

Nonlinear Goubau Line: Numerical Study of TE-polarized Waves

E. Yu. Smol'kin¹ and Yu. V. Shestopalov²

¹Penza State University, Russia

²University of Gävle, Sweden

Abstract— The propagation of monochromatic electromagnetic TE waves in the Goubau line (conducting cylinder covered by a concentric dielectric layer) filled with nonlinear inhomogeneous medium is considered. Two types of nonlinearity are studied. A physical problem is reduced to solving a nonlinear transmission eigenvalue problem for an ordinary differential equation. Eigenvalues of the problem correspond to propagation constants of the waveguide. A method is proposed for finding approximate eigenvalues of the nonlinear problem based on solving an auxiliary Cauchy problem (by the shooting method). The existence of eigenvalues that correspond to a new propagation regime is predicted. A comparison with the linear case is given.

1. INTRODUCTION

Analysis of wave propagation in open metal-dielectric waveguides constitutes an important class of vector electromagnetic problems. A conducting cylinder covered by a concentric dielectric layer, the Goubau line (GL) shown in Fig. 1 is the simplest type of such guiding structures. A complete mathematical investigation of the spectrum of symmetric surface modes in a GL is performed in [1]. Papers [2, 3] develop the theory of wave propagation in layered nonlinear dielectric waveguides. However, there are virtually no results concerning the analysis of wave propagation in a GL with an external concentric layer having variable, nonlinear, or variable and nonlinear permittivity. We aim this study to fill this gap and consider the problem of electromagnetic TE (transverse-electric) wave propagation in a GL with nonlinear inhomogeneous permittivity of the dielectric medium filling the GL layer. We consider only the intensity-dependent permittivity. The determination of TE waves is reduced to a nonlinear transmission eigenvalue problem for Maxwell's equations, which is then reduced to a system of nonlinear ordinary differential equations. Numerical experiments are carried out for two types of nonlinearities.

2. STATEMENT OF THE PROBLEM

Consider three-dimensional space \mathbb{R}^3 with a cylindrical coordinate system $O\rho\varphi z$ filled with isotropic medium with constant permittivity $\varepsilon = \varepsilon_c \varepsilon_0$, ($\varepsilon_0 > 0$ is the permittivity of free space and we assume $\mu = \mu_0$, where $\mu_0 > 0$ is magnetic permeability of vacuum). A GL with a cross-section

$$\Sigma := \{(\rho, \varphi, z) : a \leq \rho \leq b, 0 \leq \varphi < 2\pi\}$$

is placed parallel to the axis Oz (Fig. 1). We will consider TE-polarized waves in the monochromatic mode

$$\begin{aligned} \mathbf{E}e^{-i\omega t} &= e^{-i\omega t} (0, E_\varphi, 0)^T, \\ \mathbf{H}e^{-i\omega t} &= e^{-i\omega t} (H_\rho, 0, H_z)^T, \end{aligned}$$

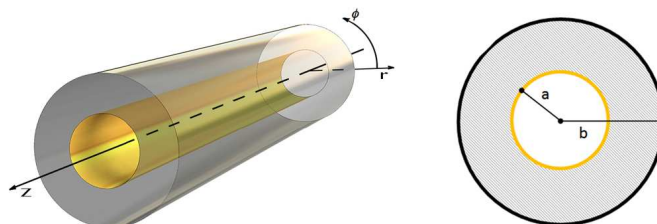


Figure 1: The Goubau line, where a and b are the radii of the internal (perfectly conducting) and external (dielectric) cylinders, respectively.

where $(\cdot)^T$ denotes the transpose operation. Each component of the field \mathbf{E} , \mathbf{H} is a function of three spatial variables. Complex amplitudes of the electromagnetic field \mathbf{E} , \mathbf{H} satisfy the Maxwell equations

$$\begin{cases} \text{rot}\mathbf{H} = -i\omega\varepsilon\mathbf{E}, \\ \text{rot}\mathbf{E} = i\omega\mu\mathbf{H}, \end{cases} \quad (1)$$

the continuity condition for the tangential components on the media interfaces (on the boundary of the waveguide) $\rho = a$, $\rho = b$ and the radiation condition at infinity: the electromagnetic field exponentially decays as $O(|\rho|^{-1})$ when $\rho \rightarrow \infty$. The solutions to the Maxwell equations are sought in the entire space. The dielectric permittivity in the whole space has the form $\varepsilon = \tilde{\varepsilon}\varepsilon_0$, where

$$\tilde{\varepsilon} = \begin{cases} \varepsilon(\rho) + \alpha f(|\mathbf{E}|^2), & a \leq \rho \leq b, \\ \varepsilon_c, & \rho > b, \end{cases} \quad (2)$$

and ε_c — positive real constant, $\varepsilon(\rho) \in C^1[R_1, R_2]$, $\varepsilon(\rho) > 0$, α is a real constants.

Remark 1. Inside the waveguide Σ quantities ε_c and $\varepsilon(\rho) + \alpha f(|\mathbf{E}|^2)$ are scalars. It is possible to consider the case where one of these quantities (or both of them) is a diagonal tensor. Such generalization will only lead to complication of formulas.

The surface waves propagating along the axis Oz of the waveguide Σ have the form

$$E_\varphi = E_\varphi(\rho)e^{i\gamma z}, \quad H_\rho = H_\rho(\rho)e^{i\gamma z}, \quad H_z = H_z(\rho)e^{i\gamma z}, \quad (3)$$

where γ is the propagation constant (spectral parameter of the problem). In what follows we often omit the arguments of functions when it does not lead to misunderstanding.

Let $k_0^2 := \omega^2\mu_0\varepsilon_0$. Substituting complex amplitude \mathbf{E} and \mathbf{H} with components (3) into equations of system (1) and introducing the notation $u(\rho) := E_\varphi(\rho)$, we obtain

$$\left(\rho^{-1}(\rho u)'\right)' + (k_0^2\tilde{\varepsilon} - \gamma^2)u = 0 \quad (4)$$

where u is a sufficiently smooth real function,

$$u \in C^1[0, +\infty) \cap C^2(0, R_1) \cap C^2(R_1, R_2) \cap C^2(R_2, +\infty). \quad (5)$$

The tangential components E_φ and H_z are continuous at the interface:

$$[u]|_{\rho=a} = [u]|_{\rho=b} = [u']|_{\rho=b} = 0, \quad (6)$$

where $[v]|_{\rho=s} = \lim_{\rho \rightarrow s-0} v(\rho) - \lim_{\rho \rightarrow s+0} v(\rho)$ is the jump of the limit values of the function at a point s defined by (5).

Formulate

Problem P_E : Find quantities $\hat{\gamma}$ such that for a given field on one of the boundaries of the waveguide, there exists a non-trivial function $u(\rho; \hat{\gamma})$ such that for $\rho \in [0, +\infty)$ $u(\rho; \hat{\gamma})$ satisfies the equation (4), transmission conditions (5), (6), and the radiation condition at infinity: functions $u(\rho; \hat{\gamma})$ exponentially decay as $\rho \rightarrow \infty$.

The quantities solving problem P_E are called eigenvalues and the corresponding $u(\rho; \hat{\gamma})$ eigenfunctions. It should be noted that an eigenvalue γ depends on the value of the eigenfunction on one of the waveguide boundaries.

3. DISPERSION EQUATION

Taking into account the radiation condition at infinity, we show that the solution and the first derivative of solution of Equation (4) in the domain $\rho > b$ have the form, respectively,

$$u(\rho) = CK_1(k\rho), \quad (7)$$

$$u'(\rho) = -Ck \left(K_0(k\rho) + \frac{K_1(k\rho)}{k\rho} \right), \quad (8)$$

where $k^2 := \gamma^2 - k_0^2\varepsilon_c$ and K_0, K_1 are the modified Bessel functions. Constant C assumed to be known. Solution (7) are real, which yields $\gamma^2 > k_0^2\varepsilon_c$.

Remark 2. *As was noted above the eigenvalues depend on the value of the field on the boundary of the waveguide; for this reason, the constant C is considered to be fixed (and known in calculations).*

Consider the Cauchy problem for

$$u'' = -\rho^{-1}u' + \rho^{-2}u - (k_0^2\varepsilon(\rho) - \gamma^2)u - \alpha f(|u|^2)u \tag{9}$$

with the initial conditions $u(b) := u(b+0)$, $u'(b) := u'(b+0)$, where the values $u(b+0)$ and $u'(b+0)$ are determined from (7) and (8).

Choosing the value of the constant $C = \frac{1}{K_1(k\rho)}$ we obtain initial conditions in the following form

$$u(b) = 1, \tag{10}$$

$$u'(b) = -k \frac{K_0(kb)}{K_1(kb)} - \frac{1}{b}. \tag{11}$$

Note that, unlike problems for linear media, in the case of nonlinear media, the propagation constants (eigenvalues) depend on the field amplitude.

To justify the solution technique, we use classical results of the theory of ordinary differential equations concerning the existence and uniqueness of the solution to the Cauchy problem and continuous dependence of the solution on parameters.

Using the transmission condition on the boundary $\rho = a$ (see (6)) and the fact that $u(a-0; \gamma) = 0$ ($\mathbf{E} = 0$ for $\rho < a$) we obtain the following dispersion equation

$$\Delta(\gamma) \equiv u(a+0; \gamma) = 0, \tag{12}$$

where $\Delta(\gamma)$ is determined explicitly and quantity $u(a+0; \gamma)$ is obtained from the solution to the Cauchy problem.

Thus, when the number $\gamma = \tilde{\gamma}$ is such that $\Delta(\gamma) = 0$, then γ is the propagation constant for problem P_E .

Remark 3. *It is known that in the linear case ($\alpha = 0$) Equation (12) has a real solution γ such that*

$$k\varepsilon_c < \gamma^2 < k \min_{\rho \in [a,b]} \varepsilon(\rho).$$

We assume that in the nonlinear case Equation (12) also has a real solution γ such that

$$k\varepsilon_c < \gamma^2 < k \min_{\rho \in [a,b]} \varepsilon(\rho) + \delta,$$

where δ is a real constant.

Equation (12) can be solved, for example, by the shooting method [9].

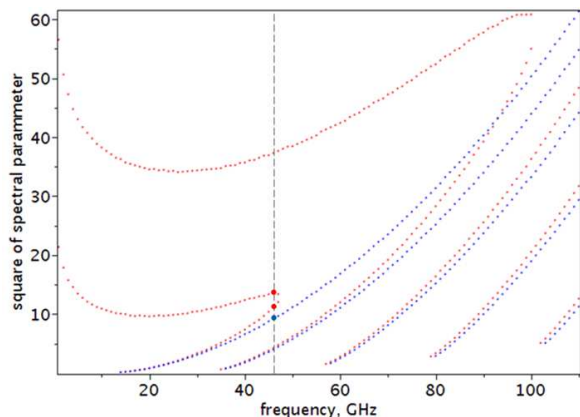


Figure 2: Red and blue curves correspond, respectively, to nonlinear ($\alpha_k = 0.25$) and linear ($\alpha_k = 0$) cases.

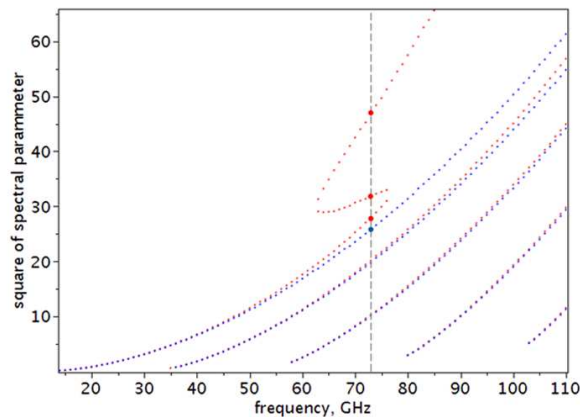


Figure 3: Red and blue curves correspond, respectively, to nonlinear ($\alpha_s = 10$, $\beta_s = 0.005$) and linear ($\alpha_s = 0$) cases.

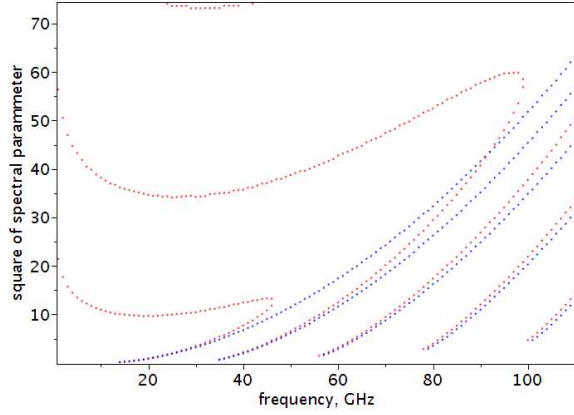


Figure 4: Red and blue curves correspond, respectively, to nonlinear ($\alpha_k = 0.25$) and linear ($\alpha_k = 0$) cases.

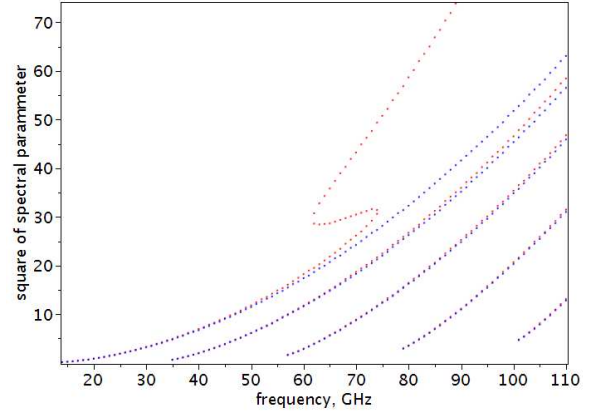


Figure 5: Red and blue curves correspond, respectively, to nonlinear ($\alpha_s = 10$, $\beta_s = 0.005$) and linear ($\alpha_s = 0$) cases.

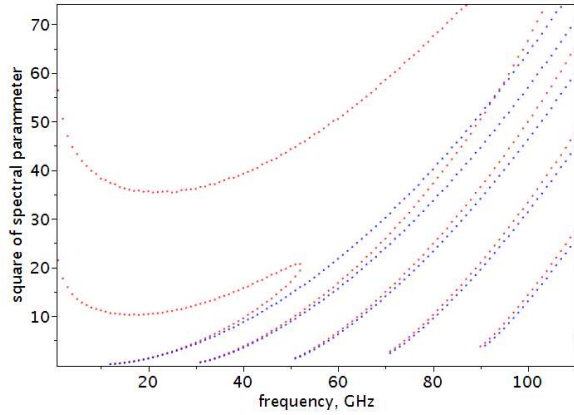


Figure 6: Red and blue curves correspond, respectively, to nonlinear ($\alpha_k = 0.25$) and linear ($\alpha_k = 0$) cases.

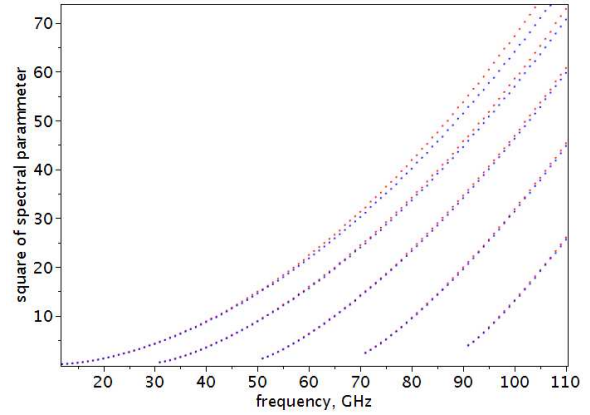


Figure 7: Red and blue curves correspond, respectively, to nonlinear ($\alpha_s = 10$, $\beta_s = 0.005$) and linear ($\alpha_s = 0$) cases.

4. NUMERICAL

Numerical experiments are carried out for two types of nonlinearities:

1. $\varepsilon = \varepsilon(\rho) + \alpha_k u^2$ (Kerr law) and
2. $\varepsilon = \varepsilon(\rho) + \alpha_s (1 - e^{-\beta_s u^2})$ (nonlinearity with saturation),

where $\varepsilon(\rho)$ is a function that specify the inhomogeneity inside GL:

1. $\varepsilon(\rho) = \varepsilon$;
2. $\varepsilon(\rho) = \varepsilon + \frac{1}{\rho}$;
3. $\varepsilon(\rho) = \varepsilon + \rho$,

where ε is a positive real constant.

In Figs. 2–7 the eigenvalues or dependence $\gamma(f)$ are shown. The following values of parameters are used in calculations: frequency $1 \text{ GHz} \leq f \leq 110 \text{ GHz}$, $\varepsilon_c = 1$ (vacuum), $\varepsilon = 12$ (silicon), $a = 2 \text{ mm}$, $b = 4 \text{ mm}$, and $\alpha_k = 0.25$ for the Kerr nonlinearity and $\alpha_s = 10$ and $\beta_s = 0.005$ for the nonlinearity with saturation.

5. CONCLUSION

The analytical approach developed in this study allows one to prove the existence of eigenvalues in the nonlinear problem that are close to eigenvalues of the corresponding linear problem.

However, as it is seen from the plots above, in the nonlinear problem, there are new eigenvalues that cannot be determined as a perturbation of eigenvalues of the linear problem. These ‘new’

eigenvalues correspond to a new (purely nonlinear) propagation regime. At the same time, the proposed numerical method enables finding all eigenvalues and proves to be efficient in the case of discrete eigenvalues. In Figures 2 and 3 the groups of eigenvalues are marked with different colors blue dots (smallest value) are eigenvalues of the linear problem (with $\alpha = 0$), and red dots are eigenvalues of the nonlinear problem. When one passes to the limit $\alpha \rightarrow 0$, the first red dot tends to the blue one, while other red dots do not tend to any eigenvalue of the linear problem when $\alpha \rightarrow 0$; these eigenvalues are ‘purely nonlinear’ and correspond to a new type of nonlinear waves.

Whether these mathematically predicted purely nonlinear waves really exist, is a hypothesis that can be proved or disproved in physical experiment.

ACKNOWLEDGMENT

The authors are grateful to Yu. G. Smirnov and D.V. Valovik for useful discussions and attention to the study.

REFERENCES

1. Shestopalov, Y., E. Kuzmina, and A. Samokhin, “On a mathematical theory of open metal-dielectric waveguides,” *FERMAT*, Vol. 5, 1–9, 2014.
2. Valovik, D. V., Y. G. Smirnov, and E. Y. Smol’kin, “Nonlinear transmission eigenvalue problem describing TE wave propagation in two-layered cylindrical dielectric waveguides,” *Computational Mathematics and Mathematical Physics*, Vol. 53, 1150–1161, 2013.
3. Valovik, D. V. and E. Y. Smol’kin, “Calculation of the propagation constants of inhomogeneous nonlinear double-layer circular cylindrical waveguide by means of the Cauchy problem method,” *Journal of Communications Technology and Electronics*, Vol. 58, 759–767, 2013.
4. Akhmediev, N. N. and A. Ankevich, *Solitons, Nonlinear Pulses and Beams*, Chapman and Hall, London, UK, 1997.
5. Smirnov, Y. G. and D. V. Valovik, *Electromagnetic Wave Propagation in Non-linear Layered Waveguide Structures*, Penza State University Press, Penza, Russia, 2011.
6. Schurmann, H. W. and V. S. Serov, Y. V. Shestopalov, “TE-polarized waves guided by a lossless nonlinear threelayer structure,” *Phys. Rev. E*, Vol. 58, No. 1, 1040–1050, 1998.
7. Smirnov, Y. G., H. W. Schurmann, and Y. V. Shestopalov, “Integral equation approach for the propagation of TE-waves in a nonlinear dielectric cylindrical waveguide,” *Journal of Nonlinear Mathematical Physics*, Vol. 11, No. 2, 256–268, 2004.
8. Schurmann, H. W., Y. G. Smirnov, and Y. V. Shestopalov, “Propagation of TE-waves in cylindrical nonlinear dielectric waveguides,” *Phys. Rev. E*, Vol. 71, No. 1, Article ID 016614, 10 Pages, 2005.
9. Smirnov, Y. G., E. Y. Smolkin, and D. V. Valovik, “Nonlinear double-layer bragg waveguide: Analytical and numerical approaches to investigate waveguiding problem,” *Advances in Numerical Analysis*, Vol. 2014, 1–11, 2014.

Unified Description of Chirped Gaussian Pulse Propagation of Arbitrary Initial Width in a Multiple Resonance Lorentz Medium

Constantinos M. Balitsis

Hellenic Telecommunications and Post Commission
60 Kifissias Avenue, Maroussi, Athens 15125, Greece

Abstract— The unified asymptotic approach yields an accurate description of chirped Gaussian pulse propagation in a causally dispersive and absorptive multiple resonance Lorentz medium, and is valid from the slowly-varying envelope to the sub-cycle pulse regimes. The dynamical evolution of the propagated field is directly related to the dynamics of the saddle points of the unified complex phase function. Accordingly, the (total) propagated field is comprised of pulse components each being due to the contribution of a respective relevant saddle point. The instantaneous oscillation frequency and the occurrence/propagation velocity of a stationary point of the envelope, of each such pulse component are intrinsically related with the dynamics of the respective relevant saddle point. Under certain conditions, a stationary point of the envelope of a pulse component occurs when the respective saddle point trajectory intersects the real frequency axis, and it travels with the group velocity at this frequency crossing value.

1. INTRODUCTION AND FORMULATION OF THE PULSE PROPAGATION PROBLEM

Research interest on ultrashort pulse-modulated signals, especially those with duration comparable to the carrier oscillation cycle, is currently increasing and extends from the RF to the XUV [1–20]. Particular emphasis is placed on the dynamical evolution of such ultrashort pulses as they propagate through, and interact with, various material media in view of their applications, among others, in optical communications, radar systems and pulse compression [1, 2, 10–13, 15–18]. Related theoretical efforts commonly invoke the slowly varying envelope approximation (SVEA) [1, 2, 4, 6–9, 11–14, 16] and are inapplicable in the sub-cycle pulse regime [1, 2, 4, 6, 8, 9, 12, 13, 16, 19]. A different stream of rigorous theoretical efforts to these pulse propagation problems employs asymptotic techniques [2–5, 8, 13, 20]. The latter efforts have elucidated the dynamical evolution of the propagated field due to rapid rise and/or fall time or exponentially varying input pulses and their accuracy has been validated upon comparison with purely numerical results.

Herein, the unified asymptotic approach is applied in order to obtain an accurate description of the dynamical evolution of the propagated field in chirped Gaussian pulse propagation of arbitrary initial width in a causal, multiple resonance Lorentz-type dielectric. The starting point is the unified, exact integral expression

$$A(z, t) = \frac{1}{2\pi} \operatorname{Re} \left\{ i \int_L \tilde{U}_U \exp \left[\frac{z}{c} \Phi_U(\omega, \theta) \right] d\omega \right\} \quad (1)$$

which describes the propagated field $A(z, t)$ in the positive z -direction of a linear, homogeneous, isotropic, temporally dispersive, non-hysteretic medium filling the semi-infinite space $z \geq 0$ (where there are no charge or current sources) and is due to an input unit-amplitude, Gaussian pulse envelope modulated chirped harmonic wave [1, 2, 7, 11, 14], whose envelope has an arbitrary initial full width $2T$ centered around $t_0 > 0$, and it modulates a harmonic wave of applied carrier frequency ω_c that is linearly chirped with a constant, arbitrary chirp parameter C . In Eq. (1), the integration contour L may be the real frequency axis, or any other homotopic to this axis contour, in the complex ω plane; hereafter, the terms $\operatorname{Re}\{\cdot\}$ and $\operatorname{Im}\{\cdot\}$ denote the real and imaginary parts, respectively, of the complex quantity inside the curly brackets. Moreover, in Eq. (1) the frequency independent unified complex spectral amplitude \tilde{U}_U is given by

$$\tilde{U}_U = \frac{2T\pi^{1/2}}{(4 + i2CT^2)^{1/2}} \exp \left[- \left(\frac{t_0^2}{T^2} + i\psi \right) \right], \quad (2)$$

and the unified complex phase $\Phi_U(\omega, \theta)$ is given by

$$\Phi_U(\omega, \theta) = \phi(\omega, \theta) - \frac{cT^2 (\omega - \omega_c - i\frac{2t_0}{T^2})^2}{z(4 + i2CT^2)}. \quad (3)$$

In Eq. (3), $\phi(\omega, \theta) = \{i\omega[n(\omega) - \theta]\}$ denotes the classical complex phase [3–5, 8, 13, 20], ψ is a constant phase term that is zero for a modulated chirped sine or $\pi/2$ for a cosine wave, $\theta = (ct)/z$ is a dimensionless space-time parameter and c is the vacuum speed of light. Throughout, the medium's refractive index $n(\omega)$ is described by the $(m + 1)$ resonance Lorentz model

$$n(\omega) = \left[1 - \sum_{j=0}^m \frac{b_{2j}^2}{\omega^2 - \omega_{2j}^2 + i2\delta_{2j}\omega} \right]^{\frac{1}{2}}, \quad (4)$$

where, for the j -th resonance, $j = 0, 1, \dots, m$, ω_{2j} is the resonance frequency, b_{2j}^2 is the square of the plasma frequency and δ_{2j} is the resonance linewidth. This causal model is often utilized [1–5, 8, 12, 13, 16] in pulse propagation problems when the field intensity is sufficiently low and the medium's nonlinearities are negligible.

2. UNIFIED ASYMPTOTIC DESCRIPTION OF CHIRPED GAUSSIAN PULSE PROPAGATION

The unified asymptotic description of the propagated field $A(z, t)$, which is obtained from an application of modern asymptotic techniques [13] on the integral expression (1), is given by

$$A(z, t) = \sum_{l=1}^n A_{Ul}(z, t), \quad n \leq 4(m + 1) + 1, \quad (5)$$

for all values of θ . Accordingly, $A(z, t)$ is composed of pulse components $A_{Ul}(z, t)$ each representing the asymptotic contribution of a respective relevant saddle point $\omega_{SP_{Ul}}(\theta)$ of $\Phi_U(\omega, \theta)$. In fact, $\Phi_U(\omega, \theta)$ has $n \leq [4(m + 1) + 1]$ saddle points which are considered to be isolated and of first-order for all values of θ .

When the first two terms in the asymptotic expansion are retained, each pulse component $A_{Ul}(z, t)$ is given by

$$A_{Ul}(z, t) = \frac{1}{2\pi} \operatorname{Re} \left\{ i \exp \left\{ \frac{z}{c} \Phi_U(\omega, \theta) \right\} \left(\frac{\pi c}{z} \right)^{\frac{1}{2}} \frac{\tilde{U}_U}{\left[-\frac{1}{2} \frac{d^2 \Phi_U(\omega, \theta)}{d\omega^2} \right]^{\frac{1}{2}}} \left[H(\omega, \theta) + O \left(z^{-\frac{5}{2}} \right) \right] \right\}_{\omega=\omega_{SP_{Ul}}(\theta)}, \quad (6)$$

where the quantity $H(\omega, \theta)$ is given by

$$H(\omega, \theta) = 1 + \left(\frac{c}{2z} \right) \left\{ \frac{\frac{15}{36} \left[\frac{d^3 \Phi_U(\omega, \theta)}{d\omega^3} \right]^2 - \frac{1}{4} \left[\frac{d^4 \Phi_U(\omega, \theta)}{d\omega^4} \right] \left[\frac{d^2 \Phi_U(\omega, \theta)}{d\omega^2} \right]}{4 \left[\frac{d^2 \Phi_U(\omega, \theta)}{d\omega^2} \right]^2 \left[-\frac{1}{2} \frac{d^2 \Phi_U(\omega, \theta)}{d\omega^2} \right]^{\frac{3}{2}}} \right\} \left[-\frac{1}{2} \frac{d^2 \Phi_U(\omega, \theta)}{d\omega^2} \right]^{\frac{1}{2}} \quad (7)$$

and is evaluated at the location of the respective relevant saddle point $\omega_{SP_{Ul}}(\theta)$, $l = 1, 2, \dots, [4(m + 1) + 1]$. From Eq. (6) it then follows that the instantaneous angular frequency of oscillation $\omega_{IFO_{Ul}}(\theta)$ of the pulse component $A_{Ul}(z, t)$ is given by

$$\omega_{IFO_{Ul}}(\theta) = \operatorname{Re} \{ \omega_{SP_{Ul}}(\theta) \} + \frac{1}{2} \frac{d}{dt} \left\{ \arg \left[\frac{d^2 \Phi_U(\omega_{SP_{Ul}}(\theta), \theta)}{d\omega^2} \right] \right\} - \frac{d}{dt} \{ \arg [H(\omega_{SP_{Ul}}(\theta), \theta)] \}. \quad (8)$$

Moreover, the envelope of $A_{Ul}(z, t)$ attains its stationary points (i.e., its local maxima and/or minima) when

$$\operatorname{Im} \{ \omega_{SP_{Ul}}(\theta) \} = \frac{d}{dt} \left\{ \ln \left[\frac{\left| -\frac{d^2 \Phi_U(\omega_{SP_{Ul}}(\theta), \theta)}{d\omega^2} \right|^{\frac{1}{2}}}{|H(\omega_{SP_{Ul}}(\theta), \theta)|} \right] \right\}. \quad (9)$$

3. DISCUSSION AND CONCLUSIONS

Hereafter, the input Gaussian pulse modulated chirped harmonic wave is chosen to have an envelope with initial width $2T = 3.891$ fs centered around $t_0 = 15$ T, and it modulates a sine wave of applied carrier frequency $\omega_c = 1.615 \times 10^{15} \text{ s}^{-1}$ which is linearly chirped with a positive chirp parameter $C^+ = 0.028 \times 10^{30} \text{ s}^{-1}$. Moreover, the dynamical evolution of the propagated field is described at a propagation distance $z = 5.0z_d$, where $z_d = 14.392 \text{ } \mu\text{m}$ is the absorption depth at ω_c , in the double resonance ($m = 1$) fluoride-type glass of Refs. [4, 8]. Notice that, ω_c is chosen to be located at the inflection point of $n_r(\omega_r)$ and the input sine wave completes a single oscillation in the unchirped case. Furthermore, for the input positive chirp case, C^+ is such that ω_c doubles over the time interval $\Delta t = 30$ T.

The dynamics of the nine saddle points in the input positive chirp case are illustrated in Fig. 1. Moreover, Figs. 2(a) and 2(b) illustrate dynamical evolution of the (total) propagated field and the angular frequency of oscillation, respectively, evaluated using both the unified asymptotic approach as well as a numerical experiment. Notice that here, only the first term of the asymptotic expansion in Eq. (6) is retained. The prediction of the numerical experiment is in close agreement with the corresponding prediction of the unified asymptotic approach, even though no optimization has been applied. The propagated field $A(z, t)$ is mainly composed of the two dominant pulse components $A_{Ul}(z, t)$ $l = 1, 2$, each being due to the asymptotic contribution of a respective relevant saddle point $\omega_{SP_{Ul}}(\theta)$ of $\Phi_U(\omega, \theta)$. The peak amplitudes of the propagated field at $\theta_{UA_{\max}}^+ = 1.381$ and at $\theta_{UB_{\max}}^+ = 1.566$ occur, approximately, when the respective saddle points $\omega_{SP_{U2}}(\theta)$ and $\omega_{SP_{U1}}(\theta)$ intersect the real frequency axis at $\theta_{stnr_{U2,1}}^+ = 1.376$ and at $\theta_{stnr_{U1,2}}^+ = 1.548$, in agreement with Eq. (9).

Moreover, $\omega_{IFO_{Ul}}(\theta)$ is given by $\text{Re}\{\omega_{SP_{Ul}}(\theta)\}$ as $\omega_{SP_{Ul}}(\theta)$ evolves with θ in the ω -plane; $\omega_{IFO_{Ul}}(\theta)$ lies in the real frequency range traversed by the $\text{Re}\{\omega_{SP_{Ul}}(\theta)\}$ as θ increases, in agreement with Eq. (8).

The unified asymptotic approach provides an accurate description of the propagated field $A(z, t)$ in chirped Gaussian pulse propagation of arbitrary initial width in a multiple ($m + 1$) resonance, causally dispersive and absorptive Lorentz-type dielectric. The propagated field is a linear superposition of pulse components $A_{Ul}(z, t)$, $l \leq [4(m + 1) + 1]$ each being due to the asymptotic

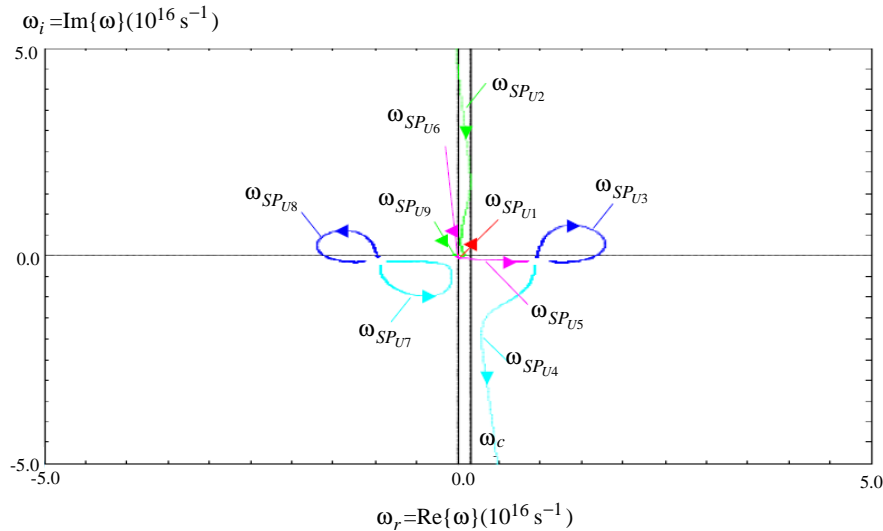


Figure 1: (Color online) dynamics of the saddle points $\omega_{SP_{Ul}}(\theta)$, $l = 1, 2, \dots, 9$, of $\Phi_U(\omega, \theta)$ in the complex ω -plane, in the positive chirp case. The arrow at each path indicates the direction of motion of the respective saddle point as θ increases in the interval $\theta \in [-5.0, 15.0]$. When a saddle point crosses the real frequency axis, its coordinates are given by: $[\theta_{stnr_{U1,1}} = 0.211; \omega_{stnr_{U1,1}} = 0.018 \times 10^{16} \text{ s}^{-1}]$ and $[\theta_{stnr_{U1,2}} = 1.548; \omega_{stnr_{U1,2}} = 0.002 \times 10^{16} \text{ s}^{-1}]$ $[\theta_{stnr_{U2,1}} = 1.376; \omega_{stnr_{U2,1}} = 0.090 \times 10^{16} \text{ s}^{-1}]$ $[\theta_{stnr_{U3,1}} = -2.786; \omega_{stnr_{U3,1}} = 0.966 \times 10^{16} \text{ s}^{-1}]$ and $[\theta_{stnr_{U3,2}} = 1.329; \omega_{stnr_{U3,2}} = 1.679 \times 10^{16} \text{ s}^{-1}]$ $[\theta_{stnr_{U8,1}} = -2.786; \omega_{stnr_{U8,1}} = -0.967 \times 10^{16} \text{ s}^{-1}]$ and $[\theta_{stnr_{U8,2}} = 1.349; \omega_{stnr_{U8,2}} = -1.613 \times 10^{16} \text{ s}^{-1}]$ $[\theta_{stnr_{U9,1}} = 0.216; \omega_{stnr_{U9,1}} = -0.018 \times 10^{16} \text{ s}^{-1}]$ and $[\theta_{stnr_{U9,2}} = 1.409; \omega_{stnr_{U9,2}} = -0.042 \times 10^{16} \text{ s}^{-1}]$.

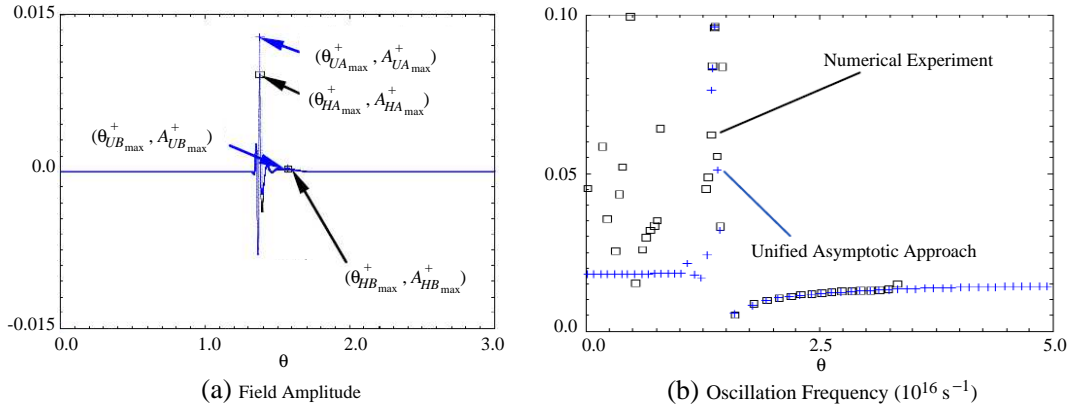


Figure 2: (Color online) (a) the propagated field in the positive chirp case. The (black) squares (' \square ') denote the (absolute) maxima ($\theta_{HA_{\max}}^+ = 1.382$, $A_{HA_{\max}}^+ = 9.314 \times 10^{-3}$) and ($\theta_{HB_{\max}}^+ = 1.575$, $A_{HB_{\max}}^+ = 0.245 \times 10^{-3}$) of the field amplitude evaluated using the numerical experiment and denoted with the solid (black) line. The (blue) crosses ('+') denote the (absolute) maxima ($\theta_{UA_{\max}}^+ = 1.381$, $A_{UA_{\max}}^+ = 12.901 \times 10^{-3}$) and ($\theta_{UB_{\max}}^+ = 1.566$, $A_{UB_{\max}}^+ = 0.309 \times 10^{-3}$) of the field amplitude $A_U(z, t) = \sum_{l=1}^{m \leq 9} A_{Ul}(z, t)$ evaluated using the unified asymptotic approach and denoted with the solid (blue) line. (b) Evolution of the instantaneous angular frequencies of oscillation for the propagated fields depicted in (a). The (black) squares (' \square ') denote the instantaneous oscillation frequency evaluated using the numerical experiment. Moreover, the instantaneous oscillation frequency evaluated using the unified asymptotic approach is denoted with the (blue) cross ('+').

contribution of a relevant saddle point $\omega_{SP_{Ul}}(\theta)$ of the unified phase $\Phi_U(\omega, \theta)$ which appears in the exact integral expression of $A(z, t)$ and is a function of both the input field and the medium parameters as well as of the propagation distance. This asymptotic approach generalizes previous findings for Gaussian pulse propagation in a single resonance Lorentz medium which is valid and accurate from the delta function limit to the SVE pulse regime [3, 5, 13]. Moreover, this asymptotic approach describes the dynamical evolution of $\omega_{IFO_{Ul}}(\theta)$ (i.e., its value range, attained maxima and/or minima and the regions of up and down chirp), identifying the spectral components of the input pulse which contribute to the dynamical evolution of $A(z, t)$. The unified asymptotic approach provides unique insight on the interaction of the pulse components $A_{Ul}(z, t)$ which lead, in the sub-cycle pulse regime, to the break-up of $A(z, t)$ (for the considered double resonance Lorentzian, into a high frequency deformed Gaussian followed by a low frequency damped oscillatory pulse structure). The insight of the unified asymptotic description is useful in applications involving chirped pulses, especially in the extremely ultrashort pulse regime.

REFERENCES

1. Agrawal, G. P., *Fiber Optic Communication Systems*, Chapter 2, John Wiley & Sons Inc., New York, 1992.
2. Akhmanov, S. A., V. A. Vysloukh, and A. S. Chirkin, *Optics of Femtosecond Laser Pulses*, Chapter 1, American Institute of Physics, New York, 1992.
3. Oughstun, K. E. and C. M. Balicstis, *Phys. Rev. Lett.*, Vol. 77, 2210–2213, 1996.
4. Oughstun, K. E. and H. Xiao, *Phys. Rev. Lett.*, Vol. 78, 642–645, 1997.
5. Balicstis, C. M. and K. E. Oughstun, *Phys. Rev. E*, Vol. 55, 1910–1921, 1997.
6. Brabec, T. and F. Krausz, *Phys. Rev. Lett.*, Vol. 78, 3282–3285, 1997.
7. Lazaridis, P., G. Debarge, and P. Gallion, *Opt. Lett.*, Vol. 22, 685–687, 1997.
8. Xiao, H. and K. E. Oughstun, *JOSA B*, Vol. 16, 1773–1785, 1999.
9. Tarasishin, A. V., S. A. Magnitskii, V. A. Shuvaev, and A. M. Zheltikov, *Opt. Express*, Vol. 8, 452–457, 2001.
10. Tsung, F. S., C. Ren, L. O. Silva, W. B. Mori, and T. Katsouleas, *Proc. Natl. Acad. Sci.*, Vol. 99, 29–32, USA, 2002.
11. Capmany, J., D. Pastor, S. Sales, and M. A. Muriel, *JOSA B*, Vol. 20, 2523–2533, 2003.
12. Agrawal, G. P., *Nonlinear Fiber Optics*, 4th Edition, Chapters 1–3, 1–77, Elsevier Inc., Orlando, Florida, 2007.

13. Oughstun, K. E., *Electromagnetic and Optical Pulse Propagation 2: Temporal Pulse Dynamics in Dispersive, Attenuative Media*, Vol. 144, Springer Series in Optical Sciences, New York, 2009.
14. Li, Q., K. Senthilnathan, K. Nakkeeran, and P. K. A. Wai, *JOSA B*, Vol. 26, 432–443, 2009.
15. Li, D., X. Lv, P. Bowlan, R. Du, S. Zeng, and Q. Luo, *Opt. Express*, Vol. 17, 17070–17081, 2009.
16. Pinhasi, Y., A. Yahalom, and G. A. Pinhasi, *JOSA B*, Vol. 26, 2404–2413, 2009.
17. Levy, E. and M. Horowitz, *Opt. Express*, Vol. 19, 17599–17608, 2011.
18. Wirth, A., et al., *Science*, Vol. 334, 195–200, 2011.
19. Cui, N. and M. A. Macovei, *New J. Phys.*, Vol. 14, 093031, 2012.
20. Balictsis, C. M., *Phys. Rev. E*, Vol. 87, 013304, 2013.

Block LU Preconditioner for the Electric Field Integral Equation

S. L. Stavtsev

INM RAS, Russian Federation

Abstract— Boundary element discretizations are used in many fields of science and engineering, for example, to solve the problem of electromagnetic scattering with electric field integral equation (EFIE). To solve the EFIE on surfaces of arbitrary shape, RWG functions are traditionally used. The matrices arising from the discretization of integral equations can be adequately approximated with low-rank matrices using the mosaic-skeleton method. However, to solve the problem of scattering with a large wave size of the object, we have to solve a large system with $n \sim 10^5$ – 10^6 . Systems of linear equations with matrices of this order are solved iteratively (GMRES). For a large wave size, the matrix is ill-conditioned and we have to use a preconditioner. In this paper, the number of iterations in the GMRES method is reduced by building a block LU preconditioner. The numerical experiments have revealed that the preconditioner makes it possible to solve the problem of electromagnetic scattering on objects with a larger wave size.

1. INTRODUCTION

The radiolocation problem is often solved using integral equations [1]. The simplest model when the given object is a perfectly conducting body is characterized by an integral equation of the electric field

$$\frac{1}{4\pi} \nabla_{\tau} \int_S \nabla_N \cdot \bar{J}(N) \frac{e^{ik|M-N|}}{|M-N|} dS_N + \frac{k^2}{4\pi} \int_S \bar{J}(N) \frac{e^{ik|M-N|}}{|M-N|} dS_N = \frac{ik}{\mu} \bar{E}_{0\tau}(M), \quad M \in S. \quad (1)$$

Equation (1) is numerically solved often by using RWG basis functions [2]. The problem is reduced to the solution of a system of linear algebraic equations with a dense matrix A . The size of this system (n) depends on the wave number k as well as on the shape and size of the surface S . The dependence on k has the form $n = \mathcal{O}(k^2)$; here, to obtain a solution of Equation (1) with an accuracy of $\varepsilon = 10^{-3}$ for an object with a typical size $a = 1$ m for $k = 100 \text{ m}^{-1}$, the system size n must be 10^4 – 10^5 .

The solution of a system with a dense matrix of size 10^4 – 10^6 requires computing systems with a large (shared or distributed) RAM or special-purpose methods for compressing the dense matrix. For example, the studies [3, 4] used the Multilevel Fast Multipole Algorithm (MLFMA) and the mosaic-skeleton method to solve electrodynamic problems.

The mosaic-skeleton method [5] is more versatile than the MLFMA and can be easily parallelized, which makes the mosaic-skeleton method suitable for both electrodynamic problems and other applications [6].

The system with a dense matrix is solved by iterative methods that use only multiplication of a matrix by a vector and ignore the explicit construction of the inverse matrix. The projective iterative methods (for example, GMRES [7]) prove to be the most efficient. The computation of the radar cross section (RCS) of a perfectly conducting object requires that Equation (1) be solved with many right-hand sides. The number of right-hand sides is determined by the number of points on the scatter diagram and reaches a few thousands.

The system with several right-hand sides is solved by a modification of GMRES that uses basis vectors of the projective subspace for all right-hand sides of the system. Of course, the system could be solved for each right-hand side or the GMRES restarts could be used. However, in this case, the system solution time increases so greatly that it becomes impossible to solve the equation for $k > 10$.

A substantial drawback of the modified GMRES method is the large amount of RAM required for storing the basis vectors. The amount of memory is proportional to the matrix dimension n and number of iterations k_i . In the GMRES method, the number of iterations k_i grows with increasing of both n and wave number k . Therefore, for large wave numbers, the solution of the system requires considerable amount of RAM. The amount of this memory is much greater than that required for storing the compressed matrix.

To reduce the number of iterations and solve Equation (1) for large wave numbers, we propose here to build a preconditioner. The authors of [8] have already proposed a preconditioner for

Equation (1) on the basis of Calderon’s formula. However, the approach proposed in [8] is suitable only for integral equations on closed surfaces. Our preconditioner can be efficiently used for both closed and open surfaces.

The papers [9, 10] also described preconditioners for compressed matrices in the \mathcal{H}^2 format. Like our preconditioner, these preconditioners contain parameters that should be chosen for a particular class of problems.

Unlike [9, 10], the preconditioner in this paper is constructed for a mosaic-skeleton rather than \mathcal{H}^2 matrix. In addition, our preconditioner is designed namely for electrodynamics problems rather than for integral equations that can be solved without preconditioners.

2. BLOCK LU PRECONDITIONER

Before constructing the preconditioner, we note that the inverse matrix that can be constructed from an LU decomposition is an ideal preconditioner. The solution of the system with a dense matrix using an LU decomposition requires $\mathcal{O}(n^3)$ operations. The solution with the help of the GMRES method requires $\mathcal{O}(n \log(n))$ operations. Nevertheless, for $n < 50000$, the system can be solved faster through an LU decomposition than using the GMRES algorithm. If the matrix is given in a compressed format, its approximate LU decomposition can be constructed in $o(n^3)$ operations. We use the approximation of L and U matrices as a preconditioner for solving the system by the iterative method.

To construct the preconditioner, we assume that the non-degenerate square matrix A corresponding to integral Equation (1) is given in the mosaic-skeleton format [5]. In other words, the matrix A is divided into blocks, some of which are represented in the skeleton format, i.e., as $A_i = V_i W_i^T$, where for a block A_i of size $p \times q$, the matrices V_i and W_i have dimensions $p \times r$ and $q \times r$, respectively. The remaining blocks are dense and can be computed explicitly. An example of matrix division into blocks is shown in Figure 1(a). The compression degree of blocks is shown by grey-scale grading: the lighter a block, the more compressed it is. It follows from the mosaic-skeleton algorithm applied to the matrix obtained from the integral equation that the diagonal blocks are dense, square, and non-degenerate.

To construct a preconditioner, we mark the nondiagonal blocks in the matrix as shown in Figure 1(b). Next, we obtain a hierarchic block construct of the decomposition factors in accordance to the formula

$$\begin{pmatrix} A_{11} & A_{12} \\ A_{21} & A_{22} \end{pmatrix} = \begin{pmatrix} L_{11} & 0 \\ L_{21} & L_{22} \end{pmatrix} \begin{pmatrix} D_1 & 0 \\ 0 & D_2 \end{pmatrix} \begin{pmatrix} U_{11} & U_{12} \\ 0 & U_{22} \end{pmatrix} \quad (2)$$

In (2), the blocks are computed in the following way:

1. $A_{11} = L_{11} D_1 U_{11}$; we compute L_{11} , D_1 , U_{11} ;
2. $A_{21} = L_{21} D_1 U_{11}$; we use the formula $L_{21} = A_{21} U_{11}^{-1} D_1^{-1}$ to find L_{21} ;
3. $A_{12} = L_{11} D_1 U_{12}$; we use the formula $U_{12} = D_1^{-1} L_{11}^{-1} A_{12}$ to find U_{12} ;
4. $A_{22} = L_{21} D_1 U_{12} + L_{22} D_2 U_{22}$; according to $L_{22} D_2 U_{22} = A_{22} - L_{21} D_1 U_{12}$ and using L_{21} and U_{12} , we find L_{22} , D_2 , U_{22} .

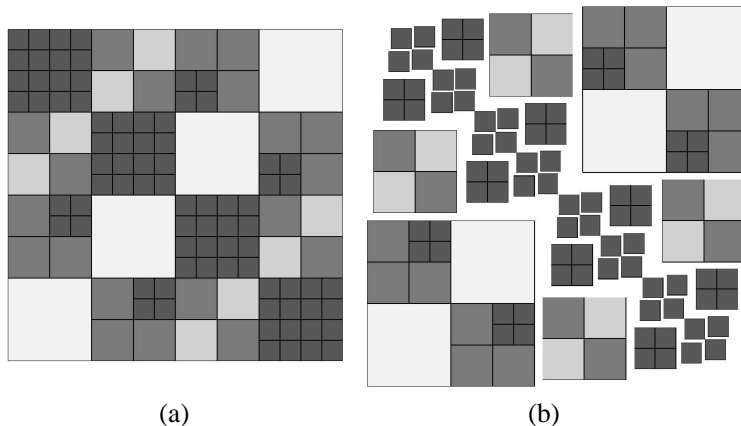


Figure 1: Mosaic division of the matrix.

In steps (2)–(4), the blocks of the matrices A , L and U are monolithic only at the initial stage. As can be seen from Figure 1(b), some parts of matrices may have a rather complex structure containing both dense and low-rank blocks. The L_{21} and U_{12} blocks cannot be computed as dense matrices because this operation is laborious and requires a considerable amount of RAM for large matrices. Therefore, the algorithm for constructing the block LU preconditioner uses the low-rank feature (i.e., the representation of original and computed blocks as VW^T).

In steps (2)–(4), as a result of the block summing operation, the ranks are summed; therefore, to ensure that the amount of data for storing the LU decomposition factors is small, the low-rank blocks are compressed up using singular value decomposition (SVD) with the truncation of a required number of lower singular numbers.

The singular numbers can be truncated using one of the following strategies:

1. fix the rank of the resulting block and assume that this rank does not exceed some value r_c ;
2. fix the approximation accuracy ε_c of the compressed block.

In each case, we obtain an additional parameter that should be chosen for the given problem, i.e., for Equation (1). The value of this parameter affects the efficiency of the preconditioner. If the value of r_c is large or the accuracy ε_c is high, the construction of the preconditioner requires considerable computational resources. This means that in this case the preconditioner requires a long time to be constructed and takes much RAM. On the other hand, a small value of r_c or low accuracy ε_c can increase the number of iterations in the relevant algorithm.

An analysis of the preconditioner shows that it is difficult to choose the parameter r_c for the integral equation. For large values of r_c , the blocks mostly become dense but the number of iterations still remains large. It is more efficient to choose the approximation accuracy ε_c of low-rank approximation blocks.

When the matrix is represented as (2), the multiplication of the preconditioner by the vector is performed by $\mathcal{O}(n \log(n))$ operations.

3. NUMERICAL RESULTS

In the calculations, we investigate the scatter diagram: the dependence of the quantity

$$\sigma = \lim_{R \rightarrow \infty} 4\pi R \frac{|\bar{E}(R)|^2}{|\bar{E}_0|^2} \tag{3}$$

on the scattering angle φ of incident wave \bar{E}_0 for different angles.

Using $\bar{J}(N)$, we can write Formula (3) as

$$\sigma = 4\pi \left| \int_S (\bar{J}(N) - \bar{k}_0(\bar{k}_0 \cdot \bar{J}(N))) k^2 e^{-ik|N|} dS_N \right|^2, \tag{4}$$

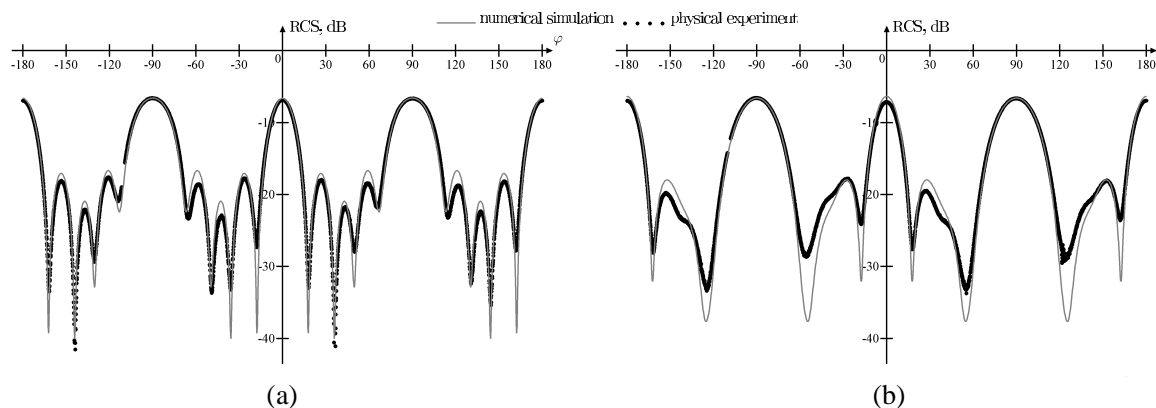


Figure 2: RCS for a cylinder with a frequency of 2 GHz ($k = 42 \text{ m}^{-1}$); the matrix dimension is $n = 21760$. (a) Horizontal polarization. (b) Vertical polarization.

where \bar{k}_0 is the unit vector of the incident wave.

We consider a circular cylinder of diameter 0.15 m and length 0.25 m.

Figures 2–4 show the comparison of RCS calculations in decibels $10 \log(\sigma/\sigma_0)$ with the results of experiments conducted by the Institute of Theoretical and Applied Electrodynamics of the Russian Academy of Sciences for two polarizations (horizontal and vertical).

It can be seen from Figure 2 that for low frequencies there is a good agreement between calculated and experimental data for both horizontal and vertical polarizations. Figures 3 and 4 show that at high frequencies the elimination of false maxima in RCS requires a much finer grid.

Table 1 gives the following data:

k is the wave number (m^{-1}),

n is the number of unknown variables in the system,

T_1 is the matrix computation time (s),

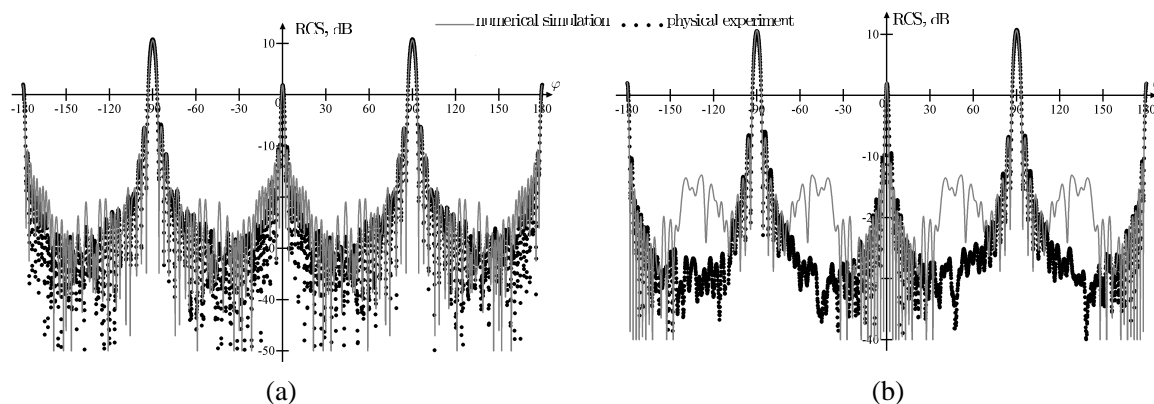


Figure 3: RCS for a cylinder with a frequency of 16 GHz ($k = 335 \text{ m}^{-1}$), the matrix dimension is $n = 21760$. (a) Horizontal polarization. (b) Vertical polarization.

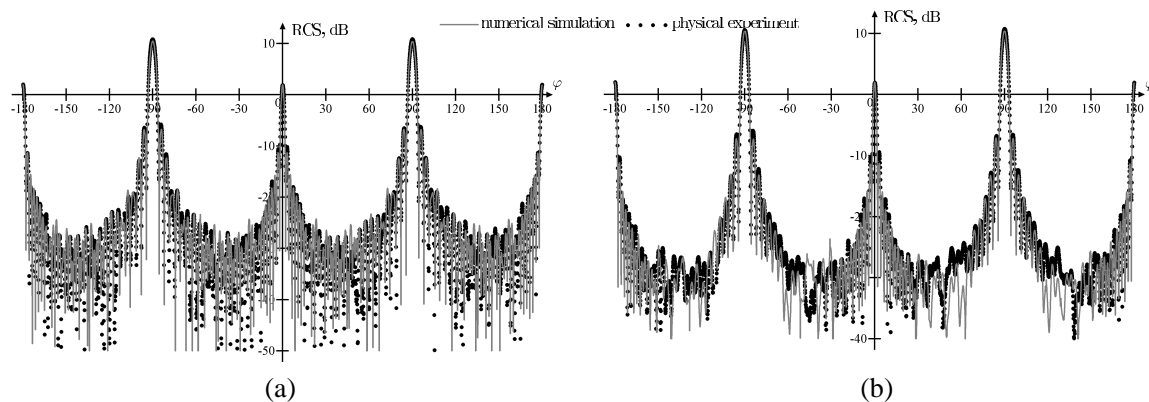


Figure 4: RCS for a cylinder with a frequency of 16 GHz ($k = 335 \text{ m}^{-1}$), the matrix dimension is $n = 192156$. (a) Horizontal polarization. (b) Vertical polarization.

Table 1: The results of calculations.

k	42	84	167	335
n	21 760	40068	90 063	192 156
T_1	1336	3981	20 013	23 376
T_2	1210	5 336	-	-
T_3	549	1 297	4 216	12 425
T_4	42	124	550	1 167
M_0	3 613	12 249	61 885	281 707
M_1	961	3 300	6 893	15 946
M_2	3 083	7 883	-	-
M_3	1 102	4 125	9 788	22 495

T_2 is the solution time without the preconditioner (s),

T_3 is the preconditioner construction time (s),

T_4 is the solution time with the preconditioner (s),

M_0 is the memory taken by the matrix without compression (Megabytes),

M_1 is the memory taken by the mosaic-skeleton matrix (Megabytes),

M_2 is the memory required for the solution of the system without the preconditioner (Megabytes),

M_3 is the memory taken by the preconditioner (Megabytes).

The calculations were conducted on a personal computer with 42 Gb of RAM for a cylinder with the parameters described above. The number of right-hand sides is 2048. The approximation accuracy and the solution accuracy were taken to be 10^{-3} . The preconditioner construction parameter ε_c was 10^{-4} .

Without the preconditioner, we managed to obtain the solution for $k = 42$ and $k = 84$. For $k = 167$ and $k = 335$, we managed to obtain the solution only with the preconditioner. Thus, the block LU preconditioner proposed in this study makes it possible to increase the solution frequency in 4 times.

ACKNOWLEDGMENT

The work was supported by the Russian Science Foundation, grant 14-11-00806.

REFERENCES

1. Colton, D. L. and R. Kress, *Integral Equation Method in Scattering Theory*, Wiley, New York, 1983.
2. Rao, S. M., D. R. Wilton, and A. W. Glisson, "Electromagnetic scattering by surfaces of arbitrary shape," *IEEE Transactions on Antennas and Propagation*, Vol. 30, No. 3, 409–418, 1982.
3. Song, J. M. and W. C. Chew, "Multilevel fast-multipole algorithm for solving combined field integral equations of electromagnetics scattering," *Microwave Opt. Tech. Lett.*, Vol. 10, No. 1, 14–19, 1995.
4. Stavtsev, S. L. and E. E. Tyrtshnikov, "Application of mosaic-skeleton approximations for solving EFIE," *PIERS Proceedings*, 1901–1904, Moscow, Aug. 18–21, 2009.
5. Tyrtshnikov, E. E., "Incomplete cross approximation in the mosaic-skeleton method," *Computing*, Vol. 64, No. 4, 367–380, 2000.
6. Stavtsev, S. L., "Application of the method of incomplete cross approximation to a non-stationary problem of vortex rings dynamics," *Russian Journal of Numerical Analysis and Mathematical Modelling*, Vol. 27, No. 3, 303–320, 2012.
7. Saad, Y. and M. H. Schultz, "GMRES: A generalized minimal residual algorithm for solving nonsymmetric linear systems," *SIAM J. Sci. Stat. Comput.*, No. 7, 856–869, 1986.
8. Guo, H., J. Hu, J. Yin, and Z. Nie, "An improved Calderon preconditioner for electric field integral equation," *Asia Pacific Microwave Conference, APMC 2009*, 92–95, 2009, Doi: 10.1109/APMC.2009.5385413.
9. Chai, W. and D. Jiao, "An LU decomposition based direct integral equation solver of linear complexity and higher-order accuracy for large-scale interconnect extraction," *IEEE Transactions on Advanced Packaging*, Vol. 33, No. 4, 794–803, 2010.
10. Bebendorf, M., "Hierarchical LU decomposition-based preconditioners for BEM," *Computing*, Vol. 74, 225–247, 2005.

Permittivity Reconstruction of a Diaphragm in a Rectangular Waveguide: Unique Solvability of Benchmark Inverse Problems

Y. Shestopalov², Y. Smirnov¹, and E. Derevyanchuk¹

¹Penza State University, Russia

²University of Gävle, Sweden

Abstract— This work is devoted to the analysis of inverse problems of permittivity reconstruction of diaphragms loaded in a rectangular waveguide including justification of the solution to a benchmark inverse problem of reconstructing permittivity of a one-sectional diaphragm. We perform comparison of theoretical and numerical results based on the measurement data to validate the efficiency of the proposed technique. The obtained solutions can be implemented in practical measurements for investigation of new artificial materials and media and can be applied in optics, nanotechnology, and design of microwave devices.

1. INTRODUCTION

Determination of electromagnetic parameters of dielectric bodies is an urgent problem for artificial materials: nanomaterials, metamaterials, and nanocomposite materials. As a rule, electromagnetic parameters of such kind of materials cannot be measured. This work is a continuation of the series of papers [1–3] devoted to the investigation of permittivity reconstruction of layered materials in the form of diaphragms (sections) in a single-mode waveguide of rectangular cross section from the transmission coefficient measured at different frequencies. The aim is the development of the mathematical technique for the analysis of the inverse problem for the case of a one- and multi-sectional diaphragms in a rectangular waveguide. We suppose that the diaphragm is made of material with real electromagnetic parameters. For this case, we obtain analytical solution of the inverse problem and the conditions providing unique solvability for the benchmark case of a one-sectional diaphragm. Based on the analytical solution we study more complicated mathematical models and present results of numerical simulation.

2. INVERSE PROBLEM

Assume that a waveguide $P = \{x : 0 < x_1 < a, 0 < x_2 < b, -\infty < x_3 < \infty\}$ with the perfectly conducting boundary surface ∂P is given in Cartesian coordinate system. A three-dimensional body Q ($Q \subset P$)

$$Q = \{x : 0 < x_1 < a, 0 < x_2 < b, 0 < x_3 < l\}$$

is placed in the waveguide; the body has the form of a diaphragm (an insert), namely, a parallelepiped separated into n sections adjacent to the waveguide walls. Domain $P \setminus \bar{Q}$ is filled with an isotropic and homogeneous layered medium having constant permeability ($\mu_0 > 0$) in whole waveguide P , the sections of the diaphragm

$$\begin{aligned} Q_0 &= \{x : 0 < x_1 < a, 0 < x_2 < b, -\infty < x_3 < 0\} \\ Q_j &= \{x : 0 < x_1 < a, 0 < x_2 < b, l_{j-1} < x_3 < l_j\}, j = 1, \dots, n \\ Q_{n+1} &= \{x : 0 < x_1 < a, 0 < x_2 < b, l < x_3 < +\infty\} \end{aligned}$$

are filled each with a medium having constant permittivity $\varepsilon_j > 0$; $l_0 := 0$, $l_n := l$.

The electromagnetic field inside and outside of the object in the waveguide is governed by Maxwells' equations:

$$\begin{aligned} \operatorname{rot} \mathbf{H} &= -i\omega \varepsilon \mathbf{E} \\ \operatorname{rot} \mathbf{E} &= i\omega \mu_0 \mathbf{H}, \end{aligned} \quad (1)$$

where \mathbf{E} and \mathbf{H} are the vectors of the electric and magnetic field intensity and ω is the circular frequency. Assume that $\pi/a < k_0 < \pi/b$, where k_0 is the wavenumber, $k_0^2 = \omega^2 \varepsilon_0 \mu_0$ [5]. In this case, only one wave H_{10} propagates in the waveguide without attenuation (we have a single-mode waveguide [5]).

The incident electrical field is

$$\mathbf{E}^0 = \mathbf{e}_2 A \sin\left(\frac{\pi x_1}{a}\right) e^{-i\gamma_0 x_3} \quad (2)$$

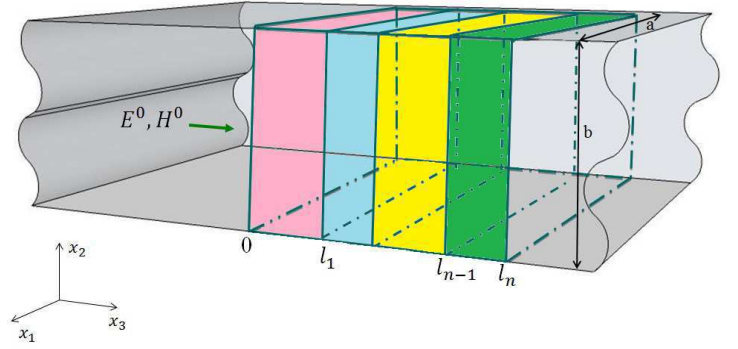


Figure 1: Multilayered diaphragms in a waveguide.

with a known A and $\gamma_0 = \sqrt{k_0^2 - \pi^2/a^2}$.

Solving the forward problem for Maxwell's equations we obtain explicit expressions for the field inside every section of diaphragm Q and outside the diaphragm:

$$E_{(0)} = \sin\left(\frac{\pi x_1}{a}\right) (Ae^{-i\gamma_0 x_3} + Be^{i\gamma_0 x_3}), \quad x \in Q_0, \quad (3)$$

$$E_{(j)} = \sin\left(\frac{\pi x_1}{a}\right) (C_j e^{-i\gamma_j x_3} + D_j e^{i\gamma_j x_3}), \quad (4)$$

$$j = 1, \dots, n+1; \quad D_{n+1} = 0, \quad x \in Q_j,$$

where $\gamma_j = \sqrt{k_j^2 - \pi^2/a^2}$ and $k_j^2 = \omega^2 \varepsilon_j \mu_0$, $\gamma_{n+1} = \gamma_0$.

From the conditions on the boundary surfaces $L := \{x_3 = 0, x_3 = l_1, \dots, x_3 = l_n\}$ of the diaphragm sections

$$[\mathbf{E}]|_L = 0; [\mathbf{H}]|_L = 0, \quad (5)$$

where square brackets $[\cdot]$ denote function jump via boundary surfaces, applied to (3) and (4) we obtain using conditions (5) a system of equations for the unknown coefficients

$$\begin{cases} A + B = C_1 + D_1 \\ \gamma_0 (B - A) = \gamma_1 (D_1 - C_1) \\ C_j e^{-i\gamma_j l_j} + D_j e^{i\gamma_j l_j} = C_{j+1} e^{-i\gamma_{j+1} l_j} + D_{j+1} e^{i\gamma_{j+1} l_j} \\ \gamma_j (D_j e^{i\gamma_j l_j} - C_j e^{-i\gamma_j l_j}) = \gamma_{j+1} (D_{j+1} e^{i\gamma_{j+1} l_j} - C_{j+1} e^{-i\gamma_{j+1} l_j}), \quad j = 1, \dots, n. \end{cases} \quad (6)$$

where $C_{n+1} = F$, $D_{n+1} = 0$. In system (6) coefficients A , B , C_j , D_j are supposed to be complex and ε_j , ($j = 1, \dots, n$) real.

Formulate the inverse problem for a multisectional diaphragm.

Inverse problem P: find (real) permittivity ε_j of each section from the known amplitude A of the incident wave and amplitude F of the transmitted wave at different frequencies.

In the case of an n -sectional diaphragm, we have [1–3] a system of n equations with n unknown permittivities

$$\operatorname{Re}(A(\omega_j)) = \operatorname{Re} \left(\frac{1}{2 \prod_{j=0}^n \gamma_j} (\gamma_n p_{n+1} + \gamma_0 q_{n+1}) F(\omega_j) e^{-i\gamma_0 l_n} \right), \quad j = 1, \dots, n, \quad (7)$$

where p and q are obtained from recurrent formulas

$$p_{j+1} = \gamma_{j-1} p_j \cos \alpha_j + \gamma_j q_j i \sin \alpha_j; \quad p_1 := 1,$$

$$q_{j+1} = \gamma_{j-1} p_j i \sin \alpha_j + \gamma_j q_j \cos \alpha_j; \quad q_1 := 1.$$

Here $\alpha_j = \gamma_j (l_j - l_{j-1})$, $j = 1, \dots, n$. Solving system (7) numerically we find permittivities ε_j ($j = 1, \dots, n$).

3. EXISTENCE AND UNIQUENESS

Consider theoretical results including the proofs of uniqueness and solvability of the inverse problems. For a one-sectional diaphragm from (7) we obtain the equation

$$\frac{F}{A} = \frac{e^{i\gamma_0 l_1}}{g(\tau)}, \quad (8)$$

$$g(\tau) = \cos(\tau) + i \left(\frac{\tau}{2\gamma_0 l_1} + \frac{\gamma_0 l_1}{2\tau} \right) \sin(\tau), \quad (9)$$

$$\tau = \gamma_1 l_1 = l_1 \sqrt{\omega^2 \varepsilon_1 \mu_0 - \frac{\pi^2}{a^2}}. \quad (10)$$

If $\varepsilon_1 > \varepsilon_0 > 0$ then

$$\tau = \gamma_1 l_1 = l_1 \sqrt{k_1^2 - \frac{\pi^2}{a^2}} > 0. \quad (11)$$

Introduce a complex variable $z = x + iy = Ae^{i\gamma_0 l_1}/F$ and separate real and imaginary parts in (8):

$$\begin{cases} x = \cos \tau \\ y = h(\tau) \sin \tau, \end{cases} \quad (12)$$

where $h(\tau) = \frac{\tau}{2\gamma_0 l_1} + \frac{\gamma_0 l_1}{2\tau}$. Equation (8) is equivalent to the system

$$\begin{cases} \cos \tau = \rho, \\ h(\tau) \sin \tau = \zeta, \end{cases} \quad (13)$$

where

$$\rho = \operatorname{Re} \left(Ae^{i\gamma_0 l_1}/F \right), \quad \zeta = \operatorname{Im} \left(Ae^{i\gamma_0 l_1}/F \right) \quad (14)$$

The following theorems justify unique solvability of the inverse problem under study.

Theorem 1 Suppose that $|\rho| < 1$ and $\rho^2 + \zeta^2 \geq 1$. Then inverse problem P has a unique solution:

$$\varepsilon_1 = \frac{1}{\omega^2 \mu_0 \varepsilon_0} \left(\left(\frac{\pi}{a} \right)^2 + \left(\frac{\tau}{l_1} \right)^2 \right), \quad (15)$$

where

$$\tau = \tau_1 = \gamma_0 l_1 \left(\frac{|\zeta| + \sqrt{\rho^2 + \zeta^2 - 1}}{\sqrt{1 - \rho^2}} \right), \quad (16)$$

if the conditions $\tau_1/\gamma_0 l_1 > 1$, $\varepsilon_1 > \varepsilon_0$, $\cos \tau_1 = \rho$, and $\operatorname{sign}(\zeta) = \operatorname{sign}(\sin \tau_1)$ are satisfied.

If $\tau_2/\gamma_0 l_1 < 1$, $\pi^2/a^2 \omega^2 \mu_0 < \varepsilon_1 < \varepsilon_0$, $\cos \tau_2 = \rho$, and $\operatorname{sign}(\zeta) = \operatorname{sign}(\sin \tau_2)$, then the inverse problem has only one solution expressed in the form

$$\tau = \tau_2 = \gamma_0 l_1 \left(\frac{\sqrt{1 - \rho^2}}{|\zeta| + \sqrt{\rho^2 + \zeta^2 - 1}} \right), \quad (17)$$

Otherwise, inverse problem P has no solution.

Remark 1. If $\rho = \pm 1$ then ζ must be equal to zero and, respectively, $\tau = 2\pi n$ or $\tau = \pi + 2\pi n$ ($n \in \mathbb{Z}$). In these cases uniqueness is violated and inverse problem P has several solutions.

Theorem 2 If

$$F = \pm Ae^{i\gamma_0 l_1}, \quad (18)$$

or

$$F = \frac{Ae^{i\gamma_0 l_1}}{g(\tau_1^*)}, \quad (19)$$

where

$$\tau_1^* = \frac{C^2}{\pi n + \sqrt{\pi^2 n^2 + C^2}}, \quad C = \gamma_0 l_1, \quad n \geq 0, \quad (20)$$

then inverse problem P has no solution in the case of a one-sectional diaphragm. If these conditions are not satisfied, then inverse problem P has a unique solution.

Proof. From (7), we have

$$g(\tau) = \frac{Ae^{i\gamma_0 l_1}}{F}$$

Suppose that $\tau \geq 0$, τ_1 and τ_2 ($\tau_2 \geq \tau_1$) exist, and $g(\tau_1) = \frac{Ae^{i\gamma_0 l_1}}{F}$ and $g(\tau_2) = \frac{Ae^{i\gamma_0 l_1}}{F}$. Then the relation $g(\tau_1) - g(\tau_2) = 0$ holds. From (8) we have that the last equality yields a system

$$\begin{cases} \cos \tau_1 - \cos \tau_2 = 0, \\ \left(\frac{\tau_1}{C} + \frac{C}{\tau_1}\right) \sin \tau_1 - \left(\frac{\tau_2}{C} + \frac{C}{\tau_2}\right) \sin \tau_2 = 0. \end{cases} \quad (21)$$

From the first equation of system (21) we obtain

$$\cos \tau_1 - \cos \tau_2 = -2 \sin \frac{\tau_1 + \tau_2}{2} \sin \frac{\tau_2 - \tau_1}{2} = 0.$$

Then $\sin \frac{\tau_1 + \tau_2}{2} = 0$, or $\sin \frac{\tau_2 - \tau_1}{2} = 0$. In the first case, we obtain

$$\begin{cases} \tau_1 = \pi m, \quad m \geq 0, \\ \tau_2 = -\pi m + 2\pi k, \end{cases}$$

and $g(\tau_1) = g(\tau_2) = (-1)^l$ which yields the proof of the first part of the theorem (relation (18)).

In the second case when $\sin \frac{\tau_2 - \tau_1}{2} = 0$, we obtain

$$\begin{cases} \tau_1^* = \frac{C^2}{\pi n + \sqrt{\pi^2 n^2 + C^2}}, \\ \tau_2 = \tau_1^* + 2\pi k, \quad n \geq 0, \end{cases}$$

and the second part of the theorem, (19) and (20), is proved.

Remark 2. Theorem 2 yields existence and uniqueness of the solution to inverse problem P when a one-sectional diaphragm is filled with a medium having real permittivity.

Statement. *In the case of a one-sectional diaphragm filled with a medium having real permittivity inverse problem P has no unique solution if only the relative amplitude $|F/A|$ is known.*

The presence of several inresction points on the graph in Fig. 2 clearly illustrates the validity of this statement.

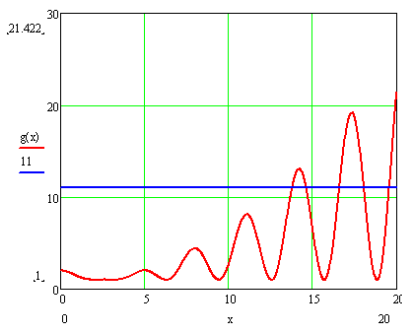


Figure 2: Graphs of functions $|g(z)|^2$. $|g(z)|^2 = \cos^2 z + \frac{1}{4} \left(\frac{z}{C} + \frac{C}{z}\right)^2 \sin^2 z$.

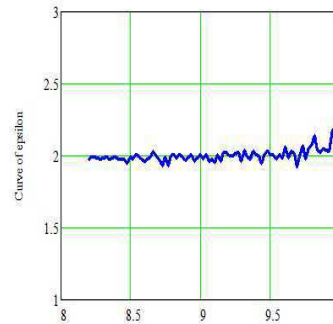


Figure 3: Real permittivity calculated from experimentally obtained values of the transmission coefficient using Equations (15) and (16), the exact value is $\varepsilon(\omega) = 2.04$, frequency range $f \in (8.2, 10)$ GHz.

4. NUMERICAL

In this section we present an example of numerical solutions to inverse problem P for a one-sectional diaphragm. Parameters of the diaphragm are $a = 2.274$ cm, $b = 1.004$ cm, and $l_1 = 1.004$ cm, and the excitation frequency $f \in (8.2, 10)$ GHz.

The permittivity was calculated on a grid of 120 (and more) frequency points taken from the indicated range using experimentally obtained values [6] of the transmission coefficient, which

explains the presence of small oscillations on the graph. We see that the average permittivity value coincides well (with accuracy less than 0.5 %) with the mean value (expectation) of the calculated data. Note that the desired permittivity value (of a homogeneous one-sectional diaphragm) can be obtained, using the developed solution to inverse problem P, from *one* (complex) value of the transmission coefficient.

5. CONCLUSION

In this work we completed theoretical justification of the solution to a benchmark inverse problem of reconstructing permittivity of a one-sectional diaphragm, proving the existence and uniqueness in the case of real permittivity. We performed comparison of results of theoretical solution to the inverse problems with the numerical data employing experimentally obtained values of the transmission coefficient, validating the efficiency of the proposed technique.

The obtained solutions can be implemented in practical measurements when new artificial materials and media are investigated by commonly used waveguide devices and analyzers.

ACKNOWLEDGMENT

This work is partially supported by the grant of the Ministry of Education and Science of Russian Federation 2.11.02.2014/K and Scholarship of the President of Russia 1311.2015.5.

REFERENCES

1. Smirnov, Yu. G., Yu. V. Shestopalov, and E. D. Derevyanchuk, “Permittivity reconstruction of layered dielectrics in a rectangular waveguide from the transmission coefficient at different frequencies,” *Inverse Problems and Large-Scale Computations, Series: Springer Proceedings in Mathematics and Statistics*, Vol. 52, No. 12, 169–181, 2013.
2. Smirnov, Yu. G., Yu. V. Shestopalov, and E. D. Derevyanchuk, “Solution to the inverse problem of reconstructing permittivity of an n-sectional diaphragm in a rectangular waveguide,” *Algebra, Geometry and Mathematical Physics, Springer Proceedings in Mathematics and Statistics*, Vol. 85, Ser. 10533-2014, 555–567, 2014.
3. Smirnov, Yu. G., Yu. V. Shestopalov, and E. D. Derevyanchuk, “Permittivity determination of multi-sectional diaphragm with metamaterial layers in rectangular waveguide,” *PIERS Proceedings*, 135–139, Taipei, Mar. 25–28, 2013.
4. Shestopalov, Y. and Y. Smirnov, “Inverse scattering in guides,” *J. of Phys.: Conf. Ser.*, Vol. 346, 2012, 012019 doi: 10.1088/1742-6596/346/1/012019.
5. Jackson, J. D., *Classical electromagnetics*, John Wiley & Sons, New York, 1967.
6. Smirnov, Yu. G., Yu. V. Shestopalov, and E. D. Derevyanchuk, “Inverse problem method for complex permittivity reconstruction of layered media in a rectangular waveguide,” *Physica Status Solidi (C) Current Topics in Solid State Physics*, Vol. 11, No. 5–6, 969–974, 2014.

The Application of Non-linear Dynamics Methods for Radar Target Identification

F. J. Rachford and T. L. Carroll
US Naval Research Laboratory, USA

Abstract— Currently radar target identification is effected by finding the downrange distribution of scatterers on a platform using high definition radar and referencing this distribution to a look-up table of measured radar returns. This method is difficult due to the rapid scintillation of the radar signal of a flying target at short wavelengths. We investigate a method of target identification in the low definition, relatively long wavelength, limit using techniques derived from the field of non-linear dynamics. In this limit the radar reflection is much less sensitive to the orientation of the target to the radar and scintillation is greatly reduced. Modern detection advances allow the digitization and processing of raw real time non-pulse compressed waveforms. We simulate the raw radar returns from several very similar small (4 to 5 wavelength) objects (i.e., cylinder, cone-cylinder, cone-ogive and double ogive) illuminated with chaotic or random modulated waveforms or a linear chirp using a commercial finite difference time domain code. In this aggressive limit we embed the target return in two dimensions using the method of delays to form an attractor. The geometric properties of the attractors are analyzed to distinguish between these similar target objects in the low definition limit. Our method selects random points on a reference attractor (or strands of points) with many Euclidean nearest neighbors and compares these with the nearest neighbor density of points (or strands) with the same time index on an attractor from an unknown target. Comparing the density of nearest neighbors at these points on two attractors allows us to calculate probabilities of correct identification. (Is the unknown signal from the reference target or from one of the other targets?) Simulation data and analyses derived from three different transmit waveforms are compared. The robustness of our target ID method is probed by the addition of white noise to the signals.

1. INTRODUCTION

In radar, a microwave wave train interacts with a complex target and is reflected to a detector. Conventional processing is used to locate the illuminated target in space ($c \times \Delta t/2$) and determine its velocity [1]. Determining the identity of the target and distinguishing one target from similar targets has proven more of a challenge [2]. Present target identification (ID) methods include using high frequency waveforms and pulse compression to find the distribution of down range locations of scatterers [3] on a complex target or studying the decay of characteristic resonant excitations [4–6]. A target is identified by matching the scatterer locations or characteristic resonances with a lookup table of measured values. The return from high frequency/high definition radar is very sensitive to target aspect and dynamic flexing leading to ambiguities in identification. Resonant ring down returns are less susceptible to aspect or dynamics of the target structure but rapidly decay and are very difficult to detect in real operational environments. Other approaches to target identification use adaptive waveform design [7–11]. In this paper we describe a method for target identification that we have recently developed [12–15] and look at its dependence on several candidate radar waveforms in the presence of Gaussian noise. To make the identification process especially challenging we choose to illuminate four very similar simple targets, Fig. 1, roughly four and a half wavelengths long by a bit more than one wavelength in diameter. We simulate the radar process using a commercial [16] finite difference time domain (FDTD) code [17].

2. WAVEFORM CONSTRUCTION

Three waveforms were constructed to illuminate the targets by concatenating one thousand individual sinusoids with varying periods. The periods of these frequency modulated CW waveforms were constrained to fall in a 400 MHz bandwidth with center frequency of 2 GHz and were selected according to three different rules: a linearly increasing frequency chirp, the output of a low dimensional chaotic map and a pseudo random number sequence. The low dimensional chaotic map used to construct the chaotically modulated wave train is described by

$$z(n+1) = 2.1z(n) \pmod{1} \quad (1)$$

the linear chirp follows $z(n+1) = z(n) + 0.001$, $z(0) = 0.001$, and the random sequence by $z(n) = \text{ran}(n)$. Each frequency modulated signal was then created from a series of concatenated sinusoids, with the frequency of the n 'th sinusoid determined by $\zeta(n) = 1.0 + \beta(z(n) - 0.5)$, where β was used to vary the modulation bandwidth. The sinusoids were matched in phase when one sinusoid ended and the other began. Mathematically, the n th sinusoid of \mathbf{s} was given by

$$s(i) = \sin(2\pi t / [600\zeta(n)]) \quad [i = 0, 1, 2, \dots, i < 600\zeta(n)] \quad (2)$$

If $\zeta(n) = 1$, then the initial period of the sinusoid was 600 points. The random waveform was generated similarly except the chaotic map was replaced by a pseudo random number generator. The chirp was generated by a linearly incremented number sequence. All waveforms were later resampled and scaled to fall within the prescribed center frequency and bandwidth for presentation to the FDTD code.

3. IDENTIFICATION METHOD

One can view the process of scattering an electromagnetic wave from a target as a filter acting on a signal. In general there is no continuous function that can reverse the effects of a filter and reconstruct the input waveform. Also there is no continuous function relating the outputs of two different filters excited by the same waveform. Since the scattering process here is deterministic, dynamical systems theory applies and can be used to calculate the probability that two received signals can be related by a function and, hence, have been scattered from the same target [18]. We emphasize we are working here with raw scattered waveforms. Simple techniques such as signal averaging can be tolerated but no matched filtering or pulse compression is applied upon detection. (Some band pass filtering is tolerable as long as it is applied equally to all signals under consideration.)

We assume that once a target of interest has been located and characterized by conventional methods that real time digitized waveforms of the return signal are available for analysis and that the waveforms can be corrected for Doppler effects by appropriate resampling. Our method proceeds by embedding the digitized normalized, non pulse compressed waveform, $s(i)$, in two dimensions by the method of delays [19–22]. We do this by constructing the set of delay vectors $\mathbf{S}(i)$:

$$\mathbf{S}(i) = [s(i), s(i + \tau)] \quad (3)$$

where the delay time τ_j is by known methods [21, 22]. The set of these vectors over time form a reconstruction (also called an embedding) of the signal in a phase space. The trajectory of these vectors carry information about the waveform interaction with the target. To discriminate between targets we look at the average Euclidean separation between nearest neighbor vectors on a reference target and compared with the average separation of the same vectors on embedded return signals from “unknown” targets. The process is initiated by selecting random points on the reference target embedding (attractor), finding their nearest neighbor points on different cycles (sufficiently separated in time) and calculating the average neighbor separation for the collection of initial seed locations. These same points and their neighbors are located in time on the “unknown” signal embedding and their average separation is recorded. In practice instead of using individual points, we use strands of 128 temporarily adjacent points in the embedding. Using strands makes the analysis less sensitive to additive noise by an effective signal averaging that takes place in the strand separation calculation. Strands also mitigate small inaccuracies in the location of reference strands in the “unknown” signal. We expect that targets that are similar to the reference target will have comparably smaller average nearest neighbor strand separations in their embedded return signals than would be the case for targets with more differing geometries. This in fact is what we find and we used this effect realize our target identification.

4. TARGETS AND SIMULATION

The four electrically small perfectly conductive targets simulated in this work are shown in Figure 1. All axially symmetric shapes have a maximum diameter of 18 cm and the *cylinder*, *double ogive* and *cone cylinder* targets are 67 cm long whereas *cone ogive* is 74 cm long. All the targets are electrically small since the waveform center frequency is 2 GHz, 15 cm. In the FDTD simulation the targets were rotated $+10^\circ$ (nose up) in elevation and the mono-static return was scanned 60° in azimuth beginning with 0° azimuth facing the elevated ends. We rotated the targets $+10^\circ$ elevation to avoid the 0° specular flash off the flat end of the cylinder. The electric polarization was in the azimuthal

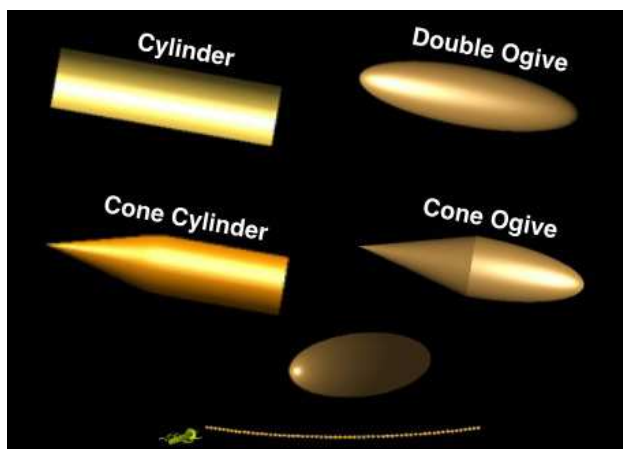


Figure 1: The four FDTD simulated shapes used in this study. All the objects simulated in this paper are 18 cm in diameter and the double ogive, cylinder and the cone ogive are all 67 cm long while the cone cylinder is 74 cm long. The objects are pitched $+10^\circ$ in elevation and are rotated in one degree increments from 0° (nose forward) to 60° in azimuth. The impinging waveform is polarized in the plane of the scan. Very similar results are seen when taking any of the other targets as reference. The best separation between target and other shape data occurs employing the chaotic waveform.

plane of the scan and data was taken at 1° intervals. 60000 FDTD time steps were executed at each degree and the back-scattered signal was low pass filtered at 3 GHz to reduce any accumulating digitizing errors.

The analysis proceeds by selecting and normalizing 50000 data points in each data set centered on the reflection from the target. The normalization was necessary since the amplitude of the return signals depends on the orientation and shape of each target. An average normalization places all signals on the same scale independent of target. Each signal is embedded in two dimensions by the method of delays with, in this case, the delay being 13 points or about a quarter of an average sinusoid cycle. One target is chosen as reference and 100 random strands are placed at random sites in the embedded data for each angle. At each test strand 5 nearest neighbor strands are located and their average separation from each original strand is noted. The average of the average nearest neighbor distances from all 100 seeded strands is then found. The embedded data from one of the four targets is then seeded with strands and positioned at the same location as the initial and nearest neighbor strand locations on the reference target. The strand separation of each of the seed strands and its associated neighbors now located in the new embedding are measured and averaged. This process is repeated for each angle and then again for each waveform. All four targets serve as reference targets in turn to complete our analysis.

The strand separation versus angle for the case of the three waveforms and four unknown targets with the cylinder data taken as the reference is shown in Figure 2. Since here the reference was the cylinder, the lowest curve corresponding to the smallest average strand separation at each angle belongs to the cylinder case (red curve noted in the legend NC for new cylinder). For the case of the chaotically modulated waveform the other three targets result in curves that are well separated from the cylinder trace. The cone cylinder (CC) and the cone ogive share (CO) the same cone on their “front” ends and their traces overlap using the cylinder reference. When using either one as reference they are well separated and distinguishable. In the case of the randomly modulated waveform the three are largely separated from the cylinder curve but are not as well separated as in the previous case. Finally for the chirp waveform, the cylinder curve and the cone cylinder and cone ogive strand separations are much closer and overlap at larger angles while only the double ogive (DO) data is well separated from the cylinder. In this case it would be difficult to distinguish the cylinder from the cone cylinder or cone ogive. In the case of the chirp similar bunching of curves is seen with the other targets taken as reference.

Addition of Gaussian Noise: To test the susceptibility of our method to noise, we add various amounts of Gaussian noise to our unknown signals. Our signals are normalized to an average amplitude of 1. The noise is added to the signal point by point at maximum amplitudes ranging from 0.01 to 10 and then the summed signal is renormalized to an average amplitude of 1. For each noise value all the calculations are rerun and at each angle a determination is made

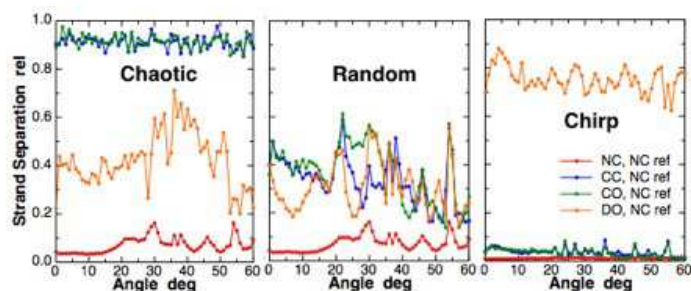


Figure 2: Three plots of strand separation versus angle for the case of the cylinder data serving as reference in the presence of zero additive noise for the cases of chaotic, random and chirp waveforms. Nearest neighbor strand locations chosen for the reference object are evaluated for data created using the each of the targets. In the legend NC = Cylinder, CC = Cone Cylinder, CO = Cone Ogive and DO = Double Ogive.

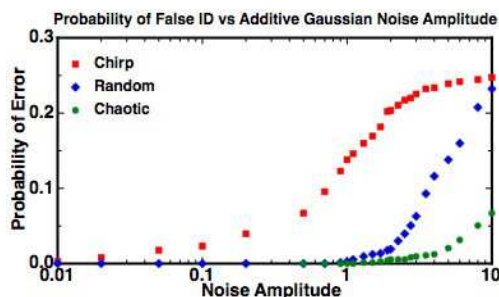


Figure 3: Probability of error in determining which of 4 shapes is present, as a function of added Gaussian noise level. Chaotic, random and chirp waveforms were reflected from the four objects. Comparisons of phase space strand separation occurred at every one degree increment between 0° and 60° in azimuth.

if the test case strand separation value is greater or less than that of the correct trace. Where the correct trace was calculated by adding the same amount of noise to the reference signal and treating it as an unknown. To calculate the probability of error in the presence of noise we log an error every time the wrong target unknown produces a strand separation less than that calculated for the correct target. The number of errors are summed and normalized to the number of trials at risk over all angles and targets and target references. The probability of error is plotted versus noise in Figure 3 for each of the three waveform types.

5. DISCUSSION

It is clear that the type of waveform modulation strongly influences the utility of our target ID technique. (See Figure 2 and Figure 3.) The chaotically modulated waveform produces a clear separation between reference and “false” target strand separation traces at zero added noise that persists as noise is added to the signal. In the case of the chirp waveform, the nearest neighbor strands tend to cluster together in time as the period of sinusoids is gradually shortened and each cluster effectively samples less of the total waveform target interaction. For random modulation the rapid variation of periods leads to blur the target interaction modulations imposed on the return waveforms. The low dimensional chaotic modulation clearly works best in this application. With the addition of noise, all the strand separations increase and separate target curves begin to overlap resulting in false identifications. For waveforms that do not produce large separations in zero noise, the addition of noise quickly causes overlapping of strand separation traces and false IDs.

We envision using this method in conjunction with conventional pulse compression to initially locate targets of interest. From time of flight and location data and the target aspect can be estimated. The target can then be queried with a low dimensional chaotic modulated waveform and the real time non-pulse compressed waveform can be detected and processed. Signal averaging and band pass filtering can reduce the noise amplitude of the raw return signal. At that point an estimate of the residual noise level can be made and a library of target of interest low noise waveforms can have noise added for comparison with the unknown signal. Finally a probability of identity should be possible in a fully deployed system assuming the availability of a library of return waveforms from a variety of targets of interest.

Clearly this method is transmission waveform dependent. Though our particular single parameter shift register chaotic map works as a waveform generator, there are probably even better waveform constructs that can do the job. It may be possible to optimize the waveform to the specific target for further assurance.

6. CONCLUSION

We have shown that using the methods of time series embedding and nearest neighbor search drawn from non-linear dynamics, we can distinguish between very similar targets sized in the few wavelength regime. This method is strongly waveform dependent. We find that a waveform assembled by the concatenation of sinusoids prescribed by a simple chaotic single parameter shift register map is superior to a simple linear chirp or random waveform. Our method is shown to be robust in the presence of added Gaussian noise in the case of the chaotic waveform.

REFERENCES

1. Knott, E. F., J. F. Shaeffer, and M. T. Tulley, *Radar Cross Section*, Artech House, Norwood, MA, 1993.
2. Rihaczek, A. W. and S. J. Hershkowitz, *Theory and Practice of Radar Target Identification*, Artech House, Norwood, MA, 2000.
3. Hu, R. and Z. Zhu, "Researches on radar target classification based on high resolution range profiles," *Proc. IEEE*, Vol. 2, 951–955, 1997.
4. Berni, A. J., "Target identification by natural resonance estimation," *IEEE Transactions on Aerospace and Electronic Systems*, Vol. 11, 147–154, Feb. 1975.
5. Baum, C. E., E. J. Rothwell, K. M. Chen, and D. P. Nyquist, "The singularity expansion method and its application to target identification," *Proc. IEEE*, Vol. 79, 1481–1491, Oct. 1991.
6. Kennaugh, E., "The K-pulse concept," *IEEE Transactions on Antennas and Propagation*, Vol. 29, 327–331, 1981.
7. Pillai, S. U., H. S. Oh, D. C. Youla, and J. R. Guerci, "Optimum Transmit & receiver design in the presence of signal-dependent interference and channel noise," *IEEE Transactions on Information Theory*, Vol. 46, No. 2, 577–584, 2000.
8. Bergin, J. S., P. M. Techau, J. E. D. Carlos, and J. R. Guerci, "Radar waveform optimization for colored noise mitigation," *2005 IEEE International Radar Conference*, 149–154, 2005.
9. Vespe, M., C. J. Baker, and H. D. Griffiths, "Automatic target recognition using multi-diversity radar," *IET Radar, Sonar & Navigation*, Vol. 1, No. 6, 470–478, 2007.
10. Carroll, T. L., "Optimizing chaos-based signals for complex radar targets," *Chaos*, Vol. 17, 033103, 2007.
11. Rachford, F. J. and T. L. Carroll, "A chaos based waveform approach to radar target identification," *PIERS Online*, Vol. 6, No. 5, 476–479, 2010.
12. Carroll, T. L. and F. J. Rachford, "Nonlinear dynamics method for target identification," *Proceedings of SPIE*, Vol. 8021, 8021L1-1–8021L1-13, 2011.
13. Carroll, T. L. and F. J. Rachford, "Using filtering effects to identify objects," *Chaos: An Interdisciplinary Journal of Nonlinear Science*, Vol. 22, 023107–023109, Feb. 2012.
14. Carroll, T. L. and F. J. Rachford, "Object identification based on filtering," *IET-RSN*, Vol. 2013, 1–6, 2013.
15. Carroll, T. L. and F. J. Rachford, "Target identification based on state space analysis," *IEEE-RADAR*, Vol. 2014, 0032–0037, 2014.
16. XFDTD, Remcom Inc., State College, PA.
17. Taflov, A. and S. C. Hagness, *Computational Electrodynamics: The Finite Difference Time Domain Method*, Artech House, Norwood, MA, 2005.
18. Pecora, L. M., T. L. Carroll, and J. F. Heagy, "Statistics for mathematical properties between time series embeddings," *Physical Review E*, Vol. 52, 3420–3439, 1995.
19. Takens, F., *Dynamical Systems and Turbulence*, Springer, Berlin, 1981.
20. Sauer, T., J. A. Yorke, and M. Casdagli, "Embedology," *Journal of Statistical Physics*, Vol. 65, 579–616, Mar.–Apr. 1991.
21. Abarbanel, H. D. I., R. Brown, J. J. Sidorowich, and L. S. Tismring, "The analysis of observed chaotic data in physical systems," *Reviews of Modern Physics*, Vol. 65, 1331–1392, Apr. 1993.
22. Pecora, L. M., L. Moniz, J. Nichols, and T. L. Carroll, "A unified approach to attractor reconstruction," *Chaos*, Vol. 17, 013110–013119, Jan. 2007.

Verification of Computational Model of Transmission Coefficients of Waveguide Filters

P. Tomasek¹ and Y. V. Shestopalov²

¹Tomas Bata University in Zlin, Czech Republic

²University of Gävle, Gävle, Sweden

Abstract— Owing to the recent research a method of estimating transmission coefficients for a waveguide of rectangular cross-section loaded with multi-layered parallel-plane dielectrics is found. Consequently, the analysis of the transmitted and reflected fields in terms of the scattering matrix formalism can be performed explicitly. This article is mainly based on comparisons between real measured and computed transmission coefficients of a waveguide filter. the computation employs analysis of closed-form solutions and numerical multi-parameter optimization. the presented waveguide filter is formed by multi-sectional diaphragms placed in a waveguide of rectangular cross-section. Comparison of the computed and measured transmission coefficients demonstrates that the difference is very low, rather marginal and thus the output of the work is considerably promising.

1. INTRODUCTION

In this work we verify a computation model aimed at direct estimation of transmission coefficients of filters created on the basis of multi-layered parallel-plane dielectric diaphragms in waveguides of rectangular cross section. Waveguide filters and their analysis, synthesis and optimization is interesting as far as alternative possibility of designing specific frequency selective filters is concerned. These filters can for example suppress a specific desired band of frequencies.

This article is mainly based on the previous research presented in [1], it enhances the theory and contains comparisons between real measured and computed transmission coefficients of a waveguide filter using a technique based on the method set forth in [2, 3]. The computation employs analysis of closed-form solutions and numerical multi-parameter optimization [4, 5]. The presented waveguide filter is formed by multi-sectional diaphragms placed in a waveguide of rectangular cross-section. the filter consists of a specific combination of diaphragms of FR4, plexi and RO4003 with defined permittivities and thicknesses.

A specific behaviour of the transmission coefficient characteristic for these structures is governed by frequency, parameters of layers, and geometry of a given filter [11].

The techniques [6, 7, 10, 13] that make use of complicated inclusions in waveguides to design FSSs and filters employ approximate numerical schemes for calculating the transmission characteristics that produce non-controllable errors in the filter design.

An approach presented in this article is virtually free from this drawback because it is based on explicit formulas for the transmission coefficient obtained and applied in [6–9] and careful investigation of its properties as a function of several complex variables (see [4]) and therefore provides more robust determination of the filter characteristics and goals. The method allows simultaneous analysis of not only narrow band-pass but also wider band-pass and band-stop filters — rectangular waveguides loaded with layered dielectric diaphragms.

2. PROBLEM STATEMENT

Assume that a single-mode waveguide [12] of rectangular cross section with a perfectly conducting boundary surface contains a body which has the form of a diaphragm, an insert separated into several sections adjacent to the waveguide walls. the waveguide is filled with an isotropic and homogeneous layered medium of constant permittivity. The sections of the diaphragm are filled each with a medium of a constant permittivity.

Solving the forward problem for Maxwell's equations we obtain explicit expressions for the field inside every section of the diaphragm and outside the diaphragm. An explicit expression for the transmission coefficient of a multi-sectional diaphragm can be obtained [1] from a system of equations related to transmission conditions on the boundary surfaces on the diaphragm sections [6–9]:

$$F = 2 \prod_{j=0}^n \gamma_j \frac{A e^{i\gamma_0 l_n}}{\gamma_n p_{n+1} + \gamma_0 q_{n+1}} \quad (1)$$

In Formula (1) the F represents the transmission coefficient, A is the amplitude of the incident wave, n is the number of sections in the diaphragm, and other quantities and symbols like γ , p , q , l are further explained in [6, 7].

If the presumptions above are correct the results of this theoretical approach and a real measurement using a calibrated measuring devices should correspond.

3. EXPERIMENTAL SETUP

The following few points describe the experiment:

- Waveguide: R100 (22.86 mm \times 10.16 mm).
- Frequency range: 8 GHz–12 GHz.
- Vector network analyzer: Rohde-Schawrz ZVB20.
- S -parameters are normed with respect to impedance (variable by frequency) TE₁₀.
- Filter consisted of the following specific combination of sections (strictly in this order, in the direction of propagation of the incident wave): RO4003, plexi glass, FR4, plexi glass, FR4, plexi glass, FR4, RO4003 (information about selected materials in more detail can be found in Table 1 below).

Table 1: Details about used materials.

<i>Material</i>	<i>Relative Permittivity</i>	<i>Thickness [mm]</i>
RO4003	3.55	1.52
Plexi glass	2.50	3.66
FR4	4.20	1.57

All important points of the experimental setup has been mentioned. Results of the measurement are presented in the next section.

4. RESULTS & COMPARISON

In this section we present and briefly analyse results of computations and output of actual measurements.

Figure 1 shows a waveguide containing a special profile loaded with sections of different material connected to a vector network analyser.

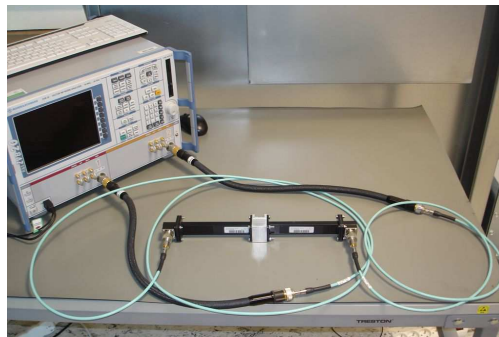


Figure 1: Photography of the experimental setup (a vector network analyser connected to the waveguide containing a profile with a multilayered diaphragm).

The output of the real measurement is presented in Figure 2 and the comparison is depicted in Figure 3.

We see that the measured and calculated data agree very well. It can be shown in addition that the observed deviation does not exceed the accuracy frames of the experimental setup and the tolerance of theoretical determination of permittivity of dielectrics.

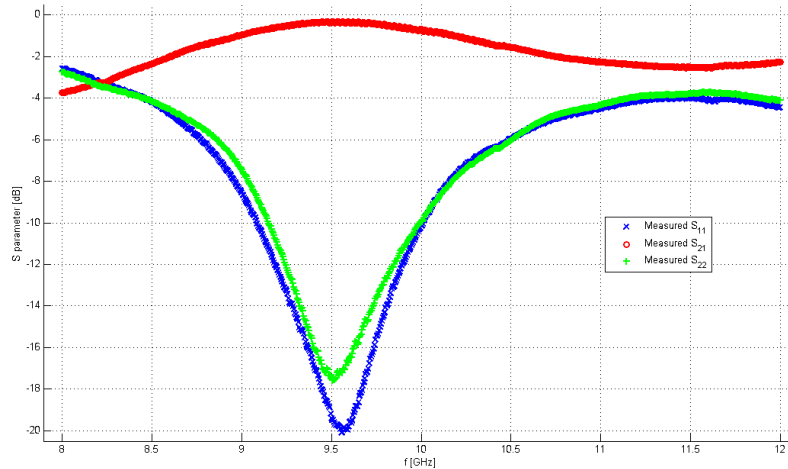


Figure 2: Results of real measurement (S_{21} , the red line, represents the transmission coefficients).

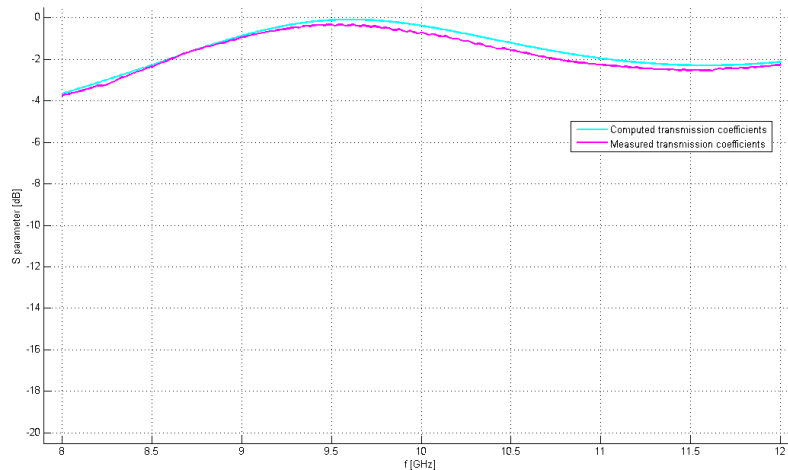


Figure 3: Transmission coefficients computed (azure colour) and measured (magenta colour).

5. CONCLUSION

Comparison of the computed and measured transmission coefficients demonstrates that the difference is very low, rather marginal and thus the output of the work is considerably promising. In this particular case the results prove the ideas, approach and the final implementation of the mathematical background used for computation of the transmission coefficients of a waveguide filter.

In further work we could aim at analysis of another more complicated filter and then estimate the relative deviation from a set of experiments.

ACKNOWLEDGMENT

This work was partially supported by Internal Grant Agency of Tomas Bata University under the project No. IGA/CebiaTech/2015/004. The work was also performed with financial support of research project NPU I No. MSMT-7778/2014 by the Ministry of Education of the Czech Republic and also by the European Regional Development Fund under the Project CEBIA-Tech No. CZ.1.05/2.1.00/03.0089.

REFERENCES

1. Tomasek, P. and Y. Shestopalov, "Parameter optimization of waveguide filters employing analysis of closed-form solution," *PIERS Proceedings*, 296–299, Stockholm, Sweden, Aug. 12–15, 2013.
2. Shestopalov, Y. and Y. Smirnov, "Inverse scattering in guides," *Journal of Physics: Conference Series*, Vol. 346, 012019, 2012.
3. Shestopalov, Y., Y. Smirnov, and E. Derevyanchuk, "Permittivity determination of multi-sectional diaphragm with metamaterial layers in rectangular waveguide," 135–139, *PIERS Proceedings*, Taipei, Mar. 25–28, 2013.
4. Chan, R., R. Mittra, and T. Cwik, "Techniques for analyzing frequency selective surfaces — A review," *Proceedings of the IEEE*, Vol. 76, No. 12, 1593–1615, 1988.
5. Antoniou, A. and W. S. Lu, *Practical Optimization: Algorithms and Engineering Applications*, Springer (India) Pvt. Limited, 2009.
6. Antoniou, A. and W. S. Lu, *Practical Optimization: Algorithms and Engineering Applications*, Springer (India) Pvt. Limited, 2009.
7. Yin, L., Z. Qian, W. Hong, X. W. Zhu, and Y. Chen, "The application of genetic algorithm in *E*-plane waveguide filter design," *Int. J. Infrared Millimeter Waves*, Vol. 21, 303–308, 2000.
8. Wu, T. K., *Frequency Selective Surfaces and Grid Arrays*, Wiley, 1995.
9. D'Errico, J., "Fminsearchbnd, fminsearchcon," File Exchange, MATLAB Central, Online: <http://www.mathworks.com/matlabcentral/fileexchange/8277-fminsearchbnd--fminsearchcon>, Feb. 6, 2012, [cit. 2015-03-23].
10. Elhawil, A., G. Koers, L. Zhang, J. Stiens, and R. Vounckx, "Comparison between two optimisation algorithms to compute the complex permittivity of dielectric multilayer structures using a free-space quasi-optical method in W-band," *IET Science, Measurement & Technology*, Vol. 3, No. 1, 13–21, Institution of Engineering and Technology, Stevenage, ROYAUME-UNI, 2009.
11. Goldsmith, P. S., "The quasi optical techniques," *Proceedings of the IEEE*, Vol. 80, 1729–1747, 1992.
12. Jackson, J. D., *Classical Electromagnetics*, Wiley, 1967.
13. Monorchioand, A., G. Manara, U. Serra, G. Marola, and E. Pagana, "Design of waveguide filters by using 21 genetically optimized frequency selective surfaces," *IEEE Microwave and Wireless Components Letters*, Vol. 15, 407–409, 2005.

Exponential Regularization of EM Dyadic Green's Functions via Green's Function-induced Dirac δ -functions

A. R. Baghai-Wadji

University of Cape Town, South Africa

Abstract— In a series of recently published contributions it was shown that singular or hyper-singular dyadic Green's functions (GFs) in computational electrostatics and electromagnetics can be utilized to construct problem-specific integral representations of the Dirac δ -function, leading to parametrized smeared out δ_η -functions, which tend to the Dirac δ -function for the parameter η approaching 0^+ . It was also shown that the constructed δ_η -functions can be employed to regularize originating GFs associated with Poisson equation in isotropic and anisotropic dielectrics. The main result of the present paper is that the constructed δ_η -function is used to regularize dyadic GFs associated with Maxwell's equations in isotropic media. The formulae arising in the formulation are all expressed in closed-form in spectral domain, allowing deep insights into the dynamics of the proposed regularization method. Complex media do not permit construction of GFs in closed form. Consequently, the integral representations for the δ_η -functions cannot be expressed in closed-form either. A recipe is proposed for numerically calculating δ_η -functions in asymptotic form. This result is claimed to present a genuine contribution to the computational physics. Applications in which near field phenomena play a role, e.g., nanoscopic and plasmonic devices will benefit from the results.

1. INTRODUCTION

Regularization problems arising in theoretical and computational field theory are fascinating and challenging at the same time; numerically, however, they may lead to catastrophically ill-conditioned results and are thus most undesirable. Singular fields, requiring regularization, have characteristic footprints in spectral domain. Electrostatic fields may possess a $1/|k|$ pole-like singularity in infrared wavenumber domain [1, 2]. Interestingly, the same $1/|k|$ functional dependence leads to slowly convergent or divergent Fourier-type integrals in ultraviolet wavenumber domain. The infrared $1/|k|$ -singularity is associated with the fields in the far-field, while the $1/|k|$ -ultraviolet slowly decaying, divergent behavior is related to the near-field in spatial domain, respectively. Singularities in electrodynamic fields manifest themselves in poles and branch points in intermediate regions in spectral domain. In computations the focus is on the regularization of slowly decaying dyadic Green's functions in spectral domain (near-field spatial domain). To this end the present author has proposed exponential — as well as algebraic regularization techniques. This paper is devoted to the exponential regularization which utilizes smeared out δ_η -functions constructed from the Green's functions themselves. (Complementary considerations in electrostatic limit have been treated in [1–5]. Static limits are illuminating and crucially important for their own right.)

2. CONVENTIONAL (SINGULAR) DYADIC GREEN'S FUNCTIONS IN 3D ELECTRODYNAMICS

Statement of the problem: Consider the dipoles $J_1 \mathbf{e}_1 \delta(x-x', y-y', z-z')$ and $J_2 \mathbf{e}_2 \delta(x-x', y-y', z-z')$ located at (x', y', z') in a medium characterized by position-independent scalar permittivity ε and permeability μ . The unit vectors in the x - and y -directions are denoted by \mathbf{e}_1 and \mathbf{e}_2 , respectively. Calculate the electric field vector $\mathbf{E}(x, y, z)$ and the magnetic field vector $\mathbf{H}(x, y, z)$, in entire (x, y, z) -space, as the response of the medium to the assumed unit dipoles.

Solution procedure: Partition (x, y, z) -space into subspaces $z > z'$ and $z < z'$ by introducing the fictitious plane $z = z'$. Find solution ansatzes for $\mathbf{E}(x, y, z)$ and $\mathbf{H}(x, y, z)$, involving *a priori* unknown coefficients, in regions $z > z'$ and $z < z'$. Satisfy Sommerfeld radiation conditions at infinity along with “interface” conditions at $z = z'$ to determine the unknown coefficients.

3. CALCULATION OF THE EIGENVALUES AND THE CORRESPONDING EIGENVECTORS

Maxwell's electrodynamic equations can be diagonalized with respect to, say, the z -coordinate, in closed form, which in spectral domain leads to a 4×4 algebraic eigenvalue equation with the

following twofold degenerate eigenvectors ([5, Ref. [17]]):

$$\begin{bmatrix} E_1(k_1, k_2) \\ E_2(k_1, k_2) \\ H_1(k_1, k_2) \\ H_2(k_1, k_2) \end{bmatrix}_{(1)}^{\pm} = \begin{bmatrix} j\omega\mu\lambda^{\pm} \\ 0 \\ k_1k_2 \\ k_2^2 - \varepsilon\mu\omega^2 \end{bmatrix}, \quad \begin{bmatrix} E_1(k_1, k_2) \\ E_2(k_1, k_2) \\ H_1(k_1, k_2) \\ H_2(k_1, k_2) \end{bmatrix}_{(2)}^{\pm} = \begin{bmatrix} 0 \\ -j\omega\mu\lambda^{\pm} \\ k_1^2 - \varepsilon\mu\omega^2 \\ k_1k_2 \end{bmatrix} \quad (1)$$

corresponding to the eigenvalues $\lambda^{\pm} = \pm\sqrt{k_1^2 + k_2^2 - \varepsilon\mu\omega^2}$. Consequently we have four linearly independent eigenvectors. It is advantageous to introduce $W(k_1, k_2)$:

$$W(k_1, k_2) = \begin{cases} \sqrt{k_1^2 + k_2^2 - \varepsilon\mu\omega^2} & \text{if } k_1^2 + k_2^2 - \varepsilon\mu\omega^2 > 0 \\ -j\sqrt{\varepsilon\mu\omega^2 - (k_1^2 + k_2^2)} & \text{if } \varepsilon\mu\omega^2 - (k_1^2 + k_2^2) > 0 \end{cases} \quad (2)$$

Since there is no danger of ambiguity same symbols are used to denote fields in spatial- and spectral domain, e.g., $E_1(x, y)$ and $E_1(k_1, k_2)$, rather than employing $E_1(x, y)$ and $\bar{E}_1(k_1, k_2)$.

Equipped with the above eigenpairs we now embark on constructing the dyadic Green's functions associated with the boundary value problem stated above, satisfying the integrability (Sommerfeld radiation) condition, and subject to the interface conditions which shall be formulated shortly.

3.1. General Field Expressions Satisfying Sommerfeld Radiation Condition

General field expressions satisfying Sommerfeld radiation condition in $z > z'$ and $z < z'$, respectively, take on the following forms:

$$\begin{bmatrix} E_1^{z>z'}(k_1, k_2) \\ E_2^{z>z'}(k_1, k_2) \\ H_1^{z>z'}(k_1, k_2) \\ H_2^{z>z'}(k_1, k_2) \end{bmatrix} = A(k_1, k_2) \begin{bmatrix} -j\omega\mu W \\ 0 \\ k_1k_2 \\ k_2^2 - \varepsilon\mu\omega^2 \end{bmatrix} e^{jk_1(x-x')} e^{jk_2(y-y')} e^{-W(z-z')} \\ + B(k_1, k_2) \begin{bmatrix} 0 \\ j\omega\mu W \\ k_1^2 - \varepsilon\mu\omega^2 \\ k_1k_2 \end{bmatrix} e^{jk_1(x-x')} e^{jk_2(y-y')} e^{-W(z-z')} \quad (3a)$$

$$\begin{bmatrix} E_1^{z<z'}(k_1, k_2) \\ E_2^{z<z'}(k_1, k_2) \\ H_1^{z<z'}(k_1, k_2) \\ H_2^{z<z'}(k_1, k_2) \end{bmatrix} = P(k_1, k_2) \begin{bmatrix} j\omega\mu W \\ 0 \\ k_1k_2 \\ k_2^2 - \varepsilon\mu\omega^2 \end{bmatrix} e^{jk_1(x-x')} e^{jk_2(y-y')} e^{W(z-z')} \\ + Q(k_1, k_2) \begin{bmatrix} 0 \\ -j\omega\mu W \\ k_1^2 - \varepsilon\mu\omega^2 \\ k_1k_2 \end{bmatrix} e^{jk_1(x-x')} e^{jk_2(y-y')} e^{W(z-z')} \quad (3b)$$

3.2. General Field Solutions at the Limits $z \rightarrow z'_+$ and $z \rightarrow z'_-$

In view of (3), and discarding the kernel $e^{jk_1(x-x')} e^{jk_2(y-y')}$, general field expressions at the limits $z \rightarrow z'_+$ and $z \rightarrow z'_-$, respectively, read:

$$\begin{bmatrix} E_1^{z>z'}(k_1, k_2) \\ E_2^{z>z'}(k_1, k_2) \\ H_1^{z>z'}(k_1, k_2) \\ H_2^{z>z'}(k_1, k_2) \end{bmatrix} = A(k_1, k_2) \begin{bmatrix} -j\omega\mu W \\ 0 \\ k_1k_2 \\ k_2^2 - \varepsilon\mu\omega^2 \end{bmatrix} + B(k_1, k_2) \begin{bmatrix} 0 \\ j\omega\mu W \\ k_1^2 - \varepsilon\mu\omega^2 \\ k_1k_2 \end{bmatrix} \quad (4a)$$

$$\begin{bmatrix} E_1^{z<z'}(k_1, k_2) \\ E_2^{z<z'}(k_1, k_2) \\ H_1^{z<z'}(k_1, k_2) \\ H_2^{z<z'}(k_1, k_2) \end{bmatrix} = P(k_1, k_2) \begin{bmatrix} j\omega\mu W \\ 0 \\ k_1k_2 \\ k_2^2 - \varepsilon\mu\omega^2 \end{bmatrix} + Q(k_1, k_2) \begin{bmatrix} 0 \\ -j\omega\mu W \\ k_1^2 - \varepsilon\mu\omega^2 \\ k_1k_2 \end{bmatrix} \quad (4b)$$

3.3. Interface Conditions (Discarding $e^{jk_1(x-x')}e^{jk_2(y-y')}$)

$$E_1^{z>z'}(k_1, k_2) - E_1^{z<z'}(k_1, k_2) = 0 \quad (5a)$$

$$E_2^{z>z'}(k_1, k_2) - E_2^{z<z'}(k_1, k_2) = 0 \quad (5b)$$

$$H_1^{z>z'}(k_1, k_2) - H_1^{z<z'}(k_1, k_2) = J_2 \quad (5c)$$

$$H_2^{z>z'}(k_1, k_2) - H_2^{z<z'}(k_1, k_2) = -J_1 \quad (5d)$$

Satisfying the interface conditions in (5) results in $P = -A$ and $Q = -B$ with:

$$A(k_1, k_2) = \frac{k_1^2 - \varepsilon\mu\omega^2}{2\varepsilon\mu\omega^2W^2}J_1 + \frac{k_1k_2}{2\varepsilon\mu\omega^2W^2}J_2 \quad (6a)$$

$$B(k_1, k_2) = -\frac{k_1k_2}{2\varepsilon\mu\omega^2W^2}J_1 - \frac{k_2^2 - \varepsilon\mu\omega^2}{2\varepsilon\mu\omega^2W^2}J_2 \quad (6b)$$

4. EXPLICIT EXPRESSIONS FOR THE GREEN'S FUNCTIONS

The Green's functions G_{E_1, J_1} and G_{E_1, J_2} : Having determined A , B , P and Q , and referring to (4) we obtain:

$$E_1^{z>z'}(k_1, k_2) = \left\{ \frac{j}{2\varepsilon\omega} \frac{k_2^2 - W^2}{W} \right\} J_1 + \left\{ \frac{j}{2\varepsilon\omega} \frac{-k_1k_2}{W} \right\} J_2 \quad (7)$$

Continuity condition, Equation (5a), dictates the equality of the expressions for $E_1^{z<z'}$ and $E_1^{z>z'}$. Thus, considering the defining equation for the Green's functions G_{E_1, J_1} and G_{E_1, J_2} ; i.e., $E_1 = \{G_{E_1, J_1}\}J_1 + \{G_{E_1, J_2}\}J_2$ we have:

$$G_{E_1, J_1}(k_1, k_2) = \frac{j}{2\varepsilon\omega} \frac{k_2^2 - W^2}{W} \quad \text{and} \quad G_{E_1, J_2}(k_1, k_2) = \frac{j}{2\varepsilon\omega} \frac{-k_1k_2}{W} \quad (8)$$

The Green's functions G_{E_2, J_1} and G_{E_2, J_2} : Similarly, from $E_2 = \{G_{E_2, J_1}\}J_1 + \{G_{E_2, J_2}\}J_2$ we obtain:

$$G_{E_2, J_1}(k_1, k_2) = \frac{j}{2\varepsilon\omega} \frac{-k_1k_2}{W} \quad \text{and} \quad G_{E_2, J_2}(k_1, k_2) = \frac{j}{2\varepsilon\omega} \frac{k_1^2 - W^2}{W} \quad (9)$$

The Green's functions G_{H_1, J_1} and G_{H_1, J_2} : Substituting for A and B into the expressions for $H_1^{z>z'}$ and $H_1^{z<z'}$ we realize that the coefficients associated with J_1 cancel out, and the coefficient of J_2 equals $\varepsilon\mu\omega^2W^2$ leading to:

$$H_1^{z>z'}(k_1, k_2) = \{0\}J_1 + \left\{ \frac{1}{2} \right\} J_2 \quad \text{and} \quad H_1^{z<z'}(k_1, k_2) = \{0\}J_1 + \left\{ -\frac{1}{2} \right\} J_2 \quad (10)$$

Introducing the sgn-function the two representations in (10) unify, resulting in:

$$H_1(k_1, k_2) = \{0\}J_1 + \left\{ \text{sgn}(z - z') \frac{1}{2} \right\} J_2 \quad (11)$$

Thus from $H_1 = \{G_{H_1, J_1}\}J_1 + \{G_{H_1, J_2}\}J_2$ we have:

$$G_{H_1, J_1}(k_1, k_2) = 0 \quad \text{and} \quad G_{H_1, J_2}(k_1, k_2) = \text{sgn}(z - z') \frac{1}{2} \quad (12)$$

The Green's functions G_{H_2, J_1} and G_{H_2, J_2} : Analogous considerations result in:

$$G_{H_2, J_1}(k_1, k_2) = -\text{sgn}(z - z') \frac{1}{2} \quad \text{and} \quad G_{H_2, J_2}(k_1, k_2) = 0 \quad (13)$$

4.1. Field Distributions $E_3(\mathbf{x}, \mathbf{x}')$ and $H_3(\mathbf{x}, \mathbf{x}')$

For the components E_3 and H_3 normal to the interface ($z = z'$)-plane we employ the relationships

$$E_3(\mathbf{x}, \mathbf{x}') = -\frac{1}{j\omega\varepsilon} (-\partial_y H_1 + \partial_x H_2) \quad \text{and} \quad H_3(\mathbf{x}, \mathbf{x}') = \frac{1}{j\omega\mu} (-\partial_y E_1 + \partial_x E_2) \quad (14)$$

or, equivalently, in spectral domain:

$$E_3(k_1, k_2) = \frac{k_2}{\omega\varepsilon} H_1(k_1, k_2) - \frac{k_1}{\omega\varepsilon} H_2(k_1, k_2) \quad \text{and} \quad H_3(k_1, k_2) = -\frac{k_2}{\omega\mu} E_1(k_1, k_2) + \frac{k_1}{\omega\mu} E_2(k_1, k_2) \quad (15)$$

The Green's functions G_{E_3, J_1} and G_{E_3, J_2} : Substitute $H_1(k_1, k_2)$ and $H_2(k_1, k_2)$ into (15) to obtain:

$$G_{E_3, J_1}(k_1, k_2) = \text{sgn}(z - z') \frac{k_1}{2\omega\varepsilon} \quad \text{and} \quad G_{E_3, J_2}(k_1, k_2) = \text{sgn}(z - z') \frac{k_2}{2\omega\varepsilon} \quad (16)$$

The Green's functions G_{H_3, J_1} and G_{H_3, J_2} : Substitute $E_1(k_1, k_2)$ and $E_2(k_1, k_2)$ into (15) to obtain:

$$G_{H_3, J_1}(k_1, k_2) = -\frac{jk_2}{2W} \quad \text{and} \quad G_{H_3, J_2}(k_1, k_2) = \frac{jk_1}{2W} \quad (17)$$

5. PROBLEM-TAILORED FIELD-INDUCED EXPRESSION FOR DIRAC δ -FUNCTION

The results obtained so far allow us gaining a deeper understanding of the properties of Green's functions which are, as we shall see momentarily, of paramount significance for numerical calculations. In this section the construction of Dirac δ -function from the associated field distribution will be pursued in terms of one example; i.e., $G_{H_2, J_1}(\mathbf{x}|\mathbf{x}')$, which is the magnetic field component in y -direction in response to a dipole oriented along the x -axis, (refer to the left equation in (13)):

$$G_{H_2, J_1}(\mathbf{x}|\mathbf{x}') = \int_{-\infty}^{\infty} \int_{-\infty}^{\infty} \frac{dk_1}{2\pi} \frac{dk_2}{2\pi} \left\{ -\text{sgn}(z - z') \frac{1}{2} \right\} e^{jk_1(x-x')} e^{jk_2(y-y')} e^{-W|z-z'|} \quad (18)$$

The term in the curly brackets is independent of the integration variables. Considering the definition of the function $\text{sgn}(z - z')$ for regions $z > z'$ and $z < z'$, respectively, we obtain:

$$G_{H_2, J_1}^{z > z'}(\mathbf{x}|\mathbf{x}') = -\frac{1}{2} \int_{-\infty}^{\infty} \int_{-\infty}^{\infty} \frac{dk_1}{2\pi} \frac{dk_2}{2\pi} e^{jk_1(x-x')} e^{jk_2(y-y')} e^{-W|z-z'|} \quad (19a)$$

$$G_{H_2, J_1}^{z < z'}(\mathbf{x}|\mathbf{x}') = \frac{1}{2} \int_{-\infty}^{\infty} \int_{-\infty}^{\infty} \frac{dk_1}{2\pi} \frac{dk_2}{2\pi} e^{jk_1(x-x')} e^{jk_2(y-y')} e^{-W|z-z'|} \quad (19b)$$

The expressions in (19a) and (19b), respectively, stand for $H_2^{z > z'}$ and $H_2^{z < z'}$ as responses to a dipole oriented along the x -axis. In view of this fact we consider the following expression:

$$\begin{aligned} & -\lim_{z \rightarrow z'_+} G_{H_2, J_1}^{z > z'}(\mathbf{x}|\mathbf{x}') + \lim_{z \rightarrow z'_-} G_{H_2, J_1}^{z < z'}(\mathbf{x}|\mathbf{x}') \\ &= \lim_{\eta \rightarrow 0^+} \frac{1}{2} \int_{-\infty}^{\infty} \int_{-\infty}^{\infty} \frac{dk_1}{2\pi} \frac{dk_2}{2\pi} e^{jk_1(x-x')} e^{jk_2(y-y')} e^{-W\eta} + \lim_{\eta \rightarrow 0^+} \frac{1}{2} \int_{-\infty}^{\infty} \int_{-\infty}^{\infty} \frac{dk_1}{2\pi} \frac{dk_2}{2\pi} e^{jk_1(x-x')} e^{jk_2(y-y')} e^{-W\eta} \\ &= \lim_{\eta \rightarrow 0^+} \int_{-\infty}^{\infty} \int_{-\infty}^{\infty} \frac{dk_1}{2\pi} \frac{dk_2}{2\pi} e^{jk_1(x-x')} e^{jk_2(y-y')} e^{-W\eta} \end{aligned} \quad (20)$$

On the other hand the interface condition for the field component H_2 reads:

$$-\lim_{z \rightarrow z'_+} G_{H_2, J_1}^{z > z'}(\mathbf{x}|\mathbf{x}') + \lim_{z \rightarrow z'_-} G_{H_2, J_1}^{z < z'}(\mathbf{x}|\mathbf{x}') = \delta(x - x', y - y') \quad (21)$$

A comparison between (20) and (21) results in:

$$\delta(x - x', y - y') = \lim_{\eta \rightarrow 0^+} \int_{-\infty}^{\infty} \int_{-\infty}^{\infty} \frac{dk_1}{2\pi} \frac{dk_2}{2\pi} e^{jk_1(x-x')} e^{jk_2(y-y')} e^{-W\eta} \quad (22)$$

Lemma: The double integrals in (22) is a valid representation for the 2D Dirac δ -function [3].

The representation in (22) enables the regularization of singular integral expressions arising in the Method of Moments (MoM) applications. The integral in (22) is well-defined for any finite value $\eta > 0$, and can be utilized for defining the “smeared out” δ -function source, $\rho_\eta(x - x', y - y')$:

$$\delta_\eta(x - x', y - y') = \int_{-\infty}^{\infty} \int_{-\infty}^{\infty} \frac{dk_1}{2\pi} \frac{dk_2}{2\pi} e^{jk_1(x-x')} e^{jk_2(y-y')} e^{-W\eta} \iff e^{-W\eta} \quad (\text{in spectral domain}) \quad (23)$$

6. EXPONENTIALLY η -REGULARIZED DYADIC GREEN'S FUNCTIONS

Rather than exciting the medium with sources $\mathbf{J}_1 = J_1 \mathbf{e}_1 \delta(x - x', y - y')$ and $\mathbf{J}_2 = J_2 \mathbf{e}_2 \delta(x - x', y - y')$, consider their corresponding field-theoretically constructed “smeared out” versions $\mathbf{J}_{1,\eta} = J_1 \mathbf{e}_1 \delta_\eta(x - x', y - y')$, and $\mathbf{J}_{2,\eta} = J_2 \mathbf{e}_2 \delta_\eta(x - x', y - y')$, respectively. Note that the support of $\mathbf{J}_{1,\eta}$ and $\mathbf{J}_{2,\eta}$ are confined to the interface. Using these problem-tailored distributed sources in the interface conditions we obtain the following exponentially η -regularized Green's functions:

$$\begin{pmatrix} G_{E_1, J_1, \eta}(\mathbf{x}|\mathbf{x}') \\ G_{E_2, J_1, \eta}(\mathbf{x}|\mathbf{x}') \\ G_{H_1, J_1, \eta}(\mathbf{x}|\mathbf{x}') \\ G_{H_1, J_1, \eta}(\mathbf{x}|\mathbf{x}') \\ G_{E_3, J_1, \eta}(\mathbf{x}|\mathbf{x}') \\ G_{H_3, J_1, \eta}(\mathbf{x}|\mathbf{x}') \end{pmatrix} = \int_{-\infty}^{\infty} \int_{-\infty}^{\infty} \frac{dk_1}{2\pi} \frac{dk_2}{2\pi} \begin{pmatrix} \frac{j}{2\varepsilon\omega} \frac{k_2^2 - W^2}{W} \\ \frac{j}{2\varepsilon\omega} \frac{-k_1 k_2}{W} \\ 0 \\ -\text{sgn}(z - z') \frac{1}{2} \\ \text{sgn}(z - z') \frac{k_1}{2\varepsilon\omega} \\ -\frac{jk_2}{2W} \end{pmatrix} e^{jk_1(x-x')} e^{jk_2(y-y')} e^{-W(|z-z'|+\eta)} \quad (24)$$

Similarly,

$$\begin{pmatrix} G_{E_1, J_2, \eta}(\mathbf{x}|\mathbf{x}') \\ G_{E_2, J_2, \eta}(\mathbf{x}|\mathbf{x}') \\ G_{H_1, J_2, \eta}(\mathbf{x}|\mathbf{x}') \\ G_{H_1, J_2, \eta}(\mathbf{x}|\mathbf{x}') \\ G_{E_3, J_2, \eta}(\mathbf{x}|\mathbf{x}') \\ G_{H_3, J_2, \eta}(\mathbf{x}|\mathbf{x}') \end{pmatrix} = \int_{-\infty}^{\infty} \int_{-\infty}^{\infty} \frac{dk_1}{2\pi} \frac{dk_2}{2\pi} \begin{pmatrix} \frac{j}{2\varepsilon\omega} \frac{-k_1 k_2}{W} \\ \frac{j}{2\varepsilon\omega} \frac{k_1^2 - W^2}{W} \\ \text{sgn}(z - z') \frac{1}{2} \\ 0 \\ \text{sgn}(z - z') \frac{k_2}{2\varepsilon\omega} \\ \frac{jk_1}{2W} \end{pmatrix} e^{jk_1(x-x')} e^{jk_2(y-y')} e^{-W(|z-z'|+\eta)} \quad (25)$$

Note that the original slowly-convergent or even divergent integrals have become regularized with a problem-specific exponential damping term. The subindex η is a reminder of this property!

7. EXPONENTIAL η -REGULARIZATION OF DYADIC GREEN'S FUNCTIONS IN COMPLEX MEDIA

Consider bi-anisotropic media characterized by material matrices $\underline{\underline{\varepsilon}}$, $\underline{\underline{\xi}}$, $\underline{\underline{\zeta}}$ and $\underline{\underline{\mu}}$, with constitutive equations $\mathbf{D} = \underline{\underline{\varepsilon}}\mathbf{E} + \underline{\underline{\xi}}\mathbf{H}$ and $\mathbf{B} = \underline{\underline{\zeta}}\mathbf{E} + \underline{\underline{\mu}}\mathbf{H}$. It can be shown that the following z -diagonalized and

(x, y) -supplementary representations are consistently equivalent with Maxwell's equations:

$$\left\{ \begin{bmatrix} \zeta_{21} & \zeta_{22} & \mu_{21} & \mu_{22} \\ -\zeta_{11} & -\zeta_{12} & -\mu_{11} & -\mu_{12} \\ -\varepsilon_{21} & -\varepsilon_{22} & -\xi_{21} & -\xi_{22} \\ \varepsilon_{11} & \varepsilon_{12} & \xi_{11} & \xi_{12} \end{bmatrix} + \begin{bmatrix} \zeta_{23} + \partial_x/j\omega & \mu_{23} \\ -\zeta_{13} + \partial_y/j\omega & -\mu_{13} \\ -\varepsilon_{23} & -\xi_{23} + \partial_x/j\omega \\ \varepsilon_{13} & \xi_{13} + \partial_y/j\omega \end{bmatrix} \begin{bmatrix} \varepsilon_{33} & \xi_{33} \\ \zeta_{33} & \mu_{33} \end{bmatrix}^{-1} \right. \\ \left. \times \begin{bmatrix} -\varepsilon_{31} & -\varepsilon_{32} & -\zeta_{31} + \partial_y/j\omega & -\zeta_{32} - \partial_x/j\omega \\ -\zeta_{31} - \partial_y/j\omega & -\zeta_{32} + \partial_x/j\omega & -\mu_{31} & -\mu_{32} \end{bmatrix} \right\} \begin{bmatrix} E_1 \\ E_2 \\ H_1 \\ H_2 \end{bmatrix} = \frac{\partial_z}{j\omega} \begin{bmatrix} E_1 \\ E_2 \\ H_1 \\ H_2 \end{bmatrix} \quad (26a)$$

$$\begin{bmatrix} E_3 \\ H_3 \end{bmatrix} = \begin{bmatrix} \varepsilon_{33} & \xi_{33} \\ \zeta_{33} & \mu_{33} \end{bmatrix}^{-1} \begin{bmatrix} -\varepsilon_{31} & -\varepsilon_{32} & -\zeta_{31} + \frac{\partial_y}{j\omega} & -\zeta_{32} - \frac{\partial_x}{j\omega} \\ -\zeta_{31} - \frac{\partial_y}{j\omega} & -\zeta_{32} + \frac{\partial_x}{j\omega} & -\mu_{31} & -\mu_{32} \end{bmatrix} \begin{bmatrix} E_1 \\ E_2 \\ H_1 \\ H_2 \end{bmatrix} \quad (26b)$$

Equation (26) in spectral domain can be used to construct asymptotic limits of the corresponding eigenpairs for $k \rightarrow 0$, and, particularly, for $k \rightarrow \infty$, to any order desired. Generally, the calculations need to be carried out numerically. The asymptotic limits of the eigenpairs allow the determination of the asymptotic limits of the Green's functions in spectral domain. Following the recipe introduced in this paper, "smeared out" parametrized δ -functions $\delta_\eta(x-x', y-y')$ can be constructed numerically. The latter functions can be employed as source functions to η -regularize Green's functions. The validity of this scheme has already been established theoretically. Current efforts concern the automatic- and symbolic implementation of the procedures involved.

8. CONCLUSIONS

A dyadic Green's functions-based smeared out δ -source function, $\delta_\eta(x-x', y-y')$ has been constructed and utilized to regularize originating Green's functions exponentially in ultraviolet region. The framework for applying the proposed method to complex media has also been provided.

ACKNOWLEDGMENT

This work is based on the research supported in part by the National Research Foundation (UID: 93114). The support provided by the University of Cape Town is greatly appreciated.

REFERENCES

1. Baghai-Wadji, A. R., "Self-consistent physics-based δ_η -regularized Green's function for 2D Poisson's equation in anisotropic dielectric media," *Proceedings of the Applied Computational Electromagnetics Society*, Jacksonville, Florida, USA, 2014.
2. Baghai-Wadji, A. R., "Self-consistent physics-based δ_η -regularized Green's function for 3D Poisson's equation in anisotropic dielectric media," *Proceedings of the Applied Computational Electromagnetics Society*, Jacksonville, Florida, USA, 2014.
3. Baghai-Wadji, A. R., "D-theorem (on regularization): Green's function-induced distributed elementary sources — First kind," *Proceedings of the IEEE Antennas and Propagation Symposium*, Memphis, Mississippi, USA, 2014.
4. Baghai-Wadji, A. R., "S-theorem (on regularization): Green's function-induced distributed elementary sources — Second kind," *Proceedings of the IEEE Antennas and Propagation Symposium*, Memphis, Mississippi, USA, 2014.
5. Baghai-Wadji, A. R., "3D electrostatic charge distribution on finitely-thick bus-bars in micro-acoustic devices: Combined regularization in the near- and far-field," *IEEE Transactions on Ultrasonics, Ferroelectrics, and Frequency Control*, Special Issue, 2015.

Superresolution Based on the Methods of Extrapolation

B. A. Lagovsky¹, A. B. Samokhin¹, and Y. V. Shestopalov²

¹Department of Applied Mathematics

Moscow State Technical University of Radio Engineering, Electronics and Automatics, Russia

²University of Gävle, Sweden

Abstract— A new method of signal processing by smart antennas is proposed and justified. It allows to improve the accuracy of angle measurement and to restore the image of the object with superresolution. The method is based on the extrapolation of the signals received by each element of the antenna array, outside the aperture. This allows introducing new virtual elements and thus synthesizing significantly larger antenna array. The method is tested in numerical experiments using a mathematical model and the maximum effective angular resolution is found for different cases and objects. Algorithms based on the method of digital aperture synthesis provide angular superresolution 3–7 times greater than that according to the Rayleigh criterion for a signal/noise ratio of 12–13 dB

1. INTRODUCTION

It is well known that to improve the quality of the target image identification we need to improve the angular resolution. Similar problems are especially important in remote sensing. The most important modern trend to improve surveillance and goniometric systems is obtaining images of objects with high angular resolution. For targets located in far zone, the angular resolution based on Rayleigh criterion is usually represented as

$$\delta\theta \cong \lambda/d, \quad (1)$$

where d is a size of antenna and λ is the wavelength. An important way to improve radar systems based on smart antennas is enhanced accuracy of angle measurements and increase in the angular resolution. In this regard, the current problem is to restore the image of the object with superresolution. This inverse problem is reduced to a Fredholm integral equation

$$U(\alpha) = \int_{\Omega} F(\alpha-\varphi)I(\varphi)d\varphi, \quad (2)$$

where $U(\alpha)$ is a signal received as a result of scanning at angle α , $\Omega = [\alpha_1, \alpha_2]$ is the angular region of location of the signal source, $I(\alpha)$ is the desired angular distribution of the reflected signal amplitude, and $F(\alpha, \varphi)$ is the radiation pattern (RP). Algebraic methods for solving problem (2) presented in [1–7] prove to be promising. They consist in representing approximate solutions in the form of finite expansions given by a sequence of functions with unknown coefficients; however it is known that this solution technique may be unstable. A new method of signal processing by smart antennas proposed in this study is based on the extrapolation of the signals received by each element of the antenna array outside the aperture.

2. PROBLEM STATEMENT

For smart antennas (SAs), a different approach to the problem is used, without direct reduction to Equation (2), which increases the stability of the algorithms. To simplify the expressions obtained we consider a large linear SA with $2N + 1$ elements. The amplitudes of the currents at the emitters assumed to be equal and the area source location Ω one-dimensional with the dimensions smaller than the width of the SA beam, $\theta_{0.5}$. Then RP is

$$F(\phi - \alpha) = \sum_{n=-N}^N \exp(ikdn(\phi - \alpha)) \quad (3)$$

where $k = 2\pi/\lambda$, d is the distance between adjacent emitters, and α is the direction of the SA maximum. Signal (2) for the formulated conditions is converted to the form

$$U(\alpha) = \sum_{n=-N}^N \exp(-ikdn\alpha) \int_{\Omega} \exp(ikdn\phi) I(\phi) d\phi = \sum_{n=-N}^N C_n \exp(-ikdn\alpha) \quad (4)$$

$$C_n = \int_{\Omega} \exp(ikdn\phi) I(\phi) d\phi, \quad n = 0, \pm 1 \dots \pm N \quad (5)$$

where coefficient C_n is a signal received by the SA element with number n . Generalization of (4) and (5), particularly to two-dimensional problems, is the case where the main difficulty is encountered. Kernel (2) in the form (3) is degenerate. It is easy to show that in this case the solution $I(\alpha)$ is expressed in terms of an expansion involving coefficients C_n as

$$I(\alpha) = A \sum_{n=-N}^N \exp(-ikdn\alpha) C_n + \Psi(\alpha), \quad (6)$$

where $\psi(\alpha)$ is an arbitrary function orthogonal to all the kernel eigenfunctions, i.e., functions from (6) on the interval $[-\lambda/d; \lambda/d]$, where A is the normalization factor. The specific form of function $\psi(\alpha)$ cannot be determined directly from the conditions of the problem and *a priori* information is required. Approximate solution, the first term in (6), repeats waveform $U(\alpha)$ and therefore permits establishing a correspondence to the Rayleigh criterion.

3. MAIN RESULTS

Consider one of the opportunities to increase angular resolution of SA. Unlike conventional phased arrays, the signals received by each transducer SA specified by C_n can be recorded in digital form and applied then in digital processing.

From (5) it follows that the difference between the values of C_n , $n = 1, 2, \dots$ are determined only by the spatial position of the individual SA emitters. Therefore, by analyzing the location of a large number of emitters and the values of the corresponding coefficients C_n , we can find a dependence, with a certain accuracy, of the received signal C_j on the coordinates of the radiator. The solution of this problem allows one to estimate the value of the received signal outside the SA aperture. Next, using the predicted values C_j , $j = \pm(N+1) \dots \pm M$ together with previously measured values C_j , $j = -N, -N+1, \dots, +N$, one can extend the summation in (3) to $2M+1$ terms. In the end we obtain a virtual RP with $2M+1$ emitters having the aperture increased in M/N times and the beam width $\theta_{0.5}$ decreased by the same order of magnitude, so that the angle accuracy and angular resolution increases correspondingly. As a result, the restored with superresolution approximate image of the object is represented as

$$I(\alpha) \cong \sum_{n=-N}^N \exp(-ikdn\alpha) C_n, \quad (7)$$

Thus, approximate solution (2)–(4) is reduced to the determination of values of the maximum possible number of complex coefficients C outside the SA aperture.

Estimation of the coefficients C for virtual SA items (i.e., outside the actual aperture) can be performed using extrapolation (linear, polynomial, spline, and so on) with different indicators of computational complexity and performance. Specialized numerical methods make it possible to carry out more effectively prediction of the behavior of diverse forms of dependence than using, e.g., polynomials. Preliminary studies show that the dependence of the values of coefficients C on the distance to the center of SA is characterized as a whole, regardless of source, as a non-periodic oscillating smooth curve. Such a firmly established regularity responds well to extrapolation using linear Berg prediction and with relatively small error if the dependence is almost periodic or oscillating. With a sufficiently large number of initial points the technique can be used successfully for a much greater distance from the target area compared with polynomial or spline extrapolation. In the algorithm based on the Berg method and developed in this work, a polynomial regression builds on the initial data which reduces the effect of random errors in the specification of initial values of C on the results of extrapolation.

Example 1. Point source. In many respects the quality of extrapolation, in particular, the size range outside the predetermined interval in which the extrapolated signal does not exceed the admissible error is determined by the signal type, more precisely, its angular size. For a point source all the coefficients C , as follows from (2), are

$$C_n = A \exp(ikdn\alpha_0), \quad n = \pm(N+1) \dots \pm \infty, \quad (8)$$

where α_0 is the angular position of the source and A is the amplitude coefficient. The values of α_0 can be found for each n from the expression

$$C_n + C_{-n} = 2A \cos(kdn\alpha_0), \quad n = 1, 2 \dots N. \quad (9)$$

Remark. It should be noted that an α_0 determines the source location and one cannot perform further synthesis of the aperture, at least for large signal/noise ratio (SNR) at each SA element. If the presence of random component becomes visible, a preference should be given to the digital processing algorithm based on aperture synthesis. A parameter extrapolation method searches for expression describing an experimental dependence C_j , $j \in [-N, N]$, taking into account the fact that the results are obtained with certain random error.

Example 2. Of practical interest is the problem of obtaining superresolution radar observations at two closely spaced point objects. In this case, assuming a predetermined target information in the form of two point objects it is useful to number aggregate signals received by SA symmetric elements using indices n and $-n$:

$$\begin{aligned} C_n + C_{-n} &= 2A_1 \cos(kdn\alpha_1) + 2A_2 \cos(kdn\alpha_2), \quad n = 1, 2 \dots N \\ c_0 &= A_1 + A_2 \end{aligned}, \quad (10)$$

where $\alpha_{1,2}$ and $A_{1,2}$ are unknown angular coordinates of the objects and the amplitudes of the received signals. The resulting system of $N+1$ nonlinear equation with unknown $\alpha_{1,2}$ and $A_{1,2}$ is overdetermined. Its solutions must be sought in the form of a minimum amount of the standard deviation of the left and right sides, reducing thus the effect of noise and random noise. Note that the remark made above applies here even to a greater extent because numerical solution of system (1) yields additional errors.

4. SIMULATION RESULTS

Characteristics of increasing angular resolution and its limits were investigated using a mathematical model. Considered RP were formed by flat equidistant SA with 31×31 elements. At the first stage the quality of extrapolation coefficients C were analyzed.

The results of image reconstruction of two identical point sources are shown in Figure 1. The algorithm is allowed to calculate with minor error the values of coefficients C for a synthetic SA, the size of which is ten times greater than the size of the original SA. Figure 2 shows the solutions found with a low level of noise.

It is known that inverse problems are very sensitive to the presence of errors in the original data. Therefore, in addition to estimating the degree of excess of the Rayleigh criterion, an important

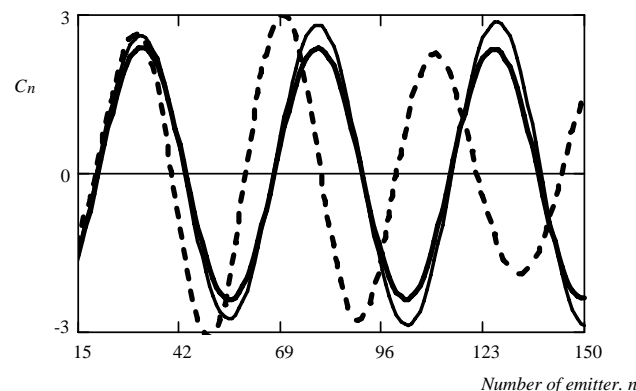


Figure 1: The values of the real part of C_n outside the aperture: the bold solid line — the true values, dashed — extrapolation using splines, and thin solid — Berg extrapolation.

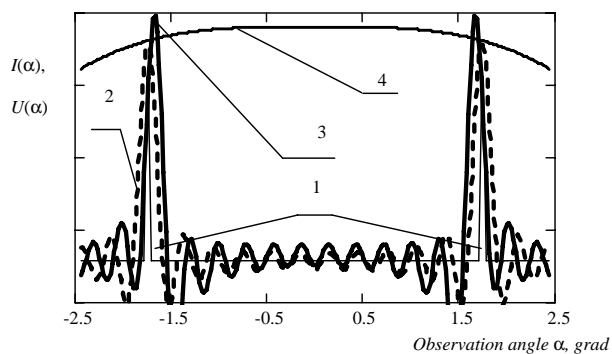


Figure 2: Results of image reconstruction of signal sources. 1 — intensity distribution of the true source; dashed 2 — signal received from the real SA; bold 3 — signal obtained on the basis of synthesis SA; 4 — real signal $U(\alpha)$.

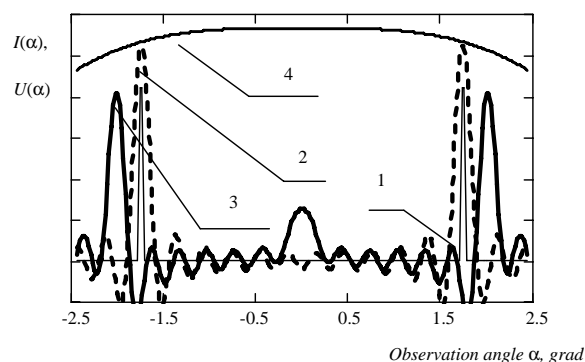


Figure 3: Results of image reconstruction at $q = 14$ dB. 1 — intensity distribution of the true source; 2 — signal received from the real SA with 300 elements; 3 — the signal obtained by synthesis SA; 4 — signal $U(\alpha)$.

characteristic of solutions is the minimum SNR at which the decision with superresolution is still possible.

Stability of the solutions and the quality of image reconstruction have been also investigated in model simulations. Figure 3 shows the solutions found with a significant level of noise when SNR $q = 14$ dB. For the elements starting with the number $N = 80$ values of the coefficients C (Figure 2) undergo significant changes as compared to the true values. Nevertheless, the quality of the reconstructed image is still good.

Due to the effects of noise the reconstructed image was somewhat offset in relation to the true one having a slightly increased amplitude of the oscillating component. With further decrease of q an increase in the source position error increases the oscillating component. Image quality begins to depend on each particular implementation of the noise component. When the signal/noise ratio is less than 10 dB the image recovery becomes impossible.

5. CONCLUSION

The proposed method of signal processing based on the digital aperture synthesis improves the accuracy of angle measurements and provides the recovery of images of objects with superresolution. The results of numerical studies have shown that the angular resolution sharply increases in SNR ranging from 12–13 dB, i.e., at substantially lower values than those provided by the known methods and algorithms. Implementation of this method as a software package in computer codes applied for the design of new systems will simplify technical solutions and reduce the costs. The developed fast algorithms of the aperture synthesis can be used in the real-time mode.

REFERENCES

1. Quinquis, A., E. Radoi, and F. Totir, "Some radar imagery results using superresolution techniques," *IEEE Trans. Antennas and Propagation*, Vol. 52, No. 5, 1230–1244, 2004.
2. Lagovsky, B. A., "Image restoration of the objects with superresolution on the basis of spline – Interpolation," *PIERS Proceedings*, 989–992, Moscow, Russia, Aug. 2012.
3. Lagovsky, B. A., "High performance angular resolution algorithm for radar systems," *PIERS Proceedings*, 1637–1641, Moscow, Russia, Aug. 18–21, 2009.
4. Lagovsky, B. A., "Algorithm for the determination of targets coordinates in structure of the multiple targets with the increased effective resolution," *PIERS Proceedings*, 1642–1645, Moscow, Russia, Aug. 18–21, 2009.
5. Herman, M. A. and T. Strohmer, "High-resolution radar via compressed sensing," *IEEE Trans. Signal Processing*, Vol. 57, No. 6, 2275–2284, 2009.
6. Lagovsky, B. A., "Superresolution: Simultaneous orthogonalization of function systems describing the received signal and its source," *PIERS Proceedings*, 993–996, Moscow, Russia, Aug. 18–21, 2009.
7. Lagovsky, B. A. and A. B. Samokhin, "Image restoration of two-dimensional signal sources with superresolution," *PIERS Proceedings*, 315–319, Moscow, Russia, Aug. 18–21, 2009.

Analysis of Quasi-circular Polarization in Near Field of Smart Shelf RFID Antenna Radiation

A. S. Andrenko

SYSU-CMU Shunde International Joint Research Institute
No. 9 Eastern Nanguo Road, Shunde, Guangdong 528300, China

Abstract— This paper presents the EM simulation and accurate analysis of quasi-circular polarization (CP) of the so-called smart shelf antenna designed for the UHF RFID retail and item-tagging applications. The design of the proposed antenna is based on the EM coupling between the open-ended or shorted-to-the ground meander microstrip (MS) line utilizing the standing wave current-voltage distribution and periodic metal strips printed on the top surface of a dielectric substrate. It has been confirmed by the series of full-wave EM simulations that the proposed antenna creates strong near field within the entire volume where multiple RFID tags are placed. The required quasi-CP near field has been numerically optimized by utilizing the three-section layout of the periodic metal strips and changing the angles of strip sections so that it results in both E_x - and E_y -components being produced. The prototypes with different layouts of the proposed antenna have been produced and their performance in the UHF RFID system has been verified.

1. INTRODUCTION

The radio frequency identification (RFID) technology continues to find numerous applications in a variety of industrial designs and solutions. Among the four different frequency bands used for RFID communications, UHF (865–960 MHz) band has attracted strong popularity and support of RF community because of its ability to provide varying read range and also high read and data rates. Recently, the concept of so-called smart shelf UHF RFID system has attracted much interest in retail industry and supply chain management [1–4]. In contrast to the conventional high gain read/write (R/W) antennas designed for maximizing the read range, the smart shelf antenna system utilizes the near field communication within a range close to a wavelength between the planar R/W antenna and several tagged items being placed on the shelf. To provide reliable detection of the multiple tags which can generally be distributed within a wide interrogation volume over the shelf surface, uniform and strong near E -field radiated over the smart shelf antenna is required. This paper presents the antenna design with an improved field distribution and analyzes the near field of such an antenna characterized by quasi-CP radiation. Quasi here means that the E -field is also having z -component (normal to antenna surface). However, the most important property of smart-shelf antenna is its ability to produce the E -field having a well-balanced x - and y -components at the different distances from antenna surface and within an entire interrogation volume.

2. NEAR FIELD CALCULATION AND OPTIMIZATION

Typical scenario of the analysis of E field radiated by a planar smart-shelf RFID antenna is shown in Fig. 1. A 50-Ohm open-ended or shorted-to-the ground MS line on FR4 substrate is covered by the 1 mm-thick FR4 layer and on its top surface a few periodic 4 mm-wide metal strips are printed so that they are EM coupled to the MS feed line. Because of an open-ended or shorted termination, a voltage-current standing wave is produced. The strongest currents on the EM coupled strips are induced when they cross over the MS line at the points of zero current and maximum voltage. By utilizing the meander MS line and by making the electric length of meander sections between the neighboring strips equal to one wavelength, in-phase excitation of periodic elements is produced which substantially improves the uniformity of E -field distribution in the near-field zone and increases the amplitude of E -field radiated by the antenna. It has also been shown by CST MS simulation that the optimum length of periodic strips is approximately one wavelength so that they operate like a full-wavelength dipoles.

At a point P over the antenna surface the total E field can be calculated as

$$\vec{E}_T(x, y, z) = \sum_{n=1}^N \left[\vec{E}_d(x, y, z) \right]_n + \sum_{n=1}^{N-1} \left[\vec{E}_m(x, y, z) \right]_n \quad (1)$$

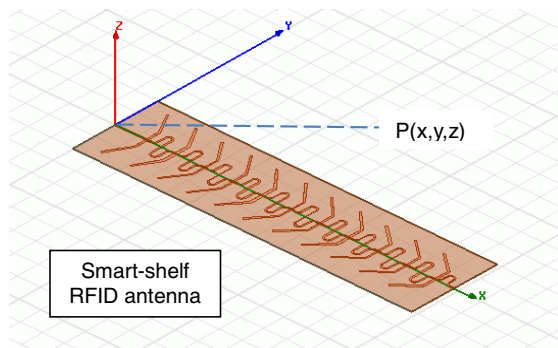


Figure 1: The geometry of a smart-shelf antenna and corresponding coordinate system.

where N is total number of EM coupled strips, E_d is an electric field radiated by each strip element while E_m is that radiated by a meander MS segment between the neighboring EM coupled strips. In a near-field zone, the total E field radiated by an antenna has Ez -component in addition to the Ex - and Ey -components being parallel to the antenna surface. Since the radiating strip elements and meander MS line are in XY -plane, it has been confirmed by EM simulation that

$$|\vec{E}_z(x, y, x)| \ll |\vec{E}_x(x, y, x)| + |\vec{E}_y(x, y, x)| \quad (2)$$

In the apparel tagging applications where tagged items are arbitrary oriented in the plane parallel to the antenna surface, the most important requirement is the antenna’s ability to radiate the E -field with a well-balanced in amplitude and quarter-period in phase x - and y -components at the different distances from the surface and within an entire interrogation volume. In such a case, the antenna would produce a quasi-CP radiation in the near-field zone.

The required near-field optimization has been achieved by the specific strip layout as illustrated in Fig. 2 showing that each of the EM coupled strips consists of 3 sections. The angle forming the strips has been optimized so that the total E -field (1) formed in the near-field zone is a quasi-CP polarized in XY -plane. To further improve the uniformity of E -field distribution over the entire antenna aperture along X -axis, the angle of 3-section strip has been gradually changed from 30-deg close to input port to 50-deg for the elements at the antenna end as shown in Fig. 2. In addition to this, the length of strip elements has also been increased to widen the impedance bandwidth. The design frequency band has been 916.8 to 920.4 MHz but the obtained impedance bandwidth is more than 60 MHz. One example of the E -field distribution calculated in XY -plane at the distance $z = 40$ cm from the 50 cm-long smart-shelf antenna is shown in Fig. 3. Over the entire antenna aperture the E field amplitude exceeds the 1.5 V/m level required to activate an IC chip in UHF RFID tag. In time domain, the field vectors rotate as a RHCP.

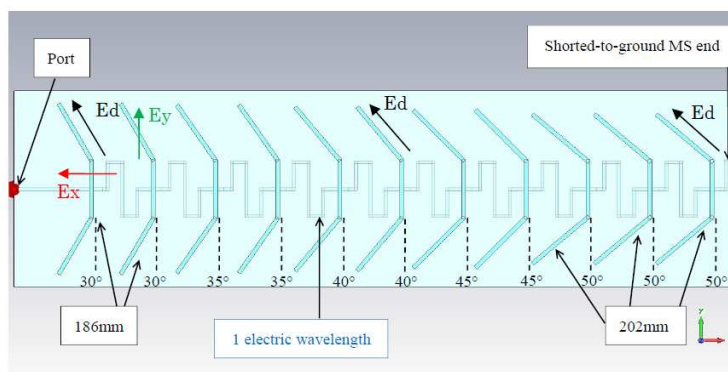


Figure 2: The detailed layout of the proposed smart-shelf antenna.

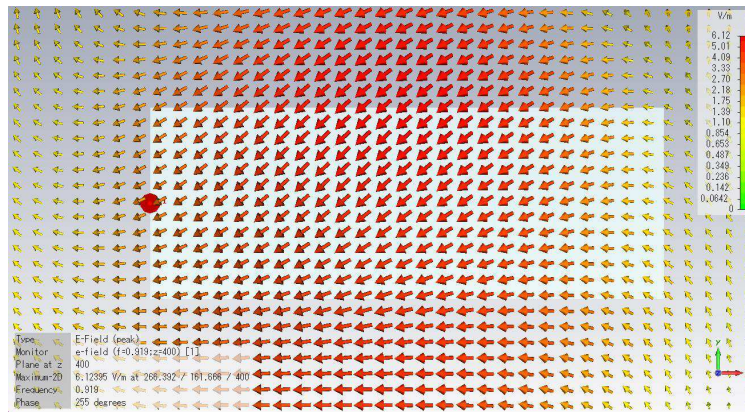


Figure 3: Time instant E field vector distribution at 919 MHz in XY -plane 40 cm over antenna.

3. MEANDER LINE EFFECT ON NEAR FIELD DISTRIBUTION

The MS line meander layout is very important for producing the required uniform E field over the antenna. As an illustration, consider the E_y -component distribution in the XY -plane at $z = 20$ cm radiated by an antenna with the straight MS line as shown in Fig. 4. Because of the symmetry in antenna elements layout with respect to x -axis, 0-field zone is produced along the x -axis in XZ -plane so that Y -oriented (and polarized) RFID tags cannot be activated there. In contrast to this, MS meander geometry produces strong E_y -component over the antenna's central part and removes such a "dead-zone" for tag interrogation as illustrated in Fig. 5.

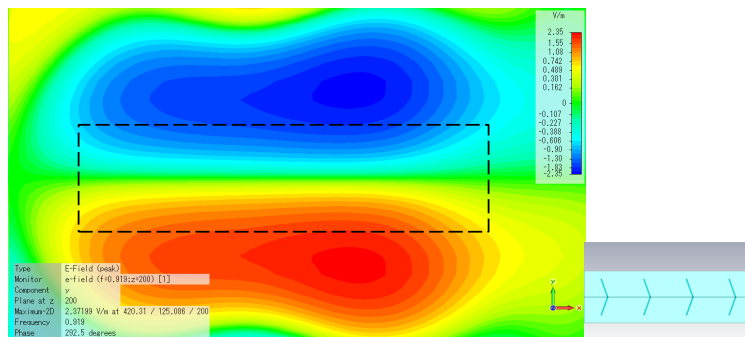


Figure 4: E_y -component distribution in the XY -plane at $z = 20$ cm, the case of straight MS line.

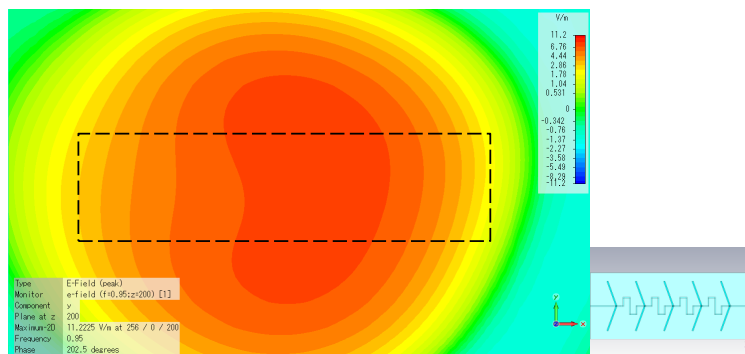


Figure 5: E_y -component distribution in the XY -plane at $z = 20$ cm, the case of meander MS line.

It has also been found out that the shape of MS meander can easily change the quasi-RHCP into quasi-LHCP field characteristics in the near field of the same antenna. Fig. 6 depicts the geometry of 1m-long antenna consisting of two parts with the same strip layout but opposite meander orientation with respect to x -axis.

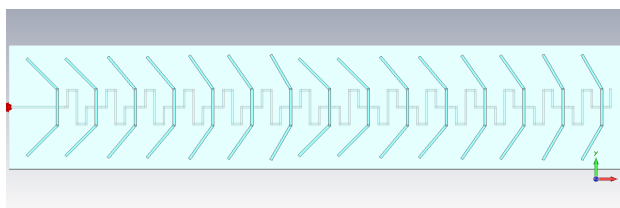


Figure 6: Geometry of 1 m-long antenna consisting of two parts with opposite meander layout.

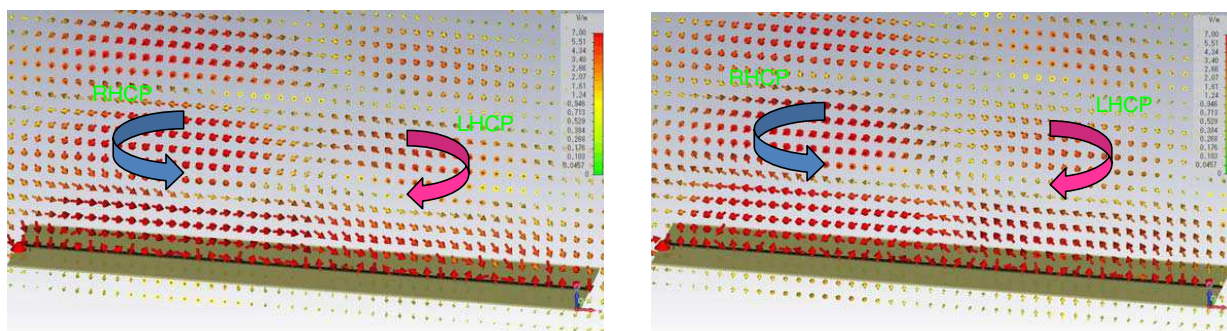


Figure 7: Two time instant vector E field distribution of the antenna shown in Fig. 6 in XZ -plane at $y = 0$.

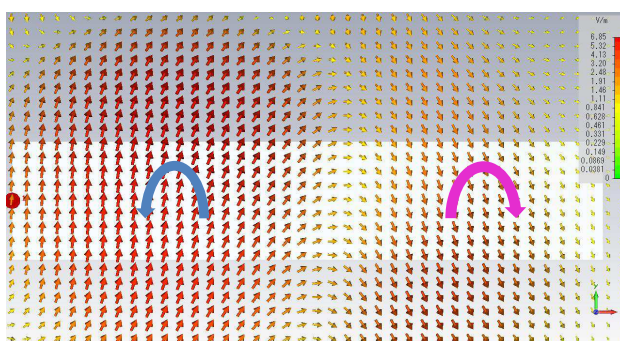


Figure 8: The same as in Fig. 7 but in XY -plane at $z = 40$ cm.

Time-domain analysis of 3D E -field vector distribution has shown that the field vectors over the antenna two segments rotate in opposite directions. Therefore, the antenna now simultaneously produces both quasi-RHCP and LHCP radiation within the different volumes over the antenna surface. The illustration of this effect is presented in Figs. 7 and 8 showing the time instants of vector E -field distribution in vertical XZ -plane at $y = 0$ and in XY -plane at $z = 40$ cm, respectively. The colored arrows here indicate the direction of the E field rotation.

4. CONCLUSION

The analysis of near field distribution of the antenna designed for smart-shelf UHF RFID applications has been presented. The required quasi-CP performance in the near-field zone has been achieved and optimized in the series of EM simulations by utilizing the three-section layout of the periodic metal strips and changing the angles of strip sections resulting in both E_x - and E_y -components being produced. Time-domain calculation of 3D E -field vector distribution has also demonstrated how a simple change of the meander line layout produces both quasi-RHCP and LHCP radiation in the near field of the same antenna. 100% detection rate and the measured read range of 40–50 cm for a large number of tagged items over the produced prototypes in UHF RFID system have confirmed the simulated near field distribution as well as an excellent performance of the proposed smart shelf antenna.

REFERENCES

1. Choi, W., J.-H. Bae, J.-S. Chae, and C.-W. Park, "U-shaped slot-array antenna for RFID shelf in the UHF," *Proceedings of 2011 IEEE AP-S/URSI International Symposium*, 1449–1451, USA, July 2011.

2. Wu, C.-Y., J. Du, A.-K. Ren, and J.-Y. Li, “Large-area RFID reader antenna for smart shelf at UHF,” *Electronics Letters*, Vol. 48, No. 15, July 2012.
3. Medeiros, C. R., J. R. Costa, and C. A. Fernandes, “RFID smart shelf with confined detection volume at UHF,” *IEEE Antennas and Wireless Propagation Letters*, Vol. 7, 773–776, 2008.
4. Andrenko, A. S. and M. Kai, “Novel design of UHF RFID near-field antenna for smart shelf applications,” *Proceedings of APMC 2013 International Conference*, 242–244, Seoul, Korea, November 2013.

Multichannel Filter Banks and Their Implementation Using Computers with a Parallel Structure

D. I. Kaplun, D. M. Klionskiy, A. S. Voznesenskiy, and V. V. Gulvanskiy

Computer Science Department

Saint Petersburg Electrotechnical University "LETI", Saint Petersburg, Russian Federation

Abstract— The paper is devoted to the development of a WOLA-algorithm (weighted overlap add algorithm) for processing vector (multichannel) signals. The algorithm is considered as a generalization of one-dimensional WOLA with certain modifications. WOLA is expounded as an algorithm for real-time signal processing and the main advantages of WOLA are provided. We also discuss software-hardware implementation of WOLA using CPU (Central Processing Unit) and CUDA (Compute Unified Device Architecture). Finally we demonstrate the possibility of reducing hardware costs for multichannel signal processing using FPGA (field programmable gate arrays) and distributed arithmetic.

1. INTRODUCTION

In the present paper we are going to consider multichannel filter banks and their implementation for wideband monitoring tasks. The term "monitoring" implies a systematic or continuous data acquisition from some object or system [1]. Monitoring is often performed in a wide frequency band (wideband monitoring) and includes tracking the main system parameters and deviation search in these parameters. Any deviation is usually caused by abnormal functioning of an object and requires immediate action in order to prevent failures.

Wideband monitoring is frequently used in the following areas [1–5]: *hydroacoustics* (monitoring of water areas (coastal and marine waters), underwater and surface objects, study of navigation canals and near-shore waters, analysis of oceanic seismicity, etc.); *radio monitoring* (time-frequency processing of radiations, noise suppression, signal classification, signal parameter estimation, signal demodulation, direction-finding, etc.); *vibration analysis* (vibration measurements, vibration parameter estimation in the time and frequency domains, resonance frequency estimation; analysis of vibrations is important for spacecraft, aircraft, engines, turbines, machinery, etc.); *geophysics* (monitoring of seismic and geomagnetic activity in various regions of our planet).

2. MULTICHANNEL DFT-MODULATED FILTER BANK AND WOLA-ALGORITHM FOR PROCESSING VECTOR SIGNALS

Wideband monitoring tasks are often handled using digital *FIR filters* [6–8] designed by the window or Chebyshev method [6–8]. Digital filters are also needed for *multichannel signal processing* [8]. One of the approaches to multichannel signal processing can be implemented by means of *digital filter banks* with the help of high-performance software-hardware tools.

The present paper is devoted to the development of a WOLA [8] modification for processing multichannel signals.

Digital filter banks and their implementations have been studied for many years and DFT-modulated filter banks (discrete Fourier transform modulated filter banks) [6–8] have long been applied to various tasks related to multirate signal processing and wideband monitoring. Among the most significant achievements are the development of the polyphase form of a filter bank and also the one-dimensional WOLA-algorithm [8].

DFT-modulated filter banks have several implementations. One of the simplest is a filter bank with complex modulation [8]. However, this implementation is not efficient since linear convolution in each channel is calculated for a large sampling rate (this leads to high computational costs). Therefore it is necessary to reduce the sampling rate, for instance, by choosing the polyphase structure [8].

One of the ways of implementing a polyphase filter bank is the WOLA algorithm, which performs *block-by-block* analysis [8]. Like a filter bank with complex modulation, the output signal is determined as

$$X_k(m) = \sum_{n=-\infty}^{\infty} h(mM - n) x(n) W_K^{-kn}, \quad (1)$$

where k is the number of a filter bank channel, m is the block number in WOLA, $h(n)$ is the impulse response of a LF-prototype (low-frequency prototype) filter, M is the decimating factor of the input signal,

$$W_K^{-kn} = e^{-j[(2\pi k/K)n]}, \quad (2)$$

where $j = \sqrt{-1}$.

According to (1) it is possible to introduce a filter with the impulse response $h(mM - n)$ as a moving analysis window for extracting the sequence $y_m(n)$, which is then subjected to short-time Fourier transform (STFT). This is the key idea behind the algorithm. In the case of critical decimation, when $M = K$, WOLA is identical to a polyphase filter bank. The main difference is that WOLA is oriented to block-by-block analysis (rather than parallel processing) and the signal in question has to be split into sections of the length N_h and overlap equal to M samples.

The main factor of the filter bank implementation that affects computational complexity is the LF-prototype filter. The magnitude response of the filter coincides with the desired one for a single channel. LF-prototype order depends on a required channel bandwidth, rectangularity shape factor, and gain flatness in the passband of one single channel.

Thus, we have to create efficient FIR-filters using the minimal computational complexity criterion for reducing hardware and software costs.

The algorithm outlined above is intended for processing *one-dimensional signals* (the term “one-dimensional signal” is used as a synonym for “single-channel signal”) presented in the form of a vector. In practice the original signal can consist of several one-dimensional signals (multichannel signal).

The WOLA-algorithm for processing vector signals can be considered as a generalization of the corresponding WOLA-algorithm for processing one-dimensional signals. However, the suggested modification will make it possible to perform efficient processing of a vector signal and then to perform efficient hardware-software implementation using high-performance software and hardware tools.

After signal computation at the output of each channel sub-band processing is carried out (the signal in each channel corresponds to some frequency band) including spectral analysis, time-frequency analysis, statistical analysis in the time domain, demodulation, etc..

Consider an input vector (multichannel) signal

$$x(n) = [x_0(n) \ \dots \ x_i(n) \ \dots \ x_{S-1}(n)]^T$$

as a set of one-dimensional (single-channel) signals

$$x_i(n), \quad i = 0, \dots, S-1; \quad n = 0, \dots, N-1.$$

The original vector signal $x(n)$ can be represented by a rectangular matrix of the dimension $S \times N$, where N is the signal length of $x_i(n)$; S is the number of one-dimensional signals.

In the following we are going to use the following notations:

1) $\mathbf{x}(n) = [\mathbf{x}_0(n), \mathbf{x}_1(n), \dots, \mathbf{x}_{S-1}(n)]$ is a multichannel signal in the matrix form, where the sub-matrices $\mathbf{x}_0(n), \mathbf{x}_1(n), \dots, \mathbf{x}_{S-1}(n)$ can be represented as

$$\mathbf{x}_0 = \begin{bmatrix} x_0(0) \\ x_0(1) \\ \vdots \\ x_0(N-1) \end{bmatrix}, \quad \mathbf{x}_1 = \begin{bmatrix} x_1(0) \\ x_1(1) \\ \vdots \\ x_1(N-1) \end{bmatrix}, \quad \dots \quad \mathbf{x}_{S-1} = \begin{bmatrix} x_{S-1}(0) \\ x_{S-1}(1) \\ \vdots \\ x_{S-1}(N-1) \end{bmatrix}. \quad (3)$$

2) S is the size of a multichannel signal (number of one-dimensional signals).

3) M is the decimation factor, $M = 1, \dots, K$, where K is the number of filter bank channels for each polyphase implementation corresponding to $x_i(n)$.

4) $g_i(m)$ and $e_i(m)$ is the impulse response of the i -th polyphase filter in the direct and inverse sections, respectively.

In the case of critical decimation when $M = K$ computation of output signals of a polyphase filter bank is equivalent to WOLA application, but the WOLA algorithm is oriented to *block-by-block analysis*.

The input of the WOLA-algorithm is a vector signal $\mathbf{x}(n) = [\mathbf{x}_0(n), \mathbf{x}_1(n), \dots, \mathbf{x}_{S-1}(n)]$, where $n = 0, \dots, N-1$. Furthermore, we need to know $h(n)$, which is the impulse response of a LF-prototype filter (vector of size $1 \times N_h$).

Next, weighting has to be applied:

$$\tilde{x}_{mi}(n) = h(mM - n)x_i(n), \quad i = 0, \dots, S - 1; \quad n = 0, \dots, N - 1, \quad (4)$$

where m is the block number (N_h is the block length). The total number of blocks P of the length N_h with the overlap ($N_h - M$) is determined as

$$P = 1 + \left\lfloor \frac{N - N_h}{M} \right\rfloor, \quad (5)$$

where $\lfloor \cdot \rfloor$ denotes rounding towards minus infinity. As a result of (4) we arrive at the matrix of weighted samples:

$$\tilde{\mathbf{x}}(n) = [\tilde{\mathbf{x}}_0(n), \tilde{\mathbf{x}}_1(n), \dots, \tilde{\mathbf{x}}_{S-1}(n)], \quad (6)$$

$$\tilde{\mathbf{x}}_0 = \begin{bmatrix} \tilde{x}_0(0) \\ \tilde{x}_0(1) \\ \vdots \\ \tilde{x}_0(N-1) \end{bmatrix}, \quad \tilde{\mathbf{x}}_1 = \begin{bmatrix} \tilde{x}_1(0) \\ \tilde{x}_1(1) \\ \vdots \\ \tilde{x}_1(N-1) \end{bmatrix}, \quad \dots, \quad \tilde{\mathbf{x}}_{S-1} = \begin{bmatrix} \tilde{x}_{S-1}(0) \\ \tilde{x}_{S-1}(1) \\ \vdots \\ \tilde{x}_{S-1}(N-1) \end{bmatrix}. \quad (7)$$

After that the blocks of the length N_h are split into non-overlapping segments of the length K and we perform summation of these segments. The total number of segments Q of the length K each within the block of the length N_h is determined as $Q = \lceil N_h/K \rceil$, where $\lceil \cdot \rceil$ denotes rounding towards infinity. As a result we obtain the following expressions:

$$z_{0,m}(r) = \sum_{l=-\infty}^{\infty} \tilde{x}_{0,m}(r + lK), \quad z_{1,m}(r) = \sum_{l=-\infty}^{\infty} \tilde{x}_{1,m}(r + lK), \quad \dots, \quad z_{S-1,m}(r) = \sum_{l=-\infty}^{\infty} \tilde{x}_{S-1,m}(r + lK), \quad (8)$$

where $m = 0, \dots, P - 1, r = 0, \dots, K - 1$. The matrix \mathbf{Z} can be written as

$$\mathbf{Z} = \begin{bmatrix} z_{00}(0) & z_{00}(1) & \dots & z_{00}(K-1) \\ \dots & \dots & \dots & \dots \\ z_{0,P-1}(0) & z_{0,P-1}(1) & \dots & z_{0,P-1}(K-1) \\ \dots & \dots & \dots & \dots \\ z_{S-1,0}(0) & z_{S-1,0}(1) & \dots & z_{S-1,0}(K-1) \\ \dots & \dots & \dots & \dots \\ z_{S-1,P-1}(0) & z_{S-1,P-1}(1) & \dots & z_{S-1,P-1}(K-1) \end{bmatrix}. \quad (9)$$

This matrix consists of sub-matrices and each one has P rows corresponding to blocks of the length N_h of each one-dimensional signal $x_i(n), i = 0, \dots, S - 1$. Thus, \mathbf{Z} has the size $P \cdot S \times K$.

Next, DFT is applied to the matrix \mathbf{Z} . This operation can be implemented on the basis of vector DFT algorithms intended for calculating DFT of multichannel data:

$$\mathbf{Y} = \text{VDFT} \{ \mathbf{Z} \}, \quad (10)$$

where \mathbf{Y} is the resulting matrix after DFT computation, VDFT is the operator of vector DFT.

There are two main approaches to vector DFT computation. One of them suggests application of one-dimensional DFT to each row of \mathbf{Z} . Overall, it is necessary to compute $P \cdot S$ one-dimensional DFTs of the length K each. The second approach is based on calculating one-dimensional DFT of the length $P \cdot S \cdot K$:

$$y = \text{DFT} (z_{00}(0) \ z_{00}(1) \ \dots \ z_{00}(K-1) \ | \ \dots \ | z_{S-1,P-1}(0) \ z_{S-1,P-1}(1) \ \dots \ z_{S-1,P-1}(K-1)), \quad (11)$$

where DFT is the operator of one-dimensional DFT. In order to compute one-dimensional DFT, the matrix \mathbf{Z} has to be converted into a vector (a sequence of matrix rows). There are several reasons for this transformation:

- an algorithm of vector DFT computation affects the total size of local memory of a DFT-processor. By reducing multichannel DFT to one-dimensional DFT it is possible to minimize computational memory and optimize the structure of a DFT-processor;

- computation of one-dimensional DFT of the length $P \cdot S \cdot K$ allows us to implement the computational procedure in a DFT-processor more efficiently in comparison with computing $P \cdot S$ different DFTs of the length K .

After computing DFT (11) of the vector \mathbf{y} it is necessary to transform the result back into a matrix. The dimension of \mathbf{Y} will coincide with the that of \mathbf{Z} . Matrix \mathbf{Y} will consist of several sub-matrices:

$$\mathbf{Y}(r) = [\mathbf{Y}_0(r), \mathbf{Y}_1(r), \dots, \mathbf{Y}_{S-1}(r)]^T, \quad (12)$$

$$\mathbf{Y}_i(r) = \begin{bmatrix} y_{i,0}(0) & y_{i,0}(1) & \dots & y_{i,0}(K-1) \\ & \dots & & \\ y_{i,P-1}(0) & y_{i,P-1}(1) & \dots & y_{i,P-1}(K-1) \end{bmatrix}, \quad i = 0, \dots, S-1; \quad r = 0, \dots, K-1. \quad (13)$$

Finally, we have to form the matrix $\tilde{\mathbf{Y}}(r)$ by multiplying all the rows of $\mathbf{Y}(r)$ by the factor W_K^{-krM} :

$$\tilde{\mathbf{Y}}_i(r) \Big|_{k\text{-th line}} = \mathbf{Y}_i(r) \Big|_{k\text{-th line}} W_K^{-krM}, \quad r = 0, \dots, K-1; \quad k = 0, \dots, P-1. \quad (14)$$

To summarize, multichannel WOLA-algorithm can be presented as a sequence of steps:

- 1) weighting the multichannel signal $\mathbf{x}(n)$ in order to obtain $\tilde{\mathbf{x}}(n)$ according to (4)–(7).
- 2) splitting the multichannel signal (6) into non-overlapping segments of the length K and summation of segments of each one-dimensional signal according to (8);
- 3) application of vector DFT (10) to the matrix \mathbf{Z} using one-dimensional DFT (11) of the length $P \cdot S \cdot K$ and computation of the matrix $\mathbf{Y}(r)$ according to (12)–(13);
- 4) computation of the matrix $\tilde{\mathbf{Y}}(r)$ according to (14).

3. SOFTWARE-HARDWARE IMPLEMENTATION OF THE WOLA FOR VECTOR SIGNAL PROCESSING

The crucial factor of computational complexity for software-hardware implementation of a multichannel filter bank is a low-frequency prototype filter (LF-prototype filter), which is responsible for forming the required magnitude response for one filter bank channel. The order of a LF-prototype filter can be found depending on the parameters of a wideband monitoring system.

The LF-prototype filter has been designed by the window technique. The parameters of the LF-prototype will define the parameters of the whole filter bank. First, it is necessary to provide small flatness of the magnitude response (no more than 1 dB) in the passband, large suppression (at least 80 dB) in the stopband and a high shape factor (the LF-prototype must have high selectivity). Below we have given the exact parameters of our LF-prototype: frequency band for wideband monitoring: [0; 1] MHz; number of filter bank channels: $K = 320$; channel bandwidth: $\Delta f = 3125$ Hz; signal suppression at the edge of the passband of a LF-prototype filter: 1 dB; signal suppression at the edge of the stopband of a LF-prototype filter: 120 dB; magnitude response flatness: 0.01 dB; rectangularity shape factor: 1.25. As a result we have designed a LF-prototype filter of the order 6245.

A filter bank performs parallel processing of an input signal and therefore in order to improve the efficiency of its hardware implementation it is reasonable to employ computers with a parallel structure. Among such computers are field programmable gate arrays (FPGA) and processing devices based on the Compute Unified Device Architecture technology (CUDA technology) [9].

CUDA technology allows us to develop software by minimizing temporal resources and satisfying high standards of information processing in real time. The main idea behind CUDA is application of a set of parallel graphical processors (Graphics Processing Unit — GPU) for handling non-graphical tasks. GPU is a specialized computational device, which has the following properties: GPU is a co-processor for CPU; GPU has its own memory; GPU allows parallel performance of a large number of data flows (in this context, a flow means several parts of a program run in a parallel way).

The experiment was made on a personal computer with the following configuration: processor Intel Core i7-3630QM (IvyBridge) 2.4 GHz; RAM DDR3 16 Gb, operating system Windows 7 64 bits; video card Nvidia GeForce GT650M (384 core CPU, core frequency 850 MHz, video card memory 2 Gb).

In Table 1 there are estimates of WOLA performance time using CUDA and CPU. When we were applying CUDA we also took into consideration the data transfer time between RAM and video card memory.

Table 1: Comparison of CPU and CUDA performance.

Data size (samples/Mbytes)	CPU and CUDA performance		
	CUDA without data transfer between RAM and video card memory	CUDA with data transfer between RAM and video card memory	CPU
3000000 / 11 Mbytes	0.293 sec.	0.508 sec.	46.931 sec.
8000000 / 30 Mbytes	0.320 sec.	0.895 sec.	122.656 sec.
16000000 / 61 Mbytes	0.346 sec.	1.496 sec.	246.834 sec.
30000000 / 114 Mbytes	0.437 sec.	2.593 sec.	459.354 sec.

Analysis of the data in Table 1 allows us to draw the following conclusions:

- application of CUDA leads to significant computational time reduction in comparison with CPU;
- increase of data size results in temporal cost rise and therefore the greater a signal set is the more reasonable it is to apply CUDA.

It is necessary to mention that the time for data transfer between RAM and video card memory can sometimes reach half of the total processing time, which is a sort of a disadvantage of the CUDA technology.

Figure 1 illustrates a general structure of a digital filter bank with FPGA (field programmable gate array) implementation.

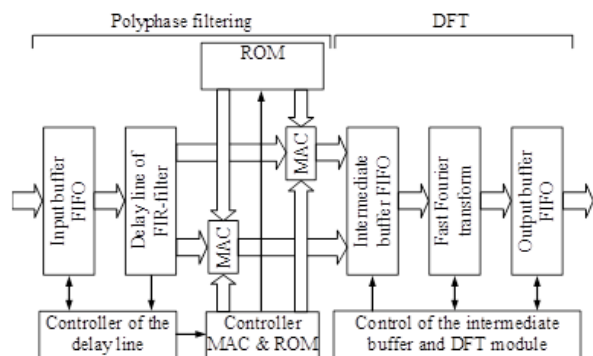


Figure 1: General structure of a digital filter bank with FPGA implementation.

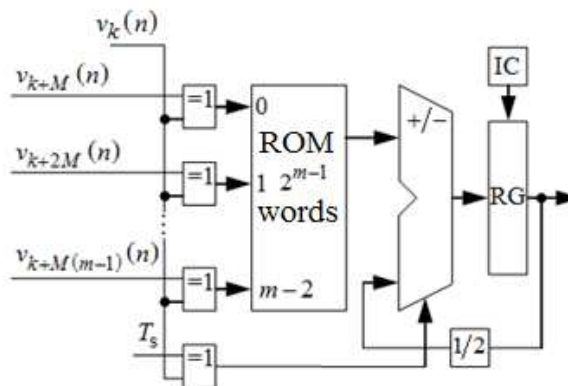


Figure 2: General structure of a digital filter bank with FPGA implementation.

By analyzing this figure we can conclude that one of the crucial factors of hardware implementation of a digital filter bank is the order of a LF-prototype filter, which defines the magnitude response of a FIR-filter of a single channel. Hardware resources of computers used for digital filter bank implementation are limited (the number of multipliers is the most critical) and the main task consists in synthesizing efficient FIR-filters (the criterion is minimum computational complexity), which will make it possible to reduce software-hardware costs and to accelerate signal analysis. In the case of using FPGA such an approach allows us to reduce the number of devices involved (primarily, the number of FPGA multipliers) and increase the number of those on a chip.

One more practical approach to digital filter bank implementation using FPGA is application of distributed arithmetic (DA) [10]. The main difference of this approach from direct implementation based on MAC cores is the fact that there are no multipliers in the DA.

Computation of the k -th polyphase component of a multichannel filter bank corresponds to computing the scalar product of $\mathbf{v}_{k+mi}(n)$ (output of a delay chain) and \mathbf{g}_{k+mi} (coefficients of the

polyphase component):

$$Y_k(n) = \sum_{i=0}^{m-1} \mathbf{v}_{k+mi}(n) \mathbf{g}_{k+mi}. \quad (15)$$

Consider the scalar product of two vectors: $Y = \sum_{k=0}^{L-1} \mathbf{A}_k \mathbf{x}_k$ and let us assume that the input data \mathbf{x}_k are the numbers in the complement code normalized to one: $x_k = -b_{k0} + \sum_{n=1}^{N-1} b_{kn} 2^{-n}$, where b_{kn} are bits for numeric representation of x_k . Having made a few transformations we can obtain the following expression:

$$Y = - \sum_{k=0}^{L-1} \mathbf{A}_k b_{k0} + \sum_{n=1}^{N-1} \left[\sum_{k=0}^{L-1} \mathbf{A}_k b_{kn} \right] 2^{-n}. \quad (16)$$

The sum $\sum_{k=0}^{L-1} \mathbf{A}_k b_{kn}$ can take 2^L different values, which can be computed in advance and saved in the memory. Then the vector $\mathbf{b}_n = [b_{0n} \ b_{1n} \ \dots \ b_{(L-1)n}]$ is the address where the value $\sum_{k=0}^{L-1} \mathbf{A}_k b_{kn}$ is stored. Thus, we need the memory size of 2^L cells of the type “adder-subtractor” and a register for storing intermediate results. The memory size can be reduced twice if we interpret the input data as those represented in the offset binary code.

Each polyphase component of a prototype-filter is a low-order FIR-filter, which can be implemented efficiently using the distributed arithmetic. The polyphase component implementation using the distributed arithmetic is shown in Fig. 2. Data $v_k(n)$ from a block of registers are sent to the input in the sequential code beginning from a low-order bit. The signal T_s follows the sign bit and after that the register RG will store the result. The control device for this circuit can be implemented using a counter. The block IC (initial condition) stores the initial value loaded in the register RG prior to the beginning of the circuit operation for representing filter coefficients in an offset binary code for reducing the size of ROM [10]. When filtering is performed, data from the register RG shifted to the right by one bit (this is equivalent to dividing by 2) are added to the contents of ROM. The number of polyphase components is determined by the number of sub-channels of one channel of a multi-channel filter bank M and the order of each polyphase component is determined by the parameter m .

Filter banks are efficient for preprocessing when the original signal is divided into a given number of parallel channels with the required parameters. Next, we can select any of the channels and apply specialized processing algorithms that are needed for solving wideband monitoring tasks. Thus, application of a filter bank makes it possible to obtain a number of parallel devices and each device improves the performance and efficiency of software-hardware wideband monitoring packages.

4. CONCLUSION

In the present paper we have provided the WOLA algorithm for processing vector (multichannel) signals in real time. We have provided the results of software-hardware implementation using CUDA and we have shown that CUDA performs much better for long data sets (the processing time has been reduced). Hardware resources for multichannel signal processing implementation can be reduced using the distributed arithmetic.

ACKNOWLEDGMENT

The paper is supported by the grant of the Russian Foundation for Basic Research (“My first grant”) No. 14-07-31250/15 and Contract No. 02.G25.31.0058 dated 12.02.2013 (Board of Education of Russia).

REFERENCES

1. Porcino, D. and W. Hirt, “Ultra-wideband radio technology: Potential and challenges ahead,” *IEEE Communications Magazine*, Vol. 41, No. 7, 66–74, 2003.
2. Li, L. and Y. H. Yen, “Wideband monitoring and measuring system for optical coatings,” *Applied Optics*, Vol. 28, No. 14, 2889–2894, Jul. 15, 1989.

3. Allen, B., T. Brown, K. Schwieger, E. Zimmermann, W. Q. Malik, D. J. Edwards, L. Ouvry, and I. Oppermann, "Ultra wideband: Applications, technology and future perspectives," *Proc. Int. Workshop Convergent Tech.*, Oulu, Finland, Jun. 2005.
4. Xu, Y., Y. Lu, H. Zhang, and Y. Wang, "An overview of ultra-wideband technique application for medical engineering," *2007 IEEE/ICME International Conference on Complex Medical Engineering (CME)*, Beijing, May 2007.
5. Hu, X.-Q., Y.-M. Chen, and J.-F. Tang, "Apparatus for wideband monitoring of optical coatings and its uses," *Applied Optics*, Vol. 28, No. 14, 2886–2888, 1989.
6. Antoniou, A., *Digital Filters: Analysis, Design, and Applications*, 689, McGraw-Hill, USA, 1993.
7. Mitra, S. K., *Digital Signal Processing: A Computer-Based Approach*, 940, McGraw-Hill, USA, 1998.
8. Crochiere, R. E. and L. R. Rabiner, *Multirate Digital Signal Processing*, 411, Prentice Hall, USA, 1983.
9. Kirk, D. B. and W. Hwu, *Programming Massively Parallel Processors: A Hands-on Approach*, 280, Morgan Kaufmann, USA, 2010.
10. White, S. A., "Applications of distributed arithmetic to digital signal processing: A tutorial review," *IEEE ASSP Magazine*, Vol. 6, 4–19, 1989.

Analysis of Multipactor Effect in Parallel-plate and Rectangular Waveguides

A. Berenguer¹, A. Coves¹, E. Bronchalo¹, B. Gimeno², and V. E. Boria³

¹Departamento de Ingeniería de Comunicaciones. Universidad Miguel Hernández de Elche, Spain

²Departamento de Física Aplicada y Electromagnetismo, Instituto de Ciencia de Materiales
Universidad de Valencia, Spain

³Departamento de Comunicaciones, Universidad Politécnica de Valencia, Spain

Abstract— In this work it is investigated, in the parallel-plate waveguide case, how the 1D, 2D or 3D motion of the electrons inside the waveguide can affect the generalized susceptibility diagrams, by means of a developed model capable of tracking the exact trajectory of multiple effective electrons which includes effects such as the spreading of the secondary electron departure kinetic energies or the dependence on elastic and inelastic electrons. On the other hand, a comparative study of the susceptibility charts in a parallel-plate and in its equivalent rectangular waveguide with the same height is performed, showing how the inhomogeneity of the electric field inside the waveguide modifies the multipactor region with respect to that predicted by the parallel-plate waveguide case. The results of this study are going to be extended to a partially dielectric-loaded rectangular waveguide, which is a problem of great interest in the space industry that has not yet been rigorously investigated in the literature.

1. INTRODUCTION

The multipactor effect is an electron discharge that may appear in particle accelerators and microwave devices such as waveguides in satellite on-board equipment under vacuum conditions. This effect has been widely studied, and many investigations have been focused on the prediction of multipactor breakdown in a wide variety of microwave passive components for signals of different frequency and power levels, in order to prevent their damage. Many works [1, 2] take advantage of available susceptibility charts in empty parallel-plate waveguides obtained with analytical models [3], and they are directly used to predict multipactor breakdown in the component under study, which is going to happen in the point of highest field intensity. Thus, they are aimed to determine such highest field intensity region, which is generally the smallest device gap. However, such susceptibility diagrams do not take into account important effects such as the dependence of these diagrams on elastic and inelastic electrons, as well as the 3D character of the motion of the electrons inside the waveguide, or the non-uniform nature of the electromagnetic fields in some particular cases. In the last years, the authors have developed a 1D model for studying the multipactor effect in a parallel-plate dielectric-loaded waveguide [4–6] including space charge effects. In this work we have extended this model to a 3D movement case, and a comparison of the obtained results with such 3D model to those provided by the 1D model has been performed in the empty parallel-plate waveguide case. On the other hand, a 3D model for studying multipactor effect in an empty rectangular waveguide has also been developed, and the obtained results for a rectangular waveguide with the same height as the the parallel-plate one have also been obtained and compared.

2. THEORY

2.1. Electron Dynamics

The key for understanding the mechanism of the multipactor discharge is to study the behavior of the electrons within a harmonically excited waveguide. An electron inside the gap space is accelerated by the RF electric field. A significant growth in the electron density in the device can only happen if the electrons hit the walls with the appropriate energy and at periodically suitable instants.

The electron dynamics is governed by the Lorentz force resulting in Eq. (1),

$$\vec{F}_L = q \left(\vec{E} + \vec{v} \times \vec{B} \right) = \frac{\partial \vec{p}}{\partial t} \quad (1)$$

where $q = -e$ is the electron charge, \vec{E} and \vec{B} are, respectively, the instantaneous electric and magnetic field vectors interacting with the electron, \vec{v} is the velocity vector of the electron, and t

is the time. The linear momentum is defined according to Eq. (2),

$$\vec{p} = m_0 \gamma \vec{v} \quad (2)$$

where m_0 is the electron mass at rest, $\gamma = \frac{1}{\sqrt{1-(\frac{v}{c})^2}}$ is the relativistic factor, v being the magnitude of the velocity vector, $c = \frac{1}{\sqrt{\mu_0 \epsilon_0}}$ is the free-space light velocity, where μ_0 is the free-space magnetic permeability and ϵ_0 is the free-space electric permittivity. Usually, when $v \ll c$, the relativistic term tends to $\gamma \rightarrow 1$. Although the relativistic component of this equation can be discarded for the typical power ranges of most space waveguide devices, it should be considered in cases when extreme speeds are reached ($\frac{v}{c} \gtrsim 0.1$), like for high-power multipactor testing simulations. Expanding then Eq. (1), Eq. (3) is obtained:

$$-\vec{E} - \vec{v} \times \vec{B} = A\gamma \vec{a} + \frac{A}{c^2} \gamma^3 (\vec{v} \cdot \vec{a}) \vec{v} \quad (3)$$

where \vec{a} is the acceleration vector and $A = m_0/e$. The acceleration is the derivative over time of the velocity, which in turn is the derivative of the position: $\vec{a} = \dot{\vec{v}} = \ddot{\vec{r}}$. The differential equation system to solve becomes then,

$$\ddot{r}_x = \frac{\dot{r}_z B_y - \dot{r}_y B_z - E_x + \dot{r}_x \cdot \vec{r} \cdot \frac{\vec{E}}{c^2}}{A\gamma} \quad (4a)$$

$$\ddot{r}_y = \frac{\dot{r}_x B_z - \dot{r}_z B_x - E_y + \dot{r}_y \cdot \vec{r} \cdot \frac{\vec{E}}{c^2}}{A\gamma} \quad (4b)$$

$$\ddot{r}_z = \frac{\dot{r}_y B_x - \dot{r}_x B_y - E_z + \dot{r}_z \cdot \vec{r} \cdot \frac{\vec{E}}{c^2}}{A\gamma} \quad (4c)$$

In the parallel-plate dielectric-loaded waveguide case, the electromagnetic fields have an analytical expression, and then such differential equation system can be analytically solved under certain approximations [4, 5]. On the other side, in a partially dielectric-loaded rectangular waveguide, the electromagnetic fields must be numerically solved. To this end, a vectorial modal method has been employed [7], and in this case the electron trajectories are found by solving such equations using a velocity Verlet algorithm which assures sufficient accuracy and good efficiency provided enough time steps are chosen.

2.2. Secondary Electron Yield (SEY)

The movement may eventually lead the electron to impact with any surface. Each collision can result in the emission or absorption of secondary electrons. The number of electrons emitted or absorbed after each impact is determined by the value of the secondary electron yield (SEY) parameter δ ($\delta > 1$ if secondary electrons are emitted, and $\delta < 1$ if they are absorbed). The value of parameter δ is calculated by means of realistic SEY functions that include the effect of reflected electrons for low impact energies of primary electrons, which must be accounted in order to obtain accurate results [8, 9]. The SEY function used assumes $\delta = 0.5$ for low impact energies of primary electrons. This value is in agreement with experimental results obtained in [10]. If total absorption were considered instead, an electron colliding with low energy would automatically be lost for the rest of the simulation. The SEY properties are defined by the following parameters: the primary electron impact kinetic energies, which yield $\delta = 1$, W_1 , and W_2 ; the impact energy W_{\max} necessary for a primary electron to yield $\delta = \delta_{\max}$, which is the maximum value of the SEY function; and the value of the primary electron impact energy W_0 ($\delta = 0$) that limits the region of elastic collisions. In the effective electron model assumed in this study, after each effective electron impacts at time t with any surface, $N_i(t)$ is modified according to the δ value provided by the SEY function by means of Eq. (5),

$$N_i(t + \Delta t) = \delta N_i(t) \quad (5)$$

where $N_i(t)$ represents the population of each effective electron inside the waveguide at the instant t , and Δt is the time step used in the simulations. If multiple effective electrons are considered, the total population of electrons inside the waveguide at each instant t is the sum of the population of all effective electrons.

On the other hand, the secondary electron departure kinetic energy W_s after each impact is assumed to follow a Rayleigh probability density function according to Eq. (6) [4],

$$f(W_s) = \frac{W_s}{W_g^2} e^{-\frac{W_s^2}{2W_g^2}} \quad (6)$$

with parameter $W_g = 3 \text{ eV}$.

3. NUMERICAL RESULTS AND DISCUSSION

The schemes of the geometries and dimensions of the problems under investigation are shown in Fig. 1. For the parallel-plate waveguide the distance is $d = 3 \text{ mm}$. Similarly, in the case of the rectangular waveguide, the distance is $b = 3 \text{ mm}$. With regard to the distance a , it has been chosen so that there is at least one propagation mode in the waveguide, i.e., $a \gg b$. Fig. 2 provides the SEY characteristics for the silver material employed in the waveguides under study. The parameters are $W_1 = 30 \text{ eV}$, $W_2 = 5000 \text{ eV}$, $W_{\max} = 165 \text{ eV}$, $W_0 = 16 \text{ eV}$, and $\delta_{\max} = 2.22$.

First, a comparative study of the susceptibility charts in a parallel-plate and in its equivalent rectangular waveguide with the same height is performed. In each susceptibility chart, for each V_0 and $f \times d$ pair, the simulation is run 72 times, corresponding to 72 equidistant phases of the RF field separated 5 degrees. In each run, a single effective electron starts at a uniformly random position and velocity inside the waveguide. Each simulation lasts 100 RF cycles, with 5000 time intervals per cycle. The arithmetic mean of the final population of electrons after 100 RF cycles is calculated using all 72 simulations. If this mean value is greater than 1, then the multipactor discharge is assumed to have occurred. In Fig. 3, the susceptibility charts of an empty silver parallel-plate waveguide considering both a 1D model and a 3D model have been compared (results obtained with a 2D model have also been obtained for this guide, although they are not shown in this study given that the results of 2D and 3D models are quite similar). The differences between the susceptibility charts shown in Fig. 3 are evident: the multipactor region experiences a relevant decrease when the 3D movement inside the waveguide is considered. Such decrease is observed not only as a multipactor threshold reduction, i.e., a decrease of the voltage threshold at each $f \times d$ point, but also in the high voltage regions. This observed decrease of the multipactor region in

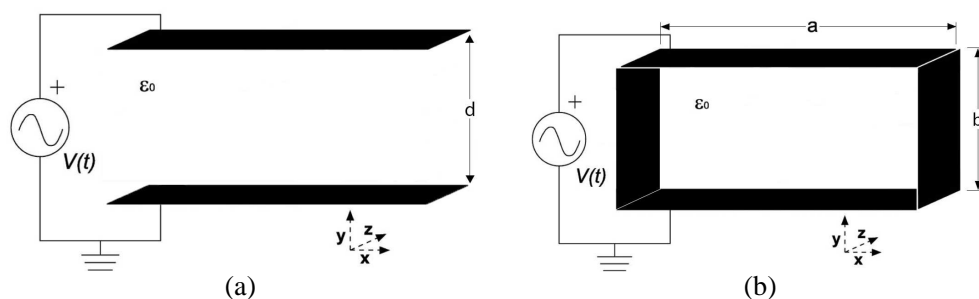


Figure 1: Geometries and dimensions of the problems under investigation. (a) Parallel-plate waveguide. (b) Rectangular waveguide.

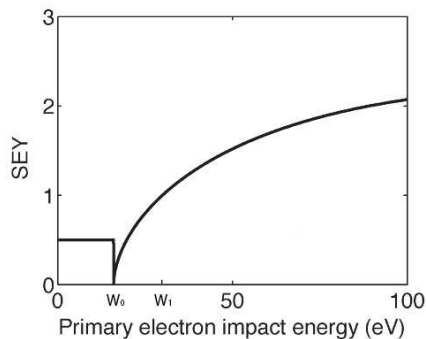


Figure 2: SEY characteristics for the silver material.

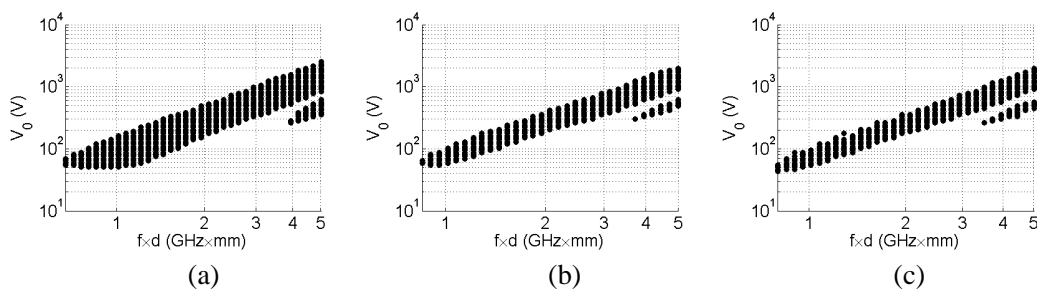


Figure 3: Susceptibility charts. (a) 1D: parallel-plate waveguide. (b) 3D: parallel-plate waveguide. (c) 3D: rectangular waveguide.

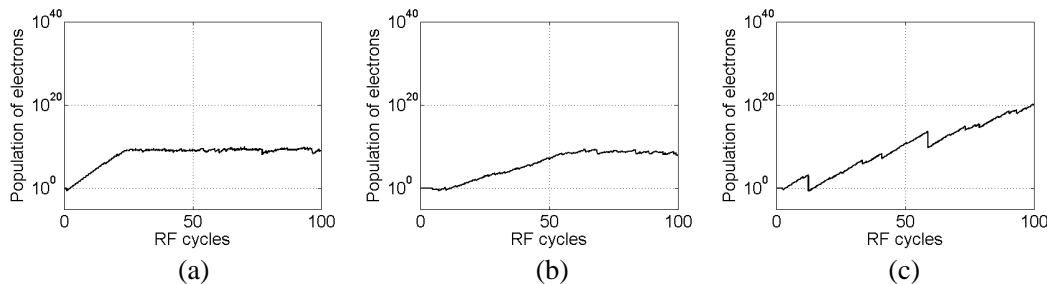


Figure 4: Populations of electrons. (a) 1D: parallel-plate waveguide. (b) 3D: parallel-plate waveguide. (c) 3D: rectangular waveguide.

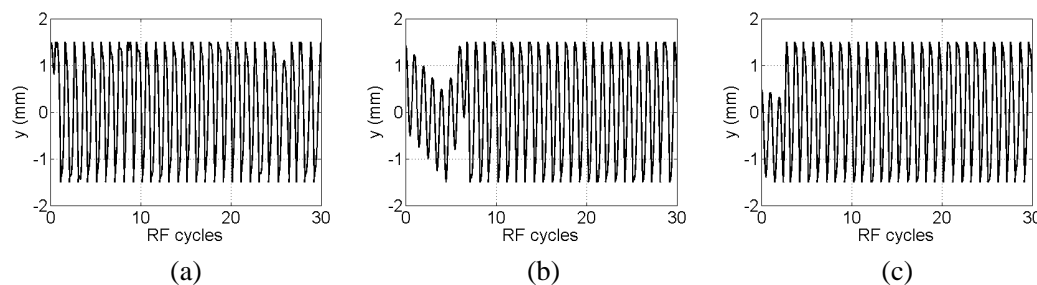


Figure 5: y position of the electron. (a) 1D: parallel-plate waveguide. (b) 3D: parallel-plate waveguide. (c) 3D: rectangular waveguide.

a 3D movement case is due to a slight desynchronization of the electron resonant movement after each impact, given that the secondary electron departure kinetic energy W_s is distributed in this case in the three velocity components (in a 1D model, all the secondary electron departure kinetic energy is used to push the effective electron towards the opposite wall). In the case of the 3D rectangular waveguide model, the susceptibility chart seems very similar to the 3D parallel-plate waveguide, i.e. a relevant decrease in the multipactor region can be appreciated when compared to the 1D parallel-plate waveguide model.

Secondly, in order to perform a detailed analysis of the physical behavior and the dynamics of the electron inside the waveguides under study, different parameters have been compared considering a bias point within the multipactor region. In all cases, $V_0 = 70$ V, $f \times d = 1$ GHz \times mm is the point under analysis.

In Fig. 4 the populations of electrons after 100 RF cycles are shown. For the 1D parallel-plate waveguide model, the population of electrons rises steadily until a saturation level around 10^{10} electrons, which is reached (due to space-charge effect) after 25 RF cycles approximately. Similar results are obtained in the 3D parallel-plate waveguide model. However, the saturation level is reached after 50 RF cycles in this case. With regard to the 3D rectangular waveguide model, no saturation level can be appreciated after 100 RF cycles since no space-charge effect has been considered in this guide. However, the same population level as in the 3D parallel-plate waveguide model is achieved again after 45 RF cycles, which corroborates that in this 3D model there is a desynchronization of the electron resonant movement after each impact.

Finally, the y position of the electron after 30 RF cycles is shown in Fig. 5. As it can be appreciated, both for the 3D parallel-plate and rectangular waveguide models, there is a slight desynchronization in the path followed by the electron, mainly on the first RF cycles.

The results of this study are going to be extended to a partially dielectric-loaded rectangular waveguide, which is a problem of great interest in the space industry that has not yet been rigorously investigated in the literature.

4. CONCLUSION

The 1D parallel-plate waveguide model, which is commonly used in the multipactor effect analysis in a wide variety of microwave passive components, is not accurate enough in the highest field intensity region. There is a x -coordinate dependency in the electromagnetic fields inside the waveguide which is not considered in 1D parallel-plate waveguide model. In this work, a 3D model which takes into account this dependency has been shown, both for parallel-plate and rectangular waveguides. The results obtained are accurate when compared to the 1D model.

ACKNOWLEDGMENT

This work was supported by the Ministerio de Economía y Competitividad, Spanish Government, under the coordinated projects TEC2013-47037-C5-4-R and TEC2013-47037-C5-1-R.

REFERENCES

1. Esteban, H., J. V. Morro, V. E. Boria, C. Bachiller, A. San Blas, and J. Gil, "Multipaction modelling of low-cost H -plane filters using an electromagnetic field analysis tool," *IEEE Antennas and Propagation Society International Symposium*, 2155–2158, San Antonio, TX, USA, Jun. 2004.
2. Quesada, F., V. E. Boria, B. Gimeno, D. Cañete, J. Pascual, A. Álvarez, J. Hueso, D. Schmitt, D. Raboso, C. Ernst, and I. Hidalgo, "Investigation of multipactor phenomena in inductively coupled passive waveguide components for space applications," *IEEE MTT-S Digest*, 246–249, San Francisco, CA, USA, 2006.
3. Hatch, A. J. and H. B. Williams, "The secondary electron resonance mechanism of low-pressure high-frequency gas breakdown," *J. Appl. Phys.*, Vol. 25, No. 4, 417–423, Apr. 1954.
4. Torregrosa, G., A. Coves, C. P. Vicente, A. M. Pérez, B. Gimeno, and V. E. Boria, "Time evolution of an electron discharge in a parallel-plate dielectric-loaded waveguide," *IEEE Electron Device Lett.*, Vol. 27, No. 7, 629–631, Jul. 2006.
5. Coves, A., G. Torregrosa, C. P. Vicente, A. M. Pérez, B. Gimeno, and V. E. Boria, "Multipactor discharges in parallel plate dielectric-loaded waveguides including space-charge effects," *IEEE Trans. Electron Devices*, Vol. 55, No. 9, 2505–2511, Sep. 2008.
6. Torregrosa, G., A. Coves, B. Gimeno, I. Montero, C. P. Vicente, and V. E. Boria, "Multipactor susceptibility charts of a parallel-plate dielectric-loaded waveguide," *IEEE Trans. Electron Devices*, Vol. 57, No. 5, 1160–1166, May 2010.
7. Soler, A. C., "Caracterización modal de sistemas guíadores inhomogéneos: Análisis de superficies selectoras de frecuencia dieléctricas," Ph.D. Thesis, Valencia, 2004.
8. Vicente, C., M. Mattes, D. Wolk, B. Mottet, H. L. Hartnagel, J. R. Mosig, and D. Raboso, "Multipactor breakdown prediction in rectangular waveguide based components," *IEEE MTT-S Digest*, 1055–1058, Long Beach, CA, USA, Jun. 2005.
9. Seviour, R., "The role of elastic and inelastic electron reflection in multipactor discharges," *IEEE Trans. Electron Devices*, Vol. 52, No. 8, 1927–1930, Aug. 2005.
10. Cimino, R., I. R. Collins, M. A. Furman, M. Pivi, F. Ruggiero, G. Rumolo, and F. Zimmermann, "Can low-energy electrons affect high-energy physics accelerators?," *Phys. Rev. Lett.*, Vol. 93, 014801, 2004.

Power Line Noise Measurements and Statistical Modelling in the Time Domain

A. M. Nyete, T. J. O. Afullo, and I. E. Davidson

Discipline of Electrical, Electronic and Computer Engineering
University of KwaZulu-Natal, Durban, South Africa

Abstract— The power grid provides a readily available medium for communication purposes. This means that the power grid is the cheapest communication medium since no new cabling is required. However, the power grid was designed for the delivery of power and not for communication applications. As such no considerations have been made in the design of power networks to accommodate communication services. However, with the application of current digital signal processing techniques, the power network can be adapted to support communication services. This adaptation requires a full understanding of the power network characteristics, which are noise, distortion and channel effects. These power network characteristics are studied through measurements, modelling and characterization. The results obtained through such studies are then utilized in the redesign of conventional receiver structures and modulation schemes so as to adequately suit them for powerline communication applications. In this paper, we present time domain power line noise measurement results, and then apply a statistical technique for the characterization and modelling of the time domain noise amplitudes in typical indoor power networks. The results obtained are validated through error analysis. The models developed are vital in the optimization of communication applications through the power network.

1. INTRODUCTION

The power network is the most expansive network in the world. Hence, given its ubiquitous nature, the power network has been attractive to communication engineers who have been busy optimizing this network for use as a communication channel. The optimization of this network for use as a communication channel is not a trivial task due to the fact that power lines were designed for the delivery of power and not communication services. The problems associated with the power network as a communication channel have mainly to do with the fact that the channel characteristics are very dynamic due to the many branches of the network, electrical equipment connected to the network and the varying cable diameters that are found in different sections of the grid. The various electrical equipment connected to the power network are a source of noise especially during switch ON/OFF. And again the different branching nodes in the network form reflection points for the signal which results in signal fading. The power network channel therefore suffers from two main impairments; reflections and temporal variations, and noise. Given the structure of a typical power network, communication signals suffer from many reflections resulting in a complex echo scenario and in turn frequency-dependent attenuation occurs [1–5].

Powerline communications (PLC) technology enables the double utilization of the power grid to deliver both communication and power services. Smart grid technologies that PLC supports include remote meter reading, load management and control, and power equipment monitoring, among a plethora of other applications. Most of the smart grid services utilize narrowband PLC technologies which operate in low frequencies and the data rates are low. Narrowband PLC technologies operate between the frequencies 3 kHz–500 kHz, with provision of data rates of up to a few kbps for single carrier cases and up to 800 kbps in multicarrier cases. However, in the recent times, PLC research has been mainly concentrated on broadband PLC technologies. This kind of shift in focus has been motivated by the possible utilization of the PLC channel (power grid) to deliver higher data rate broadband content like internet and video services. Broadband PLC or high frequency PLC operates between 1.8 MHz–250 MHz and provides data rates of up to 200 Mbps for home area networks. This PLC technology is also widely used in the networking of in-home equipment and delivery of high definition television services [1, 2, 5].

Noise in power line networks is completely different from the classical additive white Gaussian noise (AWGN) found in many other communication systems. The noise in power line networks is additive, non-white and non-Gaussian. There are three different classes of noise in power line networks, namely: colored background noise, narrowband interference and appliance (impulsive) noise. The colored background noise together with the narrowband interference constitutes what is generally referred to as background noise. On the other hand, appliance noise manifests itself in

three forms: impulsive noise that is periodic and synchronous with the mains cycle, periodic noise that is asynchronous with the mains cycle and finally non-periodic noise which is sporadic (random). Impulsive noise is the most severe type of noise and is the cause of channel degradation in many PLC systems. Impulsive noise levels can be up to 50 dB above the average background noise. PLC noise has also been studied by various authors both in frequency and time domain. Some of the time domain noise measurements, analysis and modelling have been carried out by several authors among them Chan and Donaldson [6], Degardin et al. [7], and Zimmermann and Dostert [8]. These authors have emphasized on noise properties like pulse width, arrival time and inter-arrival times, and therefore not much work has been done to characterize the noise amplitudes. In this paper, we introduce an alternative modelling approach for the measured instantaneous noise amplitudes in the time domain for indoor PLC networks. We statistically fit the instantaneous noise amplitudes using the kernel density method and then develop a stable distribution model using the kernel model as the reference model. The measurements are carried out in different rooms in the Department of Electrical, Electronic and Computer Engineering building, University of KwaZulu-Natal, Howard College, Durban, South Africa.

2. THE KERNEL DENSITY METHOD AND STABLE DISTRIBUTIONS

The kernel density method belongs to a class of density estimation tools that are non-parametric. That is to say that the estimates obtained using the kernel density methods are purely data-based with no particular form of the probability density function (pdf) being assumed. Thus, the kernel method produces the least error when compared to parametric methods which model data sets via a fixed set of parameters whose final outlook cannot be altered. The kernel density is defined by the following equation [9]:

$$f(x) = \frac{1}{nh} \sum_{i=1}^n K\left(\frac{x - X_i}{h}\right) \quad (1)$$

where n is the number of data points, h is the smoothing parameter, X_i is the i th data point and $K(\cdot)$ is the kernel function. On the other hand, the stable distribution is parametric and is defined by its characteristic function, $\emptyset(t)$, given as [10–13]:

$$\emptyset(t) = \begin{cases} \exp\left\{i\delta t - \gamma^\alpha |t|^\alpha \left[1 - i\beta \operatorname{sgn}(t) \tan \frac{\pi\alpha}{2}\right]\right\}, & \alpha \neq 1 \\ \exp\left\{i\delta t - \gamma |t| \left[1 + i\beta \frac{2}{\pi} \operatorname{sgn}(t) \ln |t|\right]\right\}, & \alpha = 1 \end{cases} \quad (2)$$

where, $\operatorname{sgn}(t)$ is the signum function and; $-\infty < \delta < \infty$, $\gamma > 0$, $0 < \alpha \leq 2$, $-1 \leq \beta \leq 1$. δ is the location parameter, γ is the dispersion parameter, α is the characteristic exponent and β is the symmetry parameter. Thus, the stable distribution is very flexible modelling tool that is controlled by the four parameters defined in Equation (2). Also, this distribution models the tail probabilities very well, an aspect that is taken care of by the characteristic exponent. Additionally, this distribution can model any degree of skewness that any data distribution may possess, an aspect that is taken care of by the symmetry parameter. The dispersion parameter models the data spread around the mean or median value. Finally, the location parameter determines the shift in the data peak. However, the closed form expression for the pdf of this distribution does not exist, and therefore it is entirely defined by the characteristic function. Hence, the four parameters that define the characteristic function have to be determined for any model. Different techniques have been proposed for the estimation of these four parameters, among them, the techniques based on extreme value theory, fractional lower moments and order statistics by Tsihrintzis and Nikias [10], the Fourier based techniques of Kogon and Williams [11] and Koutrouvelis [12], and the percentile method by McCulloch [13]. Above all, the alpha stable distribution, being a Gaussian distribution general case, is a very attractive tool for modelling phenomena that is impulsive, because it satisfies the stability property and the generalized central limit theorem.

3. MEASUREMENT METHODOLOGY, RESULTS AND DISCUSSION

Comprehensive time domain noise measurements were carried out in the Department of Electrical, Electronic and Computer Engineering building in different offices and laboratory rooms. The noise was measured using a Tektronix TDS 2024B four channel digital storage oscilloscope. A locally designed coupler was used to isolate the measurement equipment from the ac mains and filter the noise from the power lines. The noise measurement campaign was carried out for a period of eight

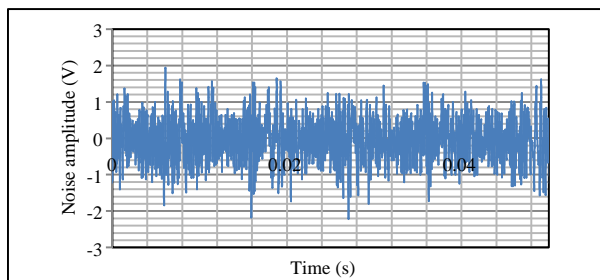


Figure 1: Noise waveform captured in an office.

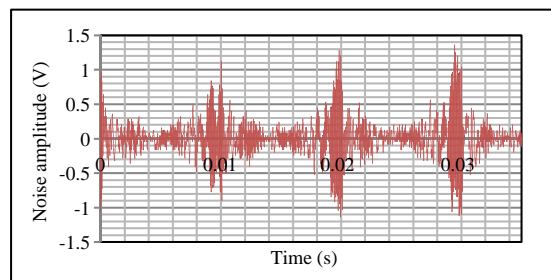


Figure 2: Noise waveform captured in a laboratory.

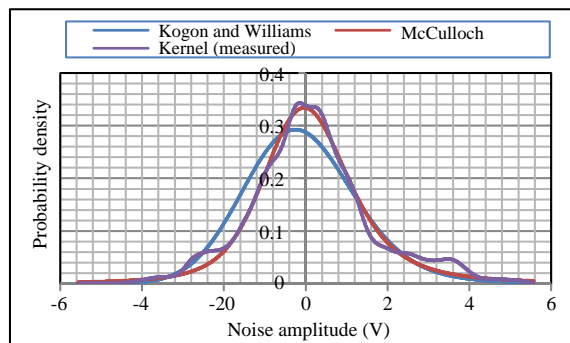


Figure 3: Alpha stable noise models.

months. Additional noise measurements were carried out in an indoor test bed environment with a 230 V 50 Hz uninterruptible power supply (UPS) used to isolate the test bed from the ac mains. Some of the noise waveform measured in different rooms are shown in Figures 1 and 2 above. Figure 1 shows the noise waveform obtained in an office room that has a printer, several desktop computers and air conditioners. Figure 2, on the other hand, shows the noise waveform measured in a laboratory which houses an anechoic chamber, and several desktop computers, lighting tubes. From Figure 1, we see that the noise measured at the office is very sporadic and does not display any periodic or synchronism features with respect to the ac mains. However, the noise measured in Figure 2 displays periodic features such that its period is half that of the ac mains, that is $T = 0.01$ sec, or $F = 100$ Hz.

From the numerous instantaneous noise amplitudes obtained, the measured pdf was developed using the kernel density technique. The pdf is shown in Figure 3, together with other parametric models developed. From this figure, we see that the pdf tails are heavier than those of the Gaussian distribution. These heavy tails are a confirmation that the measured noise contains both background and impulsive components. The heavy tails are a representative of the impulsive component of the measured noise. Such heavy tails can be modeled using the alpha stable distribution, since the heaviness of the tails can be sufficiently modeled with the right value of the characteristic exponent.

4. NOISE CHARACTERIZATION AND MODELING

From the heavy-tailed characteristic of the measured noise distribution, and for the reasons explained in Section 2 above, we have chosen the alpha stable distribution to develop a PLC noise model for indoor power networks. Since the closed form of the alpha stable pdf does not exist, but the closed form of the characteristic function exists, we have to determine the four characteristic parameters that define the PLC noise model. Two methods are used in this paper to estimate the four parameters of the noise model. These are: the Fourier based method of Kogon and Williams [11] and the quantile (percentile) method of McCulloch [13]. McCulloch's method has less computational intensity when compared with empirical characteristic function (ECF) based Fourier methods. For this method, five pre-determined sample percentiles, that are accompanied by tables, for $\beta (-1, 1)$ and $\alpha (0.6, 2.0)$, are used to consistently estimate the four parameters of the stable distribution. First we estimate the characteristic exponent α and the symmetry parameter

β using the percentiles of the empirical distribution. We define:

$$v_\alpha = \frac{x_{0.95} - x_{0.05}}{x_{0.75} - x_{0.25}}, \quad v_\beta = \frac{x_{0.95} + x_{0.05} - 2x_{0.25}}{x_{0.95} - x_{0.05}} \quad (3)$$

where x_p is the empirical distribution p th percentile, having $v_\alpha = \phi_1(\alpha, \beta)$ and $v_\beta = \phi_1(\alpha, \beta)$, or by way of inversion, $\alpha = \psi_1(v_\alpha, v_\beta)$ and $\beta = \psi_2(v_\alpha, v_\beta)$. Also,

$$\psi_1(v_\alpha, v_\beta) = \psi_1(v_\alpha, -v_\beta) \quad (4)$$

Bi-linear interpolation to estimate α and β is then carried out using tables developed for the functions $\psi_1(\cdot)$ and $\psi_2(\cdot)$ for different values of v_α and v_β . Similarly, the location parameter δ and the dispersion parameter γ are estimated using the corresponding tabulated functions and the previous estimates for α and β .

Kogon and Williams method is a modified Fourier based technique that eliminates the need for the cumbersome iterations required in Koutrouvelis technique. This is achieved by making a choice of the interval on the ECF which is robust over a wide range sample sizes on a given parameter space. The method's performance is at par with Koutrouvelis method and at the same time reduces the amount of computation intensity and the need for an interval look-up table. Here the parameter estimator is derived by considering the log-characteristic function, given by:

$$\Psi(\omega) = -|c\omega|^\alpha + j \left(\delta\omega + |c\omega|^\alpha \beta \frac{\omega}{|\omega|} \tan \frac{\pi\alpha}{2} \right) \quad (5)$$

where c is the dispersion (spread) parameter. In this case, since α is never unity in practice, the real and imaginary components of the log-characteristic function are given by:

$$\text{Re}[\Psi(\omega)] = -|c\omega|^\alpha = -c^\alpha |\omega|^\alpha \quad (6)$$

$$\text{Im}[\Psi(\omega)] = \left(\delta\omega + |c\omega|^\alpha \beta \frac{\omega}{|\omega|} \tan \frac{\pi\alpha}{2} \right) \quad (7)$$

Again, a further manipulation of the real portion of the log-characteristic can be done by taking another logarithm as follows:

$$\text{In}\{-\text{Re}[\Psi(\omega)]\} = \alpha \text{In}|\omega| + \alpha \text{In}c \quad (8)$$

The estimation of the parameters of a stable distribution of any signal that is random, $x(n)$ is done by computing the ECF and then fitting it to the parameterized characteristic function in a least squares (LS) sense. In this case, we define the ECF as follows:

$$\Phi'(\omega) = \frac{1}{N} \sum_{n=1}^N e^{j\omega x(n)} = \frac{1}{N} \sum_{n=1}^N \cos[\omega x(n)] + j \sin[\omega x(n)] \quad (9)$$

where N is the noise $x(n)$ sample size. Since, $\Psi'(\omega) = \text{In}\Phi'(\omega)$, both the log-ECF real and imaginary parts are the obtained from the ECF as follows:

$$\text{Re}[\Psi'(\omega)] = \text{In}|\Phi'(\omega)| \quad (10)$$

$$\text{Im}[\Psi'(\omega)] = \text{Arctan}\left(\frac{\text{Im}[\Phi'(\omega)]}{\text{Re}[\Phi'(\omega)]}\right) \quad (11)$$

where $\text{Arctan}(\cdot)$ is the principal value of the arctangent function. Making use of Equation (8), we then obtain the estimates of the characteristic component α' and the spread parameter c' with a LS fit on the following equation:

$$\text{In}\{-\text{Re}[\Psi'(\omega)]\} = \alpha' \text{In}|\omega| + \alpha' \text{In}c' \quad (12)$$

α' is the slope of $\text{In}\{-\text{Re}[\Psi'(\omega)]\}$ versus $\text{In}|\omega|$ plot and $\alpha' \text{In}c'$ is the y intercept of the same plot. Once α' and c' have been determined, we then estimate β' , the index of symmetry and δ' , the location parameter by computing the LS fit to Equation (7), for the log-ECF imaginary part as:

$$\text{Im}[\Psi'(\omega)] = \left(\delta'\omega + \beta' |c'\omega|^{\alpha'} \frac{\omega}{|\omega|} \tan \frac{\pi\alpha'}{2} \right) \quad (13)$$

Table 1: Alpha stable model parameters.

Method	α	β	γ	δ
McCulloch	1.469	0.238	0.844	0.231
Kogon and Williams	1.859	1	0.964	-0.002

Table 2: Model ISE errors.

Mode	ISE
McCulloch	0.172
Kogon and Williams	0.831

The alpha stable model parameters obtained using the two methods are shown in Table 1, and the models are shown in Figure 3.

From Table 1, we see that the values of the symmetry parameter for the two methods are very different from each other. The value of this parameter for Kogon and Williams's method implies that the model is fully skewed to the left. However, from Figure 3, we see that the model matches very well with both the measured model and that obtained using McCulloch's method. This is to say that as $\alpha \rightarrow 2$, the value of β doesn't matter. In this case we see that $\alpha = 1.86$, which is close to 2. The other parameters are not very different from each other for the two models. However, to determine which of the two models is optimum, we validate the models through error analysis. The error criterion employed is the integral of square error (ISE). The errors obtained are shown in Table 2. From Table 2, we see that the errors obtained are small, which means that the models obtained are a good fit to the measured data. Also, the least error is obtained for the McCulloch method, from which we conclude that this model is the best fit for the measured noise characteristics.

5. CONCLUSION AND FUTURE WORK

Communication networks suffer from degraded channel performance due to noise. This noise manifests itself in different forms. In this paper, we have developed a time domain noise model for the PLC network based on channel measurements. This model is necessary for the optimal design of receiver structures and modulation schemes for power line communications. Further measurements and alternative modeling approaches should be explored to ascertain the validity of the outcomes in the current research work.

REFERENCES

1. Galli, S., A. Scaglione, and Z. Wang, "For the grid and through the grid: The role of power line communications in the smart grid," *Proceedings of the IEEE*, Vol. 99, No. 6, 998–1027, Jun. 2011.
2. Nyete, A. M., T. J. O. Afullo, and I. Davidson, "Performance evaluation of an OFDM-based BPSK PLC system in an impulsive noise environment," *PIERS Proceedings*, 2510–2513, Aug. 25–28, Guangzhou, 2014.
3. Mosalaosi, M. and T. J. O. Afullo, "Broadband analysis and characterization of noise for in-door power-line communication channels," *PIERS Proceedings*, 719–723, Aug. 25–28, Guangzhou, 2014.
4. Philipps, H., "Performance measurements of powerline channels at high frequencies," *Proceedings of the International Symposium on Power Line Communications and Applications*, 229–237, Tokyo, Japan, Mar. 1998.
5. Nyete, A. M., T. J. O. Afullo, and I. Davidson, "On Rayleigh approximation of the multipath PLC channel: Broadband through the PLC channel," *2014 SATNAC Proceedings*, 265–270, Port Elizabeth, South Africa, Aug. 31–Sep. 3, 2014.
6. Chan, M. H. L. and R. W. Donaldson, "Amplitude, width, and interarrival distributions for noise impulses on intrabuilding power line communication networks," *IEEE Transactions on Electromagnetic Compatibility*, Vol. 31, No. 3, 320–323, Aug. 1989.
7. Degardin, V., M. Lienard, A. Zeddami, F. Gauthier, and P. Degauque, "Classification and characterization of impulsive noise on indoor power line used for data communications," *IEEE Transactions on Consumer Electronics*, Vol. 48, No. 4, 913–918, Nov. 2002.
8. Zimmermann, M. and K. Dostert, "Analysis and modeling of impulsive noise in broad-band powerline communications," *IEEE Transactions on Electromagnetic Compatibility*, Vol. 44, No. 1, 249–258, Nov. 2002.
9. Nyete, A. M. and T. J. O. Afullo, "Seasonal distribution modeling and mapping of the effective earth radius factor for microwave link design in south africa," *Progress In Electromagnetics Research B*, Vol. 51, 1–32, 2013.

10. Tsihrintzis, G. A. and C. L. Nikias, “Fast estimation of the parameters of alpha-stable impulsive interference,” *IEEE Transactions on Signal Processing*, Vol. 44, No. 6, 1492–1503, 1996.
11. Kogon, S. M. and D. B. Williams, “On the characterization of impulsive noise with alpha-stable distributions using Fourier techniques,” *1995 Conference Record of the Twenty-Ninth Asilomar Conference on Signals, Systems and Computers*, 787–791, Oct. 30–Nov. 1, 1995.
12. Koutrouvelis, I. A., “Regression-type estimation of the parameters of stable laws,” *Journal of the American Statistical Association*, Vol. 75, No. 372, 918–928, Dec. 1980.
13. McCulloch, J. H., “Simple consistent estimators of stable distributions parameters,” *Commun. Stat.-Simula.*, Vol. 15, No. 4, 1109–1136, 1986.

Wireless Transmission of Electromagnetic Energy Based on a Time Reversal Approach for Indoor Applications

R. Ibrahim^{1,2}, B. Allard¹, A. Breard¹, J. Huillery¹, C. Vollaire¹, D. Voyer¹, and Y. Zaatar²

¹Université de Lyon, Ampère (CNRS UMR 5005, École Centrale de Lyon, INSA-Lyon, UCBL)
Écully Cedex F-69134, France

²LPA, Lebanese University Faculty of Sciences 2, Campus Fanar, Jdeidet BP 90656, Lebanon

Abstract— An original approach based on a time reversal technique is proposed to fabricate a wireless transmission of electromagnetic energy for indoor applications. Experiments performed in a low- Q cavity of human size with a carrier frequency around 2.45 GHz show that the energy efficiency is greater than the one obtained with a continuous wave approach.

1. INTRODUCTION

Most of the recent developments in wireless transmission of electromagnetic energy are concentrated on systems designed to harvest the electromagnetic energy disseminated by common wireless systems such as Wi-Fi networks. However, the intermittent and unpredictable nature of these ambient sources makes energy harvesting critical for some applications [1]. In scenarios where the energy is transmitted intentionally, systems using continuous waves (CW) are not necessarily the most efficient. We investigated an alternative approach based on time reversal (TR) which was found to be promising for indoor applications. TR using electromagnetic waves was first demonstrated a decade ago [2, 3]. The implementation of this technique in indoor environment needs two stages. In a first stage called *learning stage*, a low energy pulse is transmitted through an antenna. At another place in the room, the receiver antenna records a signal constituted by a succession of many delayed pulses, more or less attenuated and related to the reflections in the medium. In a second stage called *time reversal stage*, a high energy signal built from the TR of the signal recorded during the learning stage is transmitted through one of the antennas. It follows that the time reversed waves focus spatially and temporally on the receiver antenna. These properties are particularly attractive for energy recovery. Moreover, the energy efficiency increases when the medium becomes more and more complex what makes this approach suitable for indoor applications. The paper is organized as follow: Section 2 details are given concerning the experiments performed inside a low- Q cavity. Section 3 a comparison of the energy performance is made between wireless transmissions based on the TR and CW approaches.

2. EXPERIMENTAL SETUP

2.1. Equipment

The experiment consists of transmitting electromagnetic waves between two antennas placed inside a low- Q cavity of human size ($2.45\text{ m} \times 2.45\text{ m} \times 2.45\text{ m}$) that is supposed to reproduce indoor conditions in terms of both losses and lifespan of waves in the medium. Two obstacles have been positioned between them to avoid a direct path (Figure 1). Even though, resonance related to cavity modes can be observed. This phenomena is illustrated in Figure 2 by the measurement of the transmission parameter between both antennas using a vector network analyzer. In order to perform TR, specific characteristics are required for the antennas. First large band antennas are necessary since nanosecond pulses with a frequency carrier of 2.45 GHz are handled. Second the radiation pattern of the antennas has to be omni-directional in order to investigate reflections in all the directions inside the room. Our choice focused on tap monopoles [4] since these antennas exhibit suitable properties and are easy to manufacture. A waveform generator Tektronix AWG7122C is used to transmit the different signals. This generator is particularly useful in the time reversal stage during which the manipulated signals have a complex shape. Note that the sampling frequency was set to 12 GHz, which is large enough compared to the limit defined by Shannon's theorem. The maximum output voltage of the generator is 1 V peak to peak (pk-pk) but this is not enough to transmit measurable signals because of the losses inside the room. Consequently, an amplifier with a gain value of 20 dB has been added in the transmission line. In reception, the signals are recorded using a digital oscilloscope Tektronix DPO70604C with sufficient capabilities: signals with 50000 samples can be recorded with a sampling frequency up to 25 GHz and an analogical bandwidth of 6 GHz.

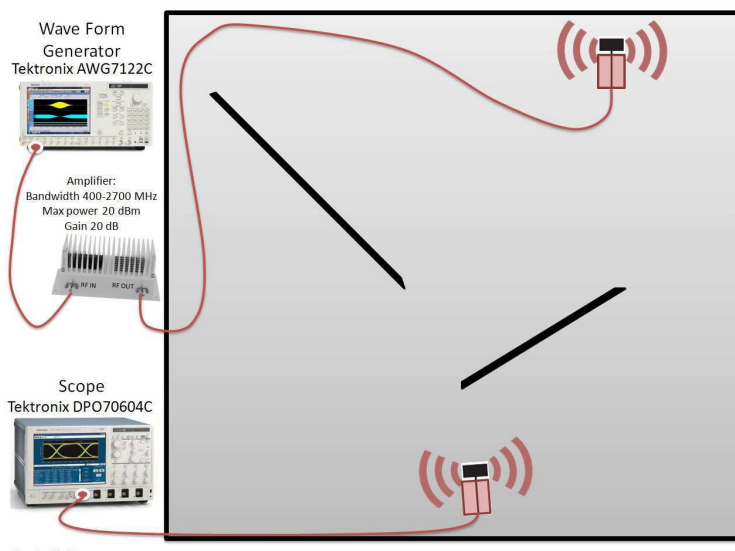


Figure 1: Top view of the cavity with the position of tap antennas and possible obstacles.

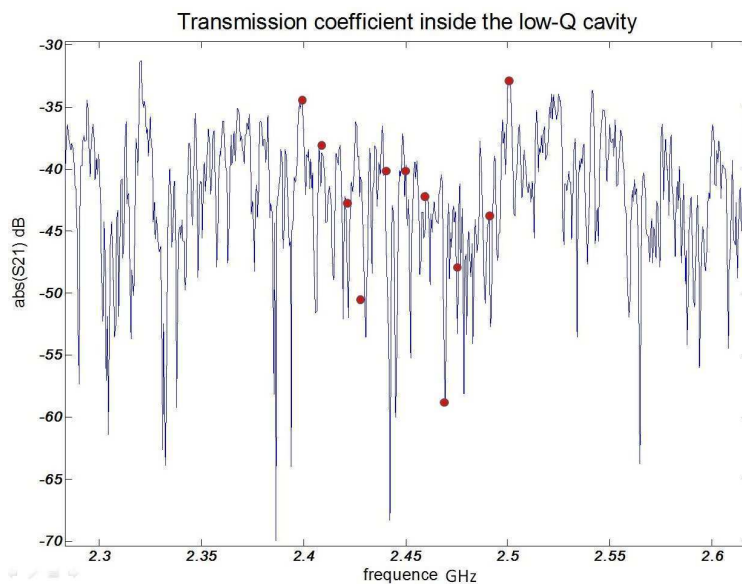


Figure 2: Response of the low- Q cavity between 2.3 GHz and 2.6 GHz. The red points mark the value of the frequency carriers chosen for the experiments see Section 3.

2.2. Time Reversal Procedure

As it is mentioned in the introduction, the TR technique is implemented following two steps (Figure 3):

- *Learning stage*

A 10 ns pulse with a carrier frequency of 2.45 GHz and an amplitude of 10 V pk-pk is transmitted through the first antenna. A hamming window has been applied such that the frequency bandwidth of the signal is 400 MHz. This signal is called $x(t)$.

In reception, a complex signal $y(t)$ with a time length of approximately 2 μ s and a maximum amplitude of 20 mV pk-pk is recorded using the digital oscilloscope. This signal is constituted of successions of delayed and attenuated reflections inside the room that provide information on the complexity of the medium.

- *Time reversal stage*

Numerical processing is applied on the signal $y(t)$ using Matlab. First a frequency filtering is performed with a Butterworth's bandpass filter to eliminate the noise outside the bandwidth

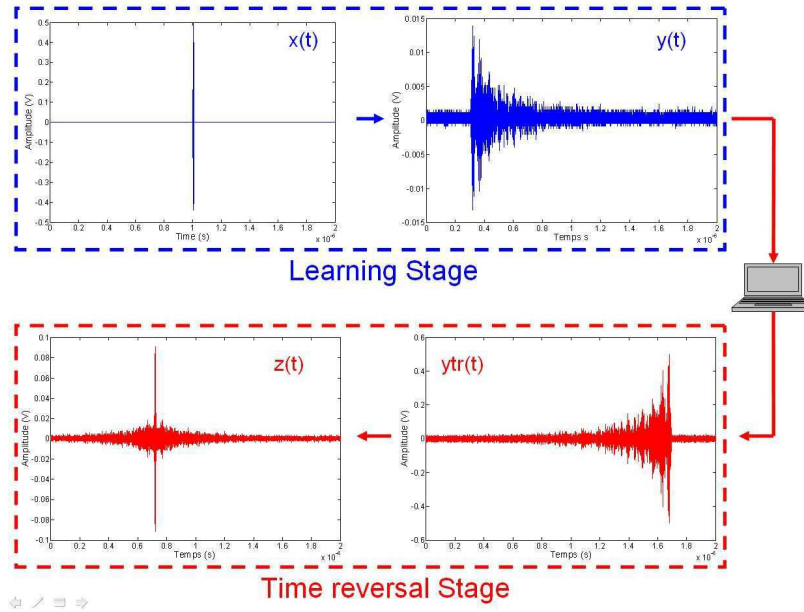


Figure 3: Steps of time reversal scheme with signal waveforms.

from 1.5 GHz to 3.5 GHz. Then the time reversal is applied. At this step, the reversed signal $y_{tr}(t)$ is transmitted from the second antenna so that the reversed waves propagate through the same path as in the learning stage but in the reverse direction. These waves are expected to converge in phase on the first antenna and build a constructive signal. But for some practical reasons, we use the same configuration as during the learning stage. The reversed signal is transmitted through the first antenna to the second. This is possible because of the reciprocity in the medium. Reciprocity implies that the received signal is the same whatever $y_{tr}(t)$ is transmitted by the first antenna or by the second one. Note that the signal $y_{tr}(t)$ generated by the waveform generator is normalized to 1 V pk-pk and the maximum amplitude of the reversed signal at the output of the amplifier is 10 V pk-pk like in the learning stage.

In reception one observes a signal $z(t)$ in which a 10 ns pulse with an amplitude of 200 mV pk-pk is recovered, this amplitude is approximately 10 times the one measured during the learning stage.

2.3. Continuous Wave Procedure

Experiments have also been performed with common wireless transmission using CW. In that case, a sinusoidal signal with an amplitude V_1' pk-pk (the voltage considered here is the one at the output of the amplifier for about 10 V) and a frequency carrier from 2.4 GHz to 2.5 GHz with a step of 0.1 GHz is transmitted by the first antenna. In reception, one measures a sinusoidal signal with an amplitude V_2 pk-pk at the frequency carrier considered.

2.4. Energy Performance Definition

The efficiency of the TR scheme has to be defined. In the experimental setup detailed in Section 2.2, the signals transmitted during the learning and time reversal stages are normalized to the same amplitude. However if one is concerned about energy performance, the learning stage should be performed using a very low energetic signal $x(t)$. Indeed, this step consists of collecting information about the medium and the amplitude of the signal is chosen based on signal to noise ratio considerations. This is why the energy of $x(t)$ is ignored in the energy performance evaluation. On the contrary, the energy E_z of the pulse recovered in reception during the time reversal stage is related to the energy $E_{y_{tr}}$ of the reversed signal $y_{tr}(t)$. However the amplifier has to be taken into account. The transmitted energy is the one carried by the signal y_{tr}' generated at the output of the amplifier. E_z should be calculated at a time interval where the signal is focused supposed to be equal to the period of time for the signal emitted in learning stage, separately from $E_{y_{tr}'}$ that must be calculated including all the signal emitted at interval of 2 μ s. Thus, the energy performance for

the TR is defined by:

$$\eta_{TR} = \frac{E_z}{E_{y_{tr}'}} = \frac{\int_{10 \text{ ns}} z(t)^2 dt}{\int_{2 \mu s} y_{tr}'(t)^2 dt} \quad (1)$$

The computation of η_{TR} is realized using Matlab. Concerning the evaluation of E_z , the recovered pulse is localized in the signal $z(t)$ and the energy is computed inside a window of 10 ns that includes the pulse. Concerning the evaluation of $E_{y_{tr}'}$, one should measure the signal y_{tr}' at the output of the amplifier. But for practical reasons, we made the computations from the signal y_{tr} built during the time reversal stage (Section 2.2). The signal y_{tr}' can approximatively be synthesized multiplying y_{tr} by a factor of 10 in order to take into account the amplification gain of 20 dB. The gain of the amplifier varies between 18 and 20 dB over the bandwidth of y_{tr} . A more precise approach consists of using the frequency response of the amplifier to compute the energy in y_{tr}' . This operation has been implemented using the discrete Fourier transform (Matlab) and the frequency response of the amplifier measured with a Vectorial Network Analyzer.

Since periodic signals are considered, the energy performance η_{CW} can be computed from power considerations, P_1 and P_2 considered as the power related for signal transmitted and received as described in Section 2.3:

$$\eta_{CW} = \frac{P_2}{P_1'} = \frac{V_2^2/8}{V_1'^2/8} = \frac{V_2^2}{V_1'^2} \quad (2)$$

3. EXPERIMENTAL RESULTS

In order to evaluate the strength of the wireless transmission, experiments for CW and TR have been performed for different sets of carrier frequency ranging from 2.4 GHz to 2.5 GHz see Figure 2.

3.1. Energy Performance for TR and CW Wireless Transmissions

Figure 4 shows the voltage measured in reception for TR and CW transmissions for different carriers frequency. In the case of TR, both the learning and time reversal maximum value of the received signal are reported. It is observed that the received amplitude after time reversal stage is 6 to 10 times higher from that of the learning stage.

In the case of CW transmission, one can observe that the voltage recovery strongly varies with the frequency. This behavior is due to the resonance of the cavity reported in Figure 2. In the case of TR transmission, the voltage recovery is nearly insensitive to the effect. This is particularly striking during the learning stage and a little bit less during the time reversal stage. This result is due to the spectral properties of the signals at hand: a 10 ns pulse with a hamming window being characterized by a bandwidth of 400 MHz, a large range of frequency is investigated inside the cavity and the effects of the resonances are attenuated.

Results in term of energy performance are reported in Table 1. It appears that the absolute value of the energy performance is very weak for both CW and TR wireless transmissions. This is due to the losses inside the low- Q cavity and to the presence of obstacles between the antennas.

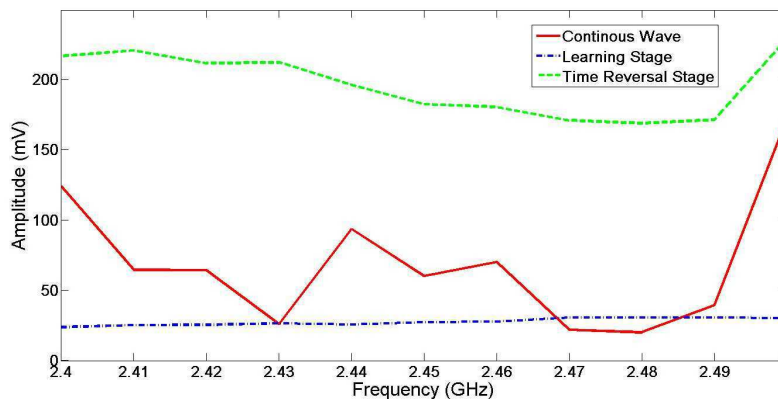


Figure 4: Voltage recovery (pk-pk) for CW and TR with different frequency carriers.

Table 1: Energy performance for CW and TR at different frequency carriers.

Frequency (GHz)	2.4	2.41	2.42	2.43	2.44	2.45	2.46	2.47	2.48	2.49	2.5
$\eta_{TR} (\times 10^{-4})$	2.8	3.0	2.7	2.7	2.3	2.3	2.5	2.3	2.4	2.4	2.4
$\eta_{CW} (\times 10^{-4})$	2.2	0.6	0.6	0.1	1.3	0.5	0.7	0.07	0.06	0.2	4.2
η_{TR}/η_{CW}	1.2	5.0	4.5	28.3	1.8	4.5	3.5	34.0	42.1	10.8	0.6

The efficiency depends strongly on the frequency in the case of CW transmission; this result is in agreement with the previous analysis concerning the voltage recovery. The comparison between CW and TR transmissions shows that TR transmission is generally more efficient than CW transmission: the gain in energy performance η_{TR}/η_{CW} is 4.5 at the frequency carrier of 2.45 GHz. It reaches 42.1 at the frequency carrier of 2.48 GHz. CW transmission can sometimes be more efficient: as it can be observed at the carrier frequency of 2.50 GHz. In this case the gain in energy performance is 0.6. The mean value of the gain in energy performance η_{TR}/η_{CW} calculated for the 11 frequency points reported in Table 1 is 12.4.

4. CONCLUSION

In this paper, it has been demonstrated that TR is a promising technique for wireless transmission of energy using electromagnetic waves for indoor applications. Experiments made inside of low- Q cavity of human size showed that the energy performance is in average about 10 times more efficient than for wireless transmission using CW. In this later case, there is a sensitivity with respect to the carrier frequency. The extreme situations observed for CW transmission are related to resonances inside the cavity. For future research, the spatial dimensions will have to be taken into account. A strong voltage recovery at one place inside the cavity leads to a low recovery at some other places inside the cavity due to the presence of nodes and anti-nodes. Concerning TR, the behavior is dramatically different. In addition with the temporal focusing, a spatial focusing is expected with a focal spot theoretically limited to a size of about one wavelength.

REFERENCES

1. Krikidis, I., S. Timotheou, S. Nikolaou, G. Zheng, D. W. K. Ng, and R. Schober, "Simultaneous wireless information and power transfer in modern communication systems," *IEEE Communications Magazine, Green Communications and Computing Networks Series*, Vol. 52, No. 11, 104–110, 2014.
2. Lerosey, G., J. De Rosny, A. Tourin, A. Derode, G. Montaldo, and M. Fink, "Time reversal of electromagnetic waves," *Physical Review Letters*, Vol. 92, No. 19, 193904, 2004.
3. Lerosey, G., J. De Rosny, A. Tourin, A. Derode, and M. Fink, "Time reversal of wideband microwaves," *Applied Physics Letters*, Vol. 88, 2006.
4. Johnson, J. M. and Y. Rahmat-Samii, "The tap monopole," *IEEE Transactions on Antennas and Propagation*, Vol. 45, No. 1, 187–188, 1997.

Use Case Analysis of Wiegand-based Energy Harvester in Mechanical Sensing Devices

Ralf Zentgraf and Ulrich Bochtler

Lab for Circuit Design, Aschaffenburg UAS, Germany

Abstract— Conventional energy harvester approaches using magnetic-inductive technologies are often realized as mass-spring systems. Due to the small resonance-bandwidth of such systems, bistable magnetic wires can be a sound solution for slow and sporadic movements. On this issue, a pressure sensor system is adapted with a so-called Wiegand-harvester to implement self-sufficient electrical feature functionalities. The Wiegand-harvester consists of an inductor coil mounted on an amorphous Vicalloy-Core (CoFeV). The large characteristic Barkhausen jump of the alloy is used to generate voltage peaks in the pickup coil in a slow changing magnetic field. Contrary to mass-spring systems or periodical induction, only the value of the coercivity field (ΔH_{ce}) is relevant for generating an energetic voltage pulse to power an electrical circuit. This technology can be used in high transients as well as in nearly static environments. A use case analysis for a pressure gauge shows the benefit of Wiegand-based systems. The power supply source is realized by placing eight harvesters circular on a PCB. Thereby a single rotation of a spindle (360°) is quantized in eight steps. A second disk equipped with eight neodymium permanent magnets is mounted parallel to the PCB. So a twist of 45° delivers a multiplied pulse in each of the eight inductor coils. An electrical energy output of approx. $13.5 \mu\text{Ws}$ and the twist-hysteresis of $0^\circ 2'$ could be achieved and verified using a magnetic FEM simulation.

1. INTRODUCTION

Motion based energy-harvesting systems using direct piezoelectric or inductive effect are often carried out as mass-spring systems. Therefore, the amount of harvested energy depends on the resonance frequency. However, systems based on large Barkhausen jumps (Wiegand effect [1, 2]) can be a sustainable solution to get voltage pulses in nearly zero speed applications. On this issue the longitudinal movement of a pressure sensor was translated to an angle of 0 to 360° . As a benefit, decentralized and battery-free sensor applications (mechanical sensing devices) can get additional electrical features by attaching a Harvesting-System based on those large Barkhausen jumps.

2. SENSOR ELEMENT

In this case a Vicalloy wire (FeCoV) with a diameter of 0.25 mm and a length of 12.5 mm was used as an energy harvesting system. Thermal and mechanical stress (tension, torsion) during the production leads to a low coercivity core and higher coercivity shell-layer (cold-worked process) [3]. Thus, the magnetization (orientation of the magnetic moment) of the layers is parallel. The exposure to an external magnetic field shows a large Hysteresis B-H-Loop plot with a characteristic jump. A high external field leads to a parallel orientation of both layers (saturation case). Initially, a saturation field applied to the sensor ensures that both layers are polarized in the same direction. As a negative field is applied the outer hard core prevent the switching of the soft layer until a sudden shift in the soft layer appears. As the strength of the external field increases, also the hard layer switches its polarity. Especially the switching of the soft layer is quite rapidly (large Barkhausen jump cf. [4–6]). This phenomenon is commonly known as the Wiegand effect.

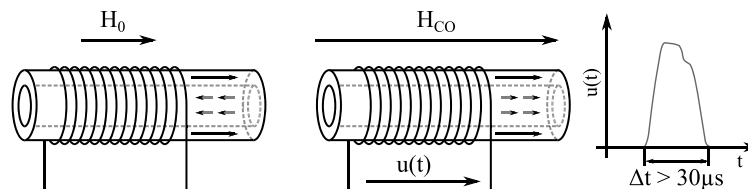


Figure 1: Domain change during increasing external magnetic field.

If a sensing coil is applied onto the wire, two different voltage pulses can be seen in one B-H loop. The voltage pulse only occurs at significant coercivity values. In contrast to classic inductive harvester technologies with ferromagnetic cores, systems based on large Barkhausen jumps are

nearly independent from the changing speed of the external magnetic flux $\frac{d\phi}{dt}$. (Equation (1)) shows the simplified output energy E_w of a harmonic induction circuit with a resistive load R_L , coil inductance L_C and windings N .

$$E_w(t) = \int_0^t \frac{N^2}{R_L + j\omega L_C} \left(\frac{d\phi(t)}{dt} \right)^2 dt \quad (1)$$

Due to the core characteristics, the parameter $\frac{d\phi(t)}{dt}$ can not be substituted by a harmonic forcing function (that depends on the characteristic jump and domain propagation). The energy output of a Wiegand system can be approximated by [7].

3. PROTOTYPE AND EXPERIMENTAL RESULTS

Mostly, non-electronic sensor are used in decentralized environment for visual monitoring or safety functionalities. An example of a use case is mechanic pressure gauge adapted on a tank to supervise the pressure. If the pressure is above a given limit, the sensor should control a safety valve. As the pressure of the tank is almost constant, a frequency optimized energy harvester is infeasible. In this case a Barkhausen sensor can be used as a sound solution to measure and control local tasks.

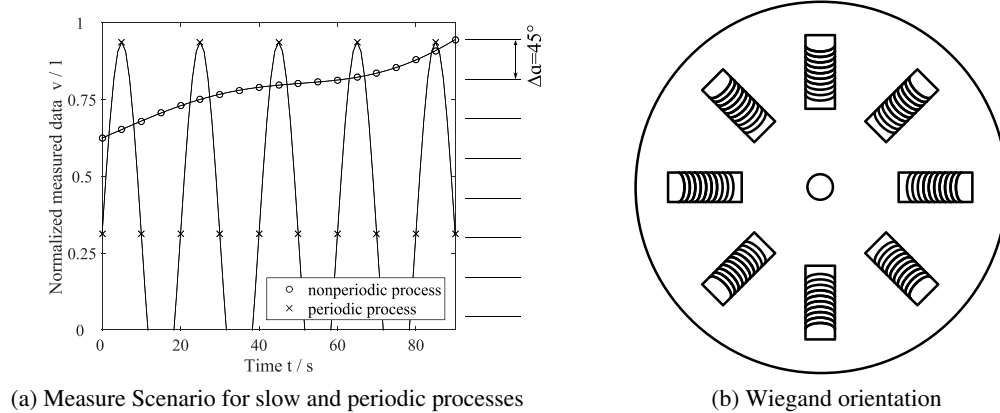


Figure 2: Measure scenario for slow and periodic processes and quantisation.

Upon the harvesting element (Co. Werap, Ch), a simple measurement application for mechanical sensing devices was developed. A small longitudinal movement (i.e., 3 mm) was translated to an full turn angular motion (Fig. 2). Two congruent disks were manufactured and positioned on top of each other. The stationary disk was assembled with eight neodymium ($\text{Nd}_2\text{Fe}_{14}\text{B}$) magnets-the moveable part is equipped with eight Wiegand-sensors. The developed prototype uses a packaged Wiegand-sensor (Co. Werap), that is not specified in detail. The eight neodymium magnets are in circular position on top of the movable disk and generate external magnetic fields upto ($H_e = 160 \frac{kA}{m}$). To minimize jitter and maximize the energy output the magnets are assembled anti-parallel. So the field gradient between the magnets is as high as possible. In this case, the rotation of 45° leads to an induction pulse in the sensing coils, which marginal depends on the rotational speed. The superposition of the eight energy pulses can be utilized to drive a small electrical circuit. In this experiment an energy output of $E_O = 13.5 \mu\text{Ws}$ by a full turn was stored in capacitors (accumulated). In this case the optimization of the power output and stabilization of the voltage is not investigated.

4. VERIFICATION AND SIMULATION

Due to the reduction of the hysteresis effect and the synchronization of the induced pulses in the sensing coils, a stationary FEM simulation of the neodymium disk (Fig. 3(b)) has been created. A high field gradient (∇H_e) between the magnets improves the synchronized pulse generation significantly. The anti-parallel orientation of the magnets ensures this behavior. As a result, the Wiegand-sensors on the stationary disk toggles between two saturation states (cf. B-H loop) quickly. The prototype shows a hysteresis, by changing the rotational direction, of approx. $0^\circ 2'$.

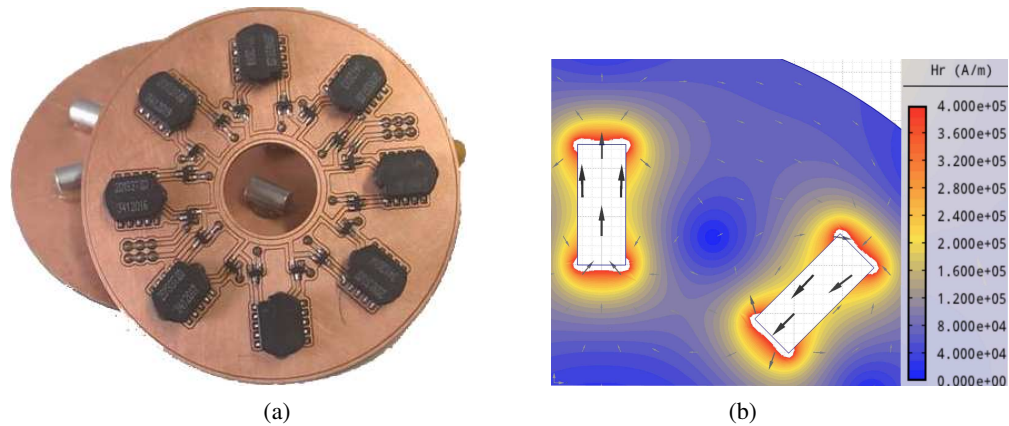


Figure 3: (a) Magnetic Harvesting PCB. (b) FEM Simulation of the neodymium magnets.

5. CONCLUSION

The experimental behavior meets perfectly the requirements for non-periodic mechanical sensors. All sensing instruments, that are converting a physical parameter (temperature, pressure etc.) into a translational or rotational movement, are suitable to be powered by such an harvesting system. Nevertheless, the energy output is not yet sufficient for powering complex electrical circuits.

ACKNOWLEDGMENT

Funding: Lab for circuit design Aschaffenburg UAS.

REFERENCES

1. Wiegand, J. R., et al., "Bistable magnetic device," U.S. Patent No. 3,820,090, 1974.
2. Wiegand, J. R., et al., "Switchable magnetic device," U.S. Patent No. 4,247,601, 1981.
3. Abe, S. and A. Matsushita, "Construction of electromagnetic rotation sensor using compound magnetic wire and measurement at extremely low frequency rotations," *IEEE Transactions on Magnetics*, Vol. 30, No. 6, 4635–4637, 1994.
4. Vazquez, M. and C. Gomez-Polo, "Amorphous and nanocrystalline wires and microwires with giant barkhausen jumps for magnetic sensor application," *Journal of the Korean Physical Society*, Vol. 31, No. 3, 471–476, 1997.
5. Takemura, Y. and M. Nishimoto, et al., "Evaluation of zero-speed sensor using NiFe/CoFe multilayer thin films and twisted FeCoV wires," *Sensors, 2004. Proceedings of IEEE*, Vol. 3, 1090–1093, 2004.
6. Takemura, Y. and T. Yamada, "Output properties of zero-speed sensors using FeCoV Wire and NiFe/CoFe multilayer thin film," *Sensors, 2004. Proceedings of IEEE*, Vol. 6, No. 5, 1186–1190, 2006.
7. Ongaro, F., S. Saggini, and L. Corradini, "Low-power energy harvester for wiegand transducers," *Applied Power Electronics Conference and Exposition (APEC), 2013 Twenty-Eighth Annual IEEE*, 453–459, 2013.

Tunable and Reconfigurable Frequency Rejection Circular Slot Antenna for UWB Communication Applications

Yingsong Li¹ and Raj Mittra²

¹College of Information and Communications Engineering, Harbin Engineering University, Harbin, China

²Electromagnetic Communication Lab, Penn State and Central Florida Universities, USA

Abstract— In this paper, a tunable and reconfigurable circular slot antenna with frequency rejection characteristics is proposed for UWB communication applications. The proposed antenna can provide triple-band-notch characteristics by using various stubs designed to filter out unwanted narrowband signals whose frequencies overlap with those of the UWB band. Center frequencies of these notch bands are tunable, and tunability is realized by adjusting the dimensions of the proposed stubs. Also, the proposed antenna has a reconfigurable frequency rejection characteristic to render the designed antenna suitable for UWB, band-notched UWB, dual band-notched UWB, tri-band-notched UWB, or multi-band communication applications. Experimental results show that the proposed antenna can provide tunability over a wide range, excellent reconfigurable frequency rejection characteristics and good omnidirectional radiation patterns, which make it attractive for indoor UWB communication applications.

1. INTRODUCTION

Even since the Federal Communications Commission (FCC) released the frequency band of 3.1–10.6 GHz for use in commercial ultra-wideband (UWB) communication systems, a large number of research studies have been directed toward UWB applications. UWB antennas are one of the crucial components for UWB communication systems and have been widely studied for many years. Recently, a wide variety of printed microstrip-fed monopole and CPW-fed UWB antennas with different configurations have been proposed to produce a broad impedance bandwidth covering the UWB band and their performance characteristics have been investigated both numerically and experimentally [1–4].

However, there exist several narrowband wireless communication systems that work in the frequency range of UWB systems such as the 3.5 GHz worldwide interoperability for microwave access (WiMAX); wireless local area network (WLAN) operating at 5.15–5.35 GHz and 5.725–5.825 GHz; and the satellite communication system operating at 8 GHz [5, 6], which may interfere with the UWB systems. Consequently, it is necessary to develop UWB antenna designs with multiple band-notch characteristics to suppress the interferences from these narrowband signals. In view of this, a large number of prototype designs for compact UWB antennas with band-notch characteristics have been presented by a number of authors [5–12]. The band-notch forming techniques reported in the literatures can be classified into three categories, namely, etching slot, stubs and parasitic strip techniques. Among these, the parasitic strip techniques including strip near patch [5], strip near ground [6] and stepped impedance resonators (SIRs) [7] are difficult to tune in practice. Many antenna designs have been carried out by embedding diverse slots in the UWB antenna designs, including those with U-shaped [8], C-shaped [9], H-shaped [8], V-shaped [10] and complementary SRR-shaped slots [11]. However, the etched slots on the radiating patch or ground plane leak electromagnetic wave, which may interfere with the adjacent radio frequency front-ends. Additionally, most of these papers are designed to generate either a single- or dual-notch band. In [12], a triple band-notched UWB antenna has been proposed by etching various slots in the radiating patch, which may excite leaky waves and, hence, limit its practical application.

Although these band-notched UWB antennas can provide designated band-notch characteristics to suppress the unwanted narrowband signal interference, they cannot cover the entire UWB band. Thus, designing a UWB antenna with desired reconfigurable characteristics is highly desired. Several reconfigurable UWB antennas have been presented by using switch techniques [13–16]; however, they are not compatible UWB antennas with triple band-notch characteristics.

In this paper, a triple band-notched UWB antenna with tunable and reconfigurable frequency rejection characteristics is proposed and its performance is investigated in detail. The triple notch-bands are generated by using an arc-shaped stub and two T-shaped stubs with an isolating element which is inserted in-between the two T-shaped stubs. The reconfigurable band-notched function is obtained by integrating five switches into the stubs. The simulated results show that the proposed

antenna can provide a wide bandwidth covering the entire UWB band, as well as a wide tunable and reconfigurable band-notched characteristic and omnidirectional radiation patterns, which render it suitable for UWB and multi-mode wireless communication applications.

2. ANTENNA DESIGN

Figure 1 depicts the configuration of the proposed tunable and reconfigurable UWB antenna with frequency rejection. The proposed antenna is fed by a coplanar waveguide and is printed on a substrate with a relative permittivity of 2.65, a loss tangent of 0.002, and a thickness of 1.6 mm. The proposed antenna consists of a wide slot with a circular shape, a circular ring radiating patch, an arc-shaped stub (AS), two T-shaped stubs (TSs), an isolation element (IE), five ideal switches integrated into the AS and TSs, and a CPW-fed structure together with a CPW ground plane. The CPW-fed structure is comprised of a CPW-fed signal strip (CFSS) with width of 3.6 mm and a gap of 0.2 mm between the CFSS and the CPW ground plane. In this study, the ideal switches are used for evaluating the proposed reconfigurable antenna and the presence of a metal bridge represents the ON state, while the absence of a metal bridge represents OFF state [13–16]. The triple band-notched function is obtained by using the arc-shaped slot and T-shaped subs, while the reconfigurable function is realized by controlling the ON/OFF states of the ideal switches.

We begin by designing a triple band-notched UWB antenna (antenna-1) and then integrate five ideal switches into this antenna to develop the reconfigurable characteristic antenna denoted as antenna-2. The proposed antenna is optimized by using the HFSS simulation code and the optimized parameters are: $L = 32$, $W = 24$, $W1 = 1.6$, $\text{Theta} = 90^\circ$, $L1 = 2$, $L2 = 2.8$, $L4 = 8.2$, $L5 = 4.8$, $d1 = d2 = d3 = d4 = d5 = 1$, $g1 = g2 = 0.5$, $R = 11.8$, $r1 = 6.7$, $r2 = 5.4$, $r3 = 10.47$, $r4 = 11.47$ (unit:mm).

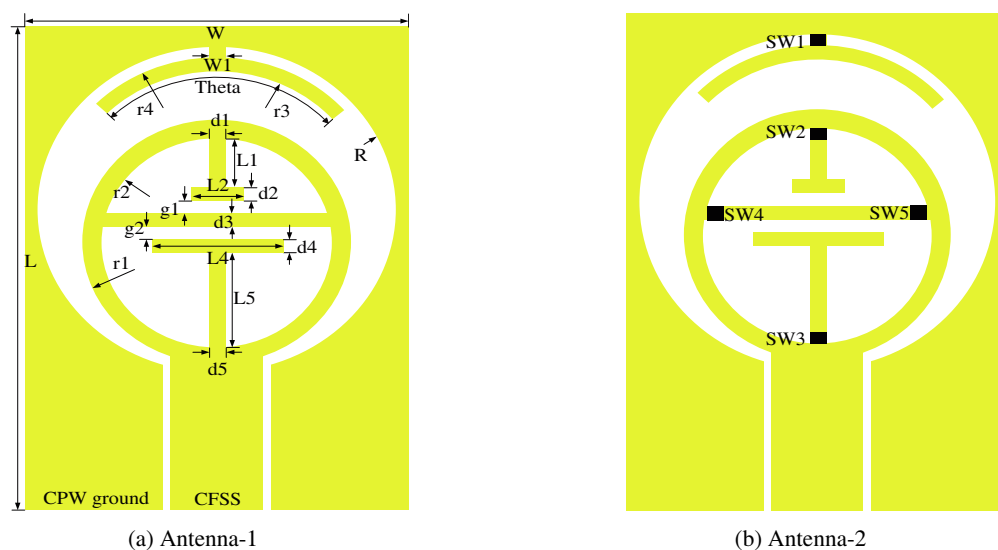


Figure 1: Configuration of the proposed antenna.

3. PERFORMANCE OF THE PROPOSED ANTENNA

In this section, tunability, reconfigurable band-notched characteristics, as well as the radiation pattern characteristics are investigated and the results are discussed in detail. Figure 2(a) shows the effects of $L5$ on the band-notch characteristics. It is observed that the center frequency of the lowest band-notch shifts from 3.9 GHz to 3.2 GHz with an increment of $L5$, which can be used to suppress the unwanted interference signal from 3.5 GHz WiMAX band. However, the center frequencies of the other two notch bands remain unchanged. In this case, increasing $L5$ increases the lower T-shaped stub, which prolongs its resonance length, which in turn modifies the location of its lowest notch band. Figure 2(b) shows the performance of the proposed antenna as the angle Theta (see Figure 1(a)) is varied. We can see that the center frequency of the middle band-notch moves to a lower frequency as we prolong the length of the AS, which can be controlled by varying the angle Theta. As Theta increases from 80° to 100° , the center frequency of the middle notch drops rapidly from 6.1 GHz to 4.8 GHz. Thus, the middle notch band can be utilized to prevent

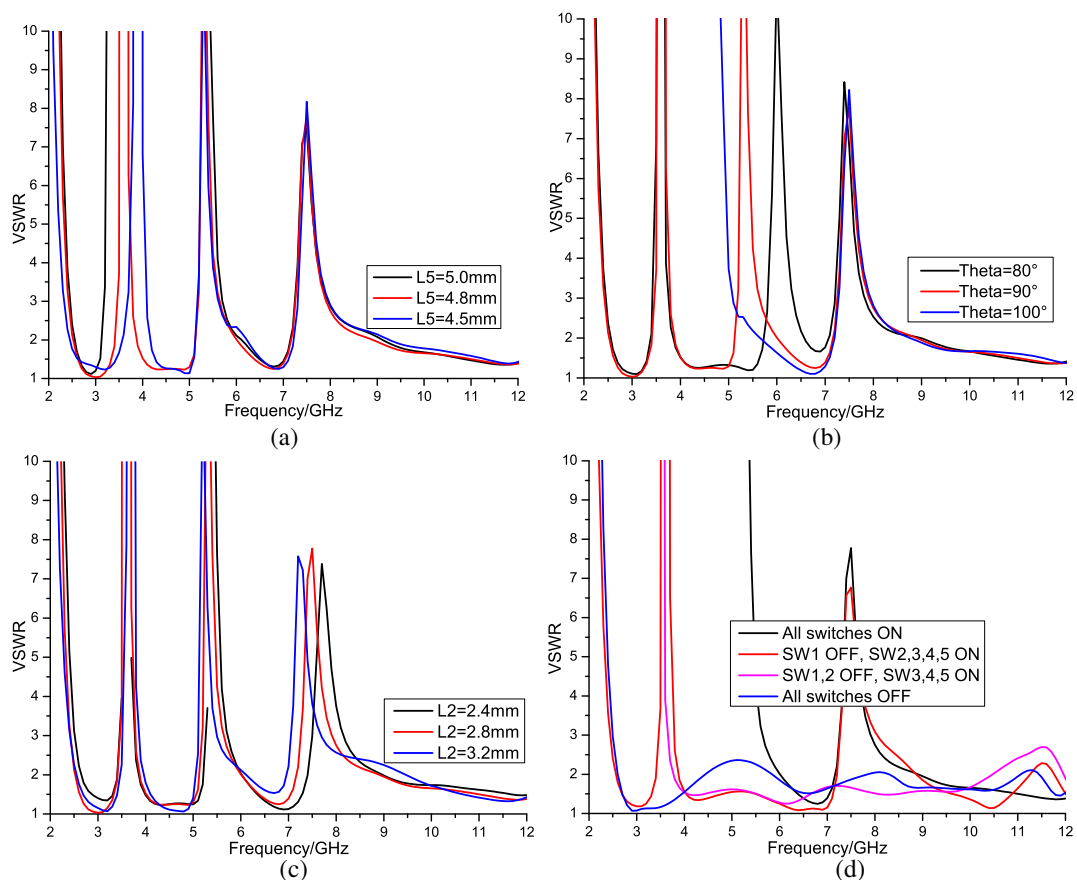


Figure 2: Parameter effects and the reconfigurable characteristics of the proposed antenna. (a) L5. (b) Theta. (c) L2. (d) Reconfigurable function.

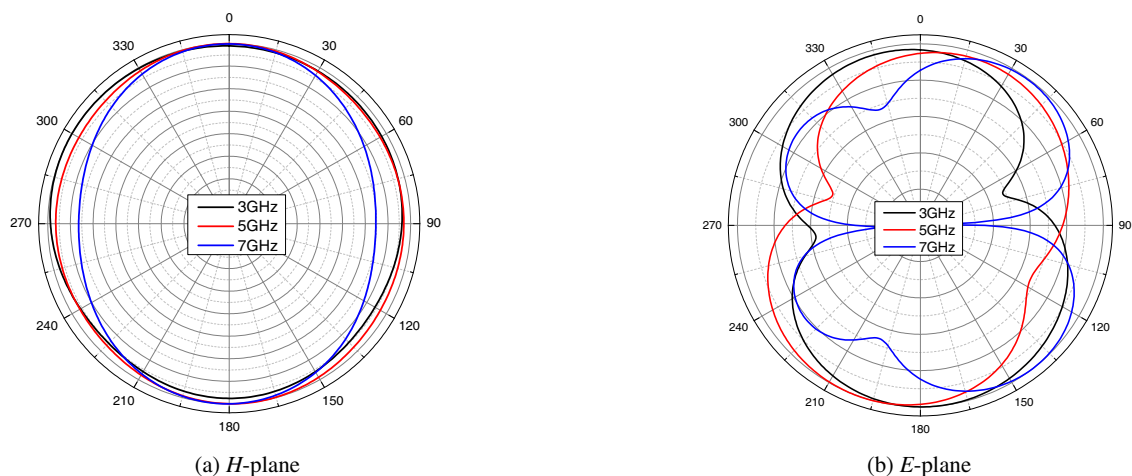


Figure 3: Radiation patterns of the proposed antenna.

the potential interference that may arise from the 5.5 GHz WLAN band. Figure 2(c) exhibits the trend of impedance bandwidth with an increment of $L2$ ranging from 2.4 mm to 3.2 mm. It is found that the center frequency of highest band-notch shifts within a range of 0.8 GHz, including the frequency band of 7.5 GHz satellite and 8.0 GHz ITU communication bands. Thus, we can conclude that the center frequencies of these three band-notches are tunable by adjusting the dimensions of the arc-shaped slot and T-shaped stubs. Figure 2(d) depicts the reconfigurable characteristics of the proposed antenna controlled by the states of the switches. When all the switches are ON, the proposed antenna is a UWB antenna with three band-notches which help to suppress the

interference from the WiMAX, WLAN and ITU bands. When SW1 is OFF and SW2, 3, 4, 5 are ON, the antenna has two band-notches at the WiMAX and ITU bands, but not at the WLAN band. As for the antenna with only SW3, 4 and 5 ON, the proposed antenna functions as a UWB antenna with a band-notch at WiMAX band. When all the switches are OFF, the antenna is a UWB antenna with a mismatch, which is caused by the coupling between the isolation element and the T-shaped stubs. The radiation patterns of the proposed antenna have been investigated for the case when all the switches are ON and are presented in Figure 3. We can see that the proposed antenna has an omnidirectional radiation pattern in the H -plane, and a figure of 8-type of radiation pattern in the E -plane.

4. CONCLUSION

A circular, wide-slot UWB antenna with tunable and reconfigurable triple band-notched characteristics has been proposed and its performance has been investigated in detail. The results show that triple notch-bands can be realized by using the arc-shaped slot and T-shaped stubs, and the tunable band-notched function is achieved by adjusting the dimensions of the slot and the T-shaped stubs. The reconfigurable band-notch characteristic has been realized by controlling the ON/OFF states of the ideal switches. Consequently, the proposed antenna can be used as a triple-band-notched UWB antenna, a dual band-notched UWB antenna, a single band-notched UWB antenna, a UWB antenna, or even a multi-band antenna, which render it suitable for UWB and multi-mode communication applications.

ACKNOWLEDGMENT

This work was supported by the Fundamental Research Funds for the Central Universities (HEUCF-D1433).

REFERENCES

1. Chen, L., S. Liu, X. Kong, B. Bian, and Z. Mao, "A novel compact UWB antenna with triple band-notched characteristics," *PIERS Proceedings*, 997–1000, Guangzhou, August 25–28, 2014.
2. Jacob, S., A. O. Lindo, C. M. Nijas, C. K. Aanandan, and P. Mohanan, "Analysis of CPW-fed UWB antenna for WiMAX and WLAN band rejection," *Progress In Electromagnetics Research C*, Vol. 52, 83–92, 2014.
3. Zaker, R. and A. Abdipour, "A very compact ultrawideband printed omnidirectional monopole antenna," *IEEE Antennas and Wireless Propagation Letters*, Vol. 9, 471–473, 2010.
4. Li, Y. S., X. D. Yang, C. Y. Liu, and T. Jiang, "Compact CPW-fed ultra-wideband antenna with band-notched characteristic," *Electronics Letters*, Vol. 46, No. 23, 1533–1534, 2010.
5. Li, Y., W. Li, and R. Mittra, "Miniaturized CPW-FED UWB antenna with dual frequency rejection bands using stepped impedance stub and arc-shaped parasitic element," *Microwave and Optical Technology Letters*, Vol. 56, No. 4, 783–787, 2014.
6. Samadi Taheri, M. M., H. R. Hassani, and M. A. Nezhad, "UWB printed slot antenna with Bluetooth and dual notch bands," *IEEE Antennas and Wireless Propagation Letters*, Vol. 10, 255–258, 2011.
7. Li, Y., W. Li, and W. Yu, "A switchable UWB slot antenna using SIS-HSIR and SIS-SIR for multi-mode wireless communications applications," *Applied Computational Electromagnetics Society Journal*, Vol. 27, No. 4, 340–351, 2012.
8. Li, Y. S., X. D. Yang, C. Y. Liu, and T. Jiang, "Compact CPW-fed ultra-wideband antenna with dual band-notched characteristic," *Electronics Letters*, Vol. 46, No. 14, 967–968, 2010.
9. Chu, Q. X. and Y. Y. Yang, "A compact ultra wideband antenna with 3.4/5.5 GHz dual band-notched characteristics," *IEEE Transactions on Antennas and Propagation*, Vol. 56, No. 12, 3637–3644, 2008.
10. Rostamzade, M., S. Mohamadi, C. Ghobadi, J. Nourinia, and M. Ojaroudi, "Square monopole antenna for UWB applications with novel rod-shaped parasitic structures and novel V-shaped slots in the ground plane," *IEEE Antennas and Wireless Propagation Letters*, Vol. 11, 446–449, 2012.
11. Kim, J., C. S. Cho, and J. W. Lee, "5.2 GHz notched ultra-wideband antenna using slot-type SRR," *Electronics Letters*, Vol. 42, No. 6, 315–316, 2006.

12. Bakariya, P. S., S. Dwari, and M. Sarkar, "Triple band notch UWB printed monopole antenna with enhanced bandwidth," *AEU — International Journal of Electronics and Communications*, Vol. 69, No. 1, 26–30, 2015.
13. Li, Y., W. Li, and Q. Ye, "A reconfigurable triple-notch-band antenna integrated with defected microstrip structure band-stop filter for ultra-wideband cognitive radio applications," *International Journal of Antennas and Propagation*, Vol. 2013, Article ID 472645, 1–13, 2013.
14. Al-Husseini, M., A. Ramadan, A. El-Hajj, K. Y. Kabalan, Y. Tawk, and C. G. Christodoulou, "Design based on complementary split-ring resonators of an antenna with controllable band notches for UWB cognitive radio applications," *Proceedings of the IEEE International Symposium on Antennas and Propagation and USNC/URSI National Radio Science Meeting (AP-SURSI '11)*, 1120–1122, July 2011.
15. Li, Y., W. Li, and Q. Ye, "Miniaturization of asymmetric coplanar strip-fed staircase ultrawideband antenna with reconfigurable notch band," *Microwave and Optical Technology Letters*, Vol. 55, No. 7, 1467–1470, 2013.
16. Li, Y., W. Li, and R. Mittra, "A CPW-fed wide slot antenna with reconfigurable notch bands for UWB and multi-band communication applications," *Microwave and Optical Technology Letters*, Vol. 55, No. 11, 2777–2782, 2013.

A Triple Band-notched UWB Antenna by Using an Arc-shaped Slot and a U-shaped Resonator Techniques

Yuanyuan Kong, Yingsong Li, and Wenhua Yu
College of Information and Communications Engineering
Harbin Engineering University, Harbin 150001, China

Abstract— In this paper, an ultra-wideband (UWB) antenna with triple notch bands is proposed and well designed by etching an arc-shaped slot (ASS) on the fan-shaped radiating patch and integrating a U-shaped resonator (USR) alongside the microstrip feed signal line. The proposed antenna consists of a microstrip feed structure, a trapezoidal ground plane, a fan-shaped radiating patch, an ASS and a USR, which are printed on a thin substrate with dielectric constant of 2.65. The three band-notched characteristics are realized by the use of the ASS and USR, while the center frequencies of these notch bands are tunable by adjusting the dimensions of the proposed ASS and USR. By using these techniques, the proposed antenna can filter out unwanted narrowband signals from WiMAX, WLAN and RFID bands. The proposed antenna is well designed and extensively investigated. The experimental results are given to verify that the proposed antenna with a wide bandwidth, three designated band-notched functions and good omnidirectional radiation patterns, which is suitable for modern high data rate UWB communication applications.

1. INTRODUCTION

Ultra-wideband technology has been rapidly developed in recent years because of its advantages, such as large communication capacity, high data rate and low cost. UWB antenna is a key component to realize a UWB system. A planar half-sized unbalance dipole antenna has been presented to reduce the size of UWB antenna [1, 2]. However, many narrow band system overlap with the UWB system and have been widely used for a long time. Thus, these narrowband signals might interfere with the UWB system. To deal with this problem, a great number of UWB antennas with notch bands have been designed and investigated. By grooving various slots into different radiating patches or ground planes, which have been widely used in microstrip-fed and CPW-fed UWB antennas, notch bands can be obtained to suppress the potential interferences from the designated narrow band systems [3–8]. Unfortunately, it is difficult to design a UWB antenna with multi-notch-band and may destroy the ground plane. After that, several UWB antennas have been designed by using T-shaped stub and U-shaped parasitic strips, which can reduce the electromagnetic leaky caused by the slots [9]. By combing the slot and stub techniques, a fractal-shaped stub and an L-shaped slot have been employed to design a dual band-notched UWB antenna [10, 11]. However, the antenna is still large in size and cannot give resistant to triple interference signals.

For these reasons, a triple band-notched UWB antenna is proposed by grooving an arc-shaped slot (ASS) into the fan-shaped radiating patch and settling a U-shaped resonator (USR) alongside the microstrip feed signal line. The triple notch band characteristics are realized by using the ASS and USR and their center frequencies can be tuned by adjusting the size of ASS and USR. The performance of the proposed triple band-notched UWB antenna has been investigated by the use of the HFSS.

2. ANTENNA CONFIGURATION

The configuration of the proposed triple band-notched UWB antenna is depicted in Fig. 1, which is modified on the basis of the original model reported in [1, 2]. The proposed antenna consists of a fan-shaped radiation patch, a trapezoid ground plane, an arc-shaped slot with an open slit, an USR and a 50-Ohm microstrip feed structure. The proposed antenna is printed on a thin substrate with dielectric constant of 2.65 and loss tangent of 0.001. To realize the band-notched characteristics, an arc-shaped slot is etched in the fan-shaped radiation patch and the arc-shaped slot is riven into two segments by an open slit. In addition, a USR is adopted and settled alongside the microstrip feed signal line. By using the arc-shaped slot and the USR, three notch bands are produced. Also, the center frequencies of these three notch bands are tunable by adjusting the dimensions of the arc-shaped slot and the USR to render the proposed antenna to filter out unwanted signals from WiMAX, WLAN and RFID systems. The proposed antenna is optimized with a small size

of $L_1 \times L_2 = 35.6 \text{ mm} \times 20 \text{ mm}$, which is slightly smaller than the reference antenna [1, 2]. The optimized parameters are $ud = 0.5$, $cd = 0.3$, $ul = 5.1$, $uw = 4$, $hu = 8$, $w1 = 1.05$, $h = 20$, $g = 0.4$, $rf = 15$, $a = 16$, $b = 20$, $wc = 3$, $hc = 1.2$, $t = 0.4$, $w2 = 6$, $hs = 1$, $d = 4$, $dw = 3$, $ug = 0.45$ (unit: mm). The angle of the arc-shaped slot is 74° and it is riven into two segments at an angle of 38.7° .

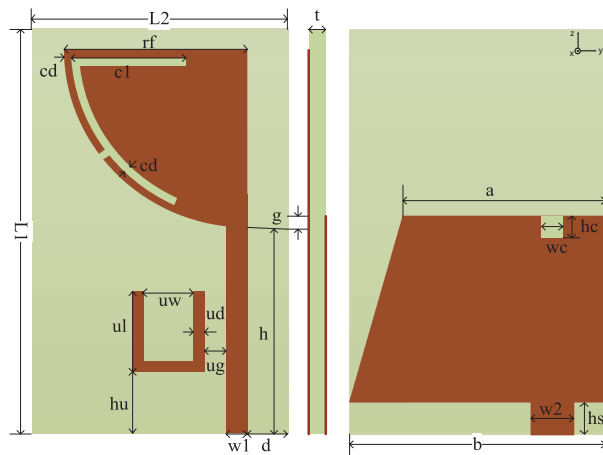


Figure 1: Physical structure of the proposed antenna.

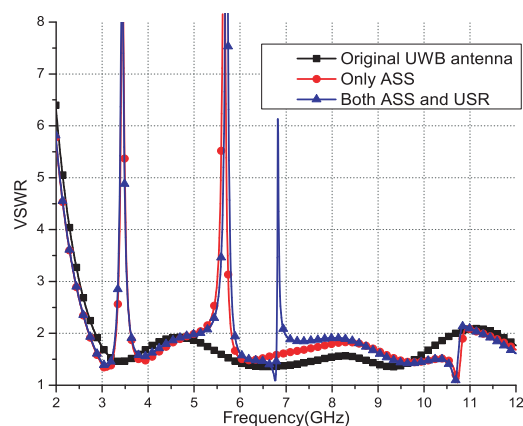


Figure 2: Notch characteristics of the antennas.

3. ANTENNA PERFORMANCE ANALYSIS

In this section, the performance of the proposed tri-band-notched UWB antenna is investigated by using the electromagnetic simulation software HFSS to verify the effectiveness of the design, including impedance characteristics, radiation patterns and the current distribution. Firstly, the band-notched characteristic is investigated by taking the ASS and USR into consideration to discuss their effects on impedance bandwidth. The effects of the ASS and USR are shown in Fig. 2. It can be seen that the proposed antenna without the ASS and USR is a UWB antenna, which has a bandwidth ranging from 2.71 GHz to 10.79 GHz with the VSWR less than 2. In this case, the proposed antenna can cover the entire UWB band released by FCC in 2002. When the proposed antenna has only ASS etched in the fan-shaped patch, it can give two notch bands at 3.4 GHz and 5.7 GHz to filter out the potential interferences from WiMAX and WLAN communication systems. When the proposed antenna integrates both the ASS and USR, it is a triple band notched UWB antenna to reject the undesired narrowband signals from WiMAX, WLAN and RFID systems.

Secondly, the key parameters are selected to discuss the effects on the band-notched characteristics. The effect of cl on the impedance bandwidth of the proposed antenna is shown in Fig. 3(a). It can be seen that the notch band at 3.4 GHz moves to the low frequency when the parameter cl increases from 5.2 mm to 7.8 mm. Also, the parameters of ul and uw have the similar effects on the corresponding notch band, which is mainly designed for the highest notch band and their performance are shown in Figs. 3(b) and (c). It is found that the center frequencies of the highest notch band moves from high frequency to low frequency, which is caused by the increased resonance length. Since the v determines the length of the two arc-shaped slots, it has been investigated and the effect of v is demonstrated in Fig. 3(d). We can see that the middle notch shifts to low frequency first and then moves to high frequency because parameter v can affect both the length of the slots. From the above discussions, we can say that the proposed antenna can give resistant to suppress the potential interferences from WiMAX, WLAN and RFID systems.

Next, the radiation patterns of proposed triple band-notched UWB antenna are studied at frequencies of 3.5 GHz, 4.5 GHz and 6.5 GHz and the results are demonstrated in Fig. 4. An omnidirectional radiation patterns are obtained in the xy -plane, while a standard eight-like radiation patterns are achieved in the xz -plane. When the frequency increases from 3.5 GHz to 6.5 GHz gradually, radiation patterns are deteriorated, which is caused by the asymmetric structure and the etched slot in the radiating patch which leaks electromagnetic waves.

Finally, surface current distribution is investigated and depicted in Fig. 5. It is observed that the current at 3.4 GHz is mainly focus on the upper segment of the etched slot, while the current at

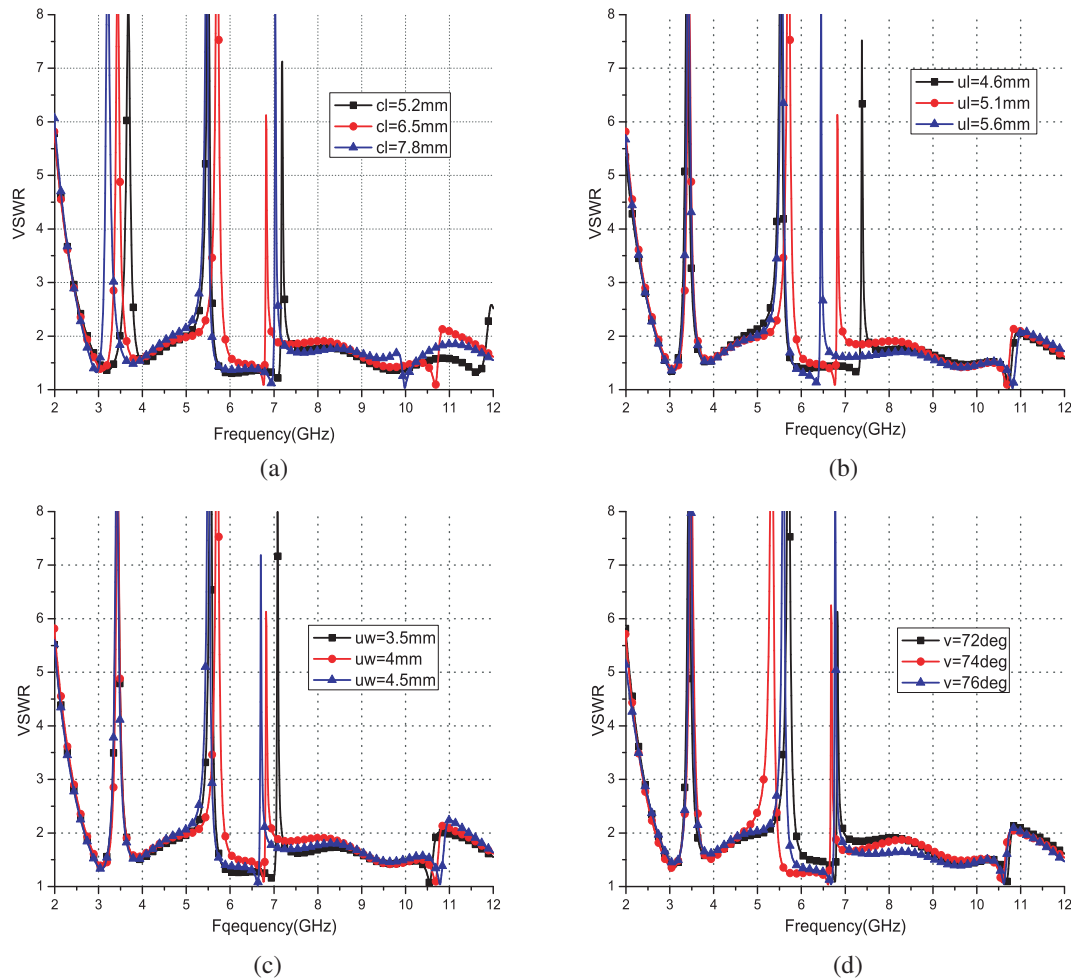


Figure 3: Effects of parameters on the proposed antenna. (a) Effects of cl . (b) Effects of ul . (c) Effects of uw . (d) Effects of v .

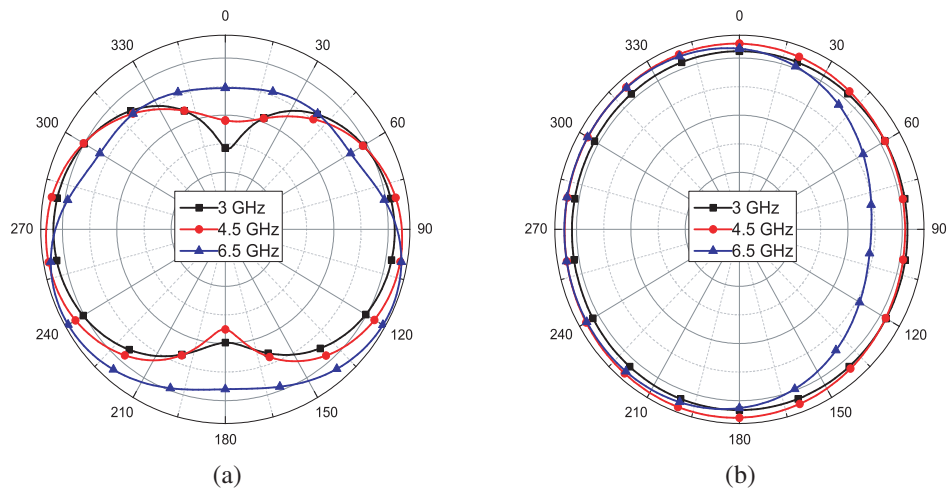


Figure 4: Radiation patterns of the proposed antenna. (a) xz -plane. (b) xy -plane.

5.7 GHz is mainly concentrate on the lower segment of the arc-shaped slot. At 6.8 GHz, the current is focused on the U-shaped resonator, while the current at the slots and the radiating patch are small. Thus, we can say that the antenna at these bands is non-resonance because the slots and the USR act as desired filters.

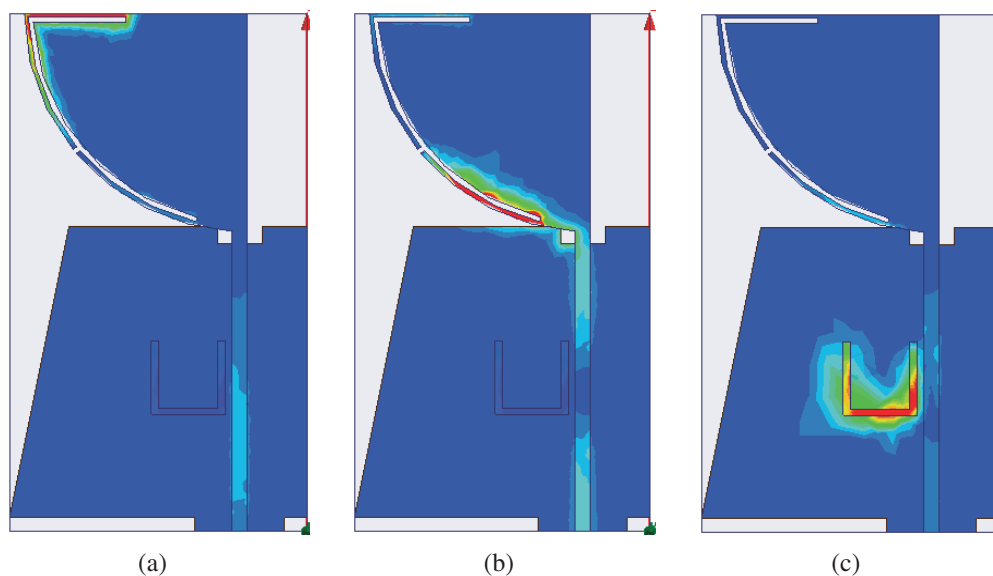


Figure 5: Surface current distributions of the proposed antenna. (a) 3.4 GHz. (b) 5.7 GHz. (c) 6.8 GHz.

4. CONCLUSION

A triple band-notched UWB antenna has been presented and well designed by the use of the HFSS. The notch bands are achieved by the slot which is split into two segments to generate two designated notch bands, while the other notch is obtained by the USR. From the simulation, we found that the proposed antenna can prevent the potential interferences from WiMAX, WLAN and RFID systems. The results showed that the proposed antenna has a wide bandwidth ranging from 2.71 GHz to 10.79 GHz, desired triple notch bands and good omnidirectional radiation patterns, which render it promising for UWB communication applications.

ACKNOWLEDGMENT

This paper is funded by the International Exchange Program of Harbin Engineering University for Innovation-oriented Talents Cultivation. This paper is also supported by Fundamental Research Funds for the Central Universities (HEUCFD1433).

REFERENCES

1. Hiraguri, K., K. Koshiji, and F. Koshiji, "A wideband antenna with fan-shaped and trapezoidal elements on printed circuit board for ultra wideband radio," *IEEE 2nd Global Conference on Consumer Electronics*, 267–268, Tokyo, Japan, 2013.
2. Koshiji, F., Y. Akiyama, S. Itaya, and K. Koshiji, "A wideband antenna with fan-shaped and trapezoidal elements for ultra wideband radio," *Proceeding of ISAP*, 838–841, Nagoya, Japan, 2012.
3. Kim, J., C. S. Cho, and J. W. Lee, "5.2 GHz notched ultra-wideband antenna using slot-type SRR," *Electronics Letters*, Vol. 42, No. 6, 315–316, 2006.
4. Li, Y., X. Yang, Q. Yang, and C. Liu, "Compact coplanar waveguide fed ultra wideband antenna with a notch band characteristic," *AEU-International Journal of Electronics and Communications*, Vol. 65, No. 11, 961–966, 2011.
5. Li, Y. S., X. D. Yang, C. Y. Liu, and T. Jiang, "Compact CPW-fed ultra-wideband antenna with band-notched characteristic," *Electronics Letters*, Vol. 46, No. 23, 1533–1534, 2010.
6. Li, Y. S., X. D. Yang, C. Y. Liu, and T. Jiang, "Compact CPW-fed ultra-wideband antenna with dual band-notched characteristic," *Electronics Letters*, Vol. 46, No. 14, 967–968, 2010.
7. Chu, Q. X. and Y.Y. Yang, "A compact ultra wideband antenna with 3.4/5.5 GHz dual band-notched characteristics," *IEEE Transactions on Antennas and Propagation*, Vol. 56, No. 12, 3637–3644, 2008.
8. Nguyen, D. T., D. H. Lee, and H. C. Park, "Very compact printed triple band-notched UWB antenna with quarter-wavelength slots," *IEEE Antennas and Wireless Propagation Letters*, Vol. 11, 411–414, 2012.

9. Jiang, W. and W. Che, “A novel UWB antenna with dual notched bands for WiMAX and WLAN applications,” *IEEE Antennas and Wireless Propagation Letters*, Vol. 11, 293–296, 2012.
10. Li, Y. S., S. Chang, M. Li, and X. D. Yang, “A compact ring UWB antenna with tri-notch band characteristics using slots and tuning stub,” *IEEE 4th International Symposium on Microwave, Antenna, Propagation, and EMC Technologies for Wireless Communications*, 27–29, 2011.
11. Taherdi, M. M. S., H. R. Hassani, and S. M. A. Nezhad, “UWB printed slot antenna with bluetooth and dual notch bands,” *IEEE Antennas and Wireless Propagation Letters*, Vol. 10, 255–258, 2011.

Design of a High Isolation Dual-band MIMO Antenna for WLAN and WiMAX Applications

Lanchao Zhang, Tao Jiang, and Yingsong Li

College of Information and Communications Engineering
Harbin Engineering University, Harbin 150001, China

Abstract— A high isolation dual-band multiple-input multiple-output (MIMO) antenna of two antenna elements is presented for WLAN and WiMAX applications. Each element consists of two meandering strips which locate at the top and bottom sides of the substrate respectively. The proposed MIMO antenna operates in the 2.45 GHz WLAN band and 3.55 GHz WiMAX band. And the antenna has high isolation over 20 dB in the two operation bands, which is obtained by the vertical structure, a neutralization line and a narrow slot between the two elements. The return loss and the isolation of the antenna are investigated simulation. The results show that the proposed MIMO antenna has high isolation and good impedance match characteristic, making it suitable for WLAN and WiMAX applications.

1. INTRODUCTION

In recent years, the demand of high data rate and wide band for modern wireless communication systems have increased rapidly [1, 2]. Multi-input and multi-output (MIMO) technology can enhance data transmission speed and give a resistant to multiple path fading, which has been widely investigated. As a MIMO system, the transmitter or receiver needs two or more antenna elements [3, 4]. However, multiple antenna elements need to be placed closely in a small space within the limitation of the space which will produce strong coupling and make it hard to satisfy the requirements of system design [5]. Hence, it is a great challenge to design a MIMO antenna system with small size and high isolation.

Consequently a large amount of methods have been presented to design MIMO antennas with low coupling. Various slots such as I-shaped slot have been successfully used to obtain high isolation in MIMO antenna systems [6, 7]. A MIMO antenna has been designed by adding a neutralization line to achieve high port-to-port isolation in the 700 MHz band [8]. Mushroom-like electromagnetic band-gap (EBG) structure has been fabricated to suppress surface waves [9, 10]. Also, loading resonators between the antenna elements were effective methods to reduce the mutual coupling [11–15].

In this paper, a dual-band MIMO antenna with small size and high isolation is presented for WLAN and WiMAX applications. The proposed MIMO antenna has two orthogonal antenna elements, each of which consists of two meandering strips located at the top and bottom sides of a FR4 substrate with the dielectric constant of 4.3. The MIMO antenna covers the bandwidths of WLAN 2.45 GHz (2.4–2.484 GHz) and WiMAX 3.55 GHz (3.4–3.69 GHz). A high isolation over 20 dB in both low and high frequency bands is obtained by orthogonally arranging antenna elements and using a neutralization line and a narrow slot.

2. ANTENNA DESIGN

The configuration of the proposed dual-band MIMO antenna is shown in Fig. 1. The proposed MIMO antenna, printing on a FR4 substrate with a thickness of 1.6 mm, consists of two orthogonal antenna elements which are connected by a neutralization line. In addition, a narrow slot is etched between the two feed ports. As for the antenna element, it is comprised of two meandering strips which are printed on the both sides of the substrate. The top strip is connected with a 50-Ohm coaxial line, while the bottom meandering strip is set under the top one. The top view and the bottom view of the MIMO antenna is depicted in Figs. 1(b) and (c) respectively. The proposed MIMO antenna is optimized by using CST and the optimal parameters are listed in Table 1. The total lengths of the top and bottom meandering strips are 26.75 mm (about quarter wavelength at 2.45 GHz) and 41.7 mm (about half wavelength at 3.55 GHz) respectively.

3. RESULTS AND DISCUSSION

The simulated S -parameters are shown in Fig. 2. It can be observed that the proposed MIMO antenna operates in both WLAN 2.45 GHz and WiMAX 3.55 GHz bands, and good impedance

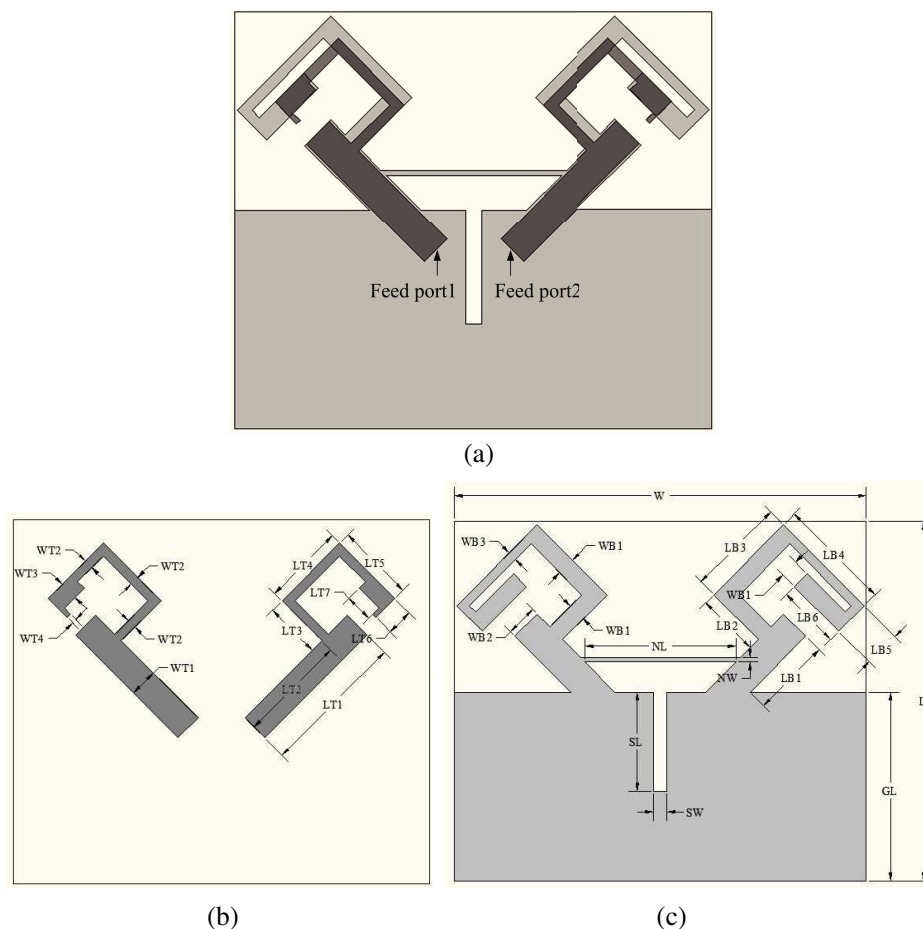


Figure 1: The configuration of the proposed MIMO antenna. (a) Total view. (b) Top view. (c) Bottom view.

Table 1: The optimal parameters of the proposed antenna.

Parameters	W	L	$WT1$	$WT2$	$WT3$	$WT4$	$LT1$	$LT2$	$LT3$
Unit (mm)	46	40	3.1	1	2	0.5	16	12	6.2
Parameters	$LT4$	$LT5$	$LT6$	$LT7$	$WB1$	$WB2$	$WB3$	$LB1$	$LB2$
Unit (mm)	9	8.6	2.95	3.1	2	3.5	1	8.78	7
Parameters	$LB3$	$LB4$	$LB5$	$LB6$	GL	NW	NL	SW	SL
Unit (mm)	11	12.7	4	7	21	0.5	16.86	1.5	11

match characteristic is achieved. In this MIMO antenna, the polarization modes of two antenna elements are different, namely one is vertical polarization and the other one is horizontal polarization. Thus, the antennas with perpendicular polarization modes are completely mismatch and cannot receive signals from each other in theory, and hence the mutual coupling caused by space waves is also reduced. Furthermore, the neutralization line connecting the two antenna elements can cancel the current because of the phase-reversal. And the narrow slot can hinder the surface currents flowing to the non-excited antenna element. The neutralization line and the narrow slot are effective on suppressing the mutual coupling caused by surface waves. Therefore, superior isolation performance beyond 20 dB is obtained. Current distributions at 2.45 GHz and 3.55 GHz for port1 are shown in Fig. 3. When port1 is excited, port2 is terminated with 50-Ohm matched load. It can be seen that the current density is very weak on the non-excited antenna element, which further verifies the good isolation characteristic of the proposed MIMO antenna.

The 3-D radiation patterns for port1 or port2 at different frequencies are displayed in Fig. 4. It can be seen that radiation directions are also orthogonal since the structures of the proposed

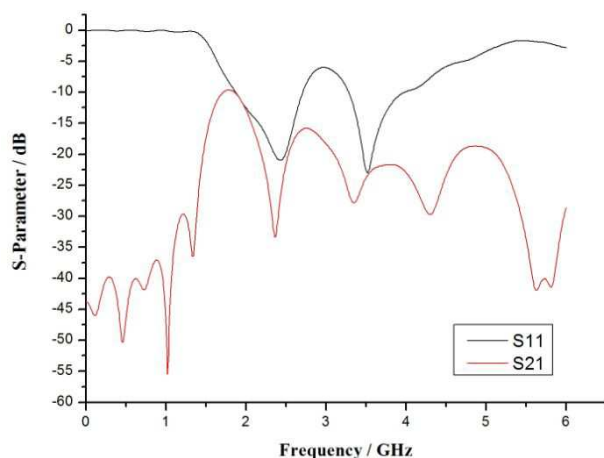


Figure 2: The simulated S -parameters.

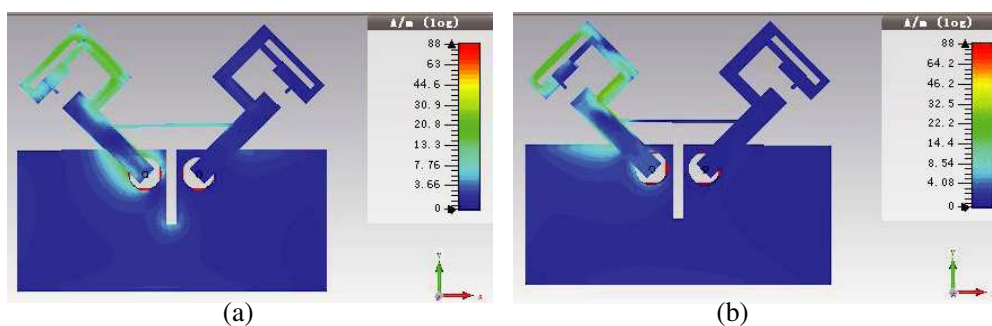


Figure 3: Current distributions at 2.45 GHz and 3.55 GHz for port1. (a) 2.45 GHz. (b) 3.55 GHz.

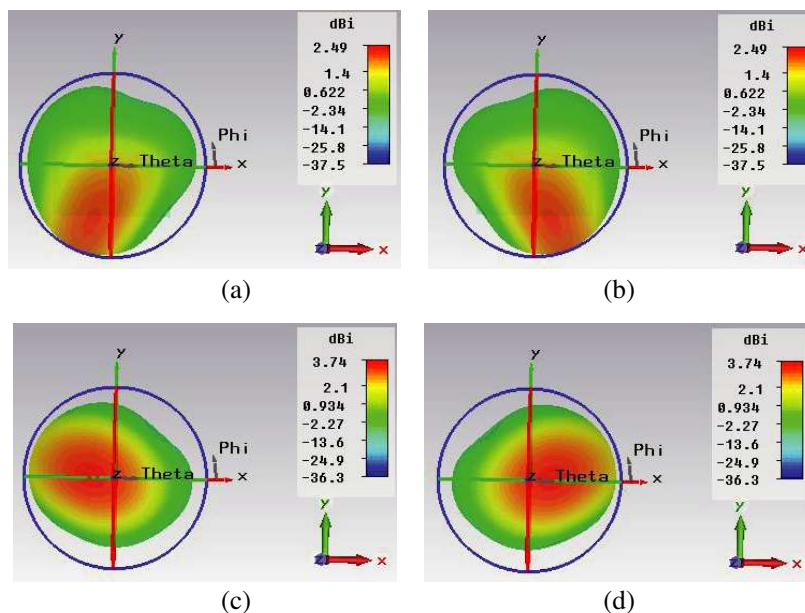


Figure 4: The 3-D radiation patterns for port1 or port2 at different frequencies. (a) Port1: 2.45 GHz. (b) Port2: 2.45 GHz. (c) Port1: 3.55 GHz. (d) Port2: 3.55 GHz.

antenna elements are orthogonal, which means it can provide pattern diversity.

4. CONCLUSION

A dual-band MIMO antenna has been designed and discussed for WLAN and WiMAX applications in this paper. The proposed MIMO antenna consists of two antenna elements which are perpendicular to each other. By using this structure, mutual coupling caused by space waves have been

effectively reduced. In addition, the neutralization line and the proposed narrow slot are fabricated to improve the isolation. Thus, it has been achieved that good isolation characteristic over 20 dB in both 2.45 GHz WLAN band and 3.55 GHz WiMAX band. The results show that the proposed MIMO antenna can be a good candidate for MIMO systems.

ACKNOWLEDGMENT

This paper is funded by the International Exchange Program of Harbin Engineering University for Innovation-oriented Talents Cultivation. This work was also partially supported by the Navy Defense Foundation of China (4010403020102), the Science and Technology innovative Talents Foundation of Harbin (2013RFXXJ083), the Foundational Research Funds for the Central Universities (HEUCF131602, HEUCFD1433).

REFERENCES

1. Foschini, G. S. and M. J. Gans, "On limits of wireless communications in a fading environment when using multiple antennas," *Wireless Personal Communications*, Vol. 6, No. 3, 311–335, 1998.
2. Yang, D. G., D. O. Kim, and C. Y. Kim, "Design of dual-band MIMO monopole antenna with high isolation using slotted CSRR for WLAN," *Microwave and Optical Technology Letters*, Vol. 56, No. 10, 2252–2257, October 2014.
3. Paulraj, A. J., D. A. Gore, R. U. Nabar, and H. Bolcskei, "An overview of MIMO communications — A key to gigabit wireless," *Proceedings of the IEEE*, Vol. 92, No. 2, 198–218, February 2004.
4. Deukhyeon, G. A., Y. Lee, T. Song, and J. Choi, "Design of MIMO antenna with decoupling network for LTE mobile application," *Proceedings of Asia-Pacific Microwave Conference*, 705–707, Kaohsiung, Taiwan, December 2012.
5. Gesbert, D., M. Sha, D. S. Shiu, P. Smith, and A. Naguib, "From theory to practice: An overview of MIMO space-time coded wireless system," *IEEE Journal on Selected Areas in Communications*, Vol. 21, No. 3, 281–302, April 2003.
6. Meshram, M. K., R. K. Amineh, A. T. Pimpale, and N. K. Nikolova, "A novel quad-band diversity antenna for LTE and Wi-Fi applications with high isolation," *IEEE Transactions on Antennas and Propagation*, Vol. 60, No. 9, 4360–4371, 2012.
7. Li, Y., W. Li, C. Liu, and T. Jiang, "A printed diversity Cantor set fractal antenna for ultra wideband communication applications," *Proceedings of 2012 Symposium on 10th International Antennas, Propagation & EM Theory*, 34–38, Xi'an, China, October 2012.
8. Dioum, I., A. Diallo, C. Luxey, and S. M. Farsi, "Dualband monopole MIMO antennas for LTE mobile phones," *Proceedings of International Conference on Applied Electromagnetics and Communications*, 20–23, Dubrovnik, September 2010.
9. Sievenpiper, D., L. Zhang, R. Broas, N. G. Alexopolus, and E. Yablonovitch, "High impedance electromagnetic surfaces with a forbidden frequency band," *IEEE Transactions on Microwave Theory and Techniques*, Vol. 47, No. 11, 2059–2074, 1999.
10. Yang, F. and Y. Rahmat-Samii, "Microstrip antennas integrated with electromagnetic-band gap structures: A low mutual coupling design for array applications," *IEEE Transactions on Antennas and Propagation*, Vol. 51, No. 10, 2936–2946, 2003.
11. Bait-Suwailam, M. M., M. S. Boybay, and O. Ramahi, "Electromagnetic coupling reduction in high-profile monopole antennas using single-negative magnetic metamaterials for MIMO applications," *IEEE Transactions on Antennas and Propagation*, Vol. 58, No. 9, 2894–2901, 2010.
12. Hsu, C. C., K. H. Lin, and H. L. Su, "Implementation of broadband isolator using metamaterial-inspired resonators and a T-shaped branch for MIMO antennas," *IEEE Transactions on Antennas and Propagation*, Vol. 59, No. 10, 3936–3939, 2011.
13. Khan, M. U. and M. S. Sharawi, "A compact 8-element MIMO antenna system for 802.11ac WLAN applications," *Proceedings of International Workshop on Antenna Technology*, 91–94, Karlsruhe, Germany, March 2013.
14. Li, Y., W. Li, C. Liu, and T. Jiang, "Two UWB-MIMO antennas with high isolation using sleeve coupled stepped impedance resonators," *Proceedings of IEEE Asia-Pacific Conference on Antennas and Propagation*, 21–22, Singapore, August 2012.

15. Li, Y., W. Li, and W. Yu, "A multi-band/UWB MIMO/diversity antenna with an enhanced isolation using radial stub loaded resonator," *Applied Computational Electromagnetics Society Journal*, Vol. 28, No. 1, 8-20, 2013.

A Compact Dual Band-notched UWB Band-pass Filter by Using a Stub and a Folded Stepped Impedance Resonator

Yanyan Wang, Tao Jiang, and Yingsong Li
College of Information and Communication Engineering
Harbin Engineering University, Harbin 150001, China

Abstract— In this paper, an ultra-wideband (UWB) band-pass filter with dual band-notch characteristic is proposed and its performance is verified numerically. The proposed UWB filter is realized by using stubs and folded stepped impedance resonators (FSIRs) to provide two desired notch bands at 5.0 GHz and 8.0 GHz, respectively. The center frequencies of these band notches can be easily tuned by adjusting the dimensions of the stubs and folded stepped impedance resonators. The proposed UWB filter with dual band-notched function can provide a wide bandwidth of 2.29–11.51 GHz. The simulated results are given to show that the proposed UWB band-pass filter with compact structure can provide desired notch bands and wide bandwidth, which make it suitable for UWB communication applications.

1. INTRODUCTION

In 2002 Federal Communications Commission (FCC) authorized the frequency band from 3.1 to 10.6 GHz for commercial UWB communication applications [1]. Consequently, the UWB wireless communication technology has attracted much more attentions in recent years. UWB filter is one of the basic components in the UWB communication system [2]. Then, many scholars in home and abroad have done a lot of studies to improve the performance of UWB band-pass filter. However, there exist several narrowband systems which have been used for a long time, such as 5.0 GHz WLAN band and 8.0 GHz ITU band. These narrowband signals may give potential interferences to ultra-wideband system. Thus, many ultra-wideband filters have been designed to eliminate or reduce the potential interferences from those narrow-band systems [3–5]. One of the effective methods is to design a band-pass UWB filter with desired notch band. Recently, a great number of band-notched band-pass UWB filters with necessary notch bands have been presented [6–11], including resonant cavity structure [8, 9], non-uniform periodic grounding slot structure [10] and asymmetric coupling structure twists [11]. Unluckily, most of these structures can only produce a single notch band which limits their applications when two interferences appear in the UWB band. In [12, 13], a stub and a folded stepped impedance resonator have been employed to design a dual notch band band-pass UWB filter. By adjusting the length of the stubs, the center frequency of the notch bands can be tuned to filter out narrow band interference signals of which the range is 5.1–5.8 GHz. By using these band-notched UWB filters, ultra-wideband communication systems can enhance the anti-jamming capability.

In this paper, a UWB band-pass filter with dual band-notched characteristic is presented and discussed on the basis of [14]. Folded stepped impedance resonators and stubs are utilized to generate the designated notch bands to filter 5.0 GHz WLAN and 8.0 GHz ITU signals. The center frequencies of the notch bands are tunable by adjusting the dimensions of the proposed folded stepped impedance resonators and stubs. The proposed filter is well designed and investigated, and the simulated results show that the proposed band-pass UWB filter can provide a good dual band notch characteristic and a wide bandwidth, which are suitable for UWB applications.

2. DESIGN OF THE PROPOSED DUAL BAND-NOTCHED UWB FILTER

A schematic of the proposed dual band-notched UWB bandpass filter is shown in Fig. 1, which is realized by using stepped impedance ports, back to back triple-mode SIR, stub and folded stepped impedance resonator. The proposed UWB filter is designed on a RT/duroid 5880 substrate with a relative dielectric constant 2.2 and a thickness of 0.7874 mm. In this design, stepped impedance ports and back to back SIR are employed to improve the performance of the filter. The width of stepped impedance ports is 3.6 mm and its length is 1.3 mm. The proposed filter is optimized by using the HFSS and the optimal parameters are given in Table 1.

In order to filter out the narrowband interference signals from 5.0 GHz WLAN band, two stubs are inserted into the input and output ports between the back to back triple-mode SIR. The

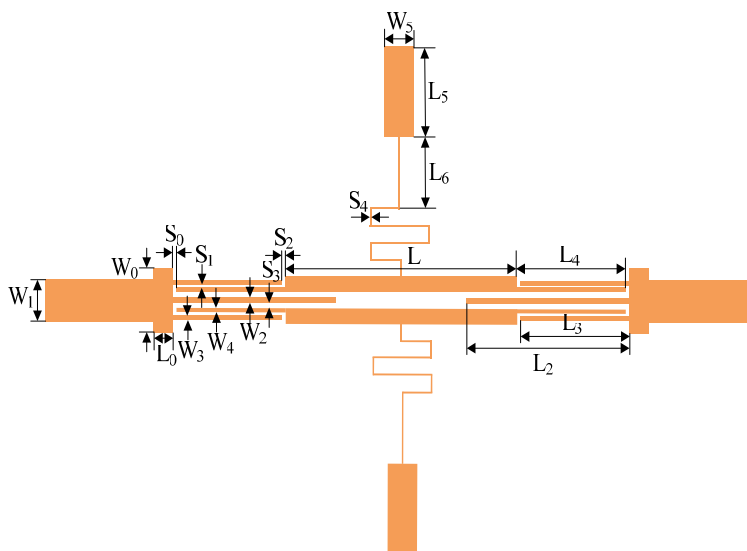


Figure 1: Schematic of the proposed dual notched-band UWB filter.

Table 1: Specifications of the designed filter (unit: mm).

L	L_0	W_0	W_1	L_2	W_2	L_3	W_3	L_4
15.7	1.3	3.6	2.35	12.5	0.3	7.4	0.23	7.4
W_4	L_5	W_5	L_6	S_0	S_1	S_2	S_3	S_4
0.23	5.0	2.0	5.0	0.1	0.05	0.1	0.3	0.1

design procedure of the proposed dual band-notched UWB filter has two steps: 1) single band-notched UWB filter; 2) dual band-notched UWB filter. Firstly, a single notch band is obtained by using stubs and the performance is in Fig. 2(a). We can note that a passband bandwidth of 3.2–11.38 GHz and a notch-band at 5.0 GHz are achieved. Also, the proposed filter has a sharp rising edge and falling edge. To realize a dual band-notched band-pass UWB filter, folded stepped impedance resonators are used to generate another notch near 8.0 GHz and its performance is shown in Fig. 2(b). It is found that the proposed UWB band-pass filter achieves a wide pass-band bandwidth of 2.29–11.51 GHz and has two notch bands operating at 4.9–5.2 GHz and 7.9–8.1 GHz, respectively.

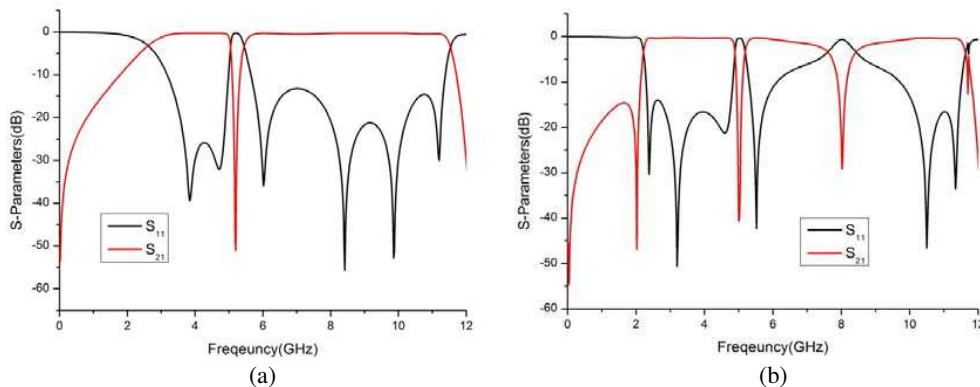


Figure 2: S -parameters of the proposed band-notched UWB filter. (a) Single notch band UWB filter. (b) Dual notch band UWB filter

3. TUNABILITIES OF THE PROPOSED DUAL BAND-NOTCHED UWB FILTER

Since the stubs and folded stepped impedance resonators have important roles in the dual notch bands, L_2 and L_6 are selected to investigate the tunable band-notched characteristics. Fig. 3(a) gives the effects of L_2 on the performance of the designed UWB filter. It is found that the lower notch band operating at 5.0 GHz moves from 5.4 GHz to 5.0 GHz when L_2 increases from 11.6 mm to 12.5 mm. This is caused by the increased resonance length of the stubs and the enhanced coupling between the stubs and the back to back triple-mode SIR. In addition, the center frequency of the upper notch band at 8.0 GHz keeps constant. The effects of L_6 are illustrated in Fig. 3(b). It is observed that the center frequency of the upper notch band shifts from 8.5 GHz to 7.9 GHz with an increment of L_6 , which is caused by the prolonged resonance length of the folded stepped impedance resonator. Thus, we can conclude that the lower notch band is produced by the stubs, while the upper notch band is realized by the use of the folded stepped impedance resonators. Additionally, the center frequencies of the notch bands can be tuned by adjusting the dimensions of the stubs and the folded stepped impedance resonators.

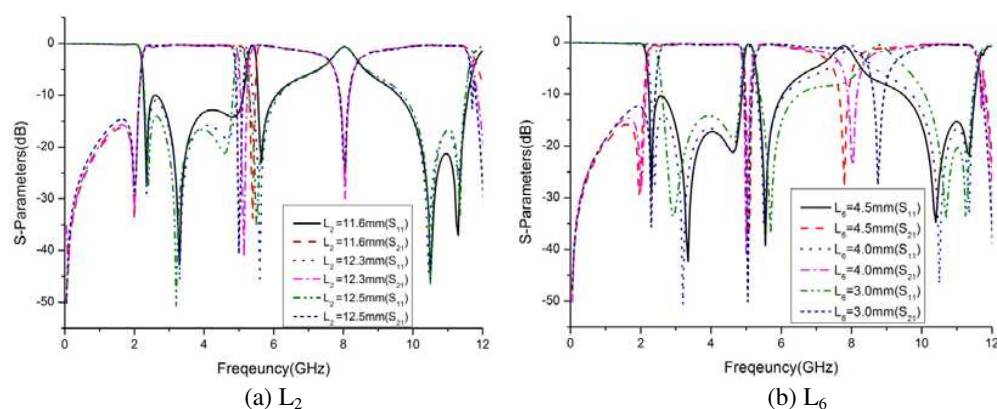


Figure 3: S -parameters with different L_2 and L_6 .

4. CONCLUSION

In this paper, we proposed a compact UWB bandpass filter with dual band notched characteristic by using stepped impedance ports, back to back triple-mode SIR, stubs and folded stepped impedance resonators. The simulated results showed that the proposed UWB filter has a wide bandwidth of 2.29–11.51 GHz and two tunable notch bands operating at 4.9–5.2 GHz and 7.9–8.1 GHz, which is promising for the application of UWB communication systems.

ACKNOWLEDGMENT

This paper is funded by the International Exchange Program of Harbin Engineering University for Innovation-oriented Talents Cultivation. This work was also partially supported by the Navy Defense Foundation of China (4010403020102), the Science and Technology innovative Talents Foundation of Harbin (2013RFXXJ083), the Foundational Research Funds for the Central Universities (HEUCF131602, HEUCFD1433).

REFERENCES

1. "Revision of part 15 of the commission's rules regarding ultra-wide-band transmission system," *First Note and Order Federal Communication Commission*, ET-Docket 98–153, 2002.
2. Jebin, S. R. and M. G. Madhan, "Design of UWB bandpass filter for wireless communication applications," *Electronics and Communication Systems*, 1–5, 2014.
3. Huang, J. M., Y. M. He, and Z. L. Deng, "An ultra-wideband band-pass filter using EBG structure," *2008 9th International Conference on Solid-State and Integrated-Circuit Technology Proceedings II*, 1373–7375, 2008.
4. Hu, H. L., X. D. Huang, and C. H. Cheng, "Ultra-wideband band-pass filter using CPW-to-microstrip coupling structure," *Electronics Letters*, Vol. 42, No. 10, 586–587, 2006.

5. Liu, Y., C. H. Liang, and Y. J. Wang, "Ultra-wideband band-pass filter using hybrid quasi-lumped elements and defected ground structure," *Electronics Letters*, Vol. 45, No. 17, 899–900, 2009.
6. Liu, D. K., C. F. Su, and X. Y. Wang, "A novel microstrip UWB bandpass filter using stub-loaded multiple-mode resonator," *Applied Superconductivity and Electromagnetic Devices*, 146–148, 2013.
7. Li, Y., W. Li, C. Liu, and Q. Ye, "A compact UWB band-pass filter with ultra-narrow tri-notch-band characteristic," *Applied Computational Electromagnetics Society Journal*, Vol. 29, No. 2, 170–177, 2014.
8. Yang, G. M., R. Jin, and C. Vittoria, "Small ultra-wideband band-pass filter with notch band," *IEEE Microwave and Wireless Components Letters*, Vol. 20, No. 1, 22–24, 2010.
9. Mondal, P. and Y. L. Guan, "A coplanar stripline ultra-wideband band-pass filter with notch band," *IEEE Microwave and Wireless Components Letters*, Vol. 20, No. 1, 22–24, 2010.
10. Hao, Z. C., J. S. Hong, and J. P. Parry, "Ultra-wideband band-pass filter with multiple notch bands using non-uniform periodical slotted ground structure," *IEEE Trans. Microwave Theory and Techniques*, Vol. 57, No. 12, 3080–3088, 2009.
11. Wichai, K. and A. Prayoot, "An ultra-wideband band-pass filter with notch implementation," *Electrical Engineering/Electronics Computer Telecommunications and Information Technology*, 933–936, 2014.
12. Li, Y., W. Li, and W. Yu, "A miniaturization band-pass filter with ultra-narrow multi-notch-band characteristics for ultra-wideband communication applications," *Applied Computational Electromagnetics Society Journal*, Vol. 29, No. 4, 289–300, 2014.
13. Liu, C., T. Jiang, Y. Li, and J. Zhang, "A novel UWB filter with WLAN and RFID stop band rejection characteristic using tri-stage radial loaded stub resonators," *Applied Computational Electromagnetics Society Journal*, Vol. 27, No. 9, 340–351, 2012.
14. Oh, S., B. Shin, J. Jeong, and J. Lee, "A UWB bandpass filter with a notched band using dual stepped-impedance stub-loaded resonators," *Microwave and Optical Technology Letters*, Vol. 56, No. 8, 1785–1787, 2014.

Miniaturized Tag Antennas with Artificial Magnetic Conductor for UHF RFID On-body Applications

Chien-Wen Chiu and Cheng-Yan Yang

Department of Electronic Engineering, National Ilan University, Ilan 260, Taiwan

Abstract— The paper presented a compact dipole tag antenna with a miniaturized artificial magnetic conductor for UHF RFID on-body applications. Two kinds of artificial magnetic conductor are designed and studied in order to insulate the influence from the human body. The miniaturized AMC structure is then placed on the button of a folded dipole tag antenna connected with a Monaz[®] 4 microchip. The tag with the AMC is designed and simulated by the simulator HFSS. The design structure is also constructed to verify the simulation results. The study finds that the tag with the AMC can increase antenna gain and reading range. When the tag is put close to a human body, the folded-dipole tag can achieve about 6 m reading distance.

1. INTRODUCTION

UHF RFID technique is popular in the logistics, inventory management or bioengineering. A UHF tag does not work well when it is put close to a human body or held in hand. The input impedance, radiation pattern, and realized gain of the tag antenna are influenced because of the body-proximity effects. The influences are caused by absorption, diffraction, and scattering of electromagnetic waves due to the lossy and conducting human body. The body-proximity effects must be considered when a tag is held or put on the body. Some literatures have studied the effect of the human body on the designed tags [1, 2].

Recently, a few scholars proposed artificial magnetic conductors (AMCs) to insulate the effect of the human body for wearable device or RFID applications [3, 4]. Ta et al. proposed a two-dimensional square metal patch as the unit cell of the artificial magnetic conductor (AMC) [5]. Then, four T-type slots are symmetrically inserted into each side of the metal patch to miniaturize the AMC size and lower the first resonant frequency. The bandwidth is limited although it is a low profile AMC structure. Recently, Hadarig et al. presented a kind of AMC using capacitive interdigital structure. The AMC structure exhibits proper bandwidth and higher angular stability under oblique incidence [6]. Using an artificial magnetic conductor (AMC) in the backplane of the tag actually helps to reduce the influence of a human body and increase reading range. However, the tag with an AMC is still large and bulky for on-body applications.

In this presentation, two kinds of AMC structure were studied for on-body applications, one is a square metal patch with T-type slots structure [5] and the other is four rectangular metal pads with interdigital capacitive structure [6]. Considering the minimum operating bandwidth and antenna sizes, we compared the performance between the two AMC structures after simulation and chose the minimum-size AMC structure. Then a miniaturized dipole tag antenna was designed and placed on the above of the AMC structure to insulate the influence from the human body. The designed tag on the AMC substrate is then placed close to a four-layer stratified elliptical cylinder human model to study the performance of the designed tags. In Section 2, we designed and compared two AMC structures. Section 3 is devoted to designing a folded-dipole tag antenna with an AMC. In Section 4, the tag with the miniaturized AMC is pasted on a human body. The gain and reading range of the folded-dipole with and without AMC are compared. Finally, Section 5 draws some conclusions.

2. AMC DESIGN

AMC structures have many kinds of physical type. An AMC is composed of a frequency selective surface (FSS) placed above a perfect ground plane and a dielectric material. A two-dimensional square metal patch was initially used as the unit cell of artificial magnetic conductor (AMC). To lower the resonance frequency, four T-type slots are symmetrically inserted into each side of the metal patch [5]. Each slot is designed with $L_p = 40$ mm and $W_p = 3$ mm so that the operating frequency is reduced to 915 MHz. The periodic square patch is built on a grounded FR4 substrate with height = 3.2 mm, $\epsilon_r = 45$ and loss tangent = 0.02. The study finds that the AMC with 3×3 T-slot patch-typed unit cells is too large and narrow band to be applied on the human body.

To miniaturize the overall size in the low frequency, the unit cell of a new AMC which consists of four rectangular metal pads with interdigital capacitors connected by two striplines is studied [6] as Figure 1 shows. The four rectangular metal pads behave like capacitors but the two striplines provide the inductive behaviour. The gap between the adjacent unit cells forms an interdigital capacitance. It is a key design factor for designing smaller unit cells at the low operating frequency [6]. The AMC structure is expected to be employed to design a tag antenna for on-body applications. Figure 1 shows the geometric configuration of the unit cells of the AMC structure. The geometric sizes are $W = 40$ mm, $a = 13.7$ mm, $b = 12$ mm, $c = 12$ mm, $d = 1.6$ mm, $e = 15.4$ mm and $f = 24.1$ mm. To reduce cost, we chose a FR4 substrate with $\epsilon_r = 45$ and loss tangent = 0.02 as the AMC carrier. The unit cell size is 34.1×34.1 mm² and the substrate thickness is 3.2 mm. The gap width between each unit cell is 1 mm.

The AMC model is established in the ANSYS's HFSS simulator. The simulated model includes two PEC walls and two PMC walls to model an infinite periodic structure and then a wave port is setup as an exciting source. Figure 2 shows the simulated reflection phase of the FSS AMC. The simulated result indicates that the miniaturized AMC has a high impedance surface at 925 MHz. The AMC surface becomes PEC as the operating frequency near 800 MHz or 1 GHz. The best operating frequency of the PMC surface is located near about 925 MHz. The useful bandwidth which ranges from 919–934 MHz is about 1.6%. The proposed AMC structure is not easy to implement so that the EM simulated software, FEKO, is evoked to verify the accuracy of the simulation results by HFSS. The simulated results by HFSS show agreement with the simulated results of FEKO. It confirms the simulation by HFSS is acceptable.

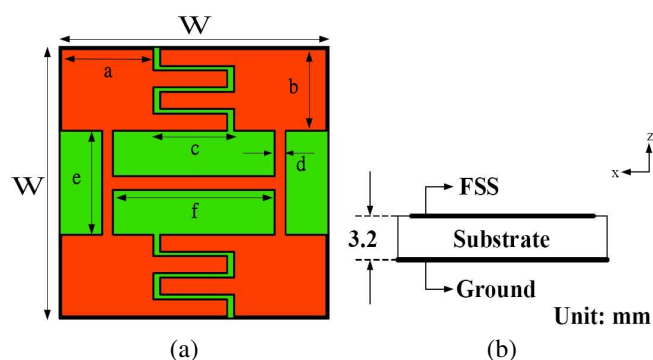


Figure 1: AMC structure, (a) top view and (b) side view and excitation method.

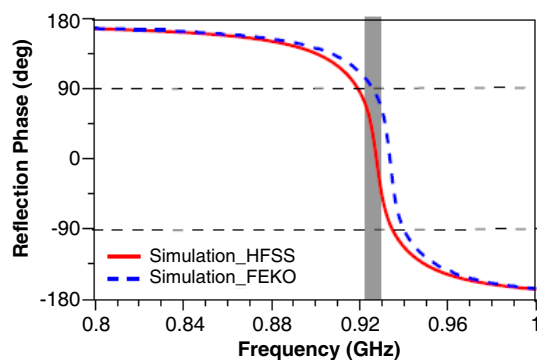


Figure 2: Simulated reflection phase on the AMC.

3. LINEARLY POLARIZED TAG DESIGN ON AMC

In this paper, a microchip of the Impinj Monaz[®] 4 is chosen to design the tag. The chip exhibits an impedance of $11-j143$ at 915 MHz [7] when its configuration is single-ended connection. A folded-dipole tag antenna printed on FR4 is proposed to miniaturize the antenna size. In order to achieve maximum power transfer, we added a T-matching structure which its coupling effect can micro tune the input impedance of the folded-dipole tag antenna. The geometric sizes of the dipole antenna with the T-matching transformer are shown in Figure 3. Figure 4 shows the input impedance for the dipole antenna with a symmetric T-matching transformer. Figure 5 shows the return loss. The tag is also fabricated to perform experiments by the Agilent EN5071B VNA. The comparison between simulation and measurement is also shown in the figures. The measured results show agreement with the simulation results. The impedance bandwidth is about 3% (902–928 MHz). The maximum realized gain is about 2.3 dBi in the free space, just like that of a half-wavelength dipole antenna.

In order to achieve minimum size, we used 3×2 miniaturized AMC unit cells. The folded-dipole is superposed on the miniaturized AMC surface with 1 mm gap. The AMC causes a little shift on the impedance so that the antenna with the AMC has less 0.8 dB gains than the original folded dipole in the free space. The advantage using the AMC is to let the tag antenna can be pasted near a lossy human body. Therefore, we optimize the folded-dipole with the miniaturized AMC and make it conjugate match the microchip with input impedance of $5-j70 \Omega$. Finally, geometric sizes of the optimized structure on the AMC are shown in Figure 6. The simple T-matching transformer is sufficient to achieve conjugate match with the microchip. Figure 7 shows the return

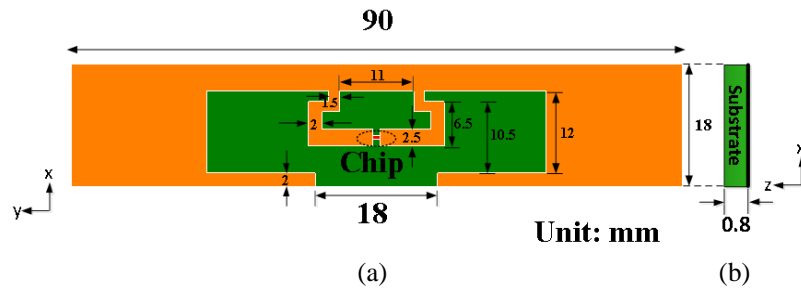


Figure 3: Folded-dipole tag antenna with a T-matching structure, (a) top view and (b) side view.

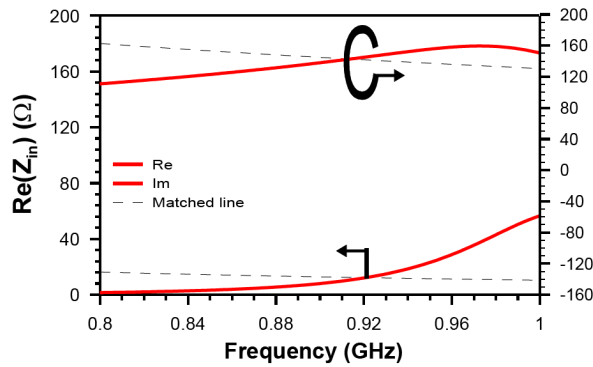


Figure 4: The input impedance of the folded-dipole with a T-matching structure.

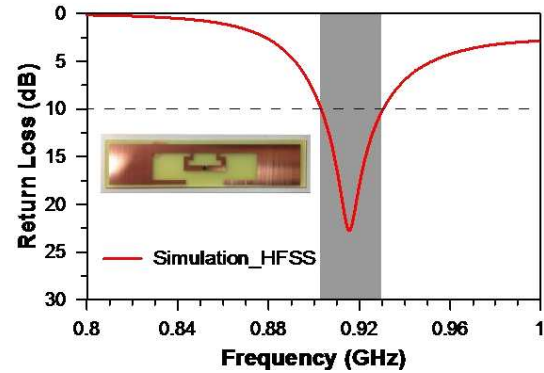


Figure 5: Simulated return loss.

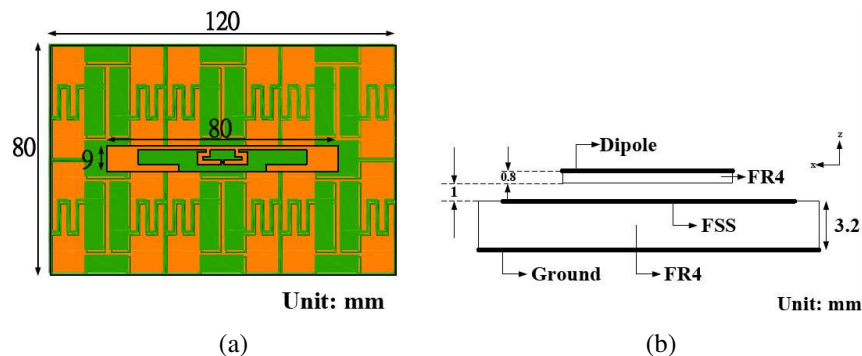


Figure 6: Geometric sizes of the optimized folded-dipole on the AMC, (a) top view and (b) side view.

loss of the optimized foldeddipole on the miniaturized AMC The impedance bandwidth is only 1.6% (917–929 MHz). The simulated results by HFSS show agreement with the simulated results by FEKO.

Figure 8 shows the realized gain of the optimized foldeddipole on the miniaturized AMC plane and the foldeddipole on a ground plane. The result indicates that the antenna gain of the folded dipole on the AMC plane is still conserved. We hope the AMC plane or PEC plane can preserve antenna gain to avoid injury from a lossy human body in the beginning. However, the study finds that the antenna with a PEC plane does not preserve the benefit. The reading range for the foldeddipole with the AMC is about 9.2m when it is predicted by the Friis formula. The foldeddipole on the miniaturized AMC has immunity against the influence of the object. Although the simulated radiation patterns at 915MHz is not shown here, the study finds the main beam is concentrated on the +Z axis. The antenna gain of the antenna with the miniaturized AMC is better than that of the original foldeddipole without the PMC or on the PEC.

The tag with AMC was constructed to measure the reading range. The reading range from a reader to the tag was measured in the aisle near our lab. The measured reading range is about 8m as the UHF RFID reader has 4W EIRP output power. The measured reading range shows

acceptable agreements with the predicted reading range which is about 9.2m. Figure 9 shows the photograph of the manufactured folded-dipole tag on the AMC. The whole antenna system is only $80 \times 120 \text{ mm}^2$, which is suitable for on-body applications if using a flexible printed circuit board.

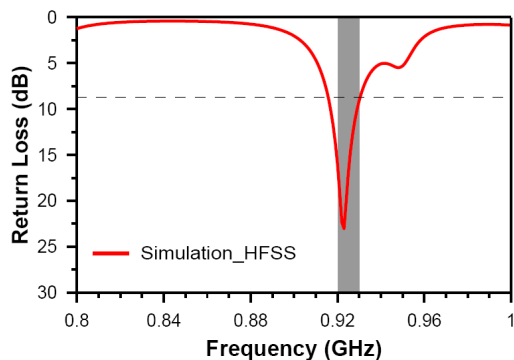


Figure 7: Return loss of the optimized T-matching folded-dipole on the designed AMC.

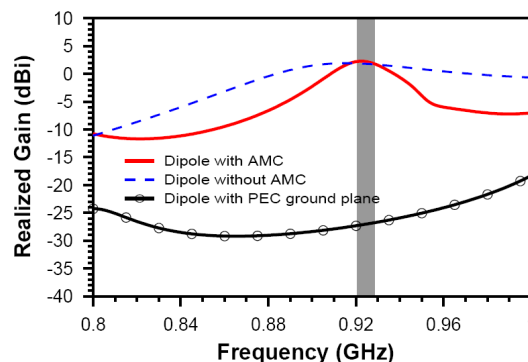


Figure 8: Realized gain of the optimized T-matching folded-dipole with and without AMC.

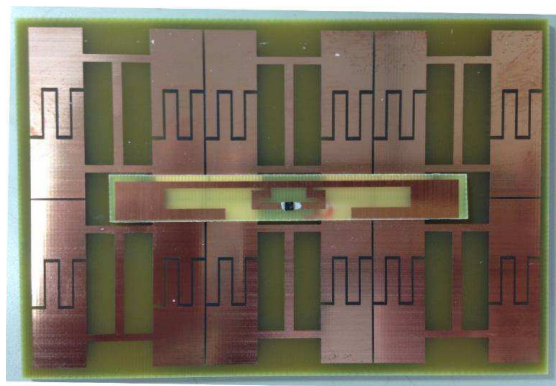


Figure 9: Photograph of the manufactured T-matching folded-dipole.

4. TAG APPLIED ON HUMAN BODY

Our original research motivation is devoted to improving reading range of the UHF RFID system for on-body applications. When the folded-dipole without AMC is put close to a human body, the realized gain of the tag antenna and reading range becomes very poor. The radiation efficiency of the folded-dipole on the human body reduces much lower than that of the folded-dipole in the free space. This section will study impacts on the tag due to the human body. Figure 10 shows a cylindrical human model. The human model consists of a stratified elliptical cylinder with four layers to model our torso. The physical and geometrical parameters can be found in the Table 1 of the reference [1]. The height of the model is 400 mm, which is similar to the length of our torso. The folded-dipole with or without the AMC in Section 3 has a good reading range in the free space. However, the AMC can help to insulate the effects of the human body on the tag. To compare fairly, the folded-dipole in the free space is 6.2 mm away from the human body but the folded-dipole with the AMC is 2 mm away from the human body. This is due to consider the thickness of the AMC.

Considering the body phantom model, we simulated the realized gain and radiation efficiency for the tags with and without AMC by HFSS. Figure 11 shows the realized gain of the folded-dipole with and without AMC when they are put close to the human model. The study finds that the influence due to the body effect is small for the tag with AMC. The maximum realized gain of the designed T-matching dipole without AMC is about 2.3 dBi in the free space. The realized gain for the designed dipole on the AMC is about 1.5 dBi since the AMC has 0 reflection phase and would not cause destructive interference between direct and reflected waves. When the tag with AMC is placed near the human model, the realized gain for the tag with AMC is about 1.0 dBi but the realized gain of the tag antenna without AMC is only -5.8 dBi . Figure 11 also shows the radiation efficiency of the folded-dipole with and without AMC when they are placed close to the

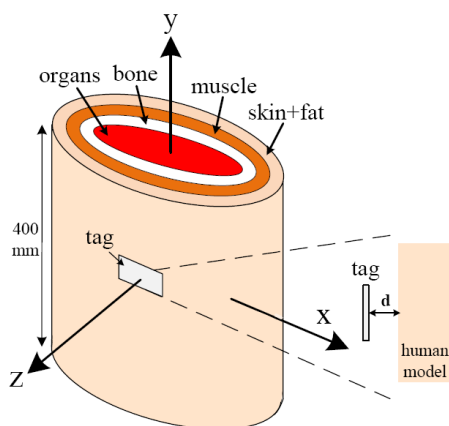


Figure 10: A cylindrical human model.

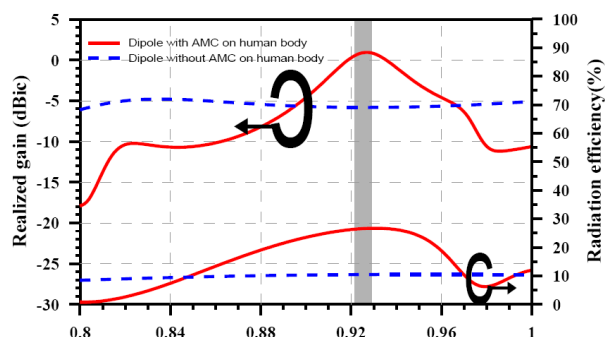


Figure 11: Radiation efficiency and realized gain of the T-matching folded-dipole tag put on the human body.

human model. The result indicates that the radiation efficiency of the folded-dipole without AMC is about 10%. The reason is because the majority EM wave is almost absorbed by the human body. However, the maximum radiation efficiency can be up to 30% for the tag with AMC.

The practical structure is constructed to measure the reading ranges when it was pasted on the chest of a practical human body. The comparisons are summarized as follows. The measured reading range is about 8.4 m for the tag with AMC in the free space and 7 m for the tag without AMC as the UHF RFID reader has 4 W EIRP output power. Considering the real body-proximity effects on the tag, the measured reading range can achieve 6 meters for the tag with AMC but only 2.8 m for the tag without AMC. Since the folded-dipole with AMC has maximum radiation efficiency of 30%, the realized gain is better than that of the dipole without AMC. Therefore, it can achieve longer reading range than that without AMC.

5. CONCLUSION

In this paper, we proposed a folded-dipole tag antenna with a symmetric T-matching transformer and a miniaturized AMC on the backplane. The artificial magnetic conductor is employed to avoid the influence of the human torso. The study finds that the miniaturized AMC is successfully applied on the tag to increase antenna gain and insulate the human body effect. The measured reading range is improved when the tag is passed on the human body. Although the antenna size is a little large for UHF RFID applications, the maximum predicted reading of the folded-dipole with FSS AMC can achieve 6 m.

REFERENCES

1. Tsai, M. C., C. W. Chiu, H. C. Wang, and T. F. Wu, "Inductively coupled loop antenna design for UHF RFID on-body applications," *Progress In Electromagnetics Research*, Vol. 143, 315–330, 2013.
2. Chiu, C. W., M. C. Tsai, H. C. Wang, and T. F. Wu, "Broadband T-matching loop tag antenna design for on-body UHF RFID applications," *Microwave and Optical Technology Letters*, Vol. 56, No. 5, 1194–1200, May 2014.
3. Raad, H. R., A. I. Abbosh, H. M. Al-rizzo, and D. G. Rucker, "Flexible and compact AMC based antenna for telemedicine applications," *IEEE Transactions on Antennas and Propagation*, Vol. 61, 524–531, Feb. 2013.
4. Hadarig, R. C., M. E. D. Cos, and F. Las-Heras, "UHF dipole-AMC combination for RFID applications," *Antennas and Wireless Propagation Letters*, Vol. 12, 1041–1044, 2013.
5. Ta, S. X. and I. Park, "Dual-band low-profile crossed asymmetric dipole antenna on dual-band AMC surface," *Antennas and Wireless Propagation Letters*, Vol. 12, 587–590, 2013.
6. Hadarig, R. C., M. E. D. Cos, and F. Las-Heras, "Novel miniaturized artificial magnetic conductor," *Antennas and Wireless Propagation Letters*, Vol. 12, 174–177, 2013.
7. Murata Manufacturing Co., [Online]. Available: <http://www.murata.com>.

A Compact VHF Antenna for Smart Meters

Paul Record and Komsan Kanjanasit

School of Engineering & Physical Sciences, Institute of Sensors, Signals and Systems
Heriot Watt University, Mountbatten Building, Riccarton, Edinburgh EH14 4AS, UK

Abstract— Energy companies have demanded two way communications between the consumer energy meter and the company to ease data collection and enable variable energy tariffs. There are several bands in use from GSM to ISM bands working at 900, 315, 434 and 868 MHz. In hilly terrains and meters located in basements these frequencies do not propagate well in these bands, however frequencies below 200 MHz are much better. This work describes a narrow band antenna derived from a perturbed microstrip patch working at 169 MHz. Its largest dimension is only 0.07λ at resonant frequency with a $ka = 0.18$. A gain of -1.2 dBi and an SII of -2 dB was achieved. The antenna was designed to fit directly to the smart meter so its radiation pattern was optimised to radiate broadside. It incorporates a novel matching element to allow ease of manufacture. From near field studies it can be described as parasitic resonator excited by a single driven electrode matching 50 ohms. The main method of tuning was by altering the separation of the top fin structures. The antenna was finally tuned to the required resonant frequency when enclosed in an polycarbonate plastic housing.

1. INTRODUCTION

Wireless mBus N-mode was introduced to read residential gas and water meters in Italy and France. The ISM band at 169 MHz with a bandwidth of 75kHz provides cost effective coverage in gathering data from in-building consumption meters minimising path losses caused by building material and partially buried meters [1, 2]. The free space wavelength, of 1775 m makes conventional antennas too large to mount conveniently near the consumer unit. The conventional approach to reducing the antenna size is either by collapsing a whip to a helix or an inverted F both of which require large ground planes to function efficiently. In this work the antenna was required to fit to a consumption meter of overall size of $234 \times 158 \times 80$ mm with a footprint of no bigger than $100 \text{ mm} \times 50 \text{ mm}$.

Taking a conventional patch antenna with an air dielectric Moon in [3] perturbed the top structure and folded the top plates to produce an antenna of size ka of 0.3 at 40 MHz where k is the wavenumber and a the radius of a minimum sphere enclosing the antenna. Its bandwidth was only 1.9% and demonstrated a gain of 0.23 dBi. This approach has a number of advantages: it has high gain relative to its size whilst maintaining an omnidirectional pattern; the antenna does not require a ground plane and lastly the construction allows rapid and economic manufacture.

2. DESIGN

Moon's design was developed from a $\lambda/4$ microstrip structure working at 40 MHz. First the structure was perturbed which enabled the top and bottom plates of the patch to be folded reducing the size by a third. Next the structure was reduced further by adding plate loading to increase the

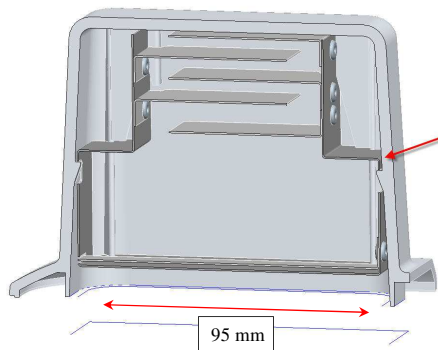


Figure 1: Antenna section within smart meter housing. Arrow indicates method of attachment.

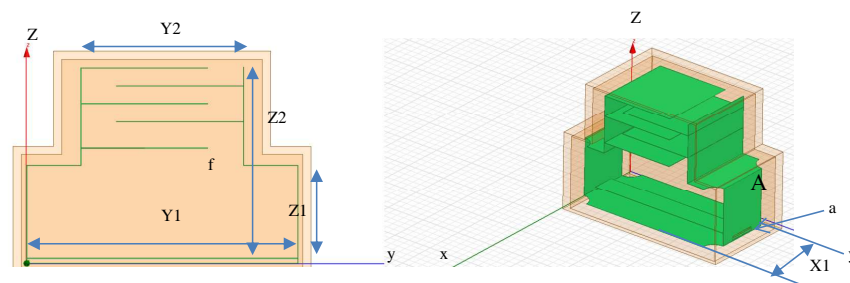


Figure 2: Antenna structure, the fawn coloured boundary surrounding the antenna represents the plastic housing. On the right the feed aperture, a , is on face A .

current path to maintain the operating frequency. A similar technique was employed in developing this design. At 169 MHz the dimensions were: $Y1 = 129$ mm, $Y2 = 60$ mm, $X1 = 70$ mm and $Z2 = 72$ mm, Figure 2. This was however still too large to fit within the required volume.

Whilst maintaining the current path the design was further reduced to $Y1 = 95$ mm, $X1 = 45$ mm whilst keeping $Z2$ to 72 mm and $Y2$ to 60 mm to allow the antenna to fit within the specified housing. The antenna was modeled using HFSS [9] and simulations had shown that reducing $X1$ had a small effect on resonant frequency. This, however, resulted in a resonance 10 MHz above 169 MHz. An additional fin, f , (Figure 2) was added and its position below the bottom fin of the initial design allowed the structure to be tuned to 169 MHz. The original feed electrode was a circular rod 5.5 mm in diameter fed from an aperture a in z - x plane on face A and terminated on the opposite face. To achieve a match of 50 ohms constrained the height above the base plate to only a few mm so to aid manufacture the electrode was developed to a flat plate of similar surface area, i.e., a width of 15 mm. Fin and electrode attachment had to be low impedance at the working frequency. The first structure was constructed from 0.5 mm copper sheet with fins soldered to the outer structure. Fast and cheap manufacture was the essence of this design and comparison by simulation between a copper structure with soldered fins and aluminium structure with fins and electrode riveted to the vertical walls showed little change in antenna performance in terms of gain and efficiency. So the final design was made from 0.5 mm thick aluminium sheet in which the fins were attached by pop rivets as in Figure 1. The rigidity of the antenna was compromised by the thinness of the aluminium so the structure was supported by a plastic clip on one face, but, small enough not to effect the antenna performance.

3. ANTENNA TUNING AND MATCHING

The ‘hot’ feed point position, $F1$, Figure 3, simulated as a lumped port, was varied horizontally from the aperture to the opposite face, from 0 (referenced at A) to 90 mm and the ‘cold’ connection, $G1$, from 2–20 mm in the vertical direction and the best match was found to be with $F1 = 2$ mm from face A and $G1$ at 2 mm. The antenna input impedance is shown in Figure 4. A good match of real 48 ohms was achieved.

The antenna input impedance is shown in Figure 4. A good match of real 48 ohms was achieved.

Without altering the feed position, fine tuning of the antenna was achieved by varying the fin size

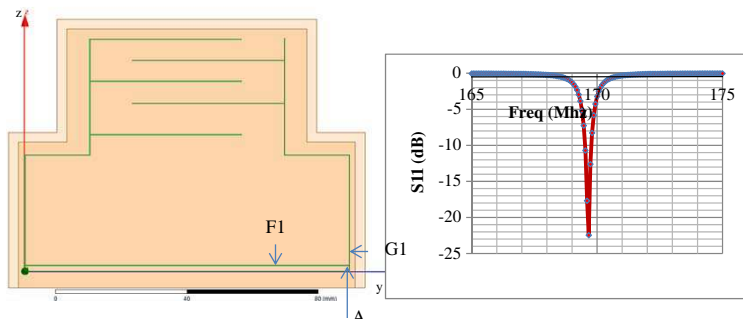


Figure 3: Left feeding points $F1$ and $G1$ with A as the reference point, right the return loss at 169.6 MHz of -22 dB at optimum feeding position.

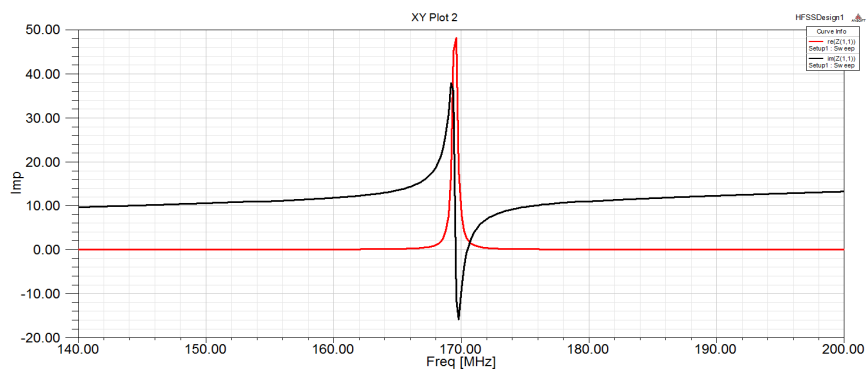


Figure 4: Antenna input impedance, the red line is real and black imaginary impedance.

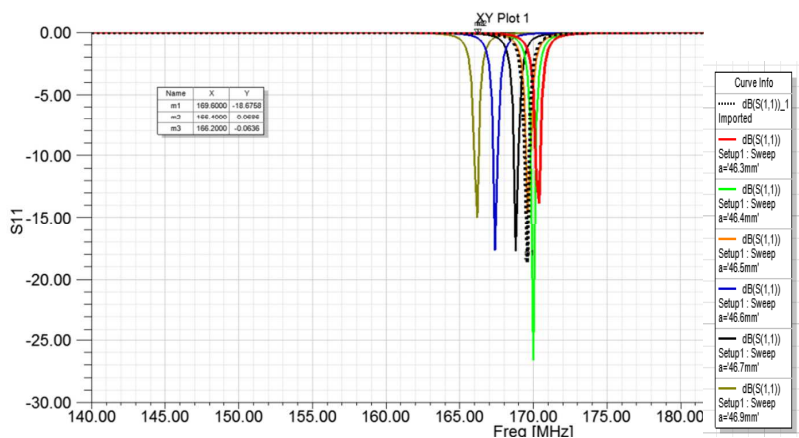


Figure 5: Return loss for fin lengths from 46.3–46.9 mm, dotted, brown = 46.5, red = 46.3, green 46.4, blue 46.6, black = 46.7, beige = 46.9.

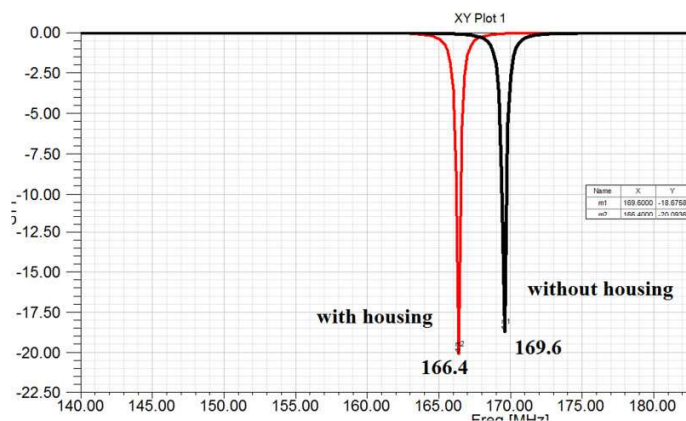


Figure 6: With and without plastic housing.

in y direction, Figure 5. At 169.6 MHz return loss of -18 dBi occurred with fin length = 46.9 mm.

In the final deployment the antenna would be enclosed in a plastic housing. Being a dielectric this would inevitably reduce the operating frequency. A reduction in frequency of 3.2 MHz was found, Figure 5, with a housing, 3 mm thick and a relative dielectric constant of 2.8, mimicking that seen with a housing made of polycarbonate.

The maximum gain simulated was -1.2 dBi omnidirectional in the y - z plane, Figure 7.

4. MEASUREMENTS

The return loss of the antenna constructed in sheet aluminium was measured in an open area with Agilent Network Analyser 8510 with and without hood attached to the gas meter.

For an independent assessment of the efficiency and radiation pattern, the antenna was measured

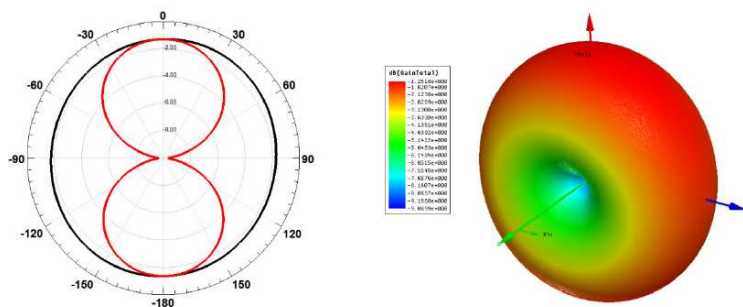


Figure 7: Gain of simulated antenna, on the left red is y - z plane, black is x - z plane, peak gain was -1.2 dBi. On the right 3D spatial gain distribution, RGB scale red = -1.2 dBi, blue = -9.5 dBi, upper is Z , to the right is Y and isometrically towards the reader on the left is X .

in an anechoic chamber by ProAnt [5]. Differences were found when the meter was attached to copper pipes, improvements in gain and efficiency were found with copper pipes the implying the antenna on its own was deficient in a ground plane.

The measured gain was lower by 0.8 dBi and the efficiency lower, 52% , than predicted, 70% , resulting from the device under test being off tune by about 3 MHz due to the devices supplied being slightly undersize.

The radiation patterns in Figure 11 demonstrate the omnidirectional pattern predicted in the YZ plane in Figure 7, and to a lesser extent the dumb bell shape in the XZ plane. The gain is lower than predicted because the antenna resonance was above 169 MHz. The tilting of the E -plane was probably caused by asymmetric ground plane resulting from the position of the antenna on the gas meter.

5. DISCUSSION

E and H field plots in Figure 12 demonstrate where the fields are positioned at maximum intensity. This can be interpreted as parallel resonant device where the top fin structures representing the capacitance and the lower part, the inductance. Erentok and Ziolkowski [7, 8] in their series of papers on metamaterial inspired antenna developed VHF and UHF antennas from resonant structures



Figure 8: Left bare antenna supported by plastic clip of the left, centre antenna mounted in hood, right antenna housed in assembled gas meter.

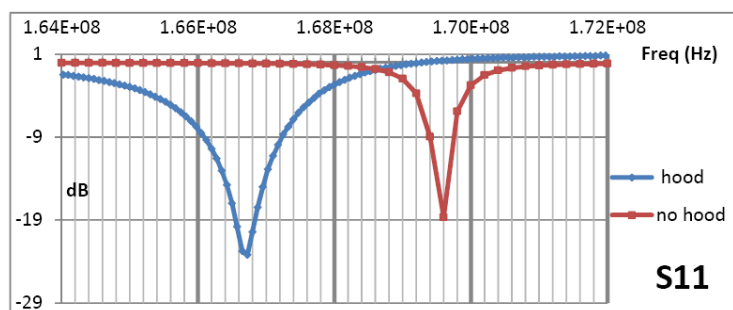


Figure 9: Return loss with and without polycarbonate shroud.

excited by a nearby electrode. However to achieve good gain and efficiency they had to use a large ground plane, comparable in size to $\lambda/4$. In this work the bottom electrode is used to excite the resonant structure in the same way, but the base plate forms the ground plane of only 94×45 mm.

Harrington [4] suggested that the efficiency of antenna is limited by its Q . But as the physical size is decreased, and loaded by capacitance or inductance to maintain a fixed frequency, the Q has to rise to maintain gain and efficiency, The Q however, is limited in practise by the conduction losses in the antenna and the coupling efficiency between the source and the antenna. The Q in this design was 211 unshrouded and 68 shrouded, the latter result from losses in the polycarbonate housing.

The minimum fractional bandwidth (FBW) required of this antenna was $\sim 0.04\%$ whereas the measured FBW was 0.5% with the antenna housing. The FBW predicted by simulation was 0.48. The return loss deepened with the antenna housing shown both by simulation, Figure 6, and measurement, Figure 9. This is to be expected because the antenna shroud is within the radian sphere increasing the energy in the electric field, deepening the return loss but losses in the plastic decrease Q broadening the bandwidth. The Q broadening however is to advantage in



Figure 10: Left antenna efficiency, 0 dB = 100%, peak -2.5 dB (52%) at 173 MHz. Blue curves are this design the green curves are an inverted F antenna for comparison. The right figure is gain plot where maximum gain out of band at 173 MHz is better than 0 dBi. Markers $a = 169.4$ MHz, marker $b = 169.8$ MHz.

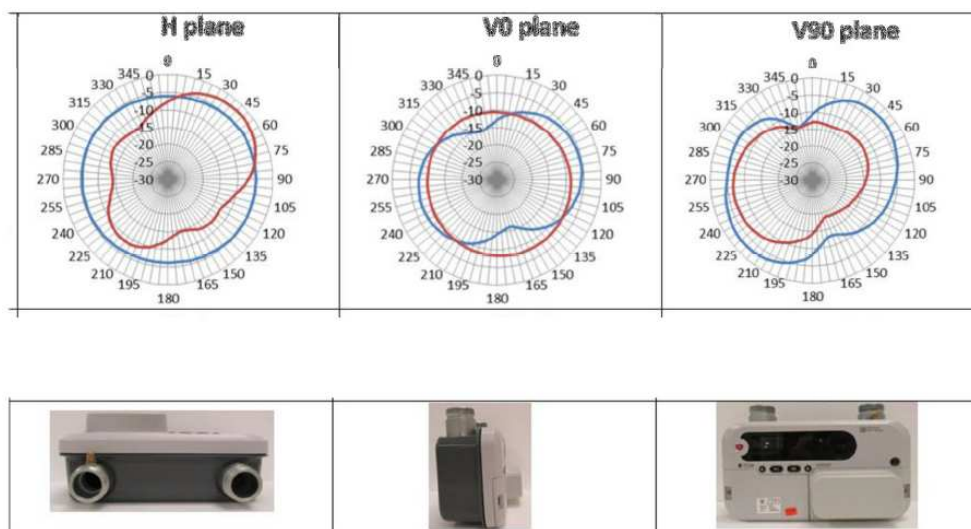


Figure 11: Top three radiation plots at 169 MHz, left H plane centre E plane 0 and right E -plane 90 degrees. The bottom three images indicate orientation of gas meter, blue curve was vertical plane, red was horizontal.

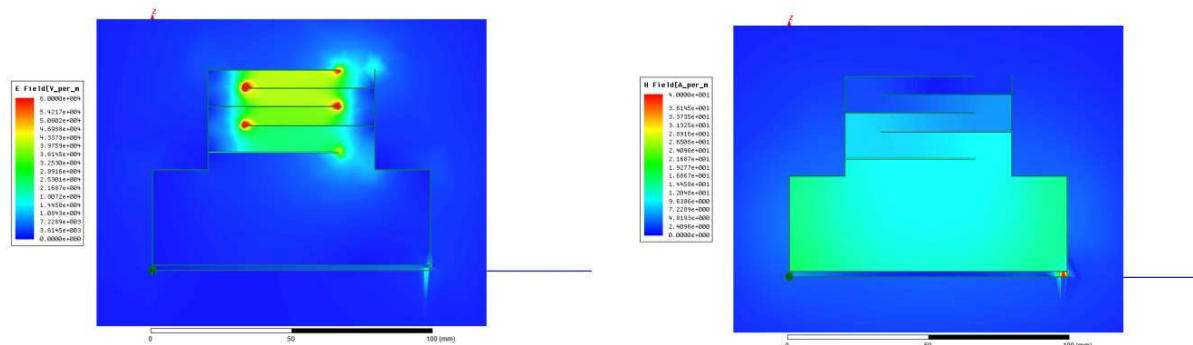


Figure 12: Left electric concentration right magnetic field concentration.

manufacturing.

6. CONCLUSION

A 169 MHz antenna was designed specifically to fit within a specified volume and be manufactured rapidly. The performance achieved exceeded the initial specification will allow the smart meters to be deployed in weak signal areas.

ACKNOWLEDGMENT

I wish to acknowledge the support of EDM I meters in particular Eric Beattie for help in providing measurements on the antenna performance. The antenna is subject to a patent application [6].

REFERENCES

1. Stefampv, M., *European Smart Meter Demand "Metering International"*, No. 3, 2013.
2. Fuschini, F., et al., "Analysis of outdoor-to-indoor propagation at 169 MHz for smart metering applications," *IEEE Transactions on Antennas and Propagation*, 2015, DOI 10.1109/TAP.2015.2399507.
3. Moon, S.-M., et al., "Miniaturisation of 1/4 microstrip antenna using perturbation effect and plate loading for low-VHF-band applications," *Electronic Letters*, Vol. 47, No. 3, 2011.
4. Harrington, R. F., *Time-harmonic Electromagnetic Fields*, McGraw-Hill, Inc., 1961.
5. <http://www.proant.se/en/home.htm>, accessed 13/4/15.
6. "Antenna for VHF band and smart meters GB1412827.6 filed," Jul. 18, 2014.
7. Ziolkowski, R., et al., "Meta-material inspired engineering of antennas," *Proceedings of IEEE*, 11/2011, 2010, DOI: 10.1109/JPROC.2010.2091610.
8. Erentok, A. and R. W. Ziolkowski, "Two dimensional efficient metamaterial inspired, electrical small antenna," *Microwave Optical Tech. Lett.*, Vol. 49, 1669, 2007.
9. Ansoft HFSS v14 www.ansys.com.

A Miniaturized Metamaterial Inspired Hexaband Antenna for GSM, GPS-L1, WLAN and WiMAX Applications

Bharath Raj, G. S. Kartikeya, K. Ullas,
Sanjji N. Manjunath, and C. Vindhya

Antenna Research Laboratory, Department of Electronics and Communication
B.M.S. Institute of Technology and Management, Bengaluru, India

Abstract— This paper illustrates the application of metamaterial inspired unit cells in the patch as well as the ground plane to obtain a compact hexaband antenna. Distinct bands were obtained at various frequencies for GPS-L1 (1.575 GHz), GSM (1800/1900 GHz), UMTS (B2/B1), WLAN (2.4 and 5.5 GHz) and WiMAX (2.5 and 3.5 GHz). This was achieved while keeping the antenna dimensions limited to $30 \times 30 \times 1.6 \text{ mm}^3$ resulting in a miniaturized antenna. The proposed antenna has a size of $0.1575\lambda_0$. The antenna was fabricated and tested to verify the simulated results.

1. INTRODUCTION

In recent years, most devices such as smart phones, tablets and portable communication systems require services from various sources that operate in distinct frequency bands. The use of antennas that are responsive to a single band of frequency is inefficient as it requires several antennas for different purposes.

Multiband antennas resonate at multiple frequencies. This reduces the amount of VLSI real estate required to set up the communication device as a single antenna can replace multiple antennas resonating at distinct frequencies. However, one of the most significant drawbacks of a multiband antenna is its considerably larger size when compared to a single band antenna. This is counterproductive when the aim is to reduce the size of the device.

In [1], the authors have presented an antenna with dimensions $30 \text{ mm} \times 43 \text{ mm}$ for WiMAX, UMTS and WLAN applications. In [2], the paper presents a compact antenna with an overall dimension of $65 \text{ mm} \times 40 \text{ mm}$ for WLAN. In [3] the authors have presented an antenna that has a compact dimension of $40 \times 5 \text{ mm}^2$ mounted on a substrate of size $40 \times 65 \text{ mm}^2$. This antenna resonates at four bands.

In the design presented, metamaterial split ring resonators and other structures such as the spiral in the ground plane are implemented to obtain a hexa-band antenna. Furthermore, the size of the patch is reduced to $20 \times 20 \text{ mm}$ square which accounts for over 50% reduction in size. Hence a miniaturized hexa-band antenna has been obtained.

One major aspect of any multiband antenna is that several other parameters are compensated for getting multiple bands. These include gain, directivity and size of the antenna. To overcome this drawback various techniques have been devised. One prominent method is the application of metamaterial structures such as the split ring resonators to decrease the size. In the design presented, several metamaterial structures like the split ring resonators have been used to increase the number of bands and to miniaturize the design.

In this paper, the discussion is divided into five sections. The first section gives an introduction into the basic concepts that are discussed in the paper. The second section covers a brief theory of antenna's and metamaterials. This is followed by the description of the proposed antenna in the third section. The fourth section discusses the graphs and the results obtained. Finally, the paper is concluded with a review of the results obtained and its significance.

2. THEORY

DNG (double negative metamaterials) are extraordinary materials that simultaneously possess negative permittivity (ϵ) and permeability (μ). In 1967, Victor Veselago did extensive research on these materials and had analytically determined that refraction of light occurs in the reverse direction (negative refractive index) at the interface between a material with negative refractive index and a material exhibiting the usual refractive index (positive) [4].

Metamaterials are composite materials artificially engineered to obtain specific properties that do not occur naturally. Properties like negative permittivity and permeability are very useful in several fields like optics (for cloaking applications) and electromagnetic radiation (antennas) but are

not found in nature. Metamaterials is a good alternative in such cases [5]. These special properties are not controlled by changing the chemical composition of the material but rather by changing its physical structure. This allows large amount of flexibility in realizing different properties.

In antennas, the utilization of microwave metamaterial structures help in shrinking the size of the antenna. One common microwave metamaterial structure is the split ring resonator (SRR). Such SRR's, which have suitable inductive and capacitive characteristics, are integrated in designing antennas that are small and compact.

One of the most common DNG structure is the split ring resonator. The splits in the rings helps in the process of making the SRR unit cell resonant at radiated wavelengths which are to a great extent larger than the diameter of the rings. Therefore, the utilization of such SRR's reduce the size of the antenna.

3. PROPOSED DESIGN

3.1. Unit Cell

The patch design consists of square split rings, which serves as the metamaterial structures for obtaining the desired operating frequencies[6]. There are three split rings each of thickness 0.5 mm. The spacing between these rings are also 0.5mm. The largest ring has a dimension of $20 \times 20 \text{ mm}^2$. The centre of the patch consists of a circular patch of radius 6.2 mm with an interlocking pattern at the middle[9]. The patch is positioned on the substrate whose dimensions are $30 \times 30 \times 1.6 \text{ mm}^3$. The antenna is excited using a line feed of length 5 mm [10]. The antenna patch design is shown in Fig. 1.

3.2. Ground Plane

The FR4 Epoxy substrate ($\epsilon_r = 4.4$) is 1.6 mm thick. The Ground plane is in the shape of a spiral which is also a meta-material structure as shown in Fig. 1. The spiral is formed by etching out copper from the ground plane. The thickness of the etched region is 0.2 mm. The spiral structure in the ground adds extra resonating bands in the antenna. The dimensions of the ground plane is $30 \times 30 \text{ mm}^2$.

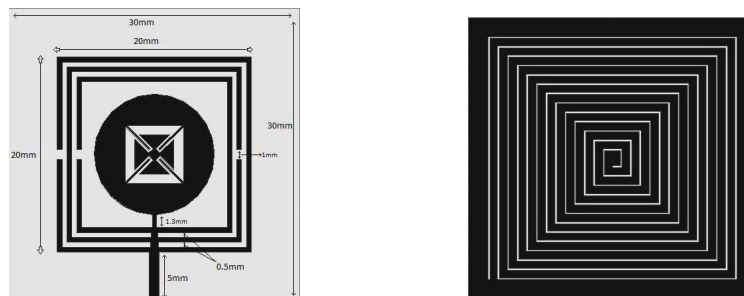


Figure 1: Antenna patch and ground plane.

The inclusion of these meta-material structures in the antenna design has facilitated good S_{11} characteristics as well as miniaturization of the design [6].

4. RESULTS AND DISCUSSION

The S_{11} characteristics have shown resonating frequencies at several commercially used frequency bands such as GPS-L1 (1.575 GHz), GSM (1800/1900 GHz), UMTS (B11/B1), WLAN(2.4 and 5.5 GHz). The overall size of the antenna is 30 mm along both length and breadth; with the largest SRR having a maximum size of 20 mm along the length and breadth.

The graph below shows the S_{11} characteristics (simulated) for the following cases:

- S_{11} without the spiral in the ground plane (dashed graph)
- S_{11} without the central circular pattern (dotted graph)
- S_{11} of the proposed antenna (solid graph)

It is observed that the presence of the spiral in the ground plane increases the number of resonating bands. In addition, we also see that the resonating frequencies have shifted towards the lower frequency region.

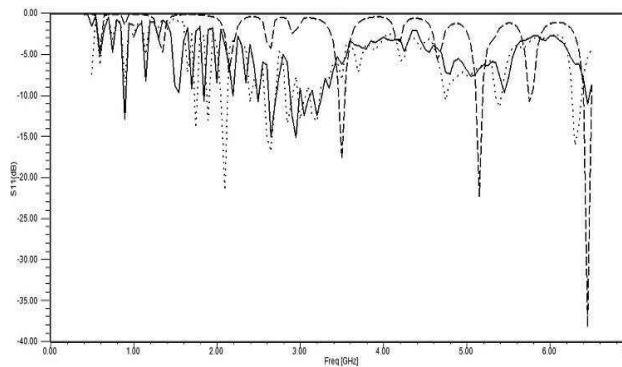


Figure 2: S_{11} graphs under different parameters.

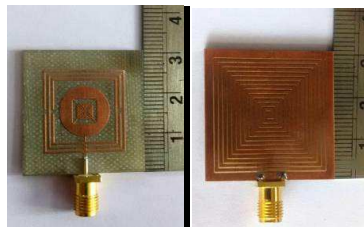


Figure 3: The fabricated antenna.

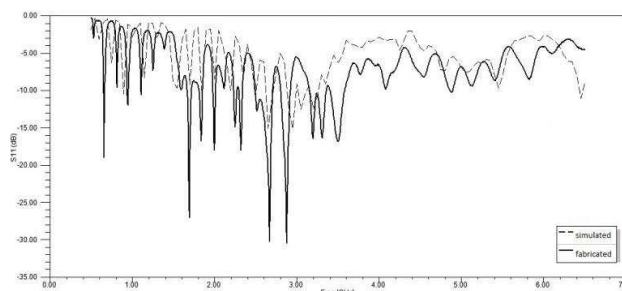


Figure 4: S_{11} graph of the proposed antenna.

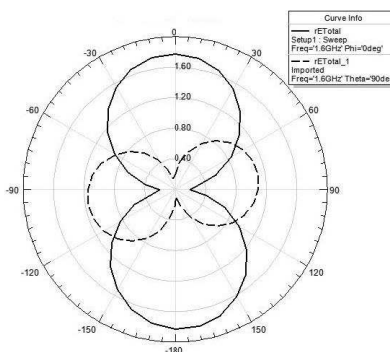


Figure 5: Radiation pattern: E & H -plane 1.6 GHz (GPS-L1).

The antenna was fabricated with the MITS machine and the S_{11} was determined and plotted in a graph.

The S_{11} graph for the proposed antenna was simulated and observed as shown by the dashed line. The fabricated antenna had an S_{11} as shown by the solid line in the figure below:

From the graph it is inferred that the antenna resonates at several frequency bands from 900MHz to 6.5 GHz. Among these, the useful bands are obtained at GSM, GPS-L1, WLAN and WiMAX ranges.

The fabricated antenna displays better S_{11} characteristics at several frequencies in comparison to the simulated results. Apart from this, the frequencies of resonance are comparably similar to the simulated antenna. Some of the bands in this antenna satisfies the -6 dB S_{11} which is good enough for compact portable wireless communication devices [7].

The graphs in the following figures show a fairly omni-directional radiation pattern at most

frequencies, which is useful in most wireless communication devices. Besides, the radiation patterns exhibit wide beam widths which is valuable in GSM communication. The radiation pattern for 5.5 GHz shows a deviation from the other ones. The pattern for this band shows a narrower beam width and increased directivity.

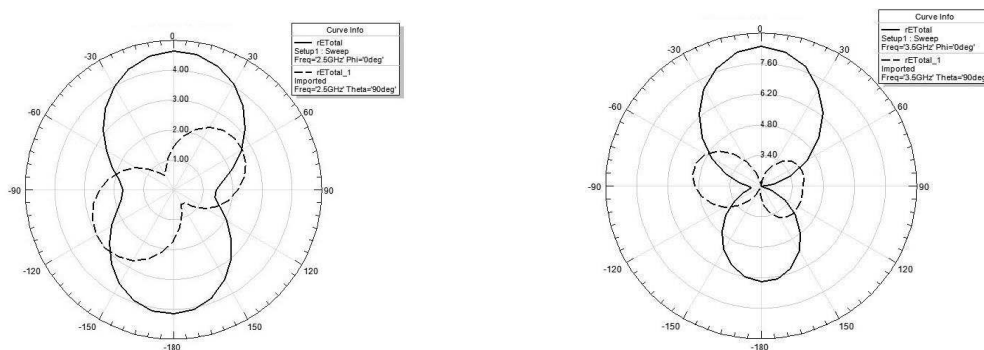


Figure 6: Radiation pattern: E & H -plane 2.5 GHz (WiMAX) and 3.5 GHz (WiMAX).

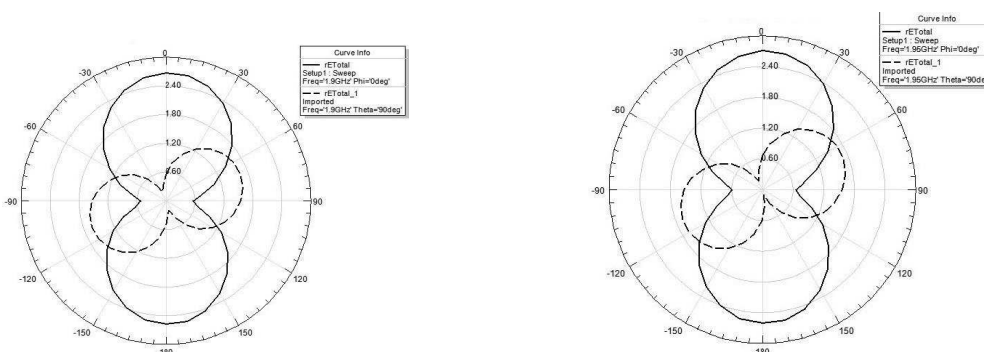


Figure 7: Radiation pattern: E & H -plane 1.9 GHz (GSM) and 1.95 GHz (GSM).

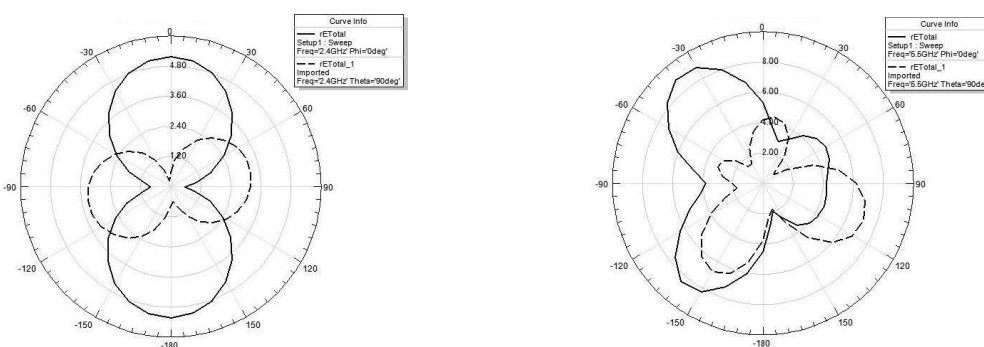


Figure 8: Radiation pattern: E & H -plane 2.4 GHz (WLAN) and 5.5 GHz (WLAN).

5. CONCLUSION

We have designed, fabricated and tested a miniaturized multiband meta-material Antenna with an overall dimension of $30 \times 30 \text{ mm}^2$ and resonating frequencies at GPS-L1 (1.575 GHz), GSM (1800/1900 GHz), UMTS (B2/B1), WLAN (2.4 and 5.5 GHz). This design, in addition to the common SRR, uses two other meta-material structures which has been implemented at the center of the patch and in the ground plane. These structures have shifted the resonating frequencies towards the lower frequency region, and increased the number of bands obtained for the specified size of the antenna.

ACKNOWLEDGMENT

We duly thank Dr. Hariprasad S. A. (H.O.D, Electronics and Communication department, BMSIT) for his support and encouragement in the preparation of this paper. We also extend our heartfelt thanks to the management of BMSIT for their support. Finally, we would like to thank the engineers of Anritsu India Pvt. Ltd for the testing of our antenna.

REFERENCES

1. Yu, Y.-C. and J.-H. Tarng, "A novel modified multiband planar inverted-F antenna," *IEEE Antennas and Wireless Propagation Letters*, Vol. 8, 189–192, 2009.
2. Chen, S.-B., et al., "Modified T-shaped planar monopole antennas for multiband operation," *IEEE Transactions on Microwave Theory and Techniques*, Vol. 54, No. 8, 3267–3270, 2006.
3. Pattnaik, S. S., J. G. Joshi, S. Devi, and M. R. Lohokare, "Electrically small rectangular microstrip patch antenna loaded with metamaterial," *2010 9th International Symposium on Antennas Propagation and EM Theory (ISAPE)*, 247–250, 2010.
4. Veselago, V. G., "The electrodynamics of substances with simultaneously negative values of ϵ and μ ," *Physics-Uspekhi*, Vol. 10, No. 4, 509–514, 1968.
5. Marqués, R., F. Martín, and M. Sorolla, *Metamaterials with Negative Parameters: Theory, Design and Microwave Applications*, Vol. 183, John Wiley & Sons, 2011.
6. Bilotti, F., A. Toscano, and L. Vegni, "Design of spiral and multiple split-ring resonators for the realization of miniaturized metamaterial samples," *IEEE Transactions on Antennas and Propagation*, Vol. 55, No. 8, 2258–2267, 2007.
7. Elsheakh, D. M. and A. M. Safwat, "Compact 3D USB dongle monopole antenna for mobile wireless communication bands," *International Journal of Microwave and Wireless Technologies*, Vol. 6, No. 6, 639–644, 2014.
8. Karthikeya, G. S., S. Kaundinya, and S. A. Hariprasad, "Dual band hexagonal microstrip antenna loaded with hexagonal and cylindrical EBG," *2014 IEEE Fifth International Conference on Communications and Electronics (ICCE)*, IEEE, 2014.
9. Liang, J., et al., "Study of a printed circular disc monopole antenna for UWB systems," *IEEE Transactions on Antennas and Propagation*, Vol. 53, No. 11, 3500–3504, 2005.
10. Si, L.-M. and X. Lv, "CPW-FED multi-band omni-directional planar microstrip antenna using composite metamaterial resonators for wireless communications," *Progress In Electromagnetics Research*, Vol. 83, 133–146, 2008.

Quad Band Split Koch Snowflake Antenna for LTE/WLAN/WiMAX Applications

K. Ullas, G. S. Karthikeya, Bharath Raj, Sanji N. Manjunath, and C. Vindhya
Antenna Research Laboratory, BMS Institute of Technology, India

Abstract— In this paper, Multiple Split Koch Snowflake Fractal is investigated as resonating element. It was found to resonate at 0.77–0.82 GHz, 2.3–2.42 GHz, 3.6–3.7 GHz and 5.3–6 GHz with center frequency of 0.8 GHz, 2.35 GHz, 3.65 GHz and 5.5 GHz which covers the LTE/WLAN/WiMAX spectrum. The antenna was realized on a FR4 epoxy substrate with dimension $0.08\lambda_o \times 0.08\lambda_o \times 0.042\lambda_o$ (30 mm \times 30 mm \times 1.6 mm). Parametric analysis was performed on the dimension of various elements of the antenna. Fractal structure was responsible for multiband resonance and the addition of split element in the fractal enhanced the ability of the antenna to resonate at lower frequency. Further the antenna was fabricated and tested.

1. INTRODUCTION

Developing an Antenna system has always been a challenging task. Recent trends in wireless communication demands a compact low profile antenna resonating at multiple frequency bands. This has resulted in the development of many multiband antennas for portable devices.

WiMAX is a standard set under IEEE 802.16 family for wireless communication providing high speed data rates for fixed stations. The IEEE 802.11 a/b/g/n/ac (2.4 & 5.2 GHz) and also known as WLAN has been utilized extensively to provide wireless service over a specified area [1]. Long term evolution which is popularly known as 4G LTE is the latest technology in wireless standards providing very high data rates for portable devices on the go. LTE TDD (Band 44 703–803 MHz) which is a subset of LTE where the uplink and downlink shares same frequency but only time multiplexed is yet to be fully exploited.

The increase in number of antennas in portable wireless devices goes hand in hand with the number of frequency bands allocated for its use, while the volume may remain the same or reduced. This has a serious consequence of reduced antenna efficiency, data rates and coverage [2]. One of the possible solutions to these problems is to use frequency reconfigurable antenna [3, 4]. A recent survey carried on various mobile phones has revealed that PIFA and Monopole are widely used antennas to achieve multiband resonance [5]. Structures like fractals, metamaterials are yet to be implemented on these devices to achieve multiband operation at compact size.

Metamaterials have recently been dealt with great enthusiasm as part of the antenna to achieve miniaturization [6, 7]. These materials exhibit negative refractive index due to simultaneous negative permittivity and permeability. A Fractal is a mathematical set which exhibits self-similarity at every scale. Fractal as antennas has been dealt with similar enthusiasm as metamaterials to achieve multiband resonance [8, 9].

In this paper, the proposed antenna structure is inspired from split ring resonator (SRR) which is a metamaterial and 1st iteration of Koch snowflake fractal.

2. ANTENNA DESIGN

The geometry and the dimension of proposed antenna is shown in the Fig. 1. The antenna is realized on a fr4 epoxy substrate ($\epsilon_r = 4.4$) with loss tangent of 0.02 at a standard thickness of 1.6 mm. The substrate dimension is 30 mm \times 30 mm \times 1.6 mm. It is excited using a normal microstrip line feed technique.

2.1. Microstrip Patch

It consists of three Koch snowflakes of first iteration with gradual increase in perimeter. The Koch snowflake fractals has split element. Each Koch fractal is of the thickness 0.5 mm with split element of width 0.4 mm is separated by a distance of 2 mm. The width of the transmission line is tapered to improve the impedance matching [10]. At the feed point, the width of the transmission line is $wf = 1.5$ mm, $wl1 = 1.2$ mm, $wl2 = 0.96$ mm.

2.2. Ground Plane

The ground plane consists of a protruding structure of length 13.63 mm. The protruding element is of the width 2.5 mm and displaced slightly to the left w.r.t center of the substrate.

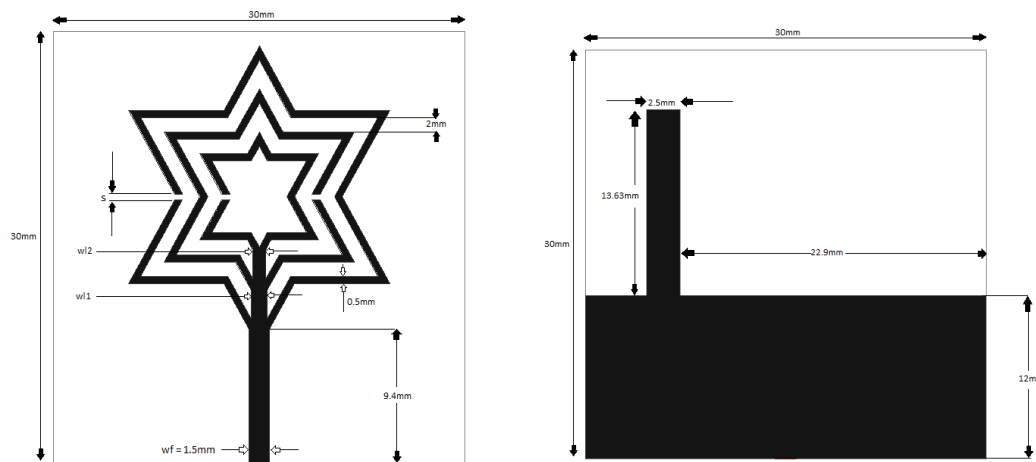


Figure 1: The geometry of proposed antenna and its ground plane with protruding element. $s = 0.4$ mm, $wl1 = 1.2$ mm, $wl2 = 0.96$.

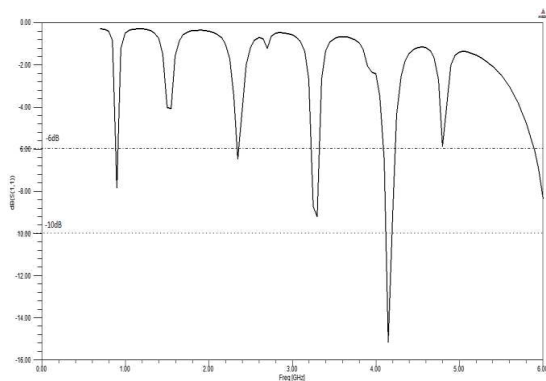


Figure 2: S_{11} with normal ground plane and split structure retained.

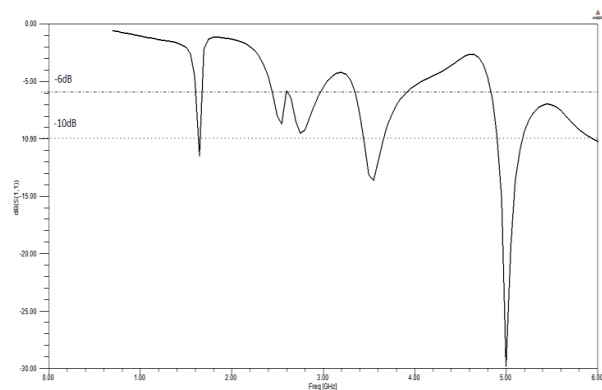


Figure 3: S_{11} without split element but retaining the proposed ground plane.

3. RESULTS AND DISCUSSION

The proposed design was simulated using a finite element method solver-HFSS and the result of these simulations are discussed below.

3.1. With Normal Ground Plane and the Split Element in Koch Snowflake Retained

Here the protruding element in the ground plane was removed and the ground plane was designed to cover the entire substrate of $30\text{ mm} \times 30\text{ mm}$ dimension. The antenna resonated at frequencies of 0.9 GHz, 2.35 GHz, 3.22 GHz–3.32 GHz with -6 dB return loss as shown in the Fig. 2. Careful observation reveals that the antenna did not resonate well at WLAN band of 5.17–5.82 GHz. The antenna resonated with -10 dB return loss bandwidth only at 4.15 GHz which was not a useful band.

3.2. Without the Split Element in the Koch Snowflake and Retaining the Proposed Ground Plane Design Containing Protruding Structure

The split element is found in the metamaterial SRR. Here the antenna was simulated without the split element in the Koch snowflake and was found to resonate with -10 dB bandwidth at 1.63–1.65 GHz, 3.44–3.65 GHz and 4.9 to 5.2 GHz as shown in Fig. 3. Comparing Fig. 2. and Fig. 3, It's clear that the lowest resonant band of 0.9 GHz was found missing due to the absence of split element in Koch snowflake

3.3. Proposed Antenna

Finally, the proposed antenna is simulated retaining both protruding structure in ground plane and split element in the Koch snowflake as shown in Fig. 1. Multiband resonance was achieved. -10 dB return loss bandwidth was obtained from 2.3–2.41 GHz, 3.6–3.7 GHz and 5.3–6 GHz bands. Further -6 dB return loss bandwidth was obtained from 0.77 GHz to 0.82 GHz. -6 dB magnitude

of return loss is sufficient for antennas in compact devices [11]. The center frequency of these bands were 0.8 GHz, 2.35 GHz, 3.65 GHz and 5.5 GHz as shown in Fig. 4. The obtained bands very well cover LTE/LTE-TDD bands (band 42, 43, 44) [12], WLAN dual band, WiMAX (2.3 GHz) band.

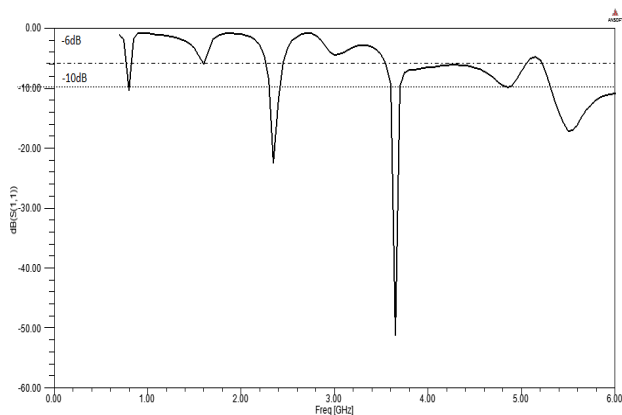


Figure 4: S_{11} graph of proposed antenna.

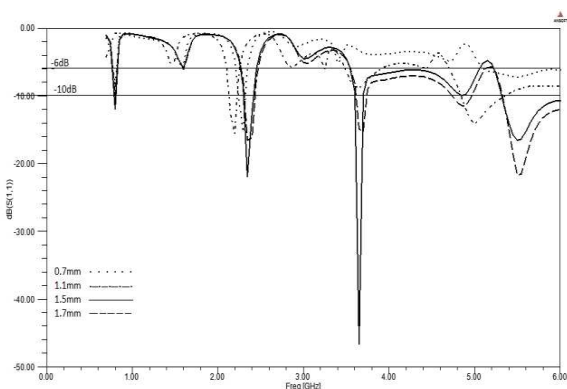


Figure 5: S_{11} graph of parametric analysis when the width of the transmission line is varied from $wf = 0.7$ mm to 1.7 mm.

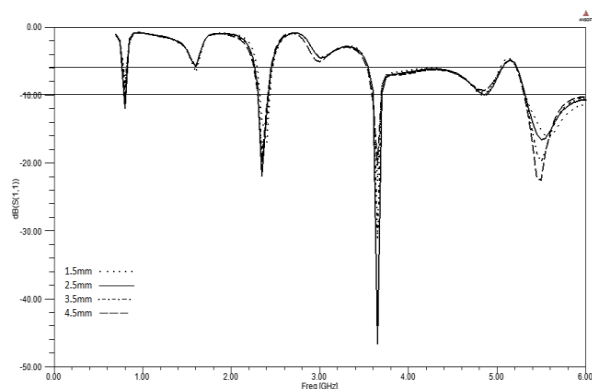


Figure 6: S_{11} graph of parametric analysis when the width of the Protruding structure in ground plane is varied from $pw = 1.5$ mm to 4.5 mm

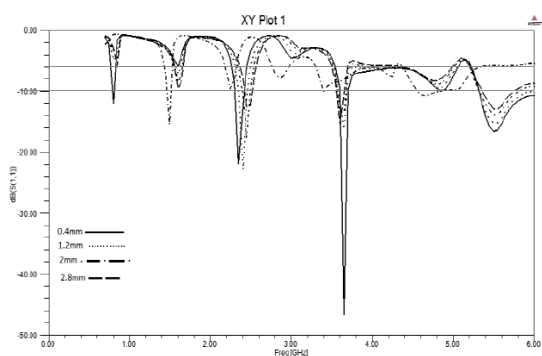


Figure 7: S_{11} graph of parametric analysis when the position of the structure in the ground plane is shifted from the original position to its left.

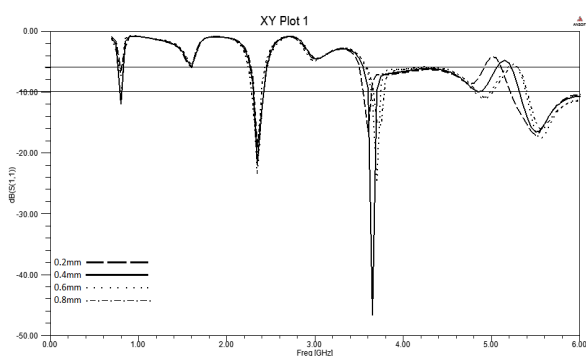


Figure 8: S_{11} graph of parametric analysis when the width of the split element is varied from $s = 0.2$ mm to 0.8 mm.

Also with the inclusion of split element in Koch snowflake fractal, the lowest resonant frequency of 0.8 GHz was achieved. Further inclusion of protruding structure in ground plane resulted in an additional 5.2–6 GHz band [13].

The transmission line is varied from $wf = 0.7$ mm to 1.7 mm. of the Protruding structure in ground plane is varied from $pw = 1.5$ mm to 4.5 mm.

3.4. Parametric Analysis

Parametric analysis were carried out extensively to study the behavior of antenna by varying the dimensions of width of transmission line, width and position of the protruding structure, and width of the split element in Koch snowflake and the results obtained are shown in Fig. 5 to Fig. 8.

3.5. Radiation Pattern

Figures 9, 10, 11 and 12 show the radiation pattern of the proposed antenna with *E* and *H* plane for the center frequency of resonant bands.

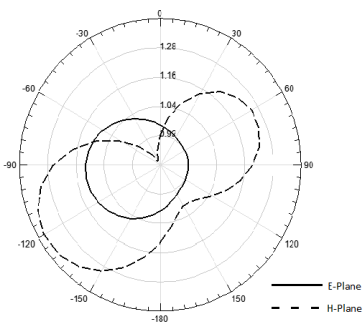


Figure 9: *E*-plane and *H*-plane Radiation pattern at 0.8 GHz.

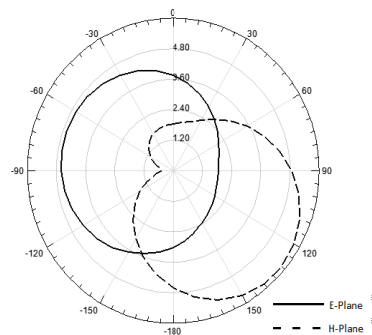


Figure 10: *E*-plane and *H*-plane Radiation pattern at 2.35 GHz.

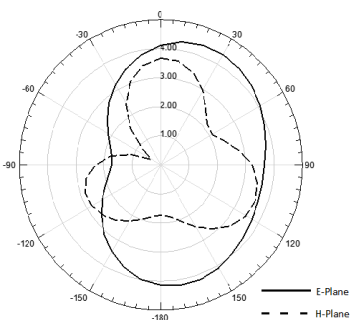


Figure 11: *E*-plane and *H*-plane Radiation pattern at 3.65 GHz.

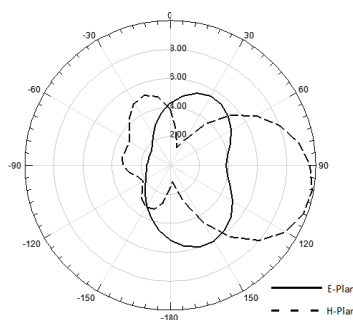


Figure 12: *E*-plane and *H*-plane Radiation pattern at 5.5 GHz.

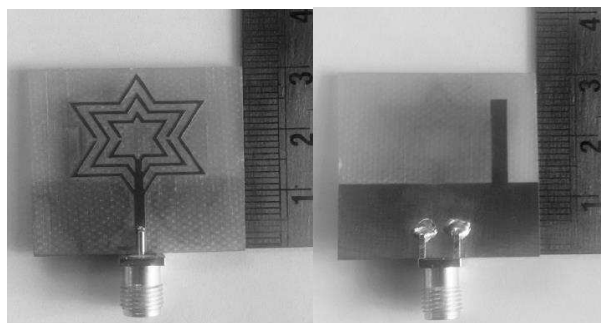


Figure 13: Fabricated antenna.

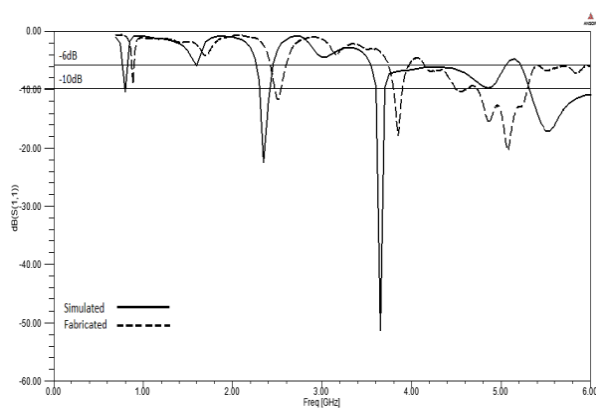


Figure 14: S_{11} graph of simulated and fabricated result.

4. FABRICATION RESULTS

Figure 13 shows the fabricated antenna. The S_{11} graph of simulated and fabricated antenna is shown in Fig. 14.

5. CONCLUSION

A quad band antenna for LTE/LTE-TDD, WLAN and WiMAX application is presented. The Koch snowflake fractal is responsible for multiband resonance. The split element inspired from metamaterial SRR in the Koch snowflake gives an additional low frequency band of 0.8 GHz. The protruding structure in ground plane is responsible for resonance at 5 GHz band. Resonant bands of 0.77–0.82 GHz, 2.3–2.4 GHz, 3.6–3.7 GHz and 5–5.3 GHz with center frequency at 0.8 GHz, 2.35 GHz, 3.65 GHz and 5.1 GHz covering all the essential bands mentioned for wireless communication and applications.

ACKNOWLEDGMENT

We duly thank Dr. Hariprasad (H.O.D, Electronics and Communication department, BMSIT&M) for his continued support and encouragement in the preparation of this paper. We also thank Entuple technologies and Anritsu for helping us in fabrication and testing of the proposed antenna.

REFERENCES

1. Karthikeya, G. S., S. Kaundinya, and S. A. Hariprasad, "Dual band hexagonal microstrip antenna loaded with hexagonal and cylindrical EBG," *2014 IEEE Fifth International Conference on Communications and Electronics (ICCE)*, IEEE, 2014.
2. Ilvonen, J., R. Valkonen, J. Holopainen, and V. Viikari, "Multiband frequency reconfigurable 4G handset antenna with MIMO capability," *Progress In Electromagnetics Research*, Vol. 148, 233–243, 2014.
3. Yang, S., et al., "Frequency-reconfigurable antennas for multiradio wireless platforms," *IEEE Microwave Magazine*, Vol. 10, No. 1, 66–83, 2009.
4. Yang, S.-L. S., A. A. Kishk, and K.-F. Lee, "Frequency reconfigurable U-slot microstrip patch antenna," *IEEE Antennas and Wireless Propagation Letters*, Vol. 7, 127–129, 2008.
5. Rowell, C. and E. Y. Lam, "Mobile-phone antenna design," *IEEE Antennas and Propagation Magazine*, Vol. 54, No. 4, 14–34, 2012.
6. Ziolkowski, R. W. and A. Erentok, "Metamaterial-based efficient electrically small antennas," *IEEE Transactions on Antennas and Propagation*, Vol. 54, No. 7, 2113–2130, 2006.
7. Ziolkowski, R. W. and A. Erentok, "At and below the Chu limit: Passive and active broad bandwidth metamaterial-based electrically small antennas," *IET Microwaves, Antennas & Propagation*, Vol. 1, No. 1, 116–128, 2007.
8. Puente-Baliarda, C., et al., "On the behavior of the Sierpinski multiband fractal antenna," *IEEE Transactions on Antennas and Propagation*, Vol. 46, No. 4, 517–524, 1998.
9. Werner, D. H. and S. Ganguly, "An overview of fractal antenna engineering research," *IEEE Antennas and Propagation Magazine*, Vol. 45, No. 1, 38–57, 2003.
10. Si, L.-M. and X. Lv, "CPW-FED multi-band omni-directional planar microstrip antenna using composite metamaterial resonators for wireless communications," *Progress In Electromagnetics Research*, Vol. 83, 133–146, 2008.
11. Elsheakh, D. M. and A. M. E. Safwat, "Compact 3D USB dongle monopole antenna for mobile wireless communication bands," *International Journal of Microwave and Wireless Technologies*, Vol. 6, No. 06, 639–644, 2014.
12. <http://www.radio-electronics.com/info/cellulartelecomms/lte-long-term-evolution/lte-frequency-spectrum.php>.
13. Panda, J. R. and R. S. Kshetrimayum, "A printed 2.4 GHz/5.8 GHz dual-band monopole antenna with a protruding stub in the ground plane for WLAN and RFID applications," *Progress In Electromagnetics Research*, Vol. 117, 425–434, 2011.

Miniaturized Multiband Antenna with Modified Split-ring Resonator for WLAN/WiMAX Applications

C. Vindhya, G. S. Karthikeya, Sanjji N. Manjunath, K. Ullas, and Bharath Raj

Antenna Research Laboratory, Department of Electronics and Communication

B.M.S. Institute of Technology and Management, Bengaluru, India

Abstract— A novel compact and planar tri-band antenna having frequency beam-scanning ability is designed using a metamaterial-inspired structure. The metamaterial (MTM) configuration consists of a marginally remodeled split-ring resonator (SRR). The antenna has a unique ground plane with a comb structure. The proposed design has dimensions $20 \times 20 \times 1.6 \text{ mm}^3$. It resonates at 2.351, 3.635 and 5.121 GHz respectively which is suited for LTE2300, WiMAX and WLAN applications. Radiation pattern shifts 90° for a change 0.2 GHz in the range 3.8–4 GHz providing beam steering applicable for MIMO LTE (4G) and WiMAX.

1. INTRODUCTION

As a consequence of rapid development in wireless communication, compact multi-band antennas attracted research interest. Significant progress is seen in the field of microstrip antenna due to its convenient features such as low cost, light-weight and flexibility. Several antennas operating in various bands such as GSM, GPS, WiFi, and WiMAX are essential in mobile phones [1]. It is desirable to have a single antenna operating at multiple bands. This enhances compactness which reduces VLSI real estate, cost and volume required in the casing of the device.

The challenge is to miniaturize the antenna to the maximum degree while retaining resonance at multiple bands. Various multiband antennas involving inverted F, slot and planar arrangement show limitations of increased size and complexity [2–4]. Several successful attempts have been made to develop compact antennas using MTM configuration [5–7]. An attempt has been made to improvise on a conventional SRR to scale-down the dimensions while retaining multifrequency functionality. Additional splits/gaps are introduced and repositioned in each ring of the SRR. The thickness is maintained standard at 1.6 mm [8, 9]. The design uses only one set of simple SRR structure and the dimensions are reduced to $20 \text{ mm} \times 20 \text{ mm}$. The proposed design has multiple frequency bands at 2.351, 3.490–3.770 and 5.041–5.256 GHz with reflection co-efficient greater than -6 , -10 and -10 dB respectively. It covers LTE2300 (2300–2400 MHz), WiMAX at 3.5 GHz and WLAN at 5.2 GHz.

The radiating face of the antenna consists of a remodeled SRR. Resonant frequencies are created by fine tuning the gaps and embedding dielectric slots in the ground plane whose positions were realized through a parametric study. Out of a total of four gaps/splits, three have a width equal to the thickness of the ring and the fourth is slightly smaller.

In addition to triple band operation, the antenna exhibits frequency beam-scanning ability inherent in a leaky wave antenna. Beam steering up to 90 degree can be achieved between 3.5–4 GHz. One of the LTE bands is centered at 3.5 GHz which is also applicable for WiMAX. This feature is similar to the property of a smart antenna used in MIMO system [10].

The paper is organized as follows. Section 2 contains the principle behind metamaterials. Design parameters are introduced in Section 3. Results are discussed in Section 4. The work is concluded in Section 5.

2. METAMATERIALS

Metamaterial is an artificial material exhibiting electromagnetic responses like negative permittivity and negative permeability which are not found in naturally available substances [11]. An SRR is one of the common metamaterial configurations [12, 13]. They form the basis for miniaturization of antennas. Conventional antennas need to be at least half the size of the wavelength they are operating in. Inclusion of metamaterial reduces the size to immensely. SRR is a composite metamaterial. It consists of concentric rings made of non-magnetic material (here, copper) separated by a gap which yields effective negative magnetic permeability [14, 15].

3. ANTENNA CONFIGURATION

The geometry of the proposed antenna is shown in Figure 1. It is fabricated on FR4 epoxy substrate of dimension $20\text{ mm} \times 20\text{ mm} \times 1.6\text{ mm}$ with dielectric constant 4.4 and loss tangent of 0.02. The patch consists of a metamaterial structure comprising a rectangular split-ring configuration with two non-opposite slits in each ring which are repositioned. The design uses a novel ground plane configuration. The size of ground plane is half the overall size, i.e., $20\text{ mm} \times 10\text{ mm}$. It is slotted with a wide gap at the centre and narrower gap on either sides. Gap between slots on either sides of the centre remains constant. It is fed by a microstrip line which can be connected by an SMA. Ansys HFSS software is used to evaluate the antenna performance. The other optimal parameters are $W = 20\text{ mm}$, $d = 2\text{ mm}$, $d_1 = 1.5\text{ mm}$, $d_2 = 7\text{ mm}$, $d_3 = 9.75\text{ mm}$, $d_4 = 4\text{ mm}$, $t = 1\text{ mm}$, $g = 1\text{ mm}$, $g_2 = 10\text{ mm}$.

4. RESULTS AND DISCUSSION

Frequency bands at 2.351, 3.635 and 5.121 GHz with reflection co-efficient -6.467 , -13.494 , -15.201 -dB respectively are presented in Figure 2(b). Bandwidths for resonances with S_{11} better than -10 dB at 3.635 GHz is 140 MHz and at 5.121 GHz is 96 MHz. The approach taken to arrive at the final design can be explained using antennas 1, 2, 3 and 4 (Figures 2(c) and 2(d)). Photograph of the fabricated antenna next to a scale is shown in Figure 2(a).

Step 1. A full patch (complete copper surface) with slotted ground is considered. Ground plane resembles comb structure with gap “ $2t$ ” at the center and gap “ t ” between slots on either sides. It results in resonance at 3.4 and 4.4 GHz with S_{11} less than -4 dB .

Step 2. Next, a conventional SRR with a complete copper ground plane of dimensions $20\text{ mm} \times$

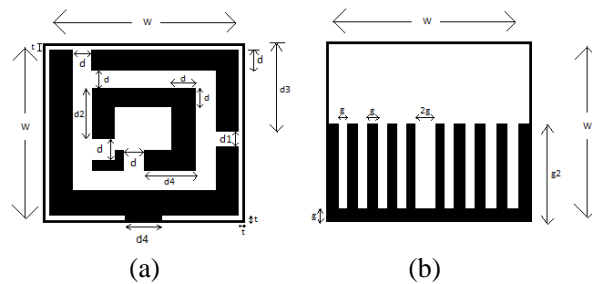


Figure 1: (a) Radiating surface and (b) ground plane of final design (antenna 4).

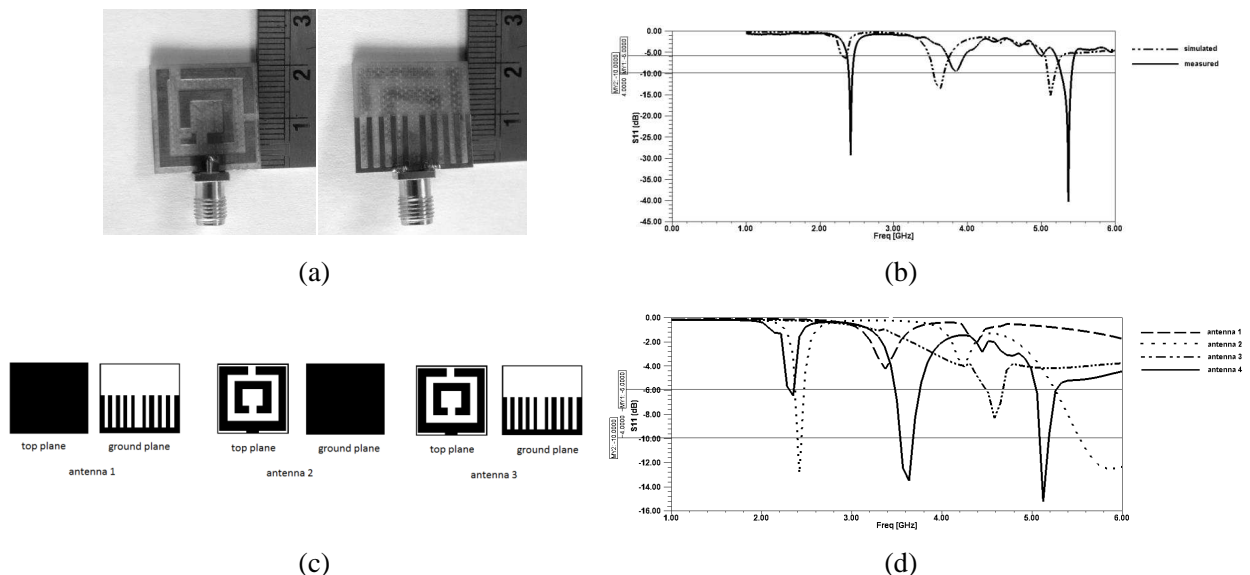


Figure 2: (a) Photograph of the fabricated antenna (1) top plane (2) ground plane. (b) Simulated and measured S_{11} for final design. (c) Preliminary designs. (d) Simulated S_{11} for antenna 1, antenna 2, antenna 3 and antenna 4.

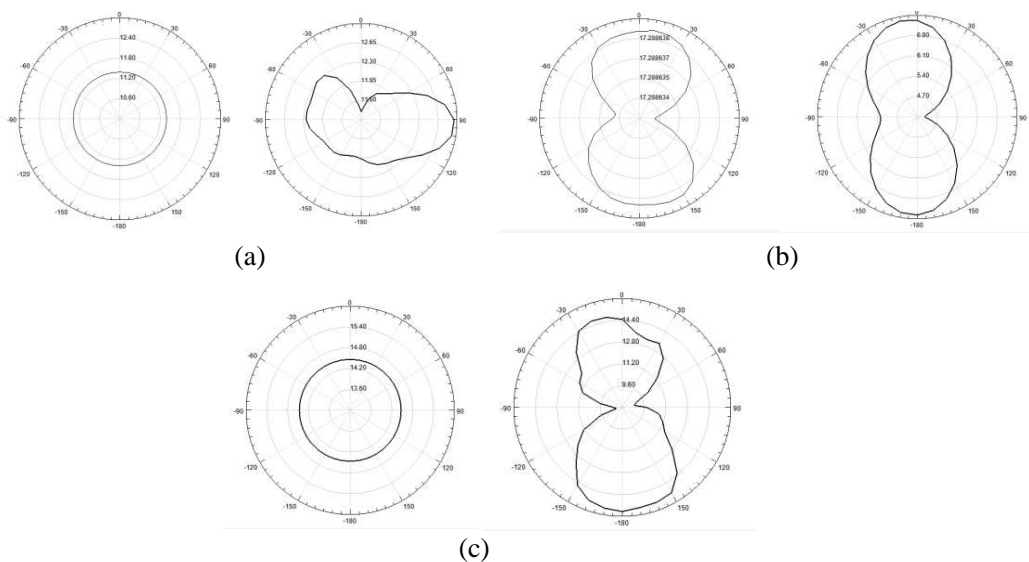


Figure 3: (a) Radiation pattern along E plane and H plane at 2.35 GHz respectively. (b) Radiation pattern along E plane and H plane at 3.63 GHz respectively. (c) Radiation pattern along E plane and H plane at 5.12 GHz respectively.

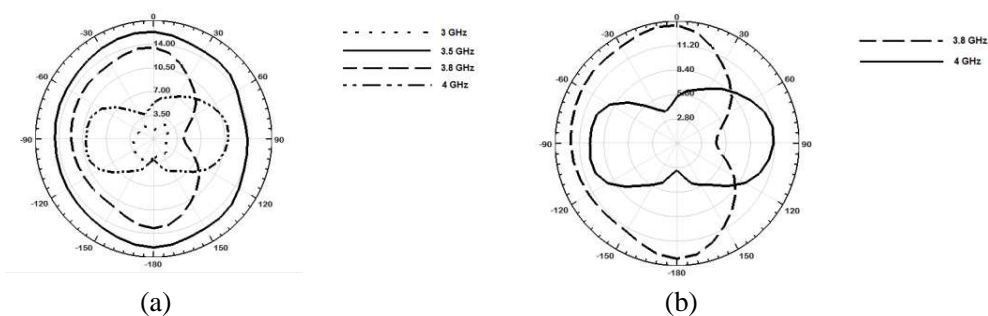


Figure 4: (a) Radiation pattern along H plane at frequencies 3, 3.5, 3.8 and 4 GHz. (b) 90° shift in radiation pattern seen between 3.8–4 GHz

10 mm is designed and simulated. Results show resonance at 2.4 and 5.9 GHz with S_{11} greater than -10 dB with approximate bandwidths 42 MHz and 500 MHz respectively.

Step 3. A typical SRR with slotted ground plane are now combined and checked. This configuration yields only one frequency band at 4.5 GHz with bandwidth 159 MHz at -6 dB.

Addition of a new set of gaps/splits resulted in multiple bizarre resonances. The position and width of each gap were tweaked to get the final result through parametric analysis.

Radiation pattern along E and H planes at resonant frequencies 2.35, 3.6 and 5 GHz is shown in Figures 3(a), (b) and (c) respectively. It can also be observed that the radiation pattern changes with frequency variation in the range 3.8–4 GHz which is a characteristic of leaky-wave antennas. A change of 0.2 GHz returns a 90° degree shift in radiation pattern along H plane. This is depicted in Figure 4. Measured S_{11} is -29.3 , -9.22 and -40.3 dB at 2.416, 3.865 and 5.361 GHz respectively. The discrepancy between simulated and measured return loss could be attributed to the interface with the connector.

5. CONCLUSION

A highly compact tri-band antenna with a modified SRR is designed and studied. In this letter, we explore improvisations on SRR architecture as well as ground plane which display simultaneous performance in WLAN and WiMAX bands. The frequency bands are centered at 2.351, 3.635 and 5.121 GHz. The design occupies a meager volume of $0.156\lambda_0 \times 0.156\lambda_0 \times 0.012\lambda_0$. Besides, beam scanning of 90° can be achieved. This feature finds applications in LTE2300 and WiMAX.

REFERENCES

1. Fujimoto, K. and J. R. James, Eds., *Mobile Antenna Systems Handbook*, Artech House, 2001.
2. Herraiz-Martínez, F. J., G. Zamora, F. Paredes, F. Martín, and J. Bonache, “Multiband printed monopole antennas loaded with OCSRRs for PANs and WLANs,” *IEEE Antennas Wireless Propag. Lett.*, Vol. 10, 1528–1532, 2011.
3. Mahmoud, N.-J. and T. A. Denidni, “A new triple-band circular ring patch antenna with monopole-like radiation pattern using a hybrid technique,” *IEEE Transactions on Antennas and Propagation*, Vol. 59, No. 10, 3512–3517, 2011.
4. Pei, J., et al., “Miniaturized triple-band antenna with a defected ground plane for WLAN/WiMAX applications,” *IEEE Antennas and Wireless Propagation Letters*, Vol. 10, 298–301, 2011.
5. Mehdipour, A., T. A. Denidni, and A.-R. Sebak, “Multi-band antenna loaded by ZOR and CSRR metamaterial structures with monopolar radiation pattern,” *IEEE Transactions on Antennas and Propagation*, Vol. 62, No. 2, 555–562, 2014.
6. Si, L.-M., W. Zhu, and H.-J. Sun, “A compact, planar, and CPW-fed metamaterial-inspired dual-band antenna,” *IEEE Antennas Wireless Propag. Lett.*, Vol. 12, 305–308, 2013.
7. Chu, Q.-X. and Y.-Y. Yang, “A compact ultrawideband antenna with 3.4/5.5 GHz dual band-notched characteristics,” *IEEE Transactions on Antennas and Propagation*, Vol. 56, No. 12, 3637–3644, 2008.
8. Gupta, S. and G. Mumcu, “Dual-band miniature coupled double loop GPS antenna loaded with lumped capacitors and inductive pins,” *IEEE Transactions on Antennas and Propagation*, Vol. 61, No. 6, 2904–2910, 2013.
9. Young, M., *The Technical Writer’s Handbook*, University Science, Mill Valley, CA, 1989.
10. Mahmoud, S. F., “A new miniaturized annular ring patch resonator partially loaded by a metamaterial ring with negative permeability and permittivity,” *IEEE Antennas Wireless Propag. Lett.*, Vol. 33, No. 1, 19–22, 2004.
11. Veselago, V. G., “The electrodynamics of substances with simultaneously negative values of ϵ and μ ,” *Physics Uspekhi*, Vol. 10, No. 4, 509–514, 1968.
12. Zhang, H., et al., “Design of circular/dual-frequency linear polarization antennas based on the anisotropic complementary split ring resonator,” *IEEE Transactions on Antennas and Propagation*, Vol. 357, No. 10, 3352–3355, 2009.
13. Quevedo-Teruel, Ó, M. N. M. Kehn, and E. Rajo-Iglesias, “Dual-band patch antennas based on short-circuited split ring resonators,” *IEEE Transactions on Antennas and Propagation*, Vol. 359, No. 8, 2758–2765, 2011.
14. Bilotti, F., A. Alu, and L. Vegni, “Design of miniaturized metamaterial patch antennas with-negative loading,” *IEEE Transactions on Antennas and Propagation*, Vol. 356, No. 6, 1640–1647, 2008.
15. Mahmoud, S. F., “A new miniaturized annular ring patch resonator partially loaded by a metamaterial ring with negative permeability and permittivity,” *IEEE Antennas Wireless Propag. Lett.*, Vol. 3, No. 1, 19–22, 2004.
16. Karthikeya, G. S., S. Kaundinya, and S. A. Hariprasad, “Dual band hexagonal microstrip antenna loaded with hexagonal and cylindrical EBG,” *2014 IEEE Fifth International Conference on Communications and Electronics (ICCE)*, IEEE, 2014.

Research on Dual Bandpass of Wide Stopband Filter with Tunable Center Frequency

Zhao-Qing Sun, Yong-Sheng Zhao, Han-Lin Duan, and Tao Jiang

College of Information and Communication Engineering

Harbin Engineering University, Harbin 150001, China

Abstract— A dual passband of wide stopband varactor tuned filter using stepped impedance resonators (SIRs) is proposed in this paper. A varactor is loaded on the middle of the E-shaped resonators, through changing the value of the bias voltage across the varactor, the center frequency of the second passband can be tuned from 1.56 GHz to 2.25 GHz, however, the center frequency of the first passband is fixed and maintained at 1.02 GHz. In fact, it is fixed during the whole process. The relative bandwidth of the first passband is 14.7%, the return loss of is 19 dB and the insertion loss is 0.2 dB. The second passband can tuning from 1.56 GHz to 2.25 GHz with the tuning range of 36.2%. The relative bandwidth almost keep unchanged. The return loss change from 16 dB to 30 dB and the insertion loss change from 0.2 dB to 0.8 dB. This filter proposed in this paper has a great characteristic of harmonic suppression, -20 dB up to 3.5 GHz. There are two advantages of the optimization process. The first is that a filter network is added in the input and output coupling line to depress stopband. The second is that spurlines are added at the input and output coupling line which can add zero between the two passbands, which improved the performance for filter. It is good to improve the selectivity of the filter. The filter proposed in this paper can achieve a compact size, lower insertion loss and wider rang harmonic suppression. Simulations show that the filter proposed is valid and has a good performance.

1. INTRODUCTION

Microwave filter as a basic part of all communication systems, its performance is directly related to the communication quality of the whole system, therefore, the filter is an integral part of communication systems which has attracted a lot of research. At the same time, there is ever increasing shortage of spectrum resources as technology become more robust. The distribution of electromagnetic field and wave in the air is becoming more and more complex, tunable filter technology emerge as the times' require, obtains the wide spread research and application microstrip filter has the advantages of miniaturization, so the tunable filter that based on the microstrip has become an interesting area of study. There is neither need to redesign the structure of the system nor reprocessing circuit board, w we need to do is transfer switch and electrically tunable filter can realize the new assume and function.

There are mainly four types of tuning methods [1]: mechanical tuning method ferrite tuning method RFMEMS tuning method and varactor diode tuning method. Mechanical tuning method has the advantage of low price and is easy to make. But its volume is too large and its tuning speed is too low and therefore it can't meet the requirements any more [2]. Ferrite circuit has a large volume too, we need to adjustable magnetic field to control it. The use of the condition is too harsh, we abandon it [3]. The RFMEMS tuning method has a very small loss and can withstand high power, however, its switching speed is slow, adjustable rate is small (relatively high tuning voltage is needed, usually tens of volts or even hundreds of volts), it is difficult to integrate it with other circuits. It requires very strict encapsulation, and this package is very expensive. Therefore, its application is limited. Varactor diode tuning method has a high tuning speed and the design cost is low, besides, it is has the advantage of planar integrated ability. That's the reason it has gained wide spread application. We conclude that it offer the best solution to solve the tuning problem.

Stopband depress of tunable filter has been a problem for a long time. The new filter network combine with traditional methods of widening the stopband can be a very effective way to solve this problem [4]. In this paper, a new filter network is added in the input and output coupling line to depress stopband. Adding spurline is a traditional method to widening the stopband [5]. In order to improve the performance of the tunable filter further, spurline of carefully designed is added in the input and output coupling lines. Bending couple line can increase the coupling degree, to some extent, reduce insertion loss of passbands, which is another way to improve the performance of the filter.

2. THEORY AND EQUATION

2.1. Basic Structure of Stepped Impedance Resonator

There are three types of stepped impedance resonators (SIRs), which are $\lambda/4$ SIR $\lambda/2$ SIR and λ SIR. This paper adopt $\lambda/2$ SIR, by changing the impedance ratio and the electrical length of the two impedance line, we can control its resonant frequency [6]. The basic structure is shown in Fig. 1. It is composed by two different transmission lines with the characteristic impedance of K and Z_2 , the corresponding electrical length is θ_1 and θ_2 respectively [7]. The Input admittance of Y_{in} is shown in Fig. 1.

$$Y_{in} = \frac{jY_2 2(K \tan \theta_1 + \tan \theta_2)(K - \tan \theta_1 \cdot \tan \theta_2)}{K(1 - \tan^2 \theta_1)(1 - \tan^2 \theta_2) - 2(1 + K^2) \cdot \tan \theta_1 \cdot \tan \theta_2} \tag{1}$$

K is the impedance ratio, we define $K = Z_1/Z_2$ [8]. We take $\theta_1 = \theta_2 = \theta$ for convenient [5], then (1) is simplified as (2)

$$Y_{in} = jY_2 \frac{2(1 + K)(K - \tan^2 \theta) \tan \theta}{K - 2(1 + K + K^2) \tan \theta} \tag{2}$$

Because the resonance condition is Y_{in} , so we put $Y_{in} = 0$, we can derive (3)

$$K = \tan \theta_1 \cdot \tan \theta_2 \tag{3}$$

We put $\theta_T = 2\theta_1 + \theta_2$ into (3), we can derive that

$$\begin{cases} \tan \frac{\theta_T}{2} = \frac{1}{1-K} \left(\frac{K}{\tan \theta_1} + \tan \theta_1 \right) & K \neq 1 \\ \theta_T = \pi = 180^\circ & K = 1 \end{cases} \tag{4}$$

We can derive that the resonance depends on electric length of θ and impedance ratio K .

2.2. Design Principle

The filter proposed in this paper is composed of a $\lambda/2$ SIR, an E-shaped resonator and a varactor [9]. The varactor series with E-shaped resonator and load on the center of the $\lambda/2$ SIR. The basic structure is shown as Fig. 2.

The center frequency of the second passband is controlled by the resonant frequency of even model. The resonant frequency of even model is decided to Z_{inc} . Z_{inc} is mainly affected by the varactor, so we can change the center frequency of the second passband by changing the voltage of the varactor. At the same time, the resonant frequency of odd model is not affected.

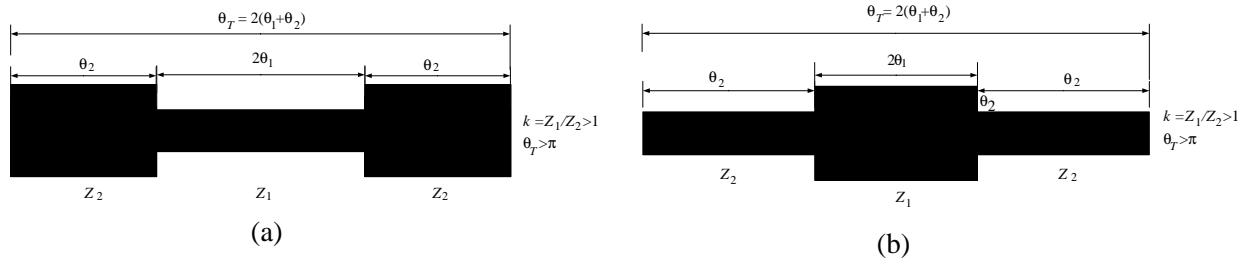


Figure 1: (a) The first form of $\lambda/2$ SIR. (b) The second form of $\lambda/2$ SIR.

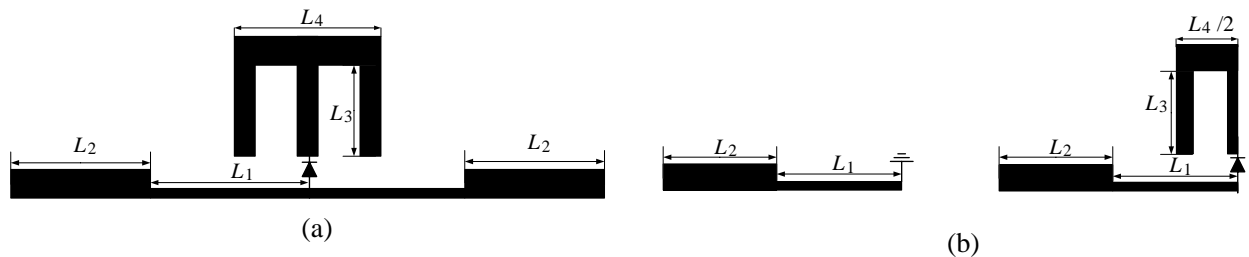


Figure 2: (a) The equivalent model of resonator. (b) The odd model. (c) The even model.

2.3. Structure of Spurline

Spurline is a coplanar microstrip defected structure that is set in the traditional microstrip. It has the advantages of simple compact, easy integration, convenient to use. Spurline as a kind of microstrip defected structure, it have influence to current distribution of filter, thus changing the characteristics of filter [10]. In addition, the spurline has excellent band gap characteristics. It can be used to structure band stop filter, have a good effect on harmonic suppression. The gap of spurline is equivalent to the resonator capacitance, the slot itself can be considered as the resonance inductance [6], the whole circuit is equivalent to a parallel resonant circuit, the resonant frequency is determined by the (6).

$$f = \frac{1}{2\pi\sqrt{LC}} \quad (5)$$

The traditional structure of spurline is shown as in Fig. 3. There are three parameters determine the structure: length a , width s , height b [11]. Typically, capacitance effect is relate to the width, and inductance effect is relate to the length. Therefore, the effective dielectric constant of dielectric substrate have change with the size of spurline [12].

The equivalent circuit structure of the traditional single spurline is shown in Fig. 4. The resonant circuit is represented by LC, the effect of radiation and transmission loss is represented by a resistor R .

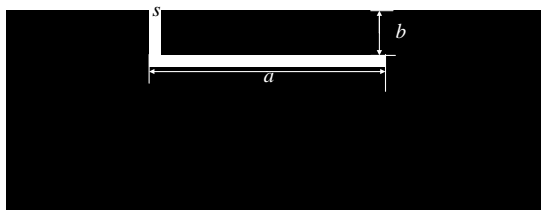


Figure 3: Conventional spurline structure.

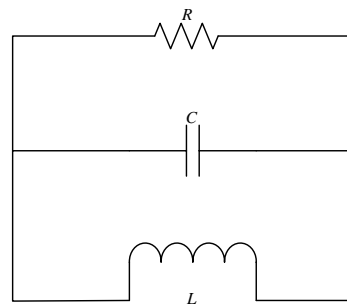


Figure 4: The equivalent circuit of single spurline.

3. SIMULATION AND RESULTS

This section we will describe the design and performance of the tunable dual passband of wide stopband filter. The proposed filter were based on a common substrate with a thickness of 20 mil and relative dielectric constant is 3.48. The type of substrate is ROGERS4350B. This is a very common substrate and easy to buy. A new asymmetric filter network is added between the input and output coupling line. As shown in Fig. 5, which is composed of four sections of curved open stub. The length L_a and L_b determine the filter network stopband characteristics; there exist additional capacitance and cross coupling between L_a and L_b and the input-output impedance line. The multipath effect of cross coupling can further expand the scope of the stop band, reduce quality factor of the passband and make the filter easier to be implemented in Engineering.

As is shown in Fig. 6, parallel coupled lines with value of 50Ω is used to feed, the structure is insensitive to the external electromagnetic environment. Spurlines is added at the input and output coupling line, it can add zero point in the two pass band, which play a good harmonic suppression function.

By changing the size of the spurline, we chose the best one, so that the performance of selection of the filter is improved. Feed coupled line is extended and bended, which can increases the coupling degree, to some extent, it reduces the insertion loss. At the center of the E-shaped resonator a varactor is loaded. The varactor involved in this proposed filter is SMV1247 with the tunable capacitance from 0.64 pF to 8.86 pF and the tunable bias voltage range from 0 to 8 V. The filter is symmetric, with the odd mode and even mode, which are independent with each other.

After analysis and simulation the filter using HFSS and ADS, the design parameters are shown as following: $L_1 = 40$ mm, $L_2 = 15.3$ mm, $L_3 = 15.5$ mm, $L_4 = 11$ mm, $L_5 = 10.4$ mm, $W_1 = 1.14$ mm, $W_2 = 2$ mm, $W_3 = 0.9$ mm, $W_4 = 5$ mm. $L_a = 11.14$ mm, $L_b = 14.14$ mm, $L_c = 11.86$ mm, $g_a = 0.86$ mm, $g_b = 0.86$ mm.

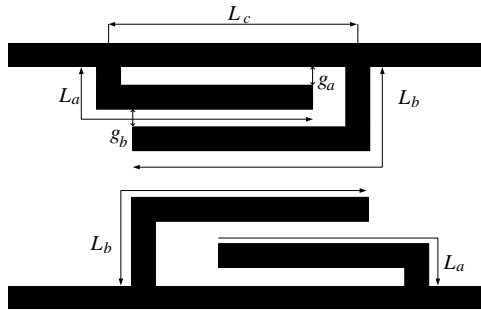


Figure 5: The structure of filtering network.

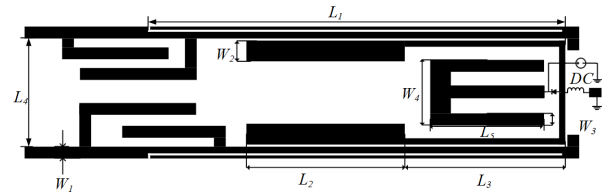
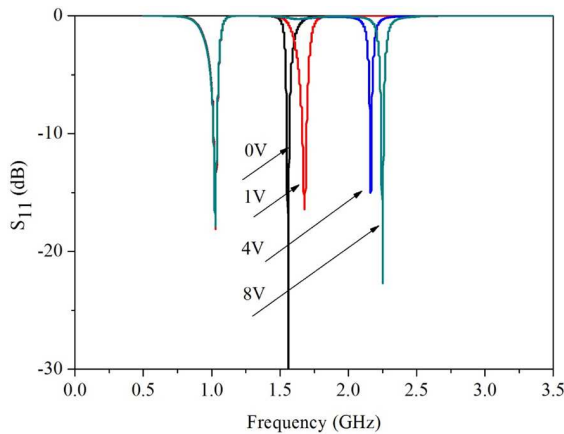
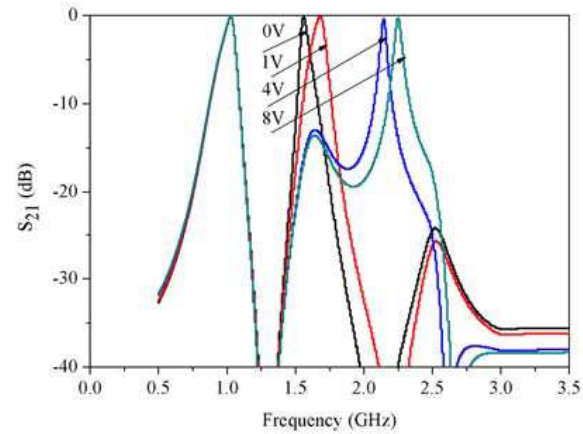


Figure 6: The structure of electrically tunable filter.

Figure 7: S_{11} -parameters of the tunable filter.Figure 8: S_{21} -parameters of the tunable filter.

The results is shown in Fig. 7 and Fig. 8, the center frequency of first passband is fixed at 1.02 GHz with the relative bandwidth of 14.7%, the return loss is 18 dB and the insertion loss is 0.2 dB. The second passband are electrically tuned, when the value of the bias voltage across the varactor is changed. The center frequency can be tuned from 1.56 GHz to 2.25 GHz with the tuning range of 36.2%. The relative bandwidths almost remain unchanged. The return loss change from 16 dB to 30 dB and the insertion loss change from 0.2 dB to 0.8 dB. The filter proposed in this paper has a good harmonic suppression of -20 dB up to 3.5 GHz ($3.5f_1$).

At the whole process the center frequency of the second passband can be tuned from 1.56 GHz to 2.25 GHz, however, the center frequency of the first passband is fixed and maintained at 1.02 GHz. The reason is that the value of the bias voltage across the varactor can change the capacitance of the varactor, the input impedance of even model is changed, resonance frequency of even model is mainly determined by input impedance. But there is no influence on the resonant frequency of odd model. Fig. 7 and Fig. 8 show the relationship between frequency and the voltage. The four curves from left to right respectively corresponding to S_{11} of 0 V, 1 V, 4 V, 8 V. When the bias voltage varies from 0 to 1 V, the center frequency of the second passband changes from 1.56 GHz to 1.66 GHz. However, when the bias voltage changes from 4 to 8 V, the center frequency of the second passband changes from 2.15 GHz to 2.25 GHz. The amplitude of voltage changes different, but the center frequency remains the same which implies that the relation between voltage and moving of center frequency are not linear. This may be attributed to the performance of the varactor. According to the datasheet of SMV1247, when the bias voltage varies from 3 to 8 V, there is no linear relationship between value of capacitance and bias voltage, which is accordance to the previous analysis.

4. CONCLUSION

In this paper, a dual passband of wide stopband varactor tuned filter using SIRs is proposed. A varactor is loaded on the middle of the E-shaped resonators, by changing the value of the bias voltage, the center frequency of the second passband can be tuned while the center frequency of

the first passband is fixed, which had been interpreted in the independence between even mode and odd mode. Feed coupled line is extended and bended to increase the coupling degree and reduce the insertion loss. Spurlines are added at the input and output coupling line is used to add zero between the two passbands and to improve the selectivity of the filter. A filter network is added in the input and output coupling line to depress stopband. The center frequency of the second passband tuning from 1.56 GHz to 2.25 GHz with the tuning range of 36.2%. The return loss changes from 16 dB to 30 dB and the insertion loss changes from 0.2 dB to 0.8 dB. The center frequency of the first passband is fixed at 1.02 GHz. The return loss is 18 dB and the insertion loss is 0.2 dB. The harmonic suppression of -20 dB is up to 3.5 GHz ($3.5f_1$). The filter has a high tuning speed of nano seconds and is easy to realize a dual passband of wide stopband varactor tuned filter by the use of SIRs with centrally loaded elements. The filter proposed in this paper has great characteristics of harmonic suppression, low insertion loss, high return loss, wide tuning range, compared with other filters of the same frequency band. The filter can be useful for many dual passband applications, which is more demanding in near future.

ACKNOWLEDGMENT

This paper is funded by the International Exchange Program of Harbin Engineering University for Innovation-oriented Talents Cultivation, the Navy Defense Foundation of China (4010403020102), the Science and Technology Innovative Talents Foundation of Harbin (2013RFXXJ083), and the Fundamental Research Funds for the Central Universities (HEUCF131602).

REFERENCES

1. Ullah, I., D. Habibi, Z. Xiaoli, and G. Kiani, "Design of RF/microwave efficient buildings using frequency selective surface," *2011 IEEE 22nd International Symposium on Personal Indoor and Mobile Radio Communications (PIMRC)*, 2070–2074, 2011.
2. Zhao, Y., T. Liu, Y. Ye, L. Cen, H. Zhang, and X. Liu, "Center frequency and bandwidth tunable filter with varactors," *2011 7th International Conference on Wireless Communications, Networking and Mobile Computing (WiCOM)*, 1–4, 2011.
3. Huang, J. M., F. Zhu, and Z. L. Deng, "A novel design of tunable band-stop filter using MEMS technology," *5th International Conference on Wireless Communications, Networking and Mobile Computing, WiCom' 09*, 1–3, 2009.
4. Kacmajor, T., P. Kant, and J. J. Michalski, "Microwave filter tuning for different center frequencies based on artificial neural network and phase compensation," *2014 20th International Conference on Microwaves, Radar, and Wireless Communication (MIKON)*, 1–4, 2014.
5. Esmaili, M. and J. Bornemann, "Substrate integrated waveguide dual-stopband filter," *Microwave and Optical Technology Letters*, Vol. 56, 1561–1563, 2014.
6. Kim, J.-S., N.-S. Kim, W.-G. Moon, and G.-B. Lee, "Novel broadband suspended substrate stripline filter using dual-mode resonators," *IEEE 19th International Symposium on Personal Indoor and Mobile Radio Communications, (PIMRC)*, 1–4, 2008.
7. Bin, D., F. Quanyuan, and Y. Shuai, "Research and design of X-band SIR microstrip filters," *International Conference on E-Business and Information System Security, EBISS' 09*, 1–4, 2009.
8. Li, Z., "Research and design of a tunable filter of highly performance," 31–37, Master, XiDian University, 2014.
9. Huang, S. Y. and Y. H. Lee, "A compact E-shaped patterned ground structure and its applications to tunable bandstop resonator," *IEEE Transactions on Microwave Theory and Techniques*, Vol. 57, 657–666, 2009.
10. Yang, Y., "Research and application of spur line in microstrip circuits," Master, University of Electronic Science and Technology, 2009.
11. Meng, L., L. Ren, and J. Huang, "Design of a SIR bandpass filter with spurious passband suppression using defected ground structure and Spurline," *2012 IEEE MTT-S International Microwave Workshop Series on Millimeter Wave Wireless Technology and Applications (IMWS)*, 1–4, 2012.
12. Liu, H., Y. Jiang, and Z. Zhang, "A design of new asymmetrical spurline resonators and its application," *Journal of East China Jiaotong University*, 29–35, 2010.

Effect of Slow Wave Structures on Scan Angles in Microstrip Leaky-wave Antennas

Saeid Mohammadpour Jaghargh, Pejman Rezaei, and Javad Soleiman Meiguni
Faculty of Electrical and Computer Engineering, Semnan University, Semnan, Iran

Abstract— This paper presents two miniaturized slow wave structures in microstrip leaky-wave antennas (MLWAs) which operate about 8 GHz. The effects of these structures on the scan angles have been compared in the paper. The designed interdigital capacitors and folded-back line have been investigated with ADS Momentum software. It has been shown that the interdigital capacitors (IDCs) yield to a broad scan angles from +53 to -74 degree, while the folded-back line inductor scans only the positive angles.

1. INTRODUCTION

Leaky-wave antennas (LWAs) are guided wave structures, which radiate electromagnetic waves by using travelling wave mechanism. Furthermore, LWAs are in classification of traveling-wave antennas [1–3]. The travelling wave mechanism consists of two structures, including fast travelling waves and slow travelling waves structures. In this type of antenna, the electromagnetic waves radiate continuously along its length, and hence the propagation wave number is complex, consisting of both a phase and an attenuation constant. Highly directive beam at an arbitrary specified angle can be achieved by this type of antenna, with a low side lobe level. In other words, beam scans with frequency inherently in LWAs. For scanning applications this is an essential advantage. Simple structure, no complicated feed network and cheap structures are the other benefits of LWAs. Moreover, they are popular in the microwave band and millimeter-wave band, because of their high directivity.

LWAs have been investigated since the 1940s, when an LWA consisting of a slotted rectangular waveguide was introduced. In [4] an LWA consisting of an inductive sheet spaced over a continuous conducting sheet, with a wave polarized in the plane of the antenna propagating between the two sheets has been represented.

LWAs can be divided into different categories depending upon the principle of operation; so uniform, quasi-uniform and periodic LWA is classification of them [1, 2]. A microstrip line that is periodically modulated in order to turn the non radiating microstrip mode into a radiating leaky mode has been reported in [2]. Recently, periodic slow wave structure has been nominated as appropriate media for LWAs. Substantially slow wave structures are special circuits that are used in microwave circuits to reduce and handle the wave velocity in certain direction. In other words, this structure controls the speed of the waves in LWAs in which non resonant periodic circuit or slow-wave structures are designed for producing large gain antennas [5].

In this paper, we present two slow-wave structures and their parameters for LWAs. Beam scanning is one of the most important parameters of LWAs and we report it here. We investigate the effect of these slow-wave structures on scan angles in periodic microstrip leaky-wave antennas (MLWAs).

2. ANTENNA DESIGN AND SIMULATION

2.1. LWA with Interdigital Capacitors

Folded-back line, zigzag line, corrugated waveguide, helical line and also interdigital capacitor, are structures that introduced as slow wave structures in [5]. Interdigital capacitors (IDCs) are widely used as lumped elements in the microwave integrated circuits (MIC), slow-wave devices, and integrated optical (IO) modulators [6]. Recently, IDCs has been utilized as slow wave structures in composite right/left handed leaky-wave antennas (CRLH LWAs) in order to control the speed of waves. CRLH LWA is another classification of LWAs that is part of the periodic LWAs. Metamaterials are usually known as periodic structures. However, there are several reports on metamaterial-inspired antennas [7, 8].

Although LWAs are cost-effective antennas in scanning the region over a large bandwidth, continuous backward to forward scanning is not reported for many of the structures [9, 10]. CRLH LWA introduces full-space continuous beam scanning, from backfire to endfire, including the broadside

direction. Moreover, it can be fabricated in microstrip technology or in coplanar technology [1–4, 9–13].

Figure 1 illustrates a 16-cell LWAs with interdigital slow wave structures. This LWA is like another structure that reported in [14], but this paper compares the 16 cells of proposed LWA. This structure is a non resonant structure with the period IDCs. The existence of the IDCs makes the capacitors for CRLH in order to propagate forward and backward scanning through broadside.

As shown in Fig. 1, conventional IDC is utilized in CRLH LWA unit cell, and each unit cell is repeated periodically.

The period of structure is 4 mm and the capacitance of a single-layer IDC can be approximated as [5]:

$$C = (l/w)(\epsilon_r + 1)[(N - 3)A_1 + A_2] \quad (1)$$

where N = number of fingers. $A_1 = 0.089$ pF/cm is the contribution of the interior finger for $h > w$. $A_2 = 0.1$ pF/cm is the contribution of the two external fingers for $h > w$. l = finger length in cm. w = finger-base width in cm which has been demonstrated in Fig. 1(b).

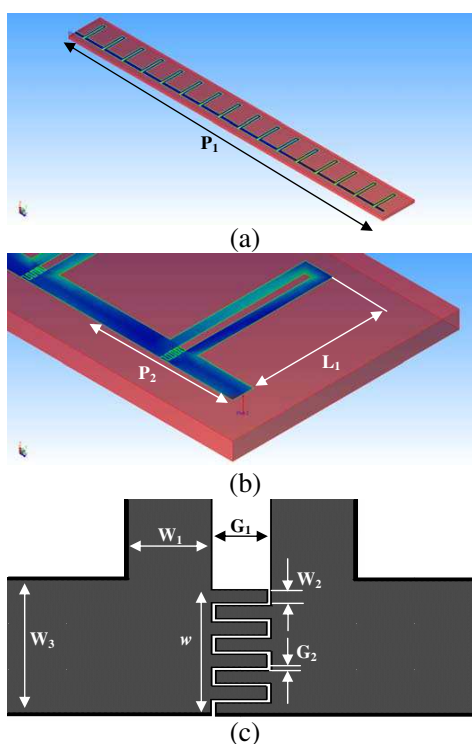


Figure 1: CRLH LWA with IDC. (a) 3D view of proposed LWA formed by 16 cells. The parameter value is: $P_1 = 64$ mm. (b) 3D view of proposed LWA with periodic IDC as slow wave structure. The parameter values are: $P_2 = 4$ mm, $L_1 = 3.9$ mm. (c) Unit cell of IDC. The parameter values are: $w = 0.55$ mm, $W_1 = 0.3$ mm, $W_2 = 0.06$ mm, $W_3 = 0.6$ mm, $G_1 = 0.2$ mm and $G_2 = 0.01$ mm.

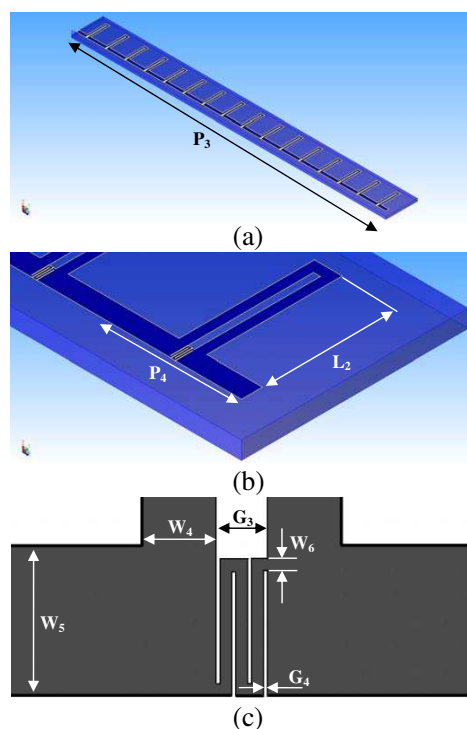


Figure 2: LWA with periodic folded-back line. (a) 3D view of proposed LWA formed by 16 cells. The parameter value is: $P_3 = 64$ mm. (b) 3D view of proposed LWA with periodic folded-back line. The parameter values are: $P_4 = 4$ mm, $L_2 = 3.9$ mm. (c) Unit cell of folded-back line inductors. The parameter values are: $W_4 = 0.3$ mm, $W_5 = 0.6$ mm, $W_6 = 0.06$ mm, $G_3 = 0.2$ mm and $G_4 = 0.01$ mm.

2.2. LWA with Folded-back Line Inductor

Folded-back line inductors are another of structures that introduced as slow wave structure in [5]. They are similar to meander-line structures.

As declared above, beam scanning is one of the most important parameters of LWAs. As reported in [15], producing maximum radiation in the range $0^\circ < \theta < 90^\circ$. For slow-wave structures appears more challenging at first, but as we investigated and analyzed in X-band, this folded-back line structure is one of the slow-wave structures that produces a maximum gain in the positive range of theta.

Figure 2 shows a folded-back line inductor LWA with 16 cells. The period of the structure is as same as the LWA with IDC.

Actually in this paper capacitor substitutes with an inductor. This substitution effects on beam scanning and on scan angles.

3. COMPARISON AND SIMULATION RESULTS

As demonstrated above, the proposed MLWAs are located on the Rogers 5880 commercial substrate. For both proposed antennas, the thickness on the substrate should be chosen 0.508 mm with $\epsilon_r = 10.2$ and finite structure formed by 16 cells. The commercial ADS Momentum software is adopted for the simulations, and the results are presented below. Fig. 3 illustrates S -parameter of proposed MLWAs. These antennas operate around X-band.

Figure 3: Magnitudes of S -parameters in proposed MLWAs.

In the designed LWA with interdigital capacitors, the main beam scans from $\theta_1 = +53$ degree to $\theta_2 = -74$ degree with increasing the frequency from 8 GHz to 10.363 GHz. This scanning investigated in $\varphi = 0^\circ$ plane. Furthermore, the gain of the antenna not changes greatly in this range which is appropriate parameter in antenna design. Also this parameter is critical for scanning applications. This is obvious from the Fig. 4 that the antenna radiates in negative values of theta with increasing the frequency. Maximum gain occurs at 9.285 GHz and it is about 17.647 dB when the scan angle is $\theta = -18$ degree.

The LWA with folded-back line scans from $\theta_1 = +3$ degree to $\theta_2 = +54$ degree with increasing the frequency from 8 GHz to 8.714 GHz. But in the broadside region, we have gain reduction. See the radiation pattern in the Fig. 5. In the other word, the folded-back line LWA only scans in the positive range of theta. It's clear that maximum gain occurs in $\theta_2 = +54$ degree too.

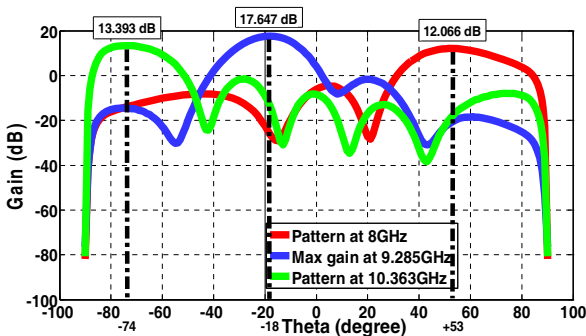


Figure 4: Radiation pattern of MLWA with IDC and scanning interval with maximum gain about 17.647 dB.

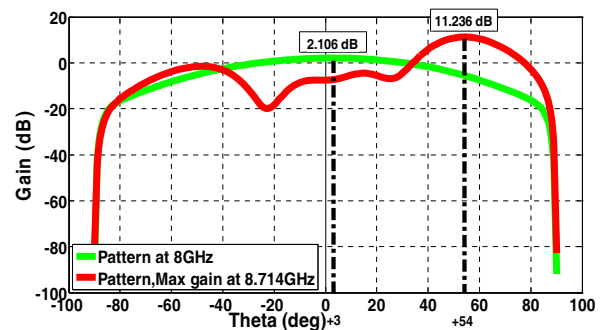


Figure 5: Radiation pattern of MLWA with folded-back line inductor and scanning interval with maximum gain about 11.236 dB.

For example, in [10] a slotted substrate integrated waveguide (SIW) LWA is proposed that has the advantages of both rectangular waveguide with transverse slots and SIW. Furthermore, this SIW LWA can only scan in the positive range of theta. As declared above, the main beam of LWAs scans the space when the frequency changes. In other words, beam scans with frequency inherently in LWAs and it's apparent from Fig. 6.

Degradation of gain in LWAs is another meaningful parameter that is examined in such a this paper. Also we have been investigated here. Notice the Fig. 7.

It is clear that, the average gain for each structure is not same and so the LWA with folded-back line inductor has less gain than LWA with interdigital capacitor. Also scanning bandwidth of LWA with folded-back line inductor is about 0.714 GHz.

As shown in Fig. 8, the average percentage of efficiency in LWA with a folded-backline inductor is less than LWA with IDC. This examinations show that LWA with a folded-backline inductor spoils the efficiency in the scanning interval because it has unbalanced unit cell. Also this reason justifies deflection of gain in LWA with the folded-backline inductor.

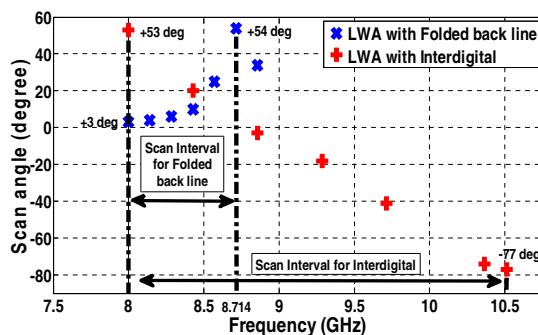


Figure 6: Details of scan angles in both proposed LWAs when frequency changes.

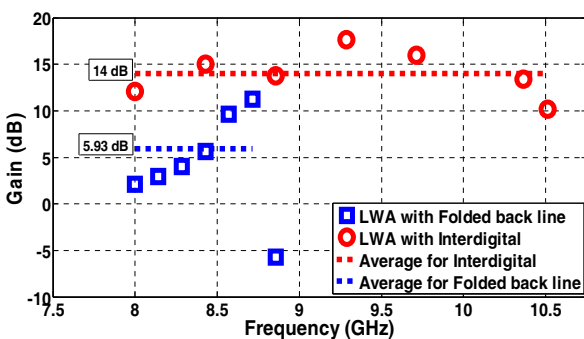


Figure 7: Details of magnitude of the gain in both proposed LWAs when frequency changes and the average of gains in interval of scan.

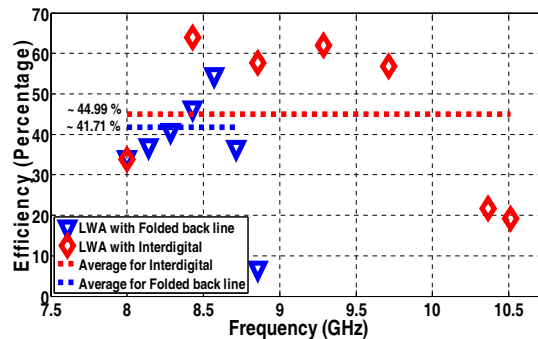


Figure 8: Details of efficiency when frequency changes and the average of gains in interval of scan.

4. CONCLUSION

This paper presented two miniaturized microstrip slow wave structures in periodic MLWAs. The effects of these structures on the scan angles have been compared. Interdigital capacitor is one of the slow wave structures and folded-back line inductor is another structure that has been investigated here. Actually in this paper a capacitor substitutes with an inductor. This substitution affects on beam scanning and on scan angles. It has been shown that IDCs yield to a broad scan angles from +53 to -74 degree, while the folded-back line inductors scan only the positive angles. This examinations show that LWA with folded-back line inductor spoils the efficiency and flat gain in the scanning interval because it has unbalanced unit cell.

ACKNOWLEDGMENT

The authors would like to thank Semnan University for its support.

REFERENCES

1. Jackson, D. R. and A. A. Oliner, *Leaky-wave Antennas in Modern Antenna Handbook*, Wiley, New York, 2008.
2. Caloz, C., D. R. Jackson, and T. Itoh, "Leaky-wave antennas," *IEEE Trans. Antennas Propag.*, Vol. 100, No. 7, 21942206, July 2012.
3. Nguyen, V., A. Parsa, and C. Caloz, "Power-recycling feedback system for maximization of leaky-wave antennas radiation efficiency," *IEEE Trans. Microw. Theory Tech.*, Vol. 58, No. 7, 1641-1650, July 2010.
4. Honey, R. C., "A flush-mounted leaky wave antenna with predictable patterns," *IRE Trans. Antennas Propag.*, Vol. 7, 320-329, Oct. 1959.
5. Liao, S. Y., *Microwave Devices and Circuits*, Prentice Hall, New Jersey, 1990.
6. Gevorgian, S. S., T. Martinsson, P. L. J. Linner, and E. L. Kollberg, "CAD models for multi-layered substrate interdigital capacitor," *IEEE Trans. Microw. Theory Tech.*, Vol. 44, No. 6, 896-904, June 1996.

7. Amani, N., M. Kamyab, A. Jafargholi, A. Hosseinbeig, and J. S. Meiguni, "Compact tri-band metamaterial-inspired antenna based on CRLH resonant structures," *Electronic Letts.*, Vol. 50, No. 12, 847–848, June 2014.
8. Jaghargh, S., P. Rezaei, and J. S. Meiguni, "Simulation and design of a novel K-band microstrip leaky-wave antenna with metamaterial unit cell and slow-wave structure," *1st National Conf. Development of Civil Eng. Archetecture, Electricity and Mechanichal in Iran*, Gorgan, Iran, Dec. 2014.
9. Cheng, G. F. and C. K. C. Tzuang, "Closely coupled half-width leaky-wave antenna array," *6th European Conf. Antennas and Propag.*, 957–960, 2012.
10. Liu, J., D. R. Jackson, and Y. Long, "Substrate integrated waveguide (SIW) leaky-wave antenna with transverse slots," *IEEE Trans. Antennas Propag.*, Vol. 60, No. 1, 20–29, Jan. 2012.
11. Calm, C., T. Itoh, and A. Renning, "CRLH metamaterial leaky-wave and resonant antennas," *IEEE Antennas Propag. Mag.*, Vol. 50, No. 5, 25–39, Oct. 2008.
12. Li, Y., Q. Xue, H. Z. Tan, and Y. Long, "The half-width microstrip leaky wave antenna with the periodic short circuits," *IEEE Trans. Antennas Propag.*, Vol. 59, No. 9, 3421–3423, Sept. 2011.
13. Pourghorban Saghati, A., M. Mirsalehi, and M. H. Neshati, "A HMSIW circularly polarized leaky-wave antenna with backward, broadside, and forward radiation," *IEEE Antennas and Wireless Propag Letts.*, Vol. 13, 451–454, Mar. 2014.
14. Paulotto, S., P. Baccarelli, F. Frezza, and D. R. Jackson, "A microstrip periodic leaky-wave antenna optimized for broadside scanning," *Antennas and Propag. Society International Symposium IEEE*, 5789–5792, 2007.
15. Sutinjo, A., M. Okoniewski, and R. H. Johnston, "Radiation from fast and slow traveling waves," *IEEE Antennas Propag. Mag.*, Vol. 50, No. 4, 175–181, Aug. 2008.

Directional Emission from Chaotic Microdisk Lasers and the Role of Boundary Imperfections

J. Kreismann¹, K. Kubo^{1,2}, P. Stockschläder¹, and M. Hentschel¹

¹Institute for Physics, Technische Universität Ilmenau
Weimarer Str. 25, Ilmenau D-98693, Germany

²MPIPKS Dresden, Nöthnitzer Str. 38, Dresden D-01187, Germany

Abstract— Optical microdisk laser provide a promising alternative to the well-known Fabry-Perot lasers as well as to VCSELs as the size of optical devices is further reduced to the scale of few micrometers. Whereas high Q -modes are available through whispering-gallery-type resonances that are trapped by total internal reflection inside the resonator, it remains a challenge to achieve directional emission by suitably breaking the rotational symmetry of the devices. In a previous work (J. Wiersig and M. Hentschel, *Phys. Rev. Lett.*, Vol. 100, 033901, 2008.) [6] we have shown that the so-called Limaçon-shape provides a robust possibility to combine directional far-field emission with high Q -factors. In detail, the far-field characteristic is determined by the unstable manifold of the cavity, a quantity well-known in the field of dynamical systems and quantum chaos. It implies that ray-based calculations, wave-simulations and experiments yield practically the same result. In particular, the easy-to-implement ray-optics methods are an appropriate tool to predict the far-field of microdisk lasers. A long-standing problem is to understand the role of boundary imperfections. Presumably these are responsible for the reduction of the Q -factors observed in experiments in comparison to the theoretical predictions. Here, we consider exemplarily the reflection of a Gaussian beam at a surface that was equipped with sharp and rounded cusps of wavelength size. We find that this changes the properties of the reflected beam considerably. We conclude that in practice, such imperfections will reduce the cavity Q -factors and will influence the far-field emission properties of microdisk lasers.

1. INTRODUCTION

The ongoing miniaturisation of photonic devices calls for new devices that provide lasing properties on the microscale. Besides the well established vertical-cavity surface-emitting lasers (VCSELs), optical microcavities [1–3] and microdisk lasers provide the unique possibility to combine ultrahigh Q -factors and directional emission characteristics in the far field. In contrast to the well-known Fabry-Perot-scheme based lasers where light is confined travelling back and forth between two mirrors, light confinement in optical microcavities is achieved using total internal reflection of light at the cavity boundary. For angles of incidence larger than the critical angle χ_c for total internal reflection, ray optics ensures that no light will leave the cavity, whereas in wave optics there remains a small evanescent leakage (tunneling). It still allows for the desired high Q -factors that are realized, for example, through the whispering gallery modes in circular microdisk cavities. However, their rotational invariance does not allow for a preferred direction of far-field emission that would be a prerequisite for every laser concept. There are many concepts how to overcome this difficulty ranging from composite systems via the use of resonance crossings [4] to specially designed geometries, see Ref. [5] for a summary on this subject.

2. ROBUST UNIDIRECTIONAL FAR-FIELD LIGHT EMISSION FROM LIMAÇON-SHAPED MICROCAVITIES

One particularly successful microdisk shape that was theoretically predicted to possess directional emission properties is the Limaçon-geometry [6]. It reads in polar coordinates (r, ϕ) : $r(\phi) = R_0(1 + \epsilon \cos \phi)$ with mean radius R_0 and a geometry parameter ϵ describing the deviation from the rotationally invariant circular shape, values around $\epsilon = 0.43$ yield the best directionality. This prediction was confirmed by four different experimental groups within one year [7–11].

In Figs. 1 and 2 examples of resonances in a Limaçon-shaped cavity are shown for two different quality factors Q , for a rather low one on top, and a higher one in the bottom rows. The refractive index of the cavity is assumed to be $n = 3.3$ corresponding to the typical case of microdisks made of semiconductor heterostructures placed in air with refractive index $n_0 = 1$. The critical angle is related to the refractive index via $\chi_c = \arcsin(1/n)$. The geometry parameter was chosen as $\epsilon = 0.43$. Although this parameter was found to optimize the directionality in light output, other ϵ

yield comparable output characteristics [11]. The two possible polarizations of light are considered, namely TM polarization (transverse magnetic case, Fig. 1), and TE polarization (transverse electric, the case with the Brewster angle feature, Fig. 1). TE polarization yields, in general, better results in

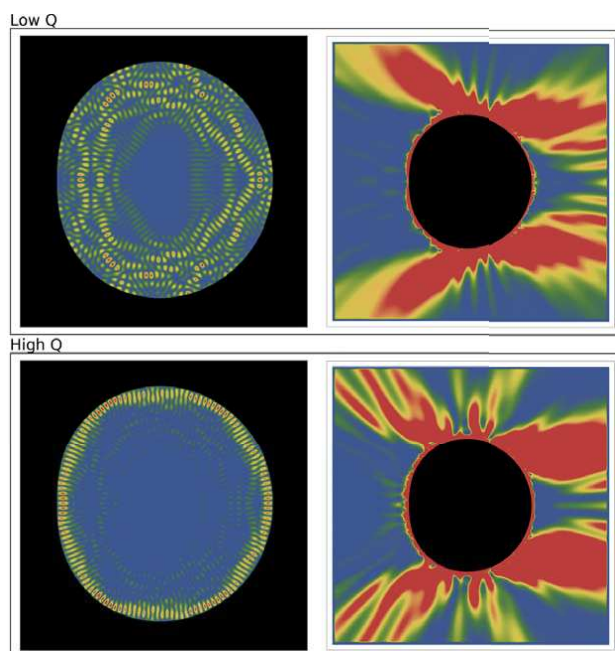


Figure 1: Resonances of TM type in the Limaçon-shaped microcavity with $n = 3.3$ and $\epsilon = 0.43$. Shown are $|E_z|$ (with E_z the electric field component perpendicular to the resonator plane) and the total intensity in the left and right panels, respectively. The mode's vacuum wavenumber k is given by $\text{Re}[kR_0] = 21.0866$ and the quality factor $Q = 8978$ in the upper row, and $\text{Re}[kR_0] = 22.1895$ and $Q = 18584$ in the lower row. The cavity wavelength is $\lambda_c = 2\pi/(nk)$. The Q -factor is obtained as $Q = \text{Re}[kR_0]/(-2\text{Im}[kR_0])$. Remarkably, the far-field pattern is practically independent from the resonance chosen.

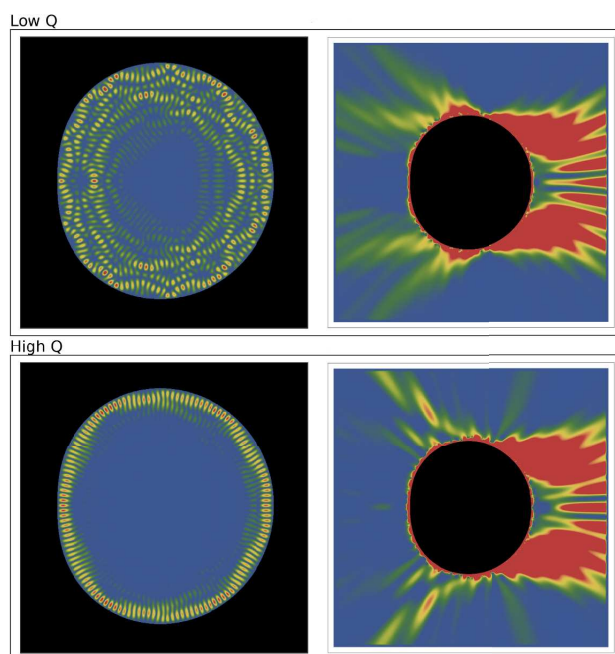


Figure 2: As before, but for resonances of TE type and the magnetic field component $|H_z|$ shown in left panels. The wavenumbers and Q -factors are $\text{Re}[kR_0] = 20.6808$ and $Q = 14878$ for the upper row, and $\text{Re}[kR_0] = 21.8779$ and $Q = 85012$ for the lower row. The better unidirectionality in the far-field characteristic of TE polarized modes in comparison to the TM case is clearly visible.

terms of unidirectionality than the TM case. The resonances and wave patterns inside (left column) and outside (right column) the resonator were obtained using the freely available simulation package MEEP [12]. The whispering-gallery-type character of the resonances is clearly visible especially for the cases of the higher Q -factors. For the examples with lower Q -factor in the top row, the chaotic character of the cavity becomes evident in form of deviations from the regular pattern of typical whispering gallery modes realized in rotationally invariant geometries. Notice that the rotational symmetry is broken in the Limaçon-case for all $\epsilon > 0$.

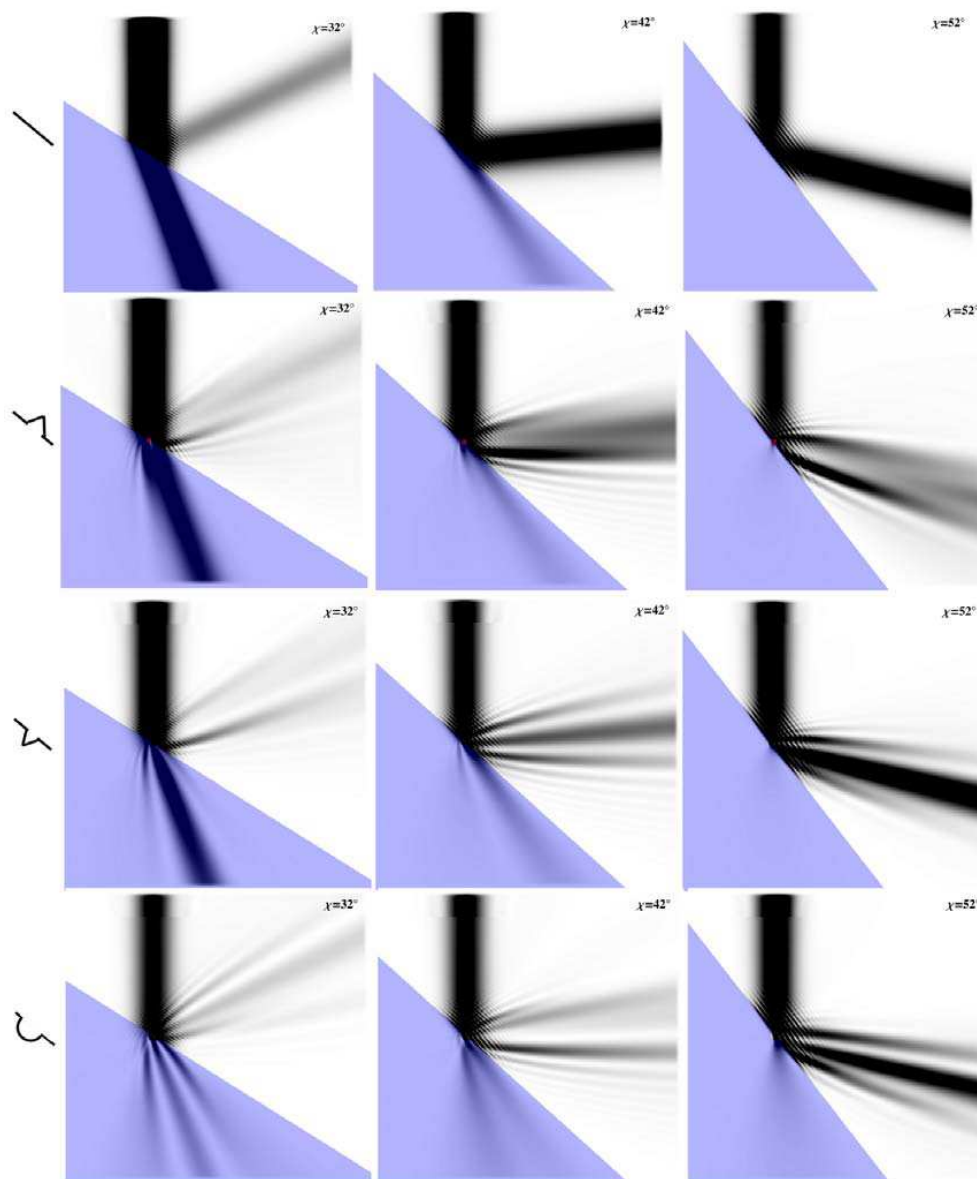


Figure 3: Role of surface roughness as function of the angle of incidence. A Gaussian beam in air is approaching an interface of refractive index $n = 2/3$ (corresponding to the reflection at a glass-air interface). The critical angle is 42° , see the central column. Subcritical incidence of 32° is depicted in the left, supercritical incidence of 52° in the right column, all for TM polarized light. The typical defect size is of the order of the wavelength λ of the material with the larger n , the beam waist of the Gaussian beam is chosen as 5λ . The upper row shows reflection at a planar interface for reference, the defect structures considered in the lower three rows are shown on the far left. The distortion of the reflected light is clearly visible. It depends, as expected, on the particular realization of the defect and amounts to a substantial broadening of the reflected beam and a substantial and varying intensity distortion of the originally Gaussian beam profile.

Remarkably, we find very robust and universal far-field emission characteristics that do not depend on the particular resonance chosen. The reason for this is that the emission characteristics of the cavity is determined by the so-called unstable manifold [6, 13]. This quantity is well known in the field of nonlinear dynamics and a characteristic of the phase-space of the corresponding ray-optical billiard, see, e.g., Ref. [6] for details. In this context we point out that ray simulations yield, therefore, very nice agreement with wave simulations [6, 11] and experiments [10]. This is remarkable because the wave simulations are not at all performed in the ray limit, and the size parameter realized in the experiments is yet in another regime. The agreement of all three data sets underlines the robustness of the proposed scheme against geometry imperfections and with respect to the mode chosen for the lasing operation.

We draw the reader's attention also to a characteristic difference between the far-field patterns of TM and TE polarized modes. It has its origin in the Brewster angle feature in the reflection coefficient important for TE polarized light. As a consequence, TE polarized light shows a better unidirectionality in the far-field, see Fig. 2, because extra emission directions (towards the left side) present for TM polarized light, Fig. 1, are missing.

3. ROLE OF SURFACE ROUGHNESS

Whereas the nice agreement between ray and wave simulation and the experiments allows one to use the straightforward and numerically cheap concept of ray simulations to determine the far-field emission characteristics of chaotic microcavity lasers, there are differences between theoretical calculations and experimental results when one looks on the Q -factors of the individual resonances. In general, the theoretically determined Q -factors can be considerably larger than the experimentally found values [11]. Boundary imperfections present in the experimental realization of optical microcavities are expected to be one important issue here.

This provides the motivation for our studies on the role of boundary imperfections. In order to concentrate on the boundary effect and avoid the influence of resonance-specific properties, our starting point is the reflection of a Gaussian beam at interfaces where different boundary defects are realized. The results of this numerical investigation are summarized in Fig. 3. We studied different kinds of wavelength-size boundary defects, in the form of sharp and rounded cusps, for subcritical, critical, and supercritical incidence of a Gaussian beam. For comparison, reflection at a perfect, planar interface is shown in the upper row. Near critical incidence, semiclassical corrections to ray optics lead to additional effects [14–18] that we, however, do not discuss here.

The effect of surface roughness is a general broadening of the reflected beam that can explain the reduction of the Q -factors observed in experiments. The details of this process in the case of resonance modes, and the role of interface curvature, will be the subject of a future work.

4. CONCLUSION

In conclusion, we have shown that the issue of achieving directional emission from microdisk lasers can be solved. We have introduced the Limaçon shape as a chaotic microcavity device that allows one to combine ultrahigh Q -factors and unidirectional output characteristics in a robust and universal scheme. This universality can be explained and understood using the concept of the unstable manifold.

The presence of boundary imperfections is argued to be one reason that reduces the Q -factor of resonant modes in experiments. In numerical simulations of the reflection of a Gaussian beam, a considerable broadening and distortion of the reflected light beam is observed and identified as a possible source for the reduced Q -factors observed in real devices.

ACKNOWLEDGMENT

The authors gratefully acknowledge funding by the German Research Society (DFG) via the Emmy Noether Program and the Research Unit FOR 760. We thank Jan Wiersig and Henning Schomerus for valuable discussions.

REFERENCES

1. Chang, R. K., *Optical Processes in Microcavities*, World Scientific, Singapore, 1996.
2. Vahala, K., *Optical Microcavities*, World Scientific, Singapore, 2004.
3. Cao, H. and J. Wiersig, "Dielectric microcavities: Model systems for wave chaos and non-Hermitian physics," *Rev. Mod. Phys.*, Vol. 87, No. 1, 61–111, 2015.

4. Wiersig, J. and M. Hentschel, "Unidirectional light emission from high- Q modes in optical microcavities," *Phys. Rev. A*, Vol. 73, No. 3, 031802(R), 2006.
5. Wiersig, J., J. Unterhinninghofen, Q. Song, H. Cao, M. Hentschel, and S. Shinohara, "Review on unidirectional light emission from ultralow-loss modes in deformed microdisks," *Trends in Nano- and Micro-Cavities*, 109–152, O. D. Kwon, B. Lee, and K. An, Eds, Bentham Science Publishers, Sharjah, UAE, 2011.
6. Wiersig, J. and M. Hentschel, "Combining directional light output and ultralow loss in deformed microdisks," *Phys. Rev. Lett.*, Vol. 100, No. 3, 033901, 2008.
7. Yi, C.-H., M.-W. Kim, and C.-M. Kim, "Lasing characteristics of a Limaçon-shaped microcavity laser," *App. Phys. Lett.*, Vol. 95, 141107, 2009.
8. Shinohara, S., M. Hentschel, J. Wiersig, T. Sasaki, and T. Harayama, "Ray-wave correspondence in limaçon-shaped semiconductor microcavities," *Phys. Rev. A*, Vol. 80, No. 3, 031801(R), 2009.
9. Song, Q., W. Fang, B. Liu, S.-T. Ho, G. Solomon, and H. Cao, "Chaotic microcavity laser with high quality factor and unidirectional output," *Phys. Rev. A*, Vol. 80, No. 4, 041807(R), 2009.
10. Yan, C., et al., "Directional emission and universal far-field behavior from semiconductor lasers with limaçon-shaped microcavity," *Appl. Phys. Lett.*, Vol. 94, 251101, 2009.
11. Wang, Q.-J., et al., "Deformed microcavity quantum cascade lasers with directional emission," *New J. Phys.* Vol. 11, 125018, 2009.
12. Oskooi, A. F., D. Roundy, M. Ibanescu, P. Bermel, J. D. Joannopoulos, and S. G. Johnson, "MEEP: A flexible free-software package for electromagnetic simulations by the FDTD method," *Comput. Phys. Commun.*, Vol. 181, No. 3, 687–702, 2010.
13. Lee, S.-Y., S. Rim, J.-W. Ryu, T.-Y. Kwon, M. Choi, and C.-M. Kim, "Quasiscattered resonances in a spiral-shaped microcavity," *Phys. Rev. Lett.*, Vol. 93, 164102, 2004.
14. Goos, F. and H. Hänchen, "Ein neuer und fundamentaler Versuch zur Totalreflexion," *Annalen der Physik*, Vol. 436, Nos. 7–8, 333–346, 1947.
15. Tureci, H. E. and A. D. Stone, "Deviation from Snell's law for beams transmitted near the critical angle: Application to microcavity lasers," *Opt. Lett.*, Vol. 27, No. 1, 7–9, 2002.
16. Schomerus, H. and M. Hentschel, "Correcting ray optics at curved dielectric microresonator interfaces: Phase-space unification of fresnel filtering and the Goos-Hänchen shift," *Phys. Rev. Lett.*, Vol. 96, No. 24, 243903, 2006.
17. Hentschel, M. and H. Schomerus, "Fresnel laws at curved dielectric interfaces of microresonators," *Phys. Rev. E*, Vol. 65, No. 4, 045603, 2002.
18. Stockschröder, P., J. Kreismann, and M. Hentschel, "Curvature dependence of semiclassical corrections to ray optics: How Goos-Hänchen shift and Fresnel filtering deviate from the planar case result," *EPL*, Vol. 107, No. 6, 64001, 2014.

Spherical Microresonators Coated with a High Refractive Index Coating for Different Applications

D. Ristić^{1,2}, A. Chiappini³, H. Gebavi^{1,2}, V. Đerek^{1,2}, A. Lukowiak⁴, R. R. Gonçalves⁵, S. Pelli⁶, G. Nunzi Conti⁶, M. Ivanda^{1,2}, G. C. Righini⁷, G. Cibiel⁸, and M. Ferrari³

¹Laboratory for Molecular Physics, Division of Materials Physics, Ruđerka Bošković Institute
Bijenička cesta 54, Zagreb 10000, Croatia

²Center of Excellence for Advanced Materials and Sensing Devices
Research Unit New Functional Materials, Bijenička cesta 54, 10000 Zagreb, Croatia

³IFN-CNR CSMFO Lab, Via alla Cascata 56/C Povo, Trento 38123, Italy

⁴Institute of Low Temperature and Structure Research, PAS, ul. Okolna 2, Wrocław 50-950, Poland

⁵Departamento de Química, Faculdade de Filosofia, Ciências e Letras de Ribeirão Preto
Universidade de São Paulo, Av. Bandeirantes, 3900, CEP 14040-901, Ribeirão Preto/SP, Brazil

⁶IFAC-CNR, MiP Lab, Sesto Fiorentino 50019, Italy

⁷Enrico Fermi Centre, Piazza del Viminale 1, Roma 00184, Italy

⁸Centre National d'Etudes Spatiales (CNES), 31401 Toulouse Cedex 9, France

Abstract— We will discuss several applications of the coating of silica microspheres. Silica microspheres fall in the group of so called whispering gallery mode (WGM) resonators. They are known to have a very high Q -factor and a low modal volume. Therefore they are suitable for a number of different applications such as lasing, frequency comb generation or sensing. In this paper we will discuss three different applications. Firstly we will discuss the sensing properties of the coated microsphere. We have found that a high refractive index coating can greatly improve the sensing properties of a silica microresonator, improving the theoretical sensing sensitivity from 5 nm/RIU for a blank silica sphere to a maximum of 145 nm/RIU for an amorphous silicon coating. We will also discuss some experimental results dealing with the coating of silica microspheres with a LPCVD a : Si coating. Second application which we will discuss is lasing and optical amplification. By coating the microsphere using an optically active material, micro-sized lasers can be produced. We have coated a silica microsphere using an erbium doped glass (70SiO₂-30HfO₂) and have shown that such a system exhibits lasing. Finally we will discuss the possibility to tailor the modal dispersion of the resonator by applying a high refractive index coating on top of the microsphere. This can be a crucial step for improving the applicability of the microsphere in non-linear optics applications, such as for four-wave mixing. We used erbium doped silica hafnia glass as a probe to study the influence of the coating on the modal dispersion inside the microresonator and have found that the coating can be used to tailor the modal dispersion in a very wide range in both the normal and anomalous regime.

1. INTRODUCTION

Optical microresonators are high quality optical resonators of μ meter dimensions. Of the many different kinds of resonators the simplest one is a silica microsphere. It can be made by melting the tip of a standard optical fiber. Upon melting, the surface tension will form a high quality silica sphere on top of the fiber. This kind of silica microresonator can exhibit very high Q -factors (10^7 up to 10^9), Q -factor defined as the average number of round trips a photon can take inside a resonator before being absorbed or scattered. Inside the microresonators the light is confined by total internal reflection, so that the light is travelling along the circumference of the resonator. The modes of such resonators are called whispering gallery modes (WGM). In addition to the high quality factors the WGMs also have a very low mode volume which means that we can confine light in a very small volume for a long period of time. This makes them very useful for different applications such as sensing, lasers and amplifiers, optoelectronic oscillators or non-linear optics. The applicability of the microspheres can be further enhanced by applying a coating on the surface of microresonator. The coating can be used to functionalize the surface of the sphere, to activate the sphere or to alter the WGM confinement. In this paper we will review some of the different effects a high refractive index coating can have upon a microsphere, in particular in respect to the tailoring of the modal dispersion of the sphere, to the enhancement of the sensing sensitivity of the sphere and to the production of microlasers [1–3].

2. EXPERIMENTAL

The microspheres were produced by melting the tip of a standard optical telecommunications fiber. The typical diameter of the microspheres was found to be around 150 μm . Two different techniques have been used to coat the sphere with a high refractive index layer. The first method consist of coating a sphere with a silica-hafnia thin film using a sol-gel route. The sphere was coated with a film of the composition 70SiO₂-30HfO₂ activated with 0.3% mol Er³⁺. The films were coated using a dip coating technique. The sol was prepared by mixing a solution of Si(OC₂H₅)₄ (TEOS), HCl, H₂O, CH₃CH₂OH (ethanol) and HfOCl₂. The molar ratio between TEOS, water and the catalyst (HCl) was $n(\text{H}_2\text{O}) : n(\text{Si}(\text{OC}_2\text{H}_5)_4) : n(\text{HCl}) = 200:100:1$. The molar ratio between the TEOS and HfOCl₂ was chosen to be $n(\text{Si}(\text{OC}_2\text{H}_5)_4) : n(\text{HfOCl}_2) = 70 : 30$ on the basis of previous experiments. The overall amount of Si and Hf in the sol was controlled so that $c(\text{Si}(\text{OC}_2\text{H}_5)_4) + c(\text{HfOCl}_2) = 4.48 \cdot 10^{-4}$ mol/mL in order to have a sol viscosity which makes the dipping rate 30 nm/dip. Er(NO₃)₃ × 5H₂O was added to activate the film so that the molar concentration of Er³⁺ in the sol is 0.3% mol. The mixture of TEOS, HCl and H₂O was prehydrolysed at 65 °C for 1 hour before adding the HfOCl₂ and the Er(NO₃)₃ × 5H₂O. The entire mixture was then stirred for 16 h until the sol became transparent. The dipping speed was 40 mm/min and the dipping time 20 s. After each dip the microspheres were densified at 900°C for 50 s and after every 10 dips an additional densification was made for 2 min. At the end of the deposition a final densification for 5 min at 900°C was made [4]. The second method consists in coating a sphere with an amorphous silicon coating using the LPCVD (Low Pressure Chemical Vapor Deposition) method. The precursor gas was 26% silane (SiH₄) diluted in argon. The silane flow was about 150 sccm resulting in the chamber working pressure of about 0.2 mbar. The reaction used to deposit silicon was the thermal pyrolysis of silane: SiH₄ → Si + 4H₂. This reaction is known to produce amorphous silicon at temperatures below 580°C and polycrystalline silicon at temperatures above 580°C. In our work we chose the temperature of 570°C as the deposition temperature in order to obtain amorphous silicon. The reason that a : Si is preferred over crystalline silicon when coating the sphere is its lower surface roughness which is needed in order to preserve the high *Q*-factor of the sphere. All the measurement of the optical properties of the spheres was done using a microsphere-taper coupling setup to couple light in and/or out of the sphere. To measure the *Q*-factor of the spheres a C-band tunable laser was used to sweep across the resonance. To measure the erbium emission in erbium doped coatings the sphere was excited using a 1480 nm laser. The emission signal was detected by a Anritsu MS9710B optical spectrum analyzer (OSA).

3. RESULTS

The microsphere themselves present a high quality optical resonator. If an optically active material is present inside this resonator and pumped to achieve population inversion the sphere can exhibit lasing provided the round trip gain is higher than the round trip loss. We have measured the lasing spectrum of a 70SiO₂-30HfO₂ coated microsphere doped with 0.3% mol Er³⁺. The sphere was excited using a 1480 nm pump laser. The laser was coupled into the sphere using a halftaper. The same taper was used to collect the luminescence and/or lasing signal from the modes which are counter propagating in respect to the pump laser.

In Figure 1 are shown typical lasing and luminescence spectra of a coated microsphere. In the left part of Figure 1 is the luminescence spectrum taken when the pump power was kept below the lasing threshold. We can see that the quasy-equidistant modes are visible, corresponding to different values of *l*. In fact, two different families of modes are visible, corresponding to the TE and TM modes. Upon increasing the pump intensity above the lasing threshold strong lasing can be observed as is shown in the right part of Figure 1. Usually the lasing is multimode, the modes corresponding to modes which are present in the luminescence spectrum as can be seen in the inset of Figure 1. Peak laser powers are around 300 nW.

Evanescent field sensing is a method which uses the evanescent field of an electromagnetic wave confined in a photonic structure (a resonator or a waveguide) to detect the presence of an analyte on the surface of the structure. A photonic structure that has been widely used for evanescent field sensing is the whispering gallery mode (WGM) microresonator [5, 6]. In this case the sensing is done by monitoring the shift of the mode eigenfrequency (wavelength) of the mode. This can be done by sweeping a tunable laser across a resonance and monitoring the shift of the resonance upon contamination of the resonator surface with an analyte. The problem with WGM sensing is that the light is confined inside the microresonator by total internal reflection and hence the evanescent tail

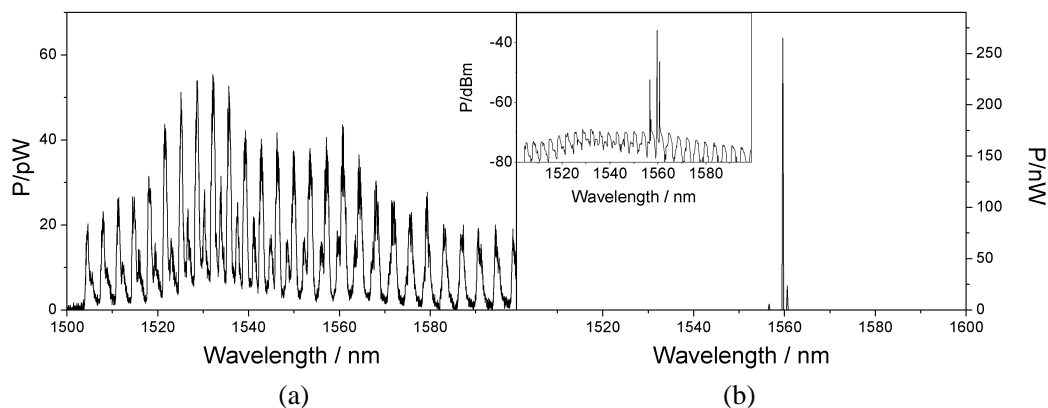


Figure 1: (a) The luminescence and (b) the lasing spectrum of an erbium doped microsphere. In the inset is the lasing spectrum in logarithmic scale.

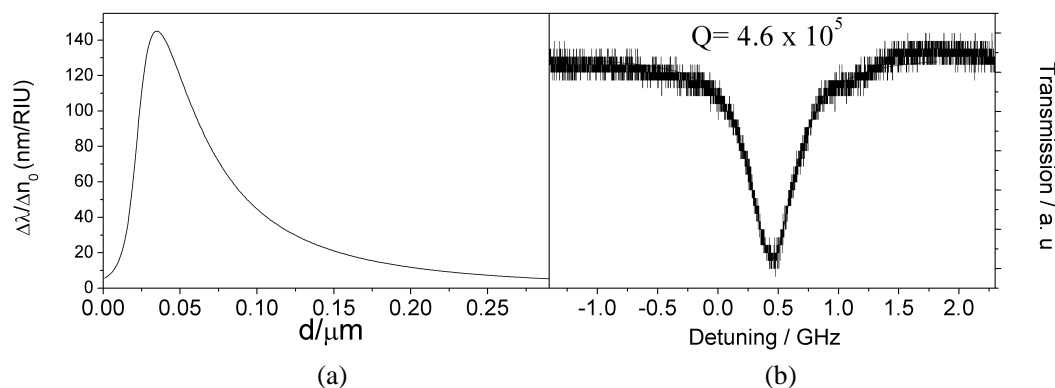


Figure 2: The sensing sensitivity vs. the coating thickness for (a) an a : Si coated microsphere and (b) the measured Q factor for a LPCVD a : Si coated microresonator, all at 1550 nm.

extending outside of the resonator is very short leading to low sensing sensitivity. If we introduce a high refractive index coating on the surface of a WGM resonator we can produce a structure which has both WGM and wave guiding properties and can have much higher sensing sensitivities than an uncoated sphere [7]. In the left part of Figure 2 is shown the theoretical calculation of the effect an amorphous silicon coating can have on the sensing sensitivity of a microsphere. The calculation shows the shift of the mode per change of the refractive index of the surrounding medium in which the sphere is located. This refractive index change is caused by the adsorption of analyte on the surface of the sphere. We can see that by choosing an appropriate coating thickness we can increase the sensing sensitivity from 5 nm/RIU in the case of an uncoated sphere to 145 nm/RIU in the case of a 35 nm a : Si coating.

In order to fully benefit from such a large increase of the sensitivity we have to make sure that the coating procedure does not degrade the Q -factor of the sphere. The coating process will necessarily introduce some scattering losses both on the sphere-coating and coating-air interfaces which could reduce the spheres Q -factor. To avoid this we must choose a coating material and procedure that allows the deposition of a highly smooth and homogenous coating. Furthermore the coating needs to be homogeneous also on the macroscopic scale meaning that the coating thickness has to be the same on all sides of the sphere. One of the few methods that allow this is the LPCVD (Low Pressure Chemical Vapor Deposition) method. Since, unlike other CVD methods, this method is not a direct flow deposition, the resulting films are highly homogenous. We have performed the coating of a 140 μm silica sphere with amorphous silicon using the LPCVD method. The Q -factor measurements of a coated sphere were made by sweeping a tunable laser across a resonance. The wavelength of the resonance divided by the transmission dip corresponding to the resonance is just the Q factor. A typical Q -factor measurement for a 150 nm coating is given in the right side of Figure 2. The measured Q -factor was 4.6×10^5 . A typical value of a blank silica microspheres

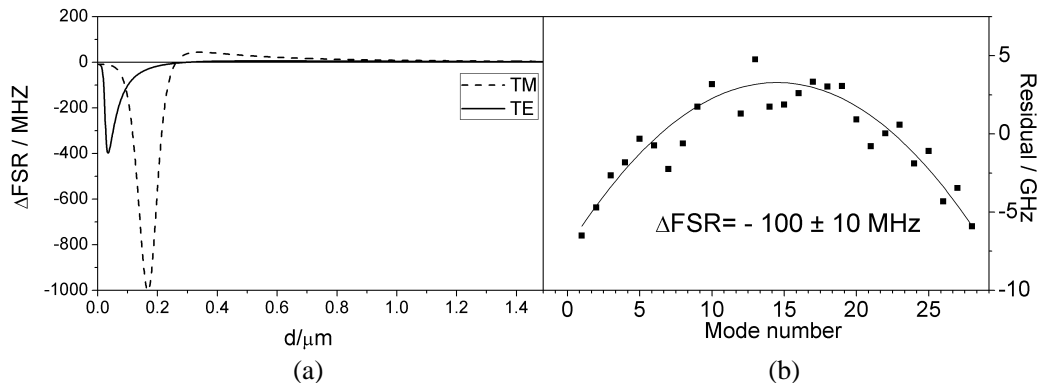


Figure 3: The sensing sensitivity vs. the coating thickness for (a) an a : Si coated microsphere and (b) the measured Q factor for a LPCVD a : Si coated microresonator, all at 1550 nm.

Q -factor is usually between 5×10^6 – 2×10^7 . We can see that even a very thick coating (150 nm) reduced the Q factor by only one order of magnitude. This makes amorphous LPCVD silicon a very promising candidate for sensing application.

A high refractive index can also be used to increase the applicability of the sphere for non-linear optics application [1]. In particular, a sphere can be coated using a material with a different refractive index in order to change its modal free spectral range (FSR) and/or modal dispersion (ΔFSR — mode to mode change of the FSR). This argument is very important for all non-linear optics applications where small anomalous dispersion is crucial, in particular frequency comb generation using four wave mixing. In fact, to achieve efficient frequency comb generation it is vital that the modes be as equidistant as possible which requires near-zero modal dispersion. In Figure 3 is shown the calculated geometrical cavity dispersion for an a : Si coating. We can see that by choosing an appropriate coating thickness we can tailor the modal dispersion in a very wide range, both in the anomalous and normal regimes. In particular, for the TE modes the dispersion can be tailored from -400 MHz normal to 6 MHz anomalous and for the TM modes from -1000 MHz normal to 50 MHz anomalous dispersion. Furthermore they both can have zero dispersion for a specific value of the coating thickness, namely 300 nm for the TE and 260 nm for the TM modes. We conclude that this method can give us a great degree of liberty in choosing a suitable geometrical cavity dispersion. For nonlinear optics application the most suitable geometrical cavity dispersion is, of course, equal in magnitude and opposite in sign to the material dispersion which depends on the materials used.

4. CONCLUSION

In conclusion we can state that a high refractive index coating can greatly increase the applicability of microresonators in a number of applications. The coating can be used to introduce optically active materials on the surface of the sphere for production of microlasers. Furthermore the coating can be used to greatly increase the sensing sensitivity of the microspheres. And finally the coating can be used to tailor the geometrical cavity dispersion of the resonator for application in non-linear optics.

ACKNOWLEDGMENT

The authors acknowledge the donation of Croatian Science Foundation (project Hybrid Silicon Nanostructures for Sensing) which supported this investigation. This research was also performed in the framework of the projects CNR-PAS (2014-2016) and CNES R&T SHYRO (2011-2014). R. R. Gonçalves and M. Ferrari acknowledge Brazilian Scientific Mobility Program “Ciências sem Fronteiras”.

REFERENCES

1. Ristić, D., M. Mazzola, A. Chiappini, A. Rasoloniaina, P. Féron, R. Ramponi, G. C. Righini, G. Cibiel, M. Ivanda, and M. Ferrari, “Tailoring of the free spectral range and geometrical cavity dispersion of a microsphere by a coating layer,” *Opt. Lett.*, Vol. 39, 5173–5176, 2014.

2. Ristić, D., A. Chiappini, M. Mazzola, D. Farnesi, G. Nunzi-Conti, G. C. Righini, P. Féron, G. Cibiel, M. Ferrari, and M. Ivanda, “Whispering gallery mode profiles in a coated microsphere,” *Eur. Phys. J. Special Topics*, Vol. 223, 1959–1969, 2014.
3. Ristić, D., A. Rasoloniaina, A. Chiappini, P. Féron, S. Pelli, G. Nunzi Conti, M. Ivanda, G. C. Righini, G. Cibiel, and M. Ferrari, “Whispering gallery mode profiles in a coated microsphere,” *Opt. Exp.*, Vol. 21, 20954–20963, 2013.
4. Gonçalves, R. R., G. Carturan, L. Zampedri, M. Ferrari, M. Montagna, G. C. Righini, S. Pelli, S. J. L. Ribeiro, and Y. Messaddeq, “Erbium-activated HfO₂-based waveguides for photonics,” *Opt. Mater.*, Vol. 25, 131–139, 2004.
5. Soria, S., F. Baldini, S. Berneschi, F. Cosi, A. Giannetti, G. Nunzi Conti, S. Pelli, and G. C. Righini, “High-*Q* polymer-coated microspheres for immunosensing applications,” *Opt. Exp.*, Vol. 17, 14694–14699, 2009.
6. Vollmer, F. and S. Arnold, “Whispering-gallery-mode biosensing: Label-free detection down to single molecules,” *Nat. Methods*, Vol. 5, 591–596, 2008.
7. Teraoka, I. and S. Arnold, “Enhancing the sensitivity of a whispering-gallery mode microsphere sensor by a high-refractive-index surface layer,” *J. Opt. Soc. Am. B*, Vol. 23, 1434–1441, 2006.

Wave-inspired Corrections for an Efficient Ray-optical Description of Micro-optics Devices

P. Stockschröder, J. Kreismann, and M. Hentschel
Institute for Physics, Technische Universität Ilmenau, Ilmenau, Germany

Abstract— Ray optics is a versatile tool to describe microscale optical systems like microlasers and their far-field emission. It is successful even in the regime where a wave-dynamical description would be expected to be appropriate. Indeed, when considering structures at length scales of a few light wavelengths, wave-inspired adjustments have to be taken into account to ensure the accuracy of ray-based predictions. These corrections to ray optics are known as the Goos-Hänchen shift, a lateral shift along the interface, and the Fresnel filtering effect, an angular shift, violating Snell's law and the principle of ray-path reversibility. In this contribution, we study in detail the influences of different factors on the exact size of the corrections paying special attention to the interplay between beam parameters and interface geometry. We obtain our results from analytical calculations using an expectation value approach to the beam shifts. These findings are supported by FDTD simulations. Knowing the influences of the different parameters, we are able to incorporate well adjusted correction terms in the ray-optical calculations for a large class of micro-optics devices with curved and planar boundaries.

1. INTRODUCTION

Optical microlasers and microcavities have attracted much interest because of their application potential in photonic and optoelectronic devices [1–3]. For the description of these micro-optics devices the concept of ray-wave correspondence has proven useful [4–6]. This concept uses geometrical optics to predict the modes and the far-field emission pattern of the devices [5, 7]. However, deviations from ray-optics occur as the system size becomes of the order of the light wavelength [8]. These deviations have to be taken into account to obtain accurate results [9].

The corrections to the laws of reflection and refraction are known as Goos-Hänchen shift [10–12] and Fresnel filtering [13]. The two contributions act in different directions in phase space [14]: The Goos-Hänchen shift (GHS) denotes a lateral shift of the reflected light beam along the interface. The Fresnel filtering (FF) effect describes a correction of Snell's law and acts on the angle of the reflected light, i.e., its momentum.

For an intuitive understanding of these effects at planar interfaces refer to Fig. 1(a) [15]. The Goos-Hänchen shift at a planar interface occurs primarily for total internal reflection (incident angle χ_{in} larger than the critical angle $\chi_c = \arcsin(1/n)$ which the relative refractive index $n = n_1/n_2$). It results from an interference effect [11] and yields a lateral shift along the interface of the order of the vacuum light wavelength λ between incident and reflected beam [12, 16, 17]. Due to the finite penetration depth γ , of the order of λ , of totally reflected light into the optically thinner medium,

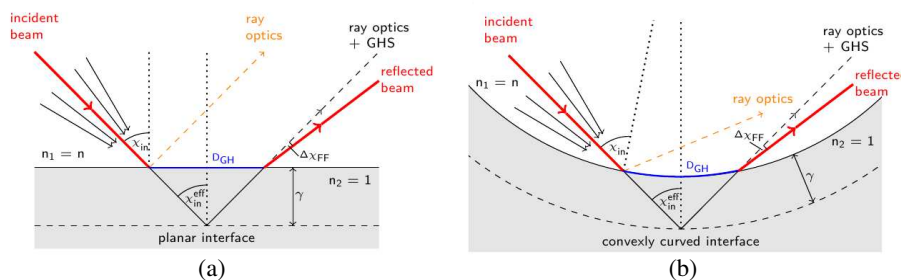


Figure 1: Schematic picture of the beam shifts at (a) planar, (b) curved interfaces. Incident and reflected beam are shown in red. The relative refractive index is $n = n_1/n_2$. The effective interface is depicted as dashed line, γ is the penetration depth. The normals to the interface and the effective interface (dotted lines) define the angle of incidence χ_{in} and the effective angle of incidence $\chi_{\text{in}}^{\text{eff}}$. The reflected beam predicted from ray optics is shown as dashed orange arrow. The lateral shift along the interface D_{GH} due to the Goos-Hänchen effect (blue) and the angular deflection $\Delta\chi_{\text{FF}}$ due to the Fresnel filtering effect are marked.

the reflection can be assumed to occur at an effective interface (dashed line in Fig. 1) under an effective angle of incidence $\chi_{\text{in}}^{\text{eff}}$ [18, 19]. The lateral shift is estimated to $D_{\text{GH}} = 2\gamma \tan(\chi_{\text{in}}^{\text{eff}})$.

The Fresnel filtering [13] (or angular Goos-Hänchen shift, [14, 20–23]) has its origin in the finite spatial extent of a light *beam* as opposed to the light *rays* of geometrical optics. This finite beam width induces angles of incidence distributed around a mean χ_{in} . Now, suppose $\chi_{\text{in}} = \chi_c$. All smaller angles in the distribution will be partially transmitted, whereas all larger angles will be totally reflected – the mean angle of the reflected light will deviate from χ_{in} : Snell’s law is violated, $\chi_{\text{out}} = \chi_{\text{in}} + \Delta\chi_{\text{FF}}$, with the FF correction $\Delta\chi_{\text{FF}}$. Consequently, FF will be most important around χ_c and for beams narrow in space, i.e., with a broad angular distribution.

At a curved interface, schematically depicted in Fig. 1(b), the beam shifts can be qualitatively understood in the same manner, though, with two major differences. Whereas $\chi_{\text{in}}^{\text{eff}} = \chi_{\text{in}}$ holds at a planar interface, we find $\chi_{\text{in}}^{\text{eff}} < \chi_{\text{in}}$ in the convexly curved case. As we can still approximate the GHS to be $D_{\text{GH}} \approx 2\gamma \tan(\chi_{\text{in}}^{\text{eff}})$, we expect the lateral shift to be smaller with increasing curvature. Furthermore, the angular spread of the incident light beam is effectively enhanced by the interface curvature which will lead to an increased FF at curved interfaces.

2. METHODOLOGY

Here, we use an expectation value approach to the beam shifts [15, 24] which is more widely applicable than the different approximative formulas discussed in literature [11, 12, 16, 22].

In the planar case, the beam is expanded in plane waves. We restrict our calculations to the interface, denoted by the z -axis. The incident beam is given by $E_I(z) = \int dk_z e_I(k_z) e^{ik_z z}$, where the transverse beam profile $e_I(k_z)$ is supposed to be centered about one momentum component $k_z = k_0$ corresponding to the central angle of incidence χ_{in} via $k_z = k \sin(\chi)$ with the wavenumber $k = 2\pi/\lambda$. The reflected beam is obtained by applying the Fresnel reflection coefficients [25] to the incident beam profile, $e_R(k_z) = \rho(k_z) e_I(k_z)$ leading to $E_R(z) = \int dk_z e_R(k_z) e^{ik_z z}$.

The beam shifts can then be defined as expectation values of the reflected beam:

$$D_{\text{GH}} = \langle z \rangle = \frac{\int_{-\infty}^{\infty} dz E_R^*(z) z E_R(z)}{\int_{-\infty}^{\infty} dz |E_R(z)|^2} \quad \text{and} \quad \Delta k_{\text{FF}} = \langle k_z - k_0 \rangle = \frac{\int dk_z e_R^*(k_z) (k_z - k_0) e_R(k_z)}{\int dk_z |e_R(k_z)|^2}. \quad (1)$$

From the shift in momentum Δk_{FF} , the angular deflection is obtained as $\Delta\chi_{\text{FF}} = \arcsin(\Delta k_{\text{FF}}/k)$.

For curved interfaces, we concentrate on circularly symmetric systems. Any curved boundary can be locally approximated by a circle. The beams are conveniently expanded in polar coordinates (r, α) using Bessel functions. Angular momentum conservation leads to a relation between the angular wavenumber m of the cylinder function J_m and the angle of incidence χ , $\sin(\chi) = m/(nkR)$ [18]. The incident light beam at the interface $r = R$, then, is $E_I(\alpha) = \sum_m e_I(m) e^{im\alpha} J_m(nkR)$. The transverse beam profile in angular momentum space $e_I(m)$ is chosen to be strongly peaked at the central angular wavenumber m_0 corresponding to χ_{in} . The reflected beam is obtained by applying the corrected Fresnel reflection coefficients for convexly curved interfaces [25] to the incident beam profile, $e_R(m) = \rho_c(m) e_I(m)$, giving $E_R(\alpha) = \sum_m e_R(m) e^{im\alpha} J_m(nkR)$.

Here, the beam shifts are obtained from the expectation values of the polar angle and the angular wavenumber

$$\Delta\alpha_{\text{GH}} = \langle \alpha \rangle = \frac{\int_{-\pi}^{\pi} d\alpha E_R^*(\alpha) \alpha E_R(\alpha)}{\int_{-\pi}^{\pi} d\alpha E_R^*(\alpha) E_R(\alpha)} \quad \text{and} \quad \Delta m_{\text{FF}} = \langle m - m_0 \rangle = \frac{\sum_m e_R^*(m) (m - m_0) e_R(m)}{\sum_m e_R^*(m) e_R(m)}. \quad (2)$$

The lateral shift D_{GH} along the interface, given in multiples of the vacuum wavelength λ , is then $D_{\text{GH}} = nkR \Delta\alpha_{\text{GH}}/(2\pi)$ and the angular deflection is $\Delta\chi_{\text{FF}} = \arcsin(\Delta m_{\text{FF}}/(nkR))$.

As transverse beam profiles we choose a Gaussian in momentum and angular momentum space for the planar and curved case, respectively,

$$e_I(k_z) = \frac{1}{\sqrt{2\pi\epsilon}} e^{-\frac{(k_z - k_0)^2}{2\epsilon^2}} \quad \text{and} \quad e_I(m) = \frac{1}{\sqrt{2\pi\sigma}} e^{-\frac{(m - m_0)^2}{2\sigma^2}} \quad (3)$$

with corresponding beam waists in real space $w/\lambda = \sqrt{2}k/(\pi\epsilon)$ and $w/\lambda = \sqrt{2}kR/(\pi\sigma)$.

Numerical results are obtained from full electromagnetic calculations simulating a Gaussian beam incident on planar and curved dielectric interfaces, see Fig. 2. These simulations have been

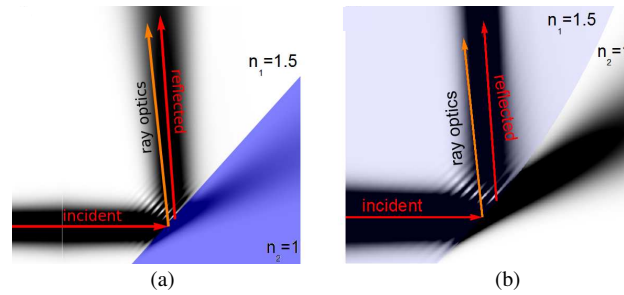


Figure 2: Real space pictures of a Gaussian beam with width $w/\lambda = 5$ reflected at a dielectric interface with relative refractive index $n = 1.5$ near critical incidence. The direction of incident and reflected beams are given by red arrows, the direction of the reflected beam expected from ray optics is given by the orange arrow. (a) TM polarized beam at a planar interface. (b) TE polarized beam at a curved interface with $kR = 400$.

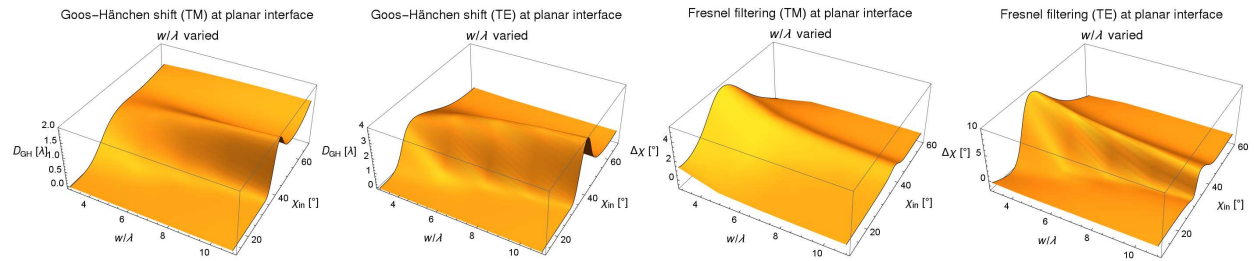


Figure 3: Effect of the beam waist on the beam shifts at a planar interface. The wavenumber k is fixed while the beam waist w/λ is varied. Goos-Hänchen shift and the Fresnel-filtering effect according to Equation (1) are shown for both, TM and TE, polarization. The relative refractive index is $n = 1.5$, $\chi_c \approx 41.8$, $\chi_B \approx 33.7$.

performed with the finite-difference time-domain (FDTD) method, using a freely available software package [26]. The ray propagation directions of the incident and reflected beams are obtained as mean value of the Poynting vectors and are denoted by red arrows. The deviation from geometrical optics, marked by the orange arrow, is clearly visible. The beam shifts are calculated as the difference between the simulated reflected beam and its ray-optics expectation.

3. RESULTS AND DISCUSSION

Now, we discuss the influence of the different parameters on the beam shifts. One important parameter is the beam width. At curved interfaces, the radius of curvature, additionally, is crucial.

In Fig. 3, the dependence on beam width of GHS and FF at planar interfaces is depicted. Firstly, both effects are broadened with reduced beam width, thus, giving a contribution for a larger range of incident angles. Secondly, GHS increases while FF decreases with increasing beam width. This is understood in the intuitive picture described in the Introduction. GHS depends on the spatial extent of the beam, whereas, FF depends on the width of the angular distribution. A broader beam in space corresponds to a narrower angular spectrum. The effects are strongest around the critical angle and the GHS has a finite value for supercritical incidence, whereas, FF drops to zero in this regime. We expect the least deviations from ray-optics for subcritical incidence, and this is indeed seen for TM polarization. The TE result, however, has a distinct contribution there, which is due to the Brewster angle, $\chi_B = \arctan(1/n) < \chi_c$, where no TE polarized light is reflected.

In Fig. 4, the effect of curvature on GHS and FF at convexly curved interfaces is studied. The radius of curvature R is changed while the angular spread σ and the beam width w/λ are kept fixed in Fig. 4(a) and 4(b), respectively. The results confirm the predictions made in the intuitive picture. When the radius is decreased, the effective angle of incidence is lower, thus, the GHS decreases in both cases. For the FF, however, the situation is more involved. In the case of fixed angular spread in the beam (Fig. 4(a)), the effective angular spread with respect to the interface is increased at a more strongly curved interface. Hence, the FF increases with decreasing radius. In the case of fixed beam width (Fig. 4(b)), however, σ changes, according to $w/\lambda = \sqrt{2kR}/(\pi\sigma)$, linearly with the radius of curvature when k and w/λ are fixed. Hence, the angular spread is increased by the same amount as the curvature is reduced. Consequently, the FF is unchanged in absolute size, only the position of the maximum is shifted and the features are broader for smaller R .

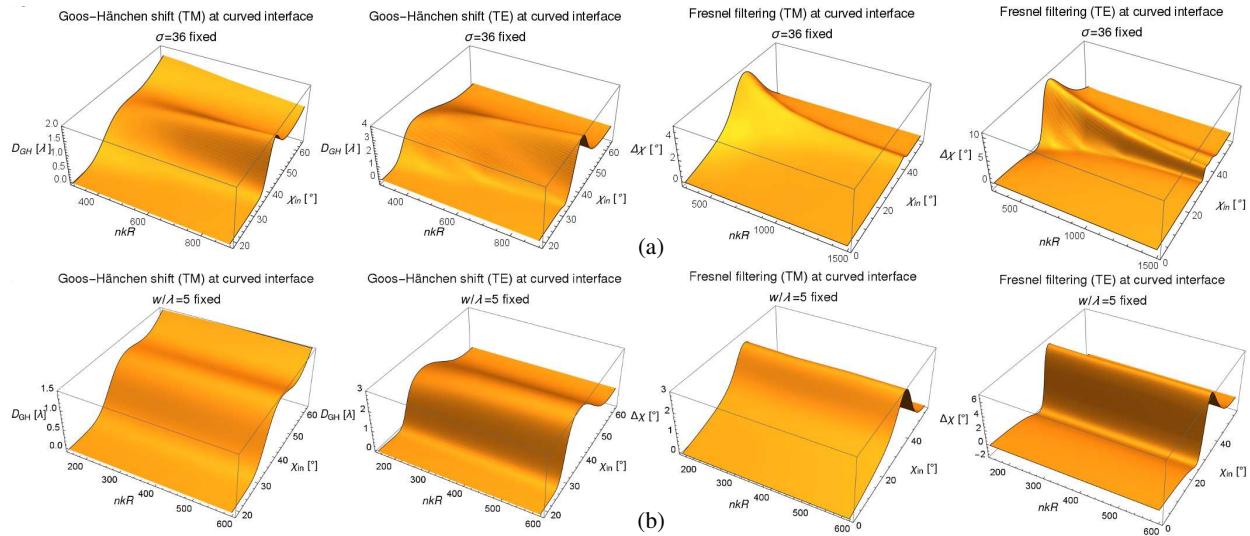


Figure 4: Effect of (a) angular spread and (b) beam waist on the beam shifts at convex interfaces. The wavenumber k and (a) the angular spread $\sigma = 36$, (b) the beam waist $w/\lambda = 5$ are fixed while the curvature $\kappa = 1/R$ is varied. Goos-Hänchen shift and the Fresnel-filtering effect according to Equation (2) are shown for both, TM and TE, polarization. The relative refractive index is $n = 1.5$, $\chi_c \approx 41.8$, $\chi_B \approx 33.7$.

4. CONCLUSION

For the inclusion of the correction terms in a ray-optical description of micro-optics devices, it is important to know how GHS and FF affect the prediction of the far-field emission. In polygonal microcavities which have only planar boundaries, only FF plays a role as it affects the emission direction. Whereas, GHS leads only to a parallel shift of the rays but not to a change in direction. For all other geometries with curved and mixed boundaries, both effects are important. Although GHS is diminished at strongly curved interfaces it still has to be taken into account as the shift along a curved boundary also affects the direction of the resulting beam. However, FF is of special importance here as it is strongly increased with curvature. Hence, it has a large impact on the prediction of the emission direction.

Furthermore, both effects are broadened with increasing curvature, thus, being important in a larger range of incident angles also far away from the critical angle. Especially in experiments with TE polarized light, the enhancement of the beam shift corrections and their Brewster angle features might lead to far-field patterns that deviate from the ray-optics expectation (e.g., [27, 28]).

Knowing the influence of polarization, beam width, angular spread and boundary curvature on the beam shift effects GHS and FF, we are now able to incorporate them in the ray-optical calculations for a large class of micro-optics devices with curved and planar boundaries. Thus, we can make predictions for these devices exploiting the simplicity and efficiency of geometrical optics while keeping the accuracy of wave calculations.

ACKNOWLEDGMENT

The authors gratefully acknowledge funding by the German Research Society (DFG) via the Emmy Noether Program and the Research Unit FOR 760. We thank Daniel Kotik, Jörg Götte, Ulf Peschel, and Henning Schomerus for discussions and valuable advice.

REFERENCES

1. Chang, R. K., *Optical Processes in Microcavities*, World Scientific, Singapore, 1996.
2. Vahala, K., *Optical Microcavities*, World Scientific, Singapore, 2004.
3. Cao, H. and J. Wiersig, "Dielectric microcavities: Model systems for wave chaos and non-Hermitian physics," *Rev. Mod. Phys.*, Vol. 87, No. 1, 61–111, 2015.
4. Schwefel, H. G. L., N. B. Rex, H. E. Tureci, R. K. Chang, A. D. Stone, T. Ben-Messaoud, and J. Zyss, "Dramatic shape sensitivity of directional emission patterns from similarly deformed cylindrical polymer lasers," *J. Opt. Soc. Am. B*, Vol. 21, No. 5, 923–934, 2004.
5. Wiersig, J. and M. Hentschel, "Combining directional light output and ultralow loss in deformed microdisks," *Phys. Rev. Lett.*, Vol. 100, No. 3, 033901, 2008.

6. Hentschel, M. and K. Richter, "Quantum chaos in optical systems: The annular billiard," *Phys. Rev. E*, Vol. 66, No. 5, 056207, 2002.
7. Tanaka, T., M. Hentschel, T. Fukushima, and T. Harayama, "Classical phase space revealed by coherent light," *Phys. Rev. Lett.*, Vol. 98, No. 3, 033902, 2007.
8. Song, Q. H., L. Ge, A. D. Stone, H. Cao, J. Wiersig, J.-B. Shim, J. Unterhinninghofen, W. Fang and G. S. Solomon, "Directional laser emission from a wavelength-scale chaotic microcavity," *Phys. Rev. Lett.*, Vol. 105, No. 10, 103902, 2010.
9. Altmann, E. G., G. Del Magno, and M. Hentschel, "Non-Hamiltonian dynamics in optical microcavities resulting from wave-inspired corrections to geometric optics," *EPL*, Vol. 84, No. 1, 10008, 2008.
10. Goos, F. and H. Hänchen, "Ein neuer und Fundamentalere Versuch Zur Totalreflexion," *Annalen der Physik*, Vol. 436, No. 7-8, 333-346, 1947.
11. Artmann, K., "Berechnung der Seitenversetzung des totalreflektierten Strahles," *Annalen der Physik*, Vol. 437, No. 1-2, 87-102, 1948.
12. Lai, H. M., F. C. Cheng, and W. K. Tang, "Goos-Hänchen effect around and off the critical angle," *J. Opt. Soc. Am. A*, Vol. 3, No. 4, 550-557, 1986.
13. Tureci, H. E. and A. D. Stone, "Deviation from Snell's law for beams transmitted near the critical angle: Application to microcavity lasers," *Opt. Lett.*, Vol. 27, No. 1, 7-9, 2002.
14. Schomerus, H. and M. Hentschel, "Correcting ray optics at curved dielectric microresonator interfaces: Phase-space unification of Fresnel filtering and the Goos-Hänchen shift," *Phys. Rev. Lett.*, Vol. 96, No. 24, 243903, 2006.
15. Stockschröder, P., J. Kreismann, and M. Hentschel, "Curvature dependence of semiclassical corrections to ray optics: How Goos-Hänchen shift and Fresnel filtering deviate from the planar case result," *EPL*, Vol. 107, No. 6, 64001, 2014.
16. Horowitz, B. R. and T. Tamir, "Lateral displacement of a light beam at a dielectric interface," *J. Opt. Soc. Am.*, Vol. 61, No. 5, 586-594, 1971.
17. Lotsch, H. K. V., "Beam displacement at total reflection: The Goos-Hänchen effect I," *OPTIK*, Vol. 32, No. 2, 116-137, 1970.
18. Hentschel, M. and H. Schomerus, "Fresnel laws at curved dielectric interfaces of microresonators," *Phys. Rev. E*, Vol. 65, No. 4, 045603, 2002.
19. Kotik, D. and M. Hentschel, "How curvature affects the far-field emission from deformed optical microcavities," *J. Opt.*, Vol. 15, No. 1, 014010, 2013.
20. Merano, M., A. Aiello, M. P. van Exter, and J. P. Woerdmann, "Observing angular deviations in the specular reflection of a light beam," *Nat. Photon.*, Vol. 3, No. 6, 337-340, 2009.
21. Fiedler-Ferrari, N., H. M. Nussenzveig, and W. J. Wiscombe, "Theory of near-critical-angle scattering from a curved interface," *Phys. Rev. A*, Vol. 43, No. 2, 1005-1038, 1991.
22. Bliokh, K. Y. and A. Aiello, "Goos-Hänchen and Imbert-Fedorov beam shifts: An overview," *J. Opt.*, Vol. 15, No. 1, 014001, 2013.
23. Götte, J. B., S. Shinohara, and M. Hentschel, "Are Fresnel filtering and the angular Goos-Hänchen shift the same?," *J. Opt.*, Vol. 15, No. 1, 014009, 2013.
24. Porras, M. A., "Moment-method evaluation of the angular and lateral shifts of reflected light beams," *Opt. Commun.*, Vol. 131, No. 1-3, 13-20, 1996.
25. Jackson, J. D., *Classical electrodynamics*, 3 Edition, Wiley, New York, 1999.
26. Oskooi, A. F., D. Roundy, M. Ibanescu, P. Bermel, J. D. Joannopoulos, and S. G. Johnson, "MEEP: A flexible free-software package for electromagnetic simulations by the FDTD method," *Comput. Phys. Commun.*, Vol. 181, No. 3, 687-702, 2010.
27. Song, Q., W. Fang, B. Liu, S.-T. Ho, G. S. Solomon, and H. Cao, "Chaotic microcavity laser with high quality factor and unidirectional output," *Phys. Rev. A*, Vol. 80, No. 4, 041807, 2009.
28. Shinohara, S., M. Hentschel, J. Wiersig, T. Sasaki, and T. Harayama, "Ray-wave correspondence in limaçon-shaped semiconductor microcavities," *Phys. Rev. A*, Vol. 80, No. 3, 031801, 2009.

Modulation of Nanolaser Output for Information Encoding

T. Wang^{1,2}, G. P. Puccioni³, and G. L. Lippi^{1,2}

¹Institut Non Linéaire de Nice, Université de Nice Sophia Antipolis, France

²CNRS, UMR 7335, 1361 Route des Lucioles, Valbonne 06560, France

⁴Istituto Sistemi Complessi, CNR, Via Madonna del Piano 10, Sesto Fiorentino 50019, Italy

Abstract— We analyze some of the fundamental issues concerning the suitability of high- β laser devices for information encoding by using a Stochastic Simulator. Modulating the pump in a square-wave fashion, to encode sequences of 0 and 1 levels, we study the influence of offset (or bias) and modulation amplitude on the fidelity of the nanolaser output. The impact of the cavity relaxation rate is also discussed.

1. INTRODUCTION

In recent years, nanolasers have gained much attention and a significant amount of work has been carried out to explore and develop them, given their potential as sources for data transmission and storage, intra-chip connections and generically for their use as on-chip light sources [1–3].

Nanoscale lasers, in the limit of $\beta = 1$ (where β represents the fraction of spontaneous emission coupled into the lasing mode) offer the advantage of allowing a unique electromagnetic cavity mode to interact with the “atoms” of the gain material (where “atoms” is to be intended as the generic quantum element transforming internal energy into electromagnetic radiation). This way, the coupling efficiency from spontaneous emission to the lasing mode approaches unity, thereby allowing for high efficiency and very low threshold [4]. In addition, their extremely small cavity size offers the potential for a short cavity lifetime (even though photons need to be *recycled* more than in a conventional laser to achieve stimulated emission), thus allowing for higher modulation bandwidth, a significant advantage for high volume information processing.

So far, different kinds of nanoscale lasers have been manufactured, and very low-threshold performance has been demonstrated, at least with optical pumping. Electrical injection is actively pursued, because of its obvious advantages, and some results in this direction have been obtained [5]. One important hurdle has so far hampered the development of these devices: the competition between the efficient fabrication of a gain medium and the manufacturing of suitable cavity “mirrors”. Indeed, the two requirements tend to impose conflicting restrictions, as particularly clear in the case of photonic crystal structures, where the “damage” inflicted on the material by the holes renders the achievement of strong gain difficult. A very recent breakthrough, decoupling the problem of achieving adequate optical gain from the construction of the cavity “mirrors”, has been obtained by accurately positioning a monolayer gain medium on top of a photonic crystal cavity [6]. This innovative configuration brings nanolasers one step closer to their actual deployment as practical devices. Thus, it is time to start asking under which conditions nanolasers may be used for effective information encoding.

Theoretically, since only a limited number of emitters is enclosed inside the cavity and therefore the number of photons is not very large, we cannot consider the *thermodynamic limit* commonly assumed for the laser [7]; thus, the quantum fluctuations in the number of inverted *atoms* and in the intracavity (as well as emitted) photons cannot be ignored [8]. Hence, the traditional rate equations [9] are no longer suitable to model such small lasers. Although sophisticated modeling has been conducted up until now on the basis of greatly enhanced rate equations which take into account the physical characteristics of the semiconducting structure both for nanolasers [10, 11] and for nanoLEDs [11], the device’s sensitivity to the intrinsic noise cannot be easily tested with these numerical approaches. Further, doubts about the suitability of nanosources for optical communications, and for information encoding and handling have been raised due to the larger intrinsic fluctuations and to the appearance of population cycles (noise-induced relaxation oscillations) in high- β devices [8].

The failure of the simplest, standard modeling choice of reliably predicting the response of a nanolaser under parameter (pump) modulation represents a serious obstacle for determining suitable operating conditions for optical encoding. More sophisticated modelling choices [12, 13] suffer from the disadvantage of requiring large computing times and/or from not allowing for dynamical investigations [14]. In order to obtain efficient predictions on the expected nanolaser

response to pump modulation for data encoding, we are going to use a recently introduced Stochastic Simulator (SS) [15], which extends an idea adopted in [8]. The model predicts the physical response of a nanolaser, taking into account the *granularity* of the processes (number of photons and of excited *atoms*) without pretending to specifically consider the construction details of any device, which would vary according to the materials, construction techniques, etc. No external noise is applied (e.g., pump noise) at the present time, since the sole *stochasticity* of the lasing process is sufficient to induce deviations — substantial for particular operating parameters — from the pattern imposed by the pump. Different regimes are considered, changing biasing, modulation amplitude and cavity quality factor.

2. STOCHASTIC SIMULATOR

The Stochastic Simulator mimics a sequence of events as a succession of possible occurrences taking place at discrete times, with a time discretization small enough compared to the fastest time scale [15]. This scheme describes the process of spontaneous or stimulated photons emitted by an excited *atom* as a random process. The individual processes considered in the SS, which in their collective interaction produce lasing or incoherent emission, are: 1. excitation of an *atom* by the pumping mechanism; 2. disexcitation of an *atom* with emission of an off-axis (i.e., in an e.m. cavity mode other than the lasing mode) spontaneous photon; 3. disexcitation of an *atom* with emission of an on-axis (i.e., in the lasing mode) spontaneous photon; 4. disexcitation of an *atom* with emission of a stimulated photon; 5. leakage (out of the cavity volume) of an off-axis spontaneous photon; 6. transmission of an on-axis spontaneous photon through the cavity output mirror; 7. transmission of a stimulated photon through the cavity output mirror [15]. The spontaneous photons emitted off-axis are collected into a single ensemble, to which we assign a (somewhat arbitrarily) same, average leakage rate, due to their low impact onto the overall dynamics. The distinction of photons into three categories is indispensable in a photon number modeling approach, since it is the most efficient way of numerically following the different populations. A Poissonian probability distribution is used for the pump, while all other processes are simulated with a binomial probability distribution. Details about the SS rules can be found in [15]. The dynamical response to the modulation of the pump is simply obtained by applying a square-wave modulation, with variable frequency and amplitude (as well as offset), to the dynamical evolution of the SS.

The parameters we used for the simulations are: material relaxation constant $\gamma_{\parallel} = 2.5 \times 10^9 \text{ s}^{-1}$, and losses for off-axis spontaneous photons $\Gamma_0 = 5 \times 10^{13} \text{ s}^{-1}$. As in [15], the value of the parameter of tuning the probability of a spontaneous photon generating a stimulated photon is set at $K = 0.05$. The time step used to follow the process is set to $\Delta\tau = 2 \times 10^{-15} \text{ s}$, allowing for a good sampling of the fastest evolution (off-axis spontaneous photons). The cavity losses for the on-axis mode (describing the transmission by the output mirror for both kinds of photons: spontaneous or stimulated) are typically assumed to be $\Gamma_c = 1 \times 10^{11} \text{ s}^{-1}$, unless otherwise noted (i.e., when changing the resonator's quality factor).

3. RESULTS AND DISCUSSION

The Stochastic Simulator is a very useful tool for predicting the laser dynamics with fast computations thus allowing for a quantification of the intrinsic noise (i.e., the spontaneous emission). The self-consistent inclusion of both populations of spontaneous photons (on- and off-axis) in addition to the traditional quantities (inverted *atoms* and stimulated photons) allows for obtaining meaningful predictions of the laser's response irrespectively of the modulation amplitude and bias (i.e., even in a region where the laser is not “properly above threshold”). In addition, the choice of stochastically simulating the discrete physical processes without introducing a differential description removes the assumptions which are normally necessary for the latter, and preserves the *granular* description of the interaction, thereby delivering predictions which maintain the strongly stochastic character typical of small-sized systems [16]. Thus, the resulting dynamical output will reflect the concomitance of the stochastic processes which contribute to the onset of lasing action even in regimes where the pump is modulated at a high rate even across the threshold region [15].

Here, we show an example of modulation in a high- β nanocavity laser, where the *lasing transition* becomes nearly linear (cf. Fig. 1, inset, $\beta = 0.9$) [17]. Since we are working with a model based on physical principles, rather than on a practical device, the parameter values are relative and do not have a direct quantitative equivalence in physical units. The region of input-output response depicted in the inset corresponds to predominantly spontaneous photons emitted for the smallest values of the pump, and to predominantly stimulated ones for the largest ones [16]. The five output

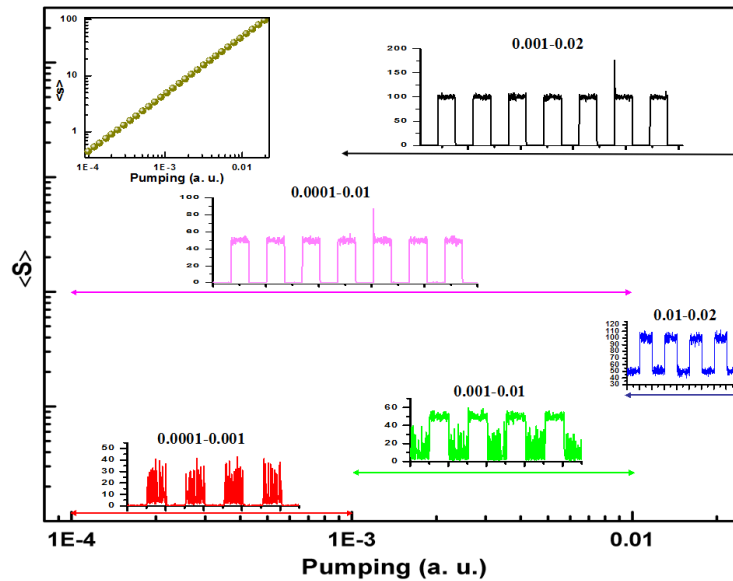


Figure 1: Illustration of principle of direct current modulation in a nanolaser with $\beta = 0.9$ computed by the SS. Inset (upper left corner): average output intensity as a function of pump. The color traces show the predicted output for a few 0–1 bit sequences for different modulation amplitude and offset. Their position is marked by color dots in the response curve (inset).

samples in the body of Fig. 1 illustrate the laser output for different values of the modulation amplitude (cf. reflected qualitatively by the horizontal placement of each graph in the figure). The exact pump values are given for each figure as a set of two numbers indicating (lower–upper) pump value, respectively, and the colored arrows give a visual representation of the modulation offset and amplitude (on the horizontal axis). The signal is computed with an integration time (0.2 ns) simulating the detector response.

First, we notice that the scale for the (total: spontaneous plus stimulated) photon number exiting the cavity does not vary more than a factor approximately 2 over the whole range explored. What changes drastically is the response of the laser to the modulation. The frequency chosen is quite low here, to highlight the different regimes (the frequency response will be analyzed elsewhere). For the lowest excitations (red curve, bottom left in the figure), the logical 1 level corresponds to a sequence of spikes corresponding to a signal whose *noise* is as large as the average (thus an entirely closed eye diagram). This is not unexpected since in the threshold region the laser operates as a sequence of spikes [15]. Moving the offset upwards one order of magnitude (green curve), we find that the lower level is extremely noisy, due to the same spiking operating regime just discussed. A large modulation amplitude (purple curve, pump driven between 10^{-4} and 10^{-2}) provides a sequence of bits which are usable, even though one remarks the presence of a spurious, large spike at the beginning of the fifth 1-level. The same occurs when the pump corresponding to the 1-level is doubled (black curve). Finally, when driving the nanolaser between two above-threshold levels one obtains a noisy, but useably encoded output (blue curve).

The cavity losses (alternately, the cavity quality factor) also play an important role in determining the encoding fidelity, as shown in Fig. 2. For large losses ($\Gamma_c = 10^{12} \text{ s}^{-1}$) the number of photons output is very small and the intrinsic fluctuations render the signal unusable (black curve). The 1-level is reminiscent of coherent oscillations [8], found also with the SS [15] (the 0-level is almost always devoid of photons, for all three values of cavity losses considered in this figure). This is plausible since for lower pump values one expects to find (less-damped) relaxation oscillations which can strongly be excited by the intrinsic fluctuations proper to the stochastic process.

Reducing the losses by one order of magnitude (red curve) the average number of photons increases by one order of magnitude and the relative fluctuations are strongly reduced, for the same pump values (from 10^{-4} to 10^{-2}). Further reduction of the cavity losses ($\Gamma_c = 10^{10} \text{ s}^{-1}$, blue curve) provides a much stronger signal with small fluctuations. It is important to remark that occasional “errors” survive, in the form of spikes, not only for the intermediate, but also for the smaller losses (cf. initial value of the fourth 1-level). Given that the number of bits computed here

is very small, it is not impossible that fidelity may be affected even under the best conditions shown here for moderately long bit sequences.

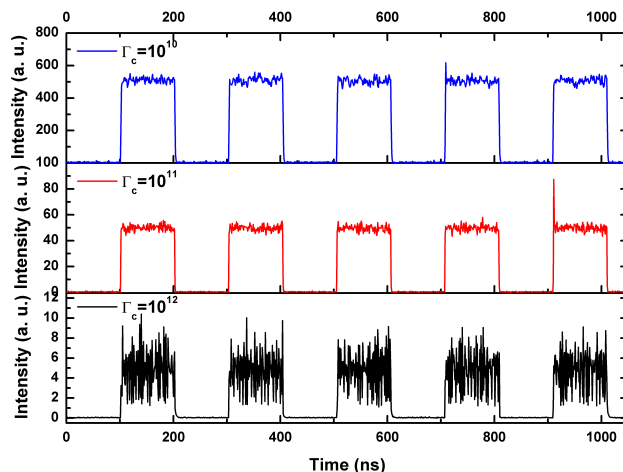


Figure 2: Laser output for a square modulation of the pump between 10^{-4} and 10^{-2} in a 0-1 level repetitive sequence for three different values of cavity losses Γ_c . Notice that the threshold is lowered as Γ_c is decreased, whence the larger output and higher-quality encoding.

The enhanced spontaneous emission, coupled with a high Q cavity (low Γ_c), is expected to result in a reduction of the laser turn-on delay, in addition to a threshold reduction. This comes from the fact that dynamically (i.e., in a rate-equation kind of analysis) the saddle point moves closer to threshold [18] and therefore can be reached faster. In the limit of $\beta = 1$ this would amount to reducing the turn-on delay to zero. However, a strong increase in cavity quality factor is accompanied by a strong reduction of the modulation bandwidth (easily checked even with a SS), thus offsetting entirely the advantage originating from the disappearance of the turn-on delay — which limits the modulation bandwidth — by an even stronger limitation on bandwidth. In addition, it is possible that the coherent oscillation conditions may worsen when the threshold is strongly lowered [8], thus calling again into question the desirability of high Q cavities. Work is under way to clarify this point.

4. CONCLUSION

With the help of a Stochastic Simulator we have analyzed some fundamental aspects of the issues which concern the suitability of a nanolaser for information encoding. Fundamental concerns raised by other authors appear to be realistic, but it seems possible to find parameter regimes in which very small devices should prove usable for digital applications.

ACKNOWLEDGMENT

We are grateful to A. Beveratos for initial discussions and to A. Politi for suggestions on modelling issues. T. W. acknowledges Ph.D. Thesis funding from the Conseil Régional PACA and support from BBright.

REFERENCES

1. Miller, D. A. B., “Device requirements for optical interconnects to silicon chips,” *Proc. IEEE*, Vol. 97, No. 7, 1166–1185, 2009.
2. Ning, C. Z., “Semiconductor nanolasers,” *Phys. Status Solidi B*, Vol. 247, No. 4, 774–788, 2010.
3. Khajavikhan, M., A. Simic, M. Katz, J. H. Lee, B. Slutsky, A. Mizrahi, V. Lomakin, and Y. Fainman, “Thresholdless nanoscale coaxial lasers,” *Nature*, Vol. 482, 204–207, 2012.
4. Björk, G., A. Karlsson, and Y. Yamamoto, “Definition of a laser threshold,” *Phys. Rev. A*, Vol. 50, No. 2, 1675–1680, 1994.
5. Matsuo, S., K. Takeda, T. Sato, M. Notomi, A. Shinya, K. Nozaki, H. Taniyama, K. Hasebe, and T. Kakitsuka, “Room-temperature continuous-wave operation of lateral current injection

- wavelength-scale embedded activeregion photonic-crystal laser,” *Opt. Express* Vol. 20, No. 4, 3773–3780, 2012.
6. Wu, A., S. Buckley, J. R. Schaibley, L. Feng, J. Yan, D. G. Mandrus, F. Hatami, W. Yao, J. Vučković, A. Majumdar, and X. Xu, “Monolayer semiconductor nanocavity lasers with ultralow thresholds,” *Nature*, Vol. 520, No. 7545, 69–73, 2015.
 7. Dohm, V., “Nonequilibrium phase transition in laser-active media,” *Solid State Commun.*, Vol. 11, No. 9, 1273–1276, 1972.
 8. Lebreton, A., I. Abram, N. Takemura, M. Kuwata-Gonokami, I. Robert-Philip, and A. Beveratos, “Stochastically sustained population oscillations in high- β nanolasers,” *New J. Phys.*, Vol. 15, No. 3, 033039 (1–11), 2013.
 9. Coldren, L. A. and S. W. Corzine, *Diode Lasers and Photonic Integrated Circuits*, Wiley, New York, 1995.
 10. Suhr, T., N. Gregersen, K. Yvind, and J. Mørk, “Modulation response of nanoLEDs and nanolasers exploiting Purcell enhanced spontaneous emission,” *Opt. Express*, Vol. 18, No. 11, 11230–11241, 2010.
 11. Ni, C.-Y. A. and S. L. Chuang, “Theory of high-speed nanolasers and nanoLEDs,” *Opt. Express*, Vol. 20, No. 15, 16450–16470, 2012.
 12. Roy-Choudhury, K., S. Haas, and A. F. J. Levi, “Quantum fluctuations in small lasers,” *Phys. Rev. Lett.*, Vol. 102, No. 5, 053902 (1–5), 2009.
 13. Lorke, M., T. Suhr, N. Gregersen, and J. Mørk, “Theory of nanolaser devices: Rate equation analysis versus microscopic theory,” *Phys. Rev. B*, Vol. 87, No. 20, 205310 (1–10), 2013.
 14. Chusseau, L., F. Philippe, and F. Disanto, “Monte Carlo modeling of the dual-mode regime in quantum-well and quantum-dot semiconductor lasers,” *Opt. Express*, Vol. 22, No. 5, 5312–5324, 2014.
 15. Puccioni, G. P. and G. L. Lippi, “Stochastic Simulator for modeling the transition to lasing,” *Opt. Express*, Vol. 23, No. 3, 2369–2374, 2015.
 16. Wang, T., G. P. Puccioni, and G. L. Lippi, “An Efficient and Innovative Modelisation for Nanolasers,” *Progress In Electromagnetic Electromagnetics Research Symposium*, Prague, Czech Republic, July 2015, paper 150204095123.
 17. Chow, W. W., F. Jahnke, and C. Gies, “Emission properties of nanolasers during the transition to lasing,” *Light: Science & Applications*, doi:10.1038/lisa.2014.82, 1–8, 2014.
 18. Lippi, G. L., S. Barland, N. Dokhane, F. Monsieur, P. A. Porta, H. Grassi, and L. M. Hoffer, “Phase space techniques for steering laser transients,” *J. Opt. B: Quantum Semiclass. Opt.*, Vol. 2, No. 3, 375–381, 2000.

FDTD Simulation of a Cylindrical Waveguide Using Longitudinal Current Distribution as an Excitation Scheme

D. V. Peponis, G. P. Latsas, Z. C. Ioannidis, and I. G. Tigelis

Faculty of Physics, National and Kapodistrian University of Athens
University Campus, Athens 157 84, Greece

Abstract— In this work we present a numerical code based on the FDTD method in the cylindrical coordinate system. In order to verify the code, the simple case of a cylindrical waveguide excited by an axial current distribution is considered. The waveguide is terminated using two CFS-PML layers in order to eliminate reflections at both ends.

1. INTRODUCTION

Recently, the demand for high-power and high-frequency microwave sources have led to the development of sophisticated microwave structures. Due to their complexity, the analytical study of those is difficult and thus numerical techniques are usually employed, one of them being the FDTD method. Such techniques often use Cartesian grids, in which obviously cylindrical structures cannot be accurately modelled. Specifically, the curvatures in these structures are approximated by a staircase scheme, which introduces undesired errors [1]. To overcome these problems, FDTD codes in cylindrical coordinates have been developed in the past based on an appropriately modified Yee algorithm, primarily used in low frequency problems [2–4]. In this work, the FDTD method (and the corresponding developed numerical code) in cylindrical coordinate system formulated for studying complex cylindrical geometries appearing in high-frequency devices (like the gyrotron beam tunnel), is used for the simple case of a smooth waveguide. The Maxwell equations are written appropriately in order to eliminate the aforementioned conformal problems [1,6]. Moreover, a CFS-PML layer [7] is used for the termination of the waveguide. As an excitation scheme, an infinitely thin wire is considered, located on the propagation axis, with a predefined current density. This type of excitation could model the case of the excitation of the waveguide modes by a thin electron beam in such a waveguide structure in the small signal regime. In this study, only the dominant TM_{01} mode is excited due to the choice of frequency range. Finally the effect of the CFS-PML on the reflection at both ends of the structure is studied in the whole frequency range under investigation.

2. MATHEMATICAL FORMULATION OF THE METHOD

The discretized Maxwell equations in Cylindrical coordinates are written appropriately taking into account the source term J , i.e., the radial component of the electric field, E_ρ , is:

$$E_\rho|_{i+1/2,j,k}^{n+1} = \frac{2\varepsilon|_{i+1/2,j,k} - \sigma|_{i+1/2,j,k}\delta t}{2\varepsilon|_{i+1/2,j,k} + \sigma|_{i+1/2,j,k}\delta t} E_\rho|_{i+1/2,j,k}^n + \frac{2\delta t}{2\varepsilon|_{i+1/2,j,k} + \sigma|_{i+1/2,j,k}\delta t} \left[-J_\rho|_{i+1/2,j,k}^{n+1/2} + \frac{H_z|_{i+1/2,j+1/2,k}^{n+1/2} - H_z|_{i+1/2,j-1/2,k}^{n+1/2}}{(i+1/2)\delta\rho\delta\varphi} - \frac{H_\varphi|_{i+1/2,j,k+1/2}^{n+1/2} - H_\varphi|_{i+1/2,j,k-1/2}^{n+1/2}}{\delta z} \right] \quad (1)$$

where δt is the timestep, $\delta\rho$, $\delta\varphi$ and δz are the mesh spatial increments in ρ , φ and z directions, respectively, σ the conductivity and ε the dielectric permittivity of the medium inside the waveguide. Indexes i , j and k refer to the grid position in ρ , φ and z directions, respectively. All the field components are properly located within the cylindrical Yee cell, which is shown in Fig. 1, in order for Ampere and Faraday laws to be valid.

The analytical field equations of Ampere and Faraday laws present a singularity at $\rho = 0$ for E_z and H_ρ time derivatives [2], and this problem appears in the discretized expressions as well. On the other hand, E_φ cannot be properly calculated at $\rho = 0$ due to the need for field values at $i = -1/2$, which are not defined. These problems can be overcome with the proper application of Ampere law at the neighbouring grid points, as presented in [2].

In order to eliminate the reflections at the terminations of the waveguide, two CFS-PML layers were used, one at each end (Fig. 2). These layers were implemented using the stretched coordinates

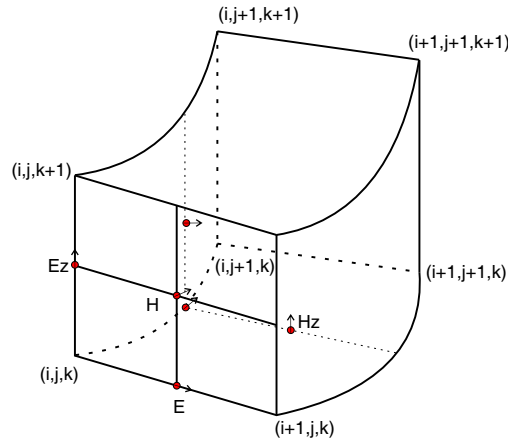


Figure 1: Cylindrical Yee cell.

formulation [7]. Coordinate stretching was applied only in the direction perpendicular to the interface of the PML-structure [8], i.e., the z -axis. The scaling characteristics of CFS-PML layer were calculated with respect to the cutoff frequency of the modes expected to excite in the structure. In detail, the complex conductivity tensor of the layer is given by [9]

$$s_i = k_i + \frac{\sigma_i}{\alpha_i + j\omega\varepsilon_0}, \quad i = \rho, \varphi, z \quad (2)$$

where s_i is the CFS-PML layer's conductivity, ω the angular velocity and ε the layer's electric permittivity. The maximum value of the a_i term can be chosen taking into account the cutoff frequencies of the expected modes. In the case, where only one mode is present, it is given by [8]

$$\alpha_{i,max} = 2\pi f_c \varepsilon_0, \quad i = \rho, \varphi, z \quad (3)$$

where f_c is the cutoff frequency of the selected mode. The conductivity σ_i , which appears in the stretching factor, can follow either a polynomial or a geometrical profile on the axis where stretching is applied. For a polynomial profile, the maximum value of the conductivity is given by [6]

$$\sigma_{i,max} = -\frac{(m+1)\ln[R(0)]}{2\eta d}, \quad i = \rho, \varphi, z \quad (4)$$

where m is the polynomial factor, $R(0)$ the desired reflection coefficient of the layer for normal incidence, η the layer impedance and d its thickness.

3. NUMERICAL RESULTS AND DISCUSSION

In order to verify the applied method and to benchmark the numerical code, the simple case of a smooth hollow cylindrical waveguide was examined, with the excitation implemented by an infinitely thin wire of specific current density located at the axis of the waveguide. The axial cross section is shown in Fig. 2 whereas the geometrical characteristics are given in Table 1. The current density is spatially constant, whereas in time it varies as a Gaussian modulated sinusoid with predefined spectral characteristics. Its frequency content is such that only TM_{01} mode (with $f_c = 8.19$ GHz) can be propagated. The central frequency of the pulse is $f_0 = 9$ GHz and the Full Width at Half Maximum (FWHM) is $FWHM = 470$ MHz. The total duration of the excitation signal is 30 ns. A field monitor (where temporal field values are recorded) is placed at $(\varrho, \varphi, z) = (0 \text{ mm}, 0, 20 \text{ mm})$ in order to be far enough from the current source and the field values to be maximum in the radial direction.

Table 1: Geometrical characteristics of the simulated waveguide.

Length L (mm)	Radius α (mm)	Current wire length L_{curr} (mm)	PML thickness (cells)
400	14	2	10

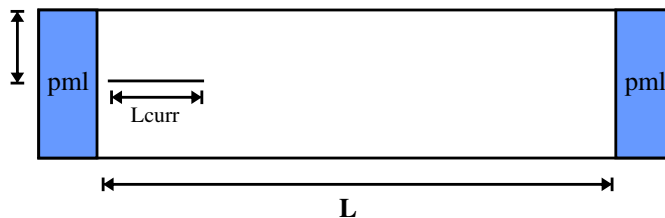


Figure 2: Axial cross section of the simulated waveguide (not in scale).

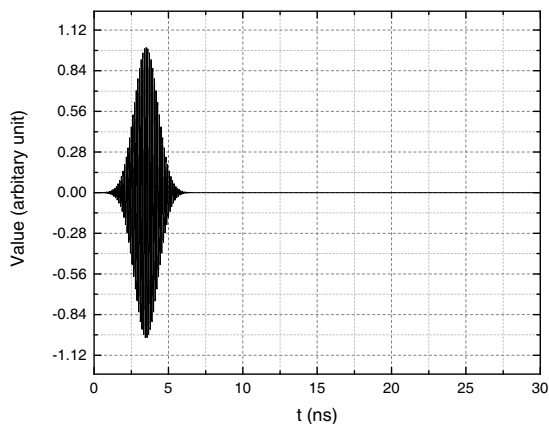


Figure 3: Excitation signal.

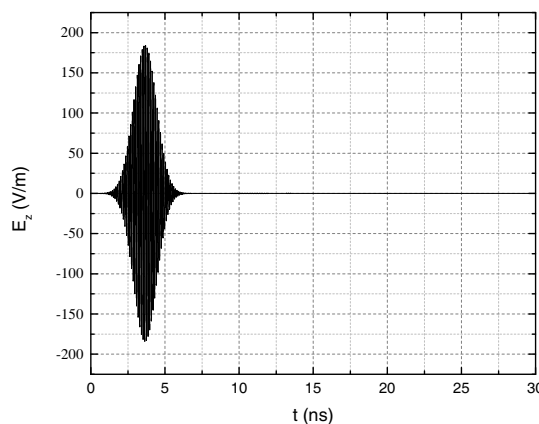


Figure 4: E_z component at $(\rho, \varphi, z) = (0, \frac{\pi}{2}, 20)$.

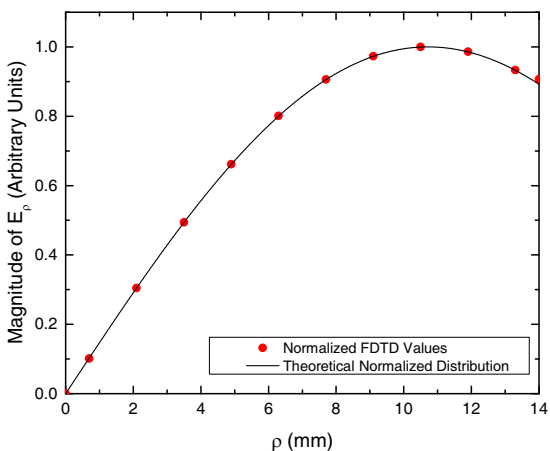


Figure 5: Radial distribution of normalized E_ρ component for $t = 3.5$ ns.

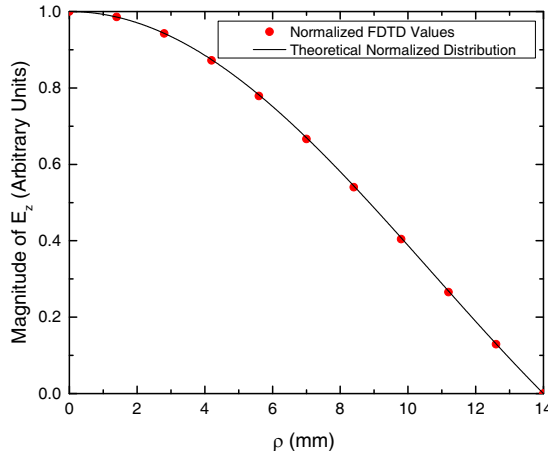


Figure 6: Radial distribution of normalized E_z component for $t = 3.5$ ns.

The time driving function is shown in Fig. 3, while the signal output of E_z , at $(\rho, \varphi, z) = (0, \frac{\pi}{2}, 20)$ is shown in Fig. 4¹. From this figure only the travelling pulse appears and therefore there is no reflection from the CFS-PML regions, leading to a macroscopical behaviour of an infinite waveguide.

The normalized radial distributions of E_ρ and E_z at $(\varphi, z) = (\frac{\pi}{2}, 20)$ are given in Fig. 5 and Fig. 6, respectively. In the same figures the values of normalized field components obtained by the theoretical analytical expressions $E_\rho \propto J'_m(k_c \rho)$ and $E_z \propto J_m(k_c \rho)$ are also plotted, where k_c is the cutoff wavenumber for the mode TM_{mn} . The values at positions where no grid points are defined, were calculated using the Richardson extrapolation method [10]. The 2D distributions for the same components are given in Fig. 7 for E_ρ and in Fig. 8 for E_z . Both radial distributions and two dimensional distributions on the $\rho - \varphi$ plane follow the theoretically expected ones of the TM_{01} mode, therefore it is evident that only this mode is excited and propagates in the waveguide.

The effect of the absence of the CFS-PML is shown in Fig. 9. The signal at the position

¹Note that the thickness of the line and the high frequency leads to a dense plot and does not allow the signals to be clearly plotted properly and thus they appear as black regions with a specific envelope function, representing the pulse function.

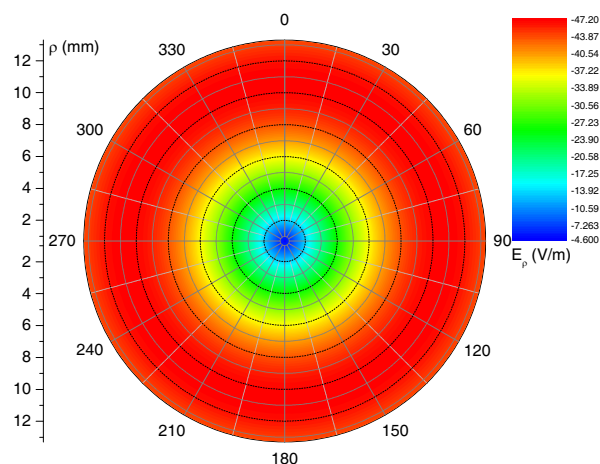


Figure 7: E_ρ distribution on $\rho - \varphi$ plane for $t = 3.5$ ns.

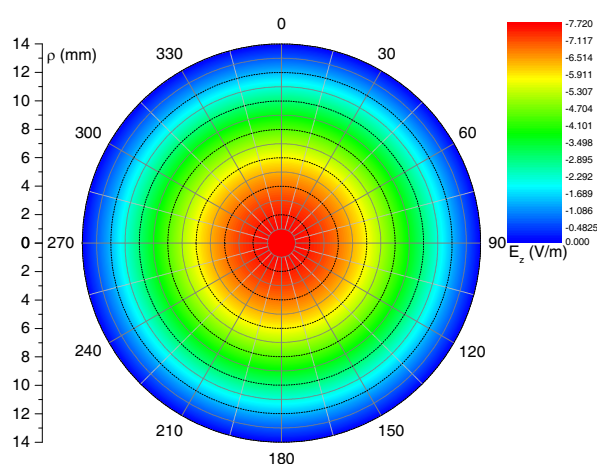


Figure 8: E_z distribution on $\rho - \varphi$ plane for $t = 3.5$ ns.

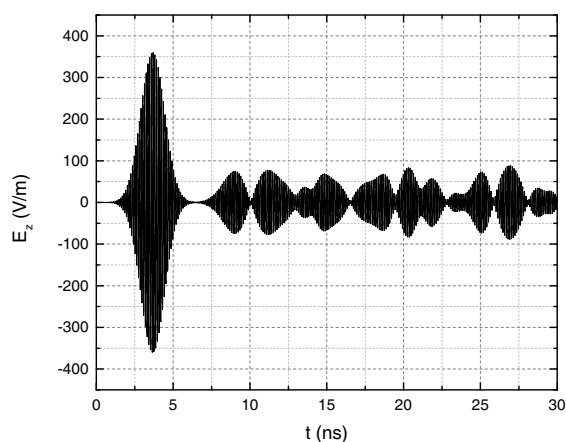


Figure 9: E_z at $(\rho, \varphi, z) = (0, \frac{\pi}{2}, 20)$ in a short-circuit ended waveguide.

$z = 20$ mm is a combination of the incident and the reflected waves originated from the two waveguide ends which are now short-circuited (PEC boundary condition). This means that the waveguide behaves now like a cylindrical cavity. Comparing the result in Fig. 9 with the one of Fig. 4 it is clear that the use of a precisely tuned CFS-PML layer in a FDTD simulation of a waveguide results in the total absorption of the incident waves at the ends.

4. CONCLUSIONS

A smooth hollow cylindrical waveguide was studied using using a numerical code developed in C and based on the FDTD method in cylindrical coordinate system with an infinitely thin wire with a constant current density as an excitation scheme. The advantage of this method is the inherit conformity to cylindrical structures. The introduction of current terms in the discretized expressions gives the flexibility to model virtually any current distribution, whose the spatial, spectral and time characteristics are defined explicitly by the user. Possible application of the presented numerical code is the simulation of a complex cylindrical structure excited by an electron beam in the small signal regime, like the gyrotron beam tunnel, cavity etc. Finally, the precise tuning of the CFS-PML layer characteristics can lead to a full absorption resulting to a more accurate simulation of the behaviour of a perfectly matched waveguide.

ACKNOWLEDGMENT

This work has been carried out within the framework of the EUROfusion Consortium and has received funding from the Euratom research and training programme 2014-2018 under grant agreement No 633053 (WPEDU). The views and opinions expressed herein do not necessarily reflect those of the European Commission.

REFERENCES

1. Harms, P. H., J.-F. Lee, and R. Mittra, "A study of the nonorthogonal FDTD method versus the conventional fdtd technique for computing resonant frequencies of cylindrical cavities," *IEEE Transactions on Microwave Theory and Techniques*, Vol. 40, No. 4, 741–746, 1992.
2. Chi, J., F. Liu, L. Xia, T. Shao, and S. Crozier, "An improved cylindrical FDTD algorithm and its application to field-tissue interaction study in MRI," *IEEE Transactions on Magnetics*, Vol. 47, No. 2, 466–470, 2011.
3. Liu, F. and S. Crozier, "An FDTD model for calculation of gradient-induced eddy currents in MRI system," *IEEE Transactions on Applied Superconductivity*, Vol. 14, No. 3, 1983–1989, 2004.
4. Trakic, A., H. Wang, F. Liu, H. Sanchez Lopez, and S. Crozier, "Cylindrical 3D FDTD algorithm for the computation of low frequency transient eddy currents in MRI," *ISMRM 14th Scientific Meeting & Exhibition*, Vol. 1, No. 1, 1373–1373, International Society for Magnetic Resonance in Medicine (ISMRM), 2006.
5. Yee, K. S., et al., "Numerical solution of initial boundary value problems involving Maxwell's equations in isotropic media," *IEEE Transactions on Antennas and Propagation*, Vol. 14, No. 3, 302–307, 1966.
6. Taflov, A. and S. C. Hagness, *Computational Electrodynamics*, Artech House, 2005.
7. Roden, J. A. and S. D. Gedney, "Convolutional PML (CPML): An efficient FDTD implementation of the CFS-PML for arbitrary media," *Microwave and Optical Technology Letters*, Vol. 27, No. 5, 334–338, 2000.
8. Berenger, J.-P., "Perfectly Matched Layer (PML) for computational electromagnetics," *Synthesis Lectures on Computational Electromagnetics*, Vol. 2, No. 1, 1–117, 2007.
9. Inan, U. S. and R. A. Marshall, *Numerical Electromagnetics: The FDTD Method*, Cambridge University Press, 2011.
10. Cheney, E. and D. Kincaid, *Numerical Mathematics and Computing*, Cengage Learning, 2012.

High Precision Range Measurement Processor Design with Low Complexity for FMCW Radar Systems

E. Hyun² and J. H. Lee

ART (Advanced Radar Technology) Lab
DGIST (Daegu Gyeongbuk Institute of Science & Technology), Korea

Abstract— The paper presents a signal processing hardware architecture with low complexity for high precision range measurement using FMCW (Frequency Modulated Continuous Wave) radar. The proposed architecture is designed based on coarse FFT processing with reduced point and a fine spectrum estimator for the specific frequency of interest. The implementation results on FPGA show that the proposed method leads to lower latency and requires fewer hardware resources than full-point FFT processing.

1. INTRODUCTION

FMCW (Frequency Modulation Continuous Wave) radar systems have been widely used for the measurement of range in a variety of industrial applications: automotive safety, traffic monitors, level gauges, security, defense seekers. Especially, level measurement is popular in almost every modern industrial plant for the measurement of bulk materials [1]. That is, digital level measurement based on FMCW radar is a trend because the digital approach is more flexible and program updates are very easy [2, 3].

In FMCW radar, when a continuous frequency modulated microwave signal is transmitted, the receive echo signal is down-converted into the baseband by the transmit frequency [4, 5]. The difference in frequency between the transmit and the receive signals is called the beat-frequency. The beat-frequency is typically obtained using FFT (Fast Fourier Transform) processing; range measurement is calculated using the detected beat-frequency. Thus, for exact level measurement in FMCW radar, it is very important to obtain a high precision beat-frequency. That can be realized using enough sample data and many FFT points. However, in a high precision FFT processor, many hardware resources and long processing time are required due to the increased computational complexity.

In this paper, we propose a low complexity frequency measurement processor. First, using the low precision FFT processor, the coarse ROI (Range Of Interest) is detected. Then, in the ROI, the fine frequency spectrum is analyzed using a frequency spectrum estimator consisting of a complex multiplier-accumulator. Compared with traditional FFT processors, even though the performance of the proposed processor is the same, the utilized hardware resources and the processing time can be decreased.

2. PROPOSED ARCHITECTURE

The structure of the proposed processor is shown in Fig. 1. Here, $a(n)$ is the digitalized sample of the received beat-signal and n ($= 0 \sim N - 1$) is the sample index of the discrete time, where N is the number of the sample.

If $a(n)$ is fully transformed by N -point FFT processing, the corresponding frequency spectrum is calculated as in Eq. (1), where d ($= 0 \sim N - 1$) is the beat-frequency index and $\Delta\omega_N$ is the radian frequency step size. Thus, the detected beat-frequency is expressed as $\Delta\omega_N \cdot n_r$, where n_r is the detected frequency index. In traditional FFT processing, the time complexity is expressed as $N \cdot \log N$.

$$X(d) = \sum_{n=0}^{N-1} \left[a(n) \cdot e^{-j(\Delta\omega_N \cdot d) \cdot n} \right] = \sum_{n=0}^{N-1} \left[a(n) \cdot e^{-j \frac{2\pi \cdot d}{N} \cdot n} \right] \quad (1)$$

On the other hand, the proposed processing is divided into two steps: the coarse frequency detection part using the reduced-point FFT and the fine frequency detection part based on the FSE (Frequency Spectrum Estimation).

In the first step, the low precision FFT processing is carried out and the result $Y(m)$ is expressed as in Eq. (2). Here, m ($= 0 \sim M - 1$) is the beat-frequency index, $\Delta\omega_M$ is the radian frequency step

²Corresponding author: E. Hyun (braham@dgist.ac.kr).

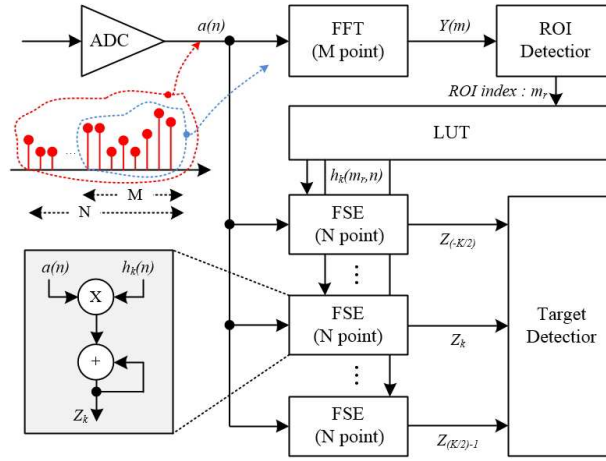


Figure 1: Structure of the proposed processor.

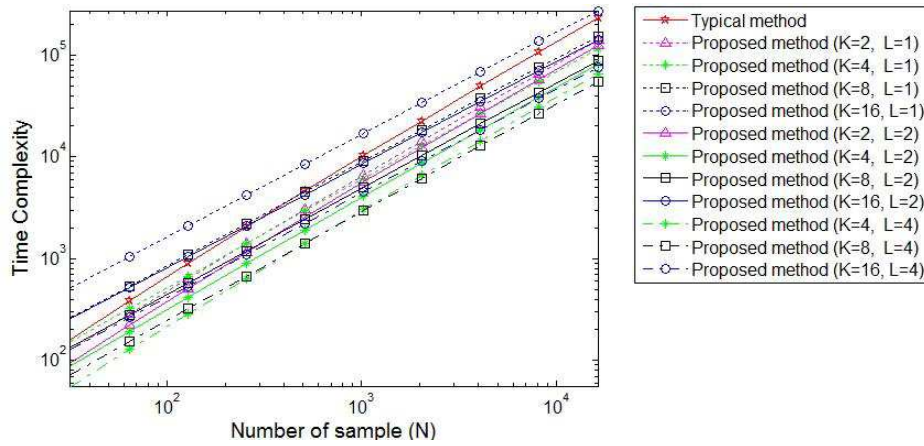


Figure 2: Time complexity comparison.

size, and M is the reduced FFT point. In this case, we define integer $K (= N/M)$, which is called ‘Reduced ratio of FFT point’.

$$Y(m) = \sum_{n=0}^{M-1} [a(n) \cdot e^{-j(\Delta\omega_M \cdot m) \cdot n}] = \sum_{n=0}^{M-1} [a(n) \cdot e^{-j\frac{2\pi \cdot m}{M} \cdot n}] \quad (2)$$

In the ROI Detector, the frequency index of interest m_r is selected. That is, the estimated coarse beat-frequency is determined according to $\Delta\omega_M \cdot m_r$. In this case, since the round-off error of the M -point FFT is K times greater than the N -point FFT, the radian frequencies between $\Delta\omega_N \cdot (m_r - K/2)$ and $\Delta\omega_N \cdot (m_r + (K/2) - 1)$ are mapped to the $\Delta\omega_M \cdot m_r$. Therefore, if the spectrum of $a(n)$ can be re-analyzed within the bound of these frequencies, we can obtain the frequency precision with the same value determined from N -point FFT.

Thus, in the paper, in order to estimate the high precision frequency from the coarse ROI frequency $\Delta\omega_M \cdot m_r$ we employ a frequency spectrum estimator consisting of a complex multiplier-accumulator. In the estimator, the fine frequency spectrum of $a(n)$ can be extracted by multiplying and summarizing the received signal $a(n)$ and $h_k \cdot (m_r, n)$ as shown in Eq. (3). The radian frequency of the complex sinusoid reference $h_k \cdot (m_r, n)$ is expressed as $\Delta\omega_N (K \cdot m_r - k)$ and k is the frequency index bounded by the coarse ROI, where $k = -K/2 \sim (K/2) - 1$.

$$\begin{aligned} Z_k &= \sum_{n=0}^{N-1} [a(n) \cdot h_k(m_r, n)] = \sum_{n=0}^{N-1} [a(n) \cdot e^{-j(\Delta\omega_M \cdot m_r - \Delta\omega_N \cdot k) \cdot n}] \\ &= \sum_{n=0}^{N-1} [a(n) \cdot e^{-j(\Delta\omega_N \cdot (K \cdot m_r - k)) \cdot n}] \end{aligned} \quad (3)$$

Since the proposed FSE consists of an N -point multiplier, its time complexity is expressed as N . If

K time processing is carried out using a single frequency spectrum estimator, the total complexity is defined as $N \cdot K$. However, if several FSEs are employed for parallel processing, the time complexity can decrease as in $N \cdot K/L$, where L is the number of FSE processors implemented for parallel processing. Therefore, the whole time complexity of the proposed hardware architecture consisting of the N -point FFT engine and the N -point FSE processor can be expressed as $M \cdot \log M + (N \cdot K)/L$.

Figure 2 provides a time complexity comparison of the traditional full-point FFT and the proposed architecture, based on the number of samples (N). Both axes are plotted in log scale. In the case in which $K = 16$ and $L = 1$, the typical full-point FFT processing has rather lower computational complexity. In these two scenarios, with $K = 16$ and $L = 2$, and $K = 8$ and $L = 1$, the more processing time of the proposed architecture is consumed in cases with a smaller sample. However, in other cases, the time complexity of the proposed method is always lower than that of the full-point FFT processor.

3. IMPLEMENTATION

In this paper, a typical architecture using an N -point FFT processor and the proposed architecture consisting of the M -point FFT processor are implemented based on the Xilinx FPGA Spartan-6 with ISE 12.1. We implement the FFT processor based on the *Xilinx LogicCORETM IP Fast Fourier Transform 7.1* [6]. Moreover, the proposed frequency spectrum estimation processor is implemented using the *LogicCORETM IP Complex Multiplier 3.1* [7].

In order to analyze used hardware resource and required processing time, we design and implement two architectures. That is, in order to support a resource optimized approach, an FFT processor with a *Radix-2 Lite Burst IO* architecture and a single FSE processor are used. On the other hand, for the processing time enhanced architecture, a *Pipelined Streaming IO* FFT structure and a parallel FSE processing are employed.

In the two implementations, the total data number N is 4096 and the reduced FFT point M for the proposed architecture is selected to be 512. Therefore, the reduced ratio of FFT point K is 8. We also determined one FSE processor ($L = 1$) for the hardware resource minimized design and eight frequency spectrum estimators ($L = 8$) for the high speed parallel processing. Moreover, we assumed that all input and output data were aligned in terms of size at 16 bit.

Table 1: Hardware cost and latency of the typical and the proposed architecture.

Design mode	Processing architecture	Used hardware resources		Latency (clocks)
		Flipflops	Slices	
Resources optimized design	Typical method	1,711	964	57,377
	Proposed method (L=1)	1,538	704	38,433
Speed enhanced design	Typical method	11,032	3,404	8,326
	Proposed method (L=8)	8,538	3,208	5,230

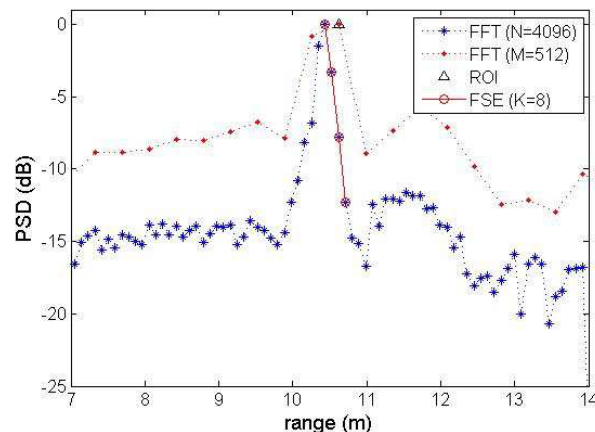


Figure 3: Range profile for target at about 11 m range.

As for implementation results from the synthesis tools with the default setting, the utilized hardware resources and the latency of the processing time are listed in Table 1. The table shows that the usages of Flipflops and Slices decreased in the proposed architecture. In particular, the processing clock is reduced by 33% and 37% in these two design modes, respectively.

Finally, the performance of the proposed architecture is estimated using a real 24 GHz FMCW radar module, developed by DGIST, as shown in Fig. 3. The x -axis is the range and the y -axis is the normalized PSD (Power Spectrum Density) with dB scale. The parameters for measurement are the same as those shown in the results in Table 1. These results show that the 4096-point FFT results and the results for the proposed architecture have an equal range profile around the ROI.

4. CONCLUSION

In this paper, we propose a high precision range measurement processor architecture for FMCW radar systems. The proposed architecture consists of an FFT processor with a reduced point and a frequency spectrum estimation processor based on a complex multiplier-accumulator. In the implemented results, the proposed architecture can reduce the utilized hardware resources by an average of 15% and the processing time by up to 30% compared with those values for the traditional method. Moreover, according to the experiment results, the range precision of the proposed architecture is the same as that of the typical method based on full-point FFT processing. Therefore, the proposed range measurement radar can be expected to be useful for level gauging systems with competitive prices.

ACKNOWLEDGMENT

This work was supported by the DGIST R&D Program of the Ministry of Science, ICT and Technology of Korea (15-RS-01).

REFERENCES

1. Kim, J.-M., Z.-S. Lim, J.-C. Chun, and T.-S. Kim, "Correlation algorithm for high-precision measurement in FM-CW radar level meters," *IEICE Trans. Commu.*, Vol. E84-B, No. 8, 2326–2329, Aug. 2001.
2. Chen, H., Y. Li, and X.-M. Wang, "Digital signal processing for a level measurement system based on FMCW radar," *IEEE International Conference on Control and Automation*, 2843–2847, May 2007.
3. Armbercht, G. and E. Denicke, "Antenna impact on the gauging accuracy of industrial radar level measurements," *IEEE Trans. Microwave Theory and Tech.*, Vol. 59, No. 10, 2554–2562, Oct. 2011.
4. Stove, A. G., "Linear FMCW radar techniques," *IEE Proceedings F (Radar and Signal Processing)*, Vol. 139, No. 5, Oct. 1992.
5. Mahafza, B. R., *Radar Systems Analysis and Design Using MATLAB*, Chapman & Hall/CRC, 2005
6. Xilinx DS260, "LogiCORE IP fast fourier transform v7.1," Mar. 2011.
7. Xilinx DS291, "LogiCORE IP complex multiplier v3.1," Mar. 2011.

Dynamic Speckle Laser Technique for the Characterization of Electrotechnical-porcelain

F. J. Salguero¹, G. Bertolini², C. I. Cabello^{2,3},
E. Grumel^{3,4}, M. Trivi^{3,4}, and G. Barbera⁵

¹Facultad de Ingeniería, UNLP

²CINDECA, (CCT CONICET La Plata-UNLP), Facultad de Ingeniería, UNLP
Calle 47 No. 257, La Plata 1900, Argentina

³CIC PBA, Argentina

⁴Centro de Investigaciones Ópticas (CCT CONICET La Plata CIC) and UID Optimo
Facultad de Ingeniería, UNLP, Casilla de Correo 3, Gonnet, La Plata 1897, Argentina

⁵IITREE, (Instituto de Investigaciones Tecnológicas para Redes y Equipos Eléctricos)
Facultad de Ingeniería, UNLP, Calle 48 No. 116 (B1900AMF), La Plata, Argentina

Abstract— This work analyzes the quality of two types of commercial electro-technical-porcelain using textural and physical-chemical methods: BET surface area and pore size by gas adsorption, X-ray powder diffraction; Electronic Microscopy and Energy dispersive X-ray analysis, Infrared Spectroscopy and their water adsorption capacity by the Dynamic Speckle Laser technique.

Experimental results showed the evolution of the speckle patterns during hydro-adsorption process, permitting to discriminate different behavior for each material. It was determined that it is possible to correlate changes in the speckle patterns with the porosity and chemical composition of materials.

1. INTRODUCTION

Dynamic speckle is a random scattering phenomenon occurring when coherent laser light illuminates an active surface [1]. The coherent electromagnetic waves beat on the detector producing light intensity variations. As a result, the surface of the samples appears to be covered by random tiny, bright and dark dots that fluctuate in time.

The study of the temporary evolution of the speckle patterns may provide an interesting tool to characterize the parameters involved in the sample dynamic processes. It has been used for several applications in biology, medicine and industry [2].

In this paper, we use this technique to analyze the hygroscopic properties of different types of porcelain for electro-technical purposes.

The typical porcelain consists of a mixture of three aluminum-silicates in a ratio: 50% kaolin, 25% quartz and 25% feldspar. This porcelain has basic electrical, mechanical, thermal and porosity properties, which naturally vary according to the composition of the mixture.

These materials are commonly used due to their insulating quality (e.g., insulation resistance) which basically depends on its porosity and hygroscopicity.

This work characterizes two types of commercial electrotechnical-porcelain using their water adsorption capacity by the Dynamic Speckle Laser technique (DLS), based on the textural, chemical composition, structural and spectroscopic characteristics.

2. EXPERIMENTAL

2.1. Materials and Methods

Dynamic speckle patterns were obtained by illuminating the samples with a 10 mW He-Ne laser and the images were recording with a CCD camera connected to a PC with an image digitizer. See Figure 1. To show the temporal evolution of speckle was used the Oulamara et al. method [3]. For each state of the adsorption process, 320 successive images of dynamic speckle are recorded, capturing 25 frames per second and select a column of them. These columns are building a pseudo-image of 320×240 so-called Temporary History Speckle Patterns (THSP). The activity of the sample changes of intensity (gray levels) in the horizontal direction. So, when a phenomenon shows low activity, time variations of the speckle pattern are slow and the THSP shows elongated shape. When the phenomenon is very active, the THSP resembles an ordinary speckle pattern. See Figure 2.

In our case, speckle high activity corresponds to the initial hydro-adsorption process. When this process is complete, the speckle activity is minimal. To establish a quantitative estimate of THSP, we use the moment of inertia of the co-occurrence matrix method [4].

Two different samples (P1 and P2) of commercial porcelains were selected.

Characterization of original porcelains was performed by Electronic microscopy using a Philips SEM 505 combined with semiquantitative analysis by EDS (Energy dispersive X-ray analysis), with an analyzer EDAX 9100.

Diagrams of X-ray diffraction powders were obtained by a Philips PW 1714 with a $\text{CuK}\alpha$ radiation and Ni filter from $2\theta = 5^\circ$ to 60° .

Infrared FTIR Spectra were performed by a Bruker IFSS 66 FT-IR equipment, from 4000 to 400 cm^{-1} wave-numbers.

Surface areas and porosity of porcelains were determined by physical N_2 adsorption at 77 K (BET method) using a Micromeritics apparatus ASAP 2010.

For DLS technique, 30 mg of each sample were wet with $10\ \mu\text{l}$ distilled water. The experiment was monitored every two minutes from the beginning of the process and then every five minutes at the end of the process. The evolution was followed for one hour. Experimental environment parameters were: Temperature: 19°C , Humidity: 60%.

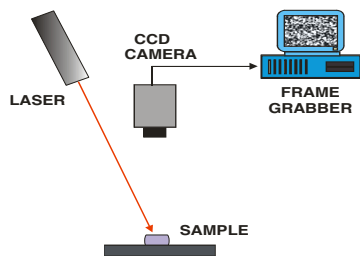


Figure 1: Dynamic speckle experimental set up.

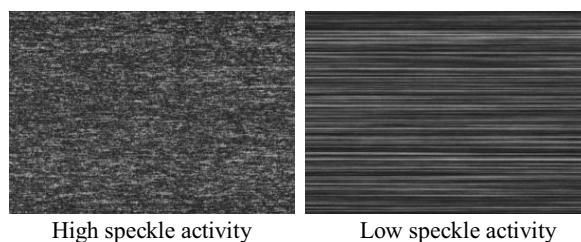


Figure 2: Temporal history of Speckle Pattern (THSP).

3. RESULTS AND DISCUSSION

3.1. Physical-chemical Analysis of Porcelain

Porcelain is the most important ceramic materials with multiple uses in electrical engineering. Typical composition comprises three aluminosilicate mixture in a ratio of 50% kaolin, 25% quartz and 25% feldspar. Its basic electrical, mechanical and thermal properties are according to the composition of the mixture. One of the characteristics that determine the quality of these materials is impermeability to water and gases depending on its porosity, as well as its Si/Al ratio. It has been considered that a high Si/Al surface is associated with increased Brønsted acidity, resulting in higher hygroscopicity.

Table 1 shows the textural characteristics by the BET method to P1 and P2. Specific surface area and pore size were slightly but P1 showed the less porosity level.

Table 1: Textural properties by the BET Method for P1 and P2.

Sample	S_{BET} (m^2/g)	Pore volume (cm^3/g)	Pore size (\AA)
P1	0.5664	0.001314	92.78
P2	0.6594	0.001775	107.65

Table 2 shows EDS chemical data (% element is the relative weight percent of the elements, Na, Mg, K, Al, Si, Ti and Fe), and Si/Al ratio for porcelain samples.

The EDS analysis revealed different composition and Si/Al ratio while SEM Micrographs (Figures 3 and 4) allowed observing the presence of porous in the porcelain surfaces.

Figure 5 shows comparative XRD patterns for P1 and P2. It is possible to observe that the main component is quartz (SiO_2) in both samples, according to the main peaks located at $2\theta = 20.5^\circ$ and 26.3° and Alumina ($\alpha\text{-Al}_2\text{O}_3$) at $2\theta = 25.5^\circ$ and 35.1° . In XRD diagram of P2 is possible to identify an additional peak of feldspar located at $2\theta = 22^\circ$.

Table 2: SEM-EDS chemical data for P1 and P2 porcelain samples.

Element Wt%	P1	P2
Na	0.81	0.80
Mg	0.41	-
Al	23.40	17.35
Si	63.26	75.41
K	5.87	4.78
Ti	1.97	-
Fe	4.28	1.66
Si/Al	2.70	4.34

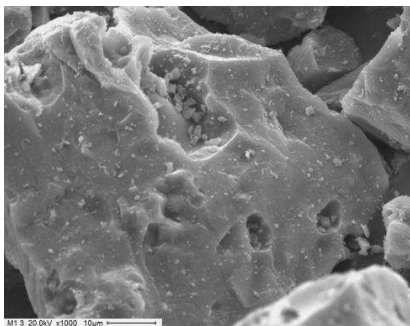
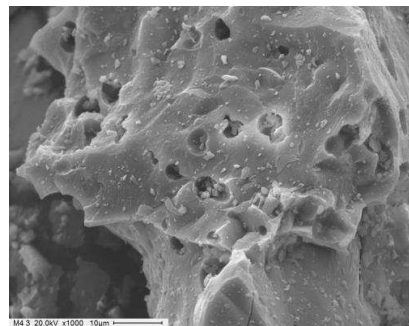
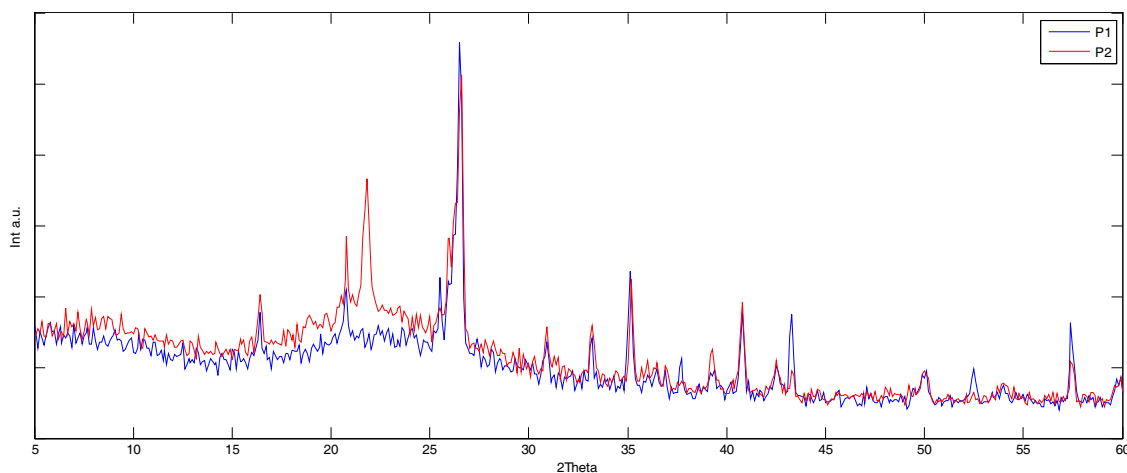
Figure 3: SEM Micrograph of P1 Magnification $\times 1000$, scale bar $10\ \mu\text{m}$.Figure 4: Micrograph of P2 Magnification $\times 1000$, scale bar $10\ \mu\text{m}$.Figure 5: XRD diagrams for P1 and P2 samples (range $2\theta = 5^\circ$ to 60°).

Figure 6 shows comparative FTIR spectra for porcelains P1 and P2. Using this technique is very difficult to differentiate between the two samples studied. Since the vibrational spectroscopy allows analyze functional groups or molecular units, which in this study are similar as Si-O-/AL-O- or Si/Al-OH, -OH etc. In these spectra are observed no bands corresponding to OH stretching, in the high frequency range. In the next range around $1000\ \text{cm}^{-1}$ intense antisymmetric stretching bands of the tetrahedral groups TO_4 ($T = \text{Si}$ or Al) appears.

3.2. DLS Technique: Hydro-adsorption Analysis of Porcelain

Analyzes were performed by Dynamic Speckle Laser during adsorption of water from both samples. DLS curves provided a quantitative measurement of this process using the Inertia Moment (IM) method.

Figure 7 shows the DLS hygroscopic behavior of porcelain. After initial fall of speckle activity, stabilization of it was reached. It can be observed that the porcelain P2 (sample b) showed the

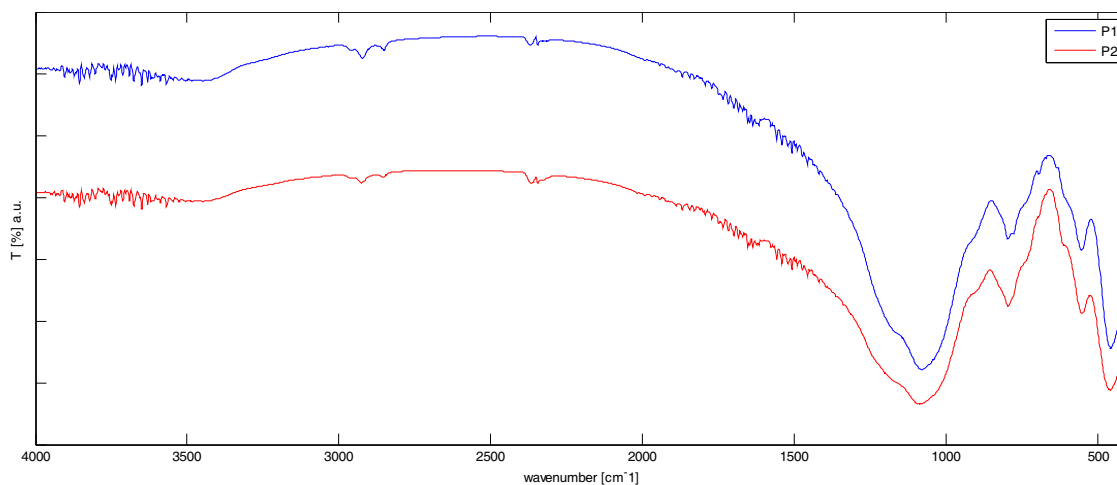


Figure 6: FTIR spectra for P1 and P2 samples (range 4000–400 cm^{-1}).

shortest stabilization time (about 200 sec), indicating a rapid hydro-adsorption process, P1 (sample a) presented the highest IM and stabilized time after 600 sec. Compared with Tables (1 and 2) it is possible to observe that the lower Si/Al, and porosity corresponds a greater IM in the H_2O adsorption process.

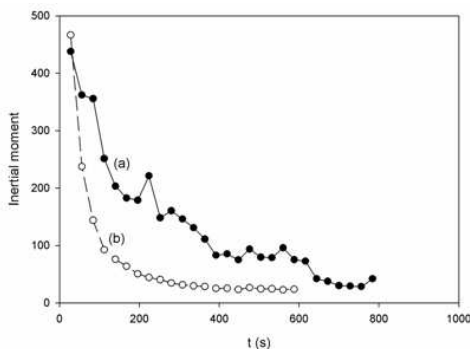


Figure 7: Dynamic speckle measurements, (a) P1, (b) P2.

4. CONCLUSIONS

The DSL technology provides a simple, more efficient and nondestructive tool with respect to other physicochemical techniques to compare different quality ceramic materials, which is important to estimate hygroscopicity.

ACKNOWLEDGMENT

This work was supported by CONICET, CIC and University of La Plata (UNLP), Argentina.

REFERENCES

1. Aizu, Y. and T. Asakura, "Biospeckle," *Trends in Optics*, A. Consortini, Ed., Chapter 2, Academic Press, 1996.
2. Rabal, H., R. Braga, Eds., *Dynamic Laser Speckle and Applications*, CRS Press, Taylor and Francis Publisher, Boca Ratón, FL, USA, 2009.
3. Oulamara, A., A. G. Tribillon, and J. Duvernoy, "Biological activity measurements on botanical specimen surfaces using a temporal decorrelation effect of laser speckle," *Journal of Modern Optics*, Vol. 36, 165, 1989.
4. Arizaga, R., M. Trivi, and H. Rabal, "Speckle time evolution characterization by the co-occurrence matrix analysis," *Optics & Laser Technology*, Vol. 31, 163–169, 1999.

Modeling of Electromagnetic Scattering from Simplified Leaf Structures by Using Spherical Wave Expansion

Paul Jason Co and Jun-Ichi Takada

Department of International Development Engineering, Tokyo Institute of Technology, Tokyo, Japan

Abstract— Leaf scatterers are a type of obstacle that is abundant in rural propagation environments. These leaf scatterers interact with propagating radio waves which may affect the performance of wireless systems operating in such environments. In this paper, deciduous leaf scatterers are modelled as thin dielectric disks. The electromagnetic scattering from these disks at 2 GHz are modelled using the generalised Rayleigh-Gans (GRG) approximation as well as using a commercial method of moment (MoM) solver. The difference between the GRG and MoM results for the single scatterer case is evaluated using the spherical wave expansion of the scattered fields from both methods. An approximation of the scattered fields for the multiple scatterer scenario based on the superposition of the GRG scattered fields is presented and is compared to MoM results.

1. INTRODUCTION

Foliage structures are one of the most dominant types of obstacles that are present in rural propagation environments. These foliage obstacles, composed of leaves, branches and trunks act as complex scatterers to propagating radio waves in such environments. This interaction between the propagating radio waves and the foliage obstacles may significantly affect the performance of radio systems operating in such environments. The proper understanding of such interactions is necessary to predict their effects on radio systems. The complex and random nature of these foliage structures provide a significant challenge in predicting their effects on these propagating radio waves.

One element that makes up these foliage obstacle are their leaf structures. These leaf geometries are generally complex, which makes it difficult to find an exact solution to their scattered fields. One approach to approximate the scattered fields from such leaf structures is to represent these leaf structures as thin dielectric disks for deciduous trees, and as thin dielectric cylinders for coniferous trees [1–3]. Approximate analytical solutions may be used to evaluate the scattered fields from these simplified leaf geometries [4]. In this paper, we take a look at the generalised Rayleigh-Gans approximation and make use of the spherical wave expansion to compare the scattering with a method of moment (MoM) solution. The scattering from multiple simplified leaf structures using the superposition of the GRG approximation is also compared to the numerical results.

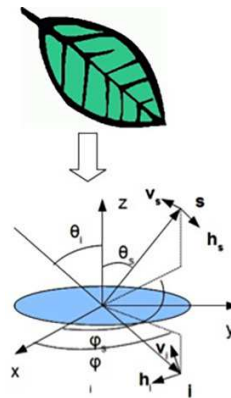


Figure 1: Simplified leaf geometry.

2. SINGLE SCATTERER

The simplified scattering geometry for deciduous leaves is illustrated in Figure 1. The deciduous leaf is modelled as a thin dielectric disk centered at the origin on the x - y plane, with radius R ,

thickness t , and relative permittivity ϵ_r . The disk is illuminated by a uniform plane wave given by Equation (1), where k is the wave number \mathbf{i} is the direction of incidence, \mathbf{r} is the position vector of the point of interest, and $\mathbf{q} = \mathbf{v}_i$ or \mathbf{h}_i are the unit vectors defining the polarization of the incident wave, where \mathbf{h} is perpendicular to the direction of propagation and the z axis, and \mathbf{v} is perpendicular to the direction of propagation and \mathbf{h} as defined in [2].

$$\vec{E}_i = \mathbf{q}E_0e^{-jk\mathbf{i}\cdot\mathbf{r}} \quad (1)$$

$$\mathbf{i} = \sin\theta_i(\mathbf{x}\cos\phi_i + \mathbf{y}\sin\phi_i) - \mathbf{z}\cos\theta_i \quad (2)$$

$$\mathbf{h}_i = \frac{\mathbf{z} \times \mathbf{i}}{|\mathbf{z} \times \mathbf{i}|} \quad (3)$$

$$\mathbf{v}_i = \mathbf{h}_i \times \mathbf{i} \quad (4)$$

The generalised Rayleigh-Gans approximation approximates the scattered fields from small scatterers in which one dimension is much smaller than the other dimensions of the scatterer. The scattered fields are dependent on the geometry of the scatterer as well as its electrical properties. The scattered fields in the direction \mathbf{s} due to an incident plane wave in the direction of \mathbf{i} approximated by the GRG approximation can be expressed as:

$$\vec{E}_S(\mathbf{s}, \mathbf{i}) = \bar{\bar{F}}(\mathbf{s}, \mathbf{i}) \cdot \mathbf{q}E_0 \frac{e^{-jkr}}{r} \quad (5)$$

The scattering amplitude tensor $\bar{\bar{F}}(\mathbf{s}, \mathbf{i})$ is as in [2].

We apply the GRG approximation to the geometry in Figure 1 with thickness of 0.1 mm and radius of 1.5 cm, with incident plane waves with a magnitude of 1, and incident angles of $0 \leq \theta_i \leq 180^\circ$, with polarisations of either $\mathbf{v}_i = 1, \mathbf{h}_i = 0$ or $\mathbf{v}_i = 0, \mathbf{h}_i = 1$. The scattered fields from the same geometries are evaluated numerically using FEKO, a commercial method of moments solver. The scattered fields from the disk for an incident angle of $\theta_i = 45^\circ$ is shown in Figure 2 for both the GRG approximation and the MoM solution. We express the error between the numerical and GRG scattered field magnitudes as:

$$\text{error}\% = \frac{\left| \left| \vec{E}_S^{\text{MoM}}(\mathbf{s}, \mathbf{i}) \right| - \left| \vec{E}_S^{\text{GRG}}(\mathbf{s}, \mathbf{i}) \right| \right|}{\left| \vec{E}_S^{\text{MoM}}(\mathbf{s}, \mathbf{i}) \right|} \times 100\% \quad (6)$$

For the vertically polarised incident wave, the average error over all scattering directions for $0 \leq \theta_i \leq 180^\circ$ was found to be approximately 1.24%. Similarly, for the horizontally polarised incident wave, the average error was found to be approximately 3.28%. Further inspection of the average error for various incidence angles is shown in Figure 3. It can be seen that the error increases as the incidence angle approaches $\theta_i = 90^\circ$ for both polarisation cases, with the h polarized incident wave having a larger error.

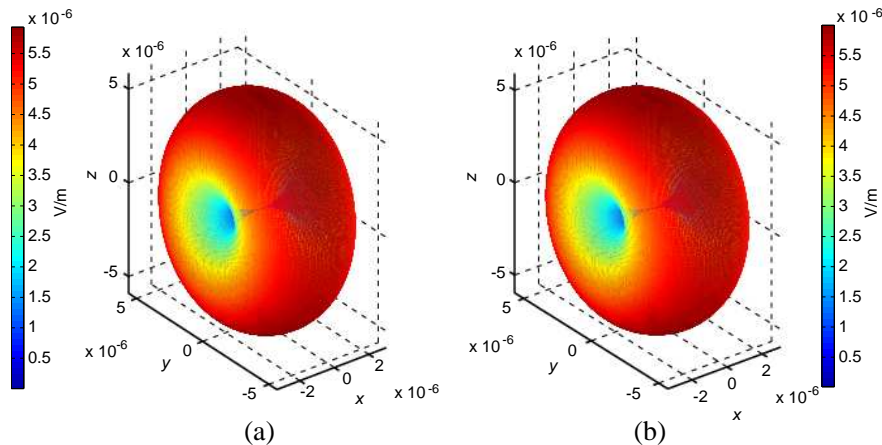


Figure 2: Scattered fields from (a) GRG and (b) MoM with $\theta_i = 45^\circ$.

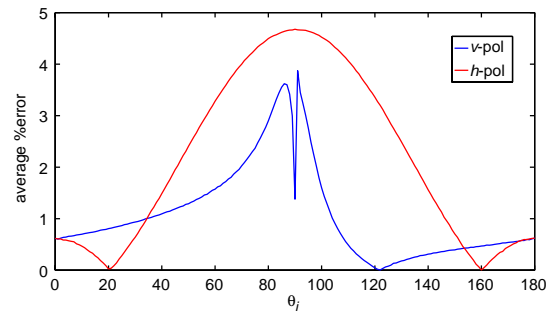


Figure 3: Average percentage error of scattered field magnitudes between MoM and GRG for varying incidence angles.

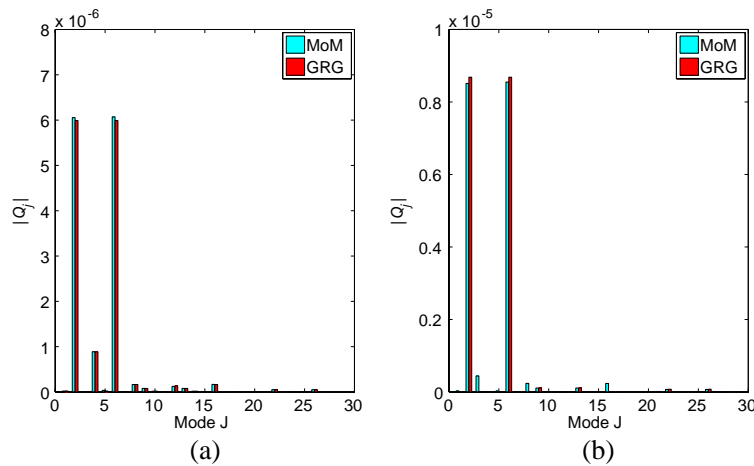


Figure 4: Spherical wave expansion coefficients of scattered fields for $\theta_i = 45^\circ$; (a) v polarized and (b) h polarized.

Spherical wave expansion was used to gain more insight on the difference of the scattered fields evaluated. The spherical wave expansion of outward traveling waves can be expressed as [5].

$$\vec{E}_S(\mathbf{r}) = \frac{k}{\sqrt{\eta}} \sum_{j=1}^J Q_j(\mathbf{i}, \mathbf{q}) \vec{F}_j^{(4)}(\mathbf{r}) \quad (7)$$

$Q_j(\mathbf{i}, \mathbf{q})$ are the spherical wave coefficients and $\vec{F}_j(\mathbf{r})$ are the associated spherical wave functions defined in [5]. The spherical wave coefficients are evaluated via point matching from the evaluated scattered fields from the GRG and MoM solutions. The spherical wave expansions are truncated to $J = 30$ spherical modes as further increasing of the mode expansion does not yield any significant improvement of the expansion. Figure 4 illustrates the spherical wave expansion coefficients for an incident angle of $\theta_i = 45^\circ$ for both v and h polarized incident waves. It can be seen from the figure that both MoM and GRG results have the same dominant modes, with small discrepancies in the magnitudes of these modes. It can also be seen that there is larger discrepancy in the h polarized incident waves. Evaluating the average error between the MoM and GRG coefficients over all incidence angles for each expansion coefficient results in Figure 5. For h polarized incident waves, we find that there is a larger error in the coefficients between the MoM and GRG results, which agrees with the results in the evaluation of the errors in the field scattering amplitudes that there is larger discrepancy in the MoM and GRG solutions for h polarized incident waves. Evaluation of the total scattered power from the spherical wave expansion using (8) [5] yields the average total scattered power tabulated in Table 1. The results show that the GRG and MoM solutions have very good agreement, with the GRG approximation underestimating the scattered fields by a small amount when the incident wave is v polarized, and overestimating the scattered fields when the

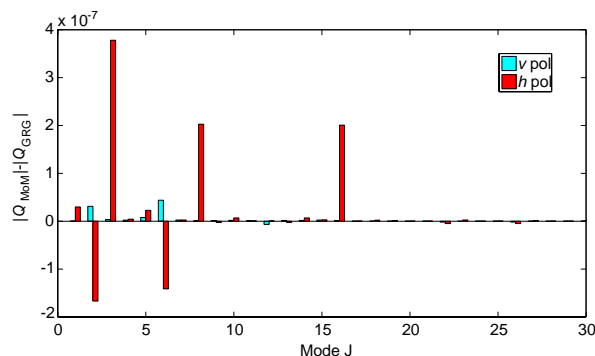


Figure 5: Average error of spherical wave coefficients.

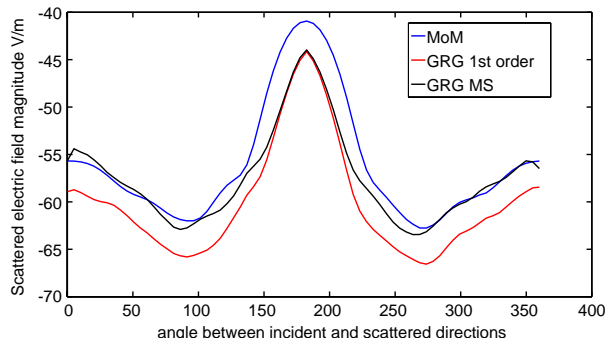


Figure 6: Scattered fields from multiple scatterers.

Table 1: Average total scattered power.

	v polarised incident wave	h polarised incident wave
MoM average total scattered power	-74.21 dBm	-71.37 dBm
GRG average total scattered power	-74.27 dBm	-71.23 dBm

incident wave is h polarised.

$$P_S = \frac{1}{2} \sum_{j=1}^J |Q_j|^2 \quad (8)$$

3. MULTIPLE SCATTERERS

An approximation for multiple scatterers is presented by applying superposition to the GRG approximation. As a first approximation, the scattering from multiple leaf structures can be expressed as a superposition of the direct scattering from each individual scatterer evaluated from the GRG approximation. In terms of the scattered fields of a single scatterer, this total first order scattered fields from multiple scatterers can be expressed as:

$$\vec{E}_S^{(1)} = \sum_{n=1}^N \vec{E}_{S,n} \quad (9)$$

where n is the index of scatterer in the volume of interest, and N is the total number of scatterers. For the second order approximation, we assume that the first order scattered fields from the scatterers in the volume of interest serve as the second order source to each of the other scatterers in the volume. Letting $\vec{E}_{S,m}$ be the second order scattered fields from scatterer m and $\vec{E}_{S,mn}$ be the scattered field from scatterer n incident to scatterer m , the scattered fields in the point of interest \mathbf{s} can be expressed as:

$$\vec{E}_{S,m} = \sum_{n=1, n \neq m}^N \vec{F}_m \vec{E}_{S,mn} \quad (10)$$

$$\vec{E}_{S,\text{Total}} = \vec{E}_S^{(1)} + \sum_{m=1}^N \vec{E}_{S,m} \quad (11)$$

where the first term corresponds to the direct scattered fields, and the second term corresponds to the second order scattering that occurs in the volume. Figure 6 shows the average scattered fields of 30 realisations of 20 randomly positioned and oriented disk scatterers within a $0.5 \text{ m} \times 0.5 \text{ m} \times 0.5 \text{ m}$ volume. The blue line corresponds to the numerical results, the red line corresponds to the first order superposition of the GRG approximation, and the black line corresponds to the second order approximation considering the second order scattering. We find that without multiple scattering, the GRG approximation underestimates the total scattered fields. Including the second order scattering improves the scattering magnitude in the back scattering direction, with minimal effect in the forward scattering direction.

4. CONCLUSION

The generalised Rayleigh-Gans approximation is considered to model the scattering from simplified leaf structures modelled as thin dielectric disks. The spherical wave expansion was used to describe the scattering from the GRG approximation and compare with a numerical method of moments solution. It was found that the GRG approximation has good agreement with the numerical results, with increasing error between the results in the region where θ_i approaches 90° , with a horizontally polarised incident wave having a larger error. The superposition approximation of the scattered fields from multiple scatterers using GRG was shown, with second order scattering considered. The introduction of backscattering shows some improvement of the approximated scattering the the backward direction, with minimal effect in the forward direction. An extension of the single scatterer spherical wave expansion to evaluate the scattering from multiple scatterers will be done in the future.

REFERENCES

1. Schiffer, R. and K. O. Thielheim, "Light scattering by dielectric needles and disks," *Journal of Applied Physics*, Vol. 50, No. 4, 2476–2483, 1979.
2. Karam, M. A., A. K. Fung, and Y. M. M. Antar, "Electromagnetic wave scattering from some vegetation samples," *IEEE Trans. Geosci. Remote Sensing*, Vol. 26, No. 6, 799–808, 1988.
3. Karam, M. A. and A. K. Fung, "Leaf shape effects in electromagnetic scattering from vegetation," *IEEE Trans. Geosci. Remote Sensing*, Vol. 27, No. 6, 687–697, 1988.
4. Oh, Y. and J. Y. Hong, "Re-examination of analytical models for microwave scattering from deciduous leaves," *IET Microw. Antennas Propag.*, Vol. 1, No. 3, 617–623, 2007.
5. Hansen, J. E., *Spherical Near-field Measurements*, IEE Electromagnetic Wave Series 26, London UK, 1988.

Behaviour of Conformal Conical Frequency Selective Surfaces

Giovanni Leone¹, Francesco Mattiello¹, Giuseppe Ruvio^{1,2}, and Rocco Pierri¹

¹Dipartimento di Ingegneria Industriale e dell'Informazione, Seconda Università di Napoli
Via Roma 29, Aversa, CE 81031, Italy

²Antenna & High Frequency Research Centre
Dublin Institute of Technology, Kevin Street, Dublin 8, Ireland

Abstract— Planar Frequency selective surfaces (FSS) have attracted large attention during the last five decades [1] because of their mechanical and electrical flexibility. FSS are spatial filters that are largely employed in applications like hybrid radomes for radars and antennas where high performance is necessary. The FSS have evolved from simple canonical forms to the complex geometries known today. This evolution has been driven primarily by increasingly stringent performance requirements of recent applications. For these structures, we must consider both the effects related to the frequency that those related to the size of the individual elements. While periodicity impacts firstly on the general reflecting properties of the surface, the shape and the size of the individual element affects its detailed both spatial and frequency filtering behaviour. In particular the frequency response is dictated mainly by the scattering of the incident plane wave by the individual element and attains its maximum at resonance conditions. Accordingly, we mean to investigate whether the same occurs also for non planar surfaces and curved elements, and in particular conical surfaces. The analysis is performed in two steps. First the frequency behaviour of input impedance of the single elements embedded within a number of similar ones is numerically computed by a commercial code. Both single, radial and circumferential strips conforming a conical shape are considered and compared with a planar and cylindrical structure. Next the FSS behaviour is fully analysed by a numerical code solving the Electric Field Integral Equation [2] for a FSS of finite size made of thin elements.

1. INTRODUCTION

Frequency selective surfaces (FSS) have been studied for the last five decades and comprehensive books have been also published (Munk, 2000) and (Wu, 1995). FSS have evolved from simple canonical forms to the complex geometries known today. This evolution has been driven primarily by increasingly stringent performance requirements of recent applications and has been made possible by the significant improvements in the methods of analysis, from the computing capacity and on the manufacturing technology. Moreover, being FSS part of the broad family of artificial materials (Ruvio & Leone, 2014), new research efforts have been dedicated to this topic.

The FSS can be fabricated as planar two-dimensional periodic arrays of metallic elements with special geometric shapes, or may be created by periodic openings in a metal screen. The transmission and reflection properties of these surfaces are dependent on the operating frequency and may also depend on the polarization and the incidence angle of the electromagnetic wave impinging the material.

Typical frequency selective behaviour is desired in the design of hybrid radomes shielding antennas from external weather conditions. They can also lower the Radar Cross Section (RCS), outside of the frequencies of interest. If we consider, for example, an antenna mounted on the nose of an airplane, one FSS disposed on the surface of the radome allows to scatter the incident radiation that operates outside the band of interest in the bi-static direction, with the consequent result of a return very low in the direction of backscatter. A similar FSS application is in the design of band-stop filters. An example of this application is related to the realization of a hybrid radome on a shipboard radar antenna.

While the frequency behaviour of the surface is dictated both by the elements spacing and the shape of the basic element, hereafter we are interested to consider the effect of the latter one. In particular, with reference to strip elements conformed on a conical surface, the aim of this work is to examine the scattering from single element of the FSS when it is illuminated by an incident plane wave, in order to show that the frequency selective character is mainly provided by this type of contribution, and that it is not lost if the structure is not planar (at least when its radius of curvature is larger than the wavelength). Finally we show the results obtained by solving the electric field integral equation using the Method of Moments to compute the induced currents on the structure and the corresponding scattered field.

2. FREQUENCY BEHAVIOR OF STRIPS ON A CONFORMAL SURFACES

For a passive FSS the main contribution to frequency selectivity is given by the interaction of the individual element with a plane wave illuminating the structure. In fact, the electromagnetic scattering by a perfectly conducting object of a prefixed shape is dependent on its electrical dimension, and for some particular values of the frequency of the impinging wave, maximum interaction can occur. For strip or filamentary objects under short circuit conditions, the scattered field depends on both the induced current under receiving conditions and on the input impedance under transmitting conditions. In particular, the input impedance of the individual strip (in presence of all the other ones) provides the main contribution to such behavior. For an isolated straight dipole it is well known that mostly the input admittance varies with the frequency and that the modulus of the impedance is minimum at resonance condition, when the length of dipole is about half a wavelength. The same behaviour is observed when the dipole is embedded within planar arrays of similar object except for very close spacing between the elements, say, less than about a quarter of wavelength. Under resonance conditions the backscattered field is also maximum.

Much less is known when the scattering strips are not flat and/or are not arranged under a planar array, as it occurs when the FSS is not a plane. However since the main frequency filtering properties are again dictated by the scattering by the individual element (embedded within an array of equal elements), it is worth to focus on the behaviour of its input impedance when acting as an antenna in the transmission mode.

In order to numerically compute a good approximation, we assume that only a neighbourhood of a single strip can affect its input impedance, so that the problem becomes to evaluate it for a radiating strip-like dipole surrounded by a number of equal ones. Such a number is determined by examining the frequency behaviour of the input impedance with increasing number of surrounding strips and stopping when convergence is achieved.

The goal is accomplished by means of a numerical electromagnetic simulation software, providing the input impedance by varying the frequency of the incident wave on the structure. In the following, for the sake of comparison, we show the input impedance of the strips of the same type and similar configuration but arranged on a plane.

Numerical results show that the general frequency filtering behaviour is not lost for a FSS conforming a conical surface (at least for surfaces with large radius of curvatures with respect to the wavelength), since the frequency selectivity is essentially connected to the interaction of the

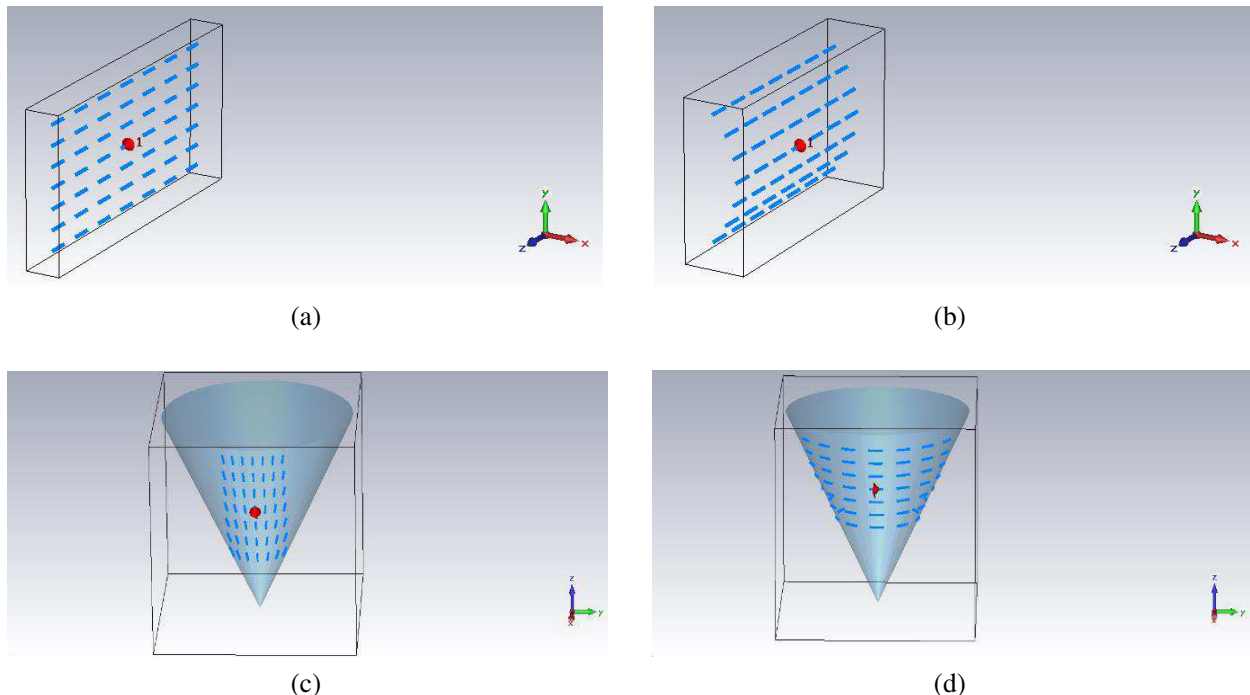


Figure 1: The geometries of the sources: (a) planar array, (b) array conforming a cylindrical surface, (c) and (d) arrays conforming conical surfaces. The feeding points are marked by a red point.

incident wave with the single element of the structure. The only apparent modification arise in the resonance frequency that can be provided by considering a limited part of the whole surface.

In order to confirm the expectations numerical experiments are performed for four finite array of two-dimensional arrays of 7×7 dipole elements, each 1.5 cm long (see Fig. 1). They are, respectively: a planar array (Fig. 1(a)), an array of rectilinear dipoles conforming a cylinder of radius 6 cm (Fig. 1(b)), an array of rectilinear dipoles radially conforming a conical surface (Fig. 1(c)), an array of curved dipoles conforming a conical surface (Fig. 1(d)). The spacing between the centers of the array elements is 3 cm along the wire direction and 1.5 cm along the orthogonal direction in all cases. The central elements are fed and the input impedance (in presence of the other passive strips) are reported in Fig. 2 within the [8–12] GHz band. The magnitude, the real and the imaginary parts of the input impedance are reported in panels (a), (b) and (c) respectively.

First of all, it can be observed that for planar and cylindrical cases the behaviours are very similar as both geometries are very similar. Accordingly the resonance frequency is the same, for

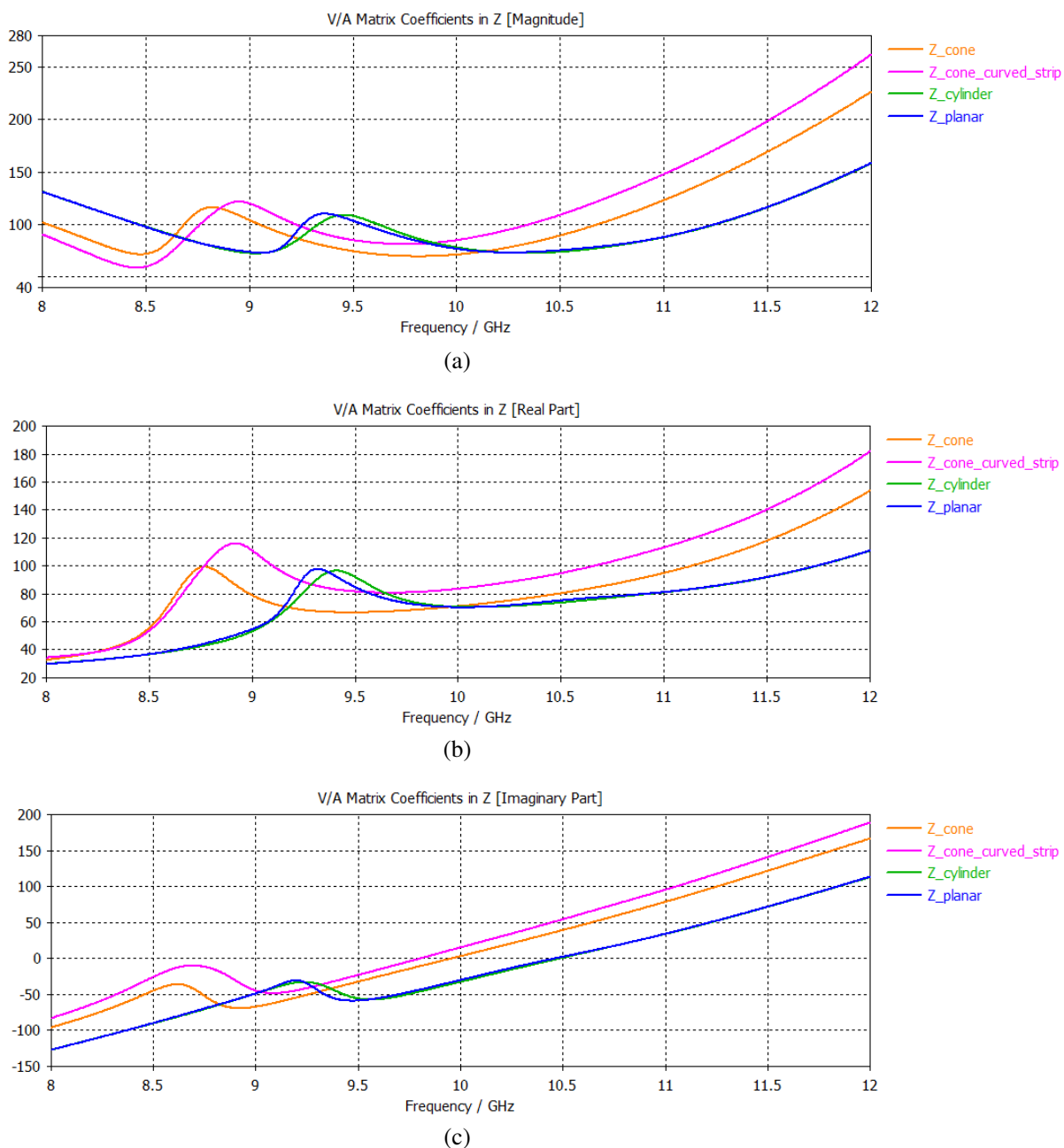


Figure 2: (a) Magnitude of the input impedance. (b) Real part of the input impedance. (c) Imaginary part of the input impedance.

a dipole length slightly more than $\lambda/2$. Moreover the frequency behaviour of both curves is not monotone due to mutual coupling between the dipoles.

The same qualitative frequency behaviour holds also when dipoles are conformed on a conical surface. However the different geometrical configuration makes it possible not only to lower slightly the main resonance point but also to occur a further resonance point at a frequency lower than about 15%. This is especially true for case d) where both the dipole shape and their alignment are markedly non planar nor rectilinear.

3. NUMERICAL SIMULATIONS OF 3D CONFORMAL FSS

In order to verify the above behaviour a code implementing the numerical solution of the Electric Field Integral Equation (EFIE) for strip objects has been developed. Plane wave incidence at different frequencies is considered. Thin, radially directed strips conforming to a conical surface are assumed as scatterers, so that the current induced over them can flow only radially. According to the Galerkin formulation of [2], surface density current is expanded as:

$$\mathbf{J}_s(\mathbf{r}) = \sum_{n=1}^N I_n \frac{f_n(r)}{r^2} \frac{1}{\Delta\varphi} \Pi\left(\frac{\varphi}{\Delta\varphi}\right) \hat{\mathbf{i}}_r$$

where the \mathbf{f}_n are the ‘triangle’ functions as basis function $\mathbf{f}_n(r) = \Lambda(1 - \frac{|r-n\Delta r|}{\Delta r})$ and the same functions are used as test ones. After computing the impedance matrix elements and the right hand side terms, the solution of the resulting linear system allows to obtain the unknown current coefficients. The next step is to calculate the far zone field scattered by the strips, using the appropriate relations [3], and the evaluation of the Radar Cross Section, into the same range [8–12] GHz band as above, and for several incidences angle.

In the first example a finite conical FSS made of rectilinear radially directed dipole strips are considered as in Fig. 3(a), where a front view is displayed. The cone aperture is 30° and five crowns of conformal strips, each 1.5 cm long, are considered. The back scattered field for some incidence angles are reported in Fig. 3(b) within the [8–12] GHz range.

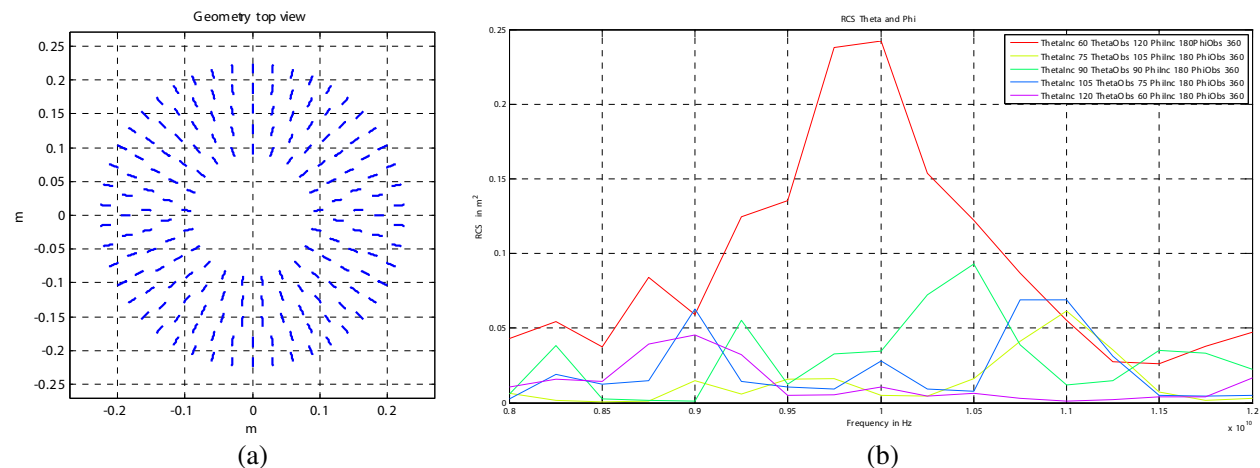


Figure 3: Scattering by a conical FSS: (a) top view of the geometry; (b) magnitude of the backscattered field.

As it can be appreciated in most circumstances the backscattered field is maximum within the same frequency range as the amplitude of input impedance, as discussed in the previous Section, is minimum.

In the second example a finite conical FSS made of curved radially directed dipole strips are considered as in Fig. 4(a), where a front view is displayed. The cone aperture is 30° and five crowns of conformal strips, each 1.5 cm long, are considered. The back scattered field for some incidence angles are reported in Fig. 3(b) within the [8–12] GHz range.

In this instance the numerical solution of the relevant EFIE is performed by expanding the

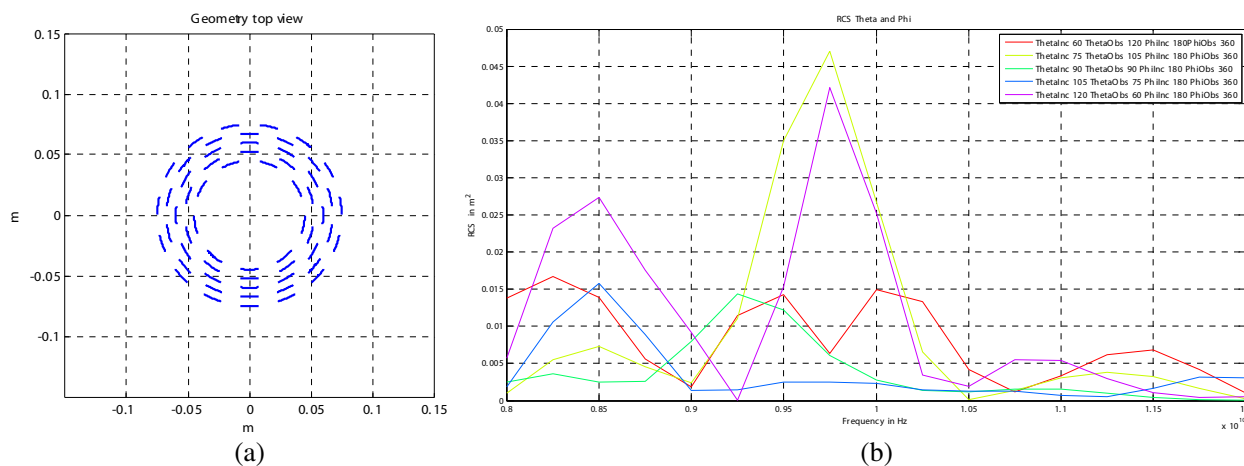


Figure 4: Scattering by a conical FSS made of curved strips: (a) top view of the geometry; (b) magnitude of the backscattered field.

surface current as

$$\mathbf{J}_s(\mathbf{r}) = \sum_{n=1}^N I_n f_n(\varphi) \frac{1}{\Delta r} \Pi\left(\frac{r}{\Delta r}\right) \hat{\mathbf{i}}_\varphi$$

and \mathbf{f}_n are again the ‘triangle’ functions.

Again the backscattered field is maximum within the same frequency range as the amplitude of input impedance, as discussed in the previous Section, is minimum.

4. CONCLUSION

As the frequency behaviour of a FSS is dictated mainly by the resonant interaction with the elementary scattering object, in this paper we have meant to verify whether the same occurs also for non planar surface. In particular, since the frequency behaviour of the electromagnetic scattering from a passive wire is dictated mainly by its (active) input impedance, we have numerically evaluated it for a single object (in presence of the closer ones). The backscattered field has turned to be maximum at the frequencies where the modulus of the input impedance is minimum, not only for planar FSS but also for a conical one.

ACKNOWLEDGMENT

This work was supported by POR Campania FSE 2007–2013 “Materiali e Strutture Intelligenti” MASTRI Excellence Network.

REFERENCES

1. Munk, B. A., *Frequency Selective Surfaces Theory and Design*, John Wiley & Sons, 2000.
2. Gibson, W. C., *The Method of Moments in Electromagnetics*, Chapman & Hall/CRC, 2008.
3. Balanis, C. A., *Advanced Engineering Electromagnetics*, John Wiley & Sons, 1989.

Time Domain Transient Analysis for Ellipsoidal and Hyperbolic Reflector Antennas

Shih-Chung Tuan¹ and Hsi-Tseng Chou²

¹Department of Communication Engineering, Oriental Institute of Technology, Pan-Chiao, Taiwan

²Department of Communication Engineering, Yuan Ze University, Chung-Li, Taiwan

Abstract— A closed-form analytical solution is developed for predicting the early-time transient electromagnetic fields which are generated by a perfectly conducting elliptical reflector antenna when it is illuminated by a transient step spherical wave due to an elemental Huygen's source located at the focus near the surface. Furthermore we discussed a transient analysis of a hyperbolic reflector antenna is performed based on a mathematic continuation of surface curvatures of an ellipsoidal reflector antenna. This work makes the time-domain (TD) analysis useful for the design of reflector antennas since both ellipsoidal and hyperbolic reflectors are widely used as sub-reflectors for dual-reflector antenna system.

1. INTRODUCTION

This work is motivated by the potential applications of elliptical reflectors. In the past, elliptical reflectors had been widely used as a sub-reflector to a parabolic reflector antenna in a Gregorian dual-reflector antenna system. The characteristics of dual-foci on the elliptical surface allow it to be used as a measure to have a longer focal length for the parabolic main reflector while, in the mean time, retaining a compact size for the dual-reflector. Recently it is also found very useful in the design of near-field focused antennas as interested in the RFID and non-contacted microwave inspection system. It is expected that it will attract more attention in the future phase of antenna applications.

The transient solution is developed here by analytically inverting, in closed form, the corresponding frequency-domain solution in terms of a radiation integral that employs an asymptotic high-frequency geometrical optics (GO)-based approximation for the fields in an equal-phase surface aperture which appears to be a sphere centered at the second focus of the ellipse. This equal-phase and spherical aperture surface allows the integration of radiation integral to be significantly simplified, and results a closed-form formulation. And then this paper we will extend the transient analysis of electromagnetic (EM) fields scattering from a perfectly conducting ellipsoidal reflector, and presents the corresponding analysis for the case of a hyperbolic reflector. This work is motivated by the fact that both ellipsoidal and hyperbolic reflectors are widely used as sub-reflectors in the dual-reflector antenna systems [1]. The transient analysis presented in this paper makes the time-domain (TD) analysis of sub-reflector antennas more complete for practical applications. In particular, the analysis is performed based on a mathematic continuation of surface curvatures of an ellipsoidal reflector, and as a result, the analysis of such ellipsoidal reflectors can be applied straightforwardly. Furthermore, the analysis successfully decomposes the scattering fields into components of reflection and edge diffractions, and allows one to interpret the scattering phenomena within the frameworks of geometrical theory of diffraction (GTD) [2, 3] and its wave propagation mechanisms. Examples are presented to demonstrate the wave scattering phenomena.

2. FORMULATION DEVELOPMENT

2.1. Near Field Focused Antenna

In the past, there experienced some applications of NF focused antennas, which were not very popular if a counterpart of far field focused antenna is compared. In the current application, it appears application advantages. Note that a “NF focused antenna” is referred because it is implemented by using an aperture antenna that is sufficiently large to radiate fields focused at a spot in the near field region of the antenna. Thus the focused fields may increase the energy to be received by the tags, and also reduce the interference caused by the scattering from adjacent portals of tags because the tags are usually located at 1–2 m from the reader's antenna aperture. This paper presents a realization of NF focused antenna using a reflector such that the number of circuit elements may be minimized to also minimize the energy loss. Usually only a single element is sufficient to provide a good feed to the reflector. In particular, an elliptic reflector will be realized.

Note that an elliptic reflector has two focal points. The radiation from a feed located at a focus will experience reflections from the reflector surface, and concentrates its energy at another focus which is usually located in the near-zone of the reader antenna. Thus it may be effectively employed to build the NF focused antenna.

2.2. Elliptic Reflector's Characteristics

An elliptic reflector is formed by taking a part of a rotationally symmetric ellipse described by the following equation:

$$\frac{z^2}{a^2} + \frac{x^2 + y^2}{b^2} = 1 \quad (1)$$

where a and b ($a > b$) are the radii of its axes. This ellipse has two foci (referred as F_1 and F_2 , respectively, hereafter) located on z -axis at $z = \pm c$ where $c = \sqrt{a^2 - b^2}$. Note that as $a = b$, $c = 0$, and the ellipse becomes a sphere. The two foci coincide at the center of the sphere. A good characteristic of this ellipse is that any ray launched from a focus (say F_1) will experience a reflection from the ellipse surface and coincide at the other focus (say F_2) as also illustrated in Fig. 1. In particular, given a point, Q , on the ellipse surface, it can be shown that

$$\overline{F_1Q} + \overline{QF_2} = 2a \quad (2)$$

which assures an in-phase superposition at F_2 if a feed's phase center is located at F_1 .

2.3. Formulations

Based on these design criteria, the fields at the NF focused region may be approximately found in the following. Let the radiation, (\vec{E}_a, \vec{H}_a) is Huygen's source, of the feed's antenna represented by

$$\vec{E}_a = V_o \left[\hat{\theta}_1 f_{\theta_f} - \hat{\phi}_1 f_{\phi_f} \right] \frac{1}{r_f} e^{-\frac{s}{v}(2a-r_1)} \quad (3)$$

$$\vec{H}_a = \hat{r}_f \times \frac{\vec{E}_a}{Z_o} \quad (4)$$

where $f_{\theta_f} = \cos \phi_1 (\cos \theta_f)^q$, $f_{\phi_f} = \sin \phi_1 (\cos \theta_f)^q$ represented by E -plane and H -plane pattern respectively where (r_f, θ_f, ϕ_f) is defined in the feed's coordinate system with \hat{z}_f pointing to $\overline{F_1Q}$. Note that $r_f = a + c \cos \theta$ if the feed is located at F_1 . The scattering near fields can be found, via Geometric Optics (GO) approximation, by

$$\vec{E}_r(\vec{r}, s) \cong \frac{Z_o}{4\pi v} \iint_{S_a} \left[\hat{R} \times \hat{R} \times \hat{z}_p \times \vec{H}_a + Y_o \hat{R} \times (\vec{E}_a \times \hat{z}_p) \right] \frac{e^{-\frac{s}{v}R}}{R} ds' \quad (5)$$

The time domain solution can be obtained via an inverse Laplace transform and the characteristic of delta function

$$\delta \left(t - \frac{R + 2a - r_1}{v} \right) = \frac{\delta(\rho - \rho_t)}{\left| \frac{\partial}{\partial \rho} \left(t - \frac{R + 2a - r_1}{v} \right) \right|_{\rho=\rho_t}} \quad (6)$$

which is a response to a transient-step incident wave and can be founded by performing a numerical integration over S_a . It can be simplified to become a line integral by considering the situations where the delta function has nonzero values at t by $\delta \left(t - \frac{R + 2a - r_1}{v} \right) \neq 0$ which occurs at $vt - 2a + r_1 = R$ that corresponds to a line contour $C_t(t)$ on the radius r_1 of spherical and shown in Fig. 1. Its projection on the x_p - y_p plane is a circular contour described by $x_1'^2 + y_1'^2 = \rho^2$ where $\rho^2 = r_1^2 - \frac{Q^2}{4z_p^2}$, thus one considers a parameter transformation by using $x' = \rho \cos \phi$, $y' = \rho \sin \phi$ and $\iint_S \dots ds' \rightarrow \iint \dots J_A(\theta, \phi) d\phi \cdot d\theta$ where $J_A(\theta, \phi)$ is the transformation Jacobian

$$J_A(\rho, \phi) = \frac{ds'}{d\rho d\phi} = \left| \vec{r}'_\rho \times \vec{r}'_\phi \right|, \quad \hat{n} = \pm \frac{\vec{r}'_\rho \times \vec{r}'_\phi}{\left| \vec{r}'_\rho \times \vec{r}'_\phi \right|} \quad (7)$$

Allows one to simplify the double integration into a line integral by

$$\vec{E}_r(\vec{r}) \cong \frac{r_1}{4\pi z_p} \left\{ \int \hat{R} \times \hat{R} \times V_o \left[-\hat{\theta}_1 f_{\theta_f} - \hat{\phi}_1 f_{\phi_f} \right] \frac{1}{r_f} d\phi - \int \hat{R} \times V_o \left[\hat{\phi}_1 f_{\theta_f} - \hat{\theta}_1 f_{\phi_f} \right] \frac{1}{r_f} d\phi \right\} \quad (8)$$

the integral in (8) can be found in a closed-form.

2.4. Analysis Description for Hyperbolic Surface

The hyperbolic reflector, illustrated in Fig. 1(a), is described by a part of the following surface

$$\frac{(z + c)^2}{a^2} - \frac{x^2 + y^2}{b^2} = 1, \quad (9)$$

and truncated at $z = z_a$, where a and b ($a > b$) are related to the radii of its two principal axes with $c = \sqrt{a^2 + b^2}$. The two foci, F_1 and F_2 , are located at $z = -c$ and $z = c$, where F_2 was selected as the origin of a global coordinate system I the following analysis while the feed is located at F_1 for a focus feeding. Given an arbitrary point, Q_s , on the hyperbolic surface, it is straightforward to show that

$$|F_1 Q_s - Q_s F_2| = 2a. \quad (10)$$

The feed’s radiation is a \hat{x}_f -polarized spherical wave with a cosine-taper and a transient step function, and is described by (9)–(10) in [4]. Here (r_f, θ_f, ϕ_f) is defined in the feed’s spherical coordinate system with $\hat{z}_f = +\hat{z}$ and $\hat{x}_f = \hat{x}$ as illustrated in Fig. 1(a).

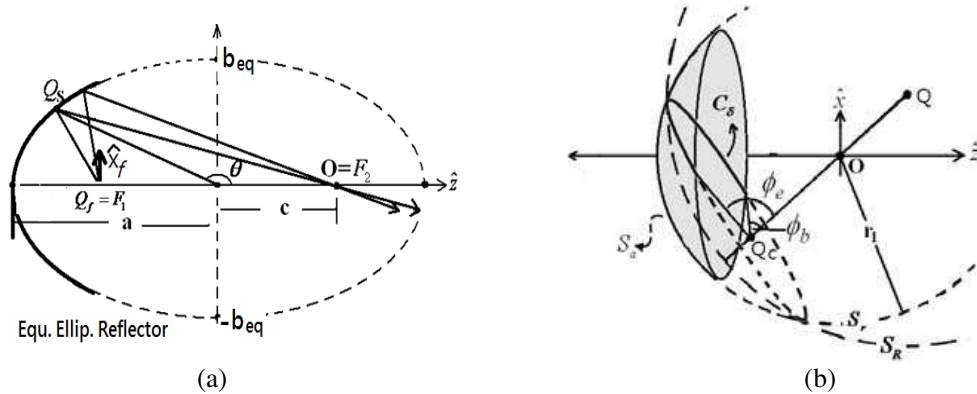


Figure 1: A rotationally symmetric hyperbolic and a near-field focused reflector which is taken from a part of hyperbolic.

2.5. The Continuation of Surface Curvature

The hyperbolic surface in (9) can be analogously described as

$$\frac{(z + c)^2}{a^2} + \frac{x^2 + y^2}{b_{eq}^2} = 1 \quad (11)$$

where $b_{eq} = jb$ is a complex radii of surface curvature, and makes the surface an ellipsoidal one. Based on this curvature continuation into a complex space, the solution in [4] can be extended for the analysis of hyperbolic reflector.

2.6. Resulting Solution

The scattering field at \vec{r}_o due to the illumination of a TD step-function feed radiation can be expressed in a closed-form as

$$\vec{E}_s(\vec{r}_o, t) = \left(\vec{E}_r(\vec{r}_o, t) \cdot T(\phi_e - \phi_b) + \vec{E}_e(\vec{r}_o, t)|_{\phi'_p = \phi_e} - \vec{E}_e(\vec{r}_o, t)|_{\phi'_p = \phi_b} \right) \Pi(t) \quad (12)$$

where $T(\varphi) = \varphi/(2\pi)$ and $\Pi(t) \equiv u(t - t_1) - u(t - t_2)$ with $u(t)$ is a Heaviside step function. In (12), t_1 and t_2 are the starting and ending time that the contributing contour, C_δ , overlaps with the reflecting surface.

3. NUMERICAL EXAMPLES

Numerical examples case 1 are presented ellipsoidal reflector to demonstrate the characteristics of scattering fields as shown Fig. 2. In this case, the reflector has a diameter of 2 m (i.e., $z_a = -7.84$ m), and $z_p = 1.06$ m. The case 2 examples consider a reflector size with the parameters in (11) given by $a = 4$ m, $b = 3$ m and $c = 5$ m. The reflector in Fig. 1 is rotationally symmetric with a radius $r_a = 1$ m. Fig. 3(a) shows the TD response on the z -axis with z_p being the distance measured from F_2 toward the $-z$ direction. In contrast to the radiation of an elliptical reflector, this reflector radiates defocusing fields. The time duration becomes shorter at the observation of farer distance. Fig. 3(b) shows the TD response at $r_o = 15$ m with various observation angles. In this case, the field at the axis corresponds to the main beam while that at the far away angles are the sidelobes.

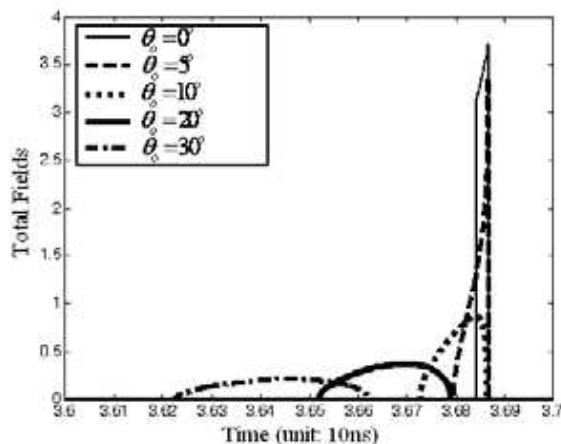


Figure 2: Transient scattering field with respect to varying observation angles.

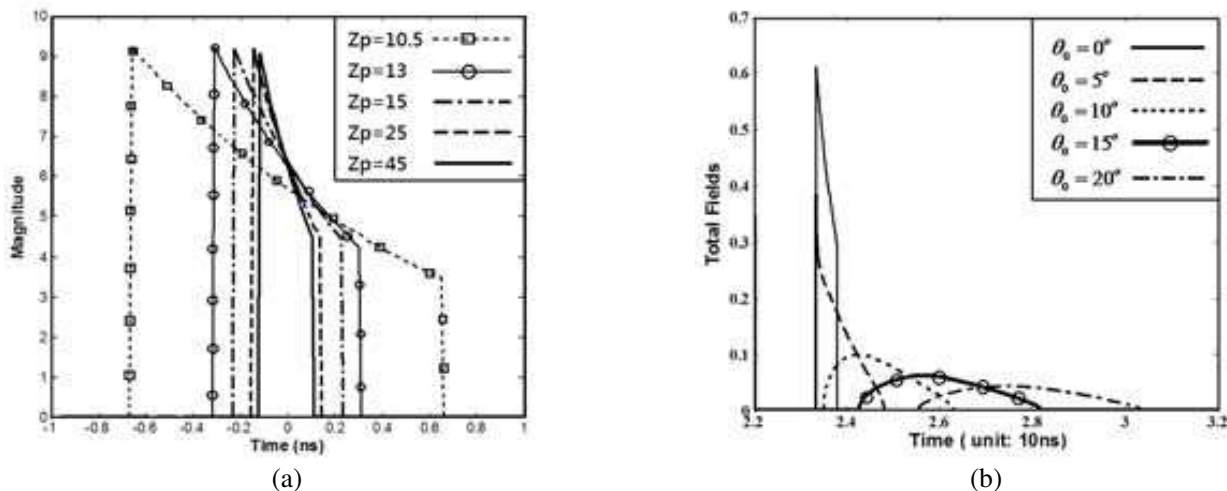


Figure 3: TD field response of scattering fields. (a) Observation on the axis. (b) Observation at $r_o = 15$ m.

4. CONCLUSIONS

This paper will present the near field time domain transient closed-form solution for elliptic reflector illuminated by Huygen's Source at the focus. That employs an asymptotic high-frequency geometrical optics (GO)-based approximation for the fields in an equal-phase surface aperture which appears to be a sphere centered at the second focus of the ellipse. Then we discuss the TD analysis of a hyperbolic reflector based on the mathematic continuation of an ellipsoidal reflector antenna. The formulation has been developed with numerical results presented to validate the results.

REFERENCES

1. Houshamand, B., Y. Rahmat-Samii, and D. W. Duan, “Time response of single and dual reflector antennas,” *Digest Held in Conjunction with: URSI Radio Science Meeting and Nuclear EMP Meeting, IEEE Antennas and Propagation Society International Symposium, 1992, AP-S. 1992*, Vol. 2, 1161–1164, Jul. 18–25, 1992.
2. Rousseau, P. R. and P. H. Pathak, “Time-domain uniform geometrical theory of diffraction for a curved wedge,” *IEEE Transactions on Antennas and Propagation*, Vol. 43, No. 12, 1375–1382, Dec. 1995.
3. Chou, H.-T. and P. H. Pathak, “Analytic solution for early-time transient radiation from pulse-excited parabolic reflector antennas,” *IEEE Transactions on Antennas and Propagation*, Vol. 45, 829–836, May 1997.
4. Tuan, S.-C., H.-T. Chou, K.-Y. Lu, and H.-H. Chou, “Analytic transient analysis of radiation from ellipsoidal reflector antennas for impulse-radiating antennas applications,” *IEEE Transactions on Antennas and Propagation*, Vol. 60, No. 1, 328–339, Jan. 2012.

A Time Domain Analytic Solution to Predict the Transient Radiation for Phased Periodic Array

Shih-Chung Tuan¹ and Hsi-Tseng Chou²

¹Department of Communication Engineering, Oriental Institute of Technology, Pan-Chiao, Taiwan

²Department of Communication Engineering, Yuan Ze University, Chung-Li, Taiwan

Abstract— Most recently the applications have been extended to treat the problems arising in the near zone of electrically large antennas such as the vital life-detection systems and noncontact microwave detection systems, where the objects under detection may locate in the near zone of antenna. A TD analytic solution to predict the transient radiation from a phased periodic array of elemental antennas is thus developed. The TD phenomena are investigated in this paper. The TD phenomena of Floquet modes in the quantity of field potentials with a transient impulse excitation in the current moments were examined. In this generalized analysis, one first considers a two dimensional finite array of current moments with phases impressed to radiate fields focused in the near zone of array aperture, where the focal field point can be arbitrarily selected.

1. INTRODUCTION

The increasing interest in the time domain (TD) analysis of ultra wideband or short pulse target identification and remote sensing applications has resulted in the development of new TD techniques to analyze the antenna radiation, which provides more physically appealing interpretation of wave phenomena. Most recently the applications have been extended to treat the problems arising in the near zone of electrically large antennas such as the vital life-detection systems and noncontact microwave detection systems, where the objects under detection may locate in the near zone of antenna. The potential applications of near-field antennas continue to grow dramatically and desire more exploration in the near future. A TD analytic solution to predict the transient radiation from a time-delayed periodic array of elemental antennas is thus developed. In this analysis, the signals of array excitations are properly delayed to radiate electromagnetic (EM) fields focused in the near zone of array aperture [1, 2]. Examples include the developments of TD uniform geometrical theory of diffraction (TD-UTD) [3, 4], physical theory of diffraction (TD-PTD) [5], physical optics (TD-PO) [6] and TD aperture integration (TD-AI) [7] techniques that were obtained by using either a direct inverse Laplace transform or an analytical time transform (ATT) [8] of the corresponding FD formulations [9]. These solutions are limited to the transient analysis of antenna radiation with scattering mechanisms such as the reflector antennas, and are not applicable to the current situation of direct antenna radiation from a time-delayed array. This paper presents an analytical transient analysis of electromagnetic field radiation from a time-delayed and finite periodic array of antennas for the near- and far-field focused applications. The elemental current moments of array are assumed with a transient impulse input for the excitations whose signals are delayed to radiate near-zone focused fields. The transient field phenomena for each of the Floquet mode expansion were analyzed. The solution reduces to the case of far-zone field radiation by moving the focus point to the far zone. The analysis shows that the radiation exhibits an impulse field at the focused point, and finite pulses at locations away from the focus point. Phenomena of partial cylindrical wave functions have been observed.

2. TIME DOMAIN IMPULSE RESPONSES WITH RESPECT TO EACH OF THE FLOQUET MODE EXPANSION

2.1. Transient Phenomena of an Unit Current Moment

Let the array be planar, rectangular and periodic with $(2N_x + 1) \times (2N_y + 1)$ identical elements of infinitesimal magnetic current moment, $d\bar{p}(\bar{r}', t)$, with periods, d_x and d_y , along the x - and y -coordinates, respectively, which is illustrated in Figure 1. In particular, this current moment has a transient behavior of Dirac delta function (impulse function) by

$$d\bar{p}(\bar{r}', t) = d\bar{P}(\bar{r}') \cdot \delta(t - t') \quad (1)$$

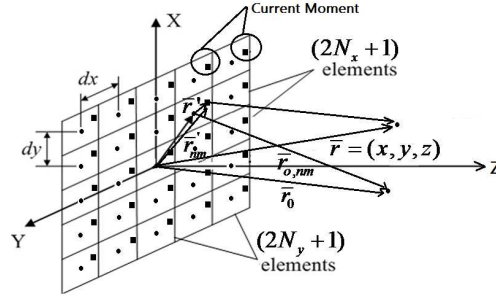


Figure 1: A two dimensional periodic array of current moments induced on the array antenna elements to radiate near-zone focused field at \bar{r}_o .

where $\delta(\cdot)$ is the Dirac delta function. The nm th element of the array is located at $\bar{r}'_{nm} = (nd_x, md_y, 0) + \bar{r}'(-N_x \leq n \leq N_x, -N_y \leq m \leq N_y)$, and has a FD potential, $d\bar{F}_{nm}(\bar{r}, s)$ by

$$d\bar{F}_{nm}(\bar{r}, s) = \frac{1}{4\pi} d\bar{P}(\bar{r}') \frac{e^{-\frac{s r_{nm}}{c}}}{r_{nm}}, \quad (2)$$

where $s = j\omega$ with ω being the angular frequency, and c is the speed of light in free space. In (2), $\bar{r}_{nm} = \bar{r} - \bar{r}'_{nm}$ with $\bar{r} = (x, y, z)$ being the coordinates of observation point. This radiation exhibits a transient behavior of impulse in TD by

$$d\bar{F}_{nm}(\bar{r}, t) = \frac{1}{4\pi} d\bar{P}(\bar{r}') \frac{\delta(t - \frac{r_{nm}}{c})}{r_{nm}}. \quad (3)$$

2.2. Transient Phenomena of an Array of Time-delayed Unit Current Moments

The net potential in FD from this array is given by

$$d\bar{F}(\bar{r}, s) = \sum_{m=-N_y}^{N_y} \sum_{n=-N_x}^{N_x} A(n, m) \frac{1}{r_{o,nm}} e^{\frac{s}{c} \phi(n,m)} d\bar{F}_{nm}(\bar{r}, s), \quad (4)$$

where $A(n, m)$ is an additional amplitude taper, which can be used to reduce the diffraction effects of a finite array. In TD, gives

$$d\bar{F}(\bar{r}, t) = \frac{d\bar{P}(\bar{r}')}{4\pi} \left[\sum_{m=-N_y}^{N_y} \sum_{n=-N_x}^{N_x} A(n, m) \frac{\delta\left(t - \frac{r_{nm} - \phi(n,m)}{c}\right)}{r_{o,nm} r_{nm}} \right]. \quad (5)$$

It is noted that a convolution in time with the impulse response in (5) can be performed to obtain the response of a general transient inputs for the elements' excitations.

2.3. Transient Floquet Mode Representation

The element-by-element summation in (5) is time-consuming and does not provide radiation phenomena with physical meanings. It is thus alternatively expressed in terms of Floquet modes by using the Poisson sum formula of a periodic structure:

$$\sum_{n=-N_1}^{N_2} f(n) = \frac{f(N_1^+)}{2} + \frac{f(N_2^-)}{2} + \sum_{p=-\infty}^{\infty} \int_{N_1^+}^{N_2^-} f(v) e^{-j2\pi p v} dv. \quad (6)$$

Thus referring to the illustration in Figure 2 and applying (6) over the double sum formulation in (5) will make (5) becoming

$$d\bar{F}(r, t) = \frac{1}{4} \sum_{\ell=1}^4 \bar{C}_{\ell}(\bar{r}, t) + \frac{1}{2} \sum_{\alpha=1}^4 \bar{G}_{\alpha}(\bar{r}, t) + \sum_{q=-\infty}^{\infty} \sum_{p=-\infty}^{\infty} \bar{F}_{pq}^w(\bar{r}, t), \quad (7)$$

which transforms the discrete source radiations into that of continuous aperture sources. The phenomena and analysis of each term are interpreted as corner, edge and Floquet wave contributions similar to these previously identified in [10]. In particular, $\bar{C}_\ell(\bar{r}, t)$ are related to the corner effects, $\bar{G}_\alpha(\bar{r}, t)$ are related to the four finite edge effects, and $\bar{F}_{pq}^w(\bar{r}, t)$ are related to the effects of a finite aperture, which are discussed in the following sections.

3. AN INTEGRATION CONTOUR AND ITS CHARACTERISTICS

The surface integral can be reduced to a line integral at the conditions that the Dirac delta function has a nonzero value. It occurs at $r_{uv} - \phi(u, v) = ct$, and with $(n, m) \rightarrow (u, v)$, which results in a line contour $C_t(t)$ on S_a as illustrated in Figure 2. It is noted that $C_t(t)$ is the intersection of a hyperbolic surface and $z = 0$ plane as illustrated in Figure 2, where the two focused points of the hyperbolic surface are located at $F_1 = (x - x', y - y', z - z')$ and $F_2 = (x_0, y_0, z_0)$, respectively. As shown in $C_t(t)$ can be described by

$$\frac{(x_{i,d} - e_{1,d})^2}{A^2} + \frac{(y_{i,d} - e_{2,d})^2}{B^2} = \rho_t^2 \tag{8}$$

4. NUMERICAL EXAMPLES

The array of antennas has a period of 0.1 m in both x - and y -dimensions. The focus point is at $(x_o, y_o, z_o) = (0, 0, 1.5 \text{ m})$, which is relatively far away from the array aperture. The observation point is at, and is in $(0, 0, 30 \text{ m})$ the near zone. In this examination, one considers the behaviors of $\bar{F}_{pq}(\bar{r}, t)$, which represents the dominating contributions in the array radiation for the impulse

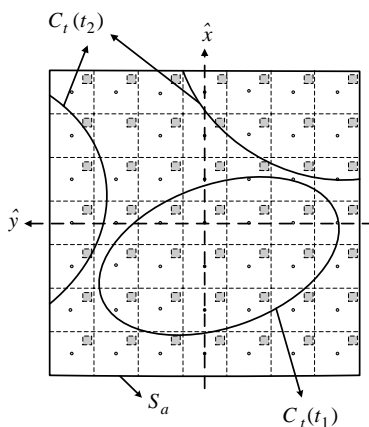


Figure 2: Illustration of S_a and $C_t(t)$, where $C_t(t_1)$ and $C_t(t_2)$ on the figure are used to indicate different types occurring at t_1 and t_2 according to which part of the hyperbolic surface intersects with S_a .

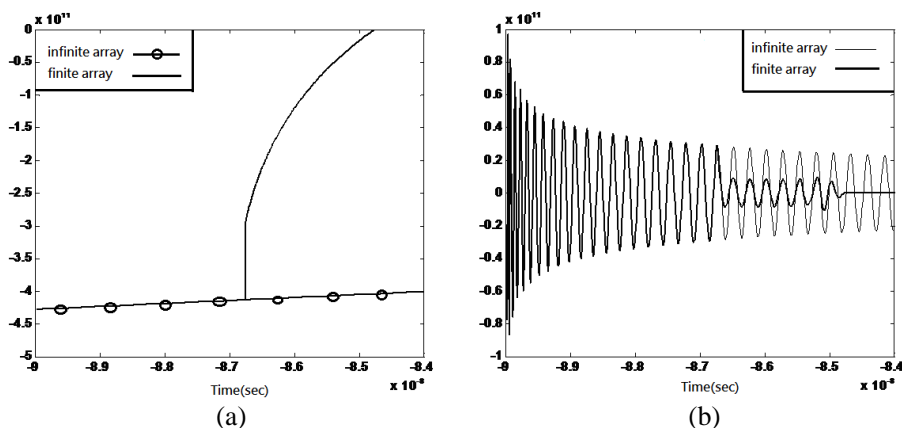


Figure 3: Transient responses of various Floquet modes for an infinite and a finite array of current sources with impulse excitations. The periods are 0.1 m in both x - and y -dimensions. The focus and observation points are at $(0, 0, 1.5 \text{ m})$ and $(0, 0, 30 \text{ m})$, respectively. (a) $(p, q) = (0, 0)$. (b) $(p, q) = (-1, 0)$.

current distributions for every element. One first considers the case of an infinite and finite array, and examines the fundamental $(p, q) = (0, 0)$ and $(-1, 0)$ modes, whose results are shown in Figures 3(a)–(b).

5. CONCLUSIONS

This paper presents a quasi-analytic TD solution to perform a transient analysis of radiation from an array of current sources. The solutions for electromagnetic radiation potential are obtained for the array with a finite size and impulse transient excitations. The array is excited to radiate fields focused in the near zone of array apertures. It is also found that each Floquet mode exhibits the characteristics of different time harmonic orders.

REFERENCES

1. Bogosanovic, M. and A. G. Williamson, “Microstrip antenna array with a beam focused in the near-field zone for application in noncontact microwave industrial inspection,” *IEEE Trans. Instrumentation Measurements*, Vol. 56, No. 6, 2186–2195, Dec. 2007.
2. Stephan, K. D., J. B. Mead, D. M. Pozar, L. Wang, and J. A. Pearce, “A near field focused microstrip array for a radiometric temperature sensor,” *IEEE Trans. Antennas Propag.*, Vol. 55, No. 4, 1199–1203, Apr. 2007.
3. Veruttipong, T. W., “Time domain version of the uniform GTD,” *IEEE Trans. Antennas Propag.*, Vol. 38, 1757–1764, Nov. 1990.
4. Rousseau, P. R. and P. H. Pathak, “Time-domain uniform geometrical theory of diffraction for a curved wedge,” *IEEE Trans. Antennas Propag.*, Vol. 43, No. 12, 1375–1382, Dec. 1995.
5. Johansen, P. M., “Time-domain version of the physical theory of diffraction,” *IEEE Trans. Antennas Propag.*, Vol. 47, No. 2, 261–270, Feb. 1999.
6. Chou, H.-T. and S.-C. Tuan, “Analytic analysis of transient scattering from a finite second-order surface illuminated by an incident plane wave,” *IEEE Trans. Antennas Propag.*, Vol. 54, No. 9, 2463–2471, Sep. 2006.
7. Chou, H.-T. and P. H. Pathak, “Analytic solution for early-time transient radiation from pulse-excited parabolic reflector antennas,” *IEEE Trans. Antennas Propag.*, Vol. 45, No. 5, 829–836, May 1997.
8. Chou, H.-T., S.-C. Tuan, and H.-H. Chou, “Transient analysis of scattering from a perfectly conducting parabolic reflector illuminated by a Gaussian beam electromagnetic field,” *IEEE Trans. Antennas Propag.*, Vol. 58, No. 5, 1711–1719, May 2010.
9. Capolino, F. and L. B. Felsen, “Time-domain Green’s function for an infinite sequentially excited periodic planar array of dipoles,” *IEEE Trans. Antennas Propag.*, Vol. 51, No. 2, 160–170, Feb. 2003.

Local Field Effects for Left-handed Planar Metamaterials

O. V. Porvatkina, A. A. Tishchenko, and M. N. Strikhanov
National Research Nuclear University “MEPhI”, Moscow, Russia

Abstract— We consider dielectric and magnetic properties of left-handed planar metamaterials with negative permittivity and permeability. In our work we investigate planar metamaterials consist of anisotropic particles. We obtain dependence of permittivity on dielectric polarizability and permeability on magnetic polarizability of the particles. Local field effects are taken into account in calculations. These effects are caused by interaction between single particles. We also obtain the generalized Clausius-Mossotti relations for planar metamaterials made of anisotropic particles in the long wave approximation. We calculate a response function to an external electromagnetic field in case of planar metamaterial. This function describes connection between external electromagnetic field and the local field. On the one hand, such connection allows us to analyze structure of electromagnetic field in the near-field regime. On the other hand, the relationship between the field interacting with particles in the planar metamaterials and the external field is of key importance for calculations of characteristics of the electromagnetic radiation generated by charged particles or particle beams passing through or near the planar structures.

1. INTRODUCTION

Metamaterials are artificially designed materials that have effective properties, such as anomalous refraction or reflection. Particularly, planar metamaterials have unusual properties such as manipulation of the polarization states of light diffracted from the surface. These structures also demonstrate extremely high confinement of electromagnetic fields and thus strong variations of field intensities, which can significantly enhance near-field optical forces [1–3]. In work [4–6] it has demonstrated that planar metamaterials with desired values of permittivity and permeability can be obtained by using different methods, for example, hybridization. Also such effective properties are achieved by the optimization of the parameters of constituent molecules of metamaterials. Therefore planar metamaterials are in the center of many modern researches. In addition the planar nature of these structures means they could be incorporated into thin-film coatings for numerous optical components.

2. PERMITTIVITY AND PERMEABILITY OF 2D METAMATERIALS WITH LOCAL FIELD EFFECTS

Let us consider planar metamaterial located at the plane $z = 0$. This material has the thickness b that is smaller than $n^{-1/2}$ — the average intermolecular distance ($n = N/S$ is the surface concentration of molecules of metamaterial). We investigate planar metamaterial which consists of anisotropic molecules with dielectric polarizability tensor and magnetic polarizability tensor:

$$\alpha_{ij}^e(\omega) = \alpha_{\perp}^e(\omega) (\delta_{ij} - e_i e_j) + \alpha_{\parallel}^e(\omega) e_i e_j, \quad (1)$$

$$\alpha_{ij}^m(\omega) = \alpha_{\perp}^m(\omega) (\delta_{ij} - e_i e_j) + \alpha_{\parallel}^m(\omega) e_i e_j. \quad (2)$$

In this medium Fourier-transform for density of micro-currents has the form:

$$\begin{aligned} \langle j_i^{mic}(\mathbf{r}', \omega) \rangle = & -i\omega \alpha_{ij}^e(\omega) \left\langle \sum_n E_j^{mic}(\mathbf{R}_b, \omega) \delta(\mathbf{r}' - \mathbf{R}_b) \right\rangle \\ & + c \alpha_{ij}^m(\omega) \left\langle \sum_n (rot \mathbf{H}^{mic}(\mathbf{R}_b, \omega))_j \delta(\mathbf{r}' - \mathbf{R}_b) \right\rangle. \end{aligned} \quad (3)$$

In our previous work [7] we obtain relation between local (electric and magnetic) fields and macroscopic fields for 3d metamaterials taken into account distributional function. In case of planar metamaterials we have:

$$w(X_{ba}, Y_{ba}, Z_a + Z_{ba}) = \frac{1}{S} \eta (Z_a + Z_{ba}) [1 - f(X_{ba}, Y_{ba})], \quad (4)$$

where $\eta(Z_b)$ is the distribution of metamaterial molecules along the z axis, $f(X_{ba}, Y_{ba})$ can be found from equation for the radial distributional function. From the Maxwell's equations taken into account Eq. (4) we obtain Fourier-transform of the resulting relations between local fields and macroscopic fields:

$$E_i(z, \omega) = T_{ik}(z, \omega) E_k^{loc}(z, \omega), \quad (5)$$

$$B_i(z, \omega) = Q_{ik}(z, \omega) B_k^{loc}(z, \omega), \quad (6)$$

where

$$T_{ik}(z, \omega) = \delta_{ik} - 4\pi n \alpha_{ij}^e(\omega) \int d^3l e^{il_z z} \frac{l_j l_k}{l^2} \eta(l_z) f(\mathbf{l}_{\parallel}), \quad (7)$$

$$Q_{ik}(z, \omega) = \delta_{ik} - 4\pi n \alpha_{ij}^m(\omega) \int d^3l e^{il_z z} \frac{l_j l_k}{l^2} \eta(l_z) f(\mathbf{l}_{\parallel}). \quad (8)$$

We do our calculations in a long-wave limit. According to this concept, if the wavelength of the field is large in comparison with the lattice constant d , the effective field acting on a molecule is formed by adding the fields of many molecules lying in some volume of the crystal with linear dimensions of L [8]:

$$c/\omega \gg L \gg d. \quad (9)$$

This limit allows us to neglect the spatial dispersion in Eqs. (5), (6). The integrals in Eqs. (7), (8) are symmetric tensors. These tensors depend on the unit normal vector to the surface of planar metamaterial. For this reason such integral can be represented as the sum of two terms which are proportional to tensors δ_{jk} and $e_j e_k$. So, the integral from Eqs. (7), (8) can be written in the form:

$$\int d^3l e^{il_z z} \frac{l_j l_k}{l^2} \eta(l_z) f(\mathbf{l}_{\parallel}) = c \delta_{jk} + b e_j e_k. \quad (10)$$

We also know that the probability of unlimited approaching of molecules is negligibly small. Using this fact one can obtain convolution of Eq. (10) with δ_{jk} :

$$3c + b = \int d^3l e^{il_z z} \eta(l_z) f(\mathbf{l}_{\parallel}) = \int d^2l_{\parallel} f(\mathbf{l}_{\parallel}) \int dl_z e^{il_z z} \eta(l_z) = \eta(z). \quad (11)$$

On the other hand, convolution of (10) with $e_j e_k$ gives:

$$c + b = \int d^3l e^{il_z z} \frac{l_z^2}{l^2} \eta(l_z) f(\mathbf{l}_{\parallel}). \quad (12)$$

In this problem the thickness b is smaller than all the characteristic lengths. For this reason the distribution function $\eta(z)$ is more rapid than other function in Eq. (12). So, integral in the right side of Eq. (12) can be represented in the form:

$$\int d^3l e^{il_z z} \frac{l_z^2}{l^2} f(\mathbf{l}_{\parallel}) = \int d^2l_{\parallel} f(\mathbf{l}_{\parallel}) \int dl_z \left(1 - \frac{l_z^2}{l_z^2 + l_{\parallel}^2}\right) e^{il_z z} \eta(l_z) = \eta(z) - \frac{1}{2} \int d^2l_{\parallel} f(\mathbf{l}_{\parallel}) l_{\parallel} e^{-|z|l_{\parallel}}. \quad (13)$$

Thus we can write Eq. (12) as follows:

$$c + b = \eta(z) - 1/2 \zeta(z), \quad (14)$$

where

$$\zeta(z) = \int d^2l_{\parallel} f(\mathbf{l}_{\parallel}) l_{\parallel} e^{-|z|l_{\parallel}}. \quad (15)$$

Combining Eqs. (11), (14), we can derive coefficients c and b :

$$c = 1/4 \zeta(z), \quad (16)$$

$$b = \eta(z) - 3/4 \zeta(z). \quad (17)$$

Taking into account these coefficients one can rewrite Eqs. (7), (8):

$$T_{ik}(z, \omega) = \left(1 - 4\pi n \alpha_{\parallel}^e \zeta(z)\right) (\delta_{ik} - e_i e_k) + (1 + 2\pi n \alpha_{\perp}^e (\zeta(z) - 2\eta(z))) e_i e_k, \quad (18)$$

$$Q_{ik}(z, \omega) = \left(1 - 4\pi n \alpha_{\parallel}^m \zeta(z)\right) (\delta_{ik} - e_i e_k) + (1 + 2\pi n \alpha_{\perp}^m (\zeta(z) - 2\eta(z))) e_i e_k. \quad (19)$$

The tensors $Q_{ik}^{-1}(z, \omega)$, $T_{ik}^{-1}(z, \omega)$ describe relations between local magnetic and macroscopic magnetic fields, local electric and macroscopic electric fields, correspondingly. Also they define magnetic and dielectric properties of planar metamaterial. Using this fact Eqs. for permittivity and permeability can be determined as:

$$\varepsilon_{ij}(z, \omega) = \delta_{ij} + 4\pi n \alpha_{ik}^e(\omega) \eta(z) T_{kj}^{-1}(z, \omega), \quad (20)$$

$$\mu_{ij}(z, \omega) = \delta_{ij} + 4\pi n \alpha_{ik}^m(\omega) \eta(z) Q_{kj}^{-1}(z, \omega). \quad (21)$$

On the other hand, the permittivity and permeability are tensors and can be submitted in the form:

$$\varepsilon_{ij}(z, \omega) = \varepsilon_{\parallel}(z, \omega) (\delta_{ij} - e_i e_j) + \varepsilon_{\perp}(z, \omega) e_i e_j, \quad (22)$$

$$\mu_{ij}(z, \omega) = \mu_{\parallel}(z, \omega) (\delta_{ij} - e_i e_j) + \mu_{\perp}(z, \omega) e_i e_j, \quad (23)$$

where

$$\mu_{\parallel}(z, \omega) = 1 + \frac{4\pi n \alpha_{\parallel}^m(\omega) \eta(z)}{1 - \pi n \alpha_{\parallel}^m(\omega) \eta(z)}, \quad (24)$$

$$\mu_{\perp}(z, \omega) = \frac{1 + 2\pi n \alpha_{\perp}^m(\omega) \zeta(z)}{1 + 2\pi n \alpha_{\perp}^m(\omega) (\zeta(z) - 2\eta(z))}. \quad (25)$$

Equations for components of permittivity are similar to Eqs. (24), (25) and depend on the components of dielectric polarizability of constituent molecules. In these equations denominators do not vanish because the dielectric polarizability and magnetic polarizability are also complex values.

3. DISCUSSION

In this work planar metamaterials are discussed. These materials draw more and more attention in the modern scientific investigations because of possibility of obtaining exotic properties via constructing their microstructure [9]. We obtain equations for permittivity (22) and permeability (23) of planar metamaterials. These equations are analogues the well-known Clausius-Mossotti relations, but for planar magnetic medium. Permittivity and permeability describe relation between macroscopic and microscopic properties of planar metamaterials. We also calculate response functions $T_{ik}^{-1}(z, \omega)$ and $Q_{ik}^{-1}(z, \omega)$ which define dielectric and magnetic properties of magnetic medium and describe relations between local and macroscopic fields (electric and magnetic). In our approach we use local field effects. This fact allows us to analyze optical properties of planar metamaterials which are very interesting for new investigations. Particularly, for design and engineering optical devices based on planar metamaterials which have extremely interesting properties (high specific rotation of polarization supported by plasmonic or waveguide resonances) [10]. Local field effects is also attractive for research nonlinear optical processes, which scale with a high power of the field. In case of nonmagnetic medium our results coincide with work [11].

REFERENCES

1. Zhang, W. A., D. M. Potts, and J. Bagnal, "Giant optical activity in dielectric planar metamaterials with two-dimensional chirality," *Opt. A: Pure Appl. Opt.*, Vol. 8, 878–890, 2006.
2. Ourir, A., R. Abdeddaim, and J. de Rosny, "Double-T metamaterial for parallel and normal transverse electric incident waves," *Opt. Lett.*, Vol. 36, 1527–1529, 2011.
3. Ryazanov, M. I., M. N. Strikhanov, and A. A. Tishchenko, "Local field effect in diffraction radiation from a periodical system of dielectric spheres," *Nucl. Instr. and Meth. B*, Vol. 266, 3811–3815, 2008.
4. Zhang, J., K. F. MacDonald, and N. I. Zheludev, "Giant optical forces in planar dielectric photonic metamaterials," *Optics Letters*, Vol. 39, 4883–4886, 2014.
5. Abdeddaim, R., A. Ourir, and J. de Rosny, "Realizing a negative index metamaterial by controlling hybridization of trapped modes," *Phys. Rev. B*, Vol. 83, 033101, 2011.
6. Ourir, A. and H. Ouslimani, "Negative refractive index in symmetric cut-wire pair metamaterial," *Appl. Phys. Lett.*, Vol. 98, 113505, 2011.

7. Porvatkina, O. V., A. A. Tishchenko, M. I. Ryazanov, and M. N. Strikhanov, “Local field effects in anisotropic metamaterials,” *IOP Conference Series*, Vol. 541, 012024, 2014.
8. Ryazanov, M. I., *Electrodynamics of Condensed Matter*, Nauka, Moscow, 1984 (in Russian).
9. Cai, W. and V. Shalaev, *Optical Metamaterials*, Springer, New York, 2010.
10. Husu, H., B. K. Canfield, J. Laukkanen, B. Bai, M. Kuittinen, J. Turunen, and M. Kauranen, “Local-field effects in the nonlinear optical response of metamaterials,” *Metamaterials*, Vol. 2, 155–168, 2008.
11. Ryazanov, M. I. and A. A. Tishchenko, “Clausius-Mossotti-type relation for planar monolayers,” *Journal of Experimental and Theoretical Physics*, Vol. 103, 539–545, 2006.

Total Internal Reflection as a Technique for Study of Surface Optical Characteristics of Left-handed Materials

A. M. Feshchenko, A. A. Tishchenko, and M. N. Strikhanov
National Research Nuclear University “MEPhI”, Moscow, Russia

Abstract— In this work we consider an effect of surface inhomogeneities of left-handed materials on light reflection and refraction. It is shown that total internal reflection could be useful for investigation of surface optical characteristics of metamaterial. Scattering of refracted wave in the near-surface layer leads to existence of radiation propagating from the boundary to the point of observation. The angular distribution of the resulting radiation is derived and the opportunity of getting information about optical properties of metamaterial surface with help of this method is discussed.

1. INTRODUCTION

Real material surface is known to differ from ideal plane surface because of the presence of non-uniform near-surface layer. The properties of the layer may influence considerably various processes of macroscopic electrodynamics, such as reflection and refraction of light, propagation of surface waves, radiation from fast charged particle beams [1–3]. As the thickness of the layer is much smaller than the light wavelength, all inhomogeneities caused by natural surface anisotropy [4–6], impurity atom adsorption, surface relaxation and reconstruction, fluctuations in surface electronic states, — all these can be taken into account via introduction of surface polarization current into boundary conditions [3]. This surface current is linearly dependent on the electrical field, and proportionality factor is the phenomenological characteristic of dielectric and magnetic surface features.

Information about surface properties can be of great use for developing of metamaterial optics. Actually the so-called gradient mediums with variable electromagnetic parameters are of interest for optics of photonic crystals, waveguides and compact antennas [7]. Also a large number of works has been focused on materials with simultaneously negative permittivity and permeability, which are called “left-handed”, because of its extraordinary features such as inverse Snell’s law, reverse Doppler effect and Cherenkov radiation [8]. This materials find the applications in near-field optics, so considerable attention is paid to the investigation of surface waves on the left-handed material border, that play an important role, for example, in multilayered structures [9], perfect lens [10], terahertz optics [11], cloaking and so on.

It is known that in case of total internal reflection there is no energy transfer from the first medium where incident and reflected waves exist to the second medium. Therefore let us consider the interface between the left-handed material and the vacuum. The presence of inhomogeneities on it gives rise to the scattering of the refracted wave in the near-surface layer so that radiation propagating from the boundary in the vacuum appears. It is convenient to describe this radiation as a result of excitation of the surface current that can be included into boundary conditions. Let us discuss the origin of this current more detailed.

2. MEDIUM RESPONSE TO ELECTROMAGNETIC FIELDS

Electromagnetic field affecting on bound electron of matter excites forced oscillations of this electron. Thus the electron deflects from its initial point \mathbf{r} and moves in the vicinity of this point. As a result average micro-current density of the bound electrons and therefore the electric induction appear:

$$D_i(\mathbf{r}, \omega) = E_i(\mathbf{r}, \omega) + \frac{4\pi i}{\omega} j_i(\mathbf{r}, \omega) \quad (1)$$

On the other hand medium properties are characterized by the constitutive equation between \mathbf{D} , \mathbf{E} and $\text{rot } \mathbf{B}$ (note that magnetic induction \mathbf{B} is an axial vector), that can be written in the most general form [12]:

$$D_i(\mathbf{r}, t) = \int d^3 r' \int dt' \{ \alpha_{is}(\mathbf{r}, t, \mathbf{r}', t') E_s(\mathbf{r} - \mathbf{r}', t - t') + \beta_{is}(\mathbf{r}, t, \mathbf{r}', t') (\text{rot } \mathbf{B}(\mathbf{r} - \mathbf{r}', t - t'))_s \} \quad (2)$$

Coefficients $\alpha_{is}(\mathbf{r}, t, \mathbf{r}', t')$ and $\beta_{is}(\mathbf{r}, t, \mathbf{r}', t')$ describe dielectric and magnetic medium properties correspondingly. Dependence of α_{is} and β_{is} on \mathbf{r} and \mathbf{r}' define local and nonlocal dielectric responses,

dependence on t — nonstationarity of the medium. So, for example, in case of the stationary medium in the absence of spatial dispersion and macroscopic inhomogeneity one can obtain:

$$D_i(\mathbf{r}, \omega) = \alpha_{is}(\omega) E_s(\mathbf{r}, \omega) + \beta_{is}(\omega) (\text{rot } \mathbf{B}(\mathbf{r}, \omega))_s \quad (3)$$

Substitution of Eq. (3) in Maxwell's equation $\text{rot } \mathbf{B}(\mathbf{r}, \omega) = -i\omega/c\mathbf{D}(\mathbf{r}, \omega) + 4\pi/c\mathbf{j}_0(\mathbf{r}, \omega)$ makes it possible to introduce the macroscopic magnetic field

$$H_i(\mathbf{r}, \omega) = \mu_{is}^{-1}(\omega) B_s(\mathbf{r}, \omega), \quad \text{where} \quad \mu_{is}(\omega) \equiv \frac{1}{1 + i\frac{\omega}{c}\beta_{is}(\omega)} \quad \text{— the permittivity,}$$

and electric displacement

$$\tilde{D}_i(\mathbf{r}, \omega) = \varepsilon_{is}(\omega) E_s(\mathbf{r}, \omega), \quad \text{where} \quad \varepsilon_{is}(\omega) \equiv \alpha_{is}(\omega) \quad \text{— the permittivity.}$$

Nevertheless, there is another approach to consideration of the matter response to applied electromagnetic field. Indeed, using Maxwell's equation $\text{rot } \mathbf{E}(\mathbf{r}, t) = -\frac{1}{c} \frac{\partial \mathbf{B}(\mathbf{r}, t)}{\partial t}$ it can be possible to move from Eq. (2) to the connection between \mathbf{D} and \mathbf{E} directly:

$$D_i(\mathbf{r}, t) = \int d^3r' \int dt' \zeta_{is}(\mathbf{r}, t, \mathbf{r}', t') E_s(\mathbf{r} - \mathbf{r}', t - t'), \quad (4)$$

where tensor $\zeta_{is}(\mathbf{r}, t, \mathbf{r}', t')$ includes both dielectric and magnetic properties of the matter. For a number of materials this approach can be more useful in case of quick-changing fields, when the permeability loses its physical meaning [13]. Thus there are two ways of description of field-matter interaction: in terms of \mathbf{E} , \mathbf{D} , \mathbf{B} and in terms of \mathbf{E} , $\tilde{\mathbf{D}}$, \mathbf{B} and \mathbf{H} . Below we shall proceed from Eq. (4), just because of its more simple form.

3. SCATTERING OF REFRACTING WAVE ON SURFACE INHOMOGENEITIES OF LEFT-HANDED MATERIAL

Let us consider the left-handed isotropic medium placed in semi-infinite space $z < 0$, where plane electromagnetic wave polarized arbitrarily towards the incident plane xz propagates. Under interaction of incident wave with the interface $z = 0$ reflected and refracted waves appear. In case of total internal reflection, when incident angle $\gamma \geq \gamma_c \equiv \arcsin |\varepsilon(\omega)\mu(\omega)|^{-1/2}$, the refracted wave propagates along the boundary. Incident and reflected fields produce volume polarization currents in the metamaterial that are usually taken into account via permittivity $\varepsilon(\omega) < 0$ and permeability $\mu(\omega) < 0$. Due to the existence of surface inhomogeneities there is an additional current in the near-surface layer, average density of which can be obtained with help of Eqs. (1) and (4):

$$\Delta \mathbf{j}(\mathbf{r}, \omega) = \frac{\omega}{4\pi i} \xi(\mathbf{r}, \omega) \mathbf{E}(\mathbf{r}, \omega) \theta(-z). \quad (5)$$

Here $\xi(\mathbf{r}, \omega)$ is a small deflection from ζ in Eq. (4), which contains additions $\varepsilon(\mathbf{r}, \omega)$ to $\varepsilon(\omega)$ and $\mu(\mathbf{r}, \omega)$ to $\mu(\omega)$, raised by surface inhomogeneities.

Then boundary conditions on the interface between the metamaterial and the vacuum can be written in a form:

$$[\mathbf{e} \{ \mathbf{H}_1(\mathbf{R}, 0, \omega) - \mathbf{H}_2(\mathbf{R}, 0, \omega) \}] = (4\pi/c) \mathbf{J}(\mathbf{R}, \omega), \quad (6)$$

$$[\mathbf{e} \{ \mathbf{E}_1(\mathbf{R}, 0, \omega) - \mathbf{E}_2(\mathbf{R}, 0, \omega) \}] = 0, \quad (7)$$

$$(\mathbf{e} \{ \varepsilon(\omega) \mathbf{E}_1(\mathbf{R}, 0, \omega) - \mathbf{E}_2(\mathbf{R}, 0, \omega) \}) = (i/\omega) \{ \partial J_x / \partial x + \partial J_y / \partial y \}, \quad (8)$$

$$(\mathbf{e} \{ \mu(\omega) \mathbf{H}_1(\mathbf{R}, 0, \omega) - \mathbf{H}_2(\mathbf{R}, 0, \omega) \}) = 0, \quad (9)$$

where

$$\mathbf{J}(\mathbf{R}, \omega) = \int_{-\infty}^{\infty} dz \tau \Delta \mathbf{j}(\mathbf{R}, z, \omega),$$

$\mathbf{R} = \mathbf{r} - \mathbf{e}(\mathbf{er})$ — radius-vector in the surface plane, \mathbf{e} — unit director vector of \mathbf{z} axis, τ — unit director vector of \mathbf{R} . Here \mathbf{E}_1 , \mathbf{H}_1 -fields in metamaterial, \mathbf{E}_2 , \mathbf{H}_2 -fields in the vacuum.

The small thickness of near-surface layer makes it possible to consider this layer as small perturbation, which lets us solve Eqs. (6)–(9) with the method of stepwise approximation, representing the fields as

$$\mathbf{E}_{1(2)} = \mathbf{E}_{1(2)}^{(0)} + \mathbf{E}_{1(2)}^{(1)}, \mathbf{H}_{1(2)} = \mathbf{H}_{1(2)}^{(0)} + \mathbf{H}_{1(2)}^{(1)}.$$

For the fields of zero approximation the surface current is absent in the boundary condition and the problem reduces to finding of reflected and refracted fields $\mathbf{E}_{1(2)}^{(0)}$, $\mathbf{H}_{1(2)}^{(0)}$ in case of ideal plane surface, which are well-known [13]. For the fields of the first approximation, which rise out of the scattering of the fields of zero approximation, so the surface current in Eqs. (6)–(9) is assumed to be set:

$$\mathbf{J}(\mathbf{R}, \omega) \rightarrow \mathbf{J}^{(0)}(\mathbf{R}, \omega) = \frac{\omega}{4\pi i} \xi(\mathbf{R}, \omega) \mathbf{E}_\tau^{(0)}(\mathbf{R}, 0, \omega), \quad (10)$$

where

$$\xi(\mathbf{R}, \omega) = \int_{-\infty}^0 dz \xi(\mathbf{R}, z, \omega), \quad \mathbf{E}_{1\tau}^{(0)} = \mathbf{E}_{2\tau}^{(0)} \equiv \mathbf{E}_\tau^{(0)}.$$

Let us find the energy flux of the scattered field, propagating out of the interface in the vacuum (similarly to the fields in the metamaterial) along the unit normal vector \mathbf{e} through the plane $z = z_0$:

$$W_z = \frac{c}{4\pi} \iiint dx dy dt \left(\mathbf{e} \left[\mathbf{E}_2^{(1)}(x, y, z_0, t) \mathbf{H}_2^{(1)}(x, y, z_0, t) \right] \right), \quad (11)$$

Applying Fourier transform in Eq. (11) and taking into account that all components of electric and magnetic field vectors can be expressed in terms of normal components by means of Maxwell's equations, we obtain:

$$W_z = 2\pi^2 \iint dq_x dq_y \int d\omega \frac{g_2 \omega}{q_x^2 + q_y^2} \left(|E_{2z}^{(1)}|^2 + |H_{2z}^{(1)}|^2 \right). \quad (12)$$

The normal components $E_{2z}^{(1)}$, $H_{2z}^{(1)}$ can easily be obtained from Eqs. (6)–(9):

$$E_{2z}^{(1)}(q_x, q_y, z, \omega) = -\frac{4\pi g_1}{\omega} \frac{(q_x J_x^{(0)}(q_x, q_y, \omega) + q_y J_y^{(0)}(q_x, q_y, \omega))}{\varepsilon_1(\omega) g_2 + \varepsilon_2(\omega) g_1} e^{ig_2 z}, \quad (13)$$

$$H_{2z}^{(1)}(q_x, q_y, z, \omega) = -\frac{4\pi \mu_1}{c} \frac{q_x J_y^{(0)}(q_x, q_y, \omega) - q_y J_x^{(0)}(q_x, q_y, \omega)}{\mu_1 g_2 + \mu_2 g_1} e^{ig_2 z}, \quad (14)$$

$$g_1 = \sqrt{\frac{\omega^2}{c^2} \varepsilon(\omega) \mu(\omega) - q_x^2 - q_y^2}, g_2 = \sqrt{\frac{\omega^2}{c^2} - q_x^2 - q_y^2}. \quad (15)$$

The surface current $\mathbf{J}^{(0)}$ is specified by tangential component of the electric field of the refracted wave $\mathbf{E}_\tau^{(0)}(x, y, z, \omega) = \mathbf{E}_\tau^{(0)} e^{-ik_x x + ik_z z} \delta(\omega - \omega_0)$, where $k_x = (\omega/c) \sqrt{\varepsilon \mu} \sin \gamma$, $k_z = i(\omega/c) \sqrt{\varepsilon \mu \sin^2 \gamma - 1}$:

$$\mathbf{J}^{(0)}(q_x, q_y, \omega) = \frac{\omega}{4\pi i} \mathbf{E}_\tau^{(0)} \xi(q_x + k_x, q_y, \omega) \delta(\omega - \omega_0) \quad (16)$$

Let us introduce substitution $q = (\omega/c) \sin \theta$. Thus, the distribution of energy $W = W_z / \cos \theta$ along unit vector $\mathbf{n} = \mathbf{r}/r$ (\mathbf{r} — point of observation) over the frequency $d\omega$ and solid angle $d\Omega = \sin \theta d\theta d\varphi$ is:

$$\begin{aligned} \frac{d^2 W(\mathbf{n}, \omega)}{d\Omega d\omega} &= \frac{T\pi \omega^4}{4 \cdot 3} \cos \theta |\xi(q_x + k_x, q_y, \omega)|^2 \delta(\omega - \omega_0) \\ &\times \left(\frac{\varepsilon \mu - \sin^2 \theta}{(\sqrt{\varepsilon \mu - \sin^2 \theta} + \varepsilon \cos \theta)^2} \left| E_x^{(0)} \cos \varphi + E_y^{(0)} \sin \varphi \right|^2 \right. \\ &\left. + \frac{\mu^2}{(\sqrt{\varepsilon \mu - \sin^2 \theta} + \mu \cos \theta)^2} \left| E_y^{(0)} \cos \varphi - E_x^{(0)} \sin \varphi \right|^2 \right), \quad (17) \end{aligned}$$

where T is the total observation time. Equation (17) gives us the dependence of spectral-angular distribution of the radiation energy on dielectric and magnetic characteristics of the magnetic medium surface that are described by the parameter ξ . We would like to notice that Equation (17) describes the radiation at positive $\cos \theta > 0$.

4. DISCUSSION

In this paper the problem of light reflection and refraction on the inhomogeneous surface of magnetic medium, in particular, on the surface of left-handed material is solved using the method of given surface current. It should be also noted that all results of this paper are obtained on the assumption of that the layer thickness is much smaller than light wavelength. Measuring of the spectral-angular radiation density resulting from scattering of refracted field can be employed for investigation surface response on electromagnetic field. The function $d^2W(\theta, \varphi, \omega)/d\Omega d\omega$ obtained from the experiment can be of use in finding $\xi(x, y, \omega)$:

$$\xi(x, y, \omega) = \int \frac{\omega^2}{c^2} \cos \theta d\Omega \sqrt{\frac{1}{f(\theta, \varphi, \omega)} \frac{d^2W(\theta, \varphi, \omega)}{d\Omega d\omega}} e^{i\frac{\omega}{c}(\cos \varphi \sin \theta + |\sqrt{\varepsilon\mu}| \sin \gamma) + i\frac{\omega}{c} \sin \varphi \sin \theta}, \quad (18)$$

where

$$f(\theta, \varphi, \omega) = \frac{T\pi \omega^4}{4} \frac{\delta(\omega - \omega_0) \cos \theta}{3} \left(\frac{\varepsilon\mu - \sin^2 \theta}{\left(\sqrt{\varepsilon\mu - \sin^2 \theta} + \varepsilon \cos \theta\right)^2} \left| E_x^{(0)} \cos \varphi + E_y^{(0)} \sin \varphi \right|^2 + \frac{\mu^2}{\left(\sqrt{\varepsilon\mu - \sin^2 \theta} + \mu \cos \theta\right)^2} \left| E_y^{(0)} \cos \varphi - E_x^{(0)} \sin \varphi \right|^2 \right). \quad (19)$$

Thus, information of parameter ξ as a function of coordinates can give clear vision of different phenomena and processes on the surface of magnetic materials.

ACKNOWLEDGMENT

This work was supported by the Ministry of Education and Science of the Russian Federation, Agreement No. 14.575.21.0002, ID RFMEFI57514X0002.

REFERENCES

1. Ryazanov, M. I., M. N. Strikhanov, and A. A. Tishchenko, "Diffraction radiation from an inhomogeneous dielectric film on the surface of a perfect conductor," *JETP*, Vol. 99, 311, 2004.
2. Koshelev, I. V. and M. I. Ryazanov, "On transition emission on an inhomogeneous interface," *Laser Physics*, Vol. 14, 897, 2004.
3. Ryazanov, M. I., "Phenomenological description of the dielectric-properties of a surface — Surface waves," *JETP*, Vol. 66, 725, 1987.
4. Ryazanov, M. I. and A. A. Tishchenko, "Clausius-Mossotti-type relation for planar monolayers," *JETP*, Vol. 103, 539, 2006.
5. Ryazanov, M. I., "The effect of the natural variation in the polarization of a near-surface layer on electromagnetic surface waves," *JETP*, Vol. 83, 529, 1996.
6. Anokhin, M., A. Tishchenko, M. Ryazanov, and M. Strikhanov, "Permittivity of anisotropic dielectric near surface with local field effects," *J. Phys.: Conf. Ser.*, Vol. 541, 012023, 2014.
7. Shvartsburg, A. B. and N. S. Erokhin, "Resonant tunneling of ultrashort electromagnetic pulses in gradient metamaterials: Paradoxes and prospects," *Phys. Usp.*, Vol. 54, 1171, 2011.
8. Veselago, V. G., "The electrodynamics of substances with simultaneously negative values of ε and μ ," *Phys. Usp.*, Vol. 10, 509, 1968.
9. Canto, J. R., C. R. Paiva, and A. M. Barbosa, "Dispersion and losses in surface waveguides containing double negative or chiral metamaterials," *Progress In Electromagnetics Research*, Vol. 116, 409–423, 2011.
10. Ambati, M., N. Fang, C. Sun, and X. Zhang, "Surface resonant states and superlensing in acoustic metamaterials," *Physical Review B*, Vol. 75, 195447, 2007.

11. Acuna, G., S. F. Heucke, F. Kuchler, H. T. Chen, A. J. Taylor, and R. Kersting, "Surface plasmons in terahertz metamaterials," *Optics Express*, Vol. 16, 18745, 2008.
12. Ryazanov, M. I., *Electrodynamics of Condensed Matter*, Nauka, Moscow, 1984 (in Russian).
13. Landau, L. D. and E. M. Lifshitz, *Electrodynamics Of Continuous Media*, Pergamon Press, 1960.

Evaluation of a Buckypaper's Electromagnetic Shielding Efficiency in X Band

N. Curreli, C. Puddu, G. Muntoni, M. Simone, and A. Fanti

Department of Electrical and Electronic Engineering, University of Cagliari, Italy

Abstract— Carbon nanotubes (CNTs) properties and applications are one of the most innovative and interesting research areas in physics and engineering. The electromagnetic behaviour of CNTs composites and plastic material such as PE and PMMA has been analyzed in several works. Recent works have highlighted how CNTs can be effectively applied in electromagnetic interference (EMI) as high shielding material. Basically, this is due to their high aspect ratio and their tunable conductivity, which allows the electrical percolation (with a little number of CNTs). It is crucial to understand and control the electromagnetic properties of these materials to apply them to devices design in several research fields. A buckypaper is a thin sheet made only with an aggregate of CNTs. A potential application is in shielding technology to protect electronic devices from electromagnetic interferences: for instance CNTs shields could be applied to avoid radar detection of military aircrafts, or to prevent equipment damaging and unintended setting modification. At the same time, CNTs shields could be applied to avoid radar detection of military aircrafts. Moreover, in the next years these structures could have a wide application in nano- and bio-science: potential application in the electromagnetic shielding concern nanoelectronic devices, nano-biomedical imaging and sensing or, in the near future, the protect medical equipments from high-frequency radiations. This paper studies the shielding efficiency of a buckypaper interposed between a multifrequency source and an electromagnetic wave detector. Our analysis is focused only on X Band frequencies.

1. INTRODUCTION

In recent years, a quick spread of wireless technologies and electronic devices led to a significant growth in terms of electromagnetic emissions within the environment, urging to find new solutions to solve various issues, including electromagnetic interference (EMI) [1]. This problem affects various branches, such as the industrial and commercial sector, and it also influences people's private life and effectively, most people are familiar with portable electronic devices, such as mobile phones. A field in which electromagnetic interference represents a severe issue is the physician-hospital one. The instrumentation which is used within hospitals and clinics consists of many electronic devices (active and passive), which might be affected by interference phenomena, due to waves generated by themselves or by other nearby devices. Thus, reduction of EM emissions is to be considered a main goal to achieve. Since a reduction in terms of intensity, regarding emissions irradiated by the source, is not always achievable, neither worthwhile, it comes as no surprise that the interest of the scientific community for EMI shielding devices is growing constantly. Despite a large number of different EM screens is present in literature, new shielding technologies are being developed by scientific community. Since the appearance of the first carbon nanotubes (CNT) devices, it was thought to use them in various applications due to electrical and mechanical characteristics, and one of these is their use in the shielding of EM radiation [2]. This article proposes a project of a screen of CNT buckypaper. The model of this structure has been simulated using ANSYS HFSS software.

2. MATERIALS AND METHODS

A buckypaper is a CNT aggregate [3]. Such a structure is too complicated to be simulated, so it has been chosen to realize a simplified model which consists of an homogeneous layer with the same electrical characteristics of a buckypaper [2]. CNT's parameters in the 8–12.4 GHz band have been considered and they have been inserted in HFSS. A spire with radius $r = 3$ mm and thickness $t = 0.15$ mm has been assumed as field source. It has been designed as a toroid made of PEC, and deprived of a small part in which the excitation port will be placed. The power on the excitation port has been set to 1 KW in order to evaluate high shielding values. A first simulation without the shield has verified the actual operation of the source, after the shield design has been started. The shield is placed at the center of an air box of $6 \times 6 \times 12$ cm, the spire is 5 mm distant from the shield. The shield edges touch the box ones to avoid undesired fields on the measuring point.

The working frequency is set to 9 GHz. The simulation consists in the evaluation of the shielding efficiency given different source's distances and different shield's thicknesses. After, also the working frequency is been varied. Moreover, a second simulation consisted in two buckypapers spaced by an air gap.

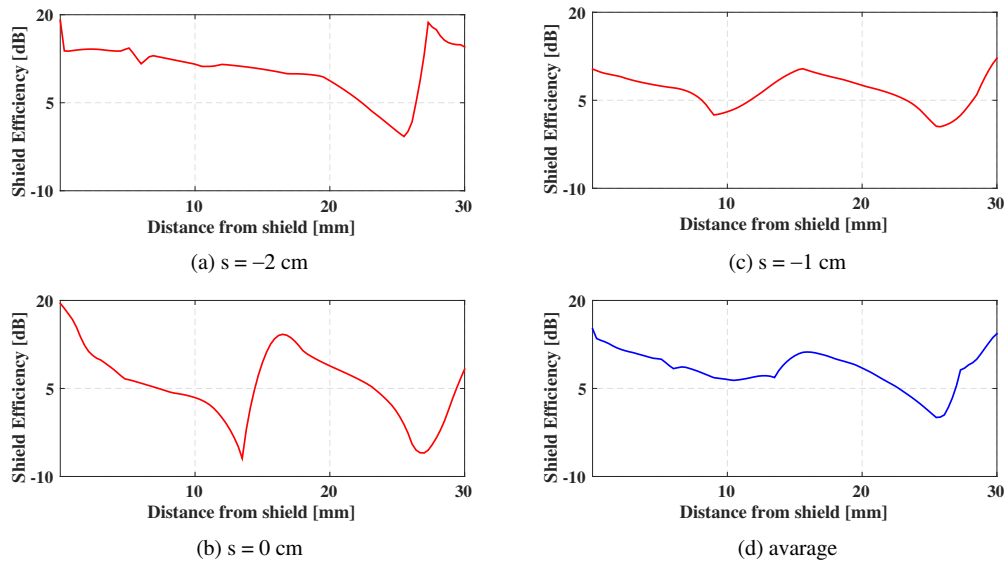


Figure 1: SE evaluated in different positions of the $5 \mu\text{m}$ shield, (a) is the SE for $s = -2$ mm, (b) is the SE for $s = 0$ mm, (c) is the SE for $s = -1$ mm, (d) is the SE for the average values of SE.

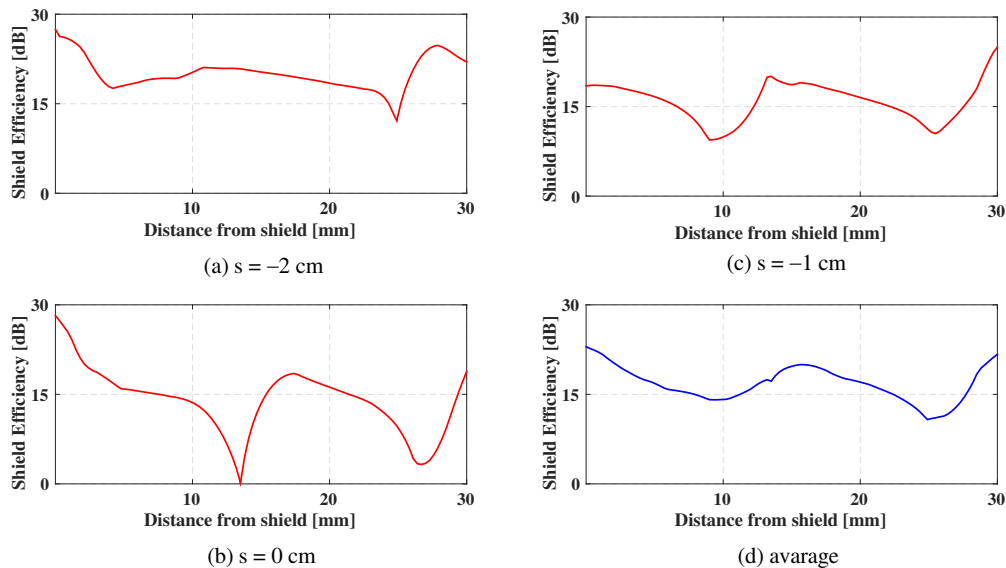


Figure 2: SE evaluated in different positions of the $20 \mu\text{m}$ shield, (a) is the SE for $s = -2$ mm, (b) is the SE for $s = 0$ mm, (c) is the SE for $s = -1$ mm, (d) is the SE for the average values of SE.

3. RESULTS

3.1. Single Screen

The field measurement has been along the screen with a step of $s = 1$ cm between two successive points, centered at $s = 0$ cm. The field intensity has been evaluated at a depth between 0 and 3 cm. For reasons of symmetry, the graphs show the shielding efficiency measured only on the right side of the screen. The results report the shielding efficiency in dB. The following results have been obtained by analyzing the shielding efficiency averaged over the points of evaluation, and by varying the shield thickness w .

With $w = 5 \mu\text{m}$ (Fig. 1(d)), the shielding efficiency varies between 0 and 15.5 dB (respectively evaluated at a distance of 0 and 25.1 mm)

With $w = 20 \mu\text{m}$ (Fig. 2(d)), the shielding efficiency varies between 11 and 23 dB (respectively evaluated at a distance of 0 and 25 mm)

With $w = 50 \mu\text{m}$ (Fig. 3(d)), the shielding efficiency varies between 16 and 25.8 dB (respectively evaluated at a distance of 0 and 25 mm)

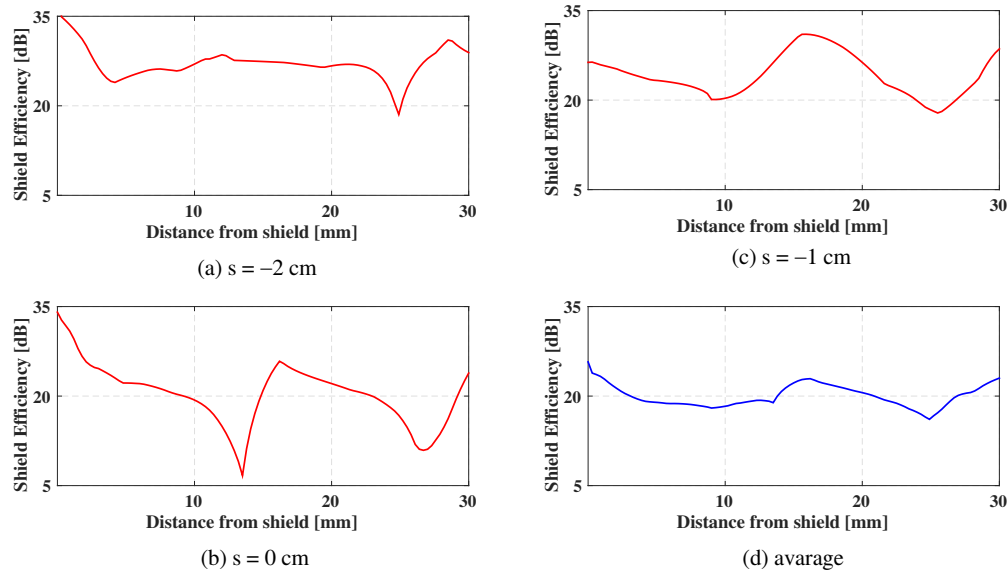


Figure 3: SE evaluated in different positions of the $50 \mu\text{m}$ shield, (a) is the SE for $s = -2 \text{ mm}$, (b) is the SE for $s = 0 \text{ mm}$, (c) is the SE for $s = -1 \text{ mm}$, (d) is the SE for the average values of SE.

3.2. Double Screen

The second simulation regards the two buckypapers case (Fig. 4(d)). It has measured a shielding efficiency which varies between 9 and 18.7 dB respectively evaluated at a distance of 0 and 25.1 mm.

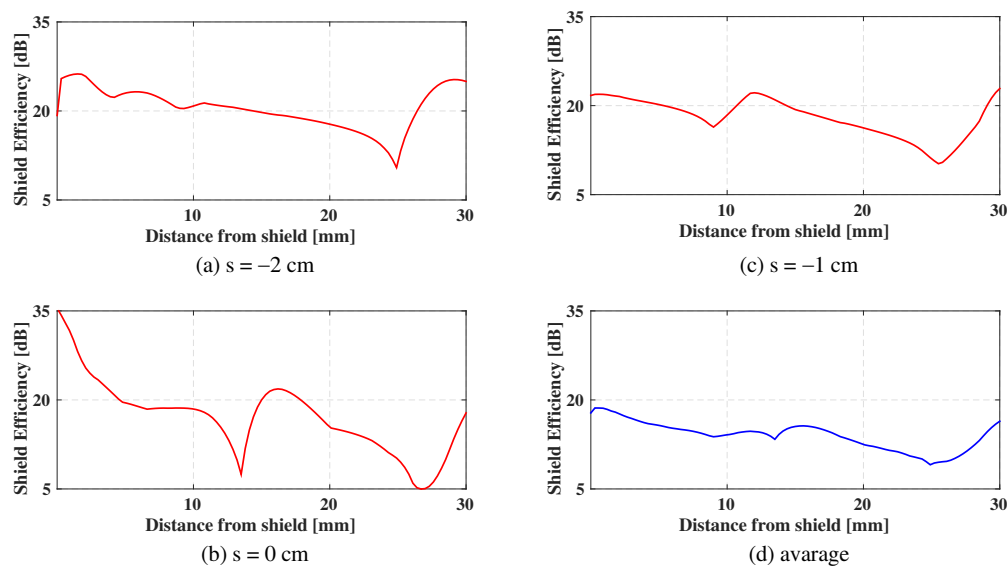


Figure 4: SE evaluated in different positions of the two shields, (a) is the SE for $s = -2 \text{ mm}$, (b) is the SE for $s = 0 \text{ mm}$, (c) is the SE for $s = -1 \text{ mm}$, (d) is the SE for the average values of SE.

As the results show, the buckypapers with a thickness of $5 \mu\text{m}$ are too thin and they don't produce useful results because the shielding efficiency is too low and too floating, so it's more

useful to analyze the cases with greater thicknesses. A thickness of 20 μm provides an higher efficiency in certain points of the screen, but it's a too floating results to be appreciate. Finally, a shield with a tickness of 50 μm provides the best results in terms of shielding efficiency and stability of the results.

4. CONCLUSION

The shielding efficiency is good only when the thickness of the screen is at least 50 μm , below which there are no significant results, but which allow us to have a screen thin enough to be used in medical equipment . Data from experiments encourage us to point out that carbon nanotubes are actually a great material to use as electromagnetic shield and they are rightly identified by the scientific community as the future universal shielding material. All this is absolutely true in electromedical equipment, in which the screen is characterized by a higher sensitivity compared to conventional electronic devices. Therefore the same solutions can be used in terms of shielding electromagnetic interference.

ACKNOWLEDGMENT

Work supported by Regione Autonoma della Sardegna, “Intervento INNOVA.RE”, under contract “Studio di Sistemi di Alimentazione di Dispositivi per la Medicina e per la Sicurezza”, number F25C10001420008. Marco Simone gratefully acknowledges Sardinia Regional Government for the financial support of his PhD scholarship (P.O.R. Sardegna F. S. E. Operational Programme of the Autonomous Region of Sardinia, European Social Fund 2007-2013 — Axis IV Human Resources, Objective 1.3, Line of Activity 1.3.1.)

REFERENCES

1. Clayton, P, R., *Introduction to Electromagnetic Compatibility*, Seconda Edizione, Ed., Wiley-Interscience, 2006.
2. Liu, L., L. B. Kong, W.-Y. Yin, and S. Matitsin, “Characterization of single- and multi-walled carbon nanotubes composites for electromagnetic shielding and tunable applications,” *IEEE Transactions on Electromagnetic Compatibility*, Vol. 53, Edizione 4, 943–949, 28 luglio 2011.
3. Wang, D., P. C. Song, C. H. Liu, W. Wu, and S. S. Fan, “Highly oriented carbon nanotube papers made of aligned carbon nanotubes” .

Secondary Instabilities of Steady Stationary Solution in Wide-aperture Lasers with Negative Detuning

D. A. Anchikov¹, A. V. Pakhomov^{1,2}, A. A. Krents^{1,2}, and N. E. Molevich^{1,2}

¹Department of Physics, Samara State Aerospace University, Samara 443086, Russia

²Theoretical Sector, Lebedev Physical Institute, Samara 443011, Russia

Abstract— Pattern formation and the evolution of complexity in spatially extended dynamical systems has been the subject of many investigations in widely diverse branches of science. In nonlinear optics, such studies have been motivated by the goal of developing a general understanding to describe the emergence of periodic and quasiperiodic patterns, vortices or spatial solitons using various nonlinear systems as well as gas, solid-state and semiconductor lasers. These systems are very complex devices having a rich spatiotemporal dynamics. The control parameter that determines the mechanism, which give rise to the transverse structure formation, is the Fresnel number.

In this work, we report on numerical and analytical investigations of the wave instability occurring for negative detuning (cavities tuned above resonance) in lasers class B. In that case, relations among the decay rate of polarization, the decay rate of population difference and the cavity rate were $\gamma_{\perp} \gg \gamma_{\parallel} \gg \kappa$. We use the Maxwell-Bloch equations to describe the dynamics of transverse patterns in single longitudinal mode lasers, where the active medium is composed of two level atoms inside a cavity with flat mirrors. An important parameter for determining the behavior of the system is the cavity detuning of field frequency from the atomic resonance transition frequency.

With increase of the pump level the homogeneous solution becomes unstable against spatiotemporal perturbations with a finite wavelength. We have numerically simulated the dynamics of laser field above the second laser threshold in one- and two-dimensional cases. In the result of stability loss of steady solution, the regime that evolves in the system consists of a sequence of switches between traveling wave solutions with different wave numbers. The laser intensity presents the areas of nearly constant values which interrupted by bursts of large amplitude oscillations. The sequence of wave numbers can be predicted as perturbation with highest growth rate.

We use analytical and numerical approaches to perform the linear stability analysis. We found that the regime of dynamical switches is the result of secondary instabilities. By both methods, the evolution may be predicted with a relatively good precision.

1. INTRODUCTION

Pattern formation and the evolution of complexity in spatially extended dynamical systems has been the subject of many investigations in widely diverse branches of science. In nonlinear optics, such studies have been motivated by the goal of developing a general understanding to describe the emergence of periodic [1] and quasiperiodic patterns [2], vortices [3] or spatial solitons [4] using various nonlinear systems as well as gas [5], solid-state [6] and semiconductor lasers [7]. These systems are very complex devices having a rich spatiotemporal dynamics. The control parameter that determines the mechanism, which gives rise to the transverse structure formation, is the Fresnel number.

In this work, we report on numerical and analytical investigations of the wave instability occurring for negative detuning (cavities tuned above resonance) in lasers class B. In that case, relations among the decay rate of polarization, the decay rate of population difference and the cavity rate were $\gamma_{\perp} \gg \gamma_{\parallel} \gg \kappa$. The large variety of spatio-temporal dynamics have been observed, including vortex lattices, high ordered structures, turbulence. In addition, class B lasers play a significant role in industrial applications, first, in communications. Therefore, the study of transverse laser field behavior becomes a relevant problem since it allow to determine the spatial coherence and the brilliance of the laser beam.

2. LINEAR ANALYSIS AND SIMULATION

We use the Maxwell-Bloch equations to describe the dynamics of transverse patterns in single longitudinal mode lasers, where the active medium is composed of two level atoms inside a cavity

with flat mirrors. These equations are normalized and take into account diffraction in one transverse direction x :

$$\begin{aligned}\frac{\partial E}{\partial t} &= ia \frac{\partial^2 E}{\partial x^2} + \sigma (P - E), \\ \frac{\partial P}{\partial t} &= -(1 + i\delta) P + DE, \\ \frac{\partial D}{\partial t} &= -\gamma \left[D - r + \frac{1}{2} (E^* P + EP^*) \right].\end{aligned}\quad (1)$$

E , P , D are obtained through normalization of the electric field, macroscopic polarization and the population inversion, respectively; $\gamma = \gamma_{\parallel}/\gamma_{\perp}$, $\sigma = k/\gamma_{\perp}$, where k , γ_{\perp} and γ_{\parallel} are the relaxation rates of field, polarization and inversion, respectively; $\delta = (\omega_{21} - \omega)/\gamma_{\perp}$ is the normalized detuning of field frequency from atomic resonant frequency; $a = c^2/(2\omega\gamma_{\perp}d^2)$ is diffraction parameter, where d is typical spatial size; r is pumping parameter.

An important parameter for determining the behavior of the system is the cavity detuning of field frequency from the atomic resonance transition frequency.

For positive detuning, the model theoretically predicts the off-axis radiation. For negative detuning, it predicts the paraxial radiation. In this work, we consider the dynamics for negative detuning. In this case, the spatially homogeneous solution is observed in the system above the lasing threshold. But, with exceeding of pumping, this mode becomes unstable against spatiotemporal perturbations with a finite wavelength (second lasing threshold).

In the result of stability loss of steady solution, the regime evolving in the system consists of a sequence of switches (Fig. 1) between traveling wave solutions with different wave numbers as described in [8].

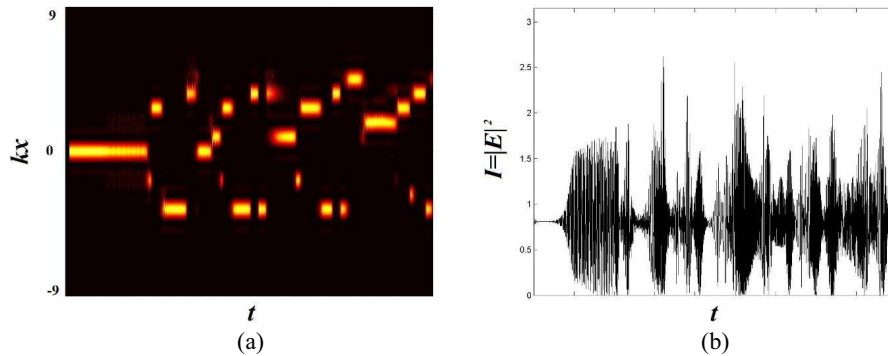


Figure 1: The time evolution of spatial Fourier spectrum (a) and intensity (b) at the parameters of the system: $\sigma = 0.03$, $\gamma = 5 \cdot 10^{-4}$, $\delta = -0.5$, $r = 2$, $a = 0.001$

An example of time dependence of spatial spectrum is presented in Fig. 1(a). The sequence of wave vectors can be predicted using linear stability analysis as perturbation with highest growth rate.

For this purpose, we apply a new analytical approach described in [9]. The wave number and frequency of mode with highest growth rate can be written as

$$q_{uns} = \sqrt[4]{\frac{2\gamma\sigma I_{st}}{(1 + \delta^2) a^2}}, \quad (2)$$

$$\Omega_{uns} = \sqrt{\frac{4\gamma\sigma I_{st}}{(1 + \delta^2)}}; \quad (3)$$

Also, we use a numerical approach to perform the linear stability analysis. At first, the system has been linearized around the homogeneous solution. The real part of eigenvalues versus wave number is plotted in Fig. 2. That curve is symmetric for negative wave numbers. The highest growth rate obtained numerically corresponds to the perturbation with the wave number $q_{uns} =$

2.28. According to (2), the analytical value of unstable wave number with the highest growth rate is $q_{uns}^T = 2.44$. As we can see, the difference is small and the results are very close to nonlinear simulation (Fig. 1(a)), where $q = 2.16$. In one-dimension case, we have two same directions for traveling waves, apparently the system selects one of them. Then we linearize the system around the next traveling wave solution with a certain wave number and so on.

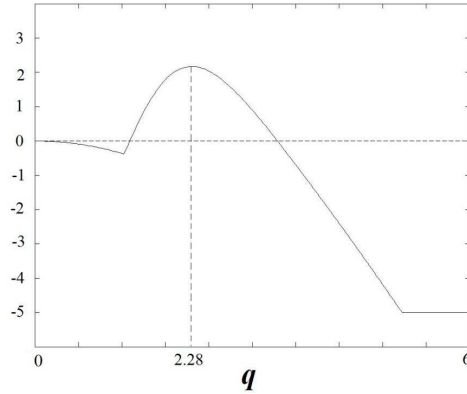


Figure 2: The growth rate of perturbation versus wave number.

Unlike dynamics in class A lasers, this case is more complex. The some noise exists in spatial spectrum and the laser intensity presents irregular large amplitude oscillations for all time evolution. But the sequence of wave numbers is repeated from cycle to cycle.

In two-dimensional simulation, we found that dynamics have not switches, but it is still irregular. In that case, a number of possible wave vector directions with the highest growth rate is infinite. And the ring-shaped image is obtained in the spatial spectrum at a linear stage of perturbation growth (Fig. 3(a)). After that, the optical turbulence takes place as shown in Fig. 3(b).

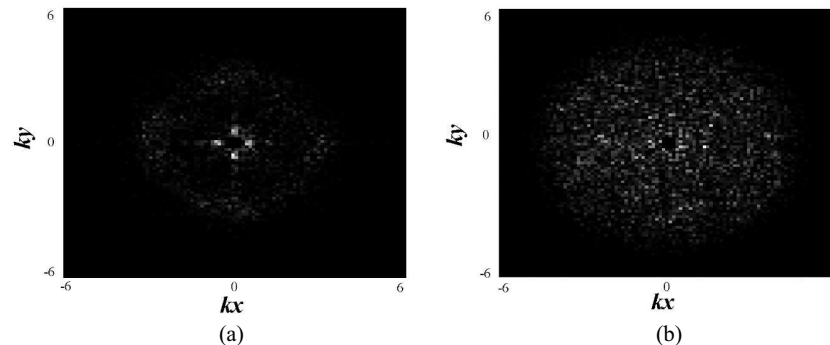


Figure 3: Spatial Fourier spectrum at a linear stage of perturbation growth (a) and optical turbulence (b), both with clipped central component.

3. CONCLUSION

Thus, we found that the regime of dynamical switches is the result of secondary instabilities. By both methods, the evolution may be predicted with a relatively good precision.

The study was supported in part by the Ministry of education and science of Russia under Competitiveness Enhancement Program of SSAU for 2013-2020 years and by State assignment to educational and research institutions under projects 1451, GR 114091840046, by RFBR under grant 14-02-31419 mol.a.

REFERENCES

1. Mamaev, A. V. and M. Saffman, *Opt. Commun.*, Vol. 128, 281, 1996.
2. Pampaloni, E., P. L. Ramazza, S. Residori, and F. T. Arecchi, *Phys. Rev. Lett.*, Vol. 82, 1434, 1999.

3. Rozas, D., Z. S. Sacks, and G. A. Swartzlander, *Phys. Rev. Lett.*, Vol. 7, 3399, 1997.
4. Barland, S., J. R. Tredicce, M. BRambilla, et al., *Nature*, 419, 699, London, 2002.
5. Encinas-Sans, F., I. Leyva, and J. M. Guera, *Phys. Rev. Lett.*, Vol. 84, 883, 2000.
6. Cabrera, E., O. Calderon, S. Melle, and J. M. Guera, *Phys. Rev. A*, Vol. 73, 053820, 2006.
7. O'Neil, E., J. Houlihan, J. G. McInerney, and G. Huyet, *Phys. Rev. Lett.*, Vol. 94, 143901, 2005.
8. Amroun, D., et al., *Physica D*, Vol. 203, 185–197, 2005.
9. Anchikov, D. A., A. V. Pakhomov, A. A. Krents, and N. E. Molevich, *Quantum Electron*, in print, 2015.

Cerenkov Radiation in Presence of Squeezed Electromagnetic Vacuum

Peter A. Meleshenko^{1,2}, Hang T. T. Nguyen³, Vladimir A. Gorlov¹,
Mikhail E. Semenov^{1,2,4}, and Alexander F. Klinskikh²

¹Zhukovsky-Gagarin Air Force Academy, Russia

²Voronezh State University, Russia

³Institute of Technology, Vietnam National University — Ho Chi Minh City, Vietnam

⁴Voronezh State University of Architecture and Civil Engineering, Russia

Abstract— In this work we investigate the Cerenkov radiation in the case of motion of a charged particle on a background of the squeezed electromagnetic vacuum. Using the quantum approach (time dependent perturbation theory) we obtain the explicit expression for the Cerenkov radiated power. The analysis of the obtained expression shows that in contrast to the “classical” case (where the Cerenkov radiation is a spontaneous process) the Cerenkov radiation in the squeezed vacuum has an induced character. The expression for radiated power contains two terms, namely the first term corresponds to radiation power, while the second one corresponds to absorption power.

1. INTRODUCTION

Cerenkov effect [1] have a long history but it remains relevant in relation to the different areas of application of such a phenomena (the wide list of publication on this subject takes place, see, e.g., [2–4] and related references). The expression for the radiated power was obtained by solving the equations of classical electrodynamics in the medium. A large number of studies have been devoted to other aspects of the Cerenkov effect. They concern the extension to the case of magnetic media, a detailed analysis of radiation in crystals, the role of boundaries, etc. The classical theory of spontaneous Cerenkov effect is fairly accurate, however the quantum analysis gives a more complete understanding of the phenomenon. Moreover, the quantum approach is most useful when considering the motion of a charged particle in a dielectric medium in the external electromagnetic wave. The radiation in this case has an induced nature and quantum approach gives a better understanding of the physical nature of phenomena.

Creation of powerful sources of electromagnetic radiation initiated extensive research in the area of particle-field interaction. The squeezed states of light [5] play an important role in such researches. These states generalize the well-known class of coherent states and are characterized by the fact that the uncertainty of one of the canonical variables of the electromagnetic field is less than in a conventional coherent state. The squeezed states are important in such areas as optical communication, interferometry, nonlinear optics, the detection of gravitational waves, etc. It should also be noted that the squeezed states are objects of purely quantum nature. So the description of the motion of a charged particle on a background of the squeezed vacuum can be performed using the quantum field theory only. This problem is of great practical interest (new sources of electromagnetic radiation such as free-electron lasers and Cerenkov lasers).

In this work we investigate the Cerenkov radiation in the case of motion of a charged particle on a background of the squeezed electromagnetic vacuum. Due to “purely” quantum nature of the squeezed vacuum we use the quantum approach, namely the time dependent perturbation theory.

2. CERENKOV RADIATION: QUANTUM DESCRIPTION

As is well known the Cerenkov radiation is electromagnetic radiation emitted when a charged particle (such as an electron) passes through a dielectric medium at a speed greater than the phase velocity of light in that medium. There are several approaches that describe this phenomenon, namely, the classical Tamm-Frank approach based on the solution of equations of classical electrodynamics, the Fermi approach based on the effect of radiative attenuation of an electron when it moves in the medium, as well as the of quantum-mechanical approach.

Here we would like to present the quantum-mechanical consideration of the Cerenkov radiation (we use the time-dependent perturbation theory). As is known, the hamiltonian of a charged

particle in the electromagnetic field in non-relativistic approach has the form

$$\hat{H} = \frac{1}{2m_e} \left(\hat{\vec{p}} - \frac{e}{c} \vec{A} \right)^2 - e\varphi. \quad (1)$$

Taking the gauge $(\nabla \cdot \vec{A}) = 0$, $\varphi = 0$ we can write

$$\hat{H} = \hat{H}_0 + \hat{V}_{int}, \hat{H}_0 = \frac{\hat{\vec{p}}^2}{2m_e}, \hat{V}_{int} = -\frac{e}{m_e c} \hat{\vec{p}} \hat{\vec{A}}, \quad (2)$$

where $\hat{\vec{A}}$ should be written in the second quantized form (also we neglect the quadratic term)

$$\hat{\vec{A}} = \sum_{\vec{k}, \sigma} \sqrt{\frac{2\pi\hbar v_c^2}{\omega_{\vec{k}} V \Sigma(\omega_{\vec{k}})}} \left(\vec{e}_{\vec{k}\sigma} \hat{a}_{\vec{k}\sigma} e^{i\vec{k}\vec{r} - i\omega_{\vec{k}}t} + \vec{e}_{\vec{k}\sigma}^* \hat{a}_{\vec{k}\sigma}^+ e^{-i\vec{k}\vec{r} + i\omega_{\vec{k}}t} \right), \quad (3)$$

where $v_c = c/n(\omega_{\vec{k}})$ is a phase velocity of the light in the medium with refractive index $n(\omega_{\vec{k}})$.

Using (2) we can write the expression for transition amplitude in the form¹:

$$a_{fi}(t) = -\frac{i}{\hbar} \int_0^t \langle f | \langle 1_{\vec{k}\sigma} | \hat{V}_{int}(t') | 0_{\vec{k}\sigma} \rangle | i \rangle dt' = -\frac{i}{\hbar} \int_0^t \langle f | \hat{V}_{\vec{k}\sigma}(t') | i \rangle dt', \hat{V}_{\vec{k}\sigma}(t') = \langle 1_{\vec{k}\sigma} | \hat{V}_{int}(t') | 0_{\vec{k}\sigma} \rangle. \quad (4)$$

The probability of single-photon process is determined by the expressions:

$$w(t) = \sum_{f, \vec{k}, \sigma} |a_{fi}(t)|^2 = \frac{1}{\hbar^2} \sum_{\vec{k}, \sigma} \int_0^t \int_0^t \langle i | \hat{V}_{\vec{k}\sigma}^+(t_1) \hat{V}_{\vec{k}\sigma}(t_2) | i \rangle dt_1 dt_2, \quad (5)$$

and

$$\hat{V}_{\vec{k}\sigma}(t') = -\frac{e}{m_e c} \sqrt{\frac{2\pi\hbar v_c^2}{\omega_{\vec{k}} V \Sigma(\omega_{\vec{k}})}} e^{-i\vec{k}\vec{r} + i\omega_{\vec{k}}t} (\vec{e}_{\vec{k}\sigma}^* \hat{\vec{p}}). \quad (6)$$

Using the explicit expression for $\hat{V}_{\vec{k}\sigma}(t)$ (6) we can write:

$$w(t) = \left(\frac{e}{\hbar m_e c} \right)^2 \sum_{\vec{k}, \sigma} \frac{2\pi\hbar v_c^2}{\omega_{\vec{k}} V \Sigma(\omega_{\vec{k}})} \int_0^t \int_0^t \langle i | (\vec{e}_{\vec{k}\sigma} \hat{\vec{p}}) e^{i\vec{k}\vec{r} - i\omega_{\vec{k}}t_1} e^{-i\vec{k}\vec{r} + i\omega_{\vec{k}}t_2} (\vec{e}_{\vec{k}\sigma}^* \hat{\vec{p}}) | i \rangle dt_1 dt_2. \quad (7)$$

Taking into account the explicit form of $\hat{\vec{r}}$ operator in Heisenberg representation² ((8) and making some transformations we obtain the following result

$$w(t) = \left(\frac{e}{\hbar m_e c} \right)^2 \sum_{\vec{k}, \sigma} \frac{2\pi\hbar v_c^2}{\omega_{\vec{k}} V \Sigma(\omega_{\vec{k}})} \int_0^t dt_1 \int_{-t}^t \langle i | (\vec{e}_{\vec{k}\sigma} \hat{\vec{p}}) \exp \left[\left(\frac{i\hbar k^2}{2m_e} - \frac{i\vec{k}\vec{p}}{m_e} + i\omega_{\vec{k}} \right) \tau \right] (\vec{e}_{\vec{k}\sigma}^* \hat{\vec{p}}) | i \rangle d\tau, \quad (9)$$

The second integral in this expression can be written in the form

$$\int_{-t}^t \exp \left[\left(\frac{i\hbar k^2}{2m_e} - \frac{i\vec{k}\vec{p}}{m_e} + i\omega_{\vec{k}} \right) \tau \right] (\vec{e}_{\vec{k}\sigma} \vec{p}) (\vec{e}_{\vec{k}\sigma}^* \vec{p}) d\tau,$$

¹In the Dirac notation the transition amplitude can be presented as [6] $a_{fi}(t) = -\frac{i}{\hbar} \int_0^t V_{fi}(t) dt = -\frac{i}{\hbar} \int_0^t \langle f | \hat{V}_{int}(t) | i \rangle dt$,

where $|i\rangle$ and $|f\rangle$ are the initial and final states of the considered system respectively.

²The explicit form of the $\hat{\vec{p}}$ and $\hat{\vec{r}}$ operators in Heisenberg representation are:

$$\hat{\vec{p}}^H = \hat{\vec{p}}^S, \hat{\vec{r}}^H \equiv \hat{\vec{r}}^H(t) = \hat{\vec{r}}^S + \frac{\hat{\vec{p}}^S}{m_e} t, \quad (8)$$

where indexes S and H indicates the Schrödinger and Heisenberg representations respectively.

where we have used the obvious relations $\hat{p}|i\rangle = \vec{p}|i\rangle$ and $\langle i|i\rangle = 1$.

After summation by photon polarization³ and summation by \vec{k} we obtain the following expression for $w(t)$:

$$w(t) = \frac{e^2 v_e^2}{4\pi^2 \hbar c^3} \int \omega n(\omega) \sin^2 \theta d\Omega d\omega \int_0^t dt_1 \int_{-t}^t \exp \left[i \left(\hbar \frac{n^2(\omega)\omega^2}{2m_e c^2} - \frac{v_e}{c} n(\omega)\omega \cos \theta + \omega \right) \tau \right] d\tau, \quad (10)$$

where $v_e = p/m_e$ is an initial velocity of an electron. The last integral in this expression can be found using the definition of the Dirac δ -function⁴.

The full radiated power can be obtained by multiplying the expression for radiation probability per time unit $dw = \lim_{t \rightarrow \infty} \frac{dw(t)}{t}$ on the energy of radiated photon $\hbar\omega$ and integrating over ω :

$$P_{rad} = \frac{e^2 v_e}{c^2} \int_0^\infty \omega \left[1 - \left(\frac{\hbar n(\omega)\omega}{2m_e c v_e} + \frac{c}{n(\omega)v_e} \right)^2 \right] \Theta \left(1 - \left| \frac{\hbar n(\omega)\omega}{2m_e c v_e} + \frac{c}{n(\omega)v_e} \right| \right) d\omega. \quad (11)$$

Transition to classical limit leads to the following well-known results:

$$P_{rad} = \frac{e^2 v_e}{c^2} \int_0^\infty \omega \left[1 - \left(\frac{c}{n(\omega)v_e} \right)^2 \right] \Theta \left(1 - \frac{c}{n(\omega)v_e} \right) d\omega. \quad (12)$$

$$\cos \theta_0(\omega) = \frac{c}{n(\omega)v_e}. \quad (13)$$

Based on the results obtained above we can take the following conclusion on the nature of Cerenkov radiation: *Cerenkov radiation is the result of interaction of charged particle with the electromagnetic vacuum which is changed by a medium, nor the interaction with a medium.*

3. CERENKOV RADIATION IN PRESENCE OF SQUEEZED ELECTROMAGNETIC VACUUM

3.1. Squeezed Electromagnetic Vacuum: Some Basic Results

Following Stoler's ideology the squeezed state is determined as an eigenstate of operator \hat{b} which is connected with \hat{a}^+ and \hat{a} as [5]:

$$\hat{b} = \mu \hat{a} + \nu \hat{a}^+, \quad \hat{b}^+ = \nu^* \hat{a} + \mu^* \hat{a}^+, \quad (14)$$

where

$$|\mu|^2 - |\nu|^2 = 1, \quad \mu \equiv \cosh r, \quad \nu \equiv e^{i\vartheta} \sinh r, \quad (15)$$

where r and ϑ are defined below. In the calculations with the squeezed states important role plays the so-called squeezing operator (the operator of unitary transformation of coherent state to squeezed state) introduced by Stoler:

$$\hat{D}(\eta) = \exp \left[\frac{1}{2} \eta^* (\hat{a})^2 - \frac{1}{2} \eta (\hat{a}^+)^2 \right], \quad (16)$$

where $\eta = r e^{i\vartheta}$ is an arbitrary complex number. The state

$$|(\eta, \alpha)\rangle \equiv \hat{T}(\alpha) \hat{D}(\eta) |0\rangle \quad (17)$$

³Summation by photon polarization can be made using the standard procedure [6], namely, $\overline{e_i e_k^*} = \frac{1}{2} (\delta_{ik} - n_i n_k)$; $\sum_\sigma (\vec{e}_{k\sigma} \vec{p})(\vec{e}_{k\sigma}^* \vec{p}) = [|\vec{p} \times \vec{n}|]^2$.

⁴We use the following well-known relations: $\delta(\omega) = \lim_{t \rightarrow \infty} \frac{1}{2\pi} \int_{-t}^t e^{-i\omega t'} dt'$; $\delta(\lambda\xi) = \frac{1}{|\lambda|} \delta(\xi)$; $\int_{-1}^1 (1-x^2)\delta(x-x_0)dx = (1-x_0^2)\Theta(1-|x_0|)$, where $\Theta(\xi)$ is a standard Heaviside step-function.

is called as *an ideal squeezed state* (here \hat{T} is the translation operator, $|0\rangle$ is an ordinary vacuum state).

Let us consider also the dynamics of ideal squeezed state (17) in time. The state $|(\eta, \alpha)(t)\rangle$ retains meaning as squeezed state, only the coefficients μ and ν change

$$\mu(t) = \mu e^{i\omega t}, \nu(t) = \nu e^{i\omega t}$$

while the condition (15) still the same.

Average number of photons in ideal squeezed state $|(\eta, \alpha)\rangle$ is determined by the expression:

$$\langle(\eta, \alpha)|\hat{a}^+\hat{a}|(\eta, \alpha)\rangle = |\alpha|^2 + |\nu|^2. \quad (18)$$

Square of dispersion of the squeezed state, minimal and maximal values of the dispersion are:

$$D^2(t) = \frac{\hbar}{2\omega} [|\mu|^2 + |\nu|^2 - 2|\mu||\nu| \cos(\vartheta + 2\omega t)], D_{min}^2 = \frac{\hbar}{2\omega} (|\mu| - |\nu|)^2, D_{max}^2 = \frac{\hbar}{2\omega} (|\mu| + |\nu|)^2. \quad (19)$$

Squeezed state is characterized by the squeezing coefficient

$$K = \sqrt{\frac{D_{max}}{D_{min}}} = |\mu| + |\nu|. \quad (20)$$

This coefficient changes in the range from 1 for coherent state ($|\nu| = 0$) to big values for strongly squeezed states ($|\nu| \rightarrow \infty$). It should also be pointed out that squeezed vacuum radically differs from usual vacuum (as a lowest state of the field). Namely, the squeezed vacuum can be a high-excited and high-energy state of the field.

3.2. Cerenkov Radiation in Presence of Squeezed Electromagnetic Vacuum

Now let us generalize the problem, namely we will find the analytic expressions for probabilities per time unit for all the transitions from initial state of an electron when it moves in the medium in the presence of the squeezed vacuum.

As previously, let $|i\rangle$ and $|f\rangle$ are the initial and final states of an electron respectively. For the squeezed states we will use the following notations: initial state of electromagnetic field with mode \vec{k} and polarization σ : $|0_{\vec{k}\sigma}\rangle \equiv |(0, \eta)_{\vec{k}\sigma}\rangle$; final state of electromagnetic field with mode \vec{k} and polarization σ : $|\zeta_{\vec{k}\sigma}\rangle \equiv |(\alpha, \eta')_{\vec{k}\sigma}\rangle$.

Taking into account the presented notations the transition amplitude in the first order of perturbation theory can be written as:

$$a_{fi}(t) = -\frac{i}{\hbar} \int_0^t \langle f | \langle \zeta_{\vec{k}\sigma} | \hat{V}_{int}(t') | 0_{\vec{k}\sigma} \rangle | i \rangle dt' = -\frac{i}{\hbar} \int_0^t \langle f | \hat{V}_{\vec{k}\sigma}(t') | i \rangle dt', \hat{V}_{\vec{k}\sigma}(t') = \langle \zeta_{\vec{k}\sigma} | \hat{V}_{int}(t') | 0_{\vec{k}\sigma} \rangle. \quad (21)$$

As previously, we assume that the time leads to infinity $t \rightarrow \infty$.

Squaring of a_{fi} and summation by final states $|\zeta_{\vec{k}\sigma}\rangle$ and $|f\rangle$ gives:

$$\sum_{f\zeta_{\vec{k}\sigma}} a_{fi}^*(t) a_{fi}(t) = \sum_{\zeta_{\vec{k}\sigma}} \frac{1}{\hbar^2} \int_0^t \int_0^t \langle i | \hat{V}_{\vec{k}\sigma}^+(t_1) \hat{V}_{\vec{k}\sigma}(t_2) | i \rangle dt_1 dt_2, \quad (22)$$

where $\hat{V}_{\vec{k}\sigma}$ is determined in (21) and \hat{V}_{int} has the form (2). Operator of electromagnetic field has the form (3) and the fact that this operator describes the squeezed vacuum state we take into account in calculations of the matrix elements. Simplification of the matrix element in the last expression can be made using these simple relations:

$$\langle 0_{\vec{k}\sigma} | (\hat{a}_{\vec{k}\sigma})^2 | 0_{\vec{k}\sigma} \rangle = -\mu^* \nu, \langle 0_{\vec{k}\sigma} | (\hat{a}_{\vec{k}\sigma}^+)^2 | 0_{\vec{k}\sigma} \rangle = -\mu \nu^*, \langle 0_{\vec{k}\sigma} | \hat{a}_{\vec{k}\sigma}^+ \hat{a}_{\vec{k}\sigma} | 0_{\vec{k}\sigma} \rangle = |\nu|^2.$$

As previously, using the expression for \hat{r} operator in Heisenberg representation (8) and making the procedures in the same way as in previous section we obtain the following expression for radiated

power⁵:

$$P = P_1 + P_2,$$

$$P_1 = (1 + |\nu|^2) \frac{e^2 v_e}{c^2} \int_0^\infty \omega \left[1 - \left(\frac{\hbar n(\omega) \omega}{2m_e c v_e} + \frac{c}{n(\omega) v_e} \right)^2 \right] \Theta \left(1 - \left| \frac{\hbar n(\omega) \omega}{2m_e c v_e} + \frac{c}{n(\omega) v_e} \right| \right) d\omega, \quad (23)$$

$$P_2 = |\nu|^2 \frac{e^2 v_e}{c^2} \int_0^\infty \omega \left[1 - \left(\frac{\hbar n(\omega) \omega}{2m_e c v_e} - \frac{c}{n(\omega) v_e} \right)^2 \right] \Theta \left(1 - \left| \frac{\hbar n(\omega) \omega}{2m_e c v_e} - \frac{c}{n(\omega) v_e} \right| \right) d\omega.$$

This expression contains two terms. First term corresponds to radiation power, and the second one corresponds to absorption power.

4. CONCLUSIONS

In this paper we have considered the Cerenkov radiation in the case when the charged particle moves in the medium in the presence of squeezed electromagnetic vacuum. Because of purely quantum nature of squeezed vacuum we use the quantum-mechanical approach (time-dependent perturbation theory) for calculation of the radiated power. We obtain the expression for single-photon process in the case when an electron moves in the medium in the presence of squeezed electromagnetic vacuum. This expression shows that in this case there are two terms: first term corresponds to radiation, while the second one corresponds to absorption. This fact is connected with the complex structure of the squeezed vacuum in contrast to the ordinary vacuum state. Moreover, application of the quantum approach to the Cerenkov radiation problem allows us to formulate the following result: *Cerenkov radiation is the result of interaction of the charged particle with the electromagnetic vacuum which is changed by a medium, nor the interaction with a medium.*

REFERENCES

1. Cherenkov, P. A., “Visible radiation produced by electrons moving in a medium with velocities exceeding that of light,” *Physical Review*, Vol. 52, 378–379, 1937.
2. Altschul, B., “Cerenkov radiation in a Lorentz-violating and birefringent vacuum,” *Phys. Rev. D*, Vol. 75, 105003(1–9), 2007.
3. Gal’tsov, D. V., E. Yu. Melkumova, and K. Salehi, “Cerenkov radiation from moving straight strings,” *Phys. Rev. D*, Vol. 75, 105013(1–22), 2007.
4. Altschul, B., “Absence of long-wavelength Cerenkov radiation with isotropic Lorentz and CPT violation,” *Phys. Rev. D*, Vol. 90, 021701(1–5), 2014.
5. Scully, M. O. and M. S. Zubairy, *Quantum Optics*, Cambridge University Press, 1997.
6. Landau, L. D. and E. M. Lifshitz, *Quantum Mechanics (Nonrelativistic Theory)*, Pergamon, Oxford, 1977.

⁵We do not present step by step calculations of the matrix elements due to a large volume of intermediate transformations which, nevertheless, are simple, but tiresome.

Frequency Characterization of Planar Resonators by THz Josephson Spectroscopy

A. V. Snezhko^{1,2}, O. Y. Volkov¹, V. N. Gubankov¹, I. I. Gundareva^{1,3},
Y. Y. Divin^{1,3}, V. V. Pavlovskiy¹, and V. I. Pokalyakin¹

¹Kotelnikov Institute of Radio Engineering and Electronics of RAS, Russian Federation

²Moscow Institute of Physics and Technology, Russian Federation

³Peter Grunberg Institute, Forschungszentrum Julich, Germany

Abstract— Broadband electromagnetic measurement at frequencies above 100 GHz is still challenging problem because of limited frequency ranges of oscillators, complicated matching networks and ambiguous deembedding procedures. It is known that Josephson junction (JJ) is very sensitive to electromagnetic environment. Josephson terahertz spectroscopy is based on ac Josephson effect in high-temperature superconducting junctions. Here we extend this method to perform spectral characterization of planar open ring resonators on separate substrates. We have studied resonator characteristics at frequencies from 50 GHz to 700 GHz, using $\text{YBa}_2\text{Cu}_3\text{O}_{7-x}$ high- T_c bicrystal grain boundary junctions on NdGaO_3 and MgO substrates. Differential resistance vs. voltage curves modified by the interaction of JJ with resonator have been analyzed. An excitation of fundamental resonance mode in the planar resonator by Josephson oscillations was demonstrated. The technique developed might be used for frequency characterization of THz photonic elements and structures.

1. INTRODUCTION

In recent years, significant efforts have been made towards development of microelectronic devices for submillimeter wave applications. Recently it was demonstrated InP high electric mobility transistor based amplifiers operating at frequencies up to 1.3 THz [1]. However, measurement and characterization of submillimeter wavelength integrated circuits and their active and passive components have always been a challenge, Network analyzers that can continuously vary the operating frequency from 40 kHz to 125 GHz are conventionally used for characterization of on-wafer planar components. Modern devices based on semiconductor frequency multipliers can increase their operating frequency up to 1 THz; however, they have narrow range of continuously tunable frequencies, which hampers their wide application. Moreover, at frequencies above 100 GHz, there are some difficulties in ensuring electromagnetic coupling of submillimeter and micron scale devices under test with the external network analyzer. This coupling is provided with the help of numerous waveguide sections and special high-frequency microprobes. Actually, measurements are performed at the external inputs of waveguides, and special deembedding procedures are used to extract parameters of the device under test [2]. These procedures include calibration measurements with the use of special calibration standards and data processing, which decreases the accuracy of the results obtained. As a result, recently, a number of on-chip characterization methods have been proposed, which should overcome drawbacks of commonly used measurement techniques. In these methods, the high-frequency part of the measurement device is integrated with the device under test on the same wafer. The main problem in realization of this method is to develop on-chip oscillator with rather high frequency. The usage of superconducting Josephson oscillator may have an advantage over other methods especially for characterization of low-temperature devices.

Few decades ago it was shown, that Josephson junction (JJ) is very sensitive to its electrodynamic environment. When Josephson junction is placed into a substance with the dispersion or attached to lumped elements with frequency-dependent characteristics, Josephson oscillations waveform is modified. This affects the dc IV -curve of the junction. It was shown that JJ can be used at the millimeter-wave wavelength range for indication of characteristic frequencies of a Fabry-Perot resonator [3], resonances in LC -circuits and coaxial lines, attached to the junction and absorption spectral lines of various substances, deposited on the weak link [4, 5]. In modern JJ, based on high- T_c superconductors (HTSC), oscillations were observed at frequencies up to 5 THz. It was demonstrated applications of HTSC JJ for frequency characterization of microstrip transmission line resonator [6] and planar antenna structures [7–9] integrated with JJ on the same wafer in frequency range from 60 to 1100 GHz. In this article we demonstrate the technique for spectral characterization of planar open-ring resonators with the usage of JJ on separate wafer.

2. THE INFLUENCE OF EXTERNAL ELECTRODYNAMIC ENVIRONMENT ON JOSEPHSON JUNCTION

It is known that dc characteristics of JJ are modified under the influence of electromagnetic environment, This modification may be caused by a variety of physical mechanisms, e.g., electromagnetic losses in materials of JJ and substrate, the influence of absorptive environment, antenna or other electromagnetic structures. In resistively-shunted junction (RSJ) model [10] the effect of all these mechanisms on JJ can be considered by a frequency-dependent complex admittance $Y_{ext}(f)$, connected to the junction in parallel. It was shown in [11] that in the case of weak binding of JJ with the environment, a deviation $\delta V(I)$ of the IV -curve, measured at current bias I , can be described by following equation:

$$\delta V(I) = R_n(IR_n - V)\text{Re}\{Y_{ext}(2eV/h)\} \quad (1)$$

where $V = R_n\sqrt{I^2 - I_c^2}$ is the unperturbed voltage at the given current I , which is proportional to the Josephson frequency f as $V = hf/2e$, I_c is the critical current and R_n is the normal-state resistance of JJ. The expression (1) performs mapping of frequency domain into voltage domain by Josephson relation $f = 2eV/h$. Therefore frequency dependent admittance of the external electrodynamic system can be reconstructed from dc characteristics of JJ. In practice to examine spectral characteristics of external circuits it is more suitable to measure differential resistance vs. voltage dependence $R_d(V)$ of JJ interacting with them.

The expression (1) was obtained for the general form of $Y_{ext}(f)$ in RSJ model, neglecting thermal fluctuations of normal currents. At finite temperatures, monochromatic spectra of Josephson oscillations are broadened by thermal fluctuations, which significantly modify characteristic features on the IV -curves, related to external resonances. Due to this broadening, Josephson spectral analysis can be carried out at frequencies above a low-frequency limit, determined by thermal fluctuations [9]. To provide spectral analysis of electromagnetic structures at frequencies not far above this limit, a modification of IV -curves and $R_d(V)$ -dependencies by thermal fluctuations should be taken into account, even at low temperatures.

Characteristics of high- T_c bicrystal junctions are described by the RSJ model with high accuracy, which simplifies the analysis. To take into account the influence of thermal fluctuations, we used an equivalent circuit of a Josephson junction with resonant electrodynamic structure, shown in Fig. 1.

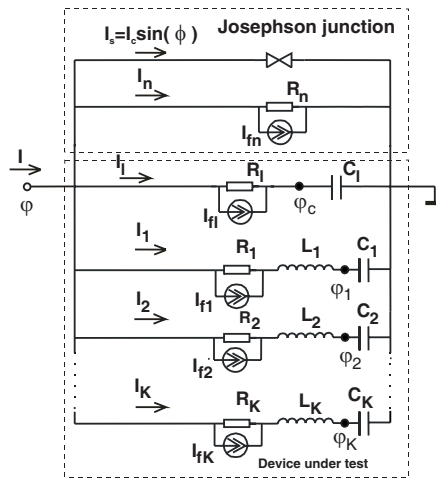


Figure 1: Equivalent circuit of Josephson junction with external electrodynamic system.

According to RSJ model, a Josephson junction is presented as an element with superconducting I_s and normal I_n currents. External structure is approximated by a set of RLC circuits. An averaged influence of the structure, which is not taken into account in the resonance circuits, and other electromagnetic environment of the junction in a broad frequency range is taken into account by $R_l C_l$ circuit, connected in parallel to the junction. Each resistor in the equivalent circuit is considered as a source of thermal fluctuation currents I_f , approximated by white noise. DC characteristics of JJ (IV -curve and voltage dependence of differential resistance $R_d(V)$) can be obtained from numerical solution of the equation set, related to the equivalent circuit. Spectral analysis of external system can be performed by fitting of calculated JJ dc characteristics to measured ones [8].

3. DETAILS OF THE EXPERIMENT

We used a grain boundary JJ to probe a $\text{Al}_2\text{O}_3/\text{Cu}/\text{PMMA}$ planar resonator. JJs were formed from epitaxial (001) $\text{YBa}_2\text{Cu}_3\text{O}_{7-x}$ thin films of 250 nm thickness deposited on the bicrystal MgO ($\epsilon=9.5$) and NdGaO_3 ($\epsilon=22$) substrates where ϵ is dielectric permittivity. Resonators had square shapes with side dimensions varied from 30 μm to 400 μm . They were formed from the copper film of 300 nm thickness on sapphire substrate with $\epsilon=10.7$ and were covered by PMMA with $\epsilon = 2.5$. Resonators were attached to JJ and were positioned in the vicinity of weak link as it shown at Figs. 2(a), (b). Resonator and JJ interlayer distance has not been controlled in our experiment (this is shown by rough line in Fig. 2(b), and may be up to few tens of microns).

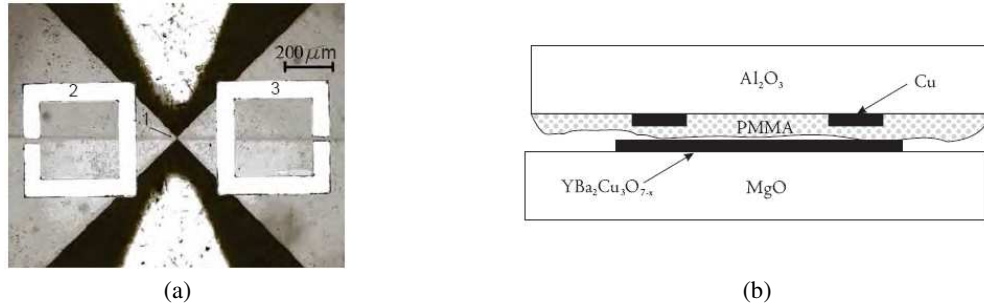


Figure 2: (a) Josephson junction 1 with open ring resonators 2,3. (b) Layers arrangement.

PMMA layer prevented ohmic contact between resonator and JJ. Excitation of resonators were performed by the Josephson oscillations through the capacitance between resonators and triangle-shaped superconducting leads. Geometry of JJ leads provides a smooth impedance vs. frequency dependence, as well as sharp features at the spectral characteristic are related to interaction with resonant structure. The junction with resonators attached was mounted on a cryogenic dipstick and was placed into a liquid-helium dewar. The IV -curves and $R_d(V)$ were measured at the temperature range from 5 to 90 K. A coupling of JJ with resonator at various frequencies is determined by JJ differential resistance which depends on JJ characteristic voltage $V_c = I_c R_n$. To cover wide frequency range we used two types of JJ: JJ on MgO substrate with $V_c = 0.8$ mV and JJ on NdGaO_3 substrate with $V_c = 3$ mV at $T = 5$ K. In addition, V_c was varied by external magnetic field up to 100 G.

4. RESULTS AND DISCUSSION

$R_d(V)$ of JJ attached to resonators of various dimensions are presented at Fig. 3. Excitations of the resonators manifest themselves as sharp features at voltages, which are scaled with resonator side length. To obtain each curve V_c was tuned by magnetic field to obtain optimal coupling at resonance frequency.

Resonance features were observed at frequencies from 50 to 120 GHz on MgO based JJ characteristics and from 80 to 700 GHz on NdGaO_3 based JJ characteristics. A feature related to 125 GHz resonance frequency of 148 μm size resonator was observed in characteristics of both resonators at 248 μV (curve 4 at Fig. 3(a)) and 257 μV (curve 4 at Fig. 3(b)). This small difference (3.5%) indicates that JJ substrate permittivity has a minor influence on resonance frequency which can be explained by rather large interlayer distance between resonator and JJ (more than 30 μm according to estimations).

Resonant frequencies and other parameters of resonators were obtained from the analysis of measurement data based on resistively shunted model of JJ and equivalent circuit (Fig. 1) of JJ interacting with the resonator [8]. Main RSJ parameters (I_c and R_n) were obtained from measured JJ IV -curve, as well as LC -circuit parameters were obtained by fitting calculated $R_d(V)$ dependence to measured one. The results for 233 μm size resonator are presented at Fig 4. It was obtained that calculated curve corresponds to excitation of a resonator with resonance $f_r = 74.9$ GHz and quality factor $Q = 25$. If we assume excitation of fundamental resonance mode (LC -mode) then physical length of the resonator should be equal to half-guided-wavelength $\lambda_r/2$ [12]. Therefore an effective permittivity of resonator environment ϵ_{eff} can be estimated: $\epsilon_{eff} = \lambda_0/f_r = 6.4$. This value is close to $\epsilon_{eff} = 0.5(\epsilon_{\text{Al}_2\text{O}_3} + \epsilon_{\text{PMMA}}) = 6.1$, estimated from the resonator layout. A 5% difference can be explained by the influence of MgO substrate.

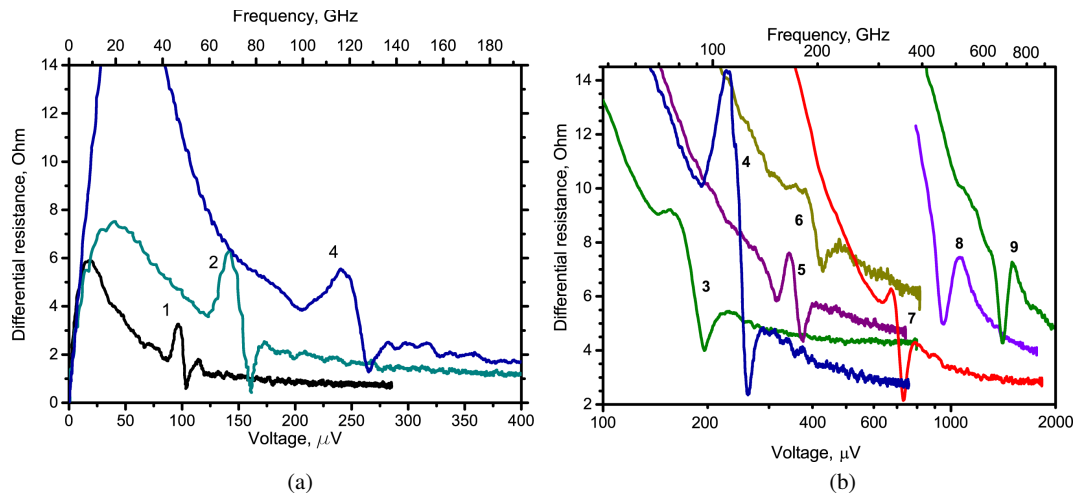


Figure 3: Differential resistance vs. voltage dependence of JJ on MgO (a) and NdGaO₃ (b) substrates with open ring resonators of various sizes: 1 — 370 μm, 2 — 233 μm, 3 — 186 μm, 4 — 148 μm, 5 — 115 μm, 6 — 92 μm, 7 — 58 μm, 8 — 46 μm, 9 — 33 μm.

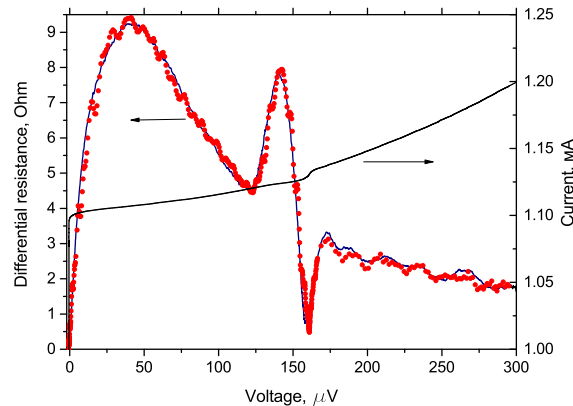


Figure 4: *IV*-curve and differential resistance vs voltage dependence of Josephson junction with 233 μm open ring resonators. Dotted line — measurement data, solid line — the results of numerical simulation.

5. CONCLUSION

Josephson spectroscopy was applied for frequency analysis of open ring resonators at frequencies from 50 to 700 GHz. Planar resonators on separate wafers were attached to HTSC bicrystal Josephson junction and junction dc characteristics (*IV*-curve and $R_d(V)$) were measured. JJ characteristics shown features at voltage values, which correspond to resonance frequencies according to Josephson relation. A detailed analysis of 233 μm side length resonator was performed using numerical simulation of JJ with resonator based on RSJ model. A resonance frequency $f_r = 74.9$ GHz was obtained and resonator quality factor was estimated. It was shown that resonance corresponds to excitation of resonator *LC*-mode.

ACKNOWLEDGMENT

This work was supported by RFBR Grant #14-07-31323.

REFERENCES

- Deal, W. R., "InP HEMT for sub-millimeter wave space applications: challenges and status," *Proceedings of 39th Int. Conf. on Infrared, Millimeter, and THz Waves*, Tucson, AZ, USA, September 14–19, 2014.
- Yau, K. H. K., I. Dacquay, I. Sarkas, et al., "Device and IC characterization above 100 GHz," *IEEE Microwave Magazine*, Vol. 13, 30–54, 2012.
- Ulrich, B. T. and E. O. Kluth, "Josephson junction millimeter microwave source and homodyne detector," *Proceedings of the IEEE*, Vol. 61, 51–54, 1973.

4. Silver, A. H. and J. E. Zimmerman, "Quantum resonance spectroscopy through weakly connected superconductors," *Applied Physics Letters*, Vol. 10, 142–145, 1967.
5. Puma, M. and B. S. Deaver, "Temperature dependence of structure on I-V curves of superconducting point contacts," *Applied Physics Letters*, Vol. 19, 539–541, 1971.
6. Edstam, J. and H. Olsson, "Josephson broadband spectroscopy to 1 THz," *Applied Physics Letters*, Vol. 64, 52733–2735, 1994.
7. Volkov, O. Y., Y. Y. Divin, V. N. Gubankov, et al., "Josephson admittance spectroscopy of log-periodic antenna at the submillimeter wavelength range," *Journal of Communications Technology and Electronics*, Vol. 54, 1310–1314, 2009.
8. Volkov, O. Y., Y. Y. Divin, V. N. Gubankov, et al., "Terahertz characterization of external resonant systems by high-Tc Josephson junctions," *IEEE Transactions on Applied Superconductivity*, Vol. 21, 306–310, 2011.
9. Pavlovskiy, V. V., I. I. Gundareva, O. Y. Volkov, et al., "Extension of the frequency range of Josephson impedance spectroscopy," *Journal of Communications Technology and Electronics*, Vol. 58, 951–955, 2013.
10. Likharev, K., *Dynamics of Josephson Junctions and Circuits*, Gordon and Breach, New York, 1986.
11. Volkov, A. F., "External circuit impedance influence on current-voltage characteristic of Josephson junction," *Radiotekhnika I Elektronika*, Vol. 17, 2581–2583, 1972.
12. Collin, R. E., *Foundations for Microwave Engineering*, McGraw-Hill, New York, 1992.

Dynamical Model of Elastic-plastic Hysteresis in Fullerenes Film

Boris M. Darinsky¹, Mikhail E. Semenov^{1, 2, 3},
Andrey M. Semenov¹, and Peter A. Meleshenko^{1, 2}

¹Voronezh State University, Voronezh, Russia

²Zhukovsky-Gagarin Air Force Academy, Voronezh, Russia

³Voronezh State University of Architecture and Civil Engineering, Voronezh, Russia

Abstract— In this paper the model of the unusual elastic-plastic hysteresis is presented and discussed in connection with the recent progress in investigation of fullerene films. The constructive model is based on the operator technique for hysteretic nonlinearities, namely, in order to describe the input-output conformity we use the Ishlinkii operator together with the probability model based on the Kolmogorov-Chapman equation.

1. INTRODUCTION

The hysteretic effects take place in various areas of material science (both in macro and micro levels). Depending on the purposes of investigation both the phenomenological and constructive models can be used and there are many literature sources on this subject (see, e.g., [1] and related references). As a rule in the constructive models which are described by the relations “input-state” “state-output” [2, 3] the dynamical properties of the hysteresis carrier have not been taken into account. It is a well-known fact that the mechanical properties almost all the materials (these properties are the elastic-plastic hysteresis) remain unchanged (hysteretic dependence of elastic-plastic materials does not depend on the speed of mechanical affection). However, the results of experiments with the fullerene nanofilms [4] show that the hysteretic curve in the coordinates “force-displacement” depends on the speed of force application.

In this work we propose the dynamical probability model of hysteresis for description of elastic-plastic properties of nanoscale fullerene film taking into account the electromagnetic nature of fullerene clusters binding. This model is based on the fact that the decay law for fullerene supercluster $[C_{60}]_n$ (especially for $n = 2$) depends on the external conditions (temperature, pressure, etc.) as well as has a probability nature. The description of the decay law in the macroscopic level can be made using the theory of random processes (Kolmogorov-Chapman equation).

2. HYSTERESIS IN NANOSCALE FILMS

In recent years the self-regenerating covers are intensively investigated [4–6]. Such covers regenerate when on its surface a little injury takes place. Usually, such covers contain the capsules with the “regenerating agent”. When the damage takes place the capsules break and as a result there are chemical reactions that lead to vanishing of injury. In this work we consider the covers that have a self-regenerating properties, but such an effect provides by the hysteretic properties of the cover’s material. This cover is coated by two beams of buckyball, namely the molecular (PVD technology) and ion (magnetron technology). In the base of the regeneration effect lies the abnormal elastic-plastic hysteresis which is caused by the depolymerization of fullerene. As was shown in [4] on the surface of nanofilm there are some “liftings” at small mechanical affection by the probe with the diameter less than 200 nm. It is also shown that the relief changing does not connect with the adhesion of the film to the probe.

As is known the elastic-plastic hysteresis manifests in macro level in such a way that the hysteresis loop get over the clockwise. Herewith, as a rule, the form and other characteristics of the loop do not depend on the speed of mechanical affections. However for the material under consideration such a dependence takes place (namely, the form of the hysteretic loop depends on the speed of force affection).

3. MODEL

In this section we present the model of the observable effect. The dependence of the loop’s form on time means that the presented model should be non-stationary.

It is well known that the physical properties of nanofilms depend on the structure of the materials. Main processes in such nanocovers occur due to the polymerization and depolymerization.

These processes can be initialized by the temperature, light or mechanical affections. It should also be pointed out that the polymerization together with the depolymerization are caused by the probability laws. The main assumption of this model consists in the fact that the depolymerization process is turning on when the cover is under temporal excess pressure.

The state of the cover can be described by the pair of parameters $(\omega_1(t); \omega_2(t))$ that are the fraction of the domains under polymerization and depolymerization respectively. The dynamics of these parameters can be described by the Kolmogorov-Chapman equation (here dot displays the time derivative):

$$\begin{cases} \dot{\omega}_1 = -\lambda_1\omega_1 + \lambda_2\omega_2, \\ \omega_1 + \omega_2 = 1, \end{cases} \quad (1)$$

with the initial conditions

$$\begin{cases} \omega_1(0) = \omega_{01}, \\ \omega_2(0) = \omega_{02}. \end{cases}$$

With each of these states is connected the linear volume, namely x_1 and x_2 respectively. At the same time the dependence on the external force u we can define as:

$$x_1 = x_1(u), \quad x_2 = x_2(u) \quad (2)$$

using the Ishlinskii operator which will be described below. Finally, the dependence of the displacement on the force can be determined by the relation:

$$l = \omega_1 x_1 + \omega_2 x_2. \quad (3)$$

The Equations (1)–(3) are the base of the proposed model.

At the same time the intensities of the transitions λ_1 and λ_2 are driven by the relations

$$\lambda_1 = \lambda_1(u), \quad \lambda_2 = \lambda_2(u).$$

Identification of these dependencies from the known experimental data is a complicated problem. Namely, there are certain facts which indicate that these functions are monotonically increasing. In this work we choose these functions in the form

$$\lambda_1(u) = \lambda_{01} + c_1 u, \quad \lambda_2(u) = \lambda_{02} + c_2 u \quad (4)$$

with positive parameters.

3.1. Ishlinskii Operator

Let us introduce the necessary definitions.

The stop is an operator $W[t_0, x_0, E, h]$ that connects every continuous input $u(t)$ ($t \geq 0$) with the output $x(t)$ by the following rule (on the monotonic inputs):

$$x(t) = \begin{cases} \min \{h, E [u(t) - u(t_0)] + x(t)\}, & \text{if } u(t) \text{ increase,} \\ \max \{-h, E [u(t) - u(t_0)] + x(t)\}, & \text{if } u(t) \text{ decrease.} \end{cases}$$

Here E is the elastic modulus of the material (we understand $u(t)$ and $x(t)$ as a stress and deformation respectively).

On the piece-wise monotonic inputs the output can be determined using the semi-group identity

$$W[t_0, x_0, E, h]u(t) = W[t_1, W[t_0, x_0, E, h]u(t_1), E, h]u(t),$$

and then, using the special limit construction such an operator can be redefined on all continuous inputs. The detailed description of this operator as well as its properties are considered in the book of Krasnosel'skii and Pokrovskii [7].

Let $U(h) = W[t_0, x_0, 1, h]$ is a single-parameter kind of stops with the elastic modulus equal 1 and the yield stress $\pm h$. Let us define the nondecreasing continuous function $\Omega = \Omega(h)$ ($h \geq 0$) which satisfies the following condition:

$$\int_0^{\infty} |\Omega(h)| dh < \infty. \quad (5)$$

In the following consideration we will use the condition (5) in the form

$$\int_0^{\infty} h d\Omega(h) < \infty. \quad (6)$$

Let us denote as Z the set of continuous functions $z(h)$ ($h \geq 0$) that satisfy the inequality $|z(h)| \leq h$ ($0 \leq h < \infty$). Then the pairs $\{u_0; z(h)\}$ form the set which determines the state space of the operator. And the dynamics of input-output relations is determined as:

$$x(t) = W [t_0, z_0(h), 1, \Omega(h)] u(t) = \int_0^{\infty} U [t_0, z_0(h), h] u(t) d\Omega(h), \quad (t \geq t_0). \quad (7)$$

Here the integral is understood in the meaning of Riemann-Stieltjes. However it should be noted that this relation is uncomfortable for calculation of the output of Ishlinsky operator.

As follows from definition, the operator $U(h)$ describes the ideal-plastic fiber with the elastic modulus $E = \xi$ and the plastic limits $\pm \xi h$. Let us consider the so-called charge function

$$\chi_+(u, \xi, h) = \begin{cases} -\xi h, & \text{at } u \leq -h, \\ \xi u, & \text{at } -h < u < h, \\ \xi h, & \text{at } u \geq h. \end{cases}$$

The analog of this function for the Ishlinsky operator is the function

$$\chi_+(u, \Omega) = \int_0^u |\Omega(|h|)| dh, \quad (-\infty < u < \infty) \quad (8)$$

and the discharge function

$$\chi_-(u, \Omega) = 2\chi_+\left(\frac{u}{2}, \Omega\right), \quad (-\infty < u < \infty).$$

In this way, the Ishlinskii operator is the model of plastic body which is composed of the continual number of ideal-plastic fibers. As follows from definition, at monotonic input and uncharged state the alternating stress can be expressed in the terms of charge function, namely

$$x(t) = \chi_+(u(t) - u(t_0), \Omega).$$

On the piece-wise monotonic inputs the Ishlinskii operator (as previously) can be determined using the semi-group identity. Unfortunately, the relation (8) allows to determine the output using the charge function only at zero initial state. However in the considered case this condition is not restrictive because at initial moment the state of a nanomaterial is natural to assume uncharged.

Finally, the model which describes the dynamics of the system under consideration is based on the Equations (1)-(3) together with the relations:

$$x_1(t) = W [t_0, z_{01}(h), 1, \Omega_1(h)] u(t), \quad (9)$$

$$x_2(t) = W [t_0, z_{02}(h), 1, \Omega_2(h)] u(t), \quad (10)$$

where $u(t)$ is an external force applied to the sample, $z_{01}(h)$ and $z_{02}(h)$ correspond to initial uncharged states of polymerized and depolymerized fractions respectively.

In the experiments described in cite the external charge is determined as a pice-wise linear function, namely

$$u(t) = \begin{cases} at, & t \in [0, \frac{T}{2}], \\ -a(t - T), & t \in (\frac{T}{2}, T]. \end{cases}$$

4. CONCLUSIONS

The numerical experiments show that the qualitative behavior of the hysteretic curves significantly depends on the choice of the parameters c_1 and c_2 that determine the intensity of transitions from depolymerized state and back. Optimization of the model by these (and other) parameters allows to obtain the results that differ from the experimental results approximately within 3 percent.

REFERENCES

1. Ikhouane, F. and T. Rodellar, *Systems with Hysteresis: Analysis, Identification and Control Using the Bouc-Wen Model*, Wiley, 2007.
2. Semenov, M. E., D. V. Shevlyakova, and P. A. Meleshenko, "Inverted pendulum under hysteretic control: Stability zones and periodic solutions," *Nonlinear Dynam.*, Vol. 75, 247–256, 2014.
3. Semenov, M. E., D. V. Grachikov, A. G. Rukavitsyn, and P. A. Meleshenko, "On the state feedback control of inverted pendulum with hysteretic nonlinearity," *MATEC Web of Conferences*, Vol. 16, 05009 (1–5), 2014.
4. Penkov, O. V., V. E. Pukha, A. Yu. Devizenko, et al., "Self-healing phenomenon and dynamic hardness of C₆₀-based nanocomposite coatings," *Nano Lett.*, Vol. 14, 2536–2540, 2014.
5. Atovmyan, E. G., A. A. Grishchuk, and T. N. Fedotova, "Polymerization of C₆₀ fullerene activated with butyllithium," *Russian Chem. Bullet*, Vol. 60, 1505–1507, 2011.
6. Wang, Y., H. Zettergren, P. Rousseau, et al., "Formation dynamics of fullerene dimers C₁₁₈, C₁₁₉ and C₁₂₀," *Phys. Rev. A*, Vol. 89, 062708, 2014.
7. Krasnosel'skii, M. A. and A. V. Pokrovskii, *Systems with Hysteresis*, Springer Verlag, 1989.

Binary Collision with Energetic Ions of Carbon Nanotubes

D. Bajalan
St. Pölten, Austria

Abstract— From various sources on processing technologies, it is expected that processing accuracy will reach the order of nano-meters in the twenty-first century. This speaks strongly for an urgent need to develop and improve nanotechnology methods in several special branches of the industry like: nanoelectronic, magnetic storage and other essential computer network devices. The field of enhancing carbon nanotube-structure science and technology has been growing very rapidly in the past few years, since the realization that creating new materials and devices so that nano-scale building blocks could access new and improved properties and functionalities. Irradiation of carbon based nanotubes creates new fields in material sciences [1]. One of the most attractive candidates for future-generation electronics field are carbon based nanotubes (for example single-walled carbon nanotubes (SWNTs): like other transistors also this tube) because flowing current along the tubes can be controlled by an external electric field [2].

Carbon nanotubes (CNTs) are very interesting technological branch. Due to their low dimensionality, nanometer size and remarkable electronic, mechanic and magnetic properties (nanotubes are promising structures for many purposes in several fields of physics, materials science or biomedicine) [3]. Channeling of energetic ions through solids is a phenomenon which should be accounted for in the present day semiconductor technology, as it gives rise to deeper implantation and less lattice disorder. The channeling effects are particularly important for materials with high crystallization and anisotropic atomic structure [4] (for example 4×10^{16} ions/cm²).

1. INTRODUCTION

While many aspects of the field existed well before nano-structure science and technology became a definable entity in the past decade, it has only become a coherent field of endeavor through the confluence of three important technological streams [5]: 1. New and improved control of the size and manipulation of nano scale building blocks 2. New and improved characterization (spatial resolution, chemical sensitivity, etc.) of materials at the nano scale 3. New and improved understanding of the relationships between nano-structure and properties and how these can be engineered Hence using nano-technology in electronic devices may solve some of problems like: 1. The size of the devices 2. The performance of the devices 3. The fabrication problems of the devices 4. The price problems, Fabrication, Marketing Nano-technology was initially proposed to provide a concrete target accuracy for fabrication processes which involve ultraprecision surface and finishing (ultra- fine mirror cutting, various kinds of energy beam processing using photon electron, and ion beams). Materials-processing in nano-technology thus consists mainly on: 1. High-precision cutting with diamond tools of low wear 2. Fine lapping and fine polishing using fine abrasives.

The invention of nano-technology was the legendary proposal of the Nobel Prize winner wonderful and respectable scientist Richard Feynman from 1957; “There is a lot of space at the bottom”. Some of the most important key fields of nano technology are [6]:

1. Electronics and communications, quantum structure electronic devices for memory and data storage, displays, optoelectronics, photonic crystal structures, (longer term) quantum information technology. Nano-sized magnetic particles facilitate small mass storage devices with capacities at multi-terabit levels, such as single electron memory [7].
2. Tissue engineering, medical implants and devices.
3. Instrumentation, tools and metrology, tools for top down manufacture e.g. high resolution and soft lithography, nanometrology.
4. Sensors and actuators; integrated nanosensor systems capable of collecting, processing, and communicating massive amounts of data with minimal size, weight, and power consumption [6, 7].
5. Nanostructured materials, smart composites, catalysis, biosensors; because biosensors are under intense development for a wide range of applications, from medical diagnostics and environmental developments [8].
6. Nanomaterials for functional interfaces.

The top-down approach, which uses techniques like photo-lithography and etching, has already been used to make so-called micro-electromechanical systems (MEMS); such systems are commercially available and have components on length scales of several microns (the acceleration sensors in airbags being a well-known example) and what to do now is shrink these systems even further to create true nano-electromechanical systems, or NEMS [9].

As dimensions reach the atomic scale, the manufacturing processes are trying to manipulate individual molecules Forces (like van der Waals and London force, which is due to a net electrostatic attraction between the electron distribution of one atom and the positive nucleus of the other) and interactions between individual molecules then become significant, and new paradigms have to come into play, Bottom-up techniques involve manipulating individual atoms and molecules (bottom-up nano usually implies controlled or directed self-assembly of atoms and molecules into nano structures) . Faster computers, advanced pharmaceuticals, controlled drug delivery, biocompatible materials, tissue repair, surface coatings, better skin care and protection, catalysts, sensors, optical communications, magnetic materials and devices — these are just some sectors of the economy where nanotechnology will have an impact.

2. CARBON NANO TUBE

Continuously improving device performance in the silicon industry has been largely achieved by downsizing device dimensions. However, this approach will soon meet scientific and technical limitations. CNTs are attractive as a solution to the forthcoming fabrication barrier. They are about 1 nm in diameter, a few micrometers in length, and are attractive semiconducting materials with a band gap of 0.5 to 1.0 eV, high mobility and large current carrying capability, and a direct band gap It is well documented that carbon nanotubes (CNTs) have excellent electrical properties both as metals and semiconductors. They can act as one-dimensional ballistic conductors at room temperature as well as Field effect transistors (FETs) with performance comparable to that of silicon FETs. Basic logic circuits have been formed by coupling such devices [10]. Moreover, nanotubes have extraordinary mechanical strength and high thermal conductivity. Recently, new functionalities of nanotube devices have been demonstrated experimentally, e.g. gate-controlled IR electroluminescence from FETs and singlewall carbon nanotubes are outstanding candidates for novel electronic applications [11].

3. ION IMPLANTATION

Experiments on the irradiation of carbon nanotubes with energetic particles poses many interesting properties. These effects may potentially be used in various practical applications, such as nanoelectronic devices (The CNs are characterized by a high Youngs modulus and varied electronic properties) [12, 13].

Carbon nanotubes (CNTs) are one of the possible building blocks for electronic devices in the transition phase from traditional silicon-based microelectronics towards the fewnanometer regime. Remaining problems in integrating CNTs to the existing technology is the low reactivity of the CNT walls which leads to low conductance between CNTs and the other components. Because recent studies have shown that ion irradiation can be used to modify both the electrical and structural properties of CNTs, we propose that it could also be possible to use ion irradiation with low energies to enhance the conductance of these connections [14].

Table 1: Calculated wave.

f_v	[THz]	0.24	0.48	0.72	0.96
-	-	1.2	2.4	12	24

Ion implantation is one of the main processes used for the fabrication of modern integrated microelectronic devices, and it allows controlled doping of the active regions [15]. The stopping of high velocity light ions in matter usually assumes two major simplifications in stopping theory: (1) the ion is moving much faster than the target electrons and is fully stripped of its electrons, and (2) the ion is much heavier than the target electrons [16].

Also important study done in channeling of heavy ions with keV energies through the wall of carbon nanotubes (for more see) [1, 4, 12, 13].

4. MODELING ENERGY AND WAVE LENGTH

The equation of Heisenberg are used to simplify the behavior of the energy and Wave length of an Energetic particles.

$$\Delta\chi \cdot \Delta\tau \geq h \quad (1)$$

in the same manner we can write the above equation in relation to the energy as

$$\Delta\tau \cdot \Delta E \geq h \quad (2)$$

and through substitution of variables and Frequency assumption as a new variable as f_v the equation changed to new relation as

$$\Delta f_v^{-1} \cdot \Delta(\mathbf{e} \cdot \mathbf{V}) \geq h \quad (3)$$

By supplying the Equations (1), (4), (3) with different wave length with different particles for optimal results and in with SWNT and MWNT at constant trigger angle (hitting angle); assuming $\theta = 30$.

5. CHALLENGE OF CHARGE TRANSPORT

The measurement of charge transport in molecules and the determination of their conductance are important goals. Such measurements are experimentally challenging and intriguing because one can test the validity of transport approximations at the molecular level. A conceptually simple configuration would be to connect a single molecule between metallic contacts. Such a metal-molecule-metal configuration would present the molecular embodiment of a system analogous to a quantum dot, with the potential barriers of the semiconductor system being replaced by any existing contact barrier of the molecule-metal interface [17].

6. SUMMERY

The interaction of heavy ions with matter has become the area of intensive concentration both experimentally and theoretically . Effective and successful applications of ion beam technology require detailed qualitative knowledge of different interaction processes. The stopping power or stopping force of any medium for different ions constitute information essential for ion-beam science and its applications. The interaction mechanism of energetic heavy ions with matter are well known at the present time, but no appropriate theoretical or semi-empirical formulations exist to calculate the stopping power of various materials for a variety of different isotopes with varying energies [18]. Irradiation of carbon NTs with energetic particles can be used for nanoengineering, e.g., for creating molecular junctions between the NTs, making NT-based quantum dots and composite materials with enhanced mechanical properties [19].

Single-Walled Carbon Nanotubes (SWNTs) have been attracting substantial interest as potential building blocks of chemical and biological sensors and future integrated circuits.

SWNTs are graphene cylinders with a wall thickness of one atomic layer and a diameter of about one nanometer. They have very exciting properties such as high aspect ratio, large surface area and hollow geometry, high current carrying capacity, superior thermal properties, fast response and good reversibility. These properties present nanotubes as viable candidates for sensing applications, such as gas sensors, pressure sensors, transistors, and thermal sensors [20].

Hence one of the most significant potential applications of single-walled nanotubes is believed to be in the domain of nano-electronics.

REFERENCES

1. Pomoell, J., A. V. Krasheninnikov, K. Nordlund, and J. Keinonen, *Nuclear Instruments and Methods in Physics Research B*, Vol. 206, 2003.
2. Jeongl, G. H., T. Izumida, T. Hirata, R. Hatakeyamal, Y. Neoz, H. Mimura, K. Omote, Y. Kasama, S. H. Jhang, and Y.-W. Park, *4th IEEE Conference on Nanotechnology*, 2004.
3. Uribe, J. D., C. Celedon, A. Cortes, and J. E. Valdes, Depto. de Fsica, Laboratorio de Colisiones Atómicas, Universidad Tecnica Federico Santa Mara, 2005.
4. Krasheninnikov, A. V. and K. Nordlund, *Nuclear Instruments and Methods in Physics Research B*, Vol. 228, 2005.
5. Siegel, R. W., *The Interagency Working Group on Nanoscience, Engineering and Technology IWGN*, Chapter 1, National Science and Technology Council (NSTC) Committee on Technology, 1999.

6. Taylor, J. M., "Report of the UK advisory group on nanotechnology applications submitted to Lord Sainsbury," Minister for Science and Innovation, 2002.
7. Zou, W., Ph.D. thesis, University of Virginia, 2001.
8. Miller, M. M., P. E. Sheehan, C. R. Tamanaha, M. Tondra, L. J. Whitmana, and E. Prairie, *Physical A*, Vol. 107, 209, 2003.
9. Bajalan, D., Ph.D. thesis, University of Wien, 2005.
10. Jang, J. H., S. C. Lim, D. L. Duong, G. Kim, W. J. Yu, K. H. Han, Y.-S. Min, and Y. H. Lee, *J. Nanosci. Nanotechnol.*, 2010.
11. Stobbez, S., P. E. Lindelof, and J. Nygaard, *Integration of Carbon Nanotubes with Semiconductor Technology; Fabrication of Hybrid Devices by III-V Molecular Beam Epitaxy Universitetsparken 5, DK-2100 Copenhagen*, Niels Bohr Institute and Nano-Science Center, Universitetsparken 5, DK-2100 Copenhagen, 2005.
12. Vincent, P., A. Brioude, C. Journet, S. Rabaste, S. T. Purcell, J. Le Brusq, and J. C. Plenet, *Journal of Non-Crystalline Solids*, 2002.
13. Brioude, A., P. Vincent, C. Journet, J. C. Plenet, and S. T. Purcell, *Applied Surface Science*, 2004.
14. Kotakoski, J. and K. Nordlund, *Mater. Res. Soc. Symp. Proc.*, 2006.
15. Hernandez-Mangas, J. M., J. Arias, L. Bailon, M. Jarayz, and J. Barbolla, *J. Appl. Phys*, 2002.
16. Ziegler, J., *Appl. Phys/Rev. Appl. Phys.*, Vol. 85, 1249–1272, 1999.
17. Zhou, C., M. A. Reed, C. J. Muller, T. P. Burgin, and J. M. Tour, *Science*, Vol. 278, 252, 1997.
18. Singh, M., L. Singh, and N. Kaur, *Materials Physics and Mechanics*, 2011.
19. Bellucci, S., *Nucl. Instr. and Meth. in Phys. Res. B*, Vol. 234, 2005.
20. Chen, C.-L., V. Agarwal, S. Sonkusale, and M. R. Dokmeci, *IEEE Nanotechnology Conference*, 2008.

Applications of Carbon Nanotubs and Other Nanomagnetic Nanowires

D. Bajalan
St. Pölten, Austria

Abstract— Ultra high data storage media need smaller spacing between head and media. Signal processing and noise problems should be included in the development of a road map of ultra high data storage systems. The fast development in magnetic recording media give the consumer and users of computer systems more hope to gain power on their systems. The magnetic recording media industry will benefit strongly from the advances in magnetic nanostructures (based on carbon or other materials). The production of ultra-high recording media with advanced lithography is possible and practical. That is why, nano-magnetic structures could be one of the best candidates for new recording technology concepts.

1. INTRODUCTION

Since their discovery, carbon nanotubes have attracted the attention of many scientist around the world [1]. In 1991, S. Iijima discovered Carbon Nanotubes by chance during investigation of fullerene production. Since then, Carbon Nanotubes have attracted the immense interest among the researchers and has been the focus of many research projects [2]. The functionalisation of carbon nanomaterials can modify their physicochemical properties, making them more suitable for chemical and biological applications. Of particular interest are CNTs with magnetic properties because of their potential applications in biological labelling, drug delivery and magnetic storage media [3]. Electrical properties of carbon nanotube structures and manifestations in related phenomena such as thermoelectricity, superconductivity, electroluminescence, and photoconductivity are important fields of research. The possibility of using naturally formed complex nanotube morphologies, such as junctions, for new device architectures are then considered. Technological applications of the electrical properties of nanotube derived structures in transistor applications, high frequency nanoelectronics, field emission, and biological sensing are also other fields of study. The technological potential of nanotubes and the need for new device architectures for nanotube systems integration has been review [4]. A widely used approach to identify the types of SWCNT is by reference to rolling up the graphene sheet. The key geometric parameter associated with this process is the roll-up vector r , which can be expressed as the linear combination of the lattice basis (a and b) [5].

$$r = na + mb \quad (1)$$

Carbon nanotubes can be visualized as a graphene sheet that has been rolled into a tube with hemispherical caps at both ends [6]. Unlike diamond, where a 3-D diamond cubic crystal structure is formed with each carbon atom having four nearest neighbours arranged in a tetrahedron, graphite is formed as a 2-D sheet of carbon atoms arranged in hexagonal array. In this case, each carbon atom is linked to three nearest neighbours. Rolling the sheets of graphite into cylinders form carbon nanotubes. The properties of nanotubes depend on atomic arrangement (how the sheets of graphite are rolled), the diameter and length of the tubes.

It is then possible to associate a particular integer pair (n, m) with each SWCNT. The relation between n and m also defines three categories of CNT: $m = 0$, Zigzag, $n = m$, Armchair, other, Chiral.

Regarding electrical conduction, carbon nanotubes show the unique property that the conductivity can be either metallic or semiconducting, depending on the tubule diameter d , and chiral angle [7, 8]. It is theoretically predicted that 1/3 of as prepared CNTs are metallic and 2/3 are semiconducting. Moreover, the band gap of the nanotube is tuned by adjusting the diameter of the nanotube. Hence electronic structure of a CNT depends only on its geometrical dimension without any doping [8].

2. CNT POSSIBLE APPLICATION

Among the organic materials, carbon Nanotubes (CNTs) are unique for their electrical and chemical properties. They are very interesting in terms of material research and electronic applications.

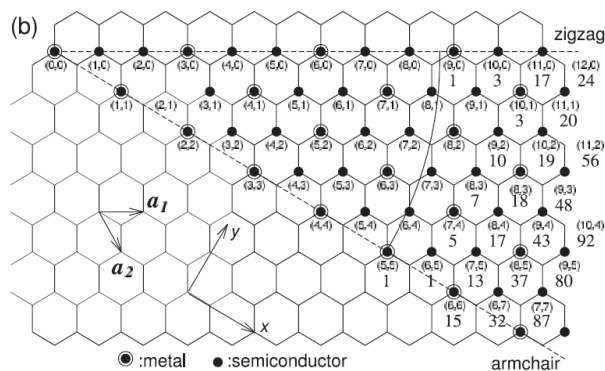


Figure 1: Possible vectors specified by the pairs of integers (n, m) for general carbon nanotubes, including zigzag, armchair, and chiral nanotubes [7].

Depending on their chemical structure, carbon nanotubes (CNTs) can be used as an alternative to organic or inorganic semiconductors as well as conductors. The chemical bonding of nanotubes is composed entirely of sp^2 bonds, similar to those of graphite. This bonding structure, which is stronger than the sp^3 bonds found in diamonds, provides the molecules with their unique strength. Nanotubes naturally align themselves into “ropes” held together by van der Waals forces. The nature of the bonding of a nanotube is described by quantum chemistry specifically, orbital hybridization. Solvents in which the CNTs can be solubilized include chlorobenzene, chloroform, methylene chloride, carbon disul.de, benzene, etc. [9].

Type	Start Atom	Vertex	End Atom	Angle (°)	Type	Start Atom	Vertex	End Atom	Angle (°)	Type	Start Atom	Vertex	End Atom	Angle (°)	Type	Start Atom	Vertex	End Atom	Angle (°)	
Angle 1	CCC	C2	C1	C8	114,6614	CCC	C2	C1	C8	114,6614	CCC	C2	C1	C8	110,5301	CCC	C2	C1	C8	114,6614
Angle 2	CCC	C1	C2	C3	115,2036	CCC	C1	C2	C3	115,2036	CCC	C1	C2	C3	110,5301	CCC	C1	C2	C3	115,2036
Angle 3	CCC	C2	C3	C4	114,6614	CCC	C2	C3	C4	114,6614	CCC	C2	C3	C4	110,5301	CCC	C2	C3	C4	114,6614
Angle 4	CCC	C3	C4	C5	115,2036	CCC	C3	C4	C5	115,2036	CCC	C3	C4	C5	110,5301	CCC	C3	C4	C5	115,2036
Angle 5	CCC	C4	C5	C6	114,6614	CCC	C4	C5	C6	114,6614	CCC	C4	C5	C6	110,5301	CCC	C4	C5	C6	114,6614
Angle 6	CCC	C5	C6	C7	115,2036	CCC	C5	C6	C7	115,2036	CCC	C5	C6	C7	116,2854	CCC	C5	C6	C7	115,2036
Angle 7	CCC	C6	C7	C8	114,6614	CCC	C6	C7	C8	114,6614	CCC	C6	C7	C8	122,8895	CCC	C6	C7	C8	114,6614
Angle 8	CCC	C1	C8	C7	115,2036	CCC	C1	C8	C7	115,2036	CCC	C1	C8	C7	105,2197	CCC	C1	C8	C7	115,2036
Type	Start Atom	End Atom	Bond Order	Rotatable	Length (Å)	Type	Atom 1	Atom 2	Atom 3	Atom 4	Torsion (°)	Type	Atom 1	Atom 2	Atom 3	Atom 4	Torsion (°)			
Bond 1	C-C	C1	C2	1	No	1,421	Torsion 1	CCCC	C8	C1	C2	C3	57,3553	CCCC	C1	C2	C3	110,4768		
Bond 2	C-C	C1	C8	1	No	1,421	Torsion 2	CCCC	C2	C1	C8	C7	54,8843	CCCC	C1	C8	C7	-73,7966		
Bond 3	C-C	C2	C3	1	No	1,421	Torsion 3	CCCC	C1	C2	C3	C4	-54,8838	CCCC	C2	C3	C4	-45,8975		
Bond 4	C-C	C5	C6	1	No	1,421	Torsion 4	CCCC	C4	C5	C6	C7	57,3557	CCCC	C5	C6	C7	48,9945		
				1	No	1,421	Torsion 5	CCCC	C6	C5	C4	C3	54,8839	CCCC	C5	C4	C3	65,0440		
								CCCC					-54,8843	CCCC	C6	C7	C8	-110,1781		
								CCCC					-57,3551	CCCC	C3	C4	C5	-67,1024		
								CCCC					-57,3556	CCCC	C7	C8	C1	72,5652		

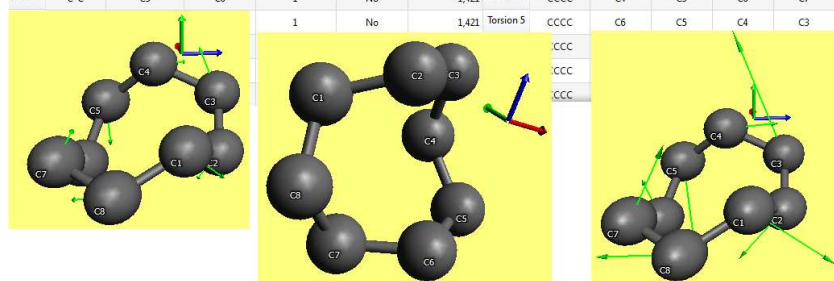


Figure 2: Torsion through c nano tube basic cell of 2×2 possible.

Carbon nanotubes (CNTs) hold a great promise in bio-medical applications, such as drug delivery agents, bio-sensors, bone scaffolds materials, and others due to their unique structural, mechanical and electronic properties. It has been reported that the modified CNTs can deliver peptides and ribonucleic acid (RNA) into cells without causing cytotoxicity. Clearly, the studies that obtained good cell viability present some kind of purification (to remove metallic particles dispersed around CNTs and amorphous carbon) or functionalization of the CNT [10].

Experimental and theoretical studies have shown that the thermal conductivity of a carbon nanotube (CNT) is up to several thousand (W/m·K SI: Watt per Meter and Kelvin), showing great potentials in the thermal management area. Many studies have been reported on the use of dispersed CNTs as thermal conducting fillers in a polymer matrix, whose thermal conductivity can be significantly improved by 65–125 percentage (very useful in packaging of electronic devices even

at a small loading of CNTs [11].

3. THERMAL STABILITY IN NANO PARTICALS

Magnetic nano particle thermal stability calculation is essential for development of patterned ultra high magnetic storage media. The use of reliable model is very important. The simulation of hysteresis opens a very big opportunities to calculate values of parameters which we then use directly for interpretation of the stability condition of stored information on a nano magnetic structure. The main idea behind that is to change the direction of the applied field H and then see the stability conditions on a given nano bit volume. Research and development teams in companies implementing nano-technology (nano wire, nano particals, nano patterned structur...etc.) are gaining more and more importance in the field of sensor systems and material science. Demands for the continuous increase in the data storage density bring the challenge to overcome physical limits for currently used magnetic recording media (example). Ferromagnetic nano-particles of different polycrystalline thin films have been formed by heavy or light ion irradiation. Although this modification technique may be a way to produce nano-magnetic particles, there are some critical size limits of nanomagnetic structures like the superparamagnetic limit (SPML) which faces magnetic nanotechnology.

The magnetic properties of thin films are strongly influenced by their structure. Small changes in the way a thin film is produced often give rise to large changes in some of the magnetic properties of the thin film. This is best understood by observing how the microstructure of the film changes with processing and then correlating the microstructure directly with the properties of the thin film. The behaviour of magnetic nanoparticles has fascinated materials scientists for decades. There are fundamental limits due to the atomic nature of matter which may impose ultimate physical bounds to nanofabrication and miniaturization. Over the past several decades, amorphous and more recently nano-crystalline materials have been investigated for applications in magnetic devices. The benefit found in the nanocrystalline alloys stem from their chemical and structural variations on a nano-scale which are important for optimizing magnetic recording devices.

4. SUMMERY

Since the discovery of CNTs, they have been the focus of frontier research [6]. It has opened vast areas of research which also include nanoscale reinforcements in composites in order to improve their mechanical, thermal and even electrical properties. Although the focus of the research in nanotube based composites has mostly been on polymer based composites, the unique properties of carbon nanotubes can also be exploited in ceramic matrix composites. But even after a decade of its discovery, the full potential of carbon nanotubes in this application has not been realized with experimental outcomes falling short of predicted values which demand an active insight in this field. Carbon nanofibers and nanotubes are promising to revolutionise several fields in material science and are a major component of nanotechnology. Further market development will depend on material availability at reasonable prices. Nanotubes have a wide range of unexplored potential applications in various technological areas such as aerospace, energy, automobile, medicine, or chemical industry, in which they can be used as gas adsorbents, templates, actuators, composite reinforcements, catalyst supports, probes, chemical sensors, nanopipes, nano-reactors etc. [12].

REFERENCES

1. Burghard, M. and K. Balasubramanian, *Small*, Vol. 1, No. 2, 180–192, 2005.
2. Tripathi, S. M. and T. S. Bholanath, *International Journal of Advance Science and Technology*, Vol. 16, 2010.
3. Korobeinyk, A. V., R. L. D. Whitby, J. J. Niu, Y. Gogotsi, and S. V. Mikhalovskya, Manuscript, 2011.
4. Bandaru, P. R., *Journal of Nanoscience and Nanotechnology*, Vol. 7, 129, 2007.
5. Ruoff, R. S., D. Qian, and W. K. Liu, *C. R. Physique*, Vol. 4, 9931008, 2003.
6. Samal, S. S. and S. Bal, *Journal of Minerals Materials Characterization Engineering*, Vol. 7, No. 4, 355–370, 2008.
7. Dresselhaus, M. S., G. Dresselhaus, and R. Saito, *Physics of Carbon Nanotubes*, Vol. 33, No. 7, 883–891, 1995.
8. Hembram, K. P. S. S., K. Reddappa Reddy, and G. M. Rao, *Open Journal of Composite Materials*, Vol. 3, 10–15, 2013.
9. Kholmurodov, K., G. Aru, and K. Yasuoka, *Natural Science*, Vol. 2, No. 8, 902–910, 2010.

10. Pan, C.-J., Y.-X. Dong, and K. D. Jandt, *Journal of Biomaterials and Nanobiotechnology*, Vol. 3, 353–361, 2012.
11. Hu, D., H. Chen, Z. Yong, M. Chen, X. Zhang, Q. Li, Z. Fan, and Z. Feng, *Materials Sciences and Applications*, Vol. 4, 453–457, 2013.
12. Khare, R. and S. Bose, *Journal of Minerals Materials Characterization Engineering*, Vol. 4, No. 1, 31–46, 2005.

Separating the Field Radiated by Two Rectilinear Sources

A. Natale, M. A. Maisto, R. Solimene, G. Leone, and R. Pierri

Dipartimento di Ingegneria Industriale e dell'Informazione, Seconda Università di Napoli
via Roma 29, Aversa 81031, Italy

Abstract— Consider two electric current sources radiating in free-space. They are assumed to be supported over two parallel strips whose positions are a priori known. Their radiated fields are collected over a single domain located in far-zone (with respect the whole radiating system). A two-dimensional scalar framework is set. The problem of separating the contributions of the two sources from their radiated field over a single domain is considered. A procedure based on two step is presented: in the first step the sources are reconstructed and in the second the field is computed by this currents. In order to reconstruct the sources, three different schemes of inversion are presented. Numerical examples are provided in order to compare the different strategies from the achievable performance and numerical complexity point of views.

1. INTRODUCTION

When dealing with electromagnetic field measurements for antenna diagnostics or even in inverse scattering problems one collects the radiated field (resp. the scattered field) over a domain and from such measurements the features of the antenna (resp. scatterer) under test have to be inferred. It often happens that beside the field due to the structure under test (SUT), the fields produced by further sources (generally unwanted) are collected as well. This give rises to clutter signals from which the useful field signals (i.e., those one due to the SUT) must be singled out. In this contribution, a related problem for a two-dimensional scalar configuration is tackled. More in detail, two strip electric currents are considered radiating in free-space. They are assumed to be supported over two parallel strips whose positions are a priori known. Their radiated fields are collected over a single domain located in far-zone (with respect the whole radiating system). The problem of concern herein is to distinguish between the contributions of two radiating sources. To this end, the problem is addressed by a two-step procedure. First, the currents are reconstructed by the radiated field measurements. This entails dealing with an inverse source problem that is tackled by comparing three different strategies of inversion. The first strategy consists in inverting the radiating operator, which rigorously describe the radiation by both the sources. In the second one, the radiated field data is inverted by considering each source as being radiating alone. Finally, the third method is a variant of the second one. Indeed, after having reconstructed one of the two sources the corresponding radiated field is synthetically computed and subtracted from the data. Then the second source is reconstructed. Same steps are applied to other source. The second step of the overall procedure then consists of computing the radiated field due to each source once they have been estimated according to the previous step. Numerical examples are provided in order to compare the different strategies from the achievable performance and numerical complexity point of views.

2. MATHEMATICAL FORMULATION

Consider two electric strip currents J_1 and J_2 directed along the \hat{y} -axis and supported over the segments of the \hat{x} -axis $\Sigma_1 = [-X_1, X_1]$ and $\Sigma_2 = [-X_2, X_2]$ located at $z_1 = 0$ and $z_2 = d$, respectively. Their radiated fields are collected over a curvilinear domain located in the far-zone of the whole radiating system. The observation is indicated by the observation angle θ which spans within the observation angular sector $\Theta = [\theta_{\min}, \theta_{\max}]$.

The field radiated (which has only the y component) by each strip source enjoys the well known far-zone integral form

$$E_i(u) = \exp(jwz_i) \int_{-X_i}^{X_i} \exp(jux) J_i(x) dx \quad (1)$$

where $i \in (1, 2)$, $u = k \sin \theta$, $w = k \cos \theta$, k being the free-space wavenumber. Now the field is regarded as a function of the spectral variable u which depends on Θ ranging within the interval $U = [u_{\min}, u_{\max}]$ for both the sources.

It is convenient to cast Eq. (1) in operator notation so to introduce the following radiation operators

$$\mathcal{A}_i : J_i \in L^2(\Sigma_i) \longrightarrow E_i \in L^2(U) \tag{2}$$

with $L^2(\Sigma_i)$ and $L^2(U)$ being the complex valued function which are square integrable in Σ_i and U .

As the sources radiate simultaneously, the field actually collected is the sum of both contributions

$$E(u) = E_1(u) + E_2(u) = \mathcal{A}_1 J_1 + \mathcal{A}_2 J_2 \tag{3}$$

Accordingly, we need to look for an operator which link the couple (J_1, J_2) to E . To this end, let us introduce the functional set

$$\Sigma = \{ \underline{f} = (f_1, f_2) : f_1 \in L^2(\Sigma_1), f_2 \in L^2(\Sigma_2) \} \tag{4}$$

equipped with the scalar product

$$\langle \underline{f}, \underline{g} \rangle_{\Sigma} = \langle f_1, g_1 \rangle_{\Sigma_1} + \langle f_2, g_2 \rangle_{\Sigma_2} \tag{5}$$

with $\langle \cdot, \cdot \rangle_{\Sigma_1}$ and $\langle \cdot, \cdot \rangle_{\Sigma_2}$ being the usual scalar products in $L^2(\Sigma_1)$ and $L^2(\Sigma_2)$, respectively. Now, the radiating operator can be compactly represented as

$$\underline{\mathcal{A}} : \underline{J} \in \Sigma \longrightarrow E \in U \tag{6}$$

with $\underline{\mathcal{A}}$ defined as

$$\underline{\mathcal{A}} = [\mathcal{A}_1 \quad \mathcal{A}_2] \tag{7}$$

so that (3) can be rewritten as

$$E(u) = \underline{\mathcal{A}} \begin{bmatrix} J_1 \\ J_2 \end{bmatrix} \tag{8}$$

3. SOURCES RECONSTRUCTION

In order to reconstruct the two sources by the radiated field measurements, the problem can be addressed following three different strategies of inversion. In the first one, the source are reconstructed by inverting the operator $\underline{\mathcal{A}}$. Let $\{v_n, \sigma_n, \underline{u}_n\}^{\infty}$ be the singular system of $\underline{\mathcal{A}}$. In particular, the v_n s and the \underline{u}_n s are the singular functions expanding the radiated field and the unknown, respectively, whereas the σ_n s are the singular values. Accordingly, the TSVD reconstruction is given by:

$$\tilde{\underline{J}} = \sum_{n=1}^{N_t} \frac{\langle E_s, v_n \rangle_U}{\sigma_n} \underline{u}_n(x) \tag{9}$$

with \langle, \rangle denoting the scalar product in the data space and N_t is the truncation index. Let $\{v_{1n}, \sigma_{1n}, u_{1n}\}^{\infty}$ and $\{v_{2n}, \sigma_{2n}, u_{2n}\}^{\infty}$ be the singular systems of \mathcal{A}_1 and \mathcal{A}_2 , respectively. Note that as \mathcal{A}_1 and \mathcal{A}_2 are related to compactly supporting Fourier Transforms, their SVD is known in closed form. Indeed, it is given in terms of the prolate spheroidal wave-functions (PSWF) [1]. This suggests the second inversion strategy, where the radiated field data is inverted by considering each source as being radiating alone. This way allows to obtain an advantage in terms of computational complexity respect to previous inversion scheme. By exploiting the apriori information about two source supports (that are two parallel strip spatially disjoint), the reconstructions can be expressed as:

$$\tilde{J}_1 = \sum_{n=1}^{N_{t1}} \frac{\langle E_s, v_{1n} \rangle_U}{\sigma_{1n}} u_{1n}(x) \tag{10}$$

$$\tilde{J}_2 = \sum_{n=1}^{N_{t2}} \frac{\langle E_s, v_{2n} \rangle_U}{\sigma_{2n}} u_{2n}(x) \tag{11}$$

The step-like behaviour of the singular values σ_{1n} and σ_{2n} suggests to choose the truncation indexes equal to $\frac{X_1[u_{\max}-u_{\min}]}{\pi}$ and $\frac{X_2[u_{\max}-u_{\min}]}{\pi}$ [1]. The third method is a variant of the second one. Indeed, after having reconstructed one of the two sources the corresponding radiated field is synthetically computed and subtracted from the data. Then the second source is reconstructed. Applying these steps to both the sources, their contributions on the field are compensated and this impacts positively the reconstructions.

The steps realizing the procedure are the following:

- \tilde{J}_2 is estimated by (9). From \tilde{J}_2 , its radiated field is obtained by:

$$\tilde{E}_2 = \mathcal{A}_2 \tilde{J}_2$$

- \tilde{E}_2 is subtracted to the total field:

$$\tilde{E}_1 = \tilde{E}_s - \tilde{E}_2;$$

- Finally, the current defined on the other support is reconstructed by its approximated radiated field:

$$\tilde{J}_1 = \sum_{n=1}^{N_t} \frac{\langle \tilde{E}_1, v_{1n} \rangle_U}{\sigma_{1n}} u_{1n}(x)$$

Same steps are applied for the other source.

4. NUMERICAL RESULTS

A numerical analysis is performed in order to compare the different procedure of inversion. Consider that the sources to be reconstructed are:

$$J_1 = \cos\left(\frac{\pi}{2X_1}x\right) \text{ with } x \in [-X_1, X_1],$$

$$J_2 = \cos\left(\frac{\pi}{2X_2}x\right) \text{ with } x \in [-X_2, X_2].$$

In Fig. 2, the reconstructions of the two sources obtained by the three inversion procedures are represented by varying of the distance d and of the truncation index N_t . In particular, the step-like behaviour of the singular values Fig. 1 suggests to choose the truncation index in correspondence of the knees: for the figures on left column the second knee is chosen and for the figures on right column the first. The singular values behaviour of $\underline{\mathcal{A}}$ exhibits a two step behaviour because of the overlapping of two sources contributions on the field in a spatial frequency band whose width depending by d ([2]). So each singular value in first step is associated both to one of \mathcal{A}_1 and \mathcal{A}_2 , accordingly to the no-orthogonality of their singular functions. The number of the singular values in the first step depends on the distance between the two sources, indeed as it increases, the band on which v_{1n} and v_{2n} are no orthogonal decreases. As consequence, the singular values behaviour of $\underline{\mathcal{A}}$ approaches to single step.

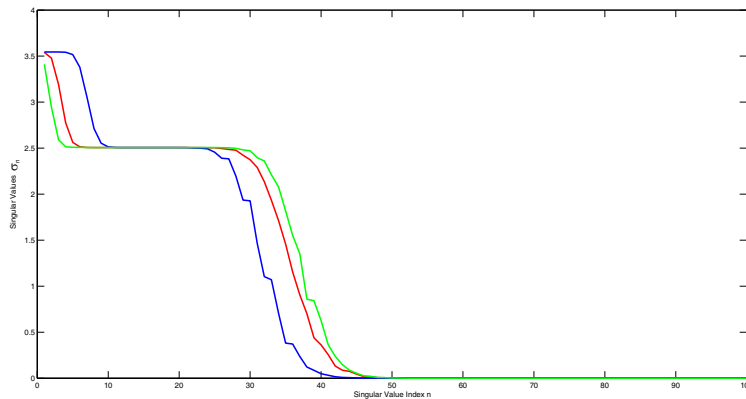


Figure 1: Singular values of the operator $\underline{\mathcal{A}}$ for $X_1 = 6\lambda$, $X_2 = 3\lambda$, $u_{\min} = -k$ and $u_{\max} = k$. The blue line refers to a distance $d = 10\lambda$, the red line to $d = 30\lambda$ and the green line to $d = 80\lambda$.

As can be seen, the performance of the third method allows to obtain better reconstruction starting from a distance $d = 80\lambda$, otherwise inverting $\underline{\mathcal{A}}$ by its eigen-spectrum gives better results only at larger d . The results obtained by the second method are the worst. Furthermore it is evident that the reconstruction of the wider source is better than the other because more singular functions associated only to wider source can be retained in 9. On the right column of Fig. 2, the role played by the truncation index is analysed. Truncating at the first knee heavily impacts the reconstruction of the wider source obtained by the first method because the singular functions associated only to this are filtered. In this case the results obtained by the third method are the best.

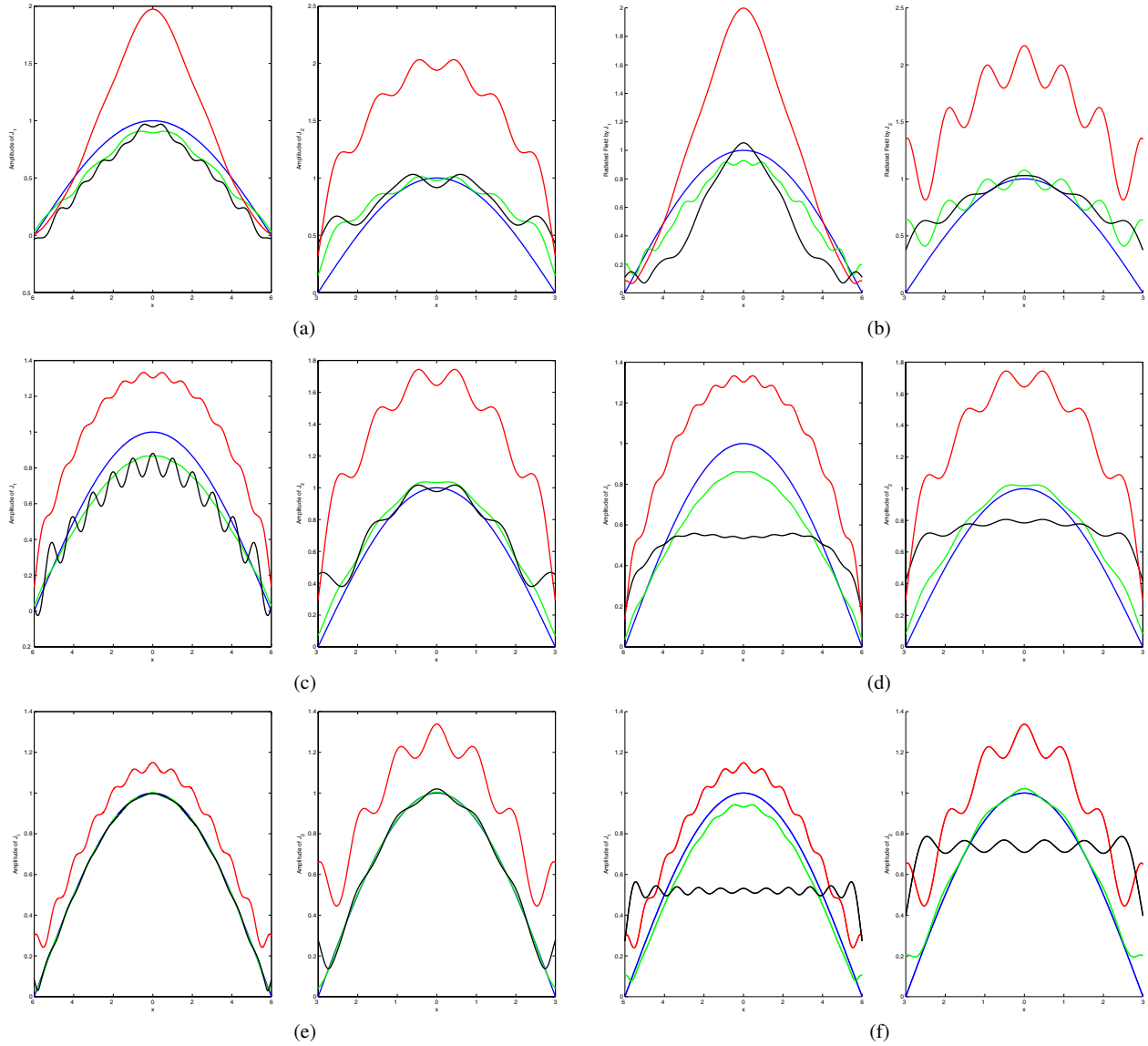


Figure 2: Reconstructions of two sources achieved by the three different methods for $X_1 = 6\lambda$, $X_2 = 3\lambda$, $u_{\min} = -k$ and $u_{\max} = k$. In particular the blue line refers to the sources to be determined, the black line to the reconstruction obtained by inverting \underline{A} by its eigen-spectrum, the red line to the reconstruction obtained by inverting the field as if each source radiates alone and the green line through the third method. On the left columns, the reconstructions are shown at varying the distance d between the source in $\{10\lambda, 80\lambda, 500\lambda\}$, respectively and the truncation index is chosen in correspondence of the second knee. On the right column same reconstructions are shown by choosing the truncation index in correspondence of the first knee.

5. FIELD SEPARATION

The second step of the overall procedure then consists of computing the radiated field due to each source once they have been estimated according to the previous section by the radiation operator.

$$E_1(u) = \mathcal{A}_1 J_{1r} \quad (12)$$

$$E_2(u) = \mathcal{A}_2 J_{2r} \quad (13)$$

where J_{1r} and J_{2r} are the sources reconstructed exploiting the seen method. In Fig. 3 the fields radiated by the sources of Fig. 2 are shown. As can be seen, the estimate of the field achieved by the second method does not approximate well the field at low frequency. The total field in 10 and 11 is spanned by a combination of two functions \tilde{v}_{1n} and \tilde{v}_{2n} linked to the singular functions of \mathcal{A}_1 and \mathcal{A}_2 that are not normalized for n belonging to the first step of σ_n . As consequence, the amplitude of the estimated field by the second method is doubled compare to the others for low

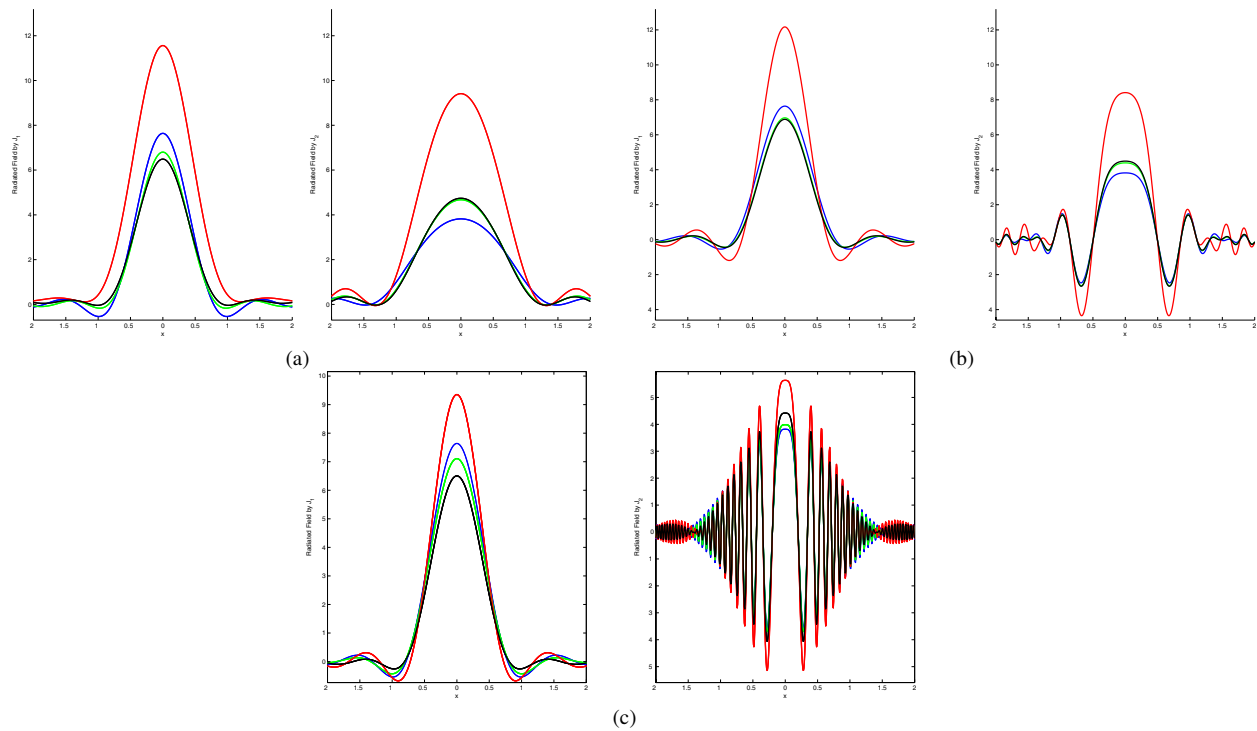


Figure 3: The radiated field due to sources shown on left column in Figure 2.

frequency because, being unitary the norm of v_{1n} , it is double compare to the norm of \tilde{v}_{1n} and \tilde{v}_{2n} for n belonging to the first step of σ_n .

6. CONCLUSION

The problem of separating the contributions of the two sources from their radiated field over a single domain has been tackled by introducing a based two step procedure. Three inversion strategies of the radiating operator realizing the first step are proposed. Their comparison has highlighted the better performance achievable by the third method by varying of the distance between the two sources and of the truncation index N_t .

ACKNOWLEDGMENT

This work was supported in part by POR Campania FSE 2007/2013-Embedded System.

REFERENCES

1. Slepian, D. and H. O. Pollak, "Prolate spheroidal wave function, Fourier analysis and uncertainty. I," *Bell Syst. Tech. J.*, Vol. 40, 43–63, 1961.
2. Solimene, R. and R. Pierri, "Number of degrees of freedom of the radiated field over multiple bounded domains," *Optics Letters*, Vol. 32, No. 21, 3113–3115, 2007.

A Bowtie Antenna Using a Broadband Microstrip to CPS Transition Balun

H. S. Ro and Y. S. Choi

Electronics and Telecommunications Research Institute, Korea

Abstract— In this paper, a bowtie antenna using a broadband microstrip to coplanar stripline transition balun is proposed. This antenna with a new transition structure has several advantages such as small size, wide bandwidth, and good impedance matching. In the balun of this antenna, the low impedance of the microstrip lines is gradually transformed to the high impedance of the CPS by a tapered bottom strip line. The proposed antenna was designed and fabricated on Teflon substrate for bandwidth from 2.2 GHz to 6 GHz. The measured return loss is less than 10 dB from 2.1 GHz to 6.5 GHz. The measured gain is from -4.5 dBi to 2.4 dBi.

1. INTRODUCTION

Patch antenna is widely used in wireless communication because of its advantages, such as low profile, low cost and easy fabrication. Especially, a wideband dipole patch element is used to obtain the performance of wideband and omnidirectional radiation pattern in this planar structure. A patch dipole element of a bowtie shape offers good performances in the bandwidth and radiation pattern. By the way, this bowtie patch has to be fed by a suitable feeding network to satisfy the requirement.

A microstrip to coplanar stripline (CPS) transition balun has been commonly used as feeding networks in this kind of antenna design. Various structures of microstrip to CPS transitions have been reported [1–4]. There are widely used two structures to provide RF continuity between the CPS strip and microstrip ground plane as follows. One of them is the transition structure via directly electrical contact and the other is the method using electromagnetic coupling between two different layers. However, the former structure has the drawback due to the fabrication of several via holes and the latter requires large surface area for sufficient coupling.

In this paper, a new wideband microstrip to CPS transition structure to solve the above problems is introduced and broadband bowtie antenna using the transition balun is designed. The proposed antenna was optimally simulated and fabricated on Teflon substrate for bandwidth from 2.2 GHz to 6 GHz.

2. ANTENNA DESIGN

Figure 1 shows a configuration of the proposed microstrip to CPS transition balun. In this structure, the electric field distribution of the microstrip line as unbalanced transmission line is transformed to one of CPS as a balance one by using a via-hole and a tapered ground line on the bottom plane. In addition, the low impedance of the microstrip lines is gradually changed to the high impedance of the CPS. We can achieve electrical contact between two different layers by only one via-hole in this transition.

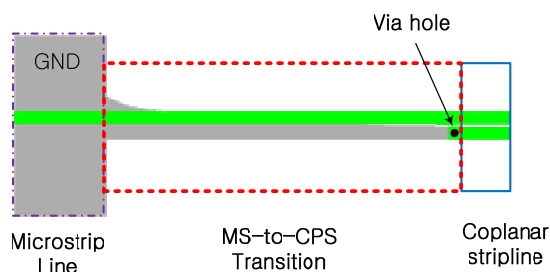


Figure 1: Configuration of the proposed microstrip to CPS transition balun.

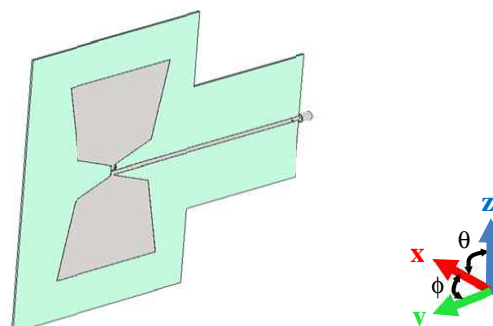


Figure 2: Designed bowtie antenna with the proposed balun.

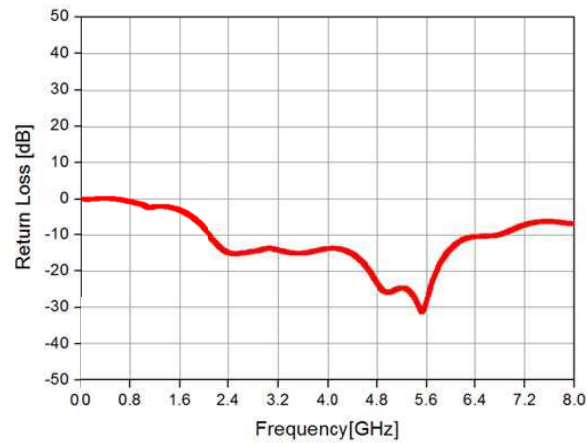
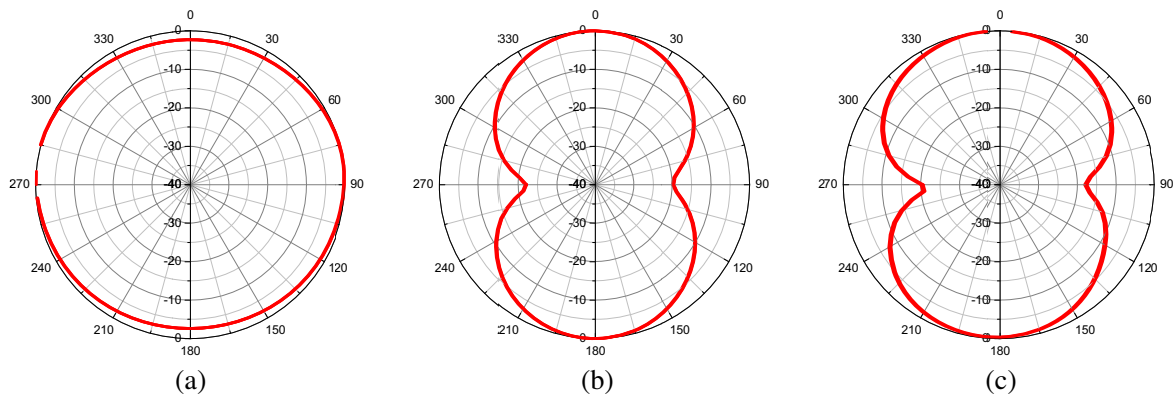


Figure 3: Return loss of the designed antenna.

Figure 4: Radiation pattern of the designed antenna. (a) Azimuth ($\theta = 90^\circ$). (b) Elevation-1 ($\varphi = 0^\circ$). (c) Elevation-2 ($\varphi = 90^\circ$).

The designed bowtie antenna using the proposed transition balun is presented in Figure 2. This antenna is designed to operate from 2.2 GHz to 6 GHz. The dielectric substrate is used as that with a dielectric constant of 3.5 and a thickness of 20 mil. The size of antenna is 73 mm (W) \times 91 mm (H). In this design, the impedance of microstrip line is $50\ \Omega$ and the characteristic impedance of CPS is $120\ \Omega$. The width of the microstrip line is 1.1 mm and the strip width and gap of the CPS are 1.1 mm and 0.2 mm. And the bottom ground line of the microstrip line is tapered to match the impedances between the microstrip line and the CPS one.

Figure 3 shows the simulation result for return loss of the designed antenna. In this result, the simulation result is less than 10 dB from 2.1 GHz to 6.5 GHz.

In Figure 4, the simulation results of radiation patterns for the proposed antenna are shown. Figure 4(a) azimuth pattern, and Figure 4(b) and Figure 4(c) are elevation patterns. From these results, we can know that the designed antenna has omnidirectional pattern.

3. RESULTS AND DISCUSSIONS

The proposed antenna is fabricated on RF-35 substrate, and fed by SMA connector. Figure 5 is the photograph of the fabricated antenna using the proposed transition balun.

Figure 6 shows the measured results for return loss of the fabricated antenna. From the result, we can see that the measured return loss is similar to above the simulated result. The measured result is less than 10 dB from 2.1 GHz to 6.5 GHz.

Figure 7 shows the measured gain. The measured gain is $-4.5 \sim 2.4$ dBi from 2.2 GHz to 6 GHz.

Figures 8(a) and 8(b) are the photographs of the measurement environment. This measurement system is installed in 10-meter-long 3D anechoic chamber. Figure 8(a) is the transmission antenna and Figure 8(b) is the fabricated antenna.

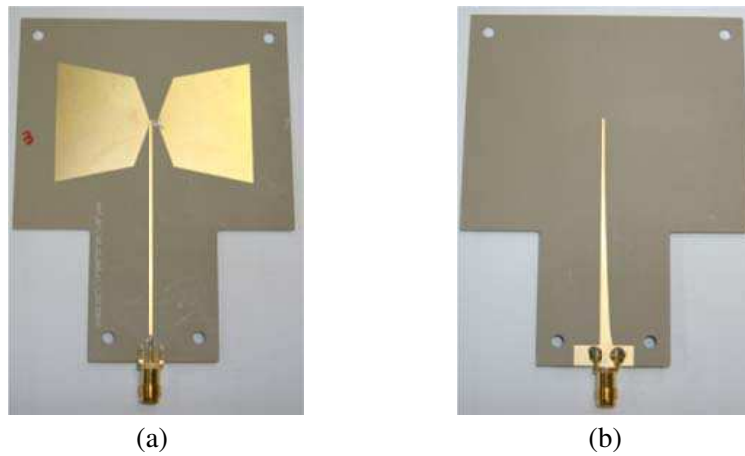


Figure 5: Fabricated bowtie antenna with the proposed balun. (a) Top view. (b) Bottom view.



Figure 6: Measured return loss of the fabricated antenna.

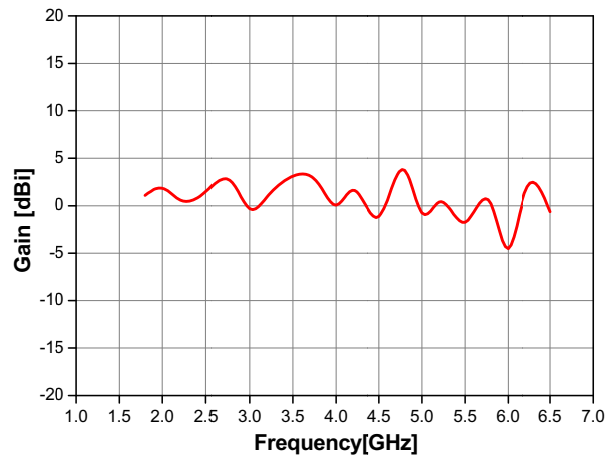
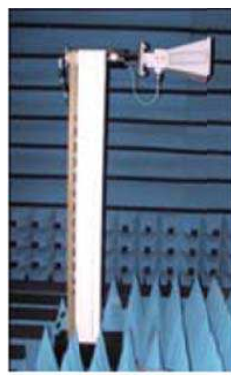


Figure 7: Measured gain of the fabricated antenna.



(a)



(b)

Figure 8: Fabricated antenna which was installed in the anechoic chamber. (a) Transmission antenna. (b) Fabricated antenna (AUT).

In Figure 9, the measured results of radiation patterns for the proposed antenna are shown. From this result, we can see that the measured results are similar to the simulated results of Figure 4 but are distorted slightly. That difference results from measurement environment, such as measurement jig, RF cable, and mast.

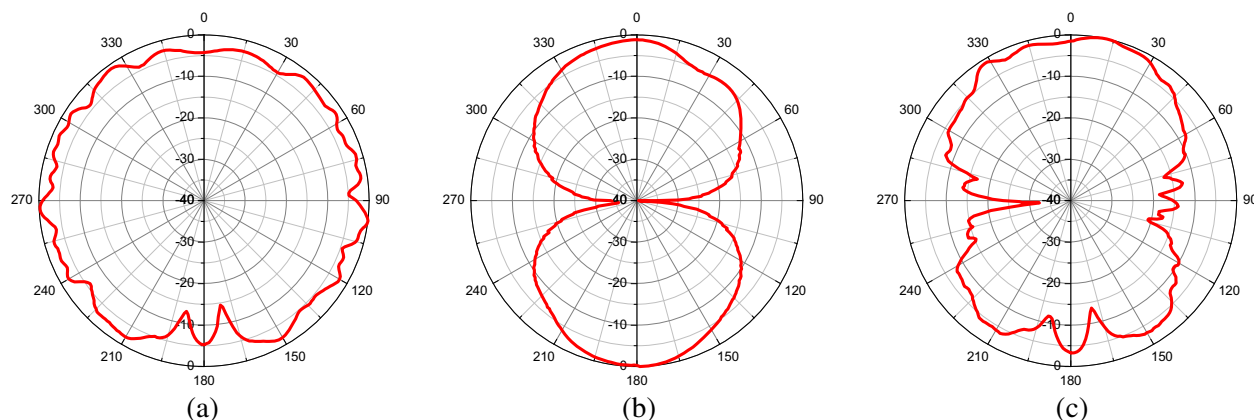


Figure 9: Measured radiation pattern of the designed antenna. (a) Azimuth ($\theta = 90^\circ$). (b) Elevation-1 ($\varphi = 0^\circ$). (c) Elevation-2 ($\varphi = 90^\circ$).

4. CONCLUSION

In this paper, a broadband bowtie antenna using a microstrip to CPS transition is proposed. The bowtie element and the transition balun are optimized for the frequency range from 2.2 GHz to 6 GHz. To verify the practicality of this antenna, we fabricated the antenna and measured the antenna performance. Both the measured and simulation results for return loss are in good agreement. The results of gain and radiation pattern also show good performances. Therefore, the proposed broadband antenna is very useful in various wireless application areas due to small size and simple structure.

ACKNOWLEDGMENT

This work was supported by Institute for Information & communications Technology Promotion(IITP) grant funded by the Korea government(MSIP) (No. B0101-15-1291, Development of Smart Radio Monitoring Platform Technology).

REFERENCES

1. Suh, Y. H. and K. Chang, "A wideband coplanar stripline to microstrip transition," *IEEE Microwave. Wireless Compon. Lett.*, Vol. 11, No. 1, 28–29, Jan. 2001.
2. Kim, Y. G., D. S. Woo, K. W. Kim, and Y. K. Cho, "A new ultra-wideband microstrip-to-CPS transition," *IEEE Int'l. Symp. Microwave*, 1563–1566, Honolulu, HI, Jun. 2007.
3. Lim, T. B. and L. Zhu, "Compact microstrip-to-CPS transition for UWB application," *IEEE MTT-S Int'l Microwave Workshop*, 153–156, Chengdu, China, Dec. 2008.
4. Chiu, T. and Y. S. Shen, "A broadband transition between microstrip and coplanar stripline," *IEEE Microwave Wireless Compon. Lett.*, Vol. 54, No. 3, 1084–1089, Mar. 2006.

Two Elements MIMO Antenna for a WLAN System

Hui Liu^{1,2}, Cheng Liu², Binjie Wang², Qibin Deng², and Youhuan Guo¹

¹Computer Science and Engineering Department, Guangdong Peizheng College, Guangzhou, China

²Centre for Optical and Electromagnetic Research, Academy of Advanced Optoelectronics
South China Normal University, Guangzhou, China

Abstract— A MIMO antenna with two elements, operating on 2.45-GHz WLAN band frequency, for asymmetric structure MIMO system was designed in this paper. The printed inverted-F and meander line structures were used for the antenna element. Because of the asymmetric structure MIMO system, each of the proposed antennas should be consisted of different dimensions to improve the performance of the MIMO antenna. The isolation, S_{11} and envelop correlation coefficient (ECC) parameters are discussed.

1. INTRODUCTION

Multiple-Input Multiple-Output (MIMO) technology, which utilizes multiple antenna to improve spectrum efficiency and increase the system channel capacity, is one of the key technologies in wireless communication system, such as 4G or WLAN system.

Due to many mounted ICs on the top or bottom PCB of the MIMO system, it is difficult for the simulation of antenna with mounted ICs and we use rectangle as the top and bottom of the PCB for simulation, it is easy to model with this method. The integration of antennas on the MIMO device with very limited space, so there will be mutual coupling between antennas and how to design a MIMO antenna with high isolation is of great importance for MIMO system.

Various printed antennas have been proposed in literature recently. In [1], the proposed antenna consists of two back-to-back planar inverted-F antennas and a fork-shaped stub for decoupling. In [2], a simple shape of L MIMO antenna with two port for the 2.4-GHz WLAN system is presented. The impedance matching for the WLAN system can easily be achieved by tuning the feeding positions. A proposed dual antenna with a Π -shape grounded strip and covering the entire LTE high band was proposed in [3]. the Π -shape grounded strip not only performs as a radiator but also serves as an isolator to enhance the isolation of the dual-antenna. Three different microstrip MIMO antennas for USB dongle were proposed in [4]. The lumped capacitance and the matching circuit was used for the second designed MIMO antenna system. The usage of a lumped decorrelation capacitance can tune the antenna coupling so that to provide high isolation.

The [5] presented a dual-band IFA-based antenna for a USB dongle application. A branch inserted in the IFA antenna to achieve the higher 5.8 GHz frequency band for the proposed configuration. All the designed antennas in [1–4] have a symmetric structure and may not be suitable for a asymmetric structure system.

In the present work, a meandered line IFA antenna was used and printed on one top layer of the FR4 substrate with a thickness of 0.8 mm. The antenna was designed to cover the 2.4 GHz WLAN band for a asymmetric structure WLAN MIMO system. It was discussed that the performance of antenna elements with different dimensions which can provide a reference for antenna design of the asymmetric structure MIMO system.

2. ANTENNA DESIGN

The basic antenna element has the shape of English character F, and hence it is called inverted-F antenna. The print IFA is a new different antenna based on the basis of monopole antenna with a short-circuit line, so the transmission line theory of the original model must be modified.

The print IFA can be similar to a transmission line which is shorted in one end and which is opened in another. It can be modeled by the equivalent circuit method and Figure 1 shows the equivalent circuit of printed IFA. According to this model, a formula for evaluating the equivalent admittance of the equivalent circuit is presented as below, Y_1 and Y_2 are equivalent admittance of L_2 and L_1 respectively. Y in is the equivalent shunt admittance of L_2 and L_1 .

Where are the characteristic admittance of the micro strip line and the radiation admittance, β is propagation constant. Where Z_0 is the characteristic impedance of transmission line.

with different dimensions of TYPE1, as in TYPE2, the resonance frequency of element *A* is different from element *B* and one of the elements' dimensions should be changed to make sure both of resonance frequencies near the 2.45 GHz band for WLAN system.

The 3D farfield radiation patterns were simulated by CST. Figure 4 shows simulated patterns of element *A* and element *B* at the typical 2.45 GHz frequency. Element 1 is shown in the right and element 2 is shown in the left.

The correlation coefficient (ρ) is a measure that describes how much the communication channels are isolated or correlated with each other. This metric considers the radiation pattern of the antenna system, and how much the patterns affect one another when operated simultaneously. The square of the correlation coefficient is known as the envelop correlation coefficient [6]. The envelop correlation coefficient (ρ_e) can be calculated using the following Formula (1).

$$\rho_e = \frac{\left| \iint_{4\pi} [\vec{F}_1(\theta, \varphi) * \vec{F}_2(\theta, \varphi)] d\Omega \right|^2}{\iint_{4\pi} |\vec{F}_1(\theta, \varphi)|^2 d\Omega \iint_{4\pi} |\vec{F}_2(\theta, \varphi)|^2 d\Omega}, \tag{1}$$

where \vec{F}_i is the three-dimensional field radiation pattern of the antenna when the *i* port is excited, and Ω is the solid angle. The asterisk is the Hermitian product operator. This is a complicated

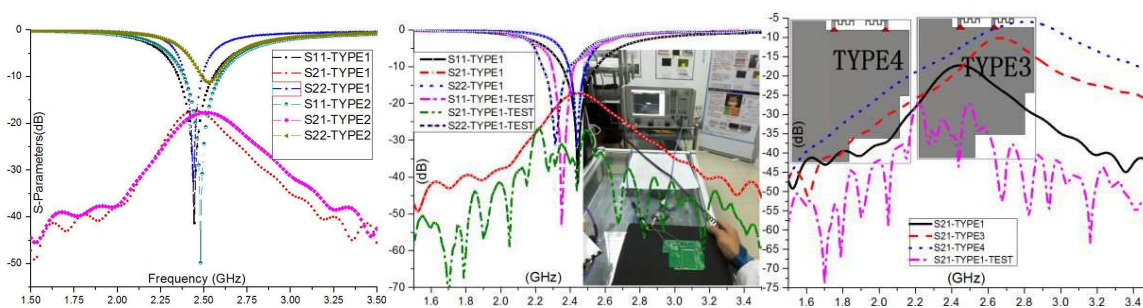


Figure 3: S-parameters.

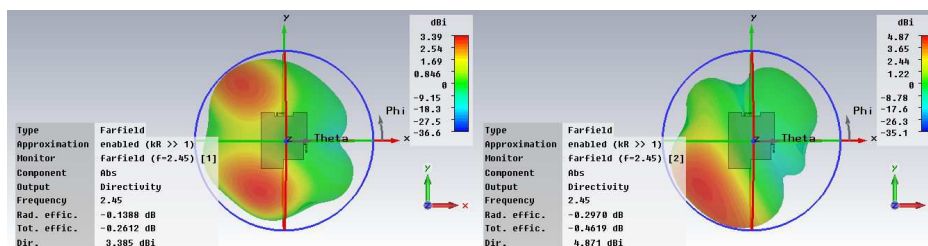


Figure 4: 3D radiation patterns.

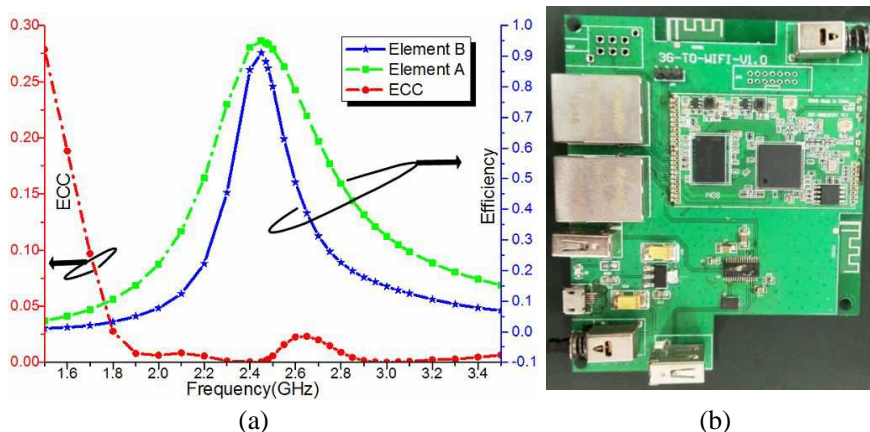


Figure 5: (a) ECC and element radiation efficiency. (b) WLAN system.

expression that requires three-dimensional radiation-pattern measurements and numerical integration.

As shown in Figure 5(a), the radiation-pattern-based ECC of the proposed MIMO antenna has the ECC of below 0.03 near 2.45-GHz frequency bands. The total efficiencies of element A and element B were shown in Figure 5(b) and both element A and B have a efficiency more than 80% at the 2.45 GHz band. Two elements meander line inverted-F antenna with different sizes integrated in the WLAN MIMO system were shown in Figure 5(b).

4. CONCLUSION

The MIMO antenna with two elements for WLAN system at the 2.45-GHz band has been simulated and test in this paper. The antenna element was of meandered line printed inverted-F structure. The antenna elements were printed on the top PCB of a WLAN system. To compare with the simulated and test results, the test resonance frequency have a shift to the lower band than simulated and the test S_{21} was better than simulated. Too many mounted ICs on the top or bottom PCB of the MIMO system might yield the different results and authors should have a consider during the process of simulation. It also can be used at 5.8-GHz band WLAN system if the dimensions of antenna elements were reduced. Unlike the conventional MIMO antennas with a symmetrical structure, this antenna verified that elements dimensions should be different to get a same working band in the practical MIMO system.

ACKNOWLEDGMENT

This work was supported by Guangdong Peizheng College Key Research Program (Nos. 14pzxmyb013 and 14pzxmzd02), the partial support of Guangdong Innovative Research Team Program (No. 201001D0104799318), the National High Technology Research and Development Program (863 Program) of China (No. 2012AA030402) and the National Natural Science Foundation of China (No. 61108022).

REFERENCES

1. Tang, Z., B. Wang, Y. Yin, and R. Lian, "Wideband planar inverted-F MIMO antenna with high isolation," *Progress In Electromagnetics Research Letters*, Vol. 51, 67–72, 2015.
2. Wang, S.-M., "A compact printed MIMO antenna integrated into a 2.4 GHz WLAN access point applications," *Asia-Pacific Microwave Conference Proceedings*, 639–641, 2013.
3. Wong, K.-L. and P.-W. Lin, "Compact dual-antenna with Π -shape grounded strip for enhanced bandwidth and decreased coupling for LTE tablet computer application," *Microwave and Optical Technology Letters*, Vol. 57, No. 1, 104–111, 2015.
4. Ssorin, V., A. Artemenko, A. Maltsev, A. Sevastyanov, and R. Maslennikov, "Compact MIMO microstrip antennas for USB dongle operating in 2.5–2.7 GHz frequency band," *International Journal of Antennas and Propagation*, Vol. 2012, Article ID 793098, 13 Pages, 2012.
5. Dias, M. H. C., B. R. Franciscatto, H. Adel, and T.-P. Vuong, "Dual-band compact planar antenna for a low-cost WLAN USB dongle," *International Journal of Antennas and Propagation*, Vol. 2014, Article ID 793191, 11 Pages, 2014.
6. Liu, H., Y. Guo, T. Pan, Z. He, and S. He, "Printed inverted-F MIMO antenna for TD-LTE mobile terminal," *PIERS Proceedings*, 1562–1566, Guangzhou, China, Aug. 25–28, 2014.

A Printed Inverted-F MIMO Antenna for WiFi Applications

Cheng Liu¹, Hui Liu¹, Binjie Wang¹, Zhibin He¹, and Sailing He^{1,2}

¹Centre for Optical and Electromagnetic Research, Academy of Advanced Optoelectronics
South China Normal University, Guangzhou, China

²The Royal Institute of Technology, Stockholm, Sweden

Abstract— A wideband printed inverted-F MIMO antenna designed for WiFi applications is presented. The proposed MIMO antenna which consists of two modified inverted-F antenna elements and an isolated structure is designed on a two-layer FR-4 printed circuit board (PCB). The occupied antenna area has the dimensions of 98 mm * 98 mm and the thickness of substrate is 0.8 mm. The functions of antenna's structure and the effects of some parameters on the antenna performance are discussed in this paper. The designed MIMO antenna system has a wide bandwidth measured more than 0.78 GHz (2.25–3.03 GHz) at the reflection coefficient level below -10 dB. Due to a folded isolated structure, in the whole measured frequency band the mutual coupling is lower than -15 dB, the MIMO antenna has good isolation. On the xy and yz planes the max gain of MIMO antenna can achieve 3 dB. The parameters of simulating and testing are shown that this MIMO antenna has good performance for WiFi applications.

1. INTRODUCTION

In recent years, WLAN applications are expected to support high data rates. Multiple-input multiple-output (MIMO) is a key technology in the good quality and high channel capacity communication. In MIMO system both antennas are transmitting and receiving data at the same time. The inverted-F antenna is a structural deformation of the monopole antenna. It has been employed in the field of short distance wireless communication due to its low profile and simple structure.

Some scholars have done many works about the MIMO antenna recently. In [1], a printed dual-antenna system operating in the GSM and 2.4 GHz WLAN bands for mobile terminals is proposed, two grounded branches are used to get good isolation, and have good performance. In [2], five elements inverted-F antenna array for MIMO communications is designed without using any specific multi-antenna isolation techniques, optimized to enhanced capacity. Another MIMO antenna at 2.45 GHz which has broad bandwidth is designed in [3, 4]. In [5], a cross branch is used at its corner of the ground to achieve a circular polarization characteristic. In [6], a compact planar inverted-F antenna system with high isolation operating in 2.5–2.7 GHz band is proposed, the two inverted-F antennas is placing mirror symmetrical orientation.

A broadband inverted-F MIMO antenna for WLAN applications printed on top layer of 0.8 mm thick with FR4 PCB substrate is proposed in this paper. The antenna covers a broad bandwidth from 2.31 GHz to 3.13 GHz. This paper also is discussed the antenna simulation and test. In [7], some comparisons have been done to study the inverted-F antenna with circuit layout or mounted ICs effects on the antenna parameters.

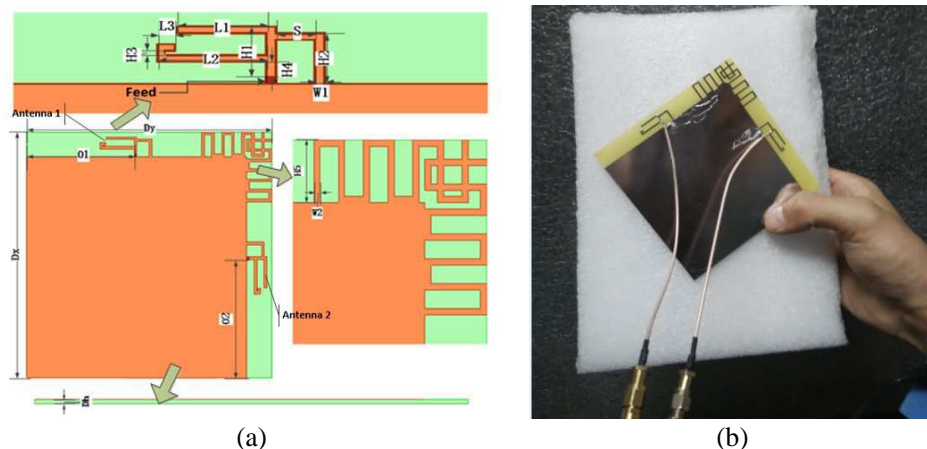


Figure 1: (a) Geometry with detailed dimensions of the MIMO antenna. (b) Photo of the MIMO antenna.

2. ANTENNA DESIGN

The geometry and photo of the proposed Inverted-F MIMO antenna for WiFi applications are shown in Figure 1. The antenna consists of two elements are placed in the two adjacent sides of a PCB with a volume of 98 mm * 98 mm * 0.8 mm. The substrate we used is FR4 layer (relative permittivity of 4.4, loss tangent of 0.02). The ground plane size is 88 mm * 88mm, and the size is suit for the PCB which is mounted ICs.

To improve the isolation between the two antennas, paper [8] layouts the antenna elements with different edges and adds two folded structures in the corner between the antennas. Table 1 shows the detailed dimensions of the inverted-F antenna.

Table 1: Dimensions of the proposed antenna (unit: mm).

L_1	L_2	L_3	L_4	W_1	W_2	H_1	H_2	H_3	H_4	H_5	S	D_x	D_y	D_h	O_1	O_2
11.2	13.7	2.2	3	1	1	7	7	0.5	2	10	5	98	98	0.8	43	44

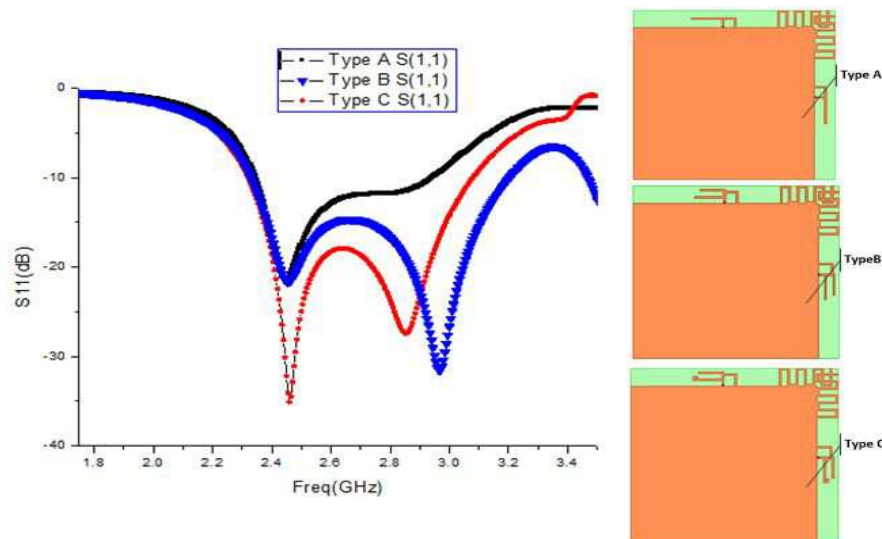


Figure 2: The S_{11} of three different type antennas.

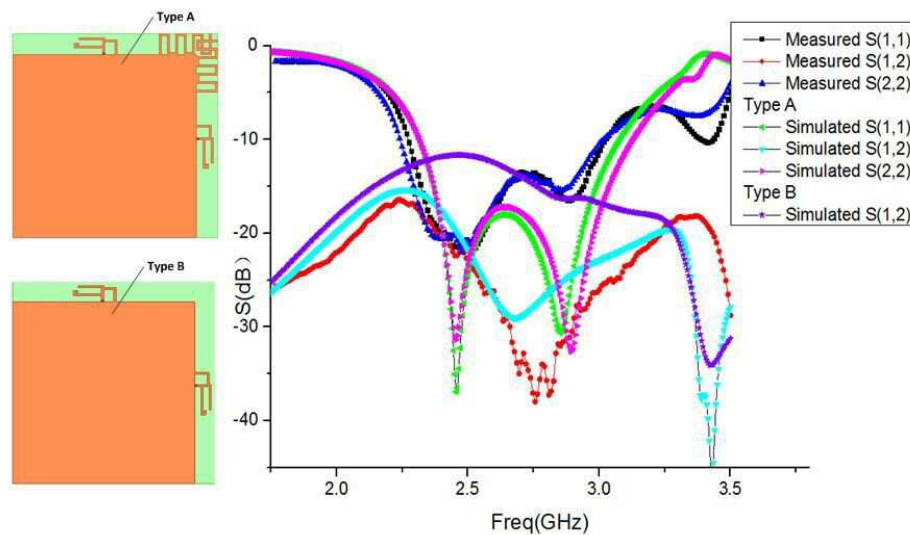


Figure 3: Simulated and measured S -parameters of proposed antenna.

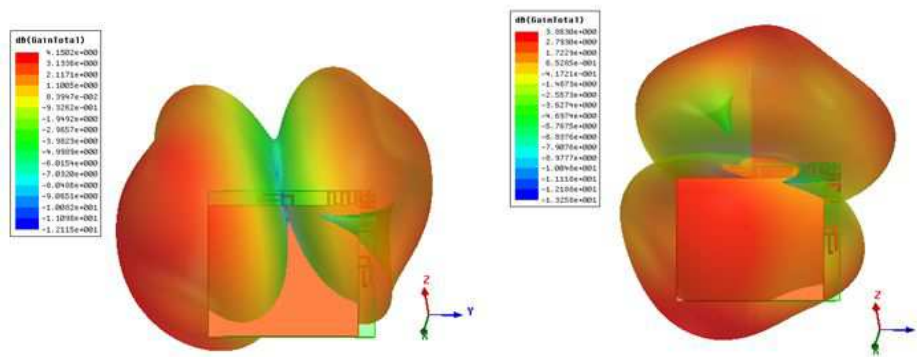


Figure 4: 3D overlay radiation field of antenna 1 and antenna 2.

Table 2: Measured and simulated S -parameters at 2.45 GHz.

S -parameters	Measured (dB)	Simulated(dB)
S_{11}	-21.4	-35
S_{12}	-22.4	-19.6
S_{22}	-20.3	-31

3. RESULTS AND DISCUSSIONS

In this paper, the inverted-F MIMO antenna is simulated and optimized by the ANSYS HFSS. In order to get broad bandwidths, another branch with the length of L_2 was used. The branch with the length of L_3 is added to get better S_{11} parameter at 2.45 GHz. The comparison of S -parameter is shown in Figure 2. The antenna only has one radiation branch with the length of L_1 is called type A antenna, type B antenna has two radiation branches with the length of L_1 and L_2 , type C antenna is added branch with the length of L_3 .

The simulated and measured S -parameters of the proposed MIMO antenna are shown in Figure 3. There are two types of antennas, type A is the whole antenna and type B antenna is the antenna without the isolation structure. While the MIMO antenna system maintaining the better isolation due to the structure. Its simulated -10 -dB impedance bandwidth is 0.82 GHz (2.31–3.13 GHz) and measured bandwidth is 0.78 GHz (2.25–3.03 GHz). Between 1.75 and 3.5 GHz, the measured mutual coupling is lower than -15 dB. Both simulated and measured all have good S -parameters. The simulated and measured S -parameters at 2.45 GHz for the MIMO antenna are tabulated in Table 2.

The simulated of 3D overlay radiation field patterns are shown in Figure 4. Antenna 1 with lumped port 1 is shown in the left side of Figure 4, antenna 2 with lumped port 2 is shown in the right side. In the radiation direction, the gain can achieve more than 3 dB.

4. CONCLUSION

A broadband Inverted-F MIMO antenna has been designed and tested in this paper. The antenna is used in WiFi application. The MIMO antenna system consists two inverted-F antenna elements, is printed on a PCB. The antenna has a wide bandwidth of more than 0.78 GHz (2.25–3.03 GHz) at the reflection coefficient level below -10 dB. Thanks to the folded isolated structure, in the whole measured frequency band the mutual coupling is lower than -15 dB. The MIMO antenna shows good performance in applications. The structure of this inverted-F MIMO antenna is simple. So the antenna is easy to design and use in practice.

ACKNOWLEDGMENT

This work was supported by Guangdong Peizheng College Key Research Program (No. 14pzxmyb013 and No. 14pzxmzd02), the partial support of Guangdong Innovative Research Team Program (No. 201001D0104799318), the National High Technology Research and Development Program (863 Program) of China (No. 2012AA030402) and the National Natural Science Foundation of China (No. 61108022).

REFERENCES

1. Wang, Y. and Z. Du, “A printed dual-antenna system operating in the GSM1800/GSM1900/UMTS/LTE2300/LTE2500/2.4-GHz WLAN bands for mobile terminals,” *IEEE Antennas and Wireless Propagation Letters*, Vol. 13, 233–236, 2014.
2. Azremi, A. A. H., M. Kyro, J. Ilvonen, J. Holopainen, S. Ranvier, C. Icheln, and P. Vainikainen, “Five-element inverted-F antenna array for MIMO communications and radio direction finding on mobile terminal,” *Loughborough Antennas & Propagation Conference*, 557–560, Nov. 2009.
3. Noordin, N. H., Y. C. Wong, A. T. Erdogan, B. Flynn, and T. Arslan, “Meandered inverted-F antenna for MIMO mobile devices,” *Loughborough Antennas & Propagation Conference*, Nov. 2012.
4. Chattha, H. T., M. Nasir, Q. H. Abbasi, Y. Huang, and S. S. AlJa’afreh, “Compact low-profile dual-port single wideband planar inverted-F MIMO antenna,” *IEEE Antennas and Wireless Propagation Letters*, Vol. 12, 1673–1675, 2013.
5. Yao, Y., J. Yu, and X. Chen, “Broadband MIMO PIFA antenna with circular polarization for RFID readers,” *Asia-Pacific Microwave Conference Proceedings*, 55–57, 2013.
6. Ssorin, V., A. Artemenko, A. Sevastyanov, and R. Maslennikov, “Compact planar inverted-F antenna system for MIMO USB dongle operating in 2.5–2.7 GHz band,” *Proceedings of the 42nd European Microwave Conference*, 408–411, 2012.
7. Kan, Y.-C. and C.-K. Chen, “Analysis of the inverted-F antennas integrated on the displacement detector for wireless sensor network applications,” *Asia-Pacific Microwave Conference Proceedings*, 1849–1851, 2009.
8. Liu, H., Y. Guo, T. Pan, Z. He, and S. He, “Printed inverted-F MIMO antenna for TD-LTE mobile terminal,” *PIERS Proceedings*, 1562–1566, Guangzhou, China, Aug. 25–28, 2014.

Design and Analysis of a Phased-MIMIO Array Antenna with Frequency Diversity

Nour El-Din Ismail, Sherif Hanafy Mahmoud, Ahmed Hamed, and Alaa Hafez
Faculty of Engineering, Alexandria University, Alexandria, Egypt

Abstract— Phased-Multiple-Input Multiple-Output (phased-MIMO) radar has been thoroughly investigated in the literature. This approach divides the transmit antenna array into multiple subarrays that are allowed to overlap. Each subarray coherently transmits a distinct waveform, which is orthogonal to the waveforms transmitted by other subarrays. While phased array radar enjoys the advantage of high coherence gain with no diversity gain, MIMO radar enjoys high diversity gain — whether waveform or spatial diversity gain — with no coherence gain. Phased-MIMO radar enjoys both advantages of coherence gain and diversity gain which enhance the main-to-side lobe levels but unfortunately decrease the antenna directivity.

Frequency diversity can improve antenna directivity by applying a small frequency increment between two successive elements but consequently increases average side lobes level. In this paper, we propose a new Phased-MIMO radar with frequency diversity which offers a tradeoff between main-to-side lobe levels and antenna directivity. This technique can exploit frequency diversity which is applied between subarray adjacent elements and between adjacent subarrays. The total beam pattern is an optimum case of the lowest side lobes level as phased-MIMO radar but with higher directivity.

1. INTRODUCTION

Phased-array antennas are called to play a fundamental role in high performance radar systems. Usually, electronic beam steering of transmitted or received electromagnetic signal with single frequency is made by means of phase shifters and attenuators associated to each one of the radiating elements that conforms the antenna array [1–4]. Thus, the beam can be steered to the desired direction by controlling the phase shifters across elements. It offers coherent gain which is useful for detecting/tracking targets and suppressing sidelobe interferences from other directions. The requirements of many emerging applications drive The need for new more advanced antenna array technologies [5–9].

The emerging concept of multiple-input multiple-output (MIMO) radar has been the focus of intensive research [10–12]. Currently, two types of MIMO radar systems are being investigated: MIMO radars with widely-separated antennas and MIMO radars with colocated antennas. Both have uniquely many advantages, but both also face many challenges.

MIMO radar with widely-separated antennas have two important features: space-diversity and spatial multiplexing. As a result, they can exploit radar cross section (RCS) diversity [13], they can handle slow moving targets by exploiting Doppler estimates from multiple directions [14], and they can support high resolution target localization [15]. However, they can also face problems with time and phase synchronization. As the data volume to be transmitted to the processing center in realtime is very large, these radars also face transmission and processing issues. Also, as they employ isotropic transmission antennas that transmit energy evenly to space [11], they cannot use most of their energy to illuminate the target and thus experience losses in signal-to-noise ratio (SNR).

MIMO radar with colocated antennas can exploit waveform diversity. This is important as it can: (a) significantly improve system identification; (b) increase target detection and parameter estimation performance when combined with adaptive arrays; (c) enhance transmit beam pattern design [12]; and (d) enable the design of airborne or ship-borne radars. However, because the antennas are colocated, the main drawback is the loss of space diversity which is needed to mitigate the effect of target fluctuations.

A. Hassanien, et al. [22] propose a new technique for MIMO radar with colocated antennas which called phased-MIMO radar. The new technique enjoys the advantages of the MIMO radar without sacrificing the main advantage of the phased-array radar which is the coherent processing gain at the transmitting side.

In this paper, we propose a new Phased-MIMO radar system technique that can exploit frequency diversity. This new system uses colocated Phased-MIMIO antenna which enjoys the advantage of phased array antenna, coherent gain, and the advantage of MIMO radar, waveform diversity

gain, in addition to the advantage of frequency diversity gain which mitigates the effect of target fluctuations and improving the antenna beam pattern by reducing the side lobes level.

The remaining sections are organized as follows.

Section 2 introduces the new approach of phased-MIMO radar with frequency diversity model compared to other models which differ in frequency diversity existence and elements correlation. In Section 3, simulation and results are illustrated for all the above models including figures and comments. Finally this paper is concluded in Section 4.

2. NEW PHASED-MIMO WITH FREQUENCY DIVERSITY MODEL

In this section, the transmit array is divided into multiple K subarrays which can be disjoint or overlapped, as shown in Figure 1. Each transmit sub-array can be composed of any number of elements ranging from 1 to M . However, unlike the general phased-MIMO array discussed in the literature, in this paper we will partition the array into K sub-arrays with transmitting elements in each sub-array following the rule $M_K = M - K + 1$ where M_K is the number of elements in each sub-array. A beam can be formed by each sub-array towards a certain direction. The beamforming weight vector can be properly designed to maximize the coherent processing gain. At the same time, different waveforms are transmitted by each sub-array. Each sub-array has a waveform ϕ_k orthogonal to other sub-array waveforms, in addition to a frequency shift $\pm\Delta f$ with respect to its neighbor sub-arrays. This orthogonality offers a waveforms diversity gain where the frequency shift offers a frequency diversity gain. Suppose the k th sub array consists of $M_k < M$ transmit elements, the equivalent baseband signal model of the k th sub array can be modeled as,

$$S_k(t) = \sqrt{\frac{M}{K}} \Phi_k(t) \tilde{w}_k^* \quad k = 1, 2, \dots, K \quad (1)$$

where K is the number of sub-arrays, \tilde{W}_k is the $M \times 1$ unit-norm complex vector which consists of M_K beamforming weights corresponding to the active antennas of the k th sub-array, that is, the number of nonzero in \tilde{W}_k equals to M_K and the number of zeros equals to $M - M_K$. Note that $\sqrt{M/K}$ is used to obtain an identical transmission power constraint for subsequent comparison, which means the transmit energy within one pulse repetition interval (PRI) is given by

$$E_k = \int_{T_p} S_k^H(t) S_k(t) dt = \frac{M}{K} \quad (2)$$

This means that the total transmitted energy for the phased-MIMO radar within one radar pulse is equal to M . The signal reflected by a hypothetical target located at direction in the far-field can be then modeled

$$S_r(t, \theta) = \sqrt{\frac{M}{K}} \sigma_s(\theta) \sum_{k=1}^K \sum_{m_k=1}^{M_K} \Phi_k(t) a_k(\theta) w_{m_k}^H b_{m_k}(\theta) \quad (3)$$

$$a_k(\theta) = e^{-j\frac{2\pi}{c}(k-1)[\Delta f R_o - f_0 d \sin \theta - (k-1)\Delta f d \sin \theta]} \quad (4)$$

$$b_{m_k}(\theta) = e^{-j\frac{2\pi}{c}(m_k-1)[\Delta f R_o - f_0 d \sin \theta - (m_k-1)\Delta f d \sin \theta]} \quad (5)$$

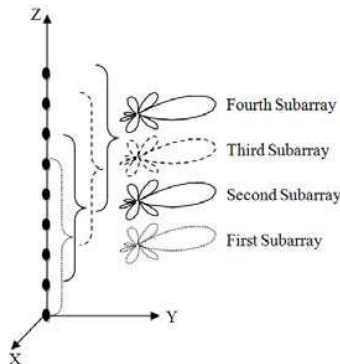


Figure 1: Illustration of the phased-MIMO array.

where σ_s is the reflection coefficient of the hypothetical target, θ is the aspect angle between target and radar boresight w_{m_k} is the complex weight of the m_k th antenna $a_k(\theta)$ is the phase shift between the signal sat the first antenna of the array and the first antenna of the k th sub-array due to both spatial displacement and frequency diversity $b_{m_k}(\theta)$ is the phase shift between the signals at the first antenna and the m_k th antenna for each subarray due to both spatial displacement and frequency diversity, R_0 is the target range measured from the first antenna of the array, d is the displacement between two successive antennas, f_0 is the carrier frequency of the 1st antenna and Δf is the increment step frequency between two successive either antennas or subarrays which equals to:

$$\Delta f = \frac{c}{2L \sin \theta} \quad (6)$$

where C is the speed of electromagnetic waves and L is the length of the target. Note that $L \sin \theta$ is the length of the target projected along the radar boresight. We assume that the first antenna is taken as a reference antenna.

It's disputable that the signal reflected $S_{r(t,\theta)}$ varies according to the existence of coherence gain, waveform diversity gain and frequency diversity gain as follows:

case (1): for phased array radar without frequency diversity ($\Delta f = 0$, $K = 1$), Equation (3) simplified to:

$$S_{r(t,\theta)} = \sqrt{M} \sigma_s(\theta) \Phi_1(t) \sum_{m_k=1}^M w_{m_k}^H e^{-j \frac{2\pi}{c} (m_k-1) (-f_0 d \sin \theta)} \quad (7)$$

case (2): for phased array radar with frequency diversity ($\Delta f \neq 0$, $K = 1$), Equation (3) simplified to:

$$S_{r(t,\theta)} = \sqrt{M} \sigma_s(\theta) \Phi_1(t) \sum_{m_k=1}^M w_{m_k}^H e^{-j \frac{2\pi}{c} (m_k-1) [\Delta f R_0 - f_0 d \sin \theta - (m_k-1) \Delta f d \sin \theta]} \quad (8)$$

case (3): for MIMO radar without frequency diversity ($\Delta f = 0$, $K = M$), Equation (3) simplified to:

$$S_{r(t,\theta)} = \sigma_s(\theta) w^H \sum_{k=1}^M \Phi_k(t) e^{-j \frac{2\pi}{c} (k-1) (-f_0 d \sin \theta)} \quad (9)$$

case (4): for MIMO radar with frequency diversity ($\Delta f \neq 0$, $K = M$), Equation (3) simplified to:

$$S_{r(t,\theta)} = \sigma_s(\theta) w^H \sum_{k=1}^M \Phi_k(t) e^{-j \frac{2\pi}{c} (k-1) [\Delta f R_0 - f_0 d \sin \theta - (k-1) \Delta f d \sin \theta]} \quad (10)$$

case (5): for Phased MIMO radar without frequency diversity ($\Delta f = 0$, $1 < K < M$), Equation (3) simplified to:

$$S_{r(t,\theta)} = \sqrt{\frac{M}{K}} \sigma_s(\theta) \sum_{k=1}^K \sum_{m_k=1}^{M_K} w_{m_k}^H \Phi_k(t) e^{-j \frac{2\pi}{c} (k-1) (-f_0 d \sin \theta)} e^{-j \frac{2\pi}{c} (m_k-1) (-f_0 d \sin \theta)} \quad (11)$$

case (6): for Phased MIMO radar with frequency diversity ($\Delta f \neq 0$, $1 < K < M$), Equation (3) express this case as:

$$S_{r(t,\theta)} = \sqrt{\frac{M}{K}} \sigma_s(\theta) \sum_{k=1}^K \sum_{m_k=1}^{M_K} W_k^H \Phi_k(t) e^{-j \frac{2\pi}{c} (k-1) [\Delta f R_0 - f_0 d \sin \theta - (k-1) \Delta f d \sin \theta]} e^{-j \frac{2\pi}{c} (m_k-1) [\Delta f R_0 - f_0 d \sin \theta - (m_k-1) \Delta f d \sin \theta]} \quad (12)$$

Now let us introduce the $K \times 1$ transmit coherent processing vector with frequency diversity

$$C(\theta) = [W_1^H B_1(\theta), \dots, W_K^H B_K(\theta)]^T \quad (13)$$

where $B_K(\theta) = [b_1(\theta), b_2(\theta), \dots, b_{M_K}(\theta)]^T$ is $M_K \times 1$ transmit steering vector and $W_K = [w_1, w_2, \dots, w_{M_K}]^T$ is $M_K \times 1$ beamforming vector which contains only the elements corresponding to the active antennas of the k th sub-array.

The $K \times 1$ diversity vector (waveform diversity vector combined with frequency diversity vector)

$$D(\theta) = [a_1(\theta), a_2(\theta) \dots, a_K(\theta)]^T \quad (14)$$

Then, the reflected signal (3) can be rewritten as,

$$S_r(t, \theta) = \sqrt{\frac{M}{K}} \sigma(\theta) (C(\theta) \odot D(\theta))^T \Phi_k(t) \quad (15)$$

where $\Phi_k(t) = [\Phi_1(t) \dots \Phi_k(t)]^T$ is the $K \times 1$ vector of waveforms. Assuming that the target of interest is observed in the background of P interfering targets with reflection coefficient $\{\sigma_i\}_{i=1}^P$ and locations $\{\theta_i\}_{i=1}^P$, the $N \times 1$ received complex vector of array observations can be written as,

$$X(t) = S_r(t, \theta_s) G(\theta_s) + \sum_{i=1}^P S_r(t, \theta_i) G(\theta_i) + n(t) \quad (16)$$

where, $S_r(t, \theta_s)$ and $S_r(t, \theta_i)$ are defined as in (15), N is the number of receiving elements, and $G(\theta)$ is the received steering vector. By matched-filtering $X(t)$ to each of the waveforms $\{\Phi_k\}_{k=1}^K$, we can form the $KN \times 1$ virtual data vector,

$$y = [x_1^T \dots x_k^T]^T = \sqrt{\frac{M}{K}} \sigma_s U(\theta_s) + \sum_{i=1}^P \sqrt{\frac{M}{K}} \sigma_i U(\theta_i) + \tilde{n} \quad (17)$$

where the $KN \times 1$ vector

$$U(\theta) = C(\theta) \odot D(\theta) \otimes G(\theta) \quad (18)$$

is the virtual steering vector associated with direction θ and \tilde{n} is the $KN \times 1$ noise term (noise received by N receivers containing K matched filters at each receiver) whose covariance is given by $\tilde{R}_n = \sigma_n^2 I_{KN}$ where σ_n^2 is the noise power.

3. SIMULATION AND RESULTS

In this section, we use the conventional transmit/receive beamforming techniques and analyze the performance of the proposed phased-MIMO radar with frequency diversity (case 6). We also compare this case to the phased array radar (without and with frequency diversity (cases (1 and 2) respectively)), MIMO radar (without and with frequency diversity (cases (3 and 4) respectively)) and phased-MIMO radar without frequency diversity (case (5)) in terms of their transmit/receive beam patterns. We assume a hypothetical target oriented at angle $\theta = 10^\circ$.

Comparing the received beam pattern of phased array radar (case 1), MIMO radar (case 3), and phased-MIMO radar (case 5), it can be noticed that phased-MIMO radar enjoys the lowest side lobes level but has lower directivity than the other two cases (wider beam width).

Comparing the received beam pattern of phased array radar without frequency diversity (case 1), and with frequency diversity (case 2), it can be noticed that frequency diversity enhances the beam directivity (narrower beam width) but with higher average side lobes level.

Using the same method, comparing the received beam pattern of MIMO radar without frequency diversity (case 3), and with frequency diversity (case 4), it can be noticed that frequency diversity enhance the beam directivity (narrower beam width) but with higher average side lobes level.

Combining the advantage of phased-MIMO technique, which is suppressing side lobes level and the advantage of frequency diversity, which is improving beam directivity (by getting narrower beam width), we achieved the proposed phased-MIMO radar with frequency diversity (case 6). Comparing the all six cases mentioned above, it can be noticed that the phased-MIMO radar with frequency directivity is optimum tradeoff between main-to-side lobe levels and antenna directivity.

It's observed that both case (1) and case (3) are identical and also case (2) and case (4) are identical too. Case (6) is the optimum beam pattern which has narrow beam width compared to case (5) and lower side lobes level compared with cases (1, 2, 3, and 4).

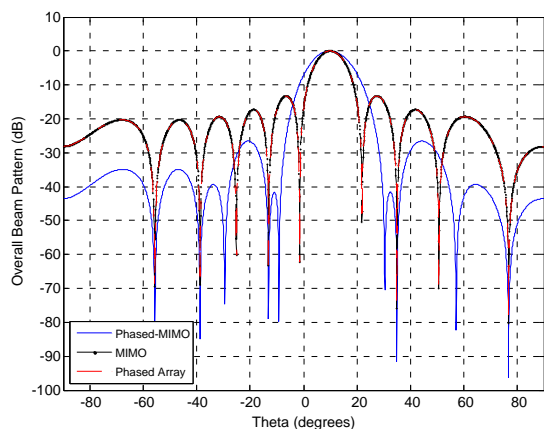


Figure 2: Overall beam pattern for phased array radar, MIMO radar, and phased-MIMO radar without frequency diversity.

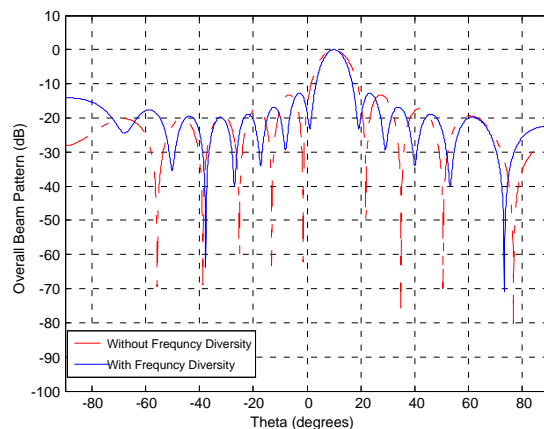


Figure 3: Overall beam pattern for phased array radar, with and without frequency diversity.

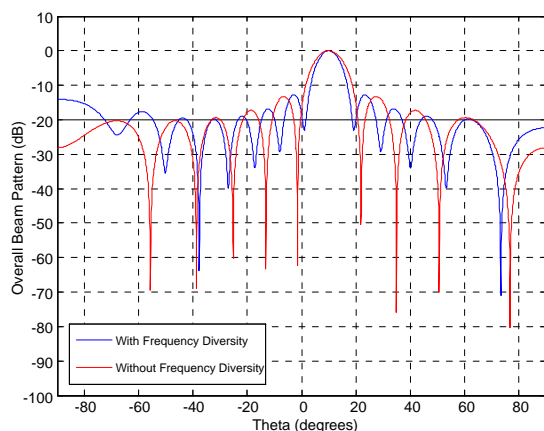


Figure 4: Overall beam pattern for MIMO radar, with and without frequency diversity.

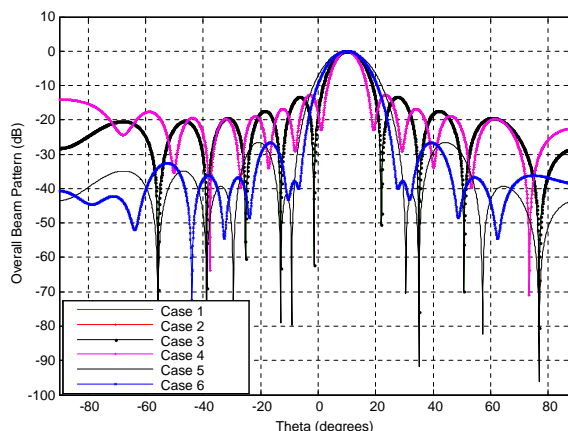


Figure 5: Overall beam pattern for the all possible six cases.

4. CONCLUSION

All possible cases of phased array, MIMO and Phased-MIMO radar in the presence and absence of frequency diversity were investigated and compared to each other. Phased-MIMO radar with frequency diversity has declared to be the optimal case of all by providing the lowest side lobes level with high directivity.

REFERENCES

1. Mailloux, R. J., *Phased Array Antenna Hand Book*, Artech House, Norwood, MA, 1994.
2. Wijnholds, S. J. and W. A. Van Cappellen, "In situ antenna performance evaluation of the LOFAR phased array radio telescope," *IEEE Transactions on Antennas and Propagation*, Vol. 59, No. 6, 1981–1989, 2011.
3. Zrnic, D. S., G. Zhang, and R. J. Doviak, "Bias correction and Doppler measurement for polarimetric phased-array radar," *IEEE Transactions on Geoscience and Remote Sensing*, Vol. 49, No. 2, 843–853, 2010.
4. Bachmann, M., M. Schwerdt, and B. Bräutigam, "Accurate antenna pattern modeling for phased array antennas in SAR applications demonstration on TerraSAR-X," *International Journal of Antennas and Propagation*, Vol. 2009, Article ID 492505, 9 Pages, 2009.
5. Wang, W. Q., "Near-space wide-swath radar imaging with multiaperture antenna," *IEEE Antennas and Wireless Propagation Letters*, Vol. 8, 461–464, 2009.
6. Younis, M., S. Huber, A. Patyuchenko, F. Bordoni, and G. Krieger, "Performance comparison of reflector- and planar antenna based digital beam-forming SAR," *International Journal of Antennas and Propagation*, Vol. 2009, Article ID 614931, 13 Pages, 2009.

7. Wang, W. Q., “Space-time coding MIMO-OFDM SAR for high-resolution remote sensing,” *IEEE Transactions on Remote Sensing*, Vol. 49, No. 8, 3094–3104, 2011.
8. Capece, P., “Active SAR antennas: Design, development, and current programs,” *International Journal of Antennas and Propagation*, Vol. 2009, Article ID 796064, 11 pages, 2009.
9. Wang, W. Q., *Near-space Remote Sensing: Potential and Challenges*, Springer, New York, NY, USA, 2011.
10. Li, J. and P. Stoica, *MIMO Radar Signal Processing*, Wiley, New Jersey, 2009.
11. Haimovich, A., R. Blum, and L. Cimini, “MIMO radar with widely separated antennas,” *IEEE Signal Processing Magazine*, Vol. 25, No. 1, 116–129, Jan. 2008.
12. Li, J. and P. Stoica, “MIMO radar with colocated antennas,” *IEEE Signal Processing Magazine*, Vol. 24, No. 5, 106–114, Sep. 2007.
13. Fishler, E., A. Haimovich, R. Blum, L. J. Cimini, Jr., D. Chizhik, and R. Valenzuela, “Spatial diversity in radars-models and detection performance,” *IEEE Transactions on Signal Processing*, Vol. 54, No. 3, 823–838, 2006.
14. Forsythe, K. W., D. W. Bliss, and G. S. Fawcett, “Multiple-input multiple-output (MIMO) radar: Performance issues,” *Proceedings of Asilomar Conference on Signals, Systems and Computers*, Vol. 1, 310–315, 2004.
15. Lehmann, N. H., A. M. Haimovich, R. S. Blum, and L. Cimini, “High resolution capabilities of MIMO radar,” *Proceedings of Asilomar Conference on Signals, Systems and Computers*, 25–30, 2006.

A Simple Monopole Slot Antenna with High Band-notch Characteristics for Ultra-wideband Communication Applications

Yingsong Li¹, Zhuqun Zhai², Wenxing Li¹, and Si Li¹

¹College of Information and Communications Engineering
Harbin Engineering University, Harbin 150001, China

²Institute of Systems, Beijing 100161, China

Abstract— In this paper, a simple ultra-wideband antenna with tunable and high rejection band-notch characteristics is proposed on the basis of a polygon slot structure. The designated notch bands are realized by the use of an inverted V-shaped stub inserted into inside of the polygon slot and a stub integrated into the radiating patch. The flexible tunable band-notch characteristics are achieved by adjusting the dimensions of the stubs. The simulation results show that the proposed antenna can provide a wide bandwidth, a flexible tunable and high rejection band-notch characteristics, and good omnidirectional radiation patterns, making it suitable for various band-notched ultra-wideband communication applications.

1. INTRODUCTION

The demand of high data rate and wide bandwidth has promoted ultra-wideband (UWB) to become an attractive technology in recent decade years. UWB antenna is one of the important components to build an indoor UWB system, which face much more challenges owing to its small size and wide bandwidth. To meet the rapidly developed UWB technologies, many printed UWB antennas with compact sizes have been proposed and investigated. However, there exist some narrowband systems, including IEEE802.11y wireless local area networks (WLAN) (3.6575–3.69 GHz), world-wide interoperability for microwave access (3.3–3.69 GHz), IEEE 802.11j WLAN band operating at 4.9–5.0 GHz and 5.03–5.091 GHz and IEEE 802.11a WLAN band operating at 5.15–5.35 GHz and 5.47–5.725 GHz, which have higher operating power than UWB systems and, hence, may interfere with UWB systems [1–13].

In order to mitigate the potential interferences from the above mentioned narrowband systems, a great number of band-notched UWB antennas have been proposed and well designed in the previous articles. Although these band-notched UWB antennas can provide desired notch band characteristics, most of them are realized by inserting various slots in the radiating patch or in the ground plane, which may leak electromagnetic waves and, hence, result in extra interferences [1–6]. Consequently, parasitic elements [7], resonators [8–12] and stub [13] have been employed to develop band-notched UWB antennas. However, some of them are complex in structure, which is difficult to tune and design in practical engineering, others are large in size or low rejection band characteristics.

For these reasons, we propose a simple ultra-wideband antenna with flexible tunable and high rejection band-notch characteristics on the basis of a polygon slot structure. The proposed band-notched characteristics are realized by using an inverted V-shaped stub inserted into inside of the pentagon slot in the coplanar waveguide (CPW) and a stub integrated into the pentagon radiating patch. The center frequencies of these band notches are tunable by adjusting the dimensions of the proposed stubs. In addition, the proposed antenna can obtain high rejection band in comparison with previously developed band-notched UWB antennas. The simulated results show that the proposed UWB antenna has a wide bandwidth, tunable band notches, high rejection notch characteristics with VSWR greater than 50, and omnidirectional radiation patterns, which makes it suitable for indoor UWB communication applications.

2. STRUCTURE OF THE PROPOSED ANTENNA

Figure 1 illustrates the geometry structure of the proposed high rejection notch band UWB antenna. The proposed antenna consists of a pentagon slot which is etched on the CPW-ground plane, a pentagon radiating patch with a polygon slot, a stub settled in the middle of the polygon slot, an inverted V-shaped stub inserted into inside of the pentagon slot and a CPW-fed structure which includes the CPW fed signal strip line and the CPW-ground plane. The UWB antenna is etched on a substrate whose relative permittivity is 2.65, and the loss tangent and the thickness of the

substrate are 0.002 and 1.6 mm, respectively. The two notch bands and high rejection function are implemented by using the inverted V-shaped stub and the stub inserted in the polygon slot. The CPW-fed signal strip (CFSS) has a width of 3.6 mm and the gap between the CFSS and the CPW ground plane is 0.2 mm. The center frequencies of the proposed antenna are tunable to cover a wide rejection band, which are used to filter out the unwanted signal from 3.5 GHz WiMAX band and 5.5 GHz WLAN band.

The proposed antenna is designed step by step and the design procedure is shown in Fig. 1. Firstly, a UWB antenna is designed and is given in Fig. 1(a), which is antenna-1. Next, a UWB antenna with a 3.5 GHz band notched is presented, which is antenna-2. Finally, another notch band is generated by using an inverted V-shaped stub inserted into inside of the pentagon slot, which is denoted as antenna-3. The antenna-3 is our proposed antenna with high rejection band notch characteristics and it has been optimized by using the HFSS. The optimized antenna geometry parameters are $L = 32$, $W = 24$, $L_1 = 1.1$, $L_2 = 13.6$, $L_3 = 9.3$, $L_4 = 3.5$, $L_5 = 14.7$, $L_6 = 3$, $L_7 = 8.5$, $W_1 = 0.5$, $W_2 = 3$, $W_3 = 0.4$ (unit: mm).

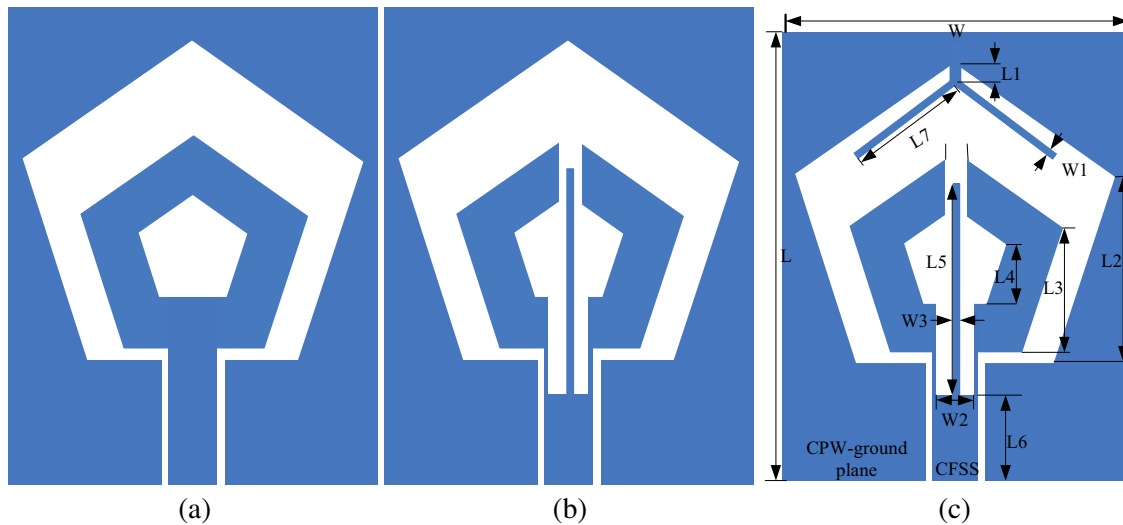


Figure 1: Geometry structure of the proposed antenna. (a) Antenna-1. (b) Antenna-2. (c) Antenna-3.

3. PERFORMANCE OF THE PROPOSED ANTENNA

In this section, parameter effects of L_5 and L_7 , band-notch characteristic, radiation patterns are investigated to exploit the performance of the proposed antenna. Fig. 2(a) shows the effects of L_5 on the impedance bandwidth. It can be seen that the center frequency of the lower notch band moves to low frequency with an increment of L_5 ranging from 13 mm to 15 mm, which is attributed to the increased L_5 that prolongs the resonance length of the stub. L_7 has important effects on the center frequency of the upper notch band. Fig. 2(b) gives the effects of L_7 on the impedance bandwidth of the proposed antenna. It is found that the center frequency of the upper notch band shifts from 6.2 GHz to 4.8 GHz when L_7 increases from 7 mm to 10 mm, while the center frequency of the lower notch keeps constant. However, the band-notched depth at the lower notch band is reduced, while the band-notched depth at the upper notch band is increased. Figure 2(c) illustrates the band-notched characteristics of the proposed antenna. It is observed that the proposed antenna without these two stubs (antenna-1) is a UWB antenna, which can cover the whole UWB band released by FCC in 2002. When the proposed antenna has only the lower stub, denoting as antenna-2, it has a notch band to filter out the unwanted narrowband interferences from 3.5 GHz WiMAX band. When the proposed antenna integrate both stubs, which is named as antenna-3, it has two notch bands operating at 3.5 GHz band and 5.5 GHz WLAN band to prevent narrowband interferences. Thus, we can say that the lower notch band is generate by using the stub which is integrated with the radiating patch together, while the upper notch band at the 5.5 GHz WLAN band is produced by the use of the inverted V-shaped stub which is inserted into inside of the pentagon slot.

The radiation patterns of the proposed antenna are investigated and are shown in Fig. 3. We can see that the proposed antenna has an omnidirectional radiation pattern in the H -plane, and a quasi-omnidirectional radiation pattern in the E -plane. However, the E -plane radiation patterns

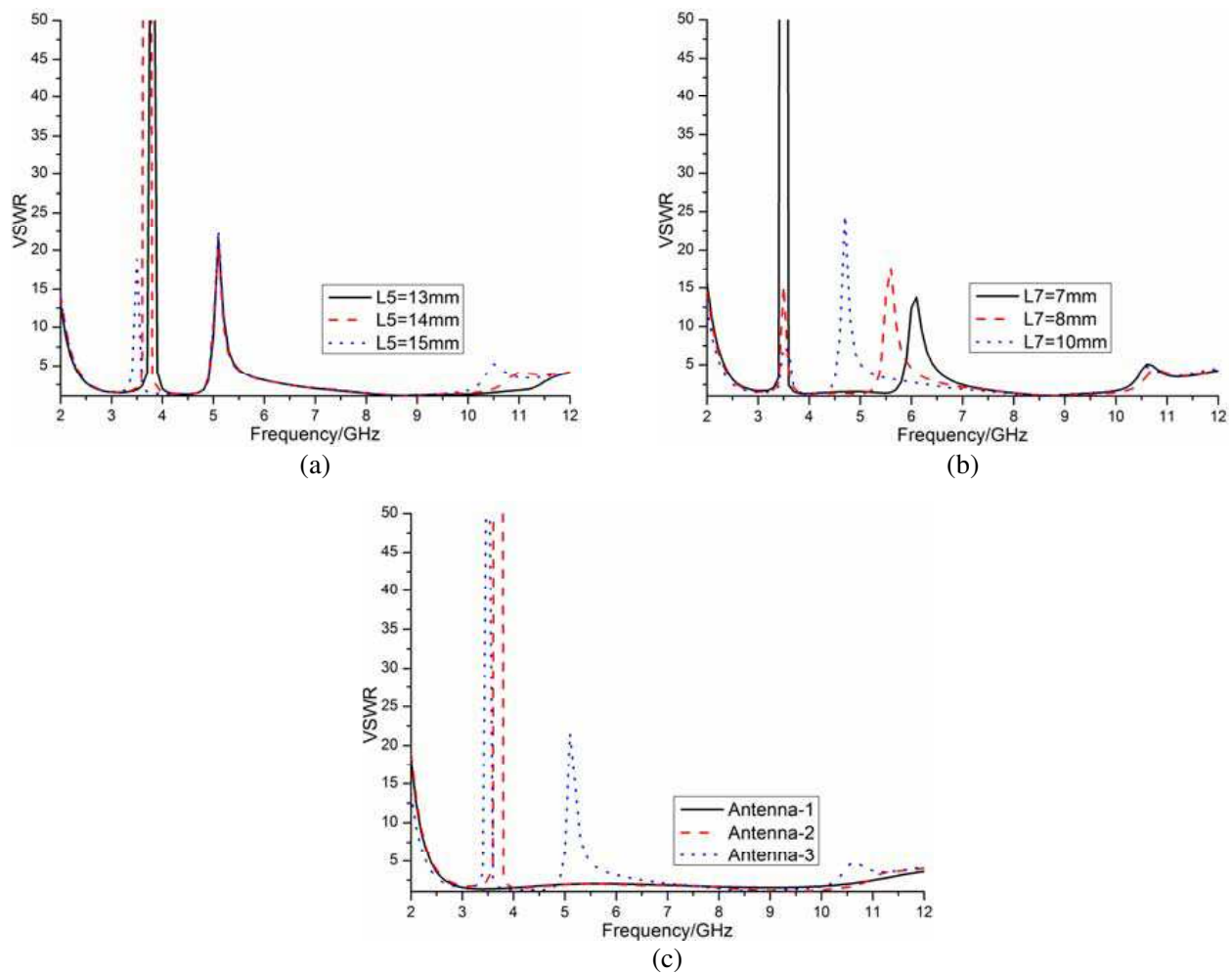


Figure 2: Performance of the proposed antenna. (a) *L5*. (b) *L7*. (c) Band-notched characteristic.

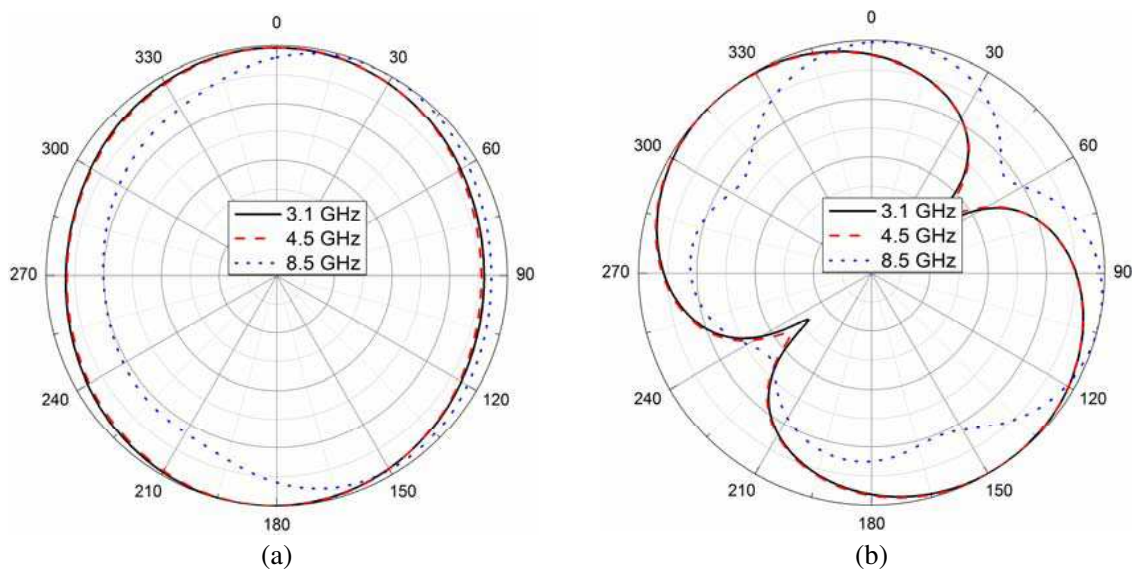


Figure 3: Radiation patterns of the proposed antenna. (a) *H*-plane. (b) *E*-plane.

are slant because of the slots which may leak extra electromagnetic waves. Table 1 compares the proposed antenna with early reported band-notched UWB antennas with respect to the size and peak VSWR which can depict the rejection depth. We note that only a few previously presented

Table 1: Comparisons of several existing band-notched UWB antennas.

References	Dimensions (mm ²)	Rejection band	Peak VSWR
[1]	28 × 21	4.5–6 GHz	> 10
[2]	40 × 31	4.13 GHz & 5.2 GHz	15
[3]	28 × 21	5–6 GHz & 8 GHz	6.3
[4]	30 × 26	3.4 GHz&5.5 GHz	9
[5]	22 × 18	3–3.8 GHz & 5–6 GHz	10
[6]	28 × 21	5–6 GHz	> 10
[7]	40 × 30	3–4 GHz & 5–6 GHz	> 8
[8]	34 × 34	5 GHz WLAN	9
[9]	40 × 31	5.15 GHz	15
[10]	34 × 27	3.23–5.93 GHz	14
[11]	33 × 25	3.5 GHz & 5.5 GHz	6
[12]	32 × 24	5–6 GHz	> 10
[13]	28 × 24	Tunable 3.55–6.8 GHz	26
Proposed	32 × 24	Tunable 3.1–7 GHz	> 50

antennas can provide peak VSWRs with their values greater than 15. Although the Reference [13] has a peak gain of 26, it can only provide a notch at each fixed dimensions. With the increment of frequency, the peak VSWR reduces quickly. At 5.5 GHz in Fig. 5 in [13], the peak VSWR is less than 10. In our design, the antenna can not only provide two tunable notch bands, but also can provide a high peak VSWR which is greater than 50 at 3.5 GHz WiMAX band and is better than 15 at the 5.5 GHz WLAN band.

4. CONCLUSION

A pentagon-slot UWB antenna with tunable and high rejection band-notched characteristics has been proposed and its performance has been evaluated in this paper. The results show that the proposed antenna has two tunable notch bands, which can filter unwanted signals from a large range. The lower notch band also has a high rejection characteristic with VSWR > 50, while the rejection depth at upper notch band reach up to 15. The results show that the antenna has two tunable notches and high rejection band, making it suitable for band-notched UWB systems.

ACKNOWLEDGMENT

This work was partially supported by the Fundamental Research Funds for the Central Universities (HEUCFD1433).

REFERENCES

1. Li, Y. S., X. D. Yang, C. Y. Liu, and T. Jiang, "Compact CPW-fed ultra-wideband antenna with band-notched characteristic," *Electronics Letters*, Vol. 46, No. 23, 1533–1534, 2010.
2. Kelly, J. R., P. S. Hall, and P. Gardner, "Planar band-notched UWB antenna," *Proc. 3rd Eur. Conf. on Antennas and Propagation (EuCAP)*, 1636–1639, 2009.
3. Li, Y. S., X. D. Yang, C. Y. Liu, and T. Jiang, "Compact CPW-fed ultra-wideband antenna with dual band-notched characteristic," *Electronics Letters*, Vol. 46, No. 14, 967–968, 2010.
4. Chu, Q. X. and Y. Y. Yang, "A compact ultra wideband antenna with 3.4/5.5 GHz dual band-notched characteristics," *IEEE Trans. Antennas Propag.*, Vol. 56, No. 12, 3637–3644, 2008.
5. Xu, J., D.-Y. Shen, G.-T. Wang, X.-H. Zhang, X.-P. Zhang, and K. Wu, "A small UWB antenna with dual band-notched characteristics," *International Journal of Antennas and Propagation*, Vol. 2012, 7 pages, Article ID 656858, 2012.
6. Li, Y., X. Yang, Q. Yang, and C. Liu, "Compact coplanar waveguide fed ultra wideband antenna with a notch band characteristic," *AEU-International Journal of Electronics and Communications*, Vol. 65, No. 11, 961–966, 2011.

7. Liu, X. L., Y.-Z. Yin, P. A. Liu, J. H. Wang, and B. Xu, "A CPW-fed dual band-notched UWB antenna with a pair of bended dual-L-shape parasitic branches," *Progress In Electromagnetics Research*, Vol. 136, 623–634, 2013.
8. Ma, T.-G., R.-C. Hua, and C.-F. Chou, "Design of a multiresonator loaded band-rejected ultrawideband planar monopole antenna with controllable notched bandwidth," *IEEE Trans. Antennas Propag.*, Vol. 56, 2875–2883, 2008.
9. Kelly, J. R., P. S. Hall, and P. Gardner, "Band-notched UWB antenna incorporating a microstrip open-loop resonator," *IEEE Trans. Antennas Propag.*, Vol. 59, 3045–3048, 2011.
10. Lin, C.-C., J. Peng, and R. W. Ziolkowski, "Single, dual and tri-band-notched ultrawideband (UWB) antennas using capacitively loaded loop (CLL) resonators," *IEEE Trans. Antennas Propag.*, Vol. 60, 102–109, 2012.
11. Sung, Y., "UWB Monopole antenna with two notched bands based on the folded stepped impedance resonator," *IEEE Antennas and Wireless Propagation Letters*, Vol. 11, 500–502, 2012.
12. Li, Y., W. Li, S. Li, C. Liu, and T. Jiang, "A CPW-fed anti-interference UWB antenna using a stepped impedance stub loaded pentagon resonator," *2012 Asia-Pacific Symposium on Electromagnetic Compatibility (APEMC)*, 901–904, Singapore, 2012.
13. Abbas, S. M., Y. Ranga, A. K. Verma, and K. P. Esselle, "A simple ultra wideband printed monopole antenna with high band rejection and wide radiation patterns," *IEEE Trans. Antennas Propag.*, Vol. 62, 4816–4820, 2014.

Design of Wideband Multi-way Power Divider with the Modified Impedance Transformer

C. W. Tang and W. M. Chuang

Center for Telecommunication Research, Advanced Institute of Manufacturing with High-Tech Innovations
Department of Communications Engineering, National Chung Cheng University, Taiwan

Abstract— An easy method for designing the multi-way wideband power divider has been proposed. In order to obtain a wide operational frequency, the corrected coefficients for the wideband impedance transformer are adopted. A wideband four-way power divider has been developed as a design example. Well-matched results of simulation and measurement can validate the proposed approach.

1. INTRODUCTION

In current wireless communication, the need for wide bandwidth is growing rapidly. Power dividers are important components in microwave applications. In addition, the multi-way power divider is a key component for phase-array antennas, power amplifiers, and multi-port circuits. Wilkinson power dividers are generally adopted for two-way power division [1]. Consequently, the multi-way power divider can be realized by interconnecting two-way Wilkinson power dividers. A general method of designing the multi-way power divider is utilizing the binominal response on the multi-stage transmission lines. However, the available bandwidth of the multi-way power divider remains limited. The multi-way power dividers with interconnection have been studied in [2–4]. In [4], a calculated method for designing the multi-way power divider with interconnecting two-way power dividers is achieved. Unfortunately, the interconnection between two-way power dividers may restrict the optimal design.

In order to obtain a wideband multi-way power divider, the corrected coefficients are adopted for the multi-stage transmission lines shown in Figure 1. With the assistance the corrected coefficients, the design of power dividers with required input reflection level can be simplified. Moreover, both even- and odd-mode analysis are provided to obtain the optimal isolation resistor values.

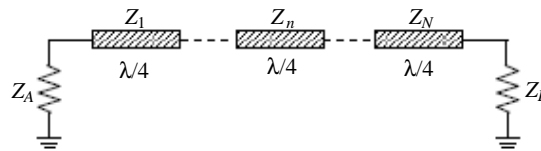


Figure 1: Diagram of the multi-stage transmission lines.

2. DESIGN FORMULAS OF THE MODIFIED IMPEDANCE TRANSFORMER

In order to obtain a wide operating bandwidth, the general binominal response utilize upon the multi-stage transmission lines can be modified by multiple the correct coefficients K_n . Consequently, the characteristic impedances Z_n can be modified by integrating the corrected coefficients K_n with transmission lines at each stage as

$$Z_n = \begin{cases} \frac{Z_A \cdot R \cdot 2^{-N} \cdot \sum_{k=0}^{n-1} C_k^N}{K_n}, & \text{for } n < \frac{N+1}{2} \\ Z_A \cdot R \cdot 2^{-N} \cdot \sum_{k=0}^{n-1} C_k^N, & \text{for } n = \frac{N+1}{2} \\ Z_A \cdot R \cdot 2^{-N} \cdot \sum_{k=0}^{n-1} C_k^N \cdot K_n, & \text{for } n > \frac{N+1}{2} \end{cases} \quad (1)$$

$$K_n = K_{N-n+1} \quad (2)$$

where $R = Z_B/Z_A$.

As for the two-stage transmission lines, Figure 2(a) shows the simulated results of $|S_{11}|$ with various corrected coefficient K_1 . It is indicated that the smaller the corrected coefficient is, the

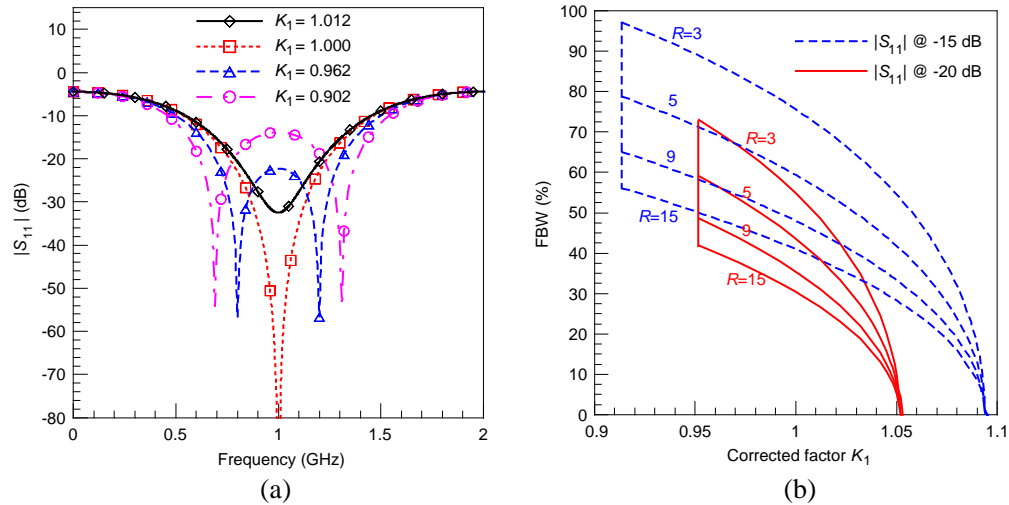


Figure 2: Simulated results of the two-stage transmission lines multiple the correct coefficient K_1 . (a) $|S_{11}|$. (b) Relation between FBW and corrected coefficient K_1 .

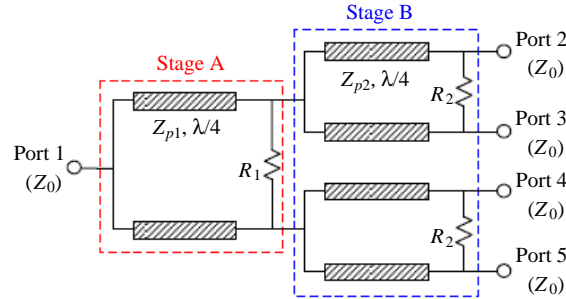


Figure 3: Structure of the exemplary four-way power divider.

larger the available fractional bandwidth (FBW), and the $|S_{11}|$ are. Moreover, there is a wider operating bandwidth with $K_1 < 1$ than that with the binomial response, $K_1 = 1$. Figure 2(b) also shows the similar tendency that the larger the impedance ratio R is, the smaller the FBW is.

3. DESIGN EXAMPLE OF THE WIDEBAND FOUR-WAY MICROSTRIP POWER DIVIDER

By interconnecting three two-way power dividers, a four-way power divider is realized with the two-stage structure, as shown in Figure 3. In Figure 3, port 1 is the input port while ports 2–5 are four output ports. The two-way power divider, indicated as Stage A in Figure 3, is composed of a resistor R_1 and two quarter-wavelength transmission lines with characteristic impedance Z_{p1} . Other two power dividers indicated as Stage B, are composed of two resistors R_2 and four quarter-wavelength transmission lines with characteristic impedances Z_{p2} . The four-way power divider is developed at 1 GHz as the central frequency and with FBW of 61.4% when the insertion loss is 20-dB. In addition, this power divider is fabricated on FR4 substrates, whose dielectric constant, loss tangent, and layer thickness are 4.4, 0.018, and 1.6 mm, respectively.

3.1. Even-mode Analysis

The even-mode equivalent circuit of the power divider shown in Figure 3 can be expressed as Figure 4(a). Moreover, in Figure 4(b), resistors R_1 and R_2 are removed from the even-mode equivalent circuit since they do not have effects on signals from input and output ports. Therefore, the two-stage transmission lines can be utilized to obtain the impedances Z_{p1} and Z_{p2} as

$$Z_{p2} = Z_1 \quad (3)$$

$$Z_{p1} = Z_2/2 \quad (4)$$

3.2. Odd-mode Analysis

The odd-mode equivalent circuit of the power divider shown in Figure 3 can be expressed as Figure 5(a). Moreover, Figure 5(b) is the odd-mode equivalent circuits of both Figures 4(a) and 5(a). In addition, Figure 5(c) is the even-mode equivalent circuit of Figure 5(a). Under the matching condition, resistors R_2 and R_1 can be derived from Figures 5(b) and 5(c), respectively, as

$$R_2 = 2Z_0 \quad (5)$$

$$R_1 = Z_{p2}^2/Z_0 \quad (6)$$

With 4 for the impedance ration R in Figure 4(b) and two-stage transmission lines adopted for the circuit, 0.962 should be selected for corrected coefficient K_1 according to Figure 2(b), where FBW is 61.4% with 20-dB for insertion loss. Consequently, from (1) to (4), the impedances Z_{p1} and Z_{p2} can be obtained as $68.02\ \Omega$ and $73.5\ \Omega$, respectively. Moreover, from (6) and (5), resistors R_1 and R_2 will be $108.05\ \Omega$ and $100\ \Omega$, respectively. In this paper, the resistor R_1 is modified as $107\ \Omega$ for real fabrication, which causes return loss degradation of 0.5 dB at four output ports. Figure 6(a) shows the theoretically modified responses. It is indicated that the bandwidth of $|S_{11}|$ at -20 dB is wider with the modified power divider proposed in this paper than the traditional Wilkinson power divider.

These theoretical parameters can be transformed into the physical dimensions shown in Table 1 with the aid of the electromagnetic (EM) simulator IE3D. Figures 6(a) and 6(b) show the layout and photograph of the fabricated four-way power divider. The total area of this prototype is $63.3 \times 74.57\ \text{mm}^2$. Figure 6(a) compares the simulated and measured results of the fabricated power divider with -20 -dB for $|S_{11}|$. Moreover, Figure 6(a) also presents measured insertion

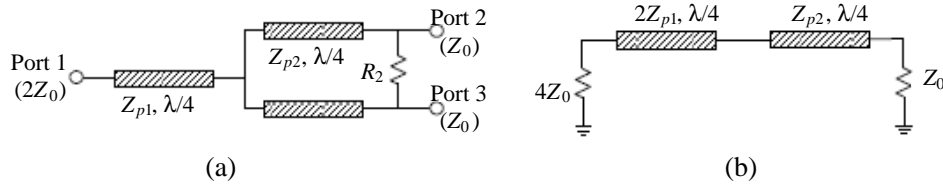


Figure 4: Half circuit of the four-way power divider with even-mode excitation. (a) Even mode of Figure 3. (b) Even mode of Figure 4(a).

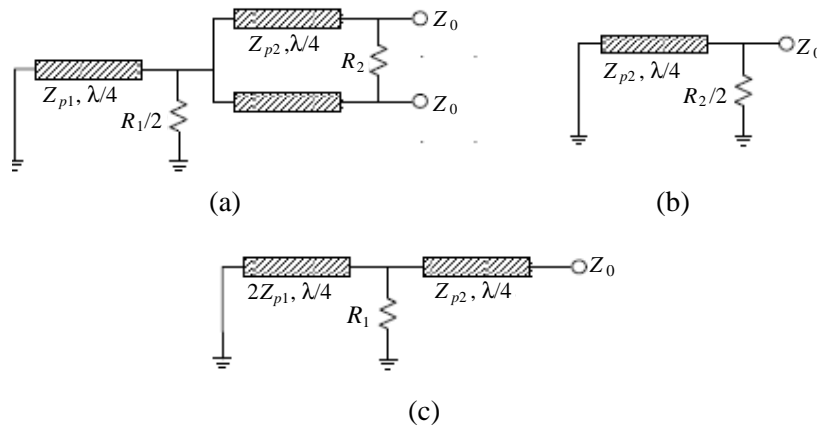


Figure 5: Half circuit of the four-way power divider with odd-mode excitation. (a) Odd mode of Figure 3. (b) Odd mode of Figure 4(a). (c) Even mode of Figure 5(a).

Table 1: Dimensions of the fabricated four-way power divider.

W_1	W_2	W_3	W_4	L_1	L_2
1.78	1.51	3.06	3.06	27.8	6.0
L_3	L_4	L_5	L_6	L_7	Unit: mm
19.35	20.0	18.65	3.0	7.0	

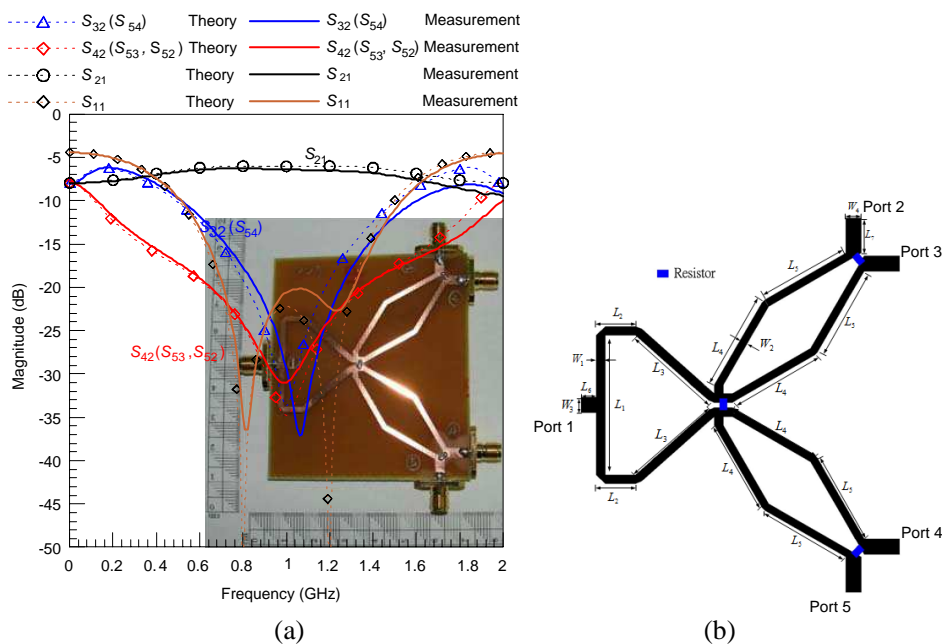


Figure 6: Proposed wideband four-way power divider. (a) Photograph and comparisons of theoretical/measured return loss, insertion loss, and isolation. (b) Layout.

loss and isolation, and the measured insertion loss is around 0.5 dB. The well matched result of simulation and measurement validates the design for a simple and wideband power divider.

4. CONCLUSION

In this paper, the corrected coefficients for the wideband impedance transformer has been proposed and adopted on the design of wideband multi-way power divider. The even- and odd-mode analyses have been presented and optimal values of isolation resistors have been obtained. Moreover, design principles and example are provided and simulated. Furthermore, a prototype of the wideband four-way power divider is designed, fabricated, and measured. With the proposed structure, performance of S_{11} can be predicated in advance. Well-matched results of simulation and measurement validate the proposed approach.

ACKNOWLEDGMENT

This work was supported in part by the National Science Council, Taiwan, under Grant NSC 102-2221-E-194-013-MY2 and Ministry of Education, Taiwan, Republic of China.

REFERENCES

1. Wilkinson, E. J., "An N -way hybrid power divider," *IEEE Trans. Microw. Theory Techn.*, Vol. 8, No. 1, 116–118, 1960.
2. Cohn, S. B., "A class of broadband three-port TEM mode hybrids," *IEEE Trans. Microw. Theory Techn.*, Vol. 16, No. 2, 110–115, 1968.
3. Yee, H. Y., F.-C. Chang, and N. F. Audeh, " N -way TEM-mode broadband power dividers," *IEEE Trans. Microw. Theory Techn.*, Vol. 18, No. 10, 682–688, 1970.
4. Zhou, J., K. A. Morris, and M. J. Lancaster, "General design of multi-way multi-section power dividers by interconnecting two-way dividers," *IEEE Trans. Microw. Theory Techn.*, Vol. 55, No. 10, 2208–2215, 2007.

Novel Module Including a Waveguide for 40 GHz High-gain Amplifier Applications

Young Chul Lee¹, Amran Bin Hj Naemat², and Zulkifli Bin Ambak²

¹Department of Electronics Engineering, Mokpo National Maritime University (MMU), Korea

²Telecom Malaysia Research & Development (TMR&D), Malaysia

Abstract— In this work, a 40 dB high-gain amplifier module has been presented for millimeter wave applications. Two amplifiers are integrated into the single module case by inserting a WR22 waveguide between them in the module case, in order to suppress oscillation. The high-gain amplifier module consists of two amplifiers and four WR22-to-microstrip line transitions which were fabricated on 5 mil thick RT5880 substrate. The transition loss of -0.44 dB per a transition was achieved from 35 to 50 GHz. The module showed the higher gain than 39.7 dB from 38 to 41 GHz. At 38.7 GHz, the maximum gain of 44.25 dB was obtained.

1. INTRODUCTION

The frequencies from 30 to 300 GHz are so-called millimeter-wave (mm-wave) ones, because their wavelength is between 10 to 1 mm. They have been utilized for gigabit wireless communications demanding greater amount of available bandwidth. Increasing several applications such as radars [1–3], point-to-point wireless communications, radio-on-fiber (RoF) links [4], cellular wireless networks [5], etc. in mm-wave band have been observed in the last decade.

One of main issues for commercialization of mm-wave radio systems is a reproducible and cost effective packaging, aside from the active radio frequency (RF) integrated circuit (IC) technology. Active RF IC chips are assembled on a metal or dielectric substrate carrier by using wire-bonding or flip-chip [6] interconnection and finally they are encapsulated in a plastic package or metal housing. In the small-sized package volume, various materials and structures like dielectric substrate, RF ICs, their mounting cavities, waveguides, etc. are integrated. Therefore, they can make difficult issues such as unwanted substrate modes [6], cavity resonance [7], feedback, or crosstalk due to discontinuities [8, 9], especially, in the mm-wave applications.

In the previously published literatures [6–9], these phenomena have been well analyzed. In order to prevent them, several approaches such as resistivity value of the flip-chip carrier [6], resonance condition of the cavity [7], chip mounting configurations [8], and resistive coating on the lid [10] has been investigated. Many oscillation-free modules [1, 2, 6] have been implemented by reflecting these investigations and have achieved good mm-wave performance. However, in the case of the high-gain amplifier block requiring over 30 dB, radiation of signals due to discontinuities can cause stability problem from the feedback effect [8, 9], that is, the radiated signals can enter the first amplifier IC in the whole high-gain amplifier block by reflecting from around structures in the module and can be amplified. This process is repeated and the high-gain amplifier module can be oscillated in final. Therefore, in order to prevent the feedback effect, a small- or medium-gain amplifier module is cascaded [2] in series by using external waveguides (WGs) until a required gain is satisfied. In addition, attenuators are inserted between amplifiers for reducing the whole gain and doing a role as an impedance buffer. However, these conventional approaches lead to bulky and expensive mm-wave radio system.

In this paper, a 40 dB amplifier module integrating a waveguide into the metal case has been presented for 40 GHz wireless communications applications.

2. MODULE CASE FOR HIGH-GAIN AMPLIFIER MODULE

In general, two amplifier modules are connected by using a WG for high-gain block applications in order to suppress oscillation. In this work, a WG between two cavities, in which two amplifier ICs are assembled, is integrated into the metal case of the high-gain amplifier as shown in Fig. 1. In this module case, because radiated signals due to discontinuities are confined to each cavity, another amplifier IC is not affected. Therefore oscillation can be prevented. Comparing to the conventional cascade high-gain block by using external WGs, the compact and low-cost mm-wave system can be implemented. However, low-loss W/G-to-MSL transition is required because of additional two W/G-to-MSL ones. The length of the cavity and MSL is 18.0 mm. The integrated WG is 15.7 mm long. The length of the WR22 ports is 18.5 mm.

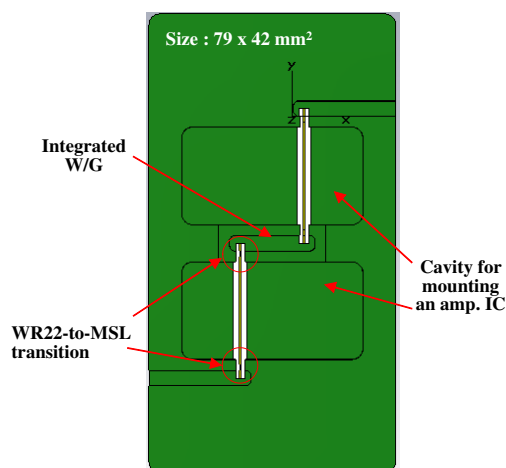


Figure 1: Proposed metal case for the high-gain amplifier module [Case size: $79 \times 42 \times 32 \text{ mm}^3$].

In this work, a WR22 WG is used as input and output (IO) port. Its rectangular size is $2.84 \times 5.68 \text{ mm}^2$. Two commercial amplifier ICs [11] are cascaded for high-gain remote antenna units (RAU) in the 40 GHz RoF system [4] having the gain of over 40 dB. The amplifier ICs and components for DC bias are mounted on a 5 mil thick RT5880 substrate [12]. Soldering pads for the amplifier ICs and 50Ω microstrip lines (MSLs) as the signal line are designed on it.

3. WAVEGUIDE-TO-MSL TRANSITION

Because of the integrated WG, additional WR22-to-MSL transitions are designed. A probe-type transition is utilized for low-loss and wideband transition and two sets of the WR22-to-MSL transitions in back-to-back configuration are mounted in order to investigate their characteristics as shown in Fig. 1.

The transition was designed on the 5 mil thick RT5880 substrate and it was inserted into the WG through a longitudinal window on its longer side. The layout of the transition part is presented at the right in Fig. 2(a) and its critical dimensions were optimized for the low loss and broad bandwidth performance by using electromagnetic (EM) analysis software [13]. Fig. 2(b) presents simulated results of the designed back-to-back structured transitions mounted on the same metal case as the high-gain amplifier module in the inset of Fig. 2(b). The return loss below -10 dB is from 34.2 to 50 GHz and its bandwidth is acceptable for the amplifier applications in this work.

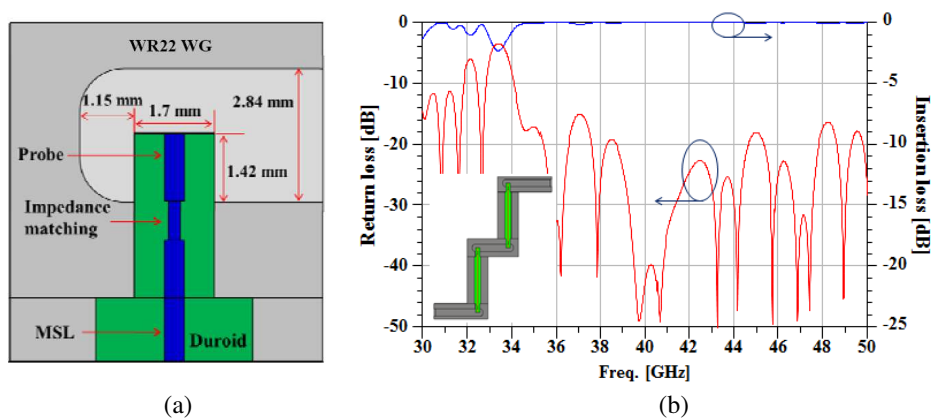


Figure 2: (a) Layout of a WR22 WG-to-MSL transition and its optimized dimensions and (b) simulated results of back-to-back structured transitions integrated into the metal case [An inset: the model designed for an EM simulation].

The transitions designed in the back-to-back type were fabricated by using the standard printed circuit board (PCB) process. A photograph of the fabricated ones assembled in the metal case for the amplifier module is illustrated in Fig. 3(a). For test of the transition performance, 2.4 mm-male-

to-WR22 W/G adapters were used in order to interconnect a vector network analyzer (VNA, Agilent N5250A) with the transition module. Adapter losses were first checked as shown in Fig. 3(b). Its measured insertion loss (IL) is from -0.26 to -0.33 dB and the return loss (RL) is less than -10 dB at all test frequencies from 30 to 50 GHz. For the case of the transitions, the measured return loss is degraded due to the adapter and is below -10 dB from 34.1 to 50 GHz. The RL bandwidth is similar to the simulated one. The measured IL is also degraded because of loss components including the adapter, substrate (dielectric), and two 18 mm long MSLs having a loss of -0.0239 dB/mm. The IL of -2.9 and -2.5 dB is observed at 38 and 41 GHz, respectively. Considering the loss components, the transition loss per a single transition is -0.44 and -0.32 dB at 38 and 41 GHz, respectively.

4. HIGH-GAIN AMPLIFIER MODULE

After removal of two sets of the transitions from the metal case, two amplifier ICs and chip capacitors to prevent low-frequency oscillation are mounted by soldering on the RT5880 substrate with transitions. The DC bias board is embedded in its back side. The assembly photograph of the high-gain amplifier module was as shown in Fig. 4(a). The overall module size is $79 \times 42 \times 32$ mm³. *S*-parameters of the fabricated high-gain amplifier module were measured at a drain supply voltage of 5 V and total DC current of 1,000 mA and the measured performance is presented in Fig. 4(b), compared to characteristics plotted from a datasheet of the amplifier IC [11]. The measured gain (M-S21) of more than 39.7 dB is achieved between 38 to 41 GHz. At 38.7 GHz, the maximum gain of 44.25 dB is obtained in spite of a little different DC bias conditions from the datasheet and assembly loss such as soldering and transitions. Compared to RLs (IC-S11 and IC-S22) of one amplifier IC, the measured output RL (M-S22) and input one (M-S11) of the high-gain module are improved and degraded, respectively. The reason comes from assembly quality of the substrate with

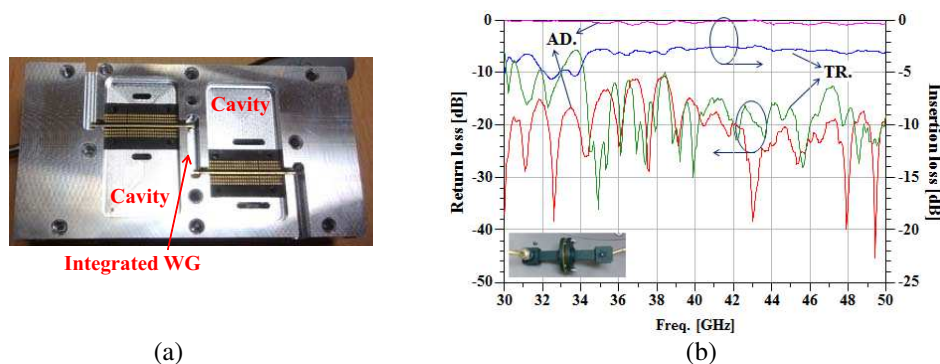


Figure 3: (a) Photograph of the fabricated transitions assembled in the metal case and (b) measured loss characteristics of the fabricated transitions [AD.: an adapter, TR.: the fabricated transitions, and an inset: the photograph of the adapter].

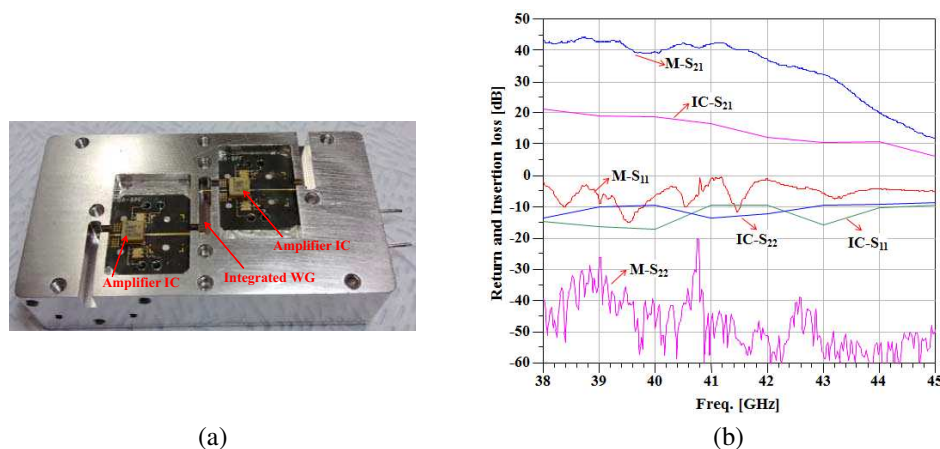


Figure 4: (a) Photo of the interior of the fabricated high-gain amplifier module and (b) its measured performances compared to AMMP-6441 characteristics from a data sheet [M: measurement and IC: the results from a data sheet of an amplifier IC (AMMP-6441)].

WR22-to-MSL transitions. The high-gain module with the gain of over 40 dB was implemented without oscillation. That demonstrates the integrated W/G can suppress the feedback effect in the high-gain amplifier module.

5. CONCLUSIONS

A 40 dB high-gain amplifier module has been presented for millimeter wave applications. In order to suppress oscillation, one WR22 waveguide (WG) is inserted between cavities for mounting chips in the metal case. The high-gain amplifier module cascades two amplifier ICs by using four WR22 WG-to-microstrip line transitions on 5 mil thick RT5880 substrate. The fabricated transition showed the transition loss of less than -0.44 dB per a transition from 35 to 50 GHz. The high-gain amplifier module achieved the gain of more than 39.7 dB from 38 to 41 GHz. At 38.7 GHz, the maximum gain of 44.25 dB was obtained

REFERENCES

1. Tessmann, A., S. Kudszus, T. Feltgen, M. Riessle, C. Sklarczyk, and W. H. Haydl, "A 94 GHz single-chip FMCW radar module for commercial sensor applications," *IEEE MTT-S International Microwave Symposium*, Vol. 3, 1, 851–1854, 2002.
2. Tessmann, A., A. Leuther, M. Kuri, H. Massler, M. Riessle, H. Essen, H. Stanko, R. Sommer, M. Zink, R. Stibal, W. Reinert, and M. Schlechtweg, "220 GHz low-noise amplifier modules for radiometric imaging applications," *The 1st European Microwave Integrated Circuits Conference*, 137–140, 2006.
3. Kim, J.-G., D.-W. Kang, B.-W. Min, and G. M. Rebeiz, "A single-chip 36–38 GHz 4-element transmit/receive phased-array with 5-bit amplitude and phase control," *IEEE MTT-S International Microwave Symposium*, 561–564, 2009.
4. Yaakob, S., N. M. Samsuri, R. Mohamad, N. E. Farid, I. M. Azmi, S. M. M. Hassan, N. Khushairi, S. A. E. A. Rahim, A. I. A. Rahim, A. Rasmi, A. K. Zamzuri, S. M. Idrus, and S. Fan, "Live HD video transmission using 40 GHz radio over fibre downlink system," *IEEE 3rd International Conference on Photonics (ICP)*, 246–249, 2012.
5. Rangan, S., S. R. Theodore, and E. Erkip, "Millimeter wave cellular wireless networks: Potentials and challenges," *Proceedings of the IEEE*, Vol. 102, 366–385, 2014.
6. Tessmann, A., M. Riessle, S. Kudszus, and H. Massler, "A flip-chip packaged coplanar 94 GHz amplifier module with efficient suppression of parasitic substrate effects," *IEEE Microwave and Wireless Components Letters*, Vol. 14, 145–147, 2004.
7. Dhar, J., R. K. Arora, A. Dasgupta, and S. S. Rana, "Enclosure effect on microwave power amplifier," *Progress In Electromagnetics Research C*, Vol. 19, 163–177, 2011.
8. Krems, T., A. Tessmann, W. H. Haydl, C. Schmelz, and P. Heide, "Avoiding cross talk and feedback effects in packaging coplanar millimeter-wave circuits," *IEEE MTT-S International Microwave Symposium*, Vol. 2, 1091–1094, 1998.
9. Beilenhoff, K. and W. Heinrich, "Excitation of the parasitic parallel-plate line mode at coplanar discontinuities," *IEEE MTT-S International Microwave Symposium*, Vol. 3, 1789–1792, 1997.
10. Yook, J.-G., L. P. B. Katehi, R. N. Simons, and K. A. Shalkhauser, "Experimental and theoretical study of parasitic leakage/resonance in a K/Ka-band MMIC package," *IEEE Transactions on Microwave Theory and Techniques*, Vol. 44, 2403–2410, 1996.
11. Avago Technologies, Available: <http://www.avagotech.com>.
12. Rogers Corporation, Available: <http://www.rogerscorp.com>.
13. CST Microwave Studio, Available: <https://www.cst.com>.

A Wideband Microstrip Line-to-waveguide Transition on LCP for 70 and 80 GHz-band Applications

Young Chul Lee

Department of Electronics Engineering, Mokpo National Maritime University (MMU), Korea

Abstract— In this paper, a broadband microstrip line-to-waveguide transition has been presented for millimeter-wave module applications. For wide bandwidth applications, the radial microstrip line (MSL) probe and extended GND plane on the low-loss organic dielectric substrate are designed. The designed and tested performance of the transition is characterized in terms of an insertion and return loss. Considering the loss contribution of the cable adapter and waveguide transition for the measurement, the loss of the fabricated transition is analyzed as -1.88 and -2.01 dB per a transition at 70 and 80 GHz, respectively and its bandwidth for reflection at -10 dB is 26 GHz from 67 to 95 GHz.

1. INTRODUCTION

Recently, because of high demands for several high-data-rate wireless services, millimeter-wave (mm-wave) frequency band has been increased to higher mm-wave band. Especially, 71 ~ 76 and 81 ~ 86 GHz bands known as “E-band” are widely used around the world for high-capacity point-to-point wireless communications applications [1]. E-band wireless systems offer the most competitive alternative to Ka-band and V-band systems and buried fiber because of very wide available bandwidth (BW) of 10 GHz, low-loss propagation characteristics in free space, and cost effective solution in terms of license and installation.

In general, mm-wave circuits, components, and modules are designed using several technologies and materials. Therefore, they are integrated and assembled in the system by using various transmission lines; microstrip line, coplanar line, waveguides et al.. Therefore, a low-loss transition between them is one of key elements in the mm-wave system integration. In nature, simple design, wide bandwidth, and low loss are key issues for mm-wave system applications.

A well-known electrical-probe (E-probe) transition [2] with a back-short waveguide on the dielectric substrate has been used because of its simple mode transformation and easy design, compared to other perpendicular transitions [3, 4] and also no additional substrate is required. However, narrow operation bandwidth is the essential drawback. For broad bandwidth applications, a waveguide transition using a quasi-Yagi Uda antenna printed on the substrate was proposed [5], but air bridges and a trenched metal block were needed. A very wide bandwidth of 24.9 GHz was achieved [6] by controlling the position of the probe and length of an extended ground (GND) [7] related to the reactance of the probe. The dielectric material as well as the transition structures should be considered for low-loss transition design. In general, RT/Duroid 5880 [3, 4, 6] and low-temperature co-fired ceramic (LTCC) [5] as a substrate have been frequently used for mm-wave applications, because of a very small loss tangent and low coefficient of thermal expansion (CTE). Considering integration into inner layers of printed circuit boards (PCBs), low-loss organic material; Liquid Crystalline Polymer (LCP) has been utilized for microwave and mm-wave module applications [8].

In this work, a wide band microstrip line (MSL)-to-waveguide (WG) transition has been presented for E-band applications. For its wide operational bandwidth, a simple radial probe and extended GND (E-GND) are designed on the LCP organic dielectric substrate. The designed and measured results are characterized in terms of an insertion and return loss.

2. DESIGN OF A MSL-TO-WR12 TRANSITION

The transitions were designed on the LCP substrate and whose relative dielectric constant, loss tangent, and height of the LCP substrate are 3.16, 0.0045, and 100 μm , respectively at 70 GHz and metal (Cu) patterns on the substrate is 8 μm thick.

Figure 1 shows the cross-sectional view of the MSL-to-WG transition. A MSL-to-WG transition is composed of a rectangular open-ended WG, short-circuit WG, and LCP dielectric substrate with the radial electrical probe. The probe and GND patterns are designed on the both side of the substrate. Via holes are formed around WG in the LCP substrate. For 70 and 80 GHz applications, the WR12 WG was used and its rectangular size is 3.1 mm \times 1.55 mm. The LCP dielectric substrate is placed on the open-ended WR12 (lower WG) and then the short-circuited WG is on it as shown

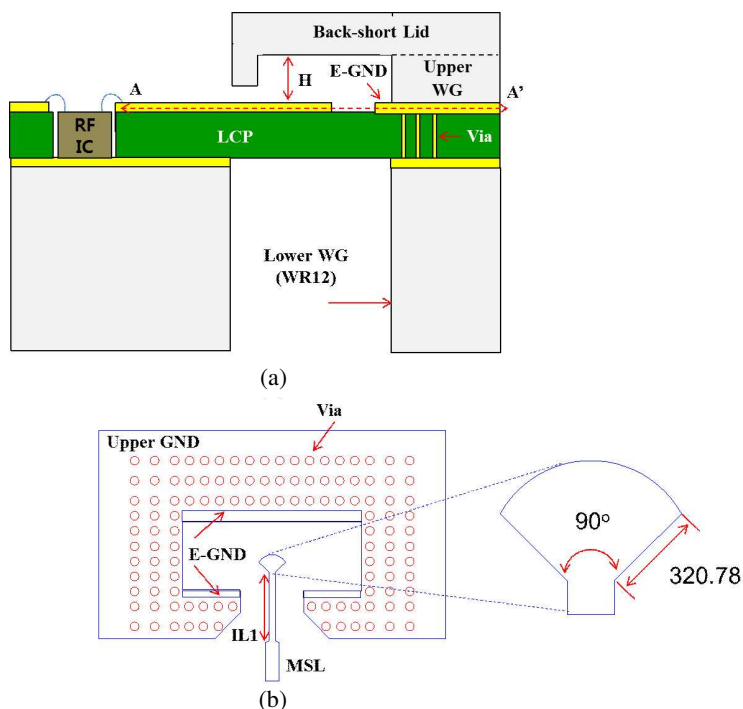


Figure 1: The cross-sectional view of (a) the MSL-to-WG transition and (b) the planar view at the $A-A'$ plane.

in Fig. 1(a). Conductor patterns on the LCP substrate are designed as shown in Fig. 1(b). A length (H) of the short-circuit WG is a quarter of guided wavelength of the WG ($\lambda_g/4$), in order to couple electric current on the probe to TE₁₀ dominant mode of the WG. For suppression of parallel-plate leakage (PPL) in the LCP substrate, vias are placed as shown in Fig. 1(b). In order to achieve a wide-band impedance matching, the extended GND and radial patch are designed as shown in Fig. 1(b). The widths of the extended GND at the upper and lower side of the WG are 230 and 130 μm , respectively. The length and angle of the radial probe are 320.78 μm and 90, respectively. They were optimized for broadband characteristics of the transition. Narrow MSL between the MSL and radial probe is designed for impedance matching. Its width and length are 0.11 and 1.184 mm, respectively. The Width of the 50- Ω MSL is 0.236 mm.

In order to evaluate the transitions, they were designed in a back-to-back structure and length between two transitions was 20.6 mm. The designed results of the back-to-back structured transition are presented in Fig. 2. Its BW for return loss (RL) at -20 dB is 26 GHz from 61 to 87 GHz. An insertion loss (IL) is -1.67 and -1.95 dB at 70 and 80 GHz, respectively.

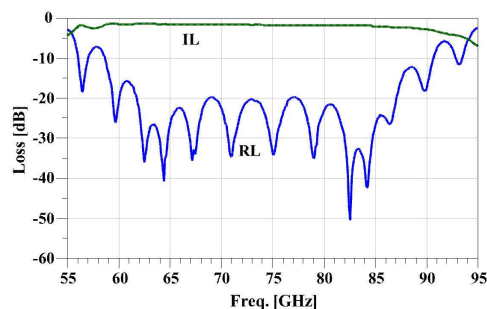


Figure 2: Designed results of the MSL-to-WG transition.

3. FABRICATION AND MEASUREMENT OF THE MSL-TO-WR12 TRANSITION

The designed transition was fabricated in a commercial printed circuit board (PCB) foundry. Fig. 3(a) shows the fabricated transition on the LCP substrate. For the test, the fabricated LCP substrate including transition patterns is attached on the lower WR12 in aluminum (Al) block by using a conductive epoxy. The upper WR12 and back-circuit cover are placed on the substrate in order. All parts are tightened by screws. By using a vector network analyzer (VNA) the fabricated back-to-back transition were tested. After calibration, adapters (1.0 mm male cable-to-WR10) and WG transitions (WR10-to-WR12) were connected to the cable of the VNA. Fig. 3(b) presents a photograph of device under test (DUT) for the fabricated board including several transitions. The test frequency was from 67 to 95 GHz. The dashed line is the size of the WR12 WG.

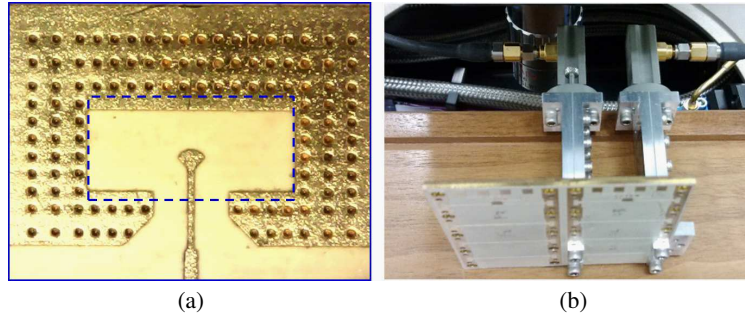


Figure 3: Fabricated transition (a) and test set-up of the fabricated transition. (b) [Two W-band adapters and waveguide transitions are used for test].

Figure 4 presents the measured insertion loss (IL) and return loss (RL) of the fabricated transition in the back-to-back structure. All test results are degraded compared to the simulated ones because of high-loss calibration using several adapters and WG transitions. The RL of the proposed transition shows less than -10 dB at all test frequencies. The IL of -8.9 and -9.2 dB is obtained at 70 and 80 GHz, respectively. The loss including the 20.6 mm long MSL, adapters, and WG transitions is -5.14 and -5.18 dB, at 70 and 80 GHz, respectively. Considering the loss contribution, the transition loss is analyzed as -1.88 and -2.01 dB per a transition

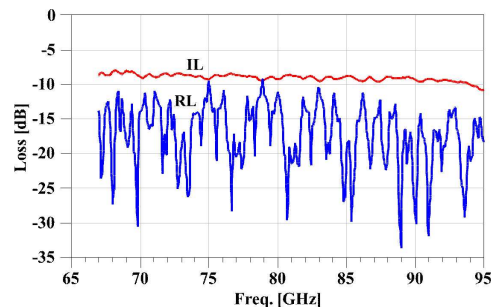


Figure 4: Measured IL and RL characteristic of the fabricated transition.

4. CONCLUSION

A wide-band microstrip (MSL)-to-waveguide transition has been presented for millimeter-wave applications. In order to improve its operational bandwidth, the radial MSL probe is designed on the low-loss organic dielectric substrate. Considering the loss contribution of the cable adapter and waveguide transition for the measurement, the proposed transition loss can be analyzed as -1.88 and -2.01 dB per a transition at 70 and 80 GHz, respectively. Its operational bandwidth of 26 GHz is obtained for reflection at -10 dB.

REFERENCES

1. Val Dyadyuk, Y. J. Guo, and J. D. Bunton, "Enabling technologies for multi-gigabit wireless communications in the E-band, mobile and wireless communications network layer and circuit

- level design,” *Salma Ait Fares and Fumiyuki Adachi (Ed.)*, 263–280, 2010, ISBN: 978-953-307-042-1, InTech, Available from: <http://www.intechopen.com/books/mobile-and-wireless-communications-network-layer-and-circuit-leveldesign/>.
2. Shih, Y.-C., T.-N. Ton, and L. Q. Bui, “Waveguide-to-microstrip transitions for millimeter-wave applications,” *IEEE MTT-s International Microwave Symposium Digest*, 473–475, 1988.
 3. Aliakbarian, H., A. Enayati, G. A. E. Vandenbosch, and W. De Raedt, “Novel low-cost end-wall microstrip-to-waveguide splitter transition,” *Progress In Electromagnetics Research*, Vol. 101, 75–96, 2010.
 4. Dong, J., T. Yang, Y. Liu, Z. Yang, and Y. Zhou, “Broadband rectangular waveguide to GCPW transition,” *Progress In Electromagnetics Research Letters*, Vol. 46, 107–112, 2014.
 5. Kaneda, N., Y. Qian, and T. Itoh, “A broad-band microstrip-to-waveguide transition using quasi-Yagi antenna,” *IEEE Transactions on Microwave Theory and Techniques*, Vol. 47, 2562–2567, 1999.
 6. Sakakibara, K., M. Hirono, N. Kikuma, and H. Hirayama, “Broadband and planar microstrip-to-waveguide transitions in millimeter-wave band,” *International Conference on Microwave and Millimeter Wave Technology (ICMMT)*, Vol. 3, 1278–1281, 2008.
 7. Marcuvitz, N., *Waveguide Handbook*, IEE Press, London, U.K., 1993.
 8. Lee, Y. C., “70 GHz Tx and Rx LCP SoP module for point-to-point millimetre wave applications,” *PIERS Proceedings*, 1264–1266, Stockholm, August 12–15, 2013.

Coaxial-line Structured SMT Pad for LTCC SiP Applications

Young Chul Lee

Department of Electronics Engineering
Mokpo National Maritime University (MMU), Korea

Abstract— In this work, a surface-mount type (SMT) pad using a coaxial-line structure is presented for low temperature co-fired ceramic (LTCC) SiP (system-in-package) applications. The vertical via transition is devised in type of the coaxial line. An overlap part between its outer conductor and a transmission line on the main board is cut off in order to eliminate their interaction. A cap on the top layer of the vertical via transition is designed in order to reduce radiation due to discontinuity. The designed SMT pad was fabricated using the standard LTCC process. The measured return and insertion loss are below -14 and -1.0 dB, respectively up to 15 GHz.

1. INTRODUCTION

SiP (system-in-package), 3-dimensional (3D) integration approach of radio systems [1, 2], have been widely used for microwave and millimeter-wave (mm-wave) package applications, because of its low loss, integration capability, similar value of temperature coefficient of expansion (TCE) to MMICs, and cost effectiveness. Most of SiP modules have been implemented in type of a surface-mount type (SMT) because of easy and lowcost assembly.

Low-loss interconnection between a main PCB board and SMT pad and the excitation [3] of package modes are key issues for mm-wave SiP applications. In general, low-loss transitions between a SMT pad and signal path in the SiP module have been investigated using vertical via structures [5–9]. Various vertical via transition such as Coplanar waveguide (CPW)-to-stripline (SL) [4, 5], microstrip (MSL)-to-SL [6, 7] and CPW-to-CPW transition [4, 8] have been developed for radio system integration. In these previous researches, several approaches have been tried for improved RF performance. There are two categories: impedance matching [5, 6, 8] and parasitic compensation [4, 5]. In order to match the impedance close to $50\ \Omega$, the coaxial-type transition using shielding vias [6, 8] and intermediate ground planes [5] have been presented. In order to reduce inductive and capacitive effects in the transition region [5, 6], S. Lei et al. [5] presented additional pads in the vertical vias to reduce the inductive effect at the transition F. J. Schmuckle et al. [6] designed the critical ground part in the SL. In addition, In order to suppress unwanted resonance modes, PBG structure in the cavity was designed, forming a kind of bandstop filter at the operation frequency [3].

In this work, the SMT pad using a coaxialline structure has been presented for mm-wave LTCC SiP module applications. Using a 9-layer LTCC dielectric substrate, CPW-to-Coaxial line-to-SMT pad transition is designed and fabricated. The SMT pad was designed and analyzed by using a 3-D Finite Integration Technique (FIT) simulator [10].

2. DESIGN OF A SMT PAD-TO-COAXIAL LINE-TO-CPW TRANSITION

A SMT pad is designed using a coaxial line-to-CPW vertical via transition in a 9-layer LTCC dielectric as shown in Fig. 1(a). For the coaxial line, a diameter of the inner conductor, which is the same as that of via for the signal path is fixed as $135\ \mu\text{m}$ and an outer one is $695\ \mu\text{m}$. In order to maintain $50\ \Omega$ impedance the outer diameter of $1,226\ \mu\text{m}$ is required. However, it leads to increase the size of the pad. Through the size optimization of the coaxial line in terms of transition loss and size, the outer diameter is determined and its impedance of the coaxial line is $37\ \Omega$. The CPW line on the seventh layer (L7) is integrated into the cavity which consists of 8th and 9th layer for interconnection with other devices or measurement. A ECPW (embedded CPW) on the same layer as the CPW in the LTCC substrate is designed for interconnection between the coaxial line and CPW. The width of the CPW and ECPW is 144 and $90\ \mu\text{m}$, respectively. Their gaps are 83 and $95\ \mu\text{m}$, respectively. Their height of the substrate is $100\ \mu\text{m}$. In order to analyze crosstalk around SMT pad, electric (E)-field distributions of the cross-sectional parts of the whole SMT pad including a LTCC and PCB substrate are presented in Fig. 1(b). The dashed rectangular shows that the outer conductors used as the ground (GND) of the coaxial line overlap with the CPW line and GND planes on the PCB board. Therefore, in the overlapped part, EM-fields are concentrated and that leads cross-talk between the PCB and pad.

Figure 2 shows the designed results of the SMT pad using the coaxial line transition. As frequencies increase above 11 GHz, return losses (RL) are severely degraded over -10 dB. At 15 GHz, an insertion loss (IL) is lower than -2 dB. The degradation of the RL and IL results from the concentrated E -fields in the overlapped part. In order to improve the performance, the structure related to the concentrated E -fields should be modified.

Figure 3 presents that (a) a perspective view of the SMT pad transition using a modified coaxial-line transition and (b) its E -field distributions at the transitions. The overlapped parts between the LTCC substrate including coaxial-line outer conductor and CPW on the PCB are cut off. In addition, in order to reduce the radiation due to discontinuities at the interconnection part of the coaxial line and CPW, a cap with a radius of $928 \mu\text{m}$ on the 9th layer (L9) of the LTCC substrate is designed.

Figure 4 shows that the simulated characteristics of the modified SMT pad transition with a cap. Compared to the previous transition in Fig. 2, the performance is clearly improved. From DC to 18 GHz, the return losses are below -10 dB.

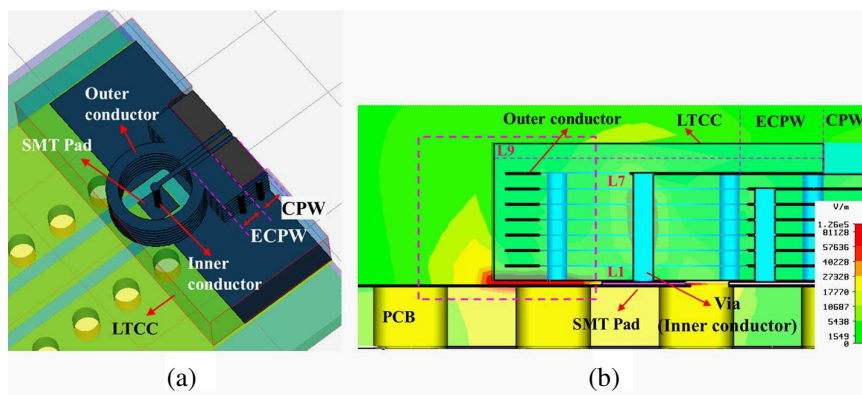


Figure 1: (a) 3D view of a SMT pad using a coaxial line transition and (b) electric (E)-field distributions the cross-sectional parts of the whole SMT.

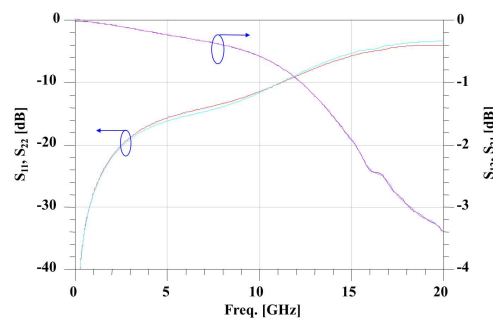


Figure 2: Designed results of the SMT pad using a coaxial line transition.

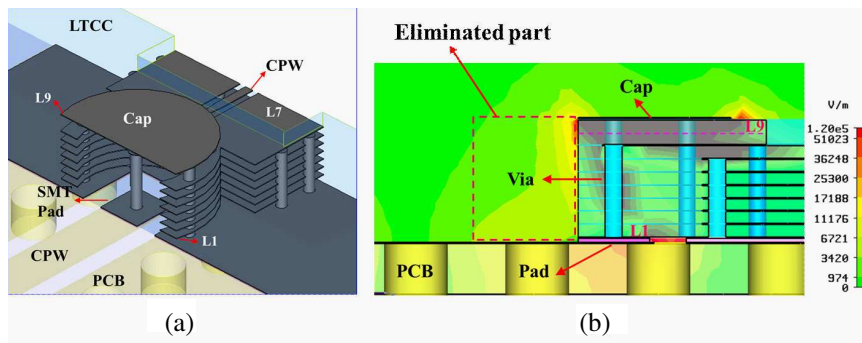


Figure 3: (a) 3D view of the modified SMT pad transition and (b) its E -field distribution.

3. FABRICATION AND MEASURED RESULTS

The modified SMT pad transition was fabricated on nine LTCC dielectric layers with a dielectric constant of 7.8 and its thickness between the metal layers is 100 μm . The Ag and Ag/Pd conductors were screen-printed on the unfired green-sheet layers for internal and external conductors, respectively. The fabricated SMT transition is shown in an inset of Fig. 5.

Using a probing method on the probe station, the fabricated SMT pad transition was measured with a VNA (vector network analyzer). Fig. 5 shows the measured characteristics of the fabricated LTCC SMT pad transition on the PCB board. The measured insertion loss is below -1.0 dB from DC to 15 GHz. The return losses are below -14 dB at the same frequency range. This SMT pad can be used for X- or Ku-band applications.

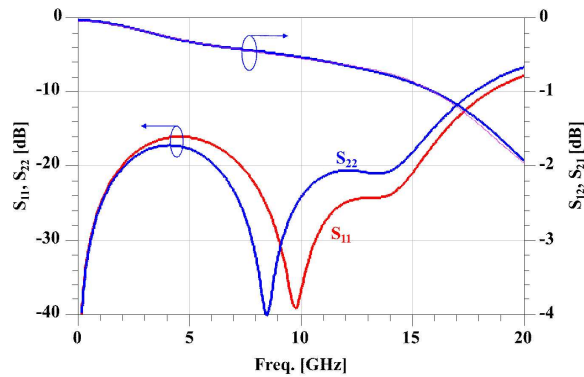


Figure 4: Designed return and insertion loss characteristics of the modified SMT pad transitions with a cap.

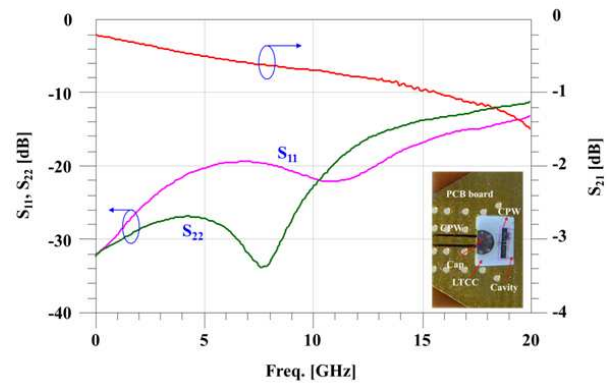


Figure 5: Measured characteristics of the fabricated SMT pad transitions [An inset: the fabricated LTCC SMT pad transition on the PCB board].

4. CONCLUSIONS

In this work, a coaxial-line structured SMT pad has been presented for LTCC SiP applications. The vertical via transition is devised in type of the coaxial line. In order to eliminate crosstalk and radiation, the overlapped parts between the LTCC substrate including coaxial-line outer conductor and CPW on the PCB are cut off and a cap at the interconnection part of the coaxial line and CPW is proposed, respectively. The designed SMT pad was fabricated using the standard LTCC process on nine LTCC dielectric layers. The measured return and insertion loss are below -14 and -1.0 dB, respectively, up to 15 GHz.

REFERENCES

1. Lee, Y. C., W.-I. Chang, and C. S. Park, "Monolithic LTCC SiP transmitter for 60 GHz wireless communication terminals," *IEEE MTT-S International Microwave Symposium Digest*, 1015–1018, 2005.
2. Lee, Y. C., T. W. Kim, A. B. Ariffin, and N.-G. Myoung, "60-GHz amplitude shift-keying receiver LTCC system-on-package module," *Microwave and Optical Technology Letters*, Vol. 53, 758–761, 2011.
3. Zirotti, A., M. Nalezinski, and W. Menzel, "A novel approach for LTCC packaging using a PBG structure for shielding and package mode suppression," *European Microwave Conference*, 419–422, 2003.
4. Lu, A. C. W., K. M. Chua, L. L. Wai, S. C. K. Wong, J. J. Wang, and Y. P. Zhang, "Integrated antenna module for broadband wireless applications," *Electronics Packaging Technology Conference*, 240–243, 2004.
5. Panther, A., C. Glaser, M. G. Stubbs, and J. S. Wight, "Vertical transitions in low temperature co-fired ceramics for LMDS applications," *IEEE MTT-S Int. Microwave Symposium Digest*, Vol. 3, 1907–1910, 2001.
6. Lei, S., Y. X. Guo, and L. C. Ong, "CPW to stripline transitions in LTCC for millimeter-wave applications," *IEEE Asia Pacific Microwave Conference (APMC) Proceedings*, 2005.

7. Schmuckle, F. J., A. Jentzch, W. Heinrich, J. Butz, and M. Spinnler, "LTCC as MCM substrate: Design of strip-line structures and flip-chip interconnections," *IEEE MTT-S Int. Microwave Symposium Digest*, Vol. 3, 1093–1096, 2001.
8. Yang, T.-H., C.-F. Chen, T.-Y. Huang, C.-L. Wang, and R.-B. Wu, "A 60 GHz LTCC transition between microstrip line and substrate integrated waveguide," *IEEE Asia Pacific Microwave Conference (APMC) Proceedings*, 2005.
9. Lee, Y. C., "SMT pad using a coaxial line structure for LTCC SoP applications," *Microwave and Optical Technology Letters*, Vol. 51, 1769–1772, 2009.
10. CST MICROWAVE STUDIO, CST Inc., <http://www.cst.com>.

InISAR Imaging of Dechirp Data under Squint Model

Biao Tian, Gang Li, Shiyong Xu, and Zengping Chen

Science and Technology on Automatic Target Recognition Laboratory
National University of Defense Technology, Changsha, China

Abstract— Aiming at InISAR imaging of dechirp data under squint model a new method based on squint iteration optimization (SIO) and distortion correction (DC) is proposed in this paper. The squint model induces the influence of accessional phase and image distortion. The 3D imaging results degrade seriously when the squint angle is big. Through a few times of squint iteration optimization and distortion correction, the estimation precision and the imaging quality are improved. Simulation results demonstrate the effectiveness of the method.

1. INTRODUCTION

Inverse synthetic aperture radar (ISAR) [1, 2] can generate 2D high resolution images of non-cooperative targets from a long distance and is widely used for military and civilian purposes. The ISAR image, however, is just the Range-Doppler plane projection of a three spatial dimensional target which results in the loss of structure information. In order to enhance the target recognition probability, the interferometric ISAR (InISAR) [3–5] technique is presented to achieve the third dimension of the target. In traditional InISAR imaging systems, three receiving antennas are mostly used [3, 4]. Using the phase difference of the three 2D complex ISAR images, the corresponding position of each scattering can be achieved.

As is known to all, the ISAR image plane is related to the targets motion with respect to the radar line of sight (LOS). For convenience, the target is generally assumed to be located close to the antenna axis in traditional InISAR imaging systems, which is called the normal mode. In practice, however, the target is usually far away from the antenna axis [6–8], which is called the squint mode. A novel InISAR imaging algorithm based on dominant scatterers is proposed in literature [6]. The phase ambiguity induced by squint is inevitable since the same reference range is used in stretch processing. Moreover, the difference of system structure limits the application of image registration using parameter estimation of targets angular motion. In literature [7], the approximation introduced to deal with the coupling of squint additive phase and target coordinates degrades the image quality. Literature [8] combines the nonlinear least square (NLS) and coordinates transform (CT) to estimate the target coordinates. The computation efficiency is decreased since NLS is applied.

Aiming at above problems we propose a new squint model InISAR imaging method based on squint iteration optimization. The remainder of this paper is organized as follows. In Section 2, the InISAR imaging geometry and signal model is described. Section 3 analyzes the influence of squint model. The new squint model InISAR imaging method based on squint iteration optimization is detailed in Section 4. Simulation results and performance analysis are reported in Section 5, followed by conclusion in Section 6.

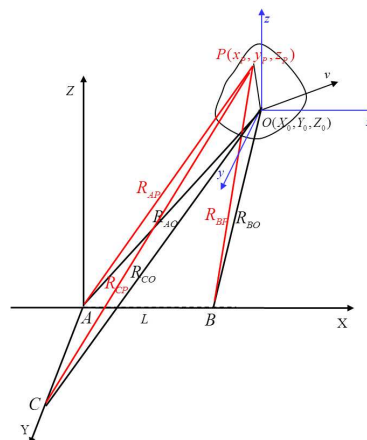


Figure 1: Three-receiver InISAR imaging geometry.

2. SIGNAL MODEL OF DECHIRP DATA FOR INISAR SYSTEM

The geometry of three-receiver InISAR imaging system is shown in Figure 1. In the system, A is the transmitter and receiver while B and C only receive signal. The initial location of the target center is (X_0, Y_0, Z_0) in the XYZ coordinate system. The initial distance from the antenna A can be denoted as $R_0 = \sqrt{X_0^2 + Y_0^2 + Z_0^2}$. The ISAR image of each antenna can be written as [8]:

$$S_A(f, f_m) = A_P T_P T_1 \text{sinc} \left[T_P \left(f + \frac{2\gamma}{c} R_{\Delta AP0} \right) \right] \text{sinc} \left[T_1 \left(f_m + \frac{2V_{AP}}{\lambda} \right) \right] \exp \left\{ -j \frac{4\pi}{\lambda} R_{\Delta AP0} \right\} \quad (1)$$

$$S_B(f, f_m) = A_P T_P T_1 \text{sinc} \left[T_P \left(f + \frac{\gamma}{c} (R_{\Delta AP0} + R_{\Delta BP0}) \right) \right] \text{sinc} \left[T_1 \left(f_m + \frac{V_{AP} + V_{BP}}{\lambda} \right) \right] \exp \left\{ -j \frac{2\pi}{\lambda} (R_{\Delta AP0} + R_{\Delta BP0}) \right\} \quad (2)$$

$$S_C(f, f_m) = A_P T_P T_1 \text{sinc} \left[T_P \left(f + \frac{\gamma}{c} (R_{\Delta AP0} + R_{\Delta CP0}) \right) \right] \text{sinc} \left[T_1 \left(f_m + \frac{V_{AP} + V_{CP}}{\lambda} \right) \right] \exp \left\{ -j \frac{2\pi}{\lambda} (R_{\Delta AP0} + R_{\Delta CP0}) \right\} \quad (3)$$

where A_P is the scattering amplitude, T_P is the pulse width, T_1 is the imaging time, $R_{\Delta AP} = R_{AP} - R_{refA}$, R_{AP} is the distance between scattering point P and antenna A, R_{refA} is the reference range, V_{AP} is the variety rate. The interferometric phase could be expressed as follows

$$\Delta\varphi_{AB} = \text{Angle} (S_B(f, f_m) S_A^*(f, f_m)) = \frac{2\pi}{\lambda} (R_{\Delta AP0} - R_{\Delta BP0}) \triangleq \frac{2\pi}{\lambda} \Delta R_{AB0} \quad (4)$$

$$\Delta\varphi_{AC} = \text{Angle} (S_C(f, f_m) S_A^*(f, f_m)) = \frac{2\pi}{\lambda} (R_{\Delta AP0} - R_{\Delta CP0}) \triangleq \frac{2\pi}{\lambda} \Delta R_{AC0} \quad (5)$$

For normal model, the same reference ranges are chosen to carry out dechirp processing for each antenna, i.e. $R_{refA} = R_{refB} = R_{refC} = R_{AO}$, then

$$\Delta R_{AB} = (R_{AP} - R_{AO}) - (R_{BP} - R_{AO}) \approx \frac{Lx_P}{R_0} \quad (6)$$

$$\Delta R_{AC} = (R_{AP} - R_{AO}) - (R_{CP} - R_{AO}) \approx \frac{Ly_P}{R_0} \quad (7)$$

From the above four formularies, we have

$$x_P = \frac{\lambda R_0 \Delta\varphi_{AB}}{2\pi L} \quad (8)$$

$$y_P = \frac{\lambda R_0 \Delta\varphi_{AC}}{2\pi L} \quad (9)$$

Meanwhile, the Z coordinate can be obtained by scaling of the ISAR image. In this way, the three dimensions of the target are achieved.

3. INFLUENCE OF SQUINT MODEL

3.1. Accessional Interferometric Phase

The interferometric phase of point P can be rewritten as

$$\Delta\varphi_{AB} = \frac{2\pi}{\lambda} (R_{\Delta AP0} - R_{\Delta BP0}) = \frac{2\pi}{\lambda} \left(\frac{2Lx_P}{R_{AP0} + R_{BP0}} + \frac{2LX_0 - L^2}{R_{AP0} + R_{BP0}} - \frac{2LX_0 - L^2}{R_{AO0} + R_{BO0}} \right) \quad (10)$$

Let $\varphi_1 = \frac{2\pi}{\lambda} \cdot \frac{2Lx_P}{R_{AP0} + R_{BP0}}$, $\varphi_2 = \frac{2\pi}{\lambda} \cdot \frac{2LX_0 - L^2}{R_{AP0} + R_{BP0}}$, $\varphi_3 = -\frac{2\pi}{\lambda} \cdot \frac{2LX_0 - L^2}{R_{AO0} + R_{BO0}}$, where φ_1 is the main interferometric phase that contains the coordinate information while φ_2 and φ_3 are the accessional phases caused by squint view of the X direction. We call them as main phase and accessional phase respectively. Then $\Delta\varphi_{AB} = \varphi_1 + \varphi_2 + \varphi_3$.

When the radar works at the normal model, namely $\varphi_2 + \varphi_3 = 0$, the coordinate x_P of the point P can be simplified as Eq. (8). When the radar works at squint model, however, the interferometric phase becomes ambiguous if $\varphi_2 + \varphi_3$ is big enough. Moreover, the accessional phases are not the same to all points, since they are correlative with the point location too. Only after they are compensated, can we achieve accurate 3D InSAR image.

3.2. Image Distortion

The down-range coordinates R of 2D ISAR image is not directly in accordance with the z -axis coordinate of the target when the squint angle is too big. Through the CT method, the true coordinates of the target (x, y, z) can be obtained from the distorted coordinates (x, y, r) .

The projection coordinate of P at R-axis of the radar LOS coordinate is

$$r = x \cos \varphi \cos \theta + y \cos \varphi \sin \theta + z \sin \varphi \quad (11)$$

where θ and φ are the azimuth and pitching angle of the LOS direction. As we can see, the obtained down-range coordinate is related to each of the three coordinates of point P , which results in distortion of the final 3D InSAR image.

4. INISAR IMAGING BASED ON SQUINT ITERATION OPTIMIZATION

As analyzed in Section 3.2, only after the compensation of the accessional phases is carried out, can high quality 3D InSAR results be achieved. In this section, we propose a method named squint iteration optimization to carry out high precision interferometric processing. From Eq. (10), we can get the true x -coordinate and y -coordinate of scattering point as

$$x_P = \frac{R_{AP0} + R_{BP0}}{2L} \cdot \left(\frac{\lambda}{2\pi} \Delta\varphi_{AB} - \frac{2LX_0 - L^2}{R_{AP0} + R_{BP0}} + \frac{2LX_0 - L^2}{R_{AO0} + R_{BO0}} \right) \quad (12)$$

$$y_P = \frac{R_{AP0} + R_{CP0}}{2L} \cdot \left(\frac{\lambda}{2\pi} \Delta\varphi_{AC} - \frac{2LX_0 - L^2}{R_{AP0} + R_{CP0}} + \frac{2LX_0 - L^2}{R_{AO0} + R_{CO0}} \right) \quad (13)$$

As can be seen from the above two equations, the true location of scattering point is related to R_{AP0} , R_{BP0} and R_{CP0} , and, which are also associated with x_P , y_P and z_P . In order to achieve accurate interferometric result, a few iterations should be carried out to achieve improvement. The initial value of the iteration can be used as that in Eqs. (8) and (9). Then we can calculate the distance value of the scattering point to each antenna

$$R_{AP0} = \sqrt{(X_0 + x_P)^2 + (Y_0 + y_P)^2 + (Z_0 + z_P)^2} \quad (14)$$

$$R_{BP0} = \sqrt{(X_0 + x_P - L)^2 + (Y_0 + y_P)^2 + (Z_0 + z_P)^2} \quad (15)$$

$$R_{CP0} = \sqrt{(X_0 + x_P)^2 + (Y_0 + y_P - L)^2 + (Z_0 + z_P)^2} \quad (16)$$

After this step, the iteration can be carried out and updated.

The image distortion correction could be achieved using the following inverse CT:

$$z_P = (r - x \cos \varphi \cos \theta + y \cos \varphi \sin \theta) / \sin \varphi \quad (17)$$

As we can see, the true z -coordinate meets the equation. To obtain 3D InSAR image more precisely, the distortion correction and squint iteration improvement should be carried out in the same step. The times of iterations should be decided by convergence condition of practical requirement.

The steps of squint iteration optimization and distortion correction can be summarized as:

- 1) Calculate the interferometric phase $\Delta\varphi_{AB}$ and $\Delta\varphi_{AC}$ using Eqs. (4) and (5).
- 2) Obtain the initial coordinate x_P and y_P using Eqs. (8) and (9), while $z_P = r$ by scaling of ISAR image.
- 3) Get the distance values of each scattering point to each antenna using Eqs. (14)–(16).
- 4) Update the coordinate x_P and y_P using Eqs. (12) and (13).
- 5) Update the coordinate z_P using Eq. (17).
- 6) Repeat steps 3–5 until the convergence condition is achieved.

Using the method, all the 3D spatial coordinates of each scattering point on the target are obtained, and the high precision 3D InSAR image is obtained.

5. SIMULATION RESULTS AND ANALYSIS

In order to test the analysis and 3D InSAR imaging algorithm under squint model, the simulation of a target with stable motion in the far-field is carried out. The parameters of the radar system are as follows. The carrier frequency is 10 GHz, the bandwidth is 500 MHz, the PRF is 200 Hz, the pulse width is 50 μ s, the pulses used for imaging is 256. The locations of antenna A/B/C are (0, 0, 0)/(100 m, 0, 0)/(0, 100 m, 0). The target contains 6 scattering points, whose three dimensional positions are (7, 5, 5), (-5, 5, 15), (3, 15, 5), (-1, 15, 15), (0, 2, 9), (7, 10, 10). The velocity of it is (1000, 5000, 1000) m/s. In the following simulations, three different instances are set. We call them normal model in which the targets initial location is (50 m, 50 m, 1000 km), and small squint model in which the targets initial location is (20 km, 20 km, 1000 km), and squint model in which the targets initial location is (200 km, 250 km, 1000 km).

Firstly, we demonstrate the influence of squint model to the interferometric phase. According

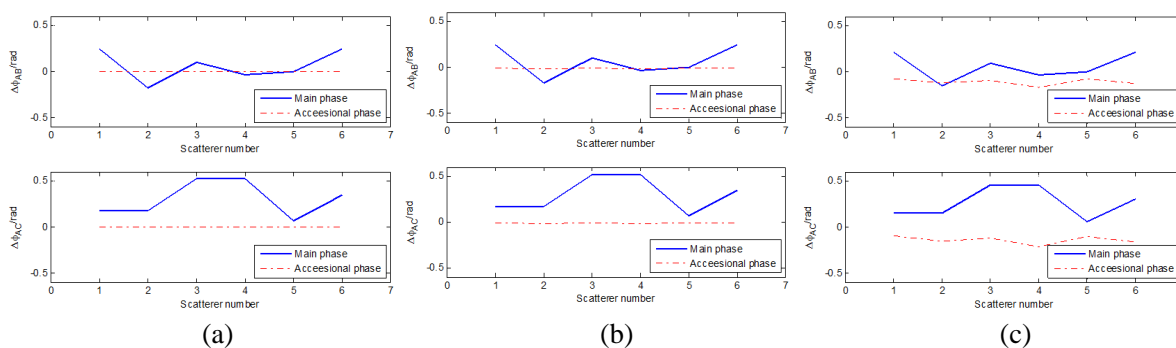


Figure 2: Comparison of main phase and accessional phase. (a) Normal model. (b) Small squint model. (c) Squint model.

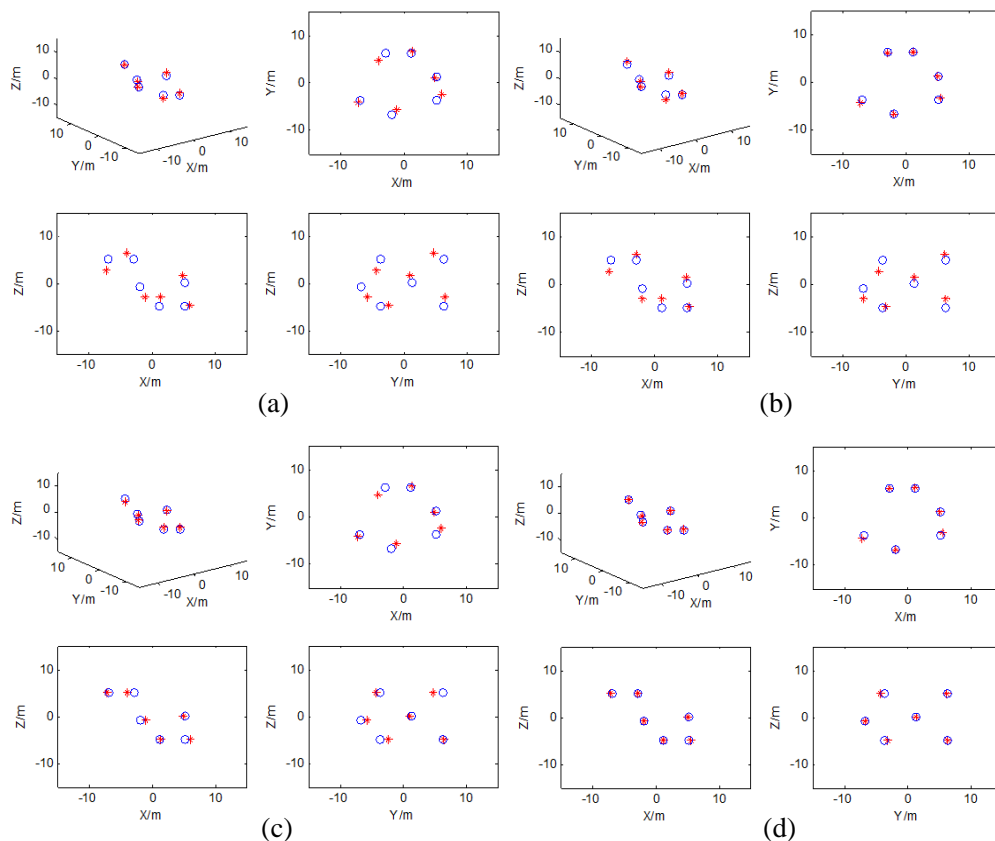


Figure 3: 3D imaging result under squint model. (a) Traditional method. (b) SIO only. (c) DC only. (d) Combination of SIO and DC.

to the analysis in Eq. (10), the main phase and accessional phase will be compared.

As Figure 2 shows, the accessional phase $\varphi_2 + \varphi_3$ is nearly zero, and it could be neglected in normal model. It increases with the increment of squint angle. The accessional phase turns comparable large as the main phase (Figure 2(c)), so we should not neglect the influence of squint model any more. Once the coordinates are simply obtained by using Eqs. (8) and (9), the 3D InISAR imaging results are in bad quality.

Then, we demonstrate the effectiveness of InISAR imaging based on squint iteration optimization and distortion correction method for squint mode. Figure 3 shows the InISAR imaging results using different methods, in which the actual scatterer distribution and the imaging results are represented by \circ and $*$, respectively. As we can see from Figures 3(a) and (b), the estimated coordinates x and y after squint iteration optimization are basically equal to the actual target model. The z coordinate, however, still departs from the target model due to the squint degree. By comparison of Figures 3(a) and (c), we can see that the z coordinates are approximately equal to the set ones after distortion correction. Figure 3(d) shows the 3D imaging results using the combination of squint iteration improvement and distortion correction. The z -coordinate is consistent with that of the target model as well. In a word, the estimated 3D coordinates based on the proposed method highly matches the actual target model.

6. CONCLUSION

For the application of InISAR, the target location usually departs from the perpendicular bisector of the baseline. The paper proposes a new 3D InISAR imaging algorithm under squint model by squint iteration optimization and distortion correction, the 3D reconstruction performance and quality are improved. Simulation results demonstrate that the algorithm is effective, achieving high quality 3D InISAR images consequently.

ACKNOWLEDGMENT

This work was supported by Hunan province innovation foundation for postgraduate (CX2014B020), and National University of Defense Technology innovation foundation for excellent postgraduate (B140405).

REFERENCES

1. Chen, C. C. and H. C. Andrews, "Target-motion-induced radar imaging," *IEEE Trans. on Aerosp. Electron. Syst.*, Vol. 16, No. 1, 2–14, 1980.
2. Delisle, G. Y. and H. Wu, "Moving target imaging and trajectory computation using ISAR," *IEEE Trans. on Aerosp. Electron. Syst.*, Vol. 30, No. 3, 887–899, 1994.
3. Zhang, Q., T. S. Yeo, G. Du, and S. Zhang, "Estimation of three-dimensional motion parameters in interferometric ISAR imaging," *IEEE Trans. Geosci. Remot. Sen.*, Vol. 42, No. 2, 292–300, 2004.
4. Wang, G. Y., X. Xia, and V. C. Chen, "Three-dimensional ISAR imaging of maneuvering targets using three receivers," *IEEE Trans. Image Proc.*, Vol. 10, No. 3, 436–447, 2001.
5. Felguera-Martin, D., J. T. Gonzalez-Partida, and M. Burgos-Garcia, "Interferometric ISAR imaging on maritime target applications: Simulation of realistic targets and dynamics," *Progress In Electromagnetics Research*, Vol. 132, 571–586, 2012.
6. Li, L. Y., H. W. Liu, B. Jiu, et al., "An interferometric inverse synthetic aperture radar imaging algorithms for squint model," *J. Xi'an Jiao Tong University*, Vol. 42, No. 10, 1290–1294, 2008.
7. Ma, C. Z., T. S. Yeo, H. S. Tan, et al., "Interferometric ISAR imaging on squint model," *Progress In Electromagnetics Research L*, Vol. 2, 125–133, 2008.
8. Liu, C. L., F. He, X. Z. Gao, et al., "Squint-mode InISAR imaging based on nonlinear least square and coordinates transform," *Sci China Tech. Sci.*, Vol. 54, No. 12, 3332–3340, 2011.

Moving Radar Target Detection Using an Improved OFDM Chirp Waveform Scheme

Jiahua Zhu, Pengzheng Lei, Chongyi Fan, Xiaotao Huang, and Zhimin Zhou

College of Electronic Science and Engineering

National University of Defense Technology, Changsha, Hunan 410073, China

Abstract— Orthogonal frequency division multiplexing (OFDM) chirp waveform has almost constant modulus, large time-bandwidth and good performance on correlation. It is a novel waveform scheme based on the OFDM principle and the linear frequency modulation (LFM) waveform. In this paper, the OFDM chirp waveform generation model is improved to the condition with arbitrary numbers of orthogonal basic signals, and the detection performance of this waveform is also analyzed. It is proved that the OFDM chirp waveform performs better than the traditional OFDM and LFM waveforms on moving target detection using the energy detector (ED) and the matched filter detector (MFD).

1. INTRODUCTION

Waveform diversity for moving target detection is always a challenging problem in radar field. Linear frequency modulation (LFM) waveform is one of the most usually used schemes for target detection, since it has the following qualities [1–3]. Firstly, it has constant envelope in time domain, which leads to a high efficiency of the transmitter modules of a phased-array antenna. Secondly, its spectrum approximates to rectangular shape with the increase of time-bandwidth product, which could maximize the spectral efficiency and signal-to-noise ratio (SNR). Thirdly, it can further exploit the linear frequency-time characteristics for easier signal processing. On the other hand, the orthogonal frequency division multiplexing (OFDM) waveform is recently introduced to radar field since it can solve the range-Doppler coupling problem caused by LFM waveform. Due to its orthogonal character in frequency domain [4, 5], the OFDM waveform could accomplish the transmission and reception in multi-channels by just one antenna and obtain much more information from targets, which means this scheme has the potential to save the cost as well as enhance the target detection performance. But unfortunately, OFDM waveform faces a drawback that its time and frequency synchronization is crucial to ensure subcarrier orthogonality [6, 7].

In order to solve the aforementioned problems, a novel waveform design scheme — the OFDM chirp waveform, which combines the OFDM principle with the LFM waveform, was proposed by Dr. Wen-Qin Wang [8, 9] and Dr. Jung-Hyo Kim [1, 10] respectively at the year 2012 and they all illustrated it has almost constant modulus, large time-bandwidth and good performance on correlation. Noticed that Dr. Kim's method only suitable for designing two orthogonal signals, Dr. Ming-Yang Zhou [7] improved the method to three orthogonal signals, and proved its better performance on the ambiguity function than the method with only two orthogonal signals.

However, the previous researches mainly discuss the processing techniques of multiple-input multiple-output (MIMO) synthetic aperture radar (SAR) systems. Few achievement about target detection based on OFDM chirp waveform was published before. Since the OFDM chirp waveform combined the orthogonality of subcarriers and intrinsic characteristics of traditional LFM waveform [1], it could be promising to have better performance than both the LFM and the OFDM waveform on moving target detection.

In this paper, the OFDM chirp waveform generation model demonstrated in [1] and [7] is extended to arbitrary numbers of orthogonal signals in theory. Moreover, the OFDM chirp waveform is proved to have good target detection performance, which is better than the traditional OFDM and chirp waveforms. The remainder sections of this paper are organized as follows. Section 2 makes a brief introduction of the OFDM chirp waveform modulation and extends its waveform generation model to arbitrary numbers of orthogonal basic signals. Based on the energy detector (ED) and the matched filter detector (MFD), Section 3 discusses the target detection performance of OFDM chirp waveform in detail. Then, some simulations and comparison analyses are given in Section 4, proving that the OFDM chirp waveform performs better than LFM and OFDM waveform on moving target detection. Finally, the paper is concluded in Section 5.

2. SIGNAL DESCRIPTION AND MODELING

According to the researches made by Dr. Jung-Hyo Kim and Dr. Ming-Yang Zhou, the orthogonality of the waveforms is independent on the types of input sequences [1], since they used the orthogonality of discrete frequency, like orthogonal subcarriers. On the basis of this quality, they built a three orthogonal basic signals model based on OFDM chirp waveform. But actually, this model could be further improved to the condition with arbitrary numbers of orthogonal basic signals.

Assume that the input sequence is $S[\bar{p}]$ with N discrete spectral components in spectrum, which are separated by $M\Delta f$ as shown in Fig. 1. Interleave $(M - 1)N$ zeros in the input sequence $S[\bar{p}]$ and we can get $\mathbf{S}_1[p]$ in Fig. 1. Then, we could shift $\mathbf{S}_1[p]$ by $\Delta f, 2\Delta f, \dots, (M - 1)\Delta f$ to obtain $\mathbf{S}_2[p], \mathbf{S}_3[p], \dots, \mathbf{S}_M[p]$ respectively. The OFDM modulation could be obtained by transforming those data sequences into the time domain through the MN point inverse discrete Fourier transform (IDFT). Therefore, the M OFDM modulators have the same number of orthogonal subcarrier, and we could get M OFDM modulators with each orthogonal subcarrier that are mutually shifted by Δf . Notice that although both modulators contain MN subcarriers, there are only N useful subcarriers that carry the input data.

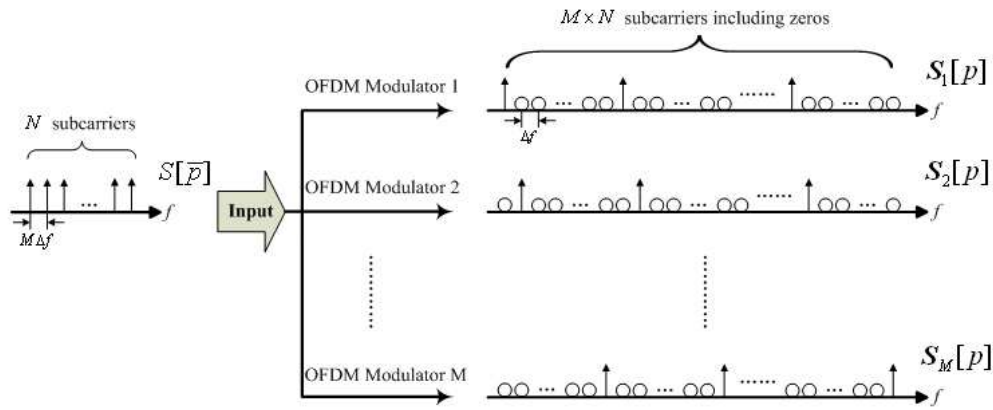


Figure 1: OFDM chirp waveform generation scheme.

In Fig. 1, the arrows represent subcarriers and the circles represent insert zeros. We first use an LFM signal spectrum as the input of each OFDM modulator, which could be given as

$$S[\bar{p}] = \mathcal{F}\{s[n]\} = \mathcal{F}\{\exp[j\pi k(nT_s)^2]\} \quad (1)$$

where $s[n]$ is the N -point discrete time samples of a complex LFM signal, k denotes the chirp rate, T_s means the sampling interval and $\mathcal{F}\{\cdot\}$ is the Fourier transform operator. Then, we can generate M input data sequence with zeros interleaved as follows using $S[\bar{p}]$.

$$\mathbf{S}_1[p] = [S[0], 0, 0, \dots, 0, 0, S[1], 0, 0, \dots, 0, 0, \dots, S[N - 1], 0, 0, \dots, 0, 0] \quad (2)$$

$$\mathbf{S}_2[p] = [0, S[0], 0, 0, \dots, 0, 0, S[1], 0, 0, \dots, 0, \dots, 0, S[N - 1], 0, 0, \dots, 0] \quad (3)$$

$$\mathbf{S}_M[p] = [0, 0, \dots, 0, 0, S[0], 0, 0, \dots, 0, 0, S[1], \dots, 0, 0, \dots, 0, 0, S[N - 1]] \quad (4)$$

where $p = 0, 1, \dots, MN - 1$. Then using the method aforementioned, we can express $s_1[n]$ as a repetition of $s[n]$ over the length of MN .

$$s_1[n] = s[n] \text{rect} \left[\frac{n}{N} \right] + s[n - N] \text{rect} \left[\frac{n - N}{N} \right] + \dots + s[n - (M - 1)N] \text{rect} \left[\frac{n - (M - 1)N}{N} \right] \quad (5)$$

In the same way, the other $M - 1$ signals could be described through a phase shift

$$s_2[n] = s_1[n] \exp \left(jn2\pi \frac{1}{MN} \right) \quad (6)$$

$$s_3[n] = s_1[n] \exp \left(jn2\pi \frac{2}{MN} \right) \quad (7)$$

$$s_M[n] = s_1[n] \exp \left(jn2\pi \frac{M - 1}{MN} \right) \quad (8)$$

By introducing $t = nT_s$ and $\Delta f = 1/(MNT_s)$, they can also be given in continuous time domain

$$s_1(t) = s(t)\text{rect}\left(\frac{t}{T_P}\right) + s(t-T_p)\text{rect}\left(\frac{t-T_p}{T_P}\right) + \dots + s(t-(M-1)T_p)\text{rect}\left(\frac{t-(M-1)T_p}{T_P}\right) \quad (9)$$

$$s_2(t) = s_1(t) \exp(j2\pi\Delta ft) \quad (10)$$

$$s_3(t) = s_1(t) \exp(2 \cdot j2\pi\Delta ft) \quad (11)$$

$$s_M(t) = s_1(t) \exp((M-1) \cdot j2\pi\Delta ft) \quad (12)$$

where T_P is the chirp duration and

$$s(t) = \exp(j\pi kt^2) \quad (13)$$

Thus, the model of OFDM chirp waveform with arbitrary numbers of orthogonal basic signals is deduced in this section. However, with the increase of M , the subcarrier numbers of each OFDM modulator would correspondingly increase M times. Although it could bring a higher processing precision, it also aggravates the burden of computing devices and needs higher cost. Without loss of generality, we then use $M = 3$ as an example in next sections to discuss its target detection performance considering the computation burden and processing precision.

3. TARGET DETECTION

There are two versions of the target detection problem. The first one we refer to as the ideal scenario, when the target channel response \mathbf{h}_t is assumed known. In the other one called realistic scenario, the target channel response \mathbf{h}_t is unknown. Although unrealistic, the ideal scenario provides straightforward bounds on the detection performance achievable by the realistic scenario [11].

In this paper, two detectors are used to analyze the detection performance under the ideal scenario:

- (1) MFD, which is the optimal detector when no clutter is presented in the scene;
- (2) ED, which is the generalized likelihood ratio test (GLRT) for conventional detection.

Given a simple radar detection scene with one moving point target and background white Gaussian noise, so the detection problem is equivalent to the binary hypothesis problem as follows:

$$\begin{cases} \mathcal{H}_0 : & \mathbf{y} = \mathbf{w} \\ \mathcal{H}_1 : & \mathbf{y} = \mathbf{s} \otimes \mathbf{h}_t + \mathbf{w} \end{cases} \quad (14)$$

where \mathbf{y} and \mathbf{s} is the receiving echo wave and the transmitting signal of each OFDM modulator respectively, “ \otimes ” is the convolution operator, $\mathbf{w} \sim \mathcal{CN}(0, \sigma^2)$ is the complex white Gaussian noise and σ^2 is its variance. Besides, all parameters in (14) are expressed in vector forms.

3.1. MFD

According to the Neyman-Pearson (NP) criterion [12], the data probability density functions (PDFs) $p(\mathbf{y}|\mathcal{H}_0)$ and $p(\mathbf{y}|\mathcal{H}_1)$ under the conditions \mathcal{H}_0 and \mathcal{H}_1 can be given as

$$p(\mathbf{y}|\mathcal{H}_0) = \frac{1}{(\pi\sigma^2)^{MN}} \exp\left[-\frac{1}{\sigma^2}\mathbf{y}^H\mathbf{y}\right] \quad (15)$$

$$p(\mathbf{y}|\mathcal{H}_1) = \frac{1}{(\pi\sigma^2)^{MN}} \exp\left[-\frac{1}{\sigma^2}(\mathbf{y}-\mathbf{s})^H(\mathbf{y}-\mathbf{s})\right] \quad (16)$$

After some algebraic manipulations we have

$$L(\mathbf{y}) = \frac{p(\mathbf{y}|\mathcal{H}_1)}{p(\mathbf{y}|\mathcal{H}_0)} > \gamma \Rightarrow \text{Re}(\mathbf{s}^H\mathbf{y}) > \gamma' \quad (17)$$

where $\gamma' = \sqrt{\sigma^2\varepsilon/2}Q^{-1}(P_{\text{FA, MF}})$, $P_{D, \text{MF}} = Q(Q^{-1}(P_{\text{FA, MF}}) - \sqrt{2\varepsilon/\sigma^2})$, $\varepsilon = \sum_{n=0}^{MN-1} |\mathbf{s}[n]|^2$, $Q(x) = \int_x^\infty \frac{1}{\sqrt{2\pi}} \exp(-\frac{1}{2}t^2)dt$, P_{FA} and P_D represent the false-alarm and detection probabilities, respectively. Besides, ε and $Q(x)$ denote the energy of \mathbf{s} and the right tail probability function, respectively.

3.2. ED

The likelihood ratio of ED should compute the total received signal energy across the operating frequency range [13], thus the likelihood ratio function is shown as

$$L(\mathbf{y}) = \frac{p(\mathbf{y}|H_1)}{p(\mathbf{y}|H_0)} = \frac{1/\sigma^2 \sum_{n=0}^{MN-1} |\mathbf{y}[n]|^2}{1/\sigma^2 \sum_{n=0}^{MN-1} |\mathbf{w}[n]|^2} > \gamma \quad (18)$$

To calculate the $P_{FA,ED}$ and $P_{D,ED}$, the Monte Carlo method [12] is introduced since the analytical expression of test statistics $L(\mathbf{y})$ cannot be obtained.

4. SIMULATIONS AND PERFORMANCE ANALYSIS

In this section, some simulation results are put forward to illustrate the target detection performance of the OFDM chirp waveform, which are compared with the counterparts of conventional OFDM and LFM waveforms.

As it is mentioned before, one moving point target was set in the radar detection scene with background white Gaussian noise. The original distance between the target and radar is 1000 m and the target has a constant velocity $v_t = 10$ m/s towards the radar. In order to compare the performance of those three kinds of waveforms, we first set some global parameters for each waveform: The operating frequency $f_c = 1$ GHz; signal bandwidth $B = 200$ MHz; pulse number is 1000; pulse repetition frequency is 500 Hz; discrete time samples of each subcarriers or the whole signal is $N = f_s \cdot T_P$. To satisfy the orthogonal quality of the OFDM, T_P should be no less than M/B and here we set $T_P = 8.5 \mu\text{s}$, $M = 3$; Δf should be no less than $1/T_P$ and here we set $\Delta f = 66.7$ MHz. For LFM signal $k = B/T_P$. Besides, the energy of each waveform is normalized to 1 and we control the noise add to them is at the same energy level. Then, the receiver operating characteristic (ROC) curves of three waveforms using two kinds of detectors when the SNR is -30 dB are shown in Fig. 2.

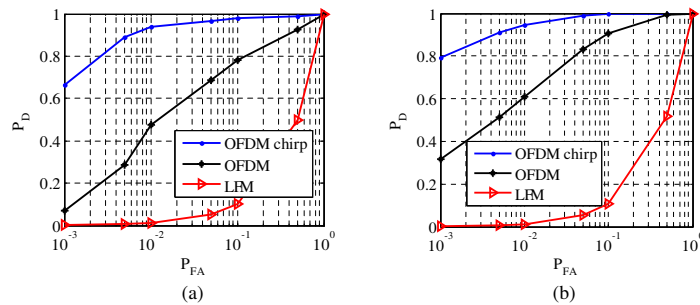


Figure 2: ROC curves of the OFDM chirp, OFDM and LFM waveforms using (a) ED; (b) MFD.

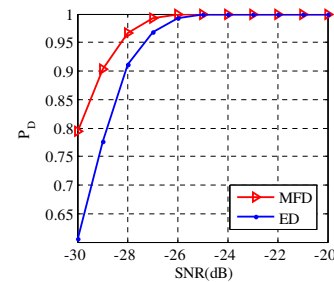


Figure 3: Detection probability versus SNR for the OFDM chirp waveform using two detectors.

From Fig. 2 it is obvious to see that the OFDM chirp waveform performs better than the other two waveforms. Exactly, the P_D of the OFDM chirp waveform using ED is about 0.63 when $P_{FA} = 10^{-3}$, while the counterparts of OFDM and LFM waveforms are only 0.07 and 0.01, respectively. Additionally, the P_D of the OFDM chirp waveform using MFD is about 0.79, while the counterparts of OFDM and LFM waveforms are only 0.31 and 0.02, respectively. As we know, it is apparent that the OFDM chirp waveform has much more orthogonal subcarriers than LFM waveform, thus more target information could be exploited for target detection algorithms and higher detection probability could be obtained. Besides, using chirp signals as the OFDM symbols can suppress the cross-correlation components better than the conventional OFDM waveform, since LFM signal is less sensitive to the time and frequency synchronization. Therefore, the OFDM chirp waveform provides higher detection probability in comparison with that of OFDM waveform.

The performance of two detectors in different SNRs when $P_{FA} = 10^{-3}$, using the OFDM chirp waveform as an example, is further compared as Fig. 3 illustrated. It proves that as the optimal detector in our detection scene, the MFD has better performance than the ED. This is because the MFD uses phase information of signals and maximizes the receiving SNR through convolution. The results also show that without clutter is presented, the MFD has about 1.5 dB gain over the ED at $P_D = 0.8$. However, it is stressed that the MFD has a lower degree of stability and robustness than

the ED [13], which means its performance may drop off significantly in dense clutter environment. This work will be discussed in our future researches.

5. CONCLUSION

In this paper, we improve a novel OFDM chirp waveform generation model to the condition with arbitrary numbers of orthogonal basic signals and introduce this waveform scheme to moving target detection. Then we use the MFD and ED respectively to evaluate the target performance of the waveforms. The simulation results prove that the OFDM chirp waveform performs better than the traditional OFDM and LFM waveforms on moving target detection, and the MFD shows a significant performance gain over the ED when clutter is not exist.

In subsequent work, the detection scene will be extended to more complex conditions such as dense clutter and multipath to further research the performance of OFDM chirp waveform.

ACKNOWLEDGMENT

This work was supported in part by the National Natural Science Foundation of China under Grant 60972121 and in part by the University Innovation Foundation for Postgraduate of National University of Defense Technology (NUDT) under Grant S140402.

REFERENCES

1. Kim, J. H., M. Younis, A. Moreira, and W. Wiesbeck, "A novel OFDM chirp waveform scheme for use of multiple transmitters in SAR," *IEEE Geoscience and Remote Sensing Letters*, Vol. 10, No. 3, 568–572, May 2013.
2. Curlander, J. C. and R. N. McDonough, *Synthetic Aperture Radar Systems and Signal Processing*, Wiley, U.S., 1991.
3. Richards, M. A., *Fundamentals of Radar Signal Processing*, McGraw-Hill Companies, U.S., 2005.
4. Le, N. P., L. C. Tran, and F. Safaei, "Energy-efficiency analysis of per-subcarrier antenna selection with peak-power reduction in MIMO-OFDM wireless systems," *International Journal of Antennas and Propagation*, Vol. 2014, 1–13, 2014.
5. Zhu, J. H., C. Y. Fan, X. T. Huang, and Z. M. Zhou, "Ground moving target detection using airborne radar based on OFDM waveform," *14th International Radar Symposium*, 929–934, Dresden, Germany, Jun. 19–21, 2013.
6. Morelli, M., C. J. Kuo, and M. Pun, "Synchronization techniques for orthogonal frequency division multiple access (OFDMA): A tutorial review," *Proceedings of the IEEE*, Vol. 95, No. 7, 1394–1427, Jul. 2007.
7. Zhou, M. Y., H. Y. Liu, W. Z. Liu, and Y. M. Gu, "An improved OFDM chirp waveform design," *2013 IEEE 5th International Symposium on Microwave, Antenna, Propagation and EMC Technologies for Wireless Communications (MAPE)*, 478–482, Chengdu, China, Oct. 29–31, 2013.
8. Wang, W. Q., "OFDM waveform diversity design for MIMO SAR imaging," *2012 IEEE International Geoscience and Remote Sensing Symposium (IGARSS)*, 2090–2093, Munich, Germany, Jul. 22–27, 2012.
9. Wang, W. Q., "Mitigating range ambiguities in high PRF SAR with OFDM waveform diversity," *IEEE Geoscience and Remote Sensing Letters*, Vol. 10, No. 1, 101–105, Jan. 2013.
10. Kim, J. H., "Multiple-input multiple-output synthetic aperture radar for multimodal operation," Ph. D. Dissertation, Karlsruhe Institute of Technology, Germany, Dec. 2011.
11. Moura, J. M. F. and Y. W. Jin, "Detection by time reversal: Single antenna," *IEEE Transactions on Signal Processing*, Vol. 55, No. 1, 187–201, Jan. 2007.
12. Kay, M. S., *Fundamentals of Statistical Signal Processing, Volume II: Detection Theory*, Prentice Hall PTR, U.S., 1998.
13. Jin, Y. W., J. M. F. Moura, Y. Jiang, D. D. Stancil, and A. G. Cepni, "Time reversal detection in clutter: Additional experimental results," *IEEE Transactions on Aerospace and Electronic Systems*, Vol. 47, No. 1, 140–154, Jan. 2011.

Methods and Experiments for the Sensing and Evaluation of Ionosphere Changes and Their Impact on the Human Organism

M. Hanzelka¹, J. Dan², P. Fiala¹, M. Friedl¹, and Vladan Holcner³

¹Department of Theoretical and Experimental Electrical Engineering
Brno University of Technology, Technická 3082/12, Brno 616 00, Czech Republic

²Rector's Office, Personnel Management Office
Masaryk University, Žerotínovo nám. 9, Brno 601 77, Czech Republic

³Faculty of Economics and Management
University of Defence, Kounicova 65, Brno 662 10, Czech Republic

Abstract— The impact of the environment upon living organisms constitutes a crucial problem examined by today's science. In this context, research institutes worldwide have analysed diverse positive and negative factors affecting the biological system of the human body. One such factor consists in the influence of the surrounding electromagnetic field. This paper presents the results of an investigation focused on ionosphere parameter changes and their impact on the basic function of the nervous system. It is a well-known fact that the frequency of the alpha waves of brain activity [1] ranges between 6–8 Hz. Changes in the electromagnetic and chemical structure of the Earth's surface may cause variation of signals in the above-defined frequency region of 6–8 Hz. Detailed examination of the overall impact of environmental factors upon the human organism is performed within a large number of medical disciplines. The research presented in this paper is concentrated on the sensing and detection of changes in the region of very low electromagnetic field frequencies; the authors test theoretical and experimental procedures to define the effects that influence brain activity.

1. INTRODUCTION

The low-level measurement of low frequencies (0.01–10 Hz) performed to evaluate the effect of magnetic fields on the human organism can be regarded as an interdisciplinary branch of science that comprises different types of research.

At this point, it is important to consider applied research disciplines, for example the measurement and radar technology in the following ranges: the ULF (Ultra Low Frequency Band: 300 Hz–3 kHz); the SLF (Super Low Frequency Band: 30 Hz–300 Hz); and the ELF (Extreme Low Frequency Band: 0.1 Hz–30 Hz).

If external magnetic fields influenced a human being to such an extent that the man or woman could change their behaviour within the social community at a higher level of statistical significance, it would be necessary to employ various questions of economics, mainly the evolution of economic value as a market phenomenon based on human behaviour and decision-making. Scientists and researchers are currently almost ready to solve special tasks related to objectivising the impact of low-level magnetic fields upon the human organism; such impact will be examined from the perspective of physical harm to cells [2] and mental condition of humans [3–6].

The state of the art in this field is relatively unsatisfactory, and certain hasty conclusions have been made and applied even in hygienic standards. An example of such standards is the guideline issued by the Council of Europe and implemented by the ICNIRP (International Commission on Non-Ionising Radiation Protection) in 1999 to establish the boundary values of magnetic flux in relation to the speed of magnetic field changes for very slowly changing currents. More concretely, this guideline introduces the value of 50 mT/s as the maximum magnetic flux change acceptable in an environment characterised by permanent presence of humans and exhibiting a variable magnetic field at the frequency of 1 Hz. This value is many millions higher than the largest changes hitherto measured during the processes referred to as magnetic storms, in which the Earth was exposed to charged particles from the Sun.

In this paper, the authors attempt to design an experiment with a comprehensive set of measurable parameters related to the human body and acquired within a homogeneous group of subjects. All the subjects were examined repeatedly to provide a dependable basis for the subsequent evaluation of these parameters in light of changes in the external magnetic field.

2. ORIENTATION OF THE METHODS FOR DETECTING IONOSPHERE DISTURBANCES

According to the conclusions produced by secondary research, there is mutual interaction between the low-level electric or magnetic fields irradiated by humans and the geomagnetic system of the Earth. This paper presents a portion of the research conducted in this province by the DTEEE, FEEC BUT; the research is built upon the current knowledge of low-level magnetic fields generated by the geomagnetic system of the Earth and the solar system. The authors of this article have focused on examining the effect of the changes in the Earth's geomagnetic system that are due to solar activity. In this context, the research was also centered on proving the existence of the effect as a result of geomagnetic storms, which substantially influence low-level magnetic fields affecting the human organism, including its behavioural patterns and decisioning. The detection of changes in geomagnetic field disturbances could be performed by means of the Schumann resonances. Until recently, this oscillation occurred at the frequency of $f_{sch} = 7.83\text{ Hz}$; this frequency changes as a result of the impact exerted by phenomena such as solar wind or greenhouse gases. In 1953, Professor W. O. Schumann of Munich university, Germany [6, 7] had found out that the cavity between the ionosphere and the Earth's surface could be interpreted as a spherical resonator. After Schumann's results were published in the Technische Physik journal, Dr. Ankermueller, a medical specialist, immediately related the resonances to brain wave rhythm (EEG). In 1954, the measurements conducted by W. O. Schumann and Herbert Koenig (who was to become Schumann's successor) confirmed the pulsation of the Earth at the frequency of $f = 7.83\text{ Hz}$. Koenig then validated the correlation between the Schumann resonances and brain wave rhythms [8]. In light of these facts, he chose a set of experimental measurements of certain instantaneous parameters of human physiology, depending on external conditions.

3. DESCRIPTION OF THE EXPERIMENTAL RESEARCH

The laboratory research comprising a homogeneous sample of 49 subjects (men and women aged 19 to 25) was launched on April 22, 2014 and lasted until June 26, 2014. The total time required for the examination of psychophysiological parameters in a subject corresponded to 19 minutes. We used a Nickelodeons Infiniti (Thought Technology Ltd.) unit to perform the entire task, and the measurement proper involved four phases: Rest; Color; Rest; Math; and Rest. At the Color stage, a special (Stroop) test was utilized to acquire the psychophysiological responses of each subject to a load on their organism. Generally, this tool demonstrates that a person performing the given task can be easily distracted due to their automatic reactions and habits; the procedure is named after John Ridley Stroop (1897–1973), an American psychologist who first described the phenomenon in 1929. In the Math phase, then, the respondents were asked to progressively subtract the number 7 from the initial value of 1081, and we examined the psychophysiological stress generated during such quiet countdown. The total number of measurements was 210, with the average of 4.29 per respondent.

The relationship between the former indicator and the number of subjects who completed the task is shown in Tab. 1. The respondents were measured in special laboratories to ensure comparable parameters and constant temperature, noise, humidity, lighting, concentration of positive and negative ions, and a homogenized component of the geomagnetic field, Fig. 2(c)).

Table 1: The relation between the number of completed measurements and the number of respondents.

Number of respondents	Number of measurements
4	1
1	2
4	3
12	4
24	5
4	6
49	SUM

4. COLLECTION OF PSYCHOLOGICAL DATA PRIOR TO THE RESEARCH

A major part of the laboratory research consisted in large-scale collection of psychological data from all participants (respondents) via several psychological tests, of which one was an ASS-SYM test; this tool measures a respondent's sensitivity to changes in the transition from load to relax. All the results were then correlated with the psychophysiological measurements.

4.1. During the Research Process

After entering the laboratory, each respondent was introduced into the input measurement according to Tab. 2. The average measurement period corresponded to 7 minutes.

Table 2: The initial measurements.

Input variables	Unit	Number of measurements
Body temperature	°C	210 (420)
Blood pressure	mmHg	210 (420)
Instant history	Writing current state of health	210
Assay for alcohol (positive only in one case)	%	0.1
Luscher psychological test colors	Index	210

The discussed input cycle was followed by the sensing of psychophysiological parameters via a BioGraph Infiniti apparatus; the related variables are listed in Tab. 3.

Table 3: An overview of dependent variables.

Dependent variable — psychophysiological measurements	Unit	Number of measurements
Skin conductance	μS	210
Skin temperature	°C	210
Peripheral blood flow BVP	%	210
Cardiac events BVP	puls/min	210
Thoracic breathing	f/min	210
Abdominal breathing	f/min	210
Trapezius muscle contractions EMG	μV	210
Contraction of muscles forehead EMG	μV	210

The final measurements performed before the respondent being dismissed from the lab included variables according to Tab. 4:

Table 4: The output variables established during the final sequences of the session.

Output variables	Unit	Number of measurements
Mirror-drawing tests: adaptability measurement	S	210
Relation to risk	index	210
Body temperature	°C	210 (420)
Blood pressure	mmHg	210 (420)

The average measurement time related to the output variables was 7 minutes.

4.2. Description of the Measurement Procedures for the Given Sample of Respondents

To measure the psychophysiological characteristics of the human body on the respondents, we used the BioGraph Infiniti devices providing bio- and neurofeedback. The following variables were measured:

B: BVP amplitude mean (Rel), B: BVP HR mean (beats/min), B: BVP HR std. dev., B: BVP peak freq. mean (Hz), B: BVP IBI std. dev. (SDRR), B: BVP VLF % power mean, B: BVP LF

% power mean, B: BVP HF % power mean ,B: BVP VLF total power mean, B: BVP LF Total power mean, B: BVP HF total power mean, B: BVP LF/HF (means), Total spectral power, C: EMG mean (uV), D: EMG mean (uV), E: Skin conductance mean (uS), E: SC as % of value mean (%),F: Temperature mean (Deg), F: Temp as % of value mean (%),G: Resp rate mean (br/min), B&G: (HR max-min) mean (b/min), G: Abd amplitude mean (rel), H: Thor amplitude mean (rel), G&H: Abd-tho ampl diff (means).

The measurement comprised three relaxation and two stress phases, with an emphasis on intensive psychological stress in the respondents. The stress stages were laboratory-generated using a low-level electromagnetic field generator, an amplifier, and Helmholtz coils to interact with the EEG brain waves of the respondent. The resulting low-level field enabled us to simulate the effect of changes in solar activity as an additional offset to the related real intensity indicators prepared for each day by NASA. The field strength in the Helmholtz coil was set to the level of terrestrial magnetic field, and the major parameters were as follows: impulse $f = 1 \text{ kHz}$; start = 100 ns; $\lambda/2 = 168 \mu\text{s}$. Fig. 1 shows a diagram of the stimulation and measurement apparatus.

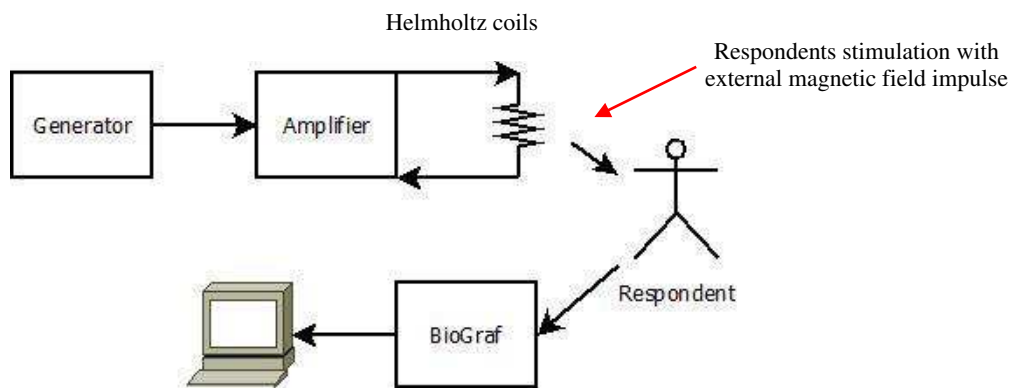


Figure 1: Scheme of measurement and simulation apparatus.

Figure 2, then presents shots of the BioGraph Infiniti measurements.

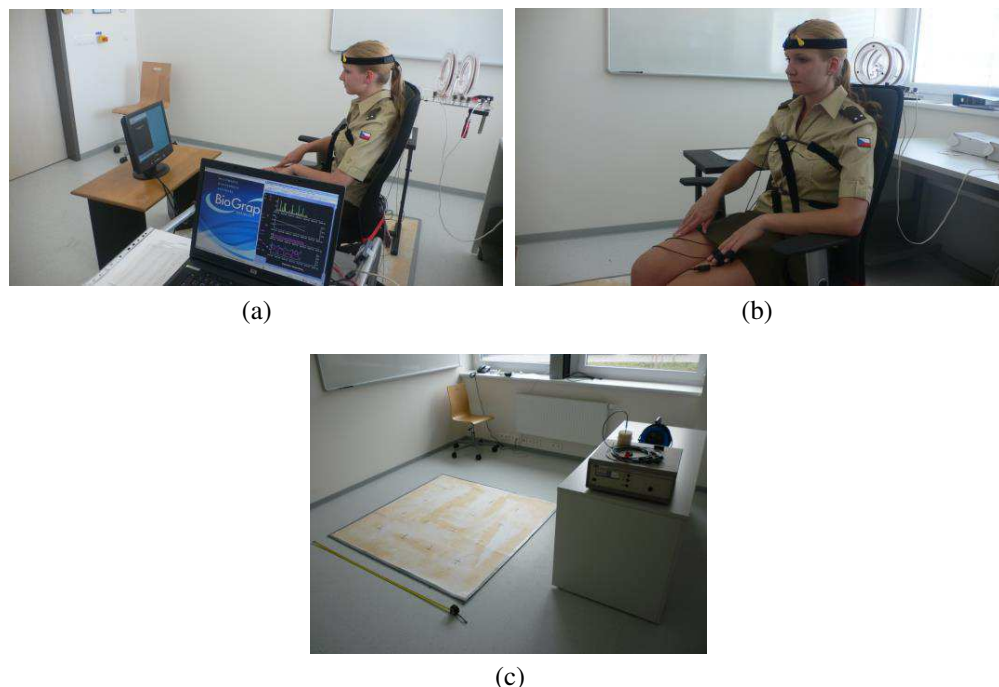


Figure 2: (a), (b) Documentation shots from measurements in laboratory conditions, (c) laboratory space of measurements with geomagnetically stable component of the magnetic field.

5. CONCLUSION

The research results will be compared with the hypotheses and the magnetic field level changes at slowly varying electric currents; further, the investigated aspects will involve possible impact of these changes on the continuous movement of population in an environment exhibiting such variable electromagnetic fields. These relationships have already been mathematically and graphically outlined within a scientific article. Moreover, the results of the materialized surveys will be processed together with the psychological tests that measure the side effects of the environment affecting human psychophysiological variables.

ACKNOWLEDGMENT

The research described in the paper was financially supported with a grant provided by Czech Science Foundation (GACR 13-09086S), the research described in this paper was carried out for the great help and support of the University of Defence, which for the purposes of research provide a homogeneous sample of respondents.

REFERENCES

1. Ferris, J., “The brain generates an electric field that influences its own activity,” *Scientific American Mind*, Vol. 21, No. 10, Oct. 28, 2010, published online: doi:10.1038/scientificamericanmind1110-10a.
2. Stuchly, M. S., “Magnetic field-induced currents in the human body in proximity of power lines,” *IEEE Transactions on Power Delivery*, Vol. 11, No. 1, Jan. 1996.
3. Scorretti, R., N. Burais, L. Nicolas, and A. Nicolas, “Modeling of induced current into the human body by low-frequency magnetic field,” *IEEE Transactions on Magnetics*, Vol. 41, No. 5, Dostupná, May 2005, z: 10.1109/TMAG.2005.846276.
4. Carrubba, S. and A. A. Marino, “The effects of low-frequency environmental-strength electromagnetic fields on brain electrical activity: A critical review of the literature,” *Electromagnetic Biology and Medical*, Vol. 27, No. 2, 83–101, Department of Orthopaedic Surgery, LSU Health Sciences Center, P. O. Box 33932, Shreveport, LA 71130-3932, United States, 2008.
5. Hashish, A. H., M. A. El-Missiry, H. I. Abdelkader, and R. H. Abou-Saleh, “Assessment of biological changes of continuous whole body exposure to static magnetic field and extremely low frequency electromagnetic fields in mice,” Department of Physics, Faculty of Science, University of Mansoura, Mansoura 35516, Egypt Department of Zoology, Faculty of Science, University of Mansoura, Mansoura 35516, Dostupná z, Feb. 21, 2008, doi:10.1016/j.ecoenv.2007.10.002.
6. Miller, R. A. and I. Miller, “The Schumann’s resonances and human psychobiology,” *News Science*, www.nexusemagazine.com, Apr. 2003.
7. Schumann, W. O., “On the free oscillations of a conducting sphere which is surrounded by an air layer and an ionosphere shell (in German),” *Z. Naturforsch*, Vol. 7A, 149–154, 1952.
8. Gray, J. A., *The Neuropsychology of Anxiety: An Enquiry into the Functions of the Septo-hippocampal System*, Oxford Univ. Press, Oxford, U.K., 1982.

The Parameters of a Special High Voltage Function Generator

P. Marcon, P. Fiala, M. Steinbauer, and P. Drexler

Department of Theoretical and Experimental Electrical Engineering
Brno University of Technology, Technicka 12, Brno 616 00, Czech Republic

Abstract— Goal of this project was to design, realize and test a special high voltage function generator. This generator was designed for special testing of soft tissues. The aim of this project was to generate electric field of defined shape. In course of design of the generator the properties of the output electrode voltage was the key element. In this article the construction and parameters measuring of the high voltage function generator is discussed.

1. INTRODUCTION

The generator was designed for special tests of soft tissues. Possibilities of the soft issue testing are described in literature [1–3]. Kriz and Vlachova-Hutova [4] also describe a numerical model of electromagnetic field in the biological cell. Designed special high voltage function generator allows to create both static field and variable electrical field. The aim of this work is describe parameters of this special high voltage generator especially frequency dependence of the generated electric field.

2. BLOCK DIAGRAM OF THE DESIGNED HIGH VOLTAGE FUNCTION GENERATOR

Designed high voltage generator has two basic parts. The first part is a low voltage and the second part is a high voltage. The low voltage part include a power source, isolation transformer, control module, optical isolation and function generator. Second part is the high voltage (HV) module. In the HV module a HV transformer as a border between low and high voltage part is the main part. The HV voltage transformer is designed as a flyback. Block diagram of the HV generator you can see in Fig. 1. Output voltage 20 kV is stabilized by the feedback signal FB — the voltage from HV output is connected through the high voltage divider and optocoupler to the control module. According to the feedback signal the control module use a PWM signal for transistor and primary coil of the HV transformer switching.

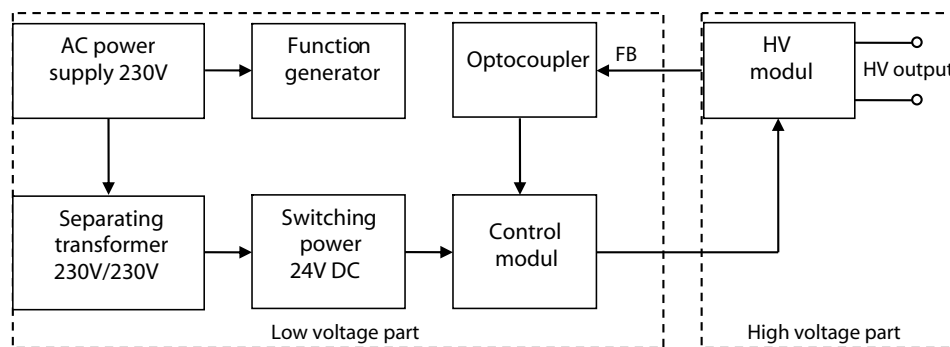


Figure 1: Block diagram of the high voltage generator.

Frequency and shape of the HV output signal is possible to change by the low voltage output signal of the function generator. Function generator signal is connected to the control module where will be actively integrated and through the optical isolation connected to the PWM controller.

2.1. HV Generator — Low Voltage Part

Basic part of the low level part is the control module. Line voltage pass through the separating transformer 230 V/230 V and consequently is in switching power supply regulated to 24 V. The switching power supply needs to be designed according to maximal output current for primary coil excitation. Primary coil voltage is switched by the PWM controlled MOSFET transistor. Used PWM controller precisely controls output voltage according to the signal on this circuit comparator. Due to this design, the circuit quickly reacts to output current changes and is able to decrease output current and voltage. This is very important for life protection in case of accidental touch.

Setting of the output frequency is done by resistor and capacitor on the resonant frequency of the transformer.

Comparator inside the PWM controller is comparing the current voltage with value of the requested voltage on the output electrode. High voltage is by HV divider decreased from 20 kV to 1 V on the input control unit. Comparison of the regulation and the output voltage is provided by an operation amplifier (OA). The operation amplifier works as a differential amplifier of the regulation deviation. OA is also compensating a voltage spikes from the HV divider. The voltage spikes could have influence on the device function and cause distortion of the output voltage. The border between low and high voltage part is the HV transformer connected as a flyback convertor. The HV function generator was designed by using equations that have been published in literature [5–10].

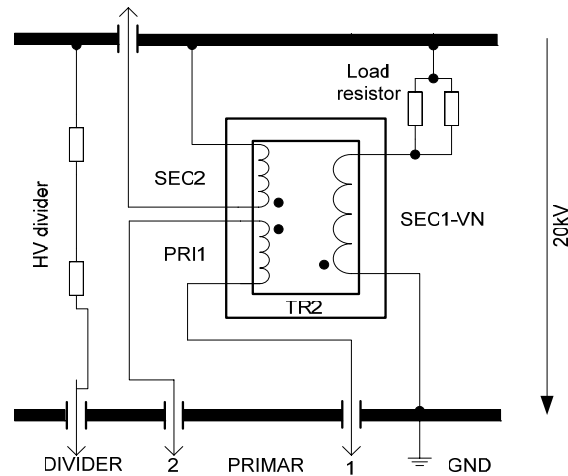


Figure 2: Block diagram of the high voltage part.

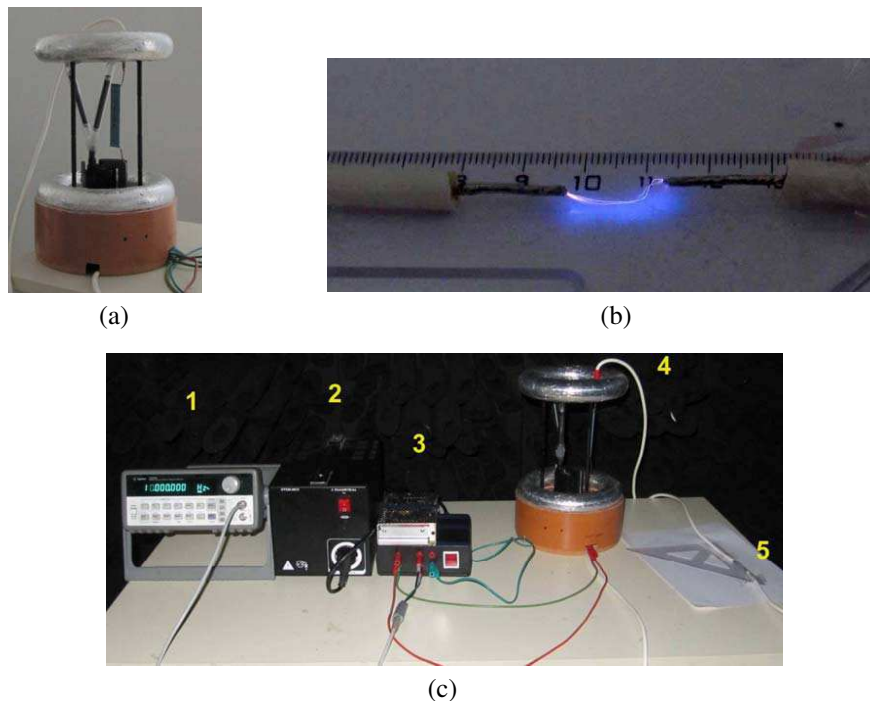


Figure 3: (a) Realized HV module. (b) Electric discharge. Electrode distance is approximately 1.5 cm. (c) Workplace with HV generator (1-function generator, 2-source, 3-control unit with power source, 4-HV module and 5-spar gap).

2.2. HV Generator — High Voltage Part

Block diagram of the high voltage part is in Fig. 2. The main part of the HV block is HV transformer TR2 working as a flyback converter. Inside the transformer a rectifier diode is connected. Secondary winding SEC2 is possible to link to next module for multiplying of the output voltage. Resistor $1\text{ G}\Omega$ and the power resistor are as the HV divider connected between the output electrodes. Exceeding of the 20 kV output voltage value cause on the $1\text{ G}\Omega$ resistor voltage drop higher then 1 V and consequently a change of pulse ratio of the PWM signal.

2.3. Realized HV Generator

Realized HV generator, in detail ring electrodes, $1\text{ G}\Omega$ resistors and flyback transformer you can see in Fig. 3. On the top the high voltage cable is connected. Voltage limit of this cable reach 30 kV . HV generator test is in Fig. 3. As you can see, discharge distance is approximately 1.5 cm .

2.4. HV Generator Parameters Measurement

Low voltage generator AGILENT was connected into the feedback loop of the flyback converter. Output square-wave voltage of the generator was set to 1 V_{pp} . Frequencies were changed in range from 1 Hz to 3 kHz . The control unit is changing the PWM signal in an effort to obtain the same shape of the secondary voltage as is the shape of the primary voltage. Amplitude of the output voltage is approximately 20 kV .

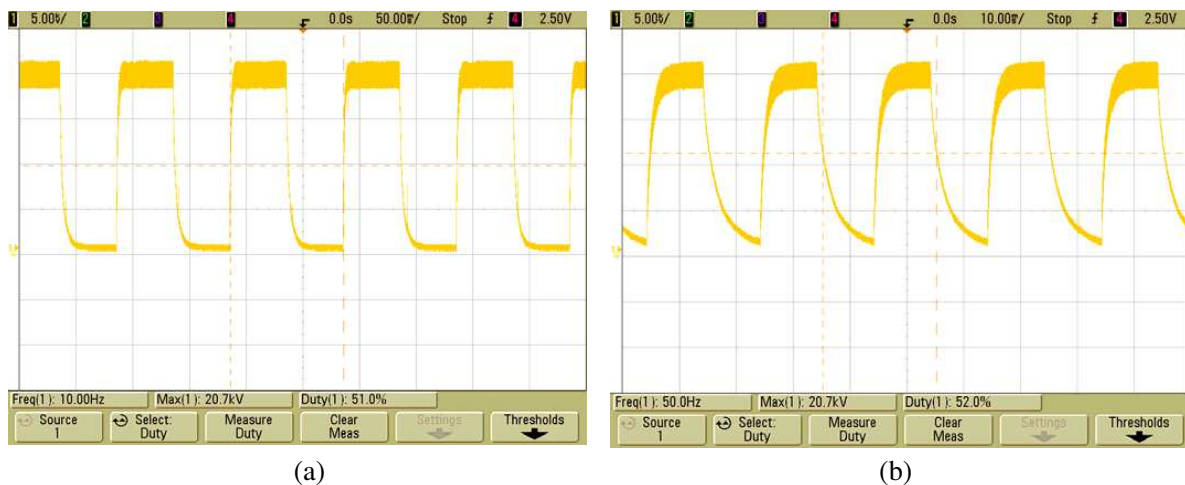


Figure 4: (a) HV generator output voltage, $V_{gen} = 1\text{ V}_{pp}$ and $f_{gen} = 10\text{ Hz}$. (b) HV generator output voltage, $V_{gen} = 1\text{ V}_{pp}$ and $f_{gen} = 50\text{ Hz}$.

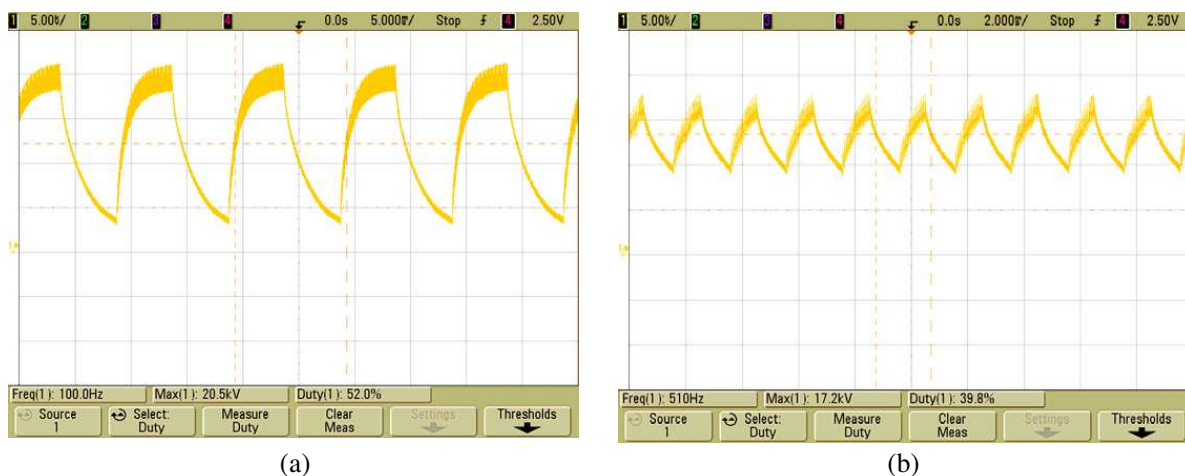


Figure 5: (a) HV generator output voltage, $V_{gen} = 1\text{ V}_{pp}$ and $f_{gen} = 100\text{ Hz}$. (b) HV generator output voltage, $V_{gen} = 1\text{ V}_{pp}$ and $f_{gen} = 500\text{ Hz}$.

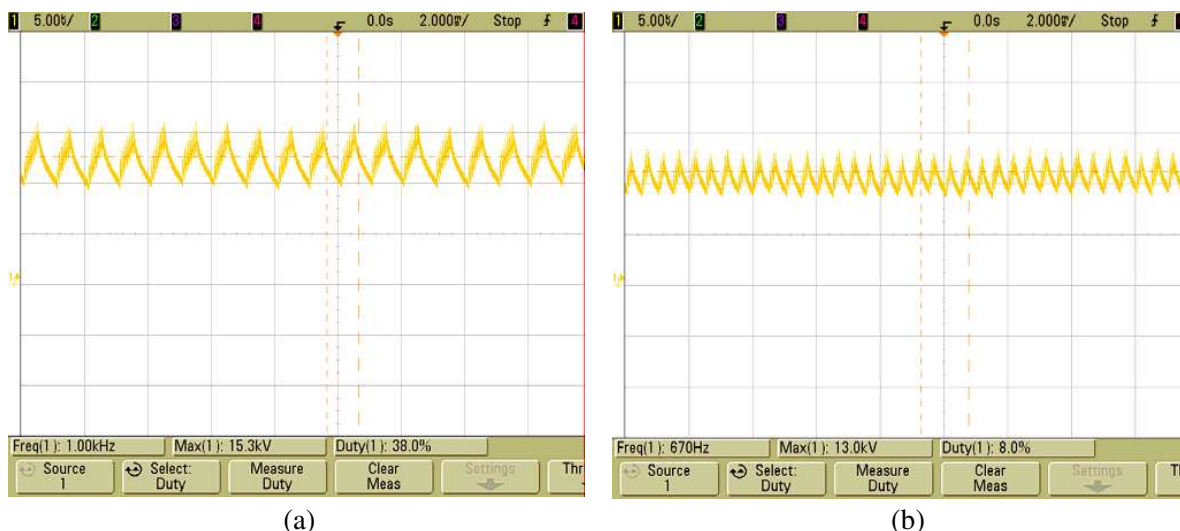


Figure 6: (a) HV generator output voltage, $V_{\text{gen}} = 1 V_{\text{pp}}$ and $f_{\text{gen}} = 1 \text{ kHz}$. (b) HV generator output voltage, $V_{\text{gen}} = 1 V_{\text{pp}}$ and $f_{\text{gen}} = 2 \text{ kHz}$.

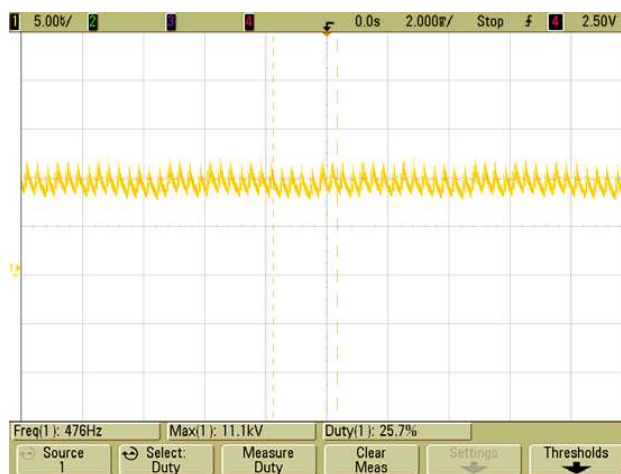


Figure 7: HV generator output voltage, $V_{\text{gen}} = 1 V_{\text{pp}}$ and $f_{\text{gen}} = 3 \text{ kHz}$.

3. RESULTS AND CONCLUSIONS

The measurement confirms that the output voltage is possible to regulate in range from 0 V to 20 kV. Frequencies of the output voltage could be changed in range from 1 Hz to 3 kHz with low distortion. Frequencies over 300 Hz are under influence of the parasitic capacities. Voltage on the output electrode needs to be soft for soft tissue testing. The output voltage of the generator can be seen in Fig. 4–Fig. 7. Input voltage has 1 Vpp amplitude and frequency in range 10 Hz to 50 Hz. Square-wave input signal is under influence of parasitic capacities changed. The influence is dependent on the frequency of the input signal. In addition, over 100 Hz the output voltage amplitude is decreasing and signal start to have offset.

ACKNOWLEDGMENT

The paper was supported by the Czech Science Foundation project 15-08803S.

REFERENCES

1. Krepelka, P., F. Perez-Rodriguez, and K. Bartusek, “Bacterial pattern identification in near-infrared spectrum,” *Pomiry w Gospodarce I Ochronie Środowiska*, 58–60, Informatyka, Automatyka, 2014.
2. Vlachova Hutova, E., T. Kriz, Z. Roubal, J. Vichova, R. Pokorny, and K. Bartusek, “Effect of static magnetic field on growth and sporulation of plant pathogenic fungi *Colletotrichum*

- acutatum,” *Proc. of 11 th Conference of the European Foundation for Plant Pathology*, 98, Publishing House of the University of Agriculture in Krakow, Kraków, Poland, 2014.
3. Pokludova, M. and P. Krepelka, “The study of the growth of tissues cultures under a layer of nanotextiles,” *PIERS Proceedings*, 195–198, Guangzhou, Aug. 25–28, 2014.
 4. Vlachova Hutova, E. and T. Kriz, “Numerical modeling of electromagnetic field in the biological cell,” *Book of Abstract CEITEC Annual Conference*, 242, Masarykova Univerzita, Brno, 2014.
 5. Gasparov-Grekhov, A. V. and V. L. Granenstein, *Applications of High-power Microwaves*, Artech House, Boston, London, 1994.
 6. Kalousek, V., F. Stanek, and J. Schieblova, “Technika vysokých napeti,” Skripta VUT FEKT v Brne, Brno, 1989.
 7. Krejcirik, A., “Napajeci zdroje II — Integrované obvody ve spinaných zdrojích,” BEN, Technická Literatura, Praha, 1997.
 8. Krejcirik, A., “Napajeci zdroje I — Zakladni zapojeni analogovych a spinaných napajecich zdroju,” BEN, Technická Literatura, Praha, 1997.
 9. Krejcirik, A., “Napajeci zdroje III — Pasivni soucastky v napajecich zdrojích a preregulatory,” BEN, Technická Literatura, Praha, ISBN 80-86056-56-2, 2002.
 10. Faktor, Z., “Transformatory a civky,” BEN, Technická Literatura, Praha, 1999.

Measurement of Tissue Cultures of Early Somatic Embryos of Norway spruce

E. Vlachova Hutova¹, R. Korinek², K. Bartusek², L. Havel¹, and P. Drexler¹

¹Department of Theoretical and Experimental Electrical Engineering
Faculty of Electrical Engineering and Communication, Brno University of Technology
Technicka 12, Brno 616 00, Czech Republic

²ASCR, Institute of Scientific Instruments, Kralovopolska 147, Brno 612 64, Czech Republic

Abstract— The objective of this study was the monitoring of the growth and development of early somatic embryos in a magnetic field strength of 4.7 T. The samples were exposed to radiofrequency (RF) field, gradient (G) field and combination of both fields. To measure longitudinal (T_1) and transverse relaxation times (T_2), the spin echo based techniques were used. The aspects of major interest for the investigation of the related biological processes are the various image contrasts and the change of the relaxation times T_1 and T_2 on the boundary between the embryo and the substrate. Control measurements of changes in the size of the investigated tissue of early somatic embryos was done using camera and subsequently evaluated in MATLAB. All measurements were realized at the Institute of Scientific Instruments in Brno.

1. INTRODUCTION

Nuclear magnetic resonance (NMR) is a physical phenomenon in which nuclei in a magnetic field absorb and re-emit electromagnetic radiation. NMR is also routinely used in advanced medical imaging techniques, such as in magnetic resonance imaging (MRI). The MRI is a non-invasive tool applied by many researchers to study molecules. The MRI approach is frequently used not only in medicine, but also in biological, biochemical, and chemical research. In plant biology, MRI is utilized to support the research of water and mineral compounds transported within a plant, the determination of plant metabolites, the investigation of cellular processes, and the examination of the growth and development of plants. MRI is also instrumental towards monitoring water changes in early somatic embryos of spruce (ESEs) [1]. These embryos constitute a unique plant model system applicable for the study of various types of environmental stresses (including metal ions) under well-controlled experimental conditions [2–4]. The earlier experimental results show that the effect of gradient magnetic fields on ESEs varies considerably [5]. Thus, it is not easy to answer the question of whether magnetic fields accelerate or suppress the growth of plant cultures but some other measurements for different settings of the external magnetic field can prove that the external magnetic field can change the dynamics of the model of matter [6].

2. METHOD

The general aim of the experiment was to perform in vivo measurement of the ESEs using MRI techniques, and the entire process comprised several stages. Within the first step, we compared the acquired T_1 - and T_2 -weighted MR images, the next stage of the experiment consisted in determining the changes of the size of ESEs. To measure the T_2 relaxation, we applied spin-echo (SE) technique (echo times (TEs): 18, 30, 50, 100 and 200 ms); the measurement of the T_1 relaxation was realized using inversion recovery spin echo (IRSE) technique (inversion times (TIs): 10, 100, 300, 1000 and 3000 ms). Other samples of ESEs were “measured” by the same techniques, but in the first case, the only gradients were switched off and in the second case, the only RF field was switched off. All the described experiments were performed on the 4.7 T (Magnex) MRI system at Institute of Scientific Instruments in Brno. The MAREVISI (8.2) and MATLAB (R2014b) programs were used for the processing. The progress of growth was evaluated from 2D images of clusters in the Petri dishes, and the area of the ESEs was calculated. The acquired images of the ESEs were processed to provide the required data. For that reason, we created an application in MATLAB, which allows for the recognition and subsequent calculation of the area occupied by the ESEs [7]. Table 1 shows the distribution of the Petri dishes during the experiment.

3. PLANT MATERIAL AND CULTIVATION CONDITIONS

A clone of early somatic embryos of the Norway spruce (*Picea abies*/L./Karst.) marked as 2/32 were used in our experiments. The cultures were maintained on a semisolid (Gelrite Gellan

Table 1: Distribution of measured samples.

Sample n.	1	2	3	4	5	6	7	8
Method	IRSE, SE	RF	G	Control/without external field	IRSE, SE	RF	G	Control/without external field
Date of measurement	2014/10/20–2014/11/06				2014/10/21–2014/11/07			

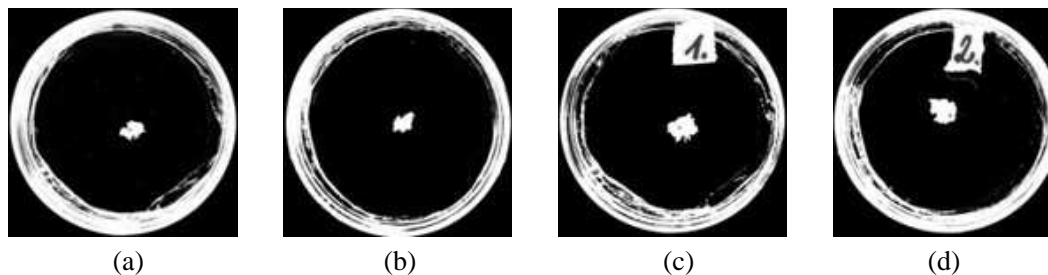


Figure 1: Petri dishes with ESEs prepared to evaluate the size of the tissue: (a), (b) images of sample 1 and 2 from the first day of experiment; (c), (d) corresponding images from the 13th day.

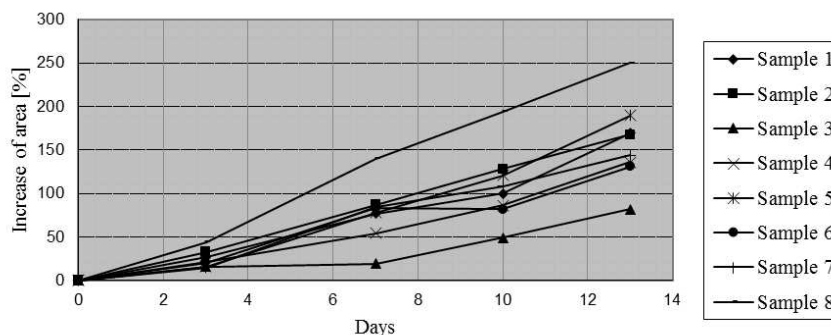


Figure 2: The growth of individual samples during the experiment.

Gum, Merck, Germany) half-strength LP medium with modifications. The concentration of 2, 4-dichlorophenoxyacetic acid and N6-benzyladenine was 4.4 and 9 μm , respectively. The pH value was adjusted to 5.7–5.8 before autoclaving (121°C, 100 kPa, 20 min). The organic part of the medium, excluding saccharose, was sterilized by filtration through a 0.2 μm polyethylenesulfone membrane (Whatman, Puradisc 25 AS). The cultivation was carried out in Petri dishes (diameter 50 mm). The sub-cultivation of stock cultures was carried out in 2-weeks intervals; the stock and experimental cultures were maintained at the temperature of $23 \pm 2^\circ\text{C}$ in a cultivation box kept in a dark place. The experiment started with colonies of early somatic embryos which weight was about 3 mg. Only one cluster per one Petri dish was cultivated.

4. RESULTS

Figure 1 shows the images of the pre-processed Petri dishes. From these images was evaluated increase tissue during the experiment.

Figure 2 shows the changes of the size of ESEs tissues. These results show that the most stable and suitable conditions for tissue growth were provided during the measurement of T_1 and T_2 . If the increase in these two samples expressed as a percentage, these values are 189.7% (sample 1) and 169.5% (sample 5). On the other side was very different growth and development of control samples that were exposed only to the influence of the magnetic field of the earth. If the increase in these two samples expressed as a percentage, these values are 136.4% (sample 4) and 250% (sample 8). Values which reflect an increase in the area may be dependent on the error, which is caused for example by bad evaluating the size of the surface tissue.

The other aspects of interest for the investigation of the related biological processes is the various image contrasts and the change of the relaxation times T_1 and T_2 on the boundary between the embryo and the substrate. Figure 3 shows the T_1 and T_2 maps and the changes in development of

sample 1 at first and last day of experiment. A comparison of the mean of the relaxation times T_1

Table 2: The relaxation times (mean value) T_1 and T_2 of the ESEs and the substrate.

B_0 field	T_1 [ms]	T_2 [ms]	Method
first day of experiment (day 0)			
ESEs	398	61	IRSE/SE
Substrate	634	36	
last day of experiment (day 13)			
ESEs	761	86	IRSE/SE
Substrate	386	46	

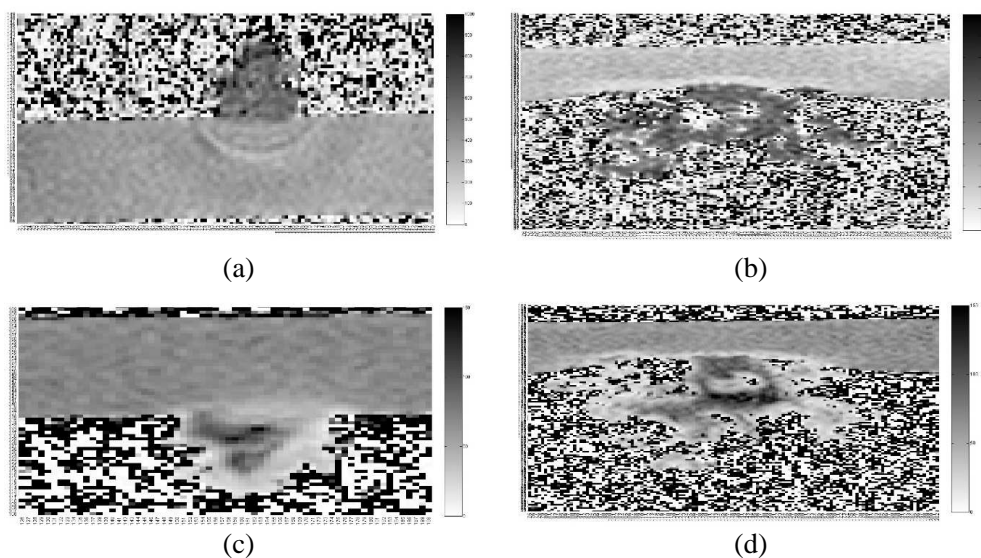


Figure 3: The changes in development of sample 1 during the experiment: (a), (c) T_1 and T_2 maps (ms) in first day of the experiment (0 day); (b), (d) T_1 and T_2 maps (ms) in 13th day.

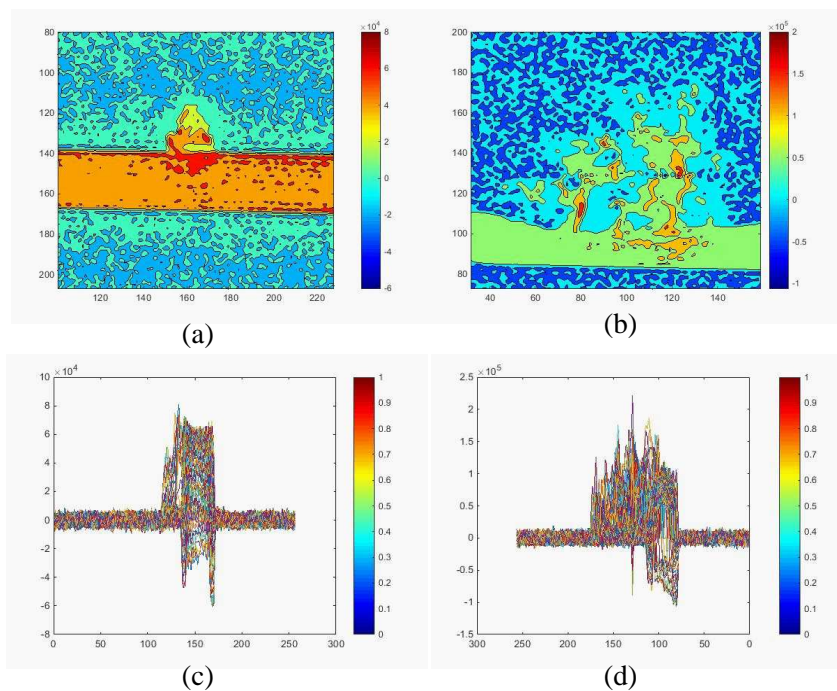


Figure 4: Changes in the development of sample 1 during the experiment: (a), (c) distribution of ESEs growth deposits in substrate; (b), (d) the image of the location of biological changes in the substrate.

and T_2 in the ESEs (sample 1) and the substrate can be seen in Table 2.

An important aspect to assess the development of ESEs is evaluating the change between the embryo and the substrate. These change in development of ESEs are shown in Figure 4. Figures 4(a) and 4(c) show the distribution of growth ESEs deposits in substrate. These place are connected by isolines. Figures 4(a) and 4(c) also show how ESEs can growth into the substrate and use the substrate for their own development. Between the substrate and the ESE are biological changes that are seen in Figure 2(b) and Figure 2(d). This change manifests itself by changing the value of the magnetic susceptibility. We can only assume that this change represent a place where the ESEs draws nutrients from the substrate. This change is also seen in Figures 4(b) and 4(d). The biological effect of this area is not confirmed yet.

5. CONCLUSION

The experimental results show that the effect of gradient magnetic fields on ESEs varies considerably (Table 1). We are still unable to assess whether the effect of stationary magnetic fields for plant organisms is positive or not but we now that the external magnetic field changes the dynamics of the model of matter and theoretically can change the growth of organisms. Table 2 shows the relaxation times T_1 and T_2 of the samples in different magnetic fields. The changes of the relaxation times T_1 and T_2 on the boundary between the embryo and the substrate are of interest for the investigation of biological processes.

ACKNOWLEDGMENT

The research described in the paper was performed within the grant of Czech ministry of industry and trade No. FR-TI1/001, it was financially supported by project of the BUT Grant Agency FEKT-S-14-2545/2014 and by the project Education for Competitiveness Operative Programme CZ.1.07.2.3.00.20.0175.

REFERENCES

1. Supalkova, V., J. Petrek, J. Baloun, V. Adam, K. Bartusek, L. Trnkova, M. Beklova, V. Diopan, L. Havel, and R. Kizek, "Multi-instrumental investigation of affecting of early somatic embryos of spruce by cadmium(II) and lead(II) ions," *Sensors* Vol. 7, No. 5, 743–759, 2007.
2. Mikelova, R., J. Baloun, J. Petrlova, V. Adam, L. Havel, H. Petrek, A. Horna, and R. Kizek, "Electrochemical determination of Ag-ions in environment waters and their action on plant embryos," *Bioelectrochemistry*, Vol. 70, No. 2, 508–518, 2007.
3. Petrek, J., J. Vitecek, H. Vlasinova, R. Kizek, K. J. Kramer, V. Adam, B. Klejdus, and L. Havel, "Application of computer imaging, stripping voltammetry and mass spectrometry for study of the effect of lead (Pb-EDTA) on growth and viability of early somatic embryos of Norway spruce (*Picea abies* /L./Karst.)," *Anal. Bioanal. Chem.*, Vol. 383, 576–586, 2007.
4. Víteček, J., V. Adam, J. Petřek, J. Vacek, R. Kizek, and L. Havel, "Esterases as a marker for growth of BY-2 tobacco cells and early somatic embryos of the Norway spruce," *Plant Cell Tissue Organ Cult.*, Vol. 79, 195–201, 2004.
5. Hutova, E., K. Bartusek, and J. Mikulka, "Study of the influence of magnetic fields on plants tissues," *PIERS Proceedings*, 57–60, Taipei, Mar. 25–28, 2013.
6. Hutova, E., K. Bartusek, and P. Fiala, "The influence of a magnetic field on the behaviour of the quantum mechanical model of matter," *PIERS Proceedings*, 1847–1851, Guangzhou, China, Aug. 25–28, 2014.
7. Bartusek, K., E. Gescheidtova, and J. Mikulka, "Data processing in studying biological tissues, using MR imaging techniques," *33th International Conference on Telecommunications and Signal Processing*, 171–175, Asszisztenda Szervezo, Budapest, Hungary, 2010,

Comparison Study of Layered Homogeneous Models with Detailed Human Tissue Models for Through-body Communications

Muhammad Ali Babar Abbasi, Dimitris Philippou, and Symeon Nikolaou

Department of Electrical Engineering, Frederick University, Nicosia, Cyprus

Abstract— Any wireless communication between implantable antenna and an external off-body antenna suffers significant link loss due to the lossy nature of living human tissues. This link degradation is normally unpredictable and varies for different parts of the human body. To study an implantable communication scenario, complete setup is generally simulated using a full wave electromagnetic simulator. Such simulation requires human body phantoms having electrical properties such as permittivity and bulk conductivity, or even mass density similar to that of real body tissues. It has been observed that geometry of such phantoms is usually chosen as simple as possible to decrease the required computational resources and the overall time for the completion of the simulation. It is difficult to predict how much error is expected when realistic phantom is replaced by such geometrically simpler phantom. This study focuses on a comparison of the usefulness of using realistic human body phantoms over geometrically simple body phantoms for through-body communication simulation. To study this comparison, an implantable antenna, placed inside a human stomach model, is set to communicate with an off-body antenna at Medical Implant Communication Service (MICS) band. Keeping the distance between implantable antenna and off-body antenna constant, the realistic human body phantom is then replaced by two types of layered body phantoms with different complexity. Results in the form of calculated s -parameters and phantom complexity metrics are further investigated to conclude the study.

1. INTRODUCTION

Implantable devices for biomedical applications play vital role in building comprehensive telemedicine wireless communication networks. Before an implantable device is proposed, it is usually thoroughly simulated at system level, using numerical methods in order to study the electromagnetic propagation loss when the DUT is placed inside human body. Computerized MRI scanner deduced, detailed body phantoms are finding increasingly important role in the attempt to test the performance of such implantable devices on system level. A number of 3D phantoms, deduced from MRI scans of living subjects [1, 2], depicting indirectly measured electrical properties of human tissues, are widely used, for case to case based, implantable device, design problems. These models generally have frequency-dependent electrical properties, and they are similar in shape to realistic human body parts and thus geometrically complex. Example of such complex phantoms for medical imaging and implantable applications are presented in [4]. Alternatively another simpler approach is widely used, where dense material blocks or homogeneous layers with constant electrical properties similar to those of predominant human tissues are built and used in EM simulations for implantable devices problems [6, 7]. These mainly homogeneous blocks, consist of simple geometric shapes which result in low mesh complexity, during modeling in 3D CAD tools, and are therefore far less resources hungry when simulated using full wave EM solvers. The main problem limiting the use of layered homogeneous models, is related to their accuracy and consequently their reliability. This study aims to assess the reliability of such simpler models in comparison with the more complex structures of realistic body-mimicking models. Towards this end, a theoretical scenario is discussed through extensive simulations, in which the communication between an implantable device, located inside a human stomach model, and an off-body device placed near the abdomen is investigated. A novel, compact, multilayered, implantable antenna, operating at 403 MHz, is used to establish a through-body communication scenario with a near-body transceivers antenna. Keeping in mind the detuning effect of implantable and near-body antennas, both antennas are matched properly with respect to the surrounding human tissue models. Three different phantom models are compared in Section 2 and the simulated results are further investigated.

2. SIMULATION SETUP

The proposed implantable setup in order to investigate through body communication consists of an implantable antenna shown in Figure 1, placed inside the stomach of a realistic body phantom. The used antenna consists of three substrate layers of Rogers RO3210 ($h = 0.635$ mm, $\epsilon_r = 9.4$ and

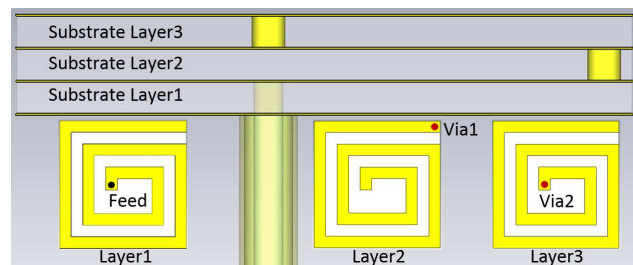


Figure 1: Geometry of implantable antenna operating at MICS band.

Tissue	ϵ_r	σ (S/m)
1- Stomach	67.51	1.00
2- Abdominal Muscle	57.15	0.79
3- Body Average	35.00	0.60
4- Gallbladder	61.25	1.13
5- Large Intestine	62.63	0.95
6- Liver	51.27	0.65
7- Pancreas	61.56	0.87
8- Small Intestine	66.19	1.90
9- Spleen	63.27	1.02

Table 1: Electrical properties of human organs at MICS band.

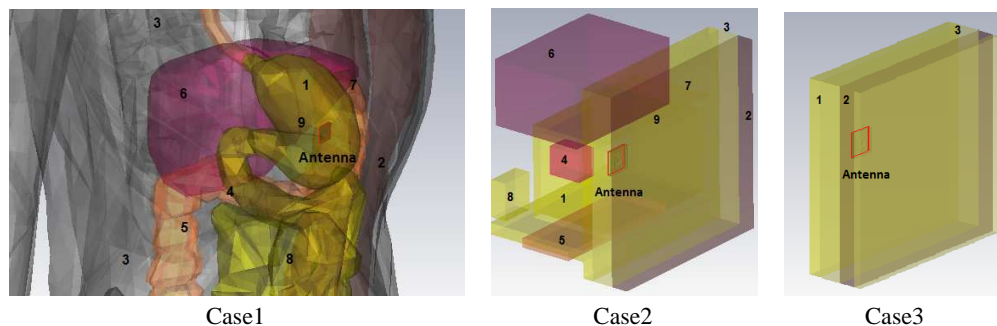


Figure 2: Implanting antenna in realistic human phantom (Case1), complex layered phantom (Case2) and simple layered phantom (Case3).

$\tan \delta = 0.006$) coated with copper having spiral and meandered configuration. Three spiral layers having 1 mm thick copper strip, connected to each other through via1 and via2, realize a radiating resonance at 403 MHz, MICS band. These layers are stacked to form a 3D meandered patch, in an attempt to achieve the desired compactness for an implantable antenna. The antenna used in this study is designed and matched in accordance to its operation inside stomach of a realistic human body phantom. On the other hand, a wideband antenna having directional radiation pattern with realizable gain ranging from 4 dB to 4.5 dB at MICS band is placed near the abdominal region of the phantom, to operate as an off-body transceiver antenna. Keeping the location and operation of implantable and off-body antennas constant, three types of phantoms, representing human tissues have been studied as described in Figure 2. The properties of human tissues considered in this study are listed in Table 1 and were presented in [8, 9]. Note that the average human tissue properties at MICS band [9] ($\epsilon_r = 35$, $\sigma = 0.60$ S/m) have been assigned to all other organs of the body phantom that are not listed in Table 1. As shown in Figure 2, Case1 represents a realistic human phantom model that can be considered as a reference phantom. Case2 represents a geometrically simpler phantom model where dense material blocks are placed at the same location where real human tissues are located. This layered phantom represents a comparatively simpler model than that of the realistic body phantom presented in Case1. The simplest phantom model is presented in Case3 in which only those tissues which are in the LOS path of the implantable to off-body antenna communication link, are modeled for the simulation setup. These tissues are represented by dense homogeneous material layers with the implantable antenna placed inside the equivalent stomach layer.

3. RESULTS AND DISCUSSION

To study the performance of each phantom, Finite Difference Time-Domain (FDTD) solver with Finite Integration Perfect Boundary Approximation (FPBA) hexahedral mesh was used. Considering only the organs listed in Table 1, full wave simulation was performed for all three cases. The number of pulses to define steady state convergence criteria was 20, and it was carefully selected to ensure accuracy up to 1%. Simulation parameters including adaptive mesh refinement were kept constant for all three cases. It was observed that a total number of FDTD mesh cells was 6.573952×10^6

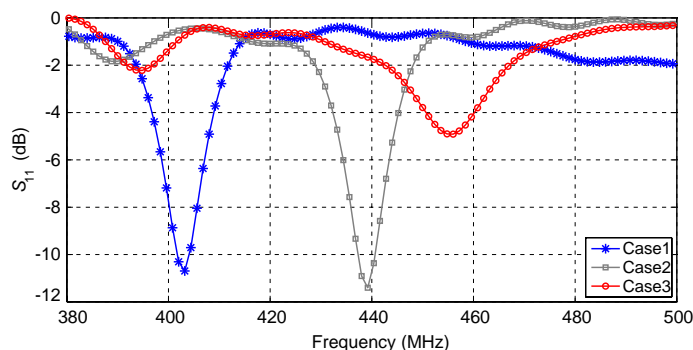


Figure 3: Return loss comparison of implantable antenna for all three cases.

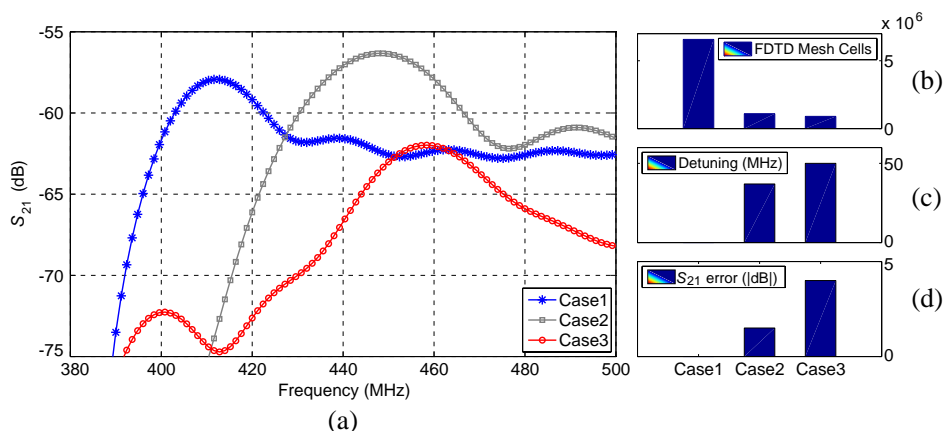


Figure 4: (a) S_{21} comparison for implantable antenna, (b) comparison of FDTD mesh cell count, (c) comparison of detuning in MHz, and (d) comparison of error observed in S -parameter for all three cases.

for Case1 as compared to that of 1.095438×10^6 and 0.898688×10^6 mesh cells generated in Case2 and Case3 respectively. In Case1, the antenna is placed inside stomach where it is surrounded by not only stomach tissue but also by other high water content and high conductivity tissues (like gallbladder, small intestine etc.). Intentionally the antenna is matched for this implant as evident by the simulated return loss shown in Figure 3. In Case2, realistic body organs are replaced by dense material blocks representing comparatively simpler models of human organs. Mesh cell count to simulate Case2 setup decreases but with the cost of significant detuning of resonant frequency from 403 MHz to 440 MHz. This shift is much greater than the total bandwidth assigned to MICS band, i.e., 3 MHz (402 MHz–405 MHz [9]) resulting in operation of the implantable antenna outside the designated, licensed, MICS band. Moreover, when this phantom is further replaced by the second even simpler layered phantom, widely used to test the performance of implantable antennas [6, 9], the resonance frequency further shifted towards higher frequencies. S_{11} for Case3 shown in Figure 3 depicts a detuning of 50 MHz, and a significant impedance mismatch. Simulation results indicate that not only the electrical properties, but also the location and even the very geometry of high conductive tissues play a significant role in through-body communication. Disregarding these tissues will introduce significant error in s -parameter calculation for any similar implantable simulation setup.

4. CONCLUSION

In this paper a realistic body phantom (Case1), a complex body phantom (Case2) and a widely used simple layered phantom (Case3) are compared in a through-body communication scenario at the MICS band. Complexity of these phantoms in terms of full wave simulator meshing density and resulting s -parameters accuracy were discussed. It was observed that when a realistic phantom was replaced by widely used simpler phantom models, significant detuning of the resonant frequency of the implantable antenna occurred. Due to the narrow bandwidth of MICS band, this detuning can be considered as unacceptable for such simulation setups. Further simulation results indicated that the additional computational requirements (computational resources and time) to simulate

a realistic body phantom model is only 6 to 7 times the computational requirements, needed to simulate simple layered phantoms. Based on this observation, it is recommended to use realistic body phantom rather than layered phantoms for simulation setups created for implantable antennas, operating in the MICS band.

REFERENCES

1. Seo, J. K. and E. J. Woo, "Electrical tissue property imaging at low frequency using MREIT," *IEEE Transactions on Biomedical Engineering*, Vol. 61, No. 5, 1390–1399, 2014.
2. Motovilova, E., J. Su, and S. Y. Huang, "MRI-based electrical property mapping for human body," *IEEE International Conference on Computational Electromagnetics (ICCEM)*, 73–75, IEEE, 2015.
3. Segars, W. P. and B. M. W. Tsui, "MCAT to XCAT: The evolution of 4-D computerized phantoms for imaging research," *Proceedings of the IEEE*, Vol. 97, No. 12, 1954–1968, 2009.
4. Veress and Segars, A. I., W. Paul, J. A. Weiss, B. M. W. Tsui, and G. T. Gullberg, "Normal and pathological NCAT image and phantom data based on physiologically realistic left ventricle finite-element models," *IEEE Transactions on Medical Imaging*, Vol. 25, No. 12, 1604–1616, 2006.
5. Xu, L., M. Q.-H. Meng, and Y. Chan, "Effects of dielectric parameters of human body on radiation characteristics of ingestible wireless device at operating frequency of 430 MHz," *IEEE Transactions on Biomedical Engineering*, Vol. 56, No. 8, 2083–2094, 2009.
6. Huang, S., M. Tofighi, and A. Rosen, "Considerations for the design and placement of implantable annular slot antennas for intracranial pressure monitoring devices," *IEEE Antennas and Wireless Propagation Letters*, Vol. 99, 2014.
7. Nawaz, H. and M. Ali Babar Abbasi, "On-body textile antenna design and development for body-centric wireless communication systems," *12th International Bhurban Conference on Applied Sciences and Technology (IBCAST)*, 650–653, 2015.
8. Sani, A., A. Alomainy, and Y. Hao, "Numerical characterization of the radiation from implanted wireless sources considering different digital body phantoms," *3rd European Conference on Antennas and Propagation, (EuCAP)*, 459–461, 2009.
9. Kiourti, A. and K. S. Nikita, "A review of implantable patch antennas for biomedical telemetry: Challenges and solutions [wireless corner]," *IEEE Antennas and Propagation Magazine*, Vol. 54, No. 3, 210–228, 2012.

Analysis on SAR Values of Commercial Mobile Phones

Ae-Kyoung Lee, Seon-Eui Hong, and Jong-Hwa Kwon

Radio Technology Research Department

Electronics and Telecommunications Research Institute, Daejeon, Korea

Abstract— For epidemiological studies on the possible association between mobile phone use and brain diseases, representative phone models had been numerically implemented based on the specific absorption rate (SAR) distributions and spatial peak 1-g SAR values from the SAR test reports of mobile phones released in Korea. The numerical phone models were intended to produce the mean SAR distribution for each corresponding phone type. However, measured SAR levels of commercial phones at the maximum power are in wide range even though they are the same type of model. This paper proposes a method to utilize SAR information of a specific commercial phone which is described in the corresponding SAR test report for SAR estimation in the human head exposed the numerical phone models.

1. INTRODUCTION

The specific absorption rate (SAR) of mobile phones has been regulated since 2002 and more than 1200 models have been tested for SAR compliance in Korea. The limits of spatial peak SAR in the head referred to IEEE Std 95.1-1999 [1]. A mobile phone model should be compatible with the spatial peak SAR, i.e., 1.6 W/kg for 1 g of mass based on the measurement procedure of IEC 62209-1 [2].

For epidemiological studies investigating the potential association between mobile phone use and the risk of brain diseases, more than 1400 SAR test reports from 2002 to June 2013 have been collected. We organized a large amount of data including a manufacturer, a frequency band, outer shape, antenna type (internal/external), a maximum output power, body dimensions, and spatial peak 1-g SAR values in the four test positions of left cheek, right cheek, left tilt and right tilt at the center frequency for all the models. SAR distributions of about 70 mobile phones were measured in the flat phantom. Eleven representative phone models different in phone shape, operating frequency and antenna type and location were numerically implemented based on the measured SAR distributions and spatial peak 1-g SAR values from the SAR test reports [3]. The numerical phone models were intended to produce the mean SAR pattern and level for each corresponding phone type. SAR distribution was calculated in the human head exposed to the numerical phone models.

However, SAR levels of commercial phones are in wide range even though they are in the same type of models. This paper analyzes SAR difference between the test positions for each type of commercial phone models and proposes a method to reflect the peak 1-g SAR data provided in the SAR test report of a specific phone to calculated SAR in the human brain.

2. SPATIAL PEAK 1-G SAR OF COMMERCIAL PHONES

Each SAR compliance test report provides the spatial peak 1-g SAR data measured in the four positions (left cheek, right cheek, left tilt, and right tilt) at center frequency of the corresponding phone. In this paper, spatial peak 1-g SAR values in the four test positions are statistically analyzed. The scatter plots of Fig. 1 represent SAR levels of commercial bar-type phone models on the right and left sides of the specific anthropomorphic mannequin (SAM) phantom along the Y- and X-axes, respectively. The scatter plots of Fig. 2 show SAR levels of commercial slider-type phone models in the tilt and cheek positions against the SAM phantom along the Y- and X-axes, respectively.

The plots indicate positive SAR correlations between the right and left sides as well as the tilt and tilt positions. Table 1 shows statistical SAR results for some types of commercial phones. Since the release of smart phones, most recent models have been bar type and the antenna of most bar-type models is located at the inside bottom of the body. The data in the table were also obtained from SAR values in SAR compliance test reports. In each type, the averaged SAR values for the left and right sides of the phantom are very similar, whose correlation was good (0.6–0.9). However, it was found that the SAR information of the test reports should be reflected for SAR estimation in the human head since SAR values are so widespread.

It is impossible to numerically implement all commercial phone models which have used by subjects participating in an epidemiological study. A previous epidemiological study had used the

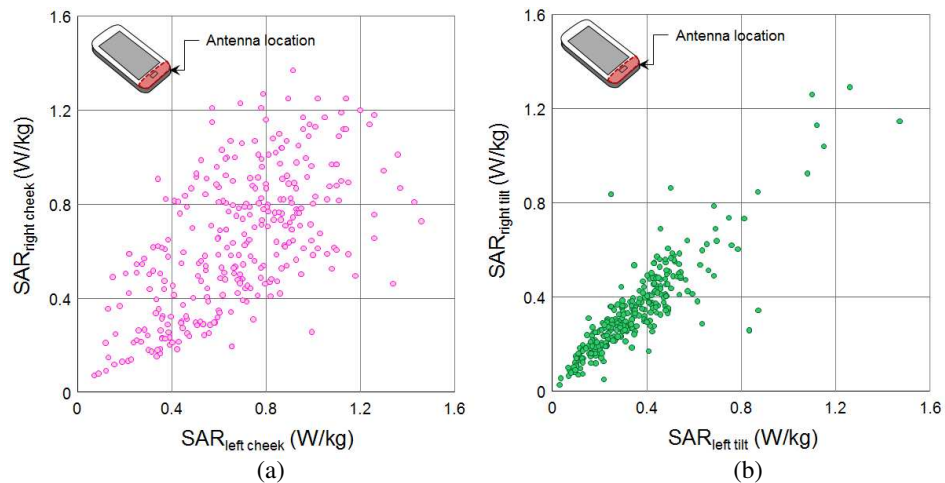


Figure 1: Scatter plot between SAR values measured on the left and right sides of the SAM phantom for the bar type of commercial phone models. (a) Cheek position. (b) Tilt position.

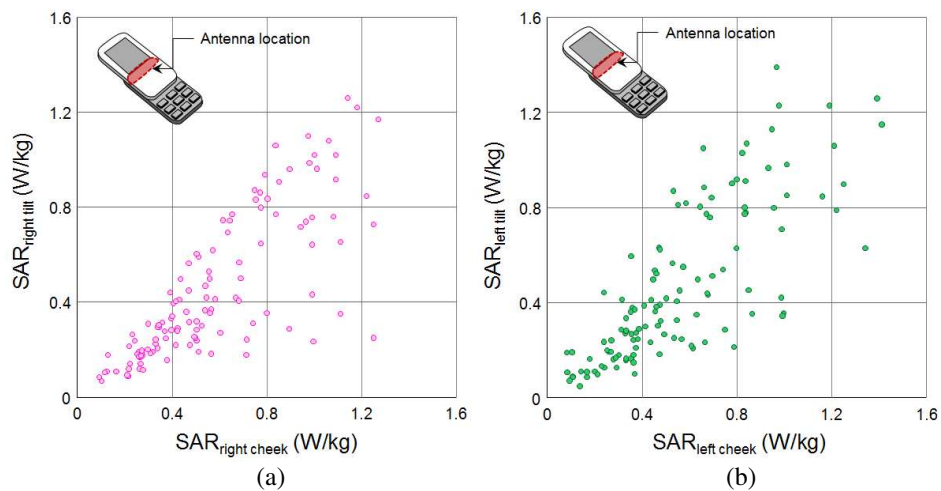


Figure 2: Scatter plot between SAR values measured in the SAM phantom under the cheek and tilt positions for the opened slider-type of commercial phone models. (a) Right side. (b) Left side.

median value of the maximum SAR (1- or 10 g-averaged spatial peak SAR) for the same type of phones [4]. The SAR factor of a specific phone using the SAR test data is proposed in the following section.

3. SAR FACTOR OF A SPECIFIC PHONE MODEL

The SAR test report of a specific phone model reported by a study subject is used to reduce the gap between the commercial model and its representative model. The spatial peak 1-g SAR in the SAM phantom had been already calculated under the four test positions for the numerical phone design. A numerical phone model had been so designed that the spatial peak 1-g SAR at each position becomes the average value of the same type of commercial phone models. Then an SAR ratio, averaged for the four positions of a representative phone model to a given commercial phone model, which is hereafter referred to as SAR factor. Fig. 3 represents the procedure to extract the SAR factor of a specific commercial phone model and apply it to the SAR data in an anatomical head model.

Subjects participating in an epidemiological study report commercial phone models which they have/had used. Assume that one of their phones is given as A-xxxx, a flip-type model with the antenna at the bottom, the SAR factor is obtained as follows.

The SAR test report of A-xxxx provides the spatial peak 1-g SAR values under the four positions, respectively; [SAR_{A-xxxx_LC}], [SAR_{A-xxxx_RC}], [SAR_{A-xxxx_LT}], and [SAR_{A-xxxx_RT}]. The

Table 1: Statistical SAR data of commercial phone models.

Phone type		Frequency	Cheek position				Tilt position			
			Left		Right		Left		Right	
Shape	Antenna		Mean	SD	Mean	SD	Mean	SD	Mean	SD
Bar	Bottom	CDMA PCS, WCDMA	0.683	0.281	0.642	0.291	0.348	0.200	0.341	0.189
Slider_c*	Top	CDMA Cellular	0.549	0.282	0.548	0.282	0.409	0.220	0.389	0.192
Slider_o*	Top	CDMA Cellular	0.570	0.295	0.572	0.298	0.300	0.204	0.289	0.183
Flip	External	CDMA PCS	0.788	0.253	0.811	0.259	0.206	0.182	0.186	0.150

*‘c’ and ‘o’ indicate closed and open states of a slider-type of phone, respectively.

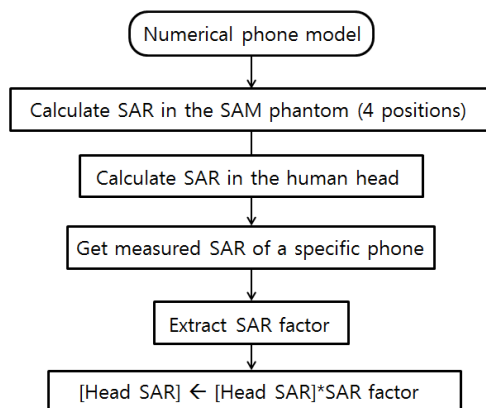


Figure 3: SAR factor.

subscripts, ‘LC’, ‘RC’, ‘LT’, and ‘RT’ indicate left cheek, right cheek, left tilt, and right tilt positions against the SAM phantom, respectively. Meanwhile, M6H is a numerical phone model, representative of flip-type phones with the antenna at the bottom. Its calculated spatial-peak 1-g SAR values in the SAM phantom are $[SAR_{M6H_{LC}}]$, $[SAR_{M6H_{RC}}]$, $[SAR_{M6H_{LT}}]$, and $[SAR_{M6H_{RT}}]$.

Since positive SAR correlations were identified between the right and left sides as well as the tilt and cheek positions, the SAR factor relating the SAR of a specific commercial phone model with that of the corresponding numerical model is written as (1).

$$\text{SAR factor} = \left\{ \frac{[SAR_{A-xxxx_{LC}}]}{[SAR_{M6H_{LC}}]} + \frac{[SAR_{A-xxxx_{RC}}]}{[SAR_{M6H_{RC}}]} \right. \\ \left. + \frac{[SAR_{A-xxxx_{LT}}]}{[SAR_{M6H_{LT}}]} + \frac{[SAR_{A-xxxx_{RT}}]}{[SAR_{M6H_{RT}}]} \right\} / 4 \quad (1)$$

The Equation (1) can be applied to other types of phones but there is one exception to it. Some slider type of phone models can answer a phone call at its closed state. SAR compliance test had to be performed at both open and closed states of the slider and the SAR test results are given in the corresponding test report. This type of models cover about 60–80% of total slider models and the percentage was a little different according to frequency band and antenna location. These phone models mostly allow two methods to answer a call: ① tap the call button at the closed state and ② push up the slider. Because a user has to push up the slider to make a call, about 25% chance to use the phone at the closed state can be assumed if incoming and outgoing call times are equal. Therefore, the average SAR distribution in the user’s head for this type of slider phone model is

obtained using the following SAR factor.

$$\text{SAR factor} = \left\{ \begin{array}{l} \frac{[\text{SAR}_{\text{B-xxxx.LC.closed}}]}{[\text{SAR}_{\text{M3L.LC}}]} + \frac{[\text{SAR}_{\text{B-xxxx.RC.closed}}]}{[\text{SAR}_{\text{M3L.RC}}]} \\ + \frac{[\text{SAR}_{\text{B-xxxx.LT.closed}}]}{[\text{SAR}_{\text{M3L.LT}}]} + \frac{[\text{SAR}_{\text{B-xxxx.RT.closed}}]}{[\text{SAR}_{\text{M3L.RT}}]} \end{array} \right\} / 4 \times 0.25$$

$$+ \left\{ \begin{array}{l} \frac{[\text{SAR}_{\text{B-xxxx.LC.open}}]}{[\text{SAR}_{\text{M5L.LC}}]} + \frac{[\text{SAR}_{\text{B-xxxx.RC.open}}]}{[\text{SAR}_{\text{M5L.RC}}]} \\ + \frac{[\text{SAR}_{\text{B-xxxx.LT.open}}]}{[\text{SAR}_{\text{M5L.LT}}]} + \frac{[\text{SAR}_{\text{B-xxxx.RT.open}}]}{[\text{SAR}_{\text{M5L.RT}}]} \end{array} \right\} / 4 \times 0.75 \quad (2)$$

where, $[\text{SAR}_{\text{B-xxxx.LC.closed}}]$ represents the spatial peak 1-g SAR value in the SAM phantom at the closed state of a slider-type of phone model, B-xxxx under the left cheek position. The specific phone model can answer a phone call at the closed state has an internal antenna at top. The corresponding numerical phone model is M3L, a closed shape of slider phone. Similarly $[\text{SAR}_{\text{B-xxxx.LC.open}}]$ is for the open state of the same phone model, under the left cheek position and the subscript M5L indicates the numerical phone model of an open shape of slider phone.

4. CONCLUSIONS

Accurate and reliable dosimetry and exposure assessment are key requirements of scientific studies on health effects of electromagnetic fields. However, there are many limitations on the estimation of cumulative exposure for radiated electromagnetic field from a series of mobile phones that a study subject had/has used from the past. One of them is that we cannot numerically implement every specific phone model for SAR calculation in the human head.

Therefore, commercial phone models were classified into 11 groups according to frequency band, outer shape, antenna type and location and a numerical phone model representative of each group was developed in the previous study. In this paper, we proposed the SAR factor of a specific commercial phone which is obtained from the spatial-peak 1-g SAR data in the SAR test report. The SAR factor relates numerically calculated SAR in the anatomical head model with the measured result in the SAM phantom for a specific commercial phone. It would work to reduce the SAR gap between a real specific phone and the corresponding numerical model.

ACKNOWLEDGMENT

This work was supported by the IT R&D program of MSIP/IITP. [B0138-15-1002, Study on the EMF exposure control in smart society]. The authors thank the officials of Samsung Electronics Co., Ltd. and LG Electronics Inc. for allowing the data use of the SAR compliance test reports in this analysis.

REFERENCES

1. *IEEE Standard for Safety Levels with Respect to Human Exposure to Radio Frequency Electromagnetic Fields, 3 kHz to 300 GHz*, IEEE Standard C95.1, 1999.
2. *Human Exposure to Radio Frequency Fields From Hand-Held and Body-Mounted Wireless Communication Devices-Human Models, Instrumentation, and Procedures, Part 1: Procedure to Determine the Specific Absorption Rate (SAR) for Hand-Held Devices Used in Close Proximity to the Ear (Frequency Range of 300 MHz to 3 GHz)*, International Electrotechnical Committee, Geneva, Switzerland, IEC 62209-1, Feb. 2005.
3. Lee, A.-K., et al., "Design of representative mobile phone models for epidemiological studies," *ETRI Journal*, submitted.
4. Cardis, E., et al., "Estimation of RF energy absorbed in the brain from mobile phones in the Interphone study," *Occup. Environ. Med.*, Vol. 68, No. 9, 686–693, Sep. 2011.

Parameter Identification of PMSM Nonlinear Part

I. Vesely^{1,2}

¹Department of Control and Instrumentation, FEEC
 Brno University of Technology, Technicka 12, Brno, Czech Republic
²Centre for Research and Utilization of Renewable Energy, FEEC
 Brno University of Technology, Technicka 12, Brno, Czech Republic

Abstract— The paper describes the identification of quadrature inductances of permanent magnet synchronous motor. The identification is based on the principle of Hammerstein model.

The electrical diagram of permanent magnet synchronous motor could be divided into two parts. First one is the static nonlinearity and the second one is the linear dynamics. The identification of quadrature inductance from nonlinear part is discussed in this paper. Only inputs and outputs can be read, when the Hammerstein model is used. Since the hessian of loss function cannot be created, the calculation is divided into two parts and the variables are computed or estimated. Because only nonlinear part is used, the outputs of this part must be calculated from system outputs. The identification is carried out on the nonlinear part by Newton method.

1. INTRODUCTION

Nowadays, permanent magnet synchronous motors are widely used in many industrial applications as well as in domestic electrical appliances. These motors are developed at the same time with more efficient control. Therefore there is a growing need to know the exact parameters of motors. The more the parameters are accurate, the more effective control can be reached. There is the question: how could these parameters be identified? There are many types of identification methods. Some of them are offline methods, that are generally based on a specific input signal and subsequent evaluation of the output [1]. Other types of identification methods are online methods. These methods obtain parameter values with the motor running and working on different principles [2, 3]. One of these methods is the injecting signal to the control signal and subsequent measurement of changes in the output [4]. Or the input and output signals are evaluated (voltage, output current, and sometime speed) and the required parameters are calculated or predictively received from them [5].

Often some systems contain nonlinear part and a linear part. Depending on the order of these parts, systems can be divided into several types. The most famous systems are Wiener model [6–8] and Hammerstein model [9–11]. In Wiener model, linear dynamics is the first part and static nonlinearity is the second part. In Hammerstein model the order is reversed. In some cases the system contains more linear and nonlinear parts, and consequently the above-mentioned models are combined [12].

In our case, the aim is the identification of the permanent magnet out-runner motor inductances. The following paper describes an inductance identification based on Hammerstein model using Gauss-Newton method.

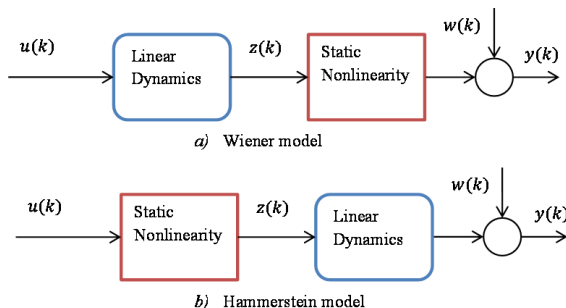


Figure 1: Wiener and Hammerstein model.

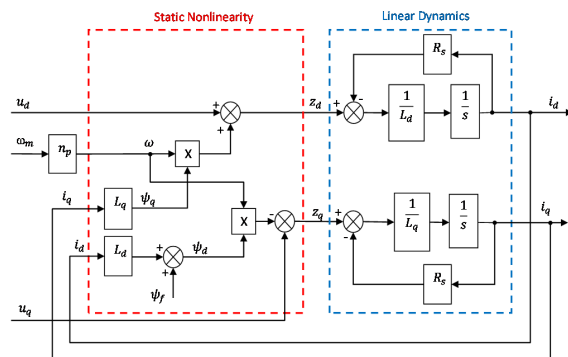


Figure 2: Wiener and Hammerstein model.

2. DISCRIPTION OF THE SYSTEM

As we can see on Figure 2. the motor model can be divided into two Hammerstein models and both models include identified inductance L_d and L_q . For greater clarity, the model was divided into Hammerstein model containing variable z_d and Hammerstein model containing variable z_q . Variables are located between linear and nonlinear part of the model and indexes of these variables are derived from the voltages that are applied to the inputs of these models. From this follows that the output of nonlinear part must be equal to the input of linear part and this equality is used for creation of loss function (Equations (4)–(5)).

Many gradient methods are suitable for identification of nonlinear system. In our case the Newton method is used [13].

In Newton method the direction matrix is calculated from the inverse of the Hessian H_{k-1}^{-1} of the loss function at the point θ_{k-1} .

$$\theta_k = \theta_{k-1} - H_{k-1}^{-1} J'_{k-1} f_{k-1} \tag{1}$$

where:

$$J = \left(\begin{array}{cccc} \frac{\partial f}{\partial \theta(1)} & \frac{\partial f}{\partial \theta(2)} & \cdots & \frac{\partial f}{\partial \theta(n)} \end{array} \right)' \tag{2}$$

$$H = \left(\begin{array}{cccc} \frac{\partial J(\theta)}{\partial \theta(1) \partial \theta(1)} & \frac{\partial J(\theta)}{\partial \theta(1) \partial \theta(2)} & \cdots & \frac{\partial J(\theta)}{\partial \theta(1) \partial \theta(n)} \\ \frac{\partial J(\theta)}{\partial \theta(2) \partial \theta(1)} & \frac{\partial J(\theta)}{\partial \theta(2) \partial \theta(2)} & \cdots & \frac{\partial J(\theta)}{\partial \theta(2) \partial \theta(n)} \\ \vdots & \vdots & \ddots & \vdots \\ \frac{\partial J(\theta)}{\partial \theta(n) \partial \theta(1)} & \frac{\partial J(\theta)}{\partial \theta(n) \partial \theta(2)} & \cdots & \frac{\partial J(\theta)}{\partial \theta(n) \partial \theta(n)} \end{array} \right) \tag{3}$$

Therefore, for Newton method all the second derivatives of the loss function, either analytical or estimated by finite difference techniques, must be found. In classical Newton method is the step size η_{k-1} set to 1. It is the optimum choice for the linear optimization problem, where the optimum should be achieved after one iteration. This follows directly from the second-order Taylor series expansion of loss function. But the nonlinear identification cannot be achieved in one iteration. Then the constant step size 1 can be either too small or too large relative to non-quadratic surface of the loss function. In our case it is set to 1000.

The problem of Newton method is that it reduces the value of the loss function only for positive definite Hessian H_{k-1}^{-1} . The fundamental importance of Newton method is based on the fact that the speed of convergence is of the second order if H_{k-1} is positive definite. This is the highest speed commonly occurring in a nonlinear identification. Disadvantages of Newton method are therefore connected with the second-order derivatives and the strong computing power needed for the calculation of the Hessian [13].

Loss functions are then as follows:

$$f1 = (-L_d \dot{i}_d(k) + L_d \dot{i}_d(k-1) - R_s T_{vz} \dot{i}_d(k-1) + L_q T_{vz} \omega(k-1) i_q(k-1) + T_{vz} u_d(k-1))^2 \tag{4}$$

$$f2 = (-L_q \dot{i}_q(k) + L_q \dot{i}_q(k-1) - R_s T_{vz} \dot{i}_q(k-1) - L_d T_{vz} \omega(k-1) i_d(k-1) + T_{vz} u_q(k-1) - \Psi_f T_{vz} \omega(k-1))^2 \tag{5}$$

However, the inverse matrix of Hessian cannot be created for these loss functions. Therefore loss function is modified. The modification lies in the fact that one part of system is always calculated from previous values and second part is identified (Figure 3).

In our case, only nonlinear part is identified and the linear part is calculated. Then calculated values z_d and z_q are constituted to loss function. This greatly simplifies the loss function and only one variable is then identified in each model.

$$z_d(k-1) = R_s \dot{i}_d(k-1) + L_d \frac{\dot{i}_d(k) - \dot{i}_d(k-1)}{T_{vz}} \tag{6}$$

$$z_q(k-1) = R_s \dot{i}_q(k-1) + L_q \frac{\dot{i}_q(k) - \dot{i}_q(k-1)}{T_{vz}} \tag{7}$$

$$f1 = (L_q T_{vz} \omega(k-1) i_q(k-1) + T_{vz} u_d(k-1) - z_d(k-1))^2 \tag{8}$$

$$f2 = (-L_d T_{vz} \omega(k-1) i_d(k-1) + T_{vz} u_q(k-1) - \Psi_f T_{vz} \omega(k-1) - z_q(k-1))^2 \tag{9}$$

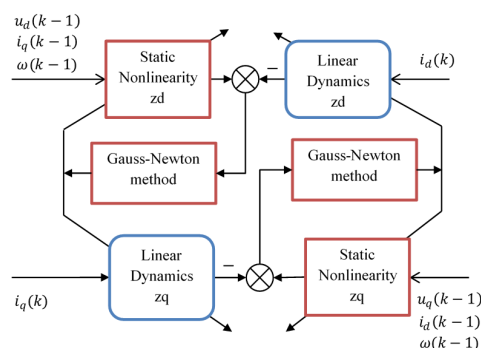


Figure 3: Wiener and Hammerstein model.

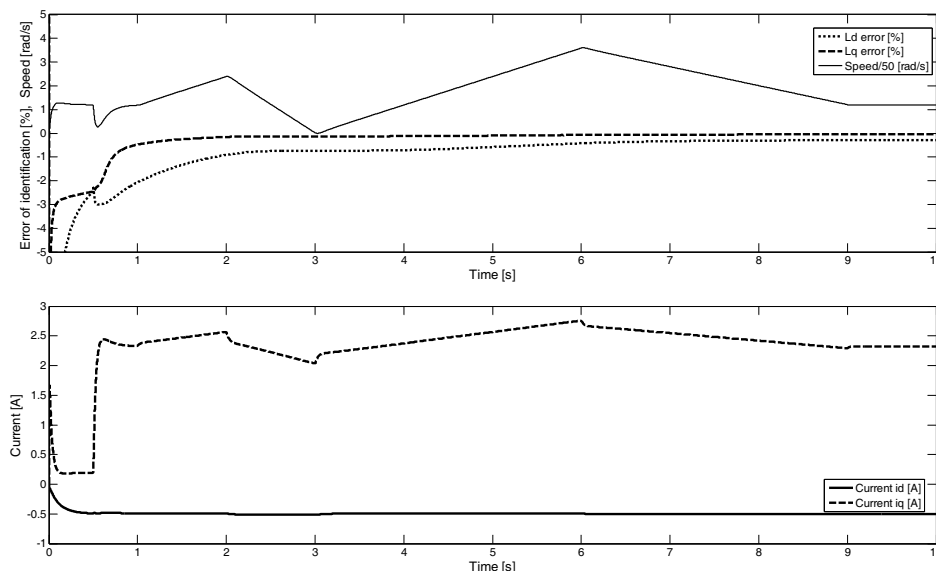


Figure 4: Error of identification.

3. CONCLUSIONS

The paper describes the permanent magnet synchronous motor as two Hammerstein models. The model contains two parts, linear dynamics and nonlinear static. The identification results from the fact that this model can be easily separated so that the output of nonlinear part is the input of linear part. Newton computational algorithm was chosen as suitable for identifying nonlinear system. After creating the loss function we found that the reverse matrix of Hessian cannot be created and the identification had to be modified. The algorithm identifies only nonlinear part and the output of this section is calculated from the output of linear part and the variables from previous identification. It is possible to identify the system with this modification. Furthermore we can greatly reduce the computational demands because Hessian is eliminated to one value. As shown in the graph chart, the method gives very good results with an error of up to 3 percent in simulations.

ACKNOWLEDGMENT

This research work has been carried out in the Centre for Research and Utilization of Renewable Energy (CVVOZE). Authors gratefully acknowledge financial support from the Ministry of Education, Youth and Sports of the Czech Republic under NPU I program (project No. LO1210).

REFERENCES

1. Vesely, I. and D. Zámečník, "A noise robust IFA identification method and their implementation at DSC," *In 10th IFAC Workshop on Programmable Devices and Embedded Systems PDeS 2010*, 201–206, 2010.

2. Khov, M., J. Regnier, and J. Faucher, "On-line parameter estimation of PMSM in open loop and closed loop," *2009 IEEE International Conference on Industrial Technology*, 1–6, 2009.
3. Briz, F. and M. Degner, "Rotor position estimation," *IEEE Ind. Electron. Mag.*, Vol. 5, No. 2, 24–36, June 2011.
4. Vesely, I., M. Sir, and D. Zamecnik, "Simplification of improved frequency analysis for on-line identification," *IEEE 16th International Conference on Intelligent Engineering Systems, Proceedings*, 185–189, 2012.
5. Underwood, S. J. and I. Husain, "Online parameter estimation and adaptive control of permanent-magnet synchronous machines," *IEEE Trans. Ind. Electron.*, Vol. 57, No. 7, 2435–2443, 2010.
6. Nowak, R. D., "Nonlinear system identification," *Circuits, Syst. Signal Process.*, Vol. 21, No. 1, 109–122, January 2002.
7. Peng, J. and R. Dubay, "Identification and adaptive neural network control of a DC motor system with dead-zone characteristics," *ISA Trans.*, Vol. 50, No. 4, 588–98, October 2011.
8. Vörös, J., "Parameter identification of Wiener systems with multisegment piecewise-linear nonlinearities," *Syst. Control Lett.*, Vol. 56, No. 2, 99–105, February 2007.
9. Liu, J., W. Xu, and J. Sun, "Nonlinear system identification of hammerstien and wiener model using swarm intelligence," *2006 IEEE International Conference on Information Acquisition*, 1219–1223, 2006.
10. Alonge, F., F. D'Ippolito, F. M. Raimondi, and S. Tumminaro, "Identification of nonlinear systems described by Hammerstein models," *42nd IEEE International Conference on Decision and Control (IEEE Cat. No.03CH37475)*, 3990–3995, December 2003.
11. Wang, F. and X. Xu, "Research on identification algorithm of Hammerstein model," *2010 IEEE Fifth International Conference on Bio-Inspired Computing: Theories and Applications (BIC-TA)*, 80–85, 2010.
12. Boutayeb, H. and M. Darouach, "Recursive identification method for MISO Wiener-Hammerstein model," *IEEE Trans. Automat. Contr.*, Vol. 40, No. 2, 287–291, 1995.
13. Nelles, O., "Nonlinear system identification," *Measurement Science and Technology*, Vol. 13, 46, 2002.

Simulation of Circulation Module

F. Solc^{1,2}, I. Vesely^{1,2}, and F. Zezulka^{1,2}

¹Department of Control and Instrumentation, FEEC
Brno University of Technology, Technicka 12, Brno, Czech Republic

²Centre for Research and Utilization of Renewable Energy, FEEC
Brno University of Technology, Technicka 12, Brno, Czech Republic

Abstract— Presented paper offers a description of a lung nutrient circulation model and its regulation. This circuit is currently being developed and it is a part of a project dealing with the transportation of lungs. Lung tissue is very sensitive and it loses its quality in a few hours without nutrition. When lungs are being transported, the transportation time has to be short, otherwise nutritional system must be used. In that case there are two conditions that must be complied. Firstly we need to keep the lung in a required temperature. The second condition is to keep the required pressure. The whole system was expressed by equations and modeled in Matlab Simulink for a better control design of the real model.

1. INTRODUCTION

Circulation module is designed for nutrition of lungs during transport [1]. The organs that are meant to be used for transplantation or ex-vivo experiments [2] must be handled with care during transportation, so as to avoid irreversible damage that would disable transplant [3]. Lungs have to be transported with the same caution even if they are used only for experiments [4, 5]. Currently, circulation modules for longer vitality of organs are being developed, which means that the time of transporting can be longer. These circulation modules must match certain requirements. In our case, these requirements are a constant flow and a constant temperature of the liquid.

The controlled system consists of several parts. The most important one of them is the reservoir where the nutrient fluid is stored and heated. From this reservoir a liquid is piped in tubes through the pump into the lungs and consequently back into the reservoir. The flow intensity of the nutritional liquid is determined by the speed of the pump that ensures a constant liquid flow in the lung. The circuit includes a feedback control, and several temperature sensors for providing a constant fluid temperature (Fig. 1). Detailed description of the entire system is described in [6].

The article discusses the equations used for creation of the model and the created model itself. Various verification tests of sensors of this model are carried out. The proposed controller performs temperature control in specific limits.

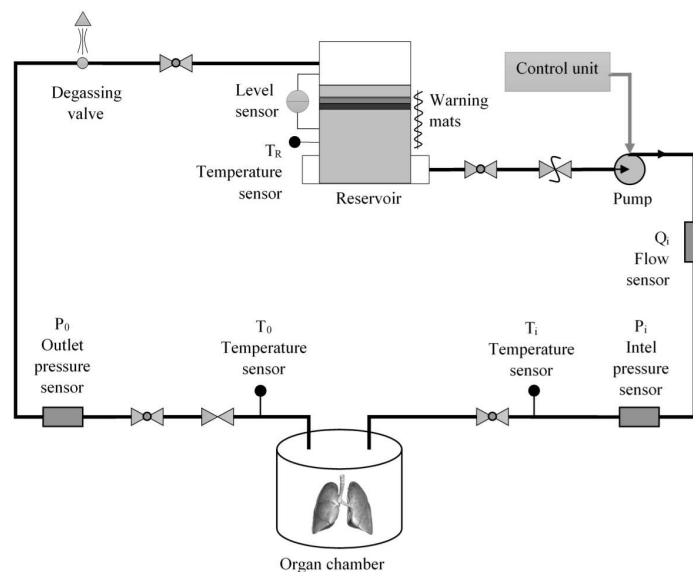


Figure 1: Principal scheme of the thermal model.

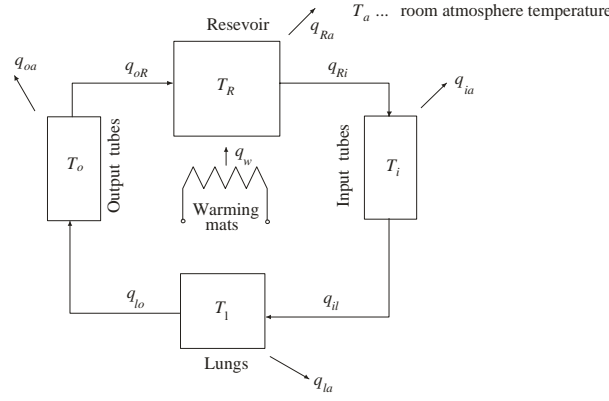


Figure 2: Principle scheme of the thermal model.

2. MATHEMATICAL MODEL OF THE THORACIC BOX

We suppose that the thermal part of the MCM can be described as a system of vessels shown on Fig. 2 [6].

The temperature of nutritional fluid in the lung must be constant. This temperature is changing due to different temperature of external atmosphere in different parts of the system. The liquid transfers the heat through the pipes into the lungs. Then it is piped back to the reservoir where it is being warmed.

Heat transfer is characterized by heat flux q . The following equations characterize heat transfer

$$cm_R \frac{dT_R}{dt} = q_w + c\rho Q (T_o - T_R) - \left(\frac{T_R - T_a}{R_R} \right) \quad (1)$$

$$cm_i \frac{dT_i}{dt} = c\rho Q (T_R - T_i) - \left(\frac{T_i - T_a}{R_i} \right) \quad (2)$$

$$cm_l \frac{dT_l}{dt} = c\rho Q (T_i - T_l) - \left(\frac{T_l - T_a}{R_l} \right) \quad (3)$$

$$cm_o \frac{dT_o}{dt} = c\rho Q (T_l - T_o) - \left(\frac{T_o - T_a}{R_o} \right) \quad (4)$$

where we denote c is a specific heat capacity of the perfusion liquid [$\text{Jkg}^{-1}\text{K}^{-1}$], q is the heat flux [W], m is the mass of nutrition liquid in the specific vessel [kg], ρ is the density of perfusion liquid [kgm^{-3}], Q is the volumetric flow of perfusion liquid [m^3s^{-1}], T is the temperature [K], R is the thermal wall resistance of the specific vessel [KW^{-1}]

Equations (1)–(4) can be rewritten into state variable form

$$\frac{dT_R}{dt} = \left(\frac{\rho Q}{m_R} + \frac{1}{cm_R R_R} \right) T_R + \frac{\rho Q}{m_R} T_o + \frac{1}{cm_R R_R} T_a + q_w \quad (5)$$

$$\frac{dT_i}{dt} = \left(\frac{\rho Q}{m_i} + \frac{1}{cm_i R_i} \right) T_i + \frac{\rho Q}{m_i} T_R + \frac{1}{cm_i R_i} T_a \quad (6)$$

$$\frac{dT_l}{dt} = \left(\frac{\rho Q}{m_l} + \frac{1}{cm_l R_l} \right) T_l + \frac{\rho Q}{m_l} T_i + \frac{1}{cm_l R_l} T_a \quad (7)$$

$$\frac{dT_o}{dt} = \left(\frac{\rho Q}{m_o} + \frac{1}{cm_o R_o} \right) T_o + \frac{\rho Q}{m_o} T_l + \frac{1}{cm_o R_o} T_a \quad (8)$$

Input variables: q_w is the control variable heat flux from warming mats, T_a is the disturbance ambient temperature.

Output variables (see Fig. 1): T_R is the temperature inside the reservoir (measured), T_i is the temperature in the input tubing (measured), T_l is the temperature inside the lungs (not measured), T_o is the temperature in the output tubing (measured).

Equations (5)–(8) can be written in more compact form

$$\dot{\mathbf{x}} = \mathbf{Ax} + \mathbf{Bu} \quad (9)$$

where

$$\mathbf{x} = [T_R \quad T_i \quad T_l \quad T_o]^T \quad \mathbf{u} = [q_w \quad T_a]^T \tag{10}$$

$$\mathbf{A} = \begin{bmatrix} -\left(\frac{\rho Q}{m_R} + \frac{1}{cm_R R_R}\right) & 0 & 0 & \frac{\rho Q}{m_R} \\ \frac{\rho Q}{m_i} & -\left(\frac{\rho Q}{m_i} + \frac{1}{cm_i R_i}\right) & 0 & 0 \\ 0 & \frac{\rho Q}{m_l} & -\left(\frac{\rho Q}{m_l} + \frac{1}{cm_l R_l}\right) & 0 \\ 0 & 0 & \frac{\rho Q}{m_o} & -\left(\frac{\rho Q}{m_o} + \frac{1}{cm_o R_o}\right) \end{bmatrix} \tag{11}$$

$$\mathbf{B} = \begin{bmatrix} \frac{1}{cm_R} & \frac{1}{cm_R R_R} \\ 0 & \frac{1}{cm_i R_i} \\ 0 & \frac{1}{cm_l R_l} \\ 0 & \frac{1}{cm_o R_o} \end{bmatrix} \tag{12}$$

Matrix form can be used for calculation of equilibrium steady state where $\mathbf{x} = \mathbf{x}_0 = \mathbf{const}$ and $\mathbf{u} = \mathbf{u}_0 = \mathbf{const}$.

$$\mathbf{x}_0 = -\mathbf{A}^{-1}\mathbf{B}\mathbf{u}_0 \tag{13}$$

This is used for the conversion to the required power of heating mats.

E.g., with parameters that are given below with the power of heating mats to be 100 W at ambient temperature 20°C Equation (13) fields steady state temperatures $\mathbf{x} = [23.41 \ 22.65 \ 22.58 \ 22.50]^T$.

3. REALIZATION OF CONTROLLER

The lung should have a constant temperature during transportation. However as mentioned above, thermal losses occur in the circulation module and the nutritional liquid must be heated constantly.

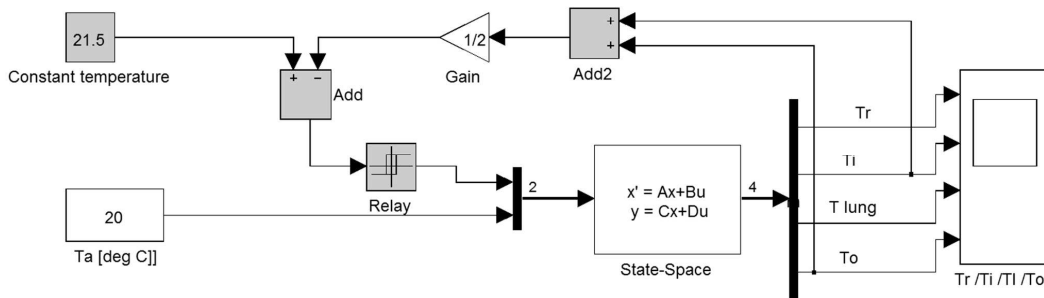


Figure 3: Simulation scheme of the thermal system.

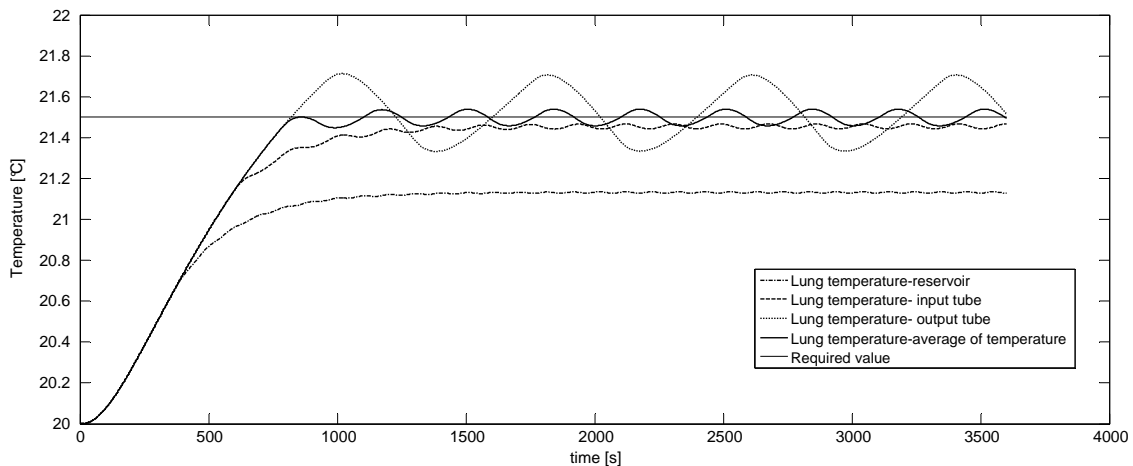


Figure 4: Temperature controls with different places of temperature measurement.

A hysteretic switch on/off with feedback is used for temperature control and data for this controller are used from temperature sensors. Therefore, the system is equipped with several temperature sensors located in the reservoir and in the input and output tubes. The temperature in the lungs is not measured.

The model consisting of the equations described earlier was used for testing various ways of control. The aim of the test was to determine the places where it is necessary to scan the temperature and how many sensors are needed for the control. The temperature of lung was controlled to 21.5°C, the hysteresis was 0.1°C. and four options of control were tested. First one: the temperature is measured in the reservoir. Second one: the temperature is measured in the input tube. Third one: the temperature is measured in the output tube. And the fourth one: the mean value of temperatures in input and output pipes is used as output temperature.

In the Figure 3, we can see the model with the control system, where the temperatures are averaged.

4. CONCLUSIONS

The time of organ transport and possible physiological changes of these organs during transport sometimes complicate the work with this material. Therefore, circulation modules are being developed to improve the transporting process. In our case it is a circulation module for the lung. The problem dealt with in the article was related to heating of the nutritional liquid and to keeping the temperature constant. The simple relay regulator with hysteresis was selected to keep the temperature within certain limits. For a simple control, the circuit is equipped with several temperature sensors which are located in the reservoir and in the tube close to the lung, but no sensor is located in the lung. The model of circulation module was created for controller testing and for the selection of correct sensors combination. As the graph shows measuring of temperature in only one reservoir is insufficient due to thermal losses. The best method is averaging data from the sensor in the tubes in front of and behind the lung.

ACKNOWLEDGMENT

This research work has been carried out in the Centre for Research and Utilization of Renewable Energy (CVVOZE). Authors gratefully acknowledge financial support from the Ministry of Education, Youth and Sports of the Czech Republic under NPU I program (project No. LO1210).

REFERENCES

1. Czech Republic, "Vyhláška č. 339/2012 Sb., kterou se mění vyhláška č. 422/2008 Sb., o stanovení bližších požadavků pro zajištění jakosti a bezpečnosti lidských tkání a buněk určených k použití u člověka," 4250–4255, Sbírka zákonů české republiky, Czech Republic, 2012.
2. Aigner, C., A. Slama, K. Hözenecker, A. Scheed, B. Urbanek, W. Schmid, F. J. Nierscher, G. Lang, and W. Klepetko, "Clinical ex vivo lung perfusion — Pushing the limits," *Am. J. Transplant.*, Vol. 12, 1839–1847, 2012.
3. Valek, J., "Organ transportation conditions sensing," Czech Technical University in Prague, 2014.
4. Wallinder, A., "Ex vivo lung perfusion clinical and experimental studies," University of Gothenburg, Sweden, 2014.
5. Okamoto, T., F. Chen, J. Zhang, T. Yamada, E. Nakayama, H. Morikawa, T. Bando, and H. Date, "Establishment of an ex vivo lung perfusion model using non-heart-beating large pigs," *Transplant. Proc.*, Vol. 42, 1598–1601, 2010.
6. Eschli, A. A., "Design of an extra corporal mobile circulatory module (mCM) for use in pig lungs," Technikum Wien, Vienna, 2013.

Analysis of Light Absorbance on the Effects of Low Frequency Magnetic Fields on Cell Proliferation

M. Sosa¹, T. Cordova-Fraga¹, A. Martinez-Longoria¹, A. Horta-Rangel²,
J. C. Villagomez³, M. Sabanero³, R. Monroy-Torres⁴, and N. Padilla-Raygoza⁵

¹Department of Physical Engineering, University of Guanajuato, Campus Leon, Mexico

²Engineering Division, University of Guanajuato, Campus Guanajuato, Mexico

³Department of Biology, University of Guanajuato, Campus Guanajuato, Mexico

⁴Department of Medicine and Nutrition, University of Guanajuato, Campus Leon, Mexico

⁵Department of Nursing and Obstetrics, University of Guanajuato, Campus Celaya-Salvatierra, Mexico

Abstract— An experiment to measure the effects of low frequency magnetic fields on cell proliferation was performed. Magnetic fields of low amplitudes, ranging from 1 to 4 mT, at frequencies of 60, 100, 800, 1500 and 2450 Hz were used to stimulate cell cultures of yeast *Saccharomyces cerevisiae*. The stimulation was carried out during 5 minutes, with intervals of 5 minutes rest, for 8 hours. A control and an experimental sample were measured two times for each frequency at the beginning of the experiment and at 2, 4, 6 and 8 hours later. In each measurement series a new cell culture was prepared for both non-stimulated and stimulated samples. The cells were grown in a liquid medium composed by 0.3 g yeast extract, 1.0 g gelatin peptone and 2.0 g dextrose for 100 ml solution of growth medium, with pH adjusted to 4.5 with NaOH. Measurements of cell proliferation were based on light absorbance using a Beckman DU-650 spectrophotometer at 600 nm wavelength. A comparison of growth rate showed an increasing of cell proliferation in stimulated cells compared to the non-stimulated ones, with differences from 8% to 16% after 8 hours of exposure, for most of the frequencies employed, except at 60 and 800 Hz, where the control sample showed an increasing larger than the stimulated cultures, particularly at the final of the experiment. For the first hours of the experiments the results are variable, coming to present a clear trend only after 4 hours. In conclusion, the results of this experiment show an influence of magnetic fields on cell evolution, which is a function of both the exposure time and the stimulation frequency.

1. INTRODUCTION

The understanding of the effects of low frequency electromagnetic fields on biological systems is still an open problem. A large number of cell cultures have been studied and reported in the literature. Studies performed using different stimulation parameters, such as intensity of the magnetic field, frequency of the signal and exposition time have been published, with often contradictory results. One biological model widely used in many experiments uses yeast *Saccharomyces cerevisiae*, because of their non-pathogenic nature for human beings, as also the possibility of working at room temperature.

Alterations in gene expression produced by 60 Hz AC magnetic fields on *Saccharomyces cerevisiae* were reported by Binninger and Ungvichian [1]. They found changes in the abundance of messenger RNAs after a continuous exposure to 20 μ T 60 Hz AC electromagnetic fields. Weisbrot [2] measured transcript levels for gene in *Saccharomyces cerevisiae* following exposures to a 60 Hz continuous wave sinusoidal field at various field strengths and exposure times. Moreover, proliferation response of yeast *saccharomyces cerevisiae* on electromagnetic field has been studied by several researchers [3–5], employing 50 and 60 Hz magnetic fields, with somewhat contradictory results. More recently Ruiz-Gómez et al. [6] published a new work where they report that a 2.45 mT, sinusoidal 50 Hz magnetic field induces alteration in the growth and survival of *saccharomyces cerevisiae*, but not induce alterations in the cell cycle and does not cause DNA damage.

In the same way, Anton-Leberre and colleagues [7] have published a study of the effects of strong static (up to 16 T) and pulsed (up to 55 T single-shot and 4×20 T repeated shots) magnetic fields on *Saccharomyces cerevisiae* cultures. They examined gene expression, proteome profile, cell viability, morphology, and growth after magnetic field exposure. They found no effects of the magnetic field on these cellular processes.

In this paper a study conducted on cell cultures of yeast *Saccharomyces cerevisiae* using magnetic fields of low amplitudes, ranging from 1 to 4 mT, at frequencies of 60, 100, 800, 1500 and 2450 Hz is reported.

2. MATERIAL AND METHODS

Cell cultures were grown in an YPD medium composed by 0.3 g yeast extract, 1.0 g gelatin peptone and 2.0 g dextrose for 100 ml solution of growth medium. The pH was adjusted to 4.5 with NaOH. In each experiment were inoculated 100 μ l of *Saccharomyces cerevisiae* culture in 1.2 ml YPD medium. The culture was grown at 28°C.

A Rodin coil system was assembled with two identical coils 2.2 cm diameter and 21 turns, arranged in series, with a total electrical resistance $R = 6.83 \Omega$.

The samples were placed in vials and stimulated during 8 hours at intervals of 5 minutes exposition and 5 minutes rest. Frequencies of 60, 100, 800, 1500 and 2450 Hz were used for stimulation.

To determine the cell proliferation the light absorbance of cell cultures was measured every 2 hours with a Beckman DU-650 spectrophotometer (American Laboratory Trading, Inc., San Diego, CA, USA) at 600 nm wavelengths. Each measurement was repeated 12 times in order to estimate the uncertainty.

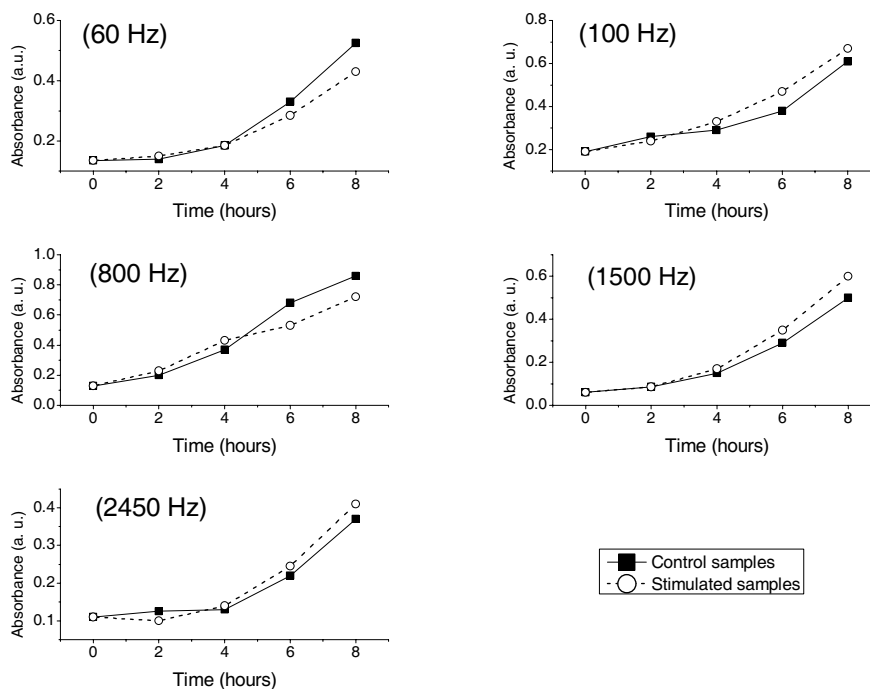


Figure 1: Growth rates for five stimulated samples at different frequencies and their comparison with the control ones.

3. RESULTS AND DISCUSSION

A comparison between a control and an experimental sample was performed in order to assess the influence of low frequency magnetic fields on *Saccharomyces cerevisiae* cell proliferation. In Figure 1 are shown the results for measurements performed at frequencies of 60, 100, 800, 1500 and 2450 Hz. In each case five evaluations of cell proliferation were determined at 0, 2, 4, 6 and 8 hours after starting the experiment.

The analysis of curves in Figure 1 show a growth rate increasing in stimulated cells compared to the non-stimulated ones, with differences from 8% to 16% after 8 hours of exposure, when frequencies of 100, 1500 and 2450 Hz were employed. On the contrary, at 60 and 800 Hz the control sample showed an increasing larger than the stimulated cultures, particularly at the final of the experiments. In all cases, for the first hours of the experiments the results were variable, coming to show a clear trend only after 4 hours.

4. CONCLUSIONS

The results of this experiment show an influence of magnetic fields on *Saccharomyces cerevisiae* cell proliferation, which is a function of both the exposure time and the stimulation frequency.

ACKNOWLEDGMENT

This work was partially supported by the University of Guanajuato, under the institutional grants for research projects DAIP 2014.

REFERENCES

1. Binninger, D. and V. Ungvichian, “Effects of 60 Hz AC magnetic fields on gene expression following exposure over multiple cell generation using *Saccharomyces cerevisiae*,” *Bioelectrochem. Bioenerget*, Vol. 43, 83–89, 1997.
2. Weisbrot, D. R., “The effect of low frequency electric and magnetic fields on gene expression in *Saccharomyces cerevisiae*,” *Bioelectrochem. Bioenerget*, Vol. 31, 167–177, 1993.
3. Ruiz-Gómez, M. J., M. I. Prieto-Barcia, E. Ristori-Bogajo, and M. Martínez-Morillo, “Static and 50 Hz magnetic fields of 0.35 and 2.45 mT have no effect on the growth of *Saccharomyces cerevisiae*,” *Bioelectrochemistry*, Vol. 64, 151–155, 2004.
4. Novák, J., L. Strasák, L. Fojt, I. Slaninová, and V. Vetterl, “Effects of low-frequency magnetic fields on the viability of yeast *Saccharomyces cerevisiae*,” *Bioelectrochemistry*, Vol. 70, 115–121, 2007.
5. Ager, D. D. and J. A. Radul, “Effect of 60-Hz magnetic fields on ultraviolet light-induced mutation and mitotic recombination in *Saccharomyces cerevisiae*,” *Mutation Research Letters*, Vol. 283, 279–286, 1992.
6. Ruiz-Gómez, M. J., F. Sendra-Portero, and M. Martínez-Morillo, “Effect of 2.45 mT sinusoidal 50 Hz magnetic field on *Saccharomyces cerevisiae* strains deficient in DNA strand breaks repair,” *International J. of Radiation Biology*, Vol. 86, 602–611, 2010.
7. Anton-Leberre, V., E. Haanappel, N. Marsaud, L. Trouilh, L. Benbadis, H. Boucherie, S. Massou, and J. M. François, “Exposure to high static or pulsed magnetic fields does not affect cellular processes in the yeast *Saccharomyces cerevisiae*,” *Bioelectromagnetics*, Vol. 31, 28–38, 2010.

An Efficiency of Broadcast Mechanisms Based on Cluster Heads in Dependence on Clustering Algorithm Type

Wojciech Bednarczyk, Jerzy Dołowski, and Jarosław Michalak

Faculty of Electronics, Military University of Technology

Gen. S. Kaliskiego 2 Str., Warsaw 00-908, Poland

Abstract— Efficiency of broadcast transmission based on Cluster Heads (CH) in clustered wireless network in dependence on clustering algorithm type has been assessed in this paper. Broadcast Communications on the basis of Gateways (GW-BC) and on the basis of Cluster Heads (CH-MPR-BC) and three types of clustering algorithms (LNIDE, HDg and WCL) were implemented and tested. Tests have been done for static network assuming Free Space Path Loss propagation model with assumed reliability of information delivery in radio link. It was shown that for clustered network, CH-MPR-BC can be reliable and effective energetically.

1. INTRODUCTION

The broadcast communication as transmission from one point to all others is a very popular type of transmission used in wireless systems for route discovering, topology dissemination, alarm notification, location update, multicast tree building etc. Technical solution is dependent on a scenario and a network topology.

When clustered network is considered, one should decide whether broadcast communication is limited to one cluster or transmission to the whole network is needed. On the other hand, certain constraints can be associated with transmission time and different system layers are involved (usually the MAC (Medium Access Control) sub-layer and/or the Network Layer).

2. RELATED WORKS

There are many proposals of achieving Broadcast Communication (BC) in the literature. Our special interest is focused on solutions related to Ad-hoc and clustered networks [1, 2].

Many studies are focused on the problem of efficient broadcasts. A lot of proposed protocols are based on Connected Dominating Sets (CDS) such as [3], or multipoint relays (MPRs), e.g., [4].

The BC algorithms described in [5–8] utilize neighbourhood and/or previous routing information to reduce redundant packets.

When radio energy is discussed, the problem can be connected with electromagnetic compatibility of military equipment [9, 10].

Energy efficient and time constrained broadcast protocols are other groups of possibilities [1, 11, 12].

An efficiency of BC can be obviously different when different clustering algorithms are used. Different clustering algorithms can be applied in dependence of system type. For mobile Ad-Hoc networks following groups of algorithms with different characteristics can be identified [13]: DS-based clustering, Low-maintenance clustering, Energy-efficient clustering, Load-balancing clustering and Combined-metrics-based clustering.

A relatively wide set of clustering algorithms for Vehicular Ad-Hoc networks was presented in [14].

A reader can find various Cluster Head election algorithms for MANETs which can be divided generally on Identifier-based clustering group, Connectivity based group, Mobility-aware group, Power-aware group and Combined weight based group [15]. Other clustering schemes and classifications of can be find, e.g., in [16, 17].

3. BROADCAST MECHANISMS ON THE BASIS OF CLUSTERED NETWORK

We assumed a clustered network with 2-levels of hierarchy (Figure 1). The clustering procedure should assure the information about a system structure and the role of nodes.

We can distinguish 3 types of functional nodes: Cluster Head (CH), Gateway (GW) and Regular Node (RN).

The broadcast protocol can use a subset of nodes, called GW set to relay packets to all nodes in the network. In such a solution, a non-CH node relays the broadcast packet if it is selected as a GW, otherwise it does nothing. If there is at least one route among all the clusters (via GWs),

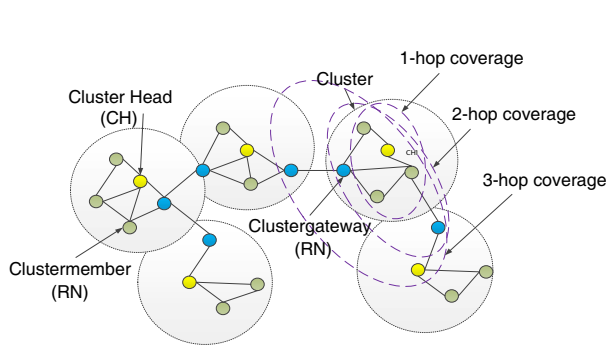


Figure 1: Clustered network.

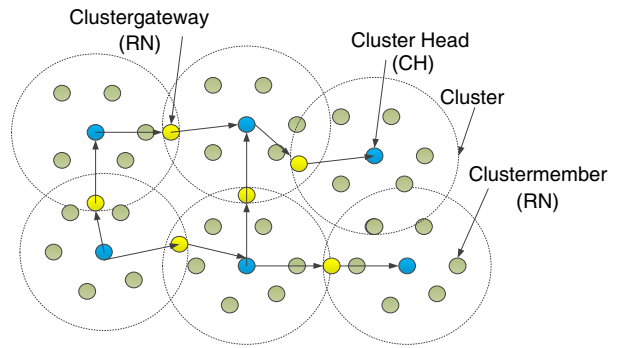


Figure 2: GW based BC (GW-BC).

a broadcast packet can be eventually delivered to the entire network. The broadcast process is limited only to the CHs and the GWs so that the broadcast redundancy is reduced.

The GW-BC process can be described as follows. A source node initiates a broadcast process, than:

1. If the source is not a CH, it sends the packet to its CH.
2. When a CH receives the packet for the first time, it chooses its GW set to forward the packet to all its neighboring CHs. If the received packet is a duplicated one, the CH does nothing.
3. When GW node receives the broadcast packet for the first time, it relays the packet (Figure 2).

The CH-MPR-BC is based on an assumption (used usually with GW-BC as well) that in one cluster (controlled by one CH) each radio can communicate with any other radio directly (peer to peer, they are in radio distance). Therefore, according to typical clustering algorithm and assumed max power of radios within the network, each CH can communicate with at least one adjacent CH [18] (Figure 3). A source node initiates a broadcast process, than:

1. If the source of BC information is not a CH, it sends the packet to its CH.
2. When a CH receives the packet for the first time, it chooses its CH-MPR set to forward the packet to all its neighboring clusters; if the received packet is a duplicated one, the CH does nothing.

4. CLUSTERS FORMATION

The main objective of clustering is to identify suitable node representatives, i.e., Cluster Heads (CHs), to store routing and topology information and maximize clusters stability. The comparison of BC efficiency in dependence of three clustering algorithms were assessed:

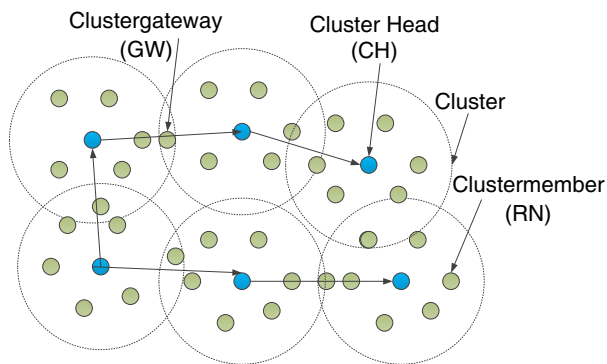


Figure 3: CH-MPR based BC (CH-MPR-BC).

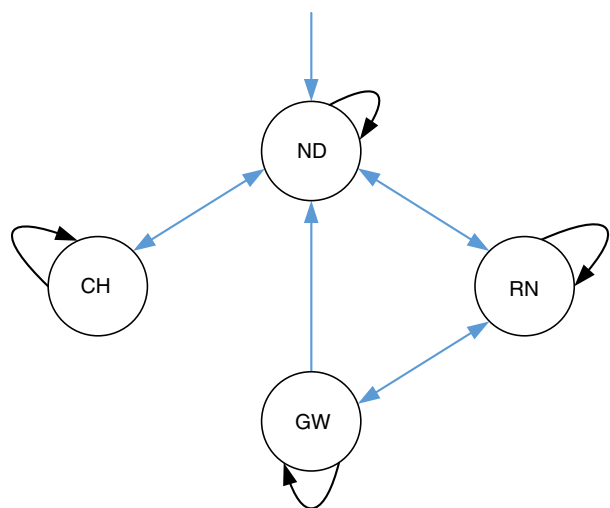


Figure 4: Node state transition diagram.

- LNIDE — own algorithm with CH election on the basis of Lowest ID concept.
- HDg — an algorithm with CH election on the basis of Highest Degree concept.
- WCL — an algorithm with CH election on the basis of weighted fitness measure concept.

As we assumed static network, only cluster formation phase was needed and cluster maintenance procedures were not implemented. Omitting details about each node state changing conditions, CHs are elected based on following criteria:

- For LNIDE (based on LID [19]) — the node can be a CH when it has the lowest MAC address among uncovered ND nodes (a node is uncovered for others when they received assumed number of Hello messages from this node).
- For HDg (based on [15]) — the node can be a CH when in comparison to other uncovered ND nodes it noticed the maximum number of uncovered nodes its vicinity.
- For WCL (based on [15]) — the node can be a CH when in comparison to other uncovered ND nodes it noticed the maximum fitness function value.

For proper deciding about its state, nodes periodically send Hello messages with following information: MAC address, Node State, List of Neighbors (MAC, State, Power), Fitness Value, My CH. In result each node can have all information about all other nodes in 2-hop distance (Figure 1). The node state transition diagram is shown in Figure 4.

5. PERFORMANCE EVALUATION

In order to determine efficiency of BC we used the OMNeT++ [20] simulation environment.

5.1. Experimental setup

The prepared network model consists of fixed number of static radio nodes, ranged from 150 to 300 and located randomly in the square area of 50 km side length. All nodes can send and receive the radio frames with path loss and transmission delay proportional to a mutual distance. The node is able to use the GW-BC or the CH-MPR-BC. The selected node periodically sends a new broadcast message. Other phenomena of transmission has been neglected, in particular, we assumed that there is no interferences nor collisions between signals from nodes. We used the following metrics to assess the efficiency of one BC process:

- *Delivery Time* — a time from first transmission (BC message from an originator node) till the moment when the last node is notified (assuming that all nodes are notified).
- *Consumed Energy* — the total energy used by a network during one completed broadcast process; this energy is calculated as the sum of energy consumed by nodes involved in this broadcast process.
- *Number Of Nodes* — the number of nodes in each state in clusterization period (CH, RN, GW, ND).
- *Nervous Measure* — the number of nodes which are changing their states during assumed period of time (a result is calculated periodically while a clusterization process lasts).

5.2. Experimental Results

Simulation results are shown in Figures 5–8. Clustering algorithms are stable and work properly (Figure 5, Figure 6).

We found that Delivery Time as well as Consumed Energy are generally dependent on clusters size and a type of BC (Figure 7, Figure 8). Assuming the same Signal to Noise power ratio constraints, CH-MPR-BC is always better than classical GW-BC. The CH election criterion can have significant influence on probability of message delivery as it decides on CH location in relation to other nodes but we didn't collect these data assuming that each node has at least one connection with the rest of network. When interference level is discussed, it is known that the level of inter-system interference is proportional to a cluster size, frequency, and the sum of transmitted power. Concluding from differences in energy observed in Figure 7, CH-MPR-BC has definitely the best potential in this area.

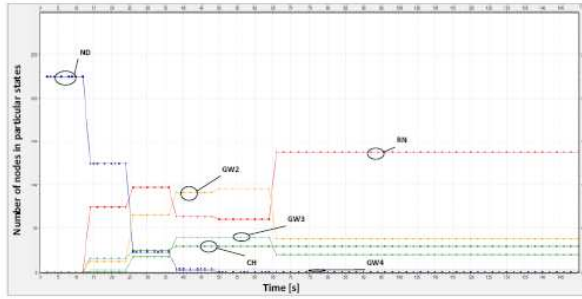


Figure 5: Number of nodes in particular state in function of time.

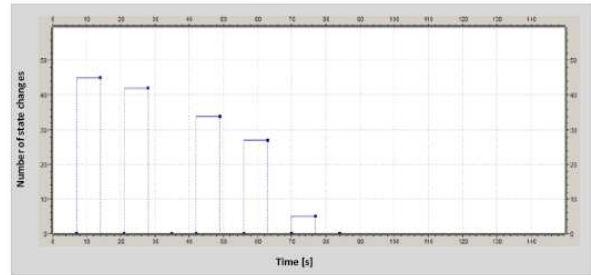


Figure 6: Number of state changes in function of time.

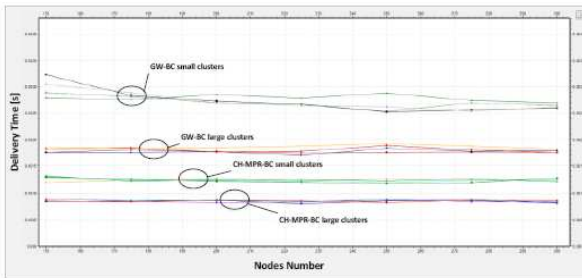


Figure 7: Delivery time in function of nodes number.

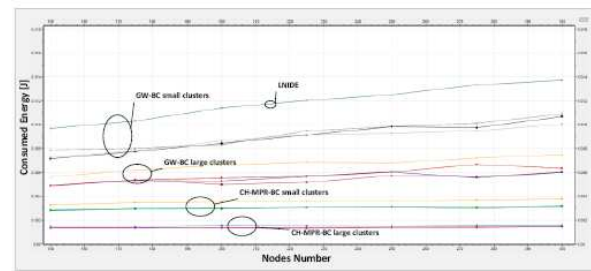


Figure 8: Consumed energy in function of nodes number.

6. CONCLUSION

According to simulation results, CH-MPR-BC is energy and time efficient. Assuming high probability of receive, influence of clustering type on BC process can be neglected. This influence is expected to be important when a signal to noise power ratio is low causing transmission errors and wrong network formation (e.g., disconnected parts of the network). Our studies will be continued for node movement with different propagation conditions.

REFERENCES

1. Zhang, X., T. Kunz, L. Li, and O. Yang, "An energy-efficient broadcast protocol in MANETs," *IEEE Computer Society*, 2010.
2. Song, Y. and J. Xie, "A QoS-based broadcast protocol for multi-hop cognitive radio Ad hoc networks under blind information," *IEEE*, 2011.
3. Wu, J. and F. Dai, "An extended localized algorithm for connected dominating set formation in Ad hoc wireless networks," *IEEE Trans. on Parallel and Distributed System*, Vol. 15, No. 10, Oct. 2004.
4. Adjih, C., T. Clausen, P. Jacquet, A. Laouiti, P. Minet, P. Muhlethaler, A. Qayyum, and L. Viennot, "Optimized link state routing protocol," *RFC 3626, IETF*, Oct. 2003.
5. Lim, H. and C. Kim, "Flooding in wireless ad hoc networks," *Computer Communications Journal*, Vol. 24, No. 3–4, 353–363, 2001.
6. Ni, S., Y. Tseng, Y. Chen, and J. Sheu, "The broadcast storm problem in a mobile Ad hoc network," *Proc. of MOBICOM'99*, 151–162, Aug. 1999.
7. Qayyum, A., L. Viennot, and A. Laouiti, "Multipoint relaying for flooding broadcast message in mobile wireless networks," *Proceedings of the Hawaii International Conference on System Sciences (HICSS'02)*, Big Island, Hawaii, Jan. 2002.
8. Sinha, P., R. Sivakumar, and V. Bharghavan, "Enhancing Ad hoc routing with dynamic virtual infrastructures," *Proc. of INFOCOM'2001*, Vol. 3, 1763–1772, 2001.
9. Nowosielski, L., J. Lopatka, and M. Siłaczuk, "Modelling of electromagnetic wave propagation with the use of the ray-tracing method," *PIERS Proceedings*, 2701–2705, Aug. 25–28, Guangzhou, 2014.
10. Kaszuba, A., R. Checinski, M. Kryk, J. Lopatka, and L. Nowosielski, "Electromagnetically shielded real-time MANET testbed," *PIERS Proceedings*, 2706–2710, Aug. 25–28, Guangzhou, 2014.

11. Cano, J. K. and P. Manzoni, "A low power protocol to broadcast real-time data traffic in a clustered Ad hoc network," *IEEE*, 2001.
12. Wieselthier, J., G. Nguyen, and A. Ephremides, "On the construction of energy-efficient broadcast and multicast trees in wireless networks," *Information Technology Division Naval Research Laboratory*, 2007.
13. Yu, J. Y. and P. H. J. Chong, "A survey of clustering schemes for mobile ad-hoc networks," *IEEE Communications Surveys & Tutorials*, 2005.
14. Vodopivec, S., J. Bešter, and A. Kos, "A survey on clustering algorithms for vehicular Ad-hoc networks," *IEEE*, 2012.
15. Mehta, S., P. Sharma, and K. Kotecha, "A survey on various cluster head election algorithms for MANET," *International Conference on Current Trends in Technology*, 2011.
16. Wei, D. and H. A. Chan, "Clustering Ad hoc networks: Schemes and classifications," *IEEE*, 2006.
17. Akbari, A., M. Soruri, and S. V. Jalali, "Survey of stable clustering for mobile Ad-hoc networks," *IEEE Computer Society*, 2010.
18. Ros, F. J. and P. M. Ruiz, "Cluster-based OLSR extensions to reduce control overhead in mobile Ad hoc networks," *IWCMC'07*, Honolulu, Hawaii, USA, Aug. 12–16, 2007.
19. Konstantopoulos, G. and B. Mamalis, "Lowest-ID with adaptive reassignment: A novel mobile Ad-hoc networks clustering algorithm," *IEEE*, 2006.
20. OMNeT++ discrete event simulation system, <http://www.omnetpp.org>.

Restoration of Antenna Patterns Using Iterative Method

Jinhwan Koh and Fan Fan

Department of Electrical and Electronic Engineering, ERI
Gyeong Sang National University, Jinju, Korea

Abstract— A new approach to reconstructing antenna far-field patterns from the missing part of the pattern is presented in this paper. The antenna far-field pattern can be reconstructed by utilizing the iterative Hilbert transform, which is based on the relationship between the real and imaginary part of the Hilbert transform. A moving average filter is used to reduce the errors in the restored signal as well as the computation load. Under the constraint of the causality of the current source in space, we could successfully reconstruct the data. Several examples dealing with line source antennas and antenna arrays are simulated to illustrate the applicability of this approach.

1. INTRODUCTION

The Hilbert transform is a commonly used technique for relating the real and imaginary parts of a spectral response under causal conditions. It results from application of Cauchy's Residue Theorem in complex variable theory, and can be expressed in both continuous and discrete forms. The conventional reconstruction algorithm involves applying the Hilbert transform to the logarithmic function of the Fourier transform to obtain the unknown component [1]. Similarly, given the phase of a spectrum, it might be desirable to compute the magnitude function [2]. So far, Hilbert transforms have been widely applied in various areas of signal reconstruction, such as image reconstruction, minimum phase signal reconstruction and phase response reconstruction [3–5]. However, as far as the authors known, there have been no studies carried out on signal reconstruction in the missing block of an antenna far-field pattern signal.

In the area of microwaves, it is desired to obtain knowledge of the transient response of a system. It is common to measure both the magnitude and phase of spectral responses using a network analyzer [6–8]. It is important to appreciate that measured patterns are usually not perfectly symmetric and nulls are often partially filled. The real and imaginary parts of a spectral response are not independent of each other. The real part includes all the information of the imaginary part, and the imaginary part also includes all the information of the real part. In other words, both of them constitute the Hilbert transform pair, whose properties can be applied to any causal signal. Since we are dealing with a linear time-invariant (LTI) system, changing the input of the system through a time shift does not change the transfer function of the original system, and the amplitude spectrum is also unchanged. An antenna problem is equivalent to a shift in the spatial coordinates.

In this paper, we take the approach of developing iterative algorithms to reconstruct the loss or distortion of data from the phase of the antenna pattern spectrum, based on the above properties, i.e., the signal's correlation of the real and imaginary parts in the Hilbert transform. The remainder of this paper is organized as follows: the computational method of the iterative Hilbert transform is in Section 2. Section 3 introduces failed signal reconstructing data from the far-field power radiation pattern in the angular domain. Three design examples are given in Section 4, followed by the conclusion in Section 5. Text including equations must be typed single spaced in any of the following font types: Times, Times Roman, Times New Roman or Symbol. Use 10 pt for the text, 12 pt for the headings and 11 pt for subheadings, and 18 pt for the title. The title should be typed in capital letters and centred. The text should be set in two columns that are 8.8 cm wide and justified, and separated by a margin of 0.4 cm.

2. PRINCIPLE OF ITERATIVE HILBERT TRANSFORM

The signal that we consider to be real has a rational frequency response. Since we are interested in conditions under which the signal can be uniquely specified by the phase of its Fourier transform, the signal is assumed to be causal. For such a signal $x(t)$, where $t > 0$, the frequency response in the Fourier transform domain, $X(\omega)$, can be obtained by using the following Fourier transform:

$$X(\omega) = \int_0^t x(t)e^{-j\omega t} dt = \text{Re}(X(\omega)) + j\text{Im}(X(\omega)) \quad (1)$$

Once the real part $\text{Re}(X(\omega))$ and imaginary part $\text{Im}(X(\omega))$ are determined, the relations are verified in the frequency domain using the expressions:

$$\begin{aligned} \text{Re}(X(\omega)) &= \frac{1}{2\pi} \left[j\text{Im}(X(\omega)) * \frac{2}{j\omega} \right] = H[\text{Im}(X(\omega))] \\ \text{Im}[X(\omega)] &= \frac{1}{2\pi} \left[\text{Re}(X(\omega)) * \frac{2}{j\omega} \right] = -H[\text{Re}(X(\omega))] \end{aligned} \quad (2)$$

where $*$ represents the convolution integral, and $H[.]$ is the Hilbert transform. We can note that one can reconstruct the real part of the spectrum from the imaginary part, and vice versa [1].

To restore the missing data one need to follow the steps shown in Fig. 1 where $\hat{\cdot}$ represents estimated data.

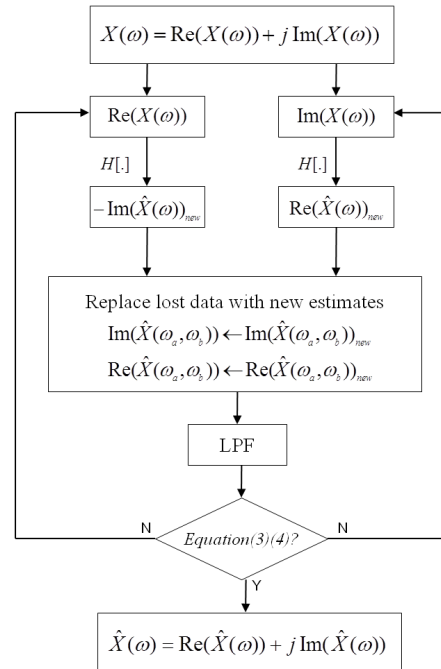


Figure 1: Flow chart of the iterative Hilbert transform.

After a number of iterations, the lost data will be reconstructed. However, there are some errors between the actual pattern and the restored pattern. The restored pattern not only has a high-frequency component but also requires a high computational load. To avoid this situation, a moving average filter is employed. The moving average filter is a linear filter, which is widely used for image enhancement [1, 9] and noise reduction in image processing. By using the MA filter at each recursive step, the fluctuating influence can be filtered out and the characteristics of these systems remain unchanged. In the meantime, the errors rapidly converge to a certain criteria, resulting in the computational load being reduced. The recursive step will not be stopped until (3) and (4) are satisfied, where ε is a small criterion. The average step size $k = 3$ is chosen in the following numerical simulations.

$$|R_c(\omega) - R_p(\omega)| < \varepsilon \quad (3)$$

$$|I_c(\omega) - I_p(\omega)| < \varepsilon \quad (4)$$

where R_c is the real part of the restored data at the current iteration step and R_p is the real part of the restored data at the previous step. The same applies to the imaginary part I_c and I_p .

3. SIGNAL RECONSTRUCTION IN A FAR FIELD PATTERN

The antenna radiation problem consists of solving for the fields that are created by an impressed current distribution J . In order to simplify the solution to solve the two Maxwell's curl equations, we use the potential function. As a result, by having a knowledge of the vector potential A one can

solve the radiation problem. It is best if the radiated electric field of an electromagnetic system is proportional to the Fourier transform of the spatial current distribution on the electromagnetic structure. If we assume a current distribution only existing along the z -axis, centered on the origin and confine the observation point to a fixed φ in the y - z plane ($\varphi = 90^\circ$), then the vector potential can be expressed as [10]:

$$\vec{A}_z = \hat{z} \frac{e^{-j\beta r}}{4\pi r} \int_{z_1}^{z_2} J_z(z) e^{j\beta z \cos \theta} dz = \hat{z} \frac{e^{-j\beta r}}{4\pi r} \int_{z_1}^{z_2} J_z(z) e^{j\beta z u} dz \quad (5)$$

where $\beta = 2\pi/\lambda$, $u = \cos \theta$, and r is the spatial far-field variable and the integral is over the extent of the current source. Then the far-field can be expressed as:

$$\vec{E} = -j\omega A_\theta \hat{\theta} = j\omega \sin \theta \vec{A}_z \hat{\theta} = j\omega \sin \theta \frac{e^{-j\beta r}}{4\pi r} \int_{z_1}^{z_2} J_z(z) e^{j\beta z u} dz \hat{\theta} \quad (6)$$

Equation (5) indicates that the vector potential A is proportional to the Fourier transform of the spatial current distribution with the variable changed from θ to u . For our proposed method, the vector potential A provides all the necessary information in the frequency domain as the difference between the vector potential A and far-field pattern is just a constant $j\omega\mu \sin \theta$.

4. NUMERICAL EXAMPLES

For the first example, as we stated in the previous section, the vector potential A can be obtained by dividing \vec{E} by $\sin \theta$ and the constant $j\omega\mu$ from the far-field pattern. Therefore, we only need

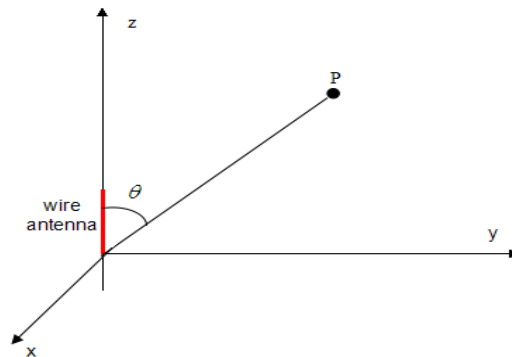


Figure 2: A line source along the z -axis.

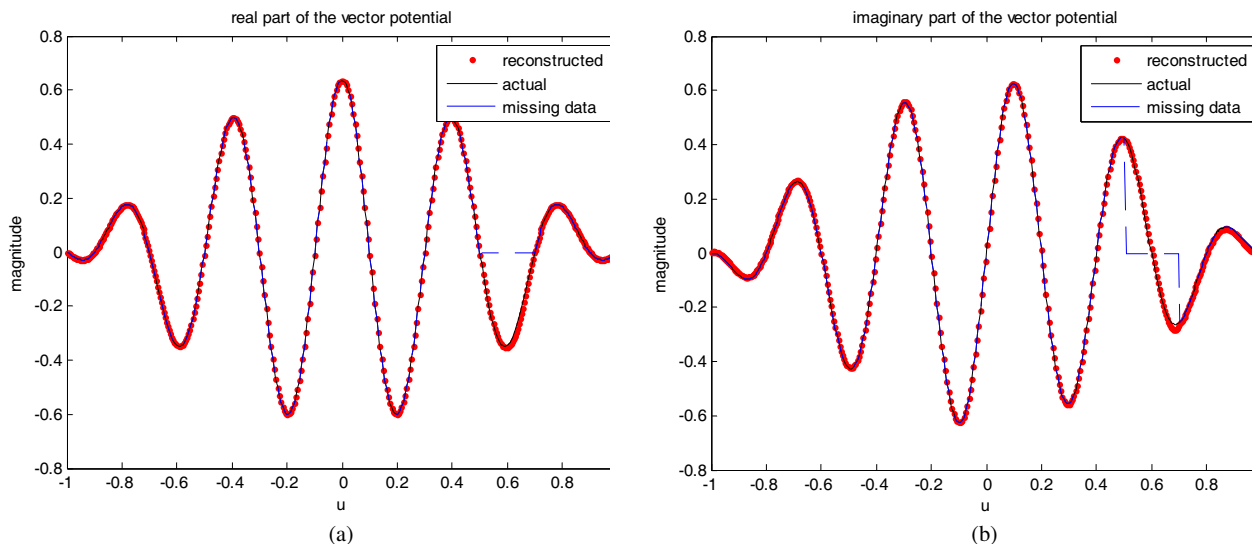


Figure 3: (a) The real part of the original, reconstructed and missing data A with a filter. (b) The imaginary part of the original, reconstructed and missing data A with a filter.

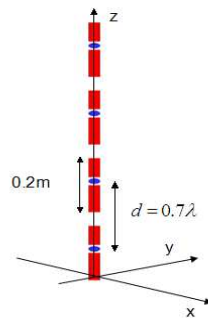


Figure 4: Straight wire antenna array.

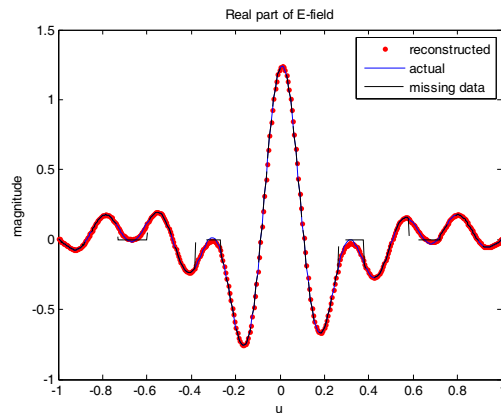


Figure 5: Real component of the actual, reconstructed and missing data.

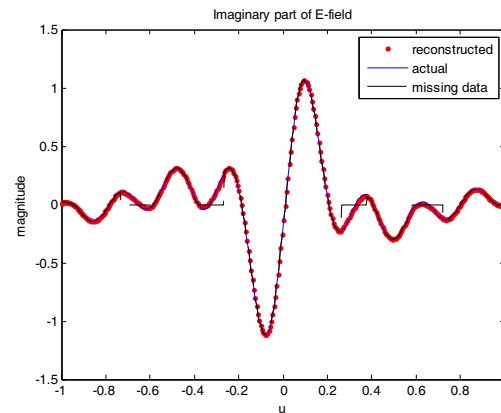


Figure 6: Imaginary component of the actual, reconstructed and missing data.

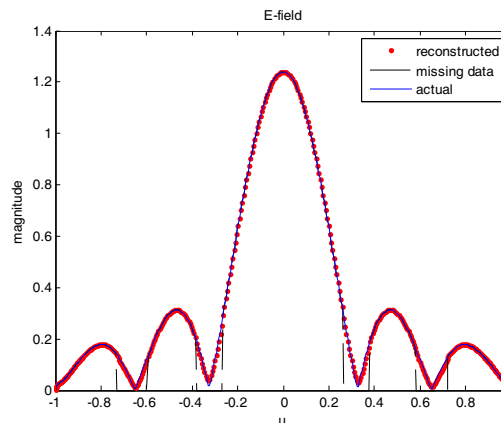


Figure 7: Far-field pattern of the actual, restored and missing data.

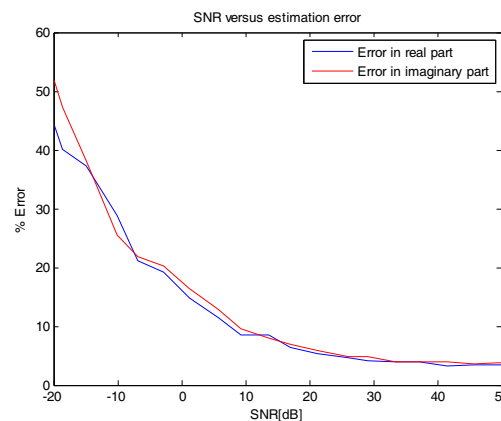


Figure 8: SNR and the estimation error.

to restore the pattern using the proposed method for vector potential. Here, we consider a short dipole as a straight wire antenna, shown in Fig. 2. The wire excited with 1V is oriented along the z -axis. The length of the wire antenna is $l = \lambda$. The far-field pattern has the variable changed with $u = \cos \theta$. We use an MA filter for a fast convergence. In addition, we can also see the actual data (solid line), restored data (dotted line), and missing data (dashed line). The missing data in the figures are reconstructed through recursive steps. The error is defined by the two norm of the difference between the actual data. The error is 10.8% and 12.8%, respectively. We can see that the restored signal fluctuates by more than 10%. In order to filter out these fluctuations, we use the moving average filter to reconstruct the missing data at each iterative step. The results are shown in Figs. 3(a) and 3(b) with errors of 4.7% and 5%, respectively. The step size of the MA filter was chosen as 3. For the second example, consider also the pattern from a straight wire antenna array. The structure of the antenna array is plotted in Fig. 4. There are 4 elements equally spaced along the z -direction. All of the elements are above the x - o - y plane. The length of each element is

$l = 0.2$ m, and diameter 2 mm. The distance between each array is $d = 0.6$ m. The driven elements are fed at the center with 1V excitation at 350 MHz. The real and imaginary parts (solid line) generated the 512 point data shown in Fig. 5 and Fig. 6. Each part includes four blocks of missing data (dashed line), with the side of the block having 30 points of missing data and the middle of the block 20 points of missing data, for a total of 100 points. As is the case with Example 2, once there are more than 100 points of missing data, the reconstructed data will have larger distortion. This iterative algorithm with an MA filter is stopped after 110 iterations. The reconstructed data (dotted line) of the real and imaginary parts are also shown in Fig. 5 and Fig. 6, respectively. The errors associated with the estimated data and the actual data are 8.59%, 8.53%, 7.66% and 10.75% in Fig. 5. The errors associated with the estimated data and the actual data are 9.02%, 7.87%, 9.97% and 9.19% in Fig. 6. From Fig. 7 we can see that the far-field pattern is well reconstructed.

5. CONCLUSION

In this paper, we presented an iterative Hilbert transform method for reconstructing missing data from an antenna pattern, on the premises that the current source exists on z -axis, has the form of a Fourier transform. In all the numerical examples, this method effectively restored the lost fragments of the antenna pattern based on the signal's relationship to the real part and imaginary part. The MA filter representation is also utilized for better estimation of the data and more efficient computation. In addition, the rates of convergence depend on the amount of data missing. In practice, we have found that the missing data can be approximately 20% of the whole data in patterns and also can be distributed in multiple blocks of the signal at the same time. Finally, the iterative algorithms, as presented, can be used in more applications where causality plays an important role

ACKNOWLEDGMENT

This work was supported by Basic Science Research Program through the National Research Foundation of Korea(NRF) funded by the Ministry of Education(NRF-2014R1A1A2055433).

REFERENCES

1. Oppenheim, A. V. and R. W. Schaffer, "Digital Signal Processing," 3rd. Englewood Cliffs, Prentice-Hall, NJ, 1999.
2. Hayes, H. M., J. S. Lim, and A. V. Oppenheim, "Signal reconstruction from phase or magnitude," *IEEE Trans. on Acoustics, Speech and Signal Processing*, Vol. 28, No. 6, Dec. 1980.
3. Gabor, D., "Theory of communication," *Institute of Electricians Engineering*, Vol. 93, No. 3, 429–457, Nov. 1946.
4. Quatieri, T. F. and A. V. Oppenheim, "Iterative techniques for minimum phase signal reconstruction from phase or magnitude," *IEEE trans. on Acoustics, Speech and Signal Processing*, Vol. 29, No. 6, 1187–1193, Dec. 1981.
5. Carballar, A. and M. A. Muriel, "Phase Reconstruction from Reflectivity in Fiber Bragg Gratings" *IEEE Light wave Technology*, vol. 15, no. 8, pp. 1314-1322, Aug. 1997.
6. Guillemin, E. A., *Synthesis of Passive Networks*, Krieger, New York, 1977.
7. Kazemipour, A., X. Begaud, and D. Allal, "E-field measurement, accuracy and uncertainties," *ECEE*, 189–191, June 2007.
8. James, G. C., "Phase retrieval and near field antenna measurements," *Processing URSI Symp, Sydney, Australia*, 510–512, 1992.
9. Martens L. J. and A. N. Venetsanopoulos, "A comparison of adaptive order statistic filters using different images," *IEEE Systems Engineering*, 77–80, Aug 1989.
10. Stuzman, W. L. and G. A. Thiele, *Antenna Theory and Design*, John Wiley & Sons, 1981.
11. Kolundzija, B., et al., *WIPL-D: Electromagnetic Modeling of Composite Metallic and Dielectric Structures-Software and User's Manual*, Artech House, Norwood, MA, 2000.

Wave Packet Propagation of Guided Optical Modes in a Thin Left-handed Film near a Frequency of Zero Power Flux

Dmitry A. Konkin, Rudol'ph V. Litvinov, and Alexander A. Shibelgut

Tomsk State University of Control Systems and Radioelectronics
40 Lenina Prospect, Tomsk 634050, Russia

Abstract— Dispersion of the propagation constants of waveguide modes of a thin left-handed film is considered. It is shown that by certain frequency the group velocity of mode can be vanished. An analysis of spatio-temporal transformation of intramode packet with spectrum near this frequency is performed. It is shown that a propagation velocity of the packet is proportional to a square root of a width of the packet spectrum and for packets with spectrum about 10 MHz can be by four orders less than the group velocity of the light in a volume left-handed material.

Modern technology of metamaterials allows creating thin left-handed waveguides on the volume substrate. These waveguides have both negative values of permittivity and permeability in optical range of wavelengths [1]. The waveguides have unique properties which considerably differ from usual waveguides. The features of dispersive characteristics of such waveguides and the features of the propagation of optical pulses in them are considered below.

It is shown in [2,3] that the propagation constants β of waveguide modes of TE -type of thin films with thickness h including on the basis of left-handed metamaterials are the real roots of the dispersion relation which can be represented in the form

$$\tanh \chi_f h + \frac{\chi_s \mu_f \chi_f^{-1} \mu_s^{-1} + \chi_c \mu_f \chi_f^{-1} \mu_c^{-1}}{1 + \chi_s \chi_c \mu_f^2 \chi_f^{-2} \mu_s^{-1} \mu_c^{-1}} = f(\beta, \omega) = 0, \quad (1)$$

where $\chi_* = \left(\beta^2 - \varepsilon_* \mu_* (\omega/c)^2\right)^{1/2}$; μ_* and ε_* are the relative permeability and the relative permittivity, respectively; c is the velocity of light in a vacuum; sign “*” at subscript is used instead of letters “c” (coating medium), “f” (film) and “s” (substrate).

We assume that the dispersion dependences of permittivity ε_f and permeability μ_f of a volume medium of left-handed metamaterial on the frequency of electromagnetic field ω are described by the well-known relations [4]

$$\varepsilon_f = 1 - \omega_p^2 / \omega^2, \quad \mu_f = 1 - F \omega^2 (\omega^2 - \omega_m^2)^{-1}, \quad (2)$$

where ω_p is a plasma frequency, ω_m is a frequency of magnetic resonance, F is a filling factor of metamaterial. The dispersion of material parameters of the usual right-handed material is negligible in comparison with the dispersion of the left-handed material and isn't taken into consideration below.

The dispersion dependences of propagation constants $\beta(\omega)$ of waveguide modes of TE -type for the left-handed film with thickness $h = 330$ nm in the case of air coating media ($\varepsilon_c = 1$ and $\mu_c = 1$) and non-magnetic substrate ($\mu_s = 1$) with relative permittivity equaled $\varepsilon_s = 2$ are represented in Fig. 1. The dependences have been calculated for parameters $\omega_p = 3.46 \cdot 10^{15}$ rad/s, $\omega_m = 1.63 \cdot 10^{15}$ rad/s and $F = 0,5$ which are in accord with data of papers [1,5]. In this case the frequency range in which both conditions $\varepsilon_f \leq 0$ and $\mu_f \leq 0$ are satisfied is within the limits from $1.63 \cdot 10^{15}$ rad/s (the wavelength equals $\lambda = 1.16$ μm) to $2.31 \cdot 10^{15}$ rad/s ($\lambda = 0.82$ μm).

The dispersion dependences $\beta(\omega)$ for modes TE_0 and TE_1 are not only in the range of fast modes ($k_s < \beta < k_f$) that typically for usual films of right-handed materials but also in the range of slow modes ($\beta > \max(k_f; k_s)$) which is absent in the usual films [6]. At the same time the dependence $\beta(\omega)$ for mode TE_1 is divided into two branches by point with infinite derivative $d\beta/d\omega = \infty$ in which the group velocity of mode is vanished $v_g = d\omega/d\beta = 0$. The phase and group velocities of mode which correspond to a lower branch of the dispersion dependence have the same directions, and which correspond to an upper branch have opposite directions. The dispersion dependences $\beta(\omega)$ of remaining modes are in the fast range. However, in contrast to usual film waveguides of right-handed materials the dispersion dependences for modes of them are monotone the dependences

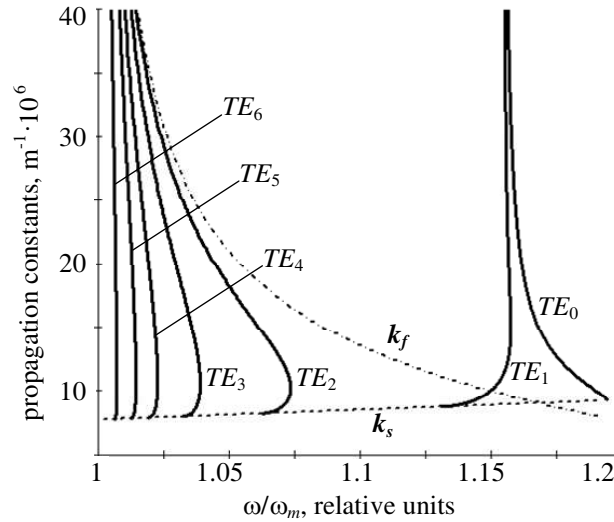


Figure 1: The dispersion dependences of the propagation constants of TE -modes of the left-handed film with thickness $h = 330$ nm in the case of the air coating medium and the non-magnetic substrate with relative permittivity $\varepsilon_s = 2$. Here k_f and k_s are dispersion dependences of wave numbers for volume materials of the film and the substrate, respectively.

$\beta(\omega)$ for fast modes of waveguides with left-handed film are divided into two branches by point that corresponds to the case $v_g = 0$ (similarly to the dependences for TE_1). At the same time by increase of mode number of the left-handed film the dispersion dependences which correspond to this mode number approach to the point of singularity of permeability μ_f and there are practically merged.

A cause of appearance on the dispersion dependences of the propagation constants of waveguide modes of the left-handed film two branches which correspond to the opposite directions of group velocity of mode is that the power flux of the light field in the film is opposite in its direction to power fluxes in right-handed coating medium and substrate [3]. Depending on the frequency ω of the light field of mode a total flux of power can have a direction either coinciding with power fluxes into the coating medium and the substrate or coinciding with the power fluxes in the film. By certain frequency ω_0 the power flux in film is equalized by fluxes in the coating medium and the substrate, the total flux of power of the mode and its group velocity are vanished. The waveguide modes of the usual right-handed films don't have the similar effect [6].

The frequency ω_0 in which the group velocity of the mode is vanished ($v_g = d\omega/d\beta = 0$) and the propagation constant β_0 corresponding to the group velocity can be determined as roots of the dispersion relation (1) that defines function $\omega(\beta)$ implicitly and equations $d\omega/d\beta = -(\partial f/\partial\beta)/(\partial f/\partial\omega) = 0$ [7]. In general case the frequency ω_0 belongs not only to the definition domain of the dispersion curve $\beta(\omega)$ of the mode (for this mode $v_g = 0$) but gets in area of definition curves $\beta(\omega)$ of other modes (see Fig. 1). Dispersion properties of these modes near the frequency ω_0 can be described within the framework of usual dispersion theory and aren't considered below.

From Fig. 1 follows that for case under consideration two waveguide modes can exist on the frequency ω in the neighborhood of point ω_0 ($\omega < \omega_0$). One of these modes corresponds to the lower branch of dependence $\beta(\omega)$ and other mode corresponds to the upper branch. The dependences $\beta(\omega)$ in the neighborhood of point ω_0 can be represented in terms of series by degrees of the square root of the frequency deviation $\Delta\omega = \omega_0 - \omega$. The dispersion dependences of the propagation constant β^+ (modes with the same directions of phase and group velocities) and the propagation constant β^- (modes with the opposite directions) to a first approximation by value $\Delta\omega^{1/2}$ can be described by following expressions:

$$\beta^\pm = \beta_0 \mp \sqrt{\Delta\omega/a} = \beta_0 (1 \mp \delta\beta), \quad (3)$$

where $a = -0.5 (d^2\omega/d\beta^2)_{\omega=\omega_0}$, $\delta\beta = \beta_0^{-1} \sqrt{\Delta\omega/a}$.

The dependence of y -component of the electric intensity vector of the light field of waveguide mode of TE -type by the frequency ω (the mode propagates in plane of the film along z -axis) on

the coordinate x along the normal to the film can be presented with accuracy at multiplier in the form:

$$E_c = (-1)^\eta \left(1 - \mu_f^2 \chi_c^2 \chi_f^{-2}\right)^{-1/2} \exp[\chi_c (h - x)], \quad x > h \quad (4)$$

$$E_f = \left(1 - \mu_f^2 \chi_s^2 \chi_f^{-2}\right)^{-1/2} \left[\cosh(\chi_f x) + \mu_f \chi_s \chi_f^{-1} \sinh(\chi_f x) \right], \quad 0 \leq x \leq h \quad (5)$$

$$E_s = \left(1 - \mu_f^2 \chi_s^2 \chi_f^{-2}\right)^{-1/2} \exp(\chi_s x), \quad x < 0 \quad (6)$$

where η is a mode number equaled to a quantity of zeros of the function $E_f(x)$.

In a first approximation by parameter $\delta\beta$ the equations which describe the dispersion of space dependences of the electric intensity E_*^\pm and x -component of the magnetic intensity vector $H_*^\pm = -\beta E_*^\pm / (\mu_* \mu_0 \omega)$ that corresponds to the electric intensity can be obtained as:

$$E_*^\pm = (1 \mp \xi_* \beta_0^2 \delta\beta) E_{*0}, \quad H_*^\pm = [1 \mp (1 + \xi_* \beta_0^2) \delta\beta] H_{*0}, \quad (7)$$

where the sign “*” denotes the same that in (1) (see the explication to (1));

$$\xi_c(x) = \frac{h-x}{\chi_{c0}} + \frac{\mu_{f0}^2 (\chi_{f0}^2 - \chi_{c0}^2)}{\chi_{f0}^2 (\chi_{f0}^2 - \mu_{f0}^2 \chi_{c0}^2)}, \quad x > h; \quad (8)$$

$$\begin{aligned} \xi_f(x) = & \mu_{f0} \frac{\chi_{f0}^2 - \chi_{s0}^2}{\chi_{s0} \chi_{f0}^3} \frac{\sinh(\chi_{f0} x)}{\cosh(\chi_{f0} x) + \mu_{f0} \chi_{s0} \chi_{f0}^{-1} \sinh(\chi_{f0} x)} \\ & + \frac{x}{\chi_{f0}^2} \frac{d}{dx} \ln \left[\cosh(\chi_{f0} x) + \mu_{f0} \chi_{s0} \chi_{f0}^{-1} \sinh(\chi_{f0} x) \right] \\ & + \frac{\mu_{f0}^2 (\chi_{f0}^2 - \chi_{s0}^2)}{\chi_{f0}^2 (\chi_{f0}^2 - \mu_{f0}^2 \chi_{s0}^2)}, \quad 0 \leq x \leq h; \end{aligned} \quad (9)$$

$$\xi_s(x) = \frac{x}{\chi_{s0}} + \frac{\mu_{f0}^2 (\chi_{f0}^2 - \chi_{s0}^2)}{\chi_{f0}^2 (\chi_{f0}^2 - \mu_{f0}^2 \chi_{s0}^2)}, \quad x < 0; \quad (10)$$

the number zero “0” at subscripts of all magnitudes signifies that they have to be calculated by the frequency ω_0 ; $\mu^{(0)}$ is the fundamental magnetic constant.

Let's consider the propagation of limited packet of the guided modes of TE -type. We assume that the propagation constants of modes from the packet belong one dispersion curve and the frequencies of them are within interval $\Delta\Omega = \omega_0 - \omega_{\min} \ll \omega_0$ (see Fig. 1). Two different pairs of intramode packets correspond to such interval. The modes of these packets have the opposite directions of phase velocities. At that the modes of one of the packet of every pair (with the propagation constants β^+) have the same directions of phase and group velocities. The modes of other packet of pair (with the propagation constants β^-) have the opposite directions of these velocities. We assume below that the spectral density of the modes in these packets is the same and normalized to unit. Analytical computation of spatio-temporal dependences of the power fluxes $S_\nu^\pm(z, t)$ of the packets of guided modes of TE -type of the first ($\nu = 1$, the phase velocity along the positive direction of z -axis) and the second ($\nu = 2$, the phase velocity along the negative direction of z -axis) pairs shows that in this case the relations are correct $S_1^+(z, t) = S_2^-(z, t) \equiv S(z, t)$ and $S_2^+(z, t) = S_1^-(z, t) \equiv -S(-z, t)$,

$$S(z, t) = \frac{4\beta_0^2}{\mu_0 \omega_0} \int_{-\infty}^{\infty} \frac{\xi(x)}{\mu(x)} (E_0^+(x))^2 dx \operatorname{Re} [\psi(z, t) (\Delta\psi(z, t))^*], \quad (11)$$

$$\psi = \frac{i}{t} \left[E x(z, t) - \frac{z}{2\sqrt{at}} \operatorname{Erf}_\Delta(z, t) \right], \quad (12)$$

$$\Delta\psi(z, t) = \frac{i}{t\sqrt{at}} \left[E x(z, t) \left(\sqrt{\Delta\Omega t} + \frac{z}{2\sqrt{at}} \right) - \frac{z}{2\sqrt{at}} + \left(\frac{i}{2} - \frac{z^2}{4at} \right) \operatorname{Erf}_\Delta(z, t) \right], \quad (13)$$

where

$$Ex(z, t) = \exp \left[i \left(\sqrt{\frac{\Delta\Omega}{a}} z - \Delta\Omega t \right) \right] - 1, \quad (14)$$

$$Erf_{\Delta}(z, t) = \frac{1+i}{\sqrt{2}} \sqrt{\pi} \exp \left(\frac{iz^2}{4at} \right) \left[erf \left(\frac{1+i}{\sqrt{2}} \frac{z}{2\sqrt{at}} \right) - erf \left(\frac{1+i}{\sqrt{2}} \left(\frac{z}{2\sqrt{at}} - \sqrt{\Delta\Omega t} \right) \right) \right], \quad (15)$$

$\mu(x)$ is a dependence of permeability on the coordinate x , $erf(\zeta)$ is an integral of errors [7].

It should be noted that the product of two functions, $\psi(z, t)(\Delta\psi(z, t))^*$, in relation (11) describes dispersive distortions of the mode packet both at the expense of the dispersion of the propagation constants of waveguide modes (see (3)) and at the expense of the dispersion of the spatial distribution shape of the fields of the waveguide modes (see (7)). Analysis and numerical simulation have showed that the function $\Delta\psi$ is degenerated into the function ψ in the case of neglect of the dispersion of shape. However such neglect is unjustified as contributions of both types of the dispersion into spatio-temporal dynamics of the mode packet have the same order.

From Fig. 1 follows that for above considered left-handed film a small neighborhood of frequency $\omega_0 \approx 1.75 \cdot 10^{15}$ rad/s ($\beta_0 \approx 1.02 \cdot 10^7$ m⁻¹) that is in the definition area of the dispersion dependence of the propagation constant of waveguide mode TE_2 with parameter $a \approx 1.66$ s/m² is outside of the definition area of the dispersion dependences of other modes. For this mode the time dependence of the power flux $s(z, t) = S(z, t)/\max[S(0, t)]$ of the wave packet with width $\Delta\Omega = 100$ GHz at different sections $z = \text{const}$ normalized to maximum of the flux by $z = 0$ is represented in Fig. 2. A considerable spreading of the mode packet with time is conditioned by both the strong material dispersion of left-handed film (see (2) and Fig. 1) and the waveguide dispersion of considered planar structure. In spite of zero group velocity by frequency ω_0 the maximum of the mode packet during 1.4 ns is shifted along the waveguide axis by 1 mm that corresponds to the propagation velocity of the mode packet approximately $6.7 \cdot 10^5$ m/s. It is almost by three orders less than the group velocity in the volume left-handed material equaled $1.1 \cdot 10^7$ m/s. From analysis of relations (11)–(15) follows that in considered case the propagation velocity of the mode packet can be approximately evaluated by means of following relation

$$v = \sqrt{2a\Delta\Omega}. \quad (16)$$

As follows from last formula the propagation velocity of group packet decreases proportionally to the square root of the spectrum width of the packet $\Delta\Omega$ and by $\Delta\Omega = 10$ MHz for the considered mode TE_2 has very small value $8.1 \cdot 10^3$ m/s.

Thus the dispersion properties of planar fibers based on the thin left-handed film have qualitative differences from the properties of usual structures based on the right-handed films. The effect of

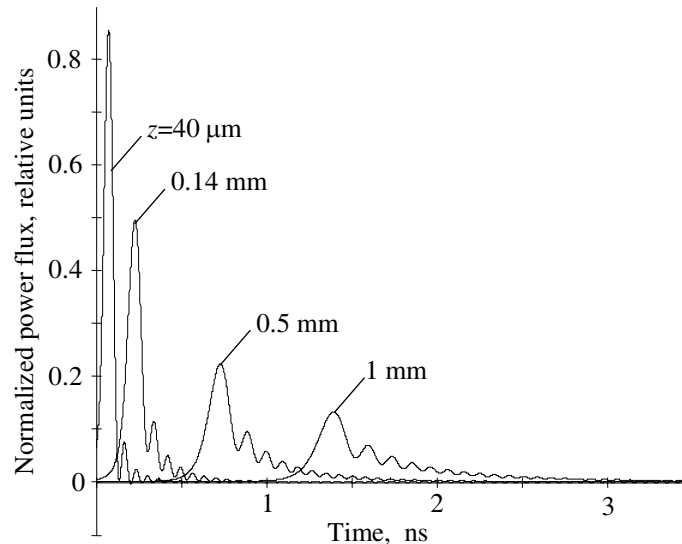


Figure 2: Normalized time dependence of the power flux of the intramode packet with width $\Delta\Omega = 100$ GHz at different sections $z = \text{const}$ for mode TE_2 with parameter $a = 1.6554$ s/m².

considerable reduction of the propagation velocity of the light in the left-handed films can be used in the integrated spatio-temporal modulators of the light.

ACKNOWLEDGMENT

This research has been partly carried out in the framework of the project 8.909.2014/K funded by the Ministry of Education and Science of the Russian Federation. Alexander A. Shibelgut is supported by scholarship of the President of the Russian Federation (project SP-4673.2013.5).

REFERENCES

1. Limberopolous, N., A. Akyurtlu, K. Higginson, A.-G. Kussow, and C. D. Merritt, "Negative refractive index metamaterials in the visible spectrum based on MgB₂/SiC composites," *Applied Physics Letters*, Vol. 95, No. 2, 023306, 2009.
2. He, Y., Z. Cao, and Q. Shen, "Guided optical modes in asymmetric left-handed waveguides," *Optics Communications*, Vol. 245, No. 1–6, 125–135, 2005.
3. Shadrivov, I. V., A. A. Sukhorukov, and Y. S. Kivshar, "Guided modes in negative-refractive-index waveguides," *Physical Review E*, Vol. 67, No. 5, 057602, 2003.
4. Smith, D. R., W. J. Padilla, D. C. Vier, S. C. Nemat-Nasser, and S. Schultz, "Composite medium with simultaneously negative permeability and permittivity," *Physical Review Letters*, Vol. 84, 4184, 2000.
5. Kussow, A.-G., A. Akyurtlu, A. Semichaevsky, and N. Angkawisittpan, "MgB₂-based negative refraction index metamaterial at visible frequencies: Theoretical analysis," *Physical Review B*, Vol. 76, No. 19, 195123, 2007.
6. Vinogradova, M. B., O. V. Rudenko, and A. P. Sukhorukov, *Theory of Waves*, Nauka, Moscow, 1979 (in Russian).
7. Korn, G. A. and T. M. Korn, *Mathematical Handbook for Scientists and Engineers*, 2nd Edition, Dover, New York, 2000.
8. Brillouin, L., *Wave Propagation and Group Velocity*, Academic Press, New York, 1960.

Mutual Coupling between Parasitic Elements of Split Ring Resonator on Antenna

Dang-Oh Kim and Uooyeol Yoon

Wireless Power Transfer Research Center

Korea Advanced Institute of Science and Technology, South Korea

Abstract— The parasitic elements on antenna have become an important issue in improving the antenna performance in various wireless devices. These elements are mostly used as radiator and resonator in antenna. However, an investigation of the mutual coupling between parasitic elements is rare to be found in metamaterial resonator antenna studies. From this unusual approach, this paper presents the new mutual coupling structure of parasitic elements with the split ring resonator (SRR) on antenna. The suggested antenna consists of two rectangular SRRs and conventional monopole antenna. These resonators play the role of the parasitic element in antenna. In order to operate these SRRs, linear monopole antenna is used as an active antenna which can provide the time-varying magnetic field with normal direction. In metamaterial technology, a negative effective permeability can be generated at resonant frequency via periodic arrangement of these SRRs which are electrically small LC resonant elements with a high quality factor. Fundamentally, mutual coupling phenomenon has been observed between adjacent resonators, so that the antenna with two resonators has the same effect on parasitic elements, too. In this study, the coupling coefficient between two parasitic element resonators on antenna is obtained from scattering parameter simulation results. On the basis of the electromagnetic field characteristics and the result of antenna parameter, this study will be exquisite from the previous studies of antennas that utilize the SRR.

1. INTRODUCTION

The split ring resonators (SRRs) have attracted considerable attention in microwave engineering. These SRRs as the metamaterial resonator are understood as artificially effective medium that exhibits some unique electromagnetic properties. They have received significant attention and have enabled numerous applications over the past decade, especially for the antenna design. Various design techniques for antenna have already been studied and developed based on the SRR [1–3]. Those studies proposed the antenna characteristics of wide bandwidth, multi-band, miniaturization, band rejection, and high directivity.

Recently, the parasitic elements are important components for antenna design, such as band rejection element, parasitic impedance stub, and resonance element. Typical parasitic elements in antenna technology have been used to improve the antenna performance. These elements act as resonators or electromagnetic coupler with antenna radiator [4–6]. The parasitic element SRR behaves as resonator which is operated by excited field, so that mutual coupling effect between the SRRs can be calculated. The conventional mutual coupling effect for resonator has been commonly obtained from coupling theory of coupling structure. In this paper, we investigated the mutual coupling effect between the SRRs as parasitic element of antenna.

2. ANTENNA CONFIGURATION

The SRR structure, which was proposed by Pendry as a metamaterial resonator in 1999 [7], is a core element in the mutual coupling effect of resonators in this study. This structure exhibits a negative-permeability medium within a local frequency range, which has resulted in the extensive development of microwave circuit and antenna using the SRR for improving electromagnetic performance. A typical SRR is made using two metallic split-ring strip, which behaves as an electrically small LC resonant tank having a high quality factor. This unusual electromagnetic property can be excited by an incident time-varying magnetic field with normal direction. Figure 1 shows the geometry and dimensions of the proposed element of the SRR. The physical parameters of the SRR are: $c = 0.9$ mm, $d = 0.3$ mm, $g = 0.5$ mm, $L1 = 11.9$ mm. The resonance frequency of the SRR depends on its geometrical parameters. Figure 2 shows the geometry and dimensions of basic monopole antenna. As shown in Figure 2, the basic monopole antenna was designed by forming the conventional linear monopole antenna on the finite ground plane and using the coaxial feeding. This antenna has a length of pole $L2 = 13.5$ mm, diameter of pole cylinder $a = 2.5$ mm. The length of monopole antenna is approximately $\lambda/4$ of 5.5 GHz. Figure 3 shows the geometry

and dimensions of the monopole antenna with two SRRs. The inserted SRRs are fabricated on a dielectric substrate of Rogers 4003 (thickness $h = 0.812$ mm, relative permittivity $\epsilon_r = 3.38$, loss tangent $\delta = 0.0023$). The geometry and dimension of two SRRs are same.

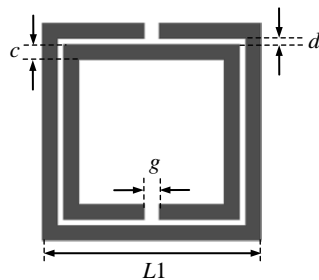


Figure 1: Geometry of the SRR.

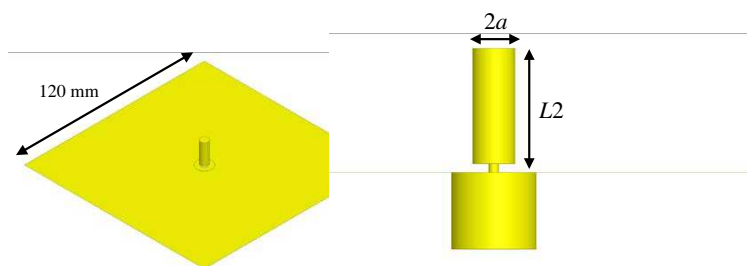


Figure 2: Geometry and dimension of the basic monopole antenna.

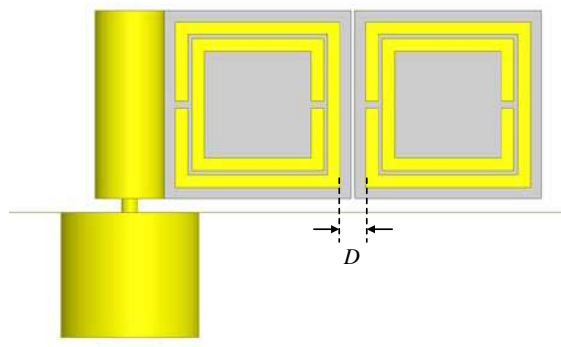


Figure 3: Geometry and dimension of the monopole antenna with SRR.

3. SIMULATION AND DISCUSSION

Figure 4 shows the simulated return loss (S_{11}) results of the proposed antenna. The return loss results were computed by 3D EM simulator of HFSS of Ansys Corporation. From the result shown in Figure 4, it is observed that an impedance bandwidth with good matching for $S_{11} < -10$ dB is from 36 to 5 GHz. Two SRRs in this antenna perform as two LC resonators which radiate and store the electromagnetic field energy, so that there are mutual coupling between them. Thus, we can find two resonance frequencies corresponding to electric coupling and magnetic coupling. Figure 5 shows the mutual coupling phenomenon between two SRRs with simple circuit model.

As two adjacent resonators make mutual coupling, it is necessary to consider the coupling coefficient of the proposed structure. To verify the effect of mutual coupling, we can calculate the coupling coefficient k , defined as Equation (1)

$$k_{ij} = \frac{f_e^2 - f_m^2}{f_e^2 + f_m^2} \quad (1)$$

In this paper, the coupling coefficient k was derived for two cases of distance between two SRRs. The calculated coupling coefficient k for $D = 1.65\text{mm}$, was 0.042, and $D = 1.85\text{mm}$ was 0.091. Considering the coupling coefficient k of the proposed structure, it is evident that the SRR as parasitic element of antenna exhibits a mutual coupling phenomenon, so that the calculation of coupling coefficient is possible.

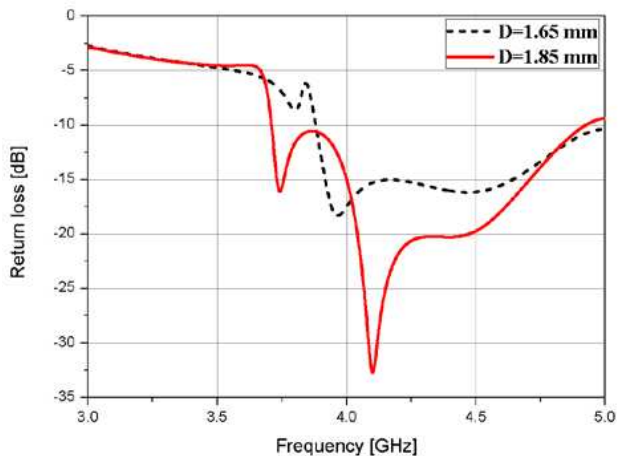


Figure 4: Return loss results of proposed antenna with two SRRs.

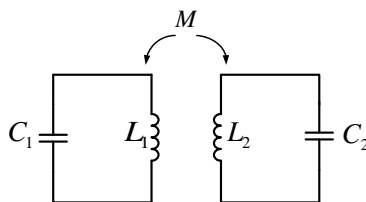


Figure 5: Simple circuit model for mutual coupling between two SRRs.

4. CONCLUSIONS

This paper explains the coupling effect between two SRRs as parasitic element of monopole antenna. A conventional linear monopole antenna is used for verification. And two SRRs are inserted on ground plane. To verify the coupling effect between two parasitic element SRRs, we show the coupling coefficient calculated. From these results, this study is helpful to design the antenna using the parasitic element of resonator type.

ACKNOWLEDGMENT

This work was supported by ICT R&D program of MSIP/IITP. [B0101-15-1369, Development of small basestation supporting multiple streams based on LTE-A systems].

REFERENCES

1. Alici, K. B. and E. Ozbay "Electrically small split ring resonator antennas," *Journal of Applied Physics*, Vol. 101, No. 8, 083104(1)–083104(4), 2007.
2. Alici, K. B. and E. Ozbay, "Radiation properties of a split ring resonator and monopole composite," *Physica Status Solidi B*, Vol. 244, No. 4, 1192–1196, 2007.
3. Kim, D. O. and C. Y. Kim, "CPW-fed ultra-wideband antenna with triple-band notch function," *Electronics Letters*, Vol. 46, No. 18, 1246–1248, 2010.
4. Alici, K. B., A. E. Serebryannikov, and E. Ozbay, "Radiation properties and coupling analysis of a metamaterial based, dual polarization, dual band, multiple split ring resonator antenna," *Journal of Electromagnetic Waves and Applications*, Vol. 24, No. 8–9, 1183–1193 2010.

5. Gemio, J., J. Parrón, P. de Paco, G. Junkin, J. Marin, and O. Menéndez, “A split-ring-resonator loaded monopole for triple band applications,” *Journal of Electromagnetic Waves and Applications*, Vol. 24, No. 2–3, 241–250, 2010.
6. Ntaikos, D. K., N. K. Bourgis, and T. V. Yioultsis, “Metamaterial-based electrically small multiband planar monopole antennas,” *IEEE Antennas and Wireless Propagation Letters*, Vol. 10, 963–966, 2011.
7. Pendry, J. B, A. J. Holden, D. J. Robbins, and W. J. Stewart, “Magnetism from conductors and enhanced nonlinear phenomena,” *IEEE Transactions on Microwave Theory and Techniques*, Vol. 47, No. 11, 2075–2084, 1999.

An Formation Algorithm of the Synthetic Aperture in an Automotive Radar with Use of the MUSIC Algorithm

Zhargal T. Erdyneev, Gleb O. Manokhin, Elena P. Velikanova, Eugeny V. Rogozhnikov,
Andrey A. Geltser, and Alexander A. Shibelgut

Tomsk State University of Control Systems and Radioelectronics
40 Lenina Prospect, Tomsk 634050, Russia

Abstract— This paper proposes an implementation of MUSIC algorithm in order to increase a range resolution after processing of synthetic aperture radar (SAR) image. SAR system operates in small ranges and uses a frequency modulated continuous wave (FMCW) in radars, offers a low-cost, low power, small earth observation system that can be placed on different types of mobile platforms. SAR operates in the side looking mode. Modified wavenumber domain algorithm (WDA) is used. WDA gives a clear sinc function on both coordinates of image. Post-processing is performed in cut-out piece of focused image after WDA. Simulation conditions are reached at the expense of available equipment intended for experimental verification.

1. INTRODUCTION

Since the middle XX century a synthetic aperture radar (SAR) is an important tool to obtain a radar image of terrain with objects located on it. The radar image is close in quality to the aerial photographs over long distances regardless of the time of day and weather conditions [1, 2]. In recent years the interest in the development of SAR systems operating on small distances has been increased [2–6]. These systems allow solving many problems in the field of earth observation, such as: monitoring flows and flood water or areas in which gas pipes and electrical power lines are buried. Operation in small ranges extends the list of possible platforms which can be used to arrange on them this system including unmanned drones, vehicles [6–10]. Moreover, this system can be applied for automatic control of the vehicle where it is important to monitor the side looking area during the movement.

In classic mode of operation the SAR use pulse signals. The use of the pulse radar by small distances imposes a number of considerable limitations. One of them is locking of receiver during transmission time of radiated signal and as a result the formation of “dead zone” in the range direction. Further the signal processing requires enough fast ADC which leads to the increase of system cost. Systems with FMCW (Frequency Modulated Continuous Wave) signal require less high-speed ADC, consumes less power and removes “dead zones”. Thus the combination of FMCW radars and SAR systems allows implementing compact, low-power, low-cost earth observation systems which can be placed on different types of mobile platforms.

The problem of increase of the azimuth resolution can be overcome by applying the synthetic aperture radar processing techniques. Range resolution depends on the bandwidth of the transmitted signal and therefore is limited by radar hardware components. The most intuitive way in order to enhance the range resolution the probe signal bandwidth can be increased or the interferometric wavenumber shift principle can be used. At the same time it is necessary to apply two different acquisitions with different viewing angles [11]. In addition there is alternative way based on the modern spectral estimation techniques like MUSIC (Multiple Signal Classification) which was first proposed to determine the angle of the arrival of signal [12]. Direct application of this algorithm to the problem has a number of drawbacks. Firstly it is desirable to know a priori the number of echo signals. Secondly the method requires high computational costs. Thirdly the MUSIC response does not give a true estimation of the power spectral density, i.e., the algorithm will give the exact position of the target but does not retain an information about power of signal reflected from the target. This paper proposes an algorithm for SAR data processing using MUSIC method implemented on the basis of the finished image obtained by Wavenumber Domain Algorithm (WDA) at the expense of the post-processing of specified cut-out of window within the image.

2. DATA MODEL

The radar signal at the out-put of FMCW transmitter can be presented as:

$$S(t) = \exp [j2\pi f_c t + j\pi\beta t^2], \quad (1)$$

where f_c is a carrier frequency; $\beta = \Delta F/\text{PRI}$ is the frequency modulation rate; ΔF is a signal bandwidth; PRI is a pulse repetition interval; t is a signal time, $0 \leq t \leq \text{PRI}$.

A side look mode of the radar mounted on a car platform is considered. The geometry of such SAR system is represented in Fig. 1. The reflected signal from the point target can be presented as:

$$S_r(t, t_{az}) = \exp \left[j2\pi f_c (t - 2R(t, t_{az})/c) + j\pi\beta (t - 2R(t, t_{az})/c)^2 \right] \quad (2)$$

where $-L_{\text{SAR}}/2V \leq t_{az} \leq L_{\text{SAR}}/2V$; L_{SAR} is an aperture length; c is the light speed; V is a velocity of the car; $R(t, t_{az})$ is range of target which depends on both azimuth time and range time: $R(t, t_{az}) = \sqrt{R_0^2 + V^2(t + t_{az})^2}$; where R_0 is minimal distance between radar and target.

After multiplication of the received signal with the reference signal (complex conjugate version of transmitted signal) a beat signal is arisen. The beat signal can be written as:

$$S(t, t_{az}) = \exp \left[-j\beta \frac{4\pi R(t, t_{az})}{c} t \right] \times \exp \left[-\frac{j4\pi f_c R(t, t_{az})}{c} \right] \times \exp \left[\frac{j4\pi\gamma R^2(t, t_{az})}{c^2} \right]. \quad (3)$$

The first exponent in (3) determines the range to the target, the second exponent is a Doppler shift in the spectrum along the azimuth, and the third exponent is called the residual video phase (RVP) [5]. For processing of the beat signal the method WDA can be used [5]. A block diagram of this algorithm is shown in Fig. 2. All formulas describing the algorithm are presented in [5].

The formula which describes the final image for a single target is shown below (4) where γ is a reflection coefficient; f_0 is a beat frequency; t_{az} is a azimuth time by which the distance between radar and target is minimal:

$$S(f_r, t_{az}) = \gamma \text{sinc}(f_r - f_0) \text{sinc}(t_{az} - t_0). \quad (4)$$

The simulation result of the considered algorithm for the two point targets with coordinates in range and azimuth [23 m, 5.5 m] for the first target and [26 m, 5.5 m] for the second target is shown in Fig. 4(a). Simulation parameters are presented in Table 1. These parameters are taken according to available equipment for the experimental proof. Simulation results show that targets can't be resolved in range direction due to the fact that the range resolution which is defined as $\rho_x = c/2\Delta F = 3.75$ m and it is greater than the distance between targets. To solve this problem we have performed the post-processing of the final image using the method MUSIC described below.

3. MUSIC POST-PROCESSING

As previously mentioned this method has been proposed for estimation of the angle of arrival of the signal which is generally described in the following way. Let's assume that there is a parameter

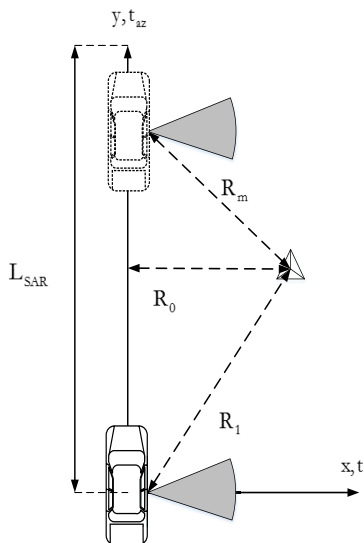


Figure 1: The geometry of the SAR system.

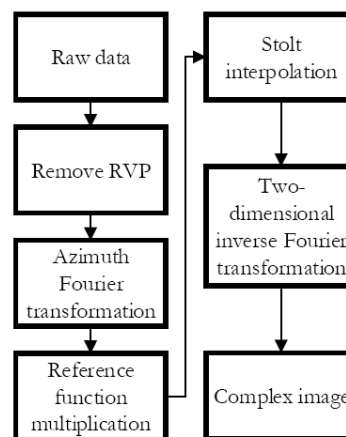


Figure 2: Block diagram of the WDA algorithm.

Table 1: System parameters.

Sampling frequency	200 kHz
Carrier frequency	10 GHz
Pulse repetition interval	320 μs
Signal bandwidth	40 MHz
Car velocity	11.1 m/s
Aperture length	11.1 m

θ which has to be evaluated in the input array \mathbf{X} . Data model with L different values of θ at the input of such system can be presented as:

$$\mathbf{X} = \mathbf{A} \cdot \mathbf{S} + \mathbf{W}, \tag{5}$$

where $\mathbf{A} = (\mathbf{a}(\theta_1) \mathbf{a}(\theta_2) \dots \mathbf{a}(\theta_L))$ are directing vectors which are corresponded to L values and described the signal shape depending on θ_L (for the frequency estimation $\mathbf{a}(\theta_k) = \exp(j \cdot 2\pi \cdot \theta_L \cdot t)$), $\mathbf{S} = (s_1 \ s_2 \ \dots \ s_L)$ is an array of complex envelopes of the signal, \mathbf{W} is the white Gaussian noise.

Before calculation of the correlation matrix for the signal model two main assumptions are done:

- signal and noise must be uncorrelated;
- full rank of autocorrelation matrix of the signal must be greater than the number of L .

After calculation of the correlation matrix $\mathbf{R} = E\{\mathbf{X}\mathbf{X}^H\}$ a singular decomposition of the matrix gives a matrix of the eigenvectors \mathbf{V} where the first L columns correspond to the signal subspace, the remaining $T-L$ columns where T is the size of the array \mathbf{X} correspond to the noise. On the basis of the orthogonality property of the noise and signal the noise eigenvectors are used to obtain a final function (6) for estimation values θ :

$$\mathbf{P}(\theta) = \frac{1}{\mathbf{a}^H(\theta) \cdot \mathbf{V}_{T-L} \cdot \mathbf{V}_{T-L}^H \cdot \mathbf{a}(\theta)} \tag{6}$$

Accordingly, the output should give L peaks with the corresponding values θ_L .

Now we should consider this method as applied to the SAR system. After the imaging it is necessary to obtain a more detailed picture within a given piece of an image of size $N \times M$. At first it is essential to estimate the correlation matrix of the signal in a given window. Before evaluation of the correlation matrix we must restore its rank because just one measurement was done [11]. A method of Spatial Smoothing is used to restore rank of the matrix. This method is represented in Fig. 3.

Matrix $\mathbf{X}(N, M)$ in Fig. 3 represents the result of 2D inverse Fourier transform of window of the function $\mathbf{S}(N, M)$ by the use of (4). Further a window is formed with size $m_1 < N$ and $m_2 < M$ and then every possible position K is scanned by this window. For each position an one-dimensional vector is formed as shown in Fig. 3 and then the correlation matrix is calculated according to (7):

$$K = (N - m_1 + 1) \cdot (M - m_2 + 1), \quad \mathbf{R} = \sum_i^K \mathbf{X}_i \cdot \mathbf{X}_i^H \tag{7}$$

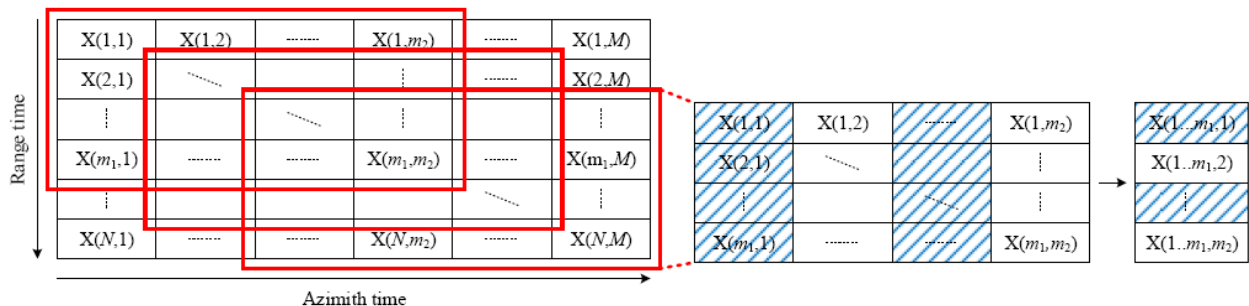


Figure 3: The method of Spatial Smoothing over 2D SAR data.

As mentioned above an array of eigenvectors $\mathbf{V}_n = \mathbf{V}(m_1 \cdot m_2, m_1 \cdot m_2 - 2L)$ corresponding to the noise subspace is formed after the singular decomposition of the matrix. Number of targets L can be estimated by the methods AIC, MDL [13]. In addition according to [14] the vectors $\mathbf{V}(m_1 \cdot m_2, m_1 \cdot m_2 - p_1 p_2)$ accurately refer to the noise subspace where p_1 and p_2 are all possible positions of the windows along the range and the azimuth, i.e., the estimation of the number of targets is not required.

Before calculation of the final function of MUSIC an array of the directing vectors are formed as:

$$\mathbf{a}(f_0, t_0) = \left[1 \ e^{jf_0} \ \dots \ e^{jf_0(m_1-1)} \ e^{jt_0} \ \dots \ e^{jf_0(m_1-1)} \ e^{jt_0(m_2-1)} \right] \quad (8)$$

Accordingly if it is necessary to keep the scale of the cut window, there is a need to form the $N \times M$ directing vectors where each vector will have its own frequency f_0 over range and azimuth delay t_0 . The MUSIC finite function is calculated as:

$$P(f_0, t_0) = \frac{1}{\mathbf{a}^H(f_0, t_0) \cdot \mathbf{V}_n \cdot \mathbf{V}_n^H \cdot \mathbf{a}(f_0, t_0)} \quad (9)$$

Then to obtain the final image like Fig. 3 but in reversed order it is essential to form a matrix of size $N \times M$ from one-dimensional vector $P(f_0, t_0)$. The results of simulation with the same system parameters before and after the post-processing by the MUSIC method are shown in Fig. 4.

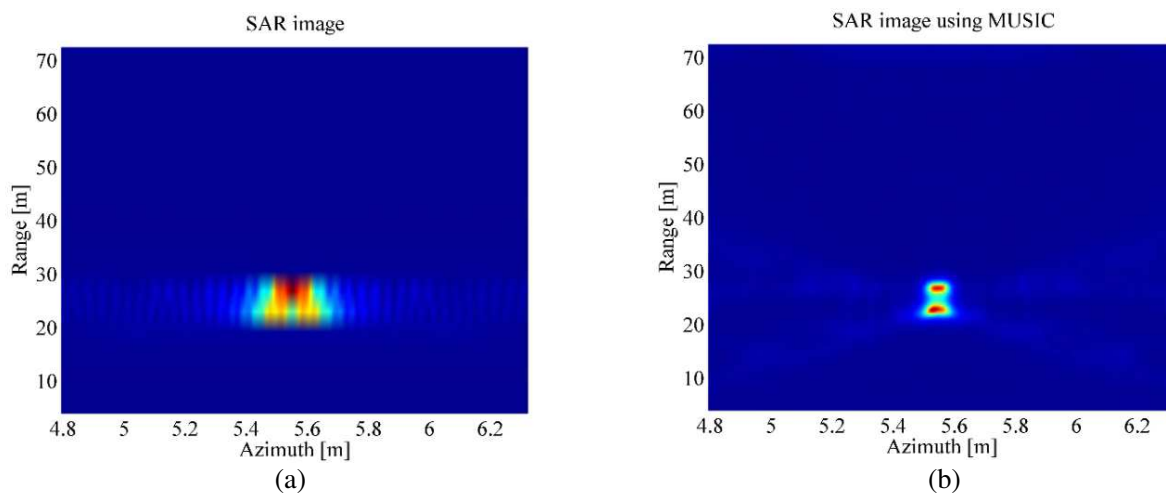


Figure 4: SAR image (a) before and (b) after the image post-processing using the MUSIC method.

4. CONCLUSION AND FUTURE WORK

The post-processing of the final image obtained by the synthetic aperture using the MUSIC method provides a more accurate picture and increases the range resolution more than two times in comparison with the original image.

One of the drawbacks of the MUSIC method is a disproportion of the power of signal reflected from the target to the output function of the method. Further researches will take into account the different reflection coefficients to obtain an accurate picture for 3-dimensional targets with a complex shape. In addition the simulation results show that it is not necessary to estimate the number of targets separately by the use of the Spatial Smoothing method and as a result a requirement to have a priori information about the number of targets is eliminated. According to [14] this statement is true only for the cases when the window size is approximately equaled $m_1 \approx 2N/3$ and $m_2 \approx 2M/3$. Therefore in the future it is necessary to assess more accurately a formula for calculation of the optimal window size.

To compare results an experiment by the conditions presented in Table 1 is planned to perform in a following research. Taking into consideration the high computational costs simplified algorithms will also be developed to get an accurate picture in real time. In addition it is planned to consider features of the image processing in the slanting SAR mode for imaging in other sector of view.

ACKNOWLEDGMENT

This research has been carried out in the framework of the project 8.909.2014/K funded by the Ministry of Education and Science of the Russian Federation.

REFERENCES

1. Antipov, V. N., V. T. Goryainov, and A. V. Kulin, *Radar Stations with Digital Synthesizing of Aperture of Antenna*, Radio and Svyaz, Moscow, 1988.
2. Franceschetti, G. and R. Lanari, *Synthetic Aperture Radar Processing*, CRC Press, 1999.
3. Meta, A., J. J. M. de Wit, and P. Hoogeboom, “Development of a high resolution airborne millimeter wave FM-CW SAR,” *Proceedings of First European Radar Conference EuRAD-2004*, 209–212, Amsterdam, the Netherlands, Oct. 11–15, 2004.
4. Meta, A. and P. Hoogeboom, “Development of signal processing algorithms for high resolution airborne millimeter wave FMCW SAR,” *Proceedings of IEEE International Radar Conference 2005*, 326–331, Arlington, USA, May 9–12, 2005.
5. Wang, R., O. Loffeld, H. Nies, S. Knedlik, M. Hagelen, and H. Essen, “Focus FMCW SAR data using the wavenumber domain algorithm,” *IEEE Transactions on Geoscience and Remote Sensing*, Vol. 48, No. 4, 2109–2118, 2010.
6. Xue, G. Y., J. G. Yang, and P. G. Liu, “Modified range migration algorithm integrated with motion compensation for FMCW SAR,” *Proceedings of IET International Radar Conference 2013*, 1–4, Xi’an, China, Apr. 14–16, 2013.
7. Wang, W.-Q., Q. Peng, and J. Cai, “Waveform-diversity-based millimeter-wave UAV SAR remote sensing,” *IEEE Transactions on Geoscience and Remote Sensing*, Vol. 47, No. 3, 691–700, 2009.
8. Luo, Y.-H., H. Song, R. Wang, and S. Zheng, “High-resolution automobile FMCW SAR and signal processing,” *Journal of Electronics*, Vol. 30, No. 6, 561–566, China, 2013.
9. Cho, B.-L., Y.-K. Kong, H.-G. Park, and Y.-S. Kim, “Automobile-based SAR/InSAR system for ground experiments,” *IEEE Geoscience and Remote Sensing Letters*, Vol. 3, No. 3, 401–405, 2006.
10. Pieraccini, M., G. Luzi, and C. Atzeni, “Terrain mapping by ground-based interferometric radar,” *IEEE Transactions on Geoscience and Remote Sensing*, Vol. 39, No. 10, 2176–2181, 2001.
11. Thompson, P., M. Nannini, and R. Scheiber, “Target separation in SAR image with the MUSIC algorithm,” *Proceedings of IEEE International Geoscience and Remote Sensing Symposium, IGARSS 2007*, 468–471, Barcelona, Spain, Jul. 23–28, 2007.
12. Schmidt, R. O., “Multiple emitter location and signal parameter estimation,” *IEEE Transactions on Antennas and Propagation*, Vol. 34, No. 3, 276–280, 1986.
13. Ermolaev, V. T., A. A. Mal’tsev, and K. V. Rodyushkin, “Statistical characteristics of the AIC and MDL criteria in the problem of estimating the number of sources of multivariate signals in the case of a short sample,” *Radiophysics and Quantum Electronics*, Vol. 44, No. 12, 977–983, 2001.
14. Marple, Jr., S. L., *Digital Spectral Analysis: With Applications*, Prentice-Hall, Englewood Cliffs, N.J., 1987.

Bioradar in Study of Low-power Radio Frequency Radiation Influence on Sleep of Laboratory Animals

L. N. Anishchenko, E. S. Gaysina, and I. L. Alborova

Remote Sensing Laboratory, Bauman Moscow State Technical University, Russia

Abstract— At present study we investigate the possibility of low-power radio frequency electromagnetic fields influence on physiological parameters of biological objects. A specially designed complex which allows generating low-power radio frequency signals with different types of modulation and remote measuring of biological object vital signs is described. The experimental data analysis reveals that respiration frequency increases in RF exposure conditions compared with non-exposure conditions ($p < 0.05$, Wilcoxon-test).

1. INTRODUCTION

At present an influence of low-power radio frequency (RF) electromagnetic fields on physiological parameters of biological objects is of high interest because the number of RF sources, which surrounds us in everyday life, is increasing. It is known that electromagnetic radiation exceeding some levels may have negative effect on biological objects. In publication the information about the parameters of radiating signal (power level, modulation type, frequency range, etc.) and the effects it causes is controversial [1, 2].

In past safety standards differed greatly from one country to another. For the USSR the standard was $10 \mu\text{Wcm}^{-2}$ for 2 h exposure per a day, for the U.S. it was 3 orders higher (10mWcm^{-2}). The origin of such huge differences was caused by a fact that the USSR standards took into account non-thermal effects of electromagnetic radiation and the U.S. ones considered only thermal effects [3]. At present the difference in standard is not so big, however they are still present.

Usually in studies of low-power RF radiation influence on biological objects mobile phones with different standards (GSM, GPRS, EDGE) are used as a sources of radiation [4]. That fact limits the variety of tested frequency ranges and modulation types.

Another limitation of studies carried out till present is post experimental estimation of vital signs of the biological object, that neglects all effects which may occur in time of applying radiation and disappear immediately after it. Moreover, even in case of monitoring vital signs during the exposure only contact sensors were used, which may have an influence on the results of the experiments.

In present work the technique that allows investigating the influence of RF signals with different frequency range and modulation type on biological objects is described. For remote contactless monitoring of biological object vital signs a method of bioradiolocation [5] is used, which minimizes the influence on the object under examination.

2. EXPERIMENTAL INSTALLATION

In experimental studies a specially designed complex, which allows generating low-power RF signals with different types of modulation and remote measuring of biological object vital signs, was used. It consists of two main blocks. Block #1 generates RF in frequency range from 1 to 20 GHz with different types of modulation and RF output lower than 3 mW. Parameters of RF modulation can be changed by an operator, who through DAC and its software gives out desired pattern to the modulator. Block #2 measures remotely the vital signs of a biological object. Scheme of the experimental procedure is presented in Figure 1.

Block #1 of the complex consists of RF synthesizer (we used FSW-0020, Phaze Matrix), modulator and radiating horn antenna. Modulator was designed by using microwave amplifier HMC326MS8G (Hittite Microwave Corporation).

For remote monitoring of biological vital signs we used a multi-frequency radar BioRASCAN-14 [6] with quadrature receiver designed at the Remote Sensing Laboratory (Bauman Moscow State Technical University). The radar has following technical characteristics:

- Number of frequencies 8
- Sampling frequency 52.5 Hz
- Operating frequency band 13.8–14.2 GHz
- Distance space resolution 0.5 m
- Recording signals band 0.03–10 Hz

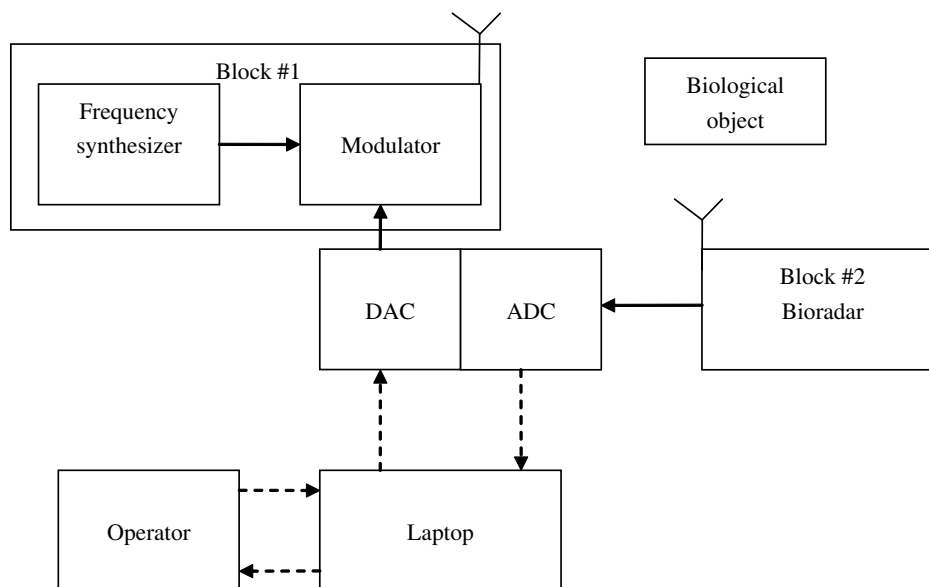


Figure 1: Scheme of the experimental procedure.

Dynamic range of the recorded signals 60 dB

This radar may be applied for distant monitoring of movement activity, respiration and heartbeat patterns of different biological objects.

Two rats (female, 4 month old each) were used as biological objects in the experiments. The complex for RF exposure and the bioradar were located at the distance of 0.5–1.0 m from a plastic box with a sleeping rat inside. For each rat, 30 records of received bioradar signals were collected for each of simulated experimental conditions (with and without additional modulated RF exposure). As a modulating signal we used harmonic wave with the frequency of 1 Hz, which is about the respiration frequency of a sleeping rat, the amplitude of the signal was 1 V. The duration of each record was not shorter than 3 hours. All experiments were conducted for the same light conditions to prevent the influence of a circadian rhythm on the experimental results.

3. RESULTS OF THE EXPERIMENTS

In this section the results of the experiments are presented. In Figure 2 record of radar signals reflected from the animal is shown. The fragment duration is 10 minutes. It is clearly seen that periods of movements with high amplitude of the pattern alternate with the calm state which corresponds to the lower amplitude of the recorded signal. For calm state, which occur if the animal was sleeping or resting, in bioradar signal the respiration pattern of the animal can be clearly seen (see insert in Figure 2).

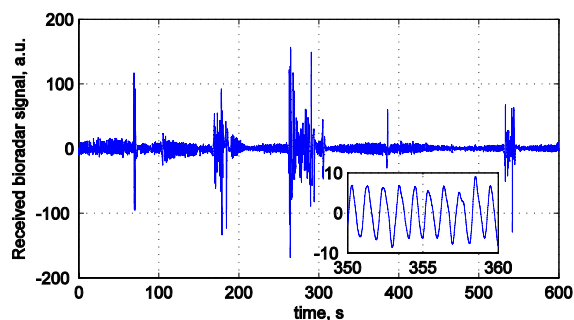


Figure 2: Radar signal reflected from an animal. The inset shows the signal over the interval [350, 360] s.

Experimental data were analyzed by using the algorithm introduced in [7]. Although the algorithm was designed for analyzing bioradar data for a sleeping human it can be also used for processing bioradar data in present case. For each bioradar record mean value of respiration frequency and total duration of movements artifacts were used for comparison of the data in different

experimental conditions (with and without RF exposure).

For rat #1 the respiration frequency is 62 ± 2 (mean \pm SD) and 71 ± 3 acts per minute for experiments without and with RF exposure conditions, respectively. For rat #2 the respiration frequency for same conditions were 81 ± 3 and 95 ± 3 acts per minute. Due to the fact that experimental data for both rats do not come from a normal distribution for their comparison in case of presence and absence of an additional RF exposure conditions Wilcoxon criteria was used, which indicated that respiration frequency increased in RF exposure conditions compared with non-exposure conditions ($p < 0.05$, Wilcoxon-test).

4. CONCLUSIONS

At present study we investigate the possibility of low-power RF electromagnetic field influence on physiological parameters of biological objects. A specially designed complex, which allows generating low- power RF signals with different types of modulation and remote measuring of biological object vital signs, was designed. The experimental data analysis reveals that respiration frequency increases in RF exposure conditions compared with non-exposure conditions ($p < 0.05$, Wilcoxon-test). Some limitations of our study should be noted. The study is limited by data peculiarities. The dataset is quite small and male/female ratio is imbalanced. Thus, the results should be accepted with caution.

The future activity will be directed towards expanding the data set and investigating the influence of parameters of RF-modulation on the vital signs of animals (in addition to the respiration frequency it is supposed to analyze changes in movement activity pattern). The research will be focused on the usage of a biologically informative modulation, which should impose on vital signs of the examinee according to several literature sources [8, 9].

ACKNOWLEDGMENT

This research has been supported by grants of the President of Russian Federation (MK-889.2014.9) and of Russian Foundation for Basic Research (#13-07-00248A).

REFERENCES

1. Adair, R. K., "Biophysical limits of athermal effects of rf and microwave radiation," *Bioelectromagnetics*, Vol. 24, 39–48, 2003.
2. Stewart, W., "Power density: Radio frequency non-ionizing radiation," *Mobile Phone and Health: A report from the Independent Expert Group on Mobile Phones*, The Stewart Report, 2000, URL: http://www.hese-project.org/hese-uk/en/niemr/power_density_effects.pdf
3. Vorst, A., A. Rosen, and Y. Kotsuka, *RF/Microwave Interaction with Biological Tissues*, 134–136, IEEE PRESS, Wiley-Interscience, 2006.
4. Croft, R. J., et al., "Effects of 2G and 3G mobile phones on human alpha rhythms: Resting EEG in adolescents, young adults, and the elderly," *Bioelectromagnetics*, Vol. 31, 434–444, 2010.
5. Anishchenko, L. N., S. I. Ivashov, and I. A. Vasiliev, "A novel approach in automatic estimation of rats' loco-motor activity," *Proc. SPIE 9077, Radar Sensor Technology XVIII*, 90771M, 1–8, Baltimore, USA, May 2014.
6. <http://www.rslab.ru/english/product/biorascan/>.
7. Tataraidze, A., L. Anishchenko, M. Alekhin, L. Korostovtseva, and Y. Sviryaev, "Estimation of respiratory rhythm during night sleep using a bio-radar," *Proc. SPIE 9077, Radar Sensor Technology XVIII*, 90770Z, 1–6, Baltimore, USA, May 2014.
8. Schmid, M. R., et al., "Sleep EEG alterations: Effects of different pulse-modulated radio frequency electromagnetic fields," *J. Sleep Re.*, Vol. 21, 50–58, 2012.
9. Hinrukus, H., et al., "Effect of modulated microwave radiation on electroencephalographic rhythms and cognitive processes," *Estonian Journal of Engineering*, Vol. 14, No. 2, 91–106, 2008.

Resonant Micro-strip Lines Analog to Electromagnetically Induced Transparency

Ben Yi Wang¹, Teh-Chau Liou^{1,2}, Jian Qi Shen³, and Shun-Feng Su²

¹Department of Electronic Engineering

Zhejiang Industry & Trade Vocational College, Wenzhou, Zhejiang 325003, China

²Department of Electrical Engineering

National Taiwan University of Science and Technology, Taipei 10607, Taiwan

³Centre for Optical and Electromagnetic Research, East Building No. 5

Zijingang Campus, Zhejiang University, Hangzhou 310058, China

Abstract— Electromagnetically induced transparency (EIT) observed in three-level atomic vapor media is a coherent quantum process whose optical response to a laser beam is modified by a second beam with a well-determined detuning. In references, some classical analogs to EIT have been presented. We propose a microstrip transmission line structure to mimic the optical behavior of a three-level Lambda type EIT phenomenon. This research may enable us to understand how the quantum coherence works in real atomic vapor experiments.

1. INTRODUCTION

Quantum coherent control effects realized via atomic phase coherence, such as three-level Lambda-type electromagnetically induced transparency, have captured interest of many researchers over the last decades [1]. EIT is such a quantum optical phenomenon, in which a resonant laser beam (probe field) incident into a medium (e.g., an rubidium atomic vapor) will get absorbed (i.e., the medium is opaque), while if there is a second resonant laser beam (control field) simultaneously incident inside the same medium, neither would be absorbed, and the medium would become transparent. There are a number of phenomena that are relevant to EIT, including multi-photon population trapping [2], inversionless light amplification [3], phase coherence control [4, 5] and cancellation of spontaneous emission [6].

Here we shall address the intriguing optical behavior of a three-level EIT atomic vapor. Consider a Lambda-configuration three-level atomic system with two lower levels $|1\rangle$, $|2\rangle$ and one upper level $|3\rangle$ (see Figure 1 for the schematic diagram of the three-level EIT system). This atomic system interacts with the electric fields of the probe and control light waves, which drive the $|1\rangle$ – $|3\rangle$ and $|2\rangle$ – $|3\rangle$ transitions, respectively. Such a three-level system can be found in metallic alkali atoms (e.g., Na, K, and Rb) [7]. The density matrix elements of the three-level atomic system is given by [7]

$$\begin{aligned}\frac{d\rho_{31}}{dt} &= -(\Gamma_3 + i\Delta_p)\rho_{31} + \frac{i\Omega_c}{2}\rho_{21} + \frac{i\Omega_p}{2}\rho_{11}, \\ \frac{d\rho_{21}}{dt} &= -[\gamma_2 + i(\Delta_p - \Delta_c)]\rho_{21} + \frac{i\Omega_c^*}{2}\rho_{31}.\end{aligned}\tag{1}$$

Here, Γ_3 and γ_2 stand for the spontaneous emission decay rate and the collisional dephasing rate, respectively. Ω_c and Ω_p denote the Rabi frequencies of the control field and the probe field. They are defined by $\Omega_c = \wp_{32}E_c/\hbar$ and $\Omega_p = \wp_{31}E_p/\hbar$ with E_c and E_p the slowly-varying amplitudes (envelopes) of the control field and the probe field, respectively. The frequency detunings of the two applied optical fields are defined as $\Delta_p = \omega_{31} - \omega_p$, $\Delta_c = \omega_{32} - \omega_c$ with ω_p and ω_c the mode frequencies of the probe field and the control field, respectively. In general, the population (ρ_{11}) in the ground level $|1\rangle$ is almost unity (i.e., $\rho_{11} \rightarrow 1$ and $\rho_{23} = \rho_{33} = 0$) [7].

We shall now concentrate our attention on the influence of the external control field on the three-level atomic population, which is analyzed based on the concepts of *quantum interference* and *dark states*. The three-level EIT occurs when the condition, $\Delta_p = \Delta_c$, of two-photon resonance is fulfilled. One can see from the second equation in (1) that the upper level $|3\rangle$ would be empty, i.e., the steady solution $\rho_{31} \rightarrow 0$. Thus, the two lower levels $|1\rangle$, $|2\rangle$ of the three-level system would form a dark state, i.e., $\Omega_c\rho_{21} + \Omega_p\rho_{11} = 0$ (destructive quantum interference). This, therefore, means that the probability amplitudes of levels $|1\rangle$ and $|2\rangle$ are $N\Omega_c$ and $-N\Omega_p$, respectively, and the dark

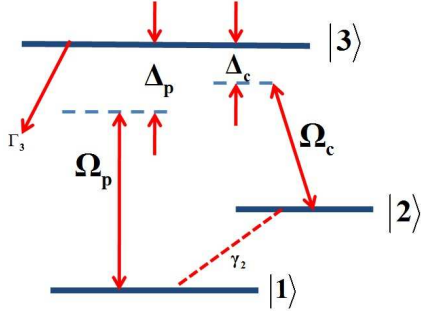


Figure 1: The schematic diagram of a three-level EIT atomic system. The control and probe laser beams drive the $|2\rangle-|3\rangle$ and $|1\rangle-|3\rangle$ transitions, respectively.

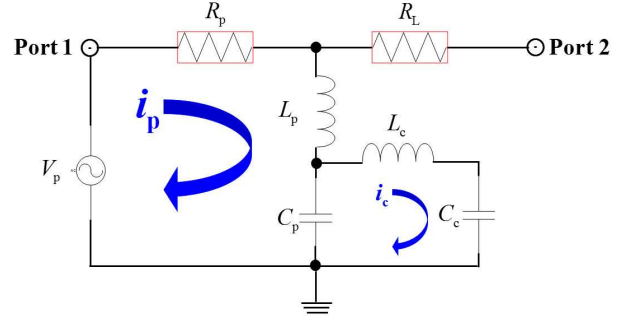


Figure 2: The circuit analog of the three-level quantum coherent effects. The circuit loop containing L_p, C_p corresponds to the $|1\rangle-|3\rangle$ transition pathway in the atomic system. The circuit loop on the bottom-right area is the analog of the $|2\rangle-|3\rangle$ atomic transition pathway.

state of the atomic system is given by $|\text{Dark}\rangle = N(\Omega_c|1\rangle - \Omega_p|2\rangle)$ with the normalized coefficient $N = 1/\sqrt{\Omega_c^*\Omega_c + \Omega_p^*\Omega_p}$. The minus sign in the dark state $|\text{Dark}\rangle$ represents an effect of destructive quantum interference between the two transition pathways $|1\rangle \rightarrow |3\rangle$ and $|2\rangle \rightarrow |3\rangle$. This leads to the effect of *electromagnetically induced transparency* to the probe field, since there is no effective interaction between the dark state and the applied fields (control and probe fields) [1], and hence no net transition from the ground level $|1\rangle$ to the upper level $|3\rangle$ occurs (i.e., $\rho_{31} \rightarrow 0$). Therefore, the multilevel atomic coherence (various quantum interference effects) can be controllably manipulated by adjusting the intensities (or the Rabi frequencies) of the control field.

EIT is a quantum coherent effect. In many classical systems, however, such an effect can be mimicked. Since a simple oscillating system (e.g., a RLC circuit and a spring oscillator) can simulate a two-level atomic system, and a coupled oscillating system (e.g., coupled circuits and double-spring oscillators) can exhibit some resonance behavior of three-level atomic system. In the literature, schemes based on optical and photonic scenarios, such as planar metamaterial analogue of EIT for plasmonic sensing, plasmonic analog of EIT, circuit analog of EIT as well as EIT-like effect in micromechanical resonators [8], have been suggested or experimentally demonstrated. Here we shall suggest a scenario of employing microstrip lines to mimic the EIT effect.

2. CIRCUIT ANALOG OF A THREE-LEVEL ATOMIC SYSTEM

Before we design the microstrip line analog of EIT, we shall address a circuit analog of the above quantum interference effect [8]. The dynamical behavior of the two-loop circuit (shown in Figure 2) is governed by

$$\begin{aligned} \frac{d^2 i_p}{dt^2} &= -\frac{R_p}{L_p} \frac{di_p}{dt} - \frac{1}{L_p C_p} i_p + \frac{1}{L_p C_p} i_c + \frac{1}{L_p} \frac{dV_p}{dt}, \\ \frac{d^2 i_c}{dt^2} &= -\frac{1}{L_c} \left(\frac{1}{C_p} + \frac{1}{C_c} \right) i_c + \frac{1}{L_c C_p} i_p. \end{aligned} \quad (2)$$

It can be easily found that the mathematical structure of the circuit Equation (2) is analogous to that of the density matrix Equation (1) of the three-level atomic system: specifically, we can have the relations $i_p \rightarrow \rho_{31}$, $i_c \rightarrow \rho_{21}$, and $1/C_c \rightarrow \Omega_c$. The term of dV_p/dt , i.e., the voltage signal source, corresponds to the Rabi frequency, Ω_p , of the probe field. For the circuit analog of the two- or three-level atomic system as shown in Figure 2, one can conclude that the curve of the parameter $20 \log |S_{21}|$ in the circuit analog of the two-level system (i.e., the simple $R_p L_p C_p$ circuit) has only one cuspidate point (a downward peak) indicating two-level resonant absorption, while in the circuit analog of three-level systems, there would be two downward cuspidate points [8]. These downward peaks can be interpreted as the ‘‘Autler-Townes effects’’. Since the circuit composed of two resonators ($L_p C_p, L_c C_c$) via capacitor coupling has one Autler-Townes doublet, there is only one EIT transparency window between the two downward cuspidate points in Autler-Townes doublet (corresponding to the circuit analog of the three-level system). This classical EIT-like RLC circuit can be viewed as the basis for designing the EIT-like microstrip lines.

3. IMPLEMENT USING TWO RESONANT MICROSTRIP LINES WITH RADIAL STUBS

The applied substrate is made up of GaAs whose relative dielectric constant is 12.9 and loss tangent is 0.0002 (See Figure 3). The microstrip line has width of 0.140473 mm, different length (in mm) for attenuation element (equivalent to a resistor, while its length is equal to half wavelength) and oscillator element (equivalent to an inductor, while its length is less than a quarter wavelength) for achieving $50\ \Omega$ characteristic impedance, 7.054 effective dielectric constant and 0.003 mm skin depth from the line surface when working at 2 GHz frequency.

The analog to the three-level system is set up by two resonant microstrip lines OSC1(See Fig-

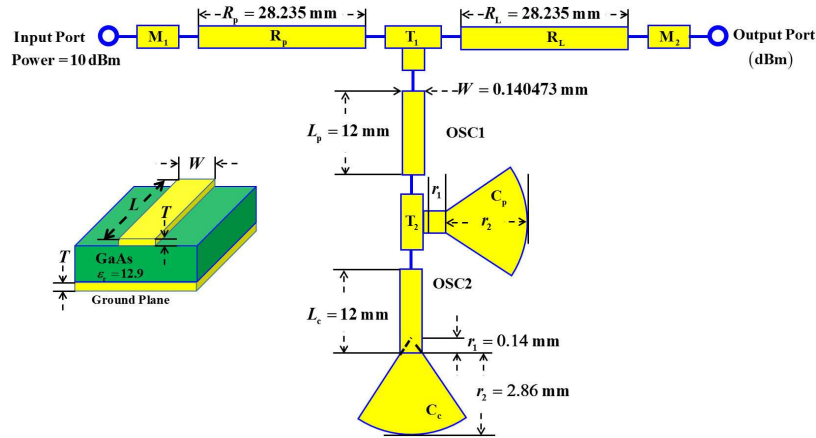


Figure 3: Scheme of EIT-like two resonant microstrip line structure. The upper one resonant microstrip line serves as the oscillator OSC1 and the lower one as the oscillator OSC2.

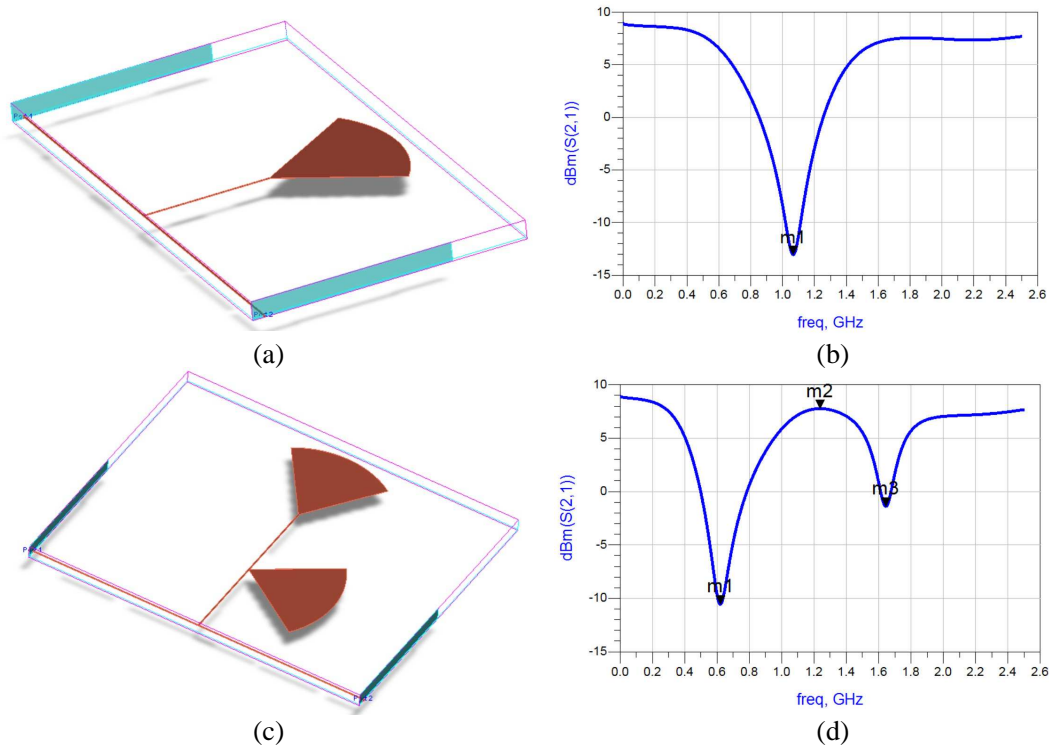


Figure 4: (a) OSC1 (an analog for a two-level atomic system). (b) A downward peak ($m_1 = (1.07, -13)$) can be found in OSC1. (c) OSC1 and OSC2 are serially connected, performing as the analog for a three-level atomic system, in which OSC2 acts as a role of modifier of OSC1. (d) Two downward peaks $m_1 = (0.6, -10.5)$ and $m_3 = (1.7, -1.5)$ corresponding to the Autler-Townes doublet are found, and one upward peak ($m_2 = (1.2, 7.8)$) corresponding to the transparency point can be acquired.

ure 4(a)) and OSC2 (See Figure 4(c), in which OSC2 has been serially connected with OSC1) using two fan-shape opened capacitive lines (i.e., two radial opened stubs). The first one resonator (i.e., OSC1) is configured by one straight microstrip line (i.e., L_p) and one series radial opened capacitance (i.e., C_p). The second resonator (i.e., OSC2) is configured by another straight microstrip line (i.e., L_c) and serially connected with another one radial opened capacitance (i.e., C_c). Combining the left-side-input port, the two resonant microstrip lines (located between the input loop and the output loop) and right-side-output port, the whole microstrip line circuit analog to EIT material is achieved. We point out that the left one straight microstrip line near the input port performs as a decaying factor (which corresponds to the spontaneous emission decay rate Γ_3 in the atomic system shown in Figure 1) and the right one (near the output port), of which the location is placed as the part-layout on microstrip line substrate for symmetry layout design with half-left amplitude, performs as attenuation factor in practice. At the input port, 10 dBm power (i.e., 10 milliwatt) is provided. Each quantity in this paper is all in dBm and acquired via s_{21} parameter for consistency and simplicity.

By adjusting the length to be the multiplication of $\lambda/2$ at the working frequency (i.e., 2 GHz), one can get an insertion loss performing as the spontaneous emission decay in the atomic system (i.e., $R_p \rightarrow \Gamma_3$). A section of micro-strip line with length scale smaller than a quarter wavelength (behaving as an inductor, L_p) is connected to a radial open stub with 3 mm axis length (behaving as a capacitor, C_p), and one can acquire a resonant microstrip line and the analog of the two-level atomic system (See Figure 4(a)). One can see a dip (downward peak, -13.048 dBm @ 1.067 GHz) corresponding to the largest absorption (See Figure 4(b)). For the three-level atomic system, two resonant microstrip lines are cascaded connected together (See Figure 4(c)). Thus, there are two downward peaks m_1 (-10.531 dBm @ 0.621 GHz) and m_3 (-1.514 dBm @ 1.657 GHz) corresponding to the Autler-Townes doublet and one upward peak m_2 (7.774 dBm @ 1.237 GHz) corresponding to the transparency point (See Figure 4(d)).

4. CONCLUSIONS

Two resonant microstrip lines can be designed for mimicking the EIT effect. One resistor line plays the role of the spontaneous emission decay of the excited state $|3\rangle$ in the three-level atomic system, two inductive lines and two capacitive radial stubs are utilized to realize two oscillators to act as the $|3\rangle-|1\rangle$ and $|3\rangle-|2\rangle$ transition frequencies, respectively. The higher quality factors of two resonators may make the transparency windows wider. Further relevant topics (such as quick intelligent floppy control on control field for EIT material or periodical layers of combination of dielectric and EIT material) will be investigated in the near future.

ACKNOWLEDGMENT

This work is supported by National Science Council of Taiwan under Grant No. NSC 101-2221-E-011-064-MY3 and National Taiwan University of Science and Technology Top University Plan under Grant No. 103TY9305. This work is also supported in part by the National Natural Science Foundations of China under Grants Nos. 11174250 and 91233119.

REFERENCES

1. Harris, S. E., "Electromagnetically induced transparency," *Phys. Today*, Vol. 50, No. 7, 36–42, 1997.
2. Champenois, C., G. Morigi, and J. Eschner, "Quantum coherence and population trapping in three-photon processes," *Phys. Rev. A*, Vol. 74, 053404, 2006.
3. Cohen, J. L. and P. R. Berman, "Amplification without inversion: Understanding probability amplitudes, quantum interference, and Feynman rules in a strongly driven system," *Phys. Rev. A*, Vol. 55, 3900–3917, 1997.
4. Zheltikov, A. M., "Phase coherence control and subcycle transient detection in nonlinear Raman scattering with ultrashort laser pulses," *Phys. Rev. A*, Vol. 74, 053403, 2006.
5. Gandman, A., L. Chuntunov, L. Rybak, and Z. Amitay, "Coherent phase control of resonance-mediated $(2 + 1)$ three-photon absorption," *Phys. Rev. A*, Vol. 75, 031401, 2007.
6. Zhu, S. Y. and M. O. Scully, "Spectral line elimination and spontaneous emission cancellation via quantum interference," *Phys. Rev. Lett.*, Vol. 76, 388–391, 1996.
7. Scully, M. O. and M. S. Zubairy, *Quantum Optics*, Chapter 7, Cambridge University Press, Cambridge, UK, 1997.

8. Chen, X., X. M. Leng, J. X. Li, Y.-T. Yeh, T.-C. Liao, J. Q. Shen, Y.-H. Kao, and T.-J. Yang, “Experimental verification of circuit analog of three- and four-level electromagnetically induced transparency,” *Adv. Mater. Res.*, Vols. 415–417, 1340–1349, Switzerland, 2012, and References therein.

Broadband Slotted Bow-tie Antennas for Terahertz Resonant Tunnelling Diode Based Oscillators

Khalid Hamed Alharbi, Afesomah Ofiare, Jue Wang,
Monageng Kgwadi, Ata Khalid, and Edward Wasige

High Frequency Electronics Group, School of Engineering, University of Glasgow
Oakfield Avenue, G12 8LP Glasgow, Scotland, UK

Abstract— A broadband slotted bow-tie antenna is presented. The antenna is fed by coplanar waveguide (CPW) and fabricated on an InP substrate for same chip integration with the promising resonant tunnelling diode (RTD) terahertz (THz) oscillator which has the capability of room temperature operation and with relative high power. The antenna exhibits a very wide bandwidth (return loss $S_{11} < -10$ dB) around the design frequency (300 GHz). However, due to the large dielectric constant of the InP substrate, most of the radiation is directed into the substrate. To re-direct the energy into air, a bow tie antenna employing a reflector ground plane underneath a thin substrate of low dielectric constant is presented. Initial simulation results of this technique are reported and experimental validation at lower frequency (17 GHz) shows the feasibility of the concept.

1. INTRODUCTION

Terahertz (THz) radiation, whose frequency range lies between millimetrewaves and infrared light in the electromagnetic spectrum has many potential applications in different scientific fields such as medical diagnostics, security imaging, and wireless communication [1–3]. Resonant tunnelling diode (RTD) based THz oscillators in integrated circuit (IC) form have recently been shown to be the technology in which many of these applications could be implemented [4, 5]. They operate at room temperature and have the potential to produce output power of around 1 mW at these frequencies [6].

An efficient antenna is a key element to couple the THz radiation into free space. A high gain and directive antenna is preferable in order to radiate most of the RF power into specific direction and, as a consequence, offer larger coverage distance. RTD THz oscillators employing integrated slot antennas [4] and planar horn antennas [7] have been demonstrated. The slot antenna is a resonant antenna with infinity input impedance at the centre of the slot and zero at the edges. For antenna dimensions of a few microns (at THz frequencies), proper impedance matching for this antenna is difficult. The planar horn antenna, on the other hand, radiates the signal energy along the substrate, whilst radiation perpendicular to the substrate would be more desirable [8]. An elevated patch antenna was proposed to suppress the substrate effects, however, the bandwidth still narrow [9].

This paper describes a bow-tie slot antenna designed for operation at 300 GHz. This antenna has a controlled input impedance of 50 Ohms. The bow-tie slot antenna is also compatible with the novel power combining RTD oscillator circuits being developed in the group [10]. Most of the radiation in the present design is directed into the substrate due to the large dielectric constant of the Indium Phosphide (InP) substrate [11]. A practical and common solution to this problem has been to use a hemispherical lens on the backside of the substrate to extract the RF power and increase the antenna gain [12–17]. Instead of using lenses, a promising alternate realisation to have most of the energy radiated away from the substrate is proposed and described in this paper. It employs a reflector ground plane underneath a thin substrate of low dielectric constant which can be spun on the top of the high dielectric constant substrate. The ground plane acts as a reflector and also isolates the high dielectric constant substrate from the high frequency radiation. The frequency of 300 GHz has been suggested for applications such as short-link and medium-link wireless communication systems. This is mainly due to the fact that it is unregulated and in moderate atmospheric attenuation band [18].

2. BOW-TIE ANTENNA ON HIGH DIELECTRIC CONSTANT SUBSTRATE

2.1. Antenna Design

A bow-tie antenna is a simple version of planar slot antennas which can offer large bandwidth. A simple CPW-fed bow-tie antenna adopted in this work was proposed in Reference [19]. Fig. 1 shows the geometry of the adopted design.

For a desired operating frequency, the dimensions (a), (b), (L), and (W) are calculated as follow:

$$a = 1.6\lambda_0/\sqrt{\epsilon_r} \quad (1)$$

$$b = 0.5\lambda_0/\sqrt{\epsilon_r} \quad (2)$$

$$L = a/0.85 \quad (3)$$

$$W = b/0.45 \quad (4)$$

The antenna was designed to operate at 300 GHz on a semi-insulating Indium Phosphide (InP) substrate with dielectric constant of $\epsilon_r = 12.56$. Thus, the dimensions a , b , L , and W are $451.5 \mu\text{m}$, $141 \mu\text{m}$, $531 \mu\text{m}$, and $313.5 \mu\text{m}$, respectively. The CPW line dimensions ($g = 20 \mu\text{m}$ and $s = 13.8 \mu\text{m}$) were calculated to give a 50Ω characteristic impedance. The conducting element is made of $0.4 \mu\text{m}$ thick gold and patterned on the top of the substrate. The antenna was simulated in HFSS simulation package which employs finite element method to solve Maxwell's equations. The antenna was fed by a waveport assigned to a rectangular patch facing the substrate side and the edge of the CPW metals.

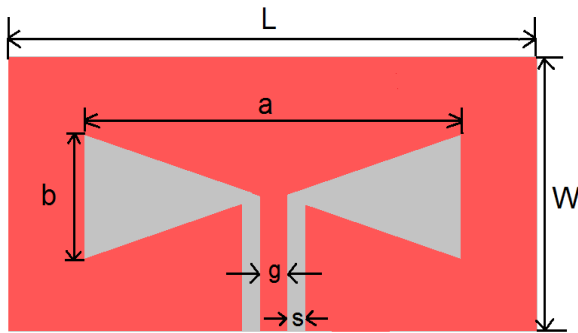


Figure 1: The geometry of the adopted bow-tie antenna [19].

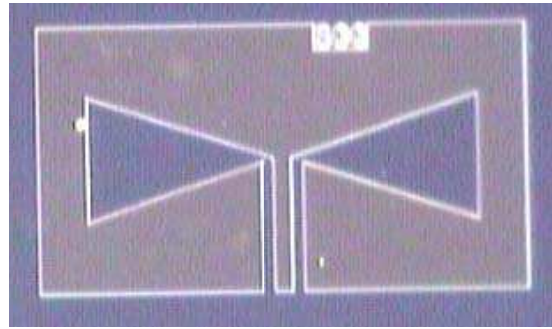


Figure 2: The fabricated bow-tie antenna.

2.2. Antenna Fabrication

The antenna was fabricated using electron beam lithography process. Electron beam resist PMMA was used. The spun PMMA on the InP sample was baked for 3 minutes at 160°C , followed by e-beam pattern writing using Vestec VB6 beam writer. After development in 1:1 IPA:MIKB, Ti/Au (20 nm/400 nm) metal scheme was deposited using an electron beam evaporator followed by lift-off in acetone. Fig. 2 is a micrograph of one of the fabricated antennas.

2.3. Results and Discussion

The antenna was measured using a J-band (220–325 GHz) Cascade Microtech millimeter wave vector network analyzer (VNA) with G-S-G infinity probes. The VNA was calibrated for 2-port S -parameter measurements using the short-open-load-thru (SOLT) two port calibration process on a Cascade impedance substrate standard. Fig. 3 shows the measured and simulated return loss of the designed bow-tie antenna. The bandwidth spans almost the entire frequency band from 220–325 GHz. This bandwidth is by far larger than that obtained from microstrip antennas. The discrepancy between the measured and simulated results can be attributed to unwanted signal reflections from surrounding objects during measurements.

The simulated radiation pattern is shown in Fig. 4. Due to the large dielectric constant of the InP substrate, most of the radiation is directed towards the substrate. This is a common problem with antennas fabricated on high dielectric constant substrates and requires a practical solution in order to enable air-side radiation [11]. A practical solution to this problem has been to use a hemispherical lens on the backside to collect the power from the bottom side of the substrate [12–17]. Our current work (Section 3) aims at designing antennas that can be integrated with RTD THz IC oscillators and which radiate into the air perpendicular to the substrate, to realise compact sources.

3. GROUNDED BOW-TIE ANTENNA ON THIN AND LOW DIELECTRIC CONSTANT SUBSTRATE

One possible way to achieve air side radiation is through employing a (thin) substrate of low dielectric constant and with a ground plane on the bottom side of the substrate to reflect the radiation upwards. The substrate used is benzocyclobutene (BCB) with dielectric constant $\epsilon_r = 2.6$. This substrate is realised by spinning it, for instance, on a carrier substrate such as InP substrate with a coating of metallisation to act as the ground plane and so isolate the high permittivity InP substrate from the high frequency radiation. The antenna dimensions were calculated following the same procedure described above with the difference that the substrate is grounded (ground plane is placed on the bottom side of the BCB substrate to act as a reflector). Therefore, the CPW dimensions (g and s) have to be calculated to get 50Ω characteristic impedance grounded-CPW line (GCPW). In initial investigations, the aim was to establish the thinnest possible BCB thickness that could provide acceptable performance and allow for simple fabrication processes. Through simulations, it was found that the antenna using a BCB thickness of $50 \mu\text{m}$ (designed for 300 GHz) gives acceptable performance. The simulated return loss for the antenna is shown in Fig. 5.

It can be seen that the antenna bandwidth extends from around 316 GHz to 338 GHz (for return loss less than -10 dB). The 3D radiation pattern of the antenna (at 321 GHz) is shown in Fig. 6. The proposed antenna exhibits unidirectional radiation with single major lobe and radiates toward the air side (perpendicular to the substrate) which proves the advantages of both the low dielectric constant material and the ground plane placed on the bottom side of the BCB substrate. The 2D radiation patterns in the xz -plane and yz -plane are shown in Figs. 7 and 8, respectively. The front-to-back ratio (FBR) is about 12 dB and the beamwidth of the antenna is about 50° in the xz -plane and 60° in yz -plane. The antenna gain is 8.3 dB and the radiation efficiency is 95.6%.

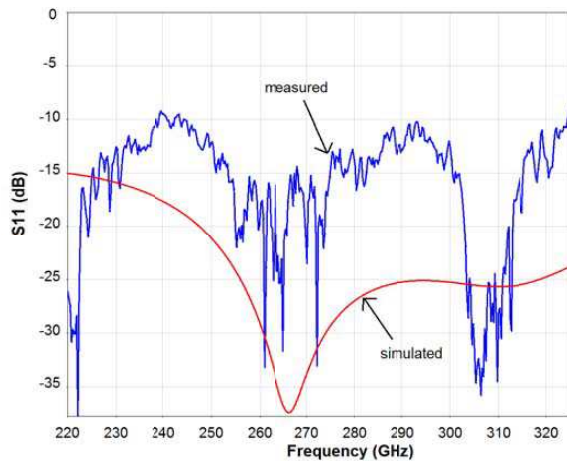


Figure 3: Return loss of the bow-tie antenna on InP substrate.

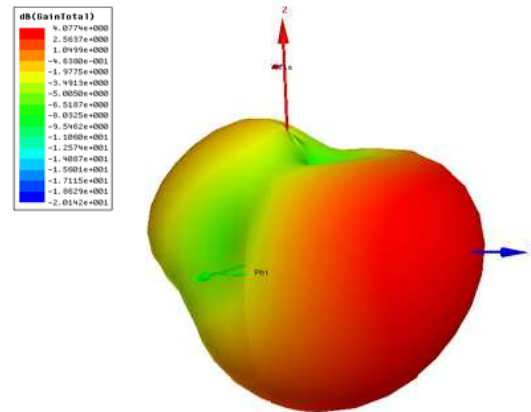


Figure 4: Radiation pattern of the bow-tie antenna on InP substrate at 300 GHz.

4. EXPERIMENTAL VALIDATION OF THE PROPOSED CONCEPT

Experimental validation of the proposed concept includes designing grounded bow-tie antenna using the Rogers substrate of thickness $762 \mu\text{m}$ at lower frequency so the antenna can be measured in the anechoic chamber in the University of Glasgow which can measure radiation pattern of antennas up to around 20 GHz. The first step is to determine the frequency of operation. In the previous design (bow tie on $50 \mu\text{m}$ BCB at 321 GHz) the $50 \mu\text{m}$ is found to be:

$$0.08\lambda_0/\sqrt{\epsilon_r} = 50 \mu\text{m} \tag{5}$$

where $\epsilon_r = 2.6$ (the dielectric constant of the BCB), and λ_0 is the free space wavelength at 321 GHz.

Now, to determine the frequency for the $762 \mu\text{m}$ Rogers ($\epsilon_r = 3.48$), we have:

$$0.08\lambda_0/\sqrt{\epsilon_r} = 762 \mu\text{m} \tag{6}$$

$$\lambda_0 = \frac{762 \times 10^{-6} \sqrt{3.48}}{0.08} \tag{7}$$

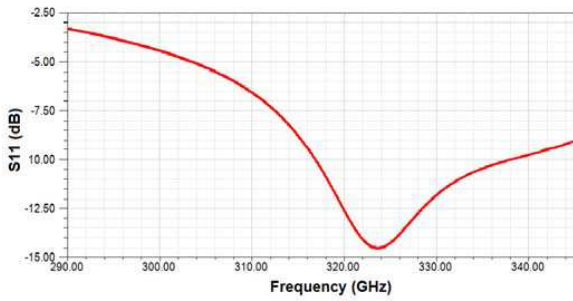


Figure 5: Return loss of the bow-tie antenna on 50 μm thick grounded BCB substrate.

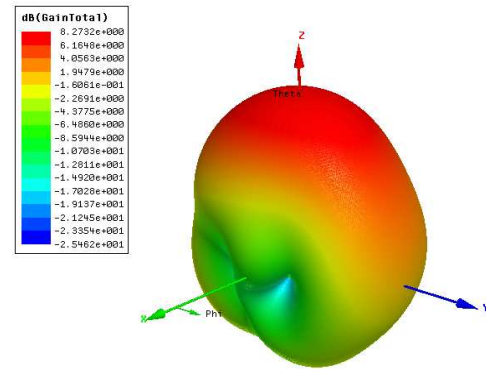


Figure 6: Radiation pattern of the proposed bow-tie antenna on 50 μm thick grounded BCB substrate at 321 GHz.

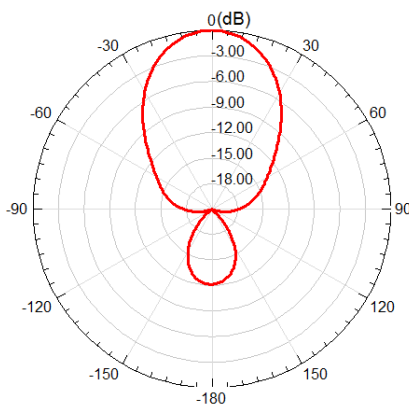


Figure 7: 2D radiation pattern of the proposed bow-tie antenna on 50 μm thick grounded BCB substrate at 321 GHz (*xz*-plane).

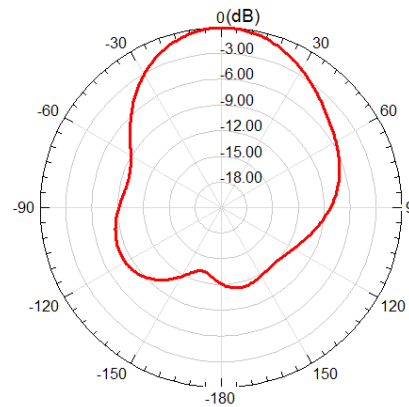


Figure 8: 2D radiation pattern of the proposed bow-tie antenna on 50 μm thick grounded BCB substrate at 321 GHz (*yz*-plane).

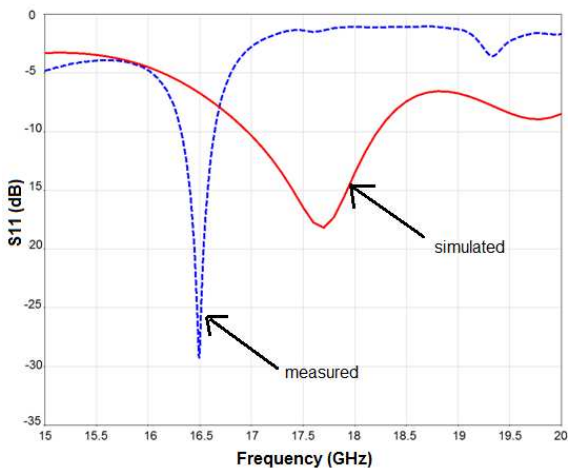


Figure 9: Return loss of the bow-tie antenna on 762 μm thick grounded Rogers substrate.

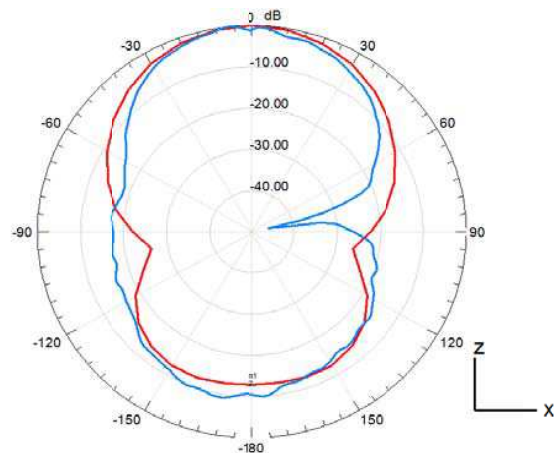


Figure 10: Radiation pattern of antenna at 16.5 GHz in *xz*-plane (Red: Simulation, Blue: Measurement).

Thus, $f_0 = 17$ GHz.

The antenna was then designed for 17 GHz, simulated in HFSS and fabricated for experimental measurements. Fig. 9 shows the return loss of the simulated and measured antennas. It can be seen that the simulation shows resonant at 17.7 GHz ($S_{11} = -18$ dB) while the measurement shows

resonant at 16.5 GHz ($S_{11} = -28$ dB). Radiation patterns at 16.5 GHz are shown in Fig. 10 and Fig. 11. Fig. 12 illustrates the planes at which the patterns were plotted. Simulated and measured pattern in Fig. 10 are in a good agreement with around 10 dB front-to-back ratio. The measured pattern in Fig. 11 (in general) follows the simulated one (at many directions) although the ripples shown which might be caused by unwanted reflections from the SMA connector which is large in size compared to the whole antenna geometry.

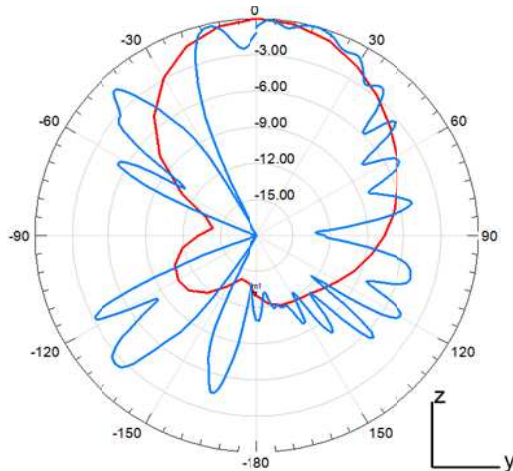


Figure 11: Radiation pattern of antenna at 16.5 GHz in yz -plane (Red: Simulation, Blue: Measurement).

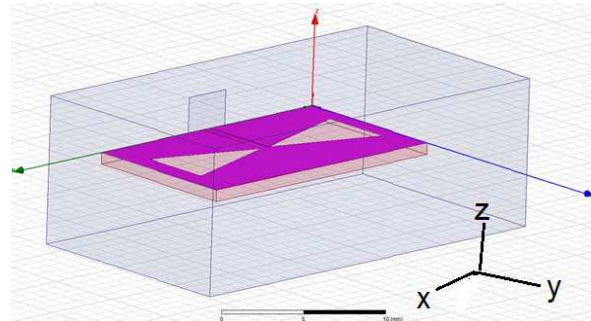


Figure 12: Antenna geometry shows the planes at which the radiation pattern were plotted.

5. CONCLUSION

In this paper, a grounded bow-tie slot antenna for terahertz applications was presented. It offers a known input impedance and radiates into the air perpendicular to the substrate. Future work is focused on integrating this antenna with InP-based RTD THz oscillators.

ACKNOWLEDGMENT

This work was supported in part by the Engineering and Physical Sciences Research Council (EPSRC) under Grant EP/J019747/1.

REFERENCES

1. Tonouchi, M., "Cutting-edge terahertz technology," *Nature Photonics*, Vol. 1, 97–105, 2007.
2. Kleine-Ostmann, T. and T. Nagatsuma, "A review on terahertz communications research," *Journal of Infrared, Millimeter, and Terahertz Waves*, Vol. 32, 143–171, 2011.
3. Liu, H. B., H. Zhon, N. Karpowicz Y. Chen, and X. C. Zhang, "Terahertz spectroscopy and imaging for defense and security applications," *Proceedings of the IEEE*, Vol. 95, 1514–1527, 2007.
4. Shiraishi, M., H. Shibayama, K. Ishigaki, S. Suzuki, M. Asada, H. Sugiyama, and H. Yokoyama, "High output power ($\sim 400 \mu\text{W}$) oscillators at around 550 GHz using resonant tunneling diodes with graded emitter and thin barriers," *Applied Physics Express*, Vol. 4, 2011.
5. Asada, M., S. Suzuki, and N. Kishimoto, "Resonant tunneling diodes for sub-terahertz and terahertz oscillators," *Japanese Journal of Applied Physics*, Vol. 47, 4375–4384, 2008.
6. Wang, J., "Monolithic microwave/millimetrewave integrated circuit resonant tunnelling diode sources with around a milliwatt output power," A thesis submitted in fulfilment for the degree of Doctor of Philosophy, University of Glasgow, 2014.
7. Urayama, K., S. Suzuki, M. Asada, H. Sugiyama, and H. Yokoyama, "Sub-THz RTD oscillators integrated with planar horn antennas for horizontal radiation," *33rd International Conference on Infrared, Millimeter and Terahertz Waves*, 1, Pasadena, Canada, Sep. 15–19, 2008.
8. Okada, K., S. Suzuki, and M. Asada, "Resonant-tunneling-diodeterahertz oscillator integrated with slot-coupled patch antenna," *26th International Conference on Indium Phosphide and Related Materials (IPRM)*, 1–2, Montpellier, May 11–15, 2014.

9. Emhemmed, A. S. and K. Elgaid, “Broadband micromachined microstrip patch antenna for G-band applications,” *European Microwave Conference*, 374–377, Rome, Sep. 29–Oct. 1, 2009.
10. Wang, J., L. Wang, C. Li, B. Romeria, and E. Wasige, “28 GHz MMIC resonant tunnelling diode oscillator of around 1 mW output power,” *Electronics Letters*, Vol. 49, 816–818, 2013.
11. Brown, E. R., C. D. Parker, and E. Yablonovitch, “Radiation properties of a planar antenna on a photonic-crystal substrate,” *Journal of the Optical Society of America B*, Vol. 10, 404–407, 1993.
12. Orihashi, N., S. Suzuki, and M. Asada, “One THz harmonic oscillation of resonant tunneling diodes,” *Applied Physics Letters*, Vol. 87, 2005.
13. Miyajima, Y., T. Nukariya, and S. Suzuki, “Terahertz detector using 70-nm T-gate In-AlAs/InGaAs HEMT integrated with bow-tie antenna,” *39rd International Conference on Infrared, Millimeter and Terahertz Waves (IRMMWTHz)*, 1–2, Tucson, AZ, 2014.
14. Compton, C. R., R. C. McPhedran, Z. Popovic, G. M. Rebeiz, P. Tong, and D. B. Rutledge, “Bow-tie antennas on a dielectric half-space: Theory and experiment,” *IEEE Transactions on Antennas and Propagation*, Vol. 35, 622–631, 1987.
15. Mir, A., J. Yu, and X. Chen, “Design and characterization of cross bow tie antenna array for focal plane array in terahertz imaging,” *39rd International Conference on Infrared, Millimeter and Terahertz Waves (IRMMWTHz)*, 1–2, Tucson, AZ, 2014.
16. Shireen, R., S. Shouyuan, and D. W. Prather, “Lens coupled bowtieantenna for millimeter wave operations,” *Antennas and Propagation Society International Symposium*, 5055–5058, Honolulu, HI, 2007.
17. Weiss, M., A. G. Steffan, S. Fedderwitz, G. Tsianos, A. Stohr, and D. Jager, “Highly-compact fibre-optic package for 30–300 GHz wireless transmitter modules,” *2nd Electronics System-Integration Technology Conference*, 1111–1114, Greenwich, 2008.
18. Koch, M., “Terahertz communications: A 2020 vision,” *Terahertz Frequency Detection and Identification of Materials and Objects. NATO Science for Peace and Security Series*, Miles, R. E., Zhang, X. C., Eisele, H. & Krotkus, Eds., Springer, Netherlands, 2007.
19. Lu, F., Q. Feng, and S. Li, “A novel CPW-fed bow-tie slot antenna for 5.8 GHz RFID tags,” *PIERS Proceedings*, 327–330, Cambridge, USA, Jul. 2–6, 2008.

Spontaneous Hemodynamic Activity in Prefrontal Cortex of Depression Patients Assessed with Functional Near-infrared Spectroscopy

Jiangxue Li¹, Huilin Zhu^{2,*}, Xinge Li^{2,4}, Hongjun Peng³,
Jie Xu², Tingting Cai², and Sailing He²

¹The Research Center of Psychological Counseling
South China Normal University (SCNU), 510006, China

²Centre for Optical and Electromagnetic Research, South China Academy of Advanced Optoelectronics
South China Normal University (SCNU), Guangzhou 510006, China

³The Department of Clinical Psychology, Guangzhou Brain Hospital
(Guangzhou Huiai Hospital, The Affiliated Brain Hospital of Guangzhou Medical School), China

⁴School of Psychology, South China Normal University (SCNU), Guangzhou 510631, China

Abstract— Patients with major depressive disorder (MDD) typically suffered from pervasive depressed mood or anhedonia, accompanied by several cognitive and physical symptoms. In this study, functional near-infrared spectroscopy (fNIRS) was applied to investigate the spontaneous activity of hemodynamic in the prefrontal cortex (PFC) of the brain. 21 patients with MDD (including 12 with antidepressant and 9 without medication) participated in 8-min resting state measurement. By analyzing the interhemispheric correlation and the correlation maps of the PFC, our results indicated that patients with MDD showed significantly reduced interhemispheric correlation in the PFC and disrupted cortical organizations in the PFC. This study showed that fNIRS could be an effective and convenient way to assess neural features of depression.

1. INTRODUCTION

Functional near infrared spectroscopy (fNIRS), as an optical method for brain imaging, measures cerebral hemodynamic parameters reflecting the neural activity of the brain. fNIRS has high temporal resolution (\sim ms) and reasonable spatial resolution (\sim cm). By providing a non-invasive and convenient imaging environment, it can be easily applied not only in laboratory, but also in clinical studies. During the 20-years' development, fNIRS was considered to have great potential in clinical populations [1], such as patients with depression.

Patients with major depressive disorder (MDD) typically suffered from pervasive depressed mood or anhedonia, accompanied by several cognitive and physical symptoms. Since patients with depressions usually show heterogeneous symptoms (i.e., emotion, cognition, sleep), it has been proposed that depression are associated with dysfunction of a brain network rather than a single area of the brain. As part of the affection network (including the prefrontal cortex, limbic system and so on) of the brain, the prefrontal cortex showed to play an important role in MDD. Many previous neuroimaging studies on depression have reported dysfunctions in the prefrontal cortex (PFC). A study found patients with MDD exhibit reduction of serotonin in the PFC [2]. Functionally, a study revealed that the ventromedial and dorsolateral areas of PFC were associated with depression, although with distinct functions [3]. Also, another study has found that, in order to achieve a similar level of performance with controls, patients with depression showed hyperactivation in the PFC [4]. Besides, by using positron emission tomography (PET) [5, 6], patient with MDD displayed an atypical metabolism pattern in the prefrontal lobe of the brain, manifesting as reduced metabolism in the lateral prefrontal area and a increased metabolism in the medial prefrontal and subgenual cingulate. Increasing studies have confirmed that PFC played a key role in the neural mechanisms of depression.

Recent years, fNIRS has been increasingly applied to investigate the brain function of clinical populations, such as patients with anxiety, major depression (unipolar) and manic-depressive (bipolar) disorder. One fNIRS study [7] has revealed that, in contrast with controls, patients with unipolar and bipolar depression both displayed decreased activation in ventro-lateral, dorso-lateral prefrontal and superior frontal cortex. A fNIRS study [8] found that the PFC played a significant role in anxiety and depression: participants with higher anxiety levels showed a more right-dominant PFC activity at resting-state. Another fNIRS study on patients with post-disaster

*Corresponding author: Huilin Zhu (huilin.zhu@coer-scnu.org).

and calculated the correlation coefficient r between the time courses of the seed and the time course of all other channels. Then, the correlation values between the seed and other channels were projected onto the channel geometry and interpolation was employed to fill the blank areas between adjacent channels. The average correlation values for each group were estimated by converting r values to z values with Fisher's r - z transformation for each participant, and then converting back to the averaged z values to obtain the averaged r values. In statistic analysis, we used Bonferroni correction to counteract Type I errors caused by multiple comparisons.

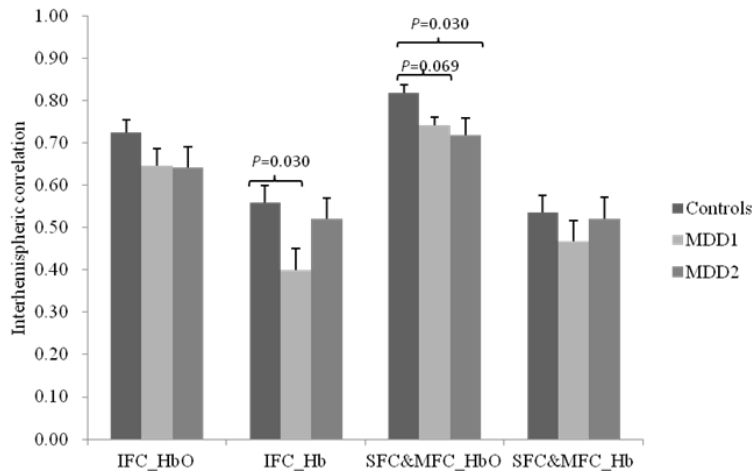


Figure 2: Interhemispheric correlation in ROIs of patients with major depression disorder in treatment with antidepressants (MDD1, $n = 12$), patients with major depression disorder without treatment by any antipsychotic (MDD2, $n = 9$) and controls ($n = 15$). Error bars are standard error of mean across participants. Compared with controls, MDD1 showed significantly reduced interhemispheric correlation in IFC (Hb) and marginally significantly reduces interhemispheric correlation in SFC & MFC (HbO), and MDD2 showed significantly reduced interhemispheric correlation in in SFC & MFC (HbO).

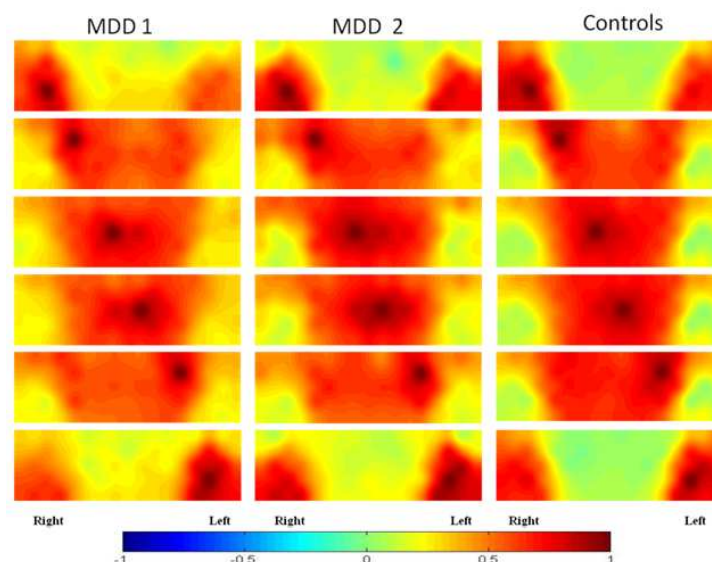


Figure 3: HbO correlation maps (the frontal view of the brain as in Figure 1) for patients with major depressive disorder in treatment with antidepressants (MDD1), patients with major depressive disorder without treatment with any antipsychotic (MDD2) and controls. The selected seeds (Channel 16, Channel 22, Channel 32 in the left hemisphere and Channel 10, Channel 21, Channel 28 in the right hemisphere) could be visually recognized by the maximal red value in each map.

3. RESULTS

Figure 2 shows the averaged interhemispheric correlation for each group. We used a General Linear Model to analyze the effect of groups (between subject factors) on the strength of interhemispheric correlation in the PFC, years of education was used as covariate. Results were shown in Figure 2.

To visualize the results, Figure 3 gives the correlation maps (HbO) for each group, separating by different seeds' locations: 3 seeds in each hemisphere. From Figure 3 (maps for controls), we could see the pattern of cortical organization of the PFC: The bilateral IFC were more functionally connected with each other (Network 1) and the bilateral SFC and the bilateral MFC was more functionally connected with other (Network 2). However, these two networks were mutually independent. Compared with controls, patients with MDD showed obviously disrupted brain network in the prefrontal cortex of the brain. Furthermore, patients with MDD who were in the treatment with antidepressant showed more disorganized brain network than patients with MDD without treatment of any antipsychotic.

4. DISCUSSION

In the present study, we employed fNIRS to detect the spontaneous hemodynamic activity of the PFC of patients with MDD. By analyzing the interhemispheric correlation and maps of functional connectivity, the results revealed that, whether in the treatments of antidepressant or not, patients with MDD showed reduced interhemispheric correlation and a disrupted organization of brain network in the PFC of the brain. In line with previous studies [3], we found the correlation between the function of the PFC and depression. Furthermore, we observed that antidepressant might have effect on the cortical organization of the prefrontal lobe.

In our study, there were two cortical networks in the prefrontal cortex. The ventromedial sectors of the PFC (including the bilateral IFC) were related to the emotion of affection, whereas the dorsolateral sectors of the PFC (including the bilateral SFC and the bilateral MFC) were related to the attention and the executive function. These two sectors of the PFC made up the critical but functionally different substrates underlying depressions [3]. Thus, pattern of the cortical organization of the PFC was an important feature to recognize the neural pathophysiology of the depression.

The limitation of the present study was that we could not clearly distinguish the effect of antidepressant and the effect of the severity of the symptom. Even though the MDD patients with or without medication reported the similar level of depression, the MDD patients in treatment would have more severity of the depression than the MDD patients without treatment. More systematic assessment should be involved in the future studies.

5. CONCLUSION

In summary, by using fNIRS to investigate the spontaneous activity of hemodynamic in the PFC of the brain and analyzing the interhemispheric correlation and the correlation maps of the PFC, we discovered that patients with MDD exhibited significantly reduced interhemispheric correlation and disrupted cortical organizations in the PFC. Our study also suggests that fNIRS is a feasible and effective technique to assess the neural features of depression.

ACKNOWLEDGMENT

This work was supported by Guangdong Innovative Research Team Program (No. 2010 01D0104799 318), the Natural Science Foundation of Guangdong province (2014A030310502).

REFERENCES

1. Boas, D. A., C. E. Elwell, M. Ferrari, et al., "Twenty years of functional near-infrared spectroscopy: Introduction for the special issue," *Neuroimage*, Vol. 85, 1–5, 2014.
2. Robbins, T. W., "Controlling stress: How the brain protects itself from depression," *Nature Neuroscience*, Vol. 8, No. 3, 261–262, 2005.
3. Koenigs, M. and J. Grafman, "The functional neuroanatomy of depression: Distinct roles for ventromedial and dorsolateral prefrontal cortex," *Behavioural Brain Research*, Vol. 201, No. 2, 239–243, 2009.
4. Harvey, P. O., P. Fossati, J. B. Pochon, et al., "Cognitive control and brain resources in major depression: An fMRI study using the n-back task," *Neuroimage*, Vol. 26, No. 3, 860–869, 2005.

5. Mayberg, H. S., "Positron emission tomography imaging in depression: A neural systems perspective," *Neuroimaging Clin N Am*, Vol. 13, 805–815, 2003.
6. Greicius, M. D., B. H. Flores, V. Menon, et al., "Resting-state functional connectivity in major depression: Abnormally increased contributions from subgenual cingulate cortex and thalamus," *Biological Psychiatry*, Vol. 62, No. 5, 429–437, 2007.
7. Schecklmann, M., T. Dresler, S. Beck, et al., "Reduced prefrontal oxygenation during object and spatial visual working memory in unipolar and bipolar depression," *Psychiatry Research: Neuroimaging*, Vol. 194, No. 3, 378–384, 2011.
8. Ishikawa, W., M. Sato, Y. Fukuda, et al., "Correlation between asymmetry of spontaneous oscillation of hemodynamic changes in the prefrontal cortex and anxiety levels: A near-infrared spectroscopy study," *Journal of Biomedical Optics*, Vol. 19, No. 2, 027005–027005, 2014.
9. Helton, W. S., U. Ossowski, and S. Malinen, "Post-disaster depression and vigilance: A functional near-infrared spectroscopy study," *Experimental Brain Research*, Vol. 226, No. 3, 357–362, 2013.
10. Zung, W. W., "A self-rating depression scale," *Archives of General Psychiatry*, Vol. 12, No. 1, 63–70, 1965.
11. Zhu, H., Y. Fan, H. Guo, et al., "Reduced interhemispheric functional connectivity of children with autism spectrum disorder: Evidence from functional near infrared spectroscopy studies," *Biomedical Optics Express*, Vol. 5, 1262–1274, 2014.

Strong Absorption in a 2D Materials-based Spiral Nanocavity

Mohammad H. Tahersima and Volker J. Sorger

Department of Electrical and Computer Engineering, The George Washington University
Washington, D.C. 20052, USA

Abstract— Recent investigations of semiconducting two-dimensional (2D) transition metal dichalcogenides have provided evidence for strong light absorption relative to its thickness attributed to high density of states. Stacking a combination of metallic, insulating, and semiconducting 2D materials enables functional devices with atomic thicknesses. While photovoltaic cells based on 2D materials have been demonstrated, the reported absorption is still just a few percent of the incident light due to their sub-wavelength thickness leading to low cell efficiencies. Here we show that taking advantage of the mechanical flexibility of 2D materials by rolling a molybdenum disulfide (MoS_2)/graphene (Gr)/hexagonal Boron Nitride (hBN) stack to a spiral solar cell allows for solar absorption up to 90%. The optical absorption of a $1\ \mu\text{m}$ long hetero-material spiral cell consisting of MoS_2 , graphene and hBN is about 50% stronger compared to a planar MoS_2 cell of the same thickness; although the ration of the absorbing material, here Gr and MoS_2 , relative to the cell volume is only 6%. We anticipate these results to provide guidance for photonic structures that take advantage of the unique properties of 2D materials in solar energy conversion applications.

1. INTRODUCTION

The most widely installed material for solar cells are amorphous, poly or single crystalline Silicon, and more recently II-VI semiconductors such as cadmium telluride have been widely studied and utilized in the photovoltaic industry. The recent isolation of two-dimensional (2D) materials [4, 5], and their combination in vertical [1, 6, 9, 24] and horizontal functional systems [7, 8] has provided opportunities to form heterostructures that are attractive candidates for solar energy conversion applications. For instance, group VI transition metal dichalcogenides (TMD) are 2D crystals that can exhibit semiconducting behavior. Such materials are constructed by the formula MX_2 (M = metal, e.g., Mo or W; X = semiconductor, e.g., S, Se, or Te) and are structured such that each layer consists of three atomic planes: a lattice of transition metal atoms sandwiched between two lattice of chalcogenides. There is strong covalent bonding between the atoms within each layer and adjacent layers are held together by weak van der Waals forces. These atomically thin heterostructures of semiconducting TMDs allow for surprisingly strong light-matter interactions, which can be utilized for harvesting sunlight via absorption and photovoltaic effects [1]. Previously TMD/Gr bilayers of vertical heterostructure stacks were studied to improve photocurrent extraction [1, 9, 24] in photovoltaic and photodetector applications. These heterostructures can utilize effective combination of good solar spectrum absorption of some TMDs such as MoS_2 and superior mobility of graphene (i.e. $200,000\ \text{cm}^2/\text{Vs}$ for suspended graphene [18]) in a Schottky barrier solar cells. Although a few layers of both graphene and MoS_2 are visually transparent, they are promising sunlight absorbers due to their large absorption per thickness and high density of states. Classically the amount of light absorbed in flat photovoltaic cells is proportional to the film thickness. However, creating an increased optical path length significantly reduces the amount of required photoactive materials. This can be achieved via light management architectures such as planar metamaterial light-director structures, Mie scattering surface nanostructures, metal-dielectric-metal waveguide or semiconductor-dielectric-semiconductor slot waveguides [21]. Here we investigate a three-dimensional solar cell structure based on a variety of stacked 2D materials each with a functional purpose (Figs. 1(a) and 1(b)); by rolling a stack of graphene, semiconducting MoS_2 , and an electrically insulating 2D material this structure creates an absorbing cylinder forming a lightconcentrating optical cavity as we discuss below. This structure is motivated by deploying the mechanical flexibility of 2D materials to enable a multilayer solar cell without the necessity to contact each of the layers separately. The electronic barrier layer needs to be flexible, wide bandgap, and optically transparent insulator to prevent electron and holes generated in a MoS_2 /Gr heterojunction from recombining in their adjacent stacked layer. Hexagonal boron nitride (hBN) is employed as barrier layer since it is an isomorph of graphene, optically transparent, electrically an insulator with a wide bandgap of about 5.9 eV, and it reduces the traps of MoS_2 layers indicated by improved mobilities [6]. Furthermore, a trilayer MoS_2 with a bandgap of 1.6 eV [11] was chosen over a monolayer since bulk behavior

is not expected to emerge beyond stacking of 3–4 monolayers [9, 19], whereas mobility improves with the number of layers [6]. In this study we contrast two absorbers, namely, the rolled up Gr/TMD/hBN “spiral” cell (Fig. 1(a)), and a metal-cladded and metal inner-post “hetero-shell” cell (Fig. 1(b)). The reason behind studying both is that as to separate the effect of the material (i.e., TMD) absorption from any optical nano-cavity effects the hetero-shell device might exhibit. For the latter design, the stack rolls around a core metallic rod and is then coated by another metallic shell, where both metals are the electrical cell’s contacts. The core metallic rod with a low work function (aluminum) is in contact with the graphene, whereas the shell contact with a higher work function (gold) contacts to the MoS₂ layer towards establishing selective cell contacts. In our experiment, we numerically investigate light absorption deploying finite difference time-domain (FDTD) techniques. Comparing this spiral design to previously reported TMD based photovoltaic cells and thick (1 μm) planar MoS₂ solar cells, we obtain a relative absorption enhancement which serves as a reference.

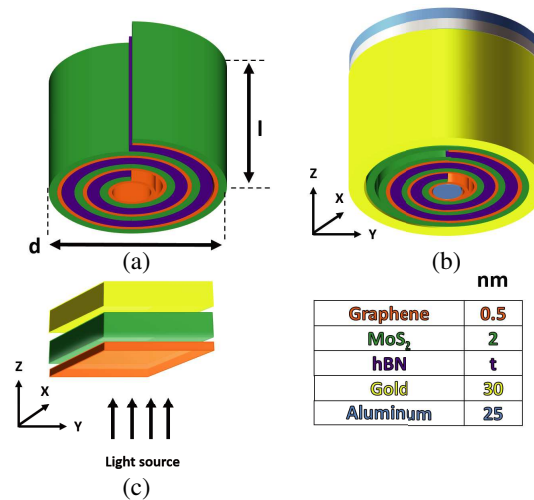


Figure 1: (a) Schematic of “spiral cell structure”; parameters, d , l , and t stand for diameter of the roll, length of the cylindrical structure, and thickness of the hBN layer. (b) “Core-shell structure” of the spiral solar cell. Back reflector is connected to the core contact. Gold (aluminum) is chosen as a shell (core) selective contact. (c) Planar MoS₂/Gr solar cell converting vertically incident photons into electron-hole pairs.

To obtain the absorption efficiency and spectral current density of the spiral cell, we perform 3D FDTD simulations to solve Maxwell’s equations as a function of time and then perform a Fourier transformation. For efficiency, this time-domain method covers a wide frequency range in a single simulation run. A multi-coefficient model was used to represent the complex refractive index of a trilayered MoS₂ [11], the Graphene monolayer [12], and hBN [13]. The approach is to send a broadband, normally incident plane wave pulse (300 to 800 nm) on the spiral structure or the planar solar cell (Fig. 1). The spiral cell was tested under both transverse electric (TE) and transverse magnetic (TM) polarization. The length of spiral structure studied are between a convenient small size for heavily meshed simulations and the length in which we obtain the highest absorption (0.5 μm and 3 μm); and their diameter range from 100 nm to 2 μm as the effect of hBN thickness on spiral cell is examined. We analyze an isolated single spiral cell and planar cell for which a perfectly matched layer and periodic boundary condition were selected, respectively, in the x and y direction. Note, a perfectly matched layer is assumed in propagation direction to absorb any back reflected waves. Furthermore, a power monitor surrounds the entire cell to obtain the net flow out of the simulation domain (P_{out}). The light source is placed inside the power analysis volume, and the absorption (A) is obtained by $A = 1 - P_{out}$. The absorption per unit volume can be calculated from the divergence of the pointing vector:

$$P_{abs} = -0.5R(\vec{\nabla} \cdot \vec{p}) = -0.5\omega E(\omega)^2 \varepsilon''(\omega)$$

where ω is the angular frequency, $\varepsilon''(\omega)$ the imaginary part of permittivity function, and $E(\omega)^2$ the electric field density. Hence, to calculate the spatial and frequency function of the absorption, we only need to know electric field intensity and imaginary part of the complex refractive index.

For a solar cell, of relevance is the current density (J), which requires knowledge of the optical generation rate (G), which is given by $G(\omega) = \frac{P_{abs}}{\hbar\omega} = \frac{-E(\omega)^2 \epsilon''(\omega)}{2\hbar}$ from which we obtain the spectral current density $J_{SC}(\lambda) = \alpha(\lambda)IQE(\lambda)\Gamma_{AM1.5}\lambda/1.24$, where α is the absorption efficiency, λ is the wavelength, and Γ is the spectral irradiance of the AM 1.5G spectrum at one sun solar intensity (data taken from [14]). Note, the internal quantum efficiency (IQE) is assumed to be unity for calculating the short circuit current (J_{SC}) is obtained by integrating $J_{SC}(\lambda)$ over the wavelength range of 300–800 nm, namely

$$J_{SC} = \int \frac{e\lambda}{hc} EQE(\lambda)\Gamma_{AM1.5}(\lambda)d\lambda.$$

The spectral scan displays resonant-like fringes in the absorption spectrum (Fig. 2(b)). We also find a higher visibility for the hetero-shell cell with the metal cladding compared to the dielectric spiral design, which can be understood from an optical field confinement inside the structure. The resonances themselves point towards the spirals resembling a nanowire like structures being a lossy Fabry-Perot cavity [22, 23], which we confirm via (i) investigating the modal features of this cavity (Figs. 2(c) and 2(d)), and (ii) analyzing their frequency profile (Fig. 3(c)). Regarding (i), the x - y mode profile (i.e., x in Fig. 2(a)) indicates a dipole for larger wavelength, which turns into quadruples and double-quadruples for blue shifting the resonance wavelength (6 to 1 in Figs. 2(c) and 2(d)). In addition the cavities' standing waves can be seen in the cross-sectional modal profile (i.e., x' in Fig. 2(a)), where the mode spacing decreases with wavelength as expected (Figs. 2(c) and 2(d)). The in Figure 2b observed higher Q-factor of the hetero-cell over the spiral cell is clearly visible in the cross-sectional mode profiles as distinct power density lobes. The apparent focusing effect in the z -direction might be connected to a changing (i.e., increasing) local effective index as experienced by the wave traveling in positive z , however more details are needed to confirm this. Regarding (ii), analyzing the resonance peak spacing from Fig. 2(b) and relating them to the inverse of the cavity length allows to test the Fabry-Perot cavity hypothesis analyzing its spectral mode spacing (Fig. 3(c)). Finding the results along a straight line confirms that the hetero-cell is a

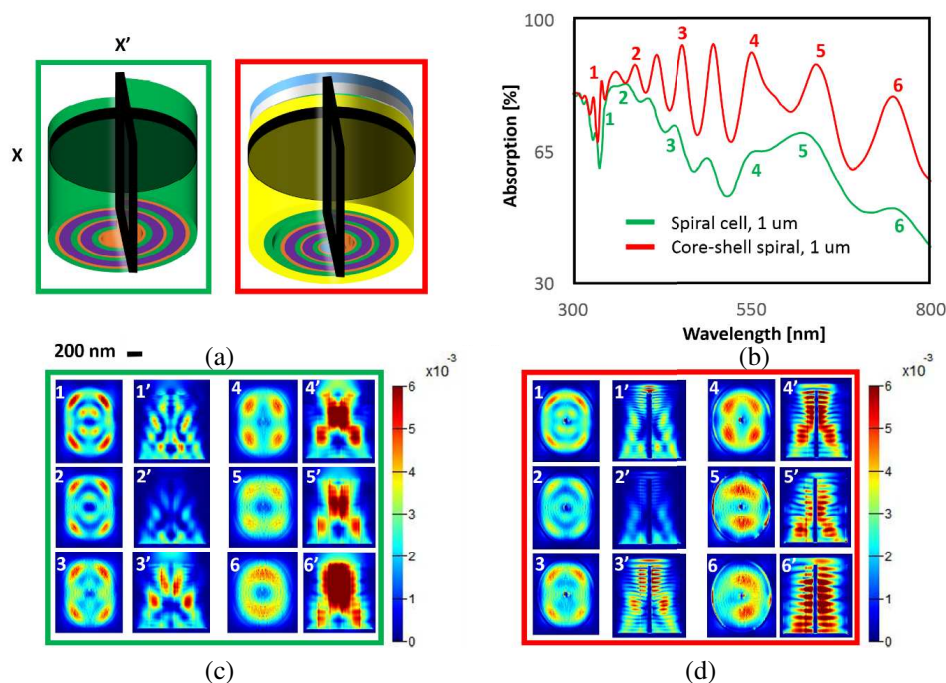


Figure 2: (a) Schematic of spiral cell (left) and core-shell structures (right). Horizontal and vertical cross sections labeled by X and X' are monitors that record the power profiles shown in (c) and (d). (b) Absorption efficiency of spiral cell and core-shell structure. (c) Power profile of absorption efficiency peaks from 1 to 6 for spiral cell structure correspond to 344, 375, 441, 550, 627, and 744 nm wavelength respectively. (d) These wavelengths correspond to wavelength of peaks of the core-shell structure at 340, 388, 455, 550, 640, and 750 nm.

nanoscale cavity. This discussion suggests that the spiral structure behaves like a circular dielectric waveguide where the end facets act as reflecting mirrors [15, 16]. Neglecting dispersion we use $m = 2nL/\lambda$, where m is the mode (an integer) and L is the length of the spiral cell (cavity), n is the effective refractive index, and λ is the wavelength. The spiral cell structure supports mode numbers between 5 and 13 that correspond to 9 visible peaks of absorption efficiency (Fig. 2(b)). This is supported by longitudinal mode profiles recorded by power monitors in Fig. 2, which demonstrates more interference visibility at core shell structure for all monitored wavelengths.

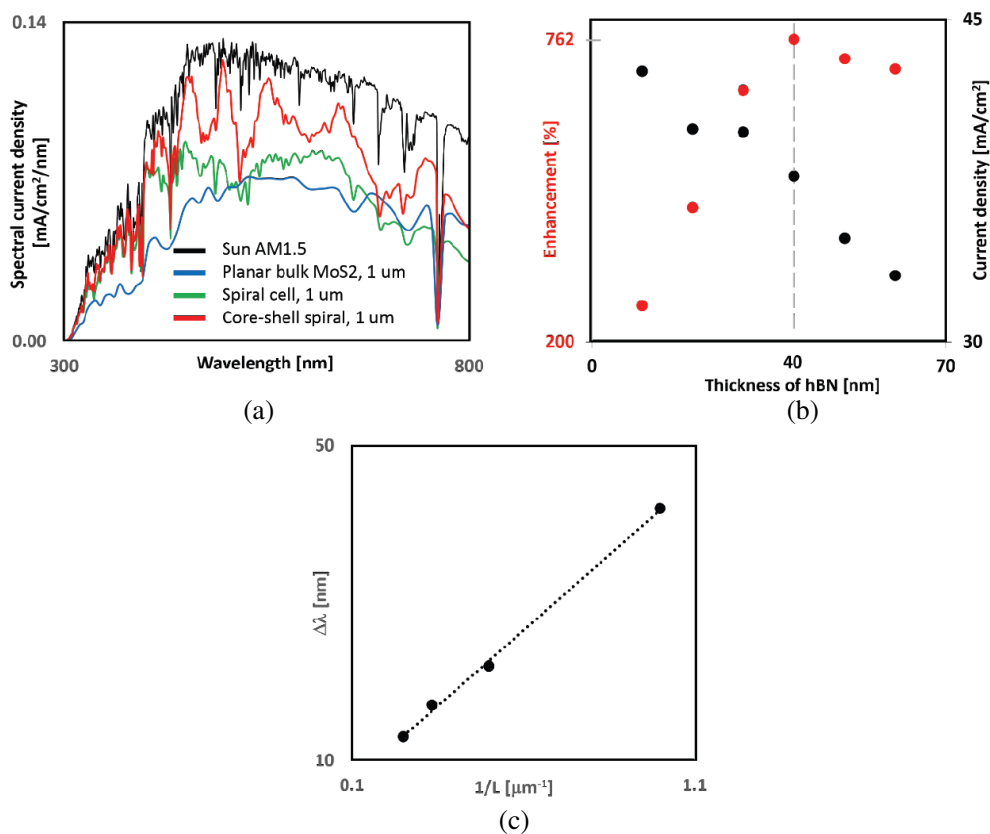


Figure 3: (a) Spectral current density of all three structures. Green, red, and blue curves correspond to Figure 1a,b,c respectively. $d = 1 \mu\text{m}$, $l = 0.8 \mu\text{m}$ (b) Optimization of hBN thickness to achieve maximum current density to photoactive material ratio. (c) Mode spacing versus inverse nanowire length.

The spectral current density of a $1 \mu\text{m}$ thick planar MoS₂ cell, the spiral cell, and the core-shell structure are compared (Fig. 3(a)). We find the spectral current density to be higher for the spiral structures over almost the entire investigated wavelength range. This is mainly because spiral structures have lower surface reflection due to lower effective refractive index of spiral structures compared to planar MoS₂ structure. Core-shell structure has an even higher absorption efficiency than the spiral cell, because the back reflector at the end of core-shell structure allows for double pass of light. The overall current densities of the planar cell, spiral cell, and core-shell structure integrated over wavelengths of 300 to 800 nm are 25.5, 29.5, and 37.2 mA/cm² respectively. The current density of the spiral (core) cell shows 16 (46)% enhancement compared to the planar structure which is expected, because the spectral current density is higher for spiral structures over almost the entire wavelength.

Note, that although the spiral length (l) was kept constant ($1 \mu\text{m}$) this does not imply that the same amount of photoactive material was used; for example in a particular simulation, the thickness of monolayer graphene, trilayer MoS₂, and few layer hBN are set to 0.5 nm, 2.0 nm and 35.0 nm, respectively; and for the planar cell thickness of MoS₂ is $1 \mu\text{m}$. Thus, the absorbing materials (graphene and MoS₂) occupy only 6% of the total volume of spiral cells. This means that the ratio of solar energy absorption to volume of photoactive material was improved by $\sim 767\%$ compared to a bulk MoS₂ photovoltaic cell of the same size. We name this ratio “enhancement” and define

it as

$$\frac{\alpha_{\text{spiral cell}} - \alpha_{\text{bulk cell}}}{\alpha_{\text{bulk cell}}} \div \frac{t_{\text{MoS}_2} + t_{\text{Gr}}}{t_{\text{MoS}_2} + t_{\text{Gr}} + t_{\text{hBN}}},$$

where α denotes absorption and t refers to the respective physical layer thickness. This enhancement is proportional to the absorption efficiency of the cell and thickness of hBN layer. However, increasing the thickness of the hBN layer, the absorption efficiency decreases due to a reduction in the amount of absorbing material (Fig. 4). Hence, to optimize the ratio of absorption enhancement to relative volume of photoactive material, the number of core shell structures with different hBN thicknesses are analyzed (Fig. 3(b), Fig. 4). For core-shell structures with 5 rings and 500 nm in length, the optimized enhancement is 762% for an hBN of 40 nm thickness. The dielectric strength of ultrathin hBN was previously studied to be 7.94 MV/cm [17], which corresponds to a breakdown voltage of 9 volts for a 10 nm thin layer of hBN. This is sufficient to prevent generated excitons to channel from one junction to another.

2. CONCLUSION

We have investigated a novel photovoltaic absorber and successfully demonstrated that rolling 2D materials into 3D structures can significantly improve their photo absorption compared to atomically thin or even bulk configurations. We optimized spiral solar cell design for the largest absorption, and optimized the hBN thickness in particular to achieve maximum absorption to photoactive material ratio. We can estimate a lower limit and a reasonable limit for power conversion efficiency of one of the spiral core-shell structure using current density (J_{SC}) of 37.2 mA/cm² for the cell with length of 1 μ m and radius of 400 nm. For the lower limit and reasonable limit, the open circuit voltage (V_{OC}) of 0.1% and 0.5 V [9], and fill factor (FF) of 0.3 and 0.7, are assumed respectively. In both cases IQE of unity and input power (P_{in}) of 475 W/m² (input power in our simulation range of 300 nm to 800 nm) are assumed. The efficiency η is then calculated from:

$$\eta = \frac{FF \times J_{SC} \times V_{OC}}{P_{in}}$$

Resulting in an overall power conversion efficiency range of 2 to 27 %. Low open circuit is one of the main drawbacks for this solar cell. One way to overcome this barrier is use of different combination of 2D materials such as aiming for type two hetero junction such as MoS₂/WSe₂. Furthermore, recent efforts on enabling horizontally tunable bandgap TMDs [7, 8] utilized in this structure could lead to a multi junction photovoltaic cell that only requires two contacts.

ACKNOWLEDGMENT

We acknowledge support from the National Science Foundations (NSF) Designing Materials to Revolutionize and Engineer our Future (DMREF) program and White House Materials Genome Initiative (MGI) under the award numbers 1436330.

REFERENCES

1. Britnell, L., et al., , *Science*, Vol. 340, No. 6138, 1311–1314, 2013.
2. Grandidier, J., et al., , *Adv. Mater.*, Vol. 23, 1272–1276, 2011.
3. Kim, S.-K., et al., , *ACS Nano*, Vol. 8, No. 4, 3707–3714, 2014.
4. Novoselov, K. S., et al., , *Science*, Vol. 306, 666, 2004.
5. Novoselov, K. S., et al., *Proc. Natl. Acad. Sci. U.S.A.*, Vol. 102, 10451, 2005.
6. Lee, G. H., et al. *ACS Nano*, Vol. 7, No. 9, 7931–7936, 2013.
7. Huang, C., et al., *Nature Materials*, Vol. 13, 1096–1101, 2014.
8. Mann, J., *Adv. Mat.*, Vol. 26, No. 9, 1399–1404,, 2014.
9. Bernardi, M., et al., *Nano Lett.*, Vol. 13, No. 8, 3664–3670, 2013.
10. Furchi, M. M., et al, *Nano Lett.*, Vol. 14, No. 8, 4785–4791, 2014.
11. Yim, C., et al., *Applied Phys. Lett.*, Vol. 104, 103114, 2014.
12. Kravets, V. G., et al., , *Phys. Rev. B*, Vol. 81, 155413, 2010.
13. Ren, S. L., et al., *Applied Physics Letters*, Vol. 62, 1760, 1993.
14. ASTM G173-03 Reference Solar Spectral Irradiance, <http://rredc.nrel.gov/solar/spectra/am1.5/ASTMG173/ASTMG173.html>.
15. Tang, J., et al., *Nature Nanotechnology*, Vol. 6, 568–572, 2011.

16. Kempaa, T. J., et al., *Proc. Natl. Acad. Sci. U. S. A. Jan.*, Vol. 31, Vol. 109, No. 5, 1407–1412, 2012.
17. Lee, G. H., et al., , *Appl. Phys. Lett.*, Vol. 99, 243114, 2011.
18. Bolotina, K. I., et al., , *Solid State Communications*, Vol. 146, No. 9–10, 351–355, June 2008.
19. Mak,, K., *Phys Rev. Lett.*, Vol. 105, 136805, 2010.
20. Zhang, W., et al., *Scientific Reports*, Vol. 4, 3826, 2014.
21. Polman, A., et al., *Nature Materials*, Vol. 11, 174–177, 2012.
22. Duan., X., et al., , *Nature*, Vol. 421, 241–245, 2003.
23. Oulton, R. F., V. J. Sorger, et al., *Nature*, Vol. 461, 629–632, 2009.
24. Hill, M. T., et al., *Optics Express*, Vol. Vol. 17, No. 13, 11107–11112, 2009.

Advanced Building Blocks in Thick Silicon on Insulator Technology: Echelle Grating Multiplexers and Reflective Multimode Interference Couplers

P. Muñoz^{1,2}, J. D. Doménech², J. S. Fandiño¹, R. Baños¹, and B. Gargallo¹

¹Universitat Politècnica de València, Spain

²VLC Photonics S.L., Spain

Abstract— In this paper we present the design, fabrication and experimental demonstration of advanced building blocks in a thick Silicon generic photonic integration platform. The platform provides a fabrication process with waveguides of different contrast ratio, through different etch levels, and the possibility of metalization in selected areas. Combining waveguiding and metals we report on Echelle Gratings (EG) multiplexers and reflective Multimode Interference (R-MMI) couplers. Several devices were designed in the same reticle and several dies were supplied by the fabrication platform. The experimental results for the individual devices are reported, as well as a die to die comparison and statistical analysis.

1. INTRODUCTION

Generic photonic integration, since its inception by 2007 [1], is becoming a foundry model for photonics, providing Multi-Project Wafers (MPWs), where users share the area of wafer, and fabrication costs. Being the technology not devoted to specific purposes, it may well serve different application domains, while the manufacturing is done in a common process. Several generic integration platforms have emerged for different photonic technologies, or material systems, and operate nowadays [2]. Very recently the Silicon-on-Insulator (SOI) platform ePIXfab, which traditionally provided Silicon technology with nanometric waveguides, of typical cross-section $W \times H$ 450×220 nm², has incorporated micrometric size Silicon waveguides [3], despite this thick Silicon technology is well known and exists since long time ago [4]. In fact, thick Si is the core technology, of several market players since 2006, but using proprietary processes [5]. Demonstrating the versatility of the generic process is key, and this is achieved by developing different photonic building blocks. Thin Si photonics, Indium Phosphide and Silicon Nitride have demonstrated a wide list of building blocks [2], ranging from passive waveguide and coupling components, through filters to active blocks as modulators, amplifiers, lasers and detectors. In generic thick Si technology the basic waveguiding and coupling components have been demonstrated [6]. However, key devices as wavelength multiplexers have not been reported yet. It is widely accepted that on-chip silicon multiplexers are central to a huge number of applications [7]. Among them, the Echelle Diffraction Grating, or Echelle Grating (EG) is recognized as the multiplexing block having smallest footprint and robustness in a wide number of applications [8] compared to other alternatives such as the Arrayed Waveguide Grating [9]. In particular, in thick Si technology where the bend radius is larger than for the thin Si nanometric waveguides, the EG proves to be very convenient. Hence, the purpose of this paper is to report on EG multiplexers using metal mirrors in a generic thick Silicon manufacturing platform. The paper is structured as follows. Section 2 provides a general review of the most relevant works addressing EGs in SOI technology. Next, Section 3 reports on the experimental outcomes of the demonstrated devices, including statistical analysis of passband features such as insertion loss, polarization dependent loss (PDL), polarization dependent wavelength shift (PDWS), bandwidth, adjacent and non-adjacent cross-talk and the comparison between devices with and without metal reflectors for both polarizations. Finally, the conclusions are presented in Section 4.

2. STATE OF THE ART AND DESIGN

A summary of devices previously reported in journals is given in Table 1. For completeness, the table includes both thick and thin Si waveguide devices. The former have a typical cross-section of 3×3 μm², and the latter typically 0.45×0.22 nm². Hence, the micrometric waveguide supports both TE and TM, whereas the nanometric mainly guides TE polarization with such a cross-section. The thin Si devices have been reported for the optical telecommunication C-band (1530–1565 nm). For thick Si devices, the EG reported in [10] is an S-C band multiplexing device for passive optical networks, whereas the one demonstrated in [8] operates at S, C and L-band as well. Regarding the

Table 1: Comparison of this work with other state of the art — journal publications — (Abbreviations: PDL, Polarization Dependent Loss; PDWS, Polarization Dependent Wavelength Shift; FSR, Free Spectral Range; n.a. does not apply; — not available; * bands may not be covered in full; † 4 channel devices with and without metalized grating lines fabricated for comparison, all the figures reported in this column are for metalized devices; ††SiO₂ 256 nm layer and 150 nm layer of Al; DBR, Distributed Bragg Reflector).

	This work†	[8]	[10]	[11]	[12]	[13]
Technology	Thick Si	Thick Si	Thick Si	Thin Si	Thin Si	Thin Si
Waveguide	$3.00 \times 3.00 \mu\text{m}^2$	$3.00 \times 3.00 \mu\text{m}^2$	$3.00 \times 3.00 \mu\text{m}^2$	$0.45 \times 0.22 \mu\text{m}^2$	$0.50 \times 0.22 \mu\text{m}^2$	$0.45 \times 0.22 \mu\text{m}^2$
Polarization (s)	TE+TMTE+TM	TE+TM	TE	TE	TE	
Operation*	S, C, L bands	S, C, L band	S,C bands	C-Band	C-Band	C-band
Grating Facet	SiO ₂ -Al/None††	Al (150 nm)	-	DBR	45 corner cube	None
# channels	4	12	2	30	-	4
focal length	275 μm	-	-	-	-	-
spacing	20 nm 8 nm	70 nm	3.2 nm	3.2 nm	20 nm	
FSR	198 nm	-	-	-	-	-
Order	8	-	-	-	20	-
Grating length	250 μm	-	-	-	-	135 μm
Grating period	5.425 μm	-	-	-	-	4.35 μm
# grooves	46	-	-	-	38	31
Passband	Gauss	Flat	Flat	Gauss	Gauss	Gauss
Results						
Insertion loss	5.68 ± 0.32 dB	1.7 dB	1.8 dB	3 dB	3 dB	7.5 dB
Loss uniformity	3.84 ± 0.90 dB	-	-	4 dB	0.5 dB	0.6 dB
PDL	0.58 ± 0.44 dB	0.2 dB	0.2 dB	n.a.	n.a.	n.a.
PDWS	0.32 ± 0.74 nm	0.3 nm	0.3 nm	n.a.	n.a.	n.a.
BW 1 dB	4.18 ± 1.12 nm	5.5 nm	-	-	-	-
BW 3 dB	7.30 ± 1.32 nm	-	20 nm	-	-	-
BW 10 dB	12.54 ± 1.20 nm	-	-	-	-	-
BW 20 dB	16.11 ± 1.06 nm	-	-	-	-	-
Adjacent Xt	-34.14 ± 2.71 dB	-25 dB	-32 dB	-15 dB	-19 dB	-30 dB
Non-adjacent Xt	-38.33 ± 3.23 dB	-	-	-25 dB	-	-
Footprint	0.12 mm ²	15.75 mm ²	3.24 mm ²	0.5 mm ²	0.05 mm ²	0.04 mm ²

grating line, some of them report different techniques to increase the reflectivity, to compensate, up to some extent, the Fresnel reflection loss [14] taking place between the Si guiding layer, and the cover layer, in some cases just air, in others SiO₂. Hence, Distributed Bragg Reflectors (DBR) [11], a 45 corner cube [12] and the deposition of metals as aluminum [8] have been reported. The latter requires additional processing steps, but the achieved reflectivity may be larger than the other techniques, albeit the former are attained within the same waveguide lithography. EGs with 4 channels were designed according to the specifications in the first two columns of Table 1. The

design process is as reported in [15]. The devices are based on a curved facet type grating and make use of input/output waveguides with the following characteristics: width $2.4\ \mu\text{m}$, side etching $1.75\ \mu\text{m}$, input waveguides center at 36° and output waveguides center at 41° . The slab mode effective and group indices were computed to be 3.46 and 3.6 respectively. In the design area, two EG devices, with and without metalization, were included.

3. EXPERIMENTAL RESULTS

3.1. Fabrication and Characterization

The devices were fabricated in the generic technology platform provided by VTT Finland [6]. The typical performance for $3\ \mu\text{m}$ width waveguides is: propagation loss $0.1\ \text{dB/cm}$, fiber i/o coupling up to 90% (lensed fibers), or 40% (regular fiber) and small polarization dependence [3]. Additional metalization steps are available in the platform, and they were employed to cover some of the grating lines in our devices. To be precise, the mirrors are formed by depositing two thin layers on top of the Silicon guiding layer: a first layer of SiO_2 (265 nm, corresponding to a quarter-wave), and a second layer of 150 nm aluminum. A cross-section of the aluminium mirror layer stack is shown in Figure 1(a). As reported by the manufacturers, reflectivity of these combined layers can be as good as 92.7% [16]. Nonetheless we employed other reflective devices within the same dies [17] based on Multimode interference reflectors (MIRs). Figures 1(b) and (c) show a schematic 3D representation of a 2-port MIR, as well as an SEM picture of a fabricated device, respectively. To assess on the MIR reflectivity, Fabry-Pérot test structures made of a concatenation of two MIRs were employed to extract the wavelength dependent reflectivity. Figure 2(a) shows an schematic diagram of the test structures, while Figure 2(b) is an SEM picture of a fabricated device. The two MIRs form an integrated resonant cavity with a periodic spectrum made of interference fringes. The depth of these fringes, also known as the extinction ratio (ER), depends on the total effective reflectivity of the MIR under test. As shown in Figure 2(c), our conclusion is the reflectivity in these chips is approximately 79.4%. Full details can be found in [17]. Finally, a SEM micrograph of the EG devices is shown in Figure 1(d), with an inset showing the view of the grating line, where the metal area is highlighted in pseudo-color. During the measurements the chips of were held on

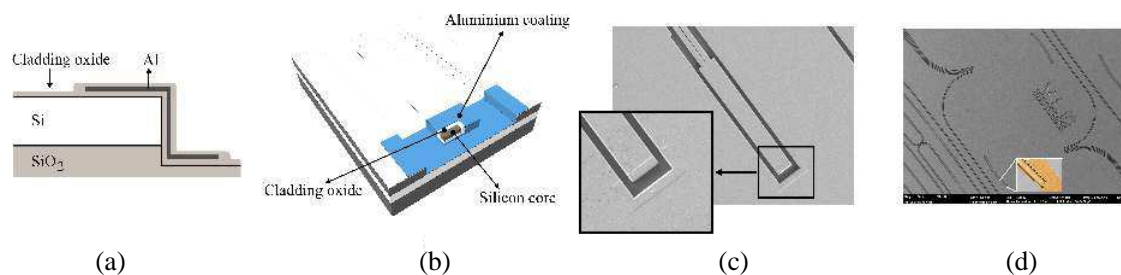


Figure 1: (a) Cross-section of the aluminium mirror layer stack. (b) 3D Model of a 2-port MIR with aluminium mirror. (c) SEM picture of a fabricated device. (d) SEM micrographs of fabricated devices, EG device, inset with detail of the grating line (metalization in pseudo-color).

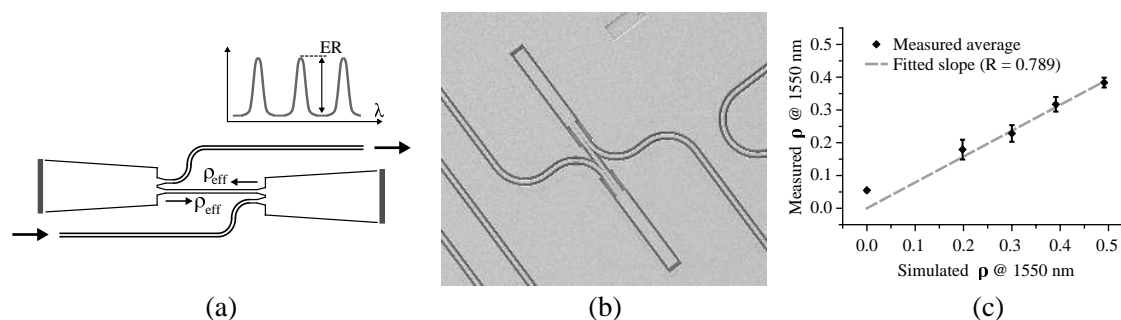


Figure 2: (a) Schematic diagram of the structures employed to measure the effective reflectivities of the devices under test. (b) SEM picture of a test structure. (c) Measured average and standard deviations of the reflectivities versus the simulated values at 1550 nm. Grey dashed line: Slope fitted to the data that provides an estimate of the average intrinsic losses both in the mirror and in the access waveguides.

top of a thermally controlled (25°C) vacuum chuck. The in/out coupling stages consists of a fiber holder, collimating lens, free space polarizer and microscope objective.

3.2. Transmission Spectra

The transmission spectra of the EG is shown in Figure 3(a). The results are normalized with respect to a straight (test structure) waveguide. The minimum insertion loss for the EG is around 5 dB, and the loss non uniformity is around 1 dB. The graph also shows the overlaid spectra for TE and TM polarizations, which were set using bulk filters in the in coupling stages mentioned previously. In accordance to the small polarization dependence of this thick Si technology, from the graphs low PDL and PDWS are observed. For these particular devices PDL is as low as 0.2 dB, except for the third channel on Figure 3(a), and PDWS is as low as 0.3 nm. Both values are in good agreement with other reported thick Si EGs [8, 10]. Finally, and less noticeable, all the passbands have a common feature, that is a small side lobe close to the left side of the main lobe (towards shorter wavelengths). This side lobe is also predicted in the design and simulation stage, where slanted grating sidewall (between $1\text{--}2^{\circ}$) were included. The slanted grating walls result into slightly increased insertion loss in the main band, due to the coupling to higher order (vertical) slab modes in the EG, which in turn result into the aforementioned left side lobe present in all the spectral traces [8].

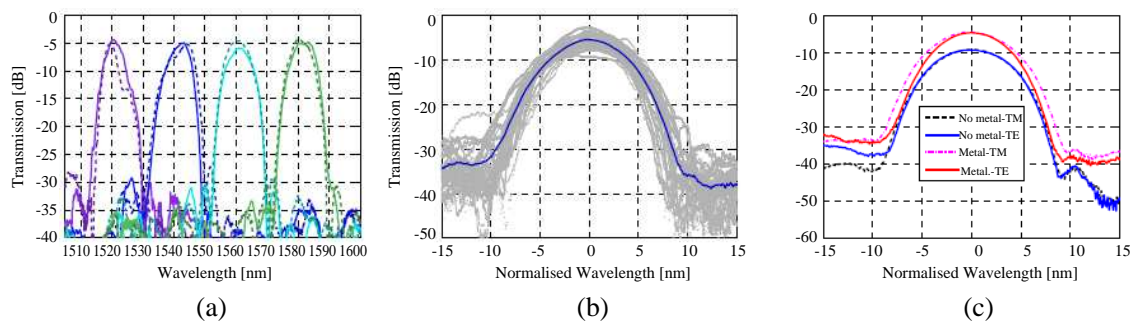


Figure 3: Transmission spectra for the EG with metal reflector. (a) Solid and dashed lines correspond to TE and TM polarization respectively. (b) Superimposed transmission spectra for all the devices and channels. Grey dots show the overlaid spectra for all measured channels from 5 chips, 1 device per chip. All the channels have been aligned to the same center wavelength. The blue line shows the average response. TE polarization, TM polarization exhibited similar performance. (c) Comparison of averaged responses from all the channels, with and without grating line metalization, and for TE and TM polarizations.

3.3. Passband Features Analysis

Several dies were retained for full measurements, having as target the analysis of variations among them. Each die includes test structures and two EGs, with and without metal mirrors. Devices from five dies were measured in full. Other dies were discarded due to randomly damaged i/o waveguide facets. The results shown onwards are only for TE polarization for the sake of clarity, since for TM similar results were obtained. Figure 3(b) shows the superimposed transmission spectra for all the channels, aligned to 3-dB bandwidth center wavelength. The collected statistical features from the passbands are summarized in the first column of Table 1. Note that a part of all the variations reported for the figures related to optical power (insertion loss, loss non-uniformity, and PDL) may be attributed to different facet condition for the different EG input/output waveguides, and that they may be reduced by facet polishing [18]. In terms of channel insertion loss, the average of the peak insertion loss for all channels and dies was calculated. The EG exhibits 5.7 dB with little variations, as detailed in the table. Compared to previous reported values, Table 1 [8, 10], these are 2–4 dB larger. This maybe attributed to a non-optimized generic process which was also used for the first time to this purpose, compared to the industrial dedicated process from [8, 10]. Next, the loss uniformity of the devices was calculated as the difference between the maximum and minimum peak transmission for each device. The mean and standard deviation over all the dies is also shown in Table 1, where an average uniformity around 3.7 dB with variations of around ± 1 dB. The PDL was calculated as the difference of the peak amplitude for TE and TM polarization of a given channel. The average PDL is close to 0.6 dB, whereas other thick Si references, Table 1 [8, 10] reported a PDL of 0.2 dB. In terms of PDWS, computed as the difference between the wavelengths were the

TE and TM maxima per channel are located, our results are on average close to those previously reported of 0.3 nm. The bandwidth was calculated from the measurements for all the devices and channels, and the obtained bandwidth values were averaged over all the channels and samples as well. The N-dB bandwidth was calculated as the wavelength difference between the two points in the passband N-dB under the maximum. The average and standard deviation interval are given in Table 1. A Gaussian power transfer function was fitted to the 3-dB bandwidth, and the band pass fit is good down the 10-dB point from the maximum. The cross-talk was computed as the maximum value of the adjacent (non-adjacent) channel(s) in a given channel 3-dB clear window [18]. The average for adjacent channel cross-talk is around -33 dB. This is slightly better than reference [8] and similar to reference [10]. The non-adjacent channel cross-talk is approximately -38 dB.

3.4. Echelle Gratings with Metal Mirrors Analysis

Figure 3(c) shows the averaged spectra for all channels and chips. The difference for the metalized and non-metalized devices is 4.62 dB and 4.67 dB for TE and TM. In all the cases, both devices (with and without mirror) sit on the same die, that is the grating line patterning is expected to be similar, despite the orientation is different, as can be seen in Figure 1(d). In an ideal situation, one would expect the loss difference between devices with and without mirrors to be close to the Fresnel reflection loss. Since the difference between the incident (input waveguide) and diffraction (output waveguides) angles is 5° , the Fresnel reflection loss contribution is calculated to be 7.83 dB for TE, and 7.51 dB for TM. Using the mirror structure described above, ideally the loss in the interface would 0.069 dB and 0.064 dB for TE and TM respectively, slightly less lossy for TM [17]. Nonetheless we measured these SiO₂-Al mirrors reflectors in the dies provide a reflectivity in average of 79.4% (1.0 dB loss) [17]. Hence, this approximately 2.0 dB variations, which may be attributed, besides to poorer performance of the mirrors in some cases, to different sources of errors: different imperfections in the grating lines of metalized and non metalized devices (roughness, rounded corners, . . .) as well as differences in the in/out coupling properties of the different samples used to average and subtract.

4. CONCLUSION AND OUTLOOK

In this paper we reported on Echelle Gratings multiplexers equipped with metal mirrors, designed and manufactured using thick Silicon photonic integration technology. Multimode interference reflectors were also designed and demonstrated, from which the reflectivity of the metal layers was derived. The paper supplies information of variations on different figures of merit for the multiplexers. Furthermore, the comparison between devices with and without metal mirrors is supplied as well, for different polarizations.

ACKNOWLEDGMENT

The authors acknowledge financial support by the Spanish CDTI NEOTEC start-up programme, the Spanish MINECO project TEC2013-42332-P, acronym PIC4ESP, project FEDER UPVOV 10-3E-492 and project FEDER UPVOV 08-3E-008. B. Gargallo acknowledges financial support through FPI grant BES-2011-046100. J. S. Fandiño acknowledge financial support through FPU grant AP2010-1595.

REFERENCES

1. "Towards a foundry model for micro- and nanophotonic ics," *European Network of Excellence on Photonic Integrated Components and Circuits*, Mar. 2007.
2. Munoz, P., J. Domenech, et al., "Evolution of fabless generic photonic integration," *2013 15th International Conference on Transparent Optical Networks (ICTON)*, Jun. 2013.
3. Aalto, T., M. Cherchi, et al., "Launching of multi-project wafer runs in epixfab with micron-scale silicon rib waveguide technology," *Proc. SPIE*, Vol. 8990, 899003-1–899003-11, 2014.
4. Soref, R. A., "Silicon-based optoelectronics," *Proceedings of the IEEE*, Vol. 81, No. 12, 1687–1706, Dec. 1993.
5. Mounier, E. and C. Troadec, "Silicon photonics 2014," Yole Development, Tech. Rep., 2014.
6. Aalto, T., M. Cherchi, et al., "Dense photonics integration on a micron-scale SOI waveguide platform," *2013 IEEE 10th International Conference on Group IV Photonics (GFP)*, 107–108, Aug. 2013.
7. Dai, D. and J. E. Bowers, "Silicon-based on-chip multiplexing technologies and devices for peta-bit optical interconnects," *Nanophotonics*, Vol. 3, Nos. 4–5, 283–311, 2014.

8. Feng, D., W. Qian, et al., "Fabrication insensitive echelle grating in silicon-on-insulator platform," *IEEE Photonics Technology Letters*, Vol. 23, No. 5, 284–286, Mar. 2011.
9. Pathak, S., P. Dumon, et al., "Comparison of AWGs and echelle gratings for wavelength division multiplexing on silicon-on-insulator," *IEEE Photonics Journal*, Vol. 6, No. 5, 1–9, Oct. 2014.
10. Bidnyk, S., D. Feng, et al., "Silicon-on-insulator-based planar circuit for passive optical network applications," *IEEE Photonics Technology Letters*, Vol. 18, No. 22, 2392–2394, Nov. 2006.
11. Bogaerts, W., S. Selvaraja, et al., "Silicon-on-insulator spectral filters fabricated with CMOS technology," *IEEE Journal of Selected Topics in Quantum Electronics*, Vol. 16, No. 1, 33–44, Jan. 2010.
12. Horst, F., W. Green, et al., "Silicon-on-insulator echelle grating WDM demultiplexers with two stigmatic points," *IEEE Photonics Technology Letters*, Vol. 21, No. 23, 1743–1745, Dec. 2009.
13. Brouckaert, J., W. Bogaerts, et al., "Planar concave grating demultiplexer fabricated on a nanophotonic silicon-on-insulator platform," *Journal of Lightwave Technology*, Vol. 25, No. 5, 1269–1275, May 2007.
14. Saleh, B. and M. Teich, *Fundamentals of Photonics*, 2nd Edition, Chapter 6, 197–242. Wiley, 2007.
15. Lycett, R., D. Gallagher, and V. Brulis, "Perfect chirped echelle grating wavelength multiplexor: Design and optimization," *IEEE Photonics Journal*, Vol. 5, No. 2, 2400123, Apr. 2013.
16. Cherchi, M., S. Ylinen, et al., "MMI resonators based on metal mirrors and MMI mirrors: An experimental comparison," *Opt. Express*, Vol. 23, No. 5, 5982–5993, Mar. 2015.
17. Fandio, J. S., J. D. Domnech, and P. Muoz, "Two-port multimode interference reflectors based on aluminium mirrors in a thick SOI platform," *Physics Optics*, arXiv: 1504.01549, Online Available: <http://arxiv.org/abs/1504.01549>.
18. Piels, M., J. Bauters, et al., "Low-loss silicon nitride AWG demultiplexer heterogeneously integrated with hybrid III-V/silicon photodetectors," *Journal of Lightwave Technology*, Vol. 32, No. 4, 817–823, Feb. 2014.

Femtosecond Laser Irradiation of Fused Silica with a Nanometric Inhomogeneity

Anton Rudenko, Jean-Philippe Colombier, and Tatiana E. Itina

Laboratoire Hubert Curien, UMR CNRS 5516, Lyon University
Bât F, 18 rue du Prof. Benoît Laurus, Saint-Etienne 42000, France

Abstract— A finite-difference time-domain (FDTD) method based on Maxwell’s equations coupled with time-dependent electron carrier density equation is proposed to investigate numerically femtosecond laser irradiation of dielectrics with a small inhomogeneity. The process of plasma generation due to multiphoton absorption near small defect in fused silica is studied in details and local field distribution around the inhomogeneity is first explained by using the Rayleigh scattering theory. Further investigation of the laser-matter interaction shows that the generated plasma properties do not significantly depend on the size of the inhomogeneity as long as it remains considerably smaller than the irradiation wavelength. The calculation results show, however, that there are several parameters which are crucial. Among such parameters, for instance, is the collision frequency, which affects strongly both the created electron density and laser propagation. In addition, the changes in the refractive index of the plasma are taken into account by the Lorentz-Drude model with time-dependent carrier density. The differences between the results calculated by using Keldysh theory for multiphoton ionization and obtained by considering only six-photon ionization are discussed. Finally, temporal changes in the behavior of scattering due to generated nanoplasma are observed and analyzed by using Mie scattering theory, which is more complete than Rayleigh one.

1. INTRODUCTION

Over past decades significant progress has been achieved in the field offemtosecond laser interaction with dielectric materials, in particular, with the possibility to induce different kind of modifications in transparent materials. Ultra-short laser beams achieve periodic nanostructuring, characterized by a sub-wavelength period [1]. These self-organized structures emerge spontaneously during multi-pulse irradiation and the conditions triggering their formation remain poorly explored. Small defects in dielectrics reinforce damage during femtosecond laser irradiation and lead to the generation of nanoplasmas, thus affecting laser propagation. Local refractive index changes in the media due to this damage lead to other nonlocal physical phenomena, as, for instance, strong interference of the incident wave with the plasma wave [1] incubation processes in plasma [2, 3] thermal diffusion or self-trapping of excitons [4, 6], thus resulting into a feedback for nanograting formation.

The nature, the size and the shape of the initial defects were found to significantly vary and potentially play an important role in the nanograting initiation. However, the processes of plasma generation after the first pulse irradiation for small impurity center typically leads to the formation of the larger defects due to the memory in nonlinear ionization of transparent solids [5]. In this article we consider inhomogeneities with different properties, by varying its size in the nanometric scale. Sphere is chosen as the simplest shape, for which there are analytical solutions of the Mie scattering problem [7]. Herein it is supposed that initial defects have nanometric scale and are smaller than the wavelength of the irradiation. FDTD method [8], based on Maxwell’s equations coupled with time-dependent electron carrier density equation is applied to investigate numerically femtosecond laser irradiation of dielectrics with inhomogeneities, where nonlinear effects of multiphoton ionization and Kerr non-linearity are included.

2. SIMULATION MODEL

To better understand the processes of laser interaction with small inhomogeneities in dielectrics, the finite-difference time-domain (FDTD) approach for nonlinear and disperse media is applied [8]. In this method Maxwell’s equations are written as:

$$\begin{cases} \frac{\partial \vec{D}}{\partial t} = \nabla \times \vec{H} - \vec{J} \\ \frac{\partial \vec{H}}{\partial t} = -\frac{\nabla \times \vec{E}}{\mu_0} \end{cases} \quad (1)$$

where \vec{D} is the displacement field, \vec{E} is the electric field, \vec{H} is the magnetic field and \vec{J} is the current density. They are numerically solved by using the standard Yee’s algorithm [8]. At the

edges of the grid absorbing boundary conditions related to convolutional perfect matched layers (CPML) are set to avoid nonphysical reflections [9]. Substitution of the constitutive equations into Maxwell-Ampere equation yields:

$$\frac{\partial \vec{E}}{\partial t} = \frac{\nabla \times \vec{H}}{\varepsilon_0} - \frac{1}{\varepsilon_0} \left(\vec{J}_{L-D} + \vec{J}_{\text{Kerr}} + \vec{J}_{\text{MPI}} \right), \quad (2)$$

where \vec{J}_{L-D} is current derived from the Lorentz-Drude model for the dispersive media; \vec{J}_{Kerr} is Kerr polarization current; and \vec{J}_{MPI} is the multiphoton ionization term. For dielectric materials, such as fused silica, the heating of the conduction band electrons is modeled by Drude model with time-dependent carrier density as follows:

$$\frac{\partial \vec{J}_D}{\partial t} = -\nu_e \vec{J}_D + \frac{e^2 n_e}{m_e} \vec{E} \quad (3)$$

where e is the elementary charge; m_e is the mass of an electron; n_e is the carrier electron density and ν_e is the electron collision frequency. For metals, as gold or silver, Lorentz-Drude model is applied.

$$\frac{\partial^2 \vec{J}_m}{\partial t^2} + \gamma_m \frac{\partial \vec{J}_m}{\partial t} + \omega_m^2 \vec{J}_m = G_m \omega_p^2 \frac{\partial \vec{E}}{\partial t} \quad (4)$$

where $\gamma_m \omega_m$ and G_m are the damping factor, resonance frequency and oscillator strength respectively for each Lorentz pole m , and $\omega_p = \frac{e^2 n_e}{m_e}$ is the plasma frequency, and $\vec{J}_L = \sum_m \vec{J}_m$ is the resulting current for dispersive medium.

In addition, nonlinearity of the third order is included, which describes Kerr effect, as follows:

$$\vec{J}_{\text{Kerr}} = \varepsilon_0 \chi_3 \frac{\partial (|\vec{E}|^2 \vec{E})}{\partial t} \quad (5)$$

where the third-order susceptibility is $\chi_3 = 2 \cdot 10^{-22} \text{ m}^2 \text{ V}^{-2}$ [10].

For multiphoton ionization, two approaches are used and compared: the complete Keldysh theoretical equation [11], including multiphoton and tunneling ionization, for which the corresponding current can be written as:

$$\vec{J}_{\text{MPI}} = E_g \frac{w_{\text{Keldysh}} \vec{E}}{I} \frac{n_a - n_e}{n_e} \quad (6)$$

and a simplified six-photon ionization model, which is as an approximation at low laser intensities for an excitation wavelength of $\lambda = 800 \text{ nm}$, as

$$\vec{J}_{\text{MPI}} = E_g \sigma_6 I^5 \vec{E} \frac{n_a - n_e}{n_e} \quad (7)$$

Here $E_g = 9 \text{ eV}$ is the electron band gap in the absence of the electric field; $n_a = 2 \cdot 10^{28} \text{ m}^{-3}$ is the saturation density; $I = \frac{n}{2} \sqrt{\frac{\varepsilon_0}{\mu_0}} |\vec{E}|^2$ — intensity; $n = 1.45$ is the refractive index of unexcited fused silica for $\lambda = 800 \text{ nm}$. Keldysh ionization rate (w_{Keldysh}) and the six-photon ionization rate ($\sigma_6 I^6$) for $\sigma_6 = 2 \cdot 10^{-65} \text{ m}^9 \text{ W}^{-6} \text{ s}^{-1}$ [9] and $\sigma_6 = 2 \cdot 10^{-67} \text{ m}^9 \text{ W}^{-6} \text{ s}^{-1}$ [12] are compared. As the intensities reached in our simulations are from $I = 10^{16}$ to 10^{18} W/m^2 and are above the ablation threshold, it is also important to take into account the tunneling ionization effect and consider the complete Keldysh ionization rate. Moreover, applying six-photon ionization model [10] typically considered as a good approximation for low intensities, leads to the overestimation of ionization rate by up to three orders of magnitude in our intensity interval. On the contrary, another approximated model [12] gives underestimated values for the ablation threshold. Therefore, the complete Keldysh expression is proven to be the most appropriate one for photoionization in our case.

Then, Maxwell's equations are coupled with the rate equation for free carrier number density as follows

$$\frac{\partial n_e}{\partial t} = W_{\text{MPI}} + W_{av} - \frac{n_e}{\tau_{tr}} \quad (8)$$

where the first term on the left corresponds to the multiphoton ionization

$$W_{\text{MPI}} = (n_a - n_e)w_{\text{Keldysh}} \quad (9)$$

and $\tau_{tr} = 150$ fs is the electron trapping time [10].

The system of nonlinear equations is resolved by the fixed-point iteration algorithm similar to the iteration algorithms developed in [13, 14].

Here, the initial Gaussian electric field profile is considered as a focused beam source taking the following form:

$$E_x(t, x, y, z) = E_0 \frac{w_0}{w(z)} \exp\left(-\frac{r^2}{w(z)^2} - ikz - ik\frac{r^2}{2R(z)} + i\zeta(z)\right) e^{-2\ln 2\left(\frac{t-t_0}{\theta}\right)^2} e^{i\omega t} \quad (10)$$

where $r^2 = x^2 + y^2 + z^2$ is the radial distance from the center axis of the beam, $w_0 = 1.5$ μm is the beam waist, $w(z) = w_0\sqrt{1 + \left(\frac{z}{z_R}\right)^2}$ is the spot size; $R(z) = z\left[1 + \left(\frac{z}{z_R}\right)^2\right]$ is the radius of curvature, $z_R = \frac{\pi w_0^2 n_0}{\lambda}$ is the Rayleigh length; $\zeta(z) = \arctan\left(\frac{z}{z_R}\right)$ is the Gouy phase shift; $\theta = 70$ fs is the pulse width at half maximum (FWHM); and $t_0 = 125$ fs is a time delay. For the given waist beam and irradiation wavelength of $\lambda = 800$ nm, the numerical aperture is $\text{NA} = n \sin\left(\frac{\lambda}{\pi w_0}\right) \approx 0.169$. Note that for this aperture the paraxial approximation of the Gaussian beam profile is still valid [15, 16].

3. RESULTS AND DISCUSSION

To better understand the process of the first femtosecond laser pulse interaction with the material in the presence of a localized defect, we consider firstly its interaction with a small spherical metallic nanoparticle. For this, it is convenient here to define two dimensionless parameters, a size parameter $q = 2\pi a/\lambda_1$, where a is radius of sphere defect, λ_1 is laser wavelength in the dielectric media; and $n^2 = \varepsilon_2/\varepsilon_1$ is a relative permeability, where $\varepsilon_1, \varepsilon_2$ are permeabilities of the media and of the inhomogeneity, respectively. The local field distribution strongly depends on these parameters according to the Mie theory.

In the present study, we consider, that the conditions $q \ll 1$ and $nq \ll 1$ are satisfied, so that the scattering has a dipole character. For instance, for nanoparticles with radius $a \ll 90$ nm the condition is valid at laser irradiation wavelength $\lambda_1 \approx 550$ nm in fused silica. In this case, the approximation of the scattered electric field can be derived from the general analytical solution of Maxwell's equations for an electromagnetic plane wave, scattered by the homogeneous sphere, or Mie scattering [7], under the discussed conditions assuming that the first electric dipole moment ${}^e B_1$ is higher than all magnetic ${}^m B_n$ and the other electric ones [17]. However, when the relative permeability is high (metallic case), the Rayleigh approximation (condition $nq \ll 1$) is no more applied and magnetic dipole moments should be also considered.

In the near-field approximation ($kr \ll 1$, r is radial distance from the center of the nanoparticle), scattered electric fields can be written in the following form [17]:

$$\begin{aligned} E_r^{(s)} &= -\frac{2i \cos \varphi \sin \theta}{(kr)^3} {}^e B_1 \\ E_\theta^{(s)} &= \frac{\cos \varphi}{kr} \left\{ \frac{i \cos \theta {}^e B_1}{(kr)^2} + \frac{{}^m B_1}{kr} \right\} \\ E_\varphi^{(s)} &= -\frac{\sin \varphi}{kr} \left\{ \frac{i {}^e B_1}{(kr)^2} + \frac{{}^m B_1 \cos \theta}{kr} \right\} \end{aligned} \quad (11)$$

In what follows, we consider the polarization along x direction and light propagation along z direction. This way, both electric field \vec{E} and wave vector \vec{k} lie in xz plane (corresponding to $\varphi = 0$) and we consider the near-field laser-matter interaction in this plane. The intensity distribution can be estimated as (neglecting the magnetic dipole moments):

$$I^2 = E_\theta^{(s)} \overline{E_\theta^{(s)}} + E_r^{(s)} \overline{E_r^{(s)}} \approx \frac{(4 \sin^2 \theta + \cos^2 \theta)({}^e B_1)^2}{(kr)^6} \quad (12)$$

From this expression, one can see that the intensity is higher in the x direction ($\theta = \pi/2$) than in the z direction ($\theta = 0, \pi$), creating elliptical distribution of intensities in the near-field of nanoparticle.

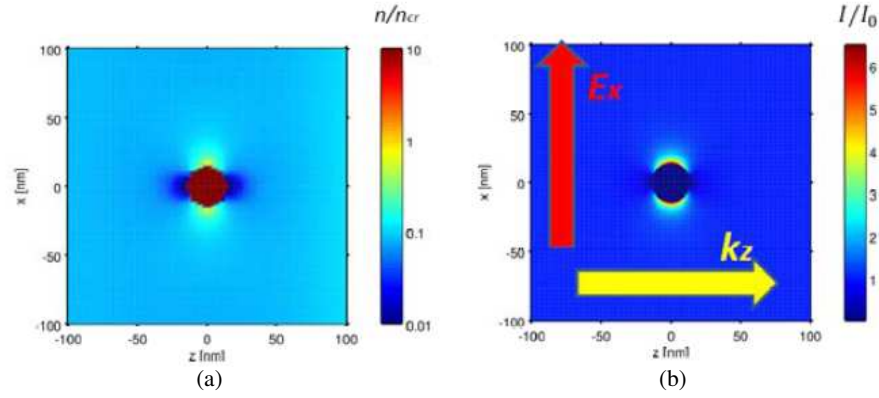


Figure 1: Near-field approximation of the intensity distribution created by small gold nanoparticle given by (b) the analytical Mie solution and electron density distribution of fused silica generated plasma, calculated by using Equations (1)–(8), normalized to critical value $n_{cr} = 1.7 \cdot 10^{27} \text{ m}^{-3}$ at $\lambda = 800 \text{ nm}$ irradiation near gold nanoparticle with parameter size $q = 0.2$ at the end of (a) the pulse. The input pulse has the energy of 250 nJ.

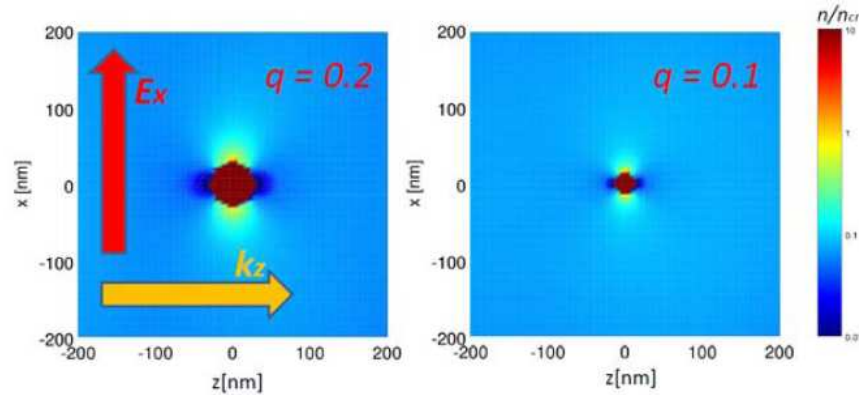


Figure 2: Electron density distributions of generated plasma, calculated by using Equations (1)–(8), normalized to critical value $n_{cr} = 1.7 \cdot 10^{27} \text{ m}^{-3}$ at $\lambda = 800 \text{ nm}$ irradiation near gold nanoparticles of different size ($q = 0.2$ and $q = 0.1$) at the end of the pulse. The input pulse has the energy of 250 nJ.

As the intensity increases and reaches the ablation threshold, the ionization processes start to play essential role and lead to the generation of plasma in the enhanced intensity regions. First hot spots will appear at the interface between fused silica and gold. An asymptotic solution of the Mie scattering problem for near-field of a small nanoparticle is presented in Fig. 1. The calculation results show that density distribution strictly follows the intensity one. The process of the plasma generation is quite similar for an inhomogeneity of a smaller size (Fig. 2), which gives us the opportunity to understand what happens in the near-field of very small defects considering nanoparticles larger in size. Assuming that after the first pulse, plasma has reached the critical density value $n_{cr} = 1.7 \cdot 10^{27} \text{ m}^{-3}$, we note that the new inhomogeneity will have metallic properties and can be considered as larger defect elongated in the polarization direction.

The process of plasma generation does not strongly depend on the size and on the exact nature of the defect. However the optical parameters of the media are crucial in the electromagnetic modeling. As frequency dependence of fused silica is described by Drude formalism, the complex permeability of the media, dependent also on the electronic carrier density, can be written in the following way:

$$\varepsilon(n_e) = \varepsilon_\infty - \frac{e^2 n_e}{m_e (\omega^2 + \nu_e^2)} + i \frac{e^2 n_e \nu_e}{m_e \omega (\omega^2 + \nu_e^2)} \quad (13)$$

where $\omega = \frac{2\pi c}{\lambda}$ is the frequency of the irradiated wavelength and ν_e is the electron collision frequency. In several works, the electron collision time, which in reality depends both on the electron carrier density and on the electron temperature, is assumed to be constant. The values commonly used

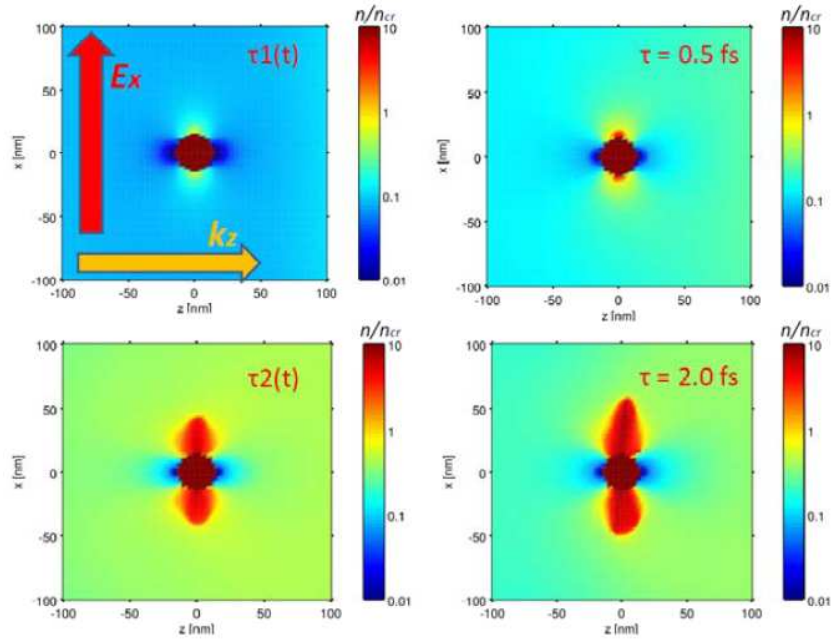


Figure 3: Electron density distributions, calculated by using Equations (1)–(8), normalized to fused silica critical value $n_{cr} = 1.7 \cdot 10^{27} \text{ m}^{-3}$ at $\lambda = 800 \text{ nm}$ irradiation near gold nanoparticle for four different electron collision times models: $\tau_1(t)$, according to (14) used in Reference [19, 21]; $\tau = 0.5 \text{ fs}$; $\tau_2(t)$, according to (15); and $\tau = 2.0 \text{ fs}$. The input pulse has the energy of 300 nJ .

in the analysis of experimental measurements and in numerical simulations vary from 0.1 fs to 10 fs [18–22].

In this work, the calculations are first performed with $\tau = 1/\nu_e = 0.5 \text{ fs}$. In addition, we take into consideration time-varying density-dependent electron collision time by using two different equations. One possibility is to use the following expression that was proposed in Drude models [20, 22]:

$$\begin{cases} \tau(t) = 3.5 \text{ fs}, & n_e(t) \leq 5 \cdot 10^{25} \text{ m}^{-3} \\ \tau(t) = \frac{16\pi\epsilon_0^2 \sqrt{m_e^* (0.1 E_g)^3}}{\sqrt{2} e^4 n_e(t)}, & n_e(t) \geq 5 \cdot 10^{25} \text{ m}^{-3} \end{cases} \quad (14)$$

where $E_g = 9 \text{ eV}$ is the electron band gap and $m_e^* = 0.64 m_e$ — reduced electron mass. In the work [19] the comparison between the calculated reflectivity for different electron collision times and the experimental results obtained in [10] has been done. This comparison gives us the maxima and minima of the parameter which can be used in simulations.

In dielectric materials electron collision time also depends on electron mobility, so that the following empirical equation is to be checked out:

$$\tau_e(t) = \tau_{\min} + \frac{\tau_{\max} - \tau_{\min}}{1 + (n_e(t)/n_{cr})^\alpha}, \quad (15)$$

where $\tau_{\min} = 0.2 \text{ fs}$; $\tau_{\max} = 2 \text{ fs}$; and $\alpha = 0.7$. Thus, with growing density we obtain smaller values for collision time, which fits well the experimental results [10, 22, 23].

The calculation results obtained by using different parameters (constant electron collision times $\tau = 0.5 \text{ fs}$ and $\tau = 2 \text{ fs}$ and empirical relationships (14) and (15)) are shown in Fig. 3. One can see that the results obtained by using Equation (14) are closer to the ones obtained for $\tau = 0.5 \text{ fs}$ and reveal smaller effects of the particles, whereas the results calculated by using Equation (15) are closer to the case with $\tau = 2 \text{ fs}$ and demonstrate stronger changes in the field around the particle. One can notice a slight asymmetry in the density distribution in “ x ” direction relative to the collision time of 2 fs in Fig. 3. This asymmetry comes from the numerical scheme which should be improved, the work is underway.

In what follows, we compare the density distributions of the fused silica plasma generated in the near-field of the gold nanoparticle after the end of the pulse. The higher the collision time is,

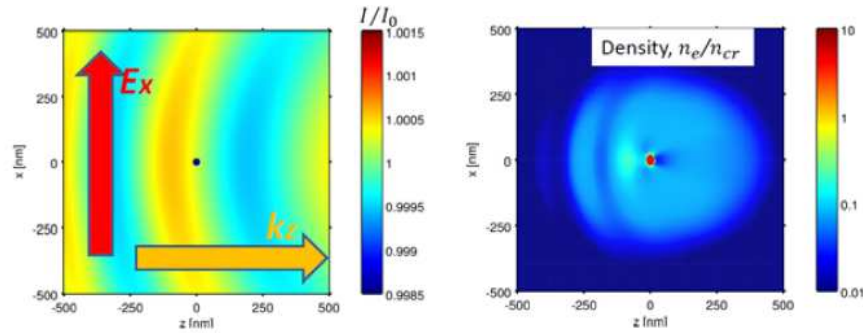


Figure 4: Far-field resulted intensity distribution (interference with plane wave) for a small gold nanoparticle and electron density distribution image of a Gaussian beam tightly focused in fused silica with a small inhomogeneity showing how the light propagation might be further affected and new plasma generated in the maxima of the resulted intensity. Electron density, calculated by using Equations (1)–(8), is normalized to fused silica critical value $n_{cr} = 1.7 \cdot 10^{27} \text{ m}^{-3}$ at $\lambda = 800 \text{ nm}$ irradiation. The input pulse has the energy of 250 nJ.

the closer the properties of the media to the metallic ones. Moreover, the one can note, that the electron collision time which corresponds to the near-critical density value plays a crucial role in plasma generation. Thus, in the first proposed empirical model (14) $\tau_1(n_{cr}) \approx 0.1 \text{ fs}$ and in the (15) $\tau_2(n_{cr}) \approx 1.1 \text{ fs}$. These facts explain the differences in the calculation results.

Finally we investigate how the generated plasma near small defect affects the laser propagation. We start from the far-field approximation ($kr \gg 1$) [17]:

$$\begin{aligned}
 E_r^{(s)} &= -\frac{2 \cos \varphi \sin \theta}{k^2 r^2} e B_1 \exp(ikr) \\
 E_\theta^{(s)} &= -\frac{i \cos \varphi}{kr} \exp(ikr) \{ {}^e B_1 \cos \theta + {}^m B_1 \} \\
 E_\varphi^{(s)} &= \frac{i \sin \varphi}{kr} \exp(ikr) \{ {}^e B_1 + {}^m B_1 \cos \theta \}
 \end{aligned} \tag{16}$$

Due to the interference of the incident wave with the scattered spherical wave, the periodic maxima and minima will be organized and they will lead to the regions of the enhanced density. However, the intensity decreases very fast in the radial direction, as $1/r^2$, explaining why local maxima are getting weaker. We consider, as for the near-field problem, the laser interaction with the defect in xz plane, corresponding to $\varphi = 0$. Note, in this case $E_\varphi^{(s)} = 0$ and in the far-field $E_\theta^{(s)} \gg E_r^{(s)}$. Converting the scattered electric field to Cartesian coordinates, we see that there is a scattered component $E_x^{(s)} \sim \frac{\exp(ikz)}{kz}$ which interferes with the incident wave $E_x^{(i)} \sim \exp(-ikz)$ and this interference leads to maxima and minima in the axis z backward direction. The interference diagram between asymptotic for the Mie scattering problem, a solution in the far-field for a small inhomogeneity and a plane wave are shown in Fig. 4. The density distribution calculated by FDTD is also presented in the figure, where the interference leads to the organization of the second nanoplasma structure created in backward direction of laser propagation.

4. CONCLUSION

We have investigated numerically nanoplasma formation near different kind of defects due to tight focusing during femtosecond laser irradiation. It is shown that the transient properties of the material surrounding the defect object strongly impact the distribution and the size of the generated plasma. Therefore, collisional frequency is the parameter which is crucial for electromagnetic modeling. The size of inhomogeneity and its associated electron number density (if they satisfy Rayleigh approximations $q \ll 1$ and $nq \ll 1$) are less important. Each considered inhomogeneity leads to the generation of the plasma in the near-field of the impurity center and spreading of the defect zone in form of ellipsoid. As the inhomogeneity grows, the scattering wave from it interacts with the incident wave. As a result of the interference in the far-field the density maxima are found to appear and new plasma regions are generated. These results demonstrate how the small defects can evaluate and how the light interaction is further affected due to their formation during the femtosecond laser irradiation.

ACKNOWLEDGMENT

This work was supported by the LABEX MANUTECHSISE (ANR-10-LABX-0075) of Université de Lyon, within the program “Investissements d’Avenir” (ANR-11-IDEX-0007) operated by the French National Research Agency (ANR).

REFERENCES

1. Shimotsuma, Y., et al., “Self-organized nanogratings in glass irradiated by ultrashort laser pulses,” *Phys. Rev. Lett.*, Vol. 91, No. 24, 2003.
2. Liang, F., et al., “Role of ablation and incubation processes on surface nanograting formation,” *Optical Materials Express*, Vol. 1, No. 7, 2011.
3. Buschlinger, R., S. Nolte, and U. Peschel, “Self-organized pattern formation in laser-induced multiphoton ionization,” *Ph. Rev. B*, Vol. 89, 184306, 2014.
4. Richter, S., et al., “The role of self-trapped excitons and defects in the formation of nanogratings in fused silica,” *Optics Letters*, Vol. 37, No. 4, 2012.
5. Rajeev, P., et al., “Memory in nonlinear ionization of transparent solids,” *Phys. Rev. Lett.*, Vol. 97, 253001, 2006.
6. Martin, P., S. Guizard, et al., “Subpicosecond study of carrier trapping dynamics in wide-band-gap crystals,” *Phys. Rev. B*, Vol. 55, No. 9, 1997.
7. Mie, G., *Ann. Phys.*, Vol. 25, 377, 1908.
8. Yee, K. S., “Numerical solution of initial boundary value problems involving Maxwell’s equations in isotropic media,” *IEEE Trans. on Antennas and Propagat.*, Vol. 14, No. 3, 302–307, 1966.
9. Roden, J. A. and S. D. Gedney, “Convolution PML (CPML): An efficient FDTD implementation of the CFS-PML for arbitrary media,” *Microwave and Optical Technology Letters*, Vol. 27, No. 5, 334–339, 2000.
10. Gamaly, E., “Laser-matter interaction in the bulk of a transparent solid: Confined microexplosion and void formation,” *Phys. Rev. B*, Vol. 73, 214101, 2006.
11. Keldysh, L. V., “Ionization in the field of a strong electromagnetic wave,” *Soviet. Phys. JETP*, Vol. 20, No. 5, 1307–1314, 1965.
12. Couairon, A., “Filamentation and damage in fused silica induced by tightly focused femtosecond laser pulses,” *Phys. Rev. B*, Vol. 71, 125435, 2005.
13. Greene, J. and A. Taflove, “General vector auxiliary differential equation finite-difference time-domain method for nonlinear optics,” *Optics Express*, Vol. 14, No. 18, 2006.
14. Ammann, M., “Non-trivial materials in EM-FDTD,” Master’s Thesis, Department of Physics, Swiss Federal Institute of Technology, 2007.
15. Bulgakova, N. M., V. P. Zhukov, and Y. P. Meshcheryakov, “Theoretical treatments of ultrashort pulse lasers processing of transparent materials: Toward understanding the volume nanograting formation and “quill” writing effect,” *Appl. Phys. B*, Vol. 113, 437–449, 2013.
16. Bulgakova, N. M., V. P. Zhukov, et al., “Pulsed laser modification of transparent dielectrics: What can be foreseen and predicted in numerical experiments?,” *J. Opt. Soc. Am. B*, Vol. 31, No. 11, 2014.
17. Born, M. and E. Wolf, *Principles of Optics*, 4th Edition, Pergamon Press, 1970.
18. Sudrie, L., et al., “Femtosecond laser-induced damage and filamentary propagation in fused silica,” *Phys. Rev. Lett.*, Vol. 89, No. 18, 2002.
19. Varkentina, N., O. Uteza, N. Sanner, B. Chimier, M. Sentis, and T. Itina, “Absorption of femtosecond laser pulse in fused silica: Experiments and modelling,” *Proc. of SPIE*, Vol. 7920, 792003-1, 2011.
20. Jing, X., et al., “Modeling validity of femtosecond laser breakdown in wide bandgap dielectrics,” *Appl. Surf. Sci.*, Vol. 258, 4741–4749, 2012.
21. Gamaly, E. and A. Rode, “Transient optical properties of dielectrics and semiconductors excited by an ultrashort laser pulse,” *J. Opt. Soc. Am. B*, Vol. 31, No. 11, 2014.
22. Starke, K., et al., “Investigations in the non-linear behavior of dielectrics by using ultrashort pulses,” *Proc. of SPIE*, Vol. 5273, 501–514, 2004.
23. Sun, Q., et al., “Measurement of the collision time of dense electronic plasma induced by a femtosecond laser in fused silica,” *Optics Letters*, Vol. 30, No. 3, 2005.

Effect of the Rock/Water/Air Interaction on the Complex Dielectric Permittivity and Electromagnetic Waves Attenuation in Water-saturated Sandstones

P. P. Bobrov, A. S. Lapina, and A. V. Repin

Omsk State Pedagogical University, Omsk, Russia

Abstract— The results of the experimental measurements of the complex relative permittivity (CRP) of the water-saturated powders of the quartz granules of different size and solid sandstones are given in the frequency range from 0.1 kHz to 1 GHz. It is shown that when the water content decreases in the powders of the fine granules and solid sandstones at the determined frequency band the increasing of the real part and decreasing of the imaginary part of the CRP are observed. This leads to the significant increasing of the skin layer, that reaches the highest values at the water content of about 60–80% of the full saturation.

In the literature, for example in [1], the properties of elastic waves in the water-saturated sandstones, particularly the dispersion and attenuation, were described in details, but the properties of electromagnetic waves were described insufficiently. It is known that the real part of complex relative permittivity (CRP) of sedimentary rocks containing clay roughly increases at frequencies below 1 GHz [2–4]. The reason is in the multifrequency relaxation processes. In completely saturated sandstones the real part of complex relative permittivity (CRP) depends on the porosity and it remains almost constant in the frequency range of 1 MHz to 1 GHz. At frequencies below 1 MHz observed abrupt increase due to the relaxation of the double layer at the rock-water interface.

It is usually assumed that reduction of water content in the rock reduces the real part of CRP. Though there are a number of works which shows the deviations from the tendency in some cases [5–7].

We measured CRP of water-saturated powders of the quartz granules and solid sandstones with a porosity from 7% to 40% in the frequency range from 100 Hz to 1 GHz by using the method described in [8]. The measurement error at different frequencies was from 0,2 to 3% for ϵ' and ϵ'' .

The schematic illustration of the experimental setup is given in Fig. 1. The complex dielectric permittivity was measured in the frequency range from 0.1 kHz to 1 GHz with Rohde & Schwarz ZNB8 vector network analyzer (VNA) and the LCR-meter 3532-50 Hioki HiTESTER. Depending on the measured frequency range, the same cell was either directly connected to the VNA (for measuring in the range from 100 MHz to 1 GHz) or included into the break of the central conductor of a coaxial line of a large cross section (for measuring in the range from 300 kHz to 100 MHz). At frequencies below 1 MHz, the cell admittance was measured ordinary by the LCR meter. CRP of the solid samples was measured in the range of frequencies from 100 Hz till 100 MHz

The characteristics of the investigated samples are in the Table 1.

Table 1: The characteristics of the investigated samples.

No.	The characteristics of the samples	The average diameter d , (μm)	The d RMSE (μm)	The porosity	The dry density (g/cm^3)
1	Powders of the quartz granules	1,35	0,42	0,434	1,50
2		29,6	11,9	0,327	1.58
3		54,5	11,6	0,420	1.57
4		71,5	17,6	0,392	1.60
5	Solid sandstones			0.173	2.21
6				0.068	2.27

The results of the measurements of the real part of the CRP of the completely deionized water-saturated samples that are shown in the table are given at Fig. 2. The temperature here and furthermore is 25°C.

At frequencies upper 1 MHz the values of ϵ' of the large granules powders (samples 2–4) don't almost depend on frequency and they are determined by general porosity. Sample 1 consisting

of fine granules contains the considerable part of bound water on the rock-water interface. At frequencies higher than 100 MHz, the dielectric permittivity of this form of water is determined by oriental polarization of water molecules and it is significantly less than the free water has [8]. At frequencies below 1 MHz the main role plays the polarization in the double layer at the rock-water interfaces, that is why the more the specific surface area (the less the pore size) the higher the ϵ' .

In the solid samples the porosity is far less therefore the dielectric permittivity ϵ' is less at frequency of 100 MHz. For all the samples except the sample 1 there is dependence between general porosity and ϵ' and the square of the correlation coefficient ($R^2 = 0.97$) that is close to linear. The increasing of the ϵ' while decreasing of the frequency begins earlier than in the powders of the quartz granules and obeys another law. Evidently the defining role plays not only the pore size but their form.

The CRP frequency dependence of the samples at different saturation levels is similar to the dielectric relaxation, described by the models of Debye or Cole-Cole.

At certain frequency range the real part of CRP is bigger than the one of the completely saturated samples, but the imaginary part of ϵ'' sharply decreases. It is necessary to note that experimental results that could be treated as the result of the dielectric relaxation were given earlier in works [4–6] as a rule at limited frequency range.

The frequency dependencies for ϵ' and ϵ'' for different saturation levels of the quartz granules powders are shown at the Figs. 2, 3. At high frequencies about 1 GHz within the water saturation level K_W increasing the values of ϵ' are monotonically raising. At the same time the values of ϵ' and ϵ'' in powders of granules of different size for the relevant values of K_W are almost identical.

In the samples containing the fine granules ($r \leq 54.5 \mu\text{m}$) at frequencies of 100 kHz–20 Hz there is a strong influence of relaxation process when K_W is between 0.2 and 0.9. The values of ϵ' are much bigger than at the completely saturation (Fig. 2), but the values of ϵ'' are much smaller. The reason of the relaxation process is in interlayer polarization at the water-air bound.

While increasing the size of granules (and consequently the size of pores) the relaxation process area moves down the frequency. Thus the rising of ϵ' at the decreasing of water saturation level is at frequency range of 50 kHz–12 MHz in the sample No. 2, and at the same frequency range there is only the upper bound of relaxation process in the sample No. 4 at frequency about 20 kHz (Fig. 2). Unfortunately the theoretical dependence of the relaxation time on the pore size wasn't found yet.

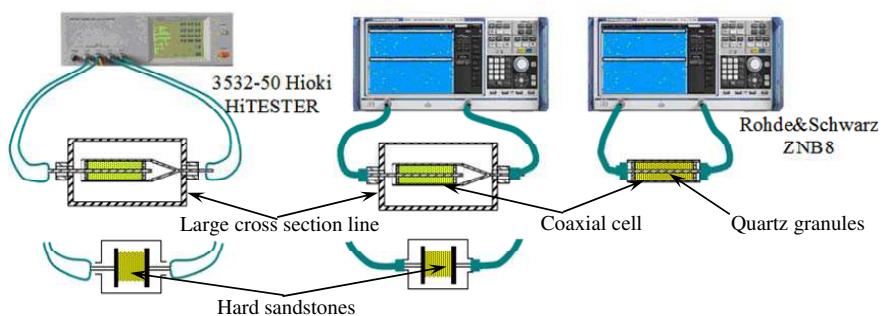


Figure 1: Schematic illustration of the experimental setup to determine the frequency dependence of the CRP.

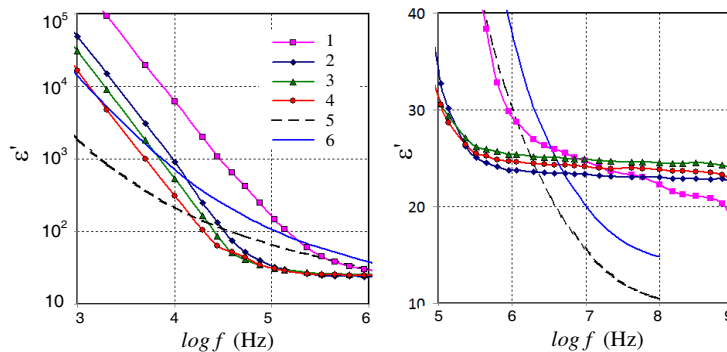


Figure 2: Real part of the dielectric permittivity of the completely saturated samples. The numbers of the curves correspond to the numbers of the samples from Table 1.

The spectra of ϵ' and ϵ'' for the solid sandstones (sample No. 6) are given in Fig. 3. The difference from the CRP of the powders of granules is caused by lower general porosity of the solid sandstones. Firstly the values of ϵ' and ϵ'' are both much smaller at high frequencies than in the powder samples, which can be explained by lower volume content of water. Secondly the values of ϵ' of the solid sandstones are higher at relaxation process areas than in the powders.

Thirdly at frequencies lower than the band of the dielectric relaxation the values of ϵ'' are one-two orders of magnitude less. In spite of the fact the water content in solid sandstones is several times less, the maximum values of ϵ' at relaxation areas are reached at the same values of K_W that are in the powders.

At the dielectric relaxation band at $K_W = 0.6-0.8$ when the values of ϵ' increase and the values of ϵ'' decrease there must be reduction of the electromagnetic wave attenuation and the extension of the skin layer thickness. The calculated values of the skin layer thickness are given in the Fig. 4.

In the powders of quartz granules (sample No. 2) the highest values of the skin layer thickness are at frequencies below 20 MHz and $K_W = 0.6-0.8$ ad these values are higher than in sample No. 4 (see the Fig. 4(a)). The reason is in the absence of dielectric relaxation in the powders with a large size of granules at the investigated frequency range, the skin layer thickness monotonically reduces

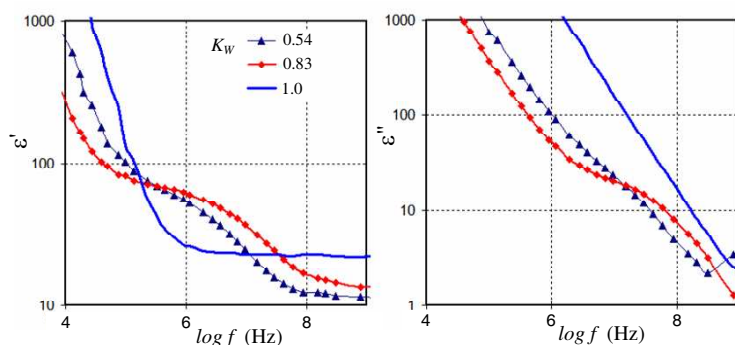


Figure 3: Dielectric permittivity ϵ' and ϵ'' of the sample No. 2, saturated with deionized water at different K_W .

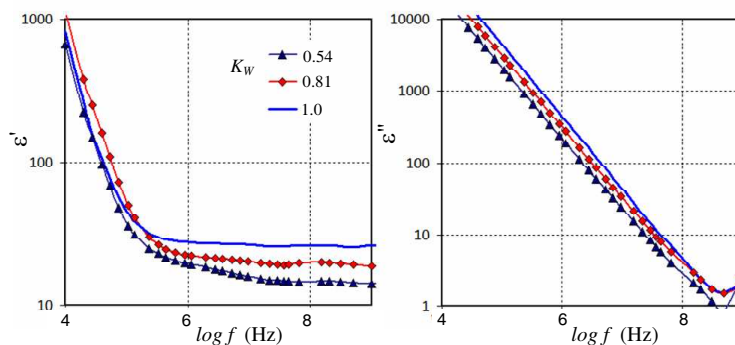


Figure 4: Dielectric permittivity ϵ' and ϵ'' of the sample No. 4, saturated with deionized water at different K_W .

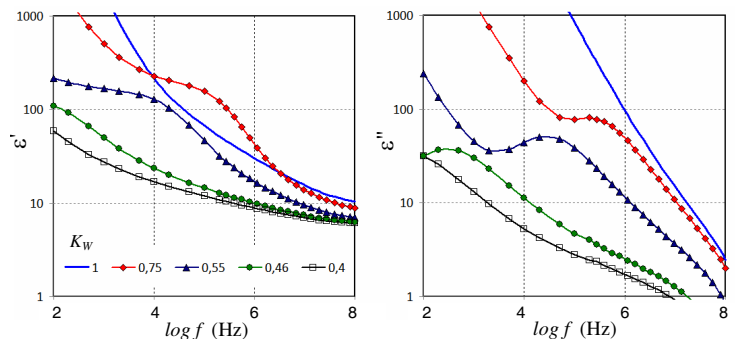


Figure 5: Dielectric permittivity ϵ' and ϵ'' of the sample No. 6, saturated with deionized water at different K_W .

with the increasing of the water saturation level.

The skin layer thickness was determined by the following formula:

$$\Delta = \frac{\lambda_0}{2\pi\kappa} \quad (1)$$

where λ_0 — is a wavelength in vacuum, κ — is an imaginary part of the complex refractive index $n^* = n - i\kappa = \sqrt{\varepsilon' - \varepsilon''}$.

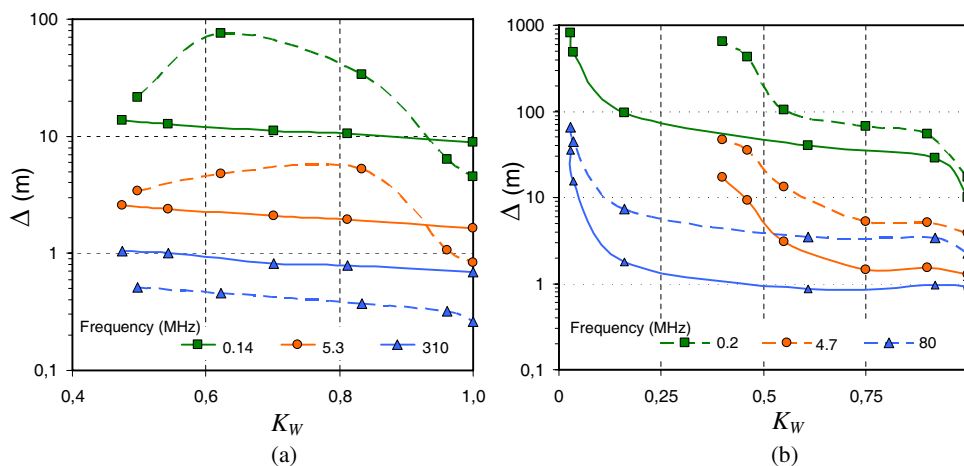


Figure 6: Skin layer thickness dependence on water saturation level at different frequencies. (a) Quartz granules, No. 2 is shaped lines, No. 4 is continuous lines; (b) solid sandstones, No. 6 is shaped lines, No. 5 is continuous lines.

The skin layer thickness is much bigger in the solid sandstones due to the less porosity and less water content. The maximum of the values are in the sample No. 5 at $K_W = 0.9-0.95$ because of the dielectric relaxation.

ACKNOWLEDGMENT

This research was supported by the Russian Foundation for Basic Research, project 14-05-00151.

REFERENCES

- David, E. C., J. Fortin, A. Schubnel, Y. Guéguen, and R. W. Zimmerman, "Laboratory measurements of low- and high-frequency elastic moduli in Fontainebleau sandstone," *Geophysics*, Vol. 78, No. 5, D369–D379, 2013.
- Levitskaya T. M. and B. K. Sternberg, "Polarization processes in rocks," *Radio Science*, Vol. 3, No. 4, 755–759, 1996.
- Ishida, T., T. Makino, and C. Wang, "Dielectric-relaxation spectroscopy of kaolinite, montmorillonite, allophane, and imogolite under moist conditions," *Clays and Clay Minerals*, Vol. 48, No. 1, 75–84, 2000.
- Epov, M. I., P. P. Bobrov, V. L. Mironov, and A. V. Repin, "Dielectric relaxation in oil-bearing clayey rocks," *Russian Geology and Geophysics*, Vol. 52, No. 9, 1028–1034, 2011.
- Endres, L. and R. Knight, "The effects of pore-scale fluid distribution on the physical properties of partially saturated tight sandstones," *J. Appl. Phys.*, Vol. 69, No. 2, 1091–1098, 1991.
- Sharma, M. M., S. L. Bryant, C. Torres-Verdín, et al., "Integrated, multi-scale characterization of imbibition and wettability phenomena using magnetic resonance and wide-band dielectric measurements," DOE Final Report DE-PS26-04NT15450-2C, The University of Texas at Austin & Rice University, 2007.
- Kavian, M., E. C. Slob, and W. A. Mulder, "Measured electric responses of unconsolidated layered and brine-saturated sand and sand-clay packs under continuous fluid flow conditions," *J. Appl. Geophys.*, Vol. 80, 83–90, 2012.
- Bobrov, P. P., A. V. Repin, and O. V. Rodionova, "Wideband frequency domain method of soil dielectric properties measurements," *IEEE Trans. Geosci. Remote Sens.*, Vol. 53, No. 5, 2366–2372, 2015.

The Electrical Characteristics of the Rocks with Different Texture

P. P. Bobrov, A. S. Yashchenko, O. V. Rodionova, A. V. Repin, and A. S. Lapina

Omsk State Pedagogical University, Russia

Abstract— The results of measuring the frequency characteristics of the complex relative permittivity (CRP) of the artificial clay-sand mixtures having different porosity and specific surface saturable deionized water and emulsion brine-oil are given. It is shown that at the frequency of 1 GHz the real part of the CRP of the water-saturated samples increases almost linearly with increasing porosity, and at 50 MHz it increases almost linearly with increasing specific surface area. Frequency dispersion is described based on the relaxation model of Cole-Cole. It is shown that the relaxation time increases with a decrease of the specific surface area of the samples saturated with deionized water. When the sample was saturated with brine-oil emulsion the relaxation time decreases with increasing of concentration of the solution and also with decreasing oil fraction.

1. INTRODUCTION

The measurements of the complex relative permittivity (CRP) in the wide frequency band allow to study the different polarization effects in clayey porous rocks. Because of the CPR sensitivity to rock texture and fluid saturation, wide-band electromagnetic measurements exhibit frequency dispersion of CPR that are influenced by a variety of petrophysical properties, including porosity, pore morphology, clay amounts, specific surface area and fluid saturation.

Many measurements have been done to study the dielectric spectra of porous saturated media saturated with fluids in different frequency ranges from 10 MHz to 40 GHz [1–7]. Usually samples are measured in narrow frequency bands because of the absence of broadband measurement methods. It does not allow continuous spectra of CPR and acquisition of full information about the frequency dispersion of CPR. Due to our method [8], we can measure the dielectric properties of the same sample in a wide frequency range.

In this paper, we focus on the dependence of the CPR frequency dispersion on the specific surface of artificial mixtures at saturation by deionized water and fluid containing oil and brine.

2. EXPERIMENT DESCRIPTION

The river sand with particle sizes of 200 to 400 microns and a specific surface area of 0.05 m²/g, or spherical quartz granules with particle sizes from 45 to 65 microm and a specific surface area of 0.08 m²/g was the sand fraction of the mixture. There were also 4 types of clay used in making mixture: bentonite (B1), Ca — bentonite (B2), Na — bentonite (B3) and kaoline (K). The areas of a specific surface were measured by a method of adsorption of nitrogen and were found to be 140 m²/g and 60 m²/g to 70 m²/g and 17 m²/g, respectively.

Samples were saturated either with deionized water or brine-oil emulsion. NaCl brine was used at a concentration of 4 g/l or 20 g/l.

We performed the dielectric measurements in the frequency range from 1 MHz to 4–8.5 GHz at 25°C. The samples after fluid saturation were kept overnight in a closed container. Samples No. 1–7 and No. 10–20 were formed into a cylinder coaxial hole with the size of the measuring cell using a press under a pressure of 10 kPa. The use of the press allows us to reduce porosity and increase the density of the sample, as well as to remove almost all the air in it. Samples number 8, 9 were not pressed.

After the measurements, the samples were dried at a temperature of 105°C for calculating the porosity P , and the water saturation level $K_W = W/P$, where W — the volume fraction of water in the sample. The specific surface area S was calculated from the amount and type of clay in the sample. Physical characteristics of the samples are given in the table.

For the dielectric measurements, coaxial line of length from 2 to 5 cm was used and the diameters of the outer and inner conductors were 16 mm and 6.96 mm, respectively. The measurement method is described in [8].

Due to the high losses of electromagnetic energy in the samples the real measurement error of the CRP ϵ' ranged from 3% to 10% in the investigated frequency band. Measurement error of the imaginary part of the CRP ϵ'' was no more than 3%.

Table 1: Physical properties of the samples.

No	Type of clay	Type of sand	K_w	Sand/clay ratio	Saturating fluid	Porosity, P	τ , nsec	S , m^2/g
1	B1	rives sand	0.1	50-50	brine 4 g/l-oil	0.365	58.89	23.03
2			0.33	50-50		0.469	55.68	23.03
3			0.66	50-50		0.469	49.47	23.03
4			0.1	50-50	brine 20 g/l-oil	0.428	52.75	23.03
5			0.33	50-50		0.481	47.60	23.03
6			0.66	50-50		0.372	37.05	23.03
7			0.9	50-50		0.482	29.15	23.03
8	quartz granules	1	50-50	deionized water	0.445	4.57	70.0	
9		1	70-30		0.454	7.73	42.0	
10	B2 (Ca-Bentonite)	river sand	0.99		0-100	0.67	4.1	60.0
11			1.00		30-70	0.59	14.3	42.0
12			1.00		50-50	0.47	19.8	30.0
13	B3 (Na-Bentonite)	river sand	0.73		70-30	0.30	43.2	18.0
14			0.80		0-100	0.64	4.2	70.0
15			0.99		30-70	0.52	7.5	49.0
16			1.00		50-50	0.45	15.7	35.0
17	K (kaoline)	river sand	0.96		70-30	0.36	26.6	21.0
18			0.97		0-100	0.46	373	17
19			0.95		50-50	0.28	63.9	8.5
20			0.93		70-30	0.23	79.6	5.1

3. EXPERIMENT RESULTS AND DISCUSSION

The real and imaginary parts of the CRP of the samples with the same content for various types of clay are given in Fig. 1. Evidently, at frequencies below 0.5–1 GHz it is observed the increase of the real and imaginary parts of the CRP, caused by interfacial polarization. Low increase for the sample with kaolin clay is due to the low specific surface of kaolin. Similar dependence was observed for all samples containing various types of clay. The results of measurements of mixtures with different sizes of sand granules showed that the grain size has very little effect on the CRP of the mixtures.

Research has shown that in sandstones [1] and in the samples containing 70% of clay saturated with water there is an almost linear dependence of the real part of CRP ϵ' at 1 GHz on the porosity P (Fig. 2(a)). The higher the porosity, the greater the water content in the sample W , and hence

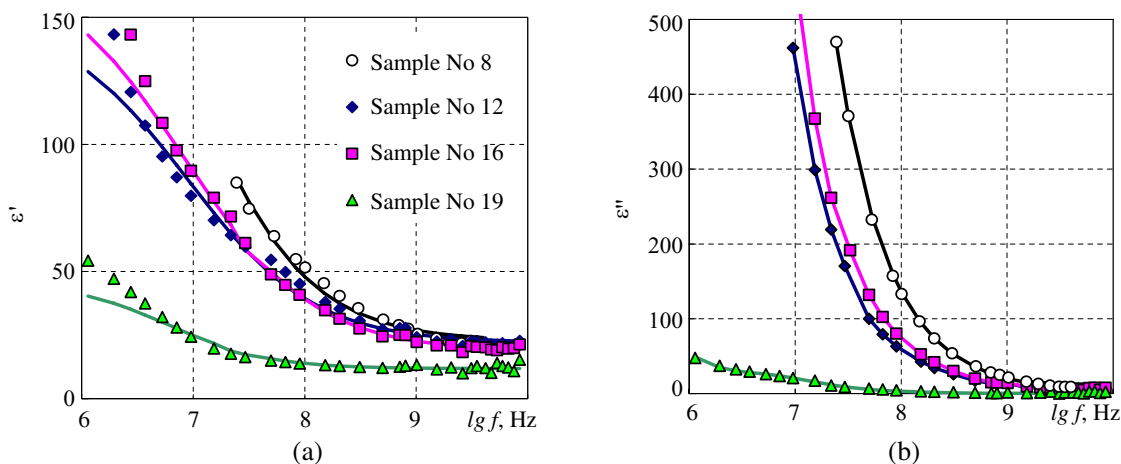


Figure 1: CRP frequency dependencies of samples No. 8, 12, 16 and 19. (a) Real and (b) imaginary parts. The solid lines are the calculation results.

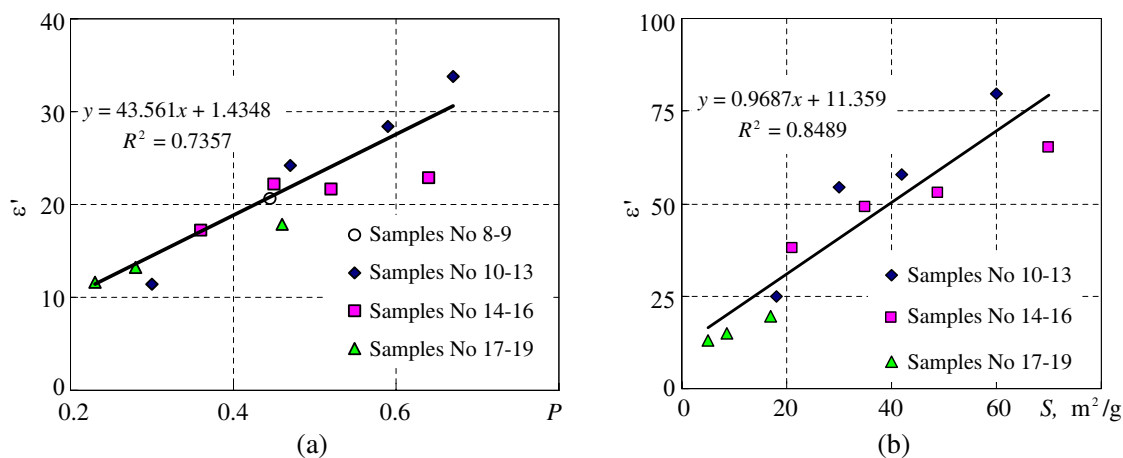


Figure 2: The dependence of the real part of CRP of the samples No 8–20 (a) on the porosity P at 1 GHz and (b) on the specific surface area S at 50 MHz.

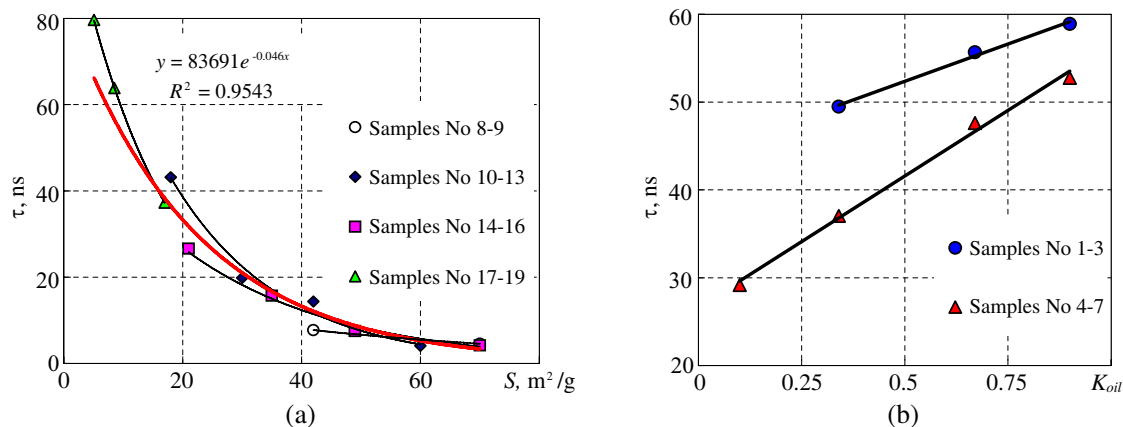


Figure 3: The dependence of the relaxation time (a) on the specific surface area for samples No. 8–20 and (b) on the oil saturation level K_{oil} for samples No. 1–7.

the higher value of ϵ' . Interfacial polarization occurs only at frequencies below 1 GHz. Its influence is stronger for greater specific surface area. You can choose the frequency at which the dependence of $\epsilon'(S)$ is the closest to a linear relationship. Fig. 2(b) shows such dependence at frequency of 50 MHz.

For the CRP dispersion modeling, we used the relaxation model of Cole-Cole:

$$\dot{\epsilon} = \epsilon_{\infty} + \frac{\epsilon_S - \epsilon_{\infty}}{1 + (j\omega\tau)^{1-\alpha}} - j \frac{\sigma}{\omega\epsilon_0}, \tag{1}$$

where ϵ_{∞} is high-frequency dielectric constant; ϵ_S is static dielectric constant; ω is the angular frequency; ϵ_0 is permittivity of free space, τ is relaxation time; σ is ionic conductivity; j is imaginary unit; α is the coefficient of distribution of relaxation times, which can vary from 0 to 1.

The constants of the Cole-Cole were chosen by minimizing the difference between the experimental and calculated data by the method of least squares. While selection of the model parameters, we used the Newton method. Depending on the initial values of the constants of the Cole-Cole model their values after solving the problem of minimizing were different. We took the solution in which the value of the relaxation time and the static dielectric constant were the lowest.

The relaxation times in different water-saturated samples, obtained from Formula (1) decrease exponentially with the increase of the specific surface area.

The solid lines in Fig. 3(a) shows the approximation of the values of the relaxation times of all the samples. The dependences for different types of clay are shown separately. It is observed that the relaxation time in the samples containing Ca-bentonite changes more rapidly at the surface changes than that in the samples containing clay of other forms.

Relaxation time in the samples with the same specific surface area depends on the proportion of oil and brine concentrations in the saturating fluid (Fig. 3(b)). The relaxation time increases with increasing proportion of oil and decreases with increasing concentration of brine.

4. CONCLUSION

As a result of the research work, the dependencies of the CDP of the sand-clay mixtures on the specific surface, porosity and properties of the saturating fluid are determined. The obtained results could be used to interpret dielectric logging, induction-based electromagnetic methods, and ground penetrating radar data to characterize the soils of vadose zone and reservoir rocks.

ACKNOWLEDGMENT

This work was supported by Ministry of Education and Science of the Russian Federation through project 2015/336/3460.

REFERENCES

1. Arulanandan, K., "Dielectric method for prediction of porosity of saturated soil," *Journal of Geotechnical Engineering*, Vol. 117, No. 2, 319–330, 1991.
2. Chelidze, T. L., Y. Gueguen, and C. Ruffet, "Electrical spectroscopy of porous rocks: A review — II. Experimental results and interpretation," *Geophysical Journal International*, Vol. 137, No. 1, 16–34, 1999.
3. Ishida, T., T. Makino, and C. Wang, "Dielectric-relaxation spectroscopy of kaolinite, montmorillonite, allophane, and imogolite under moist conditions," *Clays and Clay Minerals*, Vol. 48, No. 1, 75–84, 2000.
4. Garrouch, A. A. and M. M. Sharma, "The influence of clay content, salinity, stress, and wettability on the dielectric properties of brine-saturated rocks: 10 Hz to 1 MHz," *Geophysics*, Vol. 59, No. 6, 909–917, 1994.
5. Revil, A., "Effective conductivity and permittivity of unsaturated porous materials in the frequency range 1 MHz–1 GHz," *Water Resources Research*, Vol. 49, 306–327, 2013.
6. Schwing, M., Z. Chen, A. Scheuermann, and N. Wagner, "Dielectric properties of a clay soil determined in the frequency range from 1 MHz to 40 GHz," *ISEMA 2013: 10th International Conference on Electromagnetic Wave Interaction with Water and Moist Substances*, 242–250, Weimar, Germany, Sep. 25–27, 2013.
7. Epov, M. I., V. L. Mironov, P. P. Bobrov, and A. V. Repin, "Dielectric relaxation in oil-bearing clayey rocks," *Russian Geology and Geophysics*, Vol. 52, No. 9, 1028–1034, 2011.
8. Bobrov, P. P., A. V. Repin, and O. V. Rodionova, "Wideband frequency domain method of soil dielectric properties measurements," *IEEE Transactions on Geoscience and Remote Sensing*, Vol. 53, No. 5, 2366–2372, 2015.

An Inverse Model for Sea Ice Thickness Retrieval Using Simulated Annealing

Y. J. Lee, K. C. Yeong, and H. T. Ewe
Universiti Tunku Abdul Rahman, Malaysia

Abstract— An inverse model named the Radiative Transfer Inverse Scattering Model (RTISM) for the retrieval of sea ice thickness using Radiative Transfer Theory (RTT) had previously been developed by the authors. The model incorporates the use of the Dense Medium Phase and Amplitude Correction Theory (DMPACT) for better accuracy in the radar backscatter calculations and the application of the Levenberg-Marquardt Algorithm (LMA) to predict the sea ice thickness from the radar backscatter data. While the model has been successful in its attempts to predict the sea ice thickness from radar backscatter data, it has limitations in extending its applications to other sea ice parameters. In this paper, the study of using Simulated Annealing (SA) as an alternative solution for the LMA in the RTISM is presented. SA is appealing as a viable option to replace the LMA due to several reasons. It is a global optimizer and reduces the likelihood of being trapped in a local extremum, thus improving convergence. In addition, SA eliminates the cumbersome recalculation of the Jacobian matrices of the problem function for different applications, as required by LMA. Thus, the use of SA generalizes the inverse model and allows for more room to extend its applications. A comparison between the performances of both optimizers implemented in the RTISM shall be explored in terms of the execution time and accuracy in predicting the sea ice thickness.

1. INTRODUCTION

The physical properties of sea ice are crucial towards studies on global climate change and polar research [1]. The attempts to use inverse theoretical models to retrieve the physical properties of sea ice from microwave remote sensing data has been an ongoing study for many years [2]. Prior to the development of inverse models, many forward scattering models has been proposed and studied to relate between the sea ice characteristics and the radar backscatter data [3]. Many of the inverse models that are developed and presented in [2] use a combination of forward models to perform radar backscatter predictions, an optimization technique to optimize the target parameter and supporting theorems related to the sea ice.

Previously, the authors developed an inverse model named the Radiative Transfer Inverse Scattering Model (RTISM) for the retrieval of sea ice thickness, which is loosely based on the Radiative Transfer-Thermodynamic Inverse Model for Sea Ice Thickness from Time-Series Scattering Data [4]. In the RTISM, the forward model used to estimate radar backscatter data from a set of sea ice parameters in the algorithm is the Radiative Transfer Theory (RTT). This model has been improved with the incorporation of the Dense Medium Phase and Amplitude Correction Theory (DMPACT), which gives a better prediction in the radar backscatter calculations. The Levenberg-Marquardt Algorithm (LMA) is then used to perform prediction of the sea ice thickness from the radar backscatter data. The model has shown potential in its attempts to predict the sea ice thickness from radar backscatter data, but it has limitations in extending its applications to other sea ice parameters or multiple parameters. As such, an alternative method of optimization has been considered as a replacement for the LMA.

2. RADIATIVE TRANSFER INVERSE SCATTERING MODEL (RTISM) WITH SIMULATED ANNEALING (SA)

2.1. Background

In this paper, a modification to the RTISM is introduced by replacing the optimization technique LMA with Simulated Annealing (SA). While the LMA is robust and offers good predictions, it requires the calculation of Jacobian matrices of the problem function to cater for different applications, which can be cumbersome when multiple parameters or changes in the application are involved. The application of SA offers the following benefits. It is a global optimizer and reduces the likelihood of being trapped in a local extremum, thus improving convergence rate. In addition, SA does not require calculating the Jacobian matrices of the problem function, which allows the inverse model to become more generalized and allows for more room to extend its applications

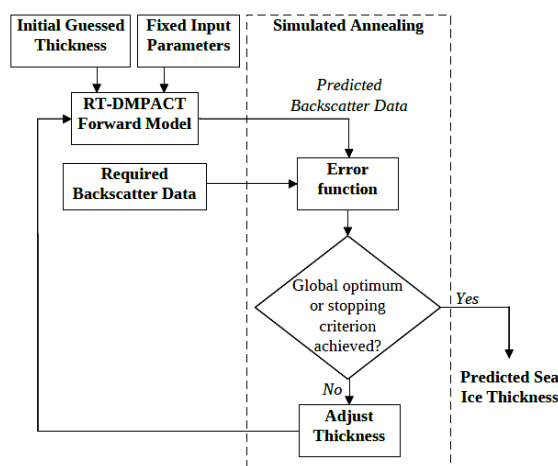


Figure 1: Flowchart of the modified RTISM.

to retrieve other sea ice parameters or to predict multiple sea ice parameters simultaneously. A flow chart of the modified RTISM is shown in Figure 1, where the SA is used as the optimization algorithm.

2.2. Simulated Annealing (SA)

SA is a global optimizer that explores a function's entire parameter space before trying to optimize a function while moving uphill or downhill [5]. This means the optimizer is largely independent of the starting values, often a critical input in other conventional algorithms, such as the LMA. In addition, SA is capable of escaping from local optima and go on to find the global optimum by the uphill and downhill moves. Another advantage of SA is that it makes less stringent assumptions regarding the function, thus making it easier to deal with functions that have ridges and plateaus. Finally, it can also optimize functions that are not defined for some parameter values.

SA is based on thermodynamics, which involves the study of a system's thermal energy, particularly in the way metals cool and anneal. In metallurgy, "annealing" is a technique involving the heating and controlled cooling of a metal to increase the size of its crystals and decrease the thermodynamic free energy of the metal. When a metal is annealed, it eventually arrives at a lower energy state. If the metal is cooled too quickly, or 'quenched', the metal may end up in a polycrystalline or amorphous state, having somewhat higher energy when fully cooled compared to an annealed metal [6]. Therefore, the essence of the process is slow cooling, giving sufficient time for the redistribution of the atoms as they lose mobility. This is the technical definition of annealing, and it is essential for ensuring that a low energy state will be achieved. The SA program used in the inverse model is based on Goffe et al., which itself is a modification of the program by Corana et al. for continuous variable problems [7].

2.3. Forward Model

In the RTISM, the RT-DMPACT forward model is used to relate between the sea ice characteristics and the radar backscatter data. Based on RTT and incorporated with the DMPACT, it is configured for a single layer medium only. In this study, the model is applied to sea ice and considers the sea ice as an electrically dense media [8]. The configuration for the forward model is shown in Figure 2 and caters for single layer only, where θ and θ_S are defined as the angle of propagation of the incident and scattered wave, respectively. In this configuration, the sea ice layer is sandwiched between the air layer (top medium) and the ocean layer (bottom medium) to simulate the actual sea ice conditions. Further details and formulations of the RT-DMPACT applied to sea ice can be found in Albert et al. [8]

3. METHODOLOGY

In order to verify the applicability and function of the modified RTISM with SA, a series of test runs were conducted using simulated results from the RT-DMPACT itself as the comparison data. The following function was to be optimized by the SA in order to predict the sea ice thickness from radar backscatter data:

$$\varepsilon_{\sigma} = \sigma'_{HH} - \sigma_{HH} \quad (1)$$

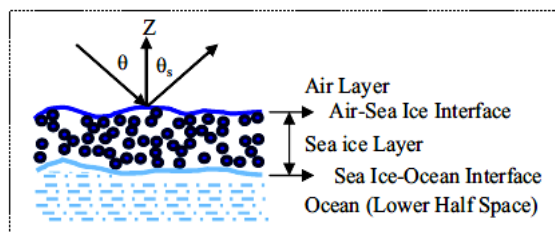


Figure 2: Model configuration for the RT-DMPACT single layer forward model.

where ε_σ is the error difference, σ'_{HH} is the estimated radar backscatter data from the forward model with guessed sea ice thickness and σ_{HH} is the required radar backscatter data (simulated using RT-DMPACT with correct sea ice thickness). The optimization will be performed by the SA by varying the sea ice thickness to find the sea ice thickness that gives the global minimum of ε_σ .

Before beginning the simulation, the RT-DMPACT is first used to simulate two sets of radar backscatter data from two test frequencies (1 GHz and 5.3 GHz), σ'_{HH} , for a range of sea ice thicknesses from 0.1–3.0 m. For this step, only the sea ice thickness is a variable while all other sea ice parameters and the incident angle are fixed. Next, the radar backscatter data, σ'_{HH} is input into the SA to begin the tests. In order to ensure consistency, the following values in Table 1 are set for all the tests:

Table 1: Input parameters for SA.

Parameter	Value
Temperature reduction factor, r_T	0.85*
Error tolerance for termination, ε	1.0E-6
Number of cycles, N_S	20*
Number of iterations before temperature reduction, N_T	20
Maximum number of function evaluations	10000
Initial temperature, T_0	5.0
Step length vector, V	1.0*
Vector that controls step length adjustment, C	2.0*
Lower bound for solution variable, L_B	0.1 m
Upper bound for solution variable, U_B	4.0 m
Starting value for variables to be optimized, X	1.2 m

*As recommended in [5]

4. RESULTS AND DISCUSSION

Figure 3 shows the comparison between predicted sea ice thickness from the RTISM with SA and also from the RTISM with LMA for 12 test cases with the wanted sea ice thickness. Preliminary tests show that the SA is able to estimate the correct sea ice thickness by finding the minimum error between σ'_{HH} and σ_{HH} . The tests prove that the modified RTISM with SA is fully functional and ready to be applied to actual case studies to find out its effectiveness under real conditions. The predictions between both models are quite close with each other, however in terms of performance, the RTISM with SA used about 15 – 20 minutes to complete each test case while the RTISM with LMA only used about 5–10 minutes.

In all the test cases, it is assumed that there are no errors coming from the forward model and that the simulated results are as accurate as possible to the actual values. In real conditions however, this is not true as the predictions from the forward model is actually a reasonable estimate of the actual value within the allowed tolerances. It will be interesting to see whether the model will still be able to give a reasonable estimate of the sea ice thickness under these circumstances.

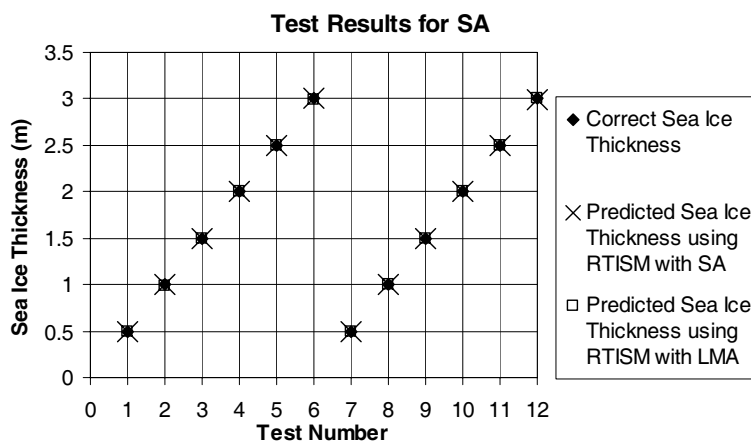


Figure 3: Comparison between sea ice thickness retrieval using RTISM with SA and LMA for data using test frequencies 1 GHz (tests 1–6) and 5.3 GHz (tests 7–12).

5. CONCLUSION AND FUTURE WORK

As a conclusion, a modification of the RTISM for the retrieval of sea ice thickness using SA has been proposed. Initial tests show promising results, with good agreements achieved between the model estimations and required sea ice thickness. In future works, more study needs to be done to find out the best configuration for the SA and also to test the model under actual conditions and measured parameters.

ACKNOWLEDGMENT

The research was supported with the research fund from MOSTI Malaysia [Grant Number: FP1213E 037.S2].

REFERENCES

- Haykin, S., E. O. Lewis, R. K. Raney, and J. R. Rossiter, *Remote Sensing of Sea Ice and Iceberg*, John Wiley & Sons, Inc., 1994.
- Golden, K. M., M. Cheney, K. H. Ding, A. K. Fung, T. C. Grenfell, D. Isaacson, J. A. Kong, S. V. Nghiem, J. Sylvester, and D. P. Winebrenner, "Forward electromagnetic scattering models for sea ice," *IEEE Transactions on Geoscience and Remote Sensing*, Vol. 36, No. 5, 1655–1674, 1998.
- Golden, K. M., D. Borup, M. Cheney, E. Cherkaeva, M. S. Dawson, K. H. Ding, A. K. Fung, D. Isaacson, S. A. Johnson, A. K. Jordan, J. A. Kong, R. Kwok, S. V. Nghiem, R. G. Onstott, J. Sylvester, D. P. Winebrenner, and I. H. H. Zabel, "Inverse electromagnetic scattering models for sea ice," *IEEE Transactions on Geoscience and Remote Sensing*, Vol. 36, No. 5, 1675–1704, 1998.
- Lee, Y. J., W. K. Lim, and H. T. Ewe, "A study of an inversion model for sea ice thickness retrieval in Ross Island, Antarctica," *Progress In Electromagnetics Research*, Vol. 111, 381–406, 2011.
- Goffe, W. L., G. D. Ferrier, and J. Rogers, "Global optimization of statistical functions with simulated annealing," *Journal of Econometrics*, Vol. 60, No. 1–2, 65–99, 1994.
- Press, W. H., S. A. Teukolsky, W. T. Vetterling, and B. P. Flannery, *Numerical Recipes: The Art of Scientific Computing*, Cambridge University Press, New York, 1986.
- Corana, A., M. Marchesi, C. Martini, and S. Ridella, "Minimizing multimodal functions of continuous variables with the 'simulated annealing algorithm'," *ACM Transactions on Mathematical Software*, Vol. 13, No. 3, 262–280, 1987.
- Albert, M. D., T. E. Tan, H. T. Ewe, and H. T. Chuah, "A theoretical and measurement study of sea ice and ice shelf in antarctica as electrically dense media," *Journal of Electromagnetic Waves and Applications*, Vol. 19, No. 14, 1973–1981, 2005.

Adaptive Boundary Approach for EMF Exposure Assessment in Broadband Measurements

Dragan Kljajic, Nikola Djuric, Karolina Kasas-Lazetic, and Danka Antic

Faculty of Technical Sciences, University of Novi Sad

Trg D. Obradovica 6, Novi Sad 21000, Serbia

Abstract— Recently proposed boundary approach for exposure assessment of humans to electromagnetic field (EMF), regarding the continuous broadband EMF monitoring, offers daily upper and lower exposure boundaries. This means that the range with the potential exposure of the general population, as well as the occupational one, can be located in real time. As an advancement of this method, this paper presents a novel approach based on the adaptation of exposure boundaries in order to reduce the difference between them and this will increase the precision of the assessment. Frequency spectrum analysis has been applied, determining the appropriate reference levels for boundary calculation on a particular in-situ location. The results of the performed in-situ test measurement of the high-frequency electric field strength have shown attainment in the reduction of boundaries difference of 36.25%, consequently resulting with the increased precision of the daily exposure assessment for the broadband EMF monitoring.

1. INTRODUCTION

Two most commonly applied approaches for the in-situ measurements of electromagnetic field (EMF) level are the frequency selective and broadband approaches. Even though worldwide researches have shown that, for many cases, the general public exposure is well below the established guidelines, long-term EMF monitoring is an important issue from an environmental protection point of view.

The broadband measuring approach seems to be a more appropriate solution, for the requirements of the continuous and long-term monitoring of the real-time EMF level fluctuations in the environment. This approach results with the single value of the overall and cumulative EMF strength, unlike the frequency selective approach, which simultaneously offers a number of EMF values for each separate frequency in a particular frequency range.

Thus, in order to provide the long-term continuous supervision of the overall and cumulative level of EMF over the observed area, the Serbian electromagnetic field monitoring network — SEMONT has been recently tested [1, 2]. The SEMONT is based on the utilization of autonomous and independent field sensors that perform broadband EMF monitoring, radiated from all active sources around the sensor nodes.

Unfortunately, due to the lack of information on the operating frequencies of EMF sources, the utilization of the broadband measuring approach leads to difficulties in performing the exposure assessment of humans. These difficulties occur since it is not known which of reference levels has to be applied when the comparison of measured values has to be done.

In order to solve this issue, the boundary exposure assessment approach has been proposed, calculating the daily upper and lower boundaries of exposure [3]. That approach has already been implemented into the SEMONT monitoring system and is applicable for both the low-frequency and the high-frequency EMF measurements.

2. THE BOUNDARY ASSESSMENT APPROACH

Regrettably, there is no recommended specific procedure for a comprehensive exposure assessment of the human population in case of the broadband EMF monitoring. On the other hand, some baseline instructions are provided in the standard SRPS EN 50492:2010 [4], suggesting the comparison of the obtained measured value with the lowest reference level in the frequency range of the used field probe in order to obtain the global exposure ratio (*GER*).

Based on this suggestion, the recently proposed boundary approach suggests the comparison of the obtained measured values with the lowest and highest reference levels in the field probe's frequency range [3]. Applying such an approach, the upper and lower boundaries of exposure can be determined. In case of the high-frequency electric field measurements, the boundaries are

calculated via following expressions:

$$GER_{low} = \left(\frac{E_m}{E_{ref\ max}} \right)^2 \quad \text{and} \quad GER_{up} = \left(\frac{E_m}{E_{ref\ min}} \right)^2, \quad (1)$$

where E_m is the broadband measured electric field strength value, while $E_{ref\ min}$ and $E_{ref\ max}$ are the minimum and maximum electric field reference levels, over the frequency range of the applied field probe, defined by the corresponding legislation for the general population, as well as the occupational exposure. In this paper, the exposure assessment has been done considering reference levels prescribed by the Serbian legislation [5].

Combining the proposed boundary approach and the results of the continuous in-situ EMF broadband monitoring, the daily boundaries can be obtained, showing the fluctuation of the potential exposure over a long period of time, as it is depicted in Fig. 1 [2].

For the purpose of this initial research, a simple test measurement of the high-frequency electric field strength was conducted on the location of the campus area of the University of Novi Sad. Four-hour broadband monitoring of the electric field strength was performed regarding the SEMONT's measurement procedure [2], in the frequency range of 100 kHz up to 6 GHz, applying Narda NBM-550 handheld broadband meter equipped with EF 0691 field probe. This equipment has very similar features as the sensor nodes of the SEMONT system.

Based on the acquired measurement results, the GER boundaries calculation was performed according to the Equation (1), where the minimum and maximum reference levels in the observed frequency range were chosen according to the Serbian legislation [5]. Results of the upper and lower GER boundaries calculation are shown in Fig. 2.

The calculation of the upper and lower exposure boundaries results with a certain difference between them, which can be described by the relative difference δ as

$$\delta = \frac{GER_{up} - GER_{low}}{GER_{up}} \cdot 100\% = \left[1 - \left(\frac{E_{ref\ min}}{E_{ref\ max}} \right)^2 \right] \cdot 100\%. \quad (2)$$

In the observed frequency range, $E_{ref\ min} = 11$ V/m (for frequency $f = 400$ MHz) and $E_{ref\ max} = 34.8$ V/m (for frequency $f = 100$ kHz) [5]. Consequently, the relative difference between GER boundaries is 90% from the upper boundary, which presents a significant discrepancy, as it can be observed from Fig. 2.

However, the real exposure is somewhere between GER boundaries and the most precise method to determine it is to use the frequency selective measuring approach, as suggested in the Guidelines of International Commission on Non-Ionizing Radiation Protection (ICNIRP) [6].

Unfortunately, the exposure per frequency approach, given in these Guidelines, could not be applied for broadband EMF measurements, since there is a lack of information on present frequencies on which EMF sources radiate. Thus, this paper proposes the investigation of GER boundaries

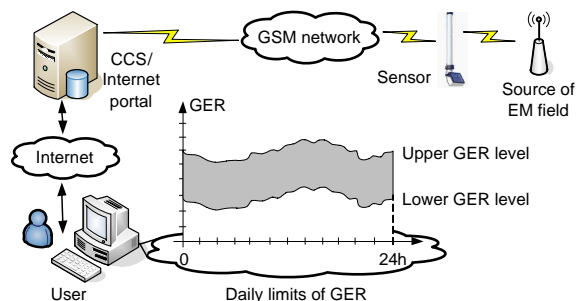


Figure 1: Presentation of daily boundaries of the GER to the public.

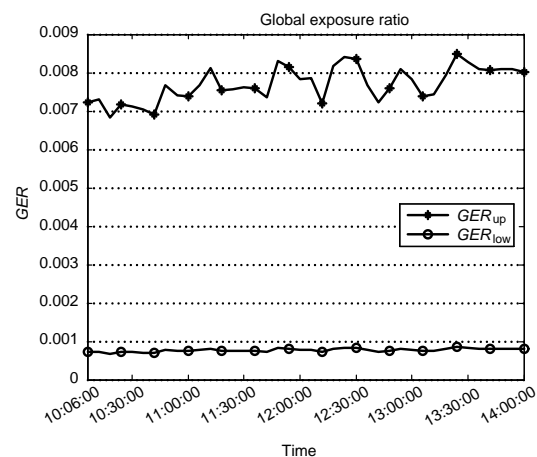


Figure 2: Broadband exposure assessment of the general population on an in-situ measurement location.

adaptation and the reduction of difference between them by adopting new and appropriate reference levels for a particular in-situ location. With the reduction of *GER* boundaries, a smaller range could be offered, where the real exposure can be positioned, resulting with a much better insight onto the exposure on a particular in-situ location.

3. THE ADAPTIVE BOUNDARY APPROACH

The broadband measuring approach offers results of the overall and cumulative value of EMF at a particular in-situ location, without the ability to identify active EMF sources in the surroundings, nor their operating frequencies. Choosing the lowest and highest prescribed reference levels in the observed broadband frequency range for $E_{ref\ min}$ and $E_{ref\ max}$, consequently leads to the underestimation and the overestimation of *GER* boundaries. This situation occurs since the measured results are compared only with these two limits, while the reference levels for other frequencies are not taken into consideration.

Regarding the particular location, it is possible that only few field components in the whole frequency spectrum contribute to the overall measured EMF value. Thus, it is clear that the observed frequency range can be narrowed and new reference levels can be chosen, reducing the gap between *GER* boundaries. This is the main idea of the adaptive boundary approach.

Latest researches have shown that the most dominant sources of the high-frequency EMF emission in the environment are those reserved for GSM 900, GSM 1800 and UMTS 2100 communications services [7, 8]. Having in mind this fact, the shrinking of the observed broadband frequency range is possible in case that it is proven that the contribution from other frequencies and EMF sources to the overall EMF strength is practically negligible, as it is presented in Fig. 3.

One way to determine in-situ active frequencies is by a spectrum scanning. Thus, the adaptation of *GER* boundaries is based on the utilization of the frequency selective in-situ measurement combined with the broadband EMF monitoring.

In order to verify the proposed adaptive approach, the spectrum scanning at a test measurement location was performed. Results of the performed scanning confirmed the assumption on the dominance of the mobile phone communications services in surroundings. Hence, the appropriate shrinking of the observed broadband frequency ranges from 925 MHz to 2200 MHz (comprising only downlink of GSM 900, GSM 1800 and UMTS 2100 services), leading to the selection of new minimum and maximum reference levels: $E_{ref\ min} = 16.728\ V/m$ (for frequency $f = 925\ MHz$) and $E_{ref\ max} = 24.597\ V/m$ (for frequency $f = 2200\ MHz$) [5]. Consequently, the relative difference between the adapted *GER* boundaries is now 53.75% from the upper boundary, while the attained reduction of the difference between the exposure boundaries is depicted in Fig. 4.

The performed analysis shows that, involving a frequency selective measurement, a reduction in

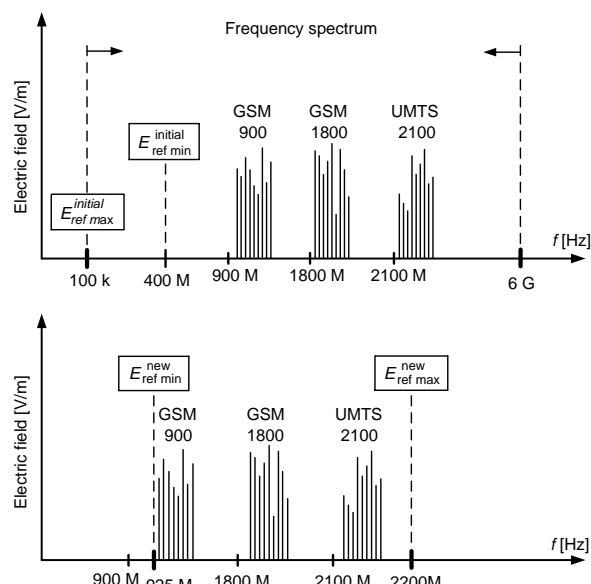


Figure 3: Shrinking of the observed frequency range.

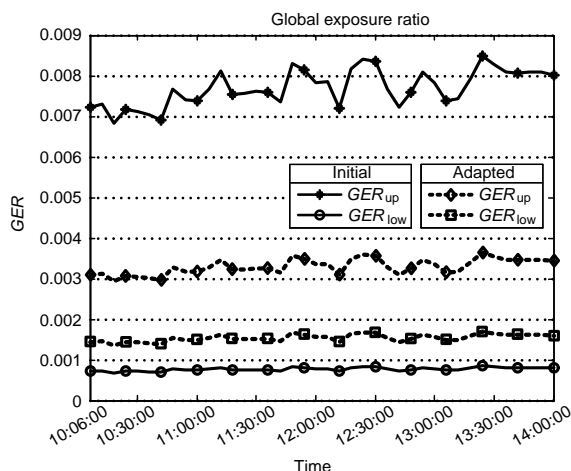


Figure 4: Adaptation of exposure boundaries.

boundaries difference of 36.25% is attained. However, the real exposure is again somewhere between *GER* boundaries, though in this case the precision of assessment is improved, accomplishing a much clearer insight of the human exposure to EMFs at a particular in-situ measurement location.

Generally, a combination of both measuring approaches at in-situ measurement locations could help in advancing the efficiency of systems for the broadband EMF observation, such as the SEMONT system. The implementation of the suggested adaptive boundary approach into those systems could offer the improvement in the accuracy of the assessment of possible long-term exposure of the public to non-ionizing radiation in the environment.

It is important to emphasize that the dominance of EMF sources varies with the measurement location; thus, depending on active frequencies in the sensor node surroundings, the corresponding narrowing of the spectrum could be performed, as well as the appropriate adaptation of exposure boundaries.

4. CONCLUSION

In this paper, one of the possible solutions for the advancement of the proposed boundary exposure assessment approach is presented. This approach is suitable for the purposes of the broadband EMF monitoring in the environment, and is already implemented into the SEMONT monitoring system.

Results of the performed test measurement showed that information on frequency spectrum in the vicinity of the measurement location could enhance the proposed boundary approach through the adaptation of calculated exposure boundaries and the reduction of difference between them.

The results also revealed that the adaptive boundary approach could offer a clearer overview of human exposure to EMF in the environment and increase the precision of the daily exposure assessment on a particular in-situ location. Moreover, performing the periodic EMF spectrum scanning at the position of the SEMONT's sensor nodes could help in the advancement of the efficiency of such monitoring system regarding the precision of the exposure assessment of human population, as well as the occupational one.

ACKNOWLEDGMENT

This work is supported by the Ministry of Education, Science and Technological Development of the Republic of Serbia, under the grant for the project TR 32055.

REFERENCES

1. Djuric, N., D. Kljajic, K. Kasas-Lazetic, M. Milutinov, M. Prsa, V. Bajovic, N. Pekaric-Nadj, and V. Milosevic, "The concept of the SEMONT monitoring system and its influence on the EM pollution protection," *IEEE AFRICON 2013 Conference*, 1298–1302, Mauritius, Sep. 9–12, 2013.
2. Djuric, N., D. Kljajic, K. Kasas-Lazetic, and V. Bajovic, "The measurement procedure in the SEMONT monitoring system," *Environmental Monitoring and Assessment*, Vol. 186, No. 3, 1865–1874, Mar. 2014.
3. Djuric, N. and D. Kljajic, "Assessment of daily exposure in the broadband continuous monitoring system — SEMONT," *IEEE AFRICON 2013 Conference*, 903–907, Mauritius, Sep. 9–12, 2013.
4. "Basic standard for the in-situ measurement of electromagnetic field strength related to human exposure in the vicinity of base stations," SRPS EN 50492:2010, 2010.
5. "Regulation on the limits of exposure to non-ionizing radiation," No. 104/09, the Law of the Republic of Serbia.
6. International Commission on Non-ionizing Radiation Protection (ICNIRP), "Guidelines for limiting exposure to time-varying electric, magnetic, and electromagnetic fields (up to 300 GHz)," 1998, <http://www.icnirp.de/documents/emfgdl.pdf>.
7. Eurobarometer 2007, Electromagnetic Fields, 2007, http://ec.europa.eu/public_opinion/archives/ebs/ebs_272a_en.pdf.
8. Gajšek, P., P. Ravazzani, J. Wiart, T. Samaras, and G. Thuróczy, "Electromagnetic field exposure assessment in Europe radiofrequency fields (10 MHz–6 GHz)," *Journal of Exposure Science and Environmental Epidemiology*, Vol. 25, No. 1, 37–44, 2013.

Topographic Effect on the Canopy Reflectance

Weiliang Fan^{1,2}, Qinhuo Liu^{1,2}, Jing Li^{1,2},
Gaofei Yin^{1,2}, Yelu Zeng^{1,2}, and Baodong Xu^{1,2}

¹State Key Laboratory of Remote Sensing Science, Institute of Remote Sensing and Digital Earth
Chinese Academy of Sciences, Beijing 100101, China

²Joint Center for Global Change Studies (JCGCS), Beijing 100875, China

Abstract— Many research works indicate that the topographic factors have strong influence on forest canopy reflectance. However, the quantitative effects of canopy reflectance by topographic is difficult to be evaluated. For this purpose, the topographic effects on sloping forest reflectance are quantitatively evaluated based on GOST model and the observed remotely-sensed images. The major findings are summarized as follows: First, the topographic factors (slope and aspect) have great impacts on sloping canopy reflectance. A case study shows that the modeled topographic index for reflectance ($[\text{bidirectional reflectance distribution of a sloping forest} - \text{bidirectional reflectance distribution of a flat forest}] / \text{bidirectional reflectance distribution of a flat forest}$), which is the relative error in modeled canopy reflectance by ignoring the topographic effects, can reach up to 58%, while the maximum observed topographic index for reflectance varies from 0.012 to 0.038. Second, model simulations show that topography has different effects on the sloping canopy reflectance in different view directions. These effects should be considered in analyzing multi-angle images. Third, topographic factors have different impacts on sloping canopy reflectance of different canopy structures. Canopy structure should also be considered in topographic correction on reflectance images because topographic factors alone is insufficient for correcting all variations of reflectance with slope and view angle.

1. INTRODUCTION

Topography modifies canopy structures and causes terrain effects on satellite observations [1]. As yet, there are rarely specific studies to quantify the topographic effects on the forest reflectance. Richter, et al. [2] indicate that in mountainous areas there is a strong influence of topography on the signals recorded by space-borne optical sensors, i.e., for the same surface cover slopes oriented away from or towards the sun will appear darker or brighter, respectively, if compared to a horizontal geometry. This behavior causes problems for a subsequent scene classification and thematic evaluation. Teillet [3] noted that not enough work has been done in this area to establish guidelines on the relative importance of topographic effects in remotely-sensed imagery.

The accurate hybrid canopy reflectance model named GOST for modeling canopy reflectance on slopes is developed and validated by Fan et al. [4, 5]. GOST has common advantages in both of GO models and RT models and the ability to simulate the reflectance of shaded forest components as well as the total BRDF (Bidirectional reflectance factor) on slopes. The validation shows that GOST has the ability to simulate the canopy structure (gap fraction and the area ratios of the 4 scene components) and canopy reflectance on sloping terrains. It also indicates that GOST has the ability to quantitatively analyze the topographic effects on sloping canopy reflectance. The topographic effects on canopy reflectance will be evaluated using the simulated results by GOST and observed results by Landsat TM5 images in this paper.

2. STUDY SITES AND METHODS

2.1. The Study Sites and Its Corresponding TM Images

A rectangular forest region (94,581 m \times 123,375 m) in the northeast of China (near to 53N, 124E) is selected as the study site 1 (SS1). The vegetation cover is predominantly conifer forest in this region. The corresponding Landsat TM5 image at a solar azimuth angle of 154° and zenith angle of 46° is acquired on August 30, 2009 and a total of 3,153 \times 4,113 nadir view pixels are selected for this study. The study site 2 (SS2) is also a conifer forest region (25,320 m \times 61,830 m) in the southwest of China (near to 30N, 107E). The corresponding Landsat TM5 image is acquired on September 2, 2009 at a solar azimuth angle of 129° and zenith angle of 32°. A total of 844 \times 2,061 nadir view pixels are selected for the forest region. The DEM (digital elevation model) datasets for SS1 and SS2 are used to produce images of the slope and aspect.

2.2. A Typical Boreal Canopies for Model Simulation

The parameters of the old Jack Pine (OJP) canopies (Latitude N $53^{\circ}54'58''$, Longitude W $-104^{\circ}41'24''$) on flat terrains are selected from Leblanc et al. [6]. Based on this parameter set, the 0° , 30° and 60° slopes are considered for evaluating the topographic effects on canopy reflectance. This forest has 1850 stems per hectare and an LAI of 2.2. The trees are 12 m–15 m in height. It exhibits large crowns with a mean radius 1.3 m. The needle-to-shoot ratio is $\gamma_E = 1.3$. In the red band, the reflectance of foliage is 0.07, the transmittance of foliage is 0.05 and the reflectance of background is 0.09.

2.3. Experiment Description

The quantitative analysis of the topographical effects on the sloping canopy reflectance is based on model simulated results by GOST, and the observed Landsat TM reflectance data are used to support the simulated results of GOST model because no ground observations are available for the sloping canopy parameters corresponding to these selected pixels.

The aspects are set as 0° and the slopes are set as 30° and 60° , respectively for OJP. The sunlight azimuth angle is set as 0° . In order to evaluate the topographic effects on reflectance, the distribution of relative error in reflectance (called topographic index) is calculated as follows (Eq. (1)).

$$RE_R = \frac{R_{\theta g} - R_{\theta g=0}}{R_{\theta g=0}} \quad (1)$$

where $R_{\theta g}$ is the bidirectional reflectance distribution of a sloping forest, and $R_{\theta g=0}$ is the bidirectional reflectance distribution of a flat forest. The greater absolute value RE_R is, the stronger the topographic factors influence the reflectance.

Figure 1 is an illustration of the topographic index distribution. The slope of the canopy is 30° in this case. The solar azimuth angle is 0° . S, N, W and E are south, north, west and east directions. The legend shows the topographic index values. The black and blue boxes show the perpendicular and principle planes, respectively.

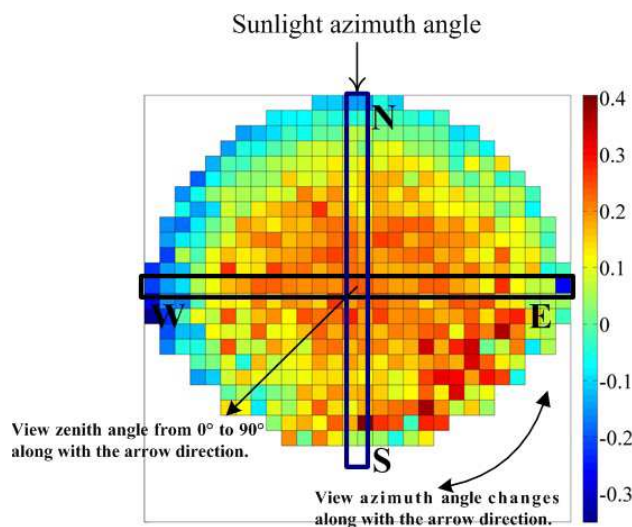


Figure 1: An illustration of the relative error distribution.

3. RESULTS AND DISCUSSIONS

Figure 2 show the variations of the red band reflectance of TM images with slope and aspect in SS1 and SS2, respectively. Fig. 3 is the topographic index distributions in reflectance of OJP forests in the red band simulated by GOST model.

3.1. The Quantitative Effects of the Topography on the Sloping Canopy Reflectance

According to the simulation results, the topographic index (RE_R) varies from -35% to 40% at a slope of 30° , and from -22% to 58% at a slope of 60° (Fig. 3). It indicates that the topographic factors have significant influences on the reflectance of sloping canopies because the area ratios of

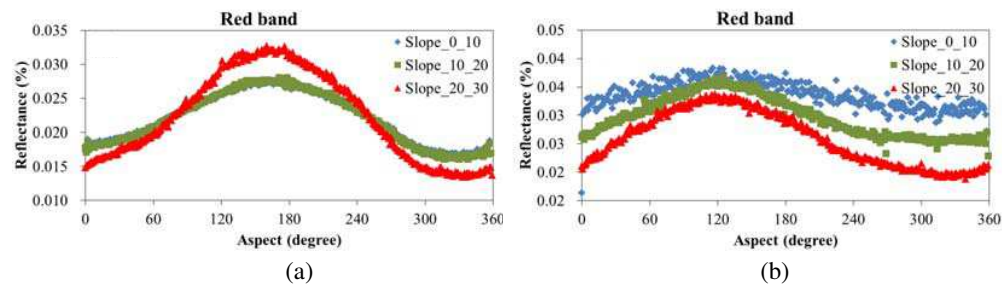


Figure 2: The reflectance vary with slope and aspect in SS1 (a) and SS2 (b). The blue, green and red dots represent the slope between 0° to 10° , between 10° to 20° and between 20° to 30° , respectively.

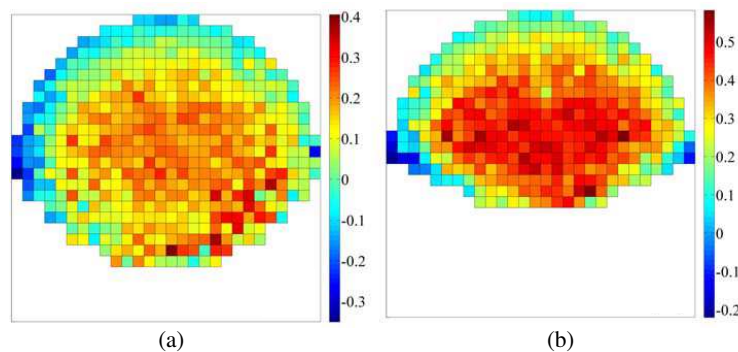


Figure 3: The topographic index distributions for OJP forest in the red band. In the red band, (a) and (b) are the forest slope equals to 30° and 60° , respectively.

the 4 scene components and the multiple scattering within the canopy are modified greatly by the topographic factors. The nadir-viewed reflectance acquired from Landsat TM5 is used to support the simulated results in these cases. Fig. 2 show that topographic factors have great effects on the observed canopy reflectance. With changes in the slope and aspect, the BRF varies from 0.012 to 0.033 in SS1 and from 0.017 to 0.038 in SS2. Although the observed reflectance is only acquired at nadir, such a large difference of reflectance at different slopes is consistent with simulated results. Both the model simulated results and observed values indicate that the topographic factors are important for the forward modeling of the canopy reflectance on slopes and should be considered in forest reflectance retrieval for non-flat surfaces.

3.2. The Topographic Effects on Multi-angle Remote Sensing of Canopy Reflectance

As for OJP on slopes in the red band, the topographic effect decreases with the view zenith angle increasing (Fig. 3). It indicates that the topographic index RE_R varies greatly in different view directions even though the canopy structure remains the same. It means that the topographic factors have different effects on the reflectance observed at different angles. Therefore, in order to establish the relevant relationship between the multi-angle reflectance and canopy parameters on sloping background, a sensor with suitable view angles should be selected according to the specific research topics or the view angle correction processes should be considered to avoid or reveal the topographic effects in different view directions.

3.3. The Topographic Effects on the Reflectance of Different Canopy Structures

The reflectance observed by Landsat TM5 (Fig. 2) also show that the reflectance of sloping canopies with different canopy structures may increase or decrease with the change of slope under the same aspect and in similar sunlight/view directions. For example, in the red band, the reflectance increases with increasing slope in SS1 when the sunlight is facing with the slope, but the reflectance decreases with increasing slope in SS2 under the same conditions. The model simulations and observations show that the canopy reflectance under different canopy structures vary greatly with slopes. The approaches for general topographic correction should consider the canopy structures in forest regions. If only the topographic factors such as slope and aspect are considered, the corrections may be erroneous. It also indicates GOST model is capable of simulating the reflectance under different canopy structures on slope.

4. CONCLUSIONS

According to the quantitative evaluation of the topographic effects on reflectance, the following conclusions are drawn. First, the topographic factors (slope and aspect) have great impacts on sloping canopy reflectance. The modeled topographic index RE_R , which is the relative error in simulated canopy reflectance by ignoring the topographic effects, can reach up to 58%, while the observed BRDF varies from 0.012 to 0.038 in SS2. Therefore, the forest reflectance models considering the topographic factors are recommended for canopy reflectance simulations and canopy parameters retrieval over non-flat terrains. Second, model simulations show that topography has variable effects on the sloping canopy reflectance and vegetation indices in different view directions. These effects should be considered in analyzing multi-angle images. Third, topographic factors have great impacts on sloping canopy reflectance and vegetation indices of different canopies with different structures. In addition, the canopy structures should also be considered in topographic correction on reflectance images because topographic factors alone is insufficient for correcting all variations of reflectance with slope and view angle.

ACKNOWLEDGMENT

This work was supported in part by the National Basic Research Program of China (973 Program) under Grant 2013CB733401, and in part by the CAS/SAFEA International Partnership Program for Creative Research Teams under Grant KZZD-EW-TZ-09 in part by China Postdoctoral Science Foundation under Grant 2014M560131, in part by the National Science Foundation of China under Grant 41401418/D0106, Grant 41271366/D0106 and Grant 41271354/D0106.

REFERENCES

1. Combal, B., H. Isaka, and C. Trotter, "Extending a turbid medium BRDF model to allow sloping terrain with a vertical plant stand," *IEEE Transactions on Geoscience and Remote Sensing*, Vol. 38, 798–810, 2000.
2. Richter, R., T. Kellenberger, and H. Kaufmann, "Comparison of topographic correction methods," *Remote Sensing*, Vol. 1, 184–196, 2009.
3. Teillet, P. M., "Image correction for radiometric errors in remote sensing," *International Journal of Remote Sensing*, Vol. 7, 1637–1651, 1986.
4. Fan, W. L., J. M. Chen, W. M., Ju, and G. L. Zhu, "GOST: A geometric-optical model for sloping terrains," *IEEE Transactions on Geoscience and Remote Sensing*, Vol. 52, No. 9, 5469–5482, 2014.
5. Fan, W. L., J. M. Chen, W. M., Ju, and N. Nesbitt, "Hybrid geometric optical-radiative transfer model suitable for forests on slopes," *IEEE Transactions on Geoscience and Remote Sensing*, Vol. 52, No. 9, 5579–5586, 2014.
6. Leblanc, S. G., P. Bicheron, J. M. Chen, M. Leroy, and J. Cihlar, "Investigation of directional reflectance in boreal forests with an improved four-scale model and airborne POLDER data," *IEEE Transactions on Geoscience and Remote Sensing*, Vol. 37, No. 3, 1396–1414, 1999.

A Study of Scattering of Scatterers Using Equivalence Principle Algorithm

Chan-Fai Lum¹, Fu Xin², Hong-Tat Ewe¹, and Li-Jun Jiang²

¹Universiti Tunku Abdul Rahman, Malaysia

²University of Hong Kong, China

Abstract— For theoretical models used in microwave remote sensing of earth terrain, it is quite common to represent the medium as a random discrete medium where the medium can be modeled as a layer of scatterers of basic shapes embedded in the host medium and bounded by upper and lower rough surfaces. By solving the wave propagation and the scattering in the medium through Radiative Transfer (RT) theory, the scattering returns from the medium can be obtained. Traditionally, analytical expression of scattering from these scatterers of basic shapes is derived and computed with simplification based on basic assumptions. However, it is generally found from ground truth measurement that the actual shapes of those scatterers are much more complex and irregular. Although it is difficult to simulate the scattering from this wide range of scatterers of different sizes, orientation and shapes, it is possible to model the medium better by representing the scatterers with major types of scatterers of particular shapes, though the shapes may not be of basic geometrical shapes like spheres. In this study, it is proposed to use the Equivalence Principle Algorithm (EPA) method under the approach of computational electromagnetics to perform the calculation of scattering from these scatterers and incorporate this for the simulation of radar scattering returns from Radiative Transfer (RT) formulation. With this approach, the theoretical model developed can be extended to cover scattering from scatterers which are not easily represented by basic geometrical shapes. Comparison results of the simulation based on Mie scattering and EPA are presented. The model prediction is also compared with satellite SAR data with physical parameters input from ground truth measurement conducted in Antarctica.

1. INTRODUCTION

There have been theoretical models based on Radiative Transfer (RT) theory that incorporate Mie scatterers to simulate scatterers like ice, brine inclusions or air bubbles which are embedded inside the snow or sea ice layer [1–3]. Studies using this kind of models and comparison of theoretical results with ground truth measurement data conducted in Antarctica and satellite SAR data have also been done. While it is convenient to model the scatterers by representing them as spherical scatterers, most of the ice particles in snow or brine inclusions or air bubbles in sea ice are not actually spherical in shape. To better represent these scatterers, a new approach is proposed where the scattering from the scatterers are computed through the Equivalence Principle Algorithm (EPA) [4, 5]. The Equivalence Principle Algorithm (EPA) was developed based on equivalence theorem, also known as Huygens' equivalence principle, which states that the fields inside or outside a closed surface can be determined by tangential components of the fields on the surface [4]. EPA is a numerical integral solution which uses the concept of equivalence surface and domain decomposition method (DDM). For complex scattering problems, EPA can also be applied by breaking the problems into sub domains for solving multi-object scattering problem and this facilitates the parallelization of solution, the reuse of solution, and also improves the conditioning of matrix system [4]. By creating an equivalence surface to enclose the scatterers inside, a new equivalence source can replace the original source which provides the same incident field inside the equivalence surface. Using the three equivalence principle operators containing the information of the inside scatterers, scattered currents are then calculated. The three equivalence principle operators, which are inside-out propagation, current solver and outside-in propagation, can form the scattering matrix which is used to solve the scattered field outside the equivalence surface that can be calculated from the scattered currents on equivalence surface. In this manner, the unknowns of the inside scatterers are transferred to the unknowns on the equivalence surface that encloses the elements in the final matrix equation [4]. Scatterers to be computed in EPA are in arbitrary 3D model, this allows EPA to operate and be independent of the shape restriction of scatterers. In this case, it is possible to extend the microwave remote sensing model for spherical scatterers embedded in the medium to include cases where the shape of scatterers is irregular or not spherical.

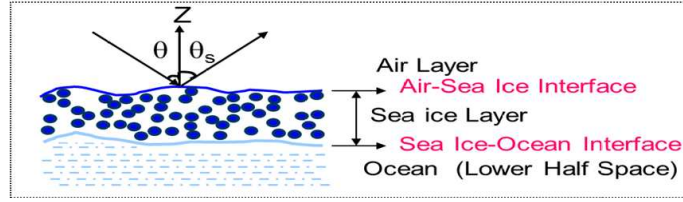


Figure 1: Model configuration.

2. MODEL DEVELOPMENT

As shown from Figure 1 above, scatterers inside a layer of sea ice are modeled as spherical objects and covered on top by air and bottom by half space of ocean. Mie scattering was previously used to calculate the phase matrix $\bar{\bar{P}}$ of the scatterers like ice, brine inclusions or air bubbles as given by:

$$\bar{\bar{P}}(\theta, \phi; \theta', \phi') = \langle |\psi|^2 \rangle_n \cdot \bar{\bar{S}} = \begin{bmatrix} P_{vv} & P_{vh} \\ P_{hv} & P_{hh} \end{bmatrix} \quad (1)$$

where $\langle |\psi|^2 \rangle_n$ is the dense medium array correction factor and $\bar{\bar{S}}$ is the Stokes matrix for a Mie scatterer with the close spacing amplitude correction [6, 7]. The dense medium array correction factor accounts for the coherency of scatterers in an electrically dense medium where the average distance between the scatterers is less than the wavelength [7, 8]. For electrically sparse medium, the dense medium array correction factor will approach to n_o where n_o is the number density of the spheres. The total backscattering from the medium will then be calculated using the Radiative Transfer (RT) equation where the method is described in [9].

For the utilization of EPA, the phase matrix of a scatterer can now be replaced by the EPA calculated values where an equivalence surface is considered enclosing the scatterer. In EPA, the components of phase matrix are calculated using the equivalence principle operators given by:

$$\begin{bmatrix} J^{sca} \\ \frac{1}{\eta} M^{sca} \end{bmatrix} = \begin{bmatrix} -\hat{n} \times K_{HJ}^S \\ -\frac{1}{\eta} \hat{n} \times L_{EJ}^S \end{bmatrix} \cdot [L_{pp}]^{-1} \cdot \begin{bmatrix} -L_{EJ}^S & -\eta K_{EM}^S \end{bmatrix} \cdot \begin{bmatrix} J^{inc} \\ \frac{1}{\eta} M^{inc} \end{bmatrix} \quad (2)$$

where J^{inc} is equivalent incident electric current and M^{inc} is equivalent incident magnetic current while J^{sca} is equivalent scattered electric current and M^{sca} is equivalent scattered magnetic current.

The first term of the equation $\begin{bmatrix} -\hat{n} \times K_{HJ}^S \\ -\frac{1}{\eta} \hat{n} \times L_{EJ}^S \end{bmatrix}$ is the inside-out propagation operator, second term $[L_{pp}]^{-1}$ is the current solver operator and third term $\begin{bmatrix} -L_{EJ}^S & -\eta K_{EM}^S \end{bmatrix}$ is the outside-in propagation operator [4]. After computing the J^{sca} and M^{sca} , the scattered fields can then be obtained and this scattered field can be used in the phase matrix in Equation (1). To verify the accuracy of the incorporation of EPA calculated scattering coefficient, several verification steps were carried out.

3. SIMULATION RESULTS AND ANALYSIS

Figure 2 and Figure 3 show the scattering coefficient of a single spherical object calculated from EPA and compared with that of Mie scattering and also FEKO software for two different sizes of sphere which were 1.2 mm and 0.5 mm (with relative permittivity $6.9 + i0.12$) at the frequencies of 5 GHz and 1 GHz, respectively. The results from the two figures show that all three methods give well agreed scattering coefficient values. Figure 4 shows the results of total backscattering coefficient from EPA and Mie scattering for a layer of medium with spherical scatterers (with relative permittivity $6.9 + i0.12$) of radius 13 mm plotted against 8 different incident angles at 5 GHz frequency. The simulated results of total backscattering coefficient from EPA agreed well with those of Mie scattering.

Figure 5 shows the backscattering coefficient comparison between EPA RT model, Mie scattering RT model and satellite SAR data for ice shelf sites A, B, C, I and P in Antarctica. The data from the RT model with Mie scattering was from paper [7] in 2012. For ground truth measurement of sites A, B, and C, data were collected in 2002, site I data were collected in 2003 and data for site P were collected in 2004 [7, 10]. From Figure 5, results computed from the EPA based

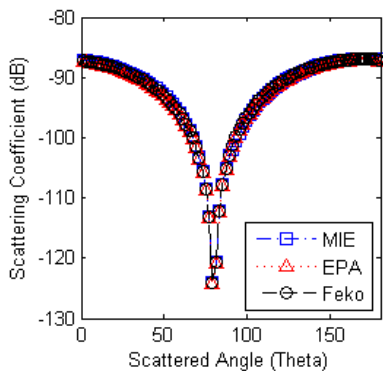


Figure 2: Scattering coefficient comparison among EPA, FEKO and MIE for a sphere with radius 1.2 mm at 5 GHz frequency.

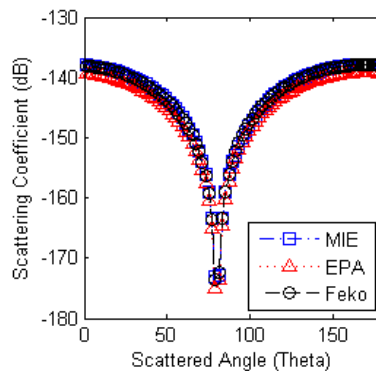


Figure 3: Scattering coefficient comparison among EPA, FEKO and MIE for a sphere with radius 0.5 mm at 1 GHz frequency.

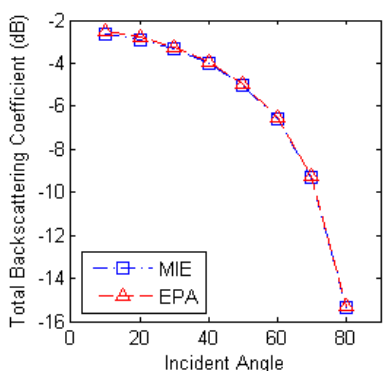


Figure 4: Total Backscattering coefficient [HH] comparison between EPA and MIE for a layer of medium with spherical scatterers of radius 13 mm at 5 GHz frequency for 8 different incident angles.

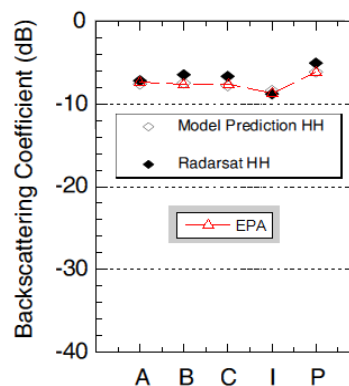


Figure 5: Backscattering coefficient comparison among EPA method, MIE model and satellite measured values for 5 ice shelf sites (Sites A, B, C, I and P) in Antarctica.

theoretical model match well with the RADARSAT-1 data measured and the Mie scattering RT model computed results. From the plotted results shown above, a new RT theoretical mode based on EPA can be extended further to simulate scatterers with non-spherical shapes.

4. CONCLUSION

In this paper, it has shown that the proposed method of incorporating EPA for the calculation of scattering from a scatterer can be combined with dense medium array correction factor and RT formulation for the calculation of radar scattering returns from a layer of embedded scatterers. With more powerful and faster computer technology, the new RT theoretical model that incorporates EPA can be further used to study the scattering of a layer of scatterers with irregular shapes.

ACKNOWLEDGMENT

The research was supported with the research fund from the Asian Office of Aerospace R&D (AOARD) [Grant Number: FA2386-12-1-4082/FA2386-13-1-4140], MOSTI Malaysia [Grant Number: FP1213E037_S2] and HKU-SIRI NSFC 61271158.

REFERENCES

1. Chuah, H. T., S. Tjuatja, A. K. Fung, and J. W. Bredow, "A phase matrix for a dense discrete random medium: Evaluation of volume scattering coefficient," *IEEE Transactions on Geoscience and Remote Sensing*, Vol. 34, No. 5, 1137–1143, 1996.
2. Chuah, H. T., S. Tjuatja, A. K. Fung, and J. W. Bredow, "Radar backscatter from a dense discrete random medium," *IEEE Transactions on Geoscience and Remote Sensing*, Vol. 35, No. 4, 892–900, 1997.

3. Fung, A. K., *Microwave Scattering and Emission Models and Their Applications*, Artech House, Norwood, Massachusetts, 1994.
4. Li, M. K., “Studies on applying the equivalence principle algorithm on multiscale problems,” Ph.D. dissertation, University of Illinois at Urbana-Champaign, 2007.
5. Lu, C. C. and W. C. Chew, “The use of Huygens’ equivalence principle for solving 3-D volume integral equation of scattering,” *IEEE Trans. Antennas Propagat.*, Vol. 43, No. 5, 500–507, May 1995.
6. Fung, A. K. and H. J. Eom, “A study of backscattering and emission from closely packed inhomogeneous media,” *IEEE Transactions on Geoscience and Remote Sensing*, Vol. 23, No. 5, 761–767, 1985.
7. Albert, M. D., Y. J. Lee, H.-T. Ewe, and H. T. Chuah, “Multilayer model formulation and analysis of radar backscattering from sea ice,” *Progress In Electromagnetics Research*, Vol. 128, 267–290, 2012.
8. Ewe, H.-T. and H. T. Chuah, “Electromagnetic scattering from an electrically dense vegetation medium,” *IEEE Transactions on Geoscience and Remote Sensing*, Vol. 38, No. 5, 2093–2105, 2000.
9. Ewe, H.-T., H. T. Chuah, and A. K. Fung, “A backscatter model for a dense discrete medium: analysis and numerical results,” *Remote Sensing of Environment*, Vol. 65, No. 2, 195–203, 1998.
10. Albert, M. D., T. E. Tan, H.-T. Ewe, and H. T. Chuah, “A theoretical and measurement study of sea ice and ice shelf in Antarctica as electrically dense media,” *Journal of Electromagnetic Waves and Applications*, Vol. 19, No. 14, 1973–1981, 2005.

The Wedding of Bioelectromagnetic and Biochemistry: Bridging a Molecule and Its Own Electromagnetic Information

Alberto Foletti^{1,2}, Mario Ledda¹, Settimio Grimaldi¹, and Antonella Lisi¹

¹Institute of Translational Pharmacology, National Research Council-CNR, Rome, Italy

²Clinical Biophysics Research Group, Lugano, Switzerland

Abstract— Previously we showed an interesting effectiveness of the electromagnetic information delivery of a specific source molecule in mimicking its specific biological effect. Nevertheless the effect was quite lower than the original positive control. Therefore we decide to assess a possible synergism between a reduced dose of a molecule and its own electromagnetic information in order to increase the efficacy of this procedure trying to disclose new possible avenues in translational pharmacology following suggestion from other works reporting synergistic effect between molecules and extremely low frequency electromagnetic fields. A reduced dose of retinoic acid, corresponding to a tenth of the usual, was delivered together with its own electromagnetic information to LAN-5 neuroblastoma cells. The signals from retinoic acid molecules was transferred to the cell culture medium employing as for our previous reports a commercial available electro medical device (Vegaselect 719). The effect on cell differentiation was significantly higher, and statistically significant, than the one obtained by the electromagnetic information delivery procedure when performed alone. A positive and effective synergism between a reduced drug dose and its own electromagnetic information seems to emerge as a promising and useful perspective in translational pharmacology outlining future applications in new drug delivery protocols allowing to reduce the amount of drug's doses especially in the elderly and in the increasing number of patients with multiple comorbidities. Bioelectromagnetic and biochemistry should, therefore, be considered on the way of a promising wedding instead of a permanently independent life. Future researches should either optimize the protocols of preparation of these potentially new drugs, either assess the lifespan of their biological effect in order to translate them into effective clinical application at the bedside through Bioelectromagnetic medicine.

1. INTRODUCTION

An increasing amount of works support of the possibility to achieve biological effects by mean of the transfer of specific electromagnetic pattern of signal through aqueous systems both *in vitro* [1–6] and in clinical applications [7–13]. Previously our group showed an interesting effectiveness of the electromagnetic information delivery of a specific source molecule in mimicking its specific biological effect [14, 15]. The effect was statistically significant and nevertheless it was quite lower than the original positive control. Therefore we decide to assess a possible synergism between a reduced dose of a molecule and its own electromagnetic information in order to increase the efficacy of this procedure trying to disclose new possible avenues in translational pharmacology [16]. We was, also, inspired to follow suggestion from other works reporting synergistic effect between molecules and extremely low frequency electromagnetic fields [17, 18]. Neuroblastoma cell lines are appropriate models “*in vitro*” for investigating the mechanisms of neuronal death and their relation to differentiation [19, 20]. It has been reported that Retinoic Acid is able to reduce the tumorigenicity of these cells through the modulation of their neuronal differentiation and cell proliferation [21].

2. MATERIAL AND METHODS

2.1. Cell Culture

LAN-5 neuroblastoma cells were grown in monolayer culture on 25 cm² plastic culture flasks, using RPMI supplemented with 10% fetal bovine serum (Euroclone), 2 mM glutamine (Sigma), 1.0 unit/ml penicillin (Sigma), and 1.0 mg/ml streptomycin (Sigma), in a humidified incubator with constant 95% air and 5% CO₂.

2.2. Growth Curves

Cells were seeded at density of 10×10^3 cells/cm² on 25 cm² plastic culture flasks. After 24 h the signals from a standard Retinoic Acid solution was captured and transferred to the target culture medium by a commercially available oscillator (Vegaselect 719). For each experimental condition, cells were grown for 4 days. At day 1, 2, 3 and 4, cells were harvested with 0.1% trypsin-EDTA

(Sigma), washed twice with PBS and the total number of nucleated and viable cells was counted by Trypan Blue dye (0.4%) (Sigma) exclusion assay using a Bürker hemocytometer chamber.

2.3. ELF-electro Magnetic Field Exposure System

The appropriate electromagnetic field (7.0 Hz) and magnetic flux 9.2 mT was generated by a commercial wave generator (Vega Select 719). Signals from the wave generator was driven to a small Helmholtz coils. The coils were 7.5 cm high with a diameter of 15 cm. Each coil constituted of 13 layers of 1 mm copper wires for a total 320 wires.

2.4. Statistical Analysis

Statistics was performed with Student's t-test. A p -value of < 0.05 was considered as being statistically significant.

3. RESULTS

LAN-5 neuroblastoma cell line was grown up for 4 days in 4 different ways: 1- Using standard medium (CTR in Fig. 1) as negative control; 2- using Retinoic Acid at the standard concentration of $1 \mu\text{M}$ (RA $1 \mu\text{M}$ in Fig. 1); 3- using Retinoic Acid at the concentration of $0.1 \mu\text{M}$ (AR $0.1 \mu\text{M}$); 4- transferring electronically the signals recorded from RA at its standard concentration to the cell medium culture and then adding a ten times reduced concentration $0.1 \mu\text{M}$ of RA (RA $0.1 \mu\text{M}$ + RA-ECM in Fig. 1).

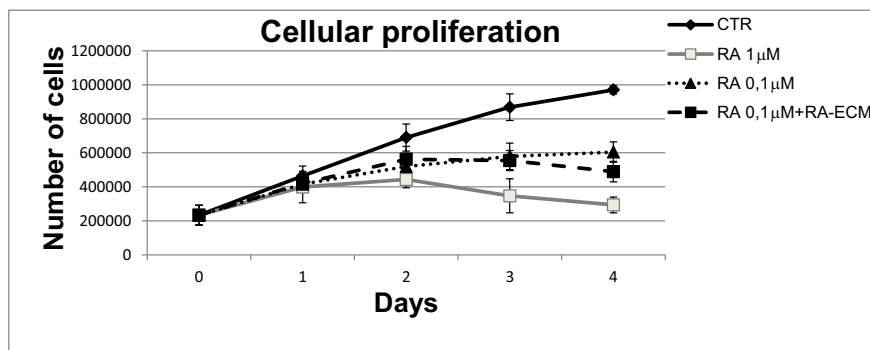


Figure 1: Effect on cellular proliferation detected by direct count for: 1- Standard cell culture medium as negative control (CTR); 2- Retinoic Acid at the standard concentration of $1 \mu\text{M}$ (RA $1 \mu\text{M}$); 3- Retinoic Acid at the concentration of $0.1 \mu\text{M}$ (AR $0.1 \mu\text{M}$); 4- Retinoic Acid at the concentration of $0.1 \mu\text{M}$ in synergy with electromagnetic information delivery of signals recorded from RA added to the cell medium culture (RA $0.1 \mu\text{M}$ + RA-ECM).

Cell proliferation was assessed by direct cell count. The results showed that LAN-5 cells treated with $1 \mu\text{M}$ of RA chemical molecule dramatically decreased their cellular proliferation. Cells proliferation was also decreased of about 40% after treatment with $0.1 \mu\text{M}$ of RA. It worth to stress that the cells cultured in the medium with the presence of the Retinoic Acid signals, together with $0.1 \mu\text{M}$ RA chemical molecule, presented a further and statistically significant ($p < 0.05$) reduction of proliferation rate as compared to negative control and to $0.1 \mu\text{M}$ RA treated cells.

4. DISCUSSION

We analysed the synergistic effect of Retinoic Acid treatment together with the electromagnetic information delivery of its own signals pattern. These data further support the possibility to yield biological effects transferring specific electromagnetic pattern of signal through aqueous systems in vitro [1–6]. It is actually very interesting to confirm that electromagnetic information delivery of a specific source molecule can mimic its specific biological activity [14, 15]. We also support the previous finding of other studies showing a fruitful potential in the combined application of retinoic acid and of direct exposure to extremely low frequency magnetic field on human neuroblastoma cell line [17] but in a water mediated way. It was acknowledged that water could play an essential role in the process of recording, storing and retrieving information through electromagnetic signalling and especially through a resonance effect [22]. A comprehensive explanations of the possible mechanisms by which these effect can occur in aqueous system and in their interactions with living cells has already been reported [16]. In particular a resonance effect can both explain the transfer of the

information pattern from the source input, like retinoic acid samples, to an aqueous system, the culture medium in our experiments, and again from the aqueous system of the cell medium to the target cultured cells [22]. Electromagnetic Information Delivery through Aqueous System has been confirmed to be feasible and effective even when applied in the perspective of enhancing the biological effect of a reduced dose of a standard biochemical drug like retinoic acid. A biophysical namely bioelectromagnetic strategy can work in alliance with a biochemical one allowing to reduce the amount of biochemical molecule to be employed to achieve a significant effect.

5. CONCLUSIONS

A positive and effective synergism between a reduced drug dose and its own electromagnetic information delivery seems to emerge as a promising and useful perspective in translational pharmacology outlining future applications in new drug delivery protocols allowing to reduce the amount of drug's doses especially in the elderly and in the increasing number of patients with multiple comorbidities. Bioelectromagnetic and biochemistry should, therefore, be considered on the way of a promising wedding instead of a permanently independent life. Future researches should either optimize the protocols of preparation of these potentially new drugs, either assess the lifespan of their biological effect in order to translate them into effective clinical application at the bedside through Bioelectromagnetic medicine [22]. The future for biophysical integrated therapies is opened.

6. DECLARATION OF INTEREST

The authors reports no declarations of interest.

REFERENCES

1. Jerman, I., R. Ružic, R. Krašovec, M. Škarja, and L. Mogilnicki, "Electrical transfer of molecule information into water, its storage, and bioeffects on plants and bacteria," *Electromagn. Biol. Med.*, Vol. 24, No. 3, 341–353, 2005.
2. Jerman, I., M. Berden, and R. Ružic, "Biological influence of ultraweak supposedly EM radiation from organisms mediated through water," *Electro. and Magnetobiology*, Vol. 15, No. 3, 229–244, 1996.
3. Endler, P. C., M. Citro, W. Pongratz, C. W. Smith, C. Vinattieri, and F. Senekowitsch, "Transfer of molecular information using a bioresonance instrument (BICOM) in amphibian trials," *Acta Medica Empirica*, Vol. 44, No. 3, 1–16, 1995.
4. Kreisl, P., "Tests on the transduction of acetic acid information via an electronic amplifier," *Acta Medica Empirica*, Vol. 47, 17–24, 1998.
5. Thomas, Y., M. Schiff, L. Belkadi, P. Jurgens, L. Kahhak, and J. Benveniste, "Activation of human neutrophils by electronically transmitted phorbol-myristate acetate," *Med. Hypotheses*, Vol. 54, 33–39, 2000.
6. Calzoni, G. L., F. Borghini, E. Del Giudice, L. Betti, F. Dal Rio, M. Migliori, G. Trebbi, and A. Speranza, "Weak extremely high frequency microwaves affect pollen-tube emergence and growth in kiwifruit: Pollen grain irradiation and water-mediated effects," *J. Altern Complement Med.*, Vol. 9, No. 2, 217–233, 2003.
7. Foletti, A., P. Baron, E. Sciauzero, G. Bucci, A. Rinaudo, and R. Rocco, "Assessment of biophysical therapy in the management of pain in current medical practice compared with ibuprofen and placebo: A pilot study," *J. Biol. Regul. Homeostat Agents*, Vol. 28, No. 3, 431–439, 2014.
8. Foletti, A. and M. Cozzolino, "A biophysical integrated approach to autoimmune nephrotic syndrome: Case report," *Recenti. Prog. Med.*, Vol. 104, No. 9, 488–489, 2013.
9. Baron, P., G. Bucci, A. Rinaudo, R. Rocco, E. Sciauzero, and A. Foletti, "System information therapy in the management of pain: A pilot study," *PIERS Proceedings*, 1698–1702, Stockholm, Sweden, Aug. 12–15, 2013.
10. Smith, C. W., "Quanta and coherence effects in water and living systems," *J. Altern Complement Med.*, Vol. 10, No. 1, 69–78, 2004.
11. Herrmann, E. and M. Galle, "Retrospective surgery study of the therapeutic effectiveness of the MORA bioresonance therapy with conventional therapy resistant patients suffering from allergies, pain and infection diseases," *Eur. J. Integrative Med.*, Vol. 2, No. 4, 257–258, 2010.
12. Foletti, A. and J. Pokorny, "Biophysical approach to low back pain: A pilot report," *Electromagn. Biol. Med.*, 2015, in press.

13. Smith, C. W., “Quanta and coherence effects in water and living systems,” *J. Altern Complement Med.*, Vol. 10, No. 1, 69–78, 2004.
14. Foletti, A., M. Ledda, E. D’Emilia, S. Grimaldi, and A. Lisi, “Differentiation of human LAN-5 neuroblastoma cells induced by extremely low frequency electronically transmitted retinoic acid,” *J. Altern Complement Med.*, Vol. 17, No. 8, 701–704, 2011.
15. Foletti, A., M. Ledda, E. D’Emilia, S. Grimaldi, and A. Lisi, “Experimental finding on the electromagnetic information transfer of specific molecular signals mediated through the aqueous system on two human cellular models,” *J. Altern Complement Med.*, Vol. 18, No. 3, 258–261, 2012.
16. Foletti, A., M. Ledda, S. Piccirillo, S. Grimaldi, and A. Lisi, “Electromagnetic information delivery as a new tool in translational medicine,” *Int. J. Clin. Exp. Med.*, Vol. 7, No. 9, 2550–2556, 2014.
17. Marcantonio, P., B. Del Re, A. Franceschini, M. Capri, S. Lukas, F. Bersani, and G. Giorgi, “Synergic effect of retinoic acid and extremely low frequency magnetic field exposure on human neuroblastoma cell line BE(2)C,” *Bioelectromagnetics*, Vol. 31, No. 6, 425–433, 2010.
18. Whissell, P. D. and M. A. Persinger, “Emerging synergisms between drugs and physiologically-patterned weak magnetic fields: Implications for neuropharmacology and the human population in the twenty-first century,” *Curr. Neuropharmacol.*, Vol. 5, No. 4, 278–288, 2007.
19. Abemayor, E. and N. Sidell, “Human neuroblastoma cell lines as models for the in vitro study of neoplastic and neuronal cell differentiation,” *Environ. Health Perspect.*, Vol. 80, No. 3, 1989.
20. Lanciotti, M., P. Montaldo, S. Folghera, E. Lucarelli, P. Cornaglia-Ferraris, and M. Ponzoni, “A combined evaluation of biochemical and morphological changes during human neuroblastoma cell differentiation,” *Cell Mol. Neurobiol.*, Vol. 12, 225–240, 1992.
21. Sidell, N., “Retinoic acid-induced growth inhibition and morphologic differentiation of human neuroblastoma cells in vitro,” *J. Natl. Cancer Inst.*, Vol. 68, 589–596, 1982.
22. Foletti, A., S. Grimaldi, A. Lisi, M. Ledda, and A. R. Liboff, “Bioelectromagnetic medicine: The role of resonance signaling,” *Electromagn. Biol. Med.*, Vol. 32, No. 4, 484–499, 2013.

Oversensing and Undersensing of Implantable Cardiac Medical Devices Exposed to EMI

I. L. Spano, A. Serpi, M. Tomasi, I. Marongiu, and G. Gatto

Department of Electrical and Electronic Engineering, University of Cagliari, Italy

Abstract— Oversensing and undersensing issues of Implantable Cardiac Medical Devices (ICMDs) are addressed in this paper. Particularly, an extensive experimental study has been performed in order to highlight that EMI affects ICMD sensing performances in correspondence of specific heartbeat status in terms of both frequency and amplitude. Experiments have been carried out on both a Pacemaker and an Implantable Cardioverter Defibrillator within an anechoic chamber. This guarantees a proper EMI injection, whose frequency has been chosen in accordance with ANSI/AAMI ISO 14117: standard 2012. In addition, such an environment also guarantees and appropriate shielding against external EMI sources, thus ensuring the reliability of the tests.

1. INTRODUCTION

Electromagnetic Compatibility (EMC) is extremely important in medical applications, where a number of electrical and electronic devices may suffer from Electromagnetic Interference (EMI). This is due to their exposition to several EMI sources, such as portable and RFID devices, telemetry systems, computers and Wi-Fi networks [1]. Particularly, EMI immunity of Implantable Cardiac Medical Devices (ICMDs) must be assured because their failure can lead to losing consciousness or, even, to death [2].

In this context, EMI immunity of ICMDs is a growing issue, particularly electromagnetic interactions between ICMDs and intentional and unintentional EMI sources may impair ICMD sensing performances [3, 4]. Consequently, the device may interpret spurious signals as threatening arrhythmias, starting unsuitable pacing activities or providing an improper defibrillation shock. Despite the use of appropriate filtering systems and/or recognition algorithms, misunderstandings can still occur, leading to undersensing or oversensing. Particularly, undersensing prevents ICMD to detect the heartbeat, whereas oversensing makes ICMD sensitive to spurious signals. Although international standards provide some procedures in order to determine EMC sensitivity of ICMDs, a more accurate testing on sensing performances should be required [5–7].

In this paper, oversensing and undersensing induced by EMI are considered and analysed in detail referring to two different types of ICMD, i.e., a pacemaker (PMK) and an Implantable Cardioverter Defibrillator (ICD). Particularly, an extensive experimental study has been performed in order to highlight that EMI affects ICMD sensing performance in correspondence of specific heartbeat status in terms of both frequency and amplitude. Experiments have been carried out within an anechoic chamber, which guarantees a proper EMI injection, the frequency of which has been chosen in accordance with ANSI/AAMI ISO 14117. In addition, such an environment also guarantees and appropriate shielding against external EMI sources, thus ensuring the reliability of the tests.

2. IMPLANTABLE CARDIAC MEDICAL DEVICES

Implantable Cardiac Medical Devices (ICMDs) are nowadays commonly employed from even a very young age, allowing more people to live a normal life. Therefore, it is no longer unusual for people wearing an ICMD to work in environments characterized by not negligible EMI levels. The most widespread ICMDs are Pacemakers (PMKs) and Implantable Cardioverter Defibrillator (ICDs), which are coupled to the heart through appropriate leads, as shown in Fig. 1. PMK operation consists of continuously monitoring the spontaneous heartbeat (sensing) and eventually stimulate the heart as needed (pacing) with the aim of preventing the bradycardia, i.e., a rapid decrease of the heartbeat frequency. Whereas ICDs are also able to deliver a certain amount of energy to the heart (up to 40 J) in order to cut off dangerous fast arrhythmias, such as ventricular tachycardia, flutter and fibrillation.

Both PMK and ICD are constituted mainly by a pacing circuit supplied by a battery and controlled through a sensing circuit, all these being enclosed into a titanium case, as shown in Fig. 2. Both these devices may be exposed to EMI, especially through their leads, which can act as antenna for several external signals. Particularly, if the sensing circuit is not able to detect an



Figure 1: Examples of ICMD: PMKs (A), ICDs (B) and leads (C).

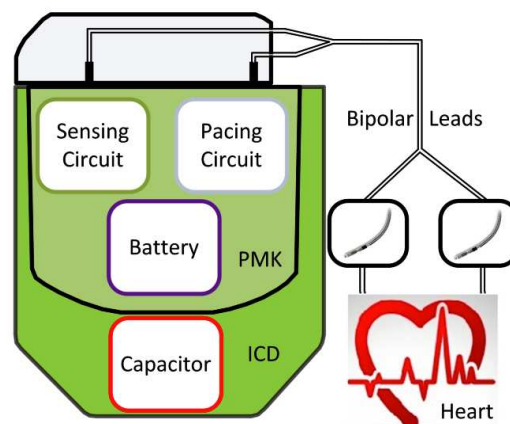


Figure 2: Schematic representation of an ICMD.

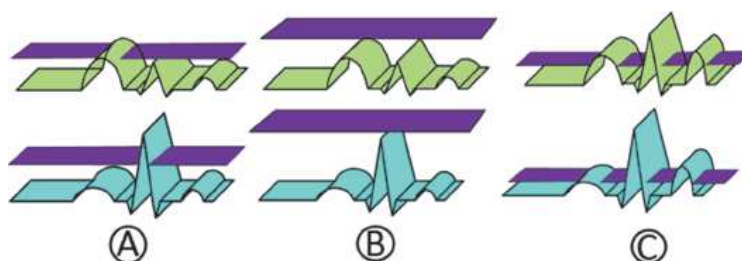


Figure 3: Atrial (top) and ventricular (bottom) sensing: (A) proper sensing, (B) undersensing, (C) oversensing.

abnormal heartbeat, no therapy is provided to the heart when needed; this is called undersensing. Alternatively, oversensing may occur when inappropriate pacing is provided due to the detection of spurious signals, which are misinterpreted as anomalous heartbeat. It is worth noting that atrial and ventricular sensing must be considered separately because they consist of detecting the *P* and *R* wave respectively, as shown in Fig. 3. From a medical point of view, atrial undersensing can cause stimulation in the vulnerable period, as well as prevent atrium contraction, leading to atrial or ventricular fibrillation respectively. Whereas ventricular undersensing may lead to dangerous and sometimes fatal arrhythmias. Similarly, atrial oversensing causes fast and irregular heartbeat, and even atrial fibrillation, whereas ventricular oversensing leads to device inhibition. All these side effects reveal the need of ensuring a high level of immunity for both PMK and ICD against EMI.

3. EMC TEST

With the aim of investigating undersensing and/or oversensing issues due to EMI, several experimental tests have been carried out inside the anechoic chamber shown in Fig. 4. Hence, referring to Fig. 5, the ICMD under test is placed inside an appropriate supporting structure, i.e., a Human Body Model or Torso Simulator, which has been accurately designed and manufactured in order to reproduce the realistic ICMD operating conditions [8]. Subsequently, the ICMD is linked to a Multifunction DAQ board (NI 6211) driven by a notebook. Particularly, the NI 6211 is used to acquire pacing signals provided by the ICMD and to emulate the human heartbeat simultaneously. Whereas EMI signals are generated in accordance with ANSI/AAMI ISO 14117 by means of a Log Periodic Antenna (Schaffner CBL6143), which is supplied by the EMI signal generator (Rohde & Schwarz SML03) through a directional coupler and an amplifier (Schaffner CBA9433). The directional coupler also allows the connection between the Log Periodic Antenna and a power meter (Rohde & Schwarz NRVD) in order to monitor the power level of EMI signals.

Experiments firstly refer to PMK that operates over AAI and VVI, which means that the pacing is provided only to atrium or ventricle respectively. The corresponding results are depicted in Fig. 6 and Fig. 7, which show the numbers of pacing events per second detected by monitoring PMK pacing activity during 50 one-minute tests. It can be seen that the number of pacing events significantly decreases in presence of EMI at 875 MHz, whereas it increases in case of EMI



Figure 4: The anechoic chamber.

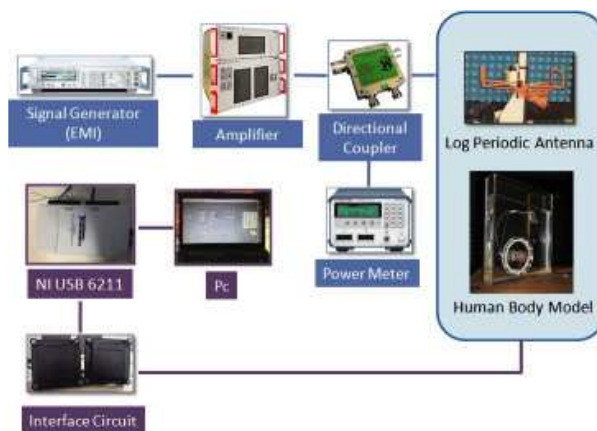


Figure 5: Experimental setup.

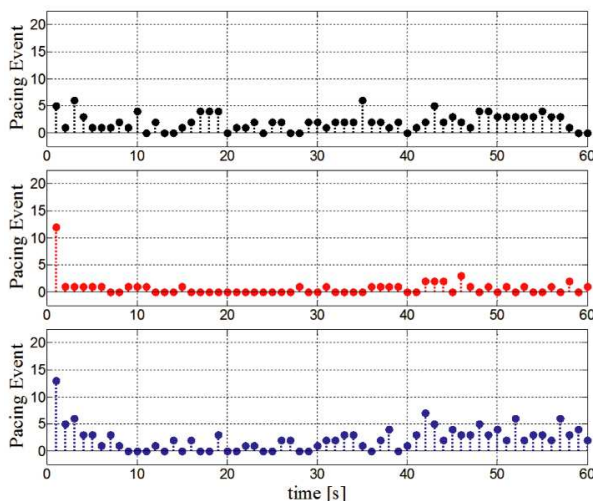


Figure 6: Experimental results (PMK, AAI): no EMI (black), 875 MHz (red) and 930 MHz (blue).

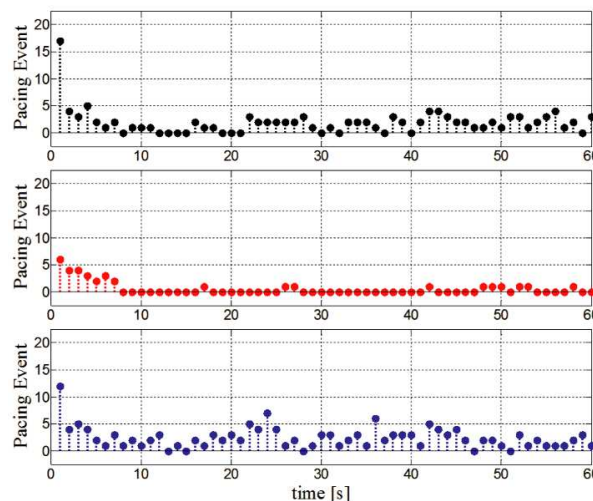


Figure 7: Experimental results (PMK, VVI): no EMI (black), 875 MHz (red) and 930 MHz (blue).

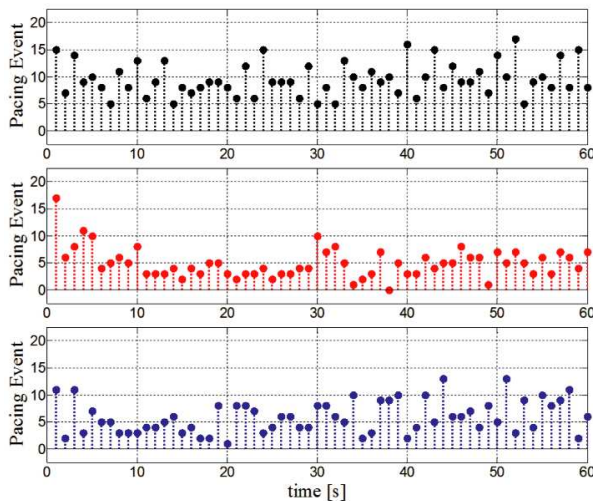


Figure 8: Experimental results (ICD, AAI): no EMI (black), 875 MHz (red) and 930 MHz (blue).

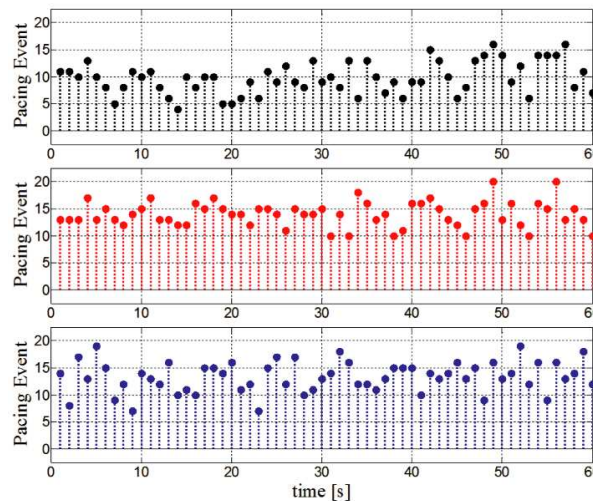


Figure 9: Experimental results (ICD, VVI): no EMI (black), 875 MHz (red) and 930 MHz (blue).

at 930 MHz. Consequently, undersensing and potential oversensing occur at 875 and 930 MHz respectively, thus revealing PMK susceptibility against EMI. It is worth noting that such results have been achieved by imposing a constant heartbeat frequency of 63 beat-per-minute. Whereas the heartbeat amplitude is set quite close to the sensitivity threshold [3], which represents the

Table 1: Overall experimental results.

		no EMI		875 MHz		930 MHz	
		N	Δ	N	Δ	N	Δ
PMK	AAI	124	---	44	-64.5%	140	+12.9%
	VVI	115	---	34	-70.4%	147	+27.8%
ICD	AAI	573	---	293	-48.9%	357	-37.7%
	VVI	586	---	840	+43.3%	802	+36.9%

worst operating condition in terms of potential undersensing and oversensing issues. This is also highlighted by the few number of pacing events occurring in absence EMI, which denote a sporadic pacing activity.

Different considerations can be made regarding an ICD, whose experimental results are depicted in Fig. 8 and Fig. 9. It can be seen that pacing events significantly decrease over AAI at both 875 and 930 MHz, the opposite occurring over VVI. It is worth noting that, also in this case, the heartbeat frequency has been set constant to 63 beat-per-minute, whereas the heartbeat amplitude has been chosen quite close to the ICD sensitivity threshold, as previously. It is also worthy of note that ICD pacing activity is more frequent than PMK, as highlighted by an increased number of pacing events in absence of EMI.

In conclusion, the overall experimental results are resumed in Table 1, which refers to the overall number of pacing events detected over 50 minutes (50 one-minute tests). These corroborates that both PMK and ICD are affected by EMI, although this occurs in correspondence of critical operating conditions, i.e., very close to the sensitivity threshold.

4. CONCLUSION

Oversensing and undersensing issues of Implantable Cardiac Medical Devices have been investigated in this paper. Particularly, several experiments have been performed in order to verify the effects of Electromagnetic Interference (EMI) on both a Pacemaker (PMK) and an Implantable Cardioverter Defibrillator (ICD). Experimental results have highlighted that oversensing and undersensing issues may arise due to EMI exposition in correspondence of critical PMK and ICD operating conditions. This reveals the need of accurate characterization of ICMD sensing performances, which should be suggested and even incorporated by international standards.

REFERENCES

1. Ott, H. W., *Electromagnetic Compatibility Engineering*, Wiley, USA, 2009.
2. Al-Ahmad, A., K. A. Ellenbogen, A. Natale, and P. J. Wang, *Pacemaker and Implantable Cardioverter Defibrillators*, Cardiotext Publishing, USA, 2010.
3. Spano, I. L., S. Sulis, A. Serpi, I. Marongiu, and G. Gatto, "EMC characterization of implantable cardiac medical devices in an anechoic chamber," *Proc. IEEE International Symposium on Electromagnetic Compatibility (EMC-Europe 2014)*, 6, Gothenburg, Sweden, Sep. 1–4, 2014.
4. Spano, I. L., A. Serpi, A. Fanti, V. Nissardi, A. Lai, V. Caredda, P. F. Orrù, G. Mazzarella, I. Marongiu, and G. Gatto, "Electromagnetic compatibility analysis of RFID and implantable medical devices," *Proc. IEEE Telecommunication Forum (TELFOR 2014)*, 4, Belgrade, Serbia & Montenegro, Nov. 25–27, 2014.
5. "Electromagnetic compatibility (EMC) — Part 4-3 Testing and measurement techniques — Radiated, radio-frequency, electromagnetic field immunity test," IEC 61000-4-3, 2008.
6. "Active implantable medical devices — Part 2 Particular requirements for active implantable medical devices intended to treat bradyarrhythmia (cardiac pacemakers)," CEI EN 45502-2-1, 2005.
7. "Active implantable medical device — Electromagnetic compatibility — EMC test protocols for implantable cardiac pacemakers and implantable defibrillators," AAMI Standard PC69, 2007.
8. Irnich, W., "Electronic security systems and active implantable medical devices," *Pacing Clin. Electrophysiol.*, Vol. 25, No. 8, 1235–1258, Aug. 2002.

Performance Evaluation of Dipole versus Modified Bow-Tie in Annular Phased Array Applicators

P. Takook, H. D. Trefná, A. Fhager, and M. Persson
Chalmers University of Technology, Sweden

Abstract— Phased arrays are the common type of applicators for deep hyperthermia systems to heat tumors selectively while keeping healthy tissues at normal temperatures. Annular array applicators with dipoles and water bolus have been improved in several studies to deposit energy efficiently in head and neck tumors. In this study we investigate the performance of a modified Bow-Tie antenna versus half-wave dipole as single elements in annular phased array applicators to heat tumors in head and neck region. Hyperthermia quality indicators have been calculated for each case to quantify the quality of treatment outcome in two different tumor positions in a head-and-neck phantom. The obtained results indicates that dipoles are appropriate phased array elements to heat superficial tumors, while modified Bow-Ties are more suitable in heating big deep-seated tumors.

1. INTRODUCTION

Combination of hyperthermia with chemotherapy and radiotherapy has proven to improve overall survival for different tumor locations [1]. The idea of hyperthermia treatment is to achieve adequate temperature increase at the tumor site while keeping temperature in healthy tissues below critical values. The required temperature increase in the tumor location depends on the ability of the hyperthermia applicator to heat the tumor efficiently.

In phased arrays the wave focusing in the tumor is given by constructive wave interference of the surrounding antennas. This can be achieved by finding the optimal excitation amplitude and phases of the antenna elements in the applicator, which is called treatment planning. The optimization methods have been used to determine the antennas amplitudes and phases, are either based on optimal SAR distribution or optimal temperature distributions.

Besides the hyperthermia treatment plans, the specific design of the applicator such as the number of antennas, number of rings and frequency has a direct effect on the final SAR pattern in the tumor and surrounding tissues. The most common applicator for treatment of head and neck tumors are phased arrays, which composed of antenna elements arranged in circular or elliptical array. To have an applicator capable of treating both shallow and deep-seated tumors, wide-band antenna design are necessary. This way the frequency of operation can be adjusted according to the size and position of the tumor. To this purpose, we have designed and analyzed a wideband Bow-Tie antenna to be used as the antenna elements in a hyperthermia applicator. The antenna has a wide-band performance over 433–900 MHz [2].

In this study 3D time-reversal focusing method is used to find the excitation settings. The advantages of this method are being fast, patient-specific and applicable to wide-band hyperthermia applications [3]. The implementation used the finite-difference time-domain (FDTD) to solve the Maxwell's equations. In a previous study, we investigated the effect of different parameters as the input settings of a 3D code, based on the time-reversal focusing method, for optimal heating of tumor models in a head-and-neck phantom [4]. There we compared the performance of dipoles and hard sources as the antenna elements of the hyperthermia applicator in the 3d code. Based on our results dipole antennas with omnidirectional radiation pattern performed better than hard sources in terms of the average absorbed power in two tumor models.

In this paper the aim is to study the behavior of the modified wideband Bow-Tie and dipole in hyperthermia treatment of two tumor models in a head-and-neck phantom. To evaluate the performance of each antenna, treatment planning outcome of Bow-Tie antenna applicator were compared with that of the half-wave dipole applicator. The efficacy of these two antennas in heating the tumors were then evaluated in terms of hyperthermia treatment quality indicators.

2. METHOD

To be able of comparing Bow-Ties and dipoles as antenna elements of a phased array, 3d time reversal method was implemented in CST commercial software. The virtual source which was placed in the center of tumors, considered as a half-wave dipole at frequency of 500 MHz. Based

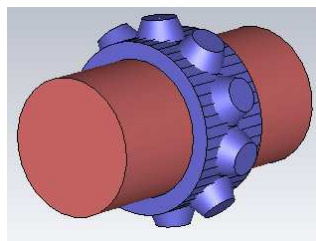


Figure 1: One-ring antenna applicator with homogeneous phantom.

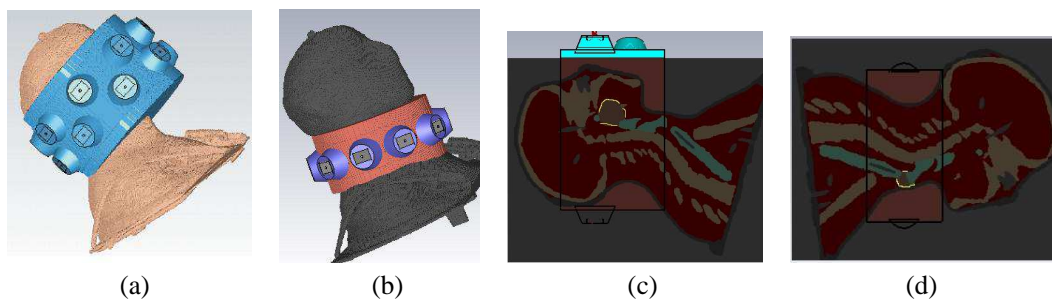


Figure 2: (a) and (b) Antenna applicators for the tongue and laryngeal tumors, (c) and (d) the position of the tongue and laryngeal tumors in the head-and-neck phantom, respectively.

on the expected target volumes in the available head-and-neck phantom, 500 MHz was considered a suitable frequency. This frequency is a good compromise between good focusing and desired penetration depth for two tumor models in our analysis.

Gaussian pulse in the frequency range of 400–1200 MHz considered as the antennas excitation. The mesh density was about 11 cells per wavelength to have a good compromise between accuracy and simulation time. In all the simulations each antenna in the applicator was immersed in a conical shape water bolus of dimension $a = 20$ mm, $b = 30$ mm and $h = 25$ mm, as the upper and lower radii and the height of the truncated cone. In the first analysis a homogeneous spherical tumor was located in 3 different positions of a homogeneous phantom with radius 80 mm. In the applicator, 10 Bow-Ties and dipoles were placed over a water-bolus of outer radius 100 mm and arranged in a one-ring setup, respectively, Figure 1. First excitation amplitudes and phases were found by the time reversal method. Then using these excitation settings, the absorbed power density in the phantom was calculated for each applicator.

In the second analysis voxel data of an available head-and-neck phantom of $430 \times 290 \times 364$ cells, was imported into CST commercial software. Here the analysis is based on two irregular-shaped tumor models in tongue and larynx. The applicator for the tongue tumor was an elliptical applicator of radii 104 and 114 mm, which consists of 16 antennas arranged in two-ring setup. For the laryngeal tumor 10 antennas were arranged in one ring. The positions of the tumors respect to the phantom and applicators are shown in Figure 2, with yellow color showing the tumor boundary. Dielectric properties of the modeled tissues in the phantom at 500 MHz are similar to those given in [4].

To evaluate the ability of the hyperthermia applicators to heat the specified tumors, the hot-spot target coefficient (HTQ) [5] and target coverage_{25%} [6] were computed for each applicator and each tumor. HTQ index shows the hot spot SAR to tumor SAR quotient, while target coverage_{25%} indicates the percentage of the tumor volume which is covered by 25% of the maximum SAR value in the patient model.

3. RESULTS

The behavior of a single Bow-Tie antenna and a single half-wave dipole, immersed in a conical shape water bolus, has been studied in the presence of a homogeneous human phantom in [4]. Recalling the analysis results of the antennas radiation at 500 MHz, the Bow-Tie antenna presented a wider bandwidth and higher effective field size than half-wave dipole over the range 0.4–1 GHz. This higher effective field size is useful for heating deep-seated larger tumors. To have a reliable measure of applicators heating efficiency, SAR distributions of the applicators were computed in the homogeneous spherical phantom, Figure 1. The quality indicators were calculated then for two

tumor radius of 10 and 20 mm at 3 different distances to the surface of the phantom,d. The analysis results are given in Table 1.

As it is shown in Table 1, for tumor at position 1, Bow-Tie antenna applicator performs better than dipole antenna applicator in terms of HTQ index. This result is independent of the tumor radius or the tumor size. For the tumor closer to the surface at position 2, while TC_{25%} are comparable for both applicators, dipole antenna applicator presents a lower HTQ index than the Bow-Tie. Finally for the shallowest tumor at position 3, dipole antenna applicator shows lower HTQ indexes for both tumor sizes.

In the second analysis, two tumors in larynx and tongue were radiated by Bow-Tie and dipole antenna applicators. As it was expected from the first analysis results, the dipole antenna applicator delivered more power into the shallow and small laryngeal tumor than Bow-Tie. This is a clear result from the calculated lower HTQ index and higher tumor coverage_{25%}, Table 2. For the tumor in tongue with larger size and more distance to the phantom surface, HTQ index and tumor coverage_{25%} are comparable for both applicators. However Bow-Tie antenna applicator presented higher value of maximum absorbed power in 2d plane of the tumor center which indicates more heating efficiency than dipole antenna applicator, Table 2.

Table 1: Quality indicators calculated for Bow-Tie and dipole antenna applicators at frequency of 500 MHz, applicator setup is shown in Figure 1.

Tumor position (mm)	Tumor radius (mm)	Bow-Tie antenna applicator		Dipole antenna applicator	
		HTQ	TC _{25%}	HTQ	TC _{25%}
Position 1 (d = 80 mm)	10	1.21	100	1.26	100
	20	1.71	95	1.79	92
Position 2 (d = 40 mm)	10	1.47	97	1.46	97
	20	1.73	60	1.7	60
Position 3 (d = 24 mm)	10	0.95	100	0.93	100
	20	0.87	70	0.84	71

Table 2: Quality indicators calculated for Bow-Tie and dipole antenna applicators at frequency of 500 MHz. The maximum power loss density in 2d plane of the tumor center is shown with PLDmax, (W/m³).

Tumor type	Bow-Tie antenna applicator			Dipole antenna applicator		
	HTQ	TC _{25%}	PLDmax	HTQ	TC _{25%}	PLDmax
Laryngeal	1.11	78	3e6	0.61	84	4.6e6
Tongue	0.85	72	3.41e6	0.84	70	2.74e6

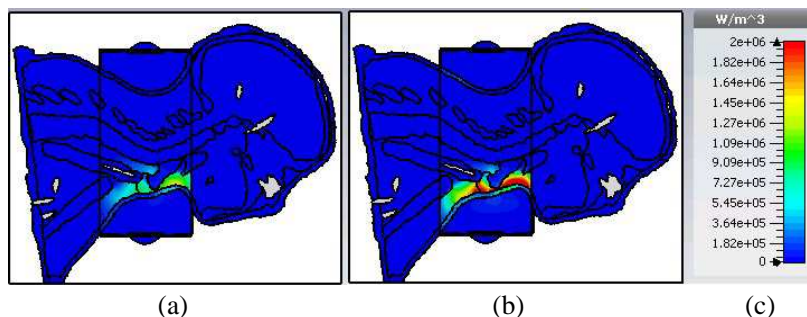


Figure 3: (a)–(c) Power absorption distribution radiated by Bow-Tie and dipole in the laryngeal tumor, shown in the sagittal plane.

4. CONCLUSION

Bow-Tie antenna and half-wave dipoles have been evaluated as the antenna elements in two different applicators for head and neck tumors. According to the calculated quality indicators in a homogeneous cylindrical phantom, Bow-Tie antennas with wider EFS performed better in heating deeper tumors while dipole-antenna applicator performed better for shallower tumors. For two specific tumors in larynx and tongue of a head-and-neck phantom conforming results were achieved. Bow-Tie-antenna applicator presented more heating into the larger, deeper tongue tumor, while dipole-antennas delivered more power to the smaller, shallower laryngeal tumor. Although Bow-Tie antennas with wideband characteristics give us the capability to adapt the treatment planning for different tumor sizes and positions, half-wave dipole antennas with lower EFS can result in a better treatment outcome for superficial tumors at the single design frequency of the dipole. Thus development of a separate hyperthermia applicator to treat superficial tumors is an alternative solution to achieve high quality treatments for all tumor types.

ACKNOWLEDGMENT

This work was supported in part by VINNOVA (Swedish Government Agency for Innovation Systems) within the VINN Excellence Center Chase.

REFERENCES

1. Moros, E. G., *Physics of Thermal Therapy: Fundamentals and Clinical Applications*, Taylor and Francis Group, CRC Press, 2013.
2. Takook, P., H. Dobšiček Trefná, and M. Persson, “A compact wideband antenna for microwave hyperthermia system over 0.4–0.9 GHz,” *ESHO 2013*, Munich, 2013.
3. Dobšiček Trefná, H., J. Vrba, and M. Persson, “Time-reversal focusing in microwave hyperthermia for deep-seated tumors,” *Phys. Med. Biol.*, Vol. 55, No. 8, Apr. 2010; Vol. 26, 185–197, 2010.
4. Takook, P., H. Dobšiček Trefná, A. Fhager, and M. Persson, “Evaluation of the 3D time reversal method for hyperthermia treatment planning in head and neck tumors,” *9th European Conference on Antennas and Propagation*, Apr. 2015, Accepted, to be Published.
5. Canters, R. A. M., P. Wust, J. F. Bakker, and G. C. Van Rhooon, “A literature survey on indicators for characterization and optimization of SAR distributions in deep hyperthermia, a plea for standardization,” *International Journal of Hyperthermia*, Vol. 25, No. 7, 593–608, 2009.
6. Rijnen, Z., J. F. Bakker, R. A. M. Canters, P. Togni, G. M. Verduijn, P. C. Levendag, G. C. Van Rhooon, and M. M. Paulides, “Clinical integration of software tool VEDO for adaptive and quantitative application of phased array hyperthermia in the head and neck,” *International Journal of Hyperthermia*, Vol. 29, No. 3, 181–193, May 2013.

Ensemble Formalism of the Orbital-free Density Functional Theory

Á. Nagy

Department of Theoretical Physics, University of Debrecen, Debrecen, Hungary

Abstract— Ensembles are constructed in the ground-state non-interacting density functional theory. The ensemble Euler equation is formulated as a one-particle Schrödinger-like equation for the square root of the ensemble density. The potential in this equation is the sum of the original Kohn-Sham potential plus the ensemble Pauli potential. The latter satisfies a first-order differential equation. The true electron density can be easily obtained from the ensemble electron density. The ensemble density or the ensemble non-interacting energy density or the ensemble angular momentum density provide a full description of a Coulomb system.

1. INTRODUCTION

Density functional calculations are generally done by solving the Kohn-Sham equations. There are several Kohn-Sham equations for systems with a lot of electrons. In orbital-free density functional theory, on the other hand, one has to solve only a single equation, the Euler equation, which is a huge simplification. Therefore, there is a growing interest in orbital-free methods [1–3]. Unfortunately, they are not accurate enough. The main problem is the lack of accurate approximation for the kinetic energy functional. In this paper we discuss a novel approach [4–7] that avoids using approximate kinetic energy functionals.

2. ENSEMBLE FORMALISM

In the construction the original Kohn-Sham equations

$$\left[-\frac{1}{2}\nabla^2 + v_{KS}(\mathbf{r}) \right] u_i(\mathbf{r}) = \varepsilon_i u_i(\mathbf{r}) \quad (1)$$

are made use of. The original ground-state density is given by

$$n_0(\mathbf{r}) = \sum_{i=1}^M \lambda_i n_i(\mathbf{r}), \quad (2)$$

where $n_i(\mathbf{r}) = |u_i(\mathbf{r})|^2$ are the one-electron densities. u_i , λ_i and v_{KS} are the Kohn-Sham orbitals, the occupation numbers and the Kohn-Sham potential, respectively. $\varepsilon_1 \leq \varepsilon_2 \leq \dots \leq \varepsilon_M$ are the one-electron energies. M denotes the number of levels with non-zero occupation numbers. Now, the ensemble density and the ensemble non-interacting energy are defined as

$$n(\mathbf{r}) = \sum_{i=1}^M \lambda_i w_i n_i(\mathbf{r}), \quad (3)$$

$$\mathcal{E} = \sum_{i=1}^M w_i \lambda_i \varepsilon_i. \quad (4)$$

Note that if all $w_i = 1$, the ensemble density and the ensemble non-interacting energy equal the true density ($n = n_0$) and the non-interacting energy ($\mathcal{E} = \mathcal{E}_0$). The generalized Rayleigh-Ritz variational principle [8] is valid for the ensembles if the weighting factors satisfy the inequalities: $w_1 \geq w_2 \geq \dots \geq w_M \geq 0$. The generalized variational principle leads to the ensemble Euler equation:

$$\frac{\delta T}{\delta n} + v_{KS} = \mu, \quad (5)$$

where μ is the Lagrange multiplier and the ensemble non-interacting kinetic energy is defined as:

$$T = \int t(\mathbf{r}) d\mathbf{r} = \int \sum_{i=1}^M \lambda_i w_i t_i(\mathbf{r}) d\mathbf{r}. \quad (6)$$

The one-electron kinetic energy densities are given by the Laplacian form $t_i(\mathbf{r}) = -\frac{1}{2}u_i^*(\mathbf{r})\nabla^2 u_i(\mathbf{r})$. Note that v_{KS} in Equation (5) is the original Kohn-Sham potential (1).

The total ensemble non-interacting kinetic energy can be partitioned as $T = T_w + T_p$, where T_w is the ensemble Weizsäcker kinetic energy

$$T_w = \frac{1}{8} \int \frac{|\nabla n|^2}{n} d\mathbf{r} \quad (7)$$

and T_p is ensemble Pauli energy. Then the ensemble Euler Equation (5) can be rewritten as

$$\left[-\frac{1}{2}\nabla^2 + v_p + v_{KS} \right] n^{1/2} = \mu n^{1/2}, \quad (8)$$

where $v_p = \frac{\delta T_p}{\delta n}$ is the Pauli potential.

3. ENSEMBLE DENSITY FOR SPHERICALLY SYMMETRIC SYSTEMS

For spherically symmetric systems the ensemble Euler Equation (8) takes the form

$$\left[-\frac{1}{2} \frac{d^2}{dr^2} + v_p + v_{KS} \right] \varrho^{1/2} = \mu \varrho^{1/2}, \quad (9)$$

where $\varrho = 4\pi r^2 n$ is the radial ensemble density. It was shown in [6] that with the choice of the weighting factors

$$w_i = e^{\beta \varepsilon_i - \gamma l_i (l_i + 1)} \quad (10)$$

(β and γ are real numbers) the ensemble Pauli potential satisfies the first-order differential equation

$$\frac{1}{2} \varrho v_p' + \varrho' v_p = f, \quad (11)$$

where

$$f = -\frac{\partial}{\partial r} \left(\frac{\partial \varrho}{\partial \beta} \right) + \mu \varrho' - \frac{1}{2r^2} \frac{\partial}{\partial r} \left(\frac{\partial \varrho}{\partial \gamma} \right) + \frac{1}{2r^3} \frac{\partial \varrho}{\partial \gamma}. \quad (12)$$

The differential Equation (11) can be solved and the Pauli potential can be written as

$$v_p = \frac{2}{\varrho^2} \int_{\infty}^r \varrho(r_1) f(r_1) dr_1. \quad (13)$$

Note that

$$\frac{\partial \varrho}{\partial \beta} = \sum_{i=1}^M w_i \lambda_i \varepsilon_i \varrho_i = \varrho_E \quad (14)$$

is the ensemble non-interacting energy density and

$$\frac{\partial \varrho}{\partial \gamma} = \sum_{i=1}^M w_i \lambda_i l_i (l_i + 1) \varrho_i = \varrho_L \quad (15)$$

is the ensemble angular momentum density.

The orbital-free solution for spherically symmetric systems can then be obtained in the following steps.

- (i) Guess an initial ensemble electron density.
- (ii) Using Equation (12) calculate the function f .
- (iii) Calculate the ensemble Pauli potential v_p using Equation (13).

- (iv) Solve the ensemble Euler Equation (8) to obtain the ensemble electron density ρ . Note that one needs the original ground-state Kohn-Sham potential. The accuracy of the results will depend on the approximate exchange-correlation functional used in solving the ensemble Euler equation.
- (v) Repeat steps (i)–(iv) until convergence. At the end the ground-state density can be obtained from the ensemble density at $\beta = \gamma = 0$.

The procedure seems to be simple, however, because of the β and γ dependence of the ensemble density, novel numerical methods have to be worked out to find the solution. This work is in progress.

4. DESCRIPTORS OF COULOMB SYSTEMS: ENSEMBLE DENSITY, ENSEMBLE NON-INTERACTING ENERGY DENSITY AND ENSEMBLE ANGULAR MOMENTUM DENSITY

It is well-known that the ground-state density determines every property of the system. In case of Coulomb systems, not only the density, but several other quantities possess this attribute. The shape function (density per particle) [9], reactivity indicators [10] as Fukui function, local softness, softness kernel, electrostatic potential, local kinetic energy and local temperature [11] are all capable of fully determining every property of a Coulomb system. The ensemble density and its derivatives with respect to β and γ appearing in Equation (13), are all provide a full description of a Coulomb system.

The external potential of a Coulomb system has the form

$$v(\mathbf{r}) = - \sum_{\alpha} \frac{Z_{\alpha}}{|\mathbf{r} - \mathbf{R}_{\alpha}|}, \quad (16)$$

where Z_{α} is the atomic number of the nucleus at the position \mathbf{R}_{α} . Consider a linear combination of one-electron densities: $\xi(\mathbf{r}) = \sum_{i=1}^M a_i n_i$, where a_i are real numbers. Using the cusp conditions for the one-electron densities [12], one can readily obtain for the spherical average of ξ around the nucleus α

$$\bar{\xi}'(\mathbf{R}_{\alpha}) = -2Z_{\alpha}\bar{\xi}(\mathbf{R}_{\alpha}). \quad (17)$$

The positions of cusps in ξ locate the nuclei and Equation (17) gives the atomic numbers Z_{α} . ξ determines also the number of electrons. The asymptotic decay of ξ is given by the highest occupied orbital [9]:

$$\xi(r \rightarrow \infty) \sim n_M(r \rightarrow \infty) \sim r^{2\left(\frac{Z_{tot}-N+1}{\sqrt{2I}}-1\right)} e^{-2r\sqrt{2I}}, \quad (18)$$

where I is the vertical ionization potential of the system and $Z_{tot} = \sum_{\alpha} Z_{\alpha}$ is the sum of the atomic numbers. Then the number of electrons can be obtained as [9]:

$$N = 1 + \left(Z_{tot} + \frac{1}{4} \left[\left(\frac{\partial \ln \xi}{\partial r} \right) \left(\frac{\partial^2 \ln \xi}{\partial r \partial \left(\frac{1}{r} \right)} + 2 \right) \right]_{r \rightarrow \infty} \right). \quad (19)$$

Equations (17)–(19) lead to the theorem: For any Coulomb system, ξ determines the external potential v up to an additive constant and the number of electrons.

ξ is the ensemble density if $a_i = \lambda_i w_i$. The choice $a_i = \lambda_i w_i \varepsilon_i$ leads to the ensemble non-interacting energy density. In case of spherically symmetric systems $a_i = w_i \lambda_i l_i (l_i + 1)$ gives the ensemble angular momentum density. That means that if we know the ensemble density or the ensemble non-interacting energy density or the ensemble angular momentum density we can, in principle, determine the external potential, that is, the total Hamiltonian of the true interacting system, therefore any property of the system.

As an illustration, the radial ensemble density, the ensemble non-interacting energy density and the ensemble angular momentum density of the Neon atom are presented as a function of the radial distance for some values of β and γ . Figure 1 shows the radial ensemble density as for $\beta = 0.00$, $\beta = -0.01$, $\beta = -0.05$ and $\gamma = 0.00$ (a) and $\gamma = 5.00$ (b). Note that the case $\beta = \gamma = 0.00$ corresponds to the ground state (solid line). The negative value of β gives larger weight to the

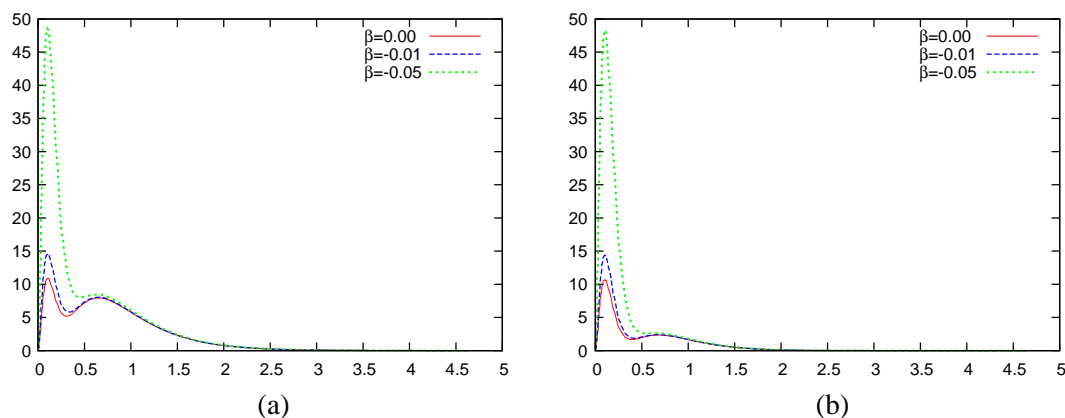


Figure 1: Radial ensemble density for (a) $\gamma = 0$ and (b) $\gamma = 5$ for some values of β as a function of the radial distance for the Neon atom. (Atomic units).

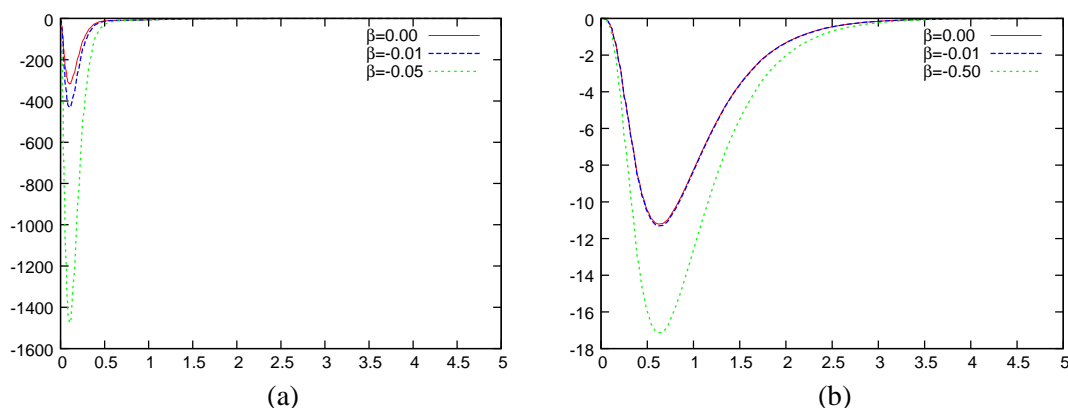


Figure 2: Derivative of the radial ensemble density with respect to (a) β and (b) γ for some values of β and $\gamma = 0$ as a function of the radial distance for the Neon atom. (Atomic units).

lower lying levels (see Equation (3)), therefore the first maximum arising from the $1s$ orbital is increased, while the second maximum is almost disappeared. Figure 2 shows the ensemble non-interacting energy density (a) and the ensemble angular momentum density (b). The ensemble non-interacting energy density, that is the derivative of the ensemble density with respect to β , is presented for $\beta = 0.00$, $\beta = -0.01$, $\beta = -0.05$ and $\gamma = 0.00$. The plots are very similar for larger values of γ . The minimum becomes deeper as β is decreased (see Equation (14)), because β is negative. The ensemble angular momentum density, that is, the derivative of the ensemble density with respect to γ , is presented for $\beta = 0.00$, $\beta = -0.01$, $\beta = -0.50$ and $\gamma = 0.00$. The plots are very similar for larger values of γ . Note that there is no contribution from s orbitals. The minimum becomes deeper as β is decreased (see Equation (15)), because β is negative.

5. CONCLUSION

In the ensemble formulation of the orbital-free density functional theory, the ensemble Euler equation takes the form of a one-particle Schrödinger-like equation for the square root of the ensemble density. The potential in this equation is the sum of the original Kohn-Sham potential plus the ensemble Pauli potential. The latter satisfies a first-order differential equation. The orbital-free problem is reduced to the solution of an equation that contains only the ensemble density and its derivatives. The ground-state problem can be recovered as a special case. The ensemble density, the ensemble non-interacting energy density and the ensemble angular momentum density are all descriptors of a Coulomb system.

ACKNOWLEDGMENT

The work is supported by the TAMOP 4.2.2.A-11/1/KONV-2012-0036 project. The project is co-financed by the European Union and the European Social Fund. Grant OTKA No. K100590 is also gratefully acknowledged.

REFERENCES

1. Chacón, E., J. E. Alvarellos, and P. Tarazona, *Phys. Rev. B*, Vol. 32, 7868, 1985.
2. Huang, C. and E. A. Carter, *Phys. Rev. B*, Vol. 81, 045206, 2010.
3. Trickey, S. B., V. V. Karasiev, and A. Vela, *Phys. Rev. B*, Vol. 84, 075146, 2011.
4. Nagy, Á., *Chem. Phys. Lett.*, Vol. 460, 343, 2008.
5. Nagy, Á., *Int. J. Quant. Chem.*, Vol. 110, 2117, 2010.
6. Nagy, Á., *J. Chem. Phys.*, Vol. 135, 044106, 2011.
7. Nagy, Á., *Recent Advances in Orbital-free Density Functional Theory*, T. A. Wesolowski, and Y. A. Wang, Eds., World Scientific, Singapore, 2013.
8. Gross, E. K. U., L. N. Oliveira, and W. Kohn, *Phys. Rev. A*, Vol. 37, 2805, 1988.
9. Ayers, P. W., *Proc. Natl. Acad. Sci.*, Vol. 97, 1959, 2000.
10. Ayers, P. W., *Chem. Phys. Lett.*, Vol. 438, 148, 2007.
11. Ayers, P. W. and Á. Nagy, *J. Chem. Phys.*, Vol. 126, 144108, 2007.
12. Nagy, Á and K. D. Sen, *J. Chem. Phys.*, Vol. 115, 6300, 2001.

Microwave Tomography Technique for Concrete Diagnosis

Z. Meng

Fukuoka University, Japan

Abstract—“Successive Estimation Technique” is introduced to microwave tomography in concrete diagnosis. It adjusts target area automatically according to the measurement of scattering wave, target range of scattering analysis and the material electromagnetic property of concrete body, and reconstructs tomography image (a distribution of permittivity, conductivity or magnetic permeability) rationally and effectively.

1. INTRODUCTION

Concrete is a very fantastic construction material and concrete buildings occupy over than 30% of whole buildings of office, hotel, and facilities for education and employee welfare. However, concrete can be affected by fire, aggregate expansion, sea water effects, bacterial corrosion, calcium leaching, physical and chemical damage, and many incidents, such as falling concrete, happen all over the world. Because some of degradation could also occur unseen in concrete, techniques for concrete diagnosis are needed in construction industry. Radiography is one of well-known non-destructive inspection techniques with very high precision, but human health risk is involved and the applicable location is limited. On the other hand, Ground Penetrating Radar is developed for concrete diagnosis [1, 2]. The device radiates electromagnetic waves to a concrete body and receives the waves scattered by the surface of the body as well as reinforcing steel bars, cavities, or other objects in the body. However, in practice it is sometimes difficult to comprehend and interpret the scattering waveforms shown on the screen of the device directly.

Microwave tomography is a hopeful technique for concrete diagnosis [3–5]. The distributions of permittivity ε , magnetic permeability μ and conductivity σ of a concrete body are computer-reconstructed by making use of the measurement of scattering waves.

Let us consider an inverse scattering problem shown in Figure 1. A microwave is illuminated from a transmitter to a concrete body, and is measured by a receiver located at the same location as the transmitter. To reconstruct the distributions of material parameters ε , μ and σ , it is assumed that the concrete body is consist of many small cubes (cells), and ε , μ and σ are uniform in each cube. A cost-function is introduced as

$$Cost(\varepsilon, \mu, \sigma) = \frac{\int_{t_{\text{begin}}}^{t_{\text{end}}} \|E^{\text{measured}} - E^{\text{estimated}}(\varepsilon, \mu, \sigma)\| dt}{\int_{t_{\text{begin}}}^{t_{\text{end}}} \|E^{\text{measured}}\| dt}, \quad (1)$$

where

$$\varepsilon = (\varepsilon_1, \varepsilon_2, \dots, \varepsilon_N), \quad \mu = (\mu_1, \mu_2, \dots, \mu_N), \quad \sigma = (\sigma_1, \sigma_2, \dots, \sigma_N),$$

ε_i , μ_i and σ_i ($i = 1, 2, \dots, N$) are material parameters of i -th cube, E^{measured} is the wave measured with the receiver from time t_{begin} to t_{end} , and $E^{\text{estimated}}$ is the wave estimated with wave scattering analysis technique, such as Finite-difference time-domain (FDTD) method. Then ε , μ and σ are estimated by minimizing the $Cost$.

Unlike common case of inverse scattering problems, usually a target of concrete diagnosis cannot be separated from the concrete structure body and taken into a radio wave darkroom for measuring.

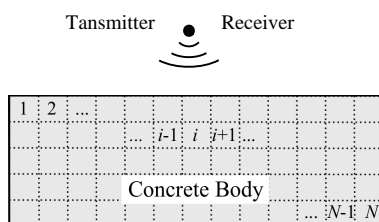


Figure 1: Transmitter, receiver and concrete body.

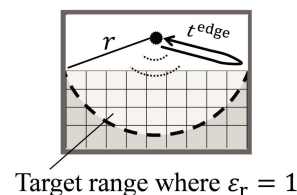


Figure 2: Simulation range and target zone.

Because computer simulation of wave scattering has to be limited in a finite range (simulation range), the time t^{end} must be less than t^{edge} , the time that a scattering wave from edge of the simulation range arrives at the receiver, refer to Figure 2. Therefore the simulation range can be divided into two parts. One is called “target zone” in which the wave scattered by any cube is measured by receiver from t^{begin} to t^{end} ($t^{\text{end}} < t^{\text{edge}}$), and the other one is “non-target zone” in which wave scattered by any cube cannot arrive at the receiver during that time. For example, the target zone becomes a circular region with radius r shown with dashed line in Figure 2, if all the cubes are free space (relative permittivity $\epsilon_r = 1$).

Obviously, only the material parameters of those cubes in the target zone are reconstructible with the cost function (1). If one estimates the material parameters of all cubes in simulation range by minimizing (1), the reconstruction results for the cubes in non-target zone will be not valid. Therefore, it is important to make sure the target and non-target zones. But in a concrete diagnosis we cannot find out the target zone in advance, because material parameters of all cubes (the concrete body) are unknown. It is one of the key problems of microwave tomography in concrete diagnosis.

2. SUCCESSIVE ESTIMATION TECHNIQUE

Successive Estimation Technique is an algorithm to reconstruct material parameters of cubes step by step.

First let us consider reconstructing material parameters of one cube in front of the transmitter(receiver) illustrated in Figure 3, which is our primary target this time. We set t^{begin} and t^{end} to the time that waves scattered by the front and back surface of the cube arrive at the receiver, where the cube is assumed as free space for the present. At the same time, other cubes from which the scattering waves may arrive at the receiver during $t^{\text{begin}} \sim t^{\text{end}}$ are regarded as secondary targets. The cubes of primary and secondary targets compose the target zone of (1) from t^{begin} to t^{end} . Just the material parameters of the primary and secondary targets are objects of the minimization, so that the number of variables is small and the minimization becomes easy to do.

It is noted that precision of the reconstruction for secondary targets may fall in some cases, because the information of scattering waves E^{measured} during the time $t^{\text{begin}} \sim t^{\text{end}}$ may be not enough for reconstructing secondary targets. However, a good reconstruction of the primary target is enough for us. We can scan a concrete surface by using a device like “handy-search” shown in Figure 4. Then the material parameters of the cubes in the first layer (surface layer) can be obtained one by one with the method.

Next let us focus on reconstructing of the cubes in the second layer. The reconstructed material parameters of primary targets in the first layer will be used as known quantities. The wave propaga-

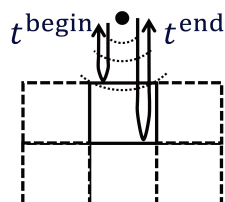


Figure 3: Time for reconstructing primary target (the cube in front of transmitter).



Figure 4: Scan a concrete surface with a handy-search device.

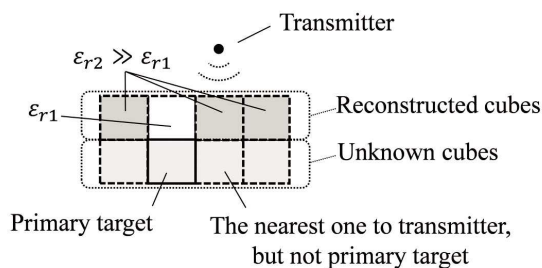


Figure 5: The cube at which the incident wave arrives first is selected as “primary target”.

tion path may become complicated in this case, because multiple scattering phenomenon may occur between different cubes. We redefine “primary target” for each transmitter position as the cube at which the incident wave arrives first. Even if a cube is the nearest one to a transmitter, it is not necessarily a “primary target” of the transmitter, as showed in Figure 5. To find out the primary target for each transmitter position, we use a pulse wave and a wave propagation simulation tool, such as a FDTD simulator, to observe the time that wave peak arrives at center of a cube, where all unknown cubes are assumed to be free space. According to the time that the incident wave arrives at the center of the primary target and pulse width of the incident wave, t_m^{begin} and t_m^{end} for primary target can be estimated and thereupon secondary targets are determined. Finally, material parameters of primary and secondary targets are estimated by minimizing the cost function.

The cubes in other layers are reconstructed by repeating previous steps. With the target layer getting deeper, the number of secondary targets becomes more and more. An effective means is to estimate the targets of all the transmitter positions in one time. In that case, cost function for M transmitter positions is defined as

$$\text{Cost}(\boldsymbol{\varepsilon}^{\text{targets}}, \boldsymbol{\mu}^{\text{targets}}, \boldsymbol{\sigma}^{\text{targets}}) = \sum_{m=1}^M \frac{\int_{t_m^{\text{begin}}}^{t_m^{\text{end}}} \|E_m^{\text{measured}} - E_m^{\text{estimated}}(\boldsymbol{\varepsilon}_m, \boldsymbol{\mu}_m, \boldsymbol{\sigma}_m)\| dt}{\int_{t_m^{\text{begin}}}^{t_m^{\text{end}}} \|E_m^{\text{measured}}\| dt}, \quad (2)$$

where E_m^{measured} is wave measured by receiver at position m from time t_m^{begin} to t_m^{end} , $\boldsymbol{\varepsilon}_m$, $\boldsymbol{\mu}_m$, $\boldsymbol{\sigma}_m$ are vectors of material parameters of primary and secondary targets for transmitter at position m , and $\boldsymbol{\varepsilon}^{\text{targets}}$, $\boldsymbol{\mu}^{\text{targets}}$, $\boldsymbol{\sigma}^{\text{targets}}$ are the sum of sets $\boldsymbol{\varepsilon}_1 \sim \boldsymbol{\varepsilon}_M$, $\boldsymbol{\mu}_1 \sim \boldsymbol{\mu}_M$, $\boldsymbol{\sigma}_1 \sim \boldsymbol{\sigma}_M$, respectively. It is noted that a secondary target for a transmitter position may be a primary target for another transmitter position, and t_m^{end} must be less than t_m^{edge} , the time that a scattering wave from edge arrives at receiver located at position m .

The procedure of successive estimation is summarized below.

1. Scan concrete surface, and measure scattering waves at M positions.
2. Make sure the minimum time that scattering waves from edges of simulation range for each position t_m^{edge} , $m = 1, 2, \dots, M$.
3. Determine primary and secondary targets for each transmitter position, as well as the period of time $t_m^{\text{begin}} \sim t_m^{\text{end}}$ during which the measurement of scattering waves E_m^{measured} will be used for reconstructing material parameters of the targets. However, the data of scattering waves measured at position m as well as the targets for the position will be discarded if t_m^{end} is larger than t_m^{edge} . If all the measurements are discarded, stop the procedure.
4. Reconstruct material parameters of the targets by minimizing the cost function (2). Material parameters of primary targets obtained in the minimization will be used as known quantities in next step, and those of secondary targets will be discarded.
5. Go to step 3 if there are any unknown cubes need to reconstruct.

3. NUMERICAL EXAMPLES

First let us have a simple 2-D example of reconstructing a uniform body where $\varepsilon_r = 9$, and other material parameters are the same as free space, as shown in Figure 6. A raised cosine pulse

$$P(t) = \begin{cases} \left[1 - \cos\left(\frac{2\pi}{T}t\right)\right]^2 & (0 \leq t \leq T) \\ 0 & \text{otherwise} \end{cases} \quad (3)$$

is used as wave source. Simulation range is meshed into 31×5 square cells, where the cell width w_c is set to half of the pulse width. Waves are measured by a transmitter and a receiver located $2w_c$ away from the surface at 23 positions. A FDTD simulator is employed to simulate wave propagation and scattering, and conjugate gradient method is employed to minimize the cost function (2). Searching space of relative permittivity is from 1 to 20.

A reconstructed result is shown in Figure 7. According to the procedure of successive estimation, we had 23 primary targets (cells) for the first iteration, 17 and 11 primary targets for the 2nd and 3rd iteration, and finally, just 1 primary target for the 4th iteration. It is noted that successive estimation technique just reconstructs the cubes in the target zone of the simulation range.

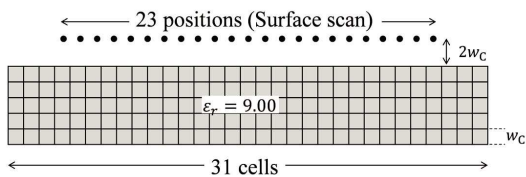


Figure 6: Model setting of example 1.

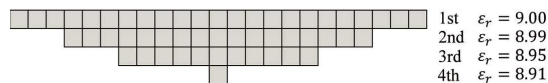


Figure 7: Reconstruction result of example 1.

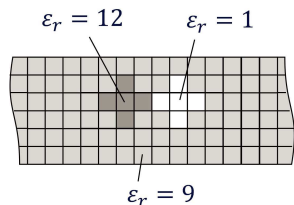


Figure 8: Model setting of example 2.

9.00	9.00	9.00	9.00	9.00	9.00	9.00	9.00	9.00
8.99	8.96	12.01	8.99	9.00	1.00	9.00	8.99	
8.94	11.96	12.06	12.03	1.00	1.01	1.00	9.10	
8.91	9.14	12.46	8.98	9.07	1.01	9.08	9.32	
8.86	9.17	9.29	9.00	9.01	8.98	9.00	9.33	

Figure 9: A part of reconstruction result of example 2.

Next let us have a little more complex example. The model is based on example 1, but one “aggregate” ($\epsilon_r = 12$) and one “hollow” ($\epsilon_r = 1$) are inserted in, as shown in Figure 8. Of course, to reconstruct a wider deep region we need a wider simulation range. A part of reconstruction result of example 2 is given in Figure 9.

4. CONCLUSIONS

Successive estimation technique is an iteration method to reconstruct target body part by part, by using time-divided information of the scattered wave. It is suitable for microwave tomography in concrete diagnosis. High accuracy tomography images are obtained efficiently in numerical experiments.

REFERENCES

1. Van der Wielen, A., L. Courard, and F. Nguyen, “GPR limits for thin layers in concrete detection: Numerical and experimental evaluation,” *PIERS Online*, Vol. 7, No. 4, 339–342, 2011.
2. Angiulli, G., V. Barrile, and M. Cacciola, “The GPR technology on the seismic damageability assessment of reinforced concrete building,” *PIERS Proceedings*, 303–307, Hangzhou, China, Aug. 22–26, 2005.
3. Soutsos, M. N., J. H. Bungey, S. G. Millard, M. R. Shaw, and A. Patterson, “Dielectric properties of concrete and their influence on radar testing,” *NDT & E International*, Vol. 34, 419–425, 2001.
4. Klysz, G., J. P. Balayssac, and X. Ferrieres, “Evaluation of dielectric properties of concrete by a numerical FDTD model of a GPR coupled antenna — Parametric study,” *NDT & E International*, Vol. 41, 621–631, 2008.
5. Li, F., X. Chen, and K.-M. Huang, “Microwave imaging a buried object by the GA and using the S_{11} parameter,” *Progress In Electromagnetics Research*, Vol. 85, 289–302, 2008.

Auto-focused Imaging of a Moving Target Using an Ultra-wideband Array Radar

T. Sakamoto¹, T. Sato², P. Aubry³, and A. Yarovoy³

¹University of Hyogo, Japan

²Kyoto University, Japan

³Delft University of Technology, The Netherlands

Abstract—The authors have developed a target speed estimation method for an ultra-wideband radar imaging system. The method is able to generate a focused image even if the target is moving at an unknown speed during the measurement, where many other techniques produce blurred images. Our technique uses the cross-range blurriness as a metric to measure the image focusing, and select the best-focused image among many generated for various candidate speeds. The target speed is estimated by finding the minimum cross-range blurriness, and the method compensates for the estimated speed to generate a focused three-dimensional image automatically. By exploiting the fact that the head size differs relatively little among individuals, we detected the head position in a radar image, and calculated the blurriness around the region to evaluate the focus of the image. The speed estimation method is applied to the measurement of a mannequin on a moving stage, and it is shown that the target speed is estimated with an accuracy of 5%. Application results show that the developed technique can estimate target speeds accurately, and produce an image with sufficient resolution for the intended application.

1. INTRODUCTION

Because of possible terrorist attacks on public transport systems such as airports, microwave body scanners are considered an important measure of ensuring public safety. Microwaves can penetrate most clothing, and such body scanners are therefore capable of detecting weapons concealed under clothes by forming an image using radar echoes from the targets. Microwave-based imaging techniques have been intensively studied to improve their resolution, accuracy and computational speed, leading to various effective technologies and commercial products [1, 2].

Recently, a new type of microwave imaging technique, revised range point migration (RRPM), has been attracting attention. The technique is faster than many existing techniques and can generate numerous images within a short time. This allows auto-focusing imaging of a moving target traveling at an unknown speed, by selecting the most focused image among many generated assuming various candidate speeds. In this paper, we review such techniques and present application results using measurement data to demonstrate the performance of the techniques. Some preliminary results have been reported at a previous conference [3], and details will be presented in an article [4] that is now under review.

2. SYSTEM MODEL

We assume a measurement system consisting of a transmitter and a receiver positioned in the $z = 0$ plane in the direction of the x axis at a fixed separation given by $2d$. The midpoint between the transmitter and receiver is labeled $(X, Y, 0)$, which means the transmitting and receiving antennas are located at $(X - d, Y, 0)$ and $(X + d, Y, 0)$, respectively. The transmitter-receiver pair scans at discrete intervals across a region of the $z = 0$ plane. Given the antenna midpoint $(X, Y, 0)$, the signal received is labeled $s(X, Y, Z)$, where $Z = ct/2$. Here, c is the speed of the electromagnetic wave and t is the time interval between transmission and reception. A schematic of the system model is shown in Figure 1.

3. IMAGING METHOD

We employ a fast imaging algorithm using the bistatic inverse boundary transform (IBST), which is a reversible transform between radar signals and radar images. The first step in imaging using the bistatic IBST is the extraction of signal peaks that exceeds a threshold T_s . These peaks are indexed as (X_i, Y_i, Z_i) for $(i = 1, 2, \dots, N)$. The corresponding amplitudes of these peaks are denoted $s_i = s(X_i, Y_i, Z_i)$. Let us assume that these points are easily connected sequentially to form multiple curved surfaces $Z(X, Y)$. This function and its derivative are used in imaging with the bistatic IBST. To obtain stable derivatives Z_X and Z_Y , we use the RRPM algorithm [4], which

is known to be fast and robust even for complicated shapes in a noisy scenario. The RRPM method estimates a derivative $Z_X = \tan(\theta_i)$, where θ_i is the inclination of the peak distribution and calculated as a weighted average over multiple peak points around the point of interest. Using multiple peak points, we can make the resultant derivative stable, leading to high-resolution imaging with in a short time.

4. TARGET SPEED ESTIMATION

The image obtained with a correctly assumed speed is well focused, where the focus can be evaluated using the image blurriness metric [3]. The proposed methodology produces multiple images corresponding to various assumed speeds, from which the optimum metric gives an estimate of the speed. It is essential to use the fast imaging technique with the bistatic IBST and RRPM in calculating these metrics because the imaging is repeated many times for various assumed speeds; this process can be impractically time consuming if conventional methods are used instead.

We introduce a metric to measure the cross-range blurriness of a radar image. Assuming that the method is applied to a human target, this metric uses only the part of a radar image that is likely to contain a head if the target is a human. First, we estimate the head position in an image by taking the largest peak of the vertical profile of the RRPM image. Because we do not yet know the exact target speed, we assume a stationary target to produce a reference image in this process. From this reference image, we estimate the head position where a strong reflection is observed. Next, the image sharpness is evaluated using the cross-range blurriness of the image at the estimated head position. If the image is focused, the blurriness is reduced; the actual target speed minimizes the value. More details on this method are found in [4].

5. MEASUREMENT SETUP

We applied the speed estimation method using the cross-range blurriness to measurements obtained for the metal-coated mannequin shown in Fig. 2. The target was placed on a moving platform. We employed frequencies from 5.0 to 25.0 GHz for the measurement. The antennas were spaced at 5.5 cm and scanned at 1.0-cm intervals over an area 75.0×75.0 cm in the x - y plane. While the antennas scanned from left to right, the target moved in the $-z$ direction over a distance of 38.0 cm, corresponding to a target speed of 1.0 m/s, assuming a total measurement time of 0.38 s. The RRPM method extracted 15 peaks for each antenna position. We set $\sigma_X = \sigma_Y = 0.8$ cm, $\sigma_Z = 0.3$ cm and $\sigma_\theta = \pi/100$. The i -th target image point (x_i, y_i, z_i) was weighted with amplitude $|s_i|$ to generate a three-dimensional image.

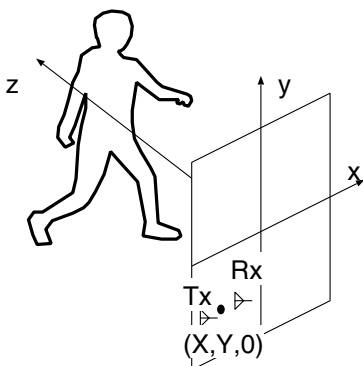


Figure 1: System model of antenna array-based radar for detecting concealed weapons worn by a person in motion.



Figure 2: Metal-coated mannequin on a moving platform used in our radar measurement.

6. APPLICATION OF THE PROPOSED METHOD

To investigate the performance of speed estimation, we apply the target speed estimation explained above. Figure 3 shows the conventional MB sharpness metric [5] and cross-range blurriness for the

mannequin target. The MB sharpness metric and cross-range blurriness are respectively plotted as dashed black and red solid lines and give the estimates of target speed. The target speeds estimated using the MB sharpness metric and cross-range blurriness are respectively 0.89 and 0.95 m/s, giving errors of 11% and 5%. Our cross-range blurriness gives a better estimate, because a mannequin is difficult to approximate as a point target, where the conventional MB sharpness metric assumes that the target is a set of point targets. In contrast, the cross-range blurriness maintains its accuracy within an acceptable range. Figure 4 shows the 3-D images generated for the speed estimated using the cross-range blurriness. It is confirmed that the shape of the target is clearly imaged, and the resolution is considered to be sufficient for many applications. The next step in this series of studies is quantitative analysis of the image resolution under various conditions such as different target motion patterns, which will reveal the applicability and limitations of the developed technique.

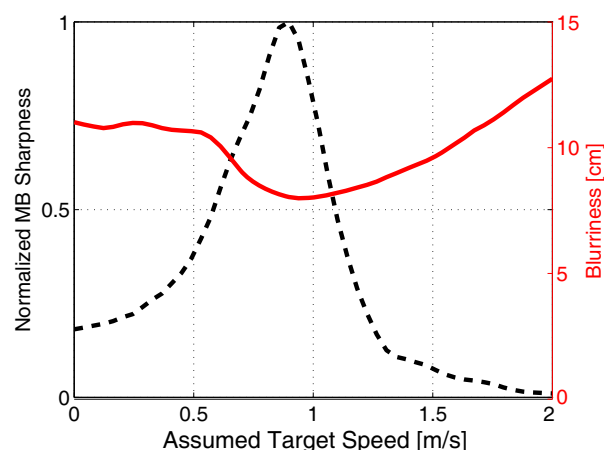


Figure 3: MB sharpness metric (black) and cross-range blurriness (red) for a mannequin. Actual speed is 1.0 m/s.

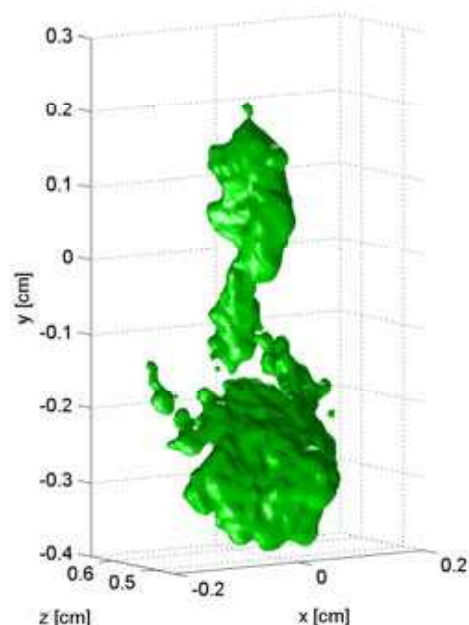


Figure 4: Focused image of the mannequin generated using the blurriness metric proposed by the authors.

7. CONCLUSION

We presented a target speed estimation technique and imaging method, and provided an application result. The method produces multiple images assuming various candidate speeds, among which we select the best-focused image and its corresponding speed as an estimate of the target motion.

Because this approach requires the production of numerous images assuming different candidate speeds, we employed a fast imaging method, RRPM, to realize fast processing sufficient for many security systems. By exploiting the fact that the head size differs relatively little among individuals, we detected the head position in a radar image, and calculated the blurriness around the region to evaluate the focusing of the image. The method was applied to measurement data for a moving mannequin, and it was shown that the target speed was estimated with an accuracy of 5%. The developed techniques were demonstrated to be effective in estimating the speed accurately and producing a focused image.

ACKNOWLEDGMENT

This research was partially supported by the Supporting Program for Interaction-based Initiative Team Studies (SPIRITS) under Japan-Netherlands joint development of sleep monitoring technology using ultra-wideband radar, the Center of Innovation Program (COI) under The Last 5X Innovation R&D Center for a Smart, Happy, and Resilient Society, JSPS KAKENHI under grant

numbers 25249057 and 15K18077, and the R&D project for expansion of radio spectrum resources for more efficient use of frequency resources for the future supported by The Ministry of Internal Affairs and Communications, Japan.

REFERENCES

1. Zhou, H., M. Sato, T. Takenaka, and G. Li, "Reconstruction from antenna-transformed radar data using a time-domain reconstruction method," *IEEE Trans. Geosci. Remote Sens.*, Vol. 45, No. 3, 689–696, 2007.
2. Oliveri, G., N. Anselmi, and A. Massa, "Compressive sensing imaging of non-sparse 2D scatterers by a total-variation approach within the born approximation," *IEEE Transactions on Antennas and Propagation*, Vol. 62, No. 10, 5157–5170, 2014.
3. Sakamoto, T., T. Sato, P. Aubry, and A. Yarovoy, "Auto-focusing UWB array radar imaging of a target in unknown motion using Muller and Buffington metrics and cross-range blurriness," *The XXXI General Assembly of the International Union of Radio Science*, 2014.
4. Sakamoto, T., T. Sato, P. Aubry, and A. Yarovoy, "Fast imaging method for security systems using ultra-wideband radar," *IEEE Trans. Aerospace & Electronic Systems*, (submitted).
5. Muller, R. A. and A. Buffington, "Real-time correction of atmospherically degraded telescope images through image sharpening," *J. Opt. Soc. Amer.*, Vol. 64, No. 9, 1200–1210, 1974.

Microwave Imaging of Dispersive Scatterers Using Vectorial Lagrange Multipliers

T. G. Papadopoulos¹, T. I. Kosmanis², and I. T. Rekanos¹

¹School of Electrical and Computer Engineering, Aristotle University of Thessaloniki, Greece

²Department of Automotive Engineering

Alexander Technological Educational Institute of Thessaloniki, Greece

Abstract— A time-domain microwave imaging method is proposed for the reconstruction of the spatial distribution of the electromagnetic properties of dispersive scatterers. The method is based on the minimization of a cost functional, which describes the discrepancy between measured and estimated scattered field data. The Maxwell's curl equations are introduced in an augmented cost functional, as equality constraints, via vectorial Lagrange multipliers. By means of the calculus of variations and the stationarity condition, it is shown that the vectorial Lagrange multipliers are the solution of the adjoint scattering problem. Moreover, the Fréchet derivatives of the cost functional with respect to the distributions of the scatterer properties are derived analytically. As a result, the Fréchet derivatives obtained can be utilized by any gradient-based optimization technique that updates the estimated scatterer properties iteratively. In this study, two-dimensional dispersive scatterers have been investigated. In the case of Debye scatterers, the spatial distributions of the relaxation time, the static and the optical permittivity, are reconstructed simultaneously. Also, the method is applied to the reconstruction of the resonant frequency, the damping factor, the static and the optical permittivity of Lorentz dispersive media.

1. INTRODUCTION

Inverse electromagnetic scattering problems have attracted significant research interest over the last years because of their applications in medical imaging, geophysical prospecting, nondestructive testing etc. [1]. The solution of an inverse scattering problem is difficult because it is an ill-posed and nonlinear problem [2]. Frequency-domain and the time-domain techniques are the two approaches for the solution of this problem, depending on the time variation of the excitations used. In the first case, the excitation is considered to be monochromatic and the inverse scattering problem is formulated in the frequency domain [3–5]. In single frequency-domain microwave imaging, the case of dispersive scatterers is tackled similarly to the case of nondispersive ones because monochromatic excitations do not generate dispersion phenomena. The second approach, namely the time-domain one, considers cases where the excitation field is wideband [6–8]. Time-domain microwave imaging results in improved reconstruction resolution of nondispersive scatterers, while it provides the ability to reconstruct dispersive scatterers. In particular, if the scatterer properties are frequency-dependent, dispersion phenomena appear, thus, time-domain techniques that estimate the parameters of dispersive media are important [9, 10].

In this study, a method to reconstruct simultaneously the electromagnetic properties of two-dimensional Debye and Lorentz dispersive scatterers is presented. The method minimizes the cost functional that describes the discrepancy between measured and estimated electric field values. By means of the calculus of variations, we derive the equations of the adjoint scattering problem. Furthermore, the Fréchet derivatives of the cost functional with respect to the medium properties are obtained. These derivatives are used by the Polak-Ribière optimization algorithm to estimate iteratively the scatterer properties while the finite-difference time-domain (FDTD) method is utilized for the solution of the direct and the adjoint scattering problem. As a result, it is possible to reconstruct the static and optical relative permittivity as well as the relaxation time of Debye scatterers, simultaneous. In the case of Lorentz dispersive scatterers, the static and optical relative permittivity as well as the resonant frequency and the damping factor are reconstructed. The numerical results that are presented, exhibit the efficiency of the proposed methodology.

2. MATHEMATICAL FORMULATION OF THE PROBLEM

2.1. Direct Scattering

The relative complex permittivity of an inhomogeneous Debye scatterer is given by

$$\varepsilon_r(\omega, \vec{r}) = \varepsilon_\infty(\vec{r}) + \Delta\varepsilon(\vec{r}) / [1 + j\omega\tau(\vec{r})] \quad (1)$$

where ε_∞ is the optical relative permittivity, τ is the relaxation time, $\Delta\varepsilon = \varepsilon_s - \varepsilon_\infty$ (ε_s is the static relative permittivity), and ω is the angular frequency. In the case of a Lorentz dispersive scatterer, the relative permittivity is given by

$$\varepsilon_r(\omega, \vec{r}) = \varepsilon_\infty(\vec{r}) + \Delta\varepsilon(\vec{r})\omega_0^2(\vec{r}) / [\omega_0^2(\vec{r}) + 2j\omega\zeta(\vec{r}) - \omega^2] \quad (2)$$

where ω_0 is the resonant frequency, and ζ is the damping factor.

The Maxwell's curl equations governing the wave propagation in a dispersive medium involve the polarization current density \vec{J} , i.e.,

$$\nabla \times \vec{E} + \mu\partial_t\vec{H} = 0, \quad \nabla \times \vec{H} - \varepsilon_0\varepsilon_\infty\partial_t\vec{E} - \vec{J} - \vec{J}_s = 0 \quad (3)$$

where \vec{J}_s is the excitation current density, while \vec{J} satisfies the differential equation

$$\vec{J} + \tau\partial_t\vec{J} - \varepsilon_0\Delta\varepsilon\partial_t\vec{E} = 0 \quad \text{or} \quad \omega_0^2\vec{J} + 2\zeta\partial_t\vec{J} + \partial_t^2\vec{J} - \varepsilon_0\Delta\varepsilon\omega_0^2\partial_t\vec{E} = 0 \quad (4)$$

in Debye or Lorentz scatterers, respectively.

2.2. Inverse Scattering

We assume that the dispersive scatterer is nonmagnetic ($\mu = \mu_0$) and lies within the scatterer domain D (see Fig. 1). The domain D is excited by I incident waves, while for each incidence the electric field is measured at K positions around the scatterer for the time interval $[0, T]$. Hence, a set of $I \times K$ electric field measurements is obtained, which are denoted as \vec{E}_{ik}^m where $i = 1, \dots, I$ and $k = 1, \dots, K$. We note that the time of measurement T is selected in a way that the measured field at the farthest receiver has significantly faded out. The reconstruction of the scatterer properties (denoted by the vector \mathbf{p}) is based on the minimization of a cost functional, which describes the difference between measured and estimated values of the electric field. The Maxwell's curl equations and the polarization relation are introduced in the augmented cost functional as equality constraints by means of vectorial Lagrange multipliers. In particular the augmented cost functional is given by

$$F(\mathbf{p}) = \frac{1}{2} \sum_{i=1}^I \sum_{k=1}^K \int_0^T \left\| \vec{E}_{ik} - \vec{E}_{ik}^m \right\|^2 dt + MC + PC \quad (5)$$

where MC is the term related to the Maxwell's equations equality constraints, i.e.,

$$MC = \sum_{i=1}^I \int_0^T \int_V \left[\vec{h}_i \cdot (\nabla \times \vec{E}_i + \mu\partial_t\vec{H}_i) + \vec{e}_i \cdot (\nabla \times \vec{H}_i - \varepsilon_0\varepsilon_\infty\partial_t\vec{E}_i - \vec{J}_i - \vec{J}_{si}) \right] dv dt \quad (6)$$

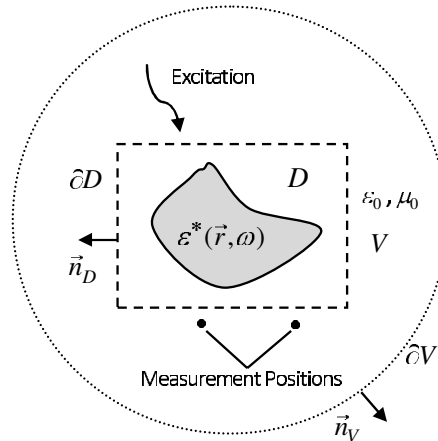


Figure 1: Geometry of the inverse scattering problem.

and PC is the term related to the polarization equality constraint and is given by

$$PC = \sum_{i=1}^I \int_0^T \int_V \vec{q}_i \cdot \left(\vec{J}_i + \tau \partial_t \vec{J}_i - \varepsilon_0 \Delta \varepsilon \partial_t \vec{E}_i \right) dv dt \quad (\text{Debye case}) \tag{7}$$

$$PC = \sum_{i=1}^I \int_0^T \int_V \vec{q}_i \cdot \left(\omega_0^2 \vec{J}_i + 2\zeta \partial_t \vec{J}_i + \partial_t^2 \vec{J}_i - \varepsilon_0 \Delta \varepsilon \omega_0^2 \partial_t \vec{E}_i \right) dv dt \quad (\text{Lorentz case})$$

In (6) and (7), \vec{h}_i , \vec{e}_i , and \vec{q}_i are the vectorial Lagrange multipliers.

2.3. Vectorial Lagrange Multipliers — Fréchet Derivatives

Using the calculus of variations, the stationarity condition of the cost functional, $\delta F = 0$, results in the differential equations (adjoint problem) satisfied by the vectorial Lagrange multipliers, i.e.,

$$\nabla \times \vec{e}_i - \mu \partial_t \vec{h}_i = 0, \quad \nabla \times \vec{h}_i + \varepsilon_0 \varepsilon_\infty \partial_t \vec{e}_i - \vec{j}_i + \sum_{k=1}^K (\vec{E}_{ik} - \vec{E}_{ik}^m) = 0, \tag{8}$$

$$\vec{j}_i - \tau \partial_t \vec{j}_i + \varepsilon_0 \Delta \varepsilon \partial_t \vec{e}_i = 0, \quad \vec{j}_i = -\varepsilon_0 \Delta \varepsilon \partial_t \vec{q}_i \quad (\text{Debye case}) \tag{9}$$

$$\omega_0^2 \vec{j}_i - 2\zeta \partial_t \vec{j}_i + \partial_t^2 \vec{j}_i + \varepsilon_0 \Delta \varepsilon \omega_0^2 \partial_t \vec{e}_i = 0, \quad \vec{j}_i = -\varepsilon_0 \Delta \varepsilon \omega_0^2 \partial_t \vec{q}_i \quad (\text{Lorentz case})$$

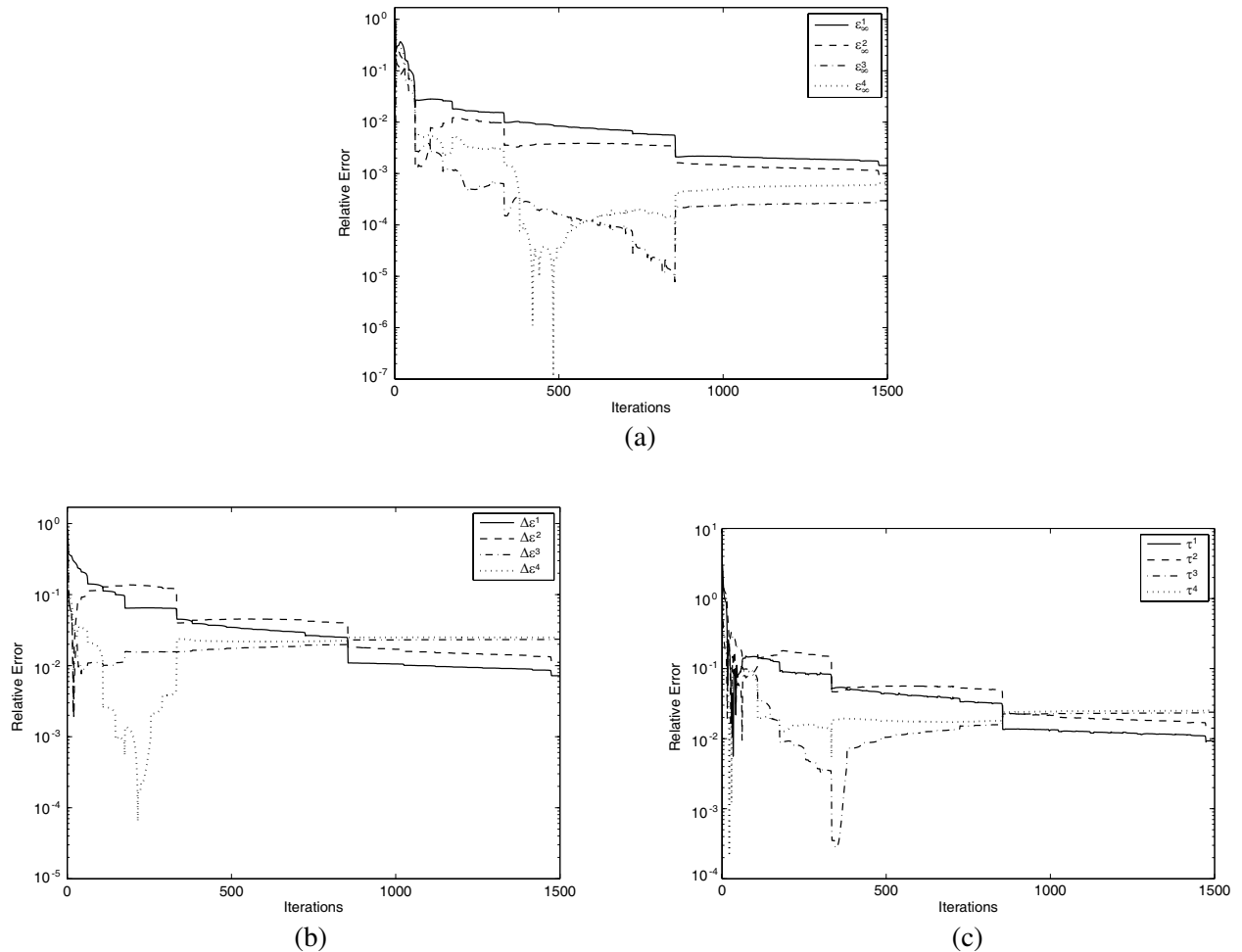


Figure 2: Relative reconstruction error vs. the number of iterations, for the case of 2D Debye scatterer divided in four subdomains. (a) ε_∞ , (b) $\Delta\varepsilon$, and (c) τ .

Furthermore, the Fréchet derivatives of the cost functional with respect to the scatterer properties are derived analytically and are given by

$$\begin{aligned} \frac{\delta F}{\delta \varepsilon_\infty} &= -\varepsilon_0 \sum_{i=1}^I \int_0^T \left(\vec{e}_i \cdot \partial_t \vec{E}_i \right) dt, \quad \frac{\delta F}{\delta \Delta \varepsilon} = -\frac{1}{\Delta \varepsilon} \sum_{i=1}^I \int_0^T \left(\vec{E}_i \cdot \vec{j}_i \right) dt, \quad \frac{\delta F}{\delta \tau} \\ &= \frac{1}{\varepsilon_0 \Delta \varepsilon} \sum_{i=1}^I \int_0^T \left(\vec{J}_i \cdot \vec{j}_i \right) dt, \\ \frac{\delta F}{\delta \omega_0} &= 2 \sum_{i=1}^I \int_0^T \left[\frac{1}{\omega_0} \vec{J}_i \cdot \vec{e}_i - \frac{\left(2\zeta \vec{j}_i - \partial_t \vec{j}_i \right) \cdot \vec{J}_i}{\varepsilon_0 \omega_0^3 \Delta \varepsilon} \right] dt, \quad \frac{\delta F}{\delta \zeta} = \frac{2}{\varepsilon_0 \omega_0^2 \Delta \varepsilon} \sum_{i=1}^I \int_0^T \left(\vec{J}_i \cdot \vec{j}_i \right) dt. \end{aligned} \quad (10)$$

The Fréchet derivatives in (10) can be utilized by any gradient-based optimization algorithm to update the dispersive scatterer properties, iteratively. In this work, the Polak-Ribière optimization algorithm is adopted, while the computation of the estimated fields and the vectorial Lagrange multipliers is based on the FDTD method.

3. NUMERICAL RESULTS

The presented method has been applied to the reconstruction of a two-dimensional Debye scatterer. The incident waves are generated by eight transmitters ($I = 8$) placed at uniformly distributed locations around the scatterer. For each incidence, the electric field is measured at sixteen positions ($K = 16$), uniformly placed around the scatterer. The scatterer is considered to be square,

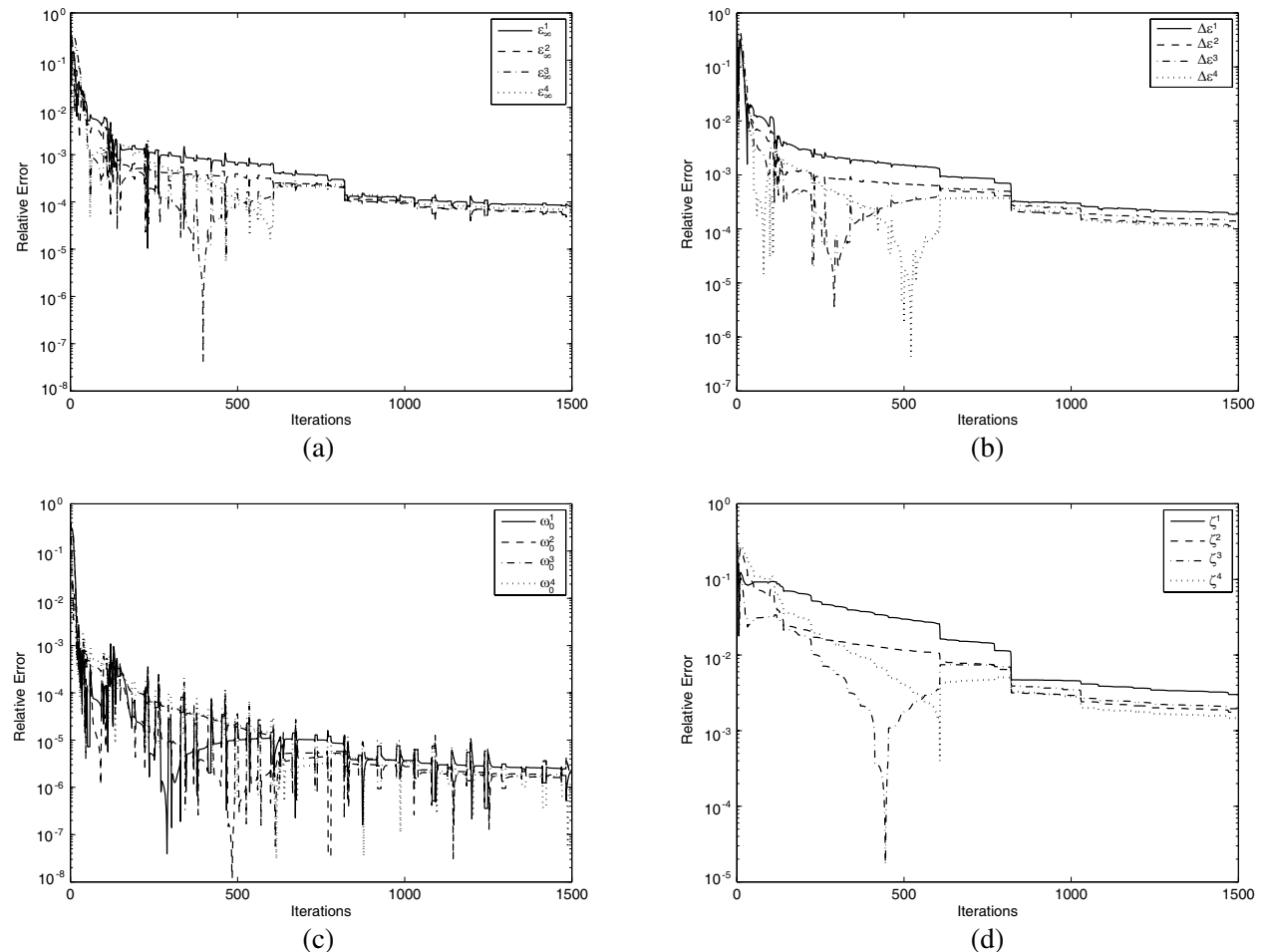


Figure 3: Relative reconstruction error vs. the number of iterations, for the case of 2D Lorentz scatterer divided in four subdomains. (a) ε_∞ , (b) $\Delta \varepsilon$, (c) ω_0 , and (d) ζ .

(0.75m \times 0.75m), and is divided in four square subdomains characterized by different parameters. Specifically, the original properties of the scatterer subdomains are $[\varepsilon_\infty^1, \varepsilon_\infty^2, \varepsilon_\infty^3, \varepsilon_\infty^4] = [2, 3, 4, 2]$, $[\Delta\varepsilon^1, \Delta\varepsilon^2, \Delta\varepsilon^3, \Delta\varepsilon^4] = [3, 2, 2, 2]$, and $[\tau^1, \tau^2, \tau^3, \tau^4] = [0.5, 0.5, 1, 1]$ ns. The excitation current density is a modulated Gaussian pulse given by

$$J_s(t) = e^{-a^2(t-4/a)^2} \sin(2\pi f_c t) u(t) \quad (11)$$

where $f_c = 5 \times 10^8$ Hz and $a = 5\pi \times 10^8$ sec $^{-1}$.

The scatterer reconstruction is based on simulated measurements obtained by the method of the FDTD. The values of the initial estimates of the scatterer parameters are $\varepsilon_\infty^{1,2,3,4} = 1.1$, $\Delta\varepsilon^{1,2,3,4} = 0.5$, and $\tau^{1,2,3,4} = 2$ ns. In addition, the widths of the four subdomains are *a priori* known. After 1500 iterations the cost function is lower than 2×10^{-4} , while the relative reconstruction errors are of order or lower than 10^{-2} , for all three Debye parameters; a fact that depicts the efficiency of the proposed technique. Figure 2 presents the relative reconstruction errors for each parameter, ε_∞ , $\Delta\varepsilon$, τ , versus the number of iterations of the algorithm.

Finally, the proposed microwave imaging method is applied to the reconstruction of a two-dimensional Lorentz dispersive scatterer. The geometry of the inverse problem, the excitation and the measurement positions are the same as in the previous Debye case. The original properties of the scatterer subdomains are $[\varepsilon_\infty^1, \varepsilon_\infty^2, \varepsilon_\infty^3, \varepsilon_\infty^4] = [2, 2.5, 2.5, 2]$, $[\Delta\varepsilon^1, \Delta\varepsilon^2, \Delta\varepsilon^3, \Delta\varepsilon^4] = [2, 3, 2.5, 3]$, $[\omega_0^1, \omega_0^2, \omega_0^3, \omega_0^4] = [\pi \times 10^9, \pi \times 10^9, \pi \times 10^9, \pi \times 10^9]$ rad/sec, and $[\zeta^1, \zeta^2, \zeta^3, \zeta^4] = [0.08\pi \times 10^8, 0.08\pi \times 10^8, 0.09\pi \times 10^8, 0.09\pi \times 10^8]$ sec $^{-1}$. The excitation current density is the same as in the previous example.

The values of the initial estimates of the scatterer parameters are $\varepsilon_\infty^{1,2,3,4} = 3.5$, $\Delta\varepsilon^{1,2,3,4} = 1.1$, $\omega_0^{1,2,3,4} = 6\pi \times 10^8$ rad/sec, $\zeta^{1,2,3,4} = 0.06\pi \times 10^8$ sec $^{-1}$ and the unknowns are now 16. As already noted, the size of the four subdomains are *a priori* known. After 1500 iterations the cost function is lower than 3×10^{-5} , while the relative reconstruction errors are of order or lower than 10^{-3} , for all four Lorentz parameters. Figure 3 presents the relative reconstruction errors for each parameter, ε_∞ , $\Delta\varepsilon$, ω_0 , and ζ versus the number of iterations of the algorithm.

4. CONCLUSION

A time-domain microwave imaging technique, which is based on the use of vectorial Lagrange multipliers, has been proposed for the reconstruction of dispersive scatterers. The Fréchet derivatives of the cost functional with respect to the scatterer properties are derived analytically. These derivatives can be utilized by any gradient-based inverse scattering technique along with any time-domain computational method employed for the solution of the electromagnetic problem. The cases of two-dimensional Debye as well as Lorentz dispersive scatterers have been investigated. Numerical results have shown that it is possible to reconstruct the spatial distributions of all the electromagnetic properties of the scatterers, accurately and simultaneously.

ACKNOWLEDGMENT

This research has been co-financed by the European Union (European Social Fund-ESF) and Greek national funds through the Operational Program “Education and Lifelong Learning” of the National Strategic Reference Framework (NSRF)-Research Funding Program: ARCHIMEDES III. Investing in knowledge society through the European Social Fund.

REFERENCES

1. Pastorino, M., *Microwave Imaging*, Wiley, New Jersey, 2010.
2. Colton, D. and R. Kress *Inverse Acoustic and Electromagnetic Scattering Theory*, Springer-Verlag, New York, 1992.
3. Pastorino, M., S. Caorsi, and A. Massa, “A global optimization technique for microwave non-destructive evaluation,” *IEEE Trans. Instrum. Meas.*, Vol. 51, No. 4, 666–673, 2002.
4. Meaney, P. M., K. D. Paulsen, and T. P. Ryan, “Two-dimensional hybrid element image reconstruction for TM illumination,” *IEEE Trans. Antennas Propag.*, Vol. 43, No. 3, 239–247, 1995.
5. Joachimowicz, N., C. Pichot, and J.-P. Hugonin, “Inverse scattering: An iterative numerical method for electromagnetic imaging,” *IEEE Trans. Antennas Propag.*, Vol. 39, No. 12, 1742–1752, 1991.

6. Gustafsson, M. and S. He, "An optimization approach to two-dimensional time domain electromagnetic inverse problems," *Radio Sci.*, Vol. 35, No. 2, 525–536, 2000.
7. Takenaka, T., H. Zhou, and T. Tanaka, "Inverse scattering for a three-dimensional object in the time domain," *JOSA A*, Vol. 20, No. 10, 1867–1874, 2003.
8. Rekanos, I. T., "Time-domain inverse scattering using Lagrange multipliers: An iterative FDTD-based optimization technique," *Journal of Electromagnetic Waves and Applications*, Vol. 17, No. 2, 271–289, 2003.
9. Papadopoulos, T. G. and I. T. Rekanos, "Estimation of the parameters of Lorentz dispersive media using a time-domain inverse scattering technique," *IEEE Trans. Magn.*, Vol. 48, No. 2, 219–222, 2012.
10. Papadopoulos, T. G. and I. T. Rekanos, "Time-domain microwave imaging of inhomogeneous Debye dispersive scatterers," *IEEE Trans. Antennas Propag.*, Vol. 60, No. 2, 1197–1202, 2012.

Analysis of Radiation from X-band Slotted-waveguide Antenna Arrays Using the Parallel DDA-FE-BI-MLFMA

Xu-Min Sun, Ming-Lin Yang, and Xin-Qing Sheng

Center for Electromagnetic Simulation, School of Information Science and Technology
Beijing Institute of Technology, Beijing 100081, China

Abstract— The hybrid finite element-boundary integral-multilevel fast multipole algorithm (FE-BI-MLFMA) approach is adopted for fast and accurate computation of radiation from large slotted-waveguide antenna arrays. A simplified model is presented by using a thin current probe as the excitation and a layer of perfectly matched layer (PML) as the termination for slotted-waveguide antenna. Since each slotted-waveguide antenna can be generally considered as a single sub-domain, the domain decomposition algorithm (DDA) is applied in the FE-BI-MLFMA to reduce computation resource and achieve high efficiency. This DDA-FE-BI-MLMFA is parallelized to further strength its capability. To validate the presented approach for computing radiation from slotted-waveguide antenna arrays, a series of numerical experiments are performed. Good agreement between our calculated results and results from commercial software CST validates accuracy of the presented approach. To show capability of the proposed DDA-FE-BI-MLFMA, a large X-band slotted-waveguide antenna array containing eighteen waveguides is designed and its radiation characteristics are studied.

1. INTRODUCTION

The slotted-waveguide antenna arrays are widely used in real-life communication and radar system applications, because of their small size, light weight, compact structure, high efficiency, and low side lobe characteristics. The computation of radiation from slotted-waveguide antenna arrays is of growing interest due to its importance in practical applications. Various methods have been developed to compute the radiation from slotted-waveguide antennas, such as the variational approach in terms of equivalent network, the method of moments (MoM), the finite-difference time-domain (FDTD) method, the finite element method (FEM) and the hybrid finite element-boundary integral (FE-BI) method [1–10].

However, due to large number of slots and the mutual coupling between the slots through the waveguides and the exterior space, previous researches mainly focus on analysis of radiation by a single slot in a waveguide, 1-D slotted-waveguide arrays or small 2-D slotted-waveguide arrays in a planar surface. In real application, fast and accurate analysis of radiation from large slotted-waveguide antenna arrays containing tens of slotted-waveguides and comprising thousands slot elements cut in the wall of the waveguides still faces great challenges.

In this paper, an efficient approach is presented for fast and accurate analysis of radiation from large slotted-waveguide antenna arrays by using the FE-BI-MLFMA [11–13]. To simplify the calculation, for each single slotted-waveguide, a short and infinitesimally thin current probe is used as the front-end excitation. A perfectly matched layer (PML) is used to terminate end of the waveguide port and absorb the reflected wave from the antenna to make each slotted-waveguide antenna work in the travelling wave mode. Since each slotted-waveguide antenna can be considered as a single sub-domain, the domain decomposition algorithm (DDA) is applied to reduce computation resource and achieve high efficiency. To improve the convergence, the sparse approximate inverse (SAI) technique is applied to construct an efficient preconditioner [14, 15]. To further improve the capability, it is parallelized on a memory distributed computer system [13, 14]. The comparison between DDA-FE-BI-MLFMA computed results and the commercial software CST results for the radiation patterns of a slotted-waveguide array validates the accuracy of the presented approach. To show capability of the presented approach, a large X-band slotted-waveguide antenna array containing eighteen waveguides with Taylor amplitude and inverse phase excitation distribution is designed and its radiation characteristics are computed and analyzed.

2. COMPUTATIONAL ALGORITHM

Consider the radiation problem of a single slotted-waveguide antenna whose surface is denoted as S . A short current probe oriented in the z -direction and located at (x_f, y_f) can be modeled as:

$$\mathbf{J}_{inp} = \hat{z}I_0\delta(x - x_f, y - y_f)e^{-jk_z z} \quad (1)$$

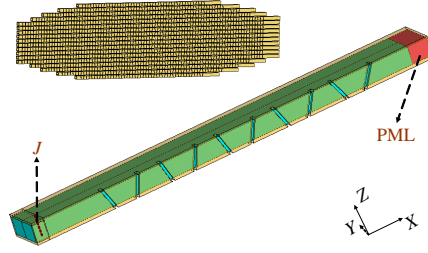


Figure 1: Simplified model for a slotted-waveguide antenna array.

where I_0 is the lumped current flowing into the antenna and φ is the phase. The location of the current is in the middle of the original waveguide excitation port. The front-end port of the waveguide is extended a small distance from the original feed location and terminated with an infinite thin PEC plate. At the end of the waveguide, it is filled with PML of thickness $0.3\lambda_g$, with λ_g being the waveguide wavelength. Then it is also terminated with infinite thin PEC plate.

According to the FE-BI-MLFMA presented in [11], the solution region is directly divided into the interior region and the exterior region by the surface S . The final FE-BI matrix equation system for a slotted-waveguide antenna array with N slotted waveguides can be written as:

$$\begin{bmatrix} \mathbf{K}^1 & 0 & 0 & \mathbf{B}^1 \mathbf{T}_g^1 \\ 0 & \ddots & 0 & \vdots \\ 0 & 0 & \mathbf{K}^N & \mathbf{B}^N \mathbf{T}_g^N \\ \mathbf{P}^1 (\mathbf{T}_g^1)^T & \dots & \mathbf{P}^N (\mathbf{T}_g^N)^T & \mathbf{Q} \end{bmatrix} \begin{bmatrix} E^1 \\ \vdots \\ E^N \\ \bar{H}_s \end{bmatrix} = \begin{bmatrix} b^1 \\ \vdots \\ b^N \\ 0 \end{bmatrix} \quad (2)$$

where $\bar{H}_s = Z_0 H_s$, with Z_0 being the free-space impedance. \mathbf{P} and \mathbf{Q} are the BI dense matrices, \mathbf{K} and \mathbf{B} are the sparse FEM matrices. \mathbf{T}_g^i denotes the projection Boolean matrix between the global BI degrees of freedom (DOFs) and the FEM degrees of freedom (DOFs) of the i th slotted waveguide. E^i denotes the discretized unknowns of the electric fields for the i th waveguide, H_s denotes the discretized unknowns of the magnetic fields on the boundary of the whole antenna array.

In a slotted-waveguide antenna array, each slotted-waveguide antenna can be considered as a single sub-domain, and the domain decomposition algorithm (DDA) can be applied to the FE-BI-MLFMA to reduce the required computation resources and achieve high efficiency [12, 13]. After solving the sparse FEM matrices of each sub-domain, we can obtain:

$$E^i = (\mathbf{K}^i)^{-1} (b^i - \mathbf{B}^i \mathbf{T}_g^i \bar{H}_s) \quad (3)$$

Substituting Equation (3) into the BI equation, we can obtain the final equation system as:

$$\left[\tilde{\mathbf{P}} + \mathbf{Q} \right] \bar{H}_s = b \quad (4)$$

with

$$\tilde{\mathbf{P}} = - \sum_{i=1}^N \mathbf{P}^i (\mathbf{T}_g^i)^T (\mathbf{K}^i)^{-1} \mathbf{B}^i \mathbf{T}_g^i \quad (5)$$

$$b = - \sum_{i=1}^N \mathbf{P}^i (\mathbf{T}_g^i)^T (\mathbf{K}^i)^{-1} b^i \quad (6)$$

The equation system of (4) can be efficiently solved by using the iterative solvers such as the GMRES. The MLFMA is employed to speed up matrix-vector multiplications. This computational approach is also parallelized on a memory distributed computer system with an efficient preconditioner constructed by using the SAI technique [15].

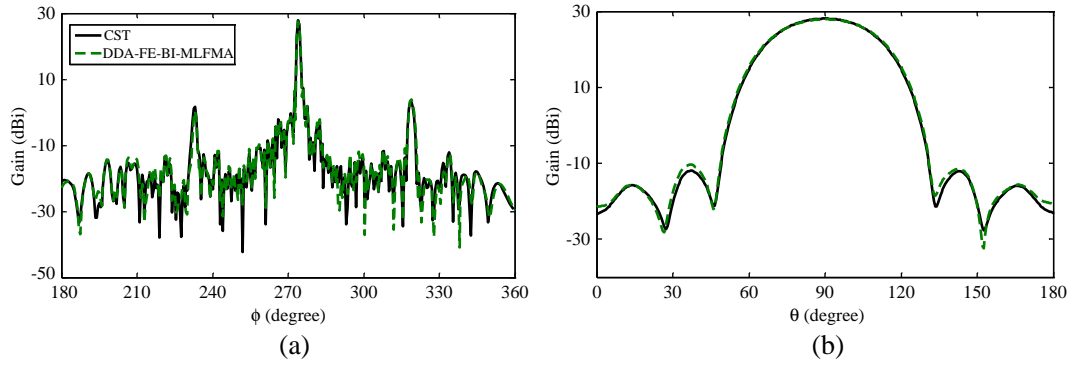


Figure 2: Radiation patterns for an antenna array containing two slotted-waveguides at 10 GHz. (a) E -plane. (b) H -plane.

Table 1: The radiation characteristics parameters of the slotted-waveguide antenna array.

Calculation method		DDA-FE-BI-MLFMA	CST
Gain (dBi)		27.9	28.1
3 dB beam width ($^{\circ}$)	E -plane	1.0	1.0
	H -plane	33.1	34.4
Side lobe level (dB)	E -plane	-21.5	-21.4
	H -plane	-40.0	-39.4

3. NUMERICAL RESULTS

A series of numerical experiments are investigated in this section. All the computations are performed on the parallel computer platform *Liuhui-II* at the Center for Electromagnetic Simulation, Beijing Institute of Technology. It has 10 nodes, each node has 2 Intel X5650 2.66 GHz CPUs with 6 cores for each CPU, 96 GB memory.

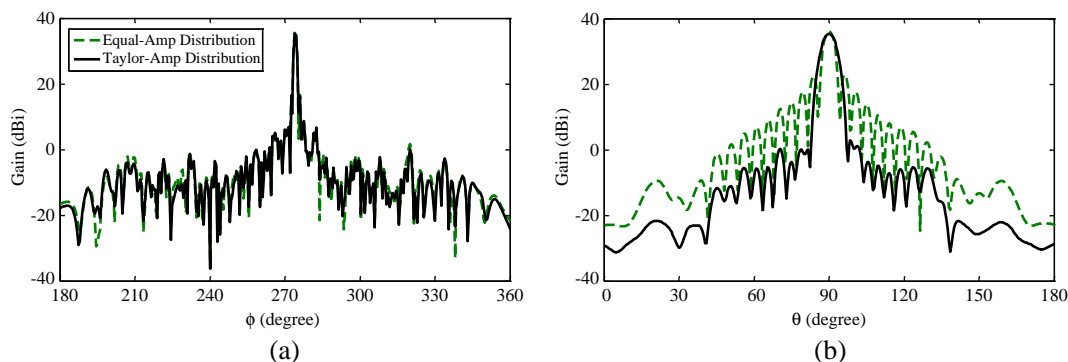
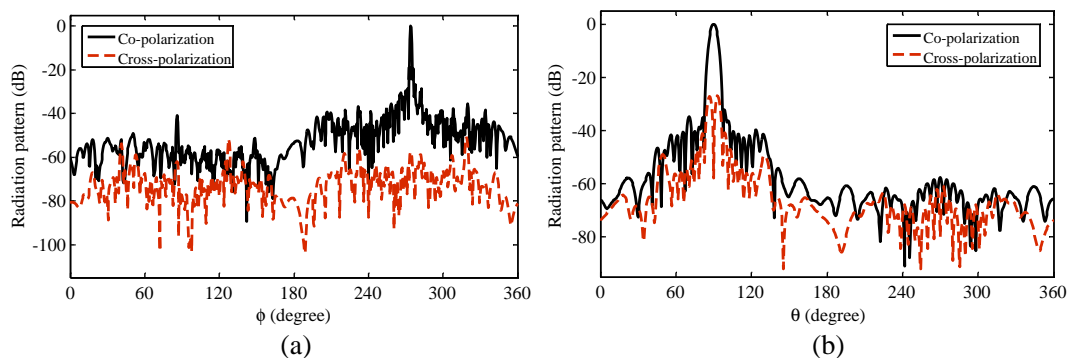
As shown in Figure 1, a typical true 3D slotted-waveguide antenna array containing eighteen slotted waveguides is specially designed. For each slotted-waveguide antenna, we choose the BJ100 waveguide (22.86×10.16 mm), the main mode frequency of which ranges from 8.2 GHz to 12.5 GHz. We set the working frequency of the antenna as 10 GHz. The vertical spacing between every two neighbor waveguides is fixed as 5.2 mm. To achieve high gain and low side-lobe performance, the fed phase and inclination angle for each slot are strictly inversed to the adjacent ones, to the corresponding one in wall of the adjacent and the mirror symmetry waveguide.

We first validate the presented approach by comparing results with the CST results for the radiation patterns of the middle two slotted-waveguides. There are total 90 narrow-wall slot-radiating elements for each slotted-waveguide. The radiation characteristics parameters of the two slotted-waveguides antennas are listed in Table 1. Figure 2 shows the calculated radiation patterns in E -plane and H -plane respectively. Good agreement can be observed between the DDA-FE-BI-MLFMA and the CST results.

To demonstrate great capability of the presented approach for electrically large arrays, we compute radiation patterns of the whole large antenna array containing eighteen waveguides as shown in Figure 1. The radiation patterns for the array with equal-amplitude/Taylor-amplitude and inverse phase distribution feed in the E -plane and H -plane are shown in Figure 3. The computed radiation characteristics parameters are listed in Table 2. We can see from Figure 3, by using the Taylor-amplitude distribution feed, better side lobe can be achieved with wider main lobe and lower gain in the H -plane, but little influence on radiation patterns in the E -plane. Figure 4 shows the normalized orthogonal polarization radiation patterns for the large antenna array with Taylor-amplitude distribution feed in the E -plane and H -plane. We can see from these figures, suppression cross-polarization characteristics are obtained in E -plane (< -50.49 dB) and in H -plane (< -26.96 dB). In this calculation, the number of unknowns for the FEM part and the BI part is 5,306,784 and 2,291,742 respectively. It takes about 91 GB memory and 4 hours of CPU time with 16 MPI processes.

Table 2: The radiation characteristics parameters of the large slotted-waveguide antenna array.

Amplitude distribution		Taylor	Equal
Gain (dBi)		35.4	36.1
3 dB beam width (°)	<i>E</i> -plane	1.0	1.0
	<i>H</i> -plane	5.1	3.9
Side lobe level (dB)	<i>E</i> -plane	-18.7	-19.2
	<i>H</i> -plane	-32.5	-13.2

Figure 3: Radiation patterns for the large slotted-waveguide antenna array containing eighteen waveguides at 10 GHz. (a) *E*-plane. (b) *H*-plane.Figure 4: Normalized orthogonal polarization radiation patterns for the large slotted-waveguide antenna array at 10 GHz. (a) *E*-plane (b) *H*-plane.

4. CONCLUSION

An efficient computational approach using the FE-BI-MLFMA is presented for analysis of radiation from large slotted-waveguide antenna arrays. A simple but flexible and efficient model is presented to simplify the calculation. Comparisons between computed results and commercial software CST results validate the presented model for fast and accurate analysis of radiation from slotted-waveguide arrays. The radiation characteristics of a large carefully designed slotted-waveguide antenna arrays are computed to show the efficiency and capability of the presented approach.

ACKNOWLEDGMENT

This work is partially supported by the National Basic Research Program (973) under Grant No. 2012CB720702 and No. 61320602, the 111 Project of China under the grant B14010, and the NSFC under grant 61371002.

REFERENCES

1. Stevenson, A. F., "The theory of slots in rectangular waveguides," *J. Appl. Phys.*, Vol. 19, 24-38, Jan. 1948.

2. Oliner, A. A., “The impedance properties of narrow radiating slots in the broad face of rectangular waveguide,” *IRE Trans. Antennas Propagat.*, Vol. 5, 4–20, Jan. 1957.
3. Jan, C. G., P. Hsu, and R. B. Wu, “Moment method analysis of sidewall inclined slots in rectangular waveguides,” *IEEE Trans. Antennas Propagat.*, Vol. 39, 68–73, Jan. 1991.
4. Hirokawa, J. and P. S. Kildal, “Excitation of an untilted narrow-wall slot in a rectangular waveguide by using etched strips on a dielectric plate,” *IEEE Trans. Antennas Propagat.*, Vol. 45, 1032–1037, Jun. 1997.
5. Prakash, V. V. S., S. Christopher, and N. Balakrishnan, “Method-of-moments analysis of the narrow-wall slot array in a rectangular waveguide,” *IEE Proc., Microw. Antennas Propagat.*, Vol. 147, 242–246, Jun. 2000.
6. Krant, E. A., J. C. Olinier, and J. B. West, “FDTD solution of Maxwell’s equations for an edge slot penetrating adjacent broadwalls of finite wall thickness waveguide,” *IEEE Trans. Antennas Propagat.*, Vol. 42, 1646–1648, Dec. 1994.
7. Vouvakis, M. N., K. Z. Zhao, and J. F. Lee, “Finite-element analysis of infinite periodic structures with nonmatching triangulations,” *IEEE Trans. Magn.*, Vol. 42, No. 4, 691–694, 2006.
8. Jin, J. M. and J. L. Volakis, “A hybrid finite element method for scattering and radiation by microstrip patch antennas and arrays residing in a cavity,” *IEEE Trans. Antennas Propagat.*, Vol. 39, 1598–1604, Nov. 1991.
9. Stupfel, B., “A hybrid finite element and integral equation domain decomposition method for the solution of the 3-D scattering problem,” *J. Comput. Phys.*, Vol. 172, 451–471, Sep. 2001.
10. Young, J. C., J. Hirokawa, and M. Ando, “Analysis of a rectangular waveguide, edge slot array with finite wall thickness,” *IEEE Trans. Antennas Propagat.*, Vol. 55, 812–819, Mar. 2007.
11. Sheng, X. Q., J. M. Song, C. C. Lu, and W. C. Chew, “On the formulation of hybrid finite-element and boundary-integral method for 3D scattering,” *IEEE Trans. Antennas Propagat.*, Vol. 46, 303–311, Mar. 1998.
12. Vouvakis, M. N., K. Zhao, S. M. Seo, and J. -F. Lee, “A domain decomposition approach for non-conformal couplings between finite and boundary elements for unbounded electromagnetic problems in R^3 ,” *J. Comput. Phys.*, Vol. 225, No. 1, 975–994, Jul. 2007.
13. Yang, M. L., H. W. Gao, and X. Q. Sheng, “Parallel domain-decomposition-based algorithm of hybrid FE-BI-MLFMA method for 3-D scattering by large inhomogeneous objects,” *IEEE Trans. Antennas Propagat.*, Vol. 50, No. 2, 4675–4684, Sep. 2013.
14. Pan, X. M. and X. Q. Sheng, “A sophisticated parallel MLFMA for scattering by extremely large targets,” *IEEE Antennas Propagat. Mag.*, Vol. 50, 129–138, Jun. 2008.
15. Lee, J., J. Zhang, and C. C. Lu, “Sparse inverse preconditioning of multilevel fast multipole algorithm for hybrid integral equations in electromagnetics,” *IEEE Trans. Antennas Propagat.*, Vol. 52, 2277–2287, Sep. 2004.

Scattering of a Gaussian Beam by an Ellipsoidal Particle with Vectorial Complex Ray Model

K. F. Ren

CORIA — UMR 6614, Normandie Université, CNRS, Université et INSA de Rouen
675 Av. de l'Université, BP 12, 76801 Saint Etienne du Rouvray, France

Abstract— By introducing the wave front curvature as a generic property of rays, the Vectorial Complex Rays Model (VCRM) improves considerably the precision of ray models. This has been already applied to the prediction of the scattering diagrams of the plane wave by large ellipsoidal particles and the two dimensional Gaussian beam scattering by an elliptical infinite cylinder at normal incidence. In this communication, the VCRM will be further extended to the scattering of a Gaussian beam by an ellipsoidal particle. The amplitude, the phase and the wave front curvature of the incident Gaussian beam are considered, but the diffraction has not been taken into account yet.

1. INTRODUCTION

The numerical prediction of the scattering properties of electromagnetic waves or light by objects of complex shape and of size much larger than the wavelength has been always a great challenge in both the field of electromagnetic computation or light interaction with particles. Among a large number of theories, models and algorithms, the methods based on the ray models seem to be the most appropriate due to their flexibility, their capability to deal with very large objects and their rapidity in term of the numerical calculation. But the precision is often not satisfactory because the wave properties (phase, divergence/convergence ...) are not properly taken into account.

In the model developed by the author — Vectorial Complex Rays Model (VCRM) [1, 2], the aforementioned wave properties are counted correctly by introducing the wave front curvature as a generic property of rays. Therefore, the VCRM improves considerably the precision of ray models. It has been validated by comparison with two rigorous methods: Lorenz-Mie theory for spherical particle [1–4] and the Multilevel Fast Multipole Algorithm (MLFMA) [5] for the ellipsoidal particles. It has been used to the prediction of the scattering diagrams of the plane wave by large ellipsoidal particles [6] and the elliptical infinite cylinders [7]. It has also been applied to the scattering of a two dimensional Gaussian beam by an elliptical infinite cylinder at normal incidence [8]. In this paper, we extend further the VCRM to the scattering of a Gaussian beam by an ellipsoidal particle. The amplitude, the phase and the wave front curvature of the incident Gaussian beam are considered in the model. But the diffraction has not yet taken into account. The results of the developed code will be compared with the rigorous Generalized Lorenz-Mie Theory (GLMT).

The rest of the paper is organized as follows. The Vectorial Complex Ray Model for the scattering of a Gaussian beam by an ellipsoidal particle is described in Section 2. The developed code is validated in Section 3 by comparison with the rigorous method, i.e., the Generalized Lorenz-Mie theory. The Section 4 is devoted to the presentation and the discussion of the numerical results. The last section is the conclusions.

2. VCRM FOR THE SCATTERING OF A GAUSSIAN BEAM

Consider an ellipsoidal particle of three semi-axes (a, b, c) respectively in (x, y, z) directions with the center located at O_P , the origin of the coordinate system O_P-xyz , referred hereafter as particle coordinate system. The particle is illuminated by a Gaussian beam of waist radius w_0 propagating in its coordinate system $O_b(u, v, w)$ along w axis which make an angle θ_0 with z axis. The coordinates of the beam center O_b in the particle coordinate system are (x_0, y_0, z_0) (Fig. 1). For simplicity, in this paper, we suppose that the beam axis is in a symmetric plane of the ellipsoid. Without lose of generality, we choose the plane (O_P-xy) . The observation is also limited in (x, z) plane, so that all rays under study remain in the same plane and we have $\phi = 0$ and $y_0 = 0$ in the case under study.

In the VCRM, each ray possesses five properties: the direction, the amplitude, the phase, the polarization and the wave front of the wave the ray represents. All these properties evolve each time a ray interacts with the particle surface and can be calculated step by step according to the standard procedure of the VCRM as described in [1, 2] and [3, 4]. It is worth, however, to note that in the VCRM, the wave vector, as well as its normal and tangent components to the particle surface,

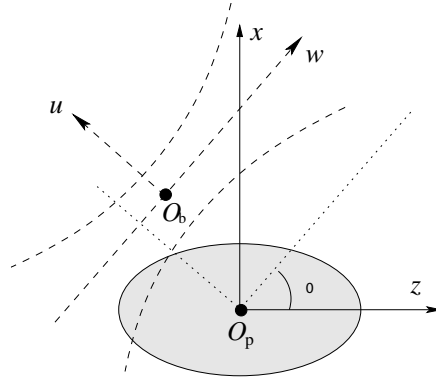


Figure 1: Definition of the coordinate systems.

are used for the determination of the propagation direction (after a reflection or a refraction) and the Fresnel coefficients. This simplifies significantly the ray tracing, especially in three dimension scattering. The divergence and the convergence of the wave on the surface of the particle are predicted directly by the wave front curvature, the latter permits also determining the phase due to the focal lines by counting the number of changes of sign of the wave front curvature radii. The reader are referred to the references cited above for the details.

The difference of the VCRM for the plane wave and for a focused beam lies in the wave front shape before the first interaction of a ray with the particle and the variation of the incident wave amplitude. We will give a detailed description in the following.

The complex amplitude (with time convention $e^{i\omega t}$) of a Gaussian beam is written as

$$S_G(u, v, w) = A_G \exp(-i\Phi)$$

where A_G and Φ present respectively the amplitude and the phase of the beam and are given by

$$A_G = \frac{w_0}{w_l} \exp\left(-\frac{u^2 + v^2}{w_l^2}\right) \quad (1)$$

and

$$\Phi(u, v, w) = k \left\{ w + \frac{u^2 + v^2}{2w[1 + (z_R/w)^2]} \right\} + \tan^{-1} \left(\frac{w}{z_R} \right) \quad (2)$$

k is the wave number and z_R is the Rayleigh length defined by

$$z_R = \pi w_0^2 / \lambda \quad (3)$$

w_l is the local radius of the beam at w and is related to the beam waist radius w_0 by

$$w_l = w_0 [1 + (w/z_R)^2]^{1/2} \quad (4)$$

To calculate the amplitude and the phase of the incident beam at the point where the ray interacts with the particle, we use the following relations between the particle coordinate system O_p-xyz and the beam coordinate system O_b-uvw given by

$$u = (x - x_0) \cos \theta_0 - (z - z_0) \sin \theta_0 \quad (5)$$

$$w = (x - x_0) \sin \theta_0 + (z - z_0) \cos \theta_0 \quad (6)$$

with $v = 0$ since the beam axis and the observation are in the plane O_p-xz .

To ensure that a ray interacts with the surface of the particle, we calculate the scalar product of the wave vector and the outward normal of the particle surface. If the result is negative the ray interacts with the particle and then we calculate the Fresnel coefficients for the two polarizations; the directions, the phase and the wave front curvatures of the reflected and the refracted rays. Then we determine the following interaction point according to the direction of the refracted ray and the equation describing the surface of the particle. We repeat the similar procedure as for the first interaction so that to determine the properties of the emergent ray and the internal reflected ray, until a order for which the amplitude of the ray is negligible. Finally, we should calculate the summation of the complex amplitudes of all emergent rays to obtain the scattering diagram.

3. VALIDATION OF THE CODE

In order to validate the code we compare firstly the scattering diagrams calculated by the VCRM and the GLMT for a spherical particle of radius $a = 30 \mu\text{m}$ and the refractive index $m = 1.333$ located at the center of a Gaussian beam of wavelength $\lambda = 0.6328 \mu\text{m}$ with two different beam waists. We found that when the beam waist radius is relatively large compared to the particle size, i.e., $w_0 = 100 \mu\text{m}$ (Fig. 2, the scattering diagrams are similar to those of a plane wave). The agreement between the two methods is good except in the two regions. one is the narrow region in forward direction, this is because the diffraction has not been taken into account. The other is in the Alexander region (between the first and the second rainbows), this is to be improved by taken into account the diffraction effect in the caustic regions.

When the beam waist radius is much less than the particle radius, i.e., $w_0 = 10 \mu\text{m}$ (Fig. 3), the scattering diagrams of the VCRM agree almost perfectly in all directions for the two polarizations. The reason of the discrepancy in forward direction (scattering angle smaller than about 5°) is the same as in Fig. 2. The disappearance of the disagreement around the Alexander region is due to the fact that the beam amplitude at the impact points of rainbow is much less than that near the beam axis. When the particle is illuminated with the same beam but off-axis, this effect may reappear (see the following section).

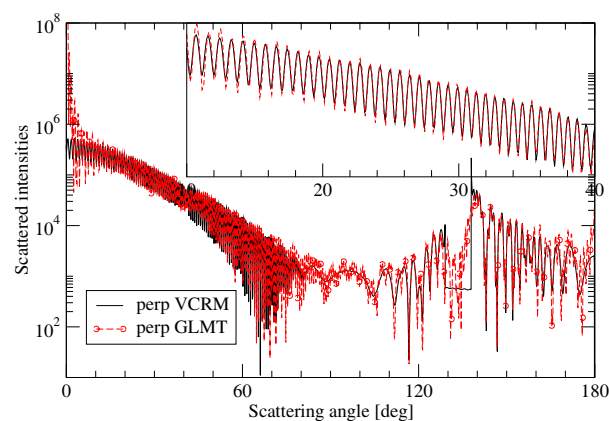


Figure 2: Comparison of the scattered diagrams calculated by VCRM and GLMT for a spherical particle of radius $a = 30 \mu\text{m}$, refractive index $m = 1.333$ illuminated by a Gaussian beam of wavelength $\lambda = 0.6328 \mu\text{m}$ and beam waist radius $w_0 = 100 \mu\text{m}$.

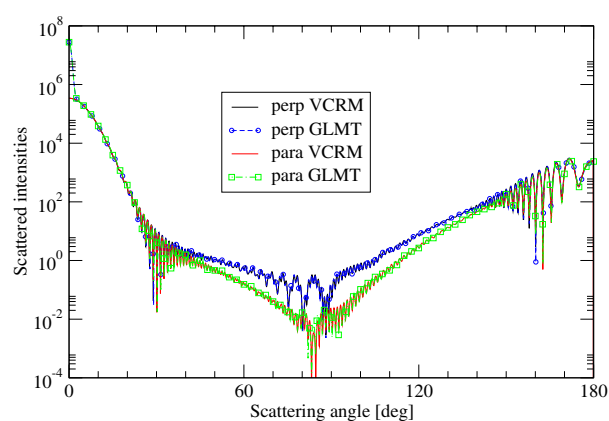


Figure 3: Comparison of the scattered diagrams calculated by VCRM and GLMT for the same parameters as in Fig. 2 except $w_0 = 10 \mu\text{m}$.

4. NUMERICAL RESULTS AND DISCUSSION

We present in this section some typical scattering diagrams of an ellipsoidal particle illuminated by a Gaussian beam. Fig. 4 shows the scattering diagrams of a particle of three different shapes illuminated by an off-axis Gaussian beam. The wavelength of the incident Gaussian beam is still $0.6328 \mu\text{m}$, its waist radius is $50 \mu\text{m}$ and its center is located at $x_0 = 30 \mu\text{m}$, $y_0 = z_0 = 0$. The polarization for the four curves is perpendicular, i.e., the incident electric field is in y direction. The black (solid line without symbol) and the red (dashed line) curves present respectively the results calculated by the GLMT and the VCRM. Similar remarks as in the last section can be made for the comparison of these two curves, but we found a dissymmetry of the scattering diagrams due to the off-axis of the incident beam. Furthermore, the second rainbow on the left (around -125°) is much less remarkable.

The other two curves in Fig. 4 are respectively the scattering diagrams of an oblate ($c = 45 \mu\text{m}$, green curve with circles) and a prolate ($c = 55 \mu\text{m}$, blue curve with diamond symbols) with the same cross circular section ($a = b = 50 \mu\text{m}$). For clarity, these two curves are off-set respectively by 10^2 and 10^3 . We may note that the profiles of the scattering diagrams between -60° and 120° are similar to that of the sphere, while the structure of the diagrams around rainbow angles and in the backward direction are very sensitive to the shape of the particle. The position of the first rainbow on the left of the figure moves about $+10^\circ$ for the oblate and -10° for the prolate relative to that of the sphere. In the other side the first and the second rainbows are merged for the oblate

particle but very significant for the prolate particle. The Alexander region is also enlarged from 8° for the sphere to about 22° for the prolate particle.

At last, we present the scattering diagrams calculated by the VCRM in the most general case: an ellipsoidal particle with different semi-axes illuminated by an off-axis Gaussian beam with an incident angle. It can be noted that the scattering diagram around the rainbows is very sensible to the shape of the particle.

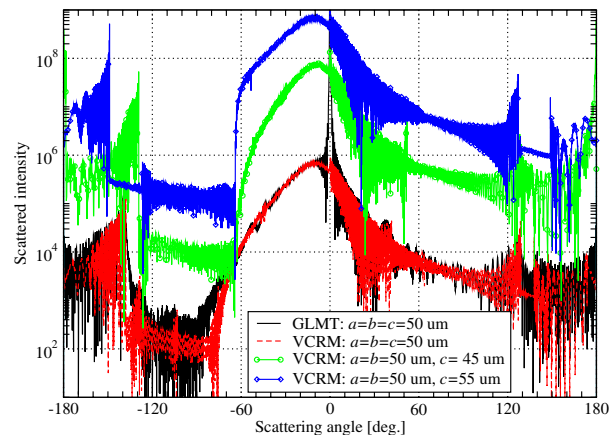


Figure 4: Scattering diagrams of particles with the same circular cross section ($a = b = 50 \mu\text{m}$) illuminated by an off-axis ($x_0 = 30 \mu\text{m}$) Gaussian beam ($\lambda = 0.6328 \mu\text{m}$ and $w_0 = 50 \mu\text{m}$). The incident beam propagates in z direction and its electric field is polarized in y direction. For clarity, the curves for the oblate in green and that for the prolate in blue are off-set respectively by 10^2 and 10^3 .

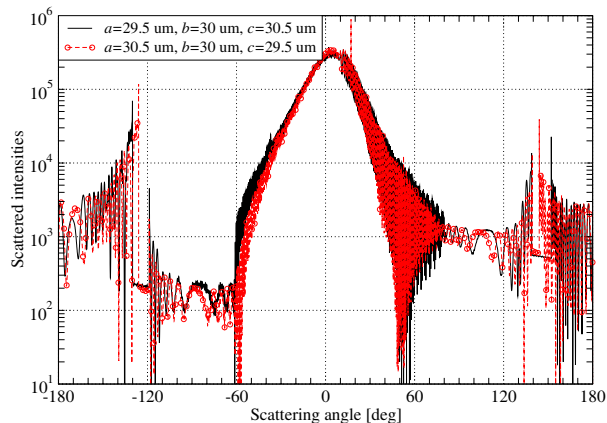


Figure 5: Scattering diagrams of an ellipsoidal particle with different semi-axes a , b and c of water $m = 1.333$ illuminated by a Gaussian beam of wavelength $\lambda = 0.6328 \mu\text{m}$ and waist radius $w_0 = 30 \mu\text{m}$. The beam axis is in the xz plane and makes an angle of 10° with z axis. The beam center is at $(10 \mu\text{m}, 0, 0)$ in the particle coordinate system.

5. CONCLUSIONS

We have applied in this paper the Vectorial Ray Tracing Model for the calculation of the scattering diagrams of a large ellipsoidal particle. The code is first validated by comparison with the rigorous solution of Maxwell equations, i.e., the generalized Lorenz-Mie theory. The comparison showed that the VCRM permits to predict correctly the scattering diagram in almost all directions except in the Alexander region. The code is then applied to the prediction of the scattering diagrams of ellipsoidal water droplets with different semi-axis illuminated by a Gaussian beam in the on-axis and off-axis cases with the propagation direction along a symmetric axis of the particle or with an incident angle. It is shown that the rainbow positions and its structure are very sensible to the position as well as the shape of the particle. This dependence may provide very useful information for the measurements of the non-spherical particle, especially in the two phase flows.

ACKNOWLEDGMENT

This work has been supported by the French National Agency under the grant number ANR-13-BS09-0008-01 (AMOCOPS).

REFERENCES

1. Ren, K. F., F. Onofri, C. Rozé, and T. Girasole, "Vectorial extended geometrical optics for scattering of a spheroid," *Progress In Electromagnetics Research Symposium Abstracts*, 145, Cambridge, USA, July 5–8, 2010.
2. Ren, K. F., F. Onofri, C. Rozé, and T. Girasole, "Vectorial complex ray model and application to twodimensional scattering of plane wave by a spheroidal particle," *Opt. Lett.*, Vol. 36, No. 3, 370–372, 2011.
3. Yuan, Y., "Diffusion de la lumière par un objet irrégulier pour l'application à l'imagerie des sprays," PhD Thesis, Rouen University, France, 2012.
4. Jiang, K., "Theoretical study of light scattering by an elliptical cylinder," PhD Thesis, Rouen University, 2013.

5. Yang, M., Y. Wu, X. Sheng, and K. F. Ren, "Comparison of scattering diagrams of large non-spherical particles calculated by VCRM and MLFMA," *J. Quant. Spect. Rad. Trans.*, Vol. 156, 88–96, 2015.
6. Ren, K. F., C. Rozé, and T. Girasole, "Scattering and transversal divergence of an ellipsoidal particle by using vectorial complex raymodel," *J. Quant. Spectrosc. Radiat. Transfer*, Vol. 113, 2419–2423, 2012.
7. Jiang, K., X. Han, and K. F. Ren, "Scattering from an elliptical cylinder by using the vectorial complex ray model," *Appl. Opt.*, Vol. 51, No. 34, 8159–8168, 2012.
8. Jiang, K., X. Han, and K. F. Ren, "Scattering of a gaussian beam by an elliptical cylinder using the vectorial complex ray model," *J. Opt. Soc. Am. A*, Vol. 8, 1548–1556, 2013.

Computation of Spheroidal Micro-organisms Cross Sections Using the Aperiodic Fourier Modal Method

M. Abboud^{1,2}, G. Granet^{1,2}, K. Edee^{1,2}, J. F. Cornet^{1,2}, and J. Dauchet^{1,2}

¹Clermont Université, Université Blaise Pascal, BP 10488, F-63000 Clermont Ferrand, France

²CNRS, UMR 6602, IP, Aubière F-63177, France

Abstract— In this paper, we investigate the light scattering properties by a spheroidal particle by using the Fourier Modal Method (FMM) equipped with the Perfectly Matched Layers (PMLs). A program which allows the computation of the scattering cross sections and efficiencies has been implemented and checked by comparing the results with those obtained in literature. The effectiveness of the PMLs appeared by plotting the field maps: the interferences from neighbouring periods in the FMM disappeared.

1. INTRODUCTION

Nowadays, our society is facing numerous ecological challenges. Cultivation of photosynthetic micro-organisms within controlled environments such as photobioreactor processes is recognized as a serious alternative to contribute to the CO₂ capture and to produce bio-diesel and bio-hydrogen. In order to optimize conversion of light energy into chemical energy within the process of photosynthesis, we have to predict the light scattering properties, such as the absorption, scattering and extinction cross sections as well as the scattering diagrams [2]. Based on the rigorous solution of Maxwell's equations, Lord Rayleigh [3] and Wait [4] introduced respectively the first formalisms to describe the interaction of a monochromatic plane wave with an isolated infinitely long circular cylinder at normal incidence and oblique incidence. In 1908, Mie [5, 6] derived the exact solution for an homogeneous spherical particle for a very wide range of parameter values. This theory is involved in several applications, e.g., in photobioreactor processes, in environmental monitoring and so on. However, most micro-organisms are not spherical and differ by their size and shape parameters. Their scattering properties are significantly different from those of spherical scatterers. Since it is much more difficult to obtain the exact solution when the scatterer loose the spherical symmetry, a number of approximations have been made in order to calculate the light scattering and absorption properties of non-spherical particles. Among the most prevalent approximations are Waterman's extended boundary condition method also called T-matrix method [7, 8], the finite-difference time-domain method (FDTD) [9] and the finite-element method (FEM) [10]. Asano and Yamamoto [11] obtained solutions for homogeneous prolate and oblate spheroidal particles by solving Maxwell's equations in the spheroidal coordinate system. The main disadvantage of this method is that the vector spheroidal wave functions are not easily calculated, especially for complex arguments that occur with absorbing particles. Nevertheless, a number of numerical results are available. Asano [1] has calculated the scattering and absorption efficiencies and the angular scattering for oriented prolate and oblate spheroids. He obtained results for particles with size parameters up to 30 and axial ratios up to 5. Most of the results are for $m = 1.33$ and $m = 1.5$ although some calculations have been made for absorbing particles with $m = 1.5 + 0.1i$.

In this paper, the Fourier Modal Method is extended to non periodic structure. This is achieved by introducing the perfectly matched layers (PMLs) concept. The remainder of the paper is organized as follows: Section 1 is devoted to the statement of the problem and the derivation of the eigenvalue equation. In Section 2, we present numerical results that are successfully compared with those obtained by Asano.

2. STATEMENT OF THE PROBLEM

Let us consider an arbitrarily particle illuminated by a monochromatic plane wave with angular frequency ω , refractive index ν_1 and wave vector \mathbf{k} which components are:

$$\mathbf{k} \begin{cases} \alpha_0 = k\nu_1 \sin \xi \cos \phi \\ \beta_0 = k\nu_1 \sin \xi \sin \phi \\ \gamma_0 = k\nu_1 \cos \xi \end{cases} . \quad (1)$$

The amplitudes of the electric field components of the incident wave are:

$$\begin{bmatrix} E_x^{inc} \\ E_y^{inc} \\ E_z^{inc} \end{bmatrix} = \begin{bmatrix} \sin \xi \cos \phi & \cos \xi \cos \phi & -\sin \phi \\ \sin \xi \sin \phi & \cos \xi \sin \phi & \cos \phi \\ \cos \phi & -\sin \xi & 0 \end{bmatrix} \begin{bmatrix} 0 \\ \cos \delta \\ \sin \delta \end{bmatrix}, \quad (2)$$

where ξ is the incidence angle, ϕ the azimuthal angle and δ the angle of polarization. The particle is approximated by a staircase profile so that it is replaced by a stack of n_{sl} layers, each of them is characterized by its thickness and its relative permittivity function $\varepsilon(x, y)$. See Figures 1(a) and (b).

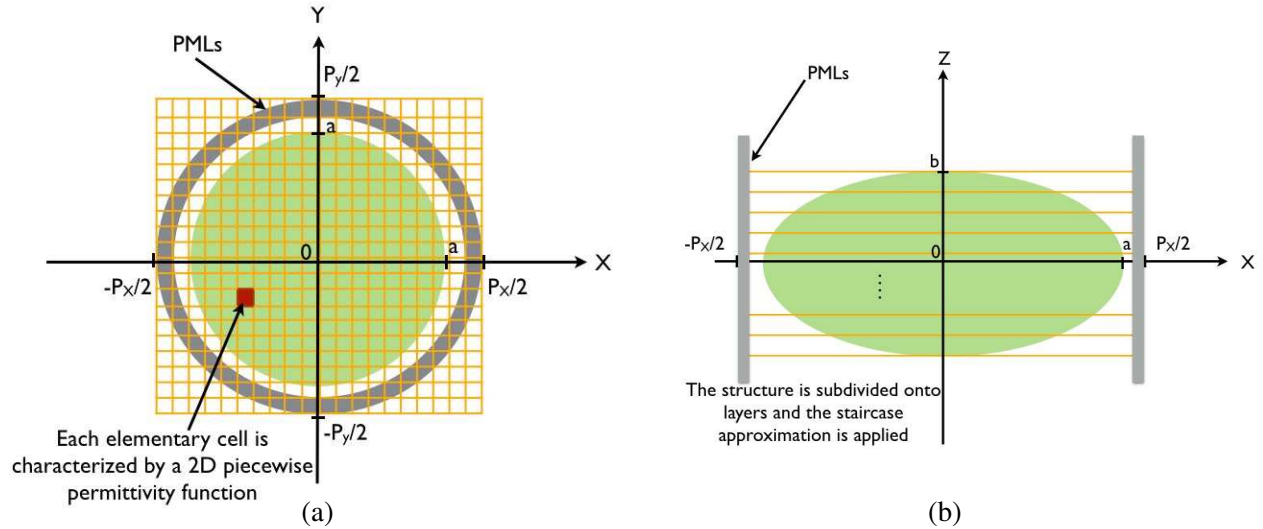


Figure 1: Configuration of the structure under study.

It can be shown that any component of electromagnetic field can be written as $\Phi(x, y)exp(-ik\gamma z)$, where $k = \omega\sqrt{\varepsilon_0\mu_0}$. ε_0 and μ_0 are the permittivity and the permeability of the vacuum. The numerical process consists in searching a numerical approximation of the functions Φ for all components of the electromagnetic field by imposing boundary conditions. By eliminating the longitudinal components E_z and H_z from Maxwell's equations, we arrive to matrix relations (3) and (4) between transversal components E_x , E_y , H_x and H_y :

$$\partial_z \begin{bmatrix} \mathbf{E}_x \\ \mathbf{E}_y \end{bmatrix} = \begin{bmatrix} \frac{i}{k} \partial_x \boldsymbol{\varepsilon}^{-1} \partial_y & -\frac{i}{k} \partial_x \boldsymbol{\varepsilon}^{-1} \partial_x - ik \\ \frac{i}{k} \partial_y \boldsymbol{\varepsilon}^{-1} \partial_y + ik & -\frac{i}{k} \partial_y \boldsymbol{\varepsilon}^{-1} \partial_x \end{bmatrix} \begin{bmatrix} H_x \\ H_y \end{bmatrix} \quad (3)$$

and

$$\partial_z \begin{bmatrix} \mathbf{H}_x \\ \mathbf{H}_y \end{bmatrix} = \begin{bmatrix} -\frac{i}{k} \partial_x \partial_y & \frac{i}{k} \partial_x \partial_x + ik\boldsymbol{\varepsilon} \\ -\frac{i}{k} \partial_y \partial_y - ik\boldsymbol{\varepsilon} & \frac{i}{k} \partial_y \partial_x \end{bmatrix} \begin{bmatrix} E_x \\ E_y \end{bmatrix}. \quad (4)$$

From these equations we can introduce a second order eigenvalue matrix relation:

$$\begin{cases} \partial_z^2 \begin{bmatrix} \mathbf{E}_x \\ \mathbf{E}_y \end{bmatrix} = \mathcal{L}_{EH} \mathcal{L}_{HE} \begin{bmatrix} \mathbf{E}_x \\ \mathbf{E}_y \end{bmatrix} \\ \text{or} \\ \partial_z^2 \begin{bmatrix} \mathbf{H}_x \\ \mathbf{H}_y \end{bmatrix} = \mathcal{L}_{HE} \mathcal{L}_{EH} \begin{bmatrix} \mathbf{H}_x \\ \mathbf{H}_y \end{bmatrix} \end{cases}, \quad (5)$$

with

$$\begin{cases} \mathcal{L}_{EH} = \frac{1}{k^2} \begin{bmatrix} -\partial_x \boldsymbol{\varepsilon}^{-1} \partial_y & \partial_x \boldsymbol{\varepsilon}^{-1} \partial_x + k^2 \boldsymbol{\mu} \\ -\partial_y \boldsymbol{\varepsilon}^{-1} \partial_x - k^2 \boldsymbol{\mu} & \partial_y \partial_x \end{bmatrix} \\ \mathcal{L}_{HE} = \frac{1}{k^2} \begin{bmatrix} -\partial_x \boldsymbol{\mu}^{-1} \partial_y & \partial_x \boldsymbol{\mu}^{-1} \partial_y + k^2 \boldsymbol{\varepsilon} \\ -\partial_y \boldsymbol{\mu}^{-1} \partial_x - k^2 \boldsymbol{\varepsilon} & \partial_y \partial_x \end{bmatrix} \end{cases}. \quad (6)$$

In each layer denoted by the superscript j , one of the eigenvalue equation of Eq. (6) is solved. For example, if the electric eigenvalue equation is solved, the electrical field is written as linear combination of the eigenvectors $[\Phi_{pq}^j, \Psi_{pq}^j]^T$ associated to the eigenvalue γ_{pq} :

$$\begin{cases} |E_x^j\rangle = \sum_{p,q=1}^{2M+1} A_{pq}^j |\Phi_{pq}\rangle \\ |E_y^j\rangle = \sum_{p,q=1}^{2M+1} A_{pq}^j |\Psi_{pq}\rangle \end{cases} . \quad (7)$$

Each eigenvector $|\Phi_{pq}\rangle$ and $|\Psi_{pq}\rangle$ are expanded on finite set of $(2M + 1) \times (2M + 1)$ Fourier basis functions. Hence, an artificial periodization P_x (resp. P_y) in x -direction (resp. y -direction) is introduced. In order to avoid the effect of this periodization, we introduce PMLs by using complex coordinates transformations in x and y directions [13, 14]. The unknown coefficients A_{pq}^j are calculated through the S matrix propagation algorithm and the reflected R_{pq} and transmitted T_{pq} efficiencies are deduced.

3. NUMERICAL RESULTS

Firstly for a sake of comparison with [1], we consider the following two examples: prolate spheroids with a refractive index $\nu = 1.5$ and oblate ones with $\nu = 1.33$. Recall that a prolate spheroid has one major semi-axis a and two equal minor semi-axes b . An oblate spheroid is characterized by two equal major semi-axes a and one minor semi-axis b . Other variables characterizing these spheroids are: the shape factor a/b and the size parameter $\alpha = 2\pi a/\lambda$. Numerical computations are performed on the spheroids of the size parameters up to 30 and for various values of the shape parameters a/b that fluctuated between 1.5 and 5.

It is of common use to normalize the cross-sections C_{sca} of a spheroid by the area of a sphere having the same volume, $C_{sca}/\pi r^2$ where $r = (a^2 b)^{1/3}$ for the oblate spheroid and $r = (ab^2)^{1/3}$ for the prolate spheroid.

Numerical investigations show that results stabilize as soon as the truncation order M reaches 12 and number of layers $n_{sl} = 80$. These results are obtained for an optimized values of $P_x = P_y = 8.33r$. The scattering efficiency factors Q_{sca} are connected with their corresponding cross-sections by this relation:

$$Q_{sca} = C_{sca}/G(\xi). \quad (8)$$

$G(\xi)$ is the area of the particle shadow also called the ‘viewing’ geometrical cross-section. It depends on the angle of incidence ξ . The geometrical cross section of the prolate spheroid is:

$$G(\xi) = \pi a(b^2 \sin^2 \xi + a^2 \cos^2 \xi)^{1/2} \quad (9)$$

and of the oblate spheroid is:

$$G(\xi) = \pi b(a^2 \sin^2 \xi + b^2 \cos^2 \xi)^{1/2}. \quad (10)$$

In Figures 2(a) and (b), the scattering cross sections of oblate and prolate spheroids are plotted at normal incidence ($\xi = 0^\circ$) with respect to the size parameter of the sphere $2\pi r/\lambda$ for different values of a/b . Those results are successfully compared with Figures 4 and 6 of Reference [1].

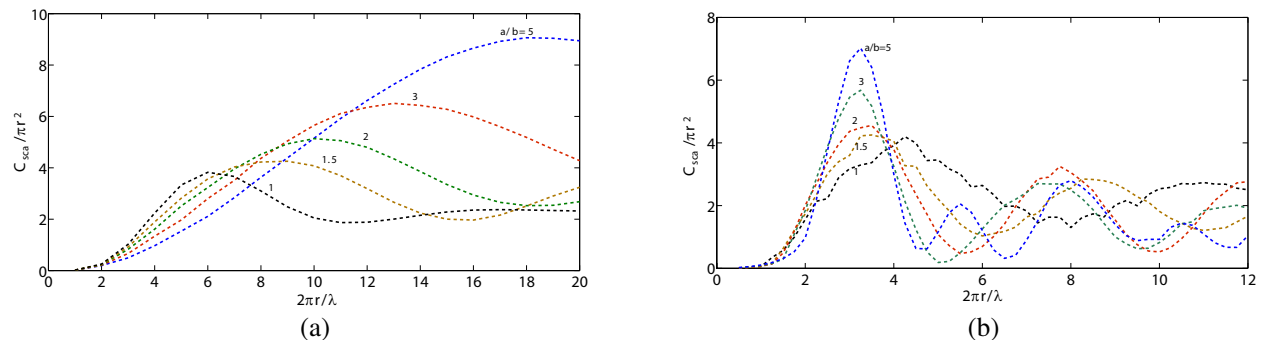


Figure 2: Scattering cross sections of particles with different ratios. (a) Oblate spheroids, (b) prolate spheroids.

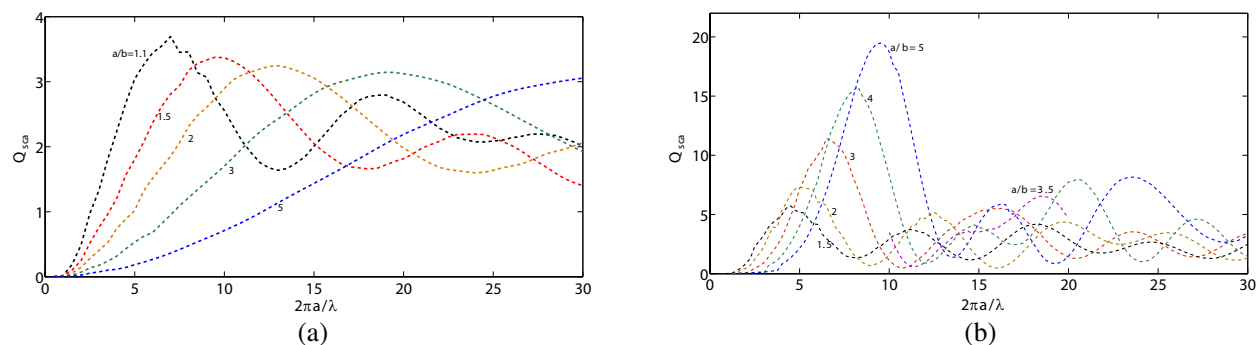


Figure 3: Scattering efficiency of particles with different ratios. (a) Oblate spheroids, (b) prolate spheroids.

Figures 3(a) and (b) show the scattering efficiency factors for the oblate and prolate spheroids at $\xi = 0^\circ$ as a function of the size parameter α for various values of the shape parameters a/b . Asano has obtained the same results in Figures 3 and 5 of Reference [1].

In Figures 4(a) and (b), the scattering efficiency factors of oblate spheroid ($a/b = 3$) and prolate spheroid ($a/b = 5$) are replotted against the size parameter α for three incidence angles $\xi = 0^\circ, 45^\circ,$ and 90° . In the case of oblique incidence ($\xi \neq 0$), the TE and TM polarizations are involved. Corresponding results are given in figures 7 and 8 in Reference [1].

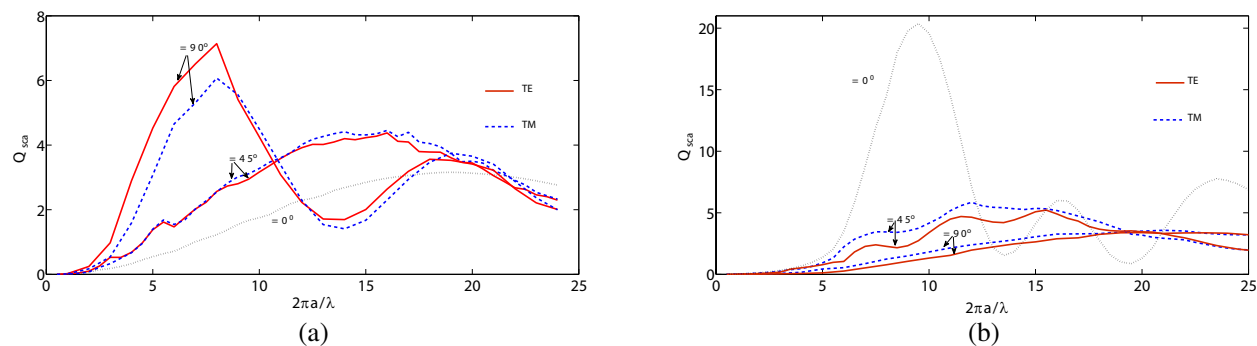


Figure 4: Scattering efficiency of particles with various angle of incidence. (a) Oblate spheroids, (b) prolate spheroids.

Secondly, to show the effectiveness of the Perfectly Matched Layers (PMLs), we compare in Figure 5 the amplitude of the transmitted electric field \mathbf{E}_y computed with and without PMLs of a prolate spheroid for the following numerical parameters: $\lambda = 16.67$ mm, $P_x = P_y = 8.33\lambda$, $\nu = 1.2$, $a = 84$ mm and $b = 17$ mm. It can be seen that, the neighbouring periods see each others and spurious interferences take place. The comparison of these results emphasizes that the field calculated with the PMLs should be valid, since the parasitic oscillations have disappeared.

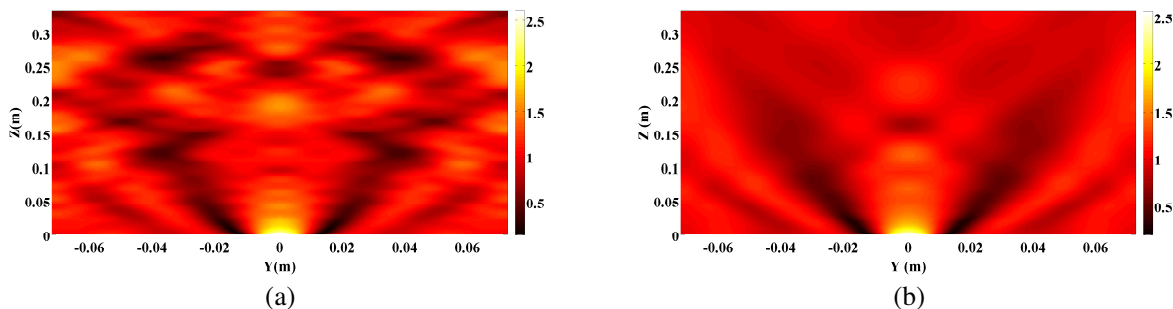


Figure 5: Field map of a prolate spheroid. (a) Without PMLs, (b) with PMLs.

4. CONCLUSION

In this paper, we applied the FMM and the staircase approximation in order to compute the light scattering by spheroidal micro-organism. To avoid the parasitic couplings introduced by the periodizations, the classical FMM is equipped with PMLs through complex coordinates concept. The scattering cross sections and the efficiencies calculated by using this method were successfully compared with results in the literature. To show the crucial role played by the PMLs, a field map, with and without using the PMLs, is presented and satisfactory results are obtained. However, the convergence of the results depends on the number of slices n_{sl} in the staircase approximation but also on the number of eigenfunctions M used to describe the field in each layer. Even though this point is not explicitly detailed in this article, the results reflect a systematic study of their convergence.

ACKNOWLEDGMENT

This work was funded by grants from the *European Commission* (Auvergne FEDER funds) and the *Region Auvergne* in the framework of the LabEx IMoBS3.

REFERENCES

1. Asano, S., "Light scattering properties of spheroidal particles," *Appl. Opt.*, Vol. 18, No. 5, 712–723, 1979.
2. Cornet, J.-F., "Calculation of optimal design and ideal productivities of volumetrically lightened photobioreactors using the constructal approach," *Chem. Eng. Sci.*, Vol. 65, No. 2, 985–998, 2010.
3. Rayleigh, L., "On the problem of random vibrations, and of random flights in one, two, or three dimension," *Phil. Mag.*, Vol. 37, No. 6, 321–347, 1919.
4. Wait, J. R., "Scattering of a plane wave from a circular dielectric cylinder at oblique incidence," *Can. J. Phys.*, Vol. 33, No. 5, 189–195, 1955.
5. Van de Hulst, H. C., *Light Scattering by Small Particles*, Dover Publication Inc., New York, 1981.
6. Bohren, C. F. and D. R. Huffman, *Absorption and Scattering of Light by Small Particles*, Wiley-Interscience, New York, 1983.
7. Waterman, P. C., "Matrix formulation of electromagnetic scattering," *Proc. IEEE*, Vol. 53, No. 8, 805–812, 1965.
8. Waterman, P. C., "Symmetry, unitarity, and geometry in electromagnetic scattering," *Phys. Rev.*, Vol. D, No. 3, 825–839, 1971.
9. Prather, D. W. and S. Shi, "Formulation and application of the finite-difference time-domain method for the analysis of axially symmetric diffractive optical elements," *J. Opt. Soc. Am.*, Vol. A, No. 16, 1131–1142, 1999.
10. Morgan, M. A. and K. K. Mei, "Finite element computation of scattering by inhomogeneous penetrable bodies of revolution," *IEEE Trans. Antennas Propagat.*, Vol. AP, No. 27, 202–214, 1979.
11. Asano, S. and G. Yamamoto, "Light scattering by spheroidal particles," *Appl. Opt.*, Vol. 14, No. 14, 29–49, 1986.
12. Asano, S. and M. Sato, "Light scattering by randomly oriented spheroidal particles," *Appl. Opt.*, Vol. 19, No. 6, 962–974, 1980.
13. Edee, K. and B. Guizal, "Modal method based on subsectional Gegenbauer polynomial expansion for nonperiodic structures: Complex coordinates implementation," *JOSA A*, Vol. 30, No. 4, 631–639, 2013.
14. Edee, K., G. Granet, and J. P. Plumey, "Complex coordinate implementation in the curvilinear coordinate method: Application to plane-wave diffraction by nonperiodic rough surfaces," *JOSA A*, Vol. 24, No. 4, 1097–1102, 2007.

A Couple of Topics in Numerical Analysis of Diffraction by a Metal Grating Using Yasuura's Method of Modal Expansion

T. Matsuda¹, X. Xu², and Y. Okuno³

¹Department of Information, Communication and Electronic Engineering
Kumamoto National College of Technology, Koshi, Kumamoto 861-1102, Japan

²Department of Electrical Engineering and Information Technology
School of Engineering, Kyushu Sangyo University, Fukuoka 813-8503, Japan

³Centre for Optical and Electromagnetic Research, South China Academy of Advanced Optoelectronics
South China Normal University, Guangzhou 510006, China

Abstract— Assuming the progress of numerical solution of grating problems by Yasuura's method of modal expansion, we pick up a couple of issues that require our countermeasure, state our step, and give our opinion if appropriate. Here we take up: choice of modal functions; observation of condition number in least-squares boundary matching; and use of refractive indices of Au taken from references.

1. INTRODUCTION

In solving the problem of scattering or diffraction on a computer, we often encounter small issues that require us to take some action. Assuming the process of numerical solution (mainly) of grating problems by Yasuura's method of modal expansion [1–4], we pick up a few of such issues or topics and state our countermeasures or opinion. The issues are:

- 1) Choice of modal functions: In the method we define an approximate solution in terms of a finite linear-combination of modal functions. The choice of a set of modal functions from among possible set of functions is an important issue because the effectiveness of the method depends on the choice.
- 2) Observation of the condition number: We employ the orthogonal decomposition of the Jacobian matrix in solving the least-squares problem and the nature of the matrix given by the condition number is important.
- 3) Refractive index of Au: The index of a metal is of a great interest in application to plasmonics. Here we show a couple of examples of plasmon resonance absorption predicted by our computer program using four different values of Au index.

2. A BRIEF INTRODUCTION TO YASUURA'S METHOD OF MODAL EXPANSION

Before taking up the issues, we briefly see the process of solution by the method. Figure 1 shows the geometry of a sample problem: 2-D E-wave (*s*-polarization) scattering by a perfectly conducting grating. We denote the cross section of the grating by *C* and assume the semi-infinite region below *C* is filled with a perfect conductor. The cross section *C* is periodic in *X* with a period *d*. We represent a point on *C* by *s*(*x*, *y*), assume *y* = *η*(*x*) (*η*(*x* + *d*) = *η*(*x*)), and let a point in the free space region *S* above *C* be **r**(*X*, *Y*). Let us consider the problem to find the diffracted field when an E-polarized plane wave

$$\mathbf{E}^i(\mathbf{r}) = \mathbf{u}_Z F(\mathbf{r}) = \mathbf{u}_Z \exp(i\alpha_0 X - i\beta_0 Y), \quad \alpha_0 = k \sin \theta, \quad \beta_0 = k \cos \theta \quad (1)$$

is incident. Here, the time factor $e^{-i\omega t}$ is suppressed and \mathbf{u}_Z denotes a unit vector in *Z*-direction.

The solution to this problem, $E_z^s(\mathbf{r}) = \Psi(\mathbf{r})$, should satisfy the following conditions:

- D1.** 2-D Helmholtz's equation in *S*, $\nabla^2 \Psi(\mathbf{r}) + k^2 \Psi(\mathbf{r}) = 0$;
- D2.** Pseudo-periodicity condition, $\Psi(X + d, Y) = \exp(i\alpha_0 d) \Psi(X, Y)$;
- D3.** 1-D radiation condition that $\Psi(X, Y)$ propagates or attenuates in the positive *Y*-direction;
- D4.** The boundary condition on a perfectly conducting surface, $\Psi(s) + F(s) = \Psi(x, \eta(x)) + F(x, \eta(x)) = 0$.

To solve this problem by using Yasuura's method of modal expansion, we first need to define a set of modal functions $\{\varphi_m(\mathbf{r}) : m = 1, 2, \dots\}$ that satisfies the requirements:

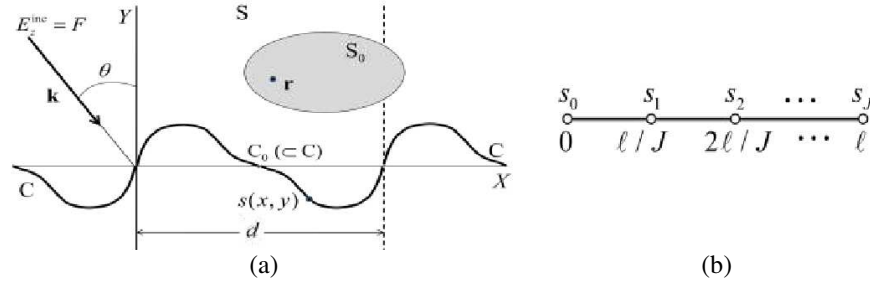


Figure 1: (a) Geometry of a sample problem: E-wave (*s*-polarization) scattering by a grating made of a perfectly-conducting metal. *C* is the cross section and *S* is a semi-infinite region above *C*. C_0 is the first period of *C* and S_0 is an arbitrary closed subregion of *S*. (b) Equally located sampling points on C_0 . s_j are the points whose *s*-coordinates are $j\ell/J$. Ed: Frame lines are for reference; please delete them.

M1. Each $\varphi_m(\mathbf{r})$ satisfies the conditions **D1**, **D2**, and **D3**.

M2. The set of boundary values $\{\varphi_m(s) : m = 1, 2, \dots\}$ is complete in the function space $L^2(C_0)$ consisting of all the square integrable functions defined on C_0 , the first period of *C*.

Next, we define an approximate solution in terms of a *finite* linear combination of the modal functions

$$\Psi_M(\mathbf{r}) = \sum_{m=1}^M A_m(M) \varphi_m(\mathbf{r}) \quad (2)$$

where $A_m(M)$ means that the A_m -coefficient depends on the number of truncation M . Because the solution satisfies the conditions **D1**, **D2**, and **D3**, we determine the coefficients in order that the solution meets the boundary condition **D4** approximately. In Yasuura's method we employ the least-squares method:

Problem C. Find the set of A_m -coefficients that minimizes a normalized mean-squares boundary residual

$$\Omega_M^C = \|\Psi_M + F\|^2 / \|F\|^2 = \int_{s=0}^{\ell} |\Psi_M(s) + F(s)|^2 ds / \int_{s=0}^{\ell} |F(s)|^2 ds \quad (3)$$

Here, ℓ denotes the length of C_0 . In a shallow grating, a definition $\|f\|^2 = \int_{x=0}^d |f(x, \eta(x))|^2 dx$ also works.

In numerical solution on a computer we need (i) the method of discretization and (ii) the method for solving the discretized problem. Discretization can be made in the following way: First, we locate equally-spaced $J = 2M$ sampling points on C_0 and denote them by $\{s_0, s_1, \dots, s_J\}$. Although this set includes $J + 1$ points, s_0 and s_J share common information (except for the $\alpha_0 d$ phase difference; see Section 3.1) and we can regard them as one point. Second, we define J -dimensional column vectors whose members are boundary values of modal functions.

$$\boldsymbol{\varphi}_m = (\varphi_m(s_1) \varphi_m(s_2) \dots \varphi_m(s_J))^T \quad (m = 1, 2, \dots, M) \quad (4)$$

Then, we set up a $J \times M$ Jacobian matrix

$$\boldsymbol{\Phi} = [\boldsymbol{\varphi}_1 \ \boldsymbol{\varphi}_2 \ \dots \ \boldsymbol{\varphi}_M] \quad (5)$$

Finally, defining an M -dimensional solution vector

$$\mathbf{A} = (A_1(M) \ A_2(M) \ \dots \ A_M(M))^T \quad (6)$$

we have a least-squares problem in a J -dimensional complex-valued vector space, a discretized form of **Problem C**.

Problem D. Find a solution vector \mathbf{A} that minimizes the discretized boundary residual

$$\Omega_M = \|\boldsymbol{\Phi} \mathbf{A} + \mathbf{F}\|^2 / J = \left\| \sum_{m=1}^M A_m(M) \boldsymbol{\varphi}_m + \mathbf{F} \right\|^2 / J \quad (7)$$

Here, \mathbf{F} is a discretized incident wave, $\|\mathbf{f}\|$ denotes the Euclidean norm of a J -dimensional vector, the denominator J comes from the line element $ds \simeq \ell/J$, and this ℓ has been canceled by the

denominator of (3). In solving **Problem D**, we usually employ the QR decomposition. In case if we need the condition number of the Jacobian matrix, we use the singular-value decomposition.

We can prove that the sequence of approximate solutions $\{\Psi_1(\mathbf{r}), \Psi_2(\mathbf{r}), \dots, \Psi_M(\mathbf{r}), \dots\}$ with the coefficients obtained by solving **Problem D** converges to the true solution $\Psi(\mathbf{r})$ uniformly in any closed sub-region S_0 in S .

3. TOPICS IN THE SOLUTION PROCESS

Here we employ three representative topics/issues that emerge in the process of numerical analysis by Yasuura's method of modal expansion.

3.1. Choice of Modal Functions

If the cross section is simple like a sinusoid, is shallow, and if the period is comparable to the wavelength, the problems are easy to solve with the commonly-employed set of separated solutions satisfying the periodicity (**D2**) and radiation condition (**D3**). They are referred to as the Floquet or grating modes and are given by

$$\begin{aligned}\varphi_m(X, Y) &= \exp(i\alpha_m X + i\beta_m Y), \\ \alpha_m &= \alpha_0 + 2m\pi/d, \quad \beta_m = \sqrt{k^2 - \alpha_m^2} \quad (\text{Re}\beta \geq 0, \text{Im}\beta \geq 0; m = 0, \pm 1, \pm 2, \dots)\end{aligned}\quad (8)$$

In using this set of modal functions, we should modify the summations in (2) and (7) to $\sum_{m=-N}^N$ and the total number of unknowns is $M = 2N + 1$. In addition, we use the functions

$$\tilde{\varphi}_m(x, y) = \exp(-i\alpha_0 x) \varphi_m(x, y) \quad \text{and} \quad \tilde{F}(x, y) = \exp(-i\alpha_0 x) F(x, y) \quad (9)$$

instead of $\varphi_m(x, y)$ and $F(x, y)$. Because the modified functions are periodic in x and s , this modification would accelerate the convergence of the solutions [5]. Further, the periodicity of functions means that the discretized boundary residual (7) is a trapezoidal approximation to (3).

Conversely, if the cross section is complicated, deep, or is electrically large, the problem is difficult and the method with Floquet modal functions often fails [6]. The same problem arises also in other methods employing modal expansion and many researchers have endeavored to develop methods of analysis that can solve the difficult problems. A lot of works can be found and we refer only a few examples [7–9]. We also have tried two approaches, which are understood as the use of alternative sets of modal functions:

(i) Location of line sources in S^c (the complement of S). This is the same as the equivalent-sources method and is useful when combined with a technique of concentrating the poles near the convex part of the obstacle. In scattering by a cylindrical obstacle $\rho = a(1 - 0.2 \cos 3\theta)$ [10], we compared three types of modal functions: separated solutions (sep), fields from monopoles located equally on an analogous curve inside the boundary (pel), and fields from monopoles densely located near the peaks of the curve (pdp). At $ka = 10$, both (pel) and (pdp) works well and the energy errors at $M = 70$ are 9×10^{-5} and $1 \times 10^{-5}\%$. It is difficult for (sep) to give good solutions for the error is 4%. At $ka = 30$, the energy errors of the solutions with $M = 100$ are $2 \times 10^{-1}\%$ (pel), $5 \times 10^{-3}\%$ (pdp), and 7% (sep). A similar choice of modal functions in grating problems seems to be more powerful than the Floquet modes. (ii) Employment of up- and down-going Floquet modes and normalization by vertical separation of groove regions. We have developed this scheme based on the following ideas: (a) Although it is commonly accepted that the diffracted field over the surface C can be represented in terms of up-going modes alone independently of the validity of the Rayleigh hypothesis, it is not unreasonable to assume down-going waves in the groove region; (b) Higher-order grating modes are often the origin of trouble in numerical computations because they oscillate in x strongly and increase/decrease in y rapidly. Hence, the scheme is a combination of (a) and (b) in the frame of Yasuura's modal expansion. The effectiveness of this method is as follows [11]: for both perfect-conductor and dielectric case, we can get solutions with high accuracy for deep gratings (sinusoidal, $1 < 2h/d < 2.4$) by separating the groove region into 20 layers.

3.2. Observation of the Condition Number

As we have mentioned after **Problem D**, we usually employ the QR decomposition (QRD) in solving the discretized problem. This is because the computational complexity of the solution by the QRD is much smaller than that of a method using the singular-value decomposition (SVD) in both time and storage. When running a computer program for a new problem for the first time, however, we employ a method using the SVD because we would like to know the nature

of the Jacobian matrix. In particular we need J dependence of $\text{cond}(\Phi)$ for a fixed M and rank deficiency check [12]. The dependence of $\text{cond}(\Phi)$ and the smallest singular value on computational parameters are also meaningful and are important sometimes. In Figure 2 we show examples of the J -dependence of a few significant quantities.

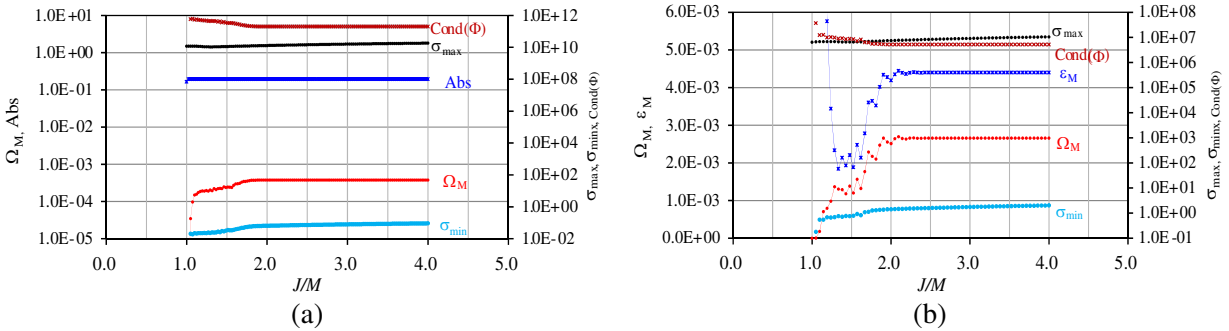


Figure 2: (a) J dependence of $\text{cond}(\Phi)$, Ω_M , maximum and minimum singular values. Conical mounting with azimuth $\varphi = 30^\circ$ and polar angle $\theta = 10^\circ$, p-wave. Au-sinusoidal grating, $d = 556$ nm, $2h = 166.8$ nm, $\lambda = 670$ nm, and $n_{\text{Au}} = (0.17393, -3.61253)$. $N = 20$, $M = 2N + 1 = 41$, total number of unknowns is 82. (b) J dependence of $\text{cond}(\Phi)$, Ω_M , maximum and minimum singular values, and energy error ϵ_M . Conical mounting with $\varphi = 30^\circ$ and $\theta = 10^\circ$. BK7-sinusoidal grating, $d = 556$ nm, $2h = 222.4$ nm, $\lambda = 670$ nm, and $n = 1.5139$. $N = 20$, $M = 2N + 1 = 41$, total number of unknowns is 82.

3.3. Refractive Index of Au

The refractive index (or permittivity) of a noble metal is an important material constant today because of the recent development of plasmonics: the plasmon wavenumber is closely related to the index. In computer simulation of a plasmonic structure, we usually employ an index value taken from a reference. Here sometimes arises a problem: In sensor application, for example, we need a precise value of the index with more than six- or seven-digit significant figures. Such a numerical value, however, is not placed in a reference available easily. Consequently, we should use an approximate value in our simulation. To see how the small difference in refractive index influences the resonance absorption, we made numerical computation about the index values from four references and compared the result in Figure 3. As we see the difference between the reflection efficiency curves cannot be neglected, which may have an influence on the fourth or fifth column of the result of an index measurement. Hence, it is an important issue for those working in plasmonics to study how to cope with the difficult situation.

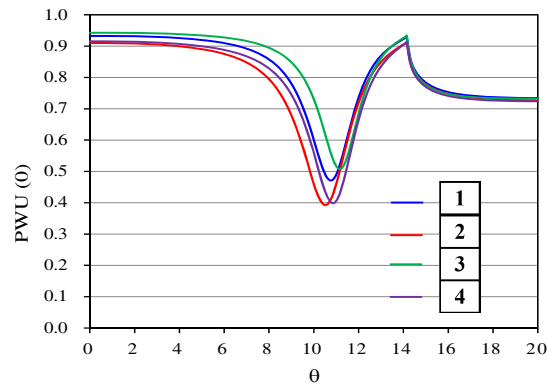


Figure 3: Comparison of the 0th order efficiency curves near the plasmon resonance absorption using Au index taken from four references. The sources are listed in Table 1. The grating is sinusoidal with $d = 556$ nm and $2h = 70$ nm. Conical mounting with $\varphi = 30^\circ$, p-wave. The abscissa shows polar angle θ and the ordinate is the 0th order reflection efficiency including both p and s-polarized wave. Note that the s-polarized component is dominant near the absorption peak ($\theta \simeq 11^\circ$). Note also that the Au index is obtained through spline interpolation when necessary.

Table 1: Refractive indices of Au for $\lambda = 670$ nm taken from four sources.

	n	k	$ n_{\text{Au}} $	sources of references
1	0.13179	3.56261	3.56505	[13]
2	0.16077	3.43942	3.44318	[14]
3	0.13225	3.79379	3.79609	[15]
4	0.17408	3.6123	3.61649	[16]

4. CONCLUSIONS

We have seen the solution process of Yasuura's method of modal expansion and have taken a few issues that require us to devise a countermeasure. Although most of the topics taken here might have been discussed elsewhere, we should consider the old topics together with many similar subjects again now to make good use of them. This is because such matters are inadequately forgotten in today's progressed computer environment.

REFERENCES

1. Yasuura, K. and T. Itakura, "Approximation method for wave functions (I), (II), and (III)," *Kyushu Univ. Tech. Rep.*, Vol. 38, No. 1, 72–77, 1965; Vol. 38, No. 4, 378–385, 1966; Vol. 39, No. 1, 51–56, 1966.
2. Ikuno, H. and K. Yasuura, "Improved point-matching method with application to scattering from a periodic surface," *IEEE Trans. Antennas Propagat.*, Vol. 21, 657–662, 1973.
3. Petit, R., et al., *Electromagnetic Theory of Gratings*, R. Petit, ed., Chapters 1 (R. Petit) and 2 (M. Cadilhac), Springer-Verlag, Berlin, 1980.
4. Okuno, Y., "An introduction to the Yasuura method," *Analytical and Numerical Methods in Electromagnetic Wave Theory*, M. Hashimoto, M. Idemen, and O. A. Tretyakov, ed., 515–565, Science House, Tokyo, 1993.
5. Recall that: the m th Fourier coefficient of a continuous and periodic function is in proportion to m^{-2} ; while that of a discontinuous periodic function is m^{-1} .
6. This is the reason why we have introduced the *Smoothing Procedure* (see e.g., Okuno [4]), but we do not go further into this subject.
7. Chandezon, J., M. T. Dupuis, G. Cornet, and D. Maystre, "Multicoated gratings: A differential formalism applicable in the entire optical region," *J. Opt. Soc. Amer.*, Vol. 72, 839–846, 1982.
8. Hafner, C., *The Generalized Multipole Technique for Computational Electromagnetics*, Artech House, Boston, 1990.
9. Wriedt, T., ed., *Generalized Multipole Techniques for Electromagnetic and Light Scattering*, Elsevier, Amsterdam, 1999.
10. Yamaguchi, H., "The idea of equivalent sources in the Yasuura method," Thesis for Master Degree, Graduate School of Science and Technology, Kumamoto University, 1993 (in Japanese).
11. Ohtsu, M., Y. Okuno, A. Matsushima, and T. Suyama, "A combination of up- and down-going Floquet modal functions used to describe the field inside grooves of a deep grating," *Progress In Electromagnetics Research*, Vol. 64, 293–316, 2006.
12. Although we gave $J = 2M$ below (3), this is an experimental rule and should be employed after examination.
13. Hass, G. and L. Hadley, "Optical properties of metals," *American Inst. Phys. Handbook*, 2nd Edition, D. G. Gray, ed., 6–107, McGraw-Hill, NY, 1963.
14. Palik, E. D., *Handbook of Optical Constants of Solids*, Academic Press, Boston, 1998.
15. Johnson, P. B. and R. W. Christy, "Optical constants of the noble metals," *Phys. Rev. B*, Vol. 6, 4370, Published Dec. 15, 1972.
16. Rakik, A. D., A. B. Djuricic, J. M. Elazar, and M. L. Majewski, "Optical properties of metallic films for vertical-cavity optoelectronic devices," *App. Opt.*, Vol. 37, 5271–5283, 1998.

Dispersion Characteristic Analysis of Open Cylindrical Waveguide and Its Metallic Closed Model

P. Kelebekler¹ and N. Yener²

¹Technical Education Faculty, Kocaeli University, Turkey

²Biomedical Engineering Department, Technology Faculty, Kocaeli University, Turkey

Abstract— In the study, complex modes dispersion characteristics of cylindrical plasma column open waveguide are obtained from exact characteristic equations system and its metallic closed model. In order to model the open waveguide with cylindrical plasma column loaded closed waveguide, firstly mathematically proper guided and complex modes are obtained. Because mathematically proper modes do not violate the boundary conditions and can be modeled with a closed waveguide structure which uses a complete set of orthogonal functions. Numerical values obtained from characteristic equations system and model structure for cylindrical isotropic plasma column open waveguide are presented in the same figure. Additionally, it is shown that the numerical results obtained from the model approach to the exact solution while radius of metallic waveguide frame gets larger.

1. INTRODUCTION

Complex waves have been investigated in numerous studies for closed and open waveguides. Complex wave modes for isotropic dielectric rod loaded closed waveguide and parallel isotropic dielectric and anisotropic ferrite sheet were presented by Clarricoats [1] and Marques [2], respectively. For open waveguides, leaky waves are the most popular complex waves. The reason is that they play very important roles at antennas, microwave circuits and a large variety of physical phenomenon [3]. The leaky wave modes are physically improper. They are not member of a complete set of orthogonal base functions. This solution for the wave equation gives a field presentation with complex propagation constant, but that the field becomes infinite at the infinite transverse spatial limit [4]. Improper nature of leaky waves originates from increase of the field while leaky wave diverges transversely from guide. If the wave exists in free space, amplitude of the wave will diverge transversely at infinity and therefore, boundary conditions at infinity will be violated. Hence these waves are characterized mathematically improper or nonspectral. It can be shown easily that the wave never arrives transverse infinity for a distance from source to infinite and it is described only within near space sector of guiding structure. It is stated in [3] that leaky wave is certainly physical and measurable in valid region and it is really a type of near field wave. Nevertheless it affects strongly nature of far field.

In our study, complex dispersion characteristics of an open waveguide is obtained by using its metallic closed model. Equations, which belong to metallic closed model, are obtained by using Method of Moment (MoM) based on generalized telegraphist's equations. Even though leaky wave modes have very large implementation field and are an important physical phenomenon, their mathematically improper nature prevents modeling these modes of open waveguide with the closed waveguide structure. Because boundary conditions for metallic closed waveguides, whose tangential component of electric field and normal component of magnetic field equal to zero at metallic wall, automatically are violated. Besides transmission line equations used in modeling consist of a complete set of orthogonal base functions [5]. The conditions which leaky waves violate the boundary conditions at infinite and they are not a member of complete set of orthogonal base functions, prevent to work the model.

In our study, firstly, mathematically proper modes are obtained, because mathematically proper modes enable to be modeled with a closed waveguide structure which uses a complete set of orthogonal functions. Additionally they do not violate the boundary conditions when the open waveguide is closed with a metallic wall. Because the fields decrease while diverging from the guiding structure. In the study, cylindrical isotropic plasma column open waveguide is taken as an example structure. Complex modes for cylindrical dielectric rod open waveguide were presented firstly by Arnbak. Later, complex modes for cylindrical dielectric rod open waveguide and cylindrical plasma column open waveguide were investigated by using Davidenko's method [6–8]. But complex modes of open waveguide structures in the studies are mathematically improper leaky modes. In the literature, mathematically proper complex modes of cylindrical isotropic plasma column open waveguide could

not be found. Guided waves of the structure were presented in [9] and they are obtained again from characteristic equation system of the structure in our study. Complex modes which correspond to mathematically proper modes of the structure are obtained from the same characteristic equation system by using “fsolve” function in Matlab.

In our study, propriety or impropriety of modes of cylindrical plasma column open waveguide are investigated analytically. It is shown that modes obtained from numerical computations correspond to proper modes. Analytic solutions of cylindrical isotropic plasma column loaded closed waveguide used as model structure in the study are obtained by using generalized telegraphist’s equations (or transmission line equivalent equations) presented in [5]. This approximation to model open waveguide with closed metallic guide was firstly used to model guided waves of rectangular dielectric open waveguide by Ogusu [10]. In our study, numerical values obtained from characteristic equations system and model structure for cylindrical isotropic plasma column open waveguide are presented in the same figure. Additionally, it is shown that the numerical results obtained from the model approach to the exact solution while radius of metallic waveguide frame gets larger.

2. CYLINDRICAL PLASMA COLUMN OPEN WAVEGUIDE

Plasma called fourth state of matter is an ionized state of matter, which exists in universe and can be obtained artificially in the earth. Plasma medium is an anisotropic medium. But it is typically tackled under special conditions which transform anisotropic medium into isotropic medium. Thus supplies simplification in solutions. One of these simplifications is that the radian electron cyclotron frequency (ω_c) is taken zero, which is called plasma column with zero magnetic field in the literature [9]. In our study, isotropic plasma medium with frequency depended permittivity, $\tilde{\varepsilon} = \varepsilon_0(1 - \frac{\omega_p^2}{\omega^2}) = \varepsilon_0\varepsilon_p$ is investigated by using the simplification. Where, ω is the angular frequency, ω_p is the radian electron plasma frequency and ε is free space permittivity.

In [9], dispersion curves of zero cyclotron frequency condition were presented for parametric values, azimuthal variation $m = 0, 1, 2$ and normalized plasma frequency (ω_p a/c) $\omega_N = 0.25, 0.5, 0.75$. Where, a indicates plasma column radius and c indicates speed of light in vacuum

Analytic solutions for cylindrical isotropic plasma column open waveguide surrounded with free space are obtained from Maxwell equations by using continuity conditions at interface between plasma-air. Variations of the fields is described as below.

$$F(r, \varphi, z) = F(r) e^{j(\omega t - \gamma z - m\varphi)} \quad (1)$$

Here, γ shows complex propagation constant and is described as $\gamma = \beta - j\alpha$. Here, α is attenuation constant and β is phase constant.

For the field variation described in Equation (1), characteristic equations system is obtained as in Equation (2) for lossless and source less cylindrical plasma column open waveguide with $\varepsilon_0\varepsilon_p$ permittivity and μ permeability. Here, μ_0 is free space permeability. In Equation (2), the points at which the determinant of the coefficient matrix vanishes, give the solution

$$\begin{bmatrix} -\frac{m}{a} \frac{\gamma}{k_1^2} J_m(k_1 a) & j \frac{1}{\omega \varepsilon_0} \frac{k_0^2}{k_1} J'_m(k_1 a) & -\frac{m}{a} \frac{\gamma}{k_2^2} K_m(k_2 a) & j \frac{1}{\omega \varepsilon_0} \frac{k_0^2}{k_2} K'_m(k_2 a) \\ 0 & J_m(k_1 a) & 0 & -K_m(k_2 a) \\ -j \frac{1}{\omega \mu_0} \frac{k_0^2 \varepsilon_p}{k_1} J'_m(k_1 a) & -\frac{m}{a} \frac{\gamma}{k_1^2} J_m(k_1 a) & -j \frac{1}{\omega \mu_0} \frac{k_0^2}{k_2} K'_m(k_2 a) & -\frac{m}{a} \frac{\gamma}{k_2^2} K_m(k_2 a) \\ J_m(k_1 a) & 0 & -K_m(k_2 a) & 0 \end{bmatrix} \begin{bmatrix} A \\ B \\ C \\ D \end{bmatrix} = 0 \quad (2)$$

where, J_m is Bessel function of first kind with m th degree, K_m is modified Bessel function of second kind with m th degree. Besides, k_1^2 , k_2^2 and k_0^2 are described as $k_1^2 = k_0^2 \varepsilon_p - \gamma^2$, $k_2^2 = \gamma^2 - k_0^2$ and $k_0^2 = \omega^2 \mu_0 \varepsilon_0$ respectively.

Complex dispersion curves generally include dispersion characteristics of forward and backward guided waves, evanescent and complex waves. In numerical computation, a noncomplex root which satisfies Equation (2) for fixed working frequency, can be easily found with simple methods as bisection method. Nevertheless obtaining complex roots gets harder while the characteristic equation gets complicated. In the study complex modes of cylindrical plasma column open waveguide are obtained from the characteristic equations system by using “fsolve” function in Matlab. “fsolve” function in Matlab requires an approximate initial value to compute noncomplex or complex root. In order to determine initial value, the complex modes reported in the literature are taken as reference. The complex waves are presented for different structures as cylindrical dielectric rod loaded

closed waveguide [11], parallel dielectric and anisotropic ferrite sheet waveguide [2]. In these studies, common feature of complex modes is that complex modes arise at points where slope of the dispersion curves changes sign. In respect of this feature, complex modes of our structure are computed about the frequency point where slope of dispersion curve changes sign by using Equation (2) and “fsolve” function in Matlab.

2.1. Analysis of Proper and Improper Complex Modes of Plasma Column Open Waveguide

Field components of open waveguides have to supply boundary conditions at infinity. Boundary conditions at infinity are given below.

$$\lim_{R \rightarrow \infty} RE = \lim_{R \rightarrow \infty} RH = 0$$

Here, R is determined as $R = \sqrt{r^2 + z^2}$, r and z are cylindrical coordinate variables.

If amplitude of wave increases while $r \rightarrow \infty$, the boundary conditions at infinity is violated and the wave is called mathematically improper. Nevertheless these waves also called leaky waves can be measurable and used in numerous electromagnetic applications. But, since leaky waves are mathematically improper, they can only exist in a restricted region of a wedge shape within which the field stays finite [6].

The characteristic equations system given in Equation (2) of cylindrical plasma column open waveguide is obtained from Maxwell equations and continuity conditions between plasma and air. All field expressions for region outside of plasma column consist of modified Bessel function of second kind or its derivatives. Since derivatives of Bessel functions can be expressed in the terms of themselves if we take limit of modified Bessel function of second kind while $r \rightarrow \infty$, we can obtain analytic results about proper or improper of fields. While $r \rightarrow \infty$, asymptotic expression of modified Bessel function of second kind is given below.

$$(kr) \simeq \frac{e^{-kr}}{\sqrt{2\pi kr}} \quad (3)$$

where, k is Bessel function parameter and called the wave number. Let's investigate Equation (3) for three cases of complex wave number, $\text{Re}(k) = k_R$ ve $\text{Im}(k) = k_I$ ($k = k_R + jk_I$). If the equation is investigated for pure real, pure imaginary and complex k while $r \rightarrow \infty$, the results below are obtained.

$$\begin{aligned} k = k_R \text{ (pure real)} &\rightarrow \begin{cases} k_R > 0 & \text{proper mode} \\ k_R < 0 & \text{improper mod.} \end{cases} \\ k = jk_I \text{ (pure imaginary)} &\rightarrow \text{proper mode (independent of value of } k_I) \\ k = k_R + jk_I \text{ (complex)} &\rightarrow \text{(independent of value of } k_I) \begin{cases} k_R > 0 & \text{proper mode} \\ k_R < 0 & \text{improper mode} \end{cases} \end{aligned}$$

Nevertheless the wave number outside of plasma column which is parameter of modified Bessel function of second kind depends on angular frequency and the propagation constant $k_2^2 = \gamma^2 - k_0^2$ constant. For real working frequency, the free space wave number k^2 is always real. Accordingly, values of k_2 depending on the propagation constant and propriety and impropriety of modes is achieved as below.

$$\begin{aligned} \gamma \text{ pure real} &\begin{cases} \gamma^2 > k_0^2 \Rightarrow k_2 = \pm |\lambda| \begin{cases} +|\lambda| & \text{positive real (proper mode)} \\ -|\lambda| & \text{negative real (improper mode)} \end{cases} \\ \gamma^2 < k_0^2 \Rightarrow k_2 \text{ pure imaginary (proper mode).} \end{cases} \\ \gamma \text{ pure imaginary } (\gamma^2 \text{ is negative real)}, &\quad \gamma^2 - k_0^2 < 0 \text{ and } k_2 \text{ is pure imaginary (proper mode)} \\ \gamma \text{ complex } (k_2 \text{ complex)} &\begin{cases} \text{Re}\{k_2\} > 0 \Rightarrow \text{proper mode} \\ \text{Re}\{k_2\} < 0 \Rightarrow \text{improper mode} \end{cases} \end{aligned}$$

2.2. Exact Dispersion Characteristic of the Structure

In this section, exact dispersion curves of cylindrical plasma column open waveguide are obtained from characteristic equations system given in Equation (2). Additionally, it is shown numerically that the modes obtained from computations correspond to proper modes.

Parametric values of cylindrical plasma column open waveguide used in numerical computations are that plasma column radius (a) is 10 mm, azimuthal variation (m) is 1 and normalized plasma frequency (ω_p) is 0.25. In numerical computations, firstly, propagation constants for a fixed frequency are obtained. Later the wave number outside of plasma column (k_2) are computed by using these propagation constants. Dispersion curves and wave number outside of plasma column which determine propriety or impropriety of wave are given together in Figure 1.

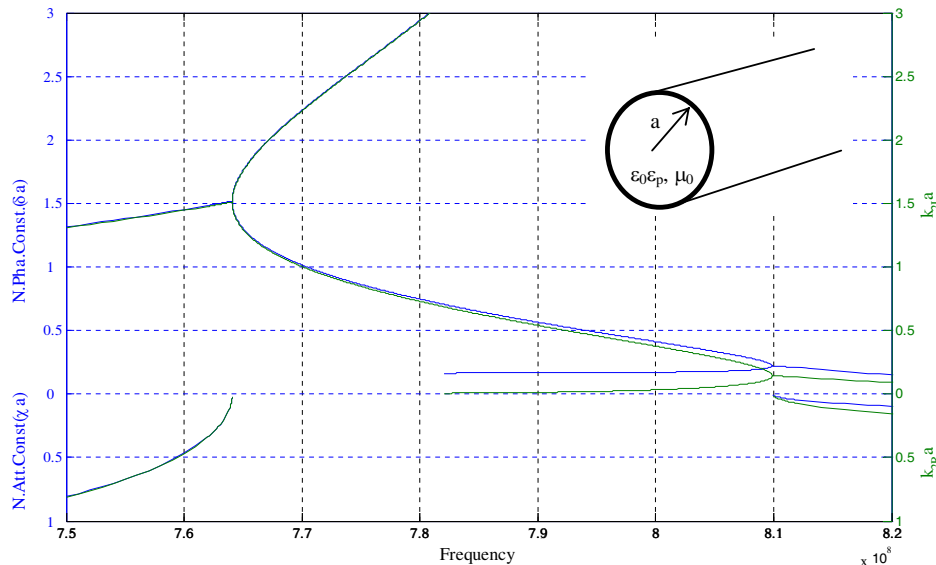


Figure 1: Left y axis: Complex dispersion curves for cylindrical isotropic plasma column open waveguide. Right y axis: Normalized wave number outside of plasma column. Inset: geometry of the problem.

In the figure, above from zero point at left y axis shows normalized phase constant (βa) and below shows normalized attenuation constant (αa). Similarly, above from zero point at right y axis shows imaginary part of normalized wave number outside of plasma column ($k_{2I}a$) and below shows real part of normalized wave number outside of plasma column ($k_{2R}a$). As shown in the figure, below from zero point are positive at both sides indicating proper nature of the complex mode observed.

As shown from blue curves in the figure, the complex modes arise at the frequency points where slope of dispersion curve changes sign. For the structure, the dispersion curve bifurcates at the frequency point 764 MHz. The complex modes exist on the left side of this point, forward and backward guided waves exist on the right side of this point. Similarly, the dispersion curve bifurcates at the frequency point 810 MHz. Forward and backward wave modes exist on the left side of this point and complex modes exist on the right side of this point. As shown from green curves in the figure, real parts of normalized wave number outside of plasma column are positive. As a result, for cylindrical plasma column open waveguide, guided modes and complex modes obtained from numerical computations and presented in Figure 1 correspond to proper modes.

3. MOM MODEL OF THE STRUCTURE

One of the strongest methods for analyzing closed waveguide structures which do not have exact solution was given by Schelkunoff [5]. In the study, Schelkunoff transformed Maxwell equations that consist of partial differential equations into an ordinary differential equations system by modeling the waveguide as an infinite system of transmission line equations. The ordinary differential equations system transforms into algebraic equations system, because derivatives with respect to propagation direction variable correspond to product with a fixed value ($-j\gamma$) for the field variation in Equation (1). So, approximate solution of the structure which does not have analytic solution can be obtained. This method is also called Method of Moment (MoM). In this section, modes of cylindrical plasma column open waveguide is obtained from model of cylindrical plasma column loaded closed waveguide. This approximation was applied to obtain guided wave characteristics of rectangular dielectric open waveguide by Ogusu [10]. In order to apply the method for our structure, cylindrical plasma column surrounded with air is closed within a metallic wall.

Investigated modes have to be mathematically proper for validation of the method. Modeling for MoM is performed by using orthogonal base functions which belong to metallic empty closed guide. The boundary conditions belonging to the closed structure are that tangential component of electric field and normal component of magnetic field on the metallic boundary are zero. Improper modes violate the boundary conditions of closed waveguide, because amplitude of their field component increase while diverging transversely from plasma column. Additionally, they are not a member of a complete set of orthogonal base functions [4]. Because amplitude of field component of proper modes decrease while diverging transversely from plasma column, if the metallic wall is placed far enough from plasma column, it is possible to model proper modes of plasma column open waveguide with closed structure. Forward and backward guided wave modes and complex wave mode, which constitute the dispersion curves of cylindrical plasma column open waveguide given in Figure 1, correspond to mathematically proper modes. Hence it is possible to model them by enclosing the plasma column in a metallic shield, since then the boundary condition at infinity can be satisfied.

4. NUMERICAL RESULTS

In this section, all modes (guided and complex) presented in Section 2 for cylindrical plasma column open waveguide are obtained by using MoM solutions belonging to cylindrical plasma column loaded closed waveguide. Results obtained from MoM for different radius values of metallic wall and from exact solution for cylindrical plasma column open waveguide are presented together in the same figure. Computations for MoM are performed by using 150 TM and 150 TE modes of empty metallic closed waveguide.

In Figure 2, dispersion curves of cylindrical plasma column open waveguide obtained from exact solution with the same parametric values used in Figure 1 and dispersion curves obtained from MoM for $b = 20$ mm (radii ratio 0.5), $b = 33$ mm (radii ratio 0.333) and $b = 100$ mm (radii ratio 0.1) are presented altogether.

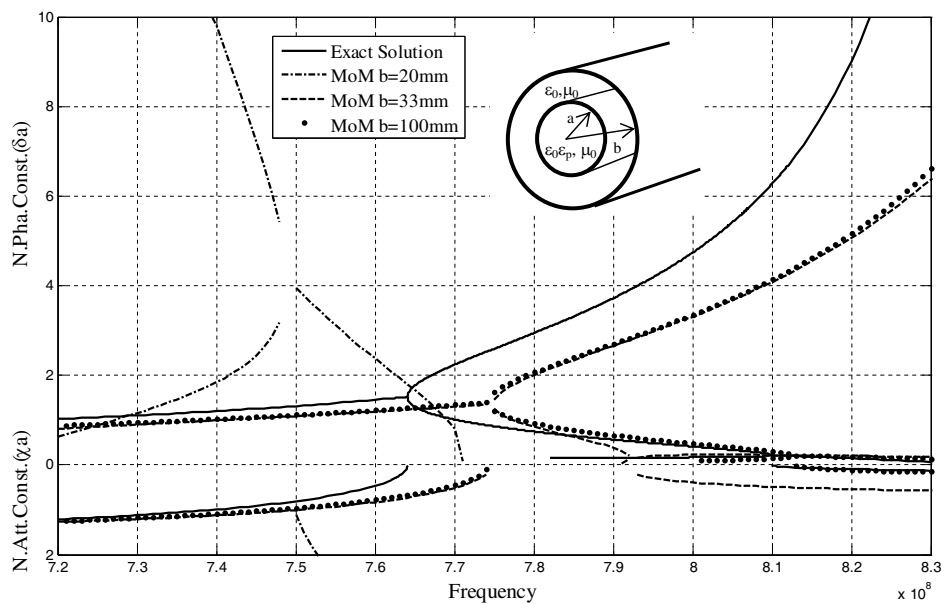


Figure 2: Dispersion curves obtained from exact solution and MoM model open plasma column.

As presented in the figure, the results obtained from MoM for $b = 20$ mm are rather far from results obtained from exact solution. Nevertheless results obtained by MoM is getting close to the exact solution while the ratio of radii is decreasing or radius of metallic wall is getting larger. For exact dispersion curve which bifurcates in the vicinity of 774 MHz, dispersion curves obtained from MoM for $b = 33$ mm and $b = 100$ mm are nearly at the same distance to the exact dispersion curve. But dispersion curve obtained from MoM for $b = 100$ mm are much more compatible with the exact solution for bifurcation point in the vicinity of 810 MHz.

Consequently, dispersion curves obtained from MoM for different values of metallic wall radius gets more compatible with exact solution while the radius is increased, as shown in Figure 2.

Nevertheless it is necessary to use more TM and TE base functions at computations of MoM

when the metallic wall radius is much increased. It is obvious that computations performed with more base functions cause to increase computational load and time. As a result of computations performed by using 150 TE and 150 TM base functions, the most suitable ratio of radii has been determined as 0.1.

5. CONCLUSION

In this study, it is aimed to obtain dispersion curves of open waveguide structure for a wide spectrum including mathematically proper complex waves from exact solution and MoM model of the structure. Cylindrical isotropic plasma column open waveguide whose forward and backward guided wave modes were presented in the literature is tackled as example structure. Guided modes and complex modes are obtained from exact characteristic equations system of the structure. The structure is transformed to cylindrical plasma column loaded closed wave guide for modeling by closing the open structure with metallic wall. MoM equations based generalized telegraphist's equations are obtained for the closed structure. Numerical results for different radius values of metallic wall are performed by using these equations. It is shown by presenting exact results and MOM results in the same figure that results obtained from MoM is getting more compatible with the exact solution while metallic wall radius is getting larger.

REFERENCES

1. Clarricoats, P. and K. Slinn, "Complex modes of propagation in dielectric-loaded circular waveguide," *Electronics Letters*, Vol. 1, 145–146, 1965.
2. Marques, R., F. Mesa, and M. Horno, "On the complex nature of higher order modes in lossless nonreciprocal transversely magnetized waveguides," *IEEE Microwave and Guided Wave Letters*, Vol. 2, 278–280, 1992.
3. Oliner, A. A., "Types and basic properties of leaky modes in microwave and millimeter-wave integrated circuits," *IEICE Trans. Electron.*, Vol. 83-C, 5, 675–686, 2000.
4. Hu, J. and C. R. Menyuk, "Understanding leaky modes: Slab waveguide revisited," *Advances in Optics and Photonics*, Vol. 1, No. 1, 58–106, 2009.
5. Schelkunoff, S. A., "Generalized telegraphist's equation for waveguide," *Bell System Tech. Journ.*, Vol. 31, 785–801, 1952.
6. Kim, K. Y., "Guided and leaky modes of circular open electromagnetic waveguides: Dielectric, plasma, and metamaterial columns," Doctoral Thesis, The Graduate School Kyungpook National University, Korea, 2004.
7. Kim, K. Y., H.-S. Tae, and J.-H. Lee, "Analysis of leaky modes in circular dielectric rod waveguides," *Electronics Letters*, Vol. 30, No. 1, 61–62, 2003.
8. Kim, K. Y., H.-S. Tae, and J.-H. Lee, "Leaky dispersion characteristics in circular dielectric rod using Davidenko's method," *Journal of the Korea Electromagnetic Engineering Society*, Vol. 5, No. 2, 72–79, 2005.
9. Granatstein, V. L., S. P. Schlesinger, and A. Vigants, "The open plasmaguide in extremes of magnetic field," *IEEE Transactions on Antennas and Propagation*, Vol. 11, No. 4, 489–496, 1963.
10. Ogusu, K., "Numerical analysis of the rectangular dielectric waveguide and its modifications," *IEEE Transaction on Microwave Theory and Techniques*, Vol. 25, No. 11, 874–885, 1977.
11. Yener, N., "Advancement of algebraic function approximation in eigenvalue problems of lossless metallic waveguides to infinite dimensions, Part III: Examples verifying the theory," *Journal of Electromagnetic Waves and Applications*, Vol. 20, 1861–1874, 2006.

Research on Ka Rough Ocean Surface Channel Modeling Based on Stochastic Processes

Xiaodong Cao¹, Xiaojun Wang^{1,2}, and Tao Jiang¹

¹College of Information and Communication Engineering, Harbin Engineering University, China

²Electrical and Computer Engineering Department, National University of Singapore, Singapore

Abstract— It is presented in this paper that a channel modeling technique based on GTD and stochastic bridge, which may boost the usage of low elevation angle Ka or higher frequency satellite down-link radio propagation prediction and estimation. First, it is introduced a random rough ocean surface modeling method under typical ocean states which is the foundation and the first step for electromagnetic simulation of telecommunication channel. Second, a huge data ocean surface reflection, scattering and diffraction based on GTD algorithm are calculated by high performance computer to provide a large number of samples for channel modeling. Third, a multipath channel model is set up to describe the statistical properties of received signal waveform which is modified by rough ocean surface. Last, all the steps are summed up and discussed to show the benefits of the presented modeling technique.

1. INTRODUCTION

Ka-band is generally applied to satellite communication. The radio waves propagation of Ka band has atmospheric attenuation, rain attenuation, atmospheric refractivity, and the loss caused by space change, in addition to the usual reflection, diffraction and scattering, etc.. The propagating process on sea surface is very complex, so, satellite down-link radio propagation prediction and estimation have important significance for maritime communications.

Typical wave propagation channel modeling methods apply experimental modeling method, stochastic modeling method and ray tracing method. Experimental modeling method, conducted by direct measurements and using statistical tools for data fitting and analysis, is not perfectly precise; Stochastic modeling method using statistical methods to analyze the statistical properties of the various parameters of the channel, can capture the channel response instantaneously and low calculation difficulty. But it has a high requirement for experimental environment and conditions. Ray tracing method taking radio waves as rays and using the Maxwell's equations and electromagnetic theory to analyze the channel and calculate the field strength is more accurate. But its calculation is complicated at the same time [1, 2]. Combining the advantages of the latter two methods, stochastic bridge channel modeling regards the electromagnetic wave as rays, and takes multipath propagation paths of rays in the wireless channel as stochastic process samples. The characteristic parameters of stochastic process is determined by the propagation environment [3].

In this paper, the first step is rough ocean surface modeling. Then calculating a huge data of ocean surface reflection, scattering and diffraction based on GTD algorithm by high performance computer to provide a large number of samples for channel modeling. In the end, modeling the the wireless channel on the sea surface.

2. RANDOM OCEAN SURFACE MODELING AND ELECTROMAGNETIC SIMULATION

With the increase in observation data and the development of the theory of the waves, there exist a lot of "experience spectrum", which are in a variety of forms respectively and the flourish logo of the simulation technique of sea wave. The wave spectrum is divided into frequency spectrum and directional spectrum. Frequency spectrum is one of the important statistical properties of the waves, so, the research of frequency spectrum is more widely. We can get wave height and period from the frequency spectrum [4]. Frequency spectrum has a good data foundation, and it is the distribution of wave energy on frequency variation. It is almost experience spectrum by measuring the data.

PM spectrum is fully growth state of the wave spectrum based on wind speed parameter, and it is detailed in the analysis of observational data and simple form. The displacement of sea surface is the the superposition of many waves with different frequency, amplitude and direction. The displacement of sea surface of every point form three-dimensional waves. Use double linear

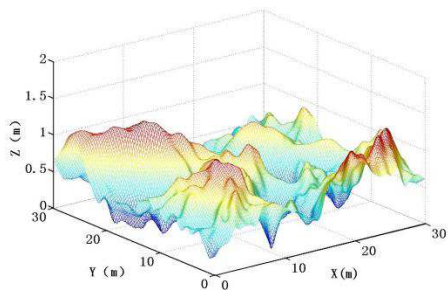


Figure 1: Wave model of level 3.

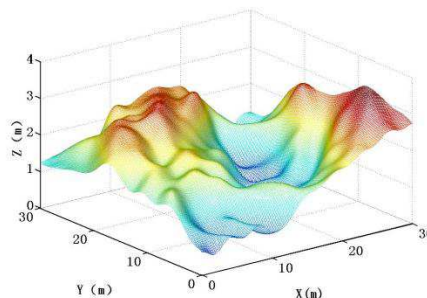


Figure 2: Wave model of level 5.

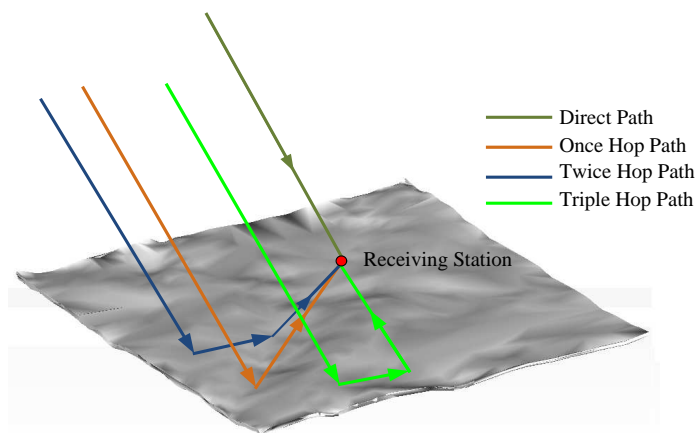


Figure 3: The scenario of ray path tracing.

superposition method to build PM spectrum wave model. The sea level is divided by the wind speed of rough sea surface [5, 6]. We take wave model of level 3 and 5 for example. As shown in Figure 1 and Figure 2, the sea level is higher, the sea level rough degree is bigger, and the waves rolled more violently.

As to the Ka band, the size of the rough surface is much greater than the wavelength, so rough sea belongs to the electrically large targets [7]. For electromagnetic simulation, at first, the waves model is built; Then put it in the electromagnetic simulation software to divide PO grid; At last, electromagnetic simulation model is generated. The scenario of ray path tracing is as shown in Figure 3. Direct path represents there is no obstacle between the launch and receiving station; Hop path includes reflection propagation and diffraction propagation.

For receiving station, its energy is contributed by a variety of rays. Because after hopping 3 times on the sea surface, the rays' energy have been very little, we just consider of direct rays and the rays that hop not more than 3 times. According to the electromagnetic simulation, we can obtain propagation characteristics of wireless channel and rays' path length, delay time and power at the receiver.

3. STOCHASTIC BRIDGE CHANNEL MODELING

The really propagation path of electromagnetic wave on the sea surface is uncertain. In mobile communications field, taking the multipath as a sample of random bridge process has been widely used [8–10]. Stochastic bridge is defined as followed: if the stochastic process $\{Y(t, \omega)\}$ meets the condition $\forall_0 \leq t \leq T$, and

$$Y_{0,r_0}^{T,r_1}(t, \omega) = r_0 + X(t, \omega) - \frac{t}{T} [X(T, \omega) - r_1 + r_0] \tag{1}$$

where, $Y_{0,w}^{T,w}(0, \omega) = r_0$, $Y_{0,w}^{T,w}(T, \omega) = r_1$, r_0 is the start point, and r_1 is the end point. Stochastic process $X(t, \omega)$ can be described by a stochastic differential equation. According to the different stochastic bridge variance and the number of paths, we can generate different samples of radio path. The parameter of the stochastic bridge is determined by the simulation of the electromagnetic.

We can get digital features of random variables on the basis of electromagnetic simulation based on GTD. Then, path length of random rays can be calculated. At last, We can obtain the time delay of the multipath component further. Under the condition of omni-directional antennas, assume that the direct signal $a_0 = 1$, multipath component amplitude (normalized) is as followed:

$$|a_{ij}| = \left(\frac{z_{ij}}{z_0} \right)^{-n/2} 10^{-\frac{1}{20} \left[\sum_{k=0}^i L_{ijk} + L_{ij} \right]} \quad (2)$$

where, Z_{ij} is the path length, and i stands for hopping i times, j stands for the j -th multipath component; Z_0 is the length of direct wave; For free space $n = 2$; L_{ijk} include reflection loss and diffraction loss, when the ij -th multipath component occurs the k times hop; L_{ij} is the atmospheric absorption loss of the ij -th multipath component. According to the above analysis, expression of channel impulse response is:

$$h(t, \tau) = \sum_{i=0}^N \sum_{j=1}^{Mi} p_{ij} |a_{ij}| \delta(\tau - \tau_{ij}(t)) \quad (3)$$

where P_{ij} represents the phase delay, $P_{ij} = \exp(j2\pi Z_{ij}/\lambda)$, j is the imaginary number; λ is wavelength of radio wave, τ_{ij} is the time delay of the multipath component.

4. SIMULATED ANALYSIS

The electromagnetic simulation conditions is as followed: The incident wave is a plane wave and the vertical polarization; The radial direction is the connecting line of radiation sources and observation point. Source location is set at the elevation direction of 5 degrees, and the height of it is 40 km above the sea surface; The receiving station is 10 m above the sea surface; The incident wave frequency is 30 GHz; The electromagnetism emulational sea is level 1, level 3, and level 5. Through the many times electromagnetic simulation for every sea condition, the mean value of number of hop rays corresponding to different sea condition is shown as followed.

There almost have no rays that thought once, twice and triple reflection can reach the receiver. As shown in Table 1, Most of the arrival rays is once diffraction. When the sea is flat, there almost is no once reflection plus once diffraction rays. Because the reflection loss is much smaller diffraction loss, even if the number of once reflection plus once diffraction rays is less than once diffraction rays, the once reflection plus once diffraction rays have big disturbance on direct path as once diffraction rays.

We assume the amplitude of direct signal is 1. Direct signal is only under the influence of path loss, and its actual amplitude is $3.9866 * 10^{-10}$. Figures 4–6 show the the impulse response of all the multipath components except the direct signal. The time delay in Figures 4–6 is relative time delay that relative to direct path. The channel impulse response of multipath components that are through reflection to arrive at the receiver have random amplitude and relative delay. As shown in Figures 4–6, we can see that multipath components have the large disturbance on direct path. With the increase of time delay, the amplitude of multipath components decrease, and with the increase of the sea level, that is to say the fluctuation of sea level is more severe, the number of components increase, the time delay is longer.

In order to validate the established model, calculate the ratio of channel input signal and output signal, then compare with RCS value that exist in literature of electromagnetic scattering characteristics of sea surface. The stochastic bridge simulation results is basically the same with the conclusions of the existing literature. So, we can draw a conclusion that stochastic bridge model can describe the channel characteristic of sea surface scattering environment.

Table 1: The mean value of number of hop rays corresponding to different sea condition.

Sea condition	The mean value of number of hop rays			
	Once reflection plus once diffraction	Once diffraction	Twice diffraction	Triple diffraction
Level 1	1	316	27	57
Level 3	68	305	49	63
Level 5	47	229	37	29

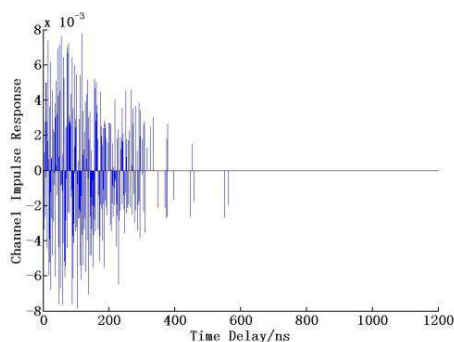


Figure 4: Channel impulse response of primary wave.

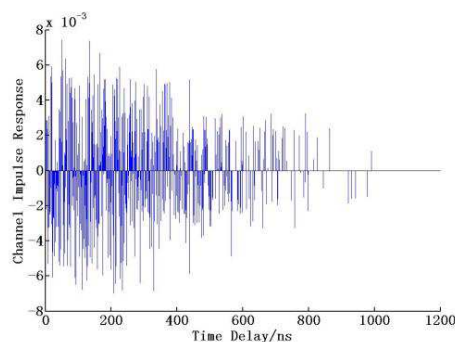


Figure 5: Channel impulse response of three stage wave.

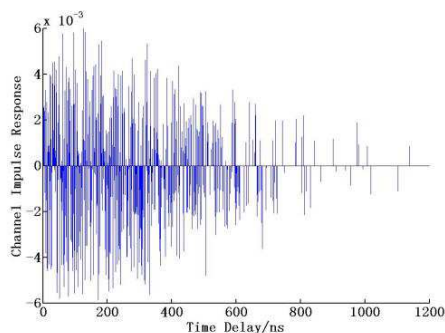


Figure 6: Channel impulse response of five level wave.

5. CONCLUSION

In this paper, we present a channel modeling technique based on GTD and stochastic bridge. At first, random rough ocean surface modeling present the displacement of sea surface under various wind speeds, and provide the basic for electromagnetic simulation of telecommunication channel. Then, electromagnetic simulation based on GTD algorithm present a huge data ocean surface reflection, scattering and diffraction, which determine the numerical characteristics of stochastic bridge and act as the samples for channel modeling. At last, a multipath channel model based on stochastic bridge provide the channel impulse response under typical ocean states. We can see clearly that the channel modeling technique we present do without a high requirement for experimental environment and conditions, and its calculation is less complicated compared with ray tracing method.

The simulations reveal that the established channel model can reflect the essential properties of radio waves propagation channel on the sea surface, and also can be verified its correctness. We can obtain the output signal based on the convolution of impulse response and the input signal, which may boost the usage of low elevation angle Ka or higher frequency satellite down-link radio propagation prediction and estimation.

ACKNOWLEDGMENT

This paper is funded by the International Exchange Program of Harbin Engineering University for Innovation-oriented Talents Cultivation. This work was also partially supported by the Navy Defense Foundation of China (4010403020102), the Science and Technology innovative Talents Foundation of Harbin (2013RFXXJ083), the Foundational Research Funds for the Central Universities (HEUCF131602, HEUCFD1433).

REFERENCES

1. Bullington, K., "Radio propagation at frequencies above 30 Megacycles," *Proceedings of the IRE — Waves and Electrons Section*, Vol. 10, 1222, 1946,.
2. Richards, J. A., *Radio Wave Propagation: An Introduction for the Non-specialist*, 6–10, Springer, 2008.

3. Hu, L. and H. Zhu, “Bounded brownian bridge model for UWB indoor multipath channel,” *IEEE Int. Symp. on Microwave, Antenna, Propagation and EMC Technol. for Wireless Commun. Proc.*, 1406–1409, Beijing, China, Aug. 2005.
4. Mouche, A. A., B. Chapron, and N. Reul, “A simplified asymptotic theory for ocean surface electromagnetic wave scattering,” *Waves in Random and Complex Media*, Vol. 17, No. 3, 321–341, 2007.
5. Kuga, Y. and P. Phu, “Experimental studies of millimeter-wave scattering in discrete random media and from rough surface,” *Progress In Eletromagnetics Reseach*, Vol. 14, No. 1, 37–88, 1996.
6. Elfouhaily, T., B. Chapron, K. Katsaros, et al., “A unified directional spectrum for long and short wind-driven waves,” *J. Geophys. Res.*, Vol. 102, 15781–15796, 1997.
7. Huang, H., D. Wang, and F. Liu, “Modeling of Ka-band mobile satellite channel and ber performance analysis,” *Journal of University of Science and Technology of China*, Vol. 35, No. 3, 346–353, 2005.
8. Hu, L. Q., *Stochastic Modeling and Applications for Radio Wave Propagation*, Huazhong University of Science and Technology Press, 2011.
9. Primak, S., V. Kontorovitch, and V. Lyandres, *Stochastic Methods and Their Applications to Communications: Stochastic Differential Equations Approach*, John Wiley & Sons, Inc., NY, 2004.
10. Molisch, A. F., A. Kuchar, J. Laurila, et al., “Geometry-based directional model for mobile radio channels-principles and implementation,” *European Transactions on Telecommunications*, Vol. 14, No. 4, 351–359, 2003.

New Intuitive Metrics for Diversity Performance Evaluation of Multi-element Antenna Systems

Vasileios C. Papamichael¹ and Petros Karadimas²

¹Department of Electrical Engineering, Technological Educational Institute of Western Greece and Wireless Systems Performance (WiSPer), Patras 26441, Greece

²Department of Computer Science and Technology, University of Bedfordshire, Luton LU1 3JU, UK

Abstract— Diversity performance of multi-element antenna (MEA) systems is evaluated using several metrics. The most common are the diversity antenna gain (DAG), the effective diversity gain (EDG) and the actual diversity gain (ADG). These metrics calculate the performance by comparing the MEA system with the reference antenna at a fixed outage probability level, i.e., usually at 1% outage level. As fixed outage levels are just an indication of probability of occurrence of specific signal levels, they provide limited insight into realistic deep-fade cases. Thus, we introduce three novel metrics, namely, the fading mitigation gain (FMG), the reliability percentage (RP) and the generalized diversity antenna gain (GDAG) for characterizing diversity performance when deep fades take place in one or more of the diversity branches. Based on the aforementioned metrics, intuitive knowledge on the diversity performance of MEA systems is provided.

1. INTRODUCTION

The mitigation of multipath fading is an issue of primary importance in wireless communications systems. Multi-element antenna (MEA) systems combat fading through diversity combining, which potentially increases the received power.

Until now, several metrics for the diversity performance have been proposed, with the most important being the diversity antenna gain (DAG) [1], the effective diversity gain (EDG) [2] and the actual diversity gain (ADG) [3]. They are derived by comparing the cumulative distribution functions (CDFs) of the received signal-to-noise ratio (SNR) of the MEA and that of a reference antenna at a specific outage probability level (usually 1% outage probability level). Their only difference lies on the choice of the reference antenna. The DAG is based on comparing the MEA with an isotropic, dual polarized reference antenna and is thus a metric of universal applicability when deriving diversity performance. The EDG arises by comparing the MEA with one of its single elements having 100% efficiency and the ADG by comparing the MEA with an arbitrarily selected antenna. Thus, both EDG and ADG are not of such universal applicability as the DAG, as they are strongly dependent on the chosen reference antenna.

As the CDF just presents probabilities of specific SNR levels, DAG, EDG and ADG do not account for performance provided by a MEA system when only deep fades take place in one or more of the diversity branches. Performance in such cases only would be a better indicator of how effectively the MEA system combats fading. Moreover, the estimated percentage of the cases where the MEA's received SNR is greater than that of the reference antenna would also provide further insights into the performance of MEA systems. Thus, in this paper, three new intuitive metrics focusing on deep-fade cases are proposed. The first metric is called *fading mitigation gain* (FMG) and accounts for the performance when at least one of the diversity branches of the MEA system has 20 dB less power with respect to the average received power of the reference antenna¹. It is thus a random variable. The second is called *reliability percentage* (RP) and accounts for the percentage of the cases when the MEA system has greater received power compared with that of the reference antenna. The third is called *generalized diversity antenna gain* (GDAG) and arises after weighting the two DAGs, i.e., the DAG (weighted by RP) when the MEA received power is greater than that of the reference antenna and the DAG (weighted by 1-RP) when is lower. An isotropic dual polarized reference antenna is considered as in [1], thus, for consistency, we maintain the term DAG in GDAG. The MEA systems and propagation environments are jointly modeled by using the stochastic approach presented in [4].

The remainder of this paper is organized as follows: In Section 2, the three new metrics, i.e., the FRG, RP and GDAG are defined. In Section 3, relevant results are presented considering a two-port compact MEA system and Section 4 draws the conclusion.

¹Considering equal noise powers between the reference antenna and the MEA system, we can consider the received power instead of the SNR.

2. NEW PERFORMANCE METRICS

2.1. Fading Mitigation Gain (FMG)

We consider A as the difference in dB of the mean received power of the reference antenna $E\{P_{ref}\}$ and a predetermined power threshold K , such that a deep fade region has resulted with respect to the mean received power of the reference antenna, e.g., $K = 20$ dB for a 20 dB deep fade region. Thus,

$$A_{dB} = E\{P_{ref}\}_{dB} - K_{dB}. \quad (1)$$

We define FMG over A as the power gain in dB that the MEA system provides when the received power of at least one of the MEA's ports is below A . Thus,

$$FMG_K = P_{div, dB} |_{\text{at least one of } P_1 \dots P_n \leq A_{dB}} - A_{dB} \quad (2)$$

where P_{div} is the power of the combined signal according to the selected diversity scheme. In (2), we use the subscript K in FMG, i.e., FMG_K , because FMG has an obvious dependence on K . It is also obvious that FMG_K is a random variable.

2.2. Reliability Percentage (RP) and Generalized Diversity Antenna Gain (GDAG)

The RP is defined as the percentage of cases where the MEA's received power is greater than the reference antenna's ones. Based on the RP, we define GDAG as

$$GDAG = RP \cdot DAG_1 + (1 - RP) \cdot DAG_2 \quad (3)$$

where DAG_1 is the diversity antenna gain evaluated when the MEA's received power is greater than the reference antenna's ones and DAG_2 when is lower.

3. RESULTS AND DISCUSSION

As a case study, we consider the two-port MEA system depicted in Fig. 1. It comprises of two inverted-F elements which have selected due to their wide bandwidth, high efficiency, omnidirectional radiation pattern and ease of fabrication. For more details about this system see [5]. The configurations depicted in Fig. 1 were simulated using IE3D, a commercial method of moment based electromagnetic field solver [6]. Also, an isotropic, dual polarized reference antenna was employed [1].

FMG_K is evaluated from (1) and (2) using the stochastic electromagnetic-circuit methodology under an isotropic propagation scenario [4]. Maximal ratio combining (MRC) is the employed diversity scheme. In Fig. 2 the CDF of the FMG_K is illustrated when $K = 20$ dB and $E\{P_{ref}\} = 0$ dB. FMG_{20} is more than 6.3 dB for 90% of the cases when the power of at least one of the received signals is below the 20 dB deep fade characterized by A . It is important to mention that 20 dB deep fades take place in only 4.8% of the whole ensemble of received powers. For other cases with less than 20 dB deep fades, FMG_K is even better. Useful statistics are also the mean value of FMG_{20} which is 13.8 dB and its standard deviation which is 5.2 dB. Thus, on average, in the 20 dB deep fade region, the combined signal will be only 6.2 dB less than that of the reference antenna whereas the signal of a single port antenna will be less by 20 dB. Such informative insights into the diversity performance of MEA systems cannot be provided by DAG, EDG or ADG.

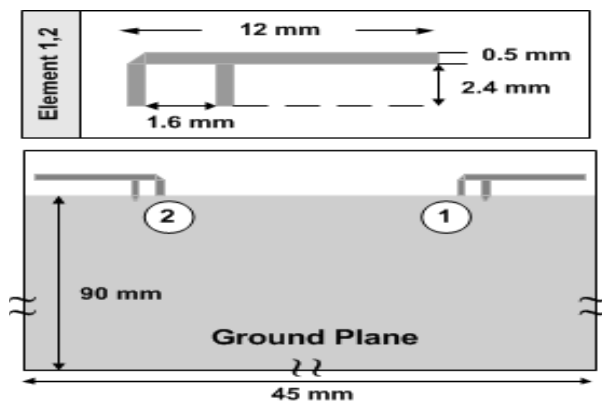


Figure 1: The layout of our two-port MEA system.

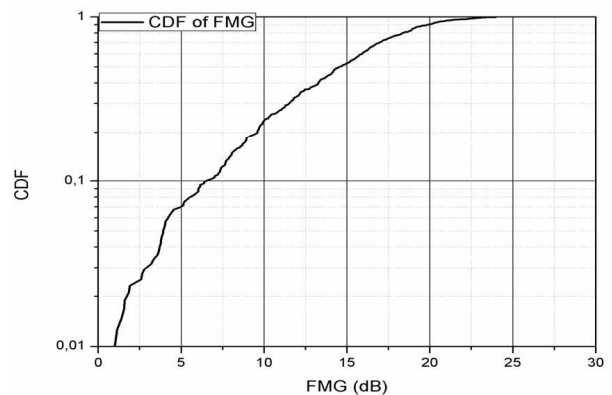


Figure 2: The CDF of FMG_{20} under MRC diversity.

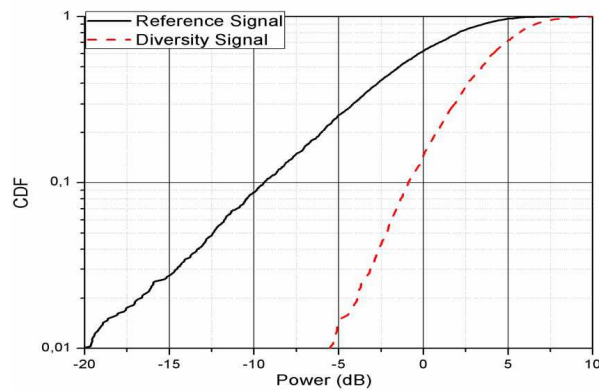


Figure 3: The CDFs of the reference antenna and the MEA system power when the MEA system's power is greater than the reference antenna's.

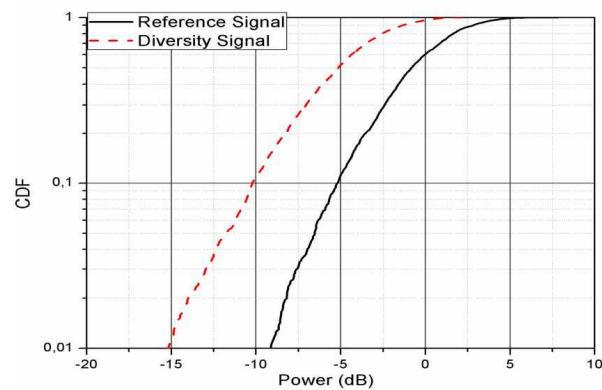


Figure 4: The CDFs of the reference antenna and the MEA system power when the MEA system's power is less than the reference antenna's.

The remaining two metrics which have evaluated are the RP and the GDAG. According to its definition in Section 2, RP was evaluated as 51%, which means that for almost half of time the MEA system performs better than the reference antenna. The GDAG is calculated from (3) using the data plotted in Figs. 3 and 4. It is found to be 4.5 dB at 1% outage probability level. More specifically, DAG_1 is 14.8 dB and DAG_2 is -6.1 dB. The latter means that when the reference antenna outperforms the MEA system, the loss in DAG is only 6.1 dB and when the opposite holds the gain is 14.8 dB. For the same MEA system, the DAG as defined in [1], was calculated in [4] and was found to be 7.8 dB. That value, as well those provided by EDG and ADG, hide information as provided by RP, DAG_1 , DAG_2 and GDAG. GDAG is thus a more realistic diversity performance indicator, since it gives the average value of gain according to its sophisticated definition.

4. CONCLUSION

In this paper, the diversity performance of MEA systems was revisited. Three novel informative metrics provided new insights into diversity performance. FMG characterizes the performance in deep-fade regions, where, in fact, their occurrence is the only reason of using MEA systems. The ultimate performance indicator is the GDAG which takes into account both the “good” and “bad” scenarios of operation of MEA systems. Based on our analysis and results, the commonly used metrics DAG, EDG and ADG give an opportunistic picture of the diversity performance since they do not exclusively focus on the “bad” scenarios, i.e., when the reference antenna outperforms the MEA system. As a matter of fact, in 49% of the time the reference antenna provides more power than our two-port MEA system and this necessitates the use of GDAG to characterize performance.

REFERENCES

1. Ogawa, K. and J. Takada, “An analysis of the effective performance of a handset diversity antenna influenced by head, hand, and shoulder effects — A proposal for a diversity antenna gain based on a signal bit error rate and analytical results for the PDC system,” *Electronics and Communications in Japan*, Part 2, Vol. 84, No. 6, 852–865, 2001.
2. Kildal, P., K. Rosengren, J. Byun, and J. Lee, “Definition of effective diversity gain and how to measure it in a reverberation chamber,” *Microwave Optical Technology Letters*, Vol. 34, No. 1, 56–59, 2002.
3. Plicanic, V., B.-K. Lau, A. Derneryd, and Z. Ying, “Actual diversity performance of a multi-band diversity antenna with hand and head effects,” *IEEE Transactions on Antennas and Propagation*, Vol. 57, No. 5, 1547–1556, May 2009.
4. Papamichael, V. and C. Soras, “Generalised selection combining diversity performance of multi-element antenna systems via a stochastic electromagnetic-circuit methodology,” *IET Microwaves, Antennas and Propagation*, Vol. 4, No. 7, 837–846, Jul. 2010.
5. M. Karaboikis, V. Papamichael, G. Tsachtisiris, C. Soras, and V. Makios, “Integrating compact printed antennas onto small diversity/MIMO terminals,” *IEEE Transactions on Antennas and Propagation*, Vol. 56, No. 7, 2067–2078, Jul. 2008.
6. Zeland Software Inc., IE3D, <http://www.zeland.com/>.

Double Broadband Balun Structure Using CRLH TL for Differential Excitation of Dual-polarized Self-grounded Bow-tie Antenna

Sadegh Mansouri¹, John Kvarnstrand², Andrés Alayon Glazunov¹,
Jian Yang¹, and Per-Simon Kildal¹

¹Department of Signals and Systems, Chalmers University of Technology, Gothenburg, Sweden

²Bluetest AB, Gothenburg, Sweden

Abstract— A broadband compact balun comprising two composite right-left handed transmission lines (CRLH TL) is designed to excite a self-grounded bow-tie antenna. The design is based on a fractal shaped CRLH TL balun modified to the frequency band of interest. This balun consists of one $+90^\circ$ branch and three -90° branches to produce the desired 180° phase difference at the output. The simulated results show an amplitude imbalance of less than 1 dB and a phase imbalance of less than 10° over most of the target bandwidth, i.e., 1.6–3 GHz. Two of the designed baluns were integrated with the bow-tie antenna in such a way that the feeding network could totally fit at the back of the antenna. The performance of the whole structure was also evaluated showing a return loss below -10 dB. The radiation pattern and the gain of the antenna with baluns are in good agreement with the ideal differential excitation, with gain degradation of only about 0.5 dB in the worst case.

1. INTRODUCTION

It is well-known that the use of multiple port antennas at both the transmitter and the receiver sides of a communication link can improve the wireless communication system performance in terms of capacity and reliability for a given system bandwidth and transmitted power [1]. These so-called Multiple Input Multiple Output (MIMO) systems are at the core of 4G, 5G and the beyond wireless systems. In that respect, communication over orthogonally polarized wireless channels will be essential to achieve the anticipated performance. Therefore designing antennas for base stations is of paramount significance to meet performance requirements. In 5G there is a particular interest in wideband micro-base stations that perform well both in rich isotropic multipath (RIMP) and in Random-Line-Of-Sight (RLOS) [2, 3]. In addition, multi-port dual polarized wideband antennas can be used in many other applications. For example, in the Over-The-Air (OTA) testing of autonomous cars in a RLOS testing environment, a dual polarized uniform linear array antenna has been proposed as an essential part of the testing procedure [4]. One promising candidate for the array antenna element in such applications is the 4-port self-grounded bow-tie antenna [5]. This antenna can be used to provide a compact realization of a wideband dual-polarized antenna. However, in order to achieve the dual polarized performance by differentially exciting two ports of the bowtie antenna, we need to incorporate two baluns together with the antenna design. Each balun excites two opposite pedals of the bow-tie with a 180 degrees phase difference and $50\ \Omega$ input impedance. So the antenna will produce two orthogonal polarizations. These baluns should satisfy the required bandwidth constraint (1.6–3 GHz) and they also should have a compact structure in order to maintain a low profile. Despite the wideband characteristics of conventional microstrip baluns [6, 7], they do not meet our compactness requirement. Furthermore, multilayer Marchand baluns [8] provide a very compact volume. On the other hand they suffer from high manufacturing complexity and cost. Another option for the balun is the Composite Right Left Handed (CRLH) Transmission line (TL) which exploits the phase advance of the left handed materials [9–11]. In this paper, we employ the fractal shaped CRLH TL balun presented in [9] as a starting point of the design, but modify it to the frequency band of interest.

2. BALUN DESIGN PRECEDURE AND RESULTS

Figure 1(a) shows the phase variation with frequency of the 90° and the 270° transmission lines which are derived from the formula $\varphi = 2\pi d/\lambda$, where λ is the wavelength and d is the length of the transmission line. Also, the frequency dependence of the phase for the LH and CRLH TL is shown in this figure. The LH and CRLH TL are designed to have a phase equal to 90° at the center frequency of 2 GHz based on the following procedure. As we can see in this figure, a 270° TL is much more frequency dependent as compared to the 90° TL. Also, in practice, the physical length of the soldering pads of the elements results in having CRLH TL instead of a perfect LH TL. Thus,

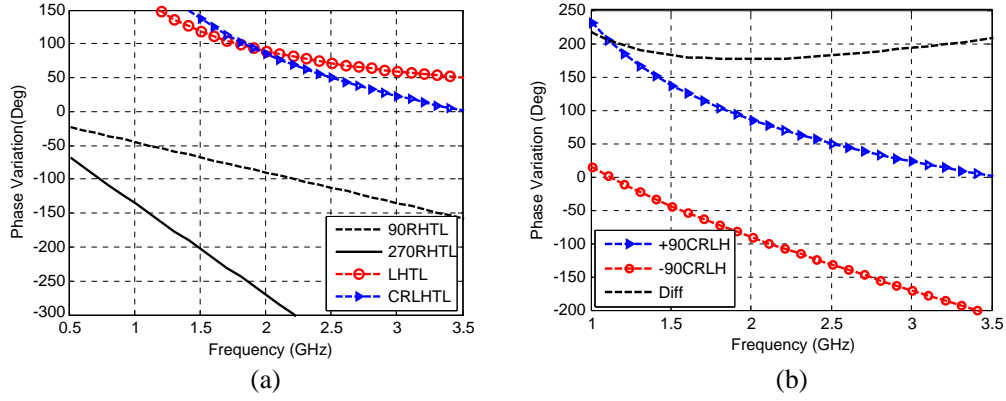


Figure 1: Phase variation of (a) 90° and 270° RHTL, LHTL and CRLHTL, (b) $+90^\circ$ CRLH and -90° CRLH and the difference.

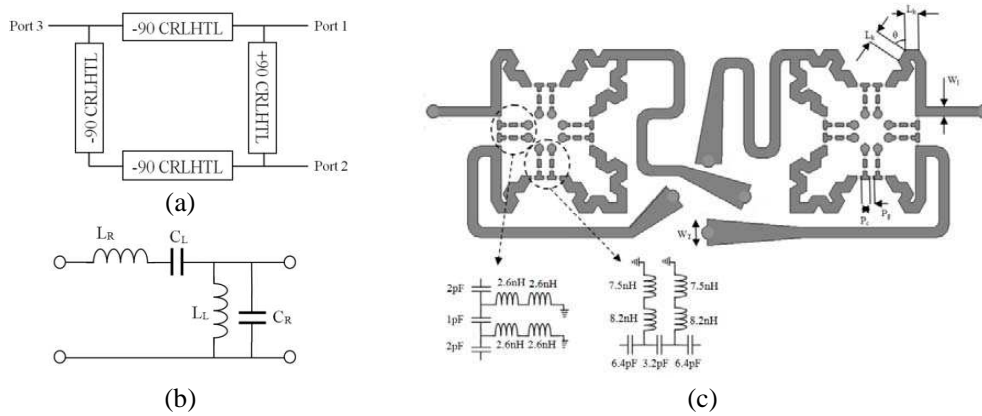


Figure 2: (a) Balun structure, (b) CRLH TL circuit model, (c) dual balun geometry

in order to meet the phase requirements, a CRLH TL is considered for both the 90° and the -90° branches.

The schematic representation of the balun and the circuit model of each CRLH TL are shown in Figures 2(a) and (b), respectively. As can be seen from Figure 2, each TL comprises a righthanded part represented by capacitor C_R and inductor L_R as the electrical equivalent of the line itself and a lefthanded part provided by the corresponding lumped elements. The balun has one 90° branch and three -90° branches.

Now, we present some conditions that are necessary to meet the phase and the amplitude requirements. First, the following condition should be satisfied for impedance matching [12]

$$Z_{C+} = \frac{Z_{C-}}{\sqrt{2Z_{C-} - Z_0}} Z_0, \quad (1)$$

where Z_{C+} and Z_{C-} are the characteristic impedances of the $+90^\circ$ and -90° branches, respectively and Z_0 is the port impedance which is 50Ω . Further assuming that Z_{C+} and Z_{C-} are equal, we obtain from (1) that $Z_{C+} = Z_{C-} = \sqrt{2}Z_0$. Secondly, we need to achieve the 180° phase difference between the output ports. The phase response of each branch can then be presented by

$$\varphi_{CRLHTL}(\omega) = -N \left(\omega \sqrt{L_R C_R} - \frac{1}{\omega \sqrt{L_L C_L}} \right), \quad (2)$$

where N is the number of CRLH cells in each branch and equals two in our case. Furthermore, in order to obtain the 180° phase difference over the required bandwidth, we set the first derivative of the phase difference respect to angular frequency equal to zero at 2 GHz. By enforcing this condition, a minimum would be appearing in $\varphi_{diff} = \varphi_{CRLHTL+} - \varphi_{CRLHTL-}$ at 2 GHz with a slow varying slope of phase difference around this frequency providing the phase requirements over the

entire bandwidth (Figure 1(b)). Using (1) and (2) together with the zero derivative condition, we can find the values of the elements of the CRLH cells in each branch. There are also some additional considerations for choosing these values. First, due to practical reasons, lumped elements should have commercially available values. Second, these values should not be large. This condition arises from the self-resonance frequency of the lumped elements above which the performance of the elements would change attributed to parasitic capacitance and inductance effects. Since elements with larger values have smaller resonance frequencies, they experience degradation in performance at higher frequencies. The third consideration is for the values which are equivalent to the length of the $+90^\circ$ branch. This length should be kept small and its minimum length will be determined, among other things, by the size of the soldering pads used in the $+90^\circ$ branch. After considering above mentioned criteria, the calculated values are shown in Table 1. The phase response of the balun outputs and the difference between these two branches calculated by using derived values are shown in Figure 1(b).

In this design, the fractal structure is used to achieve the desired compactness. A $36\text{ mm} \times 100\text{ mm}$ Rogers RO4003 with dielectric constant of 3.55 and thickness of 1.52 mm is used as substrate. The initial dimensions of the fractal structure are based on the calculated values and formula in [13] and the electrical length of transmission line for the given values of C_R and L_R . Then by using CST Microwave Studio, a parametric study was performed to optimize the dimensions including length of the meandered TLs considering standard soldering pad sizes. For our application, we integrated two baluns with the bow-tie antenna in such a way that the dual balun could totally fit at the back of the antenna. Four transmission lines were added to the outputs of the balun to feed the bowtie antenna pedals. In order to provide the same phase shift, they were chosen to have the same length. In addition, some tapering has been applied for impedance matching. The geometry of the balun is shown in Figure 2(c) with parameters given in Table 2. The schematic circuit model for the lumped elements is detailed in Figure 2(c). The structure of the lumped element has been chosen in such a way to reduce the self-resonance effect of capacitors and inductors.

The S parameters of the designed dual balun are shown in Figure 3(a). As illustrated, the amplitude of S_{11} is better than -10 dB at $1.6\text{--}3\text{ GHz}$. Figure 3(b) shows the amplitude and phase imbalance. The amplitude imbalance remains almost less than 1 dB over most of the frequency band and the phase difference stays within $\pm 10^\circ$.

Table 1: Calculated values of capacitors and inductors in CRLH circuit model of the $+90^\circ$ and the -90° branches.

C_{L-}	L_{L-}	C_{R-}	L_{R-}	C_{L+}	L_{L+}	C_{R+}	L_{R+}
3.2 pF	15.8 nH	1.3 pF	6.5 nH	1 pF	5 nH	0.4 pF	2 nH

Table 2: Designed balun parameters.

W_l	W_T	L_k	P_c	P_g	θ
2.55 mm	4 mm	2.15 mm	1.35 mm	0.6 mm	30 degrees

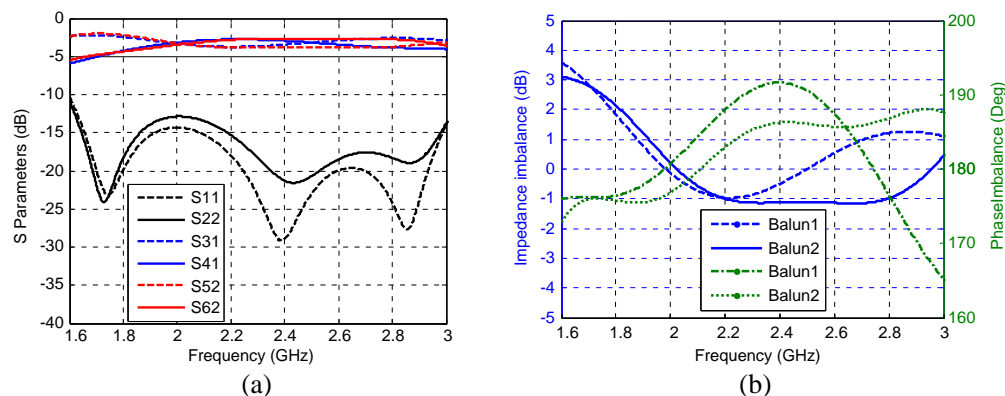


Figure 3: (a) S parameters of baluns. (b) Impedance and phase imbalance of the outputs.

3. BALUN INTEGRATION WITH THE BOW-TIE ANTENNA

The dual balun structure is integrated with the self-grounded bowtie antenna as shown in Figures 4(a) and (b). The dual balun completely fits into the area of the back side of the antenna with the four outputs connected to the each of the four pedals of the bow-tie. The reflection coefficients of the dual balun integrated with the bow-tie antenna and an ideal differentially excited bow-tie antenna are shown in Figure 4(c). To provide a more complete picture of the performance of the balun, the reflection coefficients of the dual balun alone are also included in the figure. As can be seen, the return loss will remain below -10 dB for most of the required bandwidth (1.67–3 GHz).

The radiation patterns of the bow-tie antenna integrated with the balun and the ideal excitation at the frequencies 1.6 GHz, 2.1 GHz and 3 GHz are shown in Figures 5(a), (b) and (c), respectively.

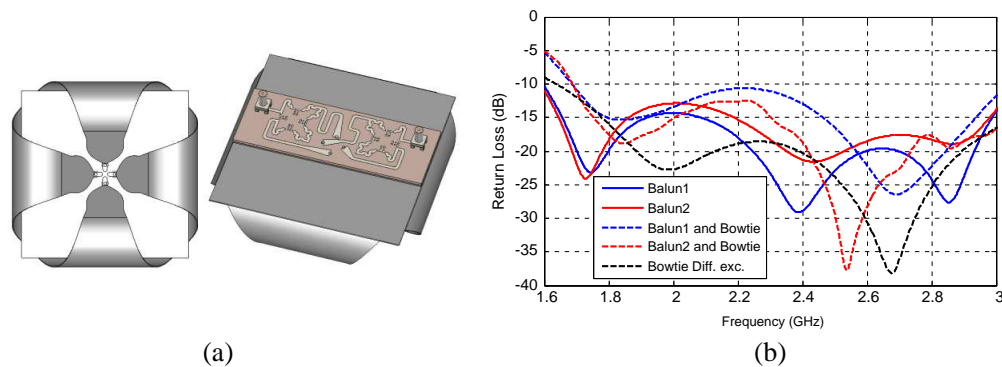


Figure 4: (a) Selfgrounded bow-tie antenna. (b) Balun attached to the back of the bow-tie. (c) Return loss of the bow-tie antenna fed with balun, differentially excited bow-tie and each balun.

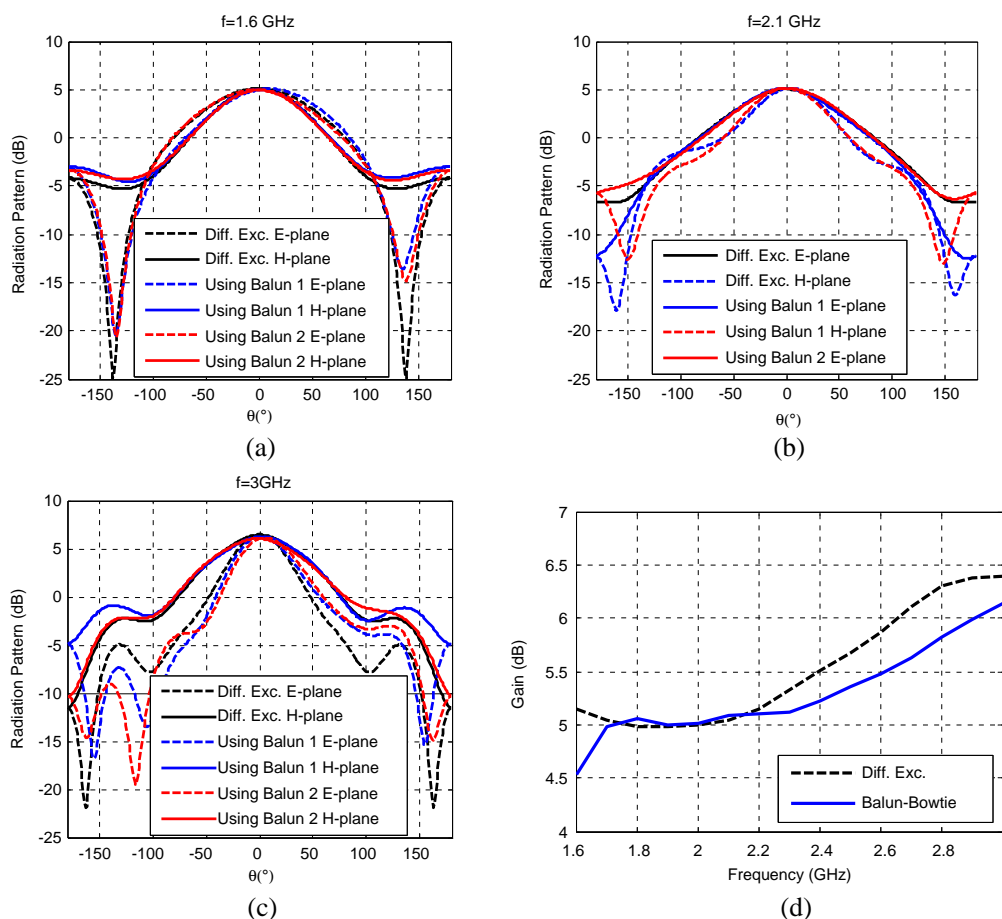


Figure 5: Antenna radiation pattern at (a) 1.6 GHz, (b) 2.1 GHz and (c) 3 GHz, and (d) gain of the bow-tie antenna with balun compared with the ideal differential excitation.

The antenna gain as function of frequency is shown in Figure 5(d). As can be seen, using the dual balun reduces the antenna gain about 0.5 dB at most. The side-lobes levels increase up to 2.5 dB at the higher frequencies and the shape of the symmetry of the pattern will be only slightly perturbed due to the magnitude and phase imbalance of the balun.

4. CONCLUSION

A compact and broadband dual balun was design for differential excitation of a dual polarized bow-tie antenna. For the balun design, CRLH TLs were used to achieve the desired bandwidth and compactness characteristics. The reflection coefficient of the simulated balun was less than -10 dB in the frequency band of 1.6–3 GHz. The amplitude and the phase imbalances were approximately less than 1 dB and 10° , respectively. In addition, the balun structure integrated with the self-grounded bow-tie antenna has shown very good simulated performance. For example, the radiation pattern of the whole structure was in good agreement with the ideal differentially excited bow-tie antenna with a gain reduction of only 0.5 dB. The reflection coefficient remained below -10 dB mostly over the entire bandwidth. Further work will include the verification of the design by measurements, as well as their evaluation in numerical and experimental Over-The-Air (OTA) setups.

REFERENCES

1. Molisch, A. F., *Wireless Communications*, 2nd Edition, John Wiley, New York, 2010, ISBN: 978-0-470-74186-3.
2. Kildal, P.-S., “Rethinking the wireless channel for OTA testing and network optimization by including user statistics: RIMP, pure-LOS, throughput and detection probability,” *SAP 2013*, Nanjing, China, Oct. 2013.
3. Kildal, P.-S., X. Chen, M. Gustafsson, and Z. Shen, “MIMO characterization on system level of 5G micro base stations subject to randomness in LOS,” *IEEE Access.*, Vol. 22, 1062–1075, Sep. 18, 2014.
4. Kildal, P.-S., A. A. Glazunov, J. Carlsson, and A. Majidzadeh, “Cost-effective measurement setups for testing wireless communication to vehicles in reverberation chambers and anechoic chambers” *2014 IEEE Conference on Antenna Measurements & Applications (CAMA)*, 1–4, Nov. 16–19, 2014, Doi: 10.1109/CAMA.2014.7003428.
5. Raza, H., A. Hussain, J. Yang, and P.-S. Kildal, “Wideband compact 4-port dual polarized self-grounded bowtie antenna,” *IEEE Trans. Antennas Propag.*, Vol. 62, No. 9, 4468–4473, Sep. 2014.
6. Wu, P., Z. Wang, and Y. Zhang, “Wideband planar balun using microstrip to CPW and microstrip to CPS transmissions,” *Electron. Lett.*, Vol. 46, No. 24, 1611–1613, Nov. 2010.
7. Zhang, Z. Y., Y. X. Guo, L. C. Ong, and M. Y. W. Chia, “A new wide-band planar balun on a single-layer PCB,” *IEEE Microwave and Wireless Components Letters*, Vol. 15, No. 6, 416–418, 2005.
8. Lan, X., F. Fong, M. Kintis, K. Kono, D. Yamauchi, W. B. Luo, and D. Farkas, “An ultra-wideband balun using multi-metal GaAs MMIC technology,” *IEEE Microwave and Wireless Components Letters*, Vol. 20, 474–476, Aug. 2010.
9. Xu, H.-X., G.-M. Wang, X. Chen, and T.-P. Li, “Broadband balun using fully artificial fractal-shaped composite right/left-handed transmission line,” *IEEE Microwave and Wireless Components Letters*, Vol. 22, No. 1, 16–18, 2012.
10. Fan, L., C. H. Ho, and K. Chang, “Wide-band reduced-size uniplanar magic-T, hybrid-ring, and de Ronde’s CPW-slot couplers,” *IEEE Trans. Microwave Theory Tech.*, Vol. 43, 2749–2758, Dec. 1995.
11. Okabe, H., C. Caloz, and T. Itoh, “A compact enhanced-bandwidth hybrid ring using an artificial lumped-element left-handed transmission-line section,” *IEEE Trans. Microwave Theory Tech.*, Vol. 52, No. 3, 798–804, Mar. 2004.
12. Li, J.-L., S.-W. Qu, and Q. Xue, “Miniaturised branch-line balun with bandwidth enhancement,” *Electron. Lett.*, Vol. 43, No. 17, 931–932, Aug. 2007.
13. Bahl, I., *Lumped Elements for RF and Microwave Circuits*, Chapter 14, 462–465, Artech House, Boston, MA, 2003,

Research on Random Wireless Channel of Radio Indicator for Mariners

Tao Jiang¹, Xiaodong Cao¹, Xiaojun Wang^{1,2}

¹College of Information and Communication Engineering, Harbin Engineering University, China

²Electrical and Computer Engineering Department, National University of Singapore, Singapore

Abstract— It is presented a random wireless channel model of marine emergence radio indicator in this paper, which describe the performance of telecommunications in difference typical ocean states. First, it is introduced a random rough ocean surface modeling method under typical ocean states which is the foundation for simulation of LOS and NLOS telecommunication channel. Second, massive data is calculated by running simulation code which is necessary for statistical analysis of linking properties. Last, the telecommunication performance is predicted by signal to noise ratio vs bit rate error in situation of typical ocean states and elevation angles which may provide key information for the design of next generation of marine indicators.

1. INTRODUCTION

Because the sea is rich in Marine products and mineral resources, it is very important to observe, research and reasonable use the the oceans. Thought a random rough ocean surface modeling under typical ocean states, we can get the background information of the sea-surface. The electromagnetic environment of the surface is very complicated. So, radio waves propagation on the surface of the time domain modeling theory and technology should be provided to research the target detection and recognition of sea surface. There is no doubt that the impact of sea clutter to the communication link is an important issue to evaluate and demonstrate [1].

Radio waves propagation of free space is divided into Line-of-sight propagation (LOS) and Non-light-of-sight propagation (NLOS). LOS is that space wave can communicate between two points in direct. In other words, there is direct path between launch and receiver. The distance of LOS is similar with the distance as far as the eyes can see, and it is generally not more than 50 km. LOS can be divided into two types. One of them is direct wave propagation. Radio wave spread by transmitting antenna go the straight line like the light to reach the receiver directly. The other one is reflection wave propagation. Radio wave transmitted by the antenna, thought the reflection, reaches the receiver finally. The waves of LOS received at the receiver is synthesized from direct wave and reflected wave. NLOS has no direct wave. We research the LOS when the radio wave spread on the sea surface [2].

According to random rough ocean surface modeling and then electromagnetic simulation, we can obtain statistical analysis of linking properties and model wireless channel based on stochastic bridge. Combined with typical DSSS/BPSK modulation, we analyze and simulate the downstream communication link model and calculate the performance of communication system.

2. OCEAN SURFACE MODELING AND CHANNEL MODELING METHOD

On the study of random waves, its model is divided into linear and nonlinear model. Linear wave model is more mature, and it take the waves as the superposition of a series of simple harmonic which have different amplitude, phase and frequency [3]. PM spectrum is fully growth state of the wave spectrum based on wind speed parameter, and it is detailed in the analysis of observational data and simple form. According to the PM spectrum and corresponding wind speed, using linear wave model method, we can generate the three-dimensional geometric model of sea surface [4–6]. The waves range from level 1 to level 6. The area of sea surface is 50 m × 50 m, and the direction of wind is crosswind. Then, the geometric model of sea surface is put into frequency domain electromagnetic simulation software which take electromagnetic waves as rays.

Before the electromagnetic simulation, the electromagnetic model of the surface should be generated, that can be done by taking the geometric model of sea surface into mesh generation and taking the triangle plane as the main way of fitting for the surface. We take wave model of level 1 and level 6 for example. From Figure 1 and Figure 2, we can find the sea surface is made up by large curved surface. We also can see that all of the electromagnetic model save the details of the geometric model of sea surface well.

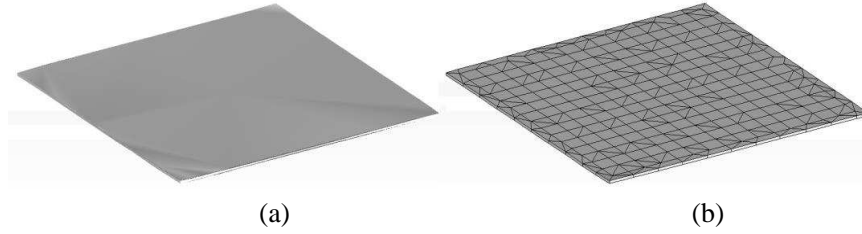


Figure 1: Sea surface model of level 1. (a) CAD model. (b) Electromagnetic model.

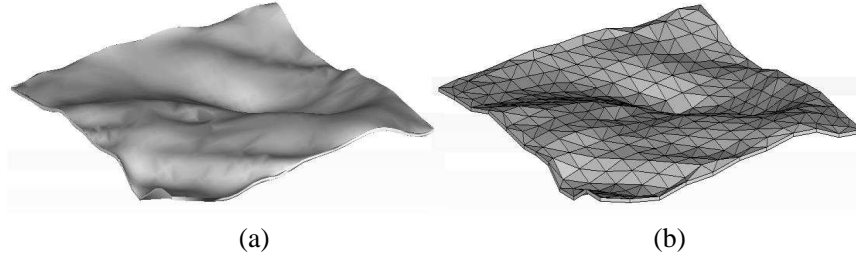


Figure 2: Sea surface model of level 6. (a) CAD model. (b) Electromagnetic model.

The height of sea surface model of level 1 is about 0–0.1 m. The surface is flat, and approximate plane; The height of level 2 is about 0.1–0.5 m. There are some ups and downs low ripple on the sea surface; the height of level 3 is about 0.5–1.25 m. The sea surface produce smaller waves; The height of level 4 is about 1.25–2.5 m. The waves get bigger, and sea surface produce obvious peaks; The height of level 5 is about 2.5–4.0 m. The wavelengths stretch, form a large wave crest, and the distance of peak valley get bigger; The height of level 6 is about 4.0–6.0 m. Towering peaks appear more, and wave breaking appear at the top of the peaks [7].

According to electromagnetic simulation, we can obtain direct ray, and the rays hop once, twice, triple at viewpoint, that is the length and number of rays. The rays path is random propagation. According to the simulation parameter, we can model wireless channel based on stochastic bridge. The stochastic bridge can be described as follows: the transmitter and the receiver are respectively taken as the starting point and the destination of a stochastic bridge process; Electromagnetic waves are considered as rays; Every ray path can be regarded as a sample of a stochastic bridge process, and all the numerical characteristics of which is determined by electromagnetic simulation. According to the length of rays, we can get the time delay of multipath components. If we want to get the impulse response of electromagnetic waves propagating on the sea, we also should know the the amplitude of multipath components.

3. THE CHARACTERISTICS OF RADIO WAVE PROPAGATION

When the electromagnetic wave propagate, the scattering loss must be considered except for path loss. The scattering coefficient can be calculated, based on the sea surface mentioned above, as well. Kirchhoff approximation (KA) and small perturbation method (SPM) are two basic approaches to calculate the scattering problem of rough surfaces which hold for the large-scale rough surface and the small scale one, respectively [8, 9]. SPM will be adopted here as the sea condition is from level 1 to level 6, under which the roughness is considered to be relative small. For a two dimensional (2D) sea surface realization, a directional function $f(k, \phi)$ is necessary. The 2D sea spectrum can be written as in terms of directional function as follows:

$$S(k, \phi) = S(k)f(k, \phi) \quad (1)$$

where $S(k)$ is the PM spectrum. The scattering coefficient developed by SPM is formulated as follows:

$$\sigma_{SPM} = 8k^4 \cos^2(\theta_i) \cos^2(\theta_s) |\alpha_{pp}|^2 S(|K_1|, \phi) \quad (2)$$

$$K_1 = \begin{bmatrix} k \sin(\theta_s) \cos(\phi_s - \phi_i) - k \sin(\theta_i) \\ k \sin(\theta_s) \sin(\phi_s - \phi_i) \end{bmatrix} \quad (3)$$

α_{pp} is polarimetric coefficient expressed as:

$$\alpha_{hh} = -\frac{(\epsilon_r - 1) \cos \phi_s}{\left[\cos \theta_i + (\epsilon_r - \sin^2 \theta_i)^{1/2} \right] \left[\cos \theta_s + (\epsilon_r - \sin^2 \theta_s)^{1/2} \right]} \quad (4)$$

$$\alpha_{vv} = \frac{(\epsilon_r - 1) \left[\epsilon_r \sin \theta_i \sin \theta_s - \cos \phi_s (\epsilon_r - \sin^2 \theta_i)^{1/2} (\epsilon_r - \sin^2 \theta_s)^{1/2} \right]}{\left[\epsilon_r \cos \theta_i + (\epsilon_r - \sin^2 \theta_i)^{1/2} \right] \left[\epsilon_r \cos \theta_s + (\epsilon_r - \sin^2 \theta_s)^{1/2} \right]} \quad (5)$$

where $\theta_i, \theta_s, \phi_i, \phi_s, \epsilon_r$ are the incidence angle, scattered angle, incidence azimuth, scattered azimuth and relative permittivity of sea water respectively. Incidence azimuth is general set as 0° .

According to scattering coefficient, scattering loss can be obtained. The amplitude of multipath components can be calculated based on ray scattering loss and paths loss. Finally, the impulse response of electromagnetic waves propagating on the sea can be obtained. We can get the output signal thought the convolution of impulse response and the input signal, and then predict telecommunication performance by signal to noise ratio vs bit rate error.

4. SIMULATION AND ANALYZE THE COMMUNICATION LINK PERFORMANCE

The electromagnetic simulation conditions is as followed: The source is the dipole antenna; The elevation direction and height of source respectively are location 45 degrees and 40 km above the sea surface; The receiver is set on the sea surface, and the height of it is 10 m; The frequency of incident wave is 1.5 GHz; We just consider the vertical polarization, and the emulational sea level is ranging from 1 to 6. Based on the channel modeling, taking wave model of level 3 for example, the probability distribution of time delay is shown in Figure 3. Its units is ns, and each value of probability distribution correspond to 10 ns time delay. The time delays have direct impact on waveform distortion, then affect the bit error rate.

For the input signal, transmitter includes the generating of original data, the generating of the C/A code, spread spectrum, BPSK modulation [10, 11]. C/A code is a 1023 bit Gold code, which consists of two m -sequences of length 10. the number of randomly generated binary sequences is

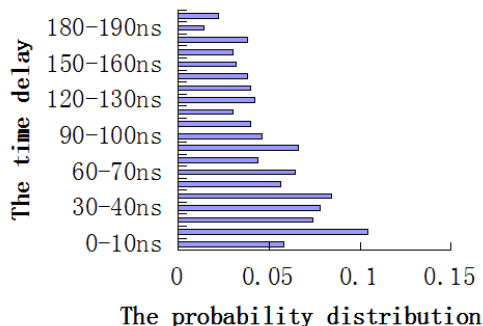


Figure 3: The probability distribution of time delay.

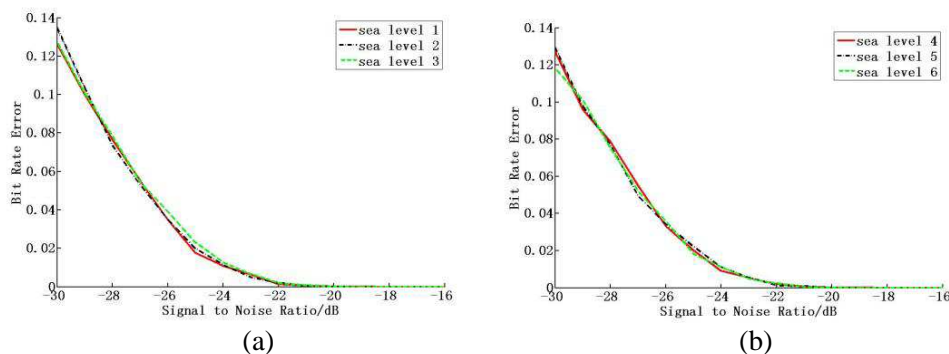


Figure 4: Performance of communication link. (a) Simulation result of BER of sea level 1–3. (b) Simulation result of BER of sea level 4–6.

10^5 . The rate is 10 kbit/s, and the spreading code rate is 10.23 Mbit/s. Select 10 step balanced Gold sequences as the pseudo-code pattern. Carrier frequency is 1.5 GHz, and the sampling frequency is 6 GHz. For the output signal, receiver has the following function: finishing demodulation and despreading the local carrier and code, restoring the original data and calculating the BER. BER is an important index to evaluate the performance of a communication link. Figure 4 is performance of communication link under typical sea level 1–6.

From Figure 4 we can see that when the SNR is greater than -22 dB, BER under different sea conditions are less than 10^{-4} . The BER is basically in the same order of magnitude when the typical grazing angle is small. Sea clutter did not contribute to the BER of the communication system significantly.

5. CONCLUSION

In this paper, we presented a random wireless channel model of marine emergence radio indicator which describe the performance of telecommunications in difference typical ocean states. At first, modeling random rough ocean surface provide the foundation for simulation of LOS and NLOS telecommunication channel. For the radio wave spreading on the sea surface, We research the LOS. Then, electromagnetic simulation and telecommunication channel modeling based on random bridge theory analyze linking properties. Last, we analyze and simulate the downstream communication link model, and calculate the performance of communication systems and the noise ratio vs bit rate error of signal in situation of typical ocean states and elevation angles.

By the finally simulation, we can obtain the preliminary conclusions of multipath channel transmission performance under the typical ocean states and elevation angles, which may provide key information for the design of next generation of marine indicators.

ACKNOWLEDGMENT

This paper is funded by the International Exchange Program of Harbin Engineering University for Innovation-oriented Talents Cultivation. This work was also partially supported by the Navy Defense Foundation of China (4010403020102), the Science and Technology innovative Talents Foundation of Harbin (2013RFXXJ083), the Foundational Research Funds for the Central Universities (HEUCF131602, HEUCFD1433).

REFERENCES

1. Mouche, A. A., B. Chapron, and N. A. Reul, "Simplified asymptotic theory for ocean surface electromagnetic wave scattering," *Waves in Random and Complex Media*, Vol. 17, No. 3, 321–341, 2007.
2. Hu, L. Q., *Stochastic Modeling and Applications for Radio Wave Propagation*, Huazhong University of Science and Technology Press, 2011.
3. Kuga, Y. and P. Phu, "Experimental studies of millimeter-wave scattering in discrete random media and from rough surface," *Progress In Electromagnetics Research*, Vol. 14, 37–88, 1996.
4. Tsang, L., J. A. Kong, K. H. Ding, and C. O. Ao, *Scattering of Electromagnetic Waves: Numerical Simulations*, 34–41, Wiley Interscience, New York, 2001.
5. Elfouhaily, T., B. Chapron, K. Katsaros, et al., "A unified directional spectrum for long and short wind-driven waves," *J. Geophys. Res.*, Vol. 102, 15781–15796, 1997.
6. Mastin, G. A., P. A. Watterberg, and J. F. Mareda, "Fourier synthesis of ocean surfaces," *IEEE. Comput. Graph. Appl.*, Vol. 7, No. 3, 16–23, 1987.
7. Min, Z., Z. H. U. Lei, Z. Ping, et al., "Time-domain techniques for transient scattering from dielectric bodies and sea surface governed by JONSWAP's sea spectra," *Chinese Physics Letters*, Vol. 26, No. 8, 84–101, 2009.
8. Soto-Crespo, J. M., M. Nieto-Vesperinas, and A. T. Friberg, "Scattering from slightly rough random surfaces: A detailed study on the validity of the small perturbation method," *J. Opt. Soc. Am. A*, Vol. 7, No. 7, 1185–1201, 1990.
9. Holliday, D., L. L. DeRaad, and G. J. St-Cyr, "Forward-backward method for scattering from imperfect conductors," *IEEE Trans. Antennas Propag.*, Vol. 46, No. 1, 101–107, 1998.
10. Li, T. and J. Y. Sun, "Balanced gold sequence generation condition," *Journal of Dalian Maritime University*, Vol. 32, 93–95, 2006.
11. Zeng, X. W., N. Liu, and X. P. Sun, *Spread Spectrum Communication and Multiple Access Technology*, Xidian University Press, 2004.

Feasibility Study of Emulating Extended Spatial Channel Models in a Multi-probe MIMO OTA Antenna Test Setup

Md Suzan Miah, Afroza Khatun, and Katsuyuki Haneda

Department of Radio Science and Engineering, School of Electrical Engineering
Aalto University, P. O. Box 13000, Aalto FI-00076, Finland

Abstract— In this paper we demonstrate the feasibility of a multi-probe based multiple-input multiple-output (MIMO) over-the-air (OTA) test method, where urban macro and microcellular scenarios of the spatial channel model — extended (SCME) are used as a target multipath channel. No work has reported the feasibility of the field synthesis aiming at emulation of the SCME using the plane-wave field synthesis (PWS) based on spherical wave theory so far. In this work we used this technique to emulate the reference channel inside the test area. The feasibility is tested by evaluating the emulated field in terms of four basic channel properties: power delay profile, temporal correlation function, spatial correlation function, and cross polarization ratio. The study shows that feasibility of the PWS technique to emulate all the basic parameters in a multi-probe based MIMO OTA test setup.

1. INTRODUCTION

Multiple input multiple output (MIMO) radios, which use multiple antennas in the two ends of the communication link, have been attracting attention because of their ability to meet the increased demand for higher data rate communications. However, the performance of MIMO links depends not only on the antenna performance but also on the propagation environment. Hence, accurate MIMO performance testing of mobile terminal devices needs to consider both the multiple terminal antennas as well as the propagation environment. Over-the-air (OTA) antenna test method has been widely used for legacy mobile devices equipped with only a single antenna, and its extension to the MIMO device has been actively investigated.

Standardization works for MIMO OTA testing have been intensively coordinated by Cellular Telecommunications Industry Association (CTIA) and 3rd Generation Partnership Project (3GPP), where several different MIMO OTA test methods have been proposed [1]. One mandatory requirement of any MIMO OTA test methods is to emulate an electromagnetic environment, which resembles the radio propagation scenario where the terminal operates. Geometry-based channel models such as the Spatial Channel Model (SCM), SCME, WINNER II or IMT-Advance constitute a good means to describe the propagation scenario, which is translated into the electromagnetic environment in the OTA testing. The use of such well-defined channel model in MIMO OTA testing makes the test methods realistic and hence well justified.

One of the proposed methods in the standardization of the MIMO OTA testing is the use of an anechoic chamber equipped with multiple probes that emulates the intended electromagnetic environment inside a confined area of the chamber, which is called a test zone. To emulate the spatial and temporal characteristics of the intended electromagnetic environment defined by the channel model, two techniques have been reported in the literature; one is the plane wave synthesis (PWS) [2–4] and another is the prefaded signal synthesis (PFS) [4, 5]. In this paper, we address the PWS technique based on the spherical wave theory, and prove its consistency with other MIMO OTA testing techniques such as the PFS.

The purpose of the paper is to demonstrate that the PWS technique is capable of emulating the intended electromagnetic environment in a multi-probe based MIMO OTA test system. In this study, we demonstrate the capability for the 3GPP SCME [1] as the intended electromagnetic environment, since no literature so far has made the demonstration. The accuracy of the emulation is evaluated in terms of power delay profile (PDP), temporal correlation function, spatial correlation, and cross-polarization ratio (XPR) as influential radio channel properties to the link data rate. Our results serve as an important reference when comparing the performance of the PWS technique with other MIMO OTA techniques such as the PFS.

The remainder of this paper is organized as follows. Section 2 describes the PWS emulation techniques. Section 3 presents the simulation set up. After Section 4 compares the emulated and intended fields to demonstrate the feasibility of the PWS technique for the SCME, Section 5 concludes the paper.

2. CHANNEL EMULATION TECHNIQUES

2.1. Configuration of the Multi-probe Anechoic Chamber

An illustration of a 2D multi-probe anechoic chamber based MIMO OTA test system is shown in Figure 1. The base station emulator feeds the downlink transmit signals to multichannel fading emulator. The output ports of the fading emulator are connected to the K probe antennas, which are equally spaced on the probe ring with radius r . Thus the radio frequency signals emitted from the probes to the air are controlled by the fading emulator to produce the intended electromagnetic environment inside a test zone. For the 2D test setup, the device under test (DUT) is at the center of the circular test zone with radius r_0 . It is required that the intended electromagnetic environment should be accurately emulated over the test zone, and hence the DUT would experience the same propagation channels as it would be in the operation environment.

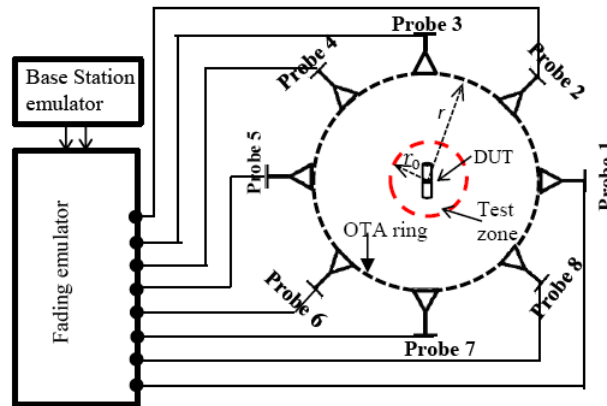


Figure 1: The 2D multi-probe based MIMO OTA test system with eight uniformly spaced probes on a ring.

2.2. Field Emulation Techniques

2.2.1. PFS Technique

The PFS technique is presented in [4, 5]. This technique focuses on clusters (i.e., groups of multipath components). The basic component of this technique is a single cluster with parameters like nominal Angle of arrival (AoA), angular spread of arrival (ASA), Doppler spectrum, and cross polarization ratio (XPR). The PFS technique emulates the intended electromagnetic environment by weighting the independent fading signals transmitted from multiple probes. The signal weighting is made so that the power angular spectrum (PAS) of the emulated field resembles that of the intended field as much as possible. This leads to accurate emulation of the spatial correlation characteristics inside the test zone.

2.2.2. PWS Technique

The PWS technique synthesizes the intended electromagnetic field inside the test zone by exciting the multiple probes with proper voltages, such that the total field from the probes resembles the intended field at a location in the test zone. This technique has a point of view in plane waves instead of clusters. The basic component generated by this technique is a plane wave with a specific AoA, Doppler shift and magnitude. The PWS reported in [2, 3] is based on the spherical wave theory [6], stating that any plane wave field in a test zone can be expressed by a finite sum of orthonormal wave modes. This spherical wave theory provides theoretical justification of the required number of probes as a result of its well-known cut-off properties of the orthonormal modes. In [2], the maximum relative error between the emulated and target field on the circumference of the test zone is evaluated.

3. CONFIGURATION OF THE SIMULATION SET-UP

A 2-D MIMO OTA test system is shown in Figure 1. The probe antennas are on a circle of radius r and are equally spaced over the circle on the horizontal plane. The antennas produce the far field towards the DUT located at the center of the test zone with the radius r_0 .

One of the main issues addressed in the multi-probe OTA test method is the number of required probe antennas. According to the PWS technique that uses the spherical wave theory, the

required number of probes K for accurate emulation of the intended field is directly related to the size of the test zone. For synthesizing both vertically and horizontally polarized plane wave fields inside a test zone, K is given as [6]

$$K_{\min}^{2-D} = 4[kr_0 + n_1] + 2, \quad (1)$$

where k is the wave number, the unknown number n_1 is a constant that determines the accuracy of the field synthesis [6]. The values of n_1 for different relative error levels of the synthesized field have been reported in [7]. In this paper, -15 dB relative error is considered and then the required number of probes considering the vertical and horizontal polarizations in 2D case becomes [7]

$$K_{\min, -15\text{dB}}^{2-D} = 4 \left[kr_0 + 0.74 \sqrt[3]{kr_0} \right] + 2. \quad (2)$$

In this paper, the field synthesis targets the radio frequency of 806 MHz. The following setup of the OTA test system is considered: a 45° slanted dipole antenna at the base station, half-wavelength dipole and magnetic loop as antennas of DUT, 8 dual-polarized Vivaldi antennas as probes. The base station antenna is taken into account in the fading emulator when calculating an excitation voltage of each probe, and the probes are placed evenly on the OTA ring with the radius of $r = 1.75$ m, and the test zone has a radius $r_0 = 0.15$ m. The required number of probes is 16 (or 8 dual-polarized) in this case, according to (2), and hence, the number of probes considered in the OTA test system here is sufficient. The intended fields are defined by the urban macro and microcellular scenarios of the SCME, are reproduced according to the channel parameters presented in Tables 8.2-1 and 8.2-2 of [1].

4. SIMULATED CHANNEL MODEL VALIDATION RESULTS

Before starting any advanced testing activity, for example, throughput measurements, the emulated fields at the DUT antenna location need to be compared with the intended field defined by the selected channel model, in order to verify their agreement and address any anomaly in the emulation. Complete verification of the emulated field against the intended one is an extensive task since it needs to involve all the relevant dimensions of the propagation channel such as space, time, delay, power and polarization. In this paper, the verification is performed in terms of four basic properties of 3GPP SCME channel model: PDP, spatial correlation function, temporal correlation function, and XPR.

4.1. Power Delay Profile

Each scenario in the 3GPP SCME channel model produces propagation channels consisting of 6 spatio-temporal propagation paths and each path has 20 sub-paths [1]. Furthermore, 20 sub-paths per path have been split into three subsets, namely “mid-paths”. Each path of the channel is associated with a delay and power. The objective of the PDP comparison is to find out the deviation between PDP in the emulated channels and in the reference channels.

The PDP is simulated with a vertically polarized half-wavelength dipole as a receiving antenna. In total 20,000 samples (i.e., a set of propagation paths) are simulated. The reference PDPs

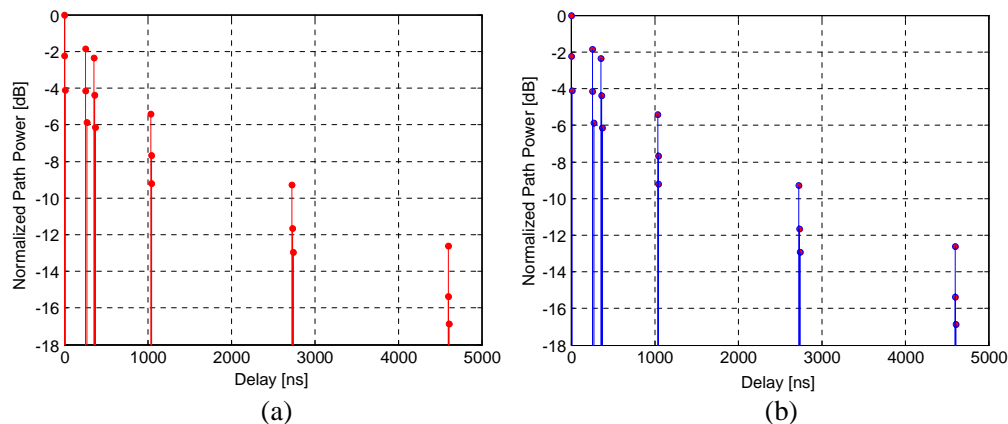


Figure 2: PDP of SCME urban macro model: (a) reference (red), and (b) emulated (blue).

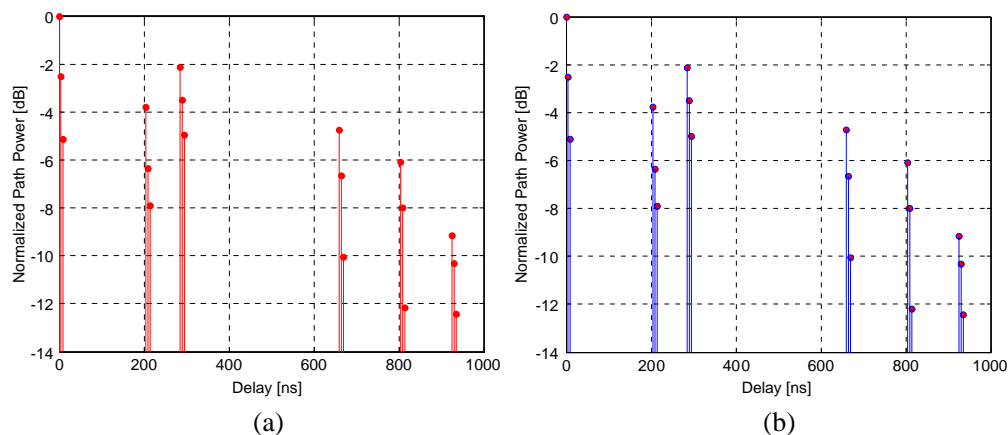


Figure 3: PDPs of SCME for the urban microcellular scenario: (a) reference (red), and (b) emulated (blue).

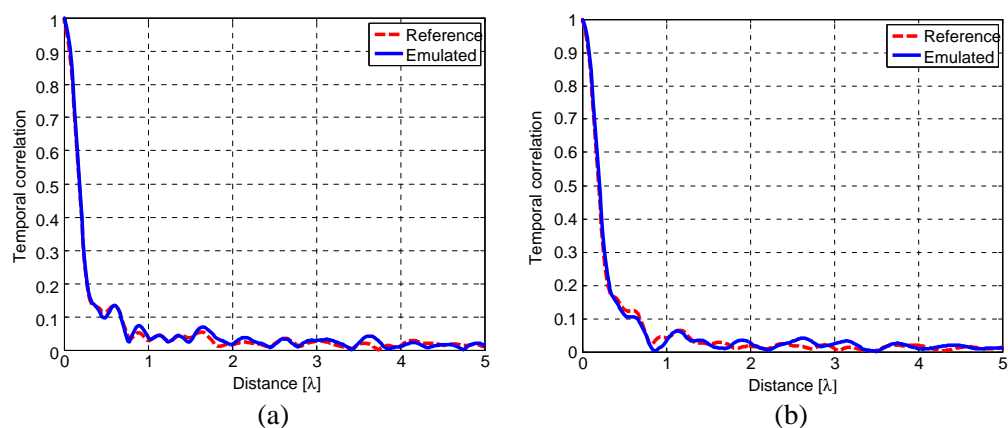


Figure 4: Reference and emulated temporal correlation: (a) SCME urban macro and (b) microcellular scenarios.

generated from the 3GPP SCME for urban macro and microcellular scenarios are presented in Figures 2(a) and 3(a), respectively, while the corresponding emulated PDPs are shown in Figures 2(b) and 3(b). Note that the figures illustrate the powers and delays associated with each mid-path of the six paths. The emulated PDP follows the reference one very well for both scenarios.

4.2. Temporal Correlation Function

The goal of comparing the temporal correlation is to see the accuracy of the temporal behavior of the emulated channel in relation to those of the reference channel. Temporal correlation function is equivalent to the power Doppler spectrum (PDS) of the channel as they are Fourier pairs. Since it is difficult to compare the PDS because of their spiky shapes, temporal correlation is used in this paper for the comparison. A half-wavelength vertically polarized dipole as a DUT antenna is used in the simulation; 32 samples per half-wavelength and a total of 50,000 samples are used to make the temporal correlation function curves smooth. In Figure 4, with constant DUT velocity of 30 km/h, the red and blue curves show the reference and emulated temporal correlation function, respectively. It can be clearly seen from Figure 4 that the emulated and reference temporal correlation functions match well for both scenarios. Note that the values of temporal correlation function left from the maximum and after five wavelengths have been cut out.

4.3. Spatial Correlation Function

Accurate reproduction of the spatial correlation function is also an important goal of the MIMO OTA antenna testing. In comparing the emulated and reference spatial correlation defined by the SCME, two vertically polarized dipole antennas are used as DUT antennas. Only the separation between the antennas has been changed to estimate the variation of the spatial correlation, while other setups of the simulation remain the same as the previous ones. For each antenna separation distance, the reference and emulated spatial correlation coefficients are calculated from 20,000

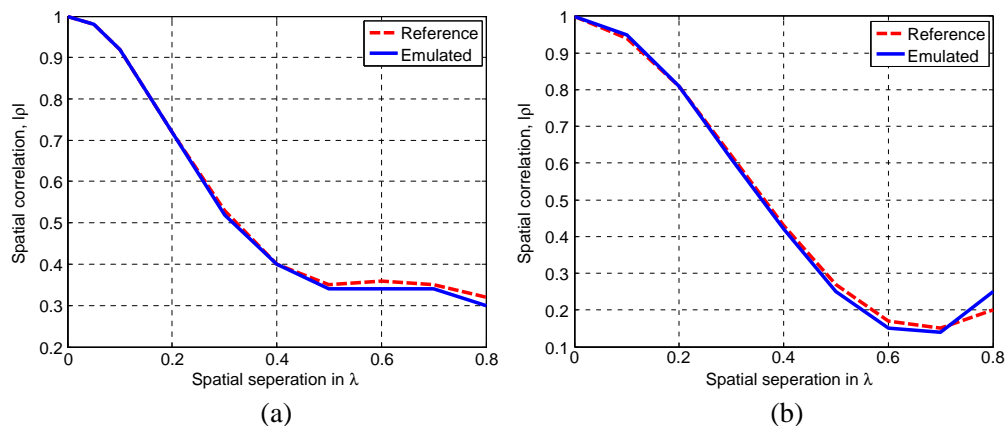


Figure 5: Reference and emulated spatial correlation: (a) SCME urban macro, and (b) microcellular scenarios.

Table 1: XPR values of the emulated and reference channels for the SCME urban macro and micro scenarios.

	Reference XPR [dB]	Emulated XPR [dB]	Delta [dB]
3GPP SCME urban macro	8.55	8.67	0.12
3GPP SCME microcellular	0.96	0.86	0.10

channel impulse responses. In Figure 5, red curve and blue curve show the reference and emulated spatial correlation function. The spatial correlation is one when the two antennas are collocated, while the correlation decreases as the separation increased up to 0.8λ . It is obvious from the figure that the emulated spatial correlation functions follow the reference one very well for both scenarios.

4.4. Cross-polarization Ratio

The polarization characteristic of the emulated channel is investigated by evaluating the XPR. In this paper, the XPR is defined as a difference of the received power by vertically and horizontally polarized antenna located at the center of the test zone. In particular, a vertically polarized half-wavelength dipole and a horizontally polarized magnetic loop were considered. Table 1 illustrates the emulated and reference XPR values for the urban macro and microcellular scenarios, estimated by 20,000 channel impulse responses generated by the SCME. The emulated XPR values deviates from the reference by 0.12 dB and 0.10 dB in the macro and microcellular scenarios, respectively. The slight deviations are likely from the difference of multipath power received at the DUT.

5. CONCLUSION

This paper presented a comparison of emulated and reference channels in a multi-probe based MIMO OTA test system. The field emulation inside the test zone was based on the PWS technique. The comparison has been performed in terms of four metrics of the radio channels that are influential to radio link performance: PDP, temporal correlation function, spatial correlation function, and XPR. A good agreement between the emulated and reference values has been achieved in all the investigated metrics. The minor deviation in the XPR values is likely introduced by slight difference of multipath profiles received at the DUT. Future work concerns the experimental validation of the emulation technique and further analysis of the MIMO performance metric, such as MIMO capacity and throughput.

ACKNOWLEDGMENT

The research was conducted in the framework of a research project, abbreviated MIMOTA-2, funded by the Finnish Funding Agency for Technology and Innovation (Tekes) and the companies Microsoft, Anite Oy, and ETS-Lindgren.

REFERENCES

1. "Verification of radiated multi-antenna reception performance of user equipment," 3GPP, TR 37.977 V12.1.0, Mar. 2014.

2. Laitinen, T., P. Kyösti, J. P. Nuutinen, and P. Vainikainen, “On the number of OTA antenna elements for planewave synthesis in a MIMO-OTA test system involving a circular antenna array,” *Proceedings of the 4th European Conference on Antennas and Propagation (EuCAP’10)*, Apr. 2010.
3. Toivanen, J. T., T. Laitinen, V. Kolmonen, and P. Vainikainen, “Reproduction of arbitrary multipath environments in laboratory conditions,” *IEEE Transactions on Instrumentation and Measurement*, Vol. 60, No. 1, 275–281, Jan. 2011.
4. Kyösti, P., T. Jämsä, and J. Nuutinen, “Channel modelling for multiprobe over-the-air MIMO testing,” *International Journal of Antennas and Propagation*, 2012.
5. Fan, W., X. Carreño, J. Ø. Nielsen, J. S. Ashta, G. F. Pedersen, and M. B. Knudsen, “Verification of emulated channels in multi-probe based MIMO OTA testing setup,” *7th European Conference on Antennas and Propagation (EuCAP)*, 97–101, Apr. 2013.
6. Hansen, J. E., *Spherical Near-field Antenna Measurements*, Peter Peregrinus, London, UK, 1988.
7. Khatun, A., T. Laitinen, V. M. Kolmonen, and P. Vainikainen, “Dependence of error level on the number of probes in over-the-air multiprobe test systems,” *International Journal of Antennas and Propagation*, Vol. 2012, Article ID 624174, 6 Pages, 2012.

Statistical Physics of Multimode Ordered and Disordered Lasers

F. Antenucci^{1,2}, A. Crisanti^{1,3}, M. Ibáñez Berganza^{1,4}, and L. Leuzzi^{1,2}

¹Dipartimento di Fisica, Università di Roma Sapienza, Piazzale A. Moro 2, Rome I-00185, Italy

²NANOTEC-CNR, Soft and Living Matter Lab, Piazzale A. Moro 2, Rome I-00185, Italy

³ISC-CNR, UOS Sapienza, Piazzale A. Moro 2, Rome I-00185, Italy

⁴INFN, Gruppo Collegato di Parma, via G.P. Usberti, Parma 7/A-43124, Italy

Abstract— The adoption of a statistical mechanical framework in optics provides realistic models for multimode laser systems, whose experimental implications are presented and critically analyzed. A model for passive mode locking lasers is analyzed beyond the mean-field approximation, accounting for the presence of many well-resolved frequencies of the lasing modes. The inhomogeneous structure in the nonlinear “mode locked” interaction network is shown to yield short pulses and phase waves with nontrivial slopes, corresponding to a phase delay of the pulsed laser signal. The analytic solution of a mean field-model for multimode laser in open and irregular cavities will be, afterwards, addressed. The complete phase diagram, in terms of degree of disorder, pumping rate of the source and strength of nonlinearity, consists of four different photonic regimes: incoherent fluorescence, mode locking, random lasing and the novel “phase locking wave”. A replica symmetry breaking transition occurs at the random lasing threshold. For a high enough strength of nonlinearity, a whole region with nonvanishing complexity anticipates the transition and the light in the disordered medium displays typical glassy behavior.

1. STATISTICAL MECHANICS FOR MULTIMODE LASERS

There have been several studies addressing the description of multimode laser systems in a statistical mechanics framework [1–5]. The approach is based on the hypothesis of effective equilibrium. Lasers are manifestly off-equilibrium and energy is pumped into the system to sustain population inversion and stimulated emission. However, as the system power is kept constant, the resulting stationary regime can be described as if at equilibrium with an effective “thermal bath” whose “temperature” is related to the pumping rate and to the true environment temperature.

The evolution of the atom-field system operators can be formalized starting from the Jaynes-Cumming Hamiltonian for matter-light interaction. The system is localized in space with discrete states. If the optical resonator is open the system is embedded in a natural environment consisting of the continuum of extended scattering states. The coupling with the scattering states of the continuum determine the lifetime of the discrete states, which is, therefore, finite. Adopting, e.g., the system-and-bath approach [6], a rigorous quantization of the field is possible also when the cavity is not closed: contributions of radiative and localized modes are separated by Feshbach projection and an effective theory in the subspace of localized modes is obtained with an effective linear damping coupling.

Adopting the semiclassical limit and assuming that the mode lifetimes are much longer than the characteristic times of pump and loss, it is possible to adiabatically remove the atomic variables and obtain the (non-linear) equations for the field alone. The evolution in the lasing regime is then conveniently expressed in the basis of the *slow amplitude modes*. These are solutions \bar{a}_k of angular frequencies ω_l with a harmonic form for long times $t \gg 1$. The mode evolution for the slow complex amplitudes $a_k(t) = \bar{a}_k(t) e^{+i\omega_k t}$ is, then, written as

$$\dot{a}_k = -\partial\mathcal{H}/\partial a_k^* \quad (1)$$

where, at the third order in the mode amplitude expansion, the functional \mathcal{H} reads

$$\mathcal{H} = - \sum_{k=1,\dots,N} G_k |a_k|^2 - \sum_{\mathbf{k}|\text{FMC}(\mathbf{k})} J_{k_1 k_2} a_{k_1}^* a_{k_2} - \sum_{\mathbf{k}|\text{FMC}(\mathbf{k})} J_{k_1 k_2 k_3 k_4} a_{k_1} a_{k_2}^* a_{k_3} a_{k_4}^*. \quad (2)$$

Here G_k is the gain curve of the active medium and the couplings between different modes are

$$J_{k_1 k_2} \propto \gamma_{k_1 k_2} - \int d\mathbf{r} \rho(\mathbf{r}) g_l^*(\mathbf{r}) g_k(\mathbf{r}), \quad J_{k_1 k_2 k_3 k_4} \propto - \int d\mathbf{r} \rho(\mathbf{r}) g_l^*(\mathbf{r}) g_{k_1}(\mathbf{r}) g_{k_2}^*(\mathbf{r}) g_{k_3}(\mathbf{r}), \quad (3)$$

the matrix γ_{lk} being the damping matrix associated to the openness of the cavity [6] and $\rho(\mathbf{r})$ the density of atoms of the active medium.

In Eq. (2), by definition of slow amplitude mode $\bar{a}_l \simeq e^{-i\omega_k t}$, the sums are restricted to terms with different indices that meet the *frequency matching conditions* (FMC):

$$\text{linear: } |\omega_{k_1} - \omega_{k_2}| \lesssim \gamma \quad \text{nonlinear: } |\omega_{k_1} - \omega_{k_2} + \omega_{k_3} - \omega_{k_4}| \lesssim \gamma. \quad (4)$$

The finite line-width γ of the modes can be obtained only in a complete quantum derivation. In general, the linear term of Eq. (2) may have non-zero off-diagonal terms. They are all zero when the frequencies are well distinct so that the frequency matching condition of the linear term is never satisfied but for the modes with overlapping frequency. While this is generally true for standard high quality-factor lasers, for a random laser (RL) [7] there can be a significant frequency overlap between the lasing modes and off-diagonal linear contributions must be considered.

For a complete statistical description one must, eventually, consider the presence of the noise $F_l(t)$ in Eq. (1), linked primarily to spontaneous emission. Though, in general, non-diagonal, a proper mode basis can be chosen where F_l is white and uncorrelated:

$$\langle F_{k_1}^*(t_1) F_{k_2}(t_2) \rangle = 2T \delta_{k_1 k_2} \delta(t_1 - t_2), \quad \langle F_{k_1}(t_1) F_{k_2}(t_2) \rangle = 0, \quad (5)$$

with T being the spectral power of the noise, proportional to the heat-bath temperature.

The functional \mathcal{H} in Eq. (2) is complex in the most general case. The real part is associated with a purely dissipative motion while the imaginary part with dispersion. Without dissipation, the total optical intensity \mathcal{E} is a constant of motion. Differently, the system remains stable because the gain decreases as the optical intensity increases. To study the equilibrium properties, this can be encoded by requiring that at any instant gain and losses balance to keep \mathcal{E} constant [1]:

$$\mathcal{E} = \epsilon N = \sum_{k=1, \dots, N} |a_k|^2 = \text{const.} \quad (6)$$

Hereinafter we consider only purely dissipative systems. These can be studied using the standard tools of the equilibrium statistical physics: the Langevin equations Eq. (1) reduce to the potential form and, hence, the steady-state solution of the associated Fokker-Planck equation is the Gibbs distribution $\rho(a_1, \dots, a_N) \propto e^{-\mathcal{H}_R/T_{\text{ph}}}$. The effective “photonic” temperature is taken $T_{\text{ph}} = T/\epsilon^2 \equiv \mathcal{P}^{-2}$, proportional to the heat-bath temperature T and with \mathcal{P} being the *pumping rate* of the source. This encodes the experimental observation that, regard to the lasing threshold, the effect of lowering T is equivalent to raise the optical intensity [8].

2. PASSIVE MODE LOCKING WITH FREQUENCY COMB

The model for passive mode locking lasers is obtained by the ordered limit of Eq. (2) [1–3]

$$\mathcal{H} = - \sum_{k=1, \dots, N} G_k |a_k|^2 - \frac{J}{2} \sum_{\mathbf{k} | \text{FMC}(\mathbf{k})} a_{k_1} a_{k_2}^* a_{k_3} a_{k_4}^*, \quad (7)$$

with the mode frequencies given by the frequency comb associated to the Fabry-Pérot resonator:

$$\omega_k = \omega_1 + (k - 1)\Delta\omega, \quad k = 1, \dots, N. \quad (8)$$

The narrow-band, low finesse, limit $\gamma \simeq \Delta\omega$ is such that the FMC in Eq. (4) is always satisfied and can be solved in mean-field theory [1]. The FMC becomes nontrivial for high-finesse, $\gamma \ll \Delta\omega$. Monte Carlo simulations of both systems have been performed to study the role of FMC [2, 3].

In both low and high finesse cases, a first order transition is observed between a continuous wave regime at low pumping and a pulsed regime at high pumping. The critical pumping value being compatible, in the thermodynamic limit, with the one obtained in mean-field, cf. Fig. 1(a).

The difference between the high and low finesse cases is in the *nature* of the pulsed regime. For low finesse, the modes are trivially phase-locked $\phi_j = \phi_0$, so the parameter of global coherence $m_x \equiv \sum \Re(a_j)/N$ is nonzero, converging on the black line of in Fig. 1(b) for high pumping. In the high finesse case, instead, the pulsed regime is not trivially phase locked, see Fig. 1(b), and the laser mode phases result to behave as $\phi_j \simeq \phi_0 + \phi' \omega$, with a nontrivial, frequency independent, slope ϕ' (see insets in Fig. 2(a)). The slope ϕ' changes in the time evolution with a distribution

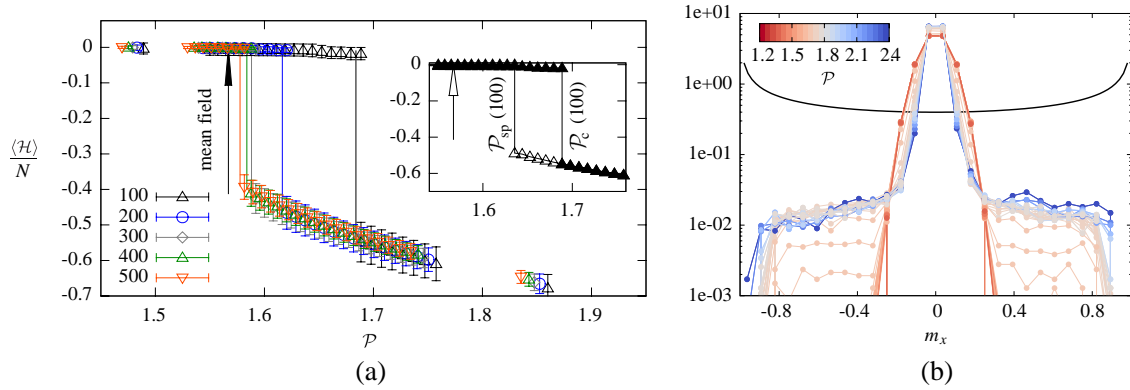


Figure 1: (a) Intensive energy vs Pumping for high-finesse systems of increasing sizes. The inset shows the metastable region between the spinodal and critical line for $N = 100$. (b) Distribution of $m_x \equiv \sum \Re(a_j) / N$ for a high-finesse system with $N = 300$ at several pumping rates above and below the mode locking threshold. The solid black line is the distribution of m_x for a trivially phase locked system $\phi_j \equiv \phi_0$.

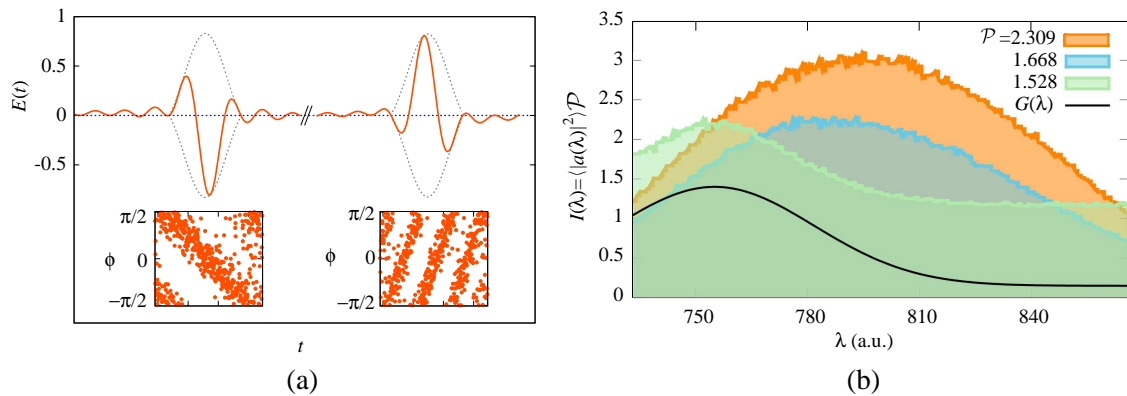


Figure 2: (a) Signal (top) and corresponding configurations plotted as Phase vs Frequency (bottom) for a high finesse system with $N = 500$ just above the critical pumping ($\mathcal{P} = 1.692, \mathcal{P}_c = 1.565(8)$). (b) Intensity spectra for three pumping for high finesse and $N = 150$ ($\mathcal{P}_c = 1.60(2)$ here). Below the threshold the spectrum is shown to follow the gain curve (black solid line).

determined by the interaction network among the modes and with a lifetime that increases with the pumping rate [2, 3]. Consequently, all the two mode correlators are zero in the high pumping regime in high finesse systems [2, 3]. The electromagnetic pulse associated with such configurations, $E(t) = \sum_j |a_j| \exp[i(\omega t + \phi_j)]$, is, accordingly, such that the phase delay between the carrier and the envelope of the signal changes at each shot, cf. Fig. 2(a). The phenomenon is observed also in high-finesse models with fixed intensities (XY and p -clock models) [2, 3, 9] and it is reminiscent of the properties of lattice gauge theories where local gauge symmetries forbid the global $O(2)$ symmetry breaking [2, 3].

The FMC results to play an essential role not only for the phase locking but for the intensity spectra as well. Indeed, for low pumping the spectrum follows the gain curve G_k . As the pumping exceeds the mode locking threshold, however, the spectrum is observed to be determined solely by the interaction network and it becomes narrow around the central frequencies of the bandwidth, cf. Fig. 2(b), because of the FMC. This furnishes a theoretical mechanism to explain the gain narrowing at the mode locking transition.

3. MEAN FIELD MODEL FOR NONLINEAR OPTICS IN RANDOM MEDIA

In the general case of RLs, the cavity is open, so the matrix $\gamma_{k_1 k_2}$ is nonzero [6], while the spatial distribution of the modes is irregular and complicated in such a way that the interactions in Eq. (3) take, in principle, a wide range of values, positive and negative. In the mean-field theory the FMC of Eq. (4) are neglected and the J_{i_1, \dots, i_p} are then taken as independent identically distributed random variables. This is exact, in particular, for systems with spatially extended modes and a

narrow bandwidth. Here we take the distributions of J_{i_1, \dots, i_p} in Eq. (2) Gaussian with ($p = 2, 4$)

$$\mathcal{P}(J_{i_1 \dots i_p}) = \frac{1}{\sqrt{2\pi\sigma_p^2}} \exp \left[-\frac{\left(J_{i_1 \dots i_p} - \tilde{J}_0^{(p)} \right)^2}{2\sigma_p^2} \right] \quad \text{with} \quad \sigma_p^2 = \frac{J_p^2}{2N^{p-1}}, \quad \tilde{J}_0^{(p)} = \frac{J_0^{(p)}}{p! N^{p-1}}. \quad (9)$$

The scaling of σ_p and $\tilde{J}_0^{(p)}$ with N assures the extensivity of the Hamiltonian. To have a direct interpretation in terms of photonic quantities we use the photonic parameters

$$J_0^{(4)} = \alpha_0 J_0, \quad J_0^{(2)} = (1 - \alpha_0) J_0, \quad R_J = \frac{J}{J_0}, \quad (10)$$

$$J_4^2 = \alpha^2 J^2, \quad J_2^2 = (1 - \alpha)^2 J^2, \quad \mathcal{P} = \epsilon \sqrt{\beta J_0}. \quad (11)$$

The parameters J_0 and J fix, respectively, the cumulative strength of the ordered and disordered part of the Hamiltonian while α_0 and α the *strength of nonlinearity* in the ordered and disordered parts. The parameter R_J is the *degree of disorder*.

The model is solved by means of the replica method for disordered systems [10] and their relative order parameters, the overlaps (i.e., the similarities) between thermodynamic states. This is achieved considering n identical replicas of the system that act as probes exploring the phase space and evaluating the physical overlaps between states from the overlap between these replicas.

In this way one obtains the free energy as a function of generalized order parameters [4, 5]

$$r_d = \frac{1}{\mathcal{E}} \sum_{k=1}^N \Re \left[(a_k^a)^2 \right], \quad m = \frac{\sqrt{2}}{N} \sum_{k=1}^N a_k^a, \quad Q_{ab} = \frac{1}{\mathcal{E}} \sum_{k=1}^N \Re \left[a_k^a (a_k^b)^* \right]. \quad (12)$$

Here r_d is the parameter of partial coherence, m is the complex parameter of global coherence and Q_{ab} is a real overlap matrix. A main point is that the simplest ansatz of assuming $Q_{ab} = Q$ for all $a \neq b$, i.e., of assuming that all replicas are equivalent, is not consistent in the whole phase space [4, 5]. Therefore, one must allow for a Replica Symmetry Breaking (RSB) to construct the solution. Following the Parisi scheme [10], the elements of Q_{ab} can take different values and the order parameter is their probability distribution. Identical copies of the system show different amplitude equilibrium configurations, as the ergodicity is broken in many distinct states.

Four different regimes are found for the photonic system varying parameters \mathcal{P} , α , α_0 and R_J :

- *Incoherent Wave (IW)*: replica symmetric solution with all order parameters equal to zero. The modes oscillate incoherently and the light is emitted in the form of a continuous wave.
- *Phase Locking Wave (PLW)*: all order parameters vanish but r_d , signaling a locking of the mode phases on a line but without a specific direction. This regime occurs in the region of the phase space intermediate between the IW and RL regimes.
- *Mode Locking Laser (ML)*: solution with $m \neq 0$, with or without replica symmetry breaking. The modes oscillate coherently with the same phase and the light is emitted in form of pulses.
- *Random Laser (RL)*: the modes do not oscillate coherently in intensity, so that $m = 0$, but the overlap matrices Q_{ab} and R_{ab} have a nontrivial structure.

Two typical phase diagrams are shown in Fig. 3. Consider the common experimental situation with an increasing pumping rate \mathcal{P} at fixed R_J , α and α_0 . Then:

- for R_J not too large a transition between the IW and the ML regimes is observed increasing the pumping. The transition is robust with respect to the introduction of small disorder;
- for systems with intermediate disorder, the high pump regime remains the ordered ML regime, but the intermediate, partially coherent, PLW regime appears between ML and IW;
- for large R_J , a further transition from ML to RL is observed at high \mathcal{P} . Moreover, if R_J exceeds a threshold the ML disappears and the only high pumping phase remains the RL.

This scenario is rather general and remains valid for different values of α and α_0 [4, 5]. The value of α_0 affects the transition toward the ML regime: for high α_0 the transition is discontinuous. On the contrary, if α_0 is low, there are regions in the phase diagram where the transition is continuous. The value of α controls the transition to the RL regime. For $\alpha > \alpha_{nl}$ ($\simeq 0.6297$ for $\epsilon = 1$) the transition is toward a RL via a *random first order transition*, typical of glassy systems, with a region of finite complexity antecedent the transition (cf. Fig. 3(a)) where the photonic glass has an exponential number of metastable states corresponding to different mode locking processes.

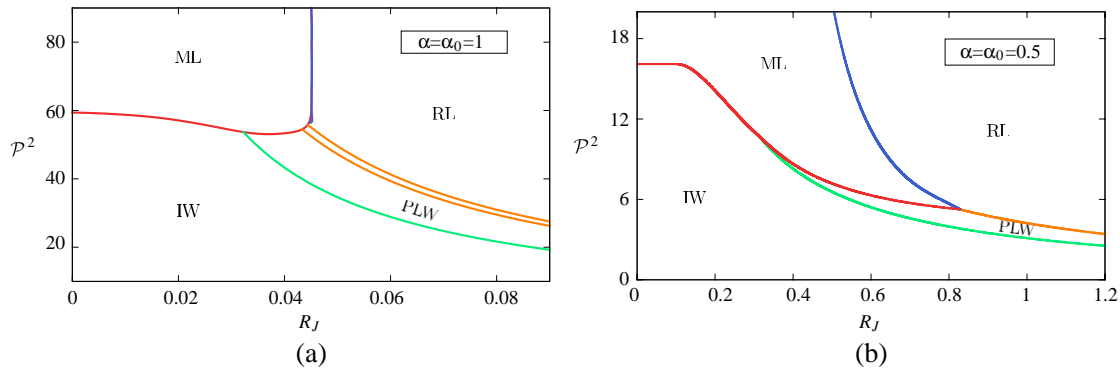


Figure 3: Phase diagram for $\epsilon = 1$ and (a) $\alpha = \alpha_0 = 1$, corresponding to a closed cavity, and (b) $\alpha = \alpha_0 = 0.5$. The solid (dashed) line between IW and ML corresponds to a continuous (discontinuous) transition. The dashed line between PLW and RL in (a) indicates the dynamic transition line with finite complexity.

4. CONCLUSIONS

We have presented statistical mechanical models for ordered and disordered multimode lasers in closed and open cavities. The approach uses equilibrium statistical mechanics tools to study the steady-state of the system via the introduction of an effective temperature.

Monte Carlo simulations for a model for passive mode locking show that the interaction network becomes inhomogeneous for high finesse, resulting in the appearance of phase waves and a nontrivial carrier-envelop phase delay in the pulsed regime. The analysis shows several other properties of experimental relevance: narrowing of the intensity spectrum, vanishing two-mode correlators, optical bistability, robustness against small homogeneous dilution while a non-equipartited condensation appears for large dilution [2, 3].

A general mean-field model for light wave systems in optically active random media is solved via the replica method. The most general phase diagram, ranging from ordered closed cavities (standard lasers) to disordered open cavities (RLs) furnishes a number of different equilibrium phases determined by nonlinearity and disorder. These include passive mode locking in standard lasers, and different coherent regimes attainable in RLs. An experimental test for the RSB predicted by this theory at the RL threshold has been put forward in Ref. [11]: the symmetry breaking in the intensity fluctuation overlap is shown to be equivalent to the one occurring in the complex amplitude overlap, proposing a test directly for shot-to-shot intensity spectra. This result establishes that the intensity fluctuations analysis of Ref. [12] is the first experimental evidence of RSB.

ACKNOWLEDGMENT

This research has received funding from the People Programme of the European Union's Seventh Framework Programme FP7/2007-2013/ under REA grant agreement No. 290038, NETADIS project, from the ERC grant agreement No. 247328 — CriPheRaSy project — and from the Italian MIUR under the Basic Research Investigation Fund FIRB2008 program, grant No. RBF08M3P4, and under the PRIN2010 program, grant code 2010HXAW77-008.

REFERENCES

1. Gordon, A. and B. Fisher, *Phys. Rev. Lett.*, Vol. 89, 103901, 2002.
2. Antenucci, F., M. Ibáñez Berganza, and L. Leuzzi, *Phys. Rev. A*, Vol. 91, 043811, 2015.
3. Antenucci, F., M. Ibáñez Berganza, and L. Leuzzi, arXiv: 1412.8610, 2015.
4. Antenucci, F., C. Conti, A. Crisanti, and L. Leuzzi, *Phys. Rev. Lett.*, Vol. 114, 043901, 2015.
5. Antenucci, F., A. Crisanti, and L. Leuzzi, *Phys. Rev. A*, Vol. 91, 053816, 2015.
6. Viviescas, C. and G. Hackenbroich, *Phys. Rev. A*, Vol. 67, 013805, 2003.
7. Cao, H., et al., *Phys. Rev. Lett.*, Vol. 82, 2278, 1999.
8. Wiersma, D. S. and S. Cavalieri, *Nature*, Vol. 414, 708, 2001.
9. Marruzzo, A. and L. Leuzzi, *Phys. Rev. B*, Vol. 91, 054201, 2015.
10. Mézard, M., G. Parisi, and M. A. Virasoro, *Spin Glass Theory and Beyond*, 1987.
11. Antenucci, F., A. Crisanti, and L. Leuzzi, arXiv: 1412.8748, 2015.
12. Ghofraniha, N., et al., *Nature Communications*, Vol. 6, 6058, 2015.

Meandering Waveguide Distributed Feedback Lightwave Elements: Phasor Diagram Analysis

C. B. Dağ¹, M. A. Anıl¹, and A. Serpengüzel²

¹Department of Electronics and Telecommunications Engineering
Istanbul Technical University, Maslak, Istanbul 34469, Turkey

²Microphotonics Research Laboratory, Department of Physics
Koç University, Rumelifeneri Yolu, Sarıyer, Istanbul 34450, Turkey

Abstract— Meandering waveguide distributed feedback (DFB) structures are introduced as novel photonic lightwave circuits elements and their amplitude and phase response are studied in frequency and phasor domain. A preliminary transfer matrix method analysis is applied for taking the coupling purely directional and with constant coefficient on geometrically symmetric and anti-symmetric elements. The meandering loop mirror is the building block of all meandering waveguide based lightwave circuit elements. The simplest uncoupled meandering DFB structure exhibits Rabi splitting in the transmittance spectrum. The symmetric and antisymmetric coupled meandering waveguide DFB geometries can be utilized as band-pass, Fano, or Lorentzian filters or Rabi splitters. Meandering waveguide DFB elements with a variety of spectral responses can be designed for a variety of lightwave circuit element functions and can be implemented with generality due to the analytic approach taken. Meandering waveguide distributed feedback structures with a variety of spectral responses can be designed for a variety of lightwave circuit element functions.

1. INTRODUCTION

Distributed meandering waveguide (DMW) structures [1] show a variety of spectral behaviors with respect to the number of meandering loop mirrors (MLMs) [2] and the coupling constants (Cs) of the structure. These spectral behavior include Fano resonances, coupled resonator induced transparency (CRIT), notch, add-drop, comb, and hitless filters. What makes the DMW special is the self-coupling property intrinsic to the DMW's nature. The basic example of DMW's nature is motivated through the analogy between the so-called symmetric meandering resonator (SMR), which consists of two coupled MLMs, and the resonator enhanced Mach-Zehnder interferometer (REMZI) [3]. A SMR shows the same spectral characteristics of Fano resonances with its self-coupling property. Recently, single, distributed [4] and binary [5] self coupled optical waveguide (SCOW) resonators, which can be considered as special cases of the DMWs, are studied. Figure 1 shows the genealogy of the DMWs studied so far for their electric field intensity and phase responses [6]. In this proceeding, we present another complementary perspective to the phase characteristics of various DMWs, namely the phasor diagrams of the transmitted electric fields. The phasor diagram contains the complete information of a transmitted electric field with amplitude and phase information for all potential DMW structures.

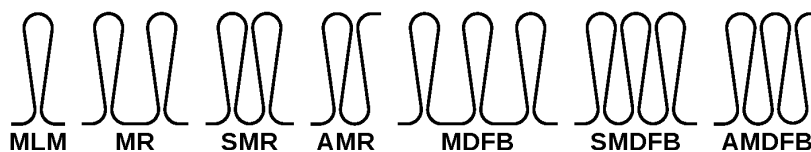


Figure 1: Genealogy of the distributed meandering waveguide structures studied in the frequency domain.

2. MEANDERING DISTRIBUTED FEEDBACK STRUCTURES

Figure 2 shows that an MDFB with 2 MLMs is capable of a phase contribution from 0 to π . There are 2 peaks (poles) in the intensity spectrum, when the normalized frequency (δ) runs from 0 to 4π . In Fig. 3, increasing the number of MLMs, results in the whole phase contribution from 0 to 2π . There are 2 peaks (poles) in the intensity spectrum, when the normalized frequency (δ) runs from 0 to 2π .

In Fig. 4, increasing the number of MLMs provides a phase interval of 4π . There are 10 peaks (poles), when the normalized frequency (δ) runs from 0 to 4π . First the blue line traverses the

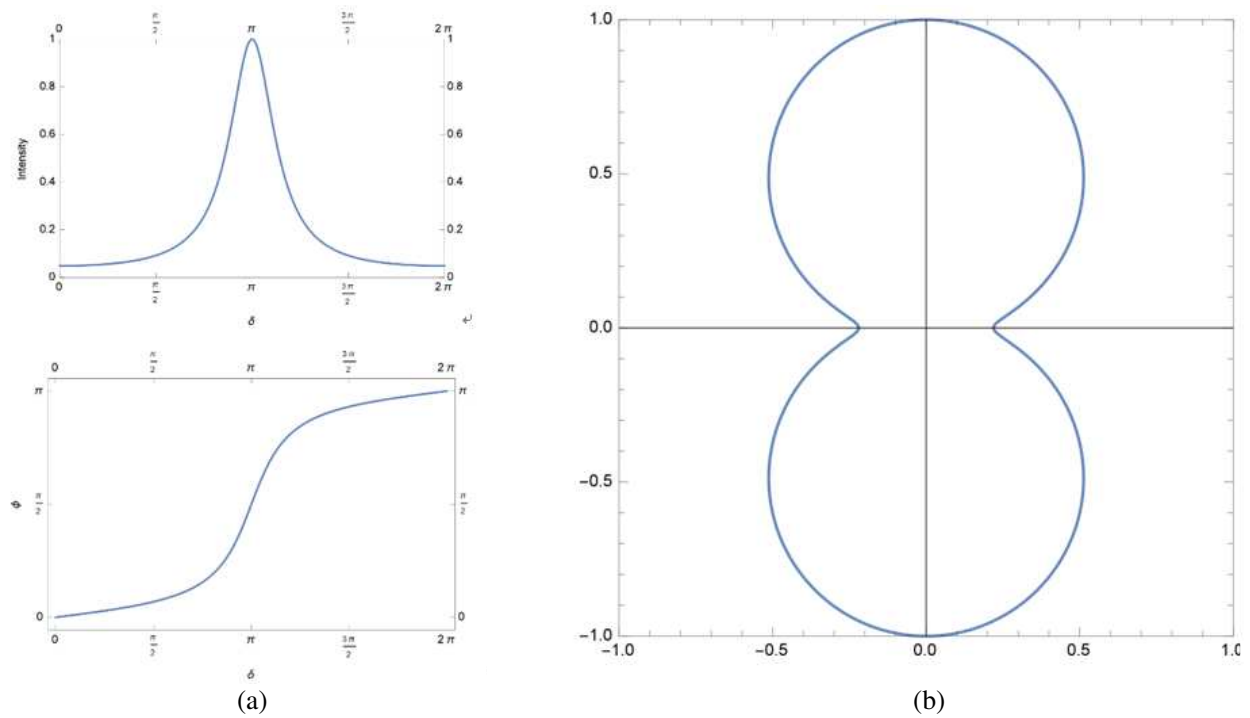


Figure 2: (a) The intensity, phase (Φ), and (b) phasor plots of an MDFB with 2 MLMs (or MR) when all coupling constants are set to 0.2. The normalized frequency (δ) runs from 0 to 2π in the intensity and phase response. Except in the phasor diagram, δ runs from 0 to 4π .

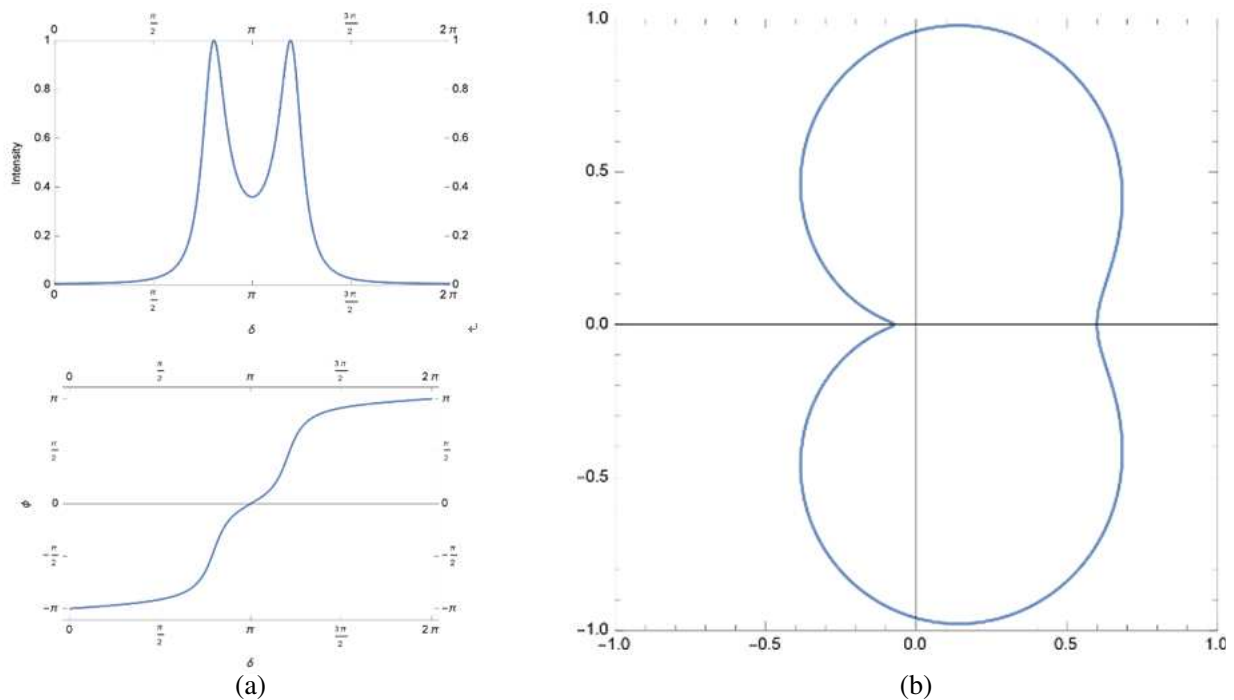


Figure 3: (a) The intensity, phase (Φ) and (b) phasor plots of an MDFB with 3 MLMs, when all coupling constants are set to 0.2. The normalized frequency (δ) runs from 0 to 2π in the intensity, phase, and phasor diagram response.

complex plane, then the orange, the green, the red, and the purple, respectively. All the coupling constants are $C = 0.2$.

3. SYMMETRIC & ANTISYMMETRIC MEANDERING RESONATOR

Figure 5 shows SMR frequency, phase and phasor diagram, depicting Fano resonances, for an SMR with 2 coupled MLMs. There are 2 peaks (poles) in the intensity spectrum, when the normalized frequency (δ) runs from 0 to 2π .

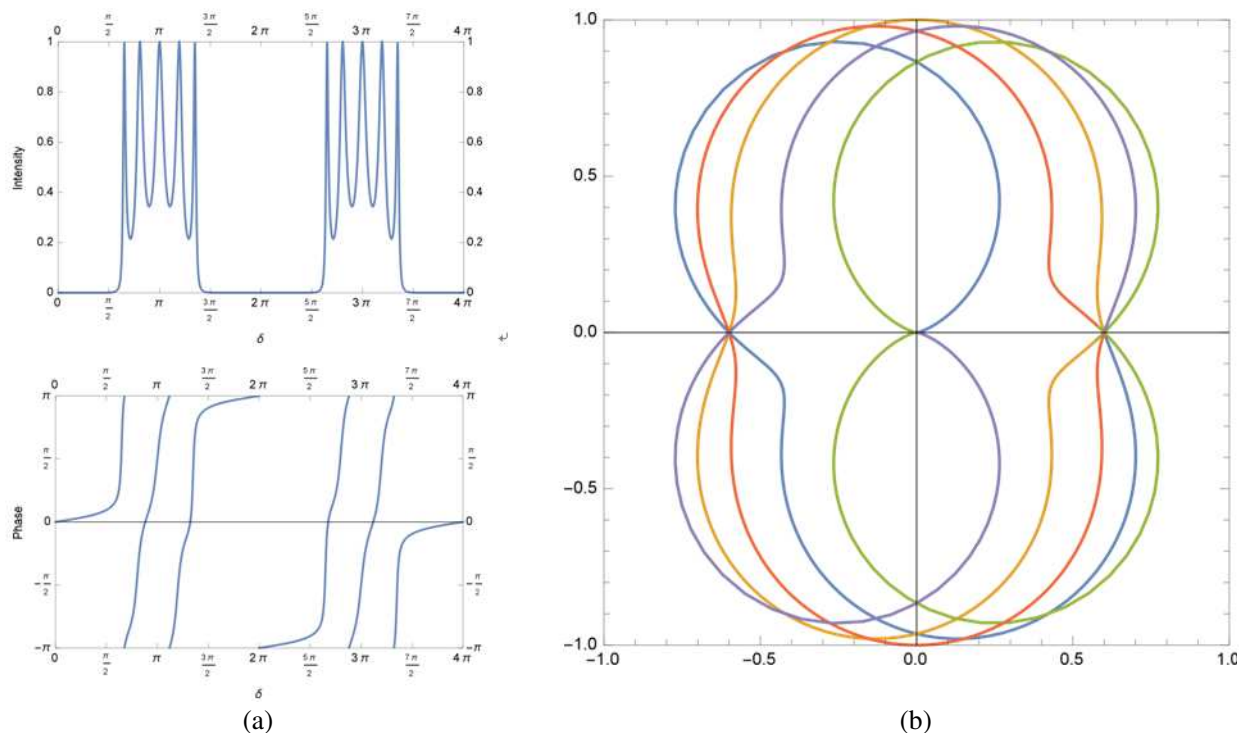


Figure 4: (a) The intensity, phase (Φ) and (b) phasor diagram of an MDFB with 6 MLMs, when the phase of the shortest path length, δ runs from 0 to 4π . The normalized frequency (δ) runs from 0 to 4π in the intensity, phase, and phasor diagram response.

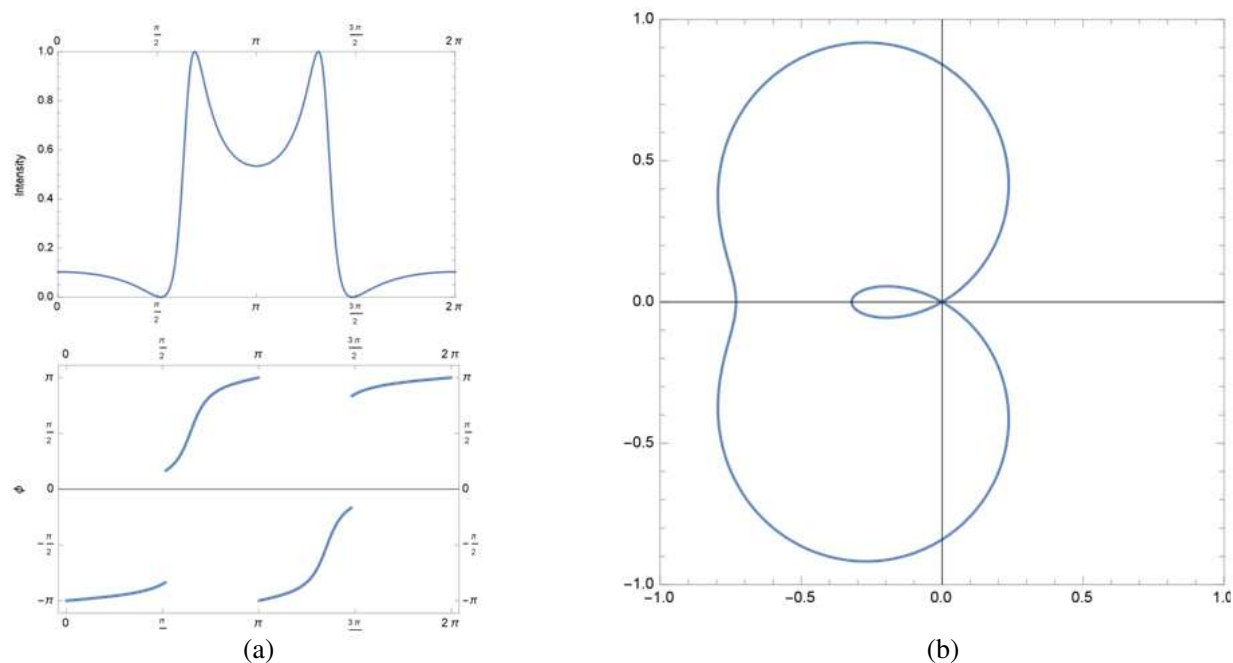


Figure 5: (a) The intensity, phase (Φ) and (b) phasor plots of an SMR, when all coupling constants are set to 0.2. The normalized frequency (δ) runs from 0 to 2π in the intensity, phase, and phasor diagram response.

Figure 6 shows an AMR frequency, phase, and phasor diagram with a narrow linewidth (orange curve) CRIT behavior for $C = 0.9$ and a broad linewidth (blue curve) CRIT behavior for $C = 0.2$. There are 2 peaks (poles) in the intensity spectrum.

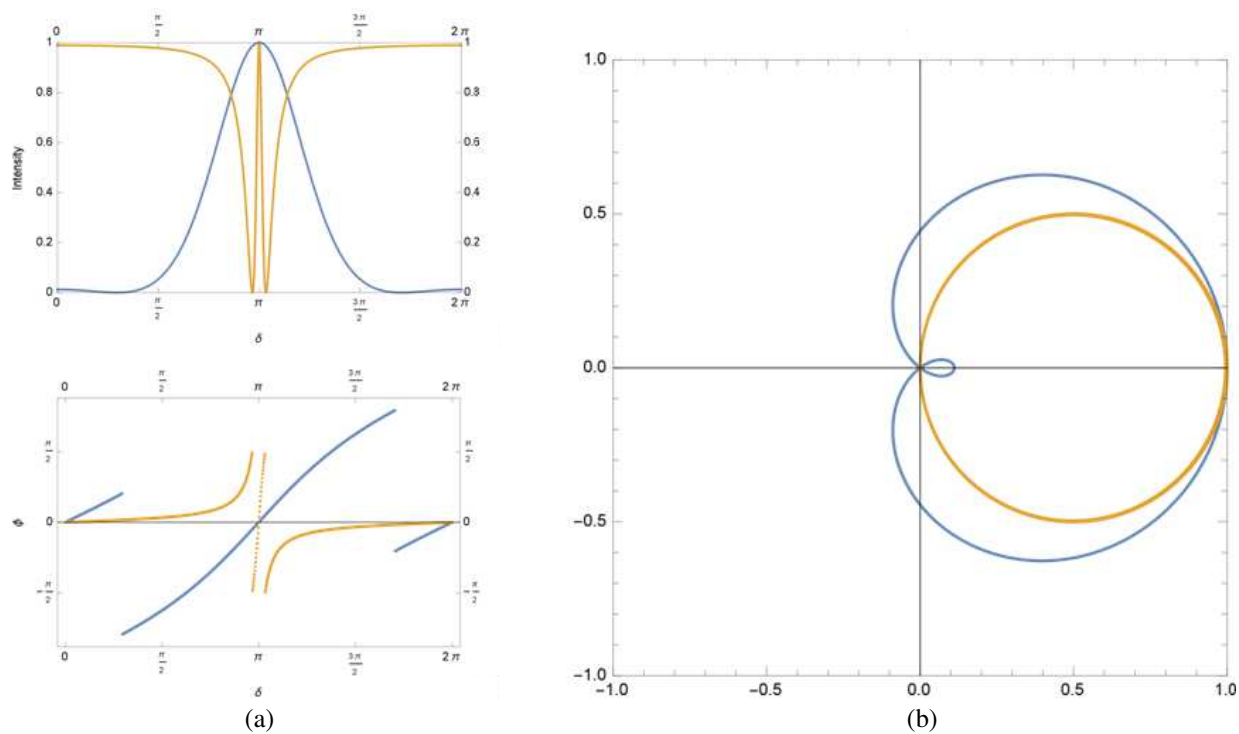


Figure 6: (a) The intensity, phase (Φ) and (b) phasor plots of an AMR, when all coupling constants are set to 0.2 (blue) and 0.9 (orange). The normalized frequency (δ) runs from 0 to 2π in the intensity, phase response, and phasor diagram response.

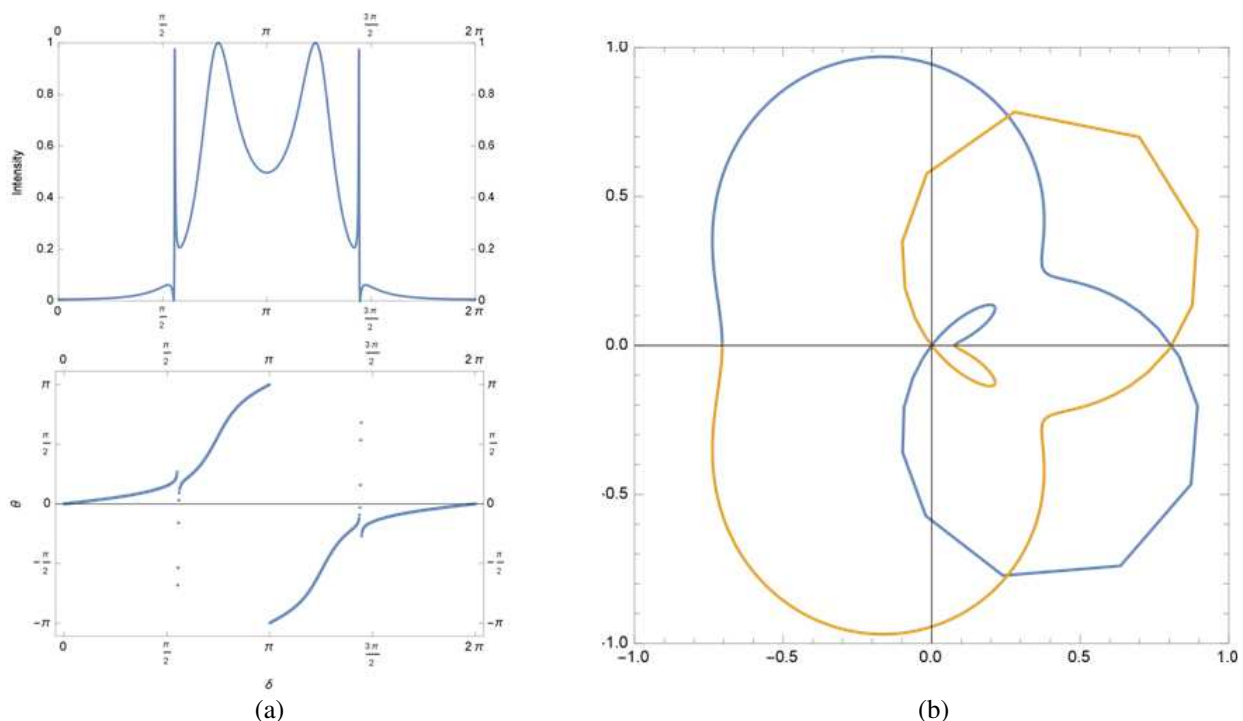


Figure 7: (a) The intensity, phase (Φ) and (b) phasor plots of an SMDFB with 3 MLMs, when all coupling constants are set to $C = 0.2$. The normalized frequency (δ) runs from 0 to 2π in the intensity, phase response, and phasor diagram response.

4. SYMMETRIC & ANTISYMMETRIC MEANDERING DISTRIBUTED FEEDBACK STRUCTURES

Figure 7 shows the SMDFB intensity, phase, and phasor diagrams as a function of the normalized frequency (δ), when all the coupling constants are set to $C = 0.2$. There are 4 peaks (poles) in the intensity spectrum. Figure 8 shows the AMDFB intensity, phase, and phasor diagrams as a function of the normalized frequency (δ), when all the coupling constants are set to $C = 0.2$. There are 3 peaks (poles) in the intensity spectrum.

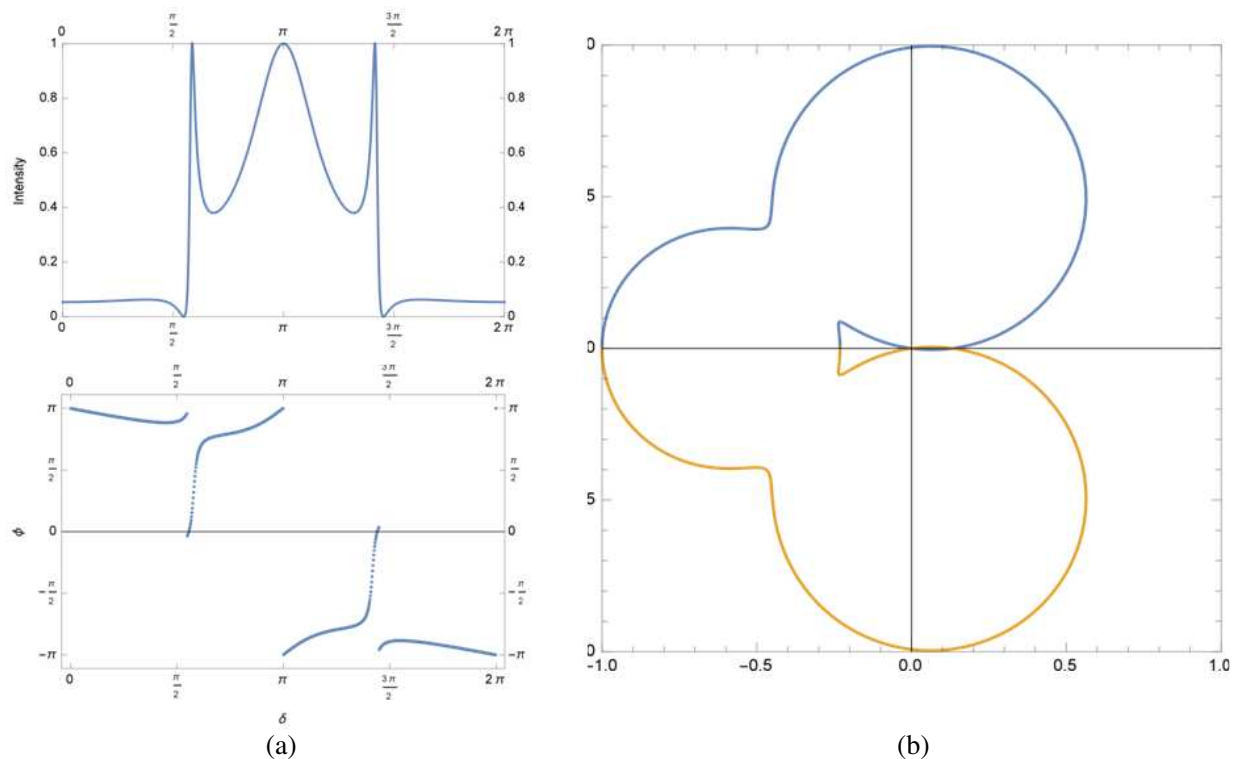


Figure 8: (a) The intensity, phase (Φ) and (b) phasor plots of an AMDFB of 2.5 MLM's, when all the coupling constants are set to $C = 0.2$. The normalized frequency (δ) runs from 0 to 2π in the intensity, phase response, and phasor diagram response.

5. CONCLUSIONS

We presented the intensity, phase, and phasor diagrams of the DMWs transmitted electric fields. The phasor diagrams give complete information of a transmitted electric field with amplitude and phase information for all the potential DMW structures.

REFERENCES

1. Dağ, C. B., M. A. Anıl, and A. Serpengüzel, "Meandering waveguide distributed feedback lightwave circuits," *J. Lightwave Technol.*, Vol. 33, No. 9, 1691–1702, May 2015.
2. Doran, N. J. and D. Wood, "Nonlinear-optical loop mirror," *Opt. Lett.*, Vol. 13, No. 1, 56–58, Jan. 1988.
3. Zhou, L. and A. W. Poon, "Fano resonance-based electrically reconfigurable add-drop filters in silicon microring resonator-coupled Mach-Zehnder interferometers," *Opt. Lett.*, Vol. 32, No. 7, 781–783, Apr. 2007.
4. Zhou, L., T. Ye, and J. Chen, "Coherent interference induced transparency in self-coupled optical waveguide-based resonators," *Opt. Lett.*, Vol. 36, No. 1, 13–15, Jan. 2011.
5. Zou, Z., L. Zhou, X. Sun, J. Xie, H. Zhu, L. Lu, X. Li, and J. Chen, "Tunable two-stage self-coupled optical waveguide resonators," *Opt. Lett.*, Vol. 38, No. 8, 1215–1217, Apr. 2013.
6. Dağ, C. B., M. A. Anıl, and A. Serpengüzel, "Novel distributed feedback lightwave circuit elements," *Proc. SPIE*, Vol. 9366, 93660A, San Francisco, 2015.

Magnetic Storms at High Latitudes and Slips in GPS Operating

V. I. Zakharov^{1,2}, Yu. V. Yasyukevich², and M. A. Titova³

¹Lomonosov Moscow State University, Moscow, Russia

²Institute of Solar-Terrestrial Physics of Siberian Branch of Russian Academy of Sciences
Irkutsk, Russia

³IZMIRAN, Moscow, Russia

Abstract— We analyzed strong magnetic storm and sub-storm influence on the GPS operating in the Arctic region. 5-years dynamic were analyzed based on IGS and CHAIN data (~ 200 receivers at more than 55°N latitude). The main studied parameters were phase and pseudorange slips as well as sharp physically unrealistic total electron (TEC) values variations (TEC slips). TEC slips were found to increase 100–200 times higher than just instrumental noises under helio-geomagnetic disturbances of different nature. The major cause of phase and pseudorange slips is GPS signal absorption in the ionosphere. The absorption is caused by high-energy particle precipitation during magnetic storms at high latitude.

1. INTRODUCTION

Analysis of the navigation and communication systems shows that currently the reliability of their operation is determined not only and not so much by instrumental failures, but increasingly influencing of different geo- and helio-physical factors, i.e., space weather, which is more pronounced at high Arctic latitudes. Strong geomagnetic disturbances can have a significant impact on the operating of radio systems using ionospheric radio channel. The same is true for the operating stability of the global navigation satellite systems such as GLONASS and GPS. The reason is influence of strong disturbances of electron density. The disturbances lead to sharp fluctuations in the group, phase and amplitude characteristics of the radio signal. Amplitude scintillation of navigation signal due to scattering of the radio signal on small-scale irregularities with size of the first Fresnel zone [1], which is of 100–300 m for GPS/GLONASS. There is a lot of papers deal with operation stability of GPS system under disturbed conditions [2–4]. A number of studies is devoted to high latitudes GPS operation [3, 5, 6].

At the same time, data on the direct measurement of navigation signal parameters failures at high latitudes is not enough and they are very fragmented. It is worth to note that geomagnetic disturbance in the majority of works were associated with sharp changing in the planetary index Dst, while at high latitudes strong substorms take place, which associated with local perturbations of currents in the magnetosphere. In addition, some fragmentary of data at high latitudes connected with lack of dense receivers network in this region. Recently the situation has changed. Development of global and regional GPS/GLONASS networks lead to increasing the statistics of navigation measurement parameters failures and total electron content (TEC) slips, including statistics at high latitudes.

2. EXPERIMENTAL DATA AND TECHNIQUE

As a slip we take two types of phenomena. First, we take “instrumental” failure, i.e., loss of pseudorange measurements or navigation signal phase for both operating frequencies. In the data files it corresponds to lack of measurement of these parameters. These slips are of technical nature and connected with the quality of electronic components of the radio transmission unit (RTU). The second group of slips is so-called TEC slips. TEC slip can be defined as sharp TEC variations, the values of which have no physical meaning (or, possibly due to unknown at this time processes and phenomena). For example, TEC rate higher than (2 ... 5) TECU/min surpass regular variability of the ionosphere, which is usually less than (0.1 ... 1) TECU/min.

The total electron content is determined based of dual-frequency phase measurements of GPS signal [7]:

$$I = \frac{1}{40.308} \frac{f_1^2 f_2^2}{f_1^2 - f_2^2} [(L_1 \lambda_1 - L_2 \lambda_2) + K + nL], \quad (1)$$

where, f_1, f_2 — operating frequency of GPS; $L_1 \lambda_1, L_2 \lambda_2$ — additional paths of radio signals caused by the phase delay in the ionosphere, m ; L_1, L_2 — the number of phase rotation at operating

frequencies; λ_1, λ_2 — wavelengths, $m; K$ — constant, due to the ambiguity of the phase definition, nL — error in determining the phase path.

The probability of slip of the parameter i (phase slip, pseudorange, TEC) for the selected station during the observation time T for a single navigation satellite is:

$$P_{T,i,\text{GPS}} = \frac{N_{i,\text{GPS}}(T)}{S_{i,\text{GPS}}(T)} \times 100\% \quad (2)$$

where $N_i(T)$ is the total number of slips of the parameter I for chosen GPS satellite during the observation time T . $S_i(T)$ is the total number of observations of the parameter i for a observation time.

To complete description of a GPS station, similar to (2) we calculated the overall probability of slips of the parameter i at the station during time T for all visible satellites. As a characteristic of the observation network consisting of M receivers we calculated N and S parameters for all line-of-sites “satellite-receiver”.

In this paper we studied the GPS slips dynamics during 2010–2014. For all stations of IGS network [8], located to the north of 55°N (Arctic region), we recorded pseudorange and phase at both operating frequencies. There were 97 stations in the IGS network in 2010 and 188 in 2014. In addition we used data from the network CHAIN (Canada), which included from 8 to 18 stations (<http://chain.physics.unb.ca>).

We used observational data in the RINEX format. All used data include more than 8.5 million hours of joint observations of P1, P2, L1, L2.

To determine the start of the geomagnetic disturbance and its strength, we used high-latitude AL, AU, AE magnetic indexes, instead of commonly used Dst and SYM-H indexes which describe the equatorial perturbations. AL, AU, AE were obtained with 1-min resolution (<http://wdc.kugi.kuoto-u.ac.jp/dstae/index.html>), but we used the 1-hour averaged indexes to better comparison with slips. In some cases, for interpretation we used magnetometers and riometers observations.

3. EXPERIMENTAL RESULTS

In the Fig. 1 we show the example of basically data of GPS slips on the subnet during strong magnetic substorm 09 March 2012 (upper panel), overall dynamics of L2 slips (middle left), L1 slips (middle, right) and TEC slips (bottom, left) for all line-of-sights “satellite receiver”. You can see slips statistic for the period of 11 days. Elevation cut were 10° . The blue curve shows the dynamics of AE-index. Bold horizontal lines define dispersion of slips over the last month against mean value (green line). One can see that response to magnetic substorm in L2 slips 5–7 times higher than in L1 slips.

It is worth to note that during strong disturbances dynamics of slips agree with AE index dynamics. The correlation during storm is usually more than 0.7 and can reach more than 0.9. Without geomagnetic disturbances slip probability is determined by internal problems of navigation equipment and generally poorly correlated with AE index. Similar situation take place when one use pseudorange measurements P1 and P2.

We also consider the time dynamics of TEC slips (see Fig. 1, left bottom panel). As the level of TEC slips we chose value 2 TECU/min. Dynamics of TEC slips corresponds to L2 slips. However, probability of TEC slips is 50–150 times greater than those of L2 slips.

In the Table 1 we show results of slips studies for 2010–2014. Overall, our studies show that the probability of L2 slips ~ 10 times larger than L1 those during magnetic storms and substorms of G3class. Growing storm strength, this ratio slightly decreases: P_{L2}/P_{L1} is up to 5–7. TEC slips are important parameters for research applications option. As we obtained, for TEC slips dynamics during geomagnetic disturbances is even more pronounced. For example, the probability of TEC slips for TEC rate more than 1 TECU/min increases depending on the class of the storm more than 6–15 times. For TEC slips supposed as a TEC rate more than 2 TECU/min, increase in the probability of slips is 4–10 times.

Right bottom panel in the Fig. 1 shows the riometer data at Dawson Station (DWS, 64.0°N , 139.1°W) recorded on March 09, 2012. There is an increase in absorption during the magnetic storm up to 8 dB. We should note that there were events with absorption increasing up to 17 dB.

The observed effects are generally easy to explain. According to the GPS interface control documents [9], they took different power for two operating frequencies. The power at f_2 is 3 dB less than those at f_1 . This fact along with significant absorption increasing due to particle precipitation during magnetic storms is a major cause of differences in slips probability.

Table 1: Maximal probabilities of slips for different substorms. Elevation cutoff is 10° .

Substorm level	AE , nT	Max $P(L1)$, %	Max $P(L2)$, %	Max $P(TEC1^*)$, %	Max $P(TEC2^*)$, %
G3	~ 600	0.1 ... 0.2	0.9 ... 1.5	1 ... 6	0.6 ... 4
G4	$\sim 600 \dots 1500$	0.15 ... 0.25	1.2 ... 3.5	5 ... 15	3 ... 6
G5	> 1500	0.25 ... 0.45	3.5 ... 5.5	15 ... 35	7 ... 15

*TEC1 and TEC2 correspond to the maximum derivative of the TEC more 1 or more 2 TECU/min, respectively.

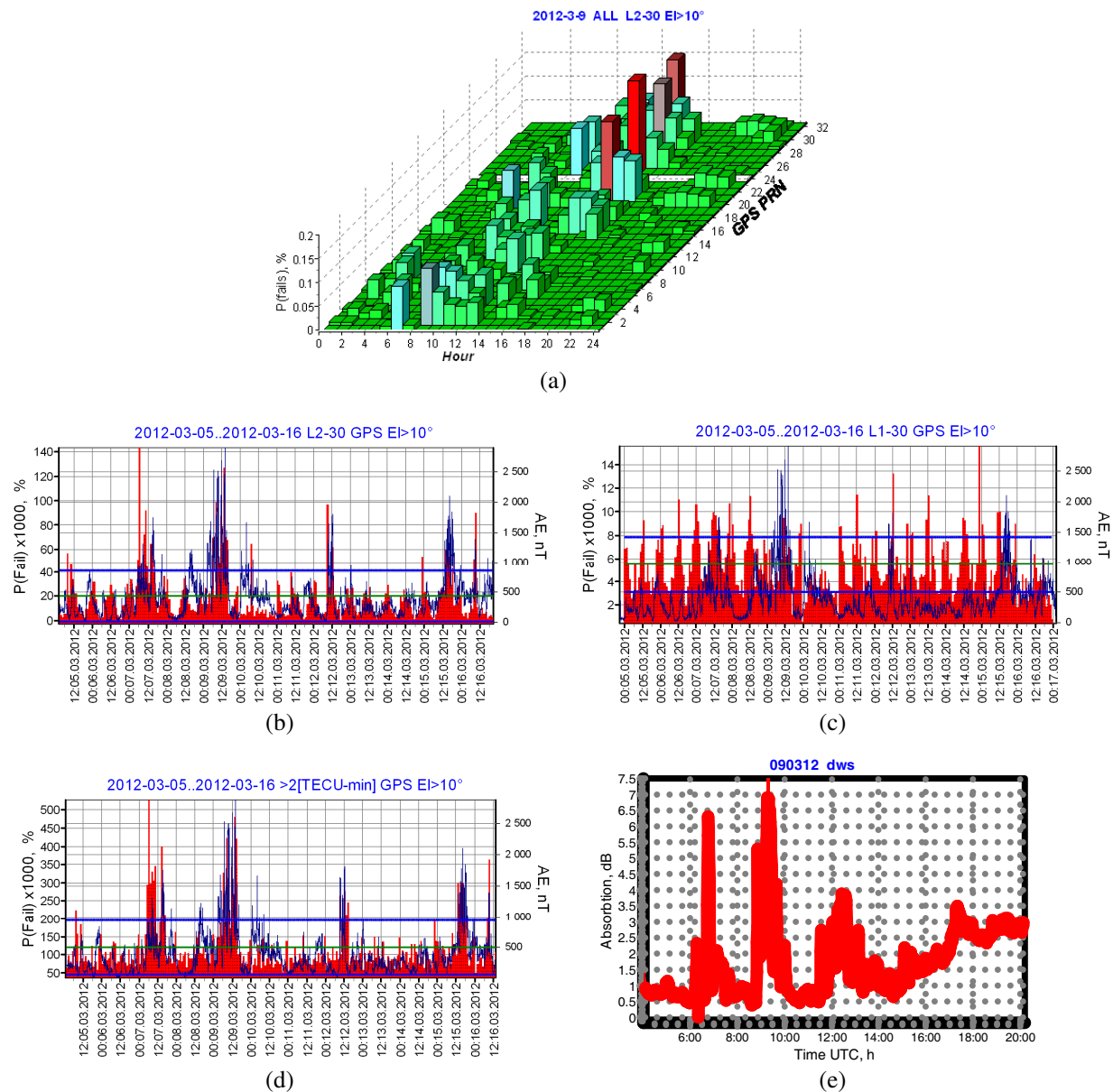


Figure 1: (a) Example of basically data of GPS slips on the subnet during strong magnetic substorm 09 March 2012. (b) The probability of L2 slips, (c) L1 slips, and (d) TEC slips on March 03–16, 2012. Thin blue curve is for AE index. (e) We show the level of radio waves absorption recorded by DWS station (64.048°N , 139.11°W).

The entire analysis we carried out for the three elevation cuts — 10° , 15° and 20° . The first two angles correspond to cuts which frequently used in the ionosphere and near-Earth space studies. 20° elevation cut is recommended for navigation applications. Analysis showed that slips probability is reduce by 15–20% when you use 20° elevation cut instead of 10° .

4. CONCLUSIONS

Our analysis showed that:

- L1 phase slips even under quiet conditions 3–15 times less than L2 those.
- Similar relation is true for slips of P2 and P1.
- The probability of L2 slips ~ 10 times larger than those of L1 slips during magnetic storms and substorms of G3 class. For G4 and G5 storms this ratio decreases slightly — up to 5–7 times. Similar results were obtained for the probability of P1 and P2 slips.
- TEC slips dynamics during magnetic storms more pronounced as compared with L1 and L2 slips. The probability of TEC slips ~ 100 – 200 times higher than those of L2 slips. Increasing the class of storm from 3 to 4 or from 4 to 5 TEC slips corresponding jumps of 1TECU/min increase more than 6–15 times. For TEC slips corresponding 2 TECU/min jump this value is 4–10 times.
- The main cause for L1, L2 slips increasing is absorption increasing, which is associated with high-energy particles precipitation at high latitudes during geomagnetic storms.
- Analysis showed that a possible solution to reduce the impact of slips on the navigation system of GPS is increasing the power of the navigation signal as well as increasing the cut-off elevation mask up to 20° .

ACKNOWLEDGMENT

The authors thank networks IGS [8] and CHAIN (<http://chain.physics.unb.ca>) for providing GPS data. Development of techniques for analyzing and investigation of slips during 2013–2014 were supported by the grant of the Russian Science Foundation (project No. 14-37-00027). Titova M. A. carried out data processing and riometers data analysis.

REFERENCES

1. Yeh, K. C. and C. H. Liu, “Radio wave scintillations in the ionosphere,” *Proc. IEEE*, Vol. 70, No. 4, 24–64, 1982.
2. Skone, S. and M. de Jong, “Limitations in GPS receiver tracking performance under ionospheric scintillation,” *Physics and Chemistry of the Earth 2001*, Part A, Vol. 26, No. 6–8, 613–621, 2001.
3. Doherty, P. H., S. H. Delay, C. E. Valladares, and J. A. Klobuchar, “Ionospheric scintillation effects in the equatorial and auroral regions,” *Proceedings of International Beacon Satellite Symposium*, 328–333, Boston College, Institute for Scientific Research, Chestnut Hill, MA, USA, Jun. 4–6, 2001.
4. Afraimovich, E. L., E. I. Astafyeva, V. V. Demyanov, I. K. Edemskiy, N. S. Gavriluk, A. B. Ishin, E. A. Kosogorov, L. A. Leonovich, O. S. Lesyuta, K. S. Palamartchouk, N. P. Perevalova, A. S. Polyakova, G. Ya. Smolkov, S. V. Voeykov, Yu. V. Yasyukevich, and I. V. Zhivetiev, “A review of GPS/GLONASS studies of the ionospheric response to natural and anthropogenic processes and phenomena,” *J. Space Weather Space Clim.*, Vol. 3, A27, 2013.
5. Aarons, J. and B. J. Lin, “Development of high latitude phase fluctuations during the January 10, April 10–11, and May 15, 1997 magnetic storms,” *Atm. Sol.-Terr. Phys.*, Vol. 61, 309–327, 1999.
6. Basu, S., S. Basu, E. MacKenzie, and H. E. Whitney, “Morphology of phase and intensity scintillations in the auroral oval and polar cap,” *Radio Sci.*, Vol. 20, No. 3, 347–356, 1985.
7. Hoffman-Wellenhoft, B., *GPS Theory and Practice*, 656, Springer-Verlag Vienna, New York, 1998.
8. Dow, J. M., R. E. Neilan, and C. Rizos, “The international GNSS service in a changing landscape of global navigation satellite systems,” *Journal of Geodesy*, Vol. 83, No. 3–4, 191–198, 2009, DOI: 10.1007.
9. “Global positioning systems directorate,” Systems Engineering & Integration, Interface Specification, IS-GPS-200, Sep. 5, 2012, www.gps.gov/technical/icwg//IS-GPS-200G.pdf.

Characteristics of HF Radio Waves Propagation along Subauroral and Mid-latitude Paths over Eastern Siberia during Magnetoactive Period in February 2014

V. I. Kurkin, N. M. Polekh, S. N. Ponomarchuk, A. V. Podlesny,
N. A. Zolotukhina, and E. B. Romanova
Institute of Solar-Terrestrial Physics SB RAS, Irkutsk, Russia

Abstract— Based on vertical and oblique-incidence sounding data, we analyzed characteristics of HF propagation during magnetoactive period in February 2014. The oblique-incidence sounding data had been obtained over subauroral and mid-latitude paths: Magadan-Irkutsk, Khabarovsk-Irkutsk, Khabarovsk-Norilsk, and Magadan-Norilsk. The period considered was characterized by a series of solar flares accompanied by intensification of proton and X-ray fluxes as well as by coronal mass ejections. These processes caused two magnetic storms of different intensity. During the main and recovery phases of the first storm, positive ionospheric disturbances were observed in the day, and negative, in the night. During the second magnetic storm, the maximum observed frequencies (MOF) over the Magadan-Irkutsk path fell sharply by 3–5 MHz. Intervals of low MOF values alternated with intervals of absence of reflected signals in ionograms. It specifies that boundaries of the main ionospheric trough could be displaced to the latitude of this path's midpoint. A similar absence of reflected signals in the ionograms was registered over the Khabarovsk-Norilsk path. Besides, during these two storms the oblique sounding ionograms showed additional signals with large time delays over the Magadan-Irkutsk and Khabarovsk-Irkutsk paths in evening and nocturnal hours. The abnormal signals were characterized by strong diffusion and their frequencies considerably exceeded MOF of standard propagation modes. Since the ionosphere is not perfectly horizontally stratified during magnetic storms, signals associated with propagation mode may arrive at a receiving point over a wide range of azimuth angles.

1. INTRODUCTION

Extreme space weather events caused by powerful solar flares and their associated magnetic storms can significantly affect radio communication, navigation and radar facilities. Numerous studies of solar flare effects on the magnetosphere-ionosphere-thermosphere system presented in reviews and original papers, for example [1, 2, 4], have showed that solar X-ray bursts and intensification of precipitation particle fluxes cause an electron density increase in the lower ionosphere, which can produce abnormally high attenuation of received HF signals and even blackouts. Heating of the ionospheric plasma due to particle precipitation and increased magnetospheric convection changes dynamics of the neutral atmosphere. During magnetic storms, boundaries of the main ionospheric trough (MIT) and auroral particle precipitation zone are displaced; activity of traveling ionospheric disturbances increases. These processes produce multipath propagation of signals as well as radio signals propagating off the great circle. Despite many years of studies of ionosphere behavior during magnetic storms, many questions remain open. This is associated with the fact that the ionospheric response to magnetic disturbances depends on many factors, therefore analyses of ionospheric parameter variations and characteristics of decametric radio wave propagation during geomagnetic events can provide additional data for studying magnetosphere-ionosphere coupling and their effects on characteristics of the ionospheric radio channel.

In this paper, using simultaneous observations over the oblique-incidence sounding paths, we analyze variations in maximum observed frequencies (MOF) during magnetically active period of February 18–28, 2014. Data on solar flares, geomagnetic indices, solar X-ray fluxes, parameters of the interplanetary magnetic field and solar wind have been taken from the following websites: <http://wdc.kugi.kyoto-u.ac.jp>, http://thesis.lebedev.ru/sun_flares.html, <ftp://ftp.ngdc.noaa.gov/S-TP>, <http://cdaweb.gsfc.nasa.gov>.

During this period, there were 12 X-ray flares of different intensity. Some of them were accompanied by coronal mass ejections and enhanced solar proton fluxes. The most powerful of solar flares with X4.9/2B intensity was registered on February 25 at 0039 UT. In consequence of it the minimum observed frequencies over the Khabarovsk-Irkutsk and Magadan-Irkutsk paths increased by 4–5 MHz. The interaction of solar wind inhomogeneities with the Earth's magnetosphere generated two magnetic storms. The first storm began on February 18 (minimum SYM-H = -127 nT

on February 19 at 0823–0824 UT) and had a long-term recovery phase. Against the background of this phase, there were substorms accompanied by a decrease in the Dst index (February 20, 22 and 23). The second storm began on February 27. Its minimum (SYM-H = -101 nT) was recorded on February 27 at 2324–2326 UT. Variations in the interplanetary magnetic field vertical component (IMFBz), geomagnetic indices Dst and Kp, AE are shown in Figure 1.

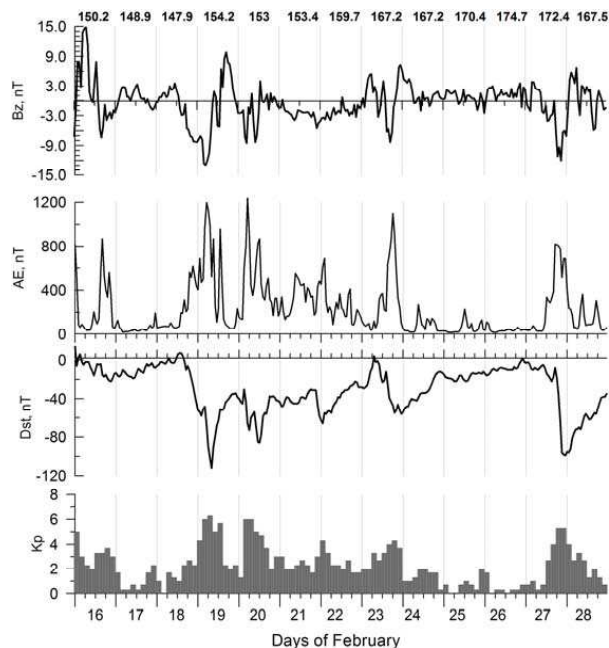


Figure 1: Variations in the IMF Bz, AE, Dst, and Kp indices on February 16–28, 2014. Numbers at the top of the figure indicate variations in the solar activity index $F_{10.7}$.

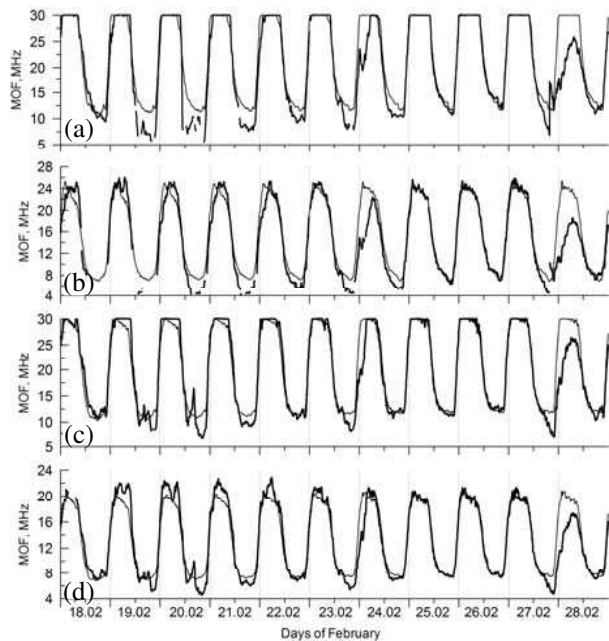


Figure 2: Variations in the MOF over the Magadan-Irkutsk ((a) MOF1F, (b) MOF2F) and Khabarovsk-Irkutsk ((c) MOF1F, (d) MOF2F) paths on February 18–28, 2014. The solid line shows current values; the dotted line, background MOF.

2. EXPERIMENTAL DATA

This study relies on oblique-incidence sounding data obtained over a network of radio paths located in the northeast region of Russia: Magadan-Irkutsk (the path length is 3034 km), Khabarovsk-Irkutsk (2297 km), Magadan-Norilsk (3000 km), Khabarovsk-Norilsk (3407 km). Sounding over the Magadan-Irkutsk and Khabarovsk-Irkutsk paths was conducted with an interval of 5 min; over the Khabarovsk-Norilsk and Magadan-Norilsk paths, with an interval of 15 min. Figure 2 shows time variations in MOF of one-hop (MOF1F) and two hop (MOF2F) modes of propagation over the Magadan-Irkutsk (a), (b) and Khabarovsk-Irkutsk (c), (d) paths. As can be seen from figure, daytime MOF1F of one-hop modes over both paths exceed the upper threshold of registration (30 MHz). According to the variations in the MOF2F mode over the Magadan-Irkutsk path, the first magnetic storm was followed by a decrease in MOF2F to 2–4 MHz in the morning, by an increase to 3.5–4.8 MHz, in the afternoon. The greatest morning decrease in MOF was recorded on February 24. It was observed during the substorm on February 23–24. The night MOF1F and MOF2F were below the background level calculated from two magnetically quiet days of February 13 and 14. The second magnetic storm caused an abrupt decrease in both MOF1F and MOF2F during the main and recovery phases of the storm. The decrease in daytime MOF2F was as much as 55%.

The most complex mode composition of reflected radio signals was observed in nighttime. Along with the basic modes, we recorded additional diffuse signals with large time delays, which propagated off the great circle. We suppose that they were caused by reflection from the polar wall of MIT. These signals were being observed on February 19 at 1000–1800 UT, on February 20 at 1030–1925 UT, on February 23 at 1445–2230 UT.

MOF variations over the Khabarovsk-Irkutsk path (Figs. 2(c)–(d)) are generally similar to variations over the Magadan-Irkutsk path. The difference is that positive disturbances occurred during all daylight hours on February 18–23. The MOF2F increase relative to background values reached

4–5 MHz (on February 19–20). In the morning on February 24, MOF1F and MOF2F variations exhibited an abrupt decrease relative to the background values. During the second magnetic storm, MOF2F decreased to 40% on February 28 in the afternoon. While the midpoint of the Khabarovsk-Irkutsk path is $\sim 7^\circ$ further south than the midpoint of the Magadan-Irkutsk path, the additional diffused signals with large delays were also recorded over this path. They were being observed on February 23 from 1800 UT to 2151 UT and on February 27 (at 1921–2236 UT as one-hop mode and 2156–2326 UT as two-hop mode).

Another remarkable feature of the MOF variations over this path is a pronounced increase in MOF observed on February 20 between 1601 and 1651 UT. This might have been caused by the passage of a large-scale ionospheric disturbance since maximum values of frequency were registered

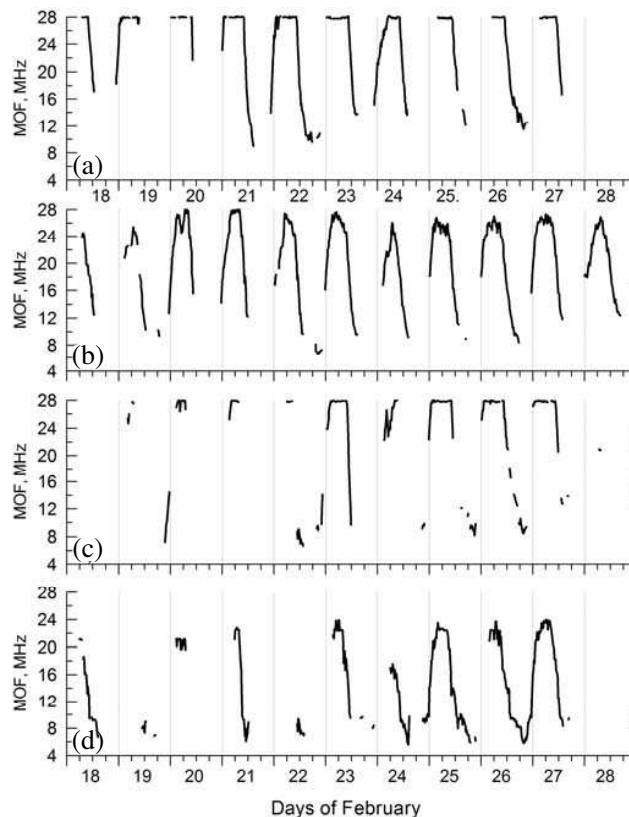


Figure 3: The same as Fig. 2 but for (a), (b) Khabarovsk-Norilsk path and (c), (d) Magadan-Norilsk.

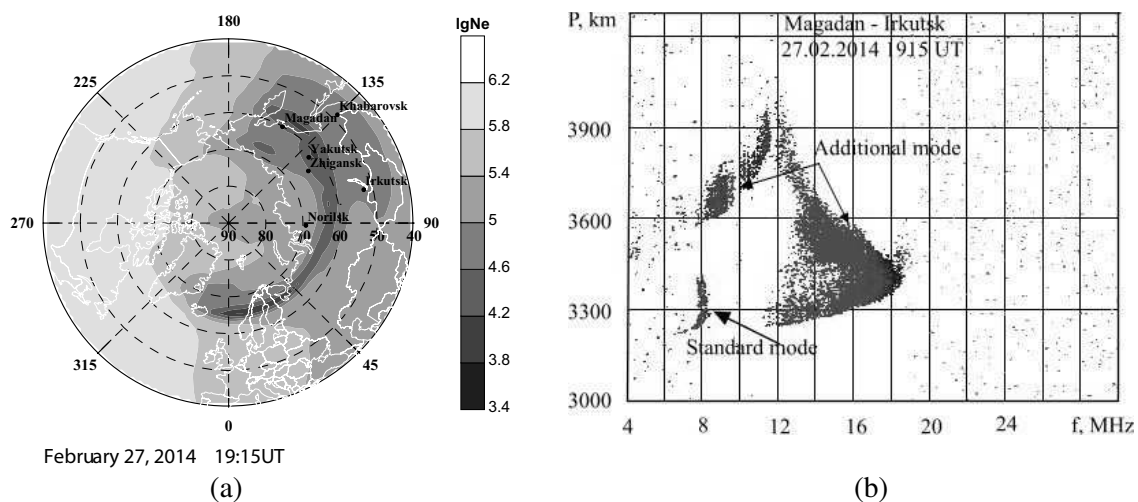


Figure 4: The simulation of electron density distribution for (a) 1915 UT on February 27, 2014 and the oblique incidence ionogram, obtained over Magadan-Irkutsk path corresponding to (b) this time.

at 1611 UT in MOF1F variations and at 1626 UT in MOF2F ones. This disturbance might have produced a slight increase in MOF1F against the extremely low values over the Magadan-Irkutsk path, which was being seen from 1536 to 1551 UT. Vertical sounding ionograms also show an increase in critical frequencies: in Khabarovsk at 1600–1615 UT, in Irkutsk at 1545–1600 UT.

Figure 3 illustrates MOF variations over the Khabarovsk-Norilsk (a), (b) and Magadan-Norilsk (c), (d) paths. It is obvious that MOF1F over both paths was registered only during the day, and its value exceeded the upper threshold of registration (28 MHz). The two-hop mode MOF was recorded more often, especially over the Khabarovsk-Norilsk path. The daytime MOF2F variations over this path are similar to variations of this mode registered over the Magadan-Irkutsk and Khabarovsk-Norilsk paths. It can be seen that the daytime MOF2F values on February 20–23 (the first storm recovery phase) are higher than those recorded on February 25–26 under quiet geomagnetic conditions. Over the Magadan-Norilsk path, most regular two-hop mode took place only under quiet geomagnetic conditions (February 25–26).

3. DISCUSSION AND CONCLUSIONS

The data have been interpreted using a theoretical model developed at ISTP SB RAS [3]. The model accounts for ionization processes, driven by UV radiation and precipitating electron fluxes, recombination, ionospheric plasma drift under the action of the magnetospheric convection electric field. By way of illustration, Figure 4(a) shows distribution of the electron density calculated for 1915 UT of February 27, 2014. The figure clearly depicts a narrow MIT near 60°N in a longitudinal sector from -10°E to 170°E . The MIT width is maximum (about 6°) in the 130°E meridian. The station Magadan was in the MIT minimum; the station Yakutsk, near the polar wall (near the MIT minimum). The same MIT shift to the geographical latitude of $55\text{--}57^{\circ}$ are shown by calculations made using empirical model [4] for other time intervals during which additional reflections with large time delays were being registered. A significant part of the Magadan-Norilsk path was located in MIT in evening and night hours. The middle part of the Khabarovsk-Norilsk path was located in a region of the lowest electron density. This explains the absence of reflections in oblique-incidence ionograms. The appearance of additional reflections over the Magadan-Irkutsk and Irkutsk-Khabarovsk paths and the decrease in their time delays are attributed to the approach of MIT boundaries to midpoints of the paths.

Similar additional signals with delays exceeding those of standard reflections were recorded at the vertical sounding stations Irkutsk.

Thus, the experimental oblique-incidence sounding data obtained during the geomagnetic period of February 18–28, 2014 revealed a complex picture of the influence of electron density distribution on characteristics of the ionospheric radio channel. Simulation of electron density allowed us to qualitatively explain the observed phenomena. The results we obtained demonstrate the importance of a precise definition of major morphological structures boundaries in the polar ionosphere, which determine characteristics of radio wave propagation.

ACKNOWLEDGMENT

This study was supported by the Grant of the Russian Scientific Foundation (Project No. 14-37-00027).

REFERENCES

1. Le, H., L. Liu, B. Ghen, J. Lei, X. Yue, and W. Wan, "Modeling the responses of the middle latitude ionosphere to solar flares," *J. Atmos. Solar-Terr. Phys.*, Vol. 69, 1587–1598, 2007.
2. Mitra, A. P., *Ionospheric Effects of Solar Flares*, D. Reidel Publishing Company, Dordrecht Holland/Boston, USA, 1974.
3. Tashchilin, A. V. and E. B. Romanova, "Numerical modeling the high-latitude ionosphere," *Proc. COSPAR Colloquia Series*, Vol. 14, 315–325, 2002.
4. Zherebtsov, G. A., O. M. Pirog, and O. I. Razuvaev, "Structure and dynamics of the high-latitude ionosphere," *Issledovaniia Po Geomagnetizmy, Aeronomii I Fizike Solntsa*, Vol. 76, 165–177, 1986.
5. Zolotukhina, N., N. Polekh, V. Kurkin, and E. Romanova, "Ionospheric effects of solar flares and their associated particle ejections in March 2012," *Advances in Space Research*, 2015, doi: <http://dx.doi.org/10.1016/j.asr.2015.03.004>.

Comparative Analysis of Geomagnetic Field and GPS-TEC Variations for Middle-latitude and Arctic Regions

Ilya K. Edemskiy¹, Nataly P. Perevalova¹, Anna S. Polyakova¹,
Olga V. Timofeeva^{1,2}, and Darya D. Katashevtseva^{1,2}

¹ISTP SB RAS, Russia

²Irkutsk State University, Russia

Abstract— We present the results of comparative analysis of geomagnetic field and total electron content (TEC) variations. The analysis is based on the long series of data from the Siberian GPS network of the Institute of solar-terrestrial physics (ISTP) of Siberian Branch of Russian Academy of Science (SB RAS) and Norilsk GPS station operated by the Geophysics Service of RAS (GS RAS.) ISTP SB RAS Siberian network makes continuous TEC measurements since 2012 and provides TEC-variation data with time resolution of 1 sec. The calculation of TEC is based on two-frequency phase measurements of GPS receivers. We analyzed TEC variations in two period ranges (0–10 min and 10–40 min), which are correspond to different types of ionospheric disturbances. Magnetic intensity data were obtained from ISTP SB RAS observatories and INTERMAGNET sites. The common level of TEC disturbance is estimated by the index of the TEC-variation intensity W_{tec} . The index is calculated for all available GPS satellites with the highest elevation angle at every moment. This method allows to investigate continuous variations of TEC disturbances intensity. The W_{tec} was calculated for all the GPS data 2013. The W_{tec} dynamics features are revealed for different times of day, seasons and levels of geomagnetic activity for middle-latitude and Arctic regions. The response of the W_{tec} to sudden storm commencements (SSC) was also investigated.

1. INTRODUCTION

Modern global navigation satellite systems (GNSS) GPS and GLONASS with wide networks of ground receivers is a unique instrument for monitoring the Earth's upper atmosphere. Space distribution of "receiver-satellite" rays during a day for only one GNSS receiver provide ionosphere observation in radius of 500–1000 km. However length of GNSS-provided continuous total electron content (TEC) series is restricted by satellite observation time (2–6 h). Such limitation obstructs investigation of long-term TEC variations connected with processes in Earth's magnetosphere and caused by solar wind via magnetic storms and sub-storms [1–3]. But in Arctic region such type of processes exactly influence ionospheric plasma dynamics. The method permitting calculation continuous TEC variations intensity investigation by single GNSS-station measurements is worked out in the Institute of solar-terrestrial physics of Siberian Branch of Russian Academy of Science (ISTP SB RAS) [4]. Moreover, ISTP SB RAS actively develop Siberian network of GPS/GLONASS stations which should increase ionospheric monitoring potential in Siberia.

Abilities of Siberian GNSS network and new data processing method allow us to carry out comparative analysis of geomagnetic field and total electron content variations for middle-latitude and Arctic regions.

2. DATA AND PROCESSING METHODS

Analysis of the common level of TEC disturbance in 2013 is made for high- and middle-latitudes. Data in middle-latitudes are obtained from the Siberian GPS/GLONASS network of ISTP SB RAS. This network makes continuous TEC measurements since 2012 and provides TEC-variation data with time resolution of 1 sec. We used data from GPS/GLONASS stations ORDA (ISTP SB RAS observatory in Usolie-Sibirskoe city), LIST (ISTP SB RAS observatory in Listvyanka village), MOND (ISTP SB RAS observatory in Mondy village), UZUR (ISTP SB RAS observatory in Uzur village). Data in high latitudes are obtained from GNSS station NRIL operated by the Geophysics Service of RAS (GS RAS) and located in Norilsk Integrated Magnetic-Ionospheric Station (69.4°N, 88.2°E) of ISTP SB RAS.

The TEC calculation is based on two-frequency phase measurements of GPS receivers. We analyzed TEC variations in two period ranges (01–10 min and 01–40 min), which are correspond to medium (MS) and large scale (LS) traveling ionospheric disturbances (TIDs). MS TIDs and LS TIDs should be associated with acoustic and gravity modes of atmospheric oscillations, respectively.

The common level of TEC disturbance was estimated by the index $W_{\text{tec}}(t)$ of the TEC variation intensity. We calculated $W_{\text{tec}}(t)$ index for all available GPS satellites with elevation angles $> 5^\circ$. First of all we filtered initial TEC series $I(t)$ in period ranges 01-10 min and 01-40 min, using a moving average method. Then for each filtered TEC series $dI(t)$ the module $A(t)$ of amplitude of TEC oscillations was computed. At a final stage we defined the intensity $W_{\text{tec}}(t)$ of TEC variations as averaged $A(t)$ over all “satellite-receiver” lines of sight (LOS). Since GPS satellites are observed in various intervals of time, sharp leaps may occur in averaged data on borders of time series from different satellites when simple averaging of data is used. So we utilized the procedure of $A(t)$ weighed averaging for all observed satellites. The described procedure of $W_{\text{tec}}(t)$ calculation allows us to obtain a continuous averaged series of TEC variation intensity filtered in the chosen period range, with any duration. The sampling rate of averaged TEC series is determined by sampling rate of GPS observations.

The $W_{\text{tec}}(t)$ behavior was compared with geomagnetic field variations, obtained from ISTP SB RAS magnetic station IRKT included in the INTERMAGNET network, and with behavior of geomagnetic Dst, Kp, AE indexes (<http://wdc.kugi.kyoto-u.ac.jp/wdc/Sec3.html>). The Dst, Kp indexes are estimated from equatorial and middle-latitude magnetic observatories data, respectively. As a first approximation the DST is supposed to be a variation of a ring current field. Perturbation in Earth’s magnetic field is considered as a magnetic storm when the Dst index falls lower than -50 nT, and Kp exceeds 4. For calculation of the high-latitude AE index, magnetograms from the observatories located on auroral and sub-auroral latitudes are used. The AE index characterizes fluctuations of a magnetic field connected with auroral zone currents (the auroral electrojet) and is the indicator of sub-storm activity.

3. RESULTS AND DISCUSSION

We calculated $W_{\text{tec}}(t)$ for both high- and middle-latitude regions and analysed correlation between them and magnetic AE, Dst, Kp indexes for every month of 2013. Variations of $W_{\text{tec}}(t)$, $AE(t)$, $Dst(t)$, $Kp(t)$ in March, June, September and December of 2013 are presented in Fig. 1. Fig. 2 shows diurnal-seasonal $W_{\text{tec}}(t)$ variations in high- and middle-latitude regions for two period ranges: 01–10 min and 01–40 min. TEC data are presented on Figs. 1 and 2 obtained on NRIL, ORDA and MOND GNSS stations.

The intensity of LS variations (periods ~ 40 min) is higher than of MS ones (~ 10 min). In high-latitude region LS and MS TID minimal intensities are about 0.12 TECU and 0.02 TECU, respectively. Minimal intensity level does not depend on season. Most pronounced diurnal variations are in March-April and September-October. Diurnal variations are more intense for MS disturbances (Figs. 1, 2). Diurnal W_{tec} variations are connected with NRIL Arctic circle location. Polar day and polar night last there about several weeks: from 30 November till 13 January and from 19 May till 25 July, respectively.

In middle-latitude region disturbance minimal intensity has certain seasonal variations. In winter, it is about 0.006 TECU for MS TIDs and 0.03 TECU for LS TIDs, in summer, it rises to 0.01 TECU and 0.07 TECU, respectively. Diurnal variations of $W_{\text{tec}}(t)$ intensity have also some seasonal features. In the summer, the disturbances are more intense at the beginning and the end of the day, whereas in all the other seasons it is higher in the middle of the day. It is also interesting that daytime $W_{\text{tec}}(t)$ level increases in the end of 2013 in both period ranges (Figs. 1(d), 2(d)). In October intensity increases and high values (0.05–0.06 TECU for MS TIDs; 0.2–0.3 TECU for LS TIDs) persist till the end of the year.

Black lines in Fig. 2(d) mark the sunrise moments at 100 km and 300 km over the station MOND. One can see that solar terminator (ST) generates intense LS disturbances. MS TIDs caused by terminator are not observed (Fig. 2(d)). Presented in Figs. 2(c), (d) $W_{\text{tec}}(t)$ variations are obtained using MOND data, but all the other middle-latitude stations demonstrates the same picture. Our results is in a good agreement with [5], where it was shown that in middle-latitudes ST generates ionospheric disturbances with periods T more than 15 min, and disturbances with $T < 10$ min are not presented. These allow us to conclude that solar terminator generates gravity waves ($T > 10$ min [3]) and does not generate acoustic ones ($T < 10$ min [3]). In Arctic region (NRIL station, Figs. 2(a), (b)) ST-caused disturbances are absent in $W_{\text{tec}}(t)$ variations of both period ranges.

Magnetic storm influence on disturbances intensity is different for high- and middle-latitude regions. High-latitude ionosphere is naturally more sensitive to magnetic field disturbances.

TEC disturbances intensity on NRIL station is significantly increases (up to 10-15 times) during

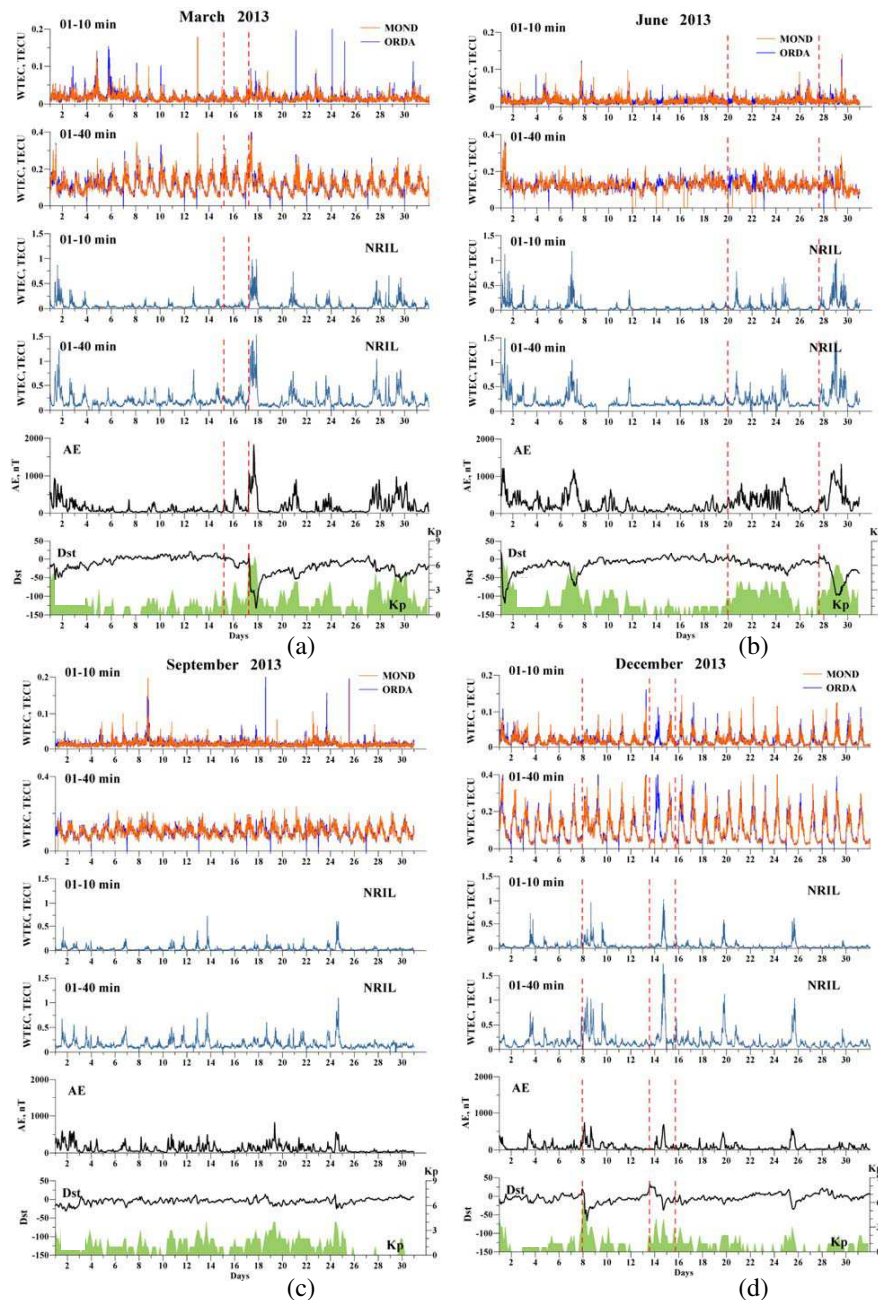


Figure 1: The TEC disturbance variations $W_{tec}(t)$ in two period ranges (01–10 min, 01–40 min) at NRIL, MOND, ORDA stations and behavior of Dst, Kp, AE geomagnetic indexes in March (a), June (b), September (c), December (d), 2013. The vertical dashed lines indicate sudden storm commencements (SSC).

geomagnetic storms (Fig. 1). Consistency between variations of $W_{tec}(t)$ and magnetic indexes Dst and Kp in this periods is also quite clear. In other periods correlation is much lower because Kp and Dst represent magnetic field dynamics in equatorial- and middle-latitudes. At the same time there is high correlation between $W_{tec}(t)$ and high-latitude AE index (correlation coefficient is 0.6–0.8). $W_{tec}(t)$ dependence on magnetic field fluctuations is prevailing in high-latitudes; it overrides diurnal $W_{tec}(t)$ variations (Figs. 1, 2).

$W_{tec}(t)$ response to magnetic field variations is less pronounced in middle latitudes. Some correlation is observed during strong magnetic storms with big falls of Dst index values. Diurnal LS TID intensity in such periods increases approximately twice. Most pronounced response is

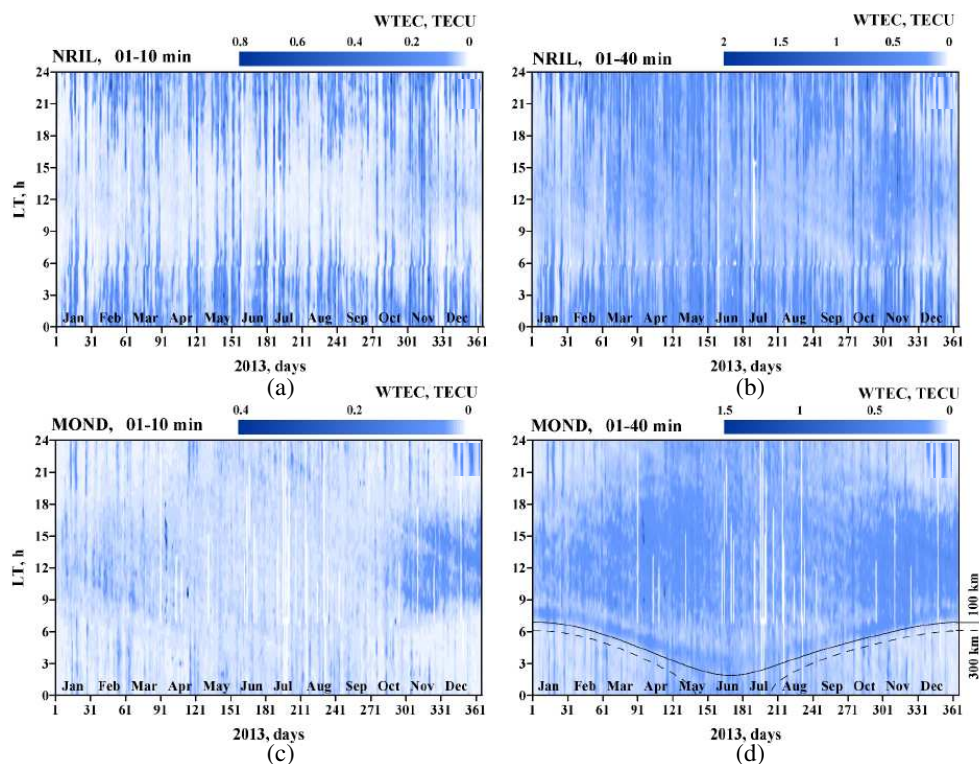


Figure 2: Diurnal-seasonal $W_{tec}(t)$ variations in period ranges of 01–10 min (a), (c) and 01–40 min (b), (d) at NRIL (a), (b) and MOND (c), (d) stations. Vertical axes are given in local time LT. For NRIL station $LT = UT + 6$ h. For MOND station $LT = UT + 7$ h. Black lines mark sunrise time at 100 km (solid line) and 300 km (dashed line).

observed in the middle of March and in the beginning of June. Apparently it is because of GNSS stations were on a illuminated side of Earth in these cases. MS TID intensity does not have any significant response to geomagnetic variations.

4. CONCLUSIONS

Analysis of the common level of TEC disturbance in two period ranges (01–10 min and 01–40 min) during 2013 was made using data from middle-latitude Siberian GPS/GLONASS network of ISTP SB RAS and high-latitude NRIL GNSS station located near Norilsk city. The common level of TEC disturbance is estimated by the index $W_{tec}(t)$ of the TEC-variation intensity.

In Arctic region (NRIL station) minimal intensity level is not depend on season. Minimal intensity is about 0.12 TECU and 0.02 TECU for LS TIDs (periods ~ 40 min) and MS TIDs (periods ~ 10 min), respectively. In the middle-latitude region minimal disturbance intensity changes over year. In winter it is about 0.006 TECU for MS disturbances and 0.03 TECU for LS ones, in summer it rises up to 0.01 TECU and 0.07 TECU, respectively. Diurnal variations are more intense for MS disturbances. In high latitudes strong $W_{tec}(t)$ dependence on magnetic field fluctuations (which is represented by the AE index) overrides diurnal variations of TEC perturbation. $W_{tec}(t)$ correlation with the Dst and Kp indexes is evident only during the magnetic storms having planetary character. TEC disturbances intensity on NRIL station rises up to 10–15 times during geomagnetic storms.

In middle latitudes diurnal $W_{tec}(t)$ variations are strongly pronounced over the year and have also some seasonal features. In the summer the disturbances are more intense at the beginning and the end of the day, whereas in all the other seasons its are higher in the middle of the day. Intensity of LS and MS disturbances increase in October and high values persist till the end of the year. During strong magnetic storms, the average daily level of LS TID intensity increases and correlates with the Kp index changes.

It is revealed that in middle latitudes solar terminator generates intense LS TIDs and doesn't cause MS TIDs, which is in a good agreement with [5]. Obtained results allow us to conclude that ST generates gravity waves ($T > 10$ min) and does not generate acoustic ones ($T < 10$ min). In

Arctic region ST-caused disturbances are absent.

ACKNOWLEDGMENT

The authors thank the Geophysics Service of RAS and INTERMAGNET for the data provided. The authors thank Sergey V. Voeykov and Oleg I. Bergardt for the Wtec calculation method development and its software realization. This work was supported by the Grant of the Russian Scientific Foundation (Project No. 14-37-00027).

REFERENCES

1. Foster, J. C. and W. Rideout, "Midlatitude TEC enhancements during the October 2003 superstorm," *Geophys. Res. Lett.*, Vol. 32, L12S04, 2005.
2. Ding, F., W. Wan, L. Liu, E. L. Afraimovich, S. V. Voeykov, and N. P. Perevalova, "Statistical study of large scale traveling ionospheric disturbances observed by GPS TEC during major magnetic storms over the years 2003–2005," *J. Geophys. Res.*, Vol. 113, A00A01, 2008.
3. Hocke, K. and K. Schlegel, "A review of atmospheric gravity waves and traveling ionospheric disturbances: 1982–1995," *Ann. Geophys.*, Vol. 14, No. 5, 917–940, 1996.
4. Bergardt, O. I., S. V. Voeykov, and K. G. Ratovsky, "Using a single GPS/GLONASS receiver for estimating the level of ionospheric disturbance," *XXXI URSI General Assembly and Scientific Symposium*, Beijing, China. August 16–23, 2014, abstracts. 2014, GP2.31, <http://www.aps-ursi.org/ursigass/program/>.
5. Afraimovich, E. L., I. K. Edemsky, S. V. Voeykov, Y. V. Yasukevich, and I. V. Zhivet'ev, "Spatio-temporal structure of the wave packets generated by the solar terminator," *Adv. Space Res.*, Vol. 44, No. 7, 824–835, 2009.

TEC Response to Geomagnetic Storms and Solar Flares as Observed with SBAS L1/L5 Signals

G. A. Kurbatov¹, V. E. Kunitsyn¹, A. M. Padokhin¹, and Yu. V. Yasyukevich²

¹Faculty of Physics, Lomonosov Moscow State University, Russia

²Institute of Solar-Terrestrial Physics SB RAS, Russia

Abstract— The development of Satellite Based Augmentation Systems (SBAS) provides the possibility to retrieve ionospheric Total Electron Content (TEC) from the dual frequency L1/L5 observations from a number of geostationary satellites using the same approach as for dual frequency GPS/GLONASS observations.

In this work we study L1/L5 signals of Indian GAGAN geostationary satellites observed with geodetic GNSS receivers at several stations at midlatitudes and estimate corresponding geostationary TEC variations. We present geostationary SBAS TEC response to X1.7 solar flare on October 25, 2013 showing good correlation between TEC and EUV flux for the stations at the sunlit hemisphere. We also present SBAS TEC response to geomagnetic field variations during moderate geomagnetic storm on June 1, 2013 showing examples of positive anomalies of order of tens TECU in TEC diurnal variations during main storm phase.

1. INTRODUCTION

Until recently the main approach for ionospheric TEC studies from geostationary orbits was based on Faraday rotation of polarization plane, which required additional information on Earth's geomagnetic field. This method was used particularly for the studies of ionospheric effects of solar flares [1, 2], statistical characteristics of traveling ionospheric disturbances [3], acoustic gravity waves [4], etc.. With the development of SBAS systems it is now possible to use coherent dual frequency transmissions compatible with GPS L1 and L5 signals from geostationary SBAS satellites to estimate TEC along “receiver-satellite” line-of-sight using the same method as for GPS/GLONASS [6]. As it was shown in [6], SBAS TEC RMS could reach up to 1.5 TECU with typical values of 0.25–0.5 TECU which is up to one order greater than for common GPS/GLONASS observations. Such large values of SBAS TEC RMS are satellite dependent and not of ionospheric origin, so they could be easily filtered out without losing significant ionospheric information providing continuous TEC datasets for selected satellite-receiver pairs instead of short 2–6 hours records as in GPS/GLONASS case. The purpose of this paper is to show the capabilities of SBAS TEC data for studying TEC anomalies during severe heliogeophysical disturbances, such as solar flares and geomagnetic storms.

2. OBSERVATIONS

Nowadays there are six SBAS satellites transmitting coherent GPS-like L1/L5 signals: SES-5, GSAT-8, GSAT-10, Intelsat Galaxy 15, TeleSat Anik F1R, Inmarsat 4-F3. As for groundbased receiving networks, the largest one was setup by International GNSS Service for The Multi-GNSS Experiment (MGEX) to track, collate and analyze all available GNSS (including SBAS L1/L5) signals [10].

For the purpose of the present work we used observations of GSAT-8 and GSAT-10 satellites from midlatitude MGEX TASH (41.33N, 69.30E) station and MSU (55.75N, 37.62E), ISTP (52.28N, 104.30E) and ORDA (52.75N, 103.66E) stations operated by Lomonosov Moscow State University and Institute of Solar-Terrestrial Physics.

Following [6], geostationary relative slant TEC can be estimated from the SBAS phase paths L_1 and L_5 at two coherent carrier frequencies $f_1 = 1575.42$ MHz and $f_5 = 1176.45$ MHz using the following relation:

$$TEC = \left(\frac{L_1}{f_1} - \frac{L_5}{f_5} \right) \frac{f_1^2 f_5^2}{f_1^2 - f_5^2} \frac{c}{K} + \text{const}, \quad (1)$$

where $K = 40.308 \frac{\text{m}^3}{\text{sec}^2}$, c is the speed of light in vacuum. The carrier phase ambiguities (leading to undefined constant term in Eq. (1)) are not estimated here.

First example we present here is SBAS TEC variations during moderate ($K_p \sim 6$) geomagnetic storm on June 1, 2013 (see Fig. 1). The Dst index reached the value -119 nT indicating moderate

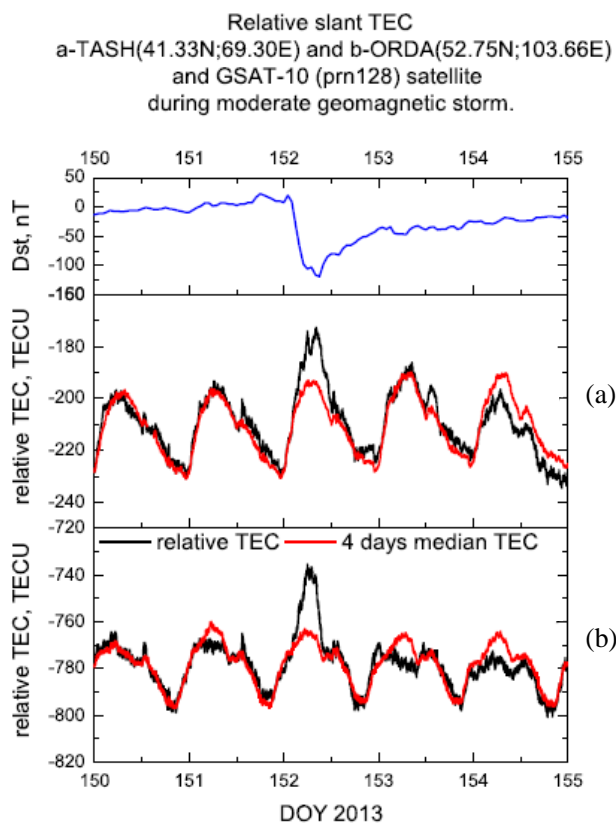


Figure 1: Dst index and relative slant SBAS TEC for GAGAN GSAT-10 satellite and ORDA and TASH receiving sites during moderate geomagnetic storm on June 1, 2013.

disturbances in midlatitude and near equatorial geomagnetic field. SBAS TEC variations during storm main and start of the recovery phases obtained at two midlatitude stations TASH and ORDA demonstrate strong positive anomaly up to 20–30 TECU compared to undisturbed 4-day median values. Two main mechanisms that can drive such positive storm are the penetration of magnetospheric electric field and the change in thermospheric circulation. In the first case, an enhanced eastward electric field induces a movement of ionospheric plasma in the direction perpendicular to the magnetic field lines (upward/poleward), whereas in the latter case the thermospheric equatorward neutral winds resulting from highlatitude energy injection drag the ionospheric plasma upward along the magnetic field lines. Rises in ionospheric height cause changes in the density and composition of the ambient atmosphere, and result in reductions in the molecular components of ionospheric plasma. Consequently, fewer O^+ ions are lost due to chemical reactions, thereby increasing the density [7]. Note also that according to [8] positive storm phases more frequently form under the winter conditions (negative storm phases tend to form during summer), while in our case positive storm was observed under summer conditions.

Finally let us demonstrate the capabilities of SBAS TEC observations in connection with ionospheric effects of solar flares. A chromospheric flare causes a sharp burst (by a few orders of magnitude) in the intensity of X-ray and EUV solar radiation, which results in the height-specific enhancement of electron density in the ionosphere of the Earth [5], and in the sudden increase in TEC, which can be detected using L1/L5 SBAS signals. Fig. 2 presents the example of processing the SBAS data recorded at MSU and ISTP stations during the X1.7-class flare on October 25, 2013. The maximum of the flare occurred at 8:01UT — at 12:01LT and 17:01LT at MSU and ISTP stations correspondingly. A sudden increase in TEC (SITEC) corresponding to variations in the X-ray and EUV radiation during the flare is observed at both stations: SITEC ~ 4 TECU within 10 min is observed at MSU station, SITEC at ISTP station is ~ 2.5 TECU for prn 127 (GSAT-8) and less than 0.5TECU for prn 128 (GSAT-10) depending on the elevation angle of the Sun at the satellites ionospheric pierce points. The MSU station is in the noon sector while ISTP is in the evening one, so higher MSU TEC variations during this flare is what was expected. Note also that elevation angles of GAGAN satellites are low at both observation sites. It provides longer ray path in

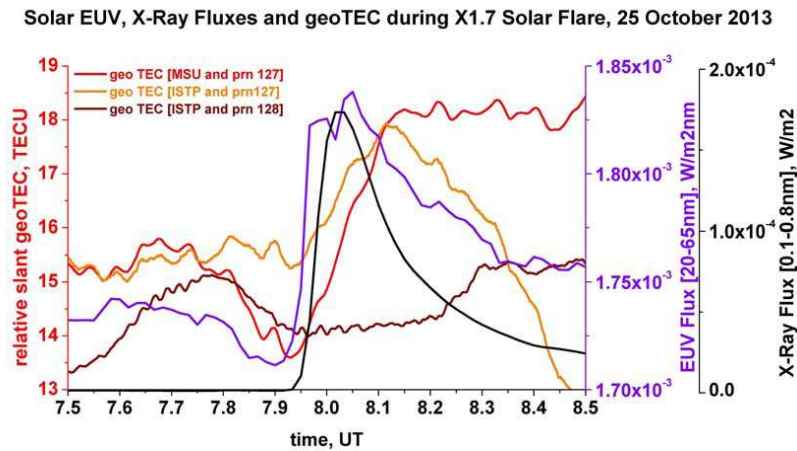


Figure 2: SBAS observation during X1.7-class Solar flare on October 25, 2013 [6].

ionosphere and thus larger SITEC values.

3. CONCLUSION

Our results show the capability of SBAS L1/L5 observations for continuous monitoring of ionospheric TEC in quite and disturbed geomagnetic conditions. Intensively growing networks of receivers capable to work with L1/L5 SBAS signals (for example MGEX network) and increasing number of dual-frequency satellites in SBAS constellation potentially make it a powerful instrument for TEC climatology. Note also that along with SBAS satellites, BeiDou/Compass geostationary satellites (currently 5 in orbit) can be used in the pretty same manner for continuous TEC monitoring [9], which doubles available constellation.

ACKNOWLEDGMENT

The authors are grateful to NGDC and IGS for the data used in presented research and to JAVAD GNSS for custom receiver firmware.

V. K. acknowledge the support of the Russian Scientific Foundation (grant 14-17-00637) in the part of analyzing geomagnetic storms effects, G. K. acknowledge the support of the Russian Foundation for Basic Research (grant 14-05-31445) in the part of studying SBAS signals, A. P. acknowledge grant of the President of Russian Federation (MK-2670.2014.5) in the part studying ionospheric effects of solar flares.

REFERENCES

1. Mendillo, M., J. A. Klobuchar, R. B. Fritz, A. V. da Rosa, L. Kersley, K. C. Yeh, B. J. Flaherty, S. Rangaswamy, P. E. Schmid, J. V. Evans, J. P. Schnödel, D. A. Matsoukas, J. R. Koster, A. R. Webster, and P. Chin, "Behavior of the ionospheric F region during the great solar flare of August 7, 1972," *Journal of Geophysical Research*, Vol. 79, No. 4, 665–672, 1974.
2. Davies, K., "Recent progress in satellite radio beacon studies with particular emphasis on the ATS-6 radio beacon experiment," *Space Science Review*, Vol. 25, No. 4, 357–430, 1980.
3. Katamzi, Z. T., N. D. Smith, C. N. Mitchell, P. Spalla, and M. Materassi, "Statistical analysis of travelling ionospheric disturbances using TEC observations from geostationary satellites," *Journal of Atmospheric and Solar-Terrestrial Physics*, Vol. 74, 64–80, 2011.
4. Dieminger, W., J. Schodel, G. Schmidt, and G. Hartmann, "Recording gravity waves by means of geostationary beacon-satellites," *Journal of Atmospheric and Terrestrial Physics*, Vol. 32, No. 9, 1615–1617, 1970.
5. Mitra, A. P., *Ionospheric Effects of Solar Flares*, D. Reidel, Norwell, MA, 1974.
6. Kunitsyn, V., G. Kurbatov, Y. Yasyukevich, and A. Padokhin, "Investigation of SBAS L1/L5 signals and their application to the ionospheric TEC studies," *IEEE Geoscience and Remote Sensing Lett.*, Vol. 12, No. 3, 547–551, 2015.
7. Prölss, G. W., "Ionospheric F-region storms," *Handbook of Atmospheric Electrodynamics*, Edited by H. Volland, CRC Press, Boca Raton, Fla, 1995.

8. Prölss, G. W., “Seasonal variation of atmospheric-ionospheric disturbances,” *Journal of Geophysical Research*, Vol. 82, 1635–1640, 1977.
9. Jin, R., S. Jin, and X. Tao, “Ionospheric anomalies during the March 2013 geomagnetic storm from BeiDou navigation satellite system (BDS) observations,” *China Satellite Navigation Conference (CSNC) 2014 Proceedings: Volume I, Lecture Notes in Electrical Engineering 303*, Springer-Verlag, Berlin, Heidelberg, 2014.
10. <http://igs.org/mgex/>.

Acoustic-gravity Waves in Space Generated by Near-ground and Volume Sources

Elena S. Andreeva¹, Viacheslav E. Kunitsyn^{1,2}, Ivan A. Nesterov¹, and Artem M. Vorontsov¹

¹M.V. Lomonosov Moscow State University, Moscow, Russia

²Institute of Physics of the Earth, Russian Academy of Sciences, Moscow, Russia

Abstract— Numerical analysis of acoustic-gravity waves (AGW) generation and propagation in the Earth's atmosphere is performed based on computer model of stratified atmosphere with dissipation. Atmospheric and ionospheric wavelike disturbances generated by near-ground or volume sources such as oscillations of the Earth's or oceanic surface, earthquakes, explosions, seiches, tsunami waves and temperature heating are studied. These wavelike phenomena in the atmosphere and ionosphere appear as the alternating areas of enhanced and depleted density (in the atmosphere) or electron concentration (in the ionosphere).

1. INTRODUCTION

Observation and investigation of various ionospheric perturbations under assumption of their correct physical interpreting and understanding of their hydrodynamic generation mechanisms commonly allows obtaining current or predictive configuration of near-ground or volume sources of disturbances. The least studied problem here is a question about acoustic energy transferring from the ground sources into near-Earth space that primarily is related with incompleteness of AGW propagation theory in the real atmosphere. Moreover, complete analysis of the observed ionospheric perturbations should be performed using conventional characteristics of ionospheric waves such as amplitude, phase, period, velocities of corresponding wave packets and angular characteristics of the wave vector. Notice, that for most near-ground or volume sources in geophysical bibliography there is a significant variance regarding values of basic AGW parameters as well as absence of unified point of view on AGW generation mechanisms. As the examples of mentioned mechanisms different authors provide infrasound wave generation [1], internal gravity waves generation [2], eddy motion of the neutral component generated by an acoustic pulses [3], the generation of shock-acoustic waves [4], etc..

The numerical simulation of upper atmosphere responses to various near-ground or volume sources can provide estimations of basic AGW characteristics and to clarify AGW generation mechanisms. The major results of the paper consist in determining of common as well as unique tendencies in AGW behavior for a wide class of sources, analysis of these tendencies and estimation of AGW wavepackets' parameters.

2. NUMERICAL MODEL OF AGW GENERATION AND PROPAGATION IN THE UPPER ATMOSPHERE

In order to analyze the propagation conditions and mechanisms of AGW generation, we follow [5] and consider the equations of geophysical hydrodynamics:

$$\begin{aligned}
 \frac{\partial \rho}{\partial t} + \nabla(\rho \mathbf{v}) &= 0 \\
 \rho \left(\frac{\partial \mathbf{v}}{\partial t} + (\mathbf{v}, \nabla) \mathbf{v} \right) &= -\nabla p + \rho \mathbf{g} + \mathbf{F}_d \\
 \rho \left(\frac{\partial (c_v T)}{\partial t} + (\mathbf{v}, \nabla) (c_v T) \right) &= -p(\nabla, \mathbf{v}) + Q_d \\
 p &= \frac{\rho}{m_0} RT
 \end{aligned} \tag{1}$$

Since our study addresses very fast motions that are commensurate to the propagation of AGWs, the Coriolis force is insignificant and it is neglected in our analysis. Here, ρ is density, T is temperature, p is pressure, \mathbf{v} is the particle velocity in the wave, \mathbf{g} is the acceleration of gravity, \mathbf{F}_d is the drag force, Q_d is the absorbed heat due to wave dissipation, c_v is the specific heat of gas at constant volume, m_0 is the relative molecular mass of air, and R is the universal gas constant. This model

takes into account the turbulent viscosity up to the heights of the tropopause and the iondrag, which takes place significantly above the tropopause. These dissipative forces are introduced as a single common drag force in the Rayleigh form $\mathbf{F}_d = -\alpha\mathbf{v}$. Here, α is the drag coefficient, whose values at different heights correspond to different mechanisms of dissipation.

For the numerical integration of the system (1), it is reasonable to represent each thermodynamic parameter as a sum of two parts: the stationary part and the perturbed part. Then the initial conditions for the velocity, perturbations of density, pressure and temperature can be chosen equals to zero. As the lower boundary condition, we require that the air particle velocity in the atmospheric boundary layer is equal to the velocity of motion of the Earth's surface or the ocean surface. The same condition governs the translation of the perturbation from the moving medium to the atmosphere. For the remaining unknowns, we assume that they are continuous at the transition through the lower boundary. On the upper and side boundaries the conventional boundary conditions are utilized that provide waves propagation through these surfaces without a significant reflection.

The numerical solution of the system (1) was obtained using the flux corrected transport algorithm (FCT) [6]. This method has proven to be quite efficient in the numerical solution of the similar problems of modeling the ionospheric responses to the explosions and earthquakes (see [7, 8]). We will seek the solution of this problem in a rectangular domain, assuming that the sphericity of the Earth does not affect the further results. Introduce the 2D Cartesian coordinates Oxz , in which the Ox axis is horizontal and the Oz axis is directed vertically upwards. In these coordinates, $\mathbf{r} = (x, z)$ and $\mathbf{v} = (u, w)$, where $u(w)$ is the horizontal (vertical) component of the particle motion velocity in the medium. For solving the given system by the FCT approach, we apply the method of time step splitting along the directions x and z so that righthand sides of (1) are separated into the horizontal and vertical components.

3. NUMERICAL SIMULATION RESULTS

The analysis of numerical simulation results shows the AGW presence in the atmosphere for all types of studied near-ground or volume sources of disturbances. The following general patterns of the AGW propagation in the upper atmosphere were observed for all types of sources: generation of acoustic perturbations above the epicenter of near-ground source at the heights or above of the mesopause having spatial scales about 1000 km along horizontal direction and about 400 km along vertical direction; generation of internal gravity waves (IGW) packets extending from two to several wavelengths that in the waveguide channel at the heights above the mesopause are captured and in the opposite horizontal directions from the Earth's disturbances source are propagated (for example see Figs. 1(a), (b)). Further IGW propagation is followed by increasing of their period and the wavelength with the distance from the source. At the distance about 2000 km from the epicenter of the near-ground disturbances increasing of the period was approximately 120–150 s in comparison with the value of the IGW period above the epicenter.

The atmospheric waves observed in the numerical simulations have contained both types of the AGW spectrums: acoustic and gravity parts. The periods of acoustic waves (AW) was about 170–290 s, the IGW periods — 750–1500 s. Note that during first 1000 s of perturbations' propagation the AW period was about 170–200 s and after the AW reaching at 400–500 km heights and forming of the stable acoustic response this period was increased to 220–290 s. The group velocity of the AW was varied from 340 m/s to 600 m/s depending on height above the ground, the IGW had corresponding velocities in the range 250–310 m/s that were slightly increased with the propagation

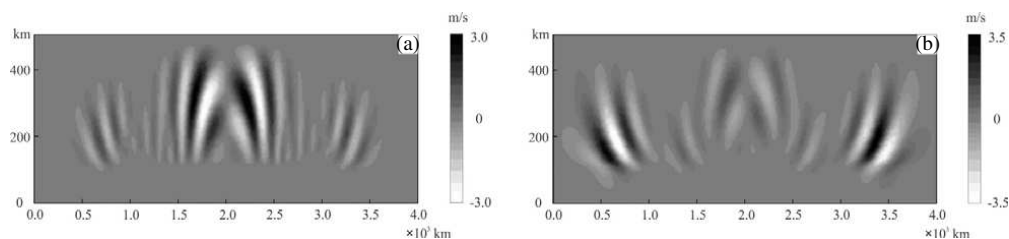


Figure 1: The spatial distributions of u at the time $t = 5500$ s after generating of (a) pulse and (b) long-period oscillations of the Earth's ground giving approximately the same amplitudes of upper atmosphere's perturbation. Here and below source of disturbances near the point $x = 2000$ km, $z = 0$ km is located.

distance. The horizontal IGW wavelength was 250–280 km, the horizontal AW wavelength was 170–200 km.

Now consider the basic properties of ionospheric responses for several examples of sources. At the beginning consider generator of short- and long-period oscillations of the Earth’s ground caused by underground explosions, shallow earthquakes and so on. For the earthquakes and explosions the spectrum of atmospheric perturbation was commonly concentrated in the acoustic range with dislocation above the source (Fig. 1(a)). The amplitudes of the w in the AW above the explosion source could reach tens of meters per second. The gravity waves was poorly represented, their periods were approximately in the range 750–900 s.

For the long-period local Earth’s surface oscillations the maximal amplitudes of the u and w in the AW were not more than 20–30 m/s and 10–30 m/s for the IGW. The atmospheric perturbation was commonly consists of the IGW of the periods $P > 1000$ s propagating without significant attenuation at the several hundreds of kilometers (Fig. 1(b)). The comparison analysis shows that the amplitude of the IGW in the case of long-period source is more than in the short-period case.

One more near-ground source having large enough ionospheric response is the seiches — the long-period oscillations of the water surface commonly taking place in a closed waters. The calculations show that seiches basically generate long-period AGW (Figs. 2(a), (b)). In the numerical simulations of the seiches at the Geneva lake, Baikal lake and Michigan lake [9] the amplitudes of the velocities u and w in the corresponding IGW, as the rule, were less than 1 m/s. The IGW propagation could be described in terms of wave packets going from the source with time delay 1.5–2.0 hours. The horizontal phase velocity of the IGW was in the range 280–300 m/s, the period was 900–1500 s, wavelength — 320–450 km.

The next important class of ionospheric perturbations’ generators includes temperature inversions in the lower atmosphere, volcano eruptions, perturbations of incoming air flow by the “warm” megalopolises, solar heating and photo dissociation in the troposphere [10]. All mentioned phenomena have a distinguishing feature — all of them connect with local near-ground temperature variation.

The numerical simulation of the atmospheric response to the temperature variations source shows presence of large scale IGW having large amplitudes ($u, w \sim 30$ –50 m/s) and low AW response (Fig. 3(a)). In contrast with previously discussed sources in this case large temperature perturbations were observed (Fig. 3(b)). The comparison analysis has demonstrated that approximately the equivalent IGW are generated by temperature source with amplitude 0.25 K as well as are formed by long-period Earth surface’s oscillations with the amplitude about ten meters and the period about 1000 s.

One more interesting example of AGW generator gives the tsunami wave propagation in the

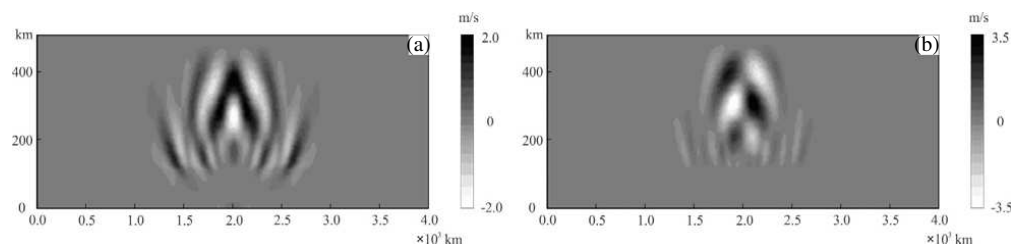


Figure 2: The spatial distributions of the velocities (a) u and (b) w at $t = 5600$ s for the numerical model of the seiches having vertical amplitude 2 m, the period 10000 s and spatial scale about 300 km.

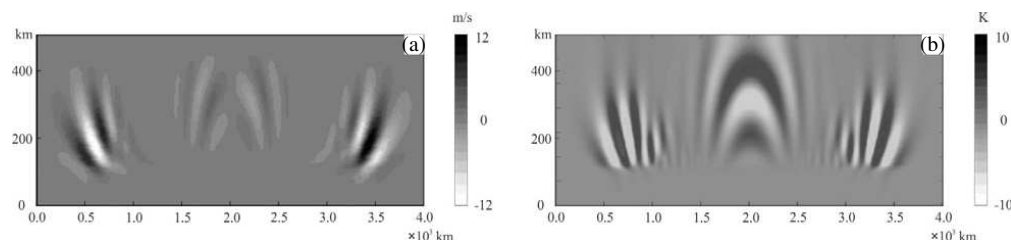


Figure 3: The spatial distribution of (a) u and (b) T at $t = 6000$ s for the temperature source with the amplitude 1 K and spatial scale 20 km. The temporal period of the source is equal to 3000 s.

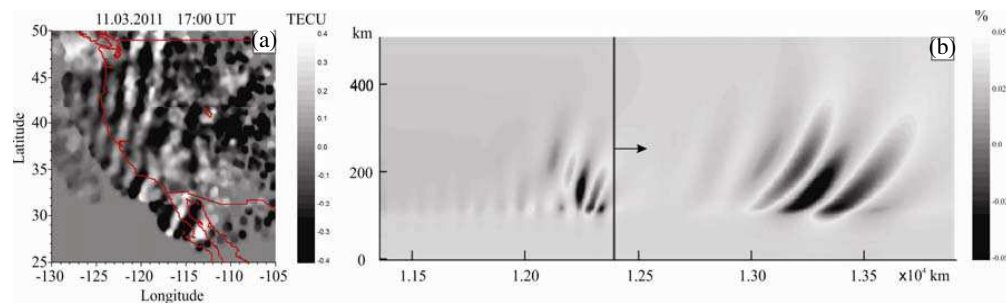


Figure 4: The TEC variation map (a) obtained by GPS RT for the west coast of the USA after 11 hours from the main shock of Tohoku earthquake. The relative density distribution ρ simulation result near the Hawaii islands (b) after 8 hours from the main shock. The position and the propagation direction of the tsunami wave are denoted by the corresponding lines.

open ocean. Consider the upper atmosphere response to the severe Tohoku earthquake of March 11, 2011. The Fig. 4(a) represents the total electron content (TEC) reconstruction in the US west coast region by the GPS radio tomography (RT) after 11 hours from the main shock. In [11] shows that ionospheric waves in this image primarily correspond to the tsunami wave propagation in the Pacific ocean. The computer simulation (Fig. 4(b)) of the tsunami-induced AGWs demonstrates a distinct precursor of the tsunami wave, which appears as a strong IGW advancing the perturbation of the ocean surface (and the accompanying AWs) and largely concentrated in the band moving 500–1000 km ahead of the tsunami.

In conclusion, note that the presented numerical simulation results show close agreement with the experimental and theoretical researches for the corresponding sources of disturbances [3, 4].

ACKNOWLEDGMENT

The work was accomplished in the scope of the contract agreement with Russian Foundation for Basic Research (grants Nos. 13-05-01122, 14-05-00855).

REFERENCES

1. Calais, E. and J. B. Minster, "GPS, earthquakes, the ionosphere, and the Space Shuttle," *Physics of Earth and Planetary Interiors*, Vol. 105, 167–181, 1998.
2. Francis, S. H., "Global propagation of atmospheric gravity waves: A review," *J. Atmos. Terr. Phys.*, Vol. 37, 1011–1054, 1975.
3. Andreeva, E. S., M. B. Gohberg, V. E. Kunitsyn, et al., "The RT registration of ionospheric perturbations from the ground explosions," *Kosmicheskie Issledovaniya (Space Research)*, Vol. 39, No. 1, 13–17, 2001.
4. Afraimovich, E. L., N. P. Perevalova, A. V. Plotnikov, and A. M. Uralov, "The shock-acoustic waves generated by earthquakes," *Ann. Geophysicae*, Vol. 19, 395–409, 2001.
5. Grigoriev, G. I., "Acoustic-gravity waves in the Earth's atmosphere (review)," *Izvestia Vuzov. Radiophysics*, Vol. XLII, No. 1, 3–25, 1999.
6. Oran, E. S. and J. P. Boris, *Numerical Simulation of Reactive Flow*, Cambridge University Press, 2000.
7. Akhmedov, R. and V. Kunitsyn, "Simulation of the ionospheric disturbances caused by earthquakes and explosions," *Geomagnetism and Aeronomy*, Vol. 44, No. 1, 95–101, 2004.
8. Kunitsyn, V. E., S. N. Suraev, and R. R. Akhmedov, "Modeling of atmospheric propagation of acoustic gravity waves generated by different surface sources," *Moscow Univ. Phys. Bulletin*, Vol. 62, No. 2, 122–125, 2007.
9. Wuest, A. and D. M. Farmer, *Seishe*, McGraw-Hill, Encyclopedia of Science & Technology, 2003.
10. Sauli, P. and J. Boska, "Tropospheric events and possible related gravity wave activity effects on the ionosphere," *J. Atmos. Sol.-Terr. Phys.*, Vol. 63, 945–950, 2001.
11. Kunitsyn, V. E. and A. M. Vorontsov, "Modeling the ionospheric propagation of acoustic gravity waves from the Tohoku tsunami of 2011," *Moscow Univ. Phys. Bulletin*, Vol. 69, No. 3, 263–269, 2014.

Adaptation of IRI-2012 Model for Estimation of IAR Harmonic Structure

A. S. Potapov¹, T. N. Polyushkina¹, A. V. Oinats¹, T. Raita², and B. Tsegmed^{1,3}

¹Institute of Solar-Terrestrial Physics SB RAS, Irkutsk, Russia

²Sodankylä Geophysical Observatory, Finland

³Institute of Astronomy and Geophysics MAS, Ulaanbaatar, Mongolia

Abstract— The ionospheric Alfvén resonator (IAR) can amplify and accumulate ultra-low frequency (ULF) wave energy in the upper ionosphere. Close connection of the IAR emission features with state of the ionosphere motivates many authors to study the details of this connection, and make suggestions about how to use observations of the spectral structure of the electromagnetic background in the range of 0.5–10 Hz for sounding ionospheric parameters and clarifying ionospheric models. In this paper we propose a new approach to analysis of emission of ionospheric Alfvén resonator (IAR). We apply the IRI-2012 version of International Reference Ionosphere model to calculate difference between frequencies of adjacent harmonics of IAR emission. The calculated values are compared with the frequency data obtained from the search-coil magnetometer observations made at two different stations, the mid-latitude observatory Mondy (Eastern Sayan, Russia) and the high-latitude Sodankylä Geophysical Observatory (Finland). The results showed a good correlation between the measured and calculated values both at medium and high latitude. The calculation results at Mondy have a systematic error of about 0.35 Hz. The reasons of this discrepancy are discussed.

1. INTRODUCTION

The ionospheric Alfvén resonator (IAR) is a structural formation in the ionosphere between two peaks of Alfvén speed in its altitude profile [1]. The IAR can amplify and accumulate ultra low frequency (ULF) wave energy in the upper ionosphere [2]. As a result of the IAR occurrence the multiband spectral resonance structure (SRS) appears in the ULF observations, both ground-based and satellite. Frequency of discrete spectral bands and spacing between them are determined by the geometry of the resonator and the Alfvén speed in its cavity; the change in band frequency during the day with a minimum around noon and a maximum after midnight or in the early morning hours is due to diurnal variation of ionospheric parameters [3]. Close connection of SRS mode and features with state of the ionosphere motivates many authors to study the details of this connection, and make suggestions about how to use observations of the spectral structure of the electromagnetic background in the range of 0.5–10 Hz for sounding ionospheric parameters and clarifying ionospheric models [4].

In this paper we propose a new approach to analysis of emission of ionospheric Alfvén resonator (IAR). We apply the IRI-2012 version of International Reference Ionosphere model to calculate difference between frequencies of adjacent harmonics (harmonic difference) of IAR emission. The calculated values are compared with the harmonic difference data obtained from search-coil magnetometer observations made at two different stations, the mid-latitude observatory Mondy (Eastern Sayan, Russia) and the high-latitude Sodankylä Geophysical Observatory (Finland). For measurements made at medium latitudes, it appears that to reach satisfactory results it is necessary to modify IRI-2012 model replacing the vertical profile of ionospheric parameters adopted in the standard model with the profile elongated along the magnetic field lines [3]. For polar latitudes, where the field lines deviate from the vertical insignificantly, such a procedure is not so important. On the other hand, irregular behavior of the polar ionosphere results in the diffusive character of the SRS. That is why the spectral bands of the SRS at SGO spectrograms are blurred which hinders precise measurements of the frequency values.

2. EQUIPMENT AND DATA PROCESSING

We used magnetic and ionospheric data from the Sodankylä Geophysical Observatory (SGO, geographic coordinates $\varphi = 67.37^\circ$, $\lambda = 26.63^\circ$; McIlwain parameter $L = 5.2$) for a period of January–March and November–December 1996 and for the same months of 1997. Both solar and magnetic activity indices were below their average levels: monthly a_p -index averaged over the above period was $a_p = 15.9$; the monthly sunspot number was $R = 8.8$. These values are typical for solar

minimum. To compare the results with those obtained basing on a mid-latitude site, we used data from the Sayan Solar Observatory Mondy (MND, geographic coordinates $\varphi = 51.6^\circ$, $\lambda = 100.9^\circ$; $L = 2.1$) which is situated near the border between Russia and Mongolia. We processed the MND data for a period of March 2010–May 2011. Magnetic activity during this period was also low; monthly averaged a_p -index never exceeded 10.3 nT. The monthly sunspot number exceeded 30 only in the last three months of the period, never rising above 57. This is consistent with low solar activity.

In SGO, data samples taken from a search-coil magnetometer with 40 Hz sampling, were stored with GPS timing. In SSO, induction magnetometer LEMI-30 with sampling rate of 60 Hz measured signals within 0.001–30 Hz frequency range. To compare magnetic data with ionospheric data above MND and SGO, we used one-hour values of the critical frequency f_0F_2 from the DPS-4 digital ionosounder installed in Irkutsk, about 260 km from the MND, and the IS-14 ionosounder at Sodankylä, respectively.

Digital magnetic records in the range of 1–10 Hz were processed using specifically developed MATLAB code. The program calculates dynamic spectrum of the signal in two components and builds daily spectrogram in coordinates “frequency-time”. The intensity of the signal at a given frequency in a given time is displayed in color. Fig. 1 shows typical examples of the IAR events at two observatories. Spectrograms obtained were analyzed visually. As a rule, we managed to make measurements of no more than 5–6 harmonics (bands), but more often three or four (two for SGO). We used these data for detailed comparison with changes in ionospheric parameters and to calculate the correlation coefficients and regression line between the harmonics and critical frequency variations of the ionosphere F2 layer.

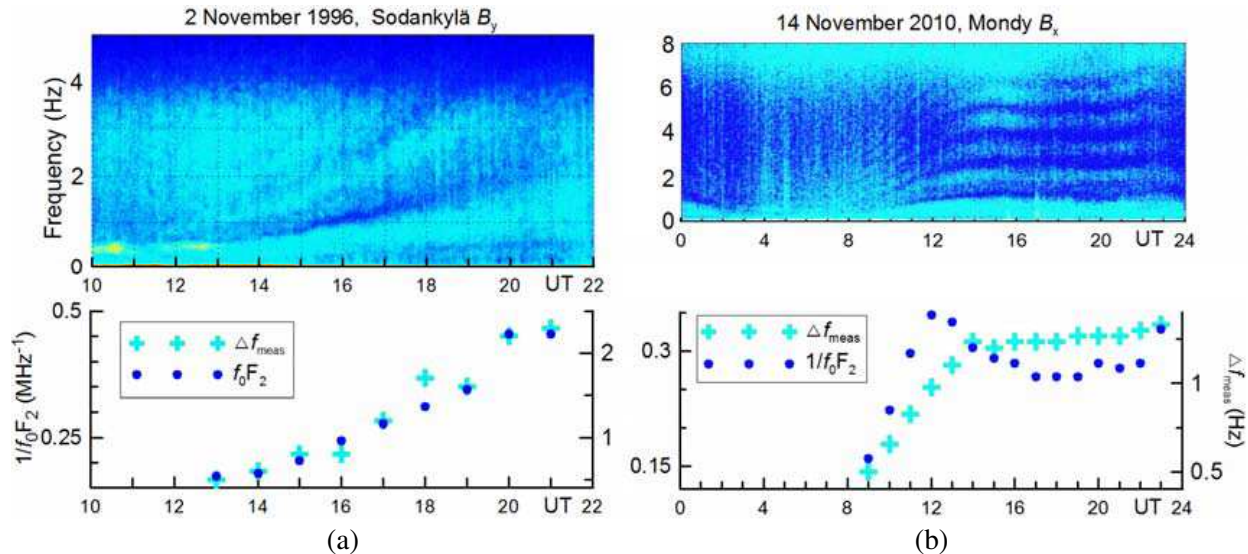


Figure 1: Two upper panels show dynamic spectra of the IAR emissions at (a) Sodankylä and (b) Mondy. Bottom panels show changes in the critical frequency f_0F_2 and the harmonic difference Δf_{meas} measured from the upper spectrograms.

3. THE SRS FREQUENCY AND THE IONOSPHERE CRITICAL FREQUENCY f_0F_2

Since the observed discrete spectral bands are formed by capturing low-frequency wave in the ionospheric Alfvén resonator being ionospheric structure, the behavior of the main characteristics of SRS should closely correlate to variations of the ionospheric parameters, primarily to changes in the electron concentration. In turn, the electron number density in the F₂ layer is uniquely linked to the critical frequency f_0F_2 , measured by ionosonde: $f_0F_2 = 8.98 * 10^{-3} N_e^{1/2}$, where the electron number density is measured in cm^{-3} , and the critical frequency in MHz.

Evidence for a connection between the measured harmonic difference Δf_{meas} and the critical frequency f_0F_2 can be seen at the bottom panels of Figure 1. In Figure 2 we compared values of the SRS frequency with the reverse value of $1/f_0F_2$ statistically for all events analyzed at the two observatories.

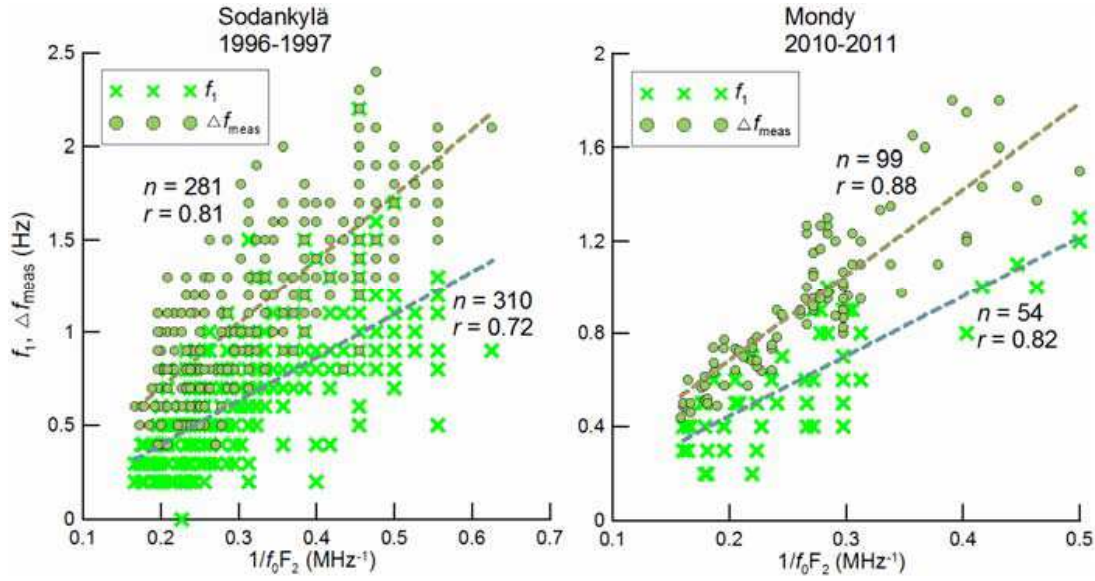


Figure 2: Scatter plots illustrating dependence of the SRS frequency structure versus the ionosphere critical frequency f_0F_2 at the two observatories. Crosses show the frequency f_1 of the emission first harmonic; circles show the SRS frequency scale Δf_{meas} versus the reverse value of $1/f_0F_2$. The observation numbers n and the correlation coefficients r are indicated for each pair of compared parameters separately.

The results show a rather high correlation between the characteristics of SRS and the ionosphere critical frequency at both observatories. The Δf_{meas} relates to the f_0F_2 closer than the f_1 . The correlation coefficients are higher for Mondy observatory. One of the reasons of the latter result can be understood if we look at the upper panels of Figure 1: the spectral bands at SGO are much wider and more blurred than at MND, which hampers precise measurements of the frequency values. But it is only one reason. The other seems to be that often the high-latitude ionosphere structure is very intricate. Therefore the wave propagation is determined not only by the plasma density within the F₂ region, but also by overall plasma distribution in the ionosphere including its upper region.

4. MODEL OF THE IAR SPECTRUM FORMATION

The literature offers different versions of the model of the ionospheric Alfvén resonator [5–7]. The models are based on the resonance conditions of Alfvén wave reflection from the lower and upper ionosphere and capture analysis of the Alfvén waves in the cavity being formed along the magnetic field lines between the local maxima of the Alfvén speed (“walls” of the resonator) below the F₂ layer and at altitude of 2,000–4,000 km. All authors agree that for resonance of waves with the wave speed A in a uniform cavity of length L , the frequency f of harmonic number n is given by $f = (n\pi)/(2L/A)$. In reality, the cavity is not uniform, and the phase factor Φ is complicated function of conditions on the walls of the resonator. To exclude phase factor Φ we can measure not the frequency f , but the harmonic difference $\Delta f = f_n - f_{n-1} = A/(2L)$. For non-uniform cavity, the latter relation can be rewritten as $\Delta f = 1/(2T_0)$, where

$$T_0 = \frac{1}{2} \int_{l_{\text{bottom}}}^{l_{\text{top}}} \frac{dl}{A(l)}. \quad (1)$$

Here l_{bottom} and l_{top} are positions of the lower and upper walls of the resonator, respectively; Alfvén speed $A(l) = B(l)/\sqrt{4\pi m_{\text{eff}}(l)N_e(l)}$, magnetic field B , electron number density N_e , and effective ion mass m_{eff} , all vary with l . Using formula (1) we calculated transit time T_0 for all hourly events. D layer height of 100 km was taken as a lower wall of the resonator. The height of the maximum Alfvén speed above the F₂ layer was taken as an upper wall. Altitude profile of the magnetic field $B(l)$ was calculated by DGRF/IGRF model. Altitude profiles of the electron density $N_e(l)$, the effective mass m_{eff} , and the Alfvén speed $A(l)$ were calculated to the height $l^* = 2,000$ km

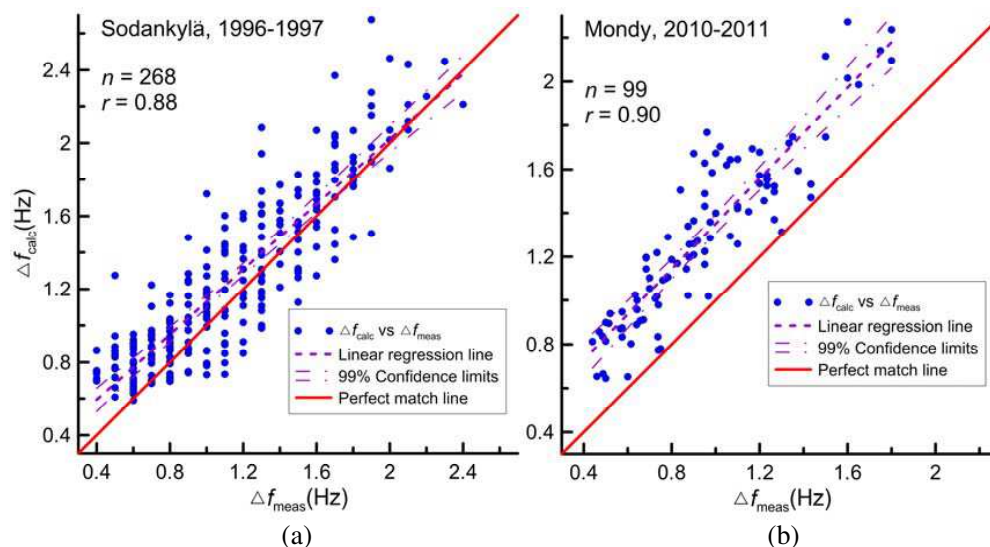


Figure 3: Calculated Δf_{calc} versus measured Δf_{meas} values of the IAR frequency scale for the (a) Sodankylä and (b) Mondy observatories. Calculations were performed using the IRI-2012 model. Dashed lines are the linear regression lines; dashed-dot lines are the 99% confidence limits; thick red line is the line of perfect match $\Delta f_{\text{calc}} = \Delta f_{\text{meas}}$.

based on the International Reference Ionosphere model IRI-2012, and above 2,000 km based on an extrapolation formula similar to that used in [8].

In total, for 13(55) selected days of observations at Mondy (Sodankylä), we have performed 99(268) calculations of the frequency scale Δf_{calc} and compared them with the measured Δf_{meas} values. A greater number of Sodankylä events included into the analysis aimed to provide better statistics for the high-latitude station. The result depicted in Fig. 3 shows that the correlation between the calculated and measured values is quite high, but at Mondy the regression line does not pass through zero, although it has the slope of nearly 45 degrees. Calculated harmonic difference Δf_{calc} exceeds measured value Δf_{meas} on average by 0.35 Hz. This means that for this station there is some systematic error in the determination of Δf_{calc} . On the contrary, at Sodankylä the regression line almost coincides with the perfect match line.

We see two possible reasons of this distinction. First, we calculated the frequency scale using the standard IRI-2012 model that gives ionospheric parameters along the vertical profile. However, the resonator cavity captures Alfvén waves along the magnetic field line. The inclination angle at the Mondy latitude is about 70 degrees, whereas at Sodankylä the field line is much closer to the vertical, the inclination here is about 77 degrees. 70-degree inclination extends the wave travel time by 6.5%, reducing equally the frequency. At Sodankylä the 77-degree inclination corresponds to only 2.5% travel time extension. Second, calculating Δf_{calc} for Mondy we used f_0F_2 values of Irkutsk as input data because we had not available digisonde data closer to Mondy. This might introduce errors in the calculated values. At Sodankylä we used digisonde data installed directly at the observatory.

5. DISCUSSION AND CONCLUSION

In this paper we compared the SRS characteristics observed at two observatories, high-latitude SGO and mid-latitude MND. We found clearer IAR emission structure at Mondy as compared to Sodankylä. Correlation coefficients between the frequency features of SRS (harmonic difference Δf and first harmonic frequency f_1) and the local ionosphere critical frequency f_0F_2 are a bit higher at Mondy with Δf vs f_0F_2 correlation being closer than f_1 vs f_0F_2 at both stations. The upper limit of Δf at Sodankylä (2.7 Hz) is higher than the Δf upper limit at Mondy (2.3 Hz) in accordance with the lower limit of f_0F_2 at Sodankylä (1.6 MHz) as compared to f_0F_2 at Mondy (2 MHz).

We also calculated values of the harmonic difference Δf at both stations within the framework of a simple time-of-travel model of the resonator. The results showed a good correlation between the measured Δf_{meas} and calculated Δf_{calc} values both at medium and high latitude. The calculation results at Mondy have a systematic error of about 0.35 Hz. The reasons of it are discussed.

In conclusion, we would like to note that studies of the IAR regularities and their dependence

on various factors can result in future development of a new method for monitoring the ionosphere. In particular, it is important for the high-latitude ionosphere that is very unstable and often non-measurable using common radio sounding. Comparing results for Sodankylä presented in Figures 2 and 3 we see sufficiently higher correlation between Δf_{meas} and Δf_{calc} than between Δf_{meas} and calculated f_0F_2 . This fact means that Δf is determined not only by plasma density in the F_2 region, but also by plasma distribution above this region. So Δf_{meas} contains information about the upper ionosphere. We plan to find the ways to reveal this information from the analysis of SRS data in our next papers.

ACKNOWLEDGMENT

Authors are grateful to the team of the IRI model. We also thank the team of the ISTP Complex Magneto-Ionospheric Observatory (Irkutsk) for providing magnetic and ionospheric data. The part of work made by A.S.P. and A.V.O. (development of the IAR spectrum formation model and ionosphere data analysis) was supported by the Russian Science Foundation, grant 14-37-00027; the part of work made by T.N.P and B.V.D. (observations and morphological studies) was supported by the Russian Foundation for Basic Research, grant 13-05-00529.

REFERENCES

1. Belyaev, P. P., S. V. Polyakov, E. N. Ermakova, and S. V. Isaev, “Experimental studies of the ionospheric Alfvén cavity using observations of electromagnetic noise background over the solar cycle of 1985 to 1995,” *Radiophysics and Quantum Electronics*, Vol. 40, No. 10, 879–889, 1997.
2. Lysak, R. L. and A. Yoshikawa, “Resonant cavities and waveguides in the ionosphere and atmosphere,” K. Takahashi, et al., (Eds.), *Magnetospheric ULF Waves*, 289–306, AGU, Washington, D.C., (Geophysical Monograph Series 169), 2006.
3. Potapov, A. S., T. N. Polyushkina, B. V. Dovbnya, B. Tsegmed, and R. A. Rakhmatulin, “Emissions of ionospheric Alfvén resonator and ionospheric conditions,” *J. Atmosph. Solar-Terr. Phys.*, Vol. 119, 91–101, 2014.
4. Yahmin, A. G., N. V. Semenova, A. A. Ostapenko, J. Kangas, J. Manninen, and T. Turunen, “Morphology of the spectral resonance structure of the electromagnetic background noise in the range of 0.1–4 Hz at $L = 5.2$,” *Ann. Geophys.*, Vol. 21, 779–786, 2003.
5. Polyakov, S. V. and V. O. Rapoport, “Ionospheric Alfvén resonator,” *Geomagnetism and Aeronomy*, Vol. 21, 816–822, 1981.
6. Demekhov, A. G., P. P. Belyaev, S. V. Isaev, et al., “Modeling the diurnal evolution of the resonance spectral structure of the atmospheric noise background in the Pc1 frequency range,” *J. Atmosph. Solar-Terr. Phys.*, Vol. 62, 257–265, 2000.
7. Hebden, S. R., T. R. Robinson, D. M. Wright, T. Yeoman, T. Raita, and T. Bösinger, “A quantitative analysis of the diurnal evolution of ionospheric Alfvén resonator magnetic resonance features and calculation of changing IAR parameters,” *Ann. Geophys.*, Vol. 23, 1711–1721, 2005.
8. Lysak, R. L., “Magnetosphere-ionosphere coupling by Alfvén waves at midlatitudes,” *J. Geophys. Res.*, Vol. 109, A07201, 2004.

Comparison of Polar, Sub-polar and Mid-latitude Ionospheric Variability Using Ionosonde and SuperDARN Data

K. G. Ratovsky¹, A. V. Oinats¹, and N. Nishitani²

¹Institute of Solar-Terrestrial Physics SB RAS, Russia

²Solar-Terrestrial Environment Laboratory, Nagoya University, Japan

Abstract— We study ionospheric variability using HF radio facilities within three latitudinal regions: polar zone (Norilsk ionosonde; 69.4N, 88.1E), sub-polar zone (Ekaterinburg SuperDARN radar; 56.4N, 58.5E) and mid-latitude zone (Hokkaido East SuperDARN radar; 43.53N, 143.61E). As characteristics we select the peak electron density (NmF2) measured with the ionosonde and the ground backscatter range corresponding to the skip distance (Rmin) from HF radar measurements. The disturbances of characteristics are the deviations of characteristics from their 27-day running median values. The variability is considered as the root mean square of disturbances. For different tasks we used different types of averaging. Annual averaging was used for studying year-to-year changes in the variability (solar cycle variations). To obtain the seasonal pattern of the variability we performed averaging over years for the daytime of each day of year. In the paper we discuss similarities and differences between the selected characteristics and between the polar, sub-polar and mid-latitude ionospheric variability.

1. INTRODUCTION

In [1] authors analyzed the 2003-2012 dataset of the Irkutsk ionosonde (52.3°N, 104.3°E). They obtained the diurnal, seasonal and solar activity pattern of the NmF2 variability for both high- and low-frequency parts of the variability.

In the current study we analyze the data of the Norilsk ionosonde (69.4N, 88.1E), the Ekaterinburg SuperDARN radar (56.4°N, 58.5°E), and the Hokkaido East SuperDARN radar (43.53°N, 143.61°E). Following [1], we analyze the variability of ionospheric characteristics in the same manner. As an ionosonde characteristic we selected the F2 peak density NmF2 calculated from the ionogram critical frequency. As a SuperDARN radar characteristic we selected the minimum slant range (Rmin) extracted from the HF radar ground backscatter data. Due to double HF focusing effect near the skip distance, the corresponding slant range can be surely determined as a slant range related to the maximum of the registered ground backscatter power. The main idea of minimum slant range extraction technique from SuperDARN radar data is described in [2]. However, in contrast with [2] in the current study we used an improved version of this technique which utilizes elevation angle information for more accurate identification of ground backscatter echoes corresponding to F2 ionospheric layer.

The main objectives of this paper are the following:

- (1) to analyze the seasonal pattern and the solar cycle variations of the NmF2 variability from the Norilsk ionosonde and make comparison with the NmF2 variability from the Irkutsk ionosonde;
- (2) to analyze the seasonal pattern and the solar cycle variations of the Rmin variability from the Hokkaido East SuperDARN radar and to make a comparison with the Rmin variability from the Ekaterinburg SuperDARN radar;
- (3) to compare the seasonal pattern and the solar cycle variations of the NmF2 and Rmin variability and discuss the reasons of the obtained distinctions.

2. TECHNIQUE OF VARIABILITY CALCULATION

A disturbance of an ionospheric characteristic is considered as deviation of the observed value from a regular behavior. The regular behavior associated with climatological specifics of the diurnal, seasonal, and long-term solar activity variations can be represented by 27-day running medians. The 27-day running median of ionospheric characteristic \mathbf{P} for given local time (LT), day of year (D) and year (Y) is the median value for the set $\{\mathbf{P}(LT, D - 13, Y), \dots, \mathbf{P}(LT, D + 13, Y)\}$. Thus, the \mathbf{P} disturbance is the difference between observed \mathbf{P}_{OBS} and the 27-day median \mathbf{P}_{MED} value:

$$\Delta\mathbf{P} = \mathbf{P}_{\text{OBS}} - \mathbf{P}_{\text{MED}}, \quad (1)$$

$$\Delta_{\text{R}}\mathbf{P}(\%) = \Delta\mathbf{P} / \mathbf{P}_{\text{MED}}100\%, \quad (2)$$

where $\Delta\mathbf{P}$ and $\Delta_R\mathbf{P}$ are the absolute and relative disturbances, respectively.

The next step is separation of low- and high frequency components of the \mathbf{P} disturbances. For the separation we used low-pass filtering with a cutoff period of 6 hours. The high-frequency part with periods less than 6 hours (denoted further as $\Delta\mathbf{P}_{\text{TID}}$, $\Delta_R\mathbf{P}_{\text{TID}}$) is related to traveling ionospheric disturbances (TID) caused by internal gravity waves (IGW). The cutoff period was selected basing on [3] statistics that showed existence of TIDs with periods up to 5 hours. The low-frequency part with periods more than 6 hours (denoted further as $\Delta\mathbf{P}_{\text{LONG-TERM}}$, $\Delta_R\mathbf{P}_{\text{LONG-TERM}}$) is related to day-to-day variability and tidal variations with diurnal, semidiurnal, and terdiurnal components.

The variability is considered as the root mean square of \mathbf{P} disturbances:

$$RMS(P) = \sqrt{\langle\Delta P^2\rangle}, \quad RMS_R(P) = \sqrt{\langle\Delta_R P^2\rangle}, \quad (3)$$

where brackets denote some averaging. For different tasks we used different types of averaging. Annual averaging was used for studying the year-to-year changes in the variability (solar cycle variations). To obtain the seasonal pattern of the variability we performed averaging over years for the daytime of each day of year. In this study we consider only the daytime variability (using ground terminator as a day-night boundary) due to the fact that the nighttime SuperDARN radar ground backscatter echoes are regularly observed only in summer period.

3. RESULTS AND DISCUSSION

Figure 1 shows the seasonal behaviors of the daytime relative NmF2 and Rmin variability. In the case of the peak electron density variability ($RMS(\text{NmF2})$), the long-term variability provides the main contribution to the total variability, and their seasonal variations are similar. These seasonal variations are characterized by the largest values at equinoxes and the smallest values in summer with intermediate values in winter. The equinoxes/summer ratio is 1.7 and the winter/summer ratio is ~ 1.3 . The short-term variability shows clear seasonal behavior with maximum in winter and minimum in summer, and the winter/summer ratio is ~ 2.3 . For all the kinds of the NmF2 variability, the main features of the seasonal behavior at polar Norilsk are close to those at mid-latitude Irkutsk [1]. The difference is that the variability in winter and equinoxes is somewhat larger at Norilsk than at Irkutsk, and as a result the winter/summer ratios are somewhat larger at Norilsk.

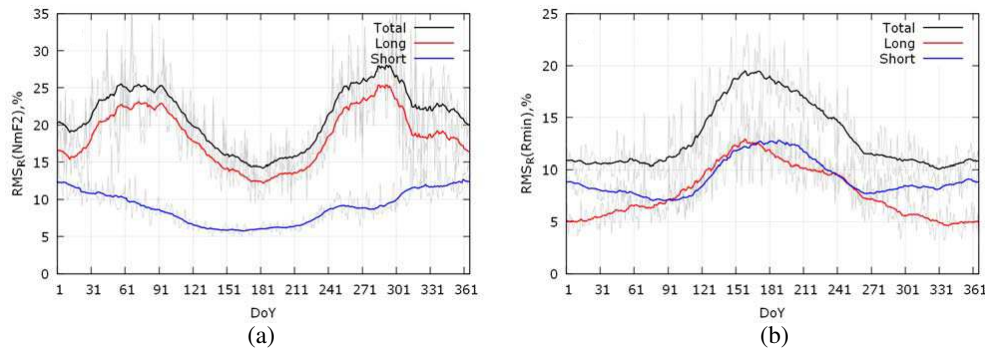


Figure 1: Seasonal behavior of daytime relative NmF2 (a) and Rmin (b) variability. Total, long-term and short-term variability averaged by running 27-day mean are shown by black, red and blue lines respectively. Grey lines are initial dependencies.

In the case of the Rmin variability ($RMS(\text{Rmin})$), the long-term variability is smaller (in winter) or comparable (in summer and equinoxes) to the short-term variability, and hence we can not make a conclusion on the main contribution to the total variability. For all the kinds of the variability, the largest $RMS(\text{Rmin})$ is seen in summer. The smallest $RMS(\text{Rmin})$ is seen in winter for the long-term variability and at equinoxes for the short-term variability. The winter/summer ratio is ~ 0.4 for the long-term variability and ~ 0.7 for the short-term variability. For all the kinds of the Rmin variability, the main features of the seasonal behavior for the mid-latitude Hokkaido SuperDARN radar are close to those for the sub-polar Ekaterinburg SuperDARN radar with somewhat greater variability for the sub-polar radar.

The main distinction between the $RMS(\text{NmF2})$ and $RMS(\text{Rmin})$ seasonal behaviors is the opposite winter-summer difference. A similar difference between the seasonal behaviors of NmF2 and

peak height (hmF2) variability was reported in [4]. Thus, we can assume that the Rmin variations are mainly caused by hmF2 variations and to a lesser extent by NmF2 variations. Under the same electron density (Ne) variations, the amplitude of hmF2 variations strongly depends on the background Ne profile thickness: the larger the thickness, the higher the amplitude. Thus, the higher hmF2 and Rmin variability in summer is most likely explained by the larger Ne profile thickness in summer compared to winter.

The other distinction between the NmF2 and Rmin variability is the different relation between the long- and short-term parts of the variability. This distinction may be explained by that the short-term part most likely corresponds to the variations with shorter vertical wavelengths that cause the higher hmF2 and Rmin variability compared to the longer wavelength variations.

The only similarity between the RMS(NmF2) and RMS(Rmin) seasonal behaviors is that the short-term part of the variability characterized by the higher winter/summer ratio compared to the long-term part.

Figure 2 demonstrates the year-to-year variations of the daytime relative NmF2 and Rmin variability. In the case of the NmF2 variability, the long-term part (as well as total variability) shows a clear increase with the solar/geomagnetic activity, whereas the short-term part does not show a clear dependence on the solar/geomagnetic activity. Both these features of the solar/geomagnetic activity dependence of the NmF2 variability at polar Norilsk are close to those at mid-latitude Irkutsk [1]. The short-term part of the Rmin variability (as well as in case of NmF2) does not show any increase with the solar/geomagnetic activity, whereas the long-term part shows some correlation with F10.7 excluding the case of 2007 when the long-term Rmin variability is the largest under enough low level of the solar/geomagnetic activity. From Figure 2 we can see that the long-term NmF2 variability noticeably exceeds the short-term NmF2 variability and the largest difference is seen under the highest solar/geomagnetic activity (2003); whereas the short-term Rmin variability is larger or comparable to the long-term Rmin variability and the largest difference is seen under the lowest solar/geomagnetic activity (2009).

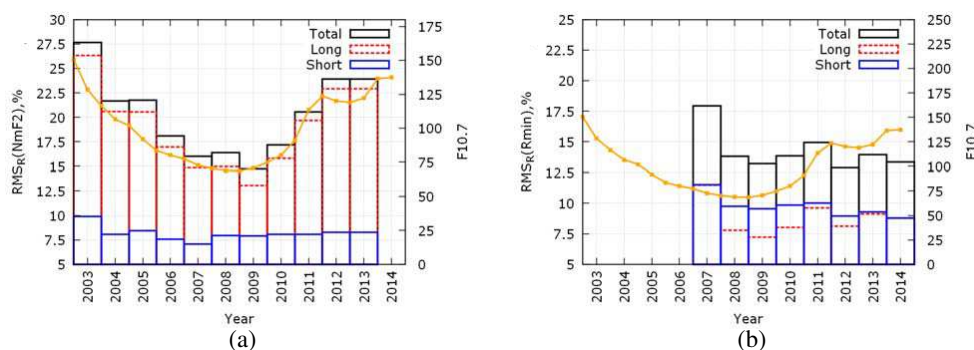


Figure 2: Year-to-year variations of daytime relative NmF2 (a) and Rmin (b) variability with variations of annual running mean F10.7 index (orange line with squares). Total, long-term and short-term are shown by black, red and blue colors respectively.

4. CONCLUSIONS

The performed analysis of the daytime relative NmF2 and Rmin variability revealed both distinctions and similarities in the seasonal behavior and year-to-year variations.

The main distinction between the seasonal behaviors is the opposite winter-summer difference. The proposed explanation is that the amplitude of Rmin variations strongly depends on the background electron density profile thickness: the larger the thickness, the higher the amplitude; and so the higher Rmin variability in summer is most likely explained by the larger profile thickness in summer compared to winter.

The long-term NmF2 variability noticeably exceeds the short-term NmF2 variability; whereas the short-term Rmin variability is larger or comparable to the long-term Rmin variability. The different relations between the long- and short-term parts of the variability may be explained by that the short-term part most likely corresponds to the variations with shorter vertical wavelengths that cause the higher Rmin variability compared to the longer wavelength variations.

The only similarity between the seasonal behaviors is that the short-term part of the variability characterized by the higher winter/summer ratio compared to the long-term part.

In solar cycle variations there are more similarities than differences. The short-term part of both the NmF2 and Rmin variability does not show any increase with the solar/geomagnetic activity, whereas the long-term part of the NmF2 variability clearly increases with the solar/geomagnetic activity and the long-term Rmin variability shows some correlation with F10.7 excluding the case of 2007.

The comparison between the NmF2 variabilities from the Norilsk and Irkutsk ionosondes as well as the comparison between the Rmin variabilities from the Ekaterinburg and Hokkaido SuperDARN radar showed that: (1) the main features of the seasonal and solar cycle behavior at polar and mid-latitudes are close to each other; and (2) the variability is somewhat larger at higher latitudes.

ACKNOWLEDGMENT

The work was supported by Russian Scientific Foundation (project 14-37-00027). We grateful Nagoya University and ISTP SB RAS for the provided experimental data.

REFERENCES

1. Ratovsky, K. G., A. V. Medvedev, and M. V. Tolstikov, “Diurnal, seasonal and solar activity pattern of ionospheric variability from Irkutsk Digisonde data,” *Adv. Space Res.*, Vol. 55, No. 8, 2041–2047, 2015.
2. Oinats, A. V., V. I. Kurkin, and N. Nishitani, “Statistical study of medium-scale traveling ionospheric disturbances using SuperDARN Hokkaido ground backscatter data for 2011,” *Earth Planets Space*, Vol. 67, 22, 2014.
3. Medvedev, A. V., K. G. Ratovsky, M. V. Tolstikov, S. S. Alsatkin, and A. A. Scherbakov, “Studying of the spatial-temporal structure of wavelike ionospheric disturbances on the base of Irkutsk incoherent scatter radar and Digisonde data,” *J. Atmos. Sol. Terr. Phys.*, Vol. 105, 350–357, 2013.
4. Deminov, M. G., G. F. Deminova, G. A. Zherebtsov, and N. M. Polekh, “Statistical properties of variability of the quiet ionosphere F2-layer maximum parameters over Irkutsk under low solar activity,” *Adv. Space Res.*, Vol. 51, No. 5, 702–711, 2013.

Geomagnetic Effects on GNSS Measurements

I. V. Bezler^{1,2}, A. B. Ishin¹, E. V. Konetskaya^{1,2},
A. V. Kulizhsky^{1,2}, M. V. Tinin^{1,2}, and S. V. Voeykov^{1,2}

¹Institute of Solar-Terrestrial Physics, SB RAS, P. O. Box 4026, Irkutsk 664033, Russia

²Irkutsk State University, 20 Gagarin Blvd, Irkutsk 664003, Russia

Abstract— In this paper, the analysis of geomagnetic effects on measurements, made by Global Navigation Satellite Systems (GNSS), relies on both the contribution of the geomagnetic field to the refractive index of ionospheric plasma and the presence of field-aligned random irregularities. The paper reports results of exploration of the possibility for simultaneous removal of first- and second-order errors by modifying the ionosphere-free combination of dual-frequency measurements. The geomagnetic field affects not only the refractive index but also the structure of ionospheric irregularities. Afraimovich et al. (Advances in Space Research, 2011, Vol. 47, 1674–1680) based on the dependence of the GNSS phase slips on the angle between the satellite-receiver line of sight (LOS) and the magnetic field line, have revealed an anisotropy effect of ionospheric irregularities. To analyze the role of this effect on GNSS measurements, we used numerical simulation for studying anisotropy effects of ionospheric irregularities on the probability of occurrence of slips in phase measurements. The simulation results allow us to study and account for the factors which mask effects of this anisotropy. In the future, we are going to exploit this method for estimating the degree of elongation of irregularities to monitor parameters of ionospheric irregularities in the Arctic region.

1. INTRODUCTION

The geomagnetic field significantly affects both the positioning accuracy and the quality of received GNSS signals. When analyzing geomagnetic effects on the positioning accuracy, the consideration of ionospheric plasma anisotropy introduces the third term into the ionospheric component of GNSS signal phase path [1]:

$$\varphi_i = D - 40.3I_1/f_i^2 - 40.3I_2/f_i^3 + \dots \quad (1)$$

Here $D = z_t - z_0$ is the satellite-receiver distance; I_1 is the total electron content: $I_1 = \int_{z_0}^{z_t} N(z')dz'$.

$I_2 = \int_{z_0}^{z_t} N(z')f_g \cos\theta dz'$, where $f_g = gB_0$ is the gyrofrequency ($g = e/(2\pi m)$), θ is the angle

between \mathbf{B}_0 and propagation direction. Neglect of the third term in (1) considering geomagnetic effects on the refractive index of ionospheric plasma allows us to take into account ionospheric plasma effects in the first (isotropic) approximation in dual-frequency measurements. The error of such measurements (second-order error) varies from 1 to 4 cm, depending on geo- and heliophysical conditions. Improvement of GNSS measurement accuracy involves considering this error.

As is seen from (1), ionospheric irregularities cause signal phase fluctuations (phase scintillations). At exceeded phase path fluctuation of a whole number of cycles, there occurs phase tracking slip [2]. Geomagnetic effects produce anisotropy of ionospheric irregularities — their sizes along magnetic field lines exceed transverse sizes. This, in turn, leads to scattering anisotropy effect, i.e., to the dependence of slips in GNSS measurements on satellite-observer LOS orientation relative to magnetic field line. Thus, observation of this dependence can provide valuable information about anisotropy of ionospheric irregularities. In [3], the GEONET network was exploited to study a large-scale “bubble” of ionization observed over Japan on February 12, 2000. The analysis of slips registered at the GPS L2 frequency has revealed that their density reaches its peak in field-aligned LOSs at ionospheric heights. This allowed the authors to conclude that the small-scale structure of the “bubble” extends along the magnetic field. However, the paper did not show how regular such situation can be observed, whether this is associated with the “bubble”, and what angular characteristics of slip density will be without such irregularities.

Our paper addresses both the geomagnetic effects on GNSS measurements. First, we, through simulation and using larger body of data, more thoroughly examine the effects of magneto-orientation of irregularities, and then report simulation results of our previously proposed method for eliminating the second-order error.

2. EXPERIMENTAL DATA ON ANISOTROPY OF PHASE SLIPS

To provide sizable observation statistics, we have processed data on 38 days from the Japanese dense network GEONET (Fig. 1(a)). We analyzed slips occurring at the L2 frequency GPS.

Using this dense network of GPS stations, we scanned a large region of the ionosphere: about 40° in latitude and longitude (Fig. 1(b)). We have separately examined four azimuthal sectors of 45° (Fig. 2) with the central direction in azimuths: 0, 90, 180, 270. For these sectors, we derived dependences of density of phase tracking slips at the L2 frequency on the satellite's elevation angle (Fig. 2).

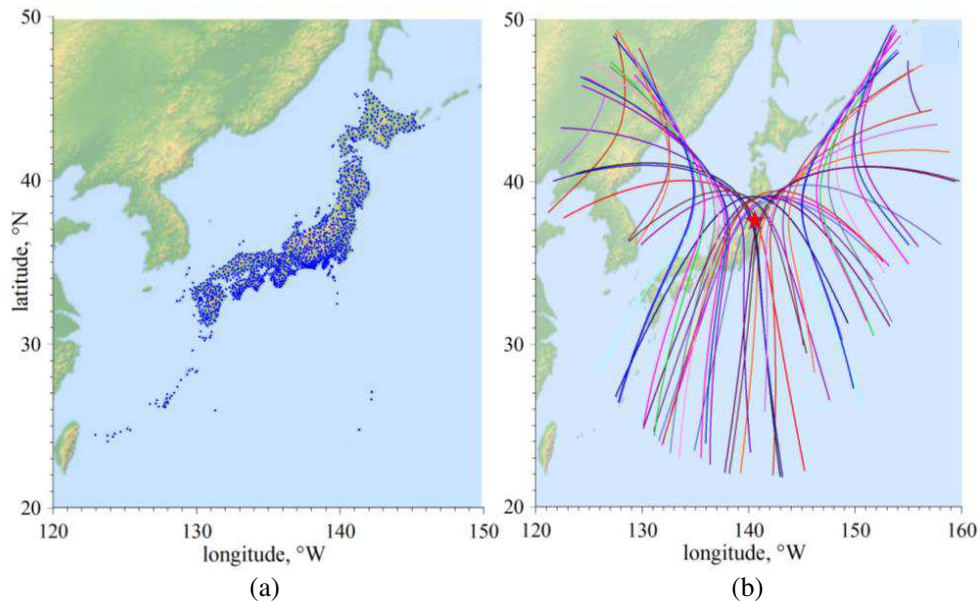


Figure 1: GEONET stations in Japan (blue points a), ionospheric points for 24 hours for one station (coordinates of the station: 37.6 N, 140.6 W).

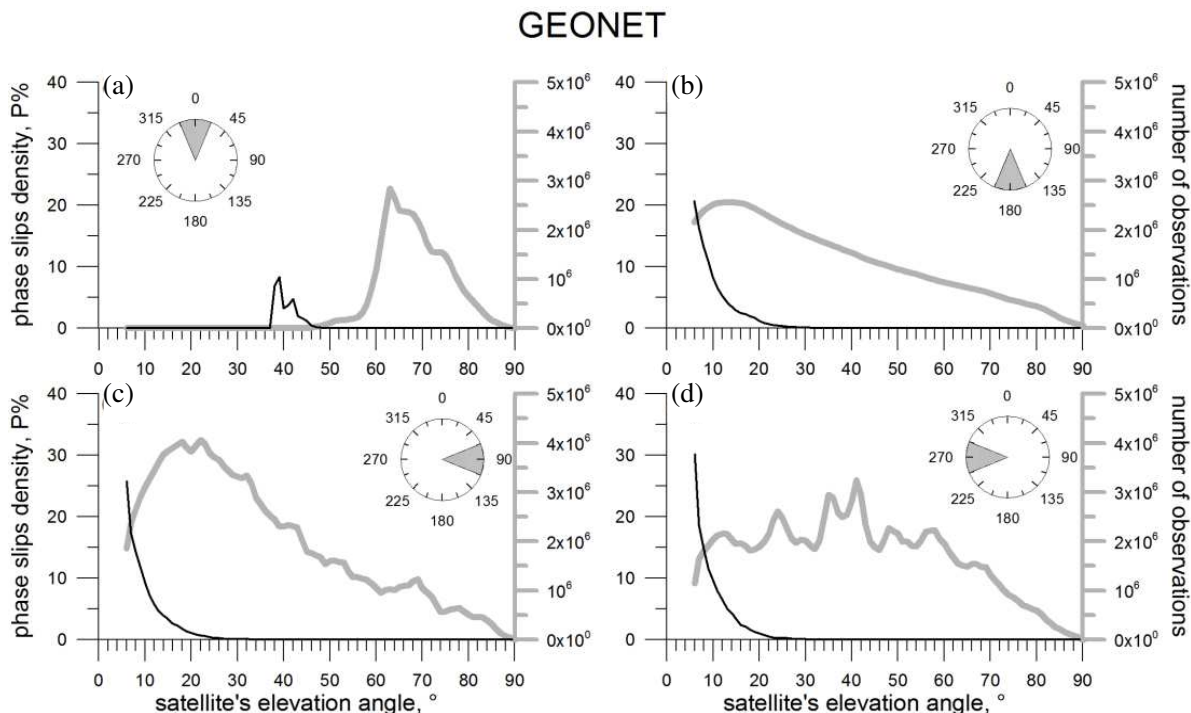


Figure 2: The dependences of the density of phase tracking slips in the GPS (black thin lines) and of the number of observations (gray lines) on the satellite's elevation angle.

We have used data with satellites' elevation angles of over 5 degrees. In the northern sector (Fig. 2(a)) at low elevation angles there are no satellites. This is also evident from the location of ionospheric points (Fig. 1(b)). Other sectors (Figs. 2(b)–(d)) exhibit increasing density of phase slips at L2 with decreasing elevation angle (for 6°, a relative number of slips may be as much as 20–30%). However, in the southern sector (Fig. 2(b)) we did not observe an increase in the density of slips in the satellite-observer LOS closely to the direction of the magnetic field.

To identify effects caused by magneto-oriented ionospheric irregularities, we plotted similar dependences separately for February 12, 2000 (Fig. 3). As expected, the effect of magnetic orientation of irregularities did appear for the southern sector (Fig. 3(b)) exhibiting a corresponding 25% increase in density for the 27–29° elevation angles. For other sectors, there is no analogous increase in the slip density (Figs. 3(c), (d)) because the condition of parallelism between the satellite-observer LOS and the magnetic field in the ionosphere is not fulfilled there.

At low elevation angles of satellites, phase slips in the GPS system increases due to the increasing length of propagation path in an inhomogeneous layer of the ionosphere. For the same reason, the amplitude of the observable TEC variations increases with decreasing elevation angle.

This has been confirmed by results of our studies of the dependence of density of occurrence of

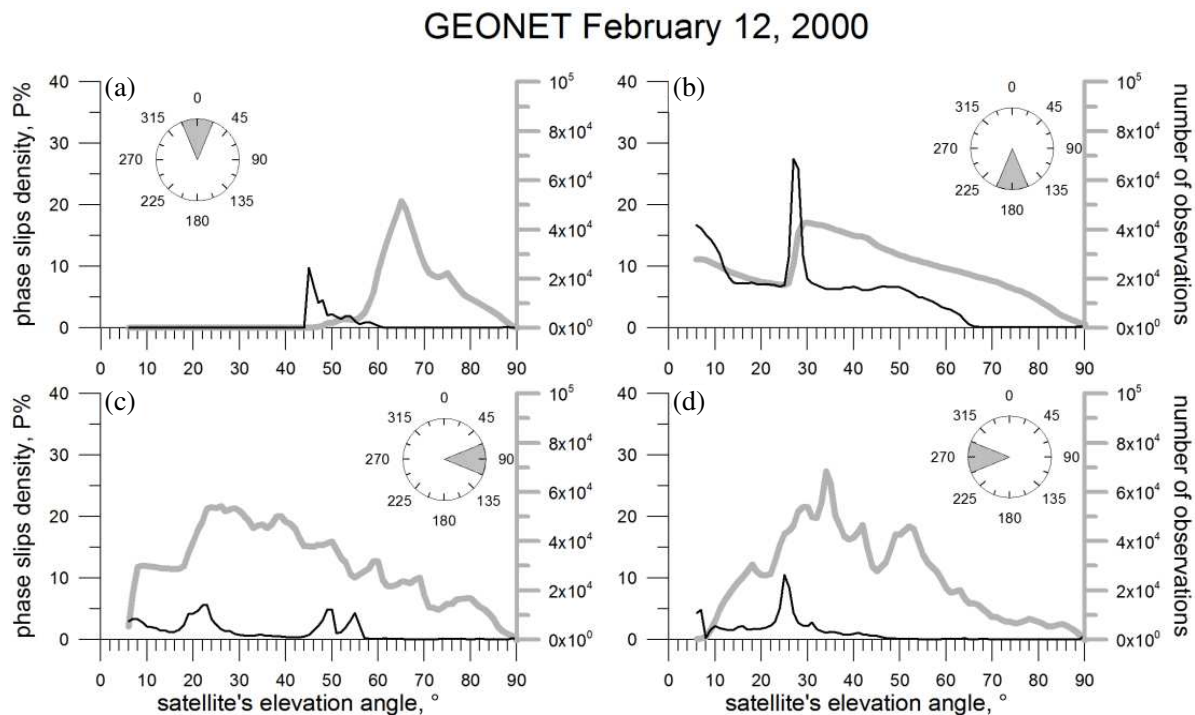


Figure 3: The dependences of the density of phase tracking slips in the GPS (black thin lines) and of the number of observations (gray lines) on the satellite's elevation angle. The data on February 12, 2000.

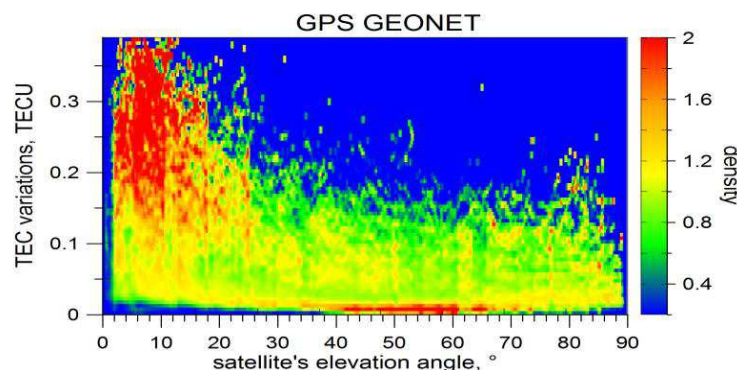


Figure 4: The dependences of the density of occurrence of TEC variations with the corresponding amplitude on GPS satellites' elevation angles. The data were calculated for the GPS station IRKJ for 2008.

oblique TEC variations with varying amplitude on the satellite's elevation angle (Fig. 4). As initial data here, we used data on 100 days from Irkutsk station IRKJ.

3. RESULTS OF SIMULATION OF SLIPS

To explain the observed effects, we simulated the probability of slips in the inhomogeneous ionosphere with the power law spectrum of irregularities. We derived the dependence of the probability of the occurrence of phase tracking slips in the GPS system on the satellite's elevation angle (Fig. 5).

In the general case, the extension of the path of signal propagation in the inhomogeneous ionosphere at decreasing elevation angle of satellite raises the probability of phase tracking slips in the GPS receiver (Fig. 5(a)). The simulation results agree with our experimental results obtained from GEONET data. If, in contrast, we take into account the extension of ionospheric irregularities along the magnetic field, the simulation of slip probability may produce a second maximum (Fig. 5(b)). The satellite's elevation angle at which the second maximum is observed will depend on the station latitude as well as on the selected azimuth. So, if the station is shifted from 37.4° to 33.4°N , this elevation angle changes from 37° to 25° (Fig. 5, right panel) at the 180° azimuth.

4. ELIMINATING GEOMAGNETIC EFFECTS FROM DUAL-FREQUENCY MEASUREMENTS

In standard dual-frequency phase measurements, second-order effects are ignored. This assumption allows us to completely remove the second term in (1) and determine the satellite-observer distance:

$$D = (\varphi_1 f_1^2 - \varphi_2 f_2^2) / (f_1^2 - f_2^2). \quad (2)$$

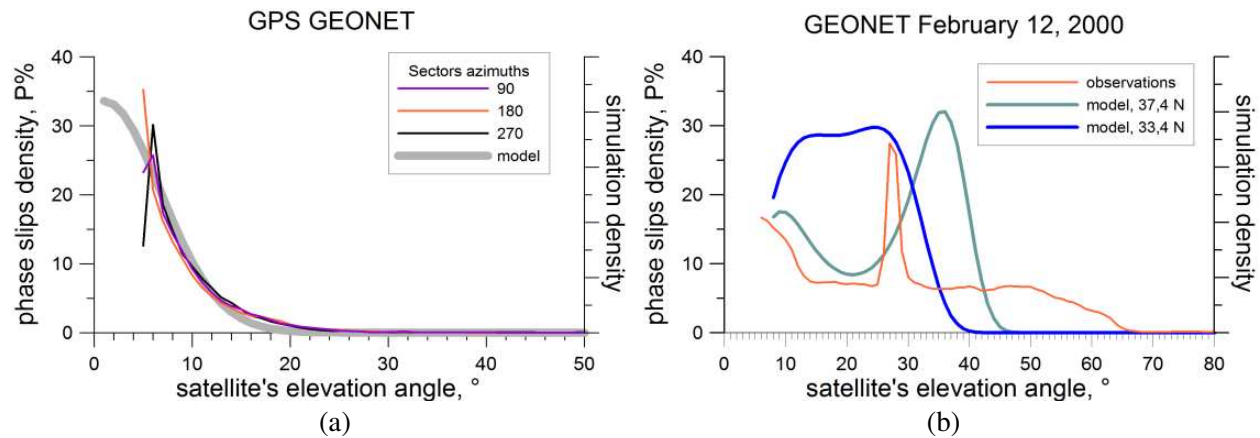


Figure 5: (a) The dependences of the density of phase tracking slips in the GPS in the regular ionosphere (simulation without considering magneto-orientation of irregularities and data on 38 days); (b) analogous dependences for the case of the ionospheric “bubble” (simulation with consideration for magneto-orientation of irregularities). The simulated probabilities are given in arbitrary units (right axes on both the panels), experimental data are in per cent (left axes on both the panels).

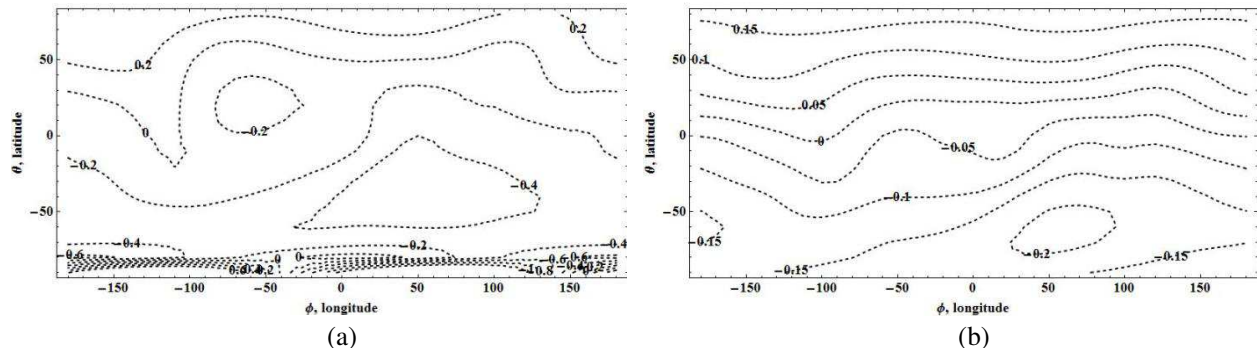


Figure 6: The distribution (in mm) of residual error (4) over the globe (a) for the elevation angle of 10° and the azimuth of -10° ; (b) for the elevation angle of 60° and the azimuth of 10° .

To take into account the second-order effects in dual-frequency measurements, we use the relationship between integral I_2 and total electron content I_1 proposed in [4]. The relationship takes into account the slow change of the geomagnetic field within the ionospheric layer:

$$I_2 \approx I_1 f_g \text{Cos}\theta|_{z=z_m}, \quad (3)$$

where z_m is usually represented by the height of the main maximum of the ionospheric layer. Approximation (3) yields a distance expression which is similar to (2) but accounts for geomagnetic effects [1]:

$$D_{\text{corr}} = (\varphi_1 f_{ef1}^2 - \varphi_2 f_{ef2}^2) / (f_{ef1}^2 - f_{ef2}^2), \quad (4)$$

where $f_{efi} = f_i - (f_g \text{Cos}\theta|_{z=z_m})/2$ is the effective frequency. Yet the residual error is less than 0.5 mm (depending on the position of the receiver) (Fig. 6).

5. CONCLUSION

Observation of slips in GNSS phase measurements may serve as a method for monitoring some parameters of ionospheric irregularities, and a relatively dense network of stations may become a tool for such monitoring. The comparison between observation and simulation results has revealed that in some cases the orientation of ionospheric irregularities manifests itself as anisotropy of observed slips. Such a situation took place on February 12, 2000. However, such an effect is not a regular phenomenon. This event might have been caused by the ionization bubble which emerged from low latitudes and was filled with smaller-scale turbulent irregularities. The slip anisotropy is associated with the anisotropy of small-scale filling and possibly with the orientation and shape of the bubble. A closer correspondence between simulation and observations can be ensured through the use of the model of anisotropic bubble of ionization against slightly anisotropic turbulent ionospheric plasma. The numerical simulation of the modification of the ionosphere-free linear combination of measurements has demonstrated the possibility of eliminating not only the first-order error, but also the second order error, associated with geomagnetic effects on the refractive index of ionospheric plasma, from dual-frequency measurements.

ACKNOWLEDGMENT

We are very grateful to O. A. Kulish for her assistance in preparing the English version of the manuscript. This study was supported by the Grant of the Russian Scientific Foundation (Project No. 14-37-00027).

REFERENCES

1. Tinin, M. V., B. C. Kim, and E. V. Konetskaya, "Possibilities of eliminating ionospheric effects in multifrequency global navigation satellite systems," S. Gardiner, K. P. Olsen, (eds.), *Recent Advances in Satellite Research and Development*, 93–120, Nova Science Publishers, New York, 2013.
2. Hofmann-Wellenhof, B., H. Lichtenegger, and E. Wasle, *GNSS — Global Navigation Satellite Systems. GPS, GLONASS, Galileo, and More*, Springer-Verlag, Wien, 2008.
3. Afraimovich, E. L., A. B. Ishin, M. V. Tinin, Yu. V. Yasyukevich, and S. G. Jin, "First evidence of anisotropy of GPS phase slips caused by the mid-latitude field-aligned ionospheric irregularities," *Advances in Space Research*, Vol. 47, 1674–1680, 2011.
4. Bassiri, S. and G. A. Hajj, "Higher-order ionospheric effects on the global positioning system observables and means of modeling them," *Manuscr. Geod.*, Vol. 18, 280–289, 1993.

Investigation of Nanoantennas Using Surface Integral Equations and the Multilevel Fast Multipole Algorithm

B. Karasmanoğlu, U. M. Gür, and Ö. Ergül

Department of Electrical and Electronics Engineering, Middle East Technical University, Ankara, Turkey

Abstract— A rigorous analysis of nanoantennas using surface integral equations and the multilevel fast multipole algorithm (MLFMA) is presented. Plasmonic properties of materials at optical frequencies are considered by using the Lorentz-Drude models and employing surface formulations for penetrable objects. The electric and magnetic current combined-field integral equation is preferred for fast and accurate solutions, which are further accelerated by an MLFMA implementation that is modified for plasmonic structures. The developed simulation environment is used to investigate popular bowtie structures with different material properties and to analyze interactions between pairs of nanoantennas.

1. INTRODUCTION

Nanoantennas, i.e., antennas designed for optical frequencies, have attracted the interest of many researchers [1–7]. Although the idea of using nanoscale antennas operating at visible lights, e.g., for harvesting solar energy, was purposed decades ago, realization of nanoantennas had to wait for the developments in nanotechnology. Recently, various nanoantennas have been designed, manufactured, and tested for diverse applications, including energy harvesting [3], optical sensing [4], and imaging. Along this direction, computational simulations of nanoantennas have become essential for designing and investigating these structures in alternative scenarios before their experimental realizations [8].

Computational analysis of nanoantennas using the conventional solvers may not be trivial. While nanoantennas are commonly made of highly conducting materials, such as silver and gold, scaled solvers with perfectly conducting assumptions fail to provide realistic and accurate modeling of nanoantennas. This is mostly due to different behaviors of metals at optical frequencies, namely plasmonic effects [9], which become dominating factors especially for nanoscale objects [10]. Incorporating plasmonic effects into the existing solvers is also a challenging task, especially for full-wave solvers. This challenge can partially be solved by resorting to Drude or Lorentz-Drude models that allow for macroscopic analysis via electromagnetic parameters. Specially, changing the electrical permittivity to a complex value with a negative real part based on these models leads to a direct analysis of a plasmonic structure using existing solvers developed for penetrable objects.

In this study, we investigate nanoantennas using surface integral equations and a powerful method, namely, the multilevel fast multipole algorithm (MLFMA). Among alternative formulations, we prefer the electric and magnetic current combined-field integral equation (JMCFIE) for accurate and fast iterative solutions using MLFMA [11]. JMCFIE is modified carefully by considering complex permittivity values with negative real parts. MLFMA is also updated for stability in handling complex wavenumbers with large imaginary parts, leading to rapidly decaying interactions. In this paper, after demonstrating the effectiveness of the developed solver on canonical problems, we present numerical simulations of bowtie nanoantennas at optical frequencies. Different material properties and frequencies are considered for single bowtie nanoantennas (see Figure 1). Electromagnetic interactions between pairs of nanoantennas and their effects in the power enhancement abilities are also investigated. Numerical results show that MLFMA is a strong alternative to space-discretization solvers for accurate and efficient full-wave analysis of nanoantennas.

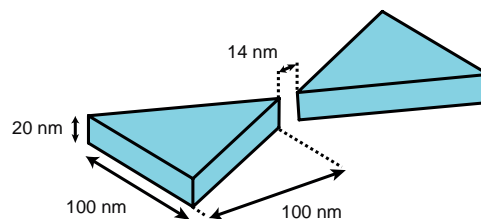


Figure 1: A single bowtie nanoantenna model [4].

2. MLFMA SOLUTIONS OF NANOANTENNAS

Consider a plasmonic object (ϵ_p, μ_p) located in a host medium (ϵ_o, μ_o) illuminated by incident electric and magnetic fields ($\mathbf{E}^{\text{inc}}, \mathbf{H}^{\text{inc}}$) created by external sources. Formulating the problem using JMC FIE discretized with the RWG functions, we obtain [12]

$$\begin{bmatrix} \bar{\mathbf{Z}}_{11} & \bar{\mathbf{Z}}_{12} \\ \bar{\mathbf{Z}}_{21} & \bar{\mathbf{Z}}_{22} \end{bmatrix} \cdot \begin{bmatrix} \mathbf{a}_J \\ \mathbf{a}_M \end{bmatrix} = \begin{bmatrix} \mathbf{w}_1 \\ \mathbf{w}_2 \end{bmatrix}, \quad (1)$$

where the matrix elements and the elements of the RHS vector are derived as

$$\bar{\mathbf{Z}}_{11} = \bar{\mathbf{Z}}_{22} = \bar{\mathbf{T}}_o^T + \bar{\mathbf{T}}_p^T + \bar{\mathbf{K}}_{PV,o}^N - \bar{\mathbf{K}}_{PV,p}^N - \bar{\mathbf{I}}^T \quad (2)$$

$$\bar{\mathbf{Z}}_{12} = -\eta_o^{-1} \bar{\mathbf{K}}_{PV,o}^T - \eta_p^{-1} \bar{\mathbf{K}}_{PV,p}^T - \frac{1}{2} (\eta_o^{-1} - \eta_p^{-1}) \bar{\mathbf{I}}^N + \eta_o^{-1} \bar{\mathbf{T}}_o^N - \eta_p^{-1} \bar{\mathbf{T}}_p^N \quad (3)$$

$$\bar{\mathbf{Z}}_{21} = \eta_o \bar{\mathbf{K}}_{PV,o}^T + \eta_p \bar{\mathbf{K}}_{PV,p}^T + \frac{1}{2} (\eta_o - \eta_p) \bar{\mathbf{I}}^N - \eta_o \bar{\mathbf{T}}_o^N + \eta_p \bar{\mathbf{T}}_p^N \quad (4)$$

$$\mathbf{w}_{1,2} = - \int_{S_m} d\mathbf{r} \mathbf{t}_m(\mathbf{r}) \cdot \left\{ [\eta_o^{-1} \mathbf{E}^{\text{inc}}(\mathbf{r}) + \hat{\mathbf{n}} \times \mathbf{H}^{\text{inc}}(\mathbf{r})], [\eta_o \mathbf{H}^{\text{inc}}(\mathbf{r}) - \hat{\mathbf{n}} \times \mathbf{E}^{\text{inc}}(\mathbf{r})] \right\}. \quad (5)$$

In the above, $\eta_u = \sqrt{\mu_u}/\sqrt{\epsilon_u}$ is the wave impedance for $u = \{o, p\}$. Discretized operators can be written as

$$\bar{\mathbf{T}}_u^{T,N}[m, n] = \int_{S_m} d\mathbf{r} \{ \mathbf{t}_m(\mathbf{r}), \mathbf{t}_m(\mathbf{r}) \times \hat{\mathbf{n}} \} \cdot \mathcal{T}_u \{ \mathbf{b}_n \}(\mathbf{r}) \quad (6)$$

$$\bar{\mathbf{K}}_{PV,u}^{T,N}[m, n] = \int_{S_m} d\mathbf{r} \{ \mathbf{t}_m(\mathbf{r}), \mathbf{t}_m(\mathbf{r}) \times \hat{\mathbf{n}} \} \cdot \mathcal{K}_{PV,u} \{ \mathbf{b}_n \}(\mathbf{r}) \quad (7)$$

$$\bar{\mathbf{I}}^{T,N}[m, n] = \int_{S_m} d\mathbf{r} \{ \mathbf{t}_m(\mathbf{r}), \mathbf{t}_m(\mathbf{r}) \times \hat{\mathbf{n}} \} \cdot \mathbf{b}_n(\mathbf{r}), \quad (8)$$

where \mathbf{t}_m and \mathbf{b}_n represent testing and basis functions, respectively, and $\hat{\mathbf{n}}$ is the outward unit normal. Integro-differential operators are defined as

$$\mathcal{T}_u \{ \mathbf{b}_n \}(\mathbf{r}) = ik_u \int d\mathbf{r}' \mathbf{b}_n(\mathbf{r}') g_u(\mathbf{r}, \mathbf{r}') + \frac{i}{k_u} \int d\mathbf{r}' \nabla' \cdot \mathbf{b}_n(\mathbf{r}') \nabla g_u(\mathbf{r}, \mathbf{r}') \quad (9)$$

$$\mathcal{K}_{PV,u} \{ \mathbf{b}_n \}(\mathbf{r}) = \int_{PV} d\mathbf{r}' \mathbf{b}_n(\mathbf{r}') \times \nabla' g_u(\mathbf{r}, \mathbf{r}'), \quad (10)$$

where $g_u(\mathbf{r}, \mathbf{r}') = \exp(ik_u |\mathbf{r} - \mathbf{r}'|)/(4\pi |\mathbf{r} - \mathbf{r}'|)$, and $k_u = 2\pi/\lambda_u = \omega \sqrt{\mu_u} \sqrt{\epsilon_u}$ is the wavenumber for $u = \{o, p\}$. In MLFMA, the Green's function is factorized and diagonalized as

$$g_u(\mathbf{r}, \mathbf{r}') = \frac{ik_u}{(4\pi)^2} \int d^2 \hat{\mathbf{k}} \exp \left(ik_u \hat{\mathbf{k}} \cdot \mathbf{d} \right) \sum_{t=0}^{\tau} i^t (2t+1) h_t^{(1)}(k_u D) P_t(\hat{\mathbf{k}} \cdot \hat{\mathbf{D}}), \quad (11)$$

where $\mathbf{r} - \mathbf{r}' = \mathbf{D} + \mathbf{d}$.

Consider a plasmonic object modeled with a permittivity of $\epsilon_p = -\epsilon_{pR} + i\epsilon_{pI}$. If $\epsilon_{pR} \gg \epsilon_{pI}$, then $\eta_p \approx -i\sqrt{\mu_p/\epsilon_{pR}}$, $k_p \approx i\omega\sqrt{\mu_p\epsilon_{pR}}$, and

$$\exp(ik_p |\mathbf{r} - \mathbf{r}'|) \approx \exp(-\omega\sqrt{\mu_p\epsilon_{pR}} |\mathbf{r} - \mathbf{r}'|) \quad (12)$$

is a rapidly decaying function. In other words, for highly plasmonic materials, inner interactions tend to be localized and captured by short-distance interactions. If the plasmonic object is located in a lossless and non-plasmonic medium, far-zone interactions in JMC FIE are dominated by the outer interactions. Then, depending on the target accuracy of matrix elements, contributions from the plasmonic material for some of the far-zone interactions can be omitted without deteriorating the accuracy of results. This approach leads to much faster matrix-vector multiplications, compared to using unnecessarily high numbers of harmonics required for large absolute values of wavenumbers encountered in highly plasmonic materials.

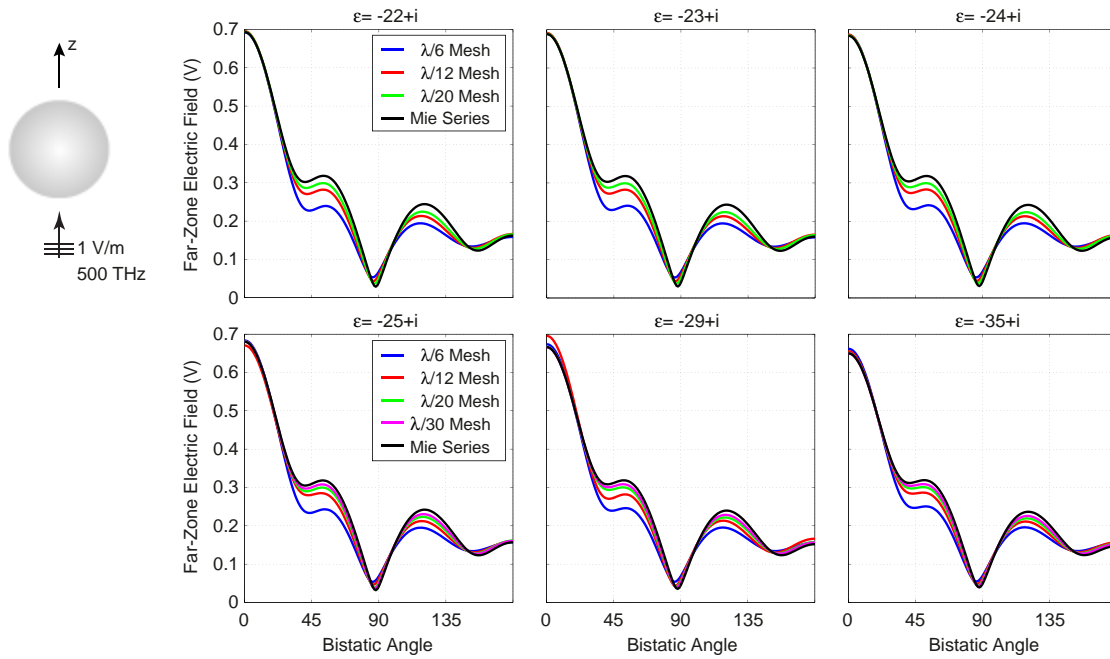


Figure 2: Solutions of scattering problems involving plasmonic spheres of radius $0.3 \mu\text{m}$ excited at 500 THz. MLFMA solutions obtained with different mesh sizes are compared to analytical Mie-series solutions.

3. NUMERICAL VERIFICATION

Figure 2 presents the results of numerical experiments involving spheres of radius $0.3 \mu\text{m}$ located in free space and illuminated by plane waves at 500 THz. Different relative permittivity values with unity imaginary parts and negative real parts from -22 to -35 are considered. Figure 2 depicts the far-zone electric field values on the E -plane with respect to the bistatic angle from 0° (forward-scattering direction) to 180° (backscattering direction). Computational values obtained by using the developed MLFMA implementation for different mesh sizes (i.e., $\lambda/6$, $\lambda/12$, $\lambda/20$, and $\lambda/30$, where λ is the free-space wavelength) are compared to those obtained with analytical Mie-series solutions. For each case, it can be observed that the computational values converge to the reference Mie-series values as the mesh size is decreased and discretization is refined. In other words, the developed MLFMA solver provides controllable accuracy for plasmonic structures.

4. NUMERICAL RESULTS

Figure 1 depicts geometric details of the nanoantenna design considered in this study. The bowtie-shaped nanoantenna has two triangular prisms with 20 nm thickness and separated by 14 nm from tip to tip. The nanoantenna is investigated at optical frequencies when the Lorentz-Drude (LD) model is used to determine the complex permittivity of the materials. Figure 3 presents the results of numerical experiments involving single nanoantennas made of silver (Ag) and gold (Au), each illuminated by a plane wave (1 V/m) from 250 THz to 600 THz. The power density values in the vicinity of the nanoantennas are investigated with respect to the frequency. It can be observed that the nanoantennas become active in different ranges of frequencies, depending on the material. Specifically, power density values in the vicinity of the nanoantennas, especially at the feed locations between the tips, increase significantly at around 400 THz. High power density values indicate the focusing ability of the nanoantennas, hence suitability for energy harvesting.

For a quantitative comparison of different materials for the purpose of energy harvesting, Figure 4(a) presents the power enhancement ratio for single nanoantennas from 250 THz to 600 THz. In addition to silver (Ag) and gold (Au), copper (Cu) and platinum (Pt) materials are considered. Among these, platinum is known to show no plasmonic activity, therefore providing a baseline for the enhancement ability. The power density at the middle of the feed location is divided by the power density of the incident wave (plane wave) to calculate the power enhancement ratio with respect to the frequency. It can be observed that the enhancement ratio of the silver nanoantenna makes a peak at 410 THz with a value of 44.4. While the copper nanoantenna behaves similar to the silver nanoantenna in the 250–370 THz range, its peak occurs with a lower value at 390 THz, fol-

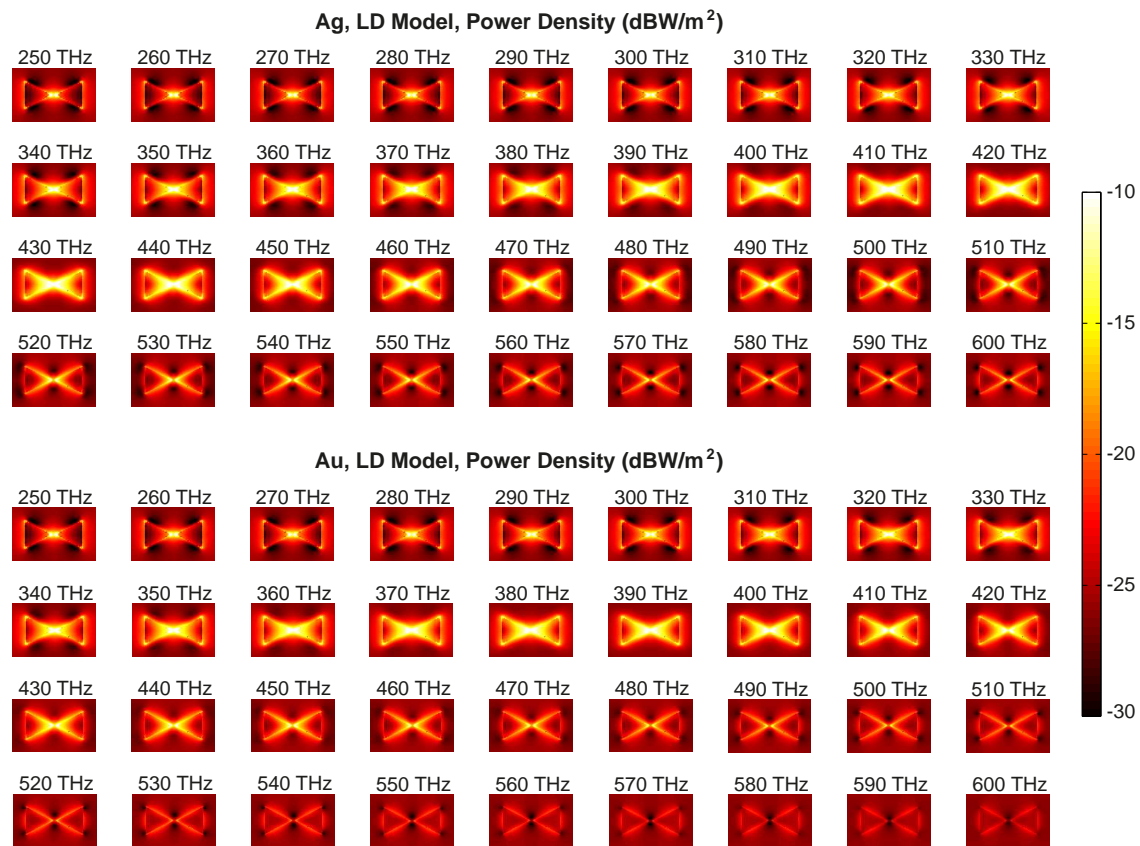


Figure 3: Power density values in the vicinity of single nanoantennas made of silver (Ag) and gold (Au), each illuminated by a plane wave (1 V/m) from 250 THz to 600 THz.

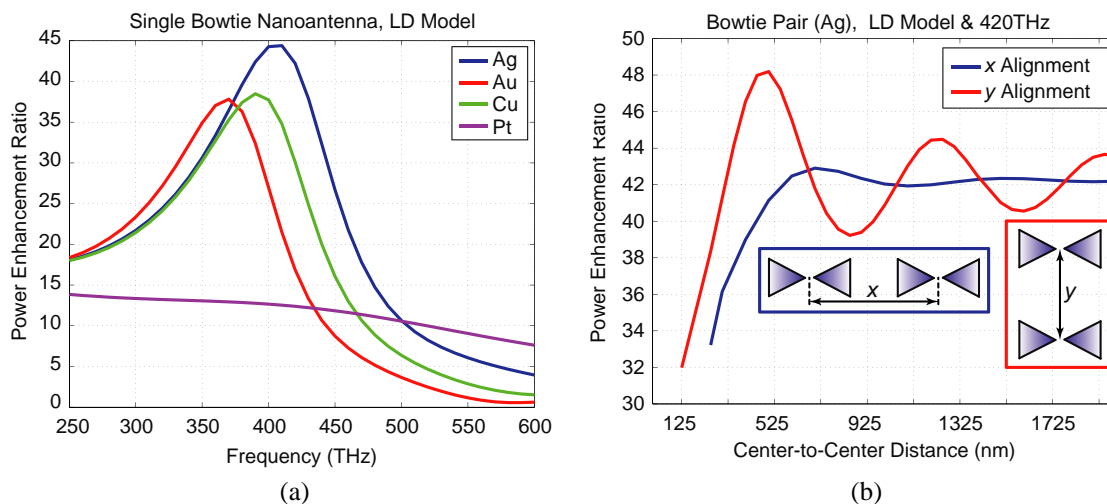


Figure 4: (a) The power enhancement ratio for single nanoantennas made of silver (Ag), gold (Au), copper (Cu), and platinum (Pt), each illuminated by a plane wave (1 V/m) from 250 THz to 600 THz. (b) The power enhancement ratio for a silver nanoantenna, while another identical nanoantenna approaches along x and y axis.

lowed by an earlier decay at higher frequencies. The peak and decay for the gold nanoantenna occur even earlier, and the enhancement ratio for this material is higher than the others from 250 THz to 370 THz, while the silver nanoantenna clearly outperforms the other nanoantennas after 390 THz. Finally, the enhancement ratio for the platinum decreases slowly from 13.8 to 7.6 in the entire range, providing a reference for measuring the performance of the plasmonic nanoantennas.

Finally, we consider pairs of silver nanoantennas and investigate the effect of mutual interactions

on the enhancement ratios. Figure 4(b) presents the power enhancement ratio at the feed location of a nanoantenna, while another nanoantenna approaches along x and y axis. The frequency is fixed to 420 THz and the pairs are illuminated by plane waves. In both cases, the enhancement ratio tends to decrease when the nanoantennas become very close to each other. For some distances, however, higher ratios in contrast to the single-nanoantenna case are observed, especially for the y alignment. Specifically, for the y alignment scenario, an optimal distance from center to center is approximately 500 nm (0.7λ), leading to an enhancement ratio of 48.2. This information can be used to construct efficient nanoantenna arrays, while mutual couplings between array elements will be more complicated, needing further analysis with MLFMA.

5. CONCLUSION

Rigorous analysis of nanoantennas using surface integral equations and MLFMA is presented. The Lorentz-Drude model is used to formulate plasmonic effects at optical frequencies. Single nanoantennas with different materials, as well as pairs of nanoantennas in alternative scenarios are investigated. MLFMA provides accurate and efficient analysis of nanoantennas, while its potential will be revealed further for much larger nanoantenna systems.

ACKNOWLEDGMENT

This work was supported by the Scientific and Technical Research Council of Turkey (TUBITAK) under the Research Grant 113E129 and by a BAGEP Grant from Bilim Akademisi — The Science Academy, Turkey.

REFERENCES

- Schuck, P. J., D. P. Fromm, A. Sundaramurthy, G. S. Kino, and W. E. Moerner, "Improving the mismatch between light and nanoscale objects with gold bowtie nanoantennas," *Phys. Rev. Lett.*, Vol. 94, 017402, 2005.
- Alda, J., J. M. Rico-Garcia, J. M. Lopez-Alonso, and G. Boreman, "Optical antennas for nano-photonic applications," *Nanotechnology*, Vol. 16, 230–234, 2005.
- Muhlschlegel, P., H.-J. Eisler, O. J. F. Martin, B. Hecht, and D. W. Pohl, "Resonant optical antennas," *Science*, Vol. 308, 1607–1609, 2005.
- Kinkhabwala, A., Z. Yu, S. Fan, Y. Avlasevich, K. Mullen, and W. E. Moerner, "Large single-molecule fluorescence enhancements produced by a bowtie nanoantenna," *Nat. Photonics*, Vol. 3, 654–657, 2009.
- Kosako, T., Y. Kadoya, and H. F. Hofmann, "Directional control of light by a nanooptical Yagi-Uda antenna," *Nat. Photonics*, Vol. 4, 312–315, 2010.
- Krasnok, A. E., A. E. Miroshnichenko, P. A. Belov, and Y. S. Kivshar, "All-dielectric optical nanoantennas," *Opt. Express*, Vol. 20, No. 18, 20599–20604, 2012.
- Chen, H., A. M. Bhuiya, L. Runyu, D. M. Wasserman, and K. C. Toussaint, Jr., "Design, fabrication, and characterization of near-IR gold bowtie nanoantenna arrays," *Phys. Chem. C*, Vol. 118, No. 35, 20553–20558, 2014.
- Solis, D. M., J. M. Taboada, F. Obelleiro, and L. Landesa, "Optimization of an optical wireless nanolink using directive nanoantennas," *Opt. Exp.*, Vol. 21, No. 2, 2369–2377, 2013.
- Johnson, P. B. and R. W. Christy, "Optical constants of the noble metals," *Phys. Rev. B*, Vol. 6, No. 12, 4370–4379, 1972.
- Ergül, Ö., "Analysis of composite nanoparticles with surface integral equations and the multilevel fast multipole algorithm," *J. Opt.*, Vol. 14, No. 6, 062701-1–062701-4, 2012.
- Ergül, Ö., "Solutions of large-scale electromagnetics problems involving dielectric objects with the parallel multilevel fast multipole algorithm," *J. Opt. Soc. Am. A*, Vol. 28, No. 11, 2261–2268, 2011.
- Ergül, Ö. and L. Gürel, *The Multilevel Fast Multipole Algorithm (MLFMA) for Solving Large-scale Computational Electromagnetics Problems*, Wiley-IEEE, 2014.

Weigert-effect in the Recording Media on the Base of the Polarization-sensitive Compositions

Valentina Shaverdova, Svetlana Petrova, Lado Tarasashvili,
Anna Purtseladze, and Nino Obolasvili

Laboratory of Holographic Recording and Processing of Information, Institute of Cybernetics
Georgian Technical University, Sandro Euli Str. 5, Tbilisi 0186, Georgia

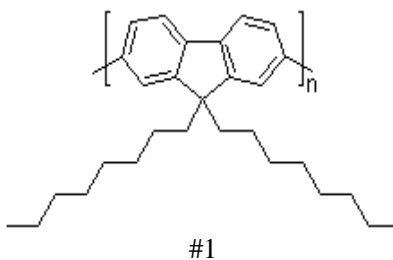
Abstract— The paper discusses the polarization properties of the compositions of the photosensitive media. The compositions have been developed — the transparent polymer in which activators were added: photo anisotropy, chiral and fluorescent impurities. Activators photo anisotropy were based on the organic dyes of different classes. Optical schemes have been created, which allows us to explore the polarized luminescence, and conduct the ellipsometric measurements of the photo anisotropic parameters obtained compositions. For polarized radiation were used standard lasers with wavelengths: ($\lambda = 405; 441.6; 532$) nm.

1. INTRODUCTION

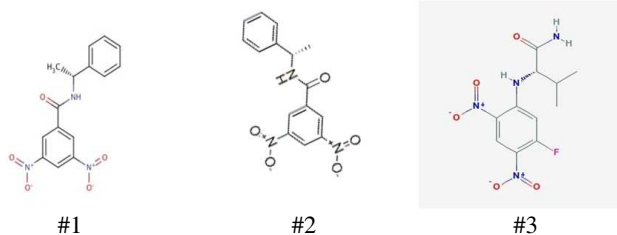
At the beginning of the last century, F. Weigert discovered the appearance of dichroic properties under radiation of the emulsions by polarized light and a variety of solid solutions of organic dyes [1, 2]. F. Weigert also discovered the phenomenon of occurrence of partial polarization of the luminescence radiation emitted by an isotropic body when it was excited with polarized light [3]. These phenomena were called collectively Weigert effect. The possibility to display the polarization of the summary field of the object and reference source of radiation by the polarization-sensitive recording medium, provided the basis for the establishment in the middle of last century, by Georgian scientist Kakichashvili — the new direction in holography — polarization holography [3]. At present this direction was further developed. Weigert-effect expands the scope of application; are created polarization-sensitive medium having new properties, allowing noticeably to increase the use of Weigert effect in various types of optical studies [4, 5]. The phenomenon of light-induced anisotropy can generally be explained by photochemical or photophysical impacts of polarized light. In the compositions presented in this paper the predominant are photochemical processes.

2. EXPERIMENTAL PART AND FORMULATIONS

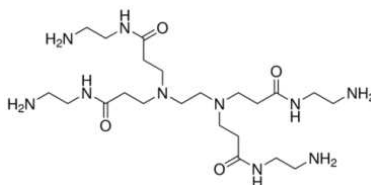
The aim of this study was to create and develop new photo anisotropic-gyrotropic (Weigert-sensitive) recording media, the study of their properties. Determination of the possibility of their use for the needs of the polarization holography and the creation of optical elements with predetermined properties. The objects of study in this paper, were photosensitive compositions created by us. That are transparent polymer films, in which for giving them functional properties — activators of photo anisotropic, fluorescent and chiral dopants were introduced. The homogeneous solution: activator + polymer were poured on glass substrates. The thicknesses of the poured layers were about 10 microns. The polymer matrix for the created media were: polycarbonate (PC), polystyrene (PS), polymethyl methacrylaterylate (PMMC). As activators of the photo anisotropy organic dyes of different classes were selected, including Dimethyl Yellow(DY) dye and its analog Dimethyl Red (DmR), Cationic Orange 5K(CO) and also fluorescent Phthalocyanine (PhC) dye. As additive-Poly (9,9-di-n- octylfluorenyl-2,7-diy) light-emitting polymer was used.



To give the photosensitive samples the chiral properties we used dopants such as:



Besides when creating the compositions PAMAM Dendrimer (DR) was used.



To investigate the fluorescent properties of the created compositions, the method of the polarized luminescence was used. Quantitative measurements were made on the optical scheme created by us, that allows the polarization state of the activating radiation to be changed. The samples were illuminated both polarized irradiation of laser wavelengths: ($\lambda = 405; 441.6; 532$) nm and unpolarized irradiation of the same wave lengths. The calculation formulas enable quantitative values of the coefficient of the anisotropic radiation $\kappa d\Delta$ ($n\tau$) and light-induced birefringence $\kappa d\Delta n$ to be obtained from measurements of the radiation intensity of the luminescence of the samples, oriented at angles of $0^\circ, 45^\circ, 90^\circ$ to the plane of polarization of the activating radiation [6].

The degree of anisotropy of the radiation $r = (I_{II} - I_{\perp}) / (I_{II} + 2I_{\perp})$, and the angles between the dipoles of radiation and absorption α was also measured $\cos^2(2\alpha) = (1 + 5r) / 15r$.

Photoinduced anisotropy can be described by an effective photo anisotropy A_{eff} obtained from a single measurement. It is numerically equal to the transmission of an anisotropic medium placed between crossed polarizers with an angle between the anisotropy axis and the axis of one of the polarizers 45° .

The use of this characteristics gives the possibility of obtaining the kinetic curves of photo anisotropy and to evaluate the influence of different components on photo anisotropy of the samples under investigation.

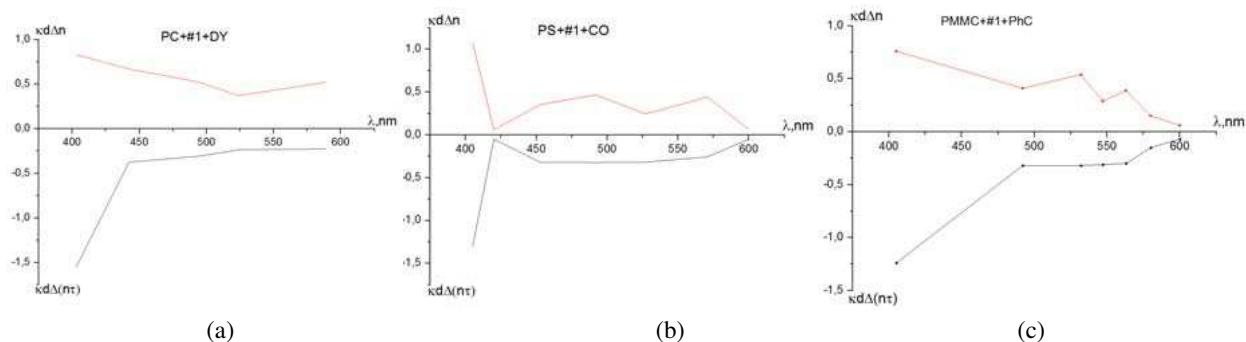


Figure 1: The spectral dependence of the anisotropic radiation coefficient for composition: matrix + fluorescent label + azo dye. Activation of the luminescence was carried out with a laser ($\lambda = 405$ nm). (a) PC + Dimethyl Yellow. (b) PS + Cationic Orange. (c) PMMC + Dimethyl Red.

For the estimation of the spatial distribution of molecules and investigation of hypothetical interactions or possibilities for bond formation between them, quantum-chemical calculations of the compositions and their components were carried out (MM2-energy minimization method, Chem3D Ultra; Total Steric Energy (TSE) as a main evaluation criterion). The most stable conformers for

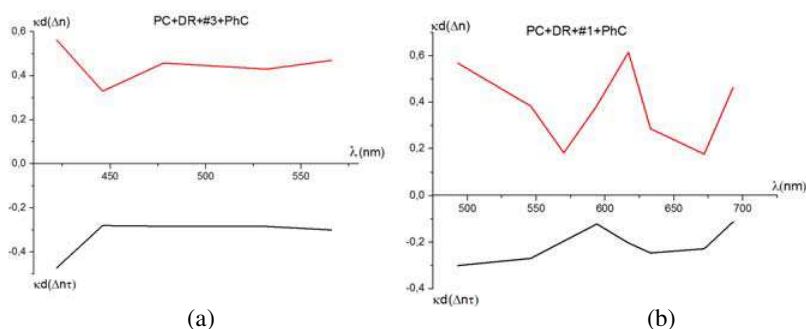


Figure 2: The spectral dependence of the coefficient anisotropic radiation for the composition: (a) PC + Dendrimer + Phthalocyanine dye + chiral dopant #3. (b) PC + Dendrimer + Phthalocyanine dye + dopant #1.

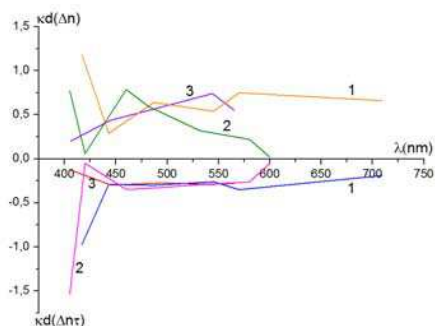


Figure 3: The spectral dependence of the coefficient of anisotropic radiation for the compositions: PC + Phthalocyanine dye + Fluorescent additive with different chiral dopants. Curve 1? #2; curve 2? #3; curve 3? #4.

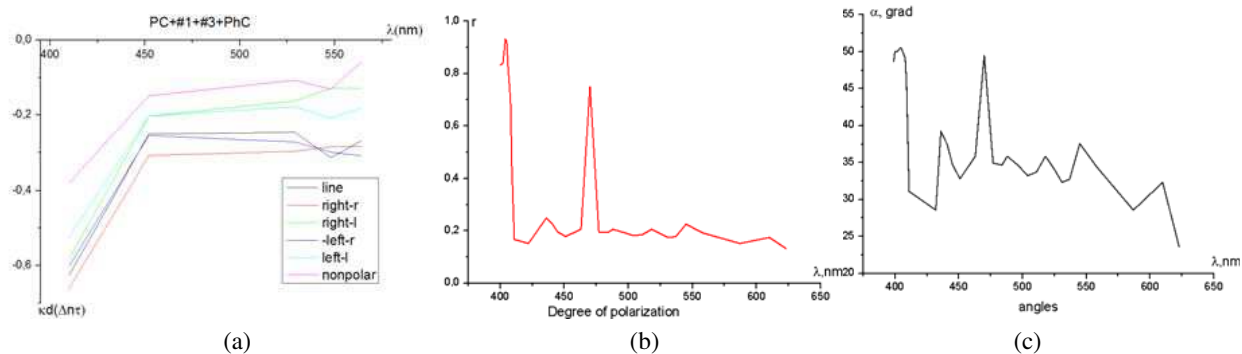


Figure 4: The spectral dependence of the coefficient of anisotropic radiation for the same composition: PC + Phthalocyanine dye + Fluorescent additive + chiral dopant. (a) With different polarization of a probing beam. (b) The spectral curve of the degree of anisotropy of the radiation. (c) The spectral curve of the angles between the dipoles of irradiation and absorption α .

each molecule were found and the models of molecules arrangement in compositions were simulated [TSE (PC) = 26.47; TSE (#3) = -17.6992; TSE (#1) = 15.69; TSE (PhC) = 28.01; TSE (PC + #3 + #1 + PhC) = 33.12]. [TSE (PC) = 26.47; TSE (#1) = 15.69; TSE (PhC) = 13.88; TSE (PC + #1 + PhC + DR) = 31.70]. According to calculations, molecules tend to move away - disperse in compositions and there are no bonds between them. We assume that arrangement of molecules in compositions in this way shouldn't influence on their photophysical properties negatively and shouldn't cause any significant changes in their photoactivity.

In order to determine the dynamic characteristics of the produced compositions the measurements photo anisotropy in real time, we used the optical scheme, which enables to be determined. The results of these studies are presented in Figs. 5(a) and 5(b).

As it is seen from the Figs. 6(a) and 6(b) anisotropy is induced only at the moment when actinic light is switched on. Thus, the data of the medium can be used as optical shutters.

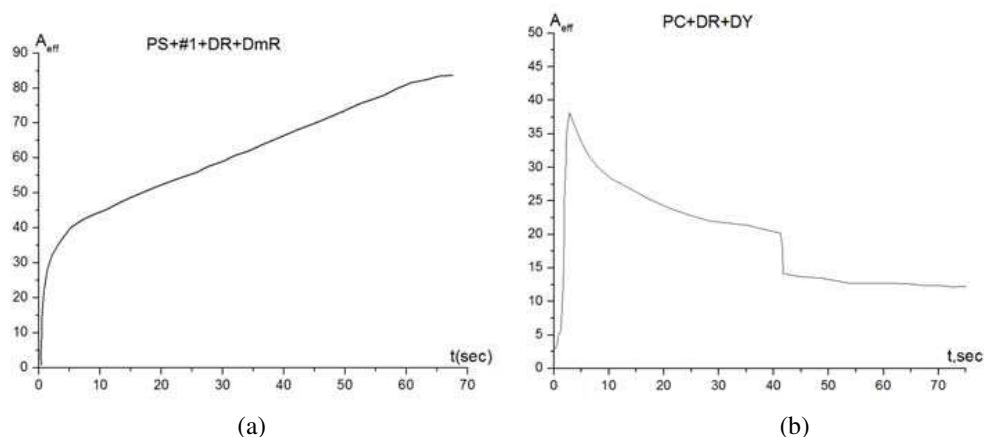


Figure 5: The kinetic curves of the effective photo anisotropy of the compositions. (a) PS + #1 + Dendrimer + Dimethyl Red. (b) PC + Dendrimer + Dimethyl Yellow.

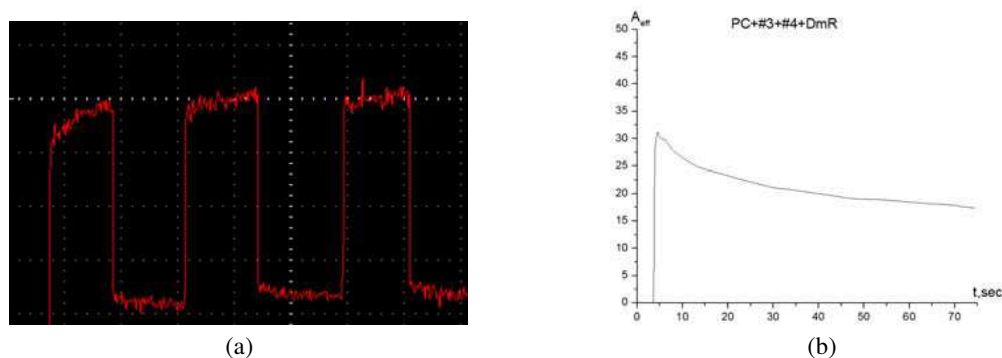


Figure 6: The kinetic curves of the effective photo anisotropy of the compositions. (a) The oscillogram of the compositions: PC + Dendrimer + Dimethyl Yellow. (b) The The kinetic curves of the effective photo anisotropy of the compositions. PC + #3 + #4 + Dimethyl Red.

3. CONCLUSION

Photosensitive compositions were created acquiring under the influence of polarized light the photo anisotropy properties (Weigert-effect), both absorption and emission (photoluminescence). In the compositions was included one of the film-forming polymers fluorescent label, photo anisotropic and chiral dopants. Dendrimer was included in the individual compositions. On the created optical scheme, by the method of polarized luminescence were obtained the spectral curves of the coefficients of anisotropic emission of the investigated compositions. The quantum mechanical calculations for a number of compositions are made. The scheme was created that enables kinetic curves of the effective photo anisotropy to be obtained. The kinetic curves for a number of anisotropy compositions are given. The oscillograms of the compositions which can be used as optical shutters are given.

REFERENCES

1. Weigert, F., "Übereinen effekt der strahlung in lichtempfindlichen schichten," *Verhandl. Dtschen Physik. Ges.*, Bd. 21, 479–483, 1919.
2. Weigert, F., "Ueber die spezifischewirkung der polarisierten strahlung," *Ann. Der Physik*, Bd. 63, 682–725, 1920.
3. ??????
4. ??????
5. Kawatsuki N., A. Yamashita, M. Kondo, T. Matsumoto, T. Shioda, A. Emoto, and H. Ono, "Photoinduced reorientation and polarization holography in photo-cross-linkable liquid crystalline polymer films with large birefringence," *Polymer*, Vol. 51, 2849–2856, 2010.
6. ??????

Investigation of the Free-space Propagation Operator Eigenfunctions in the Near-field Diffraction

Mikhail S. Kirilenko¹, Valery V. Pribylov¹, and Svetlana N. Khonina^{1,2}

¹Samara State Aerospace University Named After Academician S.P. Korolyov, Samara, Russia

²Image Processing Systems Institute of the RAS, Samara, Russia

Abstract— Finite transform, matched with free-space optical fields propagation operator and based on beam expansion of plane waves (1D case), has been considered. The spectrum is also band-limited. We demonstrate that this operator is normal, therefore, its eigenfunctions are orthogonal set. We may consider that resulting functions are eigenmodes. We produced the calculations of eigenfunctions where waves propagate at a distance of one wavelength. Elements of some functions are comparable with a half of wavelength. It is allowing to come closer for solving the problem of superresolution in free space.

1. INTRODUCTION

In recent time there are many attempts to overcome diffraction limit have been produced. It can provide the visualization of elements smaller than half of wavelength. The problems of superresolution are solved using meta-materials [1, 2], nanohole array [3, 4], superoscillation lens optical microscope [5], which includes creation the masks for superoscillation field generation [6], and flat dielectric grating reflectors with focusing abilities [7]. The possibilities of superresolution in far-field have been investigated using hyperlenses, metalenses [8], and optical eigenmodes [9, 10]. In work [11], significant progress has been achieved, where size of imaging object is equals to 25 nm. The facilities of subwave focusing have been demonstrated through development of optical needle [12].

In this work we demonstrate possibilities of creating monochromatic light distribution with details comparable with the wavelength using communication modes [13, 14]. To obtain the desired results, we investigate eigenfunctions of limited optical system. Previously, we study eigenfunctions for the limited system of two lenses where Fourier transform (or Hankel transform in case of radial symmetry) plays the role of propagation operator [15–17]. The eigenfunctions are spheroidal functions if the optical system is Cartesian [15]. The distinction of this work consists in free-space propagation in the near-field diffraction rather than through the lenses, therefore, modeling can be done at a small distance from the input plane.

2. GENERAL THEORY

We consider the propagation of one-dimensional light waves in free space on the basis of scalar diffraction theory. According to this theory, propagation equation based on plane wave expansion, is written as follows [18]:

$$F(u) = \int_{-\infty}^{+\infty} f(x)H_z(u-x)dx, \quad (1)$$

where $f(x)$ — input field, $F(u)$ — output field, $H_z(u-x)$ — the kernel of integral transformation, which depends on propagation distance z :

$$H_z(x) = \frac{1}{\lambda} \int_{-\infty}^{+\infty} e^{ikx\alpha} e^{ikz\sqrt{1-\alpha^2}} d\alpha, \quad (2)$$

where λ — light wavelength, k — wavenumber. This expression is inverse Fourier transform, and the integration is performed over the real axis. In case of infinity limits of integration, there is an analytic form of writing this integral using Hankel function of first kind [19]. We observe that if $|\alpha| > 1$ the plane wave is evanescent.

We also note that formula (1) can be rewritten as a convolution of two functions:

$$F = f * H_z. \quad (3)$$

We consider simple optical system consists of input limited aperture and observable domain at some distance z from it (Figure 1).

We consider only the propagation waves (without evanescent), because evanescent waves cannot pass in free-space at a distance more than third part of wavelength [20]. In other words, we take kernel $h_z(x)$ with finite integral limits instead of $H_z(x)$:

$$h_z(x) = \frac{1}{\lambda} \int_{-1}^1 e^{ikx\alpha} e^{ikz\sqrt{1-\alpha^2}} d\alpha. \quad (4)$$

Since optical system's input domain limited by width of $2a$, formula (1) can be rewritten as follows:

$$F_a(u) = \int_{-a}^a f(x)h_z(u-x)dx = \int_{-a}^a f_a(x)h_z(u-x)dx, \quad (5)$$

where $f_a(x)$ — function, that turns into zero outside the integration interval, $F_a(u)$ — field corresponding with it. We bound the width of observable domain by same limits: from $-a$ to a . The sets of functions defined on these domains are equal and form Hilbert space with scalar production:

$$(f, g) = \int_{-a}^a f(u)g^*(u)du, \quad (6)$$

where asterisk denotes the complex conjugation.

We try to find the functions that remain their form after propagation at a given distance z . This problem reduces itself to propagation operator eigenfunctions calculation problem. To resolve it, we write operator representations of some integrals. The operator Γ performs integral transformation in the formula (1):

$$F = \Gamma [f]. \quad (7)$$

Γ_a denotes the operator corresponding to the finite transform in the formula (5):

$$F_a = \Gamma_a [f] = \Gamma_a [f_a]. \quad (8)$$

The function defined on input of limited system $f_a(x)$ can be represented as production of unlimited field $f(x)$ and rectangular function $\text{rect}(x/2a)$:

$$\text{rect}\left(\frac{x}{2a}\right) = \begin{cases} 1, & |x| \leq 2a, \\ 0, & |x| > 2a. \end{cases} \quad (9)$$

Γ is a normal operator. We show that this property is valid for operator Γ_a too. An operator is normal, if it commutes with its adjoint operator. The adjoint operator of Γ_a is operator Γ_a^* :

$$\Gamma_a^* [f] = \int_{-a}^a f(u)h_z^*(x-u)du. \quad (10)$$

Using the above relations, we can obtain representation of operator $\Gamma_a^*\Gamma_a$:

$$\Gamma_a^*(\Gamma_a f) = \left[f(x)\text{rect}\frac{x}{2a}\text{rect}\frac{u}{2a} *_x h_z(x) \right] (u) *_u h_z^*(u), \quad (11)$$

where the convolution index means performing the integration by specified variable. Due to convolution properties of commutativity and associativity formula (11) can be rewritten as:

$$\left[f(x)\text{rect}\frac{x}{2a}\text{rect}\frac{u}{2a} *_x h_z(x) \right] (u) *_u h_z^*(u) = \left[f(x)\text{rect}\frac{x}{2a}\text{rect}\frac{u}{2a} *_x h_z^*(x) \right] (u) *_u h_z(u). \quad (12)$$

The right-hand part of (12) is action of operator $\Gamma_a\Gamma_a^*$. Thus, we have found that operator Γ_a commutes with its adjoint operator and, therefore, is normal. Its eigenfunctions corresponding to different eigenvalues is orthogonal. Hence, we can assume that the resulting basis of eigenfunctions is the set of orthogonal eigenmodes.

The problem of eigenvalues and eigenfunctions is written as follows:

$$\Gamma_a\phi_n = \mu_n\phi_n, \quad (13)$$

where μ_n — eigenvalue, ϕ_n — corresponding eigenfunction, $n \geq 1$ — the number of eigenfunction.

3. COMPUTATION OF EIGENVALUES AND EIGENFUNCTIONS

We solve the problem of eigenvalues and eigenfunctions using sampling of integral transformations by rectangle method. The calculation parameters are $\lambda = 1000$ nm, $z = 1\lambda$, $a = 5\lambda$.

The image of eigenfunctions has “step” form, as shown at Figure 2. First of 17 eigenvalues is approximately equal in modulus to 1, other values sharply fall to zero (thus, the figure shows only the first 50 eigenvalues). If we approximate arbitrary field by eigenfunctions corresponding to maximum in modulus eigenvalues, then an approximate error will be minimal.

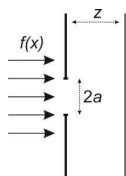


Figure 1: Image of optical system.

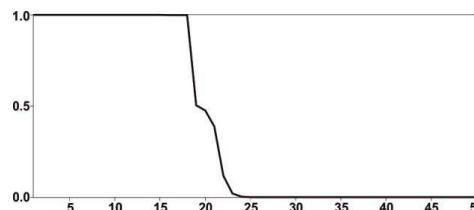


Figure 2: The modules of 50 eigenvalues.

The plots of eigenmodes have shown in Figure 3. It can be seen that fifteenth eigenmode has peaks with FWHM comparable to the half of wavelength. It is a reflection of the fact that the scalar diffraction theory allows approaching to the solution of superresolution problem.

By varying the parameter z , we can establish what kind of fields can pass the given distance without distortion, or, in other words, we can judge the degree of “survival” of optical field.

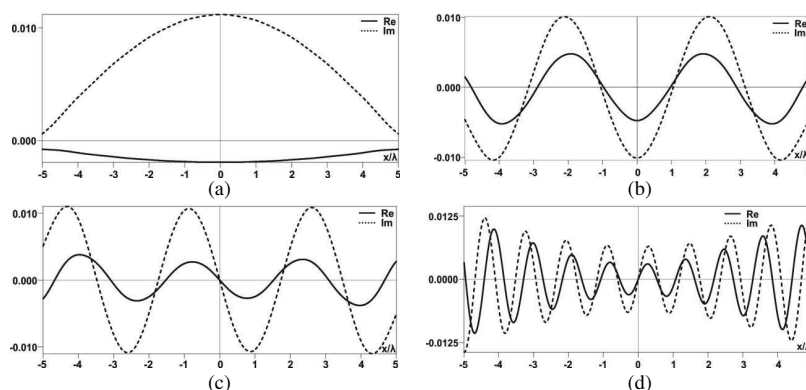


Figure 3: Eigenfunctions: (a) first; (b) second; (c) third; (d) fifteen.

4. CONCLUSION

In this work, we have studied the properties of limited operator of optical signal free-space propagation in near field (at a distance of about one wavelength). We have shown that considered operator is normal and its eigenfunctions are therefore orthogonal.

We perform the calculations of eigenvalues and eigenfunctions of monochromatic optical distribution near-field propagation operator. The beam propagation distance is a parameter of the operator and it significantly changes the set of eigenvalues and eigenfunctions. The eigenvalues modules define corresponding “survival” eigenfunction at a given distance. Thus, resulting calculations allow finding out the number of degrees of freedom in dependence of the distance.

ACKNOWLEDGMENT

The work was financially supported by the Russian Foundation for Basic Research (grant 14-01-31401 mol.a).

REFERENCES

1. Aieta, F., P. Genevet, M. A. Kats, N. Yu, R. Blanchard, Z. Gaburro, and F. Capasso, “Aberration-free ultrathin flat lenses and axicons at telecom wavelengths based on plasmonic metasurfaces,” *Nano Lett.*, Vol. 12, No. 9, 4932–4936, 2012.

2. Lin, L., X. M. Goh, L. P. McGuinness, and A. Roberts, “Plasmonic lenses formed by two-dimensional nanometric cross-shaped aperture arrays for fresnel-region focusing,” *Nano Lett.*, Vol. 10, 1936–1940, 2010.
3. Huang, F. M., T. S. Kao, V. A. Fedotov, Y. Chen, and N. I. Zheludev, “Nanohole array as a lens,” *Nano Lett.*, Vol. 8, No. 8, 2469–2472, 2008.
4. Verslegers, L., P. B. Catrysse, Z. Yu, J. S. White, E. S. Barnard, M. L. Brongersma, and S. Fan, “Planar lenses based on nanoscale slit arrays in a metallic film,” *Nano Lett.*, Vol. 9, No. 1, 235–238, 2009.
5. Rogers, E. T. F., J. Lindberg, T. Roy, S. Savo, J. E. Chad, M. R. Dennis, and N. I. Zheludev, “A super-oscillatory lens optical microscope for subwavelength imaging,” *Nature Materials*, Vol. 11, 432–435, 2012.
6. Huang, F. M. and N. I. Zheludev, “Super-resolution without evanescent waves,” *Nano Lett.*, Vol. 9, No. 3, 1249–1254, 2009.
7. Fattal, D., J. Li, Z. Peng, M. Fiorentino, and R. G. Beausoleil, “Flat dielectric grating reflectors with focusing abilities,” *Nature Photonics*, Vol. 4, 466–470, 2010.
8. Lu, D., and Z. Liu, “Hyperlenses and metalenses for far-field super-resolution imaging,” *Nature Communications*, Vol. 3, Article Number 1205, 1–9, 2012.
9. Mazilu, M., J. Baumgartl, S. Kosmeier, and K. Dholakia, “Optical Eigenmodes; exploiting the quadratic nature of the energy flux and of scattering interactions,” *Optics Express*, Vol. 19, No. 2, 933–945, 2011.
10. Baumgartl, J., S. Kosmeier, M. Mazilu, E. T. F. Rogers, N. I. Zheludev, and K. Dholakia, “Far field subwavelength focusing using optical eigenmodes,” *Applied Physics Letters*, Vol. 98, 181109 (3 pages), 2011.
11. Yan, Y., L. Li, Ch. Feng, W. Guo, S. Lee, and M. Hong, “Microsphere-coupled scanning laser confocal nanoscope for sub-diffraction-limited imaging at 25 nm lateral resolution in the visible spectrum,” *ACS Nano*, Vol. 8, No. 2, 1809–1816, 2014.
12. Rogers, E. T. F., S. Savo, J. Lindberg, T. Roy, M. R. Dennis, and N. I. Zheludev, “Super-oscillatory optical needle,” *Applied Physics Letters*, Vol. 102, 031108 (4 pages), 2013.
13. Pierri, R. and F. Soldovieri, “On the information content of the radiated fields in the near zone over bounded domains,” *Inverse Problems*, Vol. 14, 321–337, 1998.
14. Thaning, A., P. Martinsson, M. Karelín, and A. T. Friberg, “Limits of diffractive optics by communication modes,” *J. Opt. A: Pure Appl. Opt.*, Vol. 5, No. 3, 153–158, 2003.
15. Kirilenko, M. S. and S. N. Khonina, “Coding of an optical signal by a superposition of spheroidal functions for undistorted transmission of information in the lens system,” *Proc. SPIE*, Vol. 9156, 91560J (8 pages), 2014.
16. Kirilenko, M. S. and S. N. Khonina, “Calculation of the eigenfunctions of two lens imaging system,” *Proc. SPIE*, Vol. 9450, 945012 (8 pages), 2015.
17. Kirilenko, M. S. and S. N. Khonina, “Calculation of eigenfunctions for imaging two-lens system with axial symmetry,” *Computer Optics*, Vol. 38, No. 3, 412–417, 2014.
18. Luneburg, R. K., “Mathematical theory of optics,” University of California Press, Berkeley, California, 1966.
19. Kowarz, M. W., “Homogeneous and evanescent contributions in scalar near-field diffraction,” *Applied Optics*, Vol. 34, No. 17, 3055–3063, 1995.
20. Katrich, A. B., “Do evanescent waves really exist in free space?,” *Optics Communications*, Vol. 255, 169–174, 2005.

Shielding Effectiveness in Coaxial Cable Connectors in Ultra High Frequency — UHF — 1 GHz to 3 GHz

Kenedy Marconi Geraldo dos Santos^{1,2}, Marcela Silva Novo², Glauco Fontgalland³,
Marcelo Bender Perotoni⁴, and Caio Luminatti Andrade⁵

¹UFBA — Federal University of Bahia, Brazil

²IFBA — Federal Institute of Bahia, Brazil

³UFCEG — Federal University of Campina Grande, Brazil

⁴UFABC — Federal University of ABC, Brazil

⁵SENAI — CIMATEC, Brazil

Abstract— Cables and connectors are responsible to efficiently transfer energy and data between systems and so have an important role on EMI and EMC problems. The purpose of the shield of coaxial cables and connectors is the mitigation of the energy fluxes into and/or out of the circuits. There is no universally applied test method, due to the complexity of all systems and working conditions. A method to measure the electric field with and without solder on connectors in ultra-high frequency is proposed. The testing methodology is based on the integration software that controls both injected signals and measured parameters, where a constant power level is injected into the cable and then the electric field is measured.

1. INTRODUCTION

Nowadays, numerous electro-electronic system designers and product development engineers use shielded cable and connectors to protect against electromagnetic interference and comply with the strict electromagnetic compatibility requirements. Although Transfer Impedance (Z_t) is an extensively used and important parameter to test a coaxial cable, EMC engineers prefer working with the Shielding Effectiveness (SE) parameter of cables and connectors [1, 2]. The SE in terms of electric field is defined by Equation (1):

$$SE_{dB} = 20 \log \frac{E \text{ (electric field without shielding)}}{E \text{ (electric field with shielding)}} \quad (1)$$

The attenuation of semi anechoic chambers and shielded chambers are expressed in dB and the technical specification is described using the Shielding Effectiveness. Although all these procedures to measure the SE are cited in many current standards, the basic demonstration for a universal calibration of the setup measurement is frequently missing. The shielding effectiveness is a significant factor to ensure the electromagnetic compatibility of the electro-electronic systems, but there is not a universal accepted methodology to measure the SE of cable and connectors together [2].

2. PROBLEM FORMULATION AND METHODOLOGY UTILIZED

A RF connector with a poor SE can present some complications when used in the vicinity of sensitive devices or in an electromagnetic contaminated environment [4]. For instance, if conducting lines and connectors are installed near to inverters used for AC motor speed control or nearby an electric motor, they become susceptible to receive the noise emitted by these components. Such disturbs can generate frequency and amplitude variation within the conductor, which might cause errors in the communication with the electronic centrals connected to it [5]. For decreasing EMI and EMC problems, it is more efficient to act on the cause, on the receiver or on the coupling environment [3, 4]. In this paper, the connector is the component that will be investigated in order to mitigate the radiated electromagnetic energy.

In a semi-anechoic chamber, RF signal in UHF Band (1 GHz to 3 GHz) with a constant power level of 50 Watts is injected into a cable and connectors with matched 50 Ω load. The measurement setup consists of an electric field probe, the coaxial cable and connectors. Both the electric field amplitude and the voltage standing wave ratio (VSWR) are measured [5]. In order to reduce the radiated electromagnetic interference in the transmission line, a coaxial cable with a copper tube enclosing the outer conductor is used. Figure 1 and Figure 2 illustrate the measurement setup and the regions where will be soldiers in the connector, respectively.

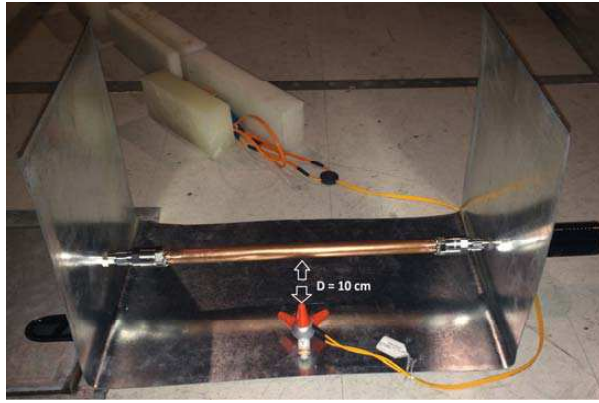


Figure 1: Measurement setup.



Figure 2: Connector without solder.

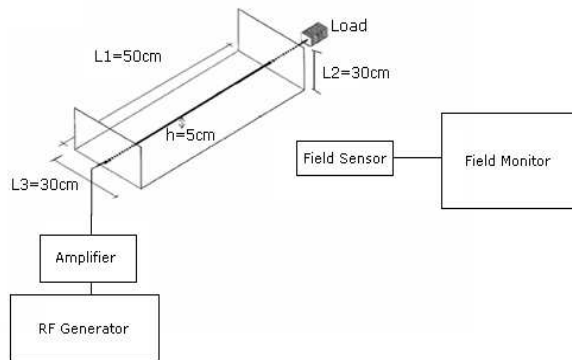


Figure 3: Measurement setup synoptic [4].

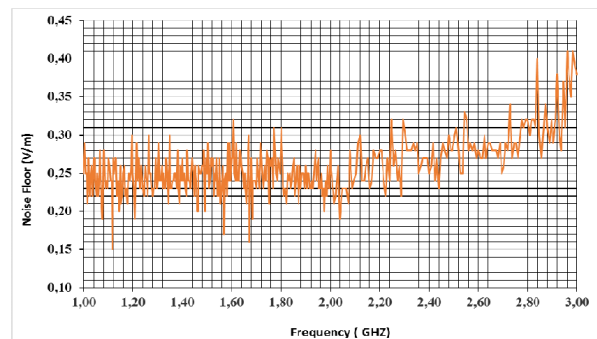


Figure 4: Noise floor of the semi-anechoic chamber.

The experimental setup shown in Figures 1 and 3 are based on the following parameters: $L_1 = 50$ cm, $L_2 = 30$ cm, $L_3 = 30$ cm, $h = 5$ cm, and load impedance of 50Ω [3]. The connector under test is a $7/8''$ 50Ω connector for $1/2''$ coaxial cable.

By using the EMC32 software that controls both injected signals and measured parameters, a 50 W constant power is injected into the cable. Both radiated electric field and the Voltage Standing Wave Ratio (VSWR) are measured with and without solder in the connector. The distance between the probe and the cable center was set to 10 cm.

3. RESULTS

In order to only measure the radiated electric field by the coaxial cable connector, and ensure consistency and repeatability of the test, the noise floor of the semi-anechoic chamber is measured. The Figure 4 shows the result for the noise floor measured with a electric field probe. The environment radio frequency levels at a test site shall be sufficiently low compared to the levels of measurements to be performed (to provide enough signal to noise ratio). In the present tests, the ambient radio frequencies had levels of at least 6 dB below the measurement levels to be performed [6].

Figure 5 illustrates the measured VSWR. The measured noise floor level shows that it can be neglected, considering that there is a good signal to noise ratio. The connector with solder has a lower VSWR and therefore it presents better performance in almost all frequency range (1 GHz to 3 GHz).

Figure 6 shows that the amplitude of the radiated electric field by the connector with solder is lower than without solder in the whole frequency range. At the frequency of 1.48 GHz, the amplitude electric field reaches values equal to 135 V/m. At the same frequency but with the connector soldered, the electric field drops to 4.7 V/m. In 1.79 GHz there is a variation of about 21.2 V/m in the electric field. At the frequency of 2.1 GHz the field level is 7.3 V/m with solder and 70 V/m without it. For frequencies higher than 2.7 GHz the difference with and without the solder is not relevant, pointing that the coupling mechanism is not anymore controlled by the solder.

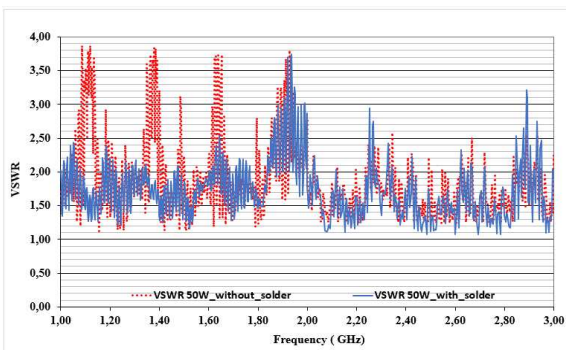


Figure 5: Voltage standing wave ratio (VSWR) with and without solder.

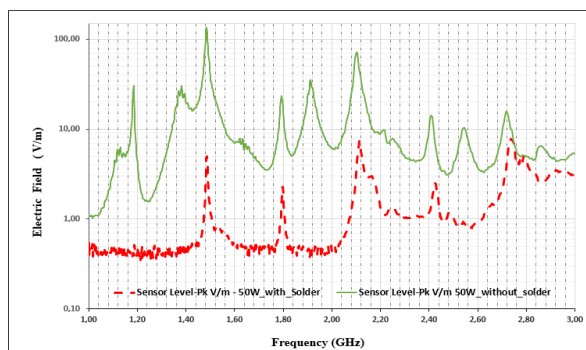


Figure 6: Electric field radiated by the connector with and without solder.

4. CONCLUSION

Differences between the measures of the electric field amplitudes in ultra-high frequency with and without solder are considerably high. For frequencies above 2.7 GHz this difference on the radiated electric field is not relevant. This article clearly shows the importance of a proper installation of RF Connectors in the UHF band. In this case even following the manufacturer recommendations it was necessary solder the connector to minimize both the VSWR and the radiated electric field. It should be also noted that in the UHF band, considering the performed measurements, there are still many challenges to determine the transfer impedance, as well as the shielding effectiveness of coaxial cables and connectors in the microwave range [7].

REFERENCES

1. Mardiguian, M., "Simple method for predicting a cable shielding factor, based on transfer impedance," *Interference Technology: The International Journal of Electromagnetic Compatibility, Interference Technology: EMC Directory & Design Guide 2012*, Vol. 1, 1–5, 2012.
2. Taghivand, M., "Correlation between shielding effectiveness and transfer impedance of shielded cable," *2004 International Symposium on Electromagnetic Compatibility, EMC 2004*, Vol. 3, 942–945, 2004.
3. Donald, R. J. and M. Mardiguian, *Electromagnetic Shielding*, Vol. 3, Interference Control Technologies, Inc., Gainesville, Virginia, 1988.
4. Santos, K. M. G., et al., "Measure of the shielding effectiveness in coaxial cables," *XIV International Symposium on Electromagnetic Fields in Mechatronics Electrical and Electronic Engineering ARRAS*, France, 2009.
5. Santos, K. M. G., et al., *Measure of the Shielding Effectiveness in Coaxial Cables*, Vol. 1, 540–548, IOS Press, Amsterdam, 2010, ISSN: 1383-728.
6. CISPR 16-1-4, "Specification for radio disturbance and immunity measuring apparatus and methods," May 2004.
7. Démoulin, B. and L. Koné, *Shielded Cable Transfer Impedance Measurements in the Microwave Range of 1 GHz to 10 GHz*, 52–61, IEEE-EMC Newsletter, 2011.

Optical Method for Investigation of the Parameters of the Thin Film

M. Bolshakov^{1,2}, N. Kundikova^{1,2}, and I. Popkov^{1,2}

¹The Institute of Electrophysics of the Ural Division of the Russian Academy of Sciences (IEP UD RAS)
Russia

²“South Ural State University” (National Research University), Russia

Abstract— We present results of computer simulation and experimental observation of the Gauss beam reflection from a thin film (an one-dimension photonic crystal). The beam splitting and the beam center of gravity shift were demonstrated after the beam reflection. The shifts were different for s and p -polarization and depended on the angle of incidence, the film thickness and the refractive indices of the film and the substrate. The computer generated intensity distributions and experimentally observed ones after the beam reflection were used to determine the film thickness.

1. INTRODUCTION

Snell's laws were formulated for rays. They are not true for laser beams. The special behavior of light beams under the total internal reflection was considered in Ref. [1]. The longitudinal shift of the linearly polarized beam under the total internal reflection was predicted in 1929 [6]. The magnitude of the shift (Goos-Hanchen shift) was of the order of the wavelength and depended on the radiation polarization. This shift was observed experimentally under the propagation of the linearly polarized radiation of different azimuths through a planar waveguide [2–5].

The transverse shift of the circularly polarized light beam under the total internal reflection was predicted in 1955 [6]. The transverse shift (Fedorov-Imbert shift) was comparable-sized the wavelength and the direction of the shift depended on the sign of the circular polarization [6, 7]. The beam transverse shift was observed experimentally under the circularly polarized beam propagation through a multifaceted prism [8–10].

The Goos-Hanchen and Imbert-Fedorov shifts are spatial shifts. The longitudinal [11] and transverse [12] spatial shifts were observed under the polarized light reflection from a metal surface. The theoretical description of the transverse shift of the polarized beams can be find in Refs. [14, 15]. Spatial shifts under reflection and refraction of the polarized beam at a non-metallic surfaces were described [13].

The deviation of the angle of reflection from the angle of incidence was described in [16]. This shift was named the angular Goos-Hanchen shift.

The Fedorov-Imbert angular displacement was predicted for the first time in Ref. [18]. The magnitude of the angular shift was proportional to the second degree of the wavelength. The Fedorov-Imbert angular displacement was observed experimentally when light was reflected from a metal surface [12].

The values of the described shifts are small. The shifts can be increased by reflection from a layed surface. It was shown theoretically that the reflection of the Gaussian beam from a thin film resulted in the beam deformation and longitudinal shift. It was found that the shift value and the deformation depended on the film thickness and refractive indecies of the film and substrate.

Here we describe the method of determination of the thin film parameters using the Gaussian beam deformation under reflection from a thin film.

2. THEORETICAL RESULTS

We calculated the Gauss beam reflection from a film as follows. The angle of the beam incidence was α_0 . The wave equation was solved by the spectral method. The Gauss beam was decomposed into plane waves in the certain range of angles. As a result we got the set of plane waves. The reflection coefficient r_s , r_p for each s - and p -polarized plane wave were calculated using the Fresnel formulas. We used the folowing parameters. The refractive index of the film n_f was equal to 1.596 (photoresist SU – 8). The refractive index of the substrate was equal to $n_s = 3.62$ (silicon). The wavelength $\lambda = 0.63 \mu\text{m}$. The film thickness was changed from $15 \mu\text{m}$ to $35 \mu\text{m}$. The obtained reflection coefficient $R_s = |r_s|^2$ and $R_p = |r_p|^2$ are shown in Fig. 1.

Figure 1 also shows the angular spectra of the Gauss beam under consideration. The angular width of the beam equals 7° . It can be seen that the Gaussian beam covers the maximum and minimum of the reflection coefficients, that can predict the Gauss beam deformation.

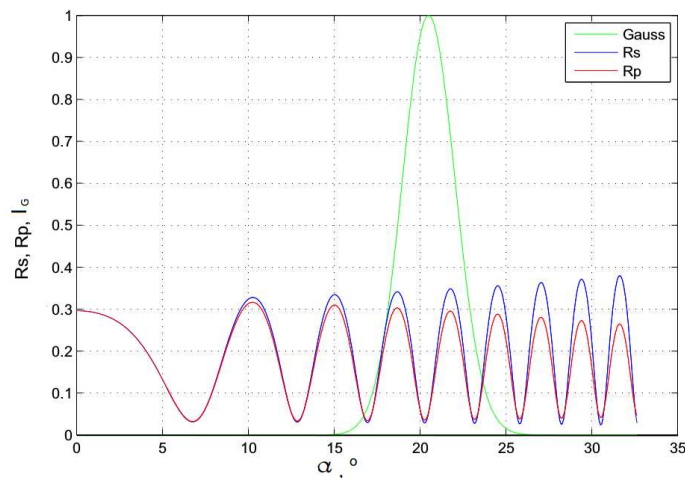


Figure 1: Reflection coefficients R_s , R_p and the angular spectra of the Gauss beam as a function of the incidence angle α .

The calculated intensity images were used to determine the center of the gravite of the reflected beam. The transverse shift wasn't observed. Figure 2 shows the dependence of the longitudinal spatial shift of the reflected Gauss beam on the angle of incidence for the different light polarizations. We can see from Figure 2 that the longitudinal shift can be positive or negative. It should be stressed that multipath light propagation through the film leads to increasing of the longitudinal spatial shift.

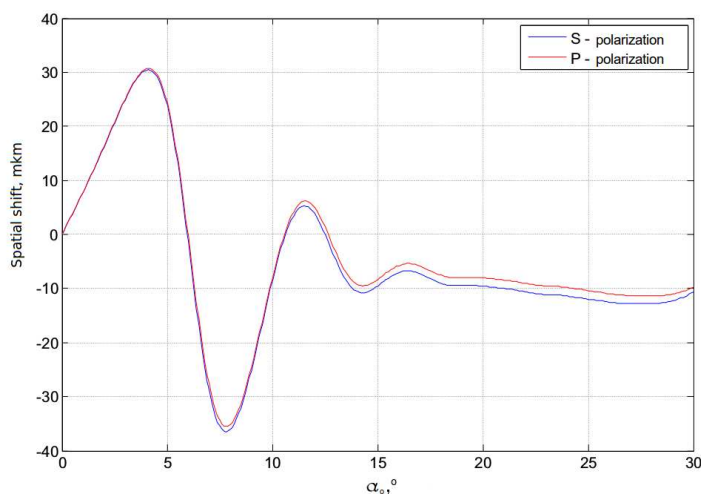


Figure 2: The dependence of the polarized beam longitudinal shift on the angle of incidence α .

To determine the angular shifts the propagation of the reflected beam was simulated and the intensity distribution in the far field was calculated. The angular shift of the beam center of gravity was determined by the deviation from the classical law of reflection. The angular longitudinal shift dependence on the angle of incidence for different polarizations. It can be seen from Ref. [2] that the angular shift depends on the angle of incidence quasi-periodically and doesn't depend on the polarization of the incident radiation. The shifts deviations are both positive and negative, the maximum value is about -1.7° .

3. EXPERIMENTAL RESULTS

The s -polarized reflected beam was investigated experimentally under the beam reflectoin from a photoresist film deposited on a silicon substrate. The angle of incidence was in the range from 5° to 24° . The beam intensity distribution was observed at a screen installed at the distance of 87 mm from the reflecting film. The image was projected at CCD camera by a lens with the focal length

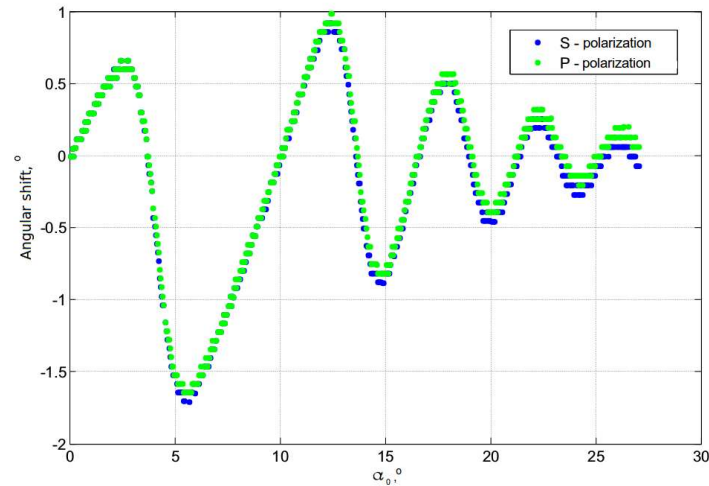


Figure 3: The dependence of the angular shift of reflection polarized beam on the angle of incidence.

$f = 25.4$ mm. The divergence angle of the beam was approximately equal to 6° .

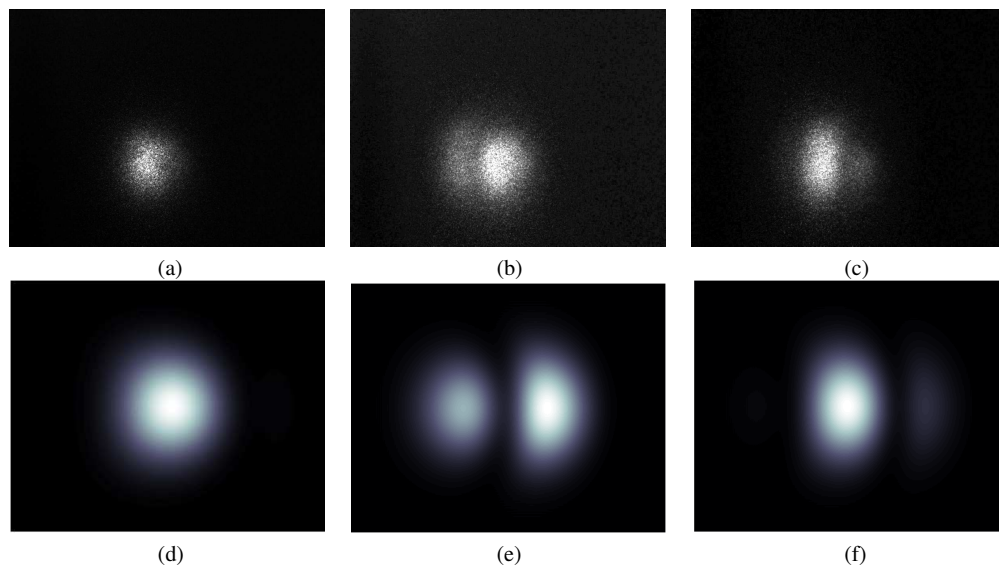


Figure 4: Experimentally observed (a), (b), (c) and calculated (d), (e), (f) intensity distributions of the reflected beam at the angles of incidence $\alpha_0 = 10^\circ$ (a), (d), $\alpha_0 = 20^\circ$, (b), (e), $\alpha = 24.5^\circ$ (c), (f).

Figures 4(a), 4(b), 4(c) show the registered beam intensity distribution for the different angles of incidence α_0 . Figures 4(d), 4(e), 4(f) show the calculated beam intensity distribution after reflection from the film with the thickness $28 \mu\text{m}$ at the same angles of incidence. The thickness of the film under investigation was measured independently and the film thickness turned out to be $28 \mu\text{m}$. The agreement between the experimental results and the results of the computer simulation allows us to use those intensity distributions for the film thickness determination.

4. CONCLUSION

The beam splitting and the beam center of gravity shift after the beam reflection were calculated. The shifts were different for *s* and *p*-polarization and depended on the angle of incidence, the film thickness and the refractive indices of the film and the substrate.

The Gauss beam splitting was observed experimentally at the different angles of incidence. It was shown that the beam deformation under the reflection can be used for the films parameters determination.

ACKNOWLEDGMENT

This work was performed under the partial support of the government program 0389-2014-0004.

REFERENCES

1. Picht, J., "Beitrag zur theorie der totalreflexion," *Ann. Physik*, Vol. 395, 433–496, 1929.
2. Goos, F. and H. Hanchen, "Ein neuer und fundamentaler versuch zur totalreflexion," *Ann. Physik.*, Vol. 436, 333–346, 1947.
3. Goos, F. and H. Hanchen, "Neumessung des strahlversetzungseffektes bei totalreflexion," *Ann. Physik.*, Vol. 440, 251–252, 1949.
4. Osterberg, H. and L. W. Smith, "Transmission of optical energy along surfaces: Part II, Inhomogeneous media," *J. Opt. Soc. Am.*, Vol. 54, 1078–1079, 1964.
5. Risset, C. A. and J. M. Vigoureux, "An elementary presentation of the Goos-Hanchen shift," *Optics Comm.*, Vol. 91, 155–157, 1992.
6. Fedorov, F. I., "On the theory of total reflection," *DAN USSR*, Vol. 105, 465–468, 1955.
7. Kristofel, N., "Total internal reflection and related effects," *Scientific Notes of Tartu State University*, Vol. 42, 94, 1956.
8. Imbert, C., "Experimental proof of the photons translational inertial spin effect," *Phys. Lett.*, Vol. 31A, 337–338, 1970.
9. Imbert, C., "Calculation and experimental proof of the transverse shift induced by total internal reflection of a circularly polarized light beam," *Phys. Rev. D*, Vol. 5, 787–796, 1972.
10. Costa de Beauregard, O. and C. Imbert, "Quantized longitudinal and transverse shifts associated with total internal reflection," *Phys. Rev. Lett.*, Vol. 28, 1211–1213, 1972.
11. Merano, M., A. Aiello, G. W. Hooft, M. P., Van Exter, E. R. Eliel, and J. P. Woerdman, "Observation of Goos-Hanchen shifts in metallic reflection," *Opt. Express*, Vol. 15, 15928–15934, 2007.
12. Hermosa, N., A. M. Nugrowati, A. Aiello, and J. P. Woerdman, "Spin Hall effect of light in metallic reflection," *Opt. Lett.*, Vol. 36, 3200–3202, 2011.
13. Onoda, M., S. Murakami, and N. Nagaosa, "Hall Effect of Light," *Phys. Rev. Lett.*, Vol. 93, 083901, 2004.
14. Fedoseyev, V. G., "Conservation laws and transverse motion of energy on reflection and transmission of electromagnetic waves," *J. Phys. A*, Vol. 21, 2045–2059, 1988.
15. Fedoseyev, V. G., "Spin-independent transverse shift of the centre of gravity of a reflected and of a refracted light beam," *Opt. Commun.*, Vol. 193, 9–18, 2001.
16. Merano, M., A. Aiello, M. P. Van Exter, and J. P. Woerdman, "Observing angular deviations in the specular reflection of a light beam," *Nat. Photonics*, Vol. 3, 337–340, 2009.
17. Krayzel, F., R. Polles, A. Moreau, M. Mihailovic, and G. Granet, "Simulation and analysis of exotic non-specular phenomena," *J. of the European Opt. Soc.*, Vol. 5, 10025, 2010.
18. Bliokh, K. Y. and Y. P. Bliokh, "Polarization, transverse shifts, and angular momentum conservation laws in partial reflection and refraction of an electromagnetic wave packet," *Phys. Rev. E*, Vol. 75, 066609, 2007.

Patterned Nano Magneticstructures

D. Bajalan
St. Pölten, Austria

Abstract— Most magnetic devices marketed nowadays still use bulk or thin film materials, this is soon to change with the advent of nano-fabrication technologies [1]. Proper scaling requires that the magnetic particle size decreases with the scaling factor at the same rate as all of the other dimensions. This is necessary in order to keep the number of particles in a bit cell constant (at a few hundred per cell) [2]. Magnetic nano-structures represents future miniaturization in magnetic recording devices, and detailed understanding of the formation of magnetic vortices in closely spaced ferromagnetic nanoparticles is important for the design of ultra-high-density magnetic devices. It is necessary to achieve ultra-high density in magnetic storage media so that the lateral size of the information bits be as small as possible, without the bit volume reaching the superparamagnetic limit beyond which the energy needed to switch the magnetization of a bit becomes less than the thermal energy, and nano-fabrication offers the technical ability to fabricate magnetic objects with nano scale precision having unique magnetic properties, which may be tailored by manipulating the size, the shape, or the composition of the nanostructures [3].

The magnetic nano-structures of have been formed by different rates of heavy ion irradiation of thin films. The fluence affects both anisotropy and spontaneous magnetization.

1. INTRODUCTION

Most recently, research interest in nanocrystalline soft magnetic alloys has dramatically increased. This is due, in part, to the properties common to both amorphous and crystalline materials and the ability of these alloys to compete with their amorphous and crystalline counterparts [4]. The magnetic properties of an ultra thin multilayer can be modified by controlled ion beam irradiation [5, 6]. Magnetic nanostructures are subjects of growing interest because of their potential applications in high density magnetic recording media and their original magnetic properties [7]. Multilayer thin films are well known for their high magnetic anisotropy, and the origin of this high magnetic anisotropy has been the subject of interest for many researchers [8].

2. BREAK THROUGH PHYSICAL LIMITS

The first hard disk recording has been based on a spinning magnetic disk with a longitudinal medium and an inductive write head. Over the past years significant developments have been made that increased the capacity, reduced the cost, and improved the performance and reliability of these magnetic storage devices. With each improved device the range and nature of the applications undertaken have expanded and, in turn, led to a need for further device improvement. The magnetic recording media industry will (also) benefit strongly from the advances in magnetic nanostructures.

Demands for the continuous increase in the data storage density bring the challenge to overcome physical limits for currently used magnetic recording media [9]. When the physical dimensions of a system become comparable to the interatomic spacing, strong modifications of the intrinsic magnetic properties (ordering temperature, magnetic anisotropy, spontaneous magnetization) are expected. Micromagnetic modeling of the behavior of a nanostructured film beautifully describes the magnetization process, but requires a high calculational effort and long computation times.

Furthermore, it is difficult to predict changes of the macroscopic physical behaviour due to variation of parameters. Phenomenological models, on the other hand, are very useful to simulate the behaviour of the magnetic material under the influence of varying parameters, especially when the parameters are based on physical constants.

2.1. Nano Magnetic Property Understanding

Patterned magnetic media could be a way of realizing ultra high density storage media. Recently, demonstrations of areal recording density over 60 GB/in² in both longitudinal and perpendicular magnetic recordings have been successfully made [10]. Determining the properties of small magnetic structures is extremely important for the development of data storage devices [11]. Better understanding of the micromagnetic processes in magnetic recording media is essential for developing novel materials for future ultrahigh density recording [12]. Good understanding of the noise mechanism in magnetic recording is required for developing heads and media for future applications [13].

In perpendicular recording, the magnetization pattern corresponding to the bits is provided perpendicular to the plane of the medium. The information is being stored in vertical domains or other structures of uniform magnetization [14]. In magnetic materials two characteristic length scales have to be considered [15–17]:

1. At the atomic level, nearest neighbor exchange interaction is dominating.
2. At a mesoscopic level, the domain wall width is the characteristic length dominating the magnetization reversal.

3. CHANGING MAGNETIC PROPERTIES

The magnetic properties of an ultra thin multilayer can be patterned by controlled ion beam irradiation. The basic step in this technique is to control the changes in the magnetic properties induced by the irradiation process. Figure 1 shows ion beam irradiation with Ga^+ [9, 16, 17]. In several works light ion irradiation was used to induced ultra-high resolution magnetic patterns on the multi-layers. High aspect ratio silica masks on the produced Co/Pt multi-layers were obtained by e-beam lithography and reactive ion etching with feature sizes down to 30 nm for dots. Hence one of the proper method was through: the use He^+ ion irradiation of the magnetic layers through proper masks to pattern the magnetic properties, without significant changes in sample roughness or optical properties. In the irradiated regions, a strong decrease in magnetic anisotropy, coercivity and Curie temperature can be controlled. After mask removal the obtained result was [18]: magnetic nano structures with high resolution and high density.

Magnetization reversal is one of the important key factors to describe the stability of the produced magnetic nano-structures. There are several studies to analyze the magnetization reversal processes with numerical simulations in magnetic patterns. It was found that this irradiation induced magnetic patterning technique is promising for both present magneto-optical storage devices and future near field recording [18].

3.1. Use of U heavy Ions for YCo_2 Sample Irradiation

An assembly of ferromagnetic nano-structures has been prepared by heavy ions irradiation of paramagnetic YCo_2 thin films on YCo_2 samples have shown that fluences in the order 10^{12} U ions/ cm^2 cause changes in magnetic properties of. the samples Changes are reported to take place after the irradiation like [19, 20]:

1. Change of spontaneous magnetization, coercivity and initial susceptibility.

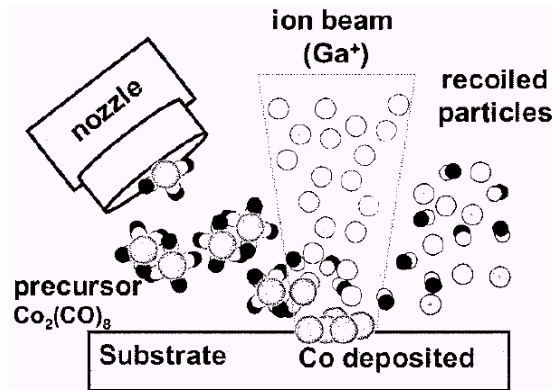


Figure 1: Cobalt dot arrays are fabricated by Ga^+ ion beam induced chemical vapor deposition with an objective to explore size limitations. Dots of about 100–150 nm in diameter are obtained as at islands [9].

Table 1: Macroscopic hysteresis features calculated for irradiated sample.

Φ	[ions/ cm^2]	10^{12}	$5 \cdot 10^{12}$	$2 \cdot 10^{13}$
M_s	[kA/m]	20	40	60
H_c	[kA/m]	43.6	21.8	14.5
M_r/H_c	[]	0,46	1.83	4.13
α	[nm]	7.3	28.6	65.6

2. A distinct change of the anisotropy perpendicular to the film.

Hysteresis loops calculated for three YCo₂ thin film samples at $T = 10$ K perpendicular and parallel to the film plane after U ion irradiation with different fluences [20].

3.2. Increase the Areal Recording

The ability to store a magnetic transition or a bit in the medium at a length as small as possible is one of the most interesting subjects to increase the areal recording density; other attempts to increase the areal recording density like low-noise thin film GMR head which consist of two ferromagnetic layers separated by a thin, non-magnetic conducting spacer, spacing between heads and media and signal processing technologies were successfully achieved [21–23]. To make the bit of information as small as possible it is important to consider the following equation [22]:

$$\alpha = \frac{M_r \delta}{2\pi H_c} \quad (1)$$

M_r [A/m] remanence magnetization of the material.

δ [m] thickness of the material.

H_c [m] coercivity of the material.

α [m] bit length.

The above equation relates important variables to each other to clarify the dependencies (to satisfy the demands) for smaller bit information. The bit length α directly depends on the thickness δ and remanence magnetization M_r of the material and is inversely proportional to the coercivity H_c of the material. Changes have to be made on the equations parameters for producing small bits.

This equation could be written for certain condition with magnetic noise (by assuming $M_r \Rightarrow M_s$ for (nano magnetic structure for ion irradiated material —)) using Equations (1), to find the dependencies as shown in the table.

4. NANO STRUCTURE PRODUCTION BY WAVE

Other method for nanostructure production are possible through different Wave, the angel and Wavelength.

Table 2: Nano pattern production with various λ .

λ Wave length	[nm]	10	12	13	14
θ Angle	[deg]	80	80	80	80
$\sin \theta$	[1]	0.9848	0.9848	0.9848	0.9848
Λ Period length	[nm]	5.0771	6.0925	6.6002	7.1079
θ Angle	[deg]	45	45	45	45
$\sin \theta$	[1]	0.7071	0.7071	0.7071	0.7071
Λ Period length	[nm]	7.0710	8.4852	9.1923	9.8994

The principle of interference lithography is simple; it uses the standing wave pattern (the interference of coherent light forms a standing wave pattern) formed between two interfering beams of light to expose a radiation sensitive material (recording on photo-resist) [24]. In traditional IL systems, the pattern is defined by the interference of spherical waves; hence the fringes produced by the spherical waves [25].

5. SUMMARY

In a conventional high density hard disk a bit with a sufficient signal to noise ratio consists of some hundred single-domain grains; the size of a grain is typically 10–30 nm. Grain size cannot be reduced liberally due to the superparamagnetic limit; a solution to that is to pattern the magnetic layer in a regular matrix of dots. Patterned media is the most prominent candidate for extremely high density magnetic recording media. Patterned media are being developed to form isolated tracks of single-domain magnetic islands. Lithography is a method for transferring a desired pattern into a thin film. Pattern transfer is achieved for example, by using light exposure to change the chemical properties of a photosensitive material, called resist, which has been deposited on top of the device

layer (thin film) to be patterned. Advances in lithography have contributed significantly to the advancement of the integrated circuit technology. In using traditional interference lithography IL to pattern a grating, one splits a laser beam in two and spatially filters them to produce two spherical waves. The waves interfere and the resulting fringes are recorded in photo-resist. Conceptually, a grating is a simple pattern constituting periodic lines and spaces.

REFERENCES

1. Henry, Y., K. Ounadjela, L. Piraux, S. Dubois, J.-M. George, and J.-L. Duvail, *The European Physical Journal B*, Vol. 20, 35, 2001.
2. Thompson, D. A. and J. S. Best, *IBM J. Res. Develop.*, Vol. 3, 321, 2000.
3. Bajalan, D., Ph.D. Thesis, University of Wien, 2005.
4. McHenry, M. E., M. A. Willard, and D. E. Laughlin, *Progress in Materials Science*, Vol. 44, 291, 1999.
5. Bajalan, D., H. Hauser, and P. L. Fulmek, *4th Int. Symposium on HMM*, University of Salamanca, Vol. 8, 78, 2003.
6. Bajalan, D., I. Groiss, G. Stangl, H. Hauser, P. L. Fulmek, and P. Haumer, "Co/Pt multi-layer production for magnetic nanostructures," *Sensors and Packaging, OVE Schriftenreihe Nr.*, Vol. 35, 193, 2003.
7. Jamet, M., W. Wernsdorfer, C. Thirion, D. Mailly, V. Dupuis, P. Mélinon, and A. Pérez, "Magnetic anisotropy of a single cobalt nanocluster," *Phys. Rev. Lett.*, Vol. 86, 4676, 2001.
8. Yamada, Y., T. Suzuki, H. Kanazawa, and J. C. Osterman, "The origin of the large perpendicular magnetic anisotropy in Co₃Pt alloy," *J. Appl. Phys.*, Vol. 85, 5094, 1999.
9. Lapicki, A., K. Kang, and T. Suzuki, "Fabrication of magnetic dot arrays by ion beam induced chemical vapor deposition," *IEEE Trans. Magn.*, Vol. 38, 589, 2002.
10. Papusoi, C. and T. Suzuki, "Anisotropy field distribution measurements for high-density recording media," *J. Magn. Magn. Mater.*, Vol. 240, 568, 2002.
11. Kirk, K. J., J. N. Chapman, and C. D. W. Wilkinson, "Lorentz microscopy of small magnetic structures," *J. Appl. Phys.*, Vol. 85, 5237, 1999.
12. Kisker, H., N. Abarra, Y. Yamada, P. Glijer, and T. Suzuki, "Micromagnetic behavior and recording performance in high density 5 Gbit/in² medium," *J. Appl. Phys.*, Vol. 81, 3937, 1997.
13. Phillips, G. N., T. Suzuki, K. Takano, and M. Takahashi, "MFM analysis of recorded bits written by trimmed and untrimmed MR heads," *J. Magn. Magn. Mater.*, Vol. 193, 434, 1999.
14. Suzuki, T. and I. M. H. Francombe, "Magneto-optic recording thin films," *Handbook of Thin Film Devices, Magnetic Thin Film Devices*, Vol. 4, 257, Academic Press, 2000.
15. Nozières, J. P., M. Ghidini, N. M. Dempsey, B. Gervais, D. Givord, G. Suran, and J. M. D. Coey, *Nucl. Instr. and Meth. in Phys. Res. B*, Vol. 146, 250, 1998.
16. Bajalan, D., H. Hauser, and P. L. Fulmek, "Calculations of magnetic nanostructure hysteresis loops for modified thin by ion irradiation," *PIERS Proceedings*, 465–468, Pisa, Italy, Mar. 28–31, 2004.
17. Bajalan, D., H. Hauser, and P. L. Fulmek, "Magnetic nanostructure in thin film multi-layer," *PIERS Proceedings*, 667–670, Pisa, Italy, Mar. 28–31, 2004.
18. Devolder, T., C. Chappert, Y. Chen, E. Cambril, H. Bernas, J. Ferre, and J. P. Jamet, "Sub-50 nm planar magnetic nanostructures fabricated by ion irradiation," *J. Appl. Phys.*, Vol. 74, 3383, 1999.
19. Solzi, M., M. Ghidini, and G. Asti, "Macroscopic magnetic properties of nanostructured and nanocomposite systems," *Magnetic Nanostructures*, Vol. 4, 123, 2002.
20. Givord, D., J. P. Nozières, M. Ghidini, B. Gervais, and Y. Otani, "Magnetization processes in amorphous nanoparticles obtained by heavy ions irradiation of nonmagnetic Y-Co films," *J. Magn. Magn. Mater.*, Vol. 148, 253, 1995.
21. Yamamoto, T., Y. Kasamatsu, and H. Hyodo, "Advanced stiction-free slider and DLC overcoat," *FUJITSU Sci. Tech. J.*, Vol. 37, 201, 2001.
22. Boboc, A., I. Z. Rahman, and M. A. Rahman, "Modelling of nanostructured magnetic network media," Paper, Surface Science Institute (MSSI) and Department of Physics, University of Limerick, Ireland, 2003.

23. Jung, K. B., H. Cho, T. Feng, Y. D. Park, S. J. Pearton, J. A. Caballero, J. R. Childress, and F. Ren, “Plasma etching of NiFeCo, NiMnSb and CoFeB-based multilayers,” Paper, Materials Science and Engineering Departments, University of Florida, Physics and Astronomy, Michigan State University, IBM Almaden Research Center, Chemical Engineering, University of Florida, Jan. 2004.
24. Walsh, M. E., “Nanostructuring magnetic thin films using interference lithography,” M.Sc. Thesis, MIT, 2000.
25. Chen, C. G., P. T. Konkola, R. K. Heilmann, G. S. Pati, and M. L. Schattenburg, “Image metrology and system controls for scanning beam interference lithography,” *J. Vac. Sci. Technol. B*, Vol. 19, 2335, 2001.

Design of Double Cladding Photonic Crystal Fibers with Low-loss and Broad Dispersion

Na Wang, Shanglin Hou, Yanjun Liu, Jingli Lei, Suoping Li, and Wenyu Zhang
School of Science, Lanzhou University of Technology, Lanzhou, Gansu 730050, China

Abstract— A novel type of photonic crystal fiber structure with double cladding is proposed by full vector finite element method. The influences of this structure on its dispersion and loss are investigated with different inner cladding diameters, outer cladding diameters and air hole pitches. The results indicate that the dispersion varies from -23 ps/(nm·km) to -10 ps/(nm·km) in the band of $1.30 \sim 1.8$ μm , which has broadband dispersion compensation characteristics. The loss is 7.39×10^{-6} dB/km at the wavelength of 1.55 μm , which is by far the smallest value that has ever been reported.

1. INTRODUCTION

Photonic crystal fibers (PCFs), which consist of a pure silica core with numerous periodically spaced airholes in the cladding region, are also called microstructure fibers or holey fibers [1]. By changing the diameters of the air holes and the air filling rate, the relative refractive index of the cladding and fiber core can be flexibly controlled so as to regulate light conduction in PCFs. According to different mechanism of light guiding, PCFs can be divided into two types, total internal reflection photonic crystal fibers (TIR-PCFs) and photonic band gap photonic crystal fibers (PBG-PCFs) [2]. PCFs have been widely applied in many fields because of these unique properties, including endlessly single-mode operation [3], controllable mode areas [4], controllable dispersion characteristic in a wide wavelength range [5], and large nonlinearity [6].

At present, researchers have already designed some new structures, such as, octagon structure, hybrid octagon structure and square structure etc.; the structure of cladding has designed from single cladding, double cladding or even multi-cladding; the fiber core has evolved from hollow-core into small-core, double-core, multi-core. These structural changes have great influence on transmission characteristics of PCFs [7–10].

This paper demonstrates a new type double-clad PCF (DC-PCF) with hexagonal air hole configuration. This kind of PCF is composed of double-cladding made by different air holes, the double-cladding structure not only makes the coupling reduced difficultly but also has a unique dispersion characteristics. In order to investigate the influences of this structure on its dispersion and loss, the effects of the inner cladding diameters, outer cladding diameters and air-hole pitches on dispersion and loss are all numerically simulated.

When the cladding structure of DC-PCF is similar as the conventional PCF, the similar dispersion characteristics can be obtained for that the dispersion characteristics of DC-PCF is mainly determined by the inner core and the surrounding air hole structure. And the loss can be reduced by optimizing the out-layer structure that affects the limited loss. In the paper, the dispersion characteristics of PCF is tailored by changing the diameters of inner and outer cladding air holes, and the effective index of which is lower than that of the fiber core so that the total internal reflection theorem is satisfied. The results indicate that values of its dispersion varies from -23 ps/(nm·km) to -10 ps/(nm·km) in the band of $1.30\text{--}1.8$ μm , which has broadband dispersion compensation characteristics. By changing these structure parameters carefully, the loss can reach $7.39 \cdot 10^{-6}$ dB/km at the wavelength of 1.55 μm , which is the smallest value that has ever been reported. The results of this DC-PCF provide a reference for designing some devices based on PCF with dispersion compensation, and also provides a theoretical basis for practical applications for the low loss characteristics which can increase the transmission efficiency of PCF.

2. THEORY AND METHOD

The cross section of the novel DC-PCF is shown in Fig. 1. The fiber core consists of one deletion air hole, the cladding consists of four layer air holes, the first and the second layer constitute the inner cladding, outer cladding consists of the third and fourth layers, and the angle between the inner cladding and the outer cladding is 30° . Λ_1 , Λ_2 and Λ_3 denote the pitch of the first layer and the second layer, the pitch of the second layer and the third layer, the pitch of the third layer and the fourth layer, respectively. d_1 and d_2 denote the diameters of the inner cladding and outer

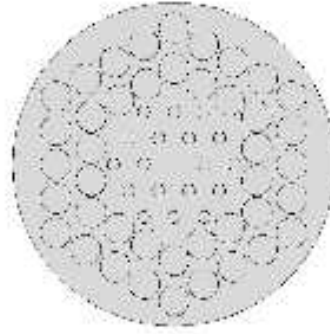


Figure 1: Cross section of DC-PCF.

cladding respectively. The background material is fused silica, whose refractive index n_1 is 1.44, and the refractive index of air hole n_0 is 1.

In this paper, we use full-vector finite element method (FEM) to compute the effective refractive index n_{eff} of fundamental mode and the confinement loss α . And according to the relationship of the effective refractive index n_{eff} and the dispersion, the dispersion and the loss can both be analyzed at wavelength of $1.30 \sim 1.80 \mu\text{m}$. The total dispersion of PCF can be described as [11]:

$$D(\lambda) = -\frac{\lambda}{c} \frac{d^2 n_{eff}(\lambda)}{d\lambda^2} + D_m(\lambda) \quad (1)$$

where λ represents wavelength, c is the speed of light in vacuum, $n_{eff}(\lambda)$ represents the effective refractive index of fundamental mode, and $D_m(\lambda)$ represents the material dispersion.

P_0 is the incident power, transmission power can be described as

$$p_T = p_0 \exp(-\alpha L) \quad (2)$$

where α is attenuation coefficient and known as fiber loss, L is the length of the fiber.

The loss of PCF represents the power attenuation of the light signal when it transmits in the fiber. The attenuation is different with different wavelength in the same fiber, and the continuous loss measurement of different wavelength is called loss spectrum measurement. In practice, the loss can be represented by the expression of attenuation coefficient

$$a = -\frac{10}{L} \lg \left(\frac{P_T}{P_0} \right) \quad (3)$$

3. NUMERICAL ANALYSIS

In the novel DC-PCF structure, the first layer of air hole plays a major role on the transmission characteristics of the PCF because the mode optical field is mainly distributed near the fiber core, the influences of inner cladding diameter d_1 , outer cladding diameter d_2 and the pitches of air holes ($\Lambda_1, \Lambda_2, \Lambda_3$) on the dispersion and the loss are analyzed by hexagonal air hole tailoring. The dispersion characteristics of the PCF are mainly depends on the fiber core and surrounding air holes, but outer cladding have a significant impact on confinement loss, thus the loss can be reduced by optimizing the outer cladding structure. Besides, according to total internal reflection, the periodic structure of the cladding has little influences on light-guiding characteristics of PCF with high index core.

It can be seen from Fig. 2(a) that the dispersion varies from -20 to $40 \text{ ps}/(\text{nm}\cdot\text{km})$, which means that the diameter of inner cladding d_1 is an important factors that affect the dispersion. From Fig. 2(b), we can see that the confinement loss increase with increasing d_1 at the wavelength range $1.30 \sim 1.80 \mu\text{m}$, the changes of confinement loss are small with increasing d_1 and λ at the wavelength of $1.30 \sim 1.55 \mu\text{m}$. However, the changes of confinement loss increase significantly at the wavelength of $1.55 \sim 1.80 \mu\text{m}$. When $d_1 = 0.5 \mu\text{m}$ and $\lambda = 1.55 \mu\text{m}$, the dispersion is $-15 \text{ ps}/(\text{nm}\cdot\text{km})$ and the confinement $\alpha = 7.39 \times 10^{-6} \text{ dB}/\text{km}$. In conclusion, the influences of the diameter of inner cladding d_1 on confinement loss are different in different wavelength range. Compared to traditional PCF, the confinement of DC-PCF is much smaller.

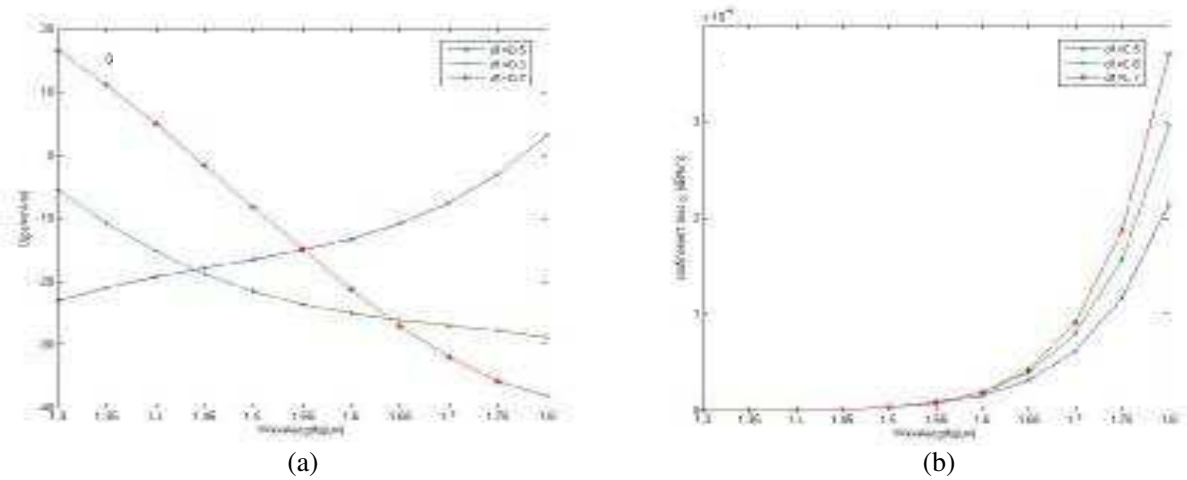


Figure 2: (a) The dispersion and (b) the loss with different d_1 .

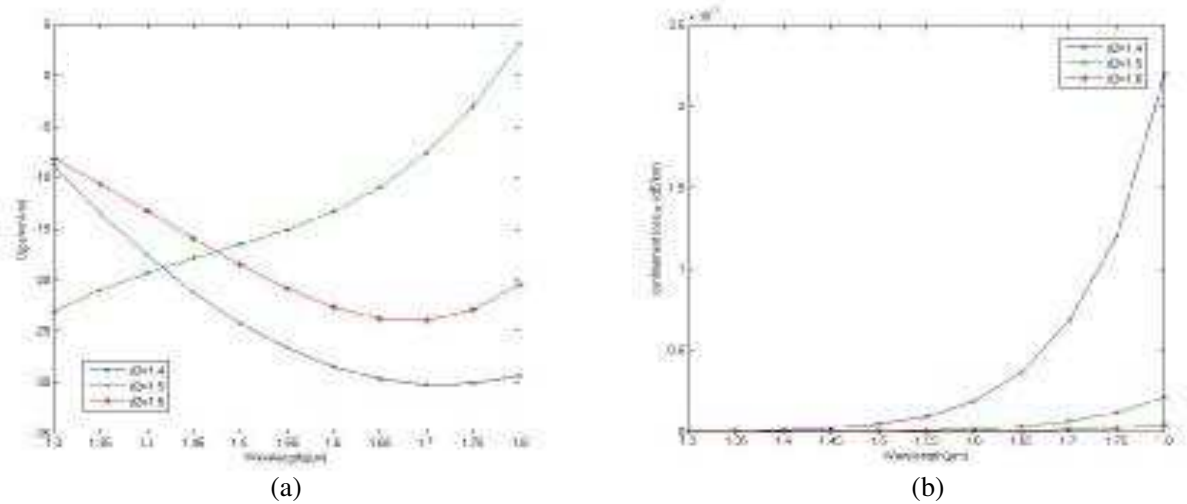


Figure 3: (a) The dispersion and (b) the loss with different d_2 .

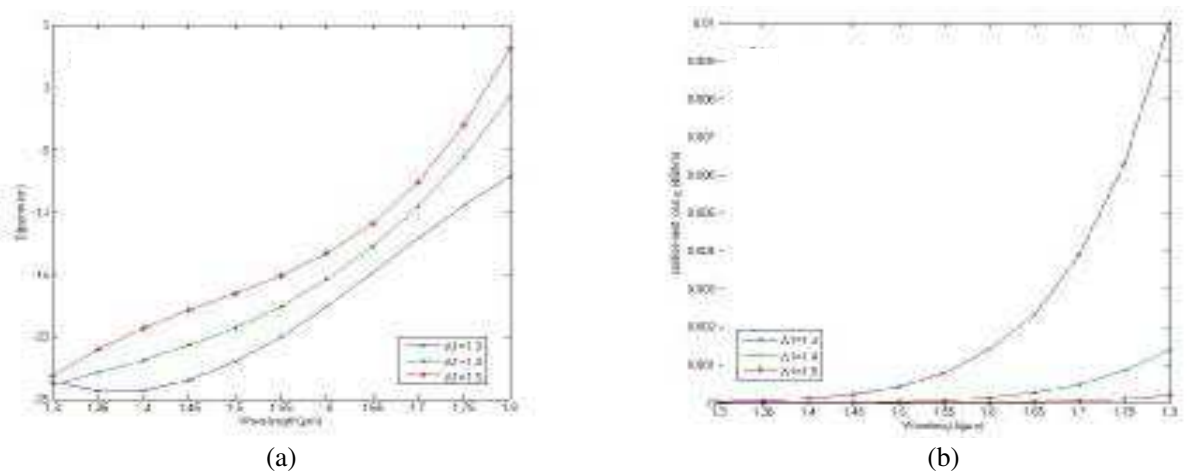


Figure 4: (a) The dispersion and (b) the loss spectrum with different Λ_1 .

In Fig. 3(a), the parameters d_1 , Λ_1 , Λ_2 , and Λ_3 are given to $0.5 \mu\text{m}$, $1.5 \mu\text{m}$, $1.75 \mu\text{m}$, $2 \mu\text{m}$, respectively. And the dispersion first decreases and then increases as wavelength increases when d_2

is $1.4 \mu\text{m}$ and $1.6 \mu\text{m}$ at the wavelength of $1.30\text{--}1.80 \mu\text{m}$, but the dispersion increases as wavelength increases when d_2 is $1.5 \mu\text{m}$. In this context, the diameter d_2 of outer cladding air hole has a significant influence to dispersion. As can be seen from Fig. 3(b), confinement loss reduces gradually as d_2 increases, and confinement loss increases gradually as d_2 increases.

In Fig. 4(a), the parameters d_1 , d_2 , Λ_2 , and Λ_3 are given to $0.5 \mu\text{m}$, $1.5 \mu\text{m}$, $1.75 \mu\text{m}$, $2 \mu\text{m}$, respectively, the dispersion increases by increasing Λ_1 and λ at the wavelength of $1.30 \sim 1.80 \mu\text{m}$, and zero dispersion point shifts toward the shorter wavelength. As shown in Fig. 4(b), confinement loss decreases with the increase of Λ_1 and reaches to zero at last. And the loss increases gradually as the wavelength increases. In conclusion, Λ_1 has a significant influence to dispersion and confinement loss.

In Fig. 5(a) and Fig. 5(b), the parameters d_1 , d_2 , Λ_1 , and Λ_3 are given to $0.5 \mu\text{m}$, $1.5 \mu\text{m}$, $1.5 \mu\text{m}$, $2 \mu\text{m}$, respectively. As can be seen from Fig. 5(a), both the dispersion becomes larger with decreasing Λ_2 and increasing λ at the wavelength of $1.30 \sim 1.80 \mu\text{m}$. The confinement loss increases with increasing Λ_2 at the wavelength of $1.30 \sim 1.80 \mu\text{m}$. But the confinement loss increases faster as the wavelength increases, and the confinement loss keeps almost flat at the wavelength of $1.30 \sim 1.55 \mu\text{m}$. Results show that Λ_2 has a significant influence to dispersion and confinement loss at the wavelength of $1.30 \sim 1.80 \mu\text{m}$. But the influence of Λ_2 on confinement loss is smaller than d_1 .

In Fig. 6(a) and Fig. 6(b), the parameters d_1 , d_2 , Λ_1 , and Λ_2 are given to $0.5 \mu\text{m}$, $1.5 \mu\text{m}$, $1.5 \mu\text{m}$, $1.75 \mu\text{m}$, respectively. As can be seen from Fig. 6(a), the dispersion increases as the wavelength

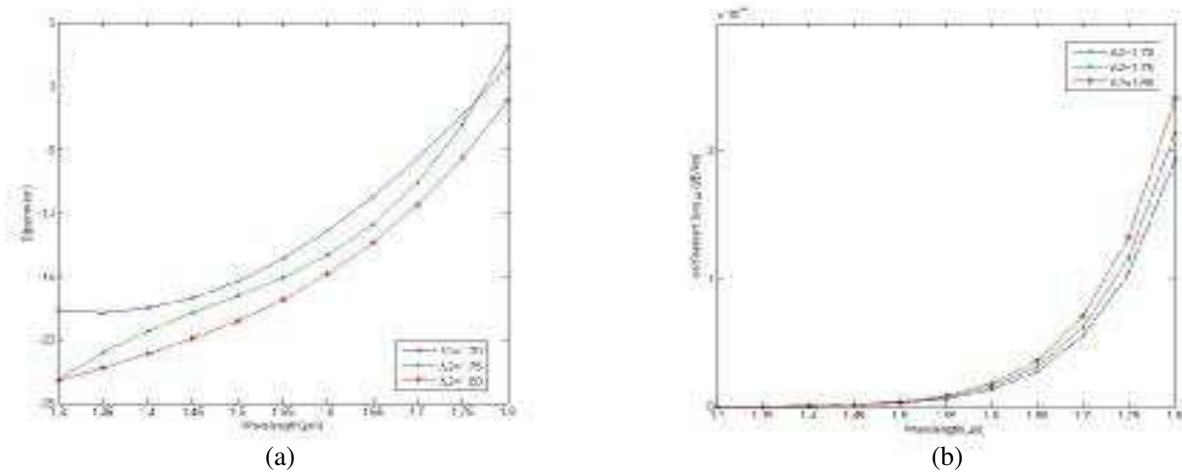


Figure 5: (a) The dispersion and (b) the loss spectrum with different Λ_2 .

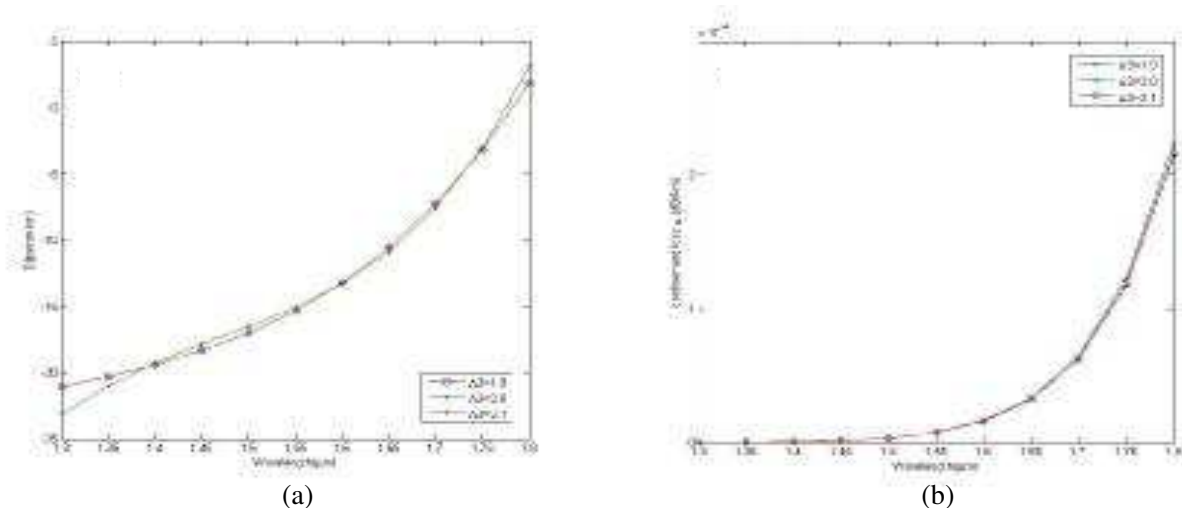


Figure 6: (a) The dispersion and (b) the loss spectrum with different Λ_3 .

increases at the wavelength of $1.30 \sim 1.80 \mu\text{m}$. And dispersion curves overlap each other when $\Lambda_3 = 1.9 \mu\text{m}$ and $\Lambda_3 = 2.1 \mu\text{m}$, which means that the values of dispersion are the same in both cases. As can be seen from Fig. 6(b), the confinement loss increases with both increasing Λ_3 and increasing λ at the wavelength of $1.30 \sim 1.80 \mu\text{m}$. It follows that Λ_3 has little influence to dispersion and confinement loss at the wavelength of $1.30 \sim 1.80 \mu\text{m}$.

4. CONCLUSION

In this paper, we simulate and analyze the double cladding photonic crystal fiber by full-vector finite element method. Results show that PCF not only compensates broadband dispersion, but also attains low loss by reasonable tailoring the diameters and the pitches of air holes. The numerical results show that the PCF present broadband dispersion characteristics at the wavelength of $1.30\text{--}1.80 \mu\text{m}$, and the confinement loss can reach 7.39×10^{-6} dB/km at wavelength of $1.55 \mu\text{m}$. This structure of PCF provide references on design and application of dispersion compensation fiber, the low loss characteristic of this structure can improve the transmission efficiency of PCF, These results provided theoretical basis for application.

ACKNOWLEDGMENT

This work was supported in part by the National Natural Science Foundation of China (Nos. 61367007, 61167005), in part by the Natural Science Fund of Gansu Province of China (Nos. 1112RJZA017, 1112RJZA018) and in part by the Research Fund for the Doctoral Program of Lanzhou University of Technology.

REFERENCES

1. Russell, P. St. J., "Photonic-crystal fibers," *J. Lightwave Technol.*, Vol. 24, 4729–4749, 2006.
2. Knight, J. C., T. A. Birks, and P. St. J. Russell, "All-silica single-mode optical fiber with photonic crystal cladding," *Opt. Lett.*, Vol. 19, No. 21, 1547–1549, 1996.
3. Yi, C. S., S. X. Dai, P. J. Zhang, X. S. Wang, X. Shen, T. F. Xu, and Q. H. Nie, "Design of a novel single-mode large mode area infrared chalcogenide glass photonic crystal fibers," *Acta. Phys. Sin.*, Vol. 62, 084206, 2013.
4. Zheng, S. W., Z. Lin, G. B. Ren, and S. Jian, "Design and analysis of novel multi-core dual-mode large-mode-area optical fiber," *Acta. Phys. Sin.*, Vol. 62, 044224, 2013.
5. Chen, X., X. B. Zhang, X. Zhu, L. Cheng, J. G. Peng, N. L. Dai, H. Q. Li, and J. Y. Li, "Effects of structure parameters on the dispersion properties of dispersion compensation photonic crystal fiber," *Acta. Phys. Sin.*, Vol. 62, 044222, 2013.
6. Cherif, R., M. Zghal, and L. Tartara, "Characterization of stimulated Brillouin scattering in small core microstructured chalcogenide fiber," *Opti. Communi.*, Vol. 285, 341–346, 2012.
7. Hou, Y., G. Y. Zhou, L. T. Hou, et al., "Analysis of dispersion properties of octagonal structural photonic crystal fiber with double cladding," *Chinese J. Lasers*, Vol. 4, No. 37, 1068–1072, 2010.
8. Wang, D. and Y. Zheng, "Numerical simulation and analysis of double cladding photonic crystal fiber with flattened dispersion," *Acta Optica Sinica*, Vol. 8, No. 21, 0806010, 2011.
9. Wang, J., C. Jiang, W. Hua, et al., "Modified design of photonic crystal fibers with flattened dispersion," *Opt. Laser Technol.*, Vol. 3, No. 38, 169–172, 2006.
10. Wang, D. and Y. Zheng, "Design and numerical investigation of a novel microstructured optical fiber," *Acta Optica Sinica*, Vol. 8, No. 32, 0806003, 2012.
11. Yuan, J. H., L. T. Hou, G. Y. Zhou, et al., "Investigation of a step-structure photonic crystal fiber with flattened dispersion," *Acta Optica Sinica*, Vol. 6, No. 28, 1167–1171, 2008.
12. Cui, Y. L. and L. T. Hou, "Dispersion characteristic of a new hybrid cladding photonic crystal fiber," *Acta Phys. Sin.*, Vol. 4, No. 59, 2571–2576, 2010.

Investigation on Reflection of Brillouin Dynamic Grating in Single Mode Optical Fibers

Junfeng Li, Shanglin Hou, Wenyu Zhang, Yanjun Liu, Jingli Lei, and Suoping Li
School of Science, Lanzhou University of Technology, Lanzhou, Gansu 730050, China

Abstract— The theory of static fiber Bragg grating was used to investigate the phenomenon that the perturbation of the refractive index modulated during the process of SBS which named as Brillouin dynamic gratings in optical fibres. Then the reflection of Brillouin dynamic gratings are studied and simulated by the coupled-mode theory in single-mode optical fibers. It is shown that the reflectivity becomes larger and the FWHM becomes narrower with the length of Brillouin dynamic grating increasing. However, with the increasing of refractive index modulation, the reflectivity becomes larger and the FWHM becomes broad. Additionally, the maximum reflectance red-shifts with the increase of core index. Finally, the maximum reflectivity is 0.9329 when the length of Brillouin dynamic grating is 100 meters and the refractive index modulation is 1×10^{-8} .

1. INTRODUCTION

Optical fiber gratings is manufactured by the photosensitive characteristic of fiber, the refractive index of fiber core is modulated periodicity, where will occurred coherence reflection when the frequency have coincidence with phase-matching condition during incident light. With this special property and the advantage of optical fiber such as low losses, anti electromagnetism etc. It have developed into a mature technology with a wide range of applications in various areas, including physical sensing for temperature, strain, acoustic waves and pressure.

Stimulated Brillouin scattering (SBS) is a nonlinear process that can occur in optical fibers, which can be described classically as a nonlinear interaction between the pump and Stokes fields through an acoustic wave. The pump field generates an acoustic wave through the process of electrostriction. The acoustic wave in turn modulates the refractive index of the medium. This pump-induced index grating scatters the pump light through Bragg diffraction. Scattered light is downshifted in frequency because of the Doppler shift associated with a grating moving at the acoustic velocity v_a which is called Brillouin dynamic gratings (BDG).

In 2008, Song et al. [1] reported BDG in polarization-maintaining (PM) fibers. Dong et al. [2] analyzed BDG in PM fibers and pointed out that BDGs were weak gratings in 2010. The four-wave mixing model was given to demonstrate the characteristics of BDG by Zhou et al. [3] in 2011, moreover, they showed that the conventional grating model is too to describe BDG. L. Thevenaz et al. [4, 5] demonstrated a novel technique for BDG by modulating two pump waves and investigated its application. Meanwhile, the reflection spectrum of BDG was calculated by S. N. Jouybari et al. [6]. And in 2013, a model of BDG was presented by Primerov et al. [7]. The characteristics of BDG were discussed in dynamic-state conditions detailedly. In 2014, Dong et al. [8] proposed an ultrahigh-resolution optical spectrometry based on BDG. But so many theory research on BDG is based on four-wave mixing model.

In this letter, the theory of static fiber Bragg grating was used to investigate the phenomenon that the perturbation of the refractive index modulated during the process of SBS. Then the reflection of Brillouin dynamic gratings are studied and simulated by the coupled-mode theory in single-mode optical fibers. some interested results are obtained, and these results provide a theoretical basis for design and application of new optical devices.

2. THEORY MODEL

2.1. The Refractive Index of BDG in Single Mode Optical Fibers

The diagram of the BDG model is shown in Figure 1. Let us denote the optical waves vector \vec{k}_i , frequency ω_i , amplitude A_i , power P_i , $i = 1$ is pump1 optical wave, $i = 2$ is pump2 optical wave, $i = 3$ is probe wave, $i = 4$ is reflected wave respectively. And $\omega_1 = \omega_3$. Pump1 and pump2 are the same polarization state, probe wave and reflected wave are the same polarization state which is orthogonal to Pump1 and pump2. Acoustic wave1 is produced by the interaction of Pump1 and pump2, whose waves vector and frequency is \vec{q}_1 , Ω_1 respectively. Acoustic wave2 is generated by

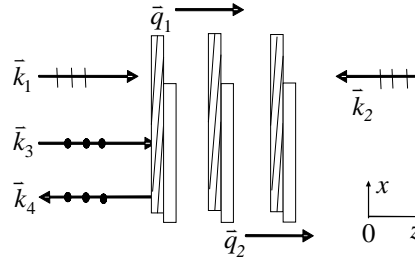


Figure 1: Diagram of the BDG model.

probe wave and reflected wave, \vec{q}_2 , Ω_2 are its waves vector and frequency. Where $\vec{q}_1 = \vec{k}_1 - \vec{k}_2$, $\Omega_1 = \omega_1 - \omega_2$, $\vec{q}_2 = \vec{k}_3 - \vec{k}_4$, $\Omega_2 = \omega_3 - \omega_4$. Acoustic wave1 and Acoustic wave2 are propagating along the $+z$ direction. we describe the acoustic field in terms of the material density distribution. Acoustic wave1 and Acoustic wave2 can be expressed as

$$\tilde{\rho}_1(z, t) = \rho_0 + \left[\rho_1(z, t)e^{i(q_1 z - \Omega_1 t)} + c \cdot c \right] \quad (1)$$

$$\tilde{\rho}_2(z, t) = \rho_0 + \left[\rho_2(z, t)e^{i(q_2 z - \Omega_2 t)} + c \cdot c \right] \quad (2)$$

ρ_0 denotes the mean density of the medium. The material density obeys the equation [10]

$$\frac{\partial^2 \tilde{\rho}}{\partial t^2} - \Gamma' \nabla^2 \frac{\partial \tilde{\rho}}{\partial t} - v^2 \nabla^2 \tilde{\rho} = \nabla \cdot \vec{f} \quad (3)$$

where v is the velocity of the acoustic wave, Γ' is damping parameter and \vec{f} is. We assume that $\Omega_1 = \Omega_2 = \Omega$. Then, under the conditions of steady-state, the variation of density that caused by acoustic wave are as follows

$$\rho_1(z, t) = \varepsilon_0 \gamma_e q_1^2 \frac{A_1 A_2^*}{(\Omega_B^2 - \Omega^2 - i\Omega \Gamma_B)} \quad (4)$$

$$\rho_2(z, t) = \varepsilon_0 \gamma_e q_2^2 \frac{A_3 A_4^*}{(\Omega_B^2 - \Omega^2 - i\Omega \Gamma_B)} \quad (5)$$

where ε_0 , γ_e , Ω_B , Γ_B are the permittivity of free space, electrostrictive constant, Brillouin frequency and Brillouin linewidth respectively. Since \vec{q}_1 , \vec{k}_1 , \vec{k}_2 and \vec{q}_2 , \vec{k}_3 , \vec{k}_4 can be regarded as two nonlinear process of SBS, considering about that the speed of acoustic wave without polarization is much smaller than the light, thus the variation of density that caused by acoustic wave is given by

$$\rho(z, t) = \varepsilon_0 \gamma_e q^2 \frac{A_1 A_2^* + A_3 A_4^*}{(\Omega_B^2 - \Omega^2 - i\Omega \Gamma_B)} \quad (6)$$

Due to the refractive index disturbance to the density is $\Delta n = \frac{\gamma_e}{2n_0 \rho_0} \rho(z, t)$. Refer to the literatures [7, 11], the variation value of refractive index modulation in fibers should be expressed as

$$\Delta n = \frac{4\pi^2 \gamma_e^2 n_{eff} (\sqrt{P_1 P_2} + \sqrt{P_3 P_4})}{n_0 \rho_0 \Omega_B \lambda_p^2 c_0 \Gamma_B A_{eff}} \quad (7)$$

where n_0 is the refractive index of the fiber core, n_{eff} is the effective mode index, λ_p is the wavelength of the pump1, c_0 is the speed of light in vacuum, A_{eff} is the acoustic-optic effective area.

2.2. The Improved Theory of Moving Gratings

We assume that the BDG can be treated as a weak uniform fiber Bragg grating with zero “dc” index and without grating chirp, the change of time can be neglected in steady-state conditions. Moreover, pump1, pump2 and probe wave are continuous wave with undepleted. Based on the

theory of grating we can get the expression of probe wave and reflected wave

$$\frac{dA_3}{dz} = i\kappa A_4 e^{-i\Delta q z} \quad (8)$$

$$\frac{dA_4}{dz} = -i\kappa A_3 e^{i\Delta q z} \quad (9)$$

where $\kappa = \frac{2\pi}{\lambda} \Delta n$, $\Delta q = |\vec{q}_1 - \vec{q}_2|$. The reflectivity could be solved by Equations (8) and (9) along with the boundary conditions $A_3|_{z=0} = A_3(0)$ and $A_4|_{z=L} = A_4(L) = 0$.

$$R_{BDG} = \frac{\sinh^2(sL)}{\cosh^2(sL) - \left(\frac{\Delta q}{2\kappa}\right)^2} \quad (10)$$

With $s^2 = \kappa^2 - \left(\frac{\Delta q}{2}\right)^2$, L is the length of the BDG, Under phase-matching condition $\Delta q = 0$, the maximum reflectivity could be expressed as

$$R_{\max} = \tanh^2(\kappa L) \quad (11)$$

For the power of the reflected wave is caused by probe wave, the Equation (7) could rewrite as

$$\Delta n = \frac{4\pi^2 \gamma_e^2 n_{eff} \left(\sqrt{P_1 P_2} + \sqrt{\theta} P_3 \right)}{n_0 \rho_0 c_0 \Omega_B \lambda_p^2 \Gamma_B A_{eff}} \quad (12)$$

where $\theta = R_{\max}|_{P_3=0}$.

3. NUMERICAL SIMULATION AND RESULT DISCUSSION

3.1. The Reflectance of BDG with Low Pump Power

In the numerical simulations, we use the same parameters in reference [3], such as $\gamma_e = 0.902$, $c_0 = 3 \times 10^8$ m/s, $\rho_0 = 2210$ kg/m³, $A_{eff} = 80$ μm^2 , $\Omega_B/2\pi = 10875$ MHz, $\Gamma_B/2\pi = 30$ MHz, $\lambda_p = 1550$ nm, $L = 13$ m. Then the maximum reflectivity of the BDG varied with P_1 , P_2 and P_3 is in Figure 2, Figure 3 and Figure 4, respectively. In Figure 2, $P_2 = 10$ mW, $P_3 = 100$ mW. $P_1 = 110$ mW, $P_3 = 63$ mW in Figure 3. And $P_1 = 110$ mW, $P_2 = 11$ mW in Figure 4.

Figure 2, Figure 3 and Figure 4 illustrate that a larger maximum reflectivity can be obtained by larger power which can be seen from Equation (11) and Equation (12). Because the value of refractive index modulation is caused by the test power, so the maximum reflectivity increases with the test power increasing. The trends of simulated results agrees very well with the results of Zhou et al. [3]. These results suggest that the BDG with Polarization-decoupled can be seen as the instructional outcome of two SBS processes in two orthogonal directions.

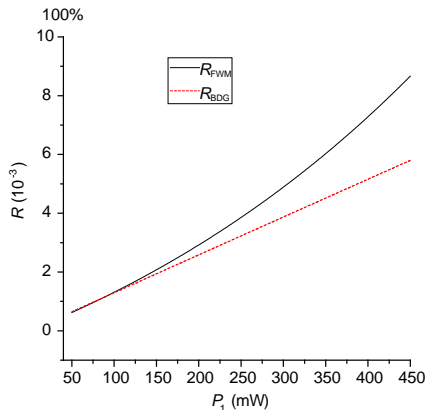


Figure 2: The reflectivity varies with P_1 for $P_2 = 10$ mW, $P_3 = 100$ mW.

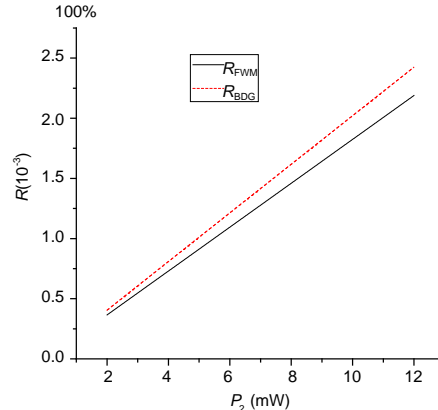


Figure 3: The reflectivity varies with P_2 for $P_1 = 110$ mW, $P_3 = 63$ mW.

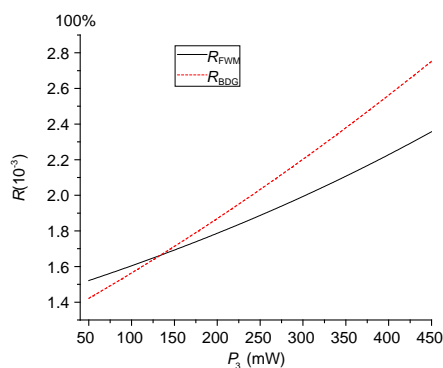


Figure 4: The reflectivity varies with P_2 for $P_1 = 110$ mW, $P_2 = 11$ mW.

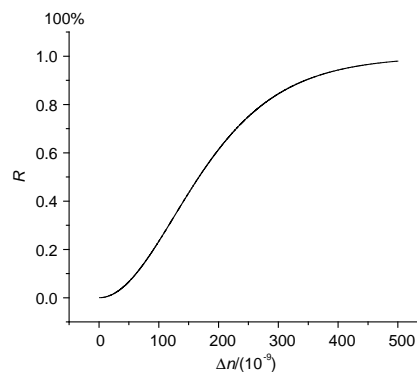


Figure 5: The relation between R_{\max} and Δn .

3.2. The Maximum Reflectivity with Various Refractive Index Modulation

To demonstrate the relation between the maximum reflectivity and various refractive index modulation, $\Delta n \approx 0.23 \times 10^{-9}$ is obtained from Equation (12) when $P_1 = 110$ mW, $P_2 = 10$ mW, $P_3 = 306$ mW. It keeps consistent with the convenient related literatures [12, 13]. Figure 5 shows the curves of the maximum reflectivity and various refractive index modulation when Δn varies from 0.1×10^{-9} to 5×10^{-8} . It is indicated that the maximum reflectivity increases with the increase of refractive index modulation. The maximum reflectivity agrees well with the simulations by Dong et al. [14] at large pump power.

4. CONCLUSION

Based on the theory of gratings, the improved model of the BDG is given. The simulate results agrees well with the results of Four-wave Mixing method. Meanwhile the relationship between the maximum reflectivity and various refractive index modulation is studied. It has been realized that the larger refractive index modulation the higher maximum reflectivity. This paper may provide a theoretical basis for the design and application of new optical devices.

ACKNOWLEDGMENT

This work was supported in part by the National Natural Science Foundation of China (Nos. 6136700-7, 61167005), in part by the Natural Science Fund of Gansu Province of China (Nos. 1112RJZA017, 1112RJZA018) and in part by the Research Fund for the Doctoral Program of Lanzhou University of Technology.

REFERENCES

1. Song, K. Y., W. Zou, Z. He, et al., "All-optical dynamic grating generation based on Brillouin scattering in polarization-maintaining fiber," *Optics Letters*, Vol. 33, No. 9, 926–928, 2008.
2. Dong, Y., L. Chen, et al., "Characterization of the Brillouin grating spectra in a polarization-maintaining fiber," *Optics Express*, Vol. 18, No. 18, 18960–18967, 2010.
3. Zhou, D. P., Y. Dong, et al., "Four-wave mixing analysis of Brillouin dynamic grating in a polarization-maintaining fiber: Theory and experiment," *Optics Express*, Vol. 19, No. 21, 20785–207984, 2011.
4. Antman, Y., N. Primerov, et al., "Localized and stationary dynamic gratings via stimulated Brillouin scattering with phase modulated pumps," *Optics Express*, Vol. 20, No. 7, 807–7821, 2012.
5. Thevenaz, L., N. Primerov, et al., "All-optical storage and processing in optical fibers," *2012 IEEE 3rd International Conference on Photonics (ICP)*, 1–5, Penang, Malaysia, Oct. 1–3, 2012.
6. Jouybari, S. N., H. Latifi, et al., "Reflection spectrum analysis of stimulated Brillouin scattering dynamic grating," *Measurement Science and Technology*, Vol. 23, No. 8, 085203(5), 2012.
7. Primerov, N. and L. Thévenaz, *Generation and Application of Dynamic Gratings in Optical Fibers Using Stimulated Brillouin Scattering*, EPFL, 2013.
8. Dong, Y., T. Jiang, et al., "Sub-MHz ultrahigh-resolution optical spectrometry based on Brillouin dynamic gratings," *Optics Letters*, Vol. 39, No. 10, 2967–2970, 2014.

9. Erdogan, T., “Fiber grating spectra,” *Journal of Lightwave Technology*, Vol. 15, No. 8, 1277–1294, 1997.
10. Boyd, R. W., *Nonlinear Optics*, 3rd Edition, 429–471, Academic Press, 2008.
11. Song, K. Y. and H. J. Yoon, “Observation of narrowband intrinsic spectra of Brillouin dynamic gratings,” *Optics Letters*, Vol. 35, No. 17, 2958–2960, 2010.
12. Agrawal, G., *Nonlinear Fiber Optics*, 4th Edition, 351, Academic Press, 2009.
13. Zhou, D. P., L. Chen, et al., “Polarization-decoupled four-wave mixing based on stimulated Brillouin scattering in a polarization-maintaining fiber,” *Journal of the Optical Society of America B*, Vol. 30, No. 4, 821–828, 2013.
14. Dong, Y., H. Zhang, et al., *Fiber Optic Sensors*, 115–136, Dr. M. Yasin, Ed., InTech, 2012.

Enhanced Femtosecond Optical Pulses Compression in Highly Nonlinear Photonic Crystal Fibers at 850 nm

Qiling Wu, Shanglin Hou, Yanjun Liu, Jingli Lei, Suoping Li, and Wenyu Zhang
School of Science, Lanzhou University of Technology, Lanzhou, Gansu 730050, China

Abstract— In this letter, we numerically investigate the soliton-effect compression of femtosecond optical pulses in highly nonlinear silica-core photonic crystal fiber (HN-PCF) at near-infrared region of the spectrum (specially at 850 nm) using full-vector finite element method and split-step Fourier method. We propose a novel photonic crystal fiber structure featuring a anomalous group velocity dispersion ($\beta_2 = -50.698 \text{ ps}^2/\text{km}$), small higher-order dispersions and enhanced nonlinearity ($\gamma = 268.4191 \text{ w}^{-1}/\text{km}$) for efficient soliton-effect compression of femtosecond optical pulses. We numerically investigate the effect of the high-order soliton compression of Gaussian pulses in HN-PCF. It shows that high-quality ultrashort optical pulses with little pedestal energy can be obtained.

1. INTRODUCTION

Ultrashort optical pulses have potential applications in ultrafast optical communication, optical signal processing, optical machining, sensing technology and other fields. Fiber-based pulse compression technology is one of effective ways for obtaining ultrashort optical pulse. However, the conventional fiber has been restricted by its geometric parameters and it's not easy to get a good pulse compression effect. Highly nonlinear photonic crystal fibers effectively overcome the deficiency of conventional fiber, and greatly improve the efficiency of pulse compression. Thus, the photonic crystal fiber-based pulse compression technology has become a hotspot in the research of pulse compression technologies.

Highly nonlinear photonic crystal fiber has important applications in various areas such as ultrashort laser pulse frequency conversion, spectrum broadening, pulse compression, wave breaking and so on. The effect of high nonlinearity can be achieved by minishing the area of core, increasing the air filling fraction or using the background material with large nonlinear refractive index. The development of optical communication system has experienced the process from the short wavelength (850 nm) to the long wavelength (1310 nm and 1550 nm), considering the communicating cost of the short wavelength of 850 nm is lower than the long wavelength, we numerically investigate the compression of femtosecond optical pulses in HN-PCF at 850 nm.

In recent years, pulse compression at near-infrared region of the spectrum were extensively investigated. In 2010, Abobaker et al. [1] investigated a new design of PCF in order to achieve efficient pulse compression at length at 850 nm, that compression factor is 21.49 which is almost 13.02 times greater than adiabatic pulse compression. Fedotov et al. [2] investigated the 20 fs pulses in the near-infrared by pulse compression in the regime of normal dispersion using a large-mode-area all-silica photonic band-gap fiber, whose central wavelength is 1140 nm. Abobaker et al. [3] designed a pulse compressor using a tapered PCF wherein dispersion as well as nonlinearity varies along the propagation direction, and discussed the generation of pedestal free ultrashort pulses around 850 nm. Olupitan et al. [4] designed a pulse compressor using a tapered PCF, and studied the possibility of generating pedestal-free ultrashort pulses around 850 nm using eight chirped cosine pulses. In 2014, Ghanbari et al. [5] proposed a novel nano-size silica PCF structure and investigated the dynamics of soliton-effect compression of femtosecond optical pulses in silica-core PCF at 850 nm.

In this paper, we designed a novel silica-core photonic crystal fiber structure, simulated the index of the fundamental guided mode using full-vector finite element method, the results show the PCF has a minimum anomalous group velocity dispersion, small higher-order dispersions and enhanced nonlinearity for efficient soliton-effect compression of femtosecond optical pulses at 850 nm. We investigated the Gaussian pulses and investigate the effect of the high-order soliton compression in HN-PCF using split-step Fourier method. It shows that high-quality ultrashort optical pulses with little pedestal energy can be provided. The parameters, such as the fiber length, chirp parameter or the soliton order, have significant influence on the pulse compression properties, such as compression ratio and peak power.

2. THEORETICAL ANALYSIS

The total dispersion of photonic crystal fibers includes waveguide dispersion and material dispersion [6]. Due to the photonic crystal fiber is generally composed of a single material such as pure silica, so the material dispersion is unchanged. The waveguide dispersion is related to the geometrical arrangement, hole pitch (Λ), wavelength (λ), and normalized air holes diameter (d/Λ) are the main factors on which the waveguide dispersion of photonic crystal fibers depends. The total dispersion is given by

$$D(\lambda) = -\frac{\lambda}{c} \frac{d^2 \text{Re}[n_{eff}(\lambda)]}{d\lambda^2} + D_m(\lambda) \quad (1)$$

where c is the velocity of light in a vacuum, λ is the wavelength, $\text{Re}[n_{eff}(\lambda)]$ is the real part of the effective refractive index, The material dispersion (D_m) which is represented by Sellmeier equation.

We consider a PCF with a triangular lattice of holes as shown in Figure 1, where d is the hole diameter, Λ is the hole pitch, an air hole is omitted to form a central high index defect serving as the fiber core [7].

The dispersion parameter, D which is commonly used in fiber optics, is related to the group velocity dispersion (GVD) parameter β_2 given by

$$\beta_2 = -\frac{\lambda^2}{2\pi c} D \quad (2)$$

The nonlinear coefficient γ is defined as

$$\gamma = \frac{n_2 \omega_0}{c A_{eff}} \quad (3)$$

where A_{eff} is the effective mode area, c denotes the speed of light, n_2 is the nonlinear refractive index.

We use the generalized nonlinear Schrödinger equation which describes the propagation of femtosecond pulses in photonic crystal fibers. In the normalized coordinates commonly used for describing optical solitons, the Equation (3) takes the form

$$\begin{aligned} \frac{\partial U}{\partial \xi} = & -\frac{i \text{sgn}(\beta_2)}{2} \frac{\partial^2 U}{\partial \tau^2} + \frac{\beta_3}{6|\beta_2|T_0} \frac{\partial^3 U}{\partial \tau^3} + \frac{i\beta_4}{24|\beta_2|T_0^2} \frac{\partial^4 U}{\partial \tau^4} - \frac{\beta_5}{120|\beta_2|T_0^3} \frac{\partial^5 U}{\partial \tau^5} \\ & - \frac{1}{2} \alpha L_D U + iN^2 \left[|U|^2 U + \frac{i}{\omega_0 T_0} \frac{\partial}{\partial \tau} (|U|^2 U) - \frac{T_R}{T_0} U \frac{\partial |U|^2}{\partial \tau} \right] \end{aligned} \quad (4)$$

where U is normalized amplitude, the parameter α represents the fiber's intrinsic loss, which is given by 0.02 dB/m, $\beta_2, \beta_3, \beta_4, \beta_5$ are GVD, TOD, FOD, and fifth-order dispersion, respectively. γ states as the nonlinear coefficient, ω_0 is the central angular frequency, $T_R = 3$ fs is the slope of Raman gain profile at the carrier frequency [8]. The last three were self-phase modulation (SPM), self-steepening (SST) and intrapulse Raman scattering (SRS), respectively.

To generate N -th order soliton, the following equation should be satisfied

$$N^2 = \frac{L_D}{L_{NL}} = \frac{\gamma p_0 T_0^2}{|\beta_2|} \quad (5)$$

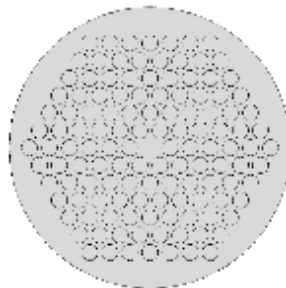


Figure 1: The model of PCF.

where P_0 is the peak power of the incident pulse, the normalized distance ξ ($\xi = z/L_D$), the dispersion length L_D ($L_D = T_0^2/|\beta_2|$), the nonlinear length L_{NL} ($L_{NL} = 1/\gamma p_0$).

The obtained pulse compression is characterized by the compression factor F_c defined by:

$$F_c = \frac{T_0}{T_c} \tag{6}$$

where T_0 and T_c are the half-width (at 1/e-intensity point) of input and output compressed pulse, respectively.

3. NUMERICAL SIMULATION

3.1. Dispersion of Photonic Crystal Fibers

The effective refractive index can be calculated by using full-vector finite element method, suppose the normalized air holes diameter ($d/\Lambda = 0.8$). Figure 2 shows the group velocity dispersion (GVD) varies with a function of wavelength. It can be seen in Figure 2, there is a minimum and nearly flat region of negative GVD, the nearly flat region is shifted to higher wavelengths by changing the pitch (Λ). By choosing the proper pitch (Λ), this region can be centered at desired wavelengths. As can be seen in Figure 3 by choosing the values $\Lambda = 0.9 \mu\text{m}$ and $d/\Lambda = 0.8$, the minimum and nearly flat region can be centered at 850 nm, β_2 is $-50.698 \text{ ps}^2/\text{km}$.

For the propagation of pulses with femtosecond duration, it is necessary to include the higher-order dispersions. Therefore, we use the generalized nonlinear Schrödinger equation which included the third-, fourth- and fifth-order dispersion. the result is that β_3 , β_4 and β_5 are $0.01982 \text{ ps}^3/\text{km}$, $2.463 \times 10^{-4} \text{ ps}^4/\text{km}$ and $-8.0362 \times 10^{-7} \text{ ps}^5/\text{km}$ at 850 nm, respectively.

3.2. Soliton Propagation in Photoniccrystal Fiber

Figure 3 shows the effective mode area of the PCF for $d/\Lambda = 0.8$ and $\Lambda = 0.9 \mu\text{m}$. A_{eff} is $0.881 \mu\text{m}^2$ at 850 nm, γ is $268.41908 \text{ W}^{-1}/\text{km}$, so this fiber is a highly nonlinear photonic crystal fiber.

Equation (4) is solved numerically by using the split-step Fourier method, the numerical simulations taking into account SPM, GVD, TOD, FOD, fifth-order dispersion, SST, SRS. The input pulses are assumed to be chirp free and have Gaussian shapes with initial width of $T_{FWHM} = 100 \text{ fs}$, $U(0, T) = \exp(-0.5\tau^2)$.

To change the soliton order N , we conduct the numerical simulation of optical pulse compression. Figure 4 shows that the compression factor F_c as a function of soliton number N , respectively. F_c reach the maximum when $N = 8$, it has a good pulse compression effect while the peak power of

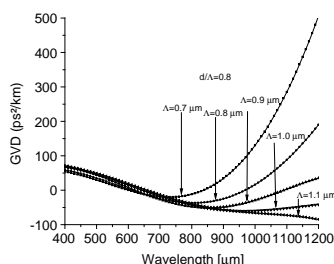


Figure 2: GVD of the PCF as a function of wavelength for different pitches and $d/\Lambda = 0.8$.

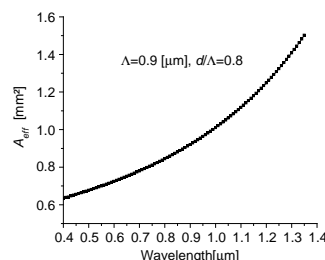


Figure 3: The effective mode area of the PCF for $d/\Lambda = 0.8$ and $\Lambda = 0.9 \mu\text{m}$.

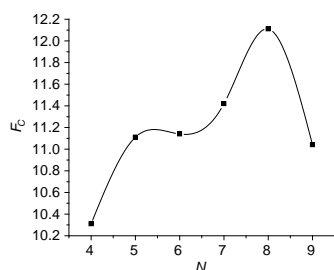


Figure 4: The compression factor F_c .

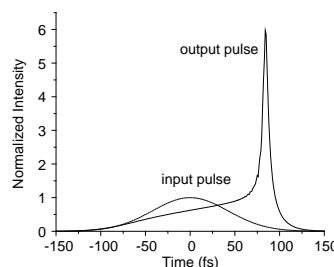


Figure 5: The input and output compressed pulse.

initial pulse $P_0=3357.8$ W. It can be seen in Figure 5 that we get an output compressed pulse of $T_0 = 4.96$ fs at the propagation distance of 5.66 mm.

4. CONCLUSION

Due to the flexible design of photonic crystal fiber structure, it has the highly nonlinear parameter and adjustable dispersion characteristics, we can obtain a high-quality compressed pulse using a shorter fiber. We propose a novel photonic crystal fiber with the normalized air holes diameter $d/\Lambda = 0.8$ and the hole pitch $\Lambda = 0.9 \mu\text{m}$, the photonic crystal fiber structure shows a anomalous group velocity dispersion, small higher-order dispersions and enhanced nonlinearity at 850 nm, a compressed pulse of $T_0 = 4.96$ fs can be obtained using a 5.66 mm highly nonlinear photonic crystal fiber.

ACKNOWLEDGMENT

This work was supported in part by the National Natural Science Foundation of China (Nos. 61367007, 61167005), in part by the Natural Science Fund of Gansu Province of China (Nos. 1112RJZA017, 1112RJZA018) and in part by the Research Fund for the Doctoral Program of Lanzhou University of Technology.

REFERENCES

1. Abobaker, A. M., R. V. J. Raja, et al., "Efficient pulse compression in photonic crystal fibre at 850 nm," *IEEE 2010 International Conference on Computer and Communication Engineering (ICCCCE)*, 1–4, 2010.
2. Fedotov, I. V., A. A. Lanin, et al., "Generation of 20 fs, 20 MW pulses in the near-infrared by pulse compression using a large-mode-area all-silica photonic band-gap fiber," *Journal of Modern Optics*, Vol. 57, No. 19, 1867–1870, 2010.
3. Abobaker, A. M., S. Olupitan, et al., "Dynamics of 850 nm optical pulses upon compression in a tapered photonic crystal fiber," *IEEE 2011 Saudi International Electronics, Communications and Photonics Conference (SIECPC)*, 1–4, 2011.
4. Olupitan, S., P. R. Babu, et al., "Generation of a train of ultrashort pulses near-infrared regime in a tapered photonic crystal fiber using raised-cosine pulses," *IEEE Photonics Journal*, Vol. 4, No. 5, 1420–1437, 2012.
5. Ghanbari, A., A. Sadr, et al., "Modeling photonic crystal fiber for efficient soliton-effect compression of femtosecond optical pulses at 850 nm," *Arabian Journal for Science and Engineering*, Vol. 39, No. 5, 3917–3923, 2014.
6. Ferrando, A., E. Silvestre, et al., "Nearly zero ultraflattened dispersion in photonic crystal fibers," *Optics Letters*, Vol. 25, No. 11, 790–792, 2000.
7. Saitoh, K. and M. Koshiba, "Empirical relations for simple design of photonic crystal fibers," *Optics Express*, Vol. 13, No. 1, 267–274, 2005.
8. Agrawal, G. P., *Nonlinear Fiber Optics*, 5th Edition, Academic Press, 2013.
9. Ma, W. W., S. G. Li, et al., "High efficiency pulse compression in tapered microstructure fibers in anomalous dispersion region," *Acta Physica Sinica*, Vol. 59, No. 7, 4720–4725, 2010.

A Universal Optical Network Unit for Hybrid TDM-PON and WDM-PON Transport Systems

Ching-Hung Chang, Liang-Shuo Tu, and Meng-Chun Tseng

Department of Electrical Engineering, National Chiayi University, Taiwan

Abstract— Based on a vertical-cavity surface-emitting laser (VCSEL)-composed wavelength selector, a universal optical network unit (ONU) is proposed for hybrid time and wavelength division multiplexing passive optical networks.

1. INTRODUCTION

Fiber to the Home (FTTH) transport systems have attracted plentiful attentions to provide triple-play multimedia services for residential and business clients due to their low loss and high capacity characteristics. By adapting this technique, the coverage range of an optical line termination (OLT) will be extended and the available bandwidth for the connected clients can be extended to Gbps range which is hundred times larger than the capacity of traditional ADSL or cable networks [1]. Time-division multiplexing (TDM)-passive optical networks (PONs) and TDM-access (TDMA) control protocols are therefore developed to share the extended bandwidth for clients. Basing on TDM-PON structure, a common type of optical network unit (ONU) installed in each client's premises can resourcefully diminish the deploying cost and more than 100 Mbps data rate is achievable for each client to enjoy convenient broadband services [2, 3]. Such economic TDM-PON architecture is popular in the beginning of deploying optical fiber in the last mile connection. Nevertheless, if the downstream bandwidth requirement is increased with the extended multimedia service environment, the network capacity of a ONU in such TDM-PON structure is difficult to be upgraded. Converting the TDM-PON structure to wavelength-division multiplexing (WDM)-PON structure will be a suitable solution to upgrade the ONUs' capacity. A WDM-PON with logical point-to-point connection for each ONU will be able to extend the available downstream bandwidth from 100 Mbps in TDM-PONs to 1 Gbps or larger bandwidth for a client [4]. There are two main methods to achieve this objective. One is to insert an optical wavelength selector, such as tunable optical bandpass filter (TOBPF) [5], in front of an TDM-ONU to select a dedicated optical wavelength and reject other inserted optical wavelengths, and another one is to replace the optical passive splitter deployed in the remote node of a TDM-PON by an optical wavelength de-multiplexer, such as arrayed waveguide grating (AWG) [6], to direct various downstream optical carriers into dedicated directions. Utilizing a TOBPF to select the inserted optical carriers in an ONU is convenient and the entire TDM-PON can be gradually migrated to WDM-PON according to consumers' requirements. However, the expensive TOBPF makes this solution unacceptable. On the other hand, the TDM-ONU is still able to be utilized in WDM-PON architecture if the optical splitter of a TDM-PON is replaced by an AWG. This can save a lot of cost but the entire network will need to be upgrade from TDM-PON to WDM-PON simultaneously. In addition, the type and amount of the employed optical wavelengths in such WDM-PON are fixed by the employed AWG. The internet service provider will not able to gradually achieve the migration according to consumers' requirements and the scale of the WDM-PON is fixed. It is clear from the discussion that utilizing a TOBPF to achieve the migration is much more flexible than employing AWG. If there is a method to provide economic wavelength selector for a TDM-ONU, a TDM-PON network will be able to migrate to WDM-PON network flexibly. To achieve this target, a novel wavelength selector is proposed and developed to compose a universal optical network unit (ONU) for both TDM- and WDM-PON architecture. Unlike the published TDM-PON to WDM-PON migration architectures which utilizing expensive tunable optical band-pass filter (TOBPF) or complicated optical routing schemes to select proper optical wavelengths, the proposed universal ONU can utilize an economic vertical-cavity surface-emitting laser (VCSEL) as a TOBPF to select a specific lightwave from multiple injected optical carriers. Besides, the VCSEL-composed wavelength selector with electrically adjustable characteristic will be able to assist the universal ONU with an ability to switch its receiver functionality for either economic TDM-PONs application or high-capacity WDM-PONs structure. Experimental results proof that by modifying the driving current of the VCSEL-based wavelength selector, both TDM-PON signal and WDM-PON signal can be received

individually. This proposal provides an economic and flexible method for clients to migrate between TMD-PON and WDM-PON architecture.

2. EXPERIMENTAL SETUP

To evaluate the proposed universal ONU in a hybrid TDM- and WDM-PON transport system, a TDM and a WDM signals generated by mixing a 1.25 Gbps PRBS signal with a 10 GHz sinusoidal signal are individually phase modulated with two different downstream optical carriers and then transmitted to a tree-topology style PON network simultaneously. As shown in Fig. 1, both downstream lightwaves are combined by an optical combiner and amplified by an Erbium doped fiber amplifier (EDFA) before be communicated over a span of 12.5 km single mode fiber (SMF) and a 1×16 optical splitter to ONUs which are composed by a wavelength selector, a photo-detector (PD) and frequency down-conversion circuit. In here, the wavelength selector in each ONU is the same and is composed by an optical circulator, a polarization controller (PC) and a commercial VCSEL. To perform both TDM-PON and WDM-PON performance, the ONU₁ is designed to receive the WDM signal (λ_1) and the ONU₂₋₁₅ are designed to receive the TDM signal (λ_2). To select each dedicated downstream carrier and reject another one, the VCSEL in the ONU₁ is driving by i_1 (5.13 mA) current and the VCSEL in the ONU₂₋₁₆ is driving by i_2 (3.5 mA) current. These two driving current values will make these VCSELs emit out two different lasing wavelengths which are aligned with the +1 sideband of the TDM and WDM signals, respectively. This process will resourcefully select and direct one of the two downstream signals into each ONU PD. In addition, the process will also convert the downstream phase modulated signals from double sideband (DSB) format to single sideband (SSB) format performing a phase modulation (PM) to intensity modulation (IM) conversion. The obtained TDM and WDM signals are then down-converted to baseband by mixing with another 10 GHz sinusoid signal and evaluated via an electrical spectrum analyzer (ESA) and eye diagrams.

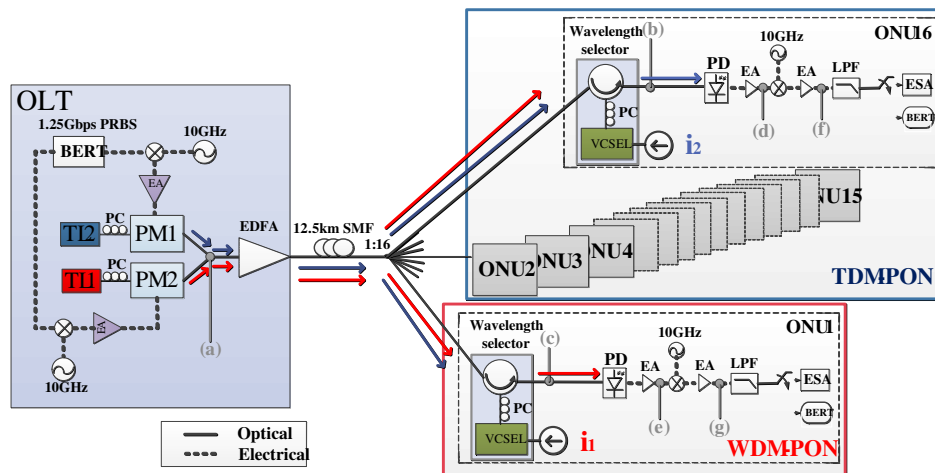


Figure 1: Experimental setup of the proposed universal ONU in a hybrid TDM- and WDM-PON transport system.

3. EXPERIMENTAL RESULT AND DISCUSSION

In this experiment, both of the downstream TDM and WDM signals will go through the VCSEL via an OC before be inserted into the PD. If the VCSEL in the TDM-ONU is driving with proper current, its lasing wavelength will align with the +1 sideband of the TDM signal, so that this sideband will go through the VCSEL quantum well and reflected back with roughly the same power. In parallel, roughly 15.28 dB attenuation will be added into the WDM signal as well as the central carrier and the -1 sideband of the TDM signal since these wavelengths are located outside the VCSEL free-running frequency. As shown in Fig. 2(a), both TDM and WDM signals originally have roughly the same optical spectra before been communicated though the downstream SMF, but both optical spectra observed before the PD of the TDM-ONU are not equal. As display in Fig. 2(b), more than 14.75 dB attenuation is added into the WDM signal (ch2) and the central carrier and -1 sideband of the TDM signal. This process will simultaneously perform wavelength selection and

PM-to-IM conversion for each TDM-ONU. Similarly, the +1 sideband of the WDM signal is also selected by the WDM-ONU, as presented in Fig. 2(c). In parallel with the optical spectra, clear electrical spectra diagrams of the obtained 1.25 Gbps/10 GHz TDM and WDM signals are presented in Figs. 3(a) and (b), respectively, and open eye diagrams for back to back and 12.5 km transmissions scenarios are presented in Figs. 4(a) and (b), respectively. These experimental results proof that the VCSEL-composed wavelength selector can provide a > 14.75 dB attenuation for the wavelengths located outside the target wavelength and its wavelength selection function can be electrically and continuously shifted by adjusting the VCSEL driving current. A roughly 3 nm shifting range is achievable for the proposed universal ONU to select the desired wavelength (signal) from the tree-topology hybrid TDM- and WDM-PON. It can be expected that by utilizing the universal ONU to deploy a passive optical access network, such as the Ethernet-PONs (EPONs) or Gigabit-capable PONs (GPONs), the clients will be able to enjoy a low capital expenditure (CAPEX) in the first beginning and any one of the client will be able to extend his/her network capacity form hundreds Mbps range (TDM-PONs) to thousands Mbps range (WDM-PONs) without replacing any deployed device or deployed network topology. The Internet service providers (ISPs) will be able to provide additional bandwidth for each specific client simply by electrically adjusting the working window of the VCSEL-composed wavelength selector inside each specific ONU and then adding a relative optical carrier to deliver the extra data in the presented network.

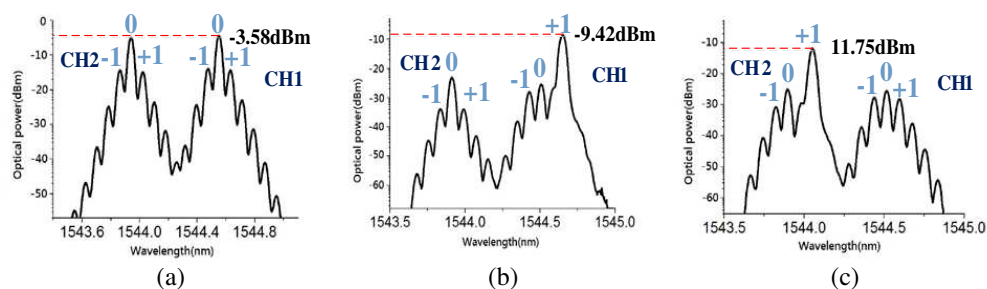


Figure 2: (a), (b) and (c) are the optical spectra diagrams obtained at the Fig. 1 observed points (a), (b) and (c) respectively.

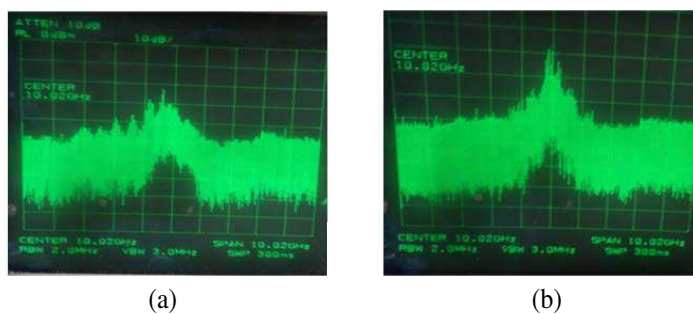


Figure 3: The electrical spectra diagram of the obtained 1.25 Gbps/10 GHz. (a) TDM signal and (b) WDM signal.

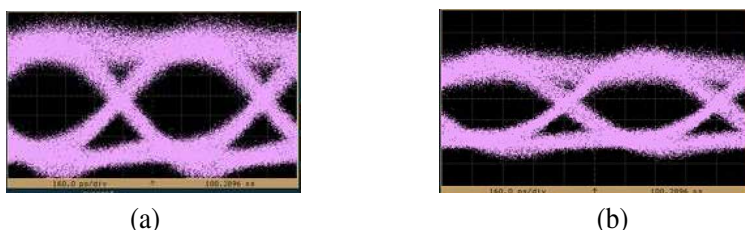


Figure 4: Electrical eye diagrams in (a) back-to-back and (b) 12.5 km transmission scenarios.

4. CONCLUSION

To provide a resourceful TDM-PON to WDM-PON migration method for clients, a universal ONU is proposed for a hybrid TDM- and WDM-PON transport system. By adding a VCSEL-composed optical wavelength selector into a general ONU, the ONU can flexibly be utilized to receive dedicated signals carried by different wavelengths. Proper optical spectra diagrams and eye diagrams prove that the proposed system can provide a proper TDM to WDM or WDM to TDM migration method for each client without changing the network structure and ONU circuit.

REFERENCES

1. Gaudino, R., D. Cárdenas, P. di Torino, M. Bellec, B. Charbonnier, N. Evanno, P. Guignard, S. Meyer, and A. Pizzinat, "Perspective in next-generation home networks: Toward optical solutions?," *IEEE Communications Magazine*, Vol. 48, 39–47, February 2010.
2. Kim, K. S., "On the evolution of PON-based FTTH solutions," *Information Sciences*, Vol. 149, 21–30, 2003.
3. Lee, C.-H., W. V. Sorin, and B. Y. Kim, "Fiber to the home using a PON infrastructure," *Journal of Lightwave Technology*, Vol. 24, No. 12, December 2006.
4. Urata, R., C. Lam, H. Liu, and C. Johnson, "High performance, low cost, colorless ONU for WDM-PON," *Optical Fiber Communication Conference and Exposition (OFC/NFOEC)*, NTh3E, 2012.
5. Wang, L. L. and T. Kowalczyk, "A novel locking technique for very narrow tunable optical filters with sub-GHz 3-dB bandpass," *IEEE Photonics Technology Letters*, Vol. 22, No. 17, September 1, 2010.
6. Liu, Z. and J. Li, "Modeling and design of arrayed waveguide gratings," *Lightwave Technology*, Vol. 20, 661–674, April 2002.

Analogy between the Ising Model and the Polarization Switching of Vertical-cavity Surface-emitting Lasers

Tsu-Chiang Yen, Yueh-Chen Li, and Yu-Heng Wu

Department of Physics, National Sun Yat-sen University

No. 70, Lienhai Rd., Kaohsiung 80424, Taiwan

Abstract— Conventional vertical-cavity surface-emitting lasers (VCSELs) have a cylindrical laser cavity, which provides an intrinsic two-degree of freedom to the polarization direction of the emitted light. This isotropic symmetry of polarization is usually broken by the anisotropy of the physical structure of VCSELs; for example, the anisotropy of the lattice structure, residual stress, or thermal distribution. In some VCSELs, the broken polarization symmetry conducts a polarization switching (PS) phenomenon. During this process, the VCSEL remains in a phase of emitting linearly polarized light around the laser's threshold, and then switches to another phase of emitting orthogonally polarized light when the laser's current surpasses a switching current. The VCSEL's PS (VPS) can help to build some components for the high speed optical computing. Accordingly, the characteristic of VPS is an important research pursuit. Recently, VPS was reported to be a second-order phase transition (SOPT). That discovery was based on the criticalities observed in the experiments, which are the unique characteristics of SOPTs. This research attempts to explore the connection between VPS and the conventional Ising model. The said model employs the spin-up and spin-down spins to study the transition of magnetic materials from the ferromagnetic state to the paramagnetic state and identifies that transition as an SOPT. Therefore, both of the phase transitions of VPS and Ising model are SOPTs between two orthogonal states. Typical Ising model employs a two dimensional spin lattice to simulate the magnetic material. In this work, a Gaussian-distributed interaction was introduced into the center of the spin lattice to simulate the laser's beam profile and the spatial coherence. The investigation focused on the examination of the relaxation time required to transit from the ferromagnetic state to the paramagnetic state. The simulation results present an exponent of the relaxation time of about 2.23. This result approximates the experimental result of 2.3 well, revealing a success of this model. Some other results will also be reported.

1. INTRODUCTION

The laser cavity of conventional vertical-cavity surface-emitting lasers (VCSELs) is a cylinder with a relatively large cross section [1, 2]. This geometry provides a two-dimensional isotropic symmetry on the laser's facet. Therefore, the polarization direction of the laser's output intrinsically has a two-degree freedom. This symmetry is usually broken by the anisotropy of the physical structure of VCSELs [1, 2]. The broken symmetry causes the laser to emit a linearly polarized light with its polarization along a specific direction as the injection current becomes greater than the threshold current. In some VCSELs, when the injection current is increased further, that polarization will switch to the orthogonal direction at a current designated as the polarization switching (PS) current, exhibiting the PS phenomenon [1–6]. Many researches attributed the VCSEL's PS (VPS) to thermal effects induced by the self-heating of the laser's current. Therefore, a deep investigation of VPS from thermodynamic point of view is an important research pursuit. The investigations of the phase transition in the VCSEL's PS (VPS) were recently reported. That phase transition was identified as an SOPT according to four criticalities observed in the experiments [7].

A typically example of SOPT in thermodynamics is the conventional Ising model [8–10]. This model investigates a system which is described by a two-dimensional square lattice and consists of $N \times N$ spins, as schematically presented in Figure 1(a). Each spin can either be in a spin-up state or a spin-down state and they interact only with the nearest neighbors. For a given temperature, the thermal agitation is applied to this system to generate a lowest energy configuration. The latter is then employed to calculate the magnetization of the system at that given temperature. Figure 1(b) presents the variation of the magnetization with respect to the temperature, exhibiting an SOPT of the magnetic material when it transits from ferromagnetic to paramagnetic state. In phase transition terminology, the magnetization plays the role of the order parameter. A continuous or gradual variation of the order parameter across the transition region is a characteristic of the SOPT [11]. The temperature at which phase transition occurred is designated as the Curie temperature.

This research tries to introduce a Gaussian-distributed interaction into the conventional Ising model to simulate the VPS. That interaction is considered to represent the spatial coherence in the laser beam. Some simulation results will be reported. Among them, a success of this Gaussian-distribution embedded Ising model (GDIM) presents that an exponent of the relaxation time of about 2.23 is obtained, which is very close to the experimental result of 2.3.

2. EXPERIMENTS OF VPS

Figure 2 presents the polarization-resolved L - I curves of a VCSEL. The inset of Figure 2 depicts the experimental setup that is typical for the VPS researches. The laser was a single-transverse mode commercial VCSEL operated at 850 nm. The threshold current of this VCSEL was about 1.06 mA. Tuning the injection current from zero, the laser started to emit a linearly polarized light as the current becomes greater than the threshold current. That polarization direction was designated as X -polarization. Further increasing the current to 3.79 mA, the polarization of the laser's output abruptly switched to the orthogonal direction, Y -polarization, and remained that polarization thereafter. Whereas, in decreasing the current from 5 mA, the laser's polarization switched back to X -polarization at 3.06 mA, exhibiting a significant PS hysteresis loop in the L - I curves, as shown in Figure 2.

The laser's current driver was set to inject a quasi-step current into the VCSEL. Figure 3 displays the oscilloscope traces of the X - and Y -polarization power detected by the photodetectors at an

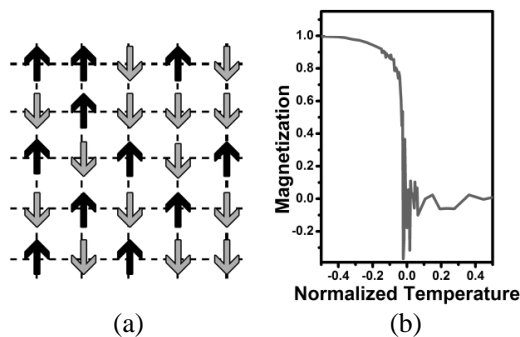


Figure 1: (a) A two-dimensional lattice consists of spins. (b) The variation of the magnetization with respect to the temperature, exhibiting a typical SOPT. The magnetization of 1.0 corresponds to a state with all spins align in the up state. The temperature is normalized with respect to the Curie temperature.

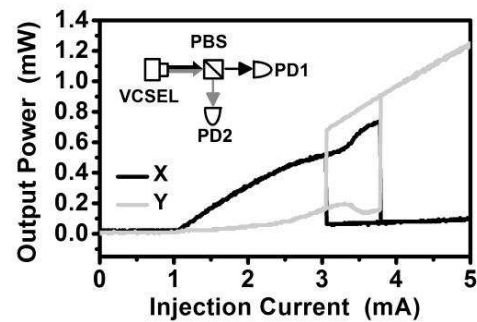


Figure 2: Polarization-resolved L - I curves of a VCSEL that can exhibit VPS. The curves were recorded at a current-modulation frequency of 10 Hz. The threshold current was 1.06 mA. PS occurred at the switching currents of 3.79 mA and 3.06 mA, respectively. The inset exhibits the experimental setup. PBS, polarized beam splitter; PD, photodetector.

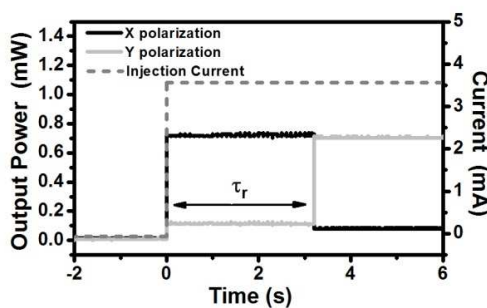


Figure 3: The oscilloscope traces of the injection current, X - and Y -polarization power in a step-current injection experiment at an injection current of 3.63 mA. The ambient temperature of the laser was stabilized at 22.4°C.

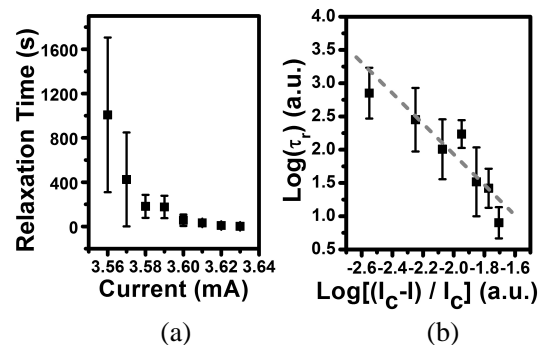


Figure 4: (a) The variation of the relaxation time with respect to the injection current obtained at 22.4°C. (b) Log-log plot of the experimental data shown in Figure 4(a). $I_c = 3.55$ mA. The plot exhibits a power law, and its slope gives the critical exponent, Δ , of about 2.3.

step injection current of 3.63 mA. This current was selected to be greater than the central current of the PS hysteresis loop.

During the leading edge of the step current, the laser was turned-on normally at the threshold current, with its output polarized in the X -direction. Then the injection current was kept constant. However, the laser still emitted stable power with X -polarization. After a significant long period, greater than 3s in Figure 3, the VCSEL's polarization switched (or relaxed) to the Y -direction within about 20 nanoseconds and remained steady both in the power and polarization thereafter. The period that the laser idles in X -polarization is a measure of the relaxation time at that injection current.

Figure 4(a) presents the variation of the relaxation times with the step injection currents. Such an extraordinary long relaxation time was identified as a CSD phenomenon [7], which is a unique characteristic of the SOPT [11]. The log-log plot in Figure 4(b) gives a critical exponent of about 2.3 for this CSD.

3. GDIM SIMULATIONS

To provide a base to simulate the VPS, the conventional Ising model is a good candidate according to the following three reasons. First, in conventional Ising model, the geometry of the system is a two-dimensional lattice which can map to the VCSEL's facet. Second, the spins that constitute the system can only be in either of two states, spin-up or spin-down, corresponding to the X -polarization or Y -polarization. Both of the spin states and the polarizations are orthogonal in mathematics. Therefore, each spin can be imagined as an atom on the laser's facet and each of them can emit either X -polarized light or Y -polarized light. The polarization distribution on the lattice can assemble the laser's beam profile. Third, the conventional Ising model is a typical SOPT and many of its analysis methods or algorithms are available.

The simulated system is set to be a 101×101 lattice. The interaction between spins is presented in Eq. (1).

$$E = - \sum_{\langle i,j,mn \rangle} \left[(1-x) + x \cdot \exp\left(-\frac{i^2+j^2}{2\sigma^2}\right) \right] S_{ij} \cdot S_{mn}, \quad (1)$$

where E is the total energy of the system and i and j are the row and column indexes of a lattice site, $-50 \leq i, j \leq 50$ in this system. $S_{ij} = +1$ or -1 for spin-up or spin-down, respectively.

The summation is over pairs of adjacent spins and every pair is counted once. The notation $\langle ij, mn \rangle$ indicates that sites ij and mn are nearest neighbors. x is the strength of the Gaussian distributed interaction and $(1-x)$ is the strength of the spin-spin interaction in conventional Ising model. σ is the width of the Gaussian interaction, and is set to 25. Therefore, in conventional Ising model the interaction between spins is a short range interaction, interacting only with the nearest neighbor. Whereas, the Gaussian distributed interaction is a long range interaction, which represents the spatial coherence in the laser's beam. Numerically, the thermal agitation is introduced into the system by the Boltzmann distribution and Monte Carlo method. They are typical methods used in conventional Ising model.

Figure 5(a) presents a simulation results of GDIM with $x = 0.2$ at a temperature of 2.45. The black and white dots indicate the lattice sites with spin orientated in up and down, respectively. The

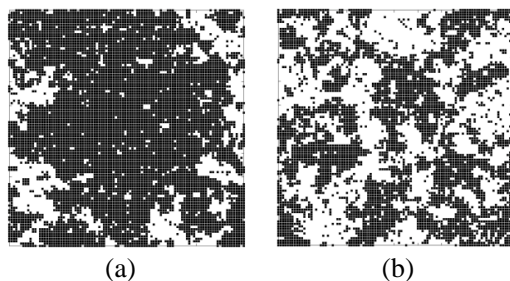


Figure 5: (a) The simulated configuration of the GDIM with $x = 0.2$ at a temperature of 2.45. (b) The simulated configuration of the conventional Ising model at a temperature of 2.47.

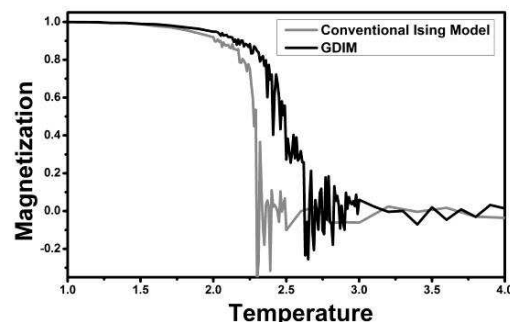


Figure 6: The dependence of the magnetization on the temperature for conventional Ising model (gray curve) and GDIM (black curve).

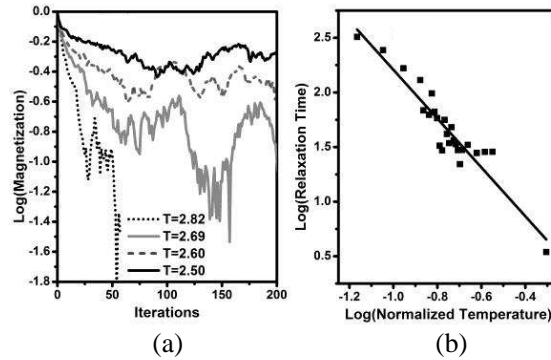


Figure 7: (a) Decay of the magnetization as a function of the iterations at various step temperatures in GDIM. (b) Log-log plot of the relaxation times versus the normalized temperatures. The later is defined by $(T - T_c)/T_c$, where T_c is the Curie temperature.

resulting configuration exhibits a significant domain of spin-up in the central region of the lattice, which reflects the effect of the Gaussian distributed interaction. For comparison, Figure 5(b) displays a similar simulation result of conventional Ising model at a temperature of 2.47. No any large structure is observed on that surface.

Figure 6 depicts the magnetization varied with the temperature both in conventional Ising model and in GDIM. Curie temperatures of about 2.27 for conventional Ising model and about 2.45 for GDIM are observed. The magnetization curve of the GDIM exhibits an SOPT-like continuous variation across the transition region.

Consider to prepare the system with all spins in the up state and at a temperature around zero. Therefore, its magnetization is 1 corresponding to a pure ferromagnetic state. Then, a step temperature profile with a temperature greater than the Curie temperature is applied to this system. Figure 7(a) depicts the variation of the magnetization with respect to the runs of the numerical iterations at various step temperatures. Here, the iteration plays the role of the time in simulations. Since the step temperatures are greater than the Curie temperature, the magnetization will decay approaching zero, which is the magnetization of the paramagnetic materials. The reciprocal of the slope of the semi-log curves in Figure 7(a) will give the time constants or relaxation time at those temperatures. The slope of the log-log plot of the relaxation times versus temperatures, as shown in Figure 7(b), will give the exponent of the relaxation time. From the analysis described above, the exponent of relaxation time of GDIM is about 2.23, which is very close to the experimental result of 2.3 presented in Figure 4(b).

4. CONCLUSIONS

In conclusion, the GDIM can present an SOPT-like characteristic of the magnetization variation with respect to the temperature in the simulation. However, in contrast to the sharp transitions observed in the VPS experiments, the simulated GDIM transition is relatively gradual. The simulations can also exhibit an exponent of the relaxation time that is very close to the experimental results, indicating a success of the GDIM.

There are many models about the physics behind the VPS; for example, the spin-flip model [12], the current-dependent gain model [13], and the stress-effect model [14]. But the question is still open. Constructing a model from the phase transition point of view for the VPS might help to explore more understanding of it. Based on some successes presented in this report, the GDIM is a good starting point. More investigations to verify the SOPT of the GDIM are required.

ACKNOWLEDGMENT

This research was supported by the Ministry of Science and Technology of the Republic of China, grant MOST 103-2112-M-110-006-MY2.

REFERENCES

1. Li, H. and K. Iga, *Vertical-cavity Surface-emitting Lasers Devices*, Springer, New York, 2003.
2. Michalzik, R., *VCSELs: Fundamentals, Technology and Applications of Vertical-cavity Surface-emitting Lasers*, Springer, New York, 2013.

3. Chang-Hasnain, C. J., J. P. Harbison, L. T. Florez, and N. G. Stoffel, "Polarization characteristics of quantum well vertical-cavity surface-emitting lasers," *Electron. Lett.*, Vol. 27, No. 2, 163–165, 1991.
4. Choquette, K. D., R. P. Schneider, Jr., K. L. Lear, and R. E. Leibenguth, "Gain-dependent polarization properties of vertical-cavity lasers," *IEEE J. Sel. Top. Quantum Electron.*, Vol. 1, No. 2, 661–666, 1995.
5. Martin-Regalado, J., F. Prati, M. San Miguel, and N. B. Abraham, "Polarization properties of vertical-cavity surface-emitting lasers," *IEEE J. Quantum Electron.*, Vol. 33, No. 5, 765–783, 1997.
6. Danckaert, J., M. Peeters, C. Mirasso, M. San Miguel, G. Verschaffelt, J. Albert, B. Nagler, H. Unold, R. Michalzik, G. Giacomelli, and F. Marin, "Stochastic polarization switching dynamics in vertical-cavity surface-emitting lasers: Theory and experiment," *IEEE J. Sel. Top. Quantum Electron.*, Vol. 10, No. 5, 911–917, 2004.
7. Kuo, W. C., Y. H. Wu, Y. C. Li, and T. C. Yen, "Criticalities and phase transitions in the polarization switching of vertical-cavity surface-emitting lasers," *IEEE Photon. Technol. Lett.*, Vol. 24, No. 24, 2262–2264, 2012.
8. Lenz, W., "Beitrag zum Verständnis der magnetischen Erscheinungen in festen Körpern," *Z. Phys.*, Vol. 21, 613–615, 1920.
9. Onsager, L., "Crystal Statistics. I. A two-dimensional model with an order-disorder transition," *Phys. Rev.*, Vol. 65, 117–149, 1944.
10. Ising, E., "Beitrag zur theorie des ferromagnetismus," *Z. Phys.*, Vol. 31, 253–258, 1925.
11. Landau, L. D. and E. M. Lifshitz, *Statistical Physics*, Pergamon Press, Oxford, 1980.
12. San Miguel, M., Q. Feng, and J. V. Moloney, "Light-polarization dynamics in surface-emitting semiconductor lasers," *Phys. Rev. A*, Vol. 52, 1728–1739, 1995.
13. Danckaert, J., B. Nagler, J. Albert, K. Panajotov, I. Veretennicoff, and T. Erneux, "Minimal rate equations describing polarization switching in vertical-cavity surface-emitting lasers," *Opt. Commun.*, Vol. 201, 129–137, 2002.
14. Van der Sande, G., M. Peeters, I. Veretennicoff, J. Danckaert, G. Verschaffelt, and S. Balle, "The effects of stress, temperature and spin flips on polarization switching in VCSELs," *IEEE J. Quantum Electron.*, Vol. 42, 896–904, 2006.

Electromagnetic Modeling of Antenna Array Based on Circular Carbon Nanotubes Bundle

M. Aidi and T. Aguli

SysCom Laboratory, National Engineering School of Tunis, BP 37 Le Belvedere 1002, Tunis, Tunisia

Abstract— A novel antenna array structure, formed by carbon nanotube bundle is proposed. The geometric structure and radiation characteristics have been investigated using a proposed integral equations system. This equations system is numerically solved using the moments method. The dependence of the radiation performance, upon geometrical parameters, e.g., nanotube length and number and the coupling distance is accurately discussed. Some illustrative numerical results have been presented to discuss the radiation performance of carbon nanotube antenna array for different coupling distances.

1. INTRODUCTION

Carbon nanotubes (CNT) are considered as one of the carbon's allotropes, formed by a rolled-up sheet of graphene. They were discovered by Iijima in 1991 [1]. Because the crystal structure of SWCNT is strongly related to that of graphene, the CNT are typically identified using graphene's lattice vectors [3]. In previous modeling works [4], CNT was considered as an antenna, but its potential performances have never been discussed. Recently, SWCNTs are synthesized with a length near to the microwave in free space, and by the way, this motivation leads to explore their properties as antenna. In the range of centimeter and millimeter applications, CNT antennas are originally proposed by Burke [5]. In [5], CNT dipole antennas are modeled using the transmission line approach, so the following transmission line parameters; kinetic inductance L_K , quantum capacitance C_Q and quantum resistance R are determined using the electrons fluid model.

Another common approach is to simulate electromagnetic wave propagation along CNT based on these electrodynamics properties [6]. This approach presents a macroscopic view for interactions of high frequency electromagnetic field with CNTs. However, the radiation efficiency of CNT antenna is very low, as a result of the slow wave surface which decreases the radiation resistance [7]. In addition, the CNT antennas are very resistive structures so the problem of impedance mismatch is strongly posed. In fact, the characteristic impedance of the CNT antenna (10–100 k Ω) is greater than each of the feeding line (50 Ω). To solve this problem the CNT bundle has been proposed and studied based on effective axial surface conductivity for low coupling distances [7–9]. In terahertz and infrared frequency range, the radiation characteristics of CNT dipole antenna arrays have been investigated by the CST MICROWAVE STUDIO simulator. It found that, $N \times N$ antennas array have a higher radiation efficiency than single CNT dipole antenna [10, 11]. In our previous works, we have proposed a general formulation based on a integral equations system which aimed at studying the coupled CNT dipole antenna. This formulation allowed a rigorously investigation of the antennas interaction for any coupling distance [13].

In this paper we propose a novel antenna array structure formed by carbon nanotube bundle. The numerical results shows that, we can obtain a higher antenna directivity with important reduction of the input impedance compared to the single CNT antenna.

2. MATHEMATIC FORMULATION

Figure 1(a) shows the antenna array structure made of $N \times N$ carbon nanotube bundles. The unit element is formed by a strongly coupled CNT, as a half wavelength dipole antenna with effective quantum mechanical conductivity σ .

2.1. Antenna Bundle

Dynamic conductivity of CNT can be calculated using the Boltzmann kinetic equation. For a small radius of CNT, the dynamic conductivity is given by [6]:

$$\sigma_{cn}(w) = \sigma_{zz}(w) \simeq -j \frac{2e^2 v_F}{\pi^2 \hbar a (w - j\nu)} \quad (1)$$

where e is the electron charge, ν is the relaxation electron frequency for CNT (equal to $3 \cdot 10^{-12} \text{ s}^{-1}$), a is the CNT radius, \hbar the reduced Planck constant and here we use the Fermi velocity as $v_F = 9,71.105 \text{ ms}^{-1}$.

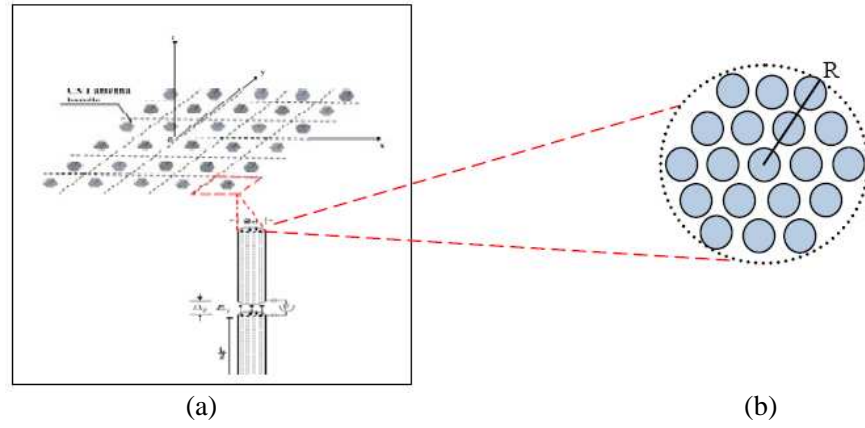


Figure 1: (a) CNT antenna array formed by $N \times N$ antenna bundle, (b) schematic structure of SWCNT bundle.

In the case of low inter-tubes distances, the array elements are strongly coupled, and the CNT bundle is considered as a single antenna with radius R , length L and effective surface conductivity σ [8]. As shown in Figure 1(b), the antenna bundle is formed by N metallic CNT with radius a , which are parallelly connected at their centers by a delta gap source with unit voltage. The effective surface conductivity is expressed as:

$$\sigma \simeq \frac{N\sigma_{cn}(w)a}{R} \quad (2)$$

The electromagnetic wave interaction between CNT antennas is modeled by the integral equation like the analysis of the single antenna. The main idea is to use the integral equation of single CNT antenna based on Hallen's integral equation, with a slight modification to include the surface conductivity of the bundle [8].

$$\left(k^2 + \frac{\partial^2}{\partial z^2}\right) \int_{-h}^h \left(\frac{e^{-jk\sqrt{(z-z')^2+a^2}}}{\sqrt{(z-z')^2+a^2}} + \frac{w\varepsilon e^{-jk|z-z'|}}{a\sigma k} \right) I(z') dz' = -j4\pi w\varepsilon E_z^{in}(z) \quad (3)$$

This integral equation can be solved numerically using the MoM method to obtain the current distribution and deduce later the input impedance and the antenna radiation pattern.

2.2. Coupled Antennas

Considering N identical parallel CNT bundle as dipole antennas center-driven by N generators $V_{1,2,\dots,N}$ and separated by the distance d . $I_{1,2,\dots,N}(z)$ are the induced currents on the dipoles antennas.

On the surfaces of each dipole antenna, the electrical field is writing as [13]:

$$\begin{cases} E_{11}^d + E_{21}^d + E_{31}^d + \dots + E_{N1}^d + E_1^{in} = Z_s I_1 \\ E_{12}^d + E_{22}^d + E_{32}^d + \dots + E_{N2}^d + E_2^{in} = Z_s I_2 \\ \vdots \\ E_{1N}^d + E_{2N}^d + E_{3N}^d + \dots + E_{NN}^d + E_N^{in} = Z_s I_N \end{cases} \quad (4)$$

where Z_s is the surface impedance per unit length of a SWCNT and E_{pq} is the z -component of the electric field on the antenna p induced by the current on the antenna q [13]:

$$E_{pq}(z) = \left(\frac{\partial^2}{\partial z^2} + k^2 \right) \int_{-\frac{l}{2}}^{\frac{l}{2}} \frac{e^{-jkR_{pq}}}{R_{pq}} I_q(z') dz' = {}_{pq} I_q \quad (5)$$

Using the MoM method, we convert this integral equations system in a matrix form and we

deduce the unknown current distribution for each dipole antenna:

$$\begin{bmatrix} \left[\langle g_{1n}, (\widehat{G}_{11} - Z_s) f_{1m} \rangle \right] & \cdots & \left[\langle g_{1n}, \widehat{G}_{N1} f_{1m} \rangle \right] \\ \vdots & \ddots & \vdots \\ \left[\langle g_{Nn}, \widehat{G}_{1N} f_{Nm} \rangle \right] & \cdots & \left[\langle g_{Nn}, (\widehat{G}_{NN} - Z_s) f_{Nm} \rangle \right] \end{bmatrix} \begin{bmatrix} I_1 \\ \vdots \\ I_N \end{bmatrix} = - \begin{bmatrix} \left[\langle g_{1n}, E_1^{in} \rangle \right] \\ \vdots \\ \left[\langle g_{Nn}, E_N^{in} \rangle \right] \end{bmatrix} \quad (6)$$

3. NUMERICAL RESULTS

We present some illustrative numerical results for antenna array formed by five CNT bundle with length $L = 20 \mu\text{m}$. Figure 2(a) shows the input impedance of a CNT bundle for different values of N . For $N = 5$, the first resonance occurs nearly at the frequency $f = 430 \text{ GHz}$ for a resonance impedance equal to 1645Ω . If we compare this results to the conventional half-wavelength dipole antenna, CNT dipole antenna has an important scale reduction factor of 0.057. For $N = 20$, the resonance frequency is nearly to $f = 600 \text{ GHz}$ and the resonance impedance is about 687Ω . Therefore, the scale reduction factor reaches a value of 0.08. It can be noted that the antenna bundle formed by $N = 120$ carbon nanotubes, does not resonate for this frequency range. So, for a fixed CNT length and radius, the input impedance is inversely proportional to the CNT number. If the CNT number increases, the resonance frequency shifts to the high values.

Next obtained results are shown for antenna array structure formed by five identical CNT antennas bundle distributed as shown in Figure 2(b). Only the antenna (1) is excited.

We present in Figure 3 the current distribution along each dipole antenna. It should be noted that, for a coupling distance $d = 0.1\lambda_p$, the excited antenna generate a current distribution more greater than each of the unexcited antenna. Furthermore, the current distribution of each antenna is approximately a half sinusoid for an operating frequency $f = 150 \text{ GHz}$ and antenna length $L = 20 \mu\text{m}$ which corresponds to the first resonance. If the coupling distance increase ($d = 0.5\lambda_p$), all the antenna current distributions keeps the same shape with lowering of the magnitude (Figure 3(b)). Figure 4 shows the Antenna array radiation pattern obtained for different coupling distances at the operating frequency $f = 150 \text{ GHz}$. from this results we can note that, the antenna directivity

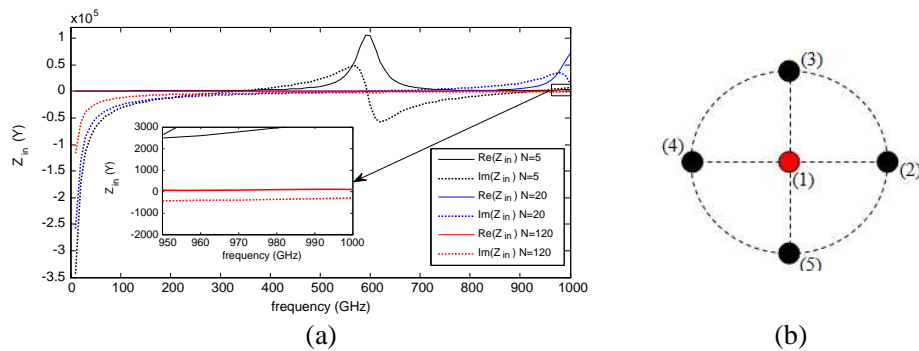


Figure 2: (a) Input impedance of CNT antenna bundle as a function of the frequency for different number of carbon nanotube, (b) five antennas array structure.

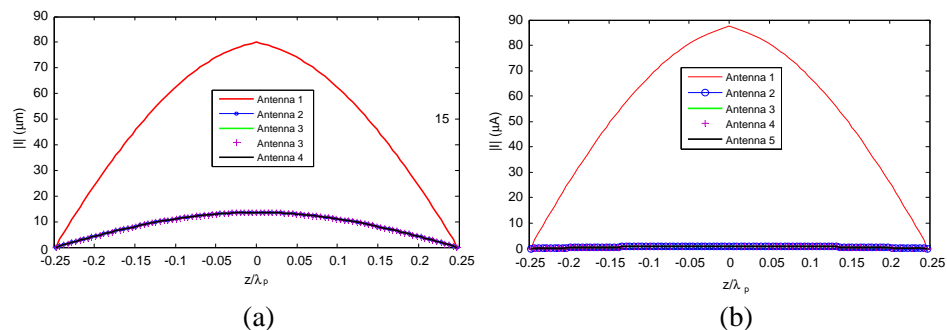


Figure 3: Current distribution along each dipole antenna bundle at the operating frequency $f = 150 \text{ GHz}$. (a) the coupling distance $d = 0.1\lambda_p$, (b) the coupling distance $d = 0.5\lambda_p$.

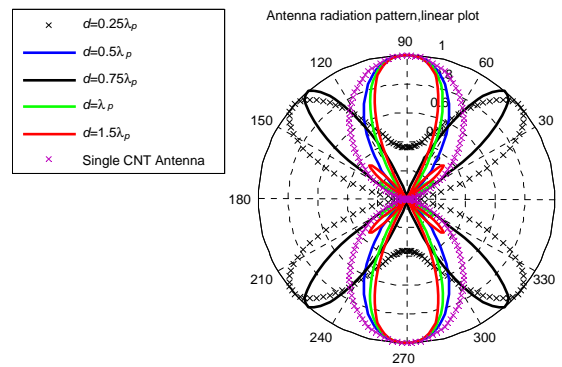


Figure 4: Antenna array radiation pattern obtained for different coupling distances at the operating frequency $f = 150$ GHz.

is significantly depends on the antenna separate distance. In fact, for a coupling distances that are greater than λ_p we observe a high directivity compared to the single CNT antenna.

4. CONCLUSION

The geometric structure and the radiation properties of the antenna formed by a CNT bundle have been studied by a proposed integral equations system. Obtained results show that, to obtain a high directivity and radiation efficiency, we can increase the array elements number with optimization of inter-elements distances and CNT length.

REFERENCES

1. Iijima, I., "Helical microtubules of graphitic carbon," *Nature*, Vol. 354, 56–58, 1991.
2. Saito, R., G. Dresselhaus, and M. S. Dresselhaus, *Physical Properties of Carbon Nanotubes*, Imperial College Press, London, UK, 2003.
3. Charlier, J.-C., X. Blase, and S. Roche, "Electronic and transport properties of nanotubes," *Reviews of Modern Physics*, Vol. 79, 677, Apr.–Jun. 2007.
4. Burke, P. J., "An RF circuit model for carbon nanotubes," *IEEE Trans. Nanotechnol.*, Vol. 2, No. 1, 55–58, Mar. 2003.
5. Burke, P. J., S. Li, and Z. Yu, "Quantitative theory of nanowire and nanotubes antenna performance," *IEEE Trans. Nanotechnol.*, Vol. 5, No. 4, 314–334, Jul. 2006.
6. Hanson, G. W., "Fundamental transmitting properties of carbon nanotubes antennas," *IEEE Transactions on Antennas and Propagation*, Vol. 53, No. 11, 3426–3435, Washington, DC, Jul. 2–3, 2005.
7. Plombon, J. J., K. P. O'Brien, F. Gstrein, and V. M. Dubin, "High-frequency electrical properties of individual and bundled carbon nanotubes," *Applied Physics Letters*, Vol. 90, 063106, 2007.
8. Attiya, A. M., "Lower frequency limit of carbon nanotube antenna," *Progress In Electromagnetics Research*, Vol. 94, 419–433, 2009.
9. Huang, Y., W.-Y. Yin, and Q. H. Liu, "Performance prediction of carbon nanotube bundle dipole antennas," *IEEE Trans. Nanotechnol.*, Vol. 7, No. 3, 331–337, May 2008.
10. Lan, Y., B. Zeng, H. Zhang, B. Chen, and Z. Yang, "Simulation of carbon nanotube THz antenna arrays," *International Journal of Infrared and Millimeter Waves*, Vol. 27, No. 6, 871–877, Jun. 2006.
11. Wang, Y., Q. Wu, W. Shi, X. He, X. Sun, and T. Gui, "Radiation properties of carbon nanotubes antenna at terahertz infrared range," *International Journal of Infrared and Millimeter Waves*, Vol. 29, No. 1, 35–42, 2008.
12. Aidi, M. and T. Aguilu, "Electromagnetic modeling of coupled carbon nanotube dipole antennas based on integral equations system," *Progress In Electromagnetics Research M*, Vol. 40, 179–183, 2014.
13. Aidi, M. and T. Aguilu, "Performance prediction of coupled carbon nanotubes dipole antennas," *IEEE Confernece on Electromagnetic Field Computation CEFC*, Annecy, May 2014.

A Compact Printed Spiral FM Antenna

Abraham Loutridis^{1,2}, Kansheng Yang^{1,2}, Matthias John², and Max Ammann¹

¹Antenna & HF Research Centre, Dublin Institute of Technology, Dublin 8, Ireland

²CTVR — The Telecommunications Research Centre, Trinity College Dublin, Dublin 2, Ireland

Abstract— In this work, a compact printed spiral monopole antenna operating in the FM frequency band (88–108 MHz) is reported. The antenna is printed on a 100 mm × 50 mm PCB layer providing more than 20 MHz bandwidth at –2 dB threshold and is easily fabricated with low manufacturing cost. The antenna was also measured and simulated on 900 mm × 900 mm ground plane which is representative of a vehicle roof

1. INTRODUCTION

Electrically Small Antennas (ESAs) are desired and essential for many applications and especially at lower frequencies such as in the HF and VHF bands. Nowadays, compact antennas have become standard for radio receivers on vehicles and mobile terminals which lead to new requirements for small, efficient and low cost designs. Good performance of a radio receiver is heavily depended on the antenna performance. A variety of FM antenna types have been reported for automotive and portable applications including, active [1] and short meander line monopoles [2], fractal Hilbert curve antenna [3], chip antennas [4], window-printed active antennas [5] and the shark type antennas [6].

The frequency range for the FM radio band which defined from FCC regulation is from 88 MHz to 108 MHz and the respective wavelength λ_0 for the centre frequency $f_0 = 98$ MHz is around 3 meters. The height of a quarter wavelength FM monopole antenna is around 750 mm. In order to reduce the size of the monopoles, helix antennas with a height of 80 mm are used for FM radio receivers. In this paper a compact spiraled monopole antenna is reported with an overall volume of 100 mm × 50 mm × 1.5 mm. A five element network matching circuit is embedded in order to increase the bandwidth to more than 20 MHz. The antenna can be easily integrated into compact volumes, is low cost and easily fabricated.

2. COMPACT SPIRAL ANTENNA

The antenna was designed and printed on a 100 mm × 50 mm double sided FR-4 substrate ($\epsilon_r = 4.3$, $\tan \delta = 0.025$, thickness = 1.5 mm) with copper metallization thickness of 0.035 mm (Figure 1(a)). The 67.9 mm × 50 mm metal ground plane is on the rear of the same PCB board. The antenna is fed by a 50 Ω microstrip line of 3 mm width which is connected to a SMA connector. The miniaturization is based on its spiral structure occupying a 33 mm ($0.01\lambda_0$) × 50 mm ($0.02\lambda_0$) area on the PCB board (Figure 1(c)). In order to improve the antenna bandwidth, a five element π -matching network circuit (Figure 1(b)) is added so that the impedance bandwidth of antenna can be wider, covering the frequency range of 31.5 MHz bandwidth at VSWR 8.5 : 1 (Figure 2). As shown in Figure 1(b) the matching network consists of two parallel capacitors of 68 pF and 82 pF, two serial inductors of 100 nH and 1.5 nH and a parallel inductor of 68 nH.

3. SIMULATED & MEASURED RESULTS

Figure 2 illustrates the measured S_{11} results of the final model and the simulated S_{11} results of the antenna with and without the matching network. The measurements were obtained using a Rohde & Schwarz ZVA 40 vector network analyzer. For the simulation model without the matching network the antenna resonates at 102.9 MHz with a –2 dB impedance bandwidth of 6.3 MHz. For the antenna with the matching network the simulation results indicate a –2 dB impedance bandwidth of 22.3 MHz (86.2–108.5 MHz), while for the measured design the impedance bandwidth at –2 dB threshold is 31.5 MHz (76.8–108.3 MHz).

The antenna was also measured and simulated on 900 mm × 900 mm ground plane which is representative of a vehicle roof (Figure 3). The spiral monopole (33 mm × 50 mm) is located on a metallic ground plane while the other part of the antenna with the microstrip line is located below it. In Figure 4 the simulated and measured results are depicted. The antenna resonates at 91.5 MHz with a –2 dB bandwidth of 30.5 MHz (77.3–107.8 MHz) which is compared to the results in Figure 2. The simulated results provide a –2 dB bandwidth of 18 MHz (83–101 MHz).

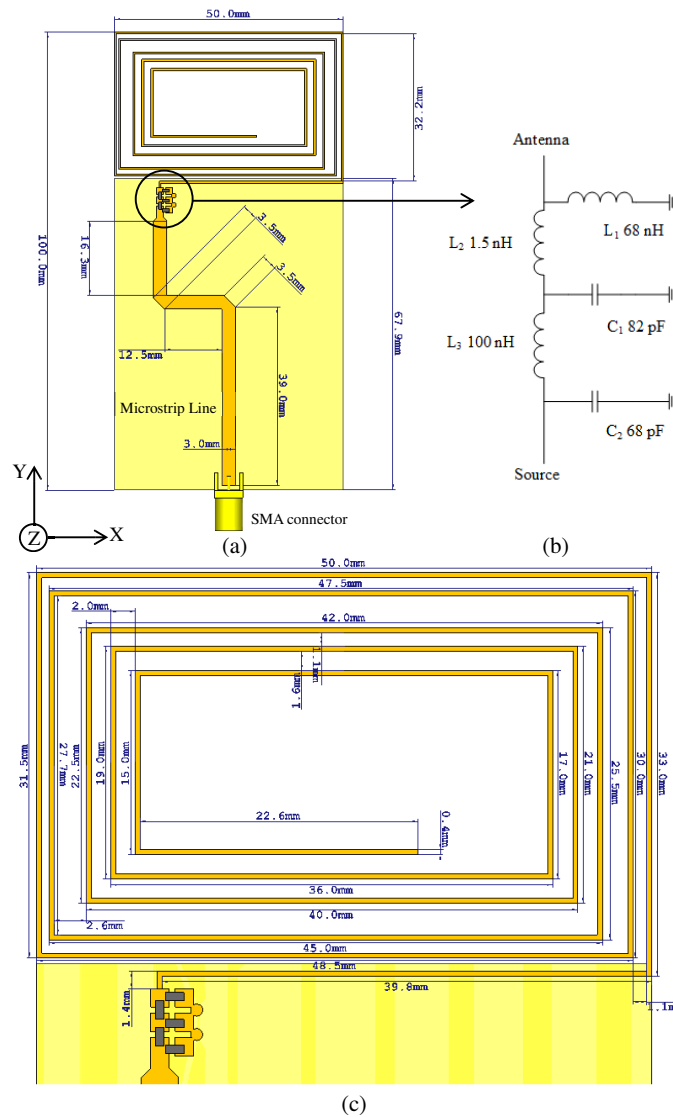


Figure 1: (a) Antenna general view, (b) π -matching network, (c) spiral monopole.

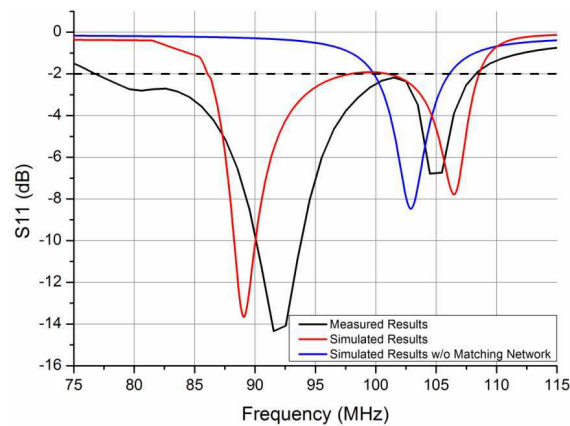


Figure 2: Simulated and measured S_{11} results.

In Figure 5 the simulated z - x and x - y plane radiation patterns at 98 MHz are illustrated. The patterns are illustrated both in 10 dB/division scaled plot. The Phi (φ) component provides omnidirectional characteristics in both planes. The simulated maximum realized gain and total efficiency is -24.9 dBi and 2% at 98 MHz respectively.

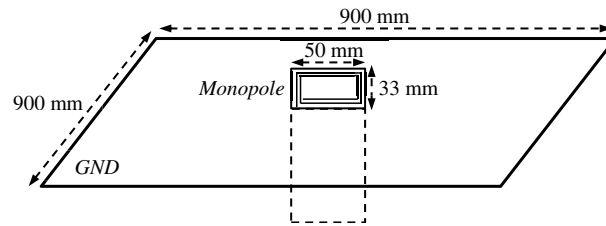


Figure 3: The FM antenna on large ground plane.

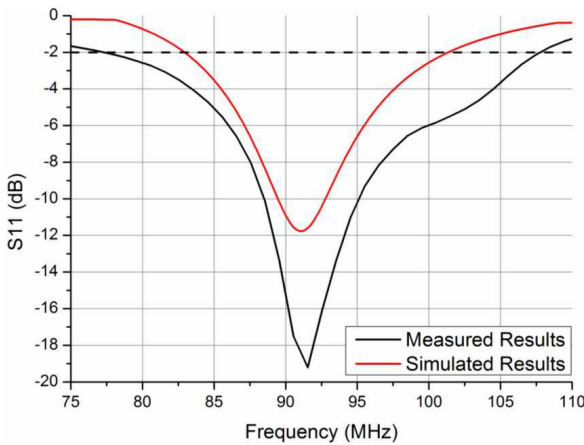
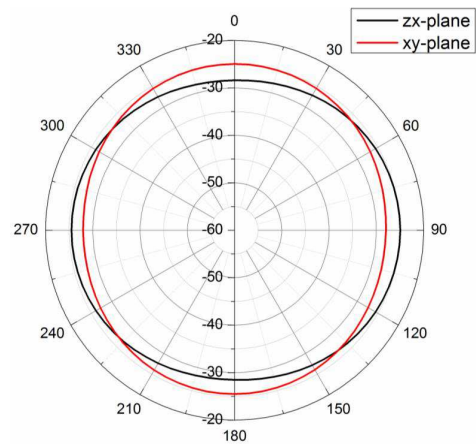


Figure 4: Simulated and measured results with the antenna on a large ground plane.

Figure 5: The simulated Phi (φ) components for the zx and xy -plane at 98 MHz.

4. CONCLUSIONS

In this work, a compact spiral FM monopole antenna is described. The proposed antenna is an electrically small antenna ($< 0.037\lambda_0$) offering a 32% fractional bandwidth (-2 dB) over the centre frequency ($f_0 = 98$ MHz) and covers the whole FM frequency band (88 MHz–108 MHz). The antenna is low cost, easily fabricated with omnidirectional radiation characteristics suitable to embed into housing. The antenna still operates with a decent wide bandwidth on large sized ground plane which makes it usable for automotive and vehicle applications.

REFERENCES

1. Negut, A., L. Reiter, J. Hopf, and S. Lindenmeier, "Performance of a 20 cm short active AM/FM monopole antenna for automotive application," *IEEE European Conference on Antennas and Propagation (EuCAP)*, 2009.
2. Perri, E. B. and S. Forcellini, "Very short meander monopole antennas," *IEEE Antennas and Propagation Society International Symposium AP-S*, 2008.
3. Borja, C., J. Anguera, C. Puente, and J. Vergés, "How much can be reduced the internal FM antenna of mobiles phones," *IEEE European Conference on Antennas and Propagation (EuCAP)*, 2010.
4. Song, S.-M., L. Jin, Y. Zheng, and G.-Q. Yang, "A miniaturized FM chip antennas for handset devices," *International Workshop on Microwave and Millimeter Wave Circuits and System Technology (MMWCST)*, 2012.
5. Schaffner, J. H., H. J. Song, A. Bekaryan, H.-P. Hsu, M. Wisniewski, and J. Graham, "The impact of vehicle structural components on radiation patterns of a window glass embedded FM antenna," *IEEE Transactions on Antennas and Propagation*, Vol. 59, No. 10, 3536–3543, 2011.
6. Chang, D.-C., F.-Y. Lin, B.-H. Zeng, and J. Chen, "Compact size antenna for car FM radio," *PIERS Proceedings*, 223–224, Taipei, Mar. 25–28, 2013.

A Wideband Matching Technique for Polarization Versatile Applications

A. G. Koutinos, G. A. Ioannopoulos, M. T. Chryssomallis, and G. A. Kyriacou

Microwaves Lab, Department of Electrical and Computer Engineering
Democritus University of Thrace, Xanthi 67100, Greece

Abstract— A rectangular patch exhibiting polarization diversity throughout a notable bandwidth is designed for operation at the 2.4 GHz WiFi band. A wideband matching technique is implemented, introducing path inequality between specular feeding points, i.e., points giving rise to a specific polarization mode. There are two pairs of such specular feeding points and two sources, offering polarization diversity when excited appropriately. Exploiting these features, linear (horizontal, vertical or diagonal) as well as RH and LH circular polarization can be achieved, over a remarkable bandwidth around the 2.4 GHz frequency band.

1. INTRODUCTION

As requirements for terminal equipment are getting more and more strict in terms of performance versus size, rectangular patch antennas are a fair solution due to their characteristics, such as ease of design and fabrication, low cost and compensatory behaviour despite their small size [1]. However, patch antennas suffer a substantial drawback, concerning their poor bandwidth performance. Many techniques have been proposed, aiming to overcome this disadvantage. Previous works includes parasitic patch loading [2], chip resistor loading [3], use of lower dielectric constant and thicker substrate [4], as well as other techniques. The technique used herein is a way of wideband matching in the sense described in [5], yet it is applied to a polarization versatile configuration. Also, the proposed configuration is designed for the 2.4 GHz band, commonly known as the WiFi band, which is allocated for Internet access and computer-to-computer communications, according to [6]. The major concept of wideband matching for a specific polarization mode is exciting the patch with a single source, by introducing a path inequality between two specular feeding points. Note that both point excite the same resonant mode (e.g., TM_{10}). This implementation splits the apparent draught at resonance frequency to two separate resonances, speaking in terms of Return Loss. Choosing an appropriate length of inequality, the overall behaviour of the Return Loss parameter follows the envelope of the resonant pair, thus enhancing the antenna bandwidth for the concerning polarization mode. This procedure is analytically described in [5]. Extending this procedure while aiming to acquire polarization diversity performance, a second pair of feeding points, biased by a second source, is introduced orthogonally to the previous pair. Again both point excite the same mode, which is orthogonal to the previous one (e.g., TM_{01}). Concerning the primary configuration, the same results are now expected, but for an orthogonal polarization. As one should guess, also circular polarization is now at hand by a simultaneous excitation of both TM_{10} and TM_{01} modes, while assigning appropriate phase to each source to get 90 degrees difference. A similar technique is described in [7], where it is stated that polarization diversity can be obtained by introducing a 90° phase difference between two adjacent linear resonances, exploiting shorting posts.

2. ANTENNA CONFIGURATION

The simulated patch is 33.5 mm long and 34 mm wide, printed on a $50 \times 50 \times 1.524$ mm Rogers dielectric substrate with $\epsilon_r = 3.4$ and $\tan \delta = 0.002$. The ground plane is printed on the back of the substrate, and a second identical substrate is attached. The feeding network is folded on the backside of the structure, consisting of transmission lines which are 1.5 mm wide. The patch is fed via circular holes in the substrates and the ground plane, which were designed as 1.975 mm rectangular holes for simulation convenience. Downwards, backside and broadside aspects of antenna configuration are depicted in Fig. 2, along with all corresponding dimensions.

Examining the proposed configuration, it becomes obvious that Source 1 excites two points for horizontal polarization, yet a path inequality is introduced between them. The same holds for Source 2, which excites two points placed along the vertical axis. This configuration, as was our primary goal, enables wideband matching for horizontal, vertical and diagonal polarization, as well as polarization diversity including circular polarization, RHCP or LHCP, depending on the relative phase assigned to the sources.

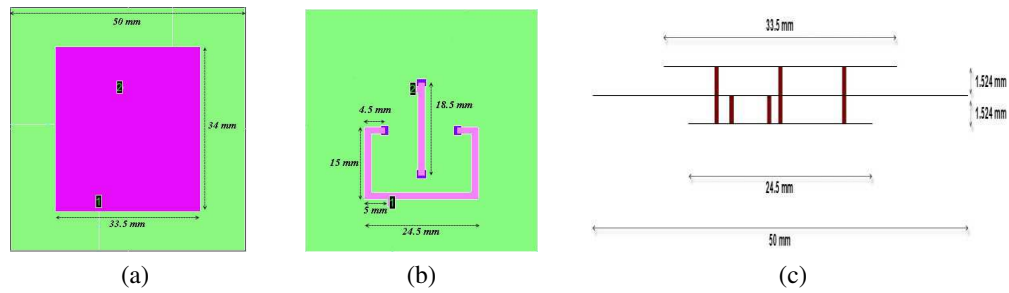


Figure 1: (a) Downwards, (b) backside and (c) broadside aspects of the proposed configuration.

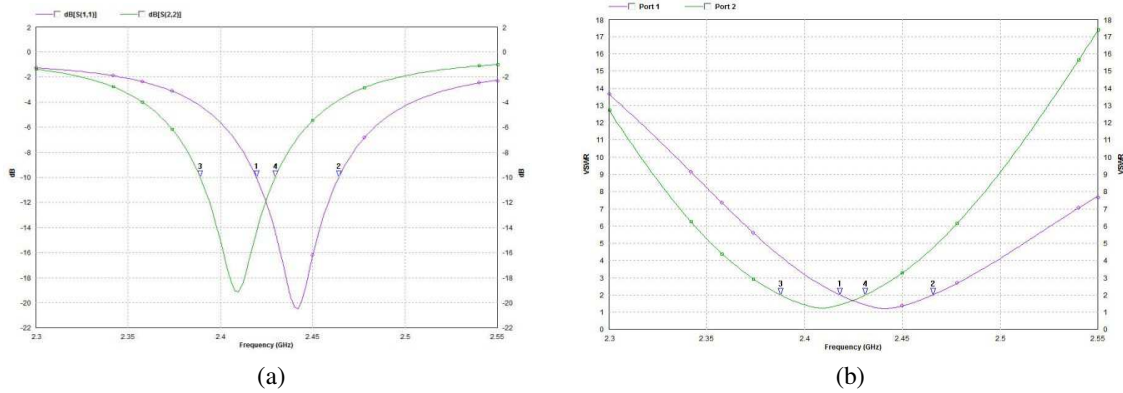


Figure 2: (a) Return Loss and (b) VSWR parameters, for horizontal (purple) and vertical (green) polarization. circular polarization modes can be excited. In Table 1 the bandwidth-defining frequency points are summarized.

3. SIMULATION RESULTS

The antenna was simulated using the Zeland IE3D[®] suite. This first section includes simulation results of parameters that are common to all polarization modes.

3.1. Return Loss and VSWR

It is common to measure Return Loss parameter bandwidth between the frequency points where the -10 dB requirement is met. Furthermore, we need $1 \leq \text{VSWR} \leq 2$, in order to obtain good radiation characteristics. Examining Fig. 2 and the corresponding frequency markers, we can assume that the useful bandwidth region is confined from the Return Loss parameter -10 dB points, as the corresponding points for VSWR allow a greater bandwidth. It is also noted, that in the region where both the S_{11} and S_{22} curves are below -10 dB, diagonal and along with rational BW for each polarization mode, and the values that shall be assigned to each source, in order to get the desirable polarization mode.

Table 1: Source voltage, centre frequency and rational bandwidth for each polarization mode.

	Source 1 Mag ^{Deg}	Source 2 Mag ^{Deg}	f_- [GHz]	f_+ [GHz]	f_{center} [GHz]	BW %
Horizontal	1^0	0	2.41951	2.46402	2.44176	1.82
Vertical	0	1^0	2.38904	2.42958	2.40931	1.68
Diagonal	1^0	1^{90}	2.41951	2.42958	2.42454	0.41
RHCP	1^0	1^0	2.41951	2.42958	2.42454	0.41
LHCP	1^0	1^{180}	2.41951	2.42958	2.42454	0.41

3.2. Horizontal Polarization

We can obtain horizontal polarization by assigning appropriate values to the voltage sources. According to our simulation results, a fractional bandwidth of 1.82% can be obtained, around the

frequency of 2.44176 GHz. Furthermore, the antenna input impedance when operating at this frequency has a magnitude that ripples from 33.1 to 64.7 Ohm, while impedance angle varies from 29.3° to -31.9° . Also, antenna efficiency is above 55% throughout the whole bandwidth, and radiation efficiency varies from 67.8% to 69.4%. Antenna current distribution and power gain patterns are depicted in Fig. 3.

3.3. Vertical Polarization

A fractional bandwidth of 1.68% is obtained for vertical polarization. Input impedance magnitude varies from 89.7 to 27 Ohm, and impedance angle takes values between 14.6° to -14.4° . Antenna efficiency is above 56% and radiation efficiency is almost stable and equal to 67%.

3.4. Diagonal Polarization

The proposed configuration can also offer diagonal polarization, yet throughout a lesser bandwidth (0.41%). For this case, the antenna efficiency reaches a maximum of 61.9%, and radiation efficiency is 60% with small variations. Input impedance takes intermediate values compared to the horizontal and vertical polarization modes. Current distribution as well as power gain patterns are depicted

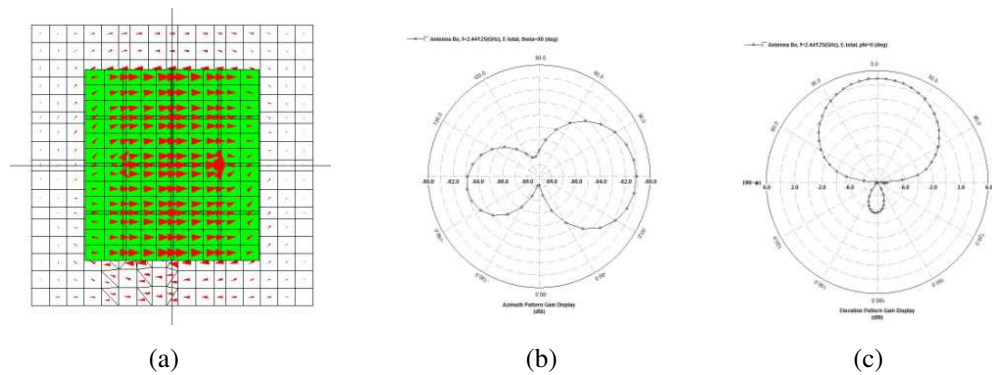


Figure 3: (a) Current distribution, (b) azimuth power gain pattern and (c) elevation power gain pattern for horizontal polarization.

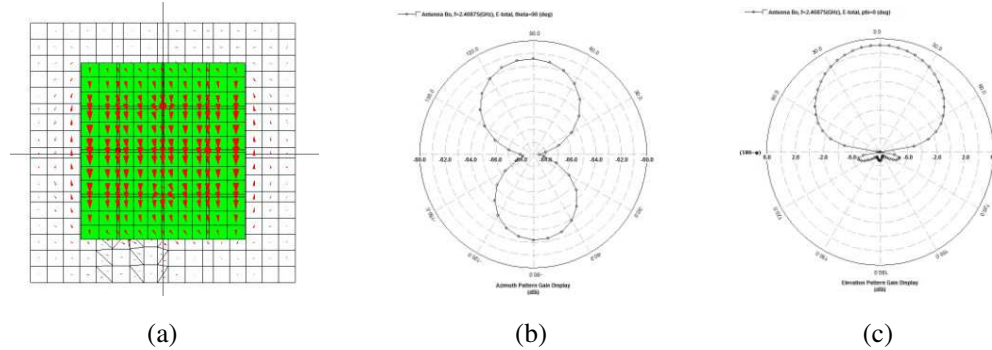


Figure 4: (a) Current distribution, (b) azimuth and (c) elevation power gain patterns for vertical polarization.

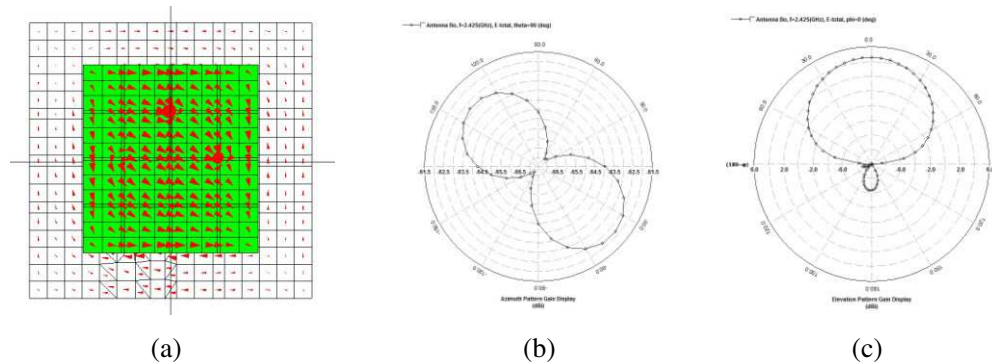


Figure 5: (a) Current distribution, (b) azimuth and (c) elevation power gain patterns for diagonal polarization.

in Fig. 5.

3.5. Right-hand Circular Polarization

RHCP mode (as well as LHCP and diagonal polarization modes) presents a fractional bandwidth of 0.41%, as it can be excited only between the frequency points where both S_{11} and S_{22} are below -10 dB. Antenna efficiency reaches a maximum of 63.2% and radiation efficiency a maximum of 68.5%. In Fig. 6, azimuth and elevation axial ratio graphs and azimuth and elevation power gain patterns are presented.

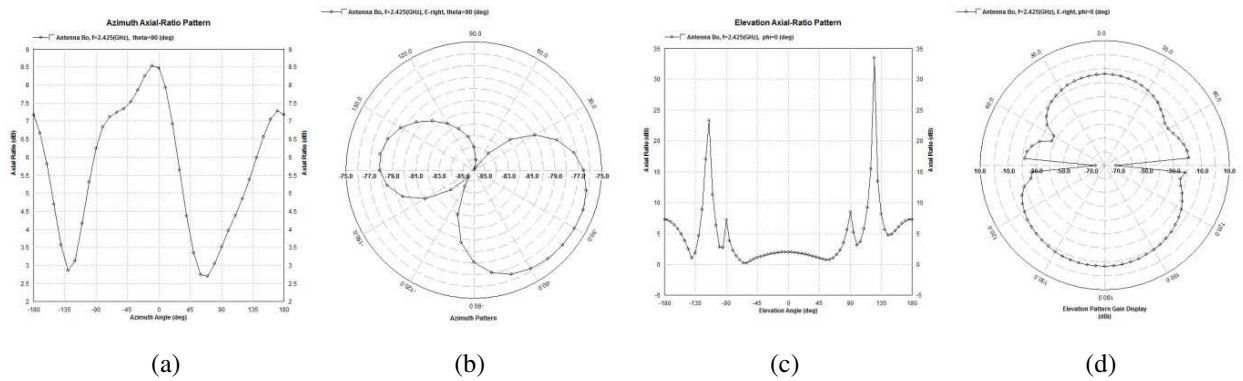


Figure 6: (a) Azimuth axial ratio, (b) azimuth power gain pattern, (c) elevation axial ratio and (d) elevation power gain pattern for RHCP.

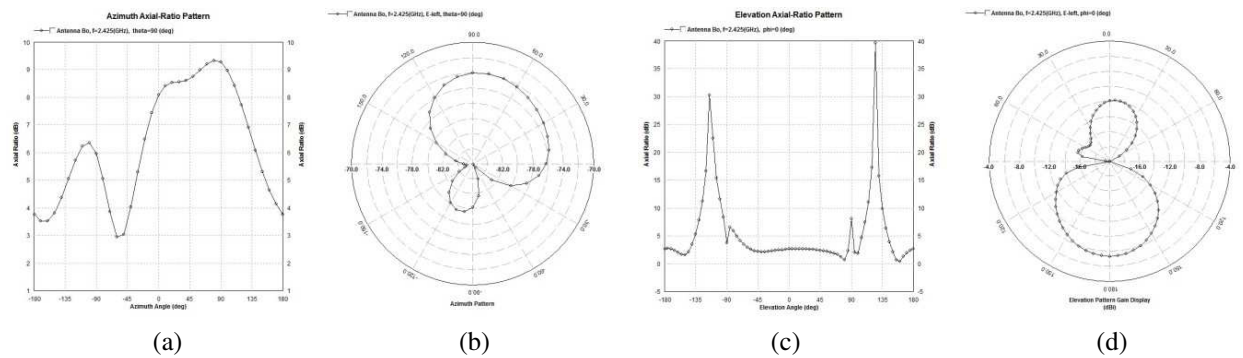


Figure 7: (a) Azimuth axial ratio, (b) azimuth power gain pattern, (c) elevation axial ratio and (d) elevation power gain pattern for LHCP.

As the azimuth power gain pattern exhibits a maximum of -76 dB, the corresponding axial ratio pattern is of little concern. On the contrary, the elevation pattern is quite uniform and the elevation axial ratio behaves well throughout the 3 dB bandwidth reaching a maximum of 7.5 dB, still remaining below 3 dB for most elevation angles of interest.

3.6. Left-hand Circular Polarization

The antenna efficiency reaches 59.7% for this case, and the radiation efficiency a maximum of 66.4%. Again, azimuth power gain pattern is negligible, and the elevation pattern is not as uniform as in the previous case. Yet still, the elevation axial ratio behaves compensatory for angles of interest, i.e., especially between -45° and 45° .

4. CONCLUSIONS

A novel patch antenna was designed and simulated. The novelty lies on the capability of polarization diversity over augmented bandwidth, reaching values of 1.82% for horizontal polarization. Bandwidth augmentation (i.e., for horizontal and vertical polarization mode) is achieved, as the pair of points exciting a specific mode are fed through a network which introduces a path inequality of 90° between them. Polarization diversity is achieved by using two voltage sources, each of them feeding a pair of specular points on the patch. Assigning the appropriate values to each source,

horizontal, vertical, diagonal, RHC or LHC polarization modes can be generated. Furthermore, all modes are well-matched and efficient throughout their corresponding bandwidth.

ACKNOWLEDGMENT

This research has been co-financed by the European Union (European Social Fund — ESF) and Greek national fund through the Operational Program “Education and Lifelong Learning” of the National Strategic Reference Framework (NSRF) — Research Funding Program: THALES. Investing in knowledge society through the European Social Fund.

REFERENCES

1. Xiong, J., Z. Ying, and S. He, “A broadband low profile patch antenna of compact size with three resonances,” *IEEE Trans. Antennas Propag.*, Vol. 57, No. 6, 1838–1843, Jun. 2009.
2. Kumar, G. and K. C. Gupta, “Directly coupled multiple resonator wideband microstrip antenna,” *IEEE Trans. Antennas Propag.*, Vol. 33, 588–593, Jun. 1985.
3. Wong, K. L. and Y. F. Lin, “Small broadband rectangular microstrip antenna with chip-resistor loading,” *Electron. Lett.*, Vol. 39, 1593–1594, 1997.
4. Garg, R., P. Bhartia, I. Bahl, and A. Ittipiboon, *Microstrip Antenna Design Handbook*, 534–538, Artech House, Boston, MA, 2001.
5. Koutinos, A. G., G. A. Ioannopoulos, M. T. Chryssomallis, and G. A. Kyriacou, “A dual-feed rectangular patch antenna for bandwidth enhancement,” *2014 Loughborough Antennas and Propagation Conference*, Loughborough, UK, Nov. 2014.
6. IEEE Std 802.11™-2012 (Revision of IEEE Std 802.11-2007), 2012.
7. Schaubert, A. D. H., F. G. Farrar, A. Sindoris, and S. T. Hayes, “Microstrip antennas with frequency agility and polarization diversity,” *IEEE Transactions on Antennas and Propagation*, Vol. 29, No. 1, Jan. 1981.

Design and Implementation of a Planar Slot Antenna for SSR

Maziar Hedayati, Gholamreza Askari, Parisa Moslemi, and Hamid Mirmohammad Sadeghi

Information and Communication Technology Institute (ICTI)
Isfahan University of Technology (IUT), Isfahan 84156, Iran

Abstract— A useful, low cost, low complexity, and one layer microstrip slot L band antenna for secondary surveillance Radar (SSR) application is presented. The printed circuit feed network is a rat-race divider to create sum and difference ports and sixteen unequal power dividers to satisfy the Chebyshev distribution. The feed network has an equally length parallel structure that create constant group delay in all output ports and wide frequency bandwidth. The suggested structure is a one-layer slot array of 2×8 slot elements that are fed with a microstrip corporate feed network. To improve total frequency bandwidth the slots are designed with unequal lengths. A substrate with low permittivity is used to decrease the side lobes. A 2:1 VSWR bandwidth of 9.4% is achieved with the presented geometry in simulation to cover the 1030 ± 10 MHz transmit and the 1090 ± 10 MHz receive frequency band. The antenna gain for the sum pattern is 18.5 dB and 19 dB at 1030 MHz and 1090 MHz, respectively with a 3 dB beam width of 52° in elevation and 9.5° in azimuth. The difference has a -19 dB null at the peak of the sum pattern and an acceptable pattern against the sum pattern for SSR applications. Furthermore, the antenna has no need of the back fill antenna to eliminate the back lobe, which is critical for SSR applications. Its low complexity structure makes it appropriate for many radar applications.

1. INTRODUCTION

The Secondary surveillance radar (SSR) mechanism is based on sending a pair of signals at the frequency of 1030 MHz for interrogation and receiving a pair of signals as an answer at 1090 MHz [1]. SSR antennas are built in the form of planar or cylindrical array [2]. Reflector and multi-layer antennas are the most common SSR antennas in the literatures that have some disadvantages like complexity and being bulky [3, 4]. One layer microstrip array antennas which is proposed in this work, are the useful antennas in mass production because of their advantages like easily printed, light weight and low cost which makes them suitable for radar applications. However they have some disadvantages like narrow bandwidth and high side lob level. To enhance the bandwidth, many attempts have been done in microstrip field. One method of increasing the bandwidth for the microstrip antennas is using stacked elements [5]. [6] proposed a stacked patch array of 1×8 elements with 14 dBi gain and the SLL of -14 dB, which is not enough low to provide the Side Lobe Suppression (SLS) for the SSR [1]. In addition using stacked element increase the complexity of the system. In this paper a slot array antenna for the secondary surveillance radar application is presented. The antenna structure against the stack patch antenna is very simple. The fed slot antenna could increase the bandwidth in addition of reducing the antenna size. However, the fed slot antennas produce back radiation. To omit the back-lobes in the microstrip antennas, a metallic box is used behind the antenna. This technique is used to enhance the performance of the proposed antenna against with standard SSR antenna. The feed network has an equally length parallel structure that create constant group delay in all output ports and so cause wide frequency bandwidth. At first the performance of the SSR is described. Then the proposed antenna parts such as: single element, the sum pattern, the difference pattern and the feed network is presented. Finally the simulation results using in 3D EM simulation software High Frequency Structure Simulator (HFSS) are presented. The substrate that is used in the design is Rogers RT Duroid5880 with the dielectric constant of 2.2 and the thickness of 0.787 mm. Also the conductor cladding is about 17 μm .

2. ANTENNA CONSIDERATIONS

The SSR uses three impulses P_1 , P_2 and P_3 for the interrogation. P_1 and P_3 are sent by a directional antenna and P_2 is sent after P_1 , by a special Omni directional antenna (Fig. 1). The configuration of these impulses provides the needed information for the transponder; with rational comparison between pulses P_1 and P_2 , the transponder will recognize whether the signal is sent by a main lobe or side lobe of the SRR antenna. In the case of sending by a main lobe, it will respond. Typically, if $P_1 > P_2 + 9$ dB the transponder will respond to the antenna but if $P_1 < P_2$ it will not respond. Otherwise, it will respond or not respond depending on the transponder characteristics.



Figure 1: The relative strengths of the impulses $P1$, $P2$ and $P3$, adapted from [10].

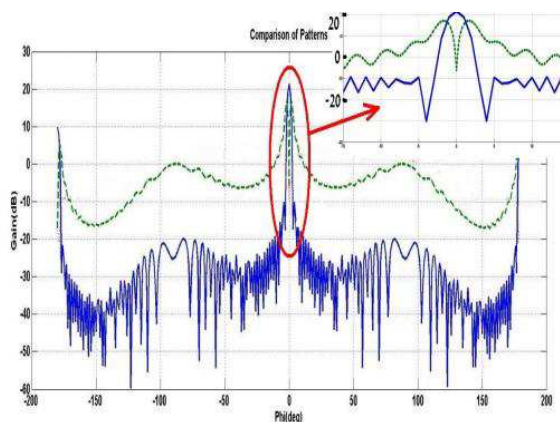


Figure 2: Typical Σ and Δ patterns.

The timing between pulses $P1$ and $P3$ shows the request content information [7]. The SSR antenna must contain of two special patterns: sum pattern (Σ) and difference pattern (Δ). Fig. 2 shows a typical sum and difference pattern. Two pulses $P1$ and $P3$ are sent by the sum pattern and pulse $P2$ is sent by the difference pattern. The Σ pattern is a directional pattern which should provide 14–16 dBi gain and 3 dB bandwidth of about 10° [1]. Typically, the sidelobe level of the Σ pattern is -20 to 30 dB [1]. To increase the accuracy, the beam width in azimuth should be narrow but in elevation should be wide to cover a large scan area. To increase the resolution in azimuth and also to enhance the dynamic range of the transponder receiver difference pattern has a null, as it is shown in Fig. 2.

3. ANTENNA DESIGN

3.1. Basic Element Design

The array element designed based on the requirement of frequency bandwidth, beam width, desired radiation patterns in E - and H -planes, compatible with microstrip structures and low mutual coupling for realizing an ultimate low side lobe pattern with vertical polarization. A slot resonated by a feed line proposed for array is shown in Fig. 3. To provide the characteristic impedance of 50 Ohms, the feed width considered 2.4 mm. The slot length (L_s) roughly is equal to $\lambda g/2$ to determines the resonate frequency at 1060 MHz [8]. As shown in Fig. 3, the slot size is 153×7.6 mm ($L_s \times W_s$). The parameter T , which is the distance from the end tip of the line to the slot (T), is equal to $\lambda g/4$ (34 mm). Finally, the L parameter, the offset from the end tip of the slot to the feed line achieved by optimization, about 42 mm. Figs. 4 and 5 show the simulation results of the slot antenna, performed by HFSS. Fig. 4 shows the parameter S_{11} of the slot element which is about -10 dB at 1.06 GHz. Fig. 5 shows the radiation pattern of the element. As discussed in the previous

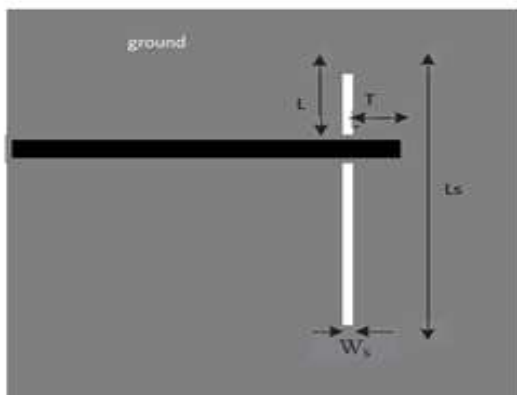


Figure 3: Microstrip fed slot antenna.

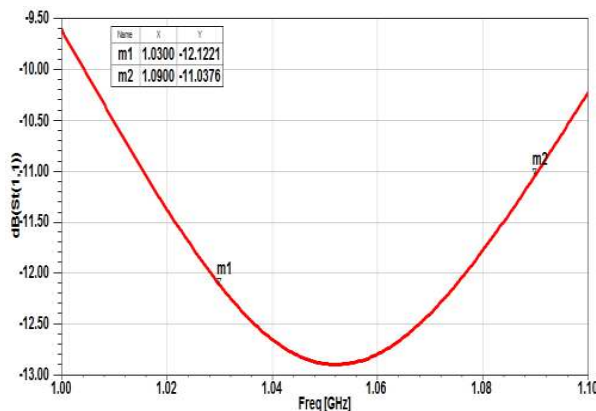


Figure 4: Return loss of the slot antenna.

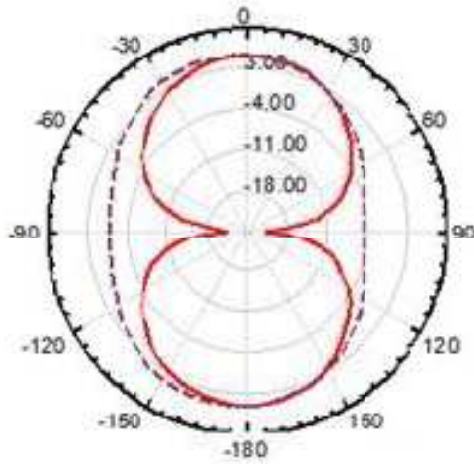


Figure 5: Radiation pattern of the slot antenna (the red line is $\phi = 0$ and the black line is $\phi = 90$).

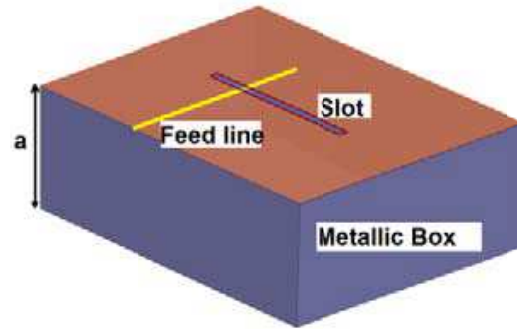


Figure 6: Metallic box behind the slot element.

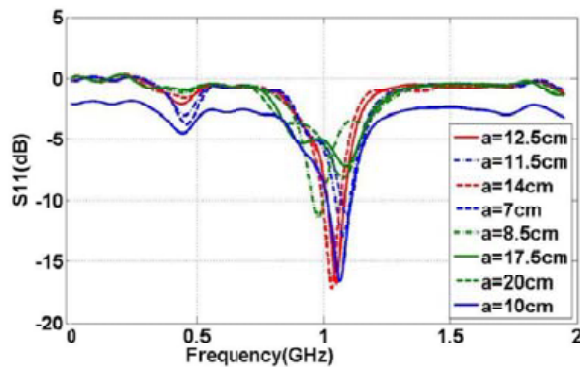


Figure 7: Optimization of the height of the metallic box against slot return loss.

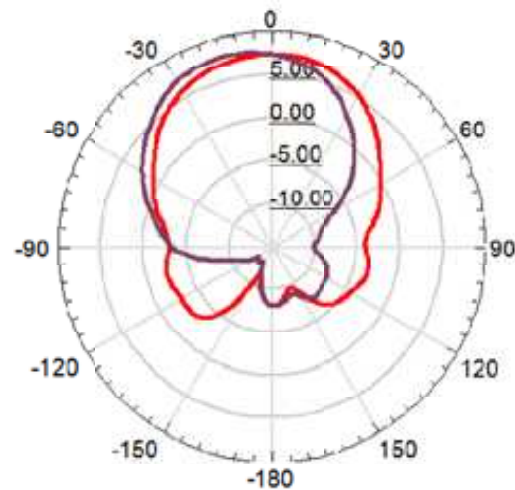


Figure 8: The single slot radiation pattern with the cavity of height 10 cm (the red line is $\phi = 0$ and the black line is $\phi = 90$).

section, sum pattern has to be a directional one. But this pattern has a back-lobe radiation around -3 dB. To improve the performance of the element, a back-lobe suppression technique is proposed by using a metallic box (Fig. 6). This box can eliminate the radiation from the back of the antenna by reflecting the backward radiation in the forward direction. The box height should be around $\lambda_0/4$ to reflect the back-lobe with 180° shift in phase. Fig. 7 shows the optimization process of the box height to obtain the best performance. 10 cm height resulted in minimizing the back-lobe and obtaining the S_{11} less than 10 dB at the 100 MHz bandwidth around the center frequency. Fig. 8 shows the radiation pattern of a single element after locating the metallic box. It shows that the back-lobe is minimized down to -17 dBc and the gain is improved up to 7 dB.

3.2. Array Design (Sum and Difference Pattern)

The design is considered a planar array with separable Dolph-Chebyshev distribution in which the elements are arranged in a rectangular grid, with a rectangular boundary. The array should be capable of generating both difference pattern as well as the sum pattern so an even number of elements should be chosen in each dimension. With the method which is discussed in [9], the number of elements are obtained 16 (2×8) with space of about 250 mm and 150 mm along X and Y axis respectively. The normalized Dolph-Chebyshev current distributions for -30 dB SLL are obtained as 1; 1.30; 1.78; 2.06; 2.06; 1.78; 1.30; 1.

To solve the frequency bandwidth limitation, the slot elements are designed with different length (about $\pm 5\%$ tolerances in length). The Δ pattern is obtained by feeding the left and right sides of the antenna with 180 degrees difference in phase which creates a null in broadside of the Δ pattern.

3.3. Feed Network

The series and parallel feed are two types of feeds architectures. The in-line feed array occupies the smallest space with the lowest insertion loss, but generally has the least polarization control and the narrowest bandwidth. In contrast the parallel feeds have more insertion loss but their bandwidth is more than series feeds. So in the array antenna, the parallel feed is chosen. The first power divider is a rat-race hybrid with equal power split to feed two antenna halves. A ratrace coupler is used to provide in phase and 180 out of phase dividing/combining to create sum and difference patterns. Then to feed the 2×8 elements, fourteen T-junction power dividers are used which create a 1×16 power dividing with Chebyshev distribution. Fig. 9 shows the width of each power divider calculated in Advanced Design System (ADS) to satisfy the currents calculated in previous section. All paths from sum ports to slot elements must have equal length because in this situation the parallel feed network has constant group delay and wide frequency bandwidth as a result. So the branch of the last power divider is blended to satisfy this condition which is shown in Fig. 10.

4. SIMULATION RESULTS

Figure 11 shows the radiation pattern of the complete array antenna at 1030 MHz considering the effect of coupling and the feed network. It shows 18.5 dB gain for the main Σ beam and 14 dB gain for the Δ beam. As it is shown the side lobe level of the Δ pattern is at least 4 dB more than Σ one in full azimuth coverage angle, which corresponds to the mentioned expectations. So it is not necessary to have back lobe antenna that is critical for SSR antennas. The SLL for the Σ pattern is optimized to be minimized down to -22 dB. Fig. 12 shows the radiation pattern of the array antenna at 1090 MHz with 19 dB gain for the main Σ beam and 15 dB gain for the Δ pattern. The side lobe level of the Δ pattern is also more than Σ one but it is not necessary for

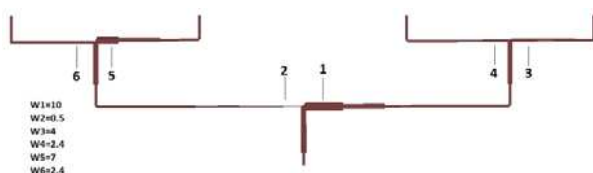


Figure 9: A part of feed network ($W1 = 10$ mm, $W2 = 0.5$ mm, $W3 = 4$ mm, $W5 = 7$ mm, $W6 = 2.4$ mm).



Figure 10: The last power divider schematic.

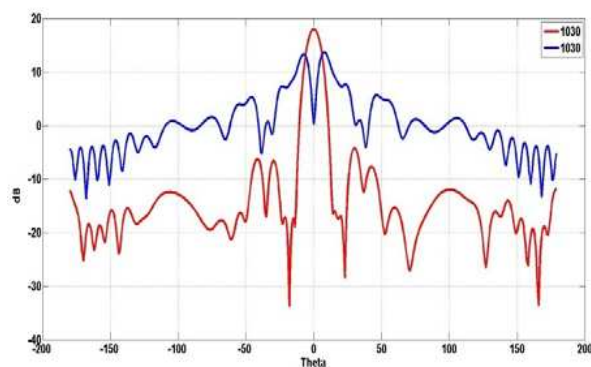


Figure 11: The radiation pattern of the array antenna with the center frequency of 1030 MHz.

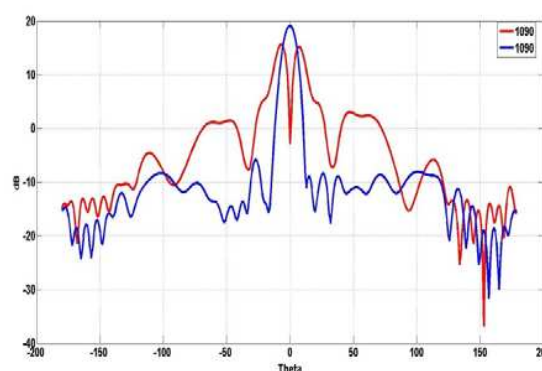


Figure 12: The radiation pattern of the array antenna with the center frequency of 1090 MHz.

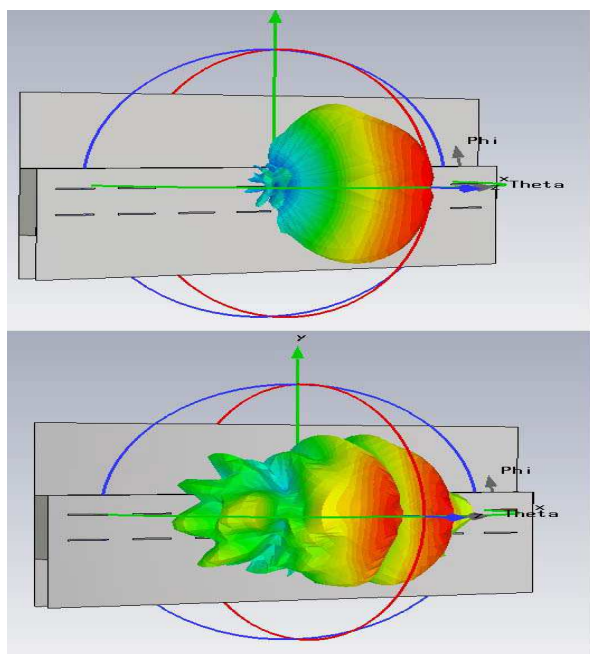


Figure 13: 3D sum and difference pattern of the array antenna at 1030 MHz.

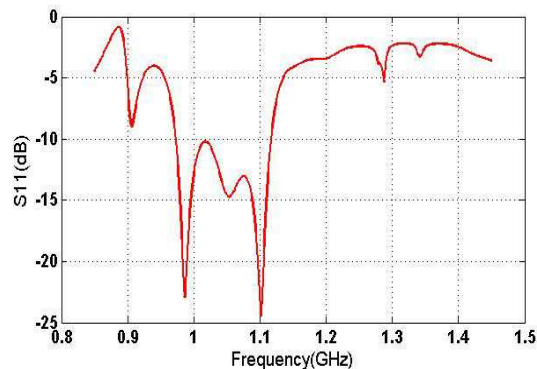


Figure 14: Simulated S_{11} of the 2×8 SSR antenna.

Table 1: Total characteristic of the proposed antenna vs goal values. The metallic box causes gain differences between desired and designed antenna.

Features	Unit	Designed Value	Goal Value
#Channels (Sum/Difference)	-	2	2
Frequency Range	MHz	$1030 \pm 5, 1090 \pm 5$	$1030 \pm 5, 1090 \pm 5$
Polarization	-	Vertical	Vertical
Sum Gain	dB	18.5	16
Sum Azimuth SLL	dB	-23	-25
Sum Azimuth BLL	dB	-28	-30
Difference Null	dB	19	20
Difference Coverage	dB	> 4	> 4
Sum Azimuth B.W	Degree	9.5	11
Sum Elevation B.W	Degree	52	50
Size	cm ³	$200 \times 10 \times 60$	
Gain at Elevation Angle ($-20^\circ, -40^\circ$) + 5 dB	> maximum Gain		
Gain at Elevation Angle (± 60) + 12 dB	< maximum Gain		
Gain at Elevation Angle (± 90) + 18 dB	< maximum Gain		
Gain at Elevation Angle (± 145) + 28 dB	< maximum Gain		
Back lobe + 30 dB	< maximum Gain		

difference pattern in 1090 MHz to cover sum at least 4 dB, because at this frequency the antenna has only receiving. Fig. 13 shows the 3D pattern of the array antenna in 1030 MHz. The return loss of antenna is shown in Fig. 14 which is better than -10 dB in the antenna bandwidth. The total characteristics of the desired and designed antenna are shown in Table which show close agreement.

5. CONCLUSION

A useful, one layer, low cost, low complexity, wideband 2×8 planar microstrip antenna array was presented to operate as SSR antenna in 1030–1090 MHz. The basic array element was designed and optimized by using microstrip fed slot antenna. The feed was designed with a ratrace and 14

power dividers. To improve the frequency bandwidth of the proposed antenna, the slot elements were considered unequal length and the parallel feed was designed to be constant group delay. Also to enhance the antenna gain and to reduce BLL a metallic box is used. As discussed, one of the most advantages of this antenna is no need to a back fell antenna. The antenna gain for the sum pattern was 18.5 dB and 19 dB at 1030 MHz and 1090 MHz, respectively with a 3 dB beam width of 52° in elevation and 9.5° in azimuth. The difference has a -19 dB null at the peak of the sum pattern. A 2:1 VSWR bandwidth of 9.4% is achieved to cover the 1030 ± 10 MHz transmit and 1090 ± 10 MHz receive band.

REFERENCES

1. Vladimir, S., et al., "Secondary surveillance radar antenna [antenna designer's notebook]," *Antennas and Propagation Magazine*, IEEE 55.2, 2013.
2. Kumar Sharma, A., C. K. Kumar, and A. Mittal, "EM coupled L-band antenna array for secondary surveillance radar," *Europea Microwave Conference, 2009, EuMC 2009*, 1465–1467, Sep. 29, 2009–Oct. 1, 2009.
3. Foster, P. R., M. W. S. Grigson, and C. W. R. Wheatley, "D band IFF for army air defence systems," *Radar 97 (Conf. Publ. No. 449)*, 705–709, Oct. 14–16, 1997.
4. El, Y. M., M. Himdi, and J. P. Daniel, "Aperture-coupled microstrip antenna for dual frequency operation," *Electron. Lett.*, Vol. 29, 1506–1508, 1993.
5. Lee, R. Q., K. F. Lee, and J. Bobinjak, "Characteristic of a two layer electromagnetically coupled rectangular patch antenna," *Electron. Lett.*, Vol. 23, No. 20, 1070–1072, Sep. 1987.
6. Yashimura, Y., "A microstrip slot antenna," *IEEE Trans. Antennas Propagat.*, Vol. 29, 2–24, Jan. 1981.
7. Sharma, S. K., N. Jacob, and L. Shafai, "Low profile wide band slot antenna for wireless communications," *Proc. IEEE AP-S Int. Symp.*, 390–393, 2002.
8. Stevens, M. C., *Secondary Surveillance Radar*, Artech House, 1936.
9. Elliott, R. S., *Antenna Theory and Design*, John Wiley & Sons, Inc., 1998.

Design And Analysis of Uniplanar Compact Electromagnetic Bandgap Structures

Shivam Gautam¹, Komalbir Kaur¹, N. S. Raghava¹, and Asok De²

¹Delhi Technological University, India

²NIT Patna, India

Abstract— A uniplanar compact electromagnetic bandgap (UCEBG) antenna and its performance analysis is presented in this paper. The antenna consists of a rectangular patch element on a dielectric substrate, micromachined with a layer of periodic unit electromagnetic bandgap (EBG) structures below the dielectric. This EBG improves the antenna's efficiency and increases its compactness, enabling it to perform better at a lower frequency. The whole structure is backed by a ground plane with an air gap of 9 mm.

1. INTRODUCTION

Microstrip Antennas are one of the most widely used type of antennas owing to their low cost and compactness. However, their low gain, efficiency and bandwidth lead to their poor performance [1]. By etching EBG structures on one side of the substrate, the performance parameters like gain, efficiency and bandwidth can be improved, in turn, leading to better operation of the antenna [2].

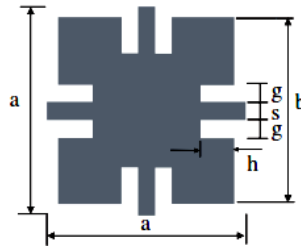


Figure 1: Unit EBG structure.

EBG structures are 3-D periodic objects that prevent the propagation of the electromagnetic waves in a specified band of frequency for all angles and for all polarization states [3]. Initial interest in the development of EBG structures was in the sphere of optics [4], but as these structures are readily scaleable and applicable to a wide range of frequencies, over the years there has been an increasing interest in the applications of these structures in microwave and millimeter wave regions. Applications of the EBG phenomena in microwave region improves the radiation pattern of antennas [5], increase the output power and efficiency of power amplifiers [6]. Apart from this, EBG structures are easy to fabricate, low cost and compatible with prevalent planar circuit technology [7]. The shape of a unit of the EBG structure may be hexagonal as in [8] or cross shaped as in [9]. The shape presented in this paper is a square pad with connecting branches [10].

2. ANTENNA DESIGN

The EBG plane is formed by periodic repetitions of a unit EBG structure depicted in Figure 1. The dimensions of the unit EBG structure, depicted in Figure 1, are as follows: $a = 11.2$ mm, $b = 10.5$ mm, $s = 1$ mm and $g = 0.9$ mm.

The antenna is composed of a reflector, an EBG plane, a dielectric substrate and a radiating patch. Figure 2(a) depicts the top view of the antenna. The length of each side of the ground plane is L which is equal to 191.2 mm. The antenna consists of a 17×17 matrix of unit UCEBG structure. The side view of the antenna is depicted in Figure 2(b). The substrate between the UCEBG layer and the radiating patch is of 0.7 mm thickness and a dielectric constant of 6.15. The reflector is introduced at the back end of the antenna to reduce the back lobe. The air gap between the reflector and the UCEBG layer is 9 mm, which has been determined by varying its position with respect to the substrate [2]. The radiating patch element is of dimension 70 mm \times 54 mm.

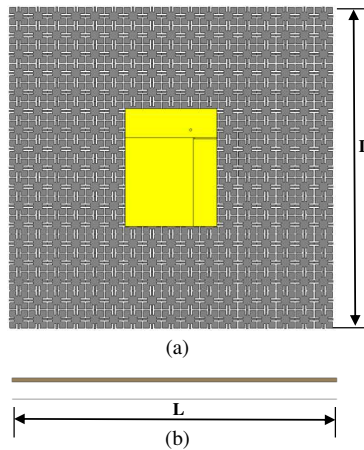


Figure 2: (a) Top view of UCEBG. (b) Side view of UCEBG.

3. RESULTS AND DISCUSSIONS

The antenna is simulated using the software Computer Simulation Technology (CST) Microwave Studio. The results obtained from the simulation show that the central frequency of operation of the antenna is 1.556 GHz. The antenna has a Voltage Standing Wave Ratio (VSWR) of 1.06 at the operating frequency. The graphical representation of reflection coefficients are shown in Figure 3 whereas the VSWR is depicted in Figure 4.

The polar plot representation of the antenna is depicted in Figure 5(a). The three dimensional depiction of radiation pattern of the antenna is shown in Figure 5(b). The antenna has a gain of 5.58 dB at $\theta = 1^\circ$, $\phi = 0^\circ$.

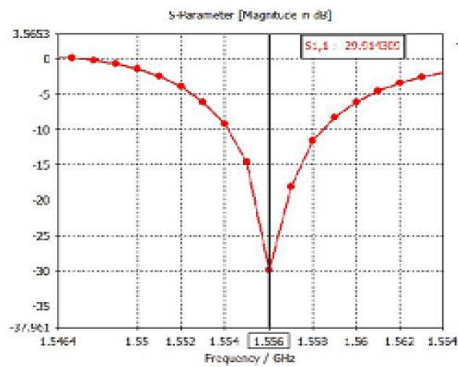


Figure 3: Reflection coefficient parameters.

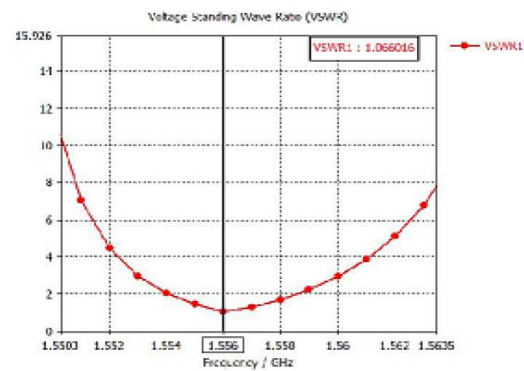


Figure 4: VSWR parameters.

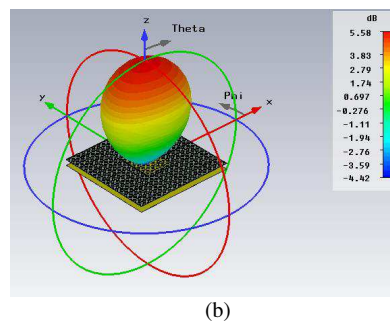
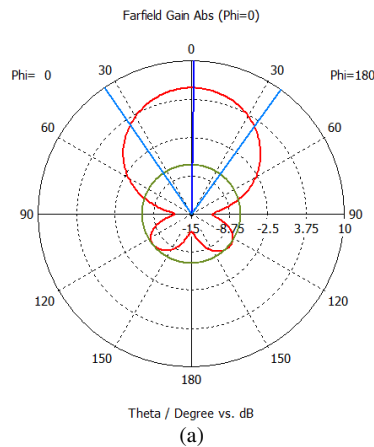


Figure 5: (a) Polar plot at $\phi = 0^\circ$. (b) Three dimensional depiction of radiation pattern.

4. CONCLUSION

The Uniplanar Compact Electromagnetic Bandgap Antenna was presented in this paper. The introduction of the EBG layer increases the compactness of the antenna and makes it possible to integrate with a wide range of applications. The structure is compact and the operational parameters of the antenna such as reflection coefficient, gain and VSWR are optimal to be integrated with suitable applications such as road vehicle communication systems [11].

REFERENCES

1. Balanis, C. A., *Antenna Theory: Analysis and Design*, John Wiley & Sons, Inc., 1997
2. Raghava, N. S. and A. De, "Effect of air gap width on the performance of a stacked square electronic band gap antenna," *IJMOT*, Vol. 4, No. 5, 315–317, Sep. 2009.
3. Rahmat-Samii, Y. and H. Mosallaei, "Electromagnetic band-gap structures: Classification, characterization and applications" *Proc. Inst. Elect-Eng. — ICAP Symp.*, 560–564, Apr. 2001.
4. Yablonovitch, E., "Inhibited spontaneous emission in solid-state physics and electronics," *Phys. Rev. Lett.*, Vol. 58, No. 20, 2059–2062, May 1987.
5. Ellis, T. J. and G. M. Rebeiz, "MM-wave tapered slot antennas on micromachined photonic bandgap dielectrics," *Proc. IEEE MTT-S Int. Microwave Symp. Dig.*, 1157–1160, Jun. 1996.
6. Radisic, V., Y. Qian, and T. Itoh, "Broadband power amplifiers using dielectric photonic band gap structure," *IEEE Microw. Guided Wave Lett.*, Vol. 8, 13–14, Jan. 1998.
7. Chang, C. C., Y. Qian, and T. Itoh, "Analysis and applications of uniplanar compact photonic bandgap structures," *Progress In Electromagnetic Research*, Vol. 41, 211–235, 2003.
8. Choudhary, A., N. S. Raghava, A. Biswas, and A. De, "A highly efficient rectangular microstrip antenna with hexagonal holes as an electromagnetic bandgap structure in the ground plane," *Proc. of International Conference on Microwave*, 152–153, 2008.
9. Raghava, N. S., A. De, N. Kataria, and S. Chatterjee, "Stacked patch antenna with cross slot electronic band gap structure," *International Journal of Information and Computation Technology*, Vol. 3, No. 5, 1–4, 2013.
10. Yang, F. R., K. P. Ma, Y. Qian, and T. Itoh, "A uniplanar compact photonic-bandgap (UC-PBG) structure and its applications for microwave circuits," *IEEE Trans. Microwave Theory Tech.*, Vol. 47, 1509–1514, Aug. 1999.
11. Raghava, N. S. and A. De, "Photonic bandgap stacked rectangular microstrip antenna for road vehicle communication," *IEEE Trans. Antennas and Wireless Propagation Letters*, Vol. 5, 421–423, Dec. 2006.

A Wide Stopband Filter with Source-load Coupling Technique

Kwok-Keung Chon¹, Ching-Jui Wu¹, Feng-Lin Jenq², Hong-Yu Jhuang¹, and Shih-Fong Chao¹

¹Department of Microelectronics Engineering, National Kaohsiung Marine University, Taiwan

²Department of Electronic Engineering, Far East University, Taiwan

Abstract— In this paper, a wide stopband bandpass filter using source-load coupling technique is proposed. With the source-load coupling structure, multiple transmission zeros are generated to suppress the harmonic responses in the stopband. By adjusting the gap space between the input/output feed lines, the locations transmission zeros can be controlled. Moreover, the open stub of the input/output feed lines are also used to generate transmission zeros in the stopband. In this design, stepped-impedance resonators (SIR) are utilized to minimize the overall circuit size and control the harmonic frequencies. The impedance and length ratios of the SIR are determined to move its first harmonic to a higher frequency. The center frequency of the filter is 2.45 GHz, and the stopband rejection is higher than 30 dB from 2.9 GHz to 13.36 GHz.

1. INTRODUCTION

Bandpass filter with small size and high performance is demanded in modern wireless communication systems. A second-order bandpass filter is a good candidate for low-loss applications, because the resonators are few in number. But the steepness of the skirts near the passband is not satisfied due to its low-order response. Moreover, the distributed resonators result in spurious responses in the stopband. In [1], a defected ground structure (DGS) is proposed to improve the stopband response, but it needs additional backside fabrication process and occupies large area. Cross-coupled technique is used to generate tunable transmission zeros to improve the stopband responses [2]. Source-load coupling technique is used generate transmission zero near the passband to improve the skirt-selectivity of the filter in [3].

The proposed filter is realized by two coupled stepped-impedance resonators (SIRs) with source-load coupling. The source-load coupling formed by the input/output feed lines can generate multiple controllable transmission zeros. By adjust the I/O coupling gap, the transmission zeros can be adjusted to suppress the harmonic response. Furthermore, the upper and lower arm of the I/O feed lines can also generate transmission zeros to improve the stopband performance. The circuit features small circuit size and wide stopband rejection. The center frequency of the filter is 2.45 GHz with stopband rejection higher than 30 dB from 2.9 GHz to 13.36 GHz.

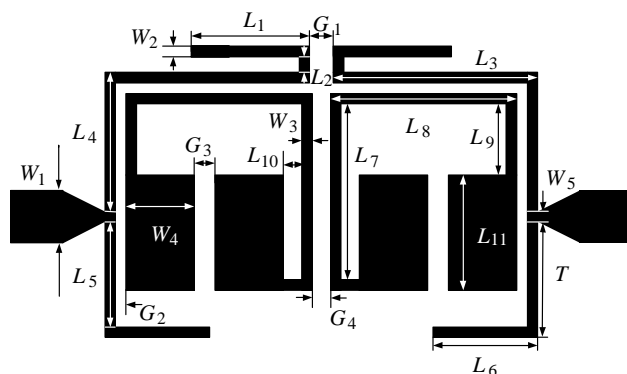


Figure 1: Layout of the bandpass filter with source-load coupling. $L_1 = 4.5$, $L_2 = 0.6$, $L_3 = 7.8$, $L_4 = 4.9$, $L_5 = 4$, $L_6 = 4$, $L_7 = 6.7$, $L_8 = 7.1$, $L_9 = 2.7$, $L_{10} = 0.7$, $L_{11} = 4.4$, $W_1 = 1.8$, $W_2 = 0.4$, $W_3 = 0.4$, $W_4 = 2.6$, $W_5 = 0.4$, $G_1 = 0.9$, $G_2 = 0.4$, $G_3 = 0.8$, $G_4 = 0.7$, $T = 4.4$ (unit: mm).

2. CIRCUIT DESIGN

Figure 1 is the circuit schematic of the proposed bandpass filter, which is composed by two SIRs with a feed structure having line width W_2 and space G_2 . Especially, the input and output feed lines are bent to form a small coupling gap G_1 to realize the source-load coupling. Stepped-impedance

resonators (SIR) have the advantages of controlling the harmonic resonance frequencies [4]. In this design, the impedance ratio and the length ratio of the SIR are determined to have its second and third harmonic resonances located at $2.6f_0$ and $4.1f_0$, respectively, where f_0 is the fundamental frequency of the SIR. This bandpass filter is designed to have a second-order Butterworth response with a center frequency of $f_0 = 2.45$ GHz and a fractional bandwidth (FBW) of 5.5%. The lumped circuit element values of the low-pass prototype filter are $g_0 = 1$, $g_1 = 1.4142$, $g_2 = 1.4142$, and $g_3 = 1$. The corresponding quality factor Q_e and coupling coefficient M_{12} can be obtained by

$$Q_e = \frac{g_1}{FBW} = 25.7$$

$$M_{12} = \frac{FBW}{\sqrt{g_1 g_2}} = 0.038$$
(1)

where M_{12} represents the coupling coefficient between the two coupled SIRs, and Q_e is the external quality factor associated with the I/O coupling. Figure 2(a) shows the trend of quality factor Q_e versus tapping position T under different values of G_2 . According to this figure, $T = 4.4$ mm and $G_2 = 0.4$ mm are chosen to have $Q_e = 26$. Figure 2(b) is the simulated coupling coefficient M_{12} versus the space G_4 . These results are extracted by the EM software Sonnet.

Figure 3 is the simulation result of the filter in Figure 1. It can be observed that total ten transmission zeros (TZ_1 - TZ_{10}) are generated. It is known that coupled lines with capacitive and inductive loads at one end can produce controllable transmission zeros [6, 7]. In this circuit, TZ_1 and TZ_8 are resulted by the coupled line section L_7 loaded with the open stub L_{11} . The low-frequency zero TZ_1 is generated when the loaded open stub is capacitive, and the transmission zero condition of TZ_8 is satisfied while the loaded open stub is inductive at a higher frequency. The equivalent circuit of gap space G_1 that forms source-load coupling in Figure 1 can be modeled as a capacitance C_g [3]. The locations of the transmission zeros generated by the source-load coupling

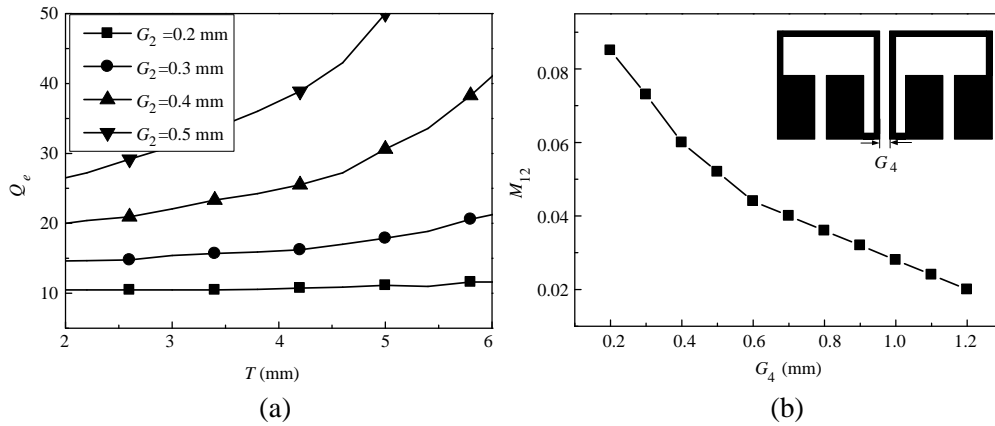


Figure 2: (a) Simulated Q_e versus tapping position T , and (b) M_{12} versus gap space G_4 at 2.45 GHz.

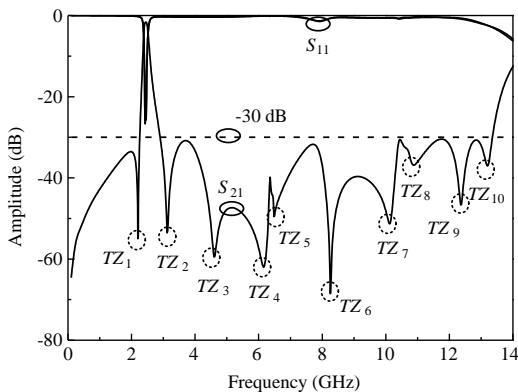


Figure 3: Simulation result of the proposed filter.

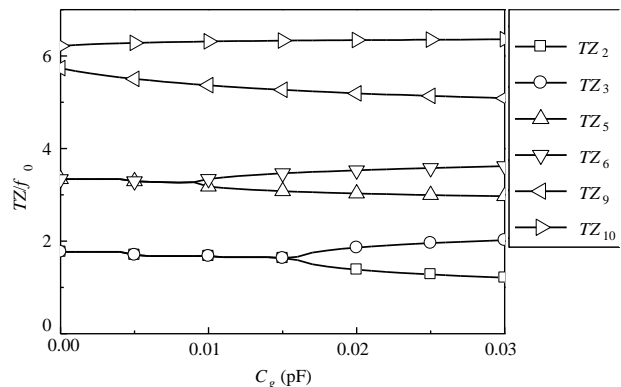


Figure 4: Transmission-zero frequencies versus gap capacitance C_g .

can be controlled by adjusting the gap space G_1 . Figure 4 shows the relations of the locations of the transmission zeros versus different values of C_g . It is seen that the three transmission zero pairs TZ_2 - TZ_3 , TZ_5 - TZ_6 , and TZ_9 - TZ_{10} split away from each other as C_g increases. Figures 5(a) and (b) show the transmission zeros resulted by the upper and lower arms of the I/O feed lines. The upper arm is composed by line sections of $L_1 + L_2 + L_3 + L_4$, and the lower arm is composed by $L_5 + L_6$. The zeros occur at the frequencies when the length equals to $(2n + 1)\lambda/4$. Thus, these zeros can be moved to lower frequencies by increasing their lengths. It is noted that once you change the line lengths of the I/O feed lines, the external quality factor Q_e will be slightly changed, and some iterations might be needed in the design process.

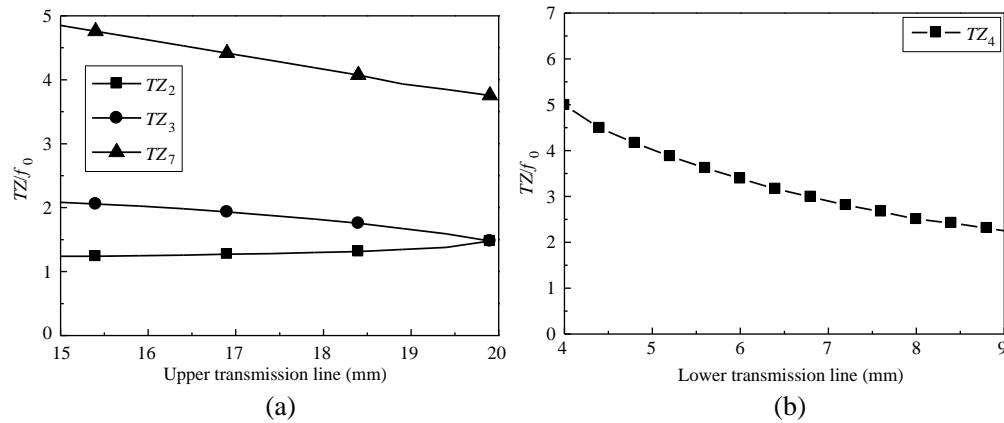


Figure 5: Transmission-zero frequencies versus the length of the input/output coupling line. (a) Upper arm and (b) lower arm.

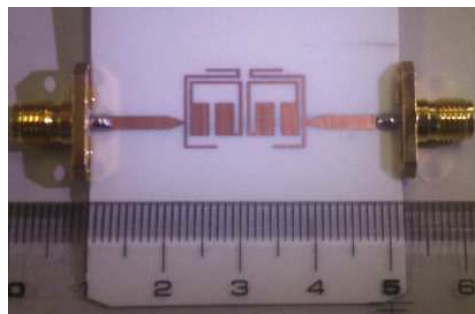


Figure 6: Photograph of the fabricated filter.

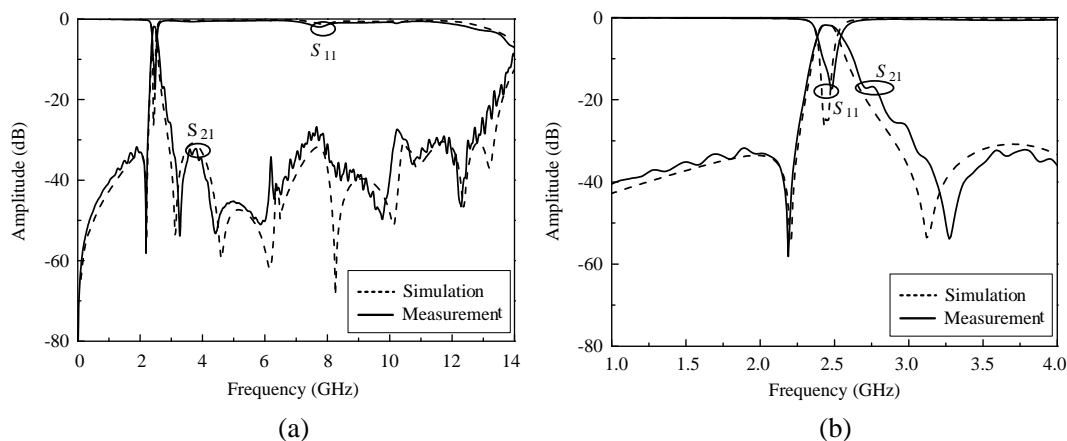


Figure 7: Measured and simulated results of the filter. (a) Wideband response and (b) narrow-band response.

3. SIMULATION AND MEASUREMENT RESULT

The filter is fabricated on the RO4003C substrate with $\epsilon_r = 3.41$, $h = 0.8$ mm, and $\tan \delta = 0.0027$. Figure 6 is the photograph of the fabricated filter. It occupies a circuit area of $0.15\lambda_g \times 0.22\lambda_g$, where λ_g is the guided wavelength of the center frequency. The measured and simulation results is shown in Figure 7. The measured center frequency is 2.45 GHz with a FBW of 5.67%, an insertion loss of 1.63 dB, and the stopband rejection better than 30dB from 2.91 GHz to 13.36 GHz.

4. CONCLUSION

In this paper, a wide stopband bandpass filter with source-load coupling is realized. The filter is composed by two coupled SIRs with coupled-line coupling structure. Transmission zeros are created by the input/output source-load coupling, the capacitive/inductive loaded coupled line, and the quarter-wavelength open stub. The center frequency of the filter is 2.45 GHz, and the stopband rejection is higher than 30 dB from 2.9 GHz to 13.36 GHz. The circuit area is $0.15\lambda_g \times 0.22\lambda_g$.

REFERENCES

1. Chen, H.-J., T.-H. Huang, C.-S. Chang, L.-S. Chen, N.-F. Wang, Y.-H. Wang, and M.-P. Hounq, "A novel cross-shape DGS applied to design ultra-wide stopband low-pass filters," *IEEE Microwave and Wireless Components Letters*, Vol. 16, 252–254, May 2006.
2. Tu, W.-H., "Compact double-mode cross-coupled microstrip bandpass filter with tunable transmission zeros," *IET Microwaves, Antennas & Propagation*, Vol. 2, No. 4, 373–377, Jun. 2008.
3. Dai, G., Y. Guo, and M. Xia, "Design of compact bandpass filter with improved selectivity using source-load coupling," *Electronics Letters*, Vol. 46, No. 7, 505–506, Apr. 2010.
4. Makimoto, M. and S. Yamashita, "Bandpass filters using parallel coupled stripline stepped impedance resonators," *IEEE Transactions on Microwave Theory and Techniques*, Vol. 28, No. 12, 1413–1417, Dec. 1980.
5. Tsai, C.-M., S.-Y. Lee, and H.-M. Lee, "Transmission-line filters with capacitively loaded coupled lines," *IEEE Transactions on Microwave Theory and Techniques*, Vol. 51, No. 5, 1517–1524, May 2003.
6. Deng, P.-H., Y.-S. Lin, C.-H. Wang, and C. H. Chen, "Compact microstrip bandpass filters with good selectivity and stopband rejection," *IEEE Transactions on Microwave Theory and Techniques*, Vol. 54, No. 2, 533–539, Feb. 2006.
7. Chao, S.-F., "Microstrip bandpass filters with series-LC resonator loaded coupled lines," *Microwave and Optical Technology Letters*, Vol. 55, No. 6, 1273–1276, Jun. 2012.

Analysis and Implementation of a Dual Mode Cavity Band Pass Filter

Zohre Pourgholamhossein, Fattah Talaei,
Gholamreza Askari, and Hamid Mirmohammad Sadeghi

Microwave and Antenna Group, Information and Communication Technology Institute (ICTI)
Isfahan University of Technology (IUT), Isfahan 84156, Iran

Abstract— In this paper a compact simple structure x-band dual mode cavity band pass filter using rectangular waveguide is presented. A cavity resonator is implemented to provide a narrow band pass filter at microwave frequency. Coaxial line probes for excitation is considered. A single cavity resonator is designed to generate a degenerate resonance of two orthogonal modes (TE_{101} and TE_{011}), enabling dual-mode operation. Using dual mode cavities that support twodegenerate resonances reduces the number of physical cavities. This improvement of compact size and weight of the filter are major advantages Also, using cross coupling technique allows to produce transmission zeros near the stop band and hence improving filter selectivity In order to couple of resonators (orthogonal modes), small perturbation by small deformation of boundary is designed. This perturbation can optimize bandwidth of the pass band to desired values. By this technique the bandwidth can be enhanced to more than 6 times of single dual mode structure. Also screw is used for tuning the resonance frequency of dual mode filtering response without disturbing the coupling of the degenerate cavity modes. A prototype is designed to operate at 9050 MHz. Simulated and experimental results are provided. The insertion loss is about 0.5 dB, return loss is better than 12.5 dB and 3 dB fractional bandwidth is about 0.66%.

1. INTRODUCTION

Microwave filters play an important role in almost every RF-microwave communications system. In communication system, narrowband filters are essential components to reject the interference signals. Therefore it is necessary to utilize high Q resonant circuits to achieve a narrow bandwidth in the pass band at high frequency. Microwave band pass filters have been typically implemented using waveguide technology or cavity due to low loss, high quality factors, narrow bandwidth and high power handling capabilities [1]. On the other hand, waveguide filters are massive and heavy. A solution has been done to reduce the size and weight of filters involves using dual mode cavities that support two degenerate resonances. Therefore, to reduce the number of physical cavities, dual mode or triple mode resonators are often employed. The advantages of these filters are the fewer number of cavities and improved performance. The first working multi-mode cavity microwave filter has been introduced by Li [2]. Elliptic dual mode filters for space applications were introduced by Atia and Williams [3]. Designs in other methods were reported by many authors [4, 5]. In addition the transmission line must be coupled together. In the coaxial case, the probe excitation is carried out in the cavity resonator by introducing the probe inside the cavity. This paper presents a structure of the dual mode rectangular cavity filter using coaxial probes for excitation. By using cross coupling technique with perturbation theory, transmission zeros in the stop band are realized, so the shape factor can be improved. Also, by this technique, bandwidth of pass band can be optimized. On the one hand, cross coupled filters are difficult to tune, due to couplings affect in the filter In section II design procedure are expressed. Also geometry and prototype values are discussed. The concept of dual mode cavity resonator is explained in Section 2.1. In Section 2.2 probe excitation is designed to excite resonance modes of the cavity filter. Moreover, direct and indirect coupling dual-mode cavity resonator filters are introduced. In Section 2.3 this technique is optimized to produce coupling resonance modes of direct and cross coupling. In addition, the realization of flexible bandwidth is discussed. In Section 3.1 simulation results are presented. The procedure to control and tune the resonant frequency is shown in Section 3.2 and the feasibility of realizing the filter has been validated with the experimental data (Section 3.3). Finally conclusion is drawn in Section 4.

2. DESIGN PROCEDURE

2.1. Dual Mode Cavity Resonator

Detailed design procedures of cavity filters can be used in several texts [1, 6]. A rectangular cavity resonator is a rectangular waveguide shorted at both ends ($z = 0$, $z = L$) as shown in Fig. 1(a).

Dual-mode resonators have been widely used to realize many RF/microwave filters [7–9]. A main feature and advantage of this type of resonator is that each of dual mode resonators can be used as a doubly tuned resonant circuit, and therefore the number of resonators required for a n -degree filter is reduced by half, resulting in a compact filter configuration [1]. The simplest dual mode filter is the two pole band pass filter using a single dual mode resonator. Fig. 1(b) shows the equivalent circuit of the dual mode resonator. This type of line resonator can support a pair of degenerate modes that have the same resonant frequencies.

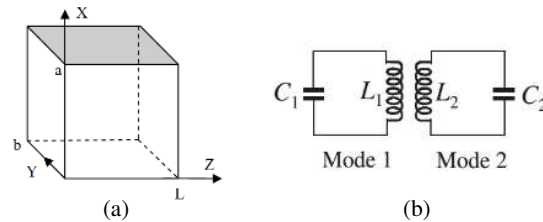


Figure 1: (a) A rectangular cavity. (b) Equivalent circuit of the dual-mode resonator.

The EM fields inside the cavity can be considered in terms of TE. Therefore, the two fundamental modes, TE_{101} and TE_{011} , are a pair of the Degenerate modes. Excitation probes position and dimensions a , b , L can be selected such that TE_{101} and TE_{011} resonate and TM_{110} does not resonate. With choosing $a = b$ (assuming the same value for two dimension of cavity) the resonance frequencies of these modes are:

$$f_{101} = f_{011} = \frac{c}{2\sqrt{\epsilon_r}} \sqrt{\left(\frac{1}{a}\right)^2 + \left(\frac{1}{L}\right)^2} \quad (1)$$

Both the degenerate modes are excited and coupled to each other, which causes resonance frequency

2.2. Probe Excitation for TE Modes

To excite a particular mode, the cavity must be properly coupled to an external source. To obtain maximum power transfer, the resonator must be matched to the feed at the resonant frequency. Fig. 2 shows the coax to waveguide feed. Since a dual mode rectangular waveguide cavity filter operates in the TE_{101} and TE_{011} modes, the position of the probes must not be in the symmetric line. For excitation of first resonant mode (TE_{101}), the probe should be orthogonal to “ xz ” plane that means the center of probe is along the electric field distribution as shown in Fig. 2(a). And for the second resonant mode (TE_{011}) it is located orthogonal to “ yz ” plane (Fig. 2(b)). On the one hand TE_{101} and TE_{011} modes have one half wave length variations in the $x-z$ and $y-z$ directions respectively. Also the positions of first and second center probes from side walls along x and y axial (L_i) can be carried out by following the technique described in [11], it is about one quarter wavelength at the resonant frequency which is the located of the shorted plane. The other position of the probe (t_i) are optimized. Therefore a direct coupling between input and output ports is created.

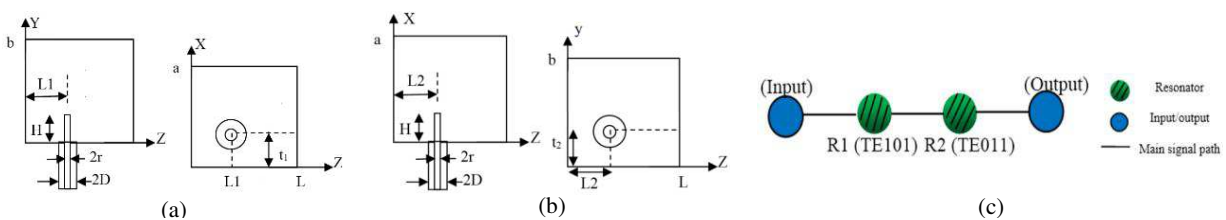


Figure 2: The geometry of the excited cavity by two probes. (a) TE_{101} mode. (b) TE_{011} mode (side view & top view). (c) Typical coupling structures of dual mode cavity filter.

Figure 2(c) shows the general coupling structure of the 2-order cavity filter, where each node represents a resonator, the full lines indicate the direct couplings. In this coupling structure, the resonators are numbered 1 to N ($N = 2$) with the input and output ports located in resonators 1 and 2, respectively. In this case the frequency response of the filter cannot be accurately predicted and

cut and try process to determining the position of t_i is difficult and time consuming. Generally the disadvantage of the structure is that there is weakly coupling between two modes and the direct coupling do not create a transmission zero in the insertion loss response of the filter. Also the maximum relative bandwidth can be achieved is about 0.1%. Therefore to obtain strong coupling, transmission zeros and more bandwidth, another design is introduced. As known, dual mode cavity filter uses two orthogonal degenerate “101” and “011” thus “xz” and “yz” plane are the location of probes. As it is shown in Fig. 3 the common axis of these planes is “z” axis and probe should be place on the middle of the axis, that is, the probe is inserted from the broad dimension of the cavity and it should be kept at the place inside the cavity where electric field is maximum. Other coordinate of probes position along “x” and “y” directions of two TE₁₀₁ and TE₀₁₁ modes are quarter wavelength of resonant frequency. Thus only the TE₁₀₁ and TE₀₁₁ modes propagate in the waveguide which are matched in both directions. In this design there are direct and cross coupling between modes. Both direct and cross coupling are realized by adding perturbation that is discussed in next section. Actually without perturbation, coupling between two resonators are not provided. By this technique, in addition to realize direct and cross coupling, the bandwidth would be able increase to arbitrary values.

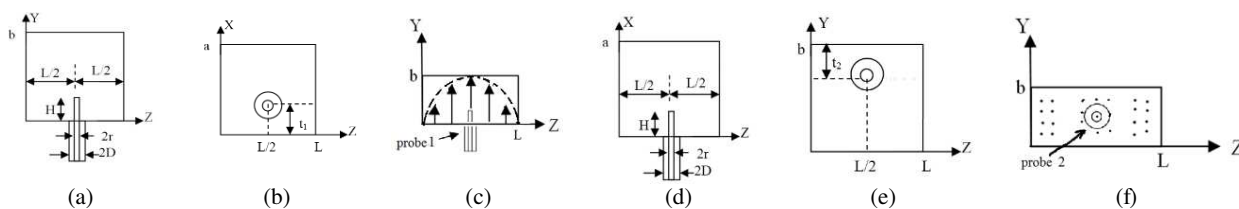


Figure 3: The geometry of the excited cavity by two probes (TE₁₀₁ and TE₀₁₁ modes). (a), (d) Side view. (b), (e) Top view. (c), (f) Electric standing wave patterns.

2.3. Perturbation Study

Cavity perturbation theory describes method to change the performance of a cavity resonator. These performance changes are caused by a small foreign object into the cavity or a small deformation of its boundary. When a resonant cavity is perturbed, i.e., when foreign object with distinct material properties is introduced into the cavity or when a general shape of the cavity is changed, electromagnetic fields inside the cavity change accordingly [6]. In this design cavity is perturbed by a small deformation of its boundary as shown in Fig. 4(a). This perturbation causes the electrical field, which induced by two resonator inside the cavity, is changed and direct coupling between them is occurred, also this cause cross coupling. The cross coupling can be designed in such a way that a pair of transmission zeros are introduced at the desired frequencies to improve the selectivity. The maximum number of zeros are equal the number of mode cavities. These zeroes increase the selectivity (slope) of the filter in the lower and upper stop band. Fig. 4(b) illustrates coupling scheme proposed for the filter structure where each node represents a resonator, the full lines indicate the main or direct coupling, and the dashed line denotes the cross couplings. This cross coupling that will produce a pair of transmission zeros at desired frequencies.

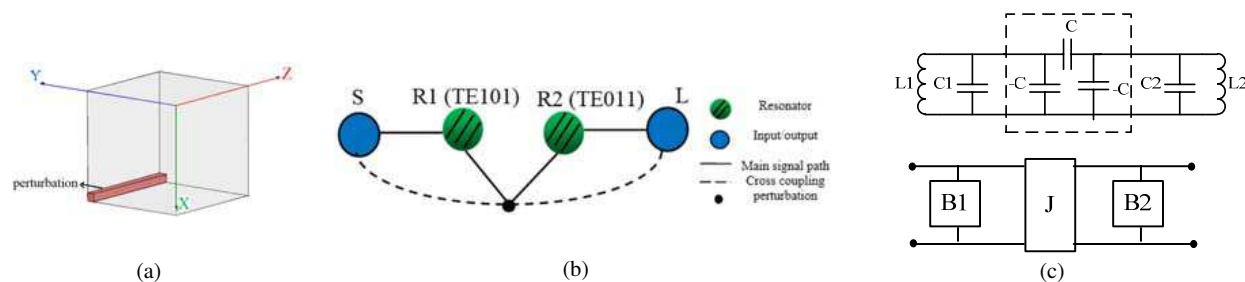


Figure 4: (a) A resonant cavity perturbed by small deformation of its boundary. (b) Coupling scheme proposed for dual mode cavity filter. (c) Equivalent circuit of the proposed second order dual-mode perturbed cavity filter along with electric coupling by an admittance inverter.

Furthermore, to indicate the effect of perturbation on the bandwidth, circuit analysis is done.

Fig. 4(c) shows the equivalent lumped element circuit of the filter. The capacitive coupling C introduced by distributed element as perturbation between two resonators. L_i and C_i ($i = 1, 2$) are inductance and capacitance of resonant loops. Actually, it can be shown that the electric coupling between the two resonant loops is represented by an admittance inverter, Fig. 4(c).

Based on admittance inverter definition [12], inductance and capacitance with an inverter J on each side looks like, a capacitance and inductance from exterior terminals. Making use of this property to analyze this technique. The resonant frequency of coupled resonators are different from uncoupled resonators. Coupling effect can reduce and increase the resonance frequencies according to:

$$f_{r_lower} = \frac{1}{2\pi\sqrt{L_1(C_1 + C')}} \quad f_{r_upper} = \frac{1}{\sqrt{2\pi(L_1||L')C_1}} \quad (2)$$

where C' and L' are transferred equivalent capacitance and inductance from exterior inverter terminal. Therefore, the bandwidth is increased. So, increasing the pass band or having flexible bandwidth is another feature of the perturbation, which is shown in Section 3 Coupling capacitance between two equal shunt resonators is calculated as follows:

1. Choose an inductor value inside the given limit, the input and output coupling capacitors will become large enough that they may be eliminated from the design.
2. Compute Susceptance slope parameter by $b = \omega_0/2 (dB/d\omega)|_{\omega=\omega_0}$ where B is the Susceptance of resonators ($B = B_1 = B_2$) that is imaginary part of input admittance of shunt resonator, ω_0 is the resonance frequency.
3. Determine coupling coefficient by: $k = J/\sqrt{b_1b_2} = w/\sqrt{g_1g_2}$, where g_1, g_2 are prototype parameter values.
4. Compute inverting circuit to calculate of admittance inverter ($J = \omega C$) which is shown in Fig. 4(c). The negative capacitances are absorbed into adjacent elements.
5. Thus the coupling capacitor is equals to: $C = wb_1/(\omega_0g_1)$.

3. SIMULATION AND EXPERIMENTAL RESULTS

In this section, a second order filter based on dual mode cavities, with square cross section perturbation and without it, are designed using techniques described above.

3.1. Filter Design

The two-pole filter is designed to meet the center frequency of 9050 MHz, 3-dB bandwidth of 60 MHz, insertion loss less than 0.5 dB, and 20 dB return loss in the pass band. Fig. 5(a) illustrates a configuration of the first design of filter structure. Fig. 5(b) shows the EM simulated response of the designed filter by HFSS software. As shown there is weakly coupling between modes, the insertion loss is about 1 dB, the B.W is 10 MHz and return loss is better than 15 dB. The dimensions of the designed filter are (all in mm) indicated in Table 1. The dimensions may be slightly altered to tune the responses toward the desired ones. The center conductor of the coaxial line (SMA connector) extends a distance H into the cavity that is obtained by simulation. As a result this way of coupling does not create a transmission zero at desired frequencies and the maximum relative bandwidth can be achieved about 0.1%. Therefore to obtain strong coupling, transmission zeros and more bandwidth, other design is used. In this design the perturbed cavity as shown in Fig. 6 is excited according the way was described before. In this structure the resonant frequency is affected by the perturbation. In addition the bandwidth can be easily tuned to flexible bandwidth by varying the square cross-sectional dimension of the perturbation since the perturbation is extending along the whole length of the cavity. The final dimensions of the perturbed filter are shown in Table 2. It can be observed that, only very small adjustments are required on the achieved dimensions in the simulation. The corresponding EM simulation result can be found in Fig. 7 (dashed lines). The filter has a center frequency of 9080 MHz, 3 dB bandwidth is about 60 MHz, insertion loss of about 0.28 dB and return loss is better than 20 dB.

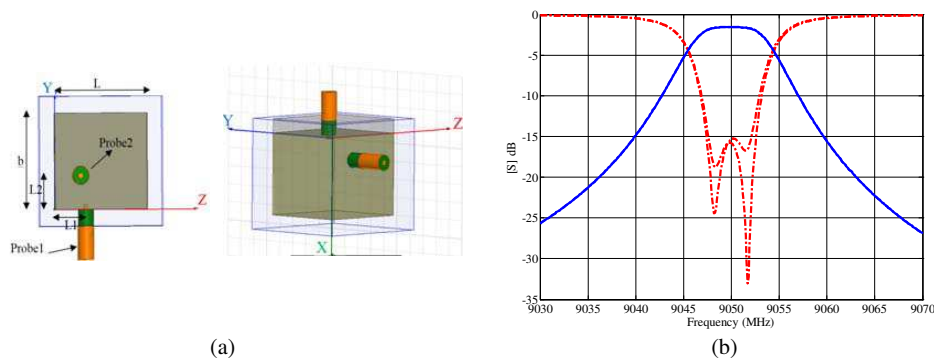


Figure 5: (a) Configuration of dual mode cavity filter with two coaxial probes without perturbation. (b) Simulated response of the cavity filter.

Table 1: Dimension of the filter shown in Fig. 5(a).

	a	b	L	L1=L2	t1=t2	H
Designed	22.9	22.9	24.02	$\lambda_r/4$	-	-
Simulated	22.8	22.8	24.05	8	0.29a	1.1

Table 2: Dimension of the perturbed dual mode cavity filter shown in Fig. 6.

	a	b	L	L1=L2	t1=t2	L.Screw	H
Designed	22.9	22.9	24.02	$\lambda_r/4$	-	-	-
Simulated	22.8	22.8	24.05	8	8.3	7.3	2.4

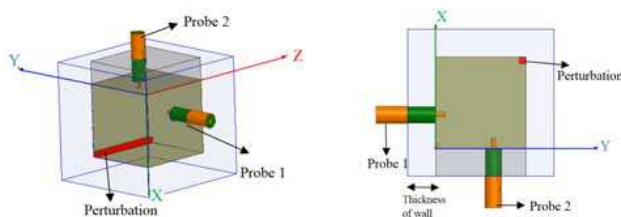


Figure 6: Configuration of dual mode cavity filter with two coaxial probes as an excitation.

3.2. Frequency Tuning

Tuning screws are screws inserted into resonant cavities which can be adjusted externally to the waveguide. But most cross coupled filters are difficult to tune since source to load couplings affect all other couplings in the filter. Whereas, this filter provide fine tuning of the resonant frequency by inserting more or less length of dielectric screw into the waveguide, thus electromagnetic fields inside the cavity change accordingly without disturbing any coupling of the degenerate cavity modes. The conventional tuning screw is used to part of the design. Fine tuning is required because of manufacturing tolerances after fabrication. Therefore, the designed frequency is considered 9080 MHz that is higher than desired frequency. Fig. 8(a) shows perturbed cavity which has a tuning dielectric screw with diameter of 4 mm on shorted wall (xy plane). Two mentioned mechanism are presented in Fig. 7 and the excellent result is obtained with screw. When the specific length of the screw has been inserted into cavity the center frequency is moved to lower frequency, from 9080 to 9050 MHz. The 3 dB bandwidth of the filter is 63 MHz centered at 9050 MHz, insertion loss is about 0.28 dB, and return loss is better than 26.4 dB in over the pass band. The dimension of the perturbation is $1.7 \times 1.7 \times L$ and the center conductor of the coaxial line (SMA connector) extends inside the cavity about H 2.4 mm. That H is the desired length of inner conductor. Moreover the proposed filter have transmission zeros at desired frequencies. Fig. 8(b) shows two transmission zeros below and above pass band. The two transmission zeros are located at $f_1 = 8.842$ GHz and $f_2 = 9.445$ GHz. Also the first spurious resonance occurs around 11.5 GHz. Fig. 9 shows the frequency responses of the unperturbed designed filter when all transmission zeros are at infinity along with the perturbed cavity filter with two transmission zeros. Also, it is obvious that the more

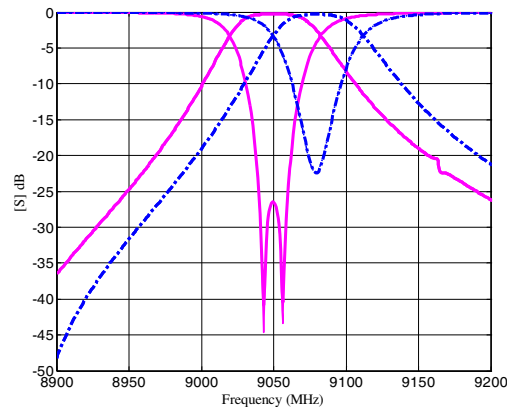


Figure 7: Simulated responses of dual mode perturbed cavity filter, dash line is without tune screw, and solid line is with tune screw.

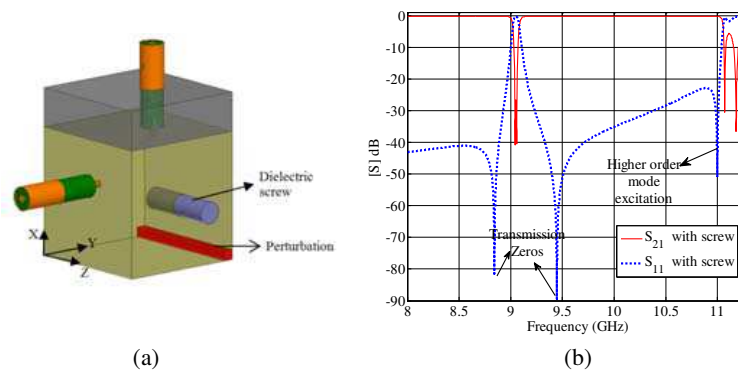


Figure 8: (a) Configuration of perturbed filter with tune screw. (b) Simulated result.

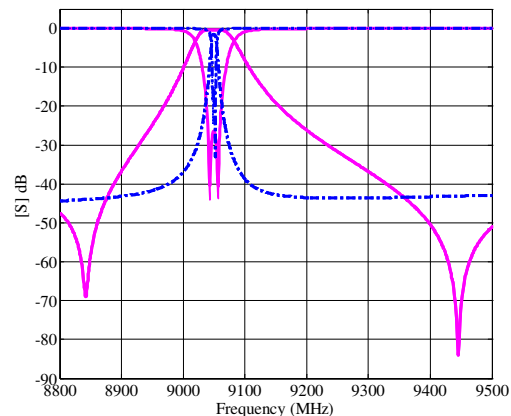


Figure 9: Comparison between unperturbed designed filter response (Dashed line) and perturbed cavity response (solid line).

bandwidth with lower insertion loss is achieved on the perturbed cavity. To analysis of electrical field inside the filter, HFSS is used as a simulator. Fig. 10(a) shows the E -field strength across the filter in 9050 MHz. Also the direction of the electrical field is important, so a vector plot uses arrows to illustrate the magnitudes of the field quantities which is shown in Fig. 10(b).

4. EXPERIMENTAL RESULTS

In order to validate the performance of the filter design, the filter was fabricated and measured. A photograph of the fabricated filter is shown in Fig. 11(a). In this work tuning screw is not part of the design, it is added only to compensate for manufacturing errors. By inserting dielectric screw on the shorted plan as shown in Fig. 11(b), the shift of resonant frequency can be completely controlled. Fabricated cavity filter was measured using the Agilent 8510C Network Analyzer. Fig. 12

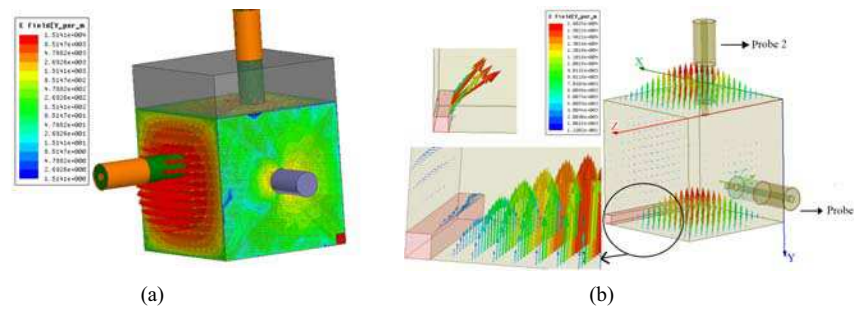


Figure 10: (a) E -field strength across the cavity filter in frequency 9050 MHz. (b) Vector E -field strength on XZ plane of cavity filter.

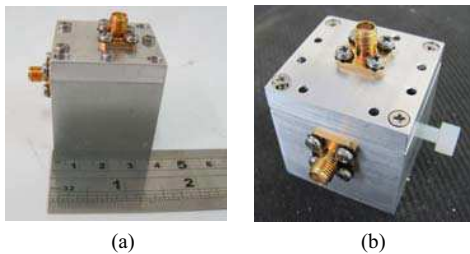


Figure 11: (a) Picture of the fabricated filter. (b) Insert dielectric screw.

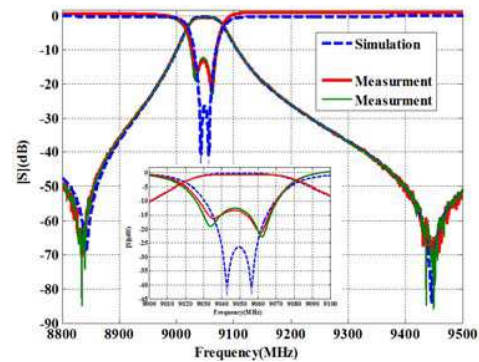


Figure 12: EM Simulated and measured results of the BPF dual mode cavity filter.

shows the comparison between the measured response as the solid curves and simulated response (dashed lines). The 3 dB bandwidth of the measured results filter is 63 MHz centered at 9050 MHz, are the return loss of better than 12.5 dB in the pass band and the insertion loss of better than 0.5 dB.

5. CONCLUSION

In this paper a compact dual mode rectangular waveguide cavity filter was presented. This dual mode cavity design was used for the implementation of second order filters with two TE_{101} and TE_{011} mode. By using cross coupling technique with perturbation theory, transmission zeros in the stop band were realized, and the shape factor was improved. Also, by this technique, bandwidth of pass band was optimized. It was obvious that the bandwidth of the filter can be altered to desired values by changing the dimension of perturbation. Furthermore, to indicate the effect of perturbation on the bandwidth, circuit analysis was done. The proposed cavity filter is structurally compact size and requires only one tuning screw. This tuning mechanism was presented to adjust the resonant frequency without causing any coupling of the degenerate cavity modes. Finally, EM simulation was done for the filter. Full wave analysis of the filter confirms the designed filter. In order to validate the performance of the filter design, the filter was fabricated and measured. The measurement results shows close agreement with the simulation results. Although there is still a little differences between the simulated and measured results due to manufacturing tolerances.

REFERENCES

1. Rizzi, P. A., *Microwave Engineering: Passive Circuits*, 1987.
2. Lin, W., "Microwave filters employing a single cavity excited in more than one mode," *J. Applied Physics*, Vol. 22, 989–1001, Aug. 1951.
3. Atia, A. E. and A. E. Williams, "Narrow bandpass waveguide filters," *IEEE Transactions on Microwave Theory and Techniques*, Vol. 20, 258–265, Apr. 1972.
4. Amari, S., U. Rosenberg, and J. Bornemann, "A novel approach to dual and triple-mode pseudo-elliptic filter design," *34th European Microwave Conference, 2004*, Vol. 2, 993–996, Oct. 12–14, 2004.

5. Shang, X., W. Xia, and M. J. Lancaster, “The design of waveguide filters based on cross-coupled resonators,” *Microw. Opt. Technol. Lett.*, Vol. 56, No. 1, Jan. 2014.
6. Pozar, D., *Microwave Engineering*, 3rd Edition, Wiley, 2005.
7. Williams, A. E. and A. E. Atia, “Dual-mode canonical waveguide filters,” *IEEE Transactions on Microwave Theory and Techniques*, Vol. 25, 1021–1026, Dec. 1977.
8. Fiedziuszko, S. J., “Dual-mode dielectric resonator loaded cavity filters,” *IEEE Transactions on Microwave Theory and Techniques*, Vol. 30, 1311–1316, Sep. 1982.
9. Wang, C., K. A. Zaki, and A. E. Atia, “Dual-mode conductor-loaded cavity filters,” *IEEE Transactions on Microwave Theory and Techniques*, Vol. 45, 1240–1246, Aug. 1997.
10. Hong, J.-S. and M. J. Lancaster, *Microstrip Filters for RF-microwave Applications*, 2001.
11. Liang, J.-F., H.-C. Chang, and K. A. Zaki, “Coaxial probe modeling in waveguides and cavities,” *IEEE Transactions on Microwave Theory and Techniques*, Vol. 40, No. 12, 2172–2180, Dec. 1992.
12. Matthaei, G. L., L. Young, and E. M. T. Jones, *Microwave Filters, Impedance-matching Networks, and Coupling Structures*, McGraw-Hill, New York, 1985.

Propagation of Electromagnetic Waves in Cylindrical Three-layers Waveguide with Metamaterial Layer

V. A. Meshcheryakov and V. A. Zhuravlev

Tomsk State University, Tomsk 634050, Russian Federation

Abstract— We present results of modeling of waveguides modes propagation coefficients in cylindrical tree-layer waveguide in this work. Intermediate layer is LHM (Left-Handed-Medium) metamaterial with negative index of refraction. The outer and inner layers are conventional materials with positive index of refraction RHM (Right-Handed-Medium). Our results indicate that in such waveguides exist complex waves and waves with a significant slowdown of phase.

1. INTRODUCTION

V. G. Veselago [1] predicted theoretically the originality of physical phenomenon's by reflection and refraction of electromagnetic waves on borders section "right" and "left" mediums. This is provided the impetus for modeling electromagnetic processes in different transmission lines [2–6]. The purpose of this work is modeling of wave processes in cylindrical waveguide that contained three layers with "right" and "left" mediums.

2. FORMULATION OF THE PROBLEM

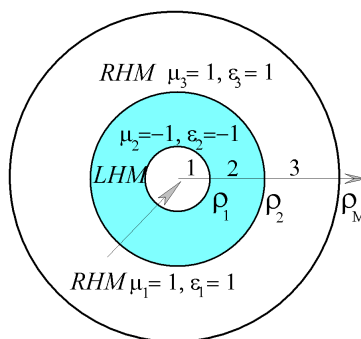


Figure 1: Three-layer waveguide.

On Figure 1 are shown cross-section three-layer waveguide with ideal conductive outer shield and geometrical characteristics of the layer's. We used cylindrical coordinate system r, ϕ, z_0 . The waves spread along coordinate z , directed into plane's drawing. The dependence of components fields on azimuth and longitudinal coordinates is selected in the form: $\exp(in\phi + i\beta z)$, where n — azimuth number, β — propagation constant. We study the behavior of the propagation constants of the guided modes. The chose of structure is specified by simplicity of dispersion equation for calculation of propagation constants of eigen waves. The dispersion equation comes from realizing boundary conditions for tangent components of EM fields on borders section medium. The propagation constant are normalized on wave number of free space: $\Gamma = \beta/k_0 = c/v$, where v — phase velocity of wave in waveguide. The complex character $\Gamma = \text{Re}(\Gamma) + i\text{Im}(\Gamma)$ means the rise of complex waves. Imaginary character of propagation constant means the absence of wave process. The radii of the layers and the longitudinal coordinate is normalized on the wave number of free space: $\rho = k_0 r, z = k_0 z_0, k_0 = \omega/c$, where c is speed of light in free space. The purpose of modeling is the explanation of the influence of the thickness of the central dielectric and its dielectric constant on the propagation constants of the guided modes.

3. THE RESULTS OF NUMERUCAL EXPERIMENTS

Figure 2 shows the dependences of the propagation constants of the waves having a field variation in azimuth (the first subscript at the bottom in the name of the wave) on the radius ρ_2 . The names of waves are specified in accordance with accepted literature recommendation [10]. In the absence

of LHM material ($\rho_1 = \rho_2$) results are well-known in the literature. On Figure 2 axis $\text{Re}(\Gamma)$ and $\text{Im}(\Gamma)$ are combined (superposed). In this case, we see the place of the “cut-off” regions and wave propagation regions.

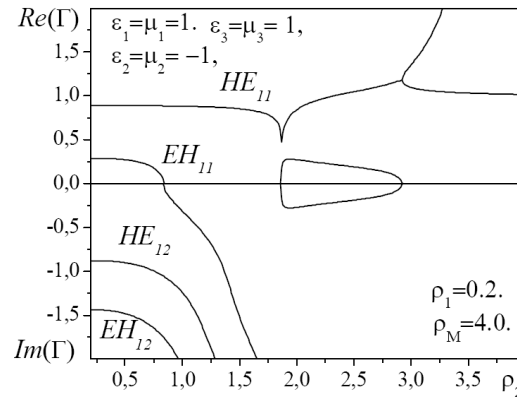


Figure 2: The radius of the first layer is 0.2. Dependences of the propagation constants on the outer radius of the second layer of waveguide.

The analysis of results shows the existence of two propagating modes (HE_{11} , EH_{11}) and two “cut off” modes (HE_{12} , EH_{12}) having an imaginary value of Γ . Increase ρ_2 makes “cut off” mode the mode EH_{11} . This fact is new. It can be explained from position of partial waves. In the LHM medium the direction of propagation ray becomes opposite. With increase of LHM layer thickness grows ray’s way in opposite direction and Γ aspires to 0. An another phenomenon observed at the growth of the radius ρ_2 . The bifurcation is observed in multilayer waveguide with increasing thickness of the second layer. The wave HE_{11} is divided into two waves. The further increase of the thickness of the layer leads to a significant increase in the propagation constant ($\Gamma \rightarrow \infty$).

Figure 3 shows the dependences of the propagation constants on the permeability of the first layer ε_1 at fixed values of the radiuses ($\rho_1 = 0.2$, $\rho_2 = 0.5$).

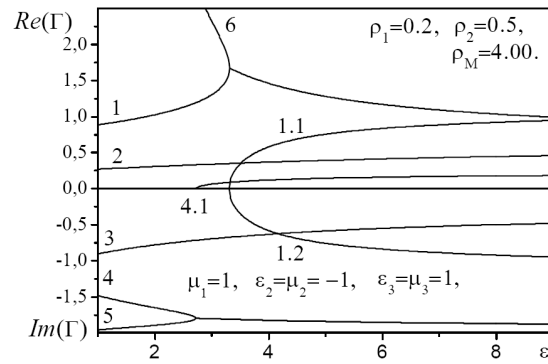


Figure 3: Three-layer waveguide. Curved 1 — HE_{11} mode, 2 — EH_{11} , 3 — HE_{12} , 4 — EH_{12} , 5 — HE_{12} .

The increase in permeability leads to an increase of the propagation constant of the mode HE_{11} (curve 1). There is a mode with very low phase velocity in the waveguide (curve 6). This is an unusual result. The bifurcation is occurs for these modes. In the spectrum there are two complex conjugate wave modes. They have anomalous behavior. For other modes, there are many different effects. The appearance of waves with a significant slowing of the phase velocity and abnormal behavior is associated with the existence of a layer of LHM.

4. CONCLUSION

We are considered various options for modifying the parameters of the multilayer waveguide at the modeling process [7–9]. The qualitative picture of the propagation constant of the waves does not change. We can talk about the features of propagation of electromagnetic waves in a waveguide with LHM and RHM layers:

1. In the waveguide can be implemented as a wave process, and the “cut off” mode process at the change of the second layer radius.

2. The emergence of LHM layer in the waveguide leads to a strong deceleration of phase velocity for some modes.

3. In the waveguide are observed complex conjugate waves and anomalous behavior of the propagation constants.

ACKNOWLEDGMENT

This Research is supported by Tomsk State University Competitiveness Improvement Program.

REFERENCES

1. Veselago, V. G., “The electrodynamics of substances with simultaneously negative values of ϵ and μ ,” *Sov. Phys. Usp.*, Vol. 10, No. 4, 509–514, 1986.
2. Smith, D. R., W. J. Padilla, D. C. Vier, et al., “Composite medium with simultaneously negative permeability and permittivity,” *J. Physical Review Letters*, Vol. 84, No. 18, 4184–4187, 2000.
3. Pendry, J. B., “Photonic band structures,” *J. Mod. Optic.*, Vol. 41, No. 2, 209–229, 1994.
4. Mousa, H. M. and M. M. Shabat, “TE waves in a cylindrical superlattices (LANs) and left handed material (LHM) waveguide structure,” *Antenna Technology (iWAT)*, 286–289, 2013.
5. Marqués, R., F. Martín, and M. Sorolla, *Metamaterials with Negative Parameters: Theory, Design and Microwave Applications*, John Wiley & Sons, 2007.
6. Salehi, H. and R. Mansour, “Analysis and design of superconducting left-handed transmission lines,” *IEEE Transactions on Applied Superconductivity*, Vol. 15, No. 2, 2005.
7. Meshcheryakov, V. A., “Modeling of electromagnetic waves in cylindrical three-layers waveguide with metamaterial layer,” *24th International Crimean Conference Microwave & Telecommunication Technology Conference Proceedings*, 553–554, Sevastopol, Crimea, Russia, September 7–13, 2014.
8. Dunaevskii, G. E., V. A. Meshcheryakov, V. A. Zhuravlev, V. I. Suslyayev, and A. K. Bashlykov, “Special features of electromagnetic wave propagation in a two-layered cylindrical waveguide with right- and left-handed media,” *Russian Physics Journal*, Vol. 52, No. 6, 1325–1330, 2009.
9. Meshcheryakov, V. A. and V. V. Ovsyannikov, “Own electromagnetic waves in a circular waveguide with chiral layers,” *Russ. Phys. J.*, 47, No. 6, 675–680, 2004.
10. Neganov, V. A., O. V. Osipov, et al., “Electrodynamics and propagation of radio waves,” *Radio Svyaz*, 2005 (in Russian).

A Broad-band End Launch Double Ridge Waveguide to Coaxial Transition Using LPDA

Maziar Hedayati, Mohsen Abdolahi, Hamid Mirmohammad Sadeghi,
Parisa Moslemi, and Gholamreza Askari

Information and Communication Technology Institute (ICTI)
Isfahan University of Technology (IUT), Isfahan 84156, Iran

Abstract— In this paper, a wideband end launch ridge waveguide to coaxial transition is proposed, which operates in 8 ~ 14 GHz. The microwave characteristics of double-ridge waveguide to coaxial transition are analyzed and simulated by full-wave analysis. Quarter wavelength Chebyshev impedance matching method used to design the middle part of the transition. Dimensions of the first part of transition have been calculated by time domain solver of Ansoft Designer based on finite element method (FEM). The compact LPDA is designed on microstrip to receive signal from the waveguide. This antenna is placed in the E -plane of the ridge waveguide to stimulate the TE_{10} dominant mode. Higher modes propagation can disturb the performance of the wide band transition. Also in this paper a C shape part is used to increase the cut off frequency of higher modes. The simulation results show that the S_{11} of the transition is below -10 dB in 8–14 GHz.

1. INTRODUCTION

Waveguide to Coaxial transition, as an important passive component has wide application in antennas radars and microwave systems Nowadays, broad band transitions are necessary for feeding wideband antenna in developing of the microwave systems. Most of designs like aperture-coupled slot [1] or aperture coupled patch element [2] have been expanded in the literature to introduce a useful transition from waveguide to microstrip. Although aperture-coupled structures are compact, but their fractional bandwidth is compact. Besides, the waveguide to microstrip transition based on the coupled probe at the E -plane [3] has been presented which is small but its bandwidth is limited ($\sim 22\%$ for less than -15 dB return loss). To modify the bandwidth, [4] has proposed transition using the stepped waveguides and [5] has presented the short-circuited tapered finline to widen the band width. However, the circuit size is also large. To decrease the size of the circuit, some researchers use the aperture slot coupling [6], and patch element [7] as a transition. The circuit size of these transitions can be reduced but in cost of narrow bandwidth. To enhance the bandwidth, waveguide to microstrip transitions using the open-circuited probe [8] and tapered coplanar strip (CPS) probe [9] were presented. But there is an additional slotline to microstrip transition in their designs. Furthermore, although [10] has presented a compact and broadband waveguide to microstrip transition using the anti-symmetric tapered probes, but there is an imbalance problem while transitioning from the ML to the rectangular waveguide. All of those transitions have been designed for simple rectangular waveguides, but for wideband application the ridge waveguides are more useful than rectangular waveguides which is not commonly presented any transition for them in the literatures.

2. TRANSITION DESIGN

The transition is designed for a double ridge waveguide with inner dimension $25.33 \text{ mm} \times 12.43 \text{ mm}$. The substrate with $\epsilon_r = 4.4$, $\tan \delta = 0.0009$, and thickness of 0.8 mm was used for planar circuit. The transition consists of three consecutive in-line sections including a double ridge waveguide, a Chebyshev matching and one LPDA. The substrate is placed in E -plane of waveguide and substrate plane must be parallel to waveguide propagation direction. An overall layout of the designed waveguide to coaxial transition is shown in Fig. 1.

2.1. Characterization of Ridge Waveguide

The dominant mode of ridge waveguide is TE_{10} mode, which is the same in rectangular waveguide. The cut of frequency TE_{10} mode of proposed ridge waveguide is 2 GHz . According to the transverse resonance condition, the cutoff wavelength (λ_c) of the ridge waveguide that works in the TE_{m0} mode can be calculated. The waveguide cross-section is shown in Fig. 2 and dominant mode and higher modes with different cut off frequency are shown in Fig. 3. As it can be seen, higher modes are propagated from 12 GHz that will effect on performance of transition. For suppressing higher modes

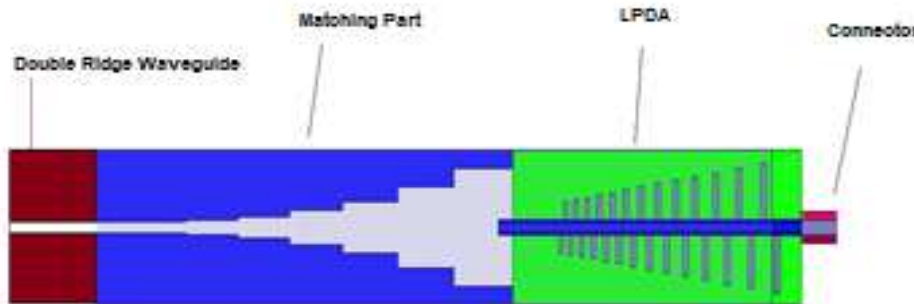


Figure 1: The layout of the proposed coaxial-to-waveguide transition.

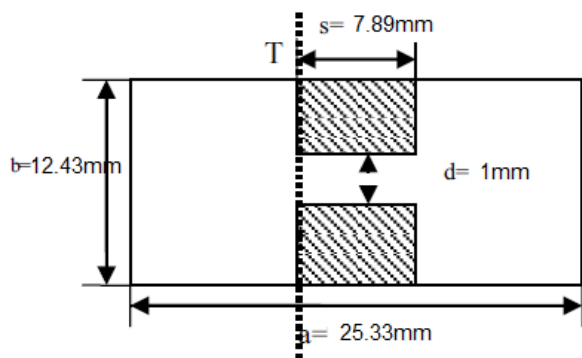


Figure 2: The size of ridge waveguide cross section.

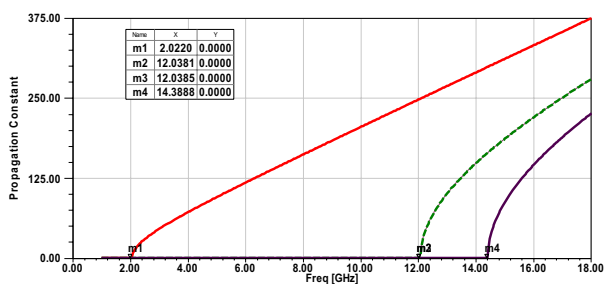


Figure 3: The Dominant mode and higher modes.

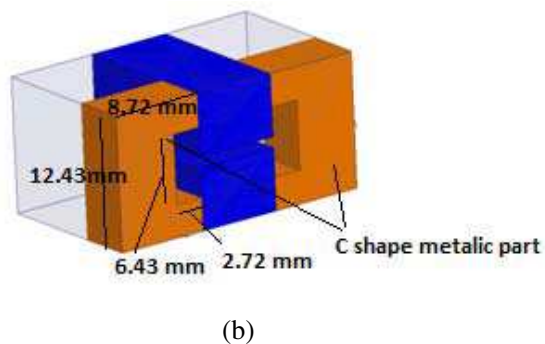
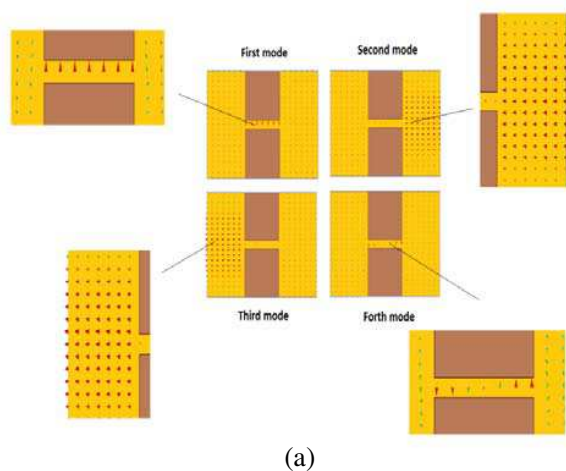


Figure 4: (a) The field of four first mode. (b) The C-shaped metallic part.

in the frequency range a C-shaped metallic part (Fig. 4) added to waveguide and as it is depicted in Fig. 5 higher modes will start on upper frequency near 17 GHz that is out of frequency performance.

The impedance of ridge waveguide depended on frequency because it is a non-TEM transmission line. So, the characteristic impedance can be expressed by the impedance at infinite frequency and the wavelengths of the waveguide [11]:

$$Z(w) = Z(\infty) \cdot \frac{\lambda_g}{\lambda_c} = \frac{Z(\infty)}{\sqrt{1 - \left(\frac{\lambda_0}{\lambda_c}\right)^2}} \quad (1)$$

where $Z(\infty)$ is the waveguide characteristic impedance of infinity frequency; λ_0 is the wavelength of free-space and λ_c is the cut-off wavelength of waveguide.

The power-voltage characteristic impedance is defined as:

$$Z_{OPV} = \frac{V_0^2}{2P} \tag{2}$$

where V_0 the peak voltage between two ridges and P is the average power propagated in z direction. The characteristic impedance of any frequency can be got through (3):

$$Z_{OPV}(w) = \frac{Z_{PV}^\infty}{\sqrt{1 - \lambda/\lambda_c}} \tag{3}$$

where Z_{PV}^∞ the impedance of infinite frequency and its expression is:

$$Z_{OPV}^\infty(w) = \frac{1}{\frac{k}{120\pi^2\beta} \left\{ m \frac{2\beta}{k} \cos^2 \frac{\pi\gamma}{k} \ln \csc \frac{\pi d}{2b} + \frac{\pi\gamma}{2k} + \frac{1}{4} \sin \frac{\pi\gamma}{k} \right\} + \frac{d}{b} \frac{\cos^2 \frac{\pi\gamma}{k}}{\sin^2 \frac{2\pi\delta}{k}} \left[\frac{\pi\delta}{k} - \frac{1}{4} \sin \frac{4\pi\delta}{k} \right]}$$

$$k = \frac{\lambda_c}{a}; \beta = \frac{d}{a}; \gamma = \frac{s}{a}; \delta = \frac{(1 - s/a)}{2} \tag{4}$$

We can get the theoretical characteristic impedance of any frequency required by formula (1)~(4). Now it is possible to calculate the value of the impedance at each frequency from the formula (Fig. 6).

2.2. Design of the Matching Structure

There are several matching methods, but with consideration of the manufacturing cost in this paper a quarter wavelength Chebyshev matching method is adopted. With the formula in Section 2.1, the input and output impedance are obtained: $Z = 37.6 \Omega$, $Z_{n+1} = 275 \Omega$. From the design table, six section transition is enough to achieve this purpose. The impedance of each section is: $Z_1 = 43.3 \Omega$, $Z_2 = 57 \Omega$, $Z_2 = 88.6 \Omega$, $Z_2 = 122 \Omega$, $Z_2 = 169 \Omega$, $Z_2 = 234.5 \Omega$. Each branch ridge has the same width (7.89 mm). Table 1 shows the dimensions of each section’s gap and length. This matching structure is depicted in Fig. 7. The simulation results of this part is shown in Fig. 8. As it is shown in figure, return loss is more than 12 dB and insertion loss is smaller than 0.2 dB that shows good matching.

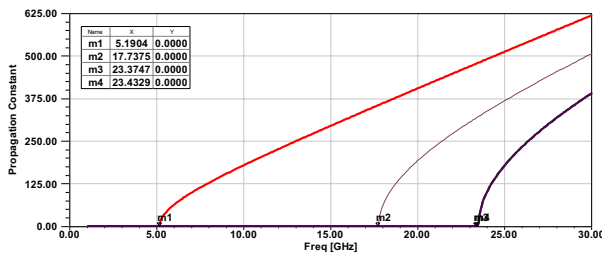


Figure 5: The dominant mode and higher modes with C-shaped metallic part.

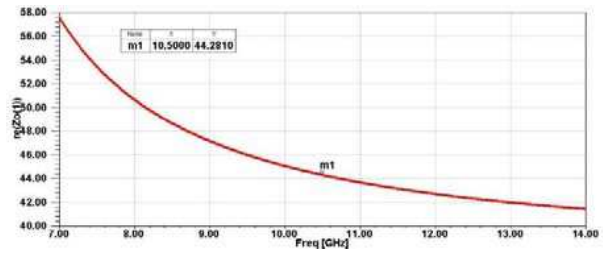


Figure 6: The characteristic impedance at each frequency.

Table 1: The dimensions and the characteristic impedance of transition.

	Gap	Length	Characteristics Impedance
	d (mm)	L (mm)	Z_0 (Ω)
First branch	1.23	7.3	43.3
Second Branch	1.63	7.3	57
Third branch	2.83	7.49	88.6
Fourth branch	4.23	7.65	122
Fifth	6.43	7.92	169
Sixth	9.41	8.27	234.5

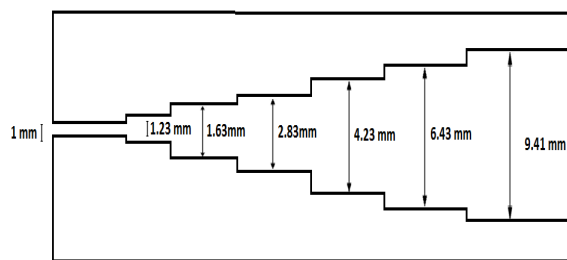


Figure 7: The matching structure and its dimensions.

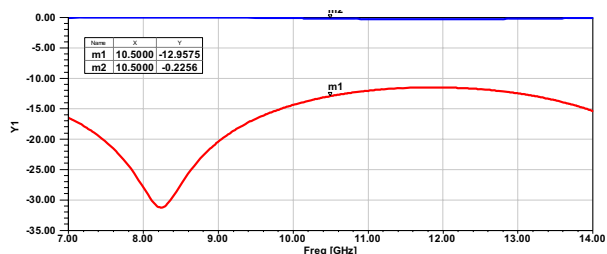


Figure 8: The simulation result of matching structure.

2.3. LPDA Design

Figure 9 shows the configuration of the proposed antenna. The antenna was designed on both sides of the 0.8 mm thick substrate with a dielectric constant 4.4 and loss tangent 0.0009. The antenna is designed to cover the X band and upper from 8 GHz to 14 GHz. With the desired directivity set at 10 dBi, the scaling factor and spacing factor were determined to be 0.96 and 0.1 based on the corrected Carrel’s tables. As it is known, the dielectric can lead to reduction in size and gain of antenna. Since, the effective dielectric constants are not the same in every region of a PLPDA antenna, two effective dielectric constants should be considered to scale the dimensions. For a substrate with $\epsilon_r = 4.4$, they are chosen about 3.5 and 1.5, respectively. The return loss of antenna has been illustrated in Fig. 10 and obvious return loss is less than 10 dB in 8–14 GHz frequencies.

3. SIMULATION RESULTS

The double ridge waveguide to coaxial transition is designed by using two individually optimized components together (LPDA and matching network) to achieve optimum performance. One prototype have been designed and simulated using dielectric with $\epsilon_r = 4.4$ and substrate thickness of 0.8 mm. The printed antenna pattern is located at the center of the waveguide. The transition was modeled and analyzed with Ansoft HFSS 12.0 which is shown in Fig. 11. The return loss is better

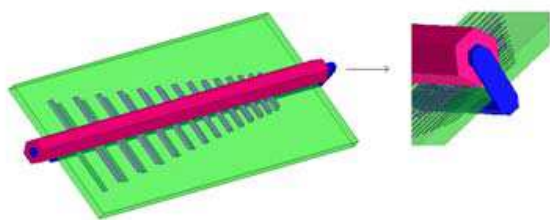


Figure 9: The designed LPDA.

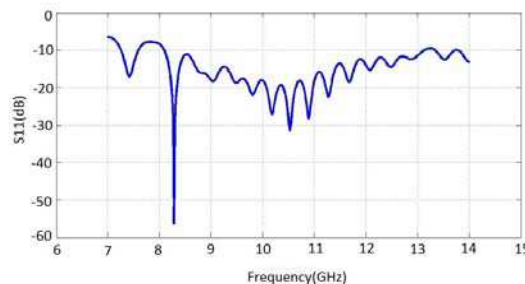


Figure 10: The return loss of antenna.

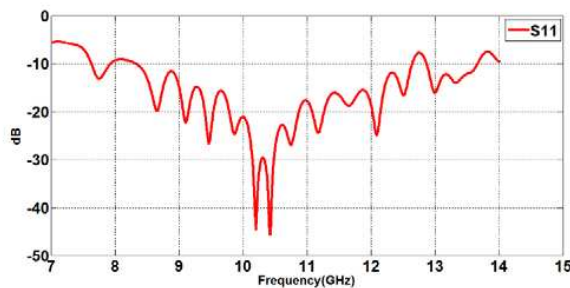


Figure 11: The return loss of final transition.

than 12 dB in X-band and better than 10 dB in the whole 8–14 GHz.

4. CONCLUSION

A broad band end launcher ridge waveguide to coaxial transition using a LPDA has been proposed and demonstrated in this paper. The transition's mechanism is presented in detail for every components to understand its broad-band characteristics. The 10 dB fractional bandwidth of the waveguide-to-coaxial transition covers the frequency range 8–14 GHz, which is calculated to be 51%.

REFERENCES

1. Das, B. N., K. V. S. V. R. Prasad, and K. V. Seshagiri Rao, "Excitation of waveguide by stripline- and microstrip-line-fed slots," *IEEE Trans. Microw. Theory Tech.*, Vol. 34, No. 3, 321–327, Mar. 1986.
2. Grabherr, W. and W. Menzel, "A new transition from microstrip line to rectangular waveguide," *Proc. 22th Eur. Microw. Conf.*, 1170–1175, Sep. 1992.
3. Lou, Y., C. H. Chan, and Q. Xue, "An in-line waveguide-to-microstrip transition using radial-shaped probe," *IEEE Microw. Wireless Compon. Lett.*, Vol. 18, No. 5, 311–313, May 2008.
4. Yao, H.-W., A. Abdelmonem, J.-F. Liang, and K. A. Zaki, "Analysis and design of microstrip-to-waveguide transitions," *IEEE Trans. Microw. Theory Tech.*, Vol. 42, No. 12, 2371–2380, Dec. 1994.
5. Van Heuven, J. H. C., "A new integrated waveguide-microstrip transition," *IEEE Trans. Microw. Theory Tech.*, Vol. 24, 144–147, 1976.
6. Herrero, P. and J. Schoebel, "A WR-6 rectangular waveguide tomicrostrip transition and patch antenna at 140 GHz using low-cost solutions," *Proc. IEEE Radio and Wireless Symp.*, 355–358, Orlando, FL, USA, 2008.
7. Wu, P., Z. Wang, Y. Zhang, S. Sun, and R. Xu, "Wideband waveguide-to-microstrip probe transition with LTCC technology," *Electron. Lett.*, Vol. 47, No. 1, 43–44, 2011.
8. Lou, Y., C. H. Chan, and Q. Xue, "An in-line waveguide-to-microstrip transition using radial-shaped probe," *IEEE Microw. Wirel. Compon. Lett.*, Vol. 18, No. 5, 311–313, 2008.
9. Lin, T.-H. and R.-B. Wu, "A broadband microstrip-to-waveguide transition with tapered CPS probe," *Proc. 32nd Eur. Microwave Conf.*, 1–4, Milan, Italy, 2002.
10. Chuang, J.-K., R.-Y. Fang, and C.-L. Wang, "Compact and broadband microstrip-to-waveguide transition using antisymmetric tapered probes," *Electron. Lett.*, Vol. 48, No. 6, 332–333, Mar. 2012.
11. Nie, R.-X., E. Li, G.-F. Guo, and Y. Wang, "Simulation and design of 18–40 GHz ridge waveguide to coaxial transition," *2011 IEEE International Conference on Microwave Technology & Computational Electromagnetics (ICMTCE)*, 183–185, May 22–25, 2011.

3D ISAR Imaging of Realistic Target Model Based on General Purpose EM Simulators

Seok Kim^{1,2}, Konstantin Nikitin¹, Inchan Paek², and Min-Ho Ka¹

¹School of Integrated Technology, Yonsei University, Seoul, South Korea

²R&D Center, Samsung Thales, Inc., Yongin, South Korea

Abstract— Recent progress in computation performance and computational electrodynamics allows various analyses on many problems related to electro-magnetic (EM) waves using general purpose EM simulators. In this paper, we describe and demonstrate 3D ISAR image generation of a realistic target using FEKO, which is one of the representative general purpose EM simulators on the commercial market. This method can benefit us many advantages like building the database of many targets for target recognition with cost-and-time effective way and designing a radar and evaluating its performance under more realistic situations.

1. INTRODUCTION

Inverse synthetic aperture radar (ISAR) has been widely used in many applications for its high resolution capability. In the traditional operation of ISAR, the coherent system directs the antenna to the target and gathers the wideband reflected energy at various look angles of the target, normally by utilizing the rotational motion of the target. Representing the target's cross-sectional area in various range points and Doppler frequencies (or cross-range points) generates the 2D ISAR image of the target [1–3]. Similarly, a 3D ISAR image of the target can be acquired when the translational and rotational motion components of the target can be measured or at least estimated precisely so that the target's profiles for two different orthogonal look angles are collected.

Recent studies on 3D ISAR imaging concept have been mainly focused on two different approaches [3]. The first approach is based on interferometric ISAR principle, where multiple antennas are used at different heights such that the second cross-range dimension is able to be resolved [4–6]. This approach has many limitations, including its high sensitivity with respect to glint noise of the target and the lack of multiple height information for a selected range cross-range point. On the other hand, the second approach that utilizes single ISAR antenna can yield radar cross section (RCS) profiles at multiple heights and multiple range cross-range points. Some of the 3D ISAR imaging algorithms are listed in [3].

In this paper, we will present 3D ISAR imaging of a realistic target using the EM simulation data from FEKO EM simulator for small frequency-bandwidth and small-angle approximation.

2. 3D ISAR IMAGING

The 3D ISAR image actually presents a 3D profile of a target in range and two cross-range domains (azimuth and elevation). Therefore, the backscattered field data must be gathered for various frequencies and different azimuth and elevation angles. The gathered data occupy a finite space in the spatial frequency domain (k_x , k_y , and k_z). If the backscattered electric field data are collected within a small bandwidth of frequencies, B (or BW_k), and width of viewing angles, BW_ϕ and BW_θ , the data grid in the spatial frequency (k_x , k_y , k_z) space becomes an equally spaced linear grid. This assumption enables to use Fast Fourier Transform (FFT) in reconstructing the 3D ISAR image.

The point scatterer to be imaged is located at $P(x_o, y_o, z_o)$. The radar illuminates the target with a wavenumber vector of $\mathbf{k} = k\hat{\mathbf{k}}$. The direction of illumination makes an angle of θ with the z -axis. It also makes an angle of α with x - y plane. Taking origin as the phase center of the scene, the far-field backscattered E -field from a point scatterer P at azimuth angle ϕ and elevation angle θ can be written as $E^s(k, \phi, \theta) = A_o e^{-j2\mathbf{k}\cdot\mathbf{r}_o}$. At this point we assume the backscattered signal is collected within a frequency bandwidth, B , that is small compared to the center frequency of operation, f_c . We further assume that the angular bandwidths in both θ and ϕ directions are also small. If the radar is located around the x -axis, the following approximations are valid: $k \approx k_c$, $\cos \alpha \cos \phi \approx 1$, $\cos \alpha \sin \phi \approx \phi$, $\sin \alpha \approx \alpha$. Then, the scattered electric field from point P is approximated as [3]

$$E^s(k, \phi, \alpha) = A_o e^{-j2k \cdot \cos \alpha \cos \phi \cdot x_o} e^{-j2k \cdot \cos \alpha \sin \phi \cdot y_o} e^{-j2k \sin \alpha \cdot z_o} \approx A_o e^{-j2k_c \cdot x_o} e^{-j2k_c \cdot \phi \cdot y_o} e^{-j2k_c \alpha \cdot z_o}$$

To be able to use the advantages of FT, we can reorganize the above equation as follows:

$$E^s(k, \phi, \alpha) \approx A_o e^{-j2\pi(\frac{2f_c}{c}) \cdot x_o} e^{-j2\pi(\frac{k_c \cdot \phi}{\pi}) \cdot y_o} e^{-j2\pi(\frac{k_c \cdot \alpha}{\pi}) \cdot z_o}$$

Then the 3D ISAR image in the spatial domain (x, y, z) can be obtained by taking the 3D inverse Fourier Transform of the above equation with respect to $(\frac{2f_c}{c})$, $(\frac{k_c \cdot \phi}{\pi})$ and $(\frac{k_c \cdot \alpha}{\pi})$ as follows:

$$\begin{aligned} ISAR(x, y, z) &= A_o \cdot F_1^{-1} \left\{ e^{-j2\pi(\frac{2f_c}{c}) \cdot x_o} \right\} F_1^{-1} \left\{ e^{-j2\pi(\frac{k_c \cdot \phi}{\pi}) \cdot y_o} \right\} F_1^{-1} \left\{ e^{-j2\pi(\frac{k_c \cdot \alpha}{\pi}) \cdot z_o} \right\} \\ &= A_o \cdot \left[\int_{-\infty}^{\infty} e^{-j2\pi(\frac{2f_c}{c}) \cdot x_o} \cdot e^{j2\pi(\frac{2f_c}{c}) \cdot x} d\left(\frac{2f_c}{c}\right) \right] \\ &\quad \cdot \left[\int_{-\infty}^{\infty} e^{-j2\pi(\frac{k_c \cdot \phi}{\pi}) \cdot y_o} \cdot e^{j2\pi(\frac{k_c \cdot \phi}{\pi}) \cdot y} d\left(\frac{k_c \cdot \phi}{\pi}\right) \right] \\ &\quad \cdot \left[\int_{-\infty}^{\infty} e^{-j2\pi(\frac{k_c \cdot \alpha}{\pi}) \cdot z_o} \cdot e^{j2\pi(\frac{k_c \cdot \alpha}{\pi}) \cdot z} d\left(\frac{k_c \cdot \alpha}{\pi}\right) \right] \\ &= A_o \cdot \delta(x - x_o, y - y_o, z - z_o) \end{aligned}$$

The backscattered electric field from a target can be approximated as the sum of scattering from a finite number of single point scatterers, called scattering centers, on the target as shown below

$$E^s(k, \phi, \alpha) \approx \sum_{i=1}^M A_i e^{-j2\mathbf{k} \cdot \mathbf{r}_i}$$

The backscattered electric field from a target is approximated as the sum of backscattered field from M different scattering centers on the target. While A_i represents the complex backscattered field amplitude for the i -th scattering center, \mathbf{r}_i is displacement vector from the origin to the location of i -th scattering center. Then, the ISAR image of the target can be found via the following inverse 3D Fourier integral

$$ISAR(x, y, z) = \iiint_{-\infty}^{\infty} E^s(k, \phi, \alpha) \cdot e^{j2\pi(\frac{2f_c}{c}) \cdot x} e^{j2\pi(\frac{k_c \cdot \phi}{\pi}) \cdot y} e^{j2\pi(\frac{k_c \cdot \alpha}{\pi}) \cdot z} d\left(\frac{2f_c}{c}\right) d\left(\frac{k_c \cdot \phi}{\pi}\right) d\left(\frac{k_c \cdot \alpha}{\pi}\right)$$

By entering the scattering center representation for the backscattered field, the small-bandwidth small-angle ISAR image can then be approximated as follows:

$$ISAR(x, y, z) \approx \sum_{i=1}^M A_i \delta(x - x_i, y - y_i, z - z_i)$$

Therefore, the resulting ISAR image is the sum of M scattering centers with their own electromagnetic reflectivity coefficients. In practical cases, the limits of the integral will be limited to finite frequency bandwidth and finite angular intervals. So, the impulse function will be blurred to the sinc function.

3. SIMULATION RESULTS

Simulation was implemented under the following environment: FEKO EM simulator v7.0 [7], Microsoft Windows™ 7 Professional (64 bit), Intel™Xeon™CPU E5-2667 2.9 GHz, RAM 64 GB. The target model for the simulation is 6.8 m in length, 17.78 m in width, and 1.64 m in height as shown in Figure 1. The direction of body length is Z axis and range direction, the direction of wing is Y axis and cross-range direction, and down direction is X axis. The angles from Z axis and X axis are θ and ϕ , respectively.

The EM simulation for frequency step $\Delta f = 1.96$ MHz, angle step $\Delta\theta = 0.3915$ degree and $\Delta\phi = 0.095$ degree under the following conditions of transmitted frequency $f_c = 9.65$ GHz (9.5~981 GHz), transmitted bandwidth $B = 310$ MHz (small bandwidth), linear polarization, look angle interval $\theta = 9.9833$ degree ($-5 \sim 4.9833$ degree), $\phi = 5.985$ degree ($-3 \sim 2.985$ degree) (small angle scan), gives total $157 \times 256 \times 64$ data samples ($N_x = 157$, $N_y = 256$, $N_z = 64$) with “Large PO” setting in FEKO. The reason for the selection of PO method is to reduce the computation time and memory

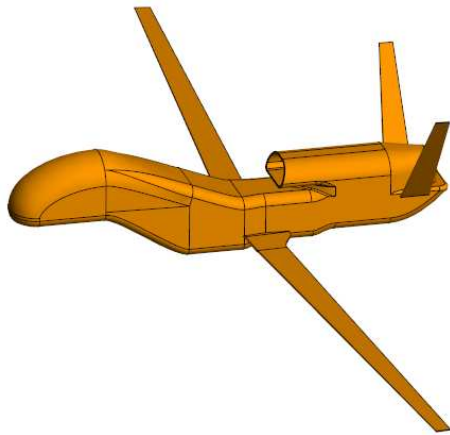


Figure 1: Target model.

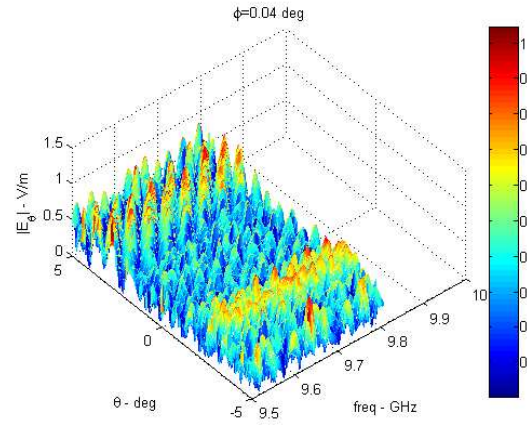


Figure 2: Electric field 2D spectrum in theta direction.

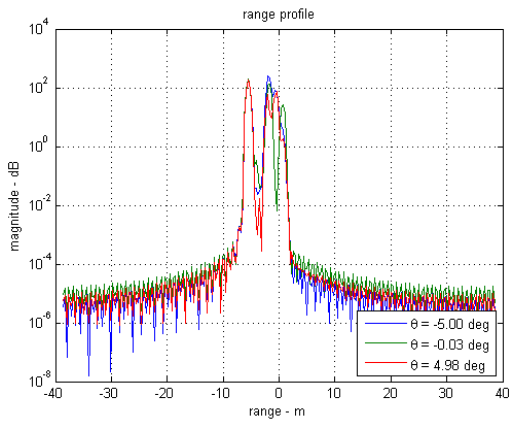


Figure 3: HRRP (high resolution range profile).

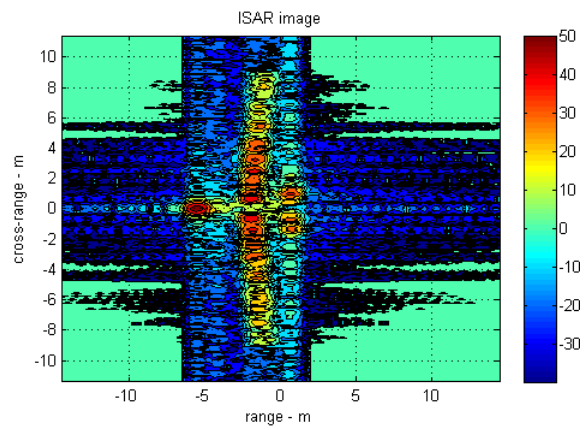


Figure 4: 2D ISAR image.

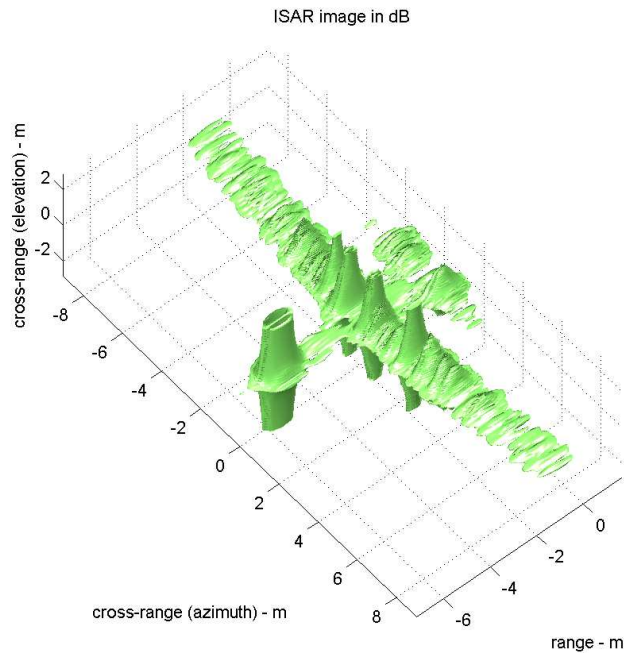


Figure 5: 3D ISAR image.

usage because of the electrically large target size. The number of meshes is 46824. The material of the target is assumed to be a PEC (Perfectly Electric Conductor) for simplicity. The EM analysis result data are saved in FEKO as an FFE file. Figure 2 shows the E -field data in θ axis $E_\theta(f)$ at frequency f .

Figure 4 depicts the 2D ISAR image of the given target. Figure 5 shows the 3D ISAR image of the given target reconstructed by 3D inverse Fourier transform under small bandwidth, small angle scan approximation. When comparing with the 2D ISAR image, we can see the 3D ISAR image gives more informative features of the target.

4. CONCLUSIONS

In this paper, we described the generation of 3D ISAR images for a realistic target model using a general purpose EM simulator, FEKO. After obtaining the EM simulation data from FEKO, we generated 3D ISAR image using 3D inverse Fourier transform under the small-bandwidth small angle assumptions. This method can benefit us many advantages like building the database of many targets for target recognition with cost-and-time effective way and designing a radar and evaluating its performance under more realistic situations.

ACKNOWLEDGMENT

This research was supported by the MSIP(Ministry of Science, ICT and Future Planning), Korea, under the “IT Consilience Creative Program” (IITP-2015-R0346-15-1008) supervised by the IITP(Institute for Information & Communications Technology Promotion); “Civil Military Technology Cooperation (13-DU-EE-11), Development of LTCC Transceiver Module for Small SAR”; “The authors gratefully acknowledge the support from Electronic Warfare Research Center at Gwangju Institute of Science and Technology (GIST), originally funded by Defense Acquisition Program Administration (DAPA) and Agency for Defense Development (ADD)”.

REFERENCES

1. Wehner, D. R., *High-resolution Radar*, 2nd Edition, Artech House, 1995.
2. Mensa, D., *High Resolution Radar Cross Section Imaging*, Artech House, 1991.
3. Ozdemir, C., *Inverse Synthetic Aperture Radar Imaging with MATLAB Algorithms*, Wiley, 2012.
4. Xu, X. J. and R. M. Narayanan, “Three-dimensional interferometric ISAR imaging for target scattering diagnosis and modeling,” *IEEE Transactions on Imaging Processing*, Vol. 10, No. 7, 1094–1102, Jul. 2001.
5. Wang, G. Y., X. G. Xia, and V. C. Chen, “Three-dimensional ISAR imaging of maneuvering targets using three receivers,” *IEEE Transactions on Imaging Processing*, Vol. 10, No. 3, 436–447, Mar. 2001.
6. Cao, X. H., F. L. Su, H. D. Sun, et al., “Three-dimensional In-ISAR imaging via the emulated bistatic radar,” *Processing of ICIEA 2007*, 2826–2830, 2007.
7. *FEKO User’s Manual*, EM Software & Systems-S.A. (Pty) Ltd., 2014.

A Comparison of SAR Imaging Performance between Matching Filter and Compressed Sensing

Gang Wang, Ze Yu, and Peng Xiao

School of Electronics and Information Engineering, Beihang University, Beijing 100191, China

Abstract— This paper is devoted to propose some new efficient indicators in comparison of synthetic aperture radar (SAR) imaging performance between matching filter (MF) and compressed sensing (CS). Generally, SAR utilizes matched filtering (MF) technique to improve resolution, whereas CS is a newly developed technology for sparse or compressible signal which can be applied to SAR imaging to achieve super-resolution images. Based on the theory derivation, the paper compares CS with MF in several aspects, such as resolution and SNR, several new indicators were also given to evaluate imaging performance because of new features caused by CS processing, such as microscopic and macroscopic resolution and group spread function (GSF). The comparison results are discussed and verified by data simulation.

1. INTRODUCTION

SAR utilizes the relative movement between target and radar to synthesize a large virtual aperture to improve azimuth resolution, and adopts MF technique to improve range resolution [1]. In 2006, Donoho proposed compressed sensing (CS) theory [2], which takes full advantage of the sparsity or compressibility of signal to reconstruct original signal while the sampling rate can be reduced considerably. In recent years, some scholars have discussed CS in SAR imaging and published some related articles [3], and it is proved that CS has the ability to achieve super resolution and decrease sampling rate.

2. THEORETICAL ANALYSIS

2.1. CS Theory

CS theory shows that when the signal is sparse in some transform domain, it can be recovered from a small amount of measurements with high probability by solving an optimization problem. A signal \mathbf{x} with a length of N can be sparsely represented in the basis $\psi = \mathbf{C}^{M \times N}$ as $\mathbf{x} = \Psi \mathbf{s}$. After \mathbf{x} is projected onto a measurement matrix $\Phi \in \mathbf{C}^{M \times N}$ with $M < N$, the measured values can be expressed as $\mathbf{y} = \Phi \mathbf{x}$. The signal can be recovered by solving a convex optimization problem as

$$\min \|\mathbf{s}\|_1, \text{ subject to } \mathbf{y} = \Phi \mathbf{x} = \Phi \Psi \mathbf{s} = \Theta \mathbf{s} \quad (1)$$

Candes and Tao pointed out that in order to ensure convergence of the algorithm, matrix Θ in (1) must satisfy the restricted isometry property (RIP) [4]. If a matrix Θ satisfies (2) for all vectors \mathbf{v} with at most k non-zero elements, the matrix Θ has RIP

$$(1 - \delta_K) \|\mathbf{v}\|_2^2 \leq \|\Theta \mathbf{v}\|_2^2 \leq (1 + \delta_K) \|\mathbf{v}\|_2^2 \quad (2)$$

where $\delta_K \in (0, 1)$ is the smallest quantity for matrix Θ to satisfy (2).

2.2. SAR Imaging Based on CS Theory

According to CS theory, sparse dictionary and recovery algorithm play crucial role in signal reconstruction. At high frequencies, target can be modeled as the sum of echoes from strong scattering centers. Assuming the target contains N strong scattering centers and radar transmits chirp signal, the target echo can be expressed as

$$s_r(t) = \sum_{n=1}^N \text{rect} \left(\frac{t - \tau_n}{T} \right) e^{j\pi K(t - \tau_n)^2} \quad (3)$$

where T is the pulse width, K is the chirp rate, τ_n is time delay caused by the round-trip distance between radar and each scattering center, and c is the speed of light.

According to above analysis, sparse dictionary Θ can be constructed by the set of echoes from target at various ranges. The construction steps are as follows: [5]

1) Assuming that $[R_0, R_0 + \Delta R]$ is the distance range of the target. Divide the distance range at intervals of Δr as $Range = \{R_0, R_0 + \Delta r, R_0 + 2\Delta r, \dots, R_0 + \lfloor \Delta R / \Delta r \rfloor \times \Delta r\}$.

2) The echo from target at different range is treated as the column vector $\Psi_{\mathbf{n}}$ of basis matrix. Let f_s be sampling rate, I be the number of samples. After discretization, the element is $\Psi_{i,n} = \text{rect}(\frac{i/f_s - 2(R_0 + (n-1)\Delta r)/c}{T}) \exp\{j\pi K(i/f_s - 2(R_0 + (n-1)\Delta r)/c)^2\}$.

3) Let $\Theta_{\mathbf{n}}$ be the column vector of Θ , and it can be obtained by extracting data from $\Psi_{\mathbf{n}}$ at intervals of d , that means $\Theta_{m,n} = \Psi_{1+(m-1)d,n}$, $m = 1, 2, \dots, \lfloor I/d \rfloor$. Each column vector $\Theta_{\mathbf{n}}$ is called an atom of sparse dictionary.

3. SIMULATION AND DISCUSSIONS

Experiments are carried out and simulation results are presented to illustrate imaging performance based on MF and CS theory.

3.1. Microscopic and Macroscopic Resolution

To prove microcosmic resolution and the effect of rank of Θ on CS reconstruction, we test with 1-D both range echoes and azimuth echoes from 10 scattering centers which have uniform amplitude and are regularly spaced in the range [3000, 3020]. By changing the value of Δr , the rank of Θ varies from less than the number of columns to greater than it.

Table 1: Simulation parameters.

Parameters	Values
Band Width B (MHz)	60
Wavelength λ (m)	0.032
Slant Range R_0 (km)	30
Sampling Rate/ f_s (MHz)	150
Pulse Width T (μs)	10
Radar Velocity v (m/s)	250
Pulse Repeat Frequency (PRF)/ f_a (Hz)	600

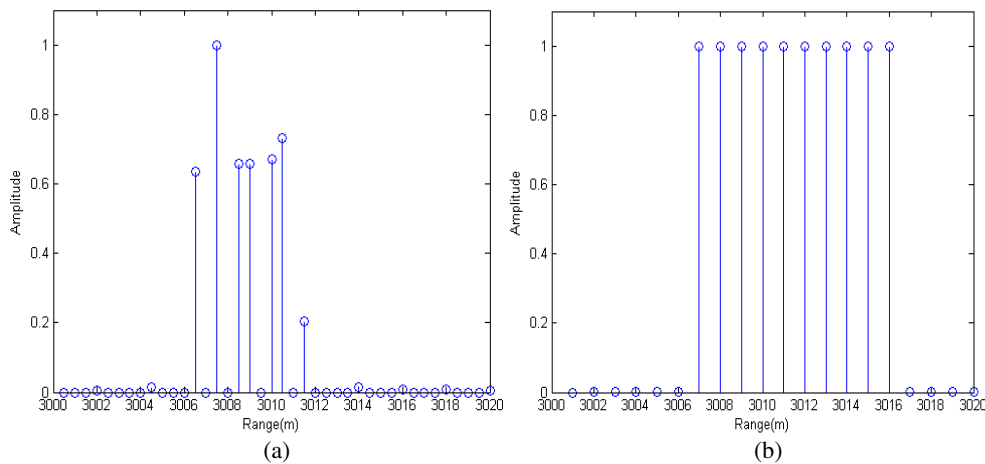


Figure 1: Reconstruction results of 1-D range signal. (a) $\Delta r < c/2f_s$. (b) $\Delta r \geq c/2f_s$.

From Fig. 1(a) and Fig. 2(b), when interval Δr is less than microcosmic resolution, or distance range R is bigger than macroscopic resolution, the signal could not be recovered correctly by utilizing CS theory as signal amplitude is not uniform in Fig. 1(a) and some signals appear in unexpected positions in Fig. 2(b) because there are some columns in sparse dictionary whose coherence is large. However, when $\Delta r \geq c/2f_s$ and $\Delta R < 2\pi V f_a / d |K_a|$, CS method can recover signal perfectly. Furthermore, the distance between two scattering centers in Fig. 1(b) is $c/2f_s = 1$ m, and the range resolution after MF should be $c/2B = 2.5$ m, which proves that the resolution can be greatly improved by using CS reconstruction.

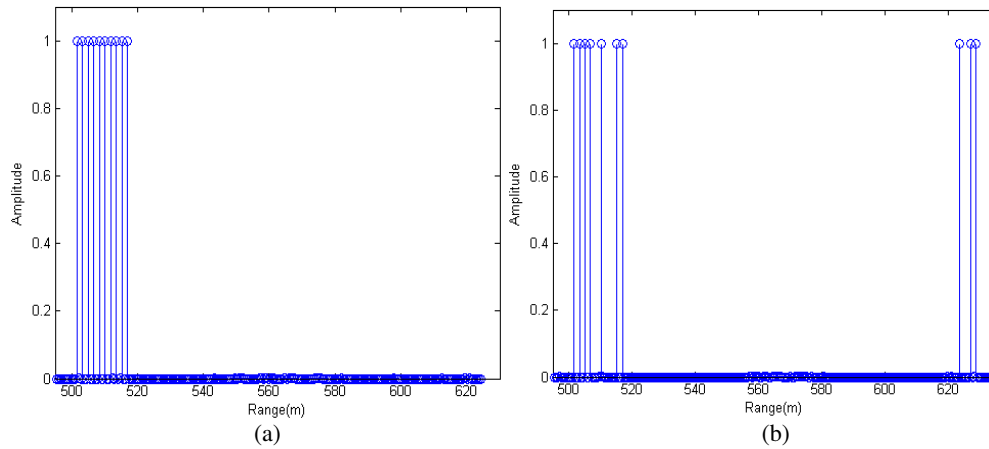


Figure 2: Reconstruction results of 1-D azimuth signal. (a) $\Delta R < 2\pi V f_a / d |K_a|$. (b) $\Delta R \geq 2\pi V f_a / d |K_a|$.

3.2. GSF Comparison

To compare GSF between MF and CS, we test with 1-D range echoes from 20 scattering centers which has uniform amplitude and are regularly spaced within a microscopic resolution cell (3000 ~ 3002.5). The radar parameters are given in Table 2 and simulation result is given in Fig. 3. As shown, the results after MF and CS processing are almost the same.

Table 2: Simulation parameters.

Parameters	Band Width B (MHz)	Sampling Rate f_s (MHz)	Pulse Width T (us)	Interval Δr (m)
Values	60	60	10	2.5

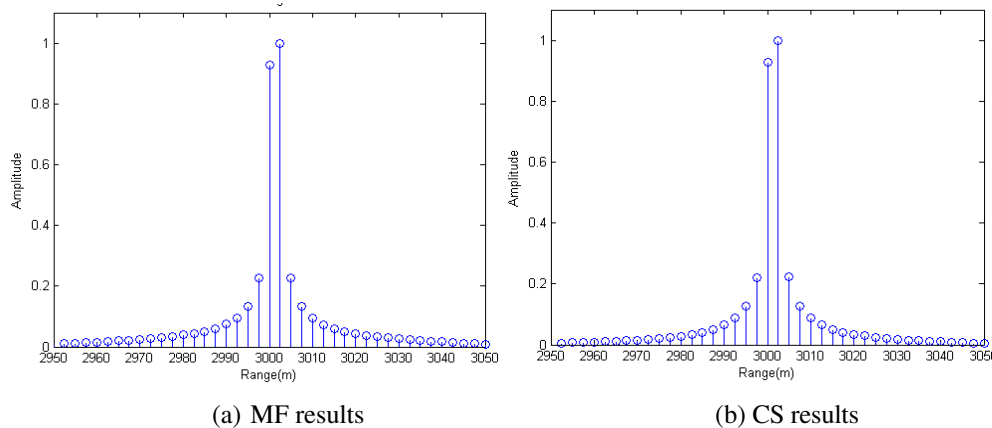


Figure 3: GSF comparison result.

3.3. SNR Comparison

To prove $SNR_{out} : SNR_{in} = M : N$, we changed input SNR and the ratio in sparse dictionary to achieve the statistical result on SNR. The results are as follows.

According to Table 4, Table 5 and Table 6, the ratio of output SNR to input SNR is around M/N , which can prove the validity of equation $SNR_{out} = \frac{P_{Sout}}{P_{Nout}} = \frac{P_{Sin}}{P_{Nin}} \cdot \frac{M}{N} = SNR_{in} \cdot \frac{M}{N}$. According to the comparison processing shown in Fig. 4, it is obvious that output SNR after MF is higher than that after CS processing when input SNR is given, which means MF has better anti-noise performance when compared to CS method.

Table 3: Simulation parameters.

Parameters	Values
Wavelength λ (m)	0.0566
Altitude H (km)	500
Slant Range R (km)	550
Antenna Length L (m)	10
Band Width B_r (MHz)	20
Sampling Rate f_s (MHz)	24
Pulse Width T_r (μ s)	40
Satellite Velocity v (m/s)	5000
Pulse Repeat Frequency (PRF) f_a (Hz)	1000

Table 4: $M : N = 4$.

SNRin	SNRout	F
9.71E+02	3.86E+03	3.98
9.80E+01	3.88E+02	3.96
9.72E+00	3.89E+01	4.00
1.00E+00	3.79E+00	3.79
9.98E-02	4.40E-01	4.41
1.00E-02	4.04E-02	4.04
1.00E-03	4.00E-03	4.00

Table 5: $M : N = 10$.

SNRin	SNRout	F
1.02E+03	1.05E+04	10.28
9.90E+01	1.02E+03	10.32
9.95E+00	1.02E+02	10.21
1.02E+00	1.01E+01	9.90
1.00E-01	1.04E+00	10.40
1.00E-02	1.00E-01	10.00
9.74E-04	9.80E-03	10.06

Table 6: $M : N = 16$.

SNRin	SNRout	F
9.83E+02	1.58E+04	16.11
1.01E+02	1.49E+03	14.72
9.90E+00	1.58E+02	15.96
1.00E+00	1.60E+01	16.00
1.00E-01	1.56E+00	15.60
1.00E-02	1.58E-01	15.80
9.90E-04	1.65E-02	16.67

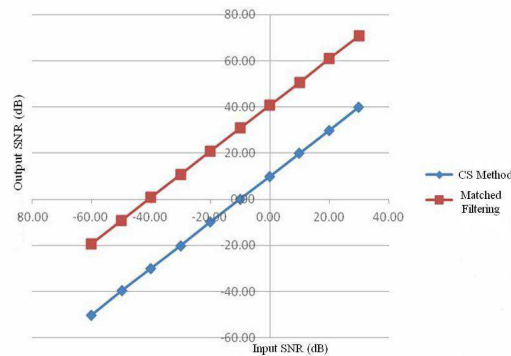


Figure 4: SNR comparison result.

4. CONCLUSIONS

According to theoretical analysis and simulation results, the resolution can be improved considerably by using CS when the sampling rate is greater than corresponding bandwidth, but ambiguity phenomenon will appear as the distance increases where does not occur when using MF. Besides macroscopic and microscopic resolution, GSF is also an important indicator to measure resolution, and it is proved that two methods' GSF are almost the same when sampling rate is close to bandwidth. In addition, output SNR for CS imaging varies with the number of rows and columns in sparse dictionary when input SNR is given, and its anti-noise ability is weaker than that when using MF which is designed to produce the maximum achievable SNR.

Each method has its own strength and weakness, and CS could not replace MF even if it has so many advantages because CS still has some characteristics not good as that of MF, such as SNR. So we must select appropriate imaging method based on specific situation.

REFERENCES

1. Cumming, I. G. and F. H. Wong, *Digital Processing of Synthetic Aperture Radar Data: Algorithms and Implementation*, Artech House Publishers, 2005.

2. Donoho, D. L., "Compressed sensing," *IEEE Trans. Inf. Theory*, Vol. 52, No. 4, 1289–1306, Apr. 2006.
3. Wei, S.-J., X.-L. Zhang, J. Shi, and G. Xiang, "Sparse reconstruction for SAR imaging based on compressed sensing," *Progress In Electromagnetics Research*, Vol. 109, 63–81, 2010.
4. Candes, E. J. and T. Tao, "Decoding by linear programming," *IEEE Trans. Information Theory*, Vol. 51, 4203–4215, Dec. 2005.
5. Ni, Z. W., M. X. Zhang, J. Li, and Q. C. Wang, "Image compressed sensing based on data-driven adaptive redundant dictionaries," *Progress In Electromagnetics Research M*, Vol. 22, 73–89, 2012.

Micro-motion Target Detection Based on Wall Envelope Alignment in Through-the-wall Ultra-wideband Radar

Lei Qiu, Tian Jin, Biying Lu, and Zhimin Zhou

College of Electronic Science and Engineering, National University of Defense Technology
Changsha, Hunan 410073, China

Abstract— Change Detection techniques are used to detect moving targets and mitigate the heavy clutter caused by strong reflections from stationary targets in through-the-wall radar. However the jitter of antenna platform results in phase distortion of scattered radar signal and decreased the performance of micro-motion target detection. This paper proposes an antenna platform jitter compensation method based on wall envelope alignment, aiming to detect micro-motion targets behind wall. Firstly, the antenna platform jitter model is established, then wall envelope alignment is applied to compensate antenna jitter in range direction and the jitter effect in cross direction is evaluated. Simulation and experimental results demonstrate that the proposed approach can compensate antenna platform jitter, eliminate the stationary clutter and detect micro-motion targets correctly and effectively.

1. INTRODUCTION

The detection of human targets behind obstacle has become a keen research topic in recent years and is highly desired in military and civil applications [1]. The jitter of through-the-wall (TTW) ultra-wideband (UWB) radar antenna platform caused by working engine wobble or environmental factors such as wind blowing, results in stationary targets position change in different data frames. Although the change is tiny, the residual energy of stationary targets after change detection [2] is much greater than that of moving targets, particularly of micro-motion human targets due to the low reflectivity of human and high signal attenuation of wall.

The error caused by antenna platform jitter includes antenna tilt error and translation error, and the former can be ignored due to the large beam angle of UWB radar. Literature [3] points out that when the jitter extension is less than a quarter of wavelength, the jitter in a frame time for stepped frequency continuous wave (SFCW) radar can be ignored. Besides, the jitter frequency is inferior to frame frequency, so it is reasonable that the platform was assumed to be unchanged during a frame time, and the jitter compensation is only performed between different frames.

Antenna platform jitter compensation, including envelope alignment and phase compensation, are widely investigated in inverse synthetic aperture radar (ISAR), where the antenna is fixed and target movement is decomposed into the rotation motion and translation motion. Envelope alignment methods, such as dominant scattering point method, envelope cross-correlation method and minimum entropy method [4], are aimed to eliminate the target dislocation relative to radar antenna. However, the received signal of different frame cannot be perfectly aligned because of the target moving, so the envelope cross-correlation method and the minimum entropy method can't achieve the optimal results. Dominant scattering point method is especially significant if there exists a stable and strong dominant scattering center. The envelope alignment of antenna jitter in TTW is distinct from that in ISAR in the following aspects: firstly, only the range direction jitter is considered in ISAR, while in TTW, the jitter in cross direction and in range direction are both required to compensate. Secondly, there is no dominant scattering center but a strong plane reflection of the wall in TTW, so the jitter in range direction can be compensated by the front surface of the wall who has the maximum amplitude in every frame data. However, the jitter in cross direction can't be compensated properly.

This paper proposes an antenna platform jitter compensation method based on wall envelope alignment. The remainder of this paper is organized as follows: in Section 2, the antenna platform jitter model is established. In Section 3, envelope alignment is applied to compensate antenna jitter and the jitter effect in cross direction is evaluated. Simulation and experiments are performed in Section 4. Section 5 gives the conclusion and acknowledge of this paper.

2. ANTENNA PLATFORM JITTER MODEL

A dual mode antenna with a transmitter and a receiver is applied to explore human target behind wall, as shown in Figure 1. The front surface of the wall is set to be X axis, and Y axis is

perpendicular to X axis, the standard Cartesian coordinate system is established in the plane of the antenna. When m_1 and m_2 frame signals are acquired, the antenna platform is located at $A(x, y)$ and $A'(x + \Delta x, y + \Delta y)$, respectively. The jitter misregistration in X axis and Y axis are denoted as Δx and Δy . A human target is located at $H(x_t, y_t)$ behind the wall, d and ε are the thickness and dielectric constant of the wall. To simplify the analysis, only the reflection of front surface of the wall and the human target are considered.

SFCW radar is applied with frequency from f_0 to f_p at a step Δf . T is the pulse interval time and N is the total frequency number, $f_p = f_0 + (N - 1)\Delta f$, and $f_c = (f_0 + f_p)/2$ is the center frequency of SFCW. The transmitter signal $s(t)$ is expressed as

$$s(t) = \sum_{n=0}^{N-1} \text{rect}\left(\frac{t - (n + 1/2)T}{T}\right) \exp[j2\pi(f_0 + n\Delta f)t] \quad (1)$$

where t is the fast time. Neglecting the transmitting loss, the received signal $s_r(t)$ is described as

$$s_r(t) = \sum_{n=0}^{N-1} \text{rect}\left(\frac{t - (n + 1/2)T - \tau_w}{T}\right) \rho_w \exp[j2\pi(f_0 + n\Delta f)(t - \tau_w)] \\ + \sum_{n=0}^{N-1} \text{rect}\left(\frac{t - (n + 1/2)T - \tau_h}{T}\right) \rho_h \exp[j2\pi(f_0 + n\Delta f)(t - \tau_h)] \quad (2)$$

where ρ_w and ρ_h are the reflectivity. $\tau_w = 2r/c$ and $\tau_h = 2R_h/c$ are time delay, c is the speed of light in free space, and r is the range between antenna and the front surface of the wall. R_h is the equivalent distance from A to H according to literature [5], R_h is described as

$$R_h = r_2 + D \left(\sqrt{\varepsilon - \sin^2 \theta} - \cos \theta \right) \quad (3)$$

where θ is the incidence angle, r_2 is the direct distance from A to H . After mixing, filtering and sampling with T interval, $s_r(t)$ is expressed as

$$s_r(m, n) = \rho_w \exp[-j2\pi(f_0 + n\Delta f)\tau_w(m, n)] + \rho_h \exp[-j2\pi(f_0 + n\Delta f)\tau_h(m, n)] \quad (4)$$

where $\tau_w(m, n) = \tau_w((m - 1)NT + nT)$, $\tau_h(m, n) = \tau_h((m - 1)NT + nT)$, $m = 1, 2, \dots, M$ is the slow-time index, $n = 0, 1, \dots, N - 1$ is frequency index. High resolution range profiles are achieved by performing the inverse fast Fourier transform (IFFT) of (4), the HRRP of m frame is expressed as

$$S(m, k) = \rho_w \exp[-j2\pi f_0 \tau_w] \exp[j\pi(N - 1)(k/N - \Delta f \tau_w)] \frac{\sin[\pi(k - N\Delta f \tau_w)]}{\sin[\pi(k/N - \Delta f \tau_w)]} \\ + \rho_h \exp[-j2\pi f_0 \tau_h] \exp[j\pi(N - 1)(k/N - \Delta f \tau_h)] \frac{\sin[\pi(k - N\Delta f \tau_h)]}{\sin[\pi(k/N - \Delta f \tau_h)]} \quad (5)$$

where $k = 0, 1, 2, \dots, N - 1$ is the range cell index, and $S(m, k)$ is the slow-time range map.

3. ENVELOPE ALIGNMENT

According to (5), there are two peak positions for ever frame of $S(m, k)$, corresponding to the front surface of the wall and human target, and the maximum amplitude of $S(m, k)$ in m_1 and m_2 frames are located at $k_1 = \Delta f \tau_{w1}$ and $k_2 = \Delta f \tau_{w2}$, respectively. So the misregistration is described as

$$k_1 - k_2 = \Delta f (\tau_{w1} - \tau_{w2}) = \frac{2\Delta f \Delta y}{c} \quad (6)$$

thus, the misregistration of m_1 and m_2 frames in range direction is

$$\Delta y = \frac{(k_1 - k_2)c}{\Delta f} \quad (7)$$

the antenna platform jitter in range direction can be compensated properly by (7). As a result of the plane reflection of the wall, the antenna jitter in cross direction which is parallel to the wall front surface has no influence on the scattered wall signal.

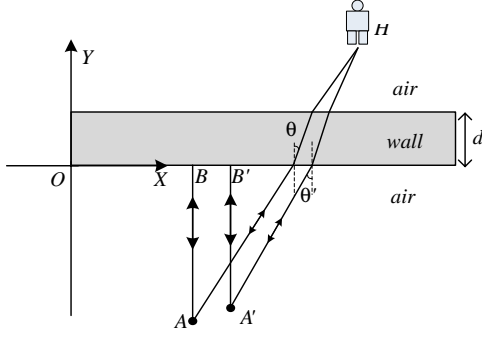


Figure 1: The scenario of human targets behind wall.

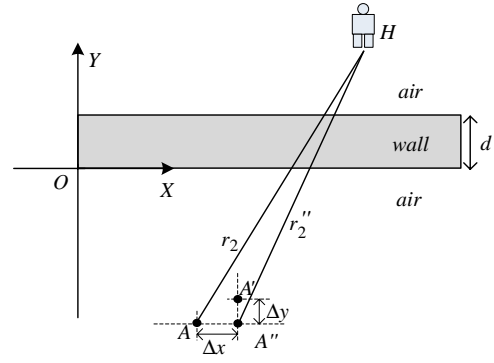


Figure 2: The scenario after envelope alignment in range direction.

After the alignment in range direction the antenna is located at $A''(x + \Delta x, y)$, as depicts in Figure 2. Δx is the antenna jitter misregistration in cross direction. Denote

$$R_h'' = r_2'' + D \left(\sqrt{\varepsilon - \sin^2 \theta''} - \cos \theta'' \right), \quad R_h' = r_2' + D \left(\sqrt{\varepsilon - \sin^2 \theta'} - \cos \theta' \right) \quad (8)$$

where R_h'' and r_2'' are the equivalent and direct range between A'' and H , R_h' and r_2' are the equivalent and direct range between A' and H . θ'' and θ' are the incidence angle, respectively. Considering $r_2'' \gg \Delta x$, $r_2 \gg \Delta x$, $\theta'' \approx \theta' \approx \theta$, the range misregistration of m_1 and m_2 frames after envelope alignment is

$$R_h - R_h'' \approx r_2 - r_2'' \approx \frac{(\Delta x)^2}{2r_2} = \frac{\Delta x}{2r_2} \Delta x \approx 0 \quad (9)$$

When the range between the target and the antenna is 10m, the antenna jitter in cross direction is 0.2m. The misregistration after jitter compensation in range direction is about 2mm by (9). Therefore, the antenna jitter in cross direction can be ignored when the jitter in range direction is compensated.

4. SIMULATION AND EXPERIMENTAL RESULTS

Simulation and experimental results are used to validate the proposed method in this section. A dual mode antenna located at $(0, 0)$ is set to be random jitter both in range direction and in cross direction. Two targets are concerned: a stationary target located at $(0, 8\text{m})$, and a harmonic motion target located at $(0, 10\text{m})$ with amplitude 1.5 cm and frequency 0.3 Hz. SFCW is used at frequency from 1.0 GHz to 3 GHz with 2 MHz frequency steps. The signal-to-noise-ratio (SNR) of radar echo is set to be -5 dB mixed with additional white gauss noise.

Figures 3(a) and 3(b) depict the raw slow-time range map and its antenna jitter compensation results based on the envelope alignment of the stationary target. In order to improve the accuracy of alignment, only the first frame is regarded as a reference. MTI is performed by average canceller to eliminate stationary clutter of every range cell, followed by accumulation of different frame data to aggrandize the micro-motion target.

The antenna platform jitter in range direction is simulated firstly, and the jitter extension is set to be 1 cm, 2 cm, 5 cm, 10 cm and 15 cm, respectively. The accumulation results before and after envelope alignment are depicted in Figure 3(c) and Figure 3(d). The residual energy of stationary target is greater than that of micro-motion target before the compensation is performed. The residual energy of stationary is approach to zero, and the micro-motion is outstanding after jitter compensation, because of the alignment in the stationary position. The SNR of accumulated data decreases along with the antenna jitter extension increases from 1 cm to 15 cm. However, when the maximum jitter in range direction is 15 cm, the proposed method can also eliminate the effect of antenna jitter correctly.

Figure 3(e) and Figure 3(f) depict the effect of antenna jitter in cross direction. The extension in range dimension is set to be 10 cm, and the jitter extension in cross direction is set to be 1 cm, 2 cm, 5 cm, 10 cm, 15 cm, respectively. After envelope alignment in range dimension, there is no significant distinction when the jitter extension varies from 1 cm to 15 cm, so the jitter in cross alignment can be ignored.

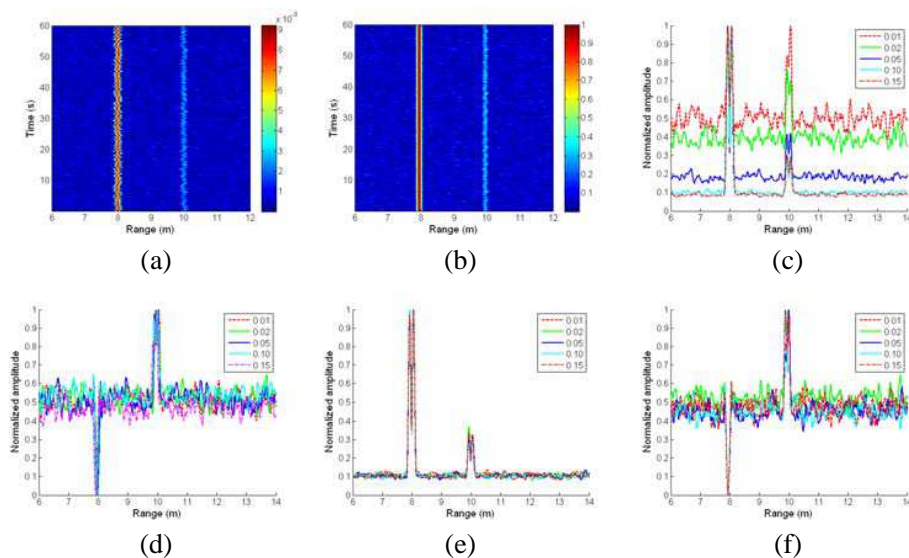


Figure 3: (a) The slow-time range map before jitter compensation; (b) the slow-time range map after jitter compensation; (c) accumulation results before envelope alignment; (d) accumulation results after envelope alignment; (e) accumulation results before envelope alignment; (f) accumulation results after envelope alignment.

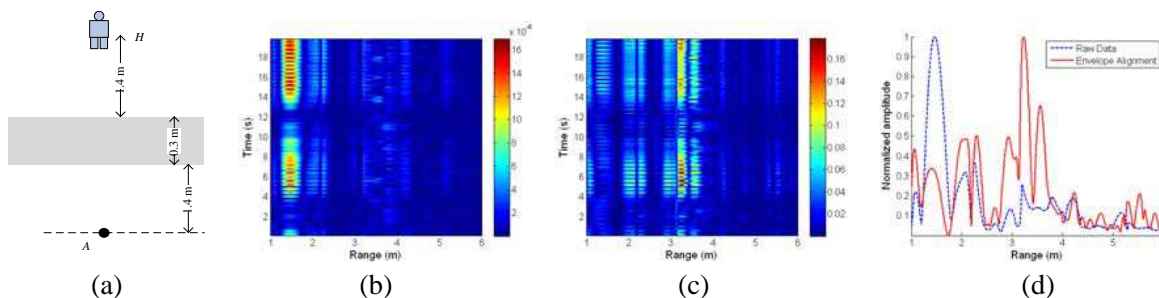


Figure 4: (a) The scenario of the experiment; (b) the slow-time range map before jitter compensation; (c) the slow-time range map after jitter compensation; (d) accumulation results.

A UWB TTW radar system is set up to test the proposed method. The antenna is on a handcart with an electrodynamic vibrator providing the jitter of the platform, and the range between the antenna location and the front surface of the concrete wall is 1.4 m, the wall thickness 30 cm, a human stands at 1.4 m behind the wall, as depicted in Figure 4(a). SFCW radar is applied at frequency from 2.0 GHz to 2.6 GHz with 4 MHz frequency steps. The raw slow-time range map and jitter compensation results are depicted in Figure 4(b) and Figure 4(c), respectively, and the accumulation data is shown in Figure 4(d). In Figure 4(b), the residual of the stationary wall after change detection is dominant due to the antenna jitter. After wall envelope alignment, the wall residual is mitigated and the micro-motion target is prominent. Besides, the human target is located at 3.4 m in the aligned range profile, but the direct range from antenna to the human is 3.1 m. This is because when transmitting signal penetrates through the wall, the free space assumption is no longer applicable. If the thickness d and dielectric constant ε are prior known, the targets range can be compensated to the real position correctly [5].

5. CONCLUSION

The antenna platform jitter results in phase distortion of scattered radar signal and decreased the performance of micro-motion target detection. The residual energy of stationary targets is much greater than that of micro-motion targets after change detection. Antenna jitter compensation based on wall envelope alignment is performed to detect micro-motion targets. Simulation and experimental results demonstrate that the proposed method can compensate antenna jitter in range direction correctly, and the cross-direction can be ignored, and the front surface of the wall

is a stable characteristic to compensate the antenna jitter.

ACKNOWLEDGMENT

This work was supported in part by the National Natural Science Foundation of China under Grant 61271441 and the research project of NUDT under Grant CJ12-04-02.

REFERENCES

1. Baranoski, E. J., “Through wall imaging: Historical perspective and future directions,” *2008 IEEE International Conference on Acoustics, Speech and Signal Processing*, Vols. 1–12, 5173–5176, 2008.
2. Amin, M. G. and F. Ahmad, “Change detection analysis of humans moving behind walls,” *IEEE Trans on AES*, Vol. 49, No. 3, 1410–1425, 2013.
3. Wehner, D. R., *High-resolution Radar*, 197–238, Artech House, Boston, MA, 1995.
4. teinberge, B. D., *Microwave Imaging of Aircraft*, *Proc. IEEE*, Vol. 76, No. 12, 1578–1592, 1988.
5. Jin, T., B. Chen, and Z. Zhou, “Image-domain estimation of wall parameters for autofocusing of through-the-wall SAR imagery,” *IEEE Trans on GRS*, Vol. 51, No. 3, 1836–1843, 2013.

Analysis of a Polycarbonate RFID Tag for Blood Chain Tracking

G. Boi, R. Secci, S. Casu, A. Fanti, and G. Mazzarella

Department of Electrical and Electronic Engineering

University of Cagliari, Italy

Abstract— In this paper we describe an antenna especially designed for a RFID passive tag working at UHF (867 MHz), for healthcare applications. In particular for the transfusional medicine and the blood supply chain. The tag has to be able to work placed on the top of a blood bag, while the bag is full of blood, and the antenna has been designed with this goal in mind. Therefore we require an antenna able to work close to a (relatively large amount of) lossy medium with high permittivity. Moreover, the bag shape is curved but its shape cannot be predicted exactly, so that the antenna must retain its behavior for a large set of different environments. In order to comply with all those requirements, a printed slot antenna built with a exible substrate has been selected, so that the whole tag can be exible too. The first step was the optimization of the working parameters of the antenna while placed on a perfect planar surface (i.e., assuming the blood bag to be a parallelepiped). Since the actual bag shape is not known, this choice allows to take into account the lossy material, but using a simple geometry. The antenna has been optimized to get the maximum reading distance. Then we consider the effects of a real blood bag (i.e., a curved one), filled with blood, on the antenna behavior. We consider a bag with a transverse section bounded by two arc of circles (with a radius quite larger than the bag size). Since we found a reasonable agreement with the planar antenna we can assume that the antenna behavior is quite insensitive to the bag shape. A robustness analysis, respect to the bag curvature radius, has been performed, too, to assess the antenna use in real environments.

1. INTRODUCTION

RFID is the acronym for Radio Frequency Identification and refers, as the name suggests, to the technology [1] that take advantage of radio frequency for identification purposes. Such a technology has been adopted in many fields. One of these is the healthcare [2].

The present leading technology for healthcare applications is the optical barcode, but recently the RFID technology has been introduced and is proving remarkably successful. Localization of critical items is one of the most promising one, in particular the localization and identification of blood bags [3].

The bag is usually filled, stored and used in different locations and, since the bag often carries with itself delicate and important informations, the RFID technology offers many improvements in this direction. Using RFID tag instead of optical one allows to store informations about the blood bag into the tag itself and improves significantly the reading distance.

To fully exploit the RFID technology in the supply chain an adaptation, or better, a re-engineering of the technology is needed. One of the part which can benefit from a re-engineering is the tag antenna, so that it can be adapted to the environment where it has to work. At the moment, the most popular solution is represented by the use of general purpose tag antennas which are not optimized to work in presence of lossy materials. Actually, the antenna environment is the blood bag, filled with a lossy dielectric with a large dielectric constant (the blood which, at UHF, has a typical relative dielectric constant of 61-j33).

The blood thus affects negatively the performances of an antenna designed to work in free space. Another important aspect is represented by the shape of the medical grade PVC bag. Since the tag is typically built using flexible substrates and the bag can easily change its shape, the tag can modify its shape and, as a consequence, the performances of the antenna can be adversely affected.

Keeping in mind all the considerations explained above, a printed slot antenna realized on a grounded slab and able to work at UHF RFID band (867 MHz) has been designed. The design of the antenna has been assessed by verifying that the antenna behavior is quite insensitive to the bag shape.

2. STRUCTURE

Printed slot antennas are not very popular as RFID tag antennas, though some proposal have appeared in the literature [4–6]. Actually, the peculiar feeding arrangement (a RFID chip) is not compatible with a standard printed slot. On the other hand, it allows to use a dipole radiating in

the slot as primary feed. This leads to the basic antenna concept shown in Figure 1, where the vertical microstrip lines act as a short dipole (with a constant current). This dipole is the source of the slot aperture field which, because of the equivalence current [7], radiates the antenna field.

Of course, this simple shape must be engineered and carefully optimized to get an high-performances RFID system. This must be done on the chosen RFID chip and material. We have selected the NXP Semiconductors UCODE G2iM+.

The G2iM+ has Z_{chip} load impedance of $27-j234\ \Omega$ at 867 MHz, good sensitivity in reading (-17.5 dBm) and high user memory (640 bit). Since the input impedance of this chip is not so different from many others, a good matching performances can be retained also with different chips.

The application we have in mind requires a flexible substrate, and we select polycarbonate. The antenna has been first designed, and optimized when located on a blood bag with a rectangular shape [8], and thus with a planar shape.

This optimized antenna has then be located on a curved blood bag, as shown in Figure 2. Since the exact bag shape is not known, we have selected an average shape, made by two cylindrical surfaces with a radius of 13.5 cm. The curved and the rectangular bag have the same volume (450 ml). The blood parameters was defined at 1 GHz and at a temperature of 4°C (while the PVC data are essentially constant up to many GHz, so that available data at 1 MHz have been used) as summarized in Table 1. To evaluate the performances we designed and simulate the antenna with the software CST Microwave Studio [9].

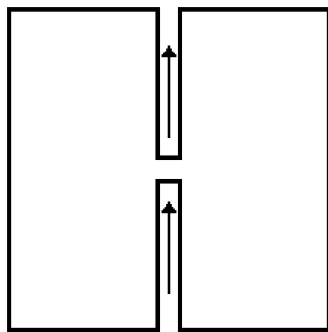


Figure 1. Feed of the patch.

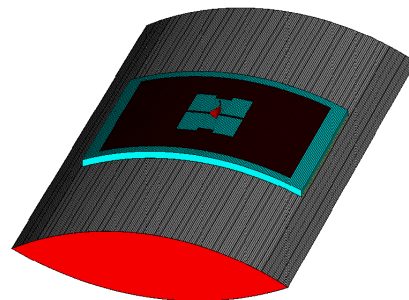


Figure 2.

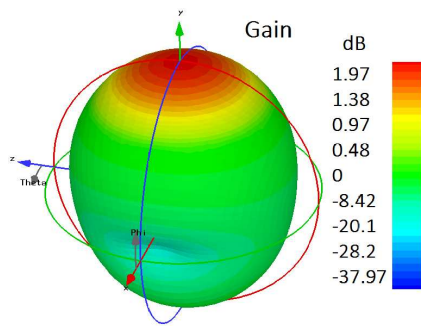


Figure 3. Radiation pattern of the antenna upon the blood bag.

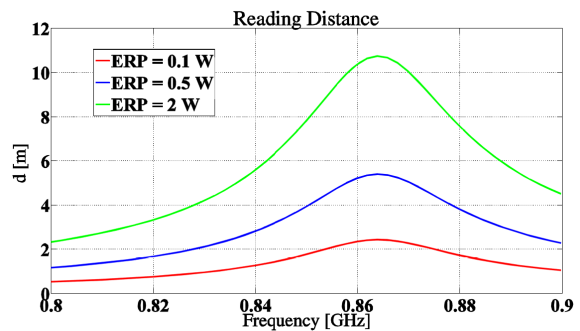


Figure 4. Reading distance.

Table 1. Blood and PVC parameters.

Layer	Dielectric constant ϵ_r	Loss Tangent	Conductivity σ [S/m]	Density [Kg/m ³]	Thickness [mm]
PVC Layer	3.1 (@ 1 MHz)	0.015 (@ 1 MHz)	-	-	0.15
Blood	61.06 (@ 1 GHz)	-	1.5830 (@ 1GHz)	1050	25.2

3. RESULTS

The 3D radiation pattern of our optimized antenna is shown in Figure 3. The pattern is omni in the upside direction, with a gain around 2 dB.

From these data, we can predict the reading distance, which is shown (for different transmission ERP, up to 3 dBW) in Figure 4. Actually, even for an ERP as low as -10 dBW (a value which comply with every national regulation) the reaching distance is larger than 1.5 m in almost all the useful bandwidth.

ACKNOWLEDGMENT

Work supported by Regione Autonoma della Sardegna, under contract Ottimizzazione della logistica in ambito sanitario attraverso l'utilizzo di sistemi RFid, No. F71J12000820002.

REFERENCES

1. Dobkin, D. M., *The RF in RFID: Passive UHF RFID in Practice*, Newnes, 2007.
2. Sani, M. R., R. Foster, and Y. Hao, "Antennas and propagation of implanted RFIDs for pervasive healthcare applications," *Proceedings of the IEEE*, 1648–1655, Sep. 2010.
3. Borrelli, G., F. V. Caredda, A. Fanti, G. Gatto, G. Mazzarella, P. F. Orr, A. Serpi, I. L. Spano, E. Tanzi, A. Volpi, and F. Zedda, "Preliminary study of RFID technologies for health-care applications," *The International Workshop on Innovative Simulation for Healthcare*, Sep. 2014.
4. Dubok, T., T. J. Coenen, A. Zamanifekri, and A. B. Smolders, "Robust UHF RFID antennas in complex environments," *7th European Conference on Antennas and Propagation (EuCAP)*, 1695–1699, Apr. 2013.
5. Ibrahim, R. A. and M. C. E. Yagoub, "Practical novel design component of microstrip patch slot antenna MSPSA for RFID applications," *IEEE 23rd Canadian Conference on Electrical and Computer Engineering (CCECE)*, May 2010.
6. Marrocco, G., "RFID antennas for the UHF remote monitoring of human subjects," *IEEE Transactions on Antennas and Propagation*, Jun. 2007.
7. Franceschetti, G., *Electromagnetics: Theory, Techniques, and Engineering Paradigms*, Plenum Press, 2013.
8. Fanti, F., R. Secci, G. Boi, S. Casu, G. A. Casula, G. Mazzarella, and G. Montisci, "A polycarbonate RFID tag for blood chain tracking," *Antennas Propagation Symposium*, Vancouver, Jul. 2015.
9. CST GmbH, CST Microwave Studio Help, CST Studio Suite Version 2011.14.01, 2011, <http://eee.guc.edu.eg/Courses/Communications/COMM905>.

28 GHz Delay Spread Measurement Using a Broadband Channel Sounder in Small Urban City

Young Keun Yoon, Jong Ho Kim, Myoung Don Kim,
Young Jun Chong, and Myoung Sun Song

ETRI (Electronics and Telecommunications Research Institute), Republic of Korea

Abstract— This paper describes the relations between the R.M.S delay spread and TX-RX separation distance for Daejeon City measurements at 28 GHz frequency with 500 MHz channel bandwidth. R.M.S delay spread is caused by multipath due to a large number of reflective and diffractive characteristics in various urban environments.

1. INTRODUCTION

Recently, the fifth generation mobile communication to satisfy the needs of high data rates in the small cell environment has attracted the attention. Millimeter frequency bands for 5G services are the lands of new frontier being able to support broadband bandwidth from 0.5 up to 2.0 GHz in [1]. We know that feasibility research at millimeter bands is carried out currently. Yet, there is still the lack of the collected field data and statistical models based on measurement. Therefore, we performed measurement in small urban city of Korea to find specific root mean square delay spread characteristics.

2. HARDWARE & MEASUREMENT CAMPAIGN

2.1. Hardware Channel Sounder

Millimeter wave Band Exploration and Channel Sounder (mBECS) developed by Electronics and Telecommunications Research Institute (ETRI) was used in the indoor/outdoor both pathloss and root mean square (R.M.S) delay spread measurement campaign. mBECS is a wideband channel sounder for measuring temporal and spatial characteristics. Using a 500 Mcps broadband channel sounder with 2.0 ns multipath resolution, we conducted R.M.S delay spread measurements at 28 GHz frequency band in Daejeon City, Korea. mBECS consists of five parts: baseband/IF modules, RF module, horn antenna, timing module and mechanical module. A measurement manager is able to control each part of the transmitter (TX) and receiver (RX). Timing module operates as rubidium oscillator which provides reference clock within 1 ns in order to synchronize the clock of TX and RX being far away. A 4095 chips pseudo-random noise (PN) sequence sliding correlator was utilized, which was modulated to a 5.2 GHz intermediate frequency (IF) and upconverted 28 GHz. The maximum TX power was 29 dBm, fed to a 30° beamwidth 12.9 dBi horn antenna that was mechanically rotated or tilted. The RX used a 10° beamwidth 21.4 dBi horn antenna and the same type of enable mechanically rotating or tilting structure such as the transmitter with antennabeamwidth of 30°.

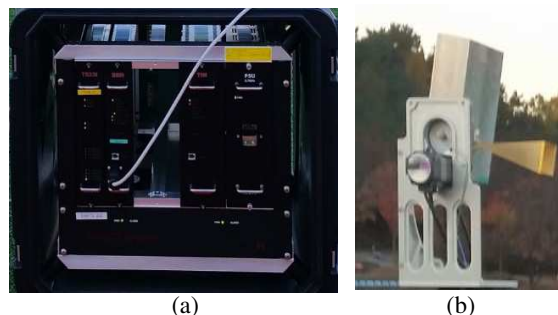


Figure 1: Channel sounder. (a) Baseband/IF module. (b) RF/antenna/positioner.

2.2. Measurement Campaign

To obtain delay spread characteristics in none line of sight(NLOS) environment, TX site locates on the side of a four-lane main road in the Daejeon City of Korea. NLOS environment includes low-rise (three to five stories which has nine to fifteen meter height) buildings, a four-lane main road, several two-lane side streets, vehicles, subsidiary facilities, and peoples. The measurement campaign was taken during daytime from 9 am to 6 pm. During measurement, TX location and antenna bore sight direction was fixed, and RX puts in two-lane side load in NLOS locations. We choose one TX at a height of 4m and 15 RX measurement locations. The distance between the TX and RX ranged from about 120 to 400 m. At RX at a height of 1.5 m, a 360° azimuth sweep at each RX position was automatically performed in steps of 10° because of using 21.4 dBi horn antenna with the 10° half power beamwidth. Extensive measurements were conducted for the thirty six different RX azimuth angles ranged from 0° to 350° , and for the three different RX elevation angles of -10° , 0° , and +10° creating one hundred eight possible antenna pointing steps. For each of one hundred eight steps, measurement data were recorded. Finally, R.M.S delay spread measurements were done at the RX locations in Daejeon, Republic of Korea



Figure 2: Measurement campaign.

3. RESULTS

3.1. Delay Spread

Multipath, which results in intersymbol interference, causes time dispersion, as described by channel impulse response (CIR). When channel is time varying, time t is needed, and τ is multipath delay.

Let equivalent complex-envelop CIR in time-variant is,

$$h(t, \tau) = \sum_{i=0}^{I-1} p_i(t, \tau) \exp(-j\varphi_i(t, \tau)) \delta(\tau - \tau_i(t)) \quad (1)$$

where, p_i , φ_i , τ_i are the amplitude, phase shift and excess delay of the i -th propagation path, respectively. I means total multipath components of transmitted signal arriving at RX. Useful to discrete τ into delay bins, each bin represents a multipath component. At time t , each bin arrives at RX with different amplitude, go through a different phase shift, and has a different excess delay.

To derive delay spread at RX in this paper, it is assumed that channel is time invariant as a special case. This means that multipath components of transmitted signals arriving at the same RX location have the same time excess delay. In time-invariant case, let equivalent complex-envelop CIR can be written as,

$$h(\tau) = \sum_{i=0}^{I-1} p_i \exp(-j\varphi_i) \delta(\tau - \tau_i) \quad (2)$$

where, p_i , φ_i , τ_i are the amplitude (Rayleigh distributed), phase shift (uniformly distributed) and excess delay (Poisson distributed) of the i -th propagation path, respectively.

R.M.S delay spread ($\tau_{R.M.S}$), which is defined as the square root of the second central moment of power delay profile, is a measurement index of multipath which results in inter-symbol interference

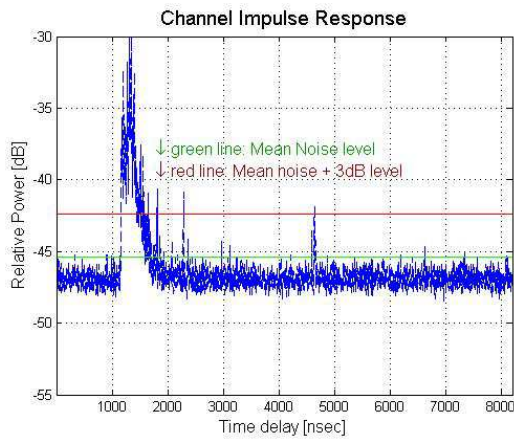


Figure 3: Power delay profile.

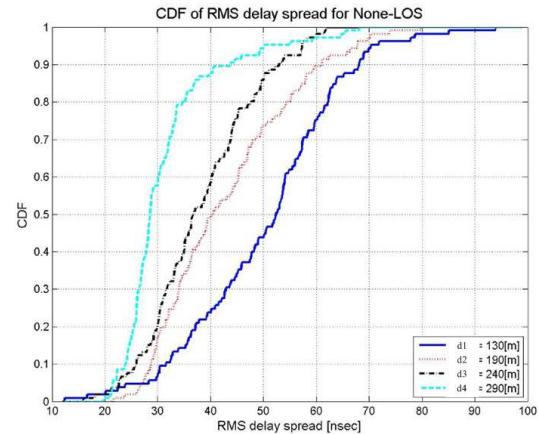


Figure 4: Delay Spread: CDF.

to communication system. With $\tau_0 = 0$, it is given by,

$$\tau_{R.M.S} = \sqrt{\frac{\sum_{i=0}^{I-1} \tau_i^2 \cdot P(\tau_i)}{\sum_{i=0}^{I-1} P(\tau_i)} - \tau_a^2} \quad (3)$$

with

$$\tau_a = \frac{\sum_{i=0}^{I-1} \tau_i P(\tau_i)}{\sum_{i=0}^{I-1} P(\tau_i)} \quad (4)$$

where, τ_a is mean excess delay, which is defined as the first moment of power delay profile, $P(\tau_i)$ is the channel power spectral density as a function of a delay, i.e., how channel power is distributed along dimension excess delay.

3.2. Analysis

We note that the maximum value of R.M.S delay spread appears to be up to 400 m TX-RX separation distance at 28 GHz frequency, and then decreases for relative large TX-RX separation distance. In NLOS case, the TX and RX antennas were indirectly pointed at each other, and large multipath existed. But, when the separation distance between a TX and Rx is too large (exceeding 400 m) in NLOS, the pathloss is so great that the power of the transmitted signal declines to zero before reaching the RX, resulting in fewer or no received multipath. For the relations between the R.M.S delay spread and TX-RX separation distance as well as the cumulative distribution function (CDF) of the R.M.S delay spread at 28 GHz, the maximum value of measured multipath components using wide band channel sounder with 2.0 ns multipath time resolution has R.M.S delay spreads below 125 ns, the average has below 58 ns to NLOS environments in small commercial urban environment of Daejeon, Republic of Korea.

4. CONCLUSION

We found that the measured values from the light urban environment of Daejeon City in Republic of Korea have substantial differences in comparison with the dense urban environment in R.M.S delay spread in [2]. To find adequate R.M.S delay spread components, we believe that the results through extensive measurement in various urban environments should be more discussed.

ACKNOWLEDGMENT

This work was supported by Institute for Information & communications Technology Promotion (IITP) grant funded by the Korea government (MSIP). [B0101-15-222, Development of core technology to improve spectral efficiency for mobile big-bang].

REFERENCES

1. Fallgren, M. and B. Timus, "Deliverable d1.1 scenarios, requirements and kpis for 5g mobile and wireless system," *METIS*, Document Number: ICT-317669-METIS/D1.1, Tech. Rep., 2013.
2. Rappaport, T., S. Sun, R. Mayzus, H. Zhao, Y. Azar, K. Wang, J. Schulz, M. Samimi, and F. Gutierrez, "Millimeter wave mobile communications for 5G cellular: It will work!," *IEEE Access*, Vol. 1, 335–349, May 2013.

Minimum Sum Algorithm Decoder for LDPC Nonregular Parity Check Matrix in BPSK System

Yi Hua Chen, Jue Hsuan Hsiao, Zong Yi Saio, and Hua Ting Syu

Oriental Institute of Technology

Institute of Information and Communication Engineering, New Taipei, Taiwan

Abstract— Referring to the approximate lower triangular low-density parity-check code check matrix of the IEEE P802.11n™/D1.04 (Part 11: Wireless Local Area Network Medium Access Control and Physical Layer specifications), this study established a decoder based on LabVIEW program language on a single program architecture that can adjust the transmission end to generate diverse codeword patterns, including three subblock sizes (27, 54, and 81 bit) and four code rates (1/2, 2/3, 3/4, and 5/6). Combined with the minimum sum algorithm (MSA), the decoder completed decoding tasks by changing the check node and variable node structures on the basis of the selected subblock size and code rate. In addition to providing an introduction on the decoding mechanism of the MSA and completing decoding program optimization and analysis of bit error rate (BER) performance curves, this study applied the LabVIEW program to simulate the BER of the ratio of energy per bit to the spectral noise density (E_b/N_0) at each point from 0 to 10 dB, when subblock sizes (27, 54, and 81 bit) were combined with code rates (1/2, 2/3, and 5/6) operating in an additive white Gaussian noise channel environment. The error rate performance curve diagrams of two studies were referenced (regular weight (3, 6) and 802.11n irregular subblock size 27 bit combined with code rate 5/6) and compared with the simulation outcome yielded in this study. The result showed that the subblock size did not affect the error rate, but the code rates substantially affected the error rates. When the code rate was set to 1/2, the error correction performance of the irregular check matrix was considerably higher than that of the regular check matrix.

1. INTRODUCTION

Shannon proposed Shannon's theory in 1948 [1], stating that by transmitting information bit through channel coding and maintaining the data rate (R_b) within the range of the channel capacity (C), the bit error rate (BER) resulting from data passing through the channel can be effectively reduced. When the encoded codeword lengthens, the data BER can approach infinitesimal. This limit is called Shannon limit [2]. Several studies have identified a considerable amount of error correcting codes [3]. In particular, the low-density parity-check (LDPC) code [4] proposed by Gallager has been the most widely applied in recent years. Despite the complex coding and decoding calculation, the LDPC code transmits at a data rate closest to the Shannon limit channel capacity. This study applied the approximate lower triangular LDPC code check matrix combined with the system architecture illustrated in Figure 1. After the information bit is encoded, binary phase-shift keying (BPSK) modulation is used. The bit then passes through the additive white Gaussian noise (AWGN) channel to the receiver end where BPSK demodulation is performed. Finally, the minimum sum algorithm (MSA) decoder [5] was used to decode the information bit.

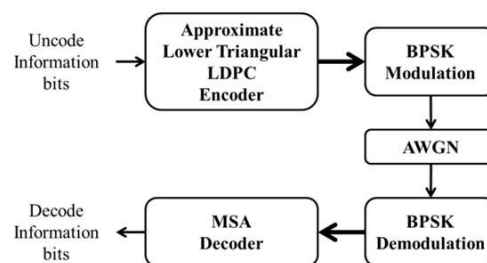


Figure 1: Diagram of the encoding and decoding system architecture.

The MSA decoding method used in this study was generated according to a simplified sum product algorithm (SPA) [6]. Unlike SPA, MSA requires no complex computation during decoding, thus increasing the speed of decoding calculation.

In this study, the MSA decoding method was applied to the approximate lower triangular LDPC encoding specifications specified in IEEE 802.11n for a wireless local area network (WLAN) [7]. The appendix in the specification records 12 code check matrices, including combinations of three subblocks (27, 54, and 81 bit) and four code rates (1/2, 2/3, 3/4, and 5/6). The MSA decoder proposed in this study integrated all 12 combinations of code check matrices into the program. Users can input different subblocks and code rates and the system automatically generates codewords for the program to decode. The decoding performance and gain of combinations of subblocks (27, 54, and 81 bit) and code rates (1/2, 2/3, and 5/6) were compared in this study.

2. APPROXIMATE LOWER TRIANGULAR LDPC CODE

2.1. Approximate Lower Triangular LDPC Code Check Matrix Architecture

The LDPC code is a type of linear block code, which is generally encoded by calculating the information bit vector and generate matrix (G) to obtain the redundancy bit. Subsequently, an encoding codeword can be determined by adding information bit and redundancy bit. During decoding, check matrices and codeword calculation were used to correct errors.

Compared with general linear block codes, LDPC codes require only check matrices to complete encoding and decoding. In this study, the encoding method programmed on the basis of the approximate lower triangular LDPC specifications in 802.11n for WLAN in [8] was adopted. This encoding method can adjust three subblocks (27, 54, and 81 bit) and four code rates (1/2, 2/3, 3/4, and 5/6) to generate 12 coding codewords that meet 802.11n specifications. Different subblocks and code rates have different code check matrices. Table 1 lists the matrix sizes.

Table 1: Size of 12 check matrices that meet the 802.11n approximate lower triangular LDPC specifications.

Code rate \ Z	1/2	2/3	3/4	5/6
27	324×648	216×648	162×648	108×648
54	648×1296	432×1296	324×1296	216×1296
81	972×1944	648×1944	486×1944	324×1944

2.2. LabVIEW Implementation of IEEE 802.11n Approximate Lower Triangular LDPC Check Matrix

Richardson and Urbanke proposed approximate lower triangular LDPC coding in 2001 [9]. This encoding method divides the designed check matrix H into six submatrices (A , B , C , D , T , and E). Through formula calculation, redundancy bits (p) p_1 and p_2 can be determined. Adding the information bit vector (m) to the resulting redundancy bits obtains codeword $X = [m \ p_1 \ p_2]$. The formulae of the redundancy bits p_1 and p_2 are expressed in (1) and (2).

$$P_1 = ET^{-1} (Am^T) + Cm^T \quad (1)$$

$$P_2 = T^{-1} (Am^T + BP_1^T) \quad (2)$$

In [8], a detailed explanation indicated that in addition to encoding formulae, implementation flows are required to satisfy the approximate lower triangular LDPC encoding specifications in the IEEE 802.11n for WLAN (Figure 2). The flow was programmed on a LabVIEW platform, and a complete program architecture and packaged SubVI are shown in Figures 3 and 4.

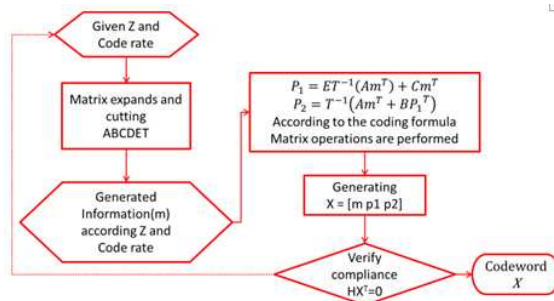


Figure 2: Approximate lower triangular LDPC encoding flowchart.

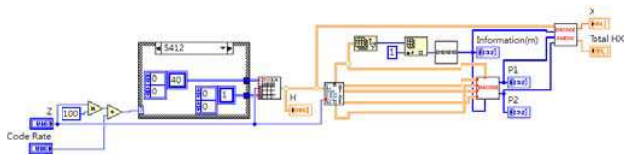


Figure 3: Approximate lower triangular LDPC encoding program architecture.

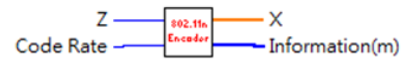


Figure 4: Complete encoding program SubVI.

3. MSA DECODING

During the decoding process, the concept of a Tanner graph [10] must be used to transform the columns and rows in check matrices into variable nodes $B_{(x_i)}$ and check nodes $C_{(x_i)}$ in the Tanner graph and observe 0 and 1 values in check matrices. Check nodes and variable nodes are linked. Through the linked paths, the soft information of signal log likelihood ratio (LLR) is transmitted. However, as shown in Table 1, the size of check matrices is counted in three digits according to the 802.11n approximate lower triangular LDPC specifications. To delineate the decoding method, the following descriptions refer to the weight (3, 6) regular parity-check matrix used in [11] (Figure 5). On the basis of this example check matrix, the generation method of the Tanner graph and the process and steps of transmitting signal LLR soft information are explained.

To clarify the corresponding situations between check and variable nodes, the researchers organized data in Figure 5 and marked $B_{(i)}$ and $C_{(i)}$ on the columns and rows and denoted the 0 and 1 values in check matrices in color blocks (Figure 6). A gray block represents 1 and a white block represents 0. Using check nodes as the main nodes and variable nodes as subsidiary nodes creates six Tanner graphs (Figure 7). By contrast, using variable nodes as the main nodes and check nodes as secondary nodes creates 12 Tanner graphs (Figure 8).

1	1	1	0	0	1	1	0	1	0	0	0
1	1	1	1	0	0	0	1	0	1	0	0
0	0	0	A	0	1	1	1	B	1	1	0
1	0	0	1	1	0	0	0	0	1	1	1
0	1	0	C	1	0	0	1	D	1	0	1
0	0	1	0	1	1	0	1	1	0	0	1

Figure 5: Weight (3, 6) regular parity check matrix.

		Variable Node											
		B1	B2	B3	B4	B5	B6	B7	B8	B9	B10	B11	B12
Check Node	C1	1	1	1	0	0	1	1	0	1	0	0	0
	C2	1	1	1	1	0	0	0	1	0	1	0	0
	C3	0	0	0	0	1	1	1	1	1	1	0	0
	C4	1	0	0	1	1	0	0	0	0	1	1	1
	C5	0	1	0	1	0	0	1	1	0	0	1	1
	C6	0	0	1	0	1	1	0	1	1	0	0	1

Figure 6: Node corresponding diagram of weight (3, 6) regular parity-check matrix.

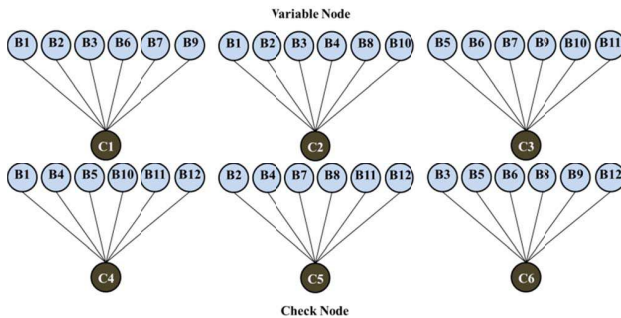


Figure 7: Tanner graph applying check nodes as main nodes and variable nodes as secondary nodes in the weight (3, 6) regular parity-check matrix.

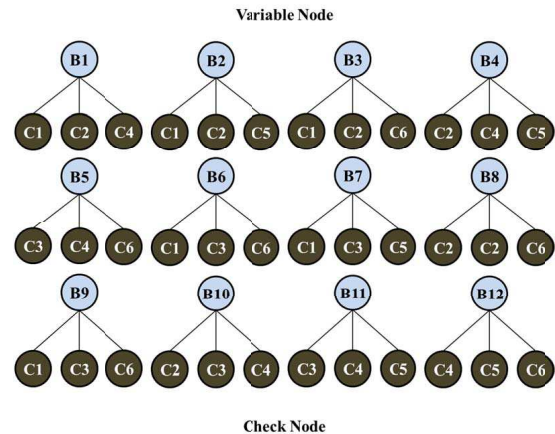


Figure 8: Twelve Tanner graphs applying variable nodes as main nodes and check nodes as secondary nodes in the weight (3, 6) regular parity-check matrix.

4. USING LABVIEW TO IMPLEMENT MSA DECODING

LabVIEW software was used to implement the MSA decoding flow (Figure 9). To ensure that the MSA flow conforms to the IEEE 802.11n LDPC specifications for WLAN, judgment is required to be incorporated into the four steps to simplify the program. The aforementioned four steps are separately packaged into four SubVIs. The program architecture and SubVI output-input relationship are introduced as follows.

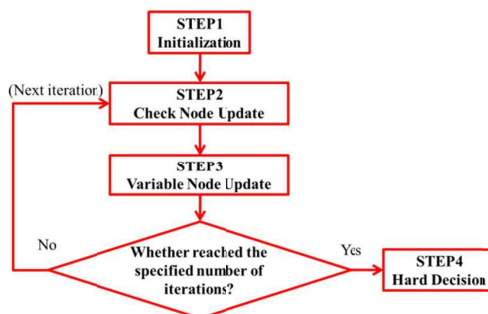


Figure 9: Decoding steps flowchart.

4.1. Transmitting Initialized LLR Soft Information to the Check Matrix

To accommodate the 12 irregular check matrices composed of three subblocks (27, 54, and 81 bit) and four code rates (1/2, 2/3, 3/4, and 5/6), and the three-digit matrix size in the specifications, Tanner graphs were not plotted during the design process. Instead, the graphs were automatically generated by the system during Steps 2 and 3. Thus, some changes were made in Step 1. After calculating the initialized LLR soft information by using (3), the information was not transmitted to variable nodes, but directly substituted into the check matrix. As shown in Figure 10, at the left side in the program structure of Step 1 SubVI, Z (subblock), code rates, σ , and encoded codewords were input to pass through the AWGN channel for information in. At the right output side, the check matrix H , corresponding to Z (subblock) and code rates, initialized LLR soft information, and the outcome of substituting initialized LLR soft information into the check matrix (STEP1) were output. Figure 11 shows the pinout of packaged SubVI.

$$L(x_i) = 2y_i/\sigma^2 \tag{3}$$

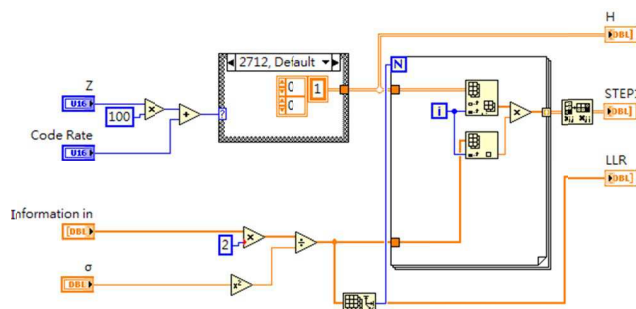


Figure 10: Program architecture of transmitting initialized LLR soft information to the check matrix.

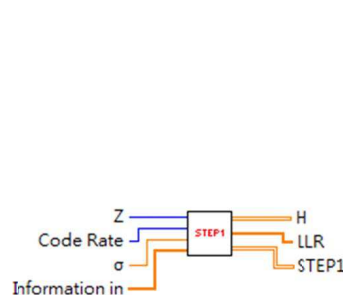


Figure 11: STEP1 SubVI pinout.

4.2. LLR Tanner Graph Generation and Variable Node LLR Soft Information Recalculation

Because the IEEE 802.11n approximate lower triangular LDPC specifications for WLAN has 12 check matrices, the Tanner graphs of each check matrix differ from each other. To simplify the program and save memory, the contacts between each node in the program were not recorded. Instead, the system automatically generated such records when necessary. In Step 2, the Tanner graph in Figure 7 is required and thus generated using the following method: the initialized LLR soft information in Step 1 is substituted into the check matrix. Subsequently, the matrix is decomposed by column to extract nonzero data, thereby obtaining the tanner graph of variable nodes

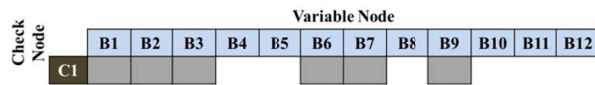


Figure 12: Tanner graph automatic generation method based on an example of weight (3, 6) regular parity-check matrix.

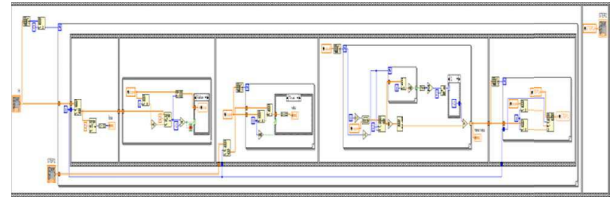


Figure 13: Program architecture of generating Tanner graphs and recalculating variable node LLR soft information.



Figure 14: STEP2 SubVI pinout.

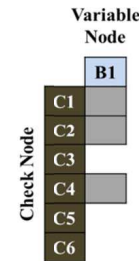


Figure 15: Tanner graph automatic generation method based on an example of weight (3, 6) regular parity-check matrix.

corresponding to single check nodes. Figure 12 shows the weight (3, 6) regular parity-check matrix with automatically generated Tanner graphs.

After the Tanner graph is generated, (4) is used to calculate new LLR soft information and feedback to the check matrix for output. Figure 13 shows the program structure of SubVI in Step 2. Figure 14 shows the pinout of packaged SubVI. At the left side of the figure, the check matrix (H) and output result of Step 1 (STEP1) are the input. At the right side, the result of new LLR soft information feedback to the check matrix is the output (STEP2).

$$\Lambda_{m \rightarrow n}(x_i) = \text{sign} \left(\prod_{n' \in N(m) \setminus n} \lambda_{n' \rightarrow m}(x_i) \right) \times \min_{n' \in N(m) \setminus n} (|\lambda_{n' \rightarrow m}(x_i)|) \quad (4)$$

4.3. LLR Tanner Graph Generation and Check Node LLR Soft Information Recalculation

This step requires the Tanner graph shown in Figure 8. Similar to the previous step, the system automatically generates the Tanner graph and decomposes the output in the previous step by rows to extract nonzero data. Subsequently, Tanner graphs of check nodes corresponding to single variable nodes can be obtained. Figure 15 shows the Tanner graph automatic generation method based on an example of weight (3, 6) regular parity-check matrix.

After the Tanner graph is generated, (5) is used to calculate new LLR soft information, which is then fed back to the check matrix input. Figure 16 shows the program structure of SubVI in Step 2. Figure 17 shows the pinout of packaged SubVI. At the left side, the check matrix (H), output results of Step 2 (STEP2), and initialized LLR soft information required for formula calculation (LLR) are the input. At the right side, the result of new LLR soft information feedback to the check matrix is the output (STEP3).

$$\lambda_{n \rightarrow m}(x_i) = L(x_i) + \sum_{m' \in M(n) \setminus m} \Lambda_{m' \rightarrow n}(x_i) \quad (5)$$

4.4. LLR Soft Information Sum

When the iteration reaches the specified number, (6) is used to sum the LLR soft information on the check nodes output in STEP3 and combine it with the initialized LLR soft information.

Figure 18 shows the program structure of SubVI in Step 4. Figure 19 shows the pinout of the packaged SubVI. At the left side, the output results of Step 3 (STEP3) and the initialized LLR

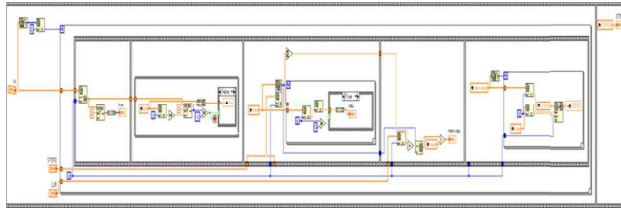


Figure 16: Program architecture of generating Tanner graphs and recalculating check node LLR soft information.

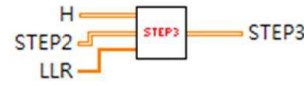


Figure 17: STEP3 SubVI pinout.

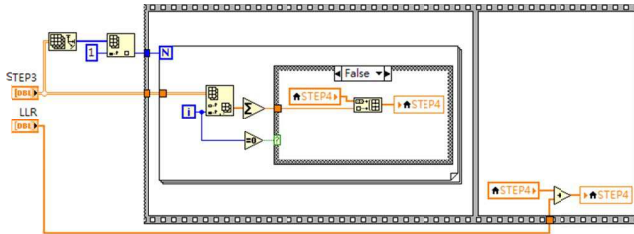


Figure 18: Program architecture of summed LLR soft information on check nodes combined with initialized LLR soft information.



Figure 19: STEP4 SubVI pinout.

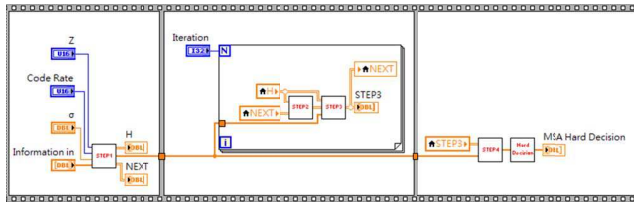


Figure 20: Complete MSA decoding program architecture.

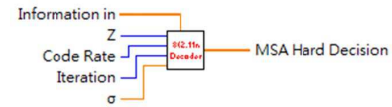


Figure 21: MSA decoding SubVI pinout.

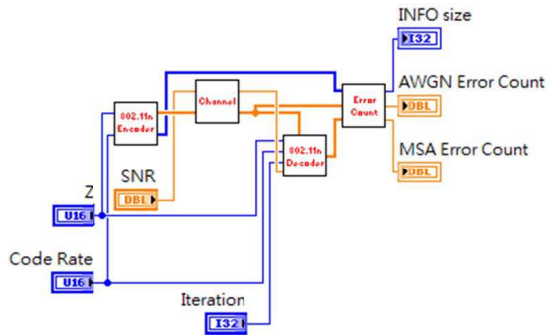


Figure 22: Complete encoding and decoding program architecture meeting IEEE 802.11n LDPC specifications.

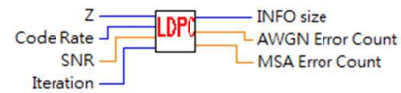


Figure 23: Complete encoding and decoding SubVI pinout satisfying IEEE 802.11n LDPC specifications

soft information (LLR) are the input. At the right side, the summed LLR soft information is the output (STEP4).

$$(x_i) = L(x_i) + \sum_{m \in M(n) \setminus m} \Lambda_{m \rightarrow n}(x_i) \quad (6)$$

Finally, the SubVIs in each step are connected and combined with the loop judgment of iteration numbers and hard decisions to complete the MSA decoding program that meets the IEEE 802.11n approximate lower triangular LDPC specifications for WLAN (Figure 20). Subsequently, the completed program is packaged as SubVI (Figure 21).

4.5. Complete Approximate Lower Triangular LDPC Decoding Structure

Incorporated with the decoder proposed by [8], the proposed MSA decoding method completes 12 check matrix decoders that meet IEEE 802.11n LDPC specifications for WLAN. An AWGN channel is added in the middle of the encoder and decoders, as shown in the complete encoding and decoding program architecture of Figure 22.

Figure 23 presents the packaged SubVI pinout. At the left side, subblock (Z), code rates, signal-to-noise ratio (SNR), and iteration are the input. At the right side, the information bit number (INFO size), number of error bits before decoding (AWGN Error Count), and number of error bits after MSA decoding (MSA Error Count) are the output.

5. ERROR RATE PERFORMANCE ANALYSIS OF IEEE 802.11N APPROXIMATE LOWER TRIANGULAR LDPC SPECIFICATIONS

The LabVIEW program was used to simulate the AWGN channel environment, with E_b/N_0 from 0 to 10 dB. For every 1 dB interval, 81 Mbit random number data were generated. The corresponding relationship of E_b/N_0 and σ is listed in Table 2. Encoding was completed by combining subblock sizes (27, 54, and 81 bit) and code rates (1/2, 2/3, and 5/6) and using BPSK modulation. The MSA single iteration was used to perform a decoding calculation.

Table 2: Comparison table of E_b/N_0 and σ .

E_b/N_0 , dB	0	1	2	3	4	5	6	7	8	9	10
σ	0.707	0.630	0.562	0.501	0.446	0.398	0.351	0.316	0.282	0.251	0.224

The result was mutually validated according to [12] the error rate curves of an irregular check matrix with $Z = 27$ and $Z = 81$ bit in the same code rate of 5/6. The validation results showed that the error rate curves were nearly identical (Figure 24). Thus, the value of Z did not influence the error rate. When the code rate is identical, the error rates yield nearly identical results. However, in this study, only AWGN channels were simulated. The Z value affected the length of codewords. If increasingly complex channel environments can be provided, such as the Rayleigh fading or burst error channels, discourse with improved integrity can be attained.

In a comparison of three error rate curves calculated at the receiver end after decoding and the error rate curve simply modulated through BPSK without adding error correcting codes (Figure 25), the results revealed that when the BER was 10^{-5} , E_b/N_0 required 9.6 dB in the AWGN environment. If approximate lower triangular LDPC codes were added to the curves, the E_b/N_0 calculated using MSA decoding, when $Z = 27$ bit, code rate = 5/6, was reduced to 6.35 dB. When $Z = 54$ bit and code rate = 2/3, E_b/N_0 was 6.0 dB. When $Z = 81$ bit, code rate = 1/2, E_b/N_0 was 5.7 dB. The coding gain increased by a range from 3.25 to 3.9 dB, compared with that of the AWGN channels. When the E_b/N_0 was higher than 7 dB, the BER approximated 0.

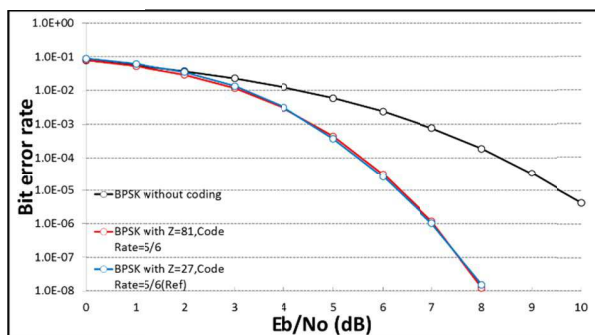


Figure 24: Error rate curve comparison of subblock size = 81 bit combined with code rate = 5/6 with the combination of subblock size = 27 bit and code rate = 5/6 in the literature.

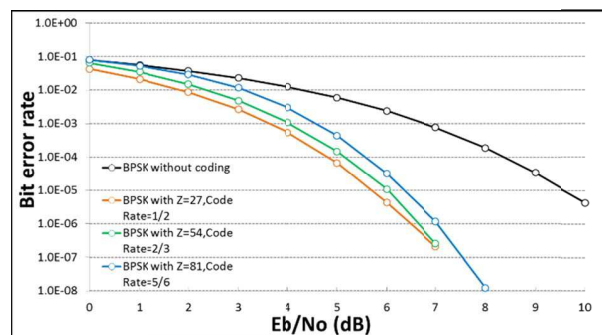


Figure 25: A comparison of error rate curve without coding and LDPC coded and decoded error rate curves generated using LabView simulation of BPSK modulation through the AWGN channel at varying subblock sizes (27, 54, 81 bit) and code rates (1/2, 2/3, and 5/6).

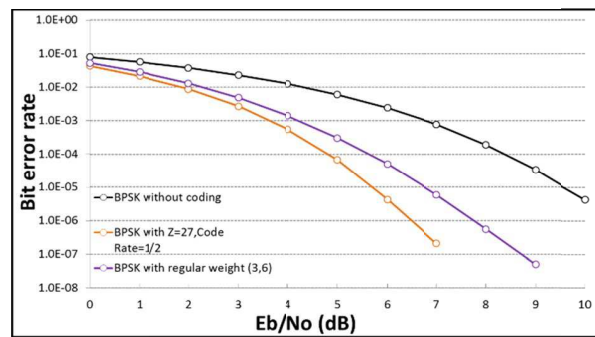


Figure 26: Comparison of error rate curves with subblock size = 27 bit, combined with code rate = 1/2 and with regular weight (3, 6) from the literature.

Finally, the results of this study were compared with the BER performance of regular weight (3, 6) from [12]. The code rate was identically 1/2. When the BER was 10^{-6} , the E_b/N_0 that the regular weight (3, 6) required was 7.75 dB, and $E_b/N_0 = 6.5$ dB when the irregular check matrix was $Z = 27$ bit. The coding gain was 1.25 dB.

6. CONCLUSION

This study applied the irregular check matrix in IEEE 802.11n specifications and adopted the LabVIEW to program and complete diverse encoders. In addition, MSA decoding methods were used to generate various decoders. The simulation adopted BPSK modulation to pass through the AWGN channel and compared the BER curves with those of previous studies. The results indicated that the subblock size in the AWGN channel environment did not affect error rates. However, different code rates yielded 3.25 to 3.9 dB coding gains when BER was 10^{-5} . The comparison results of the error correcting performances of the irregular code check matrix and weight (3, 6) regular code check matrix in 802.11n specifications showed that when the code rate was identically 1/2 and the BER was 10^{-6} , a 1.25 dB coding gain difference existed, thus verifying that the irregular check matrix outperformed the regular check matrix.

Future studies should use the sum-of product algorithm or forward-backward algorithm to complete decoding [6, 13]. Moreover, Rayleigh fading or Ricean fading can be added in the channels to further determine the variations of error rates in multiple situations.

REFERENCES

- Shannon, C. E., "A mathematical theory of communication," *Bell Syst. Tech. J.*, 379–423 (Part 1); 623–656 (Part 2), Jul. 1948.
- Berrou, C., A. Glavieux, and P. Thitimajshima, "Near Shannon limit error-correcting coding and decoding: Turbo-codes," *IEEE International Conference on Communications, ICC'93*, Vol. 2, 1064–1070, Geneva, May 1993.
- Sklar, B., *Digital Communications Fundamentals and Applications* 2nd Edition, Prentice Hall, 2001.
- Gallager, R. G., "Low-density parity-check codes," *IRE Trans. Inform. Theory*, 21–28, Jan. 1962.
- Chen, J. and P. C. Marc, "Near optimum universal belief propagation based decoding of low-density parity check codes," *IEEE Trans Commun.*, Vol. 50, No. 3, 406–414, Mar. 2002.
- Kschischang, F. R., B. J. Frey, and H.-A. Loeliger, "Factor graphs and the sum-product algorithm," *IEEE Trans. Inform. Theory*, Vol. 47, 498–519, Feb. 2001.
- IEEE P802.11nTM/D1.04, Draft Amendment to STANDARD for Information Technology-Telecommunications and Information Exchange, 2006.
- Chen, Y. H., J. H. Hsiao, and Z. Y. Siao, "Wi-Fi LDPC encoder with approximate lower triangular diverse implementation and verification," *Multi-Conference on Systems, Signals & Devices (SSD)*, 1–6, 2014.
- Richardson, T. J. and R. Urbanke, "Efficient encoding of low-density parity-check codes," *IRE Trans. Inform. Theory*, Vol. 47, No. 2, 638–656, 2001.
- Michael Tanner, R., "A recursive approach to low complexity codes," *IRE Trans. Inform. Theory*, Vol. 27, No. 5, 533–547, Sep. 1981.

11. Chen, Y.-H., C.-L. Chu, and J.-S. He, “FPGA implementation and verification of LDPC minimum sum algorithm decoder with weight (3, 6) regular parity check matrix,” *ICEMI' 2013*, 682–686, Aug. 2013.
12. He, J.-S., “Implementation of LDPC encoder and decoder on SDR wireless communication system,” Thesis-of-Master-Degree, O.I.T Institute of Information and Communication Engineer, Jul. 2013.
13. Bahl, L. R., J. Cocke, F. Jelinek, and J. Raviv, “Optimal decoding of linear codes for minimizing symbol error rate,” *IEEE Trans. Inform. Theory*, Vol. 20, 284–287, Mar. 1974.

Asymptotic Analysis of Scattering from Transmitarray for Near Field Focused

Shih-Chung Tuan¹ and Hsi-Tseng Chou²

¹Department of Communication Engineering, Oriental Institute of Technology, Pan-Chiao, Taiwan

²Department of Communication Engineering, Yuan Ze University, Chung-Li, Taiwan

Abstract— This paper presents the asymptotic formulation of ray fields in the decomposition of electromagnetic (EM) scattering mechanisms from a one-dimensional, semi-infinite and periodic array when it is illuminated by a line source. This technique can be applied to analyze the passive FSS (frequency selective surface) type periodic structure with identical elements, the transmitarray type antennas that are phased to radiate EM fields focused in the near zone of the array aperture. The solutions are built up based on the Floquet mode expansion of the scattering fields, and are obtained by asymptotically evaluating the resulted integrals to express the fields in terms of transmitted and edge diffracted fields as previously addressed in the framework of uniform geometrical theory of diffraction (UTD).

1. INTRODUCTION

This paper interprets the mechanisms in terms of ray decompositions based on the concept of uniform geometrical theory of diffractions (UTD). In this approach, the radiations of periodically located current sources are first decomposed into Floquet modes, in which every mode is equivalent to the radiation of continuous current sources with additional linear phase impressions. Fast convergence in the radiation computation can be achieved because relatively few modes will propagate to the target zone with the rest being evanescent. The ray decomposition is performed by asymptotically evaluating the radiation integral of each Floquet mode and interprets the total fields in terms of rays directly radiated from the aperture and diffracted from aperture truncations [1–5]. They have successfully decomposed the fields in terms of ray fields related to the radiation from infinite arrays and diffraction from finite truncations. The works related to the scattering problems of interested in this paper were investigated in [6], where a periodic array of identical elements illuminated by the radiation of a line source was considered. In particular, they examine the reflection type phenomena and focus on the phenomena interpretation according to the basic assumption of known equivalent distribution over the array, which appears not sufficient to become a useful tool in the realistic applications. The works presented in this paper perform a systematic investigation over the scattering problem, and extend the application scope to treat the transmitarray type antenna structures, where the array elements are periodically distributed with different elemental structures to account for the needs of phase changes in the designs of this types of array structure.

2. FORMULATIONS DEVELOPMENT

2.1. Problem Composition of the 2-D Radiation from a 1-D Array

One considers a semi-infinite, linear array of reflecting elements as illustrated in the configurations of Figure 1, where the elements are illuminated by the radiation from a line source. The line source is located at $\bar{\rho}_f = (x_f, z_f)$ and radiates EM fields by

$$u_f(\bar{\rho}) = \frac{1}{4j} I_0 H_0^{(2)}(k|\bar{\rho} - \bar{\rho}_f|) \cong \frac{e^{-j\pi/4} I_0}{4} \sqrt{\frac{2}{\pi k|\bar{\rho} - \bar{\rho}_f|}} e^{-jk|\bar{\rho} - \bar{\rho}_f|}. \quad (1)$$

The scattering field can be expressed as

$$u_s(\bar{\rho}) = \frac{1}{4j} \int_{x_a}^{x_b} u_f(\bar{\rho}_i) Q(\bar{\rho}') e^{j\phi(\bar{\rho}')} H_0^{(2)}(k|\bar{\rho} - \bar{\rho}'|) dx'. \quad (2)$$

Since the array elements are periodically located, thus substituting (1) into (2) gives

$$u_s(\bar{\rho}) = \left(\frac{I_0 d_x}{8j\pi k} \right) \sum_{n=-\infty}^N \frac{e^{-jk\ell_n} e^{-jk\rho_n} e^{j\phi_n^c}}{\sqrt{\ell_n} \sqrt{\rho_n}} G_n(k_{r,x}^n - k_{f,x}^n) \quad (3)$$

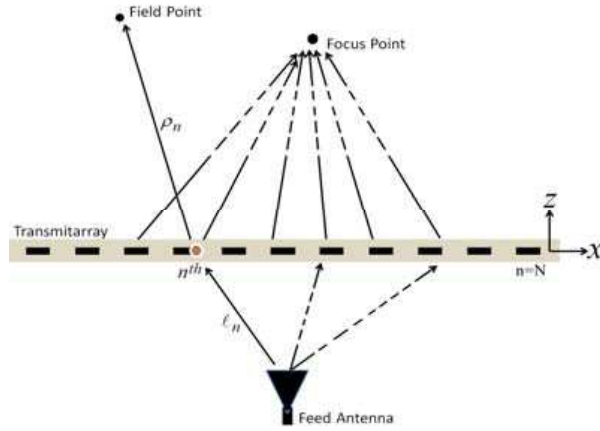


Figure 1: Illustration of 2-D transmitarray scattering/radiation problems. Where the fields are focused in the near zone at $\bar{\rho} = \bar{\rho}_o$.

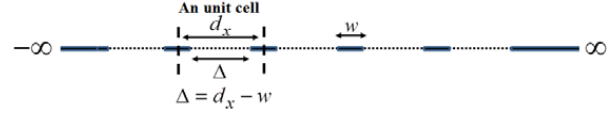


Figure 2: The array of metal strips for the scattering examination for transmitting scattering problem.

where the large argument approximation of Hankel's function has been used in (2), and

$$G_n(\xi) = \frac{1}{d_x} \int_{-d_x/2}^{d_x/2} e^{j\xi x'} Q_n(x') e^{j\phi_n^e(x')} dx' \quad (4)$$

2.2. Composition of Uniform Asymptotic Formulations

The Floquet modes are obtained by using the Poisson sum formula [7]:

$$\sum_{n=-\infty}^N f(n) = \frac{f(N^-)}{2} + \sum_{p=-\infty}^{\infty} \int_{-\infty}^{N^-} f(v) e^{-j2\pi pv} dv. \quad (5)$$

As a result, the p th Floquet mode of (4) can be expressed as

$$u_s^p(\bar{\rho}) = \left(\frac{I_0}{8j\pi k} \right) \int_{-\infty}^{x_e} \frac{e^{-j[k(\ell_v + \rho_v) + \beta_p x_i]} e^{j\phi_v^e}}{\sqrt{\ell_v} \sqrt{\rho_v}} G_v(k_{r,x}^v - k_{f,x}^v) \cdot e^{-j\beta_p x_i} dx_i \quad (6)$$

According to the UTD framework, (3) can be approximately formulated into the following format:

$$u_s^p(\bar{\rho}) = u_{dir}^p(\bar{\rho}) \cdot U(\text{Re}(x_e - x_s)) + u_{end}^p(\bar{\rho}) F(ka) \quad (7)$$

where $U(\cdot)$ is the Heaviside step function and $F(\cdot)$ is the UTD Fresnel transition function to assure the uniform field distribution when the field point is across the shadow boundary of incident/reflected fields. The asymptotic solution is given by

$$u_{dir}^p(\bar{\rho}) = u_f(\bar{\rho}_s^p) G_{v_s}(k_x^s - k_x^i) \frac{j e^{-j\beta_p x_s}}{2k_z^s} \sqrt{\frac{\rho_c}{\rho_v^s + \rho_c}} e^{-jk\rho_s^s} \quad (8)$$

In (7), $u_{end}^p(\bar{\rho})$ is the scattering field due to the truncation effect at x_e . The asymptotic solution is given by

$$u_{end}^p(\bar{\rho}) = u_f(\bar{\rho}_e^p) G_N(k_x^e - k_x^{ie}) \frac{j e^{-j\beta_p x_e} e^{-jk\rho_e}}{2\sqrt{\rho_e}} \cdot \left(\frac{e^{-j\pi/4}}{\sqrt{2k\pi} ((k_x^{ie} - k_x^e) + \beta_p)} \right) \quad (9)$$

The standard UTD Fresnel transition function is given by

$$F(\chi) = 2j\sqrt{\chi} e^{j\chi} \int_{\sqrt{\chi}}^{\infty} e^{-j\tau^2} d\tau \quad (10)$$

3. NUMERICAL EXAMPLES

One considers a finite array of infinitely thin metal strips as illustrated in Figure 2, where the period is $d_x = 0.3\lambda$, and the size of elemental strip is $w = 0.2\lambda$ at 10 GHz. The elemental structures of the array are selected by the unit cells in Figure 3, where 41 elements are considered in the examination. The line source is located at $(0, -60\lambda)$ and $(0, -80\lambda)$ respectively in front of the array.

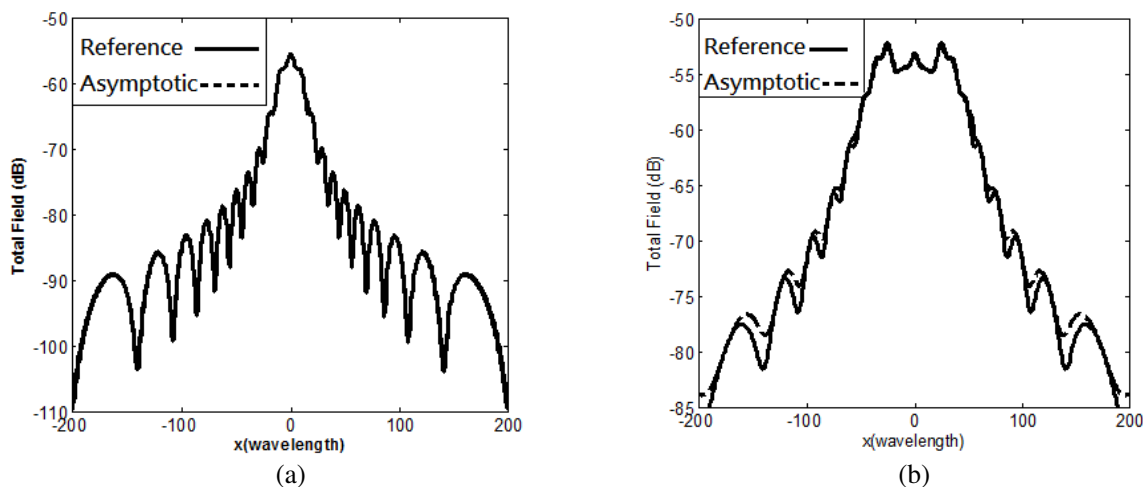


Figure 3: Numerical results to validate the solution developed in this paper. The total fields is considered at various case. (a) Without NF focused ($d_x = 0.3\lambda$). (b) NF focus point $(0, 10\lambda)$, line source located at $(0, -80\lambda)$.

4. CONCLUSIONS

This paper presents the asymptotic formulation of ray fields in the decomposition of electromagnetic (EM) scattering mechanisms from a one-dimensional, semi-infinite and periodic array when it is illuminated by a line source. The paper interprets the mechanisms in terms of ray decompositions based on the concept of uniform geometrical theory of diffractions (UTD). In this approach, the radiations of periodically located current sources are first decomposed into Floquet modes, in which every mode is equivalent to the radiation of continuous current sources with additional linear phase impressions. This technique can be applied to analyze the passive FSS (frequency selective surface) type periodic structure with identical elements, the transmit-array type antennas that are phased to radiate EM fields focused in the near zone of the array aperture.

REFERENCES

1. Neto, A., S. Maci, G. Vecchi, and M. Sabbadini, "A truncated Floquet wave diffraction method for the full wave analysis of large phased arrays. I. Basic principles and 2-D cases," *IEEE Transactions on Antennas and Propagation*, Vol. 48, No. 4, 594, 2000.
2. Chou, H.-T., "Floquet mode phenomena of infinite phased array antennas in near-field focus applications," *IEEE Transactions on Antennas and Propagation*, Vol. 61, No. 6, 3060–3068, Jun. 2013.
3. Chou, H.-T., "Asymptotic floquet mode investigation over two-dimensional infinite array antennas phased to radiate near-zone focused fields," *IEEE Transactions on Antennas and Propagation*, Vol. 61, No. 12, 6014–6021, Dec. 2013.
4. Puggelli, F., P. Pathak, M. Albani, and P. Janpugdee, "A hybrid numerical-composite UTD ray analysis of the radiation by large locally convex conformal arrays on large platforms," *Proceedings of 2013 URSI International Symposium on Electromagnetic Theory (EMTS)*, 1064–1065, May 20–24, 2013.
5. Carin, L., L. B. Felsen, and T.-T. Hsu, "High-frequency fields excited by truncated arrays of nonuniformly distributed filamentary scatterers on an infinite dielectric grounded slab: Parametrizing (leaky mode)-(Floquet mode) interaction," *IEEE Transactions on Antennas and Propagation*, Vol. 44, 1–11, 1996.

6. Felsen, L. B. and E. G. Ribas, “Ray theory for scattering by two-dimensional quasiperiodic plane finite arrays,” *IEEE Transactions on Antennas and Propagation*, Vol. 44, No. 3, 375–382, Mar. 1996.
7. Civi, O. A., P. H. Pathak, and H. Chou, “On the poisson sum formula for the analysis of wave radiation and scattering from large finite arrays,” *IEEE Transactions on Antennas and Propagation*, Vol. 47, 958–959, 1999.

Investigation on Rudimentary Geometries of Dielectric Resonator Antenna

Jitendra Kumar and Navneet Gupta

Department of Electrical and Electronics Engineering
Birla Institute of Technology and Science (BITS), Pilani, Rajasthan 333031, India

Abstract— Due to the variety of geometries available to antenna designers such as rectangular, cylindrical, hemispherical etc., a proper practice to select the best geometry for Dielectric Resonator Antenna (DRA) is required. In this paper, various rudimentary geometries of DRA excited by a coaxial probe fed is designed and investigated for selecting the preminent geometry of antenna. The rudimentary geometries of DRA are rectangular, cylindrical and hemispherical, which are used for investigation of DRA performance. The dielectric material used for rudimentary geometries is TMM10i, a ceramic thermoset polymer composite material of the Rogers high-frequency laminates. The DRA is designed to operate around 3.2 GHz. However, the resonant frequency may alter due to different rudimentary geometries. CST Microwave Studio transient solver is used to design and simulate the different rudimentary geometries of DRA. These rudimentary geometries of DRA give a better understanding of design parameters of an antenna and their effect on return losses, impedance bandwidth, VSWR, gain, efficiency and resonant frequency.

1. INTRODUCTION

Since 1960s, DRs have been used as high Q factor components in shielded microwave devices and circuits such as microwave filters, oscillators and cavity resonators [1]. In 1983, Long et al. observed that by removing the metallic shielding and with the proper feeding to excite the appropriate mode, it was found that the DRs could actually become efficient radiators [2]. The open DRs are potentially useful antenna elements. They carried out systematic study and an experiment investigation of radiation property of cylindrical, spherical and rectangular shaped antennas and their studies confirmed that the DRAs could be considered to be superior alternatives compared to the traditional antennas like monopoles, dipoles and microstrip patch antennas.

DRA has been investigated extensively in the past few decades due to its attractive features such as high radiation efficiency, zero conductor losses, wide bandwidth, and ease of fabrication [3, 4]. A DRA is a high radiation efficiency radiator, which is usually made up of high permittivity lossless dielectric material. Today, with the rapid development of wireless communications, wideband DRAs have received tremendous attention. As compared to cylindrical or hemispherical DRA, Rectangular Dielectric Resonator Antenna (RDRA) provides more degrees of freedom which can be used to control the impedance bandwidth of the antenna [3].

Significant efforts on DRAs have been reported to achieve wide bandwidth such as introducing an air gap between the DRA and ground plane [5], multilayer stacking of dielectric materials [6], fractal approach on DRA [7], etc.. Thus, a regular study to select the basic geometry of DRA is required for wireless applications. For the design of such type of DRA system, different rudimentary geometries of DRAs are required. These rudimentary geometries of DRAs play a very important for antenna society with a wide range of antenna's applications. To analyze several geometries, basic shapes of DRAs are considered and designed to resonate around 3.2 GHz.

In this paper, three rudimentary geometries of DRAs fed by coaxial probe are investigated. $|S_{11}|$ plot, radiation efficiency, radiation patterns and antenna gains were studied using CST Microwave Studio transient solver [8]. To validate the research work, simulation was carried out, and reasonable agreement is obtained.

2. ANTENNA CONFIGURATION

Different shapes of DRA have different modes of resonance, and hence different field distribution, radiating properties and resonant frequencies. Since the analytical methods cannot be used for most shapes, multiple methods were found in order to analyze the fields inside DRs. From fields inside DRs, resonant frequencies and radiation characteristics of certain modes can be determined [4]. A dielectric waveguide model (DWM) method of analysis is very good approximation for regular structure of DRs. According to the DWM method of analysis, it can be assumed that the resonator

is a truncated section of an infinite dielectric waveguide having transverse dimensions same as of the DR [9].

For the rectangular shape, the modes will also have an orientation dependency, due to symmetry. Hence, the lower energy modes are $TE_{\delta 11}^x$, $TE_{\delta 11}^y$ or $TE_{\delta 11}^z$ [10]. These modes radiate similar to a short magnetic dipole in the x , y or z direction. In cylindrical DRA, $HME_{11\delta}$ and $TM_{01\delta}$ resonant modes are radiated [3, 4] but other higher order modes excitation is also possible while the fields present in the hemispherical DRA shape can be divided into two distinct modes: TE_{111} and TM_{101} [11].

The resonant frequency of hemispherical DRA (HDRA) can be found using following equations [4]:

$$f_r \text{ (GHz)} = \frac{4.7713 \text{Re}(k(hr))}{r\sqrt{\epsilon_r}} \quad (1)$$

For TE_{111} Mode:

$$\text{Re}(k_r) = 2.8316\epsilon_r^{-0.47829} \quad (2)$$

For TM_{101} Mode:

$$\text{Re}(k_r) = 4.47226\epsilon_r^{-0.505} \quad (3)$$

The resonant frequency of cylindrical DRA (CDRA) is given as [3, 4, 12]:

$$f_{TE_{01\delta}} = \frac{2.237}{\sqrt{\epsilon_r + 1}} \left(1 + 0.2123 \frac{r}{h} - 0.00898 \left(\frac{r}{h} \right)^2 \right) \cdot \frac{4.7713}{r} \quad (4)$$

The resonant frequency (f_r) of a rectangular DRA (RDRA) is given as [13, 14]:

$$f_r = \frac{c}{2\pi\sqrt{\epsilon_r}} \sqrt{k_x^2 + k_y^2 + k_z^2} \quad (5)$$

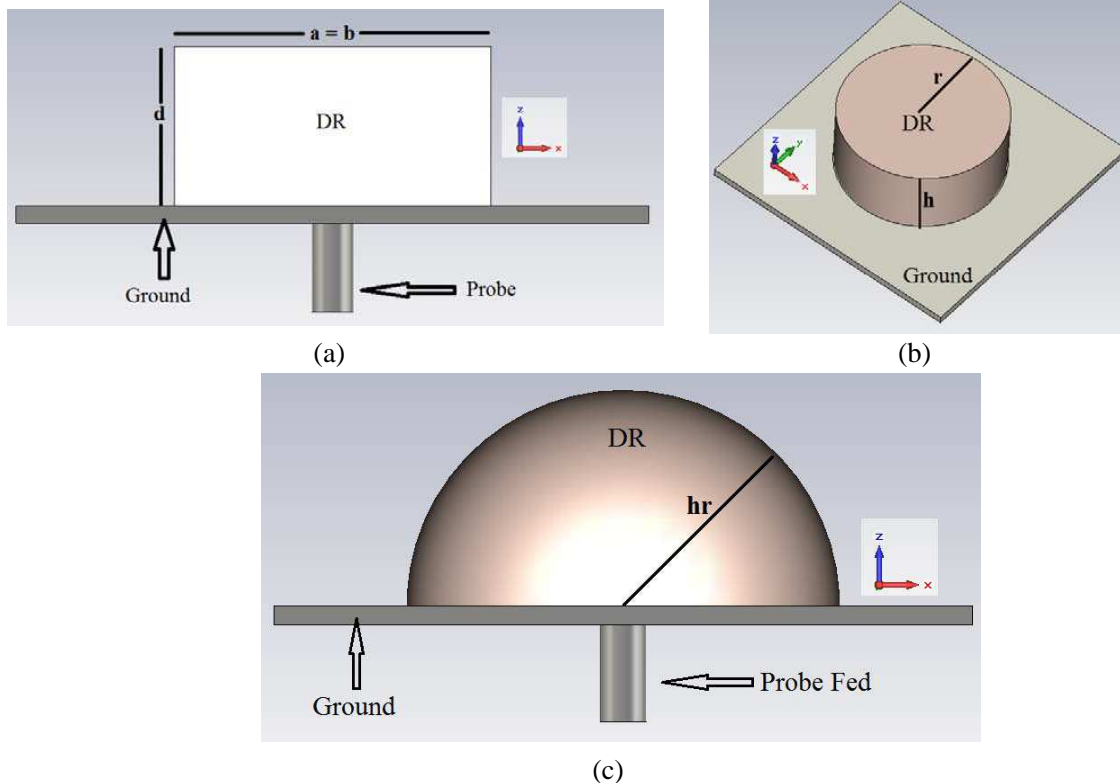


Figure 1: Configuration of rudimentary geometries of DRA: (a) rectangular, (b) cylindrical, (c) hemispherical.

In Eqs. (1)–(4) “ ϵ_r ” is the dielectric constant of the RDRA, “ c ” is the speed of light in free space and symbol “ k_x ”, “ k_y ” and “ k_z ” represents the wave numbers in the x , y and z directions respectively. The dielectric material used for simulation is Roger TMM10i, a ceramic thermoset polymer composite of the Rogers high-frequency laminates [15]. The dielectric constant (ϵ_r) of the material is 9.8, the dissipation factor ($\tan \delta$) is 0.002, and the density is 2.8 gm/cm³.

The geometry of the proposed DRA is shown in Figure 1. DRA is designed on symmetrical ground plane having the dimension of 60 × 60 mm². For Rectangular DRA, the dimensions along x -, and y -, directions are equal ($a = b = 30$ mm) and along z -, direction is d ($d = 15$ mm). While for cylindrical DRA radius of r ($r = 18$ mm) and height h ($h = 15$ mm) is taken. However, for hemispherical DRA the dimension of radius is hr ($hr = 18.61$ mm).

3. RESULTS AND DISCUSSION

Figure 2 shows the variations of $|S_{11}|$ verses frequency for different rudimentary geometries of DRAs. The simulated result shows that the impedance bandwidth (for return loss below -10 dB) of the RDRA is 56%, 46% and 50% for rectangular, hemispherical and cylindrical respectively.

Gain plots of all three geometries are shown in Figures 3–5. The peak gain is measured at 3.2 GHz, which is 1.56 dB for Rectangular DRA, 1.50 dB for Cylindrical DRA and 1.54 dB for Hemispherical DRA respectively.

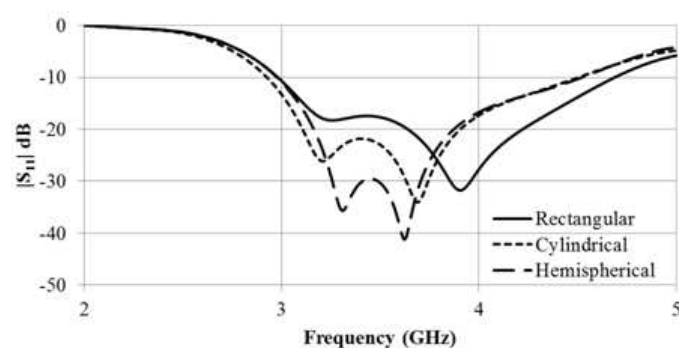


Figure 2: Variations of $|S_{11}|$ verses frequency for different rudimentary geometries of DRAs.

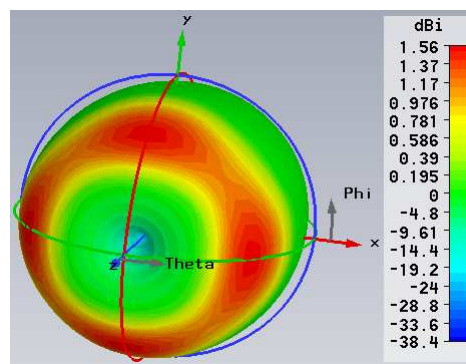


Figure 3: Gain plot of RDRA at 3.2 GHz.

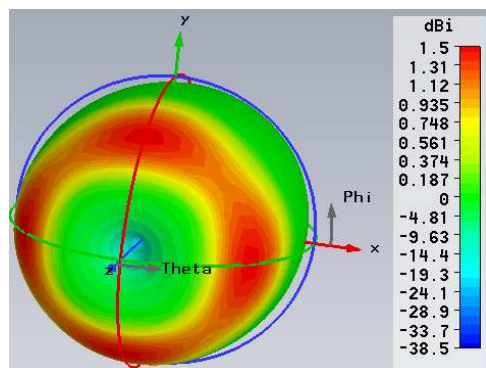


Figure 4: Gain plot of CDRA at 3.2 GHz.

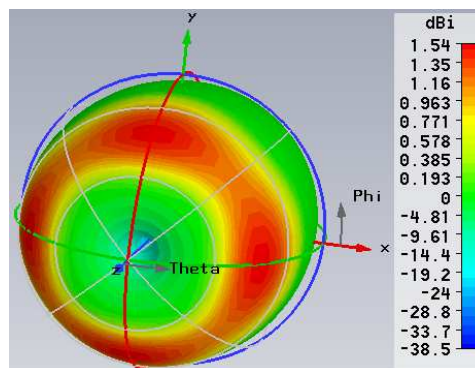


Figure 5: Gain plot of HDRA at 3.2 GHz.

Table 1: Comparison of the proposed structure.

Rudimentary Geometries	Rectangular	Cylindrical	Hemispherical
Dimensions (mm)	$a = b = 30, d = 15$	$r = 18, h = 15$	$hr = 18.61$
Resonant Frequency	3.2 GHz	3.2 GHz	3.3 GHz
Bandwidth Range	2.9–4.7 GHz	2.9–4.5 GHz	3–4.5 GHz
Bandwidth ($S_{11} < -10$ dB)	56%	50%	46%
Total Peak Gain	1.56 dBi	1.50 dBi	1.54 dBi

Table 1 summarize the all numerical results for different geometries of DRA. It can be seen that the impedance bandwidth (for return loss below -10 dB) of the DRA is 56%, 46% and 50% for rectangular, hemispherical and cylindrical respectively. It can be observed that the rectangular antenna not only achieves wider bandwidth, but also its gain is considerably higher than other DRAs.

4. CONCLUSION

In this paper comparative study of different rudimentary geometries of DRAs design has been carried out. The rudimentary geometries of DRA were rectangular, cylindrical and hemispherical, which are used for investigation of DRA performance. These rudimentary geometries of DRA give a better understanding of design parameters of an antenna and their effect on return losses, impedance bandwidth, gain, and resonant frequency. It was found that the rectangular DRA fed by coaxial probe provide better gain radiation pattern as compared to other geometries.

REFERENCES

1. Plourde, J. K. and C. L. Ren, "Application of dielectric resonators in microwave components," *IEEE Transactions on Microwave Theory and Technique*, Vol. 29, 754–770, 1981.
2. Long, S. A., M. W. McAllister, and L. C. Shen, "The resonant cylindrical dielectric cavity antenna," *IEEE Transactions on Antennas and Propagation*, Vol. 31, 406–412, 1983.
3. Luk, K. M. and K. W. Leung, *Dielectric Resonator Antennas*, Res. Studies Press, Baldock, England, 2003.
4. Petosa, A., *Dielectric Resonator Antenna Handbook*, Artech House, Norwood, MA, USA, 2007.
5. Drossos, G., Z. Wu, and L. E. Davis, "The air gap effect on a microstrip-coupled cylindrical dielectric resonator antenna," *Microwave and Optical Technology Letters*, Vol. 20, No. 1, 36–40, Jan. 1999.
6. Huang, W. and A. A. Kishk, "Compact wideband multi-layer cylindrical dielectric resonator antennas," *IET Microw. Antennas Propag.*, Vol. 1, No. 5, 998–1005, 2007.
7. Mukherjee, B., P. Patel, and J. Mukherjee, "Hemispherical dielectric resonator antenna based on Apollonian gasket of circles — A fractal approach," *IEEE Transactions on Antennas and Propagation*, Vol. 62, No. 1, 40–47, Jan. 2014.
8. CST Microwave Studio, *Computer Simulation Technology*, Framingham, MA, USA, 2015.
9. Mongia, R. K., "Theoretical and experimental resonant frequencies of rectangular dielectric resonators," *IEE Proceedings H (Microwaves, Antennas and Propagation)*, Vol. 139, 98–104, IET Digital Library, 1992.
10. Kumar, J. and N. Gupta, "Performance analysis of dielectric resonator antennas," *Wireless Personal Communications*, Vol. 75, No. 2, 1029–1049, Mar. 2014.
11. Gastine, M., L. Courtois, and J. L. Dormann, "Electromagnetic resonances of free dielectric spheres," *IEEE Transactions on Microwave Theory and Techniques*, Vol. 15, 694–700, 1967.
12. Mongia, R. K. and B. Prakash, "Dielectric resonator antennas — A review and general design relations for resonant frequency and bandwidth," *International Journal of Microwave and Millimeter-Wave Computer-Aided Engineering*, Vol. 4, 230–247, 1994.
13. Mongia, R. K., "Theoretical and experimental resonant frequencies of rectangular dielectric resonators," *IEE Proceedings H (Microwaves, Antennas and Propagation)*, Vol. 139, 98–104, IET Digital Library, 1992.
14. Mongia, R. K. and A. Ittipiboon, "Theoretical and experimental investigations on rectangular dielectric resonator antennas," *IEEE Transactions on Antennas and Propagation*, Vol. 45, No. 9, 1348–1355, Sep. 1997.
15. Kumar, J. and N. Gupta, "Investigation on microwave dielectric materials for dielectric resonator antennas," *International Journal of Applied Electromagnetics and Mechanics*, Vol. 47, No. 1, 263–272, 2015.

Two-sided Inverted F Antenna with LTE, GSM, WLAN, WiMax Frequency Bands for Mobile Phones

Chung-Jou Tsai and Bing-Yan Sie

Department of Computer and Communication

Kun Shan University, Tainan, Taiwan

Abstract— A small-size double-sided threelayers inverted-F antenna suitable to be printed on the system circuit board for LTE 700 MHz, GSM 900/1800 MHz, WLAN 2400/5200/5800 MHz and WiMax 3500/5500 MHz is presented. With meander microstrip line disperses on double-sided and coupled each other to produce enough bandwidth of low-band and multi-band of high-band, but also makes the size of the radiation side of the proposed antenna is $40 \times 13 \text{ mm}^2$. Including the ground plane, the total antenna size is $0.8 \text{ mm} \times 87 \text{ mm} \times 40 \text{ mm}$ of the FR4 substrate. This size and performance of this proposed antenna are suitable to the mobile phone.

1. INTRODUCTION

In recent years, with the rapid development of wireless communication industry, has also led to advances in mobile communications technology. The LTE (Long Term Evolution) 3GPP is the start of the latest technology in recent years, which improve and enhance the 3G air access technology, and by using OFDM and MIMO wireless network evolution as its core technology to provide fast-level bit rate of broadband up/down link of communication, which is operated in the low-frequency band 746–787 MHz. The communication system of mobile devices further comprises other necessary wireless systems, such as WLAN, Bluetooth, etc., so that the operation of multi-wireless communication systems has become a basic requirement, the antenna design must respond to such a request.

[1, 2] had proposed the antenna design using the meandering structure coupling method to make low-frequency operation in GSM, these two documents can only operate in GSM low frequency, however, no contains WiMAX 3500/5500 band and LTE700 bands. Other authors had proposed using the PIFA structure and including the radiation conductors structure [3], a coupling short circuit antenna structure [4], the ground plane extending parasitic capacitance technology [5], and fed into a compact coupling structure, such that the antenna can generate a multi-band and operating in GSM 850/900 WLAN 2400/5200/5800, WiMax 3500/5500 MHz. However, these paper [3–5] still cannot meet the application of LTE frequency bands and more bands, [6] proposed a coupling fed PIFA structure on the plate allowing this antenna operating in GSM 1800/1900, UMTS/LTE 2300/2500 MHz frequency bands, but it's size of $15 \times 48 \text{ mm}^2$ is larger.

[7, 8] proposed the loop antenna structure that can generate multi-band and operate in GSM/DCS/PCS/UMTS, but cannot meet the application LTE700 band. [9–11] using the coupled fed and distributed coupled antenna structure to achieve broadband operation, can produce LTE/WLAN bands, but was unable to provide GSM band applications. [12] proposed a slot antenna having two different lengths of a quarter wavelength and a half wavelength slot grooves, raising band covers 704–960, 1710–2690 MHz, but there is no WiMAX 3500/5500 frequency bands.

This paper presents an eight-band antenna covering LTE 700 (746–787 MHz), GSM 900/1800 (890–960/1710–1880 MHz), WLAN 2400/5200/5800 (2400–2483/5150–5350/5725–5875 MHz) and WiMax 3500/5500 (3500–3600/5250–5850 MHz), the size of the antenna radiation terminal $40 \times 13 \times 0.8 \text{ mm}^3$, comprising a ground plane of the overall size of $87 \times 40 \times 0.8 \text{ mm}^3$. This antenna is easy to manufacture and to fulfill the requirements of low cost and miniaturization, using a 50Ω coaxial cable as the fed line, to be suitable for embedded antenna of mobile phone application in size.

2. ANTENNA DESIGN

This paper presents an eight-band, double-side inverted-F antenna is suitable for LTE, GSM, WLAN, WiMax applications. The structure diagram and dimension of this proposed antenna are shown in Figure 1. This antenna is designed on FR4 substrate with total size of $0.8 \times 87 \times 40 \text{ mm}^3$, the dimension of radiating end part of antenna is $13 \times 40 \text{ mm}^2$. Figure 1(a) is a front of the antenna, the double-layer inverted F and microstrip meander line structure, main for generating

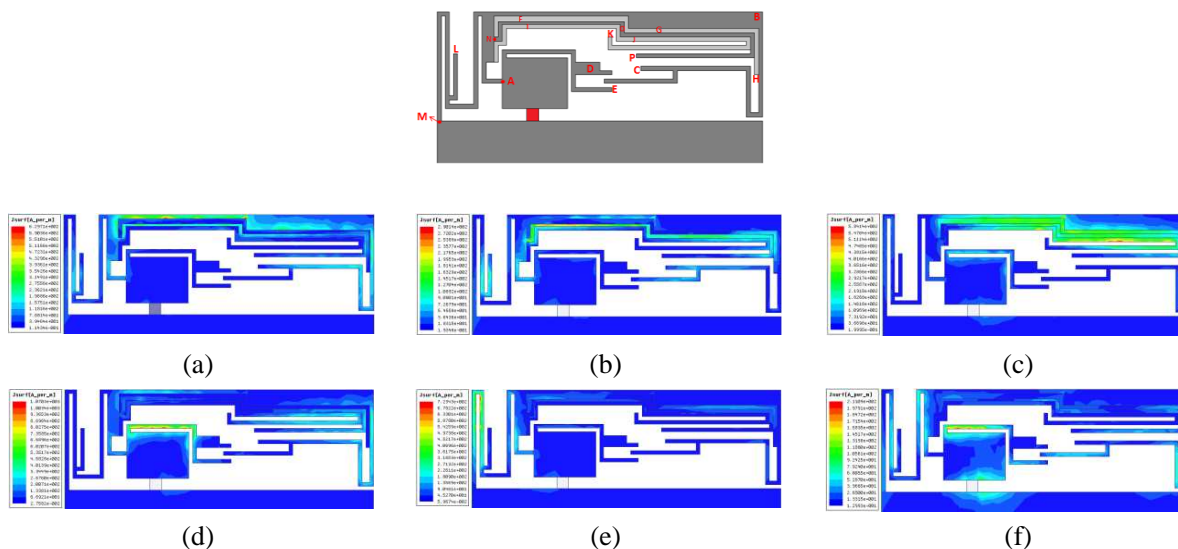


Figure 4: Current distributions at 5 oscillating frequencies of the proposed antenna, (a) 0.7 GHz, (b) 0.9 GHz, (c) 1.8 GHz, (d) 2.4 GHz, (e) 35 GHz, (f) 5.5 GHz.

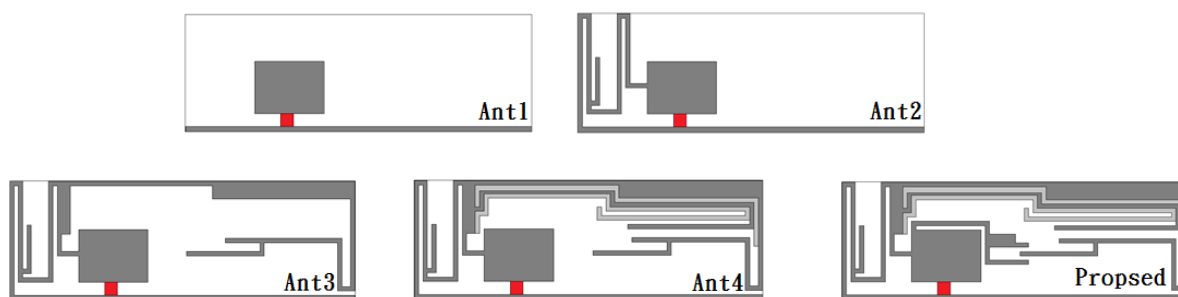


Figure 5: Design evolution of the proposed antenna.

paths at the back part, FH and IJK, were coupled from ANOP and oscillated at the relative wavelength $0.27\lambda_g$ (41 mm) GSM 1800. The current distribution path at DE corresponds to the wavelength of WLAN 2400 MHz. Finally, the current distribution path at AM corresponds to the wavelength of WiMax 3500 MHz.

Design revolution versions, Ant1~4 and the proposed, of the proposed antenna are shown in Figure 5. These corresponding return losses are shown in Figure 6. Ant1 shows the square monopole antenna structure. Ant2 add a grounding meander microstrip line. Ant3 increases meandering microstrip line structure at the top and right hand of Ant2 and makes this antenna becomes an inverted F, enhancing the LTE 700 frequency band. Ant4 adds the parasitic meander microstrip line at back part to increase the frequency band and bandwidth. The proposed antenna architecture increases the strip arm to generate 2400 MHz, making the whole antenna to become a double-sided three-layer inverted F antenna design. Ant1 operated from 3.8 to 6 GHz, Ant2 increased 3.5 GHz resonant modes, Ant3 added 0.7 GHz bandwidth and 5.8 GHz higher frequency resonant modes. Ant4 increased in 0.9 GHz and 1.8 GHz resonance frequency band through a microstrip line coupling, it also provides 5.2 GHz high resonant modes. The proposed antenna increased the 2.4 GHz by adding the inner arm of the Ant4. So, by the double-side three-layer inverted F antenna structure to generate eight bands frequencies includes LTE 700, GSM 900/1800, WLAN 2400/5150/5500, WiMax 3500 for four different communication systems.

Simulated 3D total power radiation patterns of each band are shown in Figure 7, four radiation patterns of each band from left to right are seen from different directions, the front, back, top and bottom. Observing graph types of radiation patterns, LTE 700 and WLAN 2400 are omnidirectional radiations, GSM 1800, WiMAX 3500 radiating in favor of the X-axis with the Y-axis. According to the radiating patterns directed to the back of PCB, it is a suitable antenna design mobile applications for meeting the requirement of SAR. Gain values of each band of the antenna presented

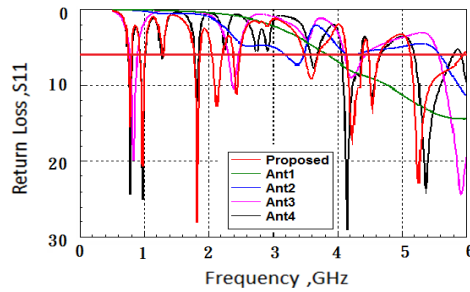


Figure 6: Return losses relative to architectures of Ant1~4 and the proposed antenna.

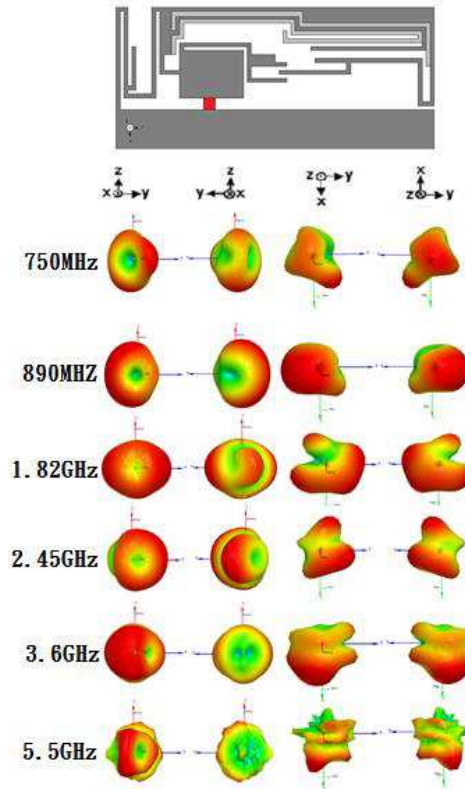


Figure 7: Radiation patterns at 6 oscillating frequencies of the proposed antenna.

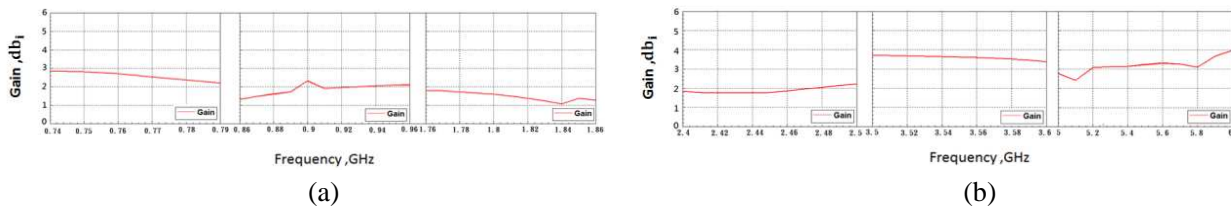


Figure 8: Antenna gain values at 6 oscillating frequencies, (a) 0.75, 0.89, and 1.82 GHz, (b) 2.45, 3.5, and 5.5 GHz of the proposed antenna.

in Figure 8, the low-frequency gain values stable at 1–2.8 dBi, the high frequency gain values is stabilized at 2.4–4 dBi.

4. CONCLUSIONS

This paper presents an eight bands antenna covering LTE 700, GSM 900/1800, WLAN 2400/5200/5800, WiMAX 3500/5500, with double-side three-layer inverted-F antenna which is transformed from the monopole antenna for minimizing the antenna size and generating eight bands. Besides,

this combined antenna structure can generate good radiation patterns and gain values, under the minimal size of the radiation area is $40 \times 13 \text{ mm}^2$. The ground plane of FR4 substrate size is $0.8 \text{ mm} \times 87 \text{ mm} \times 40 \text{ mm}$. The overall antenna size and features are consistent and meets the need of the mobile phone with limited space and good performance.

ACKNOWLEDGMENT

Thanks for the supporting of MOST 103-2632-E-168-001 and all teachers of the department of computer and communication.

REFERENCES

1. Chen, S. C. and K. L. Wong, "Small-size 11-band LTE/WWAN/WLAN internal mobile phone antenna," *Microwave Opt. Technol. Lett.*, Vol. 52, 2603–2608, Nov. 2010.
2. Chi, Y. W. and K. L. Wong, "Quarter-wavelength printed loop antenna with an internal printed matching circuit for GSM/DCS/PCS/UMTS operation in the mobile phone," *IEEE Trans. Antennas Propagat.*, Vol. 57, 2541–2547, Sep. 2009.
3. Tseng, Y.-S., Y.-H. Tseng, and W.-H. Tu, "Wideband internal antenna for tablet/laptop applications," *Proceedings of Asia-Pacific Microwave Conference (APMC)*, 310–312, 2012.
4. Lee, C. T. and K. L. Wong, "Uniplanar printed coupled-fed PIFA with a band-notching slit for WLAN/WiMAX operation in the laptop computer," *IEEE Trans. Antennas Propagat.*, Vol. 57, 1252–1258, Apr. 2009.
5. Lee, C. T. and K. L. Wong, "Uniplanar coupled-fed printed PIFA for WWAN/WLAN operation in the mobile phone," *Microwave Opt. Technol. Lett.*, Vol. 51, 1250–1257, May 2009.
6. Chen, S. C. and K. L. Wong, "Bandwidth enhancement of coupled-fed on-board printed PIFA using bypass radiating strip for eight-band LTE/GSM/UMTS slim mobile phone," *Microwave Opt. Technol. Lett.*, Vol. 52, 1059–1065, Sep. 2010.
7. Chi, Y. W. and K. L. Wong, "Quarter-wavelength printed loop antenna with an internal printed matching circuit for GSM/DCS/PCS/UMTS operation in the mobile phone," *IEEE Trans. Antennas Propagat.*, Vol. 57, 2541–2547, Sep. 2009.
8. Wong, K. L., W. Y. Chen, and T. W. Kang, "On-board printed coupled-fed loop antenna in close proximity to the surrounding ground plane for penta-band WWAN mobile phone," *IEEE Trans. Antennas Propagat.*, Vol. 59, 751–757, Mar. 2011.
9. Chen, S. C. and K. L. Wong, "Wideband monopole antenna coupled with a chip-inductor-loaded shorted strip for LTE/WWAN mobile handset," *Microwave Opt. Technol. Lett.*, Vol. 53, 1293–1298, Jun. 2011.
10. Wong, K. L., Y. C. Liu, and L. C. Chou, "Bandwidth enhancement of WWAN/LTE tablet computer antenna using embedded parallel resonant circuit," *Microwave Opt. Technol. Lett.*, Vol. 54, 426–431, Feb. 2012.
11. Wong, K. L., C. A. Lyu, and L. C. Chou, "Small-size multiband planar antenna for LTE700/2300/2500 operation in the tablet computer," *Microwave Opt. Technol. Lett.*, Vol. 54, 81–86, Jan. 2012.
12. Wong, K. L. and W. J. Lin, "WWAN/LTE printed slot antenna for tablet computer application," *Microwave Opt. Technol. Lett.*, Vol. 54, 44–49, Jan. 2012.

Analysis of the Imaging Realization of Frequency Modulated Continuous Wave Circular SAR

Gaowei Jia, Wenge Chang, and Ruibin Tu

College of Electronic Science and Engineering

National University of Defense Technology, Changsha, Hunan 410073, China

Abstract— Regarding the signal processing of frequency modulated continuous wave (FMCW) circular synthetic aperture radar (CSAR), the movement during the transmission of a pulse is considered to be one of the major problems. According to the Fourier-based imaging procedures of CSAR, the influence of intra-pulse movement is investigated and the corresponding correction method is presented. Numerical simulation tests verified the proposed correction method is feasible to remove the influence of the intra-pulse movement exactly.

1. INTRODUCTION

There has been increasing interest in frequency modulated continuous wave (FMCW) synthetic aperture radar (SAR) in the last years [1–3], which has led to the construction of several experimental systems. On the other hand, circular SAR (CSAR) has lately become of the hotspot in the field of SAR due to its characteristics like super-high resolution, three-dimensional imaging possibility, and all-aspect observation. Changing the acquisition geometry of FMCW SAR from a straight line to a circular trajectory may combine the advantages of both FMCW radar and CSAR.

As for the imaging processing of FMCW SAR, it is well known that the intra-pulse movement would introduce new range migration and affect the range cell migration correction (RCMC). Similarly, and it is found that the intra-pulse movement also leads to new range migration in the case of FMCW CSAR and further distorts the imaging results. [2] has verified that the modified BPA is feasible to focus the FMCW CSAR data very well. However, the modified BPA and its potential improvements encounter huge computation. To improve the imaging efficiency, the modified Fourier-based imaging procedures of FMCW CSAR is expected to be investigated.

2. THE SIGNAL MODEL OF CIRCULAR FMCW SAR

Let us refer to the imaging geometry of FMCW CSAR in Fig. 1.

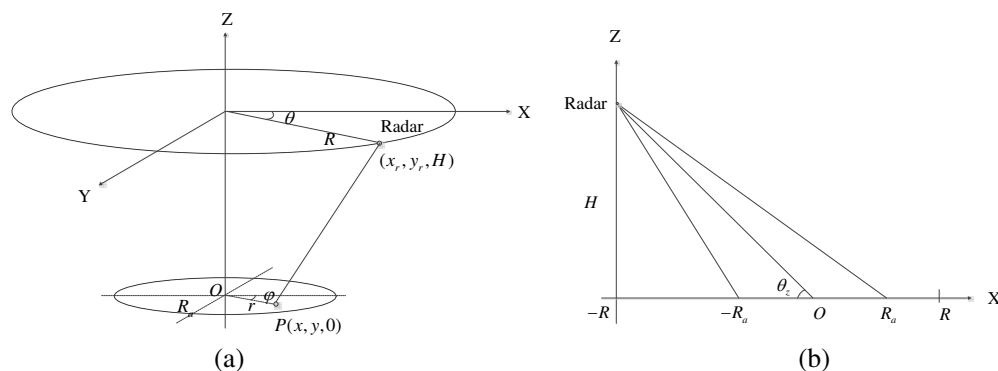


Figure 1: The imaging geometry of FMCW CSAR (a) 3-D view, (b) the side view.

Figure 1(a) stands for the imaging geometry of FMCW CSAR and Fig. 1(b) denote its side view. In Fig. 1(a), the SAR sensor moves along a circle with the radius of R , the velocity is v . $\theta \in [0, 2\pi]$ represents the aspect angle, 0 degree of θ stands for the positive x axis. O is the origin. The three dimensional (3-D) positions of the array phase center (APC) are (x_r, y_r, H) , i.e., (R, θ, H) in the polar coordinates. During the movement of SAR sensor, the beam is always spotlighted on the flat observed scene (with a radius of R_a). P is an arbitrary off-centered target located in the observed area with the 3-D positions of $(x, y, 0)$, i.e., $(r, \phi, 0)$ in the polar coordinates. In Fig. 1(b), θ_z stands for the incident angle according to the origin. With $x_r = R \cos \theta$, $y_r = R \sin \theta$ and

$x = r \cos \varphi$, $y = r \sin \varphi$, the instantaneous range from the APC to P is

$$R_r(\theta) = \sqrt{R^2 + r^2 + H^2 - 2Rr \cos(\theta - \varphi)} \quad (1)$$

It is assumed that the angular velocity of radar is w , t denotes the time axis, t_m and \hat{t} are the slow time and fast time, respectively. Based on the results in [2], we have:

$$R_r(\theta) \approx R_r(\theta_m) + \chi(\theta_m)\hat{t} \quad (2)$$

in which $\theta_m = wt_m$, $R_r(\theta_m) = \sqrt{R^2 + r^2 + H^2 - 2Rr \cos(\theta_m - \varphi)}$, and $\chi(\theta_m) = r \sin(\theta_m - \varphi)v/R_r(\theta_m)$. In (2), the term $\chi(\theta_m)\hat{t}$ denotes the new displacement introduced from the intra-pulse movement.

It is assumed that the transmitted linear modulated frequency (LFM) pulse. The intermediate frequency signal after residual video phase (RVP) filtering [4] is

$$S(\hat{t}, \theta_m) = \exp\left(-j\left(\frac{4\pi}{\lambda} + \frac{4\pi\gamma\hat{t}}{c}\right)R_r(\theta_m)\right) \exp\left(-j\frac{4\pi}{\lambda}\chi(\theta_m)\hat{t}\right) \quad (3)$$

Denoting $k = \frac{2\pi}{\lambda} + \frac{2\pi\gamma\hat{t}}{c}$, k represents the wavenumber in range. Then (3) could be rewritten as

$$S(k, \theta_m) = \exp(-j2kR_r(\theta_m)) \exp\left(-j\frac{4\pi}{\lambda}\chi(\theta_m)\hat{t}\right) \quad (4)$$

Equation (4) is the expression of the received signal of FMCW CSAR in angle time domain. To obtain the 2-D spectrum of FMCW CSAR, the Fourier transform with respect to θ_m yields

$$S(k, \xi) = \int \exp(-j2kR_r(\theta_m)) \exp\left(-j\frac{4\pi}{\lambda}\chi(\theta_m)\hat{t}\right) \exp(-j\xi\theta_m) d\theta_m \quad (5)$$

in which ξ stands for the wavenumber in the angular domain. In order to determine a closed form expression of $S(k, \xi)$, the principle of stationary phase (POSP) is used [5, 6]. The stationary point is achieved by solving the equation shown in (11).

$$\xi = -2kRr \frac{\sin(\theta_m - \varphi)}{\sqrt{\alpha^2 - 2\beta \cos(\theta_m - \varphi)}} \quad (6)$$

in which $\alpha^2 = R^2 + r^2 + H^2$, $\beta = Rr$. During the calculation of stationary points, the exponential term $\exp(j4\pi\chi(\theta_m)\hat{t}/\lambda)$ is ignored since the phase of which is much smaller than that of $\exp(-j2kR_r(\theta_m))$. Solving the Equation (11) yields two stationary points θ_1^* and θ_2^* , which follow the relationship shown in (12) and (13), respectively.

$$\cos(\theta_1^* - \varphi) = \frac{\xi^2 + \sqrt{\xi^4 - 4k^2\xi^2\alpha^2 + 16k^4\beta^2}}{4k^2\beta} \quad (7)$$

$$\cos(\theta_2^* - \varphi) = \frac{\xi^2 - \sqrt{\xi^4 - 4k^2\xi^2\alpha^2 + 16k^4\beta^2}}{4k^2\beta} \quad (8)$$

With the solutions from (7) and (8) we could obtain the 2-D spectrum of FMCW CSAR in the domain of (k, ξ) , i.e.,

$$\begin{aligned} S(k, \xi) = & \exp\left\{-j\sqrt{4k^2\alpha^2 - 2\xi^2 - 2\sqrt{\xi^4 - 4k^2\xi^2\alpha^2 + 16k^4\beta^2}}\right. \\ & \left.+ j|\xi| \cos^{-1}\left(\frac{\xi^2 + \sqrt{\xi^4 - 4k^2\xi^2\alpha^2 + 16k^4\beta^2}}{4k^2\beta}\right) - j\xi\varphi + j\frac{4\pi}{\lambda}\frac{\xi}{2kR}v\hat{t}\right\} \\ & + \exp\left\{-j\sqrt{4k^2\alpha^2 - 2\xi^2 + 2\sqrt{\xi^4 - 4k^2\xi^2\alpha^2 + 16k^4\beta^2}}\right. \\ & \left.+ j|\xi| \cos^{-1}\left(\frac{\xi^2 - \sqrt{\xi^4 - 4k^2\xi^2\alpha^2 + 16k^4\beta^2}}{4k^2\beta}\right) - j\xi\varphi + j\frac{4\pi}{\lambda}\frac{\xi}{2kR}v\hat{t}\right\} \quad (9) \end{aligned}$$

The expression shown in (9) represent the spectrum of FMCW CSAR in the slant plane, it is the basis for further imaging processing. In (9), the exponential term $\exp(j4\pi\xi v\hat{t}/2kR\lambda)$ is introduced from $\exp(-j4\pi\chi(\theta_m)\hat{t}/\lambda)$, i.e., from the intra-pulse continuous movement.

The main contributions of this section are the proposals of the signal model and the spectrum expression of FMCW CSAR. Equation (9) is the basis of the imaging processing of FMCW CSAR.

3. THE INFLUENCE AND REMOVAL OF THE INTRA-PULSE MOVEMENT

According to the spectrum of FMCW CSAR shown in (9), the phase term derived from the movement during the pulse is rewritten as

$$P(\hat{t}, \xi) = \frac{4\pi}{\lambda} \frac{\xi}{2kR} v\hat{t} \quad (10)$$

$P(\hat{t}, \xi)$ is considered as phase errors and may distort the final CSAR images. Firstly it is necessary to measure the relative variation of the phase error. Based on Equation (6), it is learnt that the absolute value of ξ has its maximum, i.e.,

$$|\xi| \leq 2kRr \frac{\sqrt{2\alpha^2 - 2\sqrt{\alpha^4 - 4\beta^2}}}{2\beta} \approx 2kr \cos \theta_z \quad (11)$$

where $|\cdot|$ denotes the absolute value. In addition, it is known $k = 2\pi/\lambda + 2\pi\gamma\hat{t}/c$ and $\hat{t} \in [0, T_p]$, T_p is the time duration of LFM. Thus the relative maximum phase variation within the whole spectrum support domain is

$$P_{\max} = 2 \frac{4\pi}{\lambda} \frac{r \cos \theta_z}{R} vT_p \quad (12)$$

It is learnt that the value of P_{\max} increases against with r , denoting the target with larger radius would suffer higher phase errors. When P_{\max} is larger than $\pi/4$, distortion of CSAR image may appear thus proper operation is expected to remove $P(\hat{t}, \xi)$ exactly. To have a better insight of the phase error, quantitative calculation is carried out. The parameters according to an X-band FMCW CSAR are adopted and listed in Table 1.

Table 1: parameters.

Carrier frequency	10 GHz	Radius of the circular track	1000 m
Bandwidth	600 MHz	Height of track	500 m
Pulse duration	4 ms	Velocity of carrier	40 m/s

During the simulation test, several target points is used. Taking one target (40 m, 0 m) for example, the corresponding phase history and the variation of $P(\hat{t}, \xi)$ are figured out and shown in Fig. 2.

Figure 2(a) stands for the phase history according to target (40 m, 0 m), in which assumes that the radar is stationary during the transmission of a sweep. Correspondingly, Fig. 2(b) stands for the phase history which has taken the intra-pulse movement into accounted. The mixing between the phase history shown in Figs. 2(a) and (b) yields the phase errors derived from the intra-pulse movement, as shown in Fig. 2(c). Fig. 2(d) represents the phase errors calculated with Equation (12). Compared Fig. 2(c) with Fig. 2(d), it is found that they matched each other well, denoting the signal model analysis in Section 2 is correct. In addition, it is seen that the relative maximum phase error at $r = 40$ m is 4.79 rad, which is larger than $\pi/4$ and will degrade the final FMCW CSAR images.

Fortunately, it is learnt that $\exp(j4\pi\xi v\hat{t}/2kR\lambda)$ has no dependence on the position of target, thus it is space-invariant and easy to be removed by matched filtering. Specifically, the matched filter is defined as

$$H_r(k, \xi) = \exp\left(-j \frac{4\pi}{\lambda} \frac{\xi}{2kR} v\hat{t}\right) \quad (13)$$

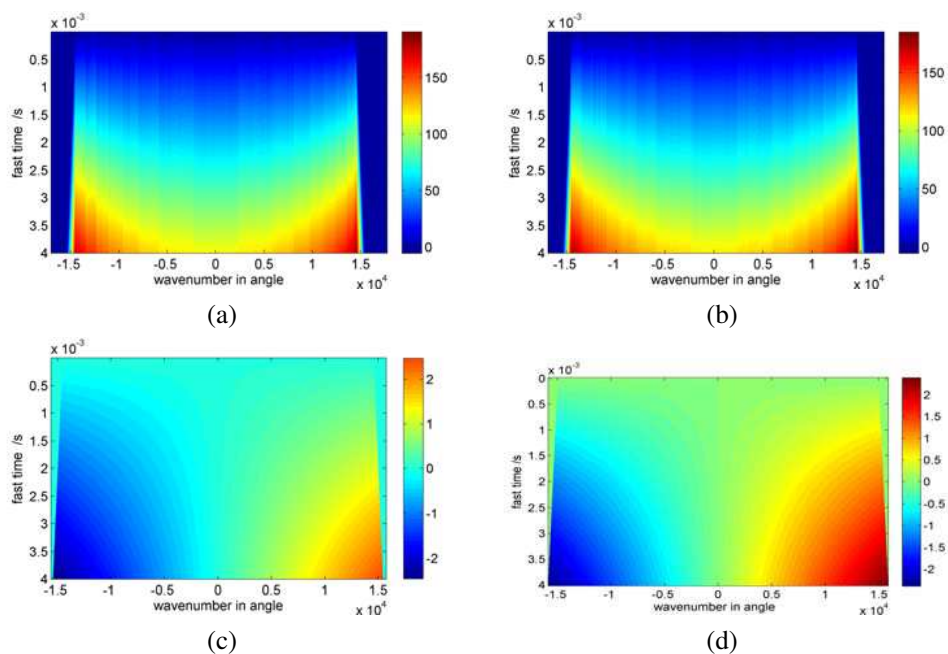


Figure 2: The phase error analysis, (a) phase history without intra-pulse movement, (b) phase history with intra-pulse movement, (c) the extracted phase error, (d) the phase error calculated by (12).

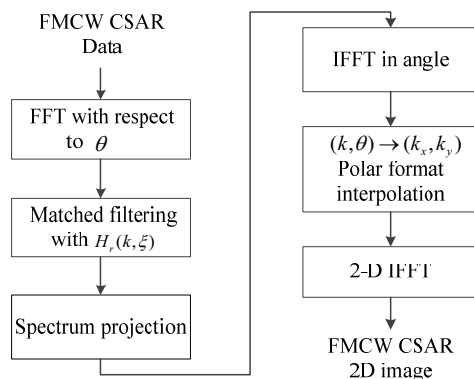


Figure 3: The modified Fourier-based imaging flow of FMCW CSAR.

After the matched filtering, the spectrum of FMCW CSAR is same with that of pulsed CSAR. Based on the former analysis about CSAR in [5], the Fourier-based imaging flow of FMCW CSAR is given in Fig. 3.

In Fig. 3, the correction procedure is performed by phase multiplication, to the benefit of high efficiency. As for the spectrum projection operation, it is independent on the removal of intra-pulse movement, although it is another important procedure within the imaging flow of FMCW CSAR. The main contributions of this section contain: On one hand, it is learnt that the intra-pulse movement would introduce phase errors, and it is necessary to remove the phase error properly once the relative variation of which is larger than $\pi/4$. On the other hand, the corresponding correction method is proposed to remove the influence of intra-pulse movement.

4. SIMULATION TESTS

Simulation test is carried out in this section and the parameters are same with that listed in Table 1. During the imaging processing, the modified BPA [2] is used to produce ideal imaging results. Figs. 4(a) and (d) stand for the imaging result of FMCW CSAR data processed by Fourier-based imaging methods without and with the correction operation, respectively. Fig. 4(b) denotes the imaging results processed with the modified BPA. Fig. 4(c) denotes the CSAR spectrum in ground plane.

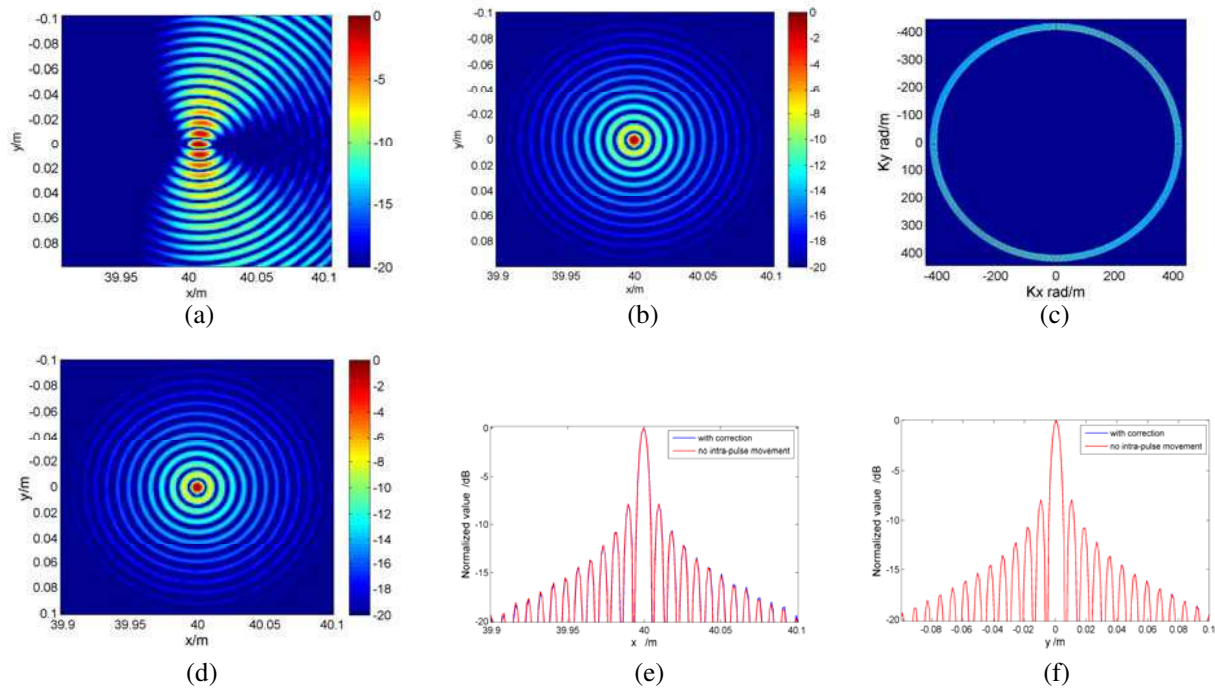


Figure 4: The imaging result with simulated CSAR data, (a) processed without the correction of intra-pulse movement, (b) processed with modified BPA, (c) the spectrum after polar formatting resampling, (d) processed with the proposed method, (e) and (f) denote the profiles.

According to the PSFs shown in Figs. 4(b) and (d), the corresponding profiles in x and y are shown in Figs. 4(e) and (f), respectively. Specifically, the blue and red curves stand for the profiles processed with the proposed improvement and the modified BPA, respectively. It is seen that the results processed with the proposed method coincides the ideal results very well, denoting again that the first proposed improvement is valid and is helpful to figure out the well-focused FMCW CSAR image.

5. CONCLUSION

Removing the influence of intra-pulse movement is proposed in this paper. During the Fourier-based imaging processing of FMCW CSAR, the movement within the pulse leads to the emergence of phase errors and eventually distorts the final image. Correspondingly, a modified Fourier-based imaging method is proposed for FMCW CSAR.

REFERENCES

1. Jia, G. W. and W. G. Chang, "Study on the improvements for the high-resolution frequency modulated continuous wave synthetic aperture radar imaging," *IET Radar, Sonar and Nav.*, 2014.
2. Jia, G. W. and W. G. Chang, "Modified back projection reconstruction for circular FMCW SAR," *International Radar Conference 2014*, Oct. 13–17, 2014.
3. Palm, S., A. Maresch, and U. Stilla, "Investigation on circular mapping by fmcw-sar on small airplanes," *Int. Arch. Photogramm. Remote Sens. Spatial Inf. Sci.*, XL-1/W1, 281–286, May 21–24, 2013.
4. Meta, A., P. Hoogeboom, and L. P. Ligthart, "Signal processing for FMCW SAR," *IEEE Trans. Geosci. Remote Sens.*, Vol. 45, No. 11, 3519–3532, 2007.
5. Soumekh, M., *Synthetic Aperture Radar Signal Processing with Matlab Algorithms*, John Wiley & Sons, Inc., New York, NY, 1999.
6. Carrara, W. G., R. S. Goodman, and R. M. Majewski, *Spotlight Synthetic Aperture Radar Signal Processing Algorithms*, Artch House, Boston, London, 1995.